STATE OF THE CLIMATE IN 2025

Special Supplement to the
Bulletin of the American Meteorological Society
Vol. 107, No. 8, August 2026

Cover Credit:
An artist's rendering of NOAA's GOES-19 satellite (formerly known as GOES-U), operating in orbit above Earth as GOES East. (Credit: NOAA/NASA.)

Background image: Portion of the first full disk image from GOES-19. (Credit: NOAA/NASA.)

How to cite this document:
Special Supplement to the Bulletin of the American Meteorological Society, Vol. 107, No. 8, August 2026 https://doi.org/10.1175/2026BAMSStateoftheClimate.1. Compiled by NOAA's National Centers for Environmental Information, *State of the Climate in 2025* is based on contributions from scientists from around the world. It provides a detailed update on global climate indicators, notable weather events, and other data collected by environmental monitoring stations and instruments located on land, water, ice, and in space.

Citing the complete report:
Blunden, J. and J. Reagan, Eds., 2026: State of the Climate in 2025 . Bull. Amer. Meteor. Soc., 107 (8), Si–S512, https://doi.org/10.1175/2026BAMSStateoftheClimate.1.

Corresponding author: Full Report: Jessica Blunden / jessica.blunden@noaa.gov

2026 American Meteorological Society
For information regarding reuse of this content and general copyright information, consult the AMS Copyright Policy.

STATE OF THE CLIMATE IN 2025

Table of Contents

Abstract ..... Siii

1. Introduction S1

Essential Climate Variables S7

2. Global Climate S12

3. Global Oceans S168

4. The Tropics S235

5. The Arctic S296

6. Antarctica and the Southern Ocean S352

7. Regional Climates S401

Abstract

—J. BLUNDEN, J. REAGAN, AND R. J. H. DUNN

In 2025, weak La Niña-like conditions were present at both the beginning and end of the year with neutral, albeit still cool, conditions present from boreal spring to autumn. Atmospheric concentrations of Earth's major greenhouse gases—carbon dioxide, methane, and nitrous oxide—continued to climb to record-high levels, with fossil fuel emissions also setting a new record. The annual global average carbon dioxide concentration in the atmosphere rose to 425.6±0.1 ppm, an increase of 2.9 ppm from 2024, which contributed to a cumulative 53% increase overall from the pre-industrial level of ~278 ppm. The ocean plays a major role in removing carbon dioxide from the atmosphere by absorbing close to 30% of anthropogenic carbon dioxide emissions. The oceanic absorption of carbon dioxide in 2025 increased compared to the prior decade.

The global surface temperature in 2025 was the third highest in the record dating to 1850, according to most of the datasets used in the analysis, only lower than 2023 and 2024, both of which experienced strong El Niño conditions. Europe reported its warmest year on record, and Russia, China, the Republic of Korea, and Argentina each reported their second warmest. Monthly and seasonal records were set in numerous countries, and some new national daily maximum temperature records were broken: 46.6°C on 29 June in Mora, Portugal; 50.5°C on 25 July in Silopi, Türkiye; and 41.8°C on 8 August in Isesaki in Gunma Prefecture, Japan.

The oceans absorb almost 90% of the excess heat in Earth's climate system. In 2025, the globally averaged ocean heat content from the surface to 2000 meters depth—the amount of heat stored in this portion of the oceans—reached a record high, surpassing the previous record set in 2024. In tandem, global sea surface temperatures marked the third consecutive year of extreme warmth. Marine heatwaves were observed over 87% of the global ocean during 2025, while marine cold spells became even less frequent, reaching their lowest occurrence in the observational record. Increasing ocean temperatures and melting glaciers and ice caps contribute to sea level rise. The average global mean sea level for 2025 also set a new record, for the 14th year in a row, rising to 111.2 millimeters above the average for 1993, the year when satellite altimetry measurements began.

Among other factors, warm sea surface temperatures contribute to tropical cyclone formation. There were 97 named tropical cyclones during the 2025 Northern Hemisphere season (January–December 2025) and the 2024/25 Southern Hemisphere season (July 2024–June 2025), which is 10 more than the 1991–2020 global average of 87. Five storms reached Category 5 intensity; three of these storms occurred in the North Atlantic, tying for the second most on record for that basin. Hurricane Melissa was the strongest tropical cyclone globally in 2025 and set several historical records over the course of its lifetime. The storm became one of the strongest Atlantic hurricanes on record, with a maximum intensity of 165 kt and a minimum central pressure of 892 hPa on 28 October, also making Melissa the latest calendar year Category 5 hurricane since Hattie on 31 October in 1961. Melissa made landfall in Jamaica with 160 kt maximum sustained winds, shattering the record for the strongest hurricane landfall over Jamaica and causing massive destruction on the western part of the island with its intense rains, strong winds, and powerful storm surge. Melissa also made landfall in Cuba (Category 3) and two landfalls in the Bahamas (Category 1). In total, the storm caused 95 fatalities and resulted in at least $12.2 billion (U.S. dollars) in damage. Twelve named storms were in the Australian basin during the 2024/25 season, which was the most in a season since 2005/06. In February, Tropical Cyclone Zelia reached Category 5 intensity at sea and made landfall as a Category 4 storm in Western Australia. Flood heights at the town of Marble Bar due to heavy rainbands were nearly two meters above previous records.

In frozen areas around the world, land-based glaciers continued to lose ice for the 38th consecutive year, losing more than one-meter water equivalent on average for the fourth straight year. About 41% of the loss experienced by glaciers since 1976 has occurred in the last decade. Permafrost temperatures and active layer thickness—the portion of ground that thaws and refreezes each year—continued to increase in most locations, and many new records were set. During the winter of 2024/25, lakes in the Northern Hemisphere continued to exhibit later ice formation and earlier ice breakup, with ice durations 15.0 days shorter on average compared to the 1991–2020 mean.

In Antarctica, the polar ice cap observed its warmest year since the start of the record in 1979. Surface melt on the continent was above average on most ice shelves, and melt on the Antarctic Peninsula approached record levels in early January. Accompanying the melt was record-high supraglacial meltwater. Surrounding the continent, sea ice remained below average in 2025, following a nearly decade-long trend. Annual daily maxima and minima of sea ice extent were the third and fourth lowest on record, respectively. In the stratosphere above Earth's surface, the 2025 Antarctic ozone hole was smaller than average and was among the weakest ozone holes observed since 1992.

On the other side of the world, the Arctic observed its second warmest year, with records dating to 1900. Arctic surface air temperatures are increasing about three times faster compared to the entire planet. Precipitation is also increasing across the region. In response to the precipitation and temperature

increases, tundra plants have been increasing; 2025 marked the third highest value in the record with respect to greenness, a measure of the increase in plants and productivity. The Greenland Ice Sheet—the second largest reservoir of frozen fresh water on the planet—lost an estimated 129±50 Gigatons of ice overall for the year. In the Arctic waters, maximum sea ice extent in 2025 was the lowest in the 47-year record, while the minimum extent was the 11th lowest. The thickness of the sea ice, which is related to its age, has also been decreasing over time. Ice older than four years old is nearly absent, with only 95,000 km^2 of older ice in September 2025 as compared to 1.5 million km^2 in the 1980s.

The global mean cloud coverage was the second lowest since records began in 1980 at 68.5%. On average, precipitation was below normal over the oceans but above normal over land, which is typical during La Niña conditions. Intense precipitation occurred in many locations and over varying time periods. In Colombia, extreme rainfall in Istmina (Chocó) in July broke the national record for maximum 24-hour precipitation with 274 mm. During 10–11 August, Tropical Storm Erin brought heavy rains to Cabo Verde off the coast of West Africa. Rainfall recorded in just a few hours exceeded the annual average. During a catastrophic rainfall event in Central Texas during 3–6 July, 180 mm–300 mm of rain fell in a three-hour period near Hunt and San Angelo, exceeding the 1-in-1000-year event probability. In September and October, central North China received three times its normal total, resulting in severe flooding that affected over seven million people and led to $25 billion (U.S. dollars) in direct economic losses.

Intense dryness, drought, and wildfires also occurred. In eastern Africa, severe drought resulting from the failure of both the Short and the Deyr/Hageya rain seasons led to more than 10 million people across Somalia, Ethiopia, and Kenya needing humanitarian food assistance in December 2025. In the Middle East, Türkiye reported its driest year on record, and Syria, Lebanon, and Cyprus each reported their second driest. Syria experienced its worst fire season in over 10 years, with about 3.7% of the total forest area burnt. From May through September, record-breaking heatwaves and nationwide drought conditions contributed to Canada's second-worst wildfire season on record, burning about 8.9 million hectares. Smoke plumes spread across thousands of kilometers caused prolonged poor air quality for millions of people. In Southern Europe, the Iberian Peninsula had unprecedented fire activity, which contributed to a record for fire emissions in Europe. Overall, however, 2025 had the lowest fire activity in the 23-year record at the global scale, driven by low activity in South America and Africa.

Editor and Author Affiliations (alphabetical by name)

Ades, Melanie, European Centre for Medium-Range Weather Forecasts, Reading, United Kingdom

Adjou, Mohamed, ISEN Engineering School, LaBISEN, Knowledge Learning and Information Modeling (KLaIM), Brest, France; University of Brest, Institut Universitaire Européen de la Mer (IUEM) UAR3113, Plouzané, France

Adler, Robert, Earth System Science Interdisciplinary Center, University of Maryland, College Park, Maryland

Adusumilli, Susheel, Department of Earth Sciences, University of Oregon, Eugene, Oregon

Agyakwah, W., ERT, Inc., College Park, Maryland; NOAA/NWS National Centers for Environmental Prediction Climate Prediction Center, College Park, Maryland

Aldeco, Laura S., Servicio Meteorológico Nacional, Buenos Aires, Argentina

Alemanno, Marco, Italian Air Force Meteorological Service, Pratica di Mare (Rome), Italy

Alfaro, Eric J., Center for Geophysical Research, University of Costa Rica, San José, Costa Rica; Center for Research in Marine Sciences and Limnology, University of Costa Rica, San José, Costa Rica

Allan, Richard P., National Centre for Earth Observation (NCEO), University of Leicester, Leicester, United Kingdom; University of Reading, Reading, United Kingdom

Allen, Teddy, Caribbean Institute for Meteorology and Hydrology, Bridgetown, Barbados

Allgood, Adam, NOAA/NWS National Centers for Environmental Prediction Climate Prediction Center, College Park, Maryland

Alves, Lincoln. M., National Institute for Space Research (INPE), São José dos Campos, São Paulo, Brazil

Amador, Jorge A., Center for Geophysical Research, University of Costa Rica, San José, Costa Rica; School of Physics, University of Costa Rica, San José, Costa Rica

Amory, Charles, Université Grenoble Alpes, Institut des Géosciences de l'Environnement, IRD, CNRS, Grenoble INP, Grenoble, France

Andreassen, Liss Marie, Section for Glaciers, Ice and Snow, Norwegian Water Resources and Energy Directorate, Oslo, Norway

Anneville, Orlane, Université Savoie Mont Blanc, INRAE, CARRTEL, Thonon-les-Bains, France

Aono, Yasuyuki, Graduate School of Agriculture, Osaka Metropolitan University, Sakai, Japan

Arguez, Anthony, NOAA/NESDIS National Centers for Environmental Information, Asheville, North Carolina

Armenteras, Dolors, Instituto de Ciencias Forestales (ICIFOR-INIA), Consejo Superior De Investigaciones Científicas (CSIC), Madrid, Spain; Science Faculty, Universidad Nacional de Colombia, Bogotá, Colombia

Arosio, Carlo, University of Bremen, Bremen, Germany

Asher, Elizabeth, Cooperative Institute for Research in Environmental Sciences, University of Colorado Boulder, Boulder, Colorado; NOAA Global Monitoring Laboratory, Boulder, Colorado

Askjaer, Thomas G., Danish Meteorological Institute, Copenhagen, Denmark

Atkinson, Christopher P., Met Office Hadley Centre, Exeter, United Kingdom

Augustine, John A., NOAA Global Monitoring Laboratory, Retired, Boulder, Colorado

Avalos, Grinia, Servicio Nacional de Meteorología e Hidrología del Perú, Lima, Peru

Azorin-Molina, Cesar, Centro de Investigaciones sobre Desertificación – Spanish National Research Council (CSIC-UV-GVA), Valencia, Spain

Baez-Villanueva, Oscar M., Hydro-Climate Extremes Lab (H-CEL), Ghent University, Ghent, Belgium

Bahrami, Mahsa, Department of Geography, Pennsylvania State University, State College, Pennsylvania

Baiman, Rebecca, Department of Atmospheric Science, Colorado State University, Fort Collins, Colorado

Ballinger, Andrew, NOAA/NESDIS National Centers for Environmental Information, Asheville, North Carolina

Ballinger, Thomas J., International Arctic Research Center, University of Alaska Fairbanks, Fairbanks, Alaska

Bandgar, Arti, India Meteorological Department, Pune, India

Banwell, Alison F., Centre for Polar Observation and Modelling, School of Geography and Natural Sciences, Northumbria University, Newcastle upon Tyne, United Kingdom; Cooperative Institute for Research in Environmental Sciences, University of Colorado Boulder, Boulder, Colorado

Barichivich, Jonathan, Laboratoire des Sciences du Climat et de l'Environnement (LSCE), LSCE/IPSL, CEA-CNRS-UVSQ, Gif-sur-Yvette, France

Barreira, Sandra, Argentine Naval Hydrographic Service, Buenos Aires, Argentina

Basckenstrass, Claire, Météo-France, Direction Interregionale Pour L'Ocean Indien, Réunion, France

Beadling, Rebecca L., Department of Earth and Environmental Science, Temple University, Philadelphia, Pennsylvania

Beauchemin, Marc, Environment and Climate Change Canada, Montreal, Canada

Beck, Hylke E., Physical Science and Engineering Division, King Abdullah University of Science and Technology, Thuwal, Saudi Arabia

Becker, Emily J., Rosenstiel School of Marine, Atmospheric, and Earth Science, University of Miami, Miami, Florida

Beckley, Brian, Earth Resources Technology, Inc., Greenbelt, Maryland

Bekele, E., NOAA/NWS National Centers for Environmental Prediction Climate Prediction Center, College Park, Maryland

Bellouin, Nicolas, University of Reading, Reading, United Kingdom; Institute Pierre Simon Laplace (IPSL), Guyancourt, France

Berne, Christine, Météo-France, Toulouse, France

Berner, Logan T., School of Informatics, Computing, and Cyber Systems, Northern Arizona University, Flagstaff, Arizona

Bernhard, Germar H., Biospherical Instruments Inc., San Diego, California

Bezanilla-Morlot, Arnoldo, Institute of Meteorology, La Habana, Cuba

Bhatt, Uma S., Geophysical Institute, University of Alaska Fairbanks, Fairbanks, Alaska

Bhuiyan, Md. E., Entarian, Greenbelt, Maryland; NOAA/NWS National Centers for Environmental Prediction, Climate Prediction Center, College Park, Maryland

Biernacik, Dawid, Institute of Meteorology and Water Management, National Research Institute, Warsaw, Poland

Bigalke, Siiri, Department of Geography, Portland State University, Portland, Oregon

Bilotta, Rocky, NOAA/NESDIS National Centers for Environmental Information, Asheville, North Carolina

Bissolli, Peter, Deutscher Wetterdienst, WMO RA VI Regional Climate Centre Network, Offenbach, Germany

Bjerke, Jarle W., FRAM – High North Research Centre for Climate and the Environment, Tromsø, Norway; Norwegian Institute for Nature Research, Trondheim, Norway

Black, T., NASA Goddard Space Flight Center, Greenbelt, Maryland

Blake, Eric S., NOAA/NWS National Hurricane Center, Miami, Florida

Blannin, Josh, Met Office Hadley Centre, Exeter, United Kingdom

Bliss, Angela, NASA Goddard Space Flight Center, Greenbelt, Maryland

Bock, Olivier, Univ Gustave Eiffel, Géodata Paris, IGN, Paris, France; Université Paris Cité, Institut de physique du globe de Paris, CNRS, IGN, Paris, France

Bonte, Olivier, Hydro-Climate Extremes Lab (H-CEL), Ghent University, Ghent, Belgium

Bosilovich, Michael G., Global Modeling and Assimilation Office, NASA Goddard Space Flight Center, Greenbelt, Maryland

Bowman, Kevin, Jet Propulsion Laboratory, California Institute of Technology, Pasadena, California

Box, Jason E., Geological Survey of Denmark and Greenland (GEUS), Copenhagen, Denmark

Brettschneider, Brian, NOAA/NWS Alaska Region, Anchorage, Alaska

Brown, Meghan, Department of Earth Sciences, University of Oregon, Eugene, Oregon
Buehler, Stefan, Universität Hamburg, Hamburg, Germany
Bukunt, Brandon, NOAA/NWS Pacific Region Headquarters, Honolulu, Hawaii
Bunno, Ayaka, Japan Meteorological Agency, Tokyo, Japan
Burgess, D., Geological Survey of Canada, Ottawa, Ontario, Canada
Butler, Amy H., NOAA Chemical Sciences Laboratory, Boulder, Colorado
Byrne, Michael P., University of St Andrews, St Andrews, Fife, United Kingdom
Calderón, Blanca, Center for Geophysical Research, University of Costa Rica, San José, Costa Rica
Camargo, Suzana J., Columbia Climate School, Columbia University, New York, New York
Campbell, Jayaka, Department of Physics, The University of the West Indies, Kingston, Jamaica
Campos, Diego, Barcelona Supercomputing Centre, Barcelona, Spain
Cappucci, Fabrizio, European Commission Joint Research Centre, Ispra, Italy
Carere, Francesco, Hydro-Climate Extremes Lab (H-CEL), Ghent University, Ghent, Belgium
Carrea, Laura, University of Reading, Reading, United Kingdom
Carter, Brendan R., NOAA/OAR Pacific Marine Environmental Laboratory, Seattle, Washington
Casado-Rodríguez, Jesús, KAjO Services, Bytča, Slovakia
Casella, Ana, Instituto Nacional de Meteorología e Hidrología de Venezuela (INAMEH), Caracas, Venezuela
Centella-Artola, Abel, La Habana, Cuba
Cetinić, Ivona, NASA Goddard Space Flight Center, Greenbelt, Maryland; Universities Space Research Association, Columbia, Maryland
Chan, Duo, School of Ocean and Earth Science, University of Southampton, Southampton, United Kingdom
Chan, Steven, National Oceanography Centre, Southampton, United Kingdom
Chang, Kai-Lan, Cooperative Institute for Research in Environmental Sciences, University of Colorado Boulder, Boulder, Colorado; NOAA Chemical Sciences Laboratory, Boulder, Colorado
Charlton, Candice S., Department of Physics, The University of the West Indies, Kingston, Jamaica
Chen, Hua, Nanjing University of Information Science and Technology, Nanjing, China
Chen, Lin, Institute for Climate and Application Research (ICAR)/KLME/ILCEC/CIC-FEMD, Nanjing University of Information Science and Technology, Nanjing, China
Cheng, Lijing, State Key Laboratory of Earth System Numerical Modeling and Application, Institute of Atmospheric Physics, Chinese Academy of Sciences, Beijing, China
Cheng, Vincent Y. S., Environment and Climate Change Canada, Toronto, Ontario, Canada
Christiansen, Hanne H., University of the Arctic, Aarhus University, Aarhus, Denmark; Department of Environmental Science, Aarhus University, Roskilde, Denmark
Chung, Eui-Seok, Korea Polar Research Institute, Incheon, South Korea
Ciasto, Laura M., NOAA/NWS National Centers for Environmental Prediction Climate Prediction Center, College Park, Maryland
Clarke, Leonardo, Department of Physics, The University of the West Indies, Kingston, Jamaica
Clem, Kyle R., School of Geography, Environment and Earth Sciences, Victoria University of Wellington, Wellington, New Zealand
Clingan, Scott, Cooperative Institute for Research in Earth Science, University of Colorado, Boulder, Colorado
Coelho, Caio A. S., Centro de Previsão do Tempo e Estudos Climáticos/National Institute for Space Research, Center for Weather Forecasts and Climate Studies, Cachoeira Paulista, Brazil
Coldewey-Egbers, Melanie, German Aerospace Center (DLR), Oberpfaffenhofen, Germany
Colwell, Steve, British Antarctic Survey, Cambridge, United Kingdom
Cooper, Owen R., NOAA Chemical Sciences Laboratory, Boulder, Colorado
Cornes, Richard C., National Oceanography Centre, Southampton, United Kingdom
Correa, Kris, Servicio Nacional de Meteorología e Hidrología del Perú, Lima, Peru
Costa, Felipe, Centro Internacional para la Investigación del Fenómeno de El Niño (CIIFEN), Guayaquil, Ecuador
Covey, Curt, Lawrence Livermore National Laboratory, Livermore, California
Coy, Lawrence, NASA Goddard Space Flight Center, Greenbelt, Maryland; Science Systems and Applications, Inc., Lanham, Maryland
Crawford, Alex, Department of Environment and Geography, University of Manitoba, Winnipeg, Manitoba, Canada
Crétaux, Jean-Francois, LEGOS (CNES/CNRS/IRD/UPS), Université de Toulouse, Toulouse, France
Crimmins, Theresa, USA National Phenology Network, School of Natural Resources and the Environment, University of Arizona, Tucson, Arizona
Crotwell, Molly, Cooperative Institute for Research in Environmental Sciences, University of Colorado, Boulder, Boulder, Colorado
Cullis, P., NOAA/OAR Earth System Research Laboratory, Global Monitoring Division, Boulder, Colorado; University of Colorado Boulder, Boulder, Colorado
Culpepper, Joshua, Department of Biology, York University, Toronto, Ontario, Canada
Cunha, Ana P., Centro Nacional de Monitoramento e Alertas de Desastres Naturais CEMADEN, São José dos Campos, São Paulo, Brazil
Danzer, Julia, Wegener Center for Climate and Global Change, University of Graz, Graz, Austria
Datta, Rajashree T., Department of Civil Engineering and Geosciences, TU Delft, Delft, The Netherlands
Davis, Sean M., NOAA Chemical Sciences Laboratory, Boulder, Colorado
De Bock, Veerle, Royal Meteorological Institute of Belgium, Brussels, Belgium
de Jeu, Richard A. M., Transmissivity B.V., Alphen aan den Rijn, The Netherlands
de Laat, Jos, Royal Netherlands Meteorological Institute (KNMI), De Bilt, The Netherlands
Decharme, Bertrand, Centre National de Recherches Météorologiques, Météo-France/CNRS, Toulouse, France
Degenstein, Doug, University of Saskatchewan, Saskatoon, Canada
Delbare, Kwint, Hydro-Climate Extremes Lab (H-CEL), Ghent University, Ghent, Belgium
Dell, R. L., University of Cambridge, Cambridge, United Kingdom
Derksen, Chris, Climate Research Division, Environment and Climate Change Canada, Toronto, Canada
Di Tomaso, Enza, European Centre for Medium-Range Weather Forecasts, Bonn, Germany
Diamond, Howard J., NOAA/OAR Air Resources Laboratory, College Park, Maryland
DiGangi, Elizabeth, AEM R&D, Germantown, Maryland
Divine, Dmitry, Norwegian Polar Institute, Fram Centre, Tromsø, Norway
Dokulil, Martin T., Research Institute for Limnology, University of Innsbruck, Mondsee, Austria
Domingues, Catia M., Global Climate, National Oceanography Centre, Southampton, United Kingdom
Donat, Markus G., Barcelona Supercomputing Centre, Barcelona, Spain; Catalan Institution for Research and Advanced Studies (ICREA), Barcelona, Spain
Dong, Shenfu, NOAA/OAR Atlantic Oceanographic and Meteorological Laboratory, Miami, Florida
Dorigo, Wouter A., Department of Geodesy and Geoinformation, TU Wien, Vienna, Austria
Dostalova, Alena, EODC GmbH, Vienna, Austria

Druckenmiller, Matthew L., National Snow and Ice Data Center, Cooperative Institute for Research in Environmental Sciences, University of Colorado, Boulder, Colorado

Du, Juan, International Center for Climate and Environment Sciences, Institute of Atmospheric Physics, Chinese Academy of Sciences, Beijing, China

du Plessis, Marcel, Department of Marine Sciences, University of Gothenburg, Gothenburg, Sweden

Duchemin, Diane, CESBIO, Université de Toulouse, CNES/CNRS/INRAe/IRD/UPS, Toulouse, France

Dugan, Hilary, Center of Limnology, University of Wisconsin-Madison, Madison, Wisconsin

Dulamsuren, Dashkhuu, Information Research Institute of Meteorology, Hydrology and Environment, Ulaanbaatar, Mongolia

Dunn, Robert J. H., Met Office Hadley Centre, Exeter, United Kingdom

Dutton, Geoff, Cooperative Institute for Research in Environmental Sciences, University of Colorado, Boulder, Boulder, Colorado

Effertz, Peter, Cooperative Institute for Research in Environmental Sciences, University of Colorado Boulder, Boulder, Colorado; NOAA Global Monitoring Laboratory, Boulder, Colorado

Ekici, Mithat, Turkish State Meteorological Service, Ankara, Türkiye

Ekwacu, S., Seychelles Meteorological Authority, Mahe, Seychelles

Elias Chereque, Aleksandra, Department of Physics, University of Toronto, Toronto, Canada

Elipot, Shane, Rosenstiel School of Marine, Atmospheric, and Earth Science, University of Miami, Miami, Florida

ElKharrim, M., General Directorate of Meteorology, Rabat, Morocco

Epstein, Howard E., Department of Environmental Sciences, University of Virginia, Charlottesville, Virginia

Espinoza, Jhan-Carlo, Institut des Géosciences de l'Environnement (IGE), Institut de Recherche pour le Dévelopement (IRD), OSUG-B, Domaine Universitaire, Saint-Martin-d'Hères, France; Instituto de Investigación Sobre la Enseñanza de las Matemáticas, Pontificia Universidad Católica del Perú, Lima, Peru

Estilow, Thomas W., Rutgers University, Piscataway, New Jersey

Estrella, Nicole, Ecoclimatology, Department of Life Science Systems, TUM School of Life Sciences, Technical University of Munich, Freising, Germany

Farrell, Sinead, Department of Geographical Sciences, University of Maryland, College Park, Maryland

Fauchereau, Nicolas, Earth Sciences New Zealand, Auckland, New Zealand

Fausto, Robert S., Geological Survey of Denmark and Greenland (GEUS), Copenhagen, Denmark

Faye, A., University Corporation for Atmospheric Research Cooperative Programs for the Advancement of Earth System Science (CPAESS), College Park, Maryland

Feely, Richard A., NOAA/OAR Pacific Marine Environmental Laboratory, Seattle, Washington

Fenimore, Chris, NOAA/NESDIS National Centers for Environmental Information, Asheville, North Carolina

Fereday, David, Met Office Hadley Centre, Exeter, United Kingdom

Fettweis, Xavier, SPHERES Research Unit, University of Liège, Liège, Belgium

Fioletov, Vitali E., Environment and Climate Change Canada, Toronto, Ontario, Canada

Flemming, Johannes, European Centre for Medium-Range Weather Forecasts, Bonn, Germany

Fleury, Michèle, Environment and Climate Change Canada, Montreal, Canada

Florentine, Caitlyn, U.S. Geological Survey, Northern Rocky Mountain Science Center, Bozeman, Montana

Flynn, Lawrence E., NOAA/NESDIS Center for Satellite Applications and Research, College Park, Maryland

Fogarty, Chris, Canadian Hurricane Centre, Dartmouth, Canada

Fogt, Ryan L., Department of Geography, Ohio University, Athens, Ohio

Forbes, Bruce C., Arctic Centre, University of Lapland, Rovaniemi, Finland

Forde, Brendan, Environment and Climate Change Canada, Toronto, Ontario, Canada

Formanek, Maud, Department of Geodesy and Geoinformation, TU Wien, Vienna, Austria

Foster, Michael J., Cooperative Institute for Meteorological Satellite Studies, Space Science and Engineering Center, University of Wisconsin-Madison, Madison, Wisconsin

Franz, Bryan A., NASA Goddard Space Flight Center, Greenbelt, Maryland

Frederikse, Thomas, Planet Labs, Haarlem, The Netherlands

Fricker, Helen A., Scripps Institution of Oceanography, University of California, San Diego, La Jolla, California

Friedman, A. R., Climatic Research Unit, School of Environmental Sciences, University of East Anglia, Norwich, United Kingdom; National Centre for Atmospheric Science (NCAS), University of East Anglia, Norwich, United Kingdom

Frith, Stacey M., Adnet Systems, Inc., Lanham, Maryland; NASA Goddard Space Flight Center, Greenbelt, Maryland

Froidevaux, Lucien, Jet Propulsion Laboratory, California Institute of Technology, Pasadena, California; Retired, Pasadena, California

Frost, Gerald V. (JJ), Alaska Biological Research, Inc., Fairbanks, Alaska

Fu, Yao, College of Marine Science, University of South Florida, St. Petersburg, Florida

Fuhrman, S., ERT, Inc., College Park, Maryland; NOAA/NWS National Centers for Environmental Prediction Climate Prediction Center, College Park, Maryland

Füllekrug, Martin, University of Bath, Bath, United Kingdom

Gallemann, Thomas, Bavarian Environment Agency, Augsburg, Germany

Ganter, Catherine, Bureau of Meteorology, Melbourne, Australia

Gao, Meng, NASA Goddard Space Flight Center, Greenbelt, Maryland; Science Systems and Applications, Inc., Lanham, Maryland

Garcia, Hernan, NOAA/NESDIS National Centers for Environmental Information, Silver Spring, Maryland

García Jiménez, Alejandro Jair, Servicio Meteorológico Nacional, Mexico City, Mexico

Gerland, Sebastian, Norwegian Polar Institute, Fram Centre, Tromsø, Norway

Ghent, Darren, National Centre for Earth Observation (NCEO), University of Leicester, Leicester, United Kingdom; School of Physics and Astronomy, University of Leicester, Leicester, United Kingdom

Gleason, Karin, NOAA/NESDIS National Centers for Environmental Information, Asheville, North Carolina

Glen, E., Department of Geography, Pennsylvania State University, State College, Pennsylvania

Gobron, Nadine, European Commission Joint Research Centre, Ispra, Italy

Godin-Beekmann, Sophie, LATMOS/IPSL, Sorbonne Universite, Paris, France

Goldenberg, Stanley B., NOAA/OAR Atlantic Oceanographic and Meteorological Laboratory, Miami, Florida

González, José, Instituto Nacional de Meteorología e Hidrología de Ecuador (INAMHI), Guayaquil, Ecuador

Good, Elizabeth, Met Office Hadley Centre, Exeter, United Kingdom

Goodman, Steven, Thunderbolt Global Analytics, Huntsville, Alabama

Goto, Atsushi, Japan Meteorological Agency, Tokyo, Japan

Graham, Garrett, North Carolina Institute for Climate Studies, North Carolina State University, Asheville, North Carolina

Gray, Jessie, Bureau of Meteorology, Melbourne, Australia

Grimaldi, Stefania, European Commission Joint Research Centre, Ispra, Italy

Grooß, Jens-Uwe, Forschungszentrum Jülich (ICE-4), Jülich, Germany

Gruber, Alexander, Department of Geodesy and Geoinformation, TU Wien, Vienna, Austria

Gu, Guojun, Earth System Science Interdisciplinary Center, University of Maryland, College Park, Maryland

Guglielmin, Mauro, Department of Theoretical and Applied Sciences, Insubria University, Varese, Italy

Hahn, Sebastian, Department of Geodesy and Geoinformation, TU Wien, Vienna, Austria

Haimberger, Leopold, Department of Meteorology and Geophysics, University of Vienna, Vienna, Austria

Hakmi, S., General Directorate of Meteorology, Rabat, Morocco

Hamlington, Benjamin D., Jet Propulsion Laboratory, California Institute of Technology, Pasadena, California

Han, Mingyu, School of Oceanography, Shanghai Jiao Tong University, Shanghai, China

Hancock, Alyce M., Institute for Marine and Antarctic Studies, University of Tasmania, Hobart, Tasmania, Australia

Hanna, Edward, Department of Geography and Lincoln Climate Research Group, Lincoln, United Kingdom

Hänsch, Martje, Centro Internacional para la Investigación del Fenómeno de El Niño (CIIFEN), Guayaquil, Ecuador

Harder, Paula, European Centre for Medium-Range Weather Forecasts, Bonn, Germany

Harlan, Merritt E., U.S. Geological Survey, Denver, Colorado

Harnos, Daniel S., NOAA/NWS National Centers for Environmental Prediction Climate Prediction Center, College Park, Maryland

Harris, Bethan L., National Centre for Earth Observation, UK Centre for Ecology & Hydrology, Wallingford, United Kingdom

Harris, Ian, Climatic Research Unit, School of Environmental Sciences, University of East Anglia, Norwich, United Kingdom

He, Qiong, State Key Laboratory of Climate System Prediction and Risk Management/KLME/CIC-FEMD/School of Atmospheric Sciences, Nanjing University of Information Science and Technology, Nanjing, China

Hemming, Deborah L., Met Office Hadley Centre, Exeter, United Kingdom

Hendricks, Stefan, Alfred Wegener Institute, Helmholtz Centre for Polar and Marine Research, Bremerhaven, Germany

Hidalgo, Hugo G., Center for Geophysical Research, Center for Research in Pure and Applied Mathematics, University of Costa Rica, San José, Costa Rica; School of Physics, University of Costa Rica, San José, Costa Rica

Hobbs, Will, Australian Antarctic Program Partnership (AAPP), Hobart, Tasmania, Australia; Institute for Marine and Antarctic Studies, University of Tasmania, Hobart, Tasmania, Australia

Holliday, Rebecca, Met Office Hadley Centre, Exeter, United Kingdom

Holzworth, Robert, University of Washington, Seattle, Washington

Horton, Radley M., Columbia Climate School, Columbia University, New York, New York; Lamont-Doherty Earth Observatory, Columbia University, Palisades, New York

Hrbáček, Filip, Department of Geography, Masaryk University, Brno, Czech Republic

Hu, Guojie, Cryosphere Research Station on Qinghai-Tibet Plateau, Northwestern Institute of Eco-Environment and Resources, CAS, Beijing, China

Hu, Zeng-Zhen, NOAA/NWS National Centers for Environmental Prediction Climate Prediction Center, College Park, Maryland

Huang, Boyin, NOAA/NESDIS National Centers for Environmental Information, Asheville, North Carolina

Hutchins, Benjamin W., University of Reading, Reading, United Kingdom

Ialongo, Iolanda, Finnish Meteorological Institute, Helsinki, Finland

Inness, Antje, European Centre for Medium-Range Weather Forecasts, Reading, United Kingdom

Isaksen, Ketil, Climate and Environment Department, Norwegian Meteorological Institute, Oslo, Norway

Ishibumi, Nozomi, Japan Meteorological Agency, Tokyo, Japan

Ito, Takamitsu, School of Earth and Atmospheric Sciences, Georgia Institute of Technology, Atlanta, Georgia

Ivanov, Mirjana, Institute of Hydrometeorology and Seismology, Podgorica, Montenegro

Jackson, P., Scott Polar Research Institute, University of Cambridge, Cambridge, United Kingdom

Jadra, G., Instituto Uruguayo de Meteorología, Montevideo, Uruguay

Jersild, Annika, Earth System Science Interdisciplinary Center/Cooperative Institute for Satellite Earth System Studies, University of Maryland, College Park, Maryland

Jevrejeva, Svetlana, National Oceanography Centre, Liverpool, United Kingdom

Jha, B., ERT, Inc., College Park, Maryland; NOAA/NWS National Centers for Environmental Prediction Climate Prediction Center, College Park, Maryland

Jia, Gensuo, Institute of Atmospheric Physics, Chinese Academy of Sciences, Beijing, China

John, Viju O., EUMETSAT, Darmstadt, Germany

Johnsen, Bjørn, Norwegian Radiation and Nuclear Safety Authority, Østerås, Norway

Johnson, Bryan, NOAA/OAR Earth System Research Laboratory, Global Monitoring Division, Boulder, Colorado; University of Colorado Boulder, Boulder, Colorado

Johnson, Gregory C., NOAA/OAR Pacific Marine Environmental Laboratory, Seattle, Washington; School of Oceanography, University of Washington, Seattle, Washington

Jones, Philip D., Climatic Research Unit, School of Environmental Sciences, University of East Anglia, Norwich, United Kingdom

Josey, Simon A., National Oceanography Centre, Southampton, United Kingdom

Junod, Robert, Earth System Science Center, University of Alabama in Huntsville, Huntsville, Alabama

Kabidi, K., General Directorate of Meteorology, Rabat, Morocco

Kaiser, Johannes W., NILU, Kjeller, Norway

Kaleschke, Lars, Alfred Wegener Institute, Helmholtz Centre for Polar and Marine Research, Bremerhaven, Germany

Kalluri, Satya, NOAA Office of Low Earth Observations, Greenbelt, Maryland

Kazemi, Amin Fazl, Iran National Climate and Drought Crisis Management Center, Iran National Meteorological Organization, Tehran, Iran

Keller, Linda M., Antarctic Meteorological Research and Data Center, Space Science and Engineering Center, University of Wisconsin-Madison, Madison, Wisconsin

Kendon, Michael, Met Office Hadley Centre, Exeter, United Kingdom

Kennedy, John, Independent Researcher, Verdun, France

Kent, Elizabeth C., National Oceanography Centre, Southampton, United Kingdom

Khaykin, Sergey, Laboratoire Atmosphères, Observations Spatiales (LATMOS), UVSQ, Sorbonne Université, CNRS, IPSL, Guyancourt, France

Khiem, Mai Van, National Center of Hydro-Meteorological Forecasting, Vietnam Meteorological and Hydrological Administration, Hanoi, Vietnam

Killick, Rachel. E., Met Office Hadley Centre, Exeter, United Kingdom

Kim, Hyungjun, Department of AI and Futures Studies, Korea Advanced Institute of Science and Technology, Daejeon, South Korea

Kim, Seong-Joong, Korea Polar Research Institute, Incheon, South Korea

Kirchner, Nina, Department of Physical Geography, Stockholm University, Stockholm, Sweden; Tarfala Research Station, Stockholm University, Stockholm, Sweden

Kittel, Chri, Department of Geography, University of Liège, Liège, Belgium; Physical Geography Research Group, Department of Geography, Vrije Universiteit Brussel, Brussels, Belgium

Klotzbach, Philip J., Department of Atmospheric Science, Colorado State University, Fort Collins, Colorado

Knaff, John A., NOAA/NESDIS Center for Satellite Applications and Research, Fort Collins, Colorado

Kohler, J., Norwegian Polar Institute, Fram Centre, Tromsø, Norway

Kondragunta, Shobha, NOAA/NESDIS Center for Satellite Applications and Research, College Park, Maryland

Korshunova, Natalia N., All-Russia Research Institute of Hydrometeorological Information, World Data Center, Obninsk, Russia

Kovács, Dávid D., Department of Geodesy and Geoinformation, TU Wien, Vienna, Austria

Kraemer, Benjamin M., University of Freiburg, Freiburg, Germany

Kramarova, Natalya A., NASA Goddard Space Flight Center, Greenbelt, Maryland

Kruger, A. C., Climate Service, South African Weather Service, Pretoria, South Africa

Kuniyuki, Darryl T., NOAA/OAR Global Monitoring Laboratory, Hilo, Hawaii

Kuramochi, Masaya, Tokyo Climate Center, Japan Meteorological Agency, Tokyo, Japan

L'Heureux, Michelle, NOAA/NWS National Centers for Environmental Prediction Climate Prediction Center, College Park, Maryland

Laas, Alo, Institute of Agricultural and Environmental Sciences, Estonian University of Life Sciences, Tartu, Estonia

Labe, Zachary M., Climate Central, Princeton, New Jersey

Lader, Rick, International Arctic Research Center, University of Alaska Fairbanks, Fairbanks, Alaska

Lait, Leslie R., NASA Ames Research Center, Moffett Field, California

Lakkala, Kaisa, Finnish Meteorological Institute, Sodankylä, Finland

Lam, Hoang Phuc, National Center of Hydro-Meteorological Forecasting, Vietnam Meteorological and Hydrological Administration, Hanoi, Vietnam

Lan, Xin, Cooperative Institute for Research in Environmental Sciences, University of Colorado Boulder, Boulder, Colorado; NOAA Global Monitoring Laboratory, Boulder, Colorado

Landerer, Felix W., Jet Propulsion Laboratory, California Institute of Technology, Pasadena, California

Landschützer, Peter, Flanders Marine Institute, InnovOcean Campus, Ostend, Belgium

Landsea, Chris W., NOAA/NWS National Hurricane Center, Miami, Florida

Lapierre, Jeff, AEM R&D, Germantown, Maryland

Lara, Mark J., Department of Plant Biology, University of Illinois, Urbana, Illinois; Department of Geography, University of Illinois, Urbana, Illinois

Laughner, Joshua L., Jet Propulsion Laboratory, California Institute of Technology, Pasadena, California

Lazzara, Matthew A., Antarctic Meteorological Research and Data Center, Space Science and Engineering Center, University of Wisconsin-Madison, Madison, Wisconsin; Department of Physical Sciences, School of Arts and Sciences, Madison Area Technical College, Madison, Wisconsin

Le Hénaff, Matthieu, NOAA/OAR Atlantic Oceanographic and Meteorological Laboratory, Miami, Florida

Leblanc, Thierry, JPL Table Mountain Facility, Wrightwood, California

Lee, Simon H., School of Earth and Environmental Sciences, University of St Andrews, St Andrews, United Kingdom

Leibensperger, Eric, Department of Physics and Astronomy, Ithaca College, Ithaca, New York

Lems, Johanna, Department of Geodesy and Geoinformation, TU Wien, Vienna, Austria

Leuliette, Eric, NOAA/NWS NCWCP Laboratory for Satellite Altimetry, College Park, Maryland

Li, Juan, State Key Laboratory of Climate System Prediction and Risk Management/KLME/CIC-FEMD/School of Atmospheric Sciences, Nanjing University of Information Science and Technology, Nanjing, China

Liang, Ping, Shanghai Climate Center, Shanghai, China

Libonati, R., Federal University of Rio de Janeiro, Rio de Janeiro, Brazil

Lieser, Jan L., Bureau of Meteorology, Hobart, Tasmania, Australia; Institute for Marine and Antarctic Studies, University of Tasmania, Hobart, Tasmania, Australia

Liley, Ben, New Zealand Institute for Earth Science Limited, Lauder, New Zealand

Lin, I-I., National Taiwan University, Taipei, Taiwan

Liu, Xuefeng, Nanjing University of Information Science and Technology, Nanjing, China

Liu, Zibin, Nanjing University of Information Science and Technology, Nanjing, China

Lo, Y. T. Eunice, Cabot Institute for the Environment, University of Bristol, Bristol, United Kingdom

Locarnini, Ricardo, NOAA/NESDIS National Centers for Environmental Information, Silver Spring, Maryland

Loeb, Norman G., NASA Langley Research Center, Hampton, Virginia

Long, Lindsey N., NOAA/NWS National Centers for Environmental Prediction Climate Prediction Center, College Park, Maryland

Loomis, Bryant D., NASA Goddard Space Flight Center, Greenbelt, Maryland

Lopez, Hosmay, NOAA/OAR Atlantic Oceanographic and Meteorological Laboratory, Miami, Florida

López-Blanco, E., Department of Ecoscience, Arctic Research Center, Aarhus University, Roskilde, Denmark

Lorrey, Andrew M., Earth Sciences New Zealand, Auckland, New Zealand

Loyola, Diego, German Aerospace Center (DLR), Oberpfaffenhofen, Germany

Lozier, M. Susan, School of Earth and Atmospheric Sciences, Georgia Institute of Technology, Atlanta, Georgia

Lu, Bin, School of Information Science and Electronic Engineering, Shanghai Jiao Tong University, Shanghai, China

Lui, Yuk Sing, Hong Kong Observatory, Hong Kong, China

Luks, B., Institute of Geophysics, Polish Academy of Sciences, Warsaw, Poland

Luo, Jing-Jia, Institute for Climate and Application Research, Nanjing University of Information Science and Technology, Nanjing, China

Luojus, Kari, Arctic Research Centre, Finnish Meteorological Institute, Helsinki, Finland

Lyman, John M., Cooperative Institute for Marine and Atmospheric Research, University of Hawaii, Honolulu, Hawaii; NOAA/OAR Pacific Marine Environmental Laboratory, Seattle, Washington

Macander, Matthew J., Alaska Biological Research, Inc., Fairbanks, Alaska

Macara, Gregor, Earth Sciences New Zealand, Lauder, New Zealand

MacFerrin, Michael, Earth Science and Observation Center, Cooperative Institute for Research in Environmental Sciences (ESOC/CIRES), University of Colorado Boulder, Boulder, Colorado

MacLennan, Michelle L., British Antarctic Survey, Cambridge, United Kingdom

Magee, Andrew D., JBA Global Resilience, Brisbane, Australia

Magnin, Florence, Laboratoire EDYTEM, CNRS/Université Savoie Mont-Blanc, Le Bourget-du-Lac, France

Magnússon, Rúna Í., Plant Ecology and Nature Conservation Group, Wageningen University & Research, Wageningen, The Netherlands

Maillard-Barras, Eliane, MeteoSwiss, Payerne, Switzerland

Mamara, Anna, Climate Division, Hellenic National Meteorological Service, Elliniko, Greece

Mamen, Jostein, Climate Division, Norwegian Meteorological Institute, Oslo, Norway

Mankoff, Ken D., Business Integra, New York, New York; NASA Goddard Institute for Space Studies, New York, New York

Marcinonienė, Izolda, Lithuanian Hydrometeorological Service, Vilnius, Lithuania

Marengo, Jose A., Centro Nacional de Monitoramento e Alertas de Desastres Naturais CEMADEN, São José dos Campos, São Paulo, Brazil

Marshall, Alex, Woodland Trust, Grantham, United Kingdom

Martinez, Rodney, World Meteorological Organization, San Jose, Costa Rica

Massant, Joppe, Hydro-Climate Extremes Lab (H-CEL), Ghent University, Ghent, Belgium

Massom, Robert A., Australian Antarctic Division, Australian Antarctic Program Partnership (AAPP) and Australian Centre for Excellence in Antarctic Science (ACEAS), Hobart, Tasmania, Australia

Matsuzaki, Shin-Ichiro, National Institute for Environmental Studies, Tsukuba, Ibaraki, Japan

Matthews, Jessica L., NOAA/NESDIS National Centers for Environmental Information, Asheville, North Carolina

Matthews, Tom, King's College London, United Kingdom

Mayer, Michael, Department of Meteorology and Geophysics, University of Vienna, Austria; Research Department, European Centre for Medium-Range Weather Forecasts, Bonn, Germany

McBride, C., Climate Service, South African Weather Service, Pretoria, South Africa

McNamara, Laura, University of Reading, Reading, United Kingdom

McVicar, Tim R., CSIRO Environment, Canberra, Australia

Mears, Carl A., Remote Sensing Systems, Santa Rosa, California

Medley, Brooke, Cryospheric Sciences Laboratory, NASA Goddard Space Flight Center, Greenbelt, Maryland

Meier, Walter N., National Snow and Ice Data Center, Cooperative Institute for Research in Environmental Sciences, University of Colorado, Boulder, Colorado

Menzel, Annette, Ecoclimatology, Department of Life Science Systems, TUM School of Life Sciences, Technical University of Munich, Freising, Germany; Institute for Advanced Study, Technical University of Munich, Garching, Germany

Merchant, Christopher J., University of Reading, Reading, United Kingdom

Meyer, Michael F., U.S. Geological Survey, Portland, Oregon

Mikolajczyk, David E., Antarctic Meteorological Research and Data Center, Space Science and Engineering Center, University of Wisconsin-Madison, Madison, Wisconsin

Milward, James, Department of Earth and Environmental Science, Temple University, Philadelphia, Pennsylvania

Minney, Caitlin, Bureau of Meteorology, Melbourne, Australia

Minobe, Shoshiro, Faculty of Science, Hokkaido University, Sapporo, Japan

Miralles, Diego G., Hydro-Climate Extremes Lab (H-CEL), Ghent University, Ghent, Belgium

Mishonov, Alexey, Earth System Science Interdisciplinary Center/Cooperative Institute for Satellite Earth System Studies, University of Maryland, College Park, Maryland; NOAA/NESDIS National Centers for Environmental Information, Silver Spring, Maryland

Mitchum, Gary T., College of Marine Science, University of South Florida, St. Petersburg, Florida

Miyamoto, Masatoshi, Japan Meteorological Agency, Tokyo, Japan

Moat, Ben I., National Oceanography Centre, Southampton, United Kingdom

Mohammadi, Marjan, Iran National Climate and Drought Crisis Management Center, Iran National Meteorological Organization, Tehran, Iran

Moise, Aurel, Centre for Climate Research Singapore, Meteorological Service Singapore, Singapore

Moldenhauer, Colin, Department of Geodesy and Geoinformation, TU Wien, Vienna, Austria

Molina-Carpio, Jorge, Universidad Mayor de San Andrés, La Paz, Bolivia

Monerie, Paul-Arthur, National Centre for Atmospheric Science, Reading, United Kingdom

Monselesan, Didier P., CSIRO, Environment Research Unit, Climate Intelligence, Climate Variability and Hazards, Hobart, Tasmania, Australia

Montesano, Paul M., NASA Goddard Space Flight Center, Greenbelt, Maryland

Montzka, Stephen A., NOAA Global Monitoring Laboratory, Boulder, Colorado

Moody, Ronald, Meteorological Service, Jamaica

Moon, Suyeon, Climate Services and Research Division, Asia-Pacific Economic Cooperation Climate Center, Busan, South Korea

Moon, Twila A., National Snow and Ice Data Center, Cooperative Institute for Research in Environmental Sciences, University of Colorado, Boulder, Colorado

Mora, Natali, Center for Geophysical Research, University of Costa Rica, San José, Costa Rica

Morata Gasca, Ana, Agencia Estatal de Meteorología, Madrid, Spain

Morice, Colin P., Met Office Hadley Centre, Exeter, United Kingdom

Morino, Isamu, National Institute for Environmental Studies, Tsukuba, Ibaraki, Japan

Morris, Gary, NOAA Global Monitoring Laboratory, Boulder, Colorado

Mostafa, A. E., Department of Seasonal Forecast and Climate Research, Cairo Numerical Weather Prediction, Egyptian Meteorological Authority, Cairo, Egypt

Mote, Thomas L., Department of Geography, University of Georgia, Athens, Georgia

Motrøen Gjelten, Herdis, Norwegian Meteorological Institute, Oslo, Norway

Mrekaj, Ivan, Technical University in Zvolen, Zvolen, Slovakia

Mudryk, Lawrence, Climate Research Division, Environment and Climate Change Canada, Toronto, Canada

Mühle, Jens, Scripps Institution of Oceanography, San Diego, California

Müller, Peter, GeoSphere Austria, Vienna, Austria

Müller, Rolf, Forschungszentrum Jülich (ICE-4), Jülich, Germany

Nakayama, Naoki, Tokyo Climate Center, Japan Meteorological Agency, Tokyo, Japan

Nance, David, Cooperative Institute for Research in Environmental Sciences, University of Colorado, Boulder, Boulder, Colorado

Natali, S. M., Woodwell Climate Research Center, Falmouth, Massachusetts

Navarra, Gian G., Atmospheric and Oceanic Sciences, Princeton University, Princeton, New Jersey

Neigh, Christopher S. R., NASA Goddard Space Flight Center, Greenbelt, Maryland

Nerem, R. Steven, Colorado Center for Astrodynamics Research, Cooperative Institute for Research in Environmental Sciences, University of Colorado Boulder, Boulder, Colorado

Newman, Paul A., NASA Goddard Space Flight Center, Greenbelt, Maryland; University of Maryland, Baltimore County, Baltimore, Maryland

Nicolas, Julien P., European Centre for Medium-Range Weather Forecasts, Bonn, Germany

Nielson-Gammon, John, Texas A&M University, College Station, Texas

Noetzli, Jeannette, Climate Change, Extremes and Natural Hazards in Alpine Regions Research Centre (CERC), Davos Dorf, Switzerland; WSL Institute for Snow and Avalanche Research SLF, Davos Dorf, Switzerland

Nomenjanahary, T., Seychelles Meteorological Authority, Mahe, Seychelles

Norton, Taylor, Antarctic Meteorological Research and Data Center, Space Science and Engineering Center, University of Wisconsin-Madison, Madison, Wisconsin

Nyland, Kelsey E., George Washington University, Washington, District of Columbia

O'Keefe, John, The Harvard Forest, Harvard University, Petersham, Massachusetts

Orlik, Alexander, GeoSphere Austria, Vienna, Austria

Orndahl, K. M., School of Informatics, Computing, and Cyber Systems, Northern Arizona University, Flagstaff, Arizona

Osborn, Timothy J., Climatic Research Unit, School of Environmental Sciences, University of East Anglia, Norwich, United Kingdom

Overland, James E., NOAA/OAR Pacific Marine Environmental Laboratory, Seattle, Washington

Pálsson, F., Institute of Earth Sciences, University of Iceland, Reykjavík, Iceland

Parrington, Mark, European Centre for Medium-Range Weather Forecasts, Bonn, Germany

Pasch, Richard J., NOAA/NWS National Hurricane Center, Miami, Florida

Payne, Vivienne H., Jet Propulsion Laboratory, California Institute of Technology, Pasadena, California

Peltier, Alexandre, Météo France, Nouméa, New Caledonia

Pelto, Mauri, Nichols College, Dudley, Massachusetts

Perez, Renellys C., NOAA/OAR Atlantic Oceanographic and Meteorological Laboratory, Miami, Florida

Perovich, Donald K., Dartmouth College, Hanover, New Hampshire

Petersen, Kyle, Cooperative Institute for Research in Environmental Sciences, University of Colorado, Boulder, Boulder, Colorado

Petit, Tyllis, National Oceanography Centre, Southampton, United Kingdom

Petropavlovskikh, Irina, NOAA/OAR Earth System Research Laboratory, Global Monitoring Division, Boulder, Colorado; University of Colorado Boulder, Boulder, Colorado

Petty, Alek, NASA Goddard Space Flight Center, Greenbelt, Maryland

Pezza, Alexandre B., Greater Wellington Regional Council, Wellington, New Zealand

Pezzi, Luciano P., Laboratory of Ocean and Atmosphere Studies (LOA), Earth Observation and Geoinformatics Division (DIOTG), National Institute for Space Research (INPE), São José dos Campos, São Paulo, Brazil

Phillips, Coda, Cooperative Institute for Meteorological Satellite Studies, Space Science and Engineering Center, University of Wisconsin-Madison, Madison, Wisconsin

Phoenix, Gareth K., School of Biosciences, University of Sheffield, Sheffield, United Kingdom

Pierson, Don, Department of Ecology and Genetics, Uppsala University, Uppsala, Sweden

Piervitali, Emanuela, Italian Institute for Environmental Protection and Research (ISPRA), Rome, Italy

Pilch-Kedzierski, Robin, Department of Meteorology and Geophysics, University of Vienna, Vienna, Austria

Po-Chedley, Stephen, Lawrence Livermore National Laboratory, Livermore, California

Pogliotti, Paolo, Environmental Protection Agency of Valle d'Aosta, Saint Christophe, Italy

Poinar, Kristin, University at Buffalo, Buffalo, New York

Polvani, Lorenzo, Columbia University, New York, New York

Porat, Amos, Israel Meteorological Service, Bet Dagan, Israel

Prajapati, Richa, CESBIO, Université de Toulouse, CNES/CNRS/INRAe/IRD/UPS, Toulouse, France

Preimesberger, Wolfgang, Department of Geodesy and Geoinformation, TU Wien, Vienna, Austria

Price, Colin, Tel Aviv University, Tel Aviv, Israel

Pulkkanen, Merja, Finnish Environment Institute (SYKE), Helsinki, Finland

Quagraine, Kwesi A., National Center for Atmospheric Research, Boulder, Colorado

Querel, Richard, Earth Sciences New Zealand, Lauder, New Zealand

Räike, Antti, Finnish Environment Institute (SYKE), Helsinki, Finland

Randel, William J., NSF National Center for Atmospheric Research, Boulder, Colorado

Raphael, Marilyn N., Department of Geography, University of California, Los Angeles, Los Angeles, California

Ratri, Dian Nur, BMKG, Jakarta, Indonesia

Raymond, Colin, Joint Institute for Regional Earth System Science and Engineering, University of California, Los Angeles, Los Angeles, California

Reagan, James, NOAA/NESDIS National Centers for Environmental Information, Silver Spring, Maryland

Reid, Phillip, Australian Antarctic Program Partnership (AAPP), Hobart, Tasmania, Australia; Bureau of Meteorology, Hobart, Tasmania, Australia

Reiter, Annika, Wegener Center for Climate and Global Change, University of Graz, Graz, Austria

Remy, Samuel, HYGEOS, Lille, France

Rennie, Jared, NOAA/NESDIS National Centers for Environmental Information, Asheville, North Carolina

Reyes Kohler, A. J., Dirección Meteorológica de Chile, Santiago de Chile, Chile

Ricciardulli, Lucrezia, Remote Sensing Systems, Santa Rosa, California

Richardson, Andrew D., Center for Ecosystem Science and Society, Northern Arizona University, Flagstaff, Arizona; School of Informatics, Computing, and Cyber Systems, Northern Arizona University, Flagstaff, Arizona

Ricker, Robert, NORCE Norwegian Research Centre, Tromsø, Norway

Riedl, Claudia, GeoSphere Austria, Salzburg, Austria

Riihimaki, Laura D., Cooperative Institute for Research in Environmental Sciences, University of Colorado Boulder, Boulder, Colorado; NOAA Global Monitoring Laboratory, Boulder, Colorado

Rivera, P. P., Servicio Nacional de Meteorología e Hidrología del Perú, Lima, Peru

Roach, Christopher J., Institute for Marine and Antarctic Studies, University of Tasmania, Hobart, Tasmania, Australia

Robinson, David A., Rutgers University, Piscataway, New Jersey

Robjhon, M., ERT, Inc., College Park, Maryland; NOAA/NWS National Centers for Environmental Prediction Climate Prediction Center, College Park, Maryland

Rodell, Matthew, NASA Goddard Space Flight Center, Greenbelt, Maryland

Rodríguez, Nathalie, Centro Internacional para la Investigación del Fenómeno de El Niño (CIIFEN), Guayaquil, Ecuador

Rodriguez-Fernandez, Nemesio, CESBIO, Université de Toulouse, CNES/CNRS/INRAe/IRD/UPS, Toulouse, France

Roebeling, Maarit, Deutscher Wetterdienst, WMO RA VI Regional Climate Centre Network, Offenbach, Germany

Rogers, Cassandra D. W., Bureau of Meteorology, Melbourne, Australia

Rohini, P., India Meteorological Department, Pune, India

Romanovsky, Vladimir E., Geophysical Institute, University of Alaska Fairbanks, Fairbanks, Alaska

Ronchail, Josyane, Laboratoire LOCEAN-IPSL, Paris, France

Rosencrans, Matthew, NOAA/NWS National Centers for Environmental Prediction Climate Prediction Center, College Park, Maryland

Rosenlof, Karen H., NOAA Chemical Sciences Laboratory, Boulder, Colorado; Retired, Boulder, Colorado

Rozanov, Alexei, University of Bremen, Bremen, Germany

Rozkošný, Jozef, Slovak Hydrometeorological Institute, Bratislava, Slovakia

Rubek, Frans, Danish Meteorological Institute, Copenhagen, Denmark

Runyen, Jason, NOAA National Weather Service Austin/San Antonio Office, New Braunfels, Texas

Rusanovskaya, Olga O., Irkutsk State University, Institute of Lake Baikal Biology, Irkutsk, Russia

Russo, Emmanuele, European Centre for Medium-Range Weather Forecasts, Bonn, Germany

Rutishauser, This, Swiss Academy of Sciences (SCNAT), Bern, Switzerland

Ryan-Keogh, Thomas J., Southern Ocean Carbon-Climate Observatory, Council for Scientific and Industrial Research (CSIR), Cape Town, South Africa

Sabeerali, C. T., India Meteorological Department, Pune, India

Said, Ryan, Vaisala R&D, Louisville, Colorado

Sakai, Tetsu, Meteorological Research Institute, Japan Meteorological Agency, Tsukuba, Ibaraki, Japan

Salamon, Peter, European Commission Joint Research Centre, Ispra, Italy

Salazar, Iliana, Centro Internacional para la Investigación del Fenómeno de El Niño (CIIFEN), Guayaquil, Ecuador

Samokhina, Olga. F., Yu. A. Izrael Institute of Global Climate and Ecology, Moscow, Russia

Sánchez-Lugo, Ahira, NOAA/NESDIS National Centers for Environmental Information, Asheville, North Carolina

Santee, Michelle L., Jet Propulsion Laboratory, California Institute of Technology, Pasadena, California

Sass, L., U.S. Geological Survey, Alaska Science Center, Anchorage, Alaska

Savita, Abhishek, Centre for Atmospheric Sciences, Indian Institute of Technology Delhi, Delhi, India

Sawaengphokhai, Parnchai, ADNET Systems, Inc., Hampton, Virginia

Scambos, Theodore, Earth Science and Observation Center, Cooperative Institute for Research in Environmental Sciences (ESOC/CIRES), University of Colorado Boulder, Boulder, Colorado

Schaffhauser, Timo, European Commission Joint Research Centre, Ispra, Italy

Schenzinger, Verena, India Meteorological Department, Pune, India

Schlegel, Robert W., Laboratoire d'Océanographie de Villefranche, Sorbonne Université, Villefranche-sur-mer, France

Schmid, Martin, Eawag, Department Surface Waters - Research and Management, Kastanienbaum, Switzerland

Schreck, Carl J., Cooperative Institute for Satellite Earth System Studies, North Carolina Institute for Climate Studies, North Carolina State University, Asheville, North Carolina

Schulz, Cristina, Department of Marine and Environmental Sciences, Northeastern University, Boston, Massachusetts

Schuur, E. A. G., Center for Ecosystem Science and Society, Northern Arizona University, Flagstaff, Arizona

Segele, Z. T., NOAA/NWS National Centers for Environmental Prediction Climate Prediction Center, College Park, Maryland

Sensoy, Serhat, Turkish State Meteorological Service, Ankara, Türkiye

Seong, Ji-In, Climate Change Monitoring Division, Korea Meteorological Administration, Seoul, South Korea

Serna Cuenca, Julieta, Instituto de Hidrología, Meteorología y Estudios Ambientales de Colombia (IDEAM), Bogotá, Colombia

Serreze, Mark C., National Snow and Ice Data Center, Cooperative Institute for Research in Environmental Sciences, University of Colorado, Boulder, Colorado

Sezaki, Fumi, Tokyo Climate Center, Japan Meteorological Agency, Tokyo, Japan

Sharma, Sapna, Department of Biology, York University, Toronto, Ontario, Canada

Sharp, Jonathan D., Cooperative Institute for Climate, Ocean, and Ecosystem Studies, University of Washington, Seattle, Washington; NOAA/OAR Pacific Marine Environmental Laboratory, Seattle, Washington

Shi, Jia-Rui, Courant Institute of Mathematical Sciences, New York University, New York City, New York

Shimaraeva, Svetlana V., Irkutsk State University, Institute of Lake Baikal Biology, Irkutsk, Russia

Shinohara, Ryuichiro, Regional Environment Conservation Division, National Institute for Environmental Studies, Tsukuba, Ibaraki, Japan

Shukla, R. P., Entarian, Greenbelt, Maryland; NOAA/NWS National Centers for Environmental Prediction, Climate Prediction Center, College Park, Maryland

Siddons, Joseph, National Oceanography Centre, Southampton, United Kingdom

Silow, Eugene A., Irkutsk State University, Institute of Lake Baikal Biology, Irkutsk, Russia

Sima, F., Retired, Banjul, The Gambia

Simmons, Adrian J., European Centre for Medium-Range Weather Forecasts, Reading, United Kingdom

Singh, B., NOAA/NWS National Centers for Environmental Prediction Climate Prediction Center, College Park, Maryland

Smeed, David A., National Oceanography Centre, Southampton, United Kingdom

Smith, Benjamin E., Polar Science Center, Applied Physics Laboratory, University of Washington, Seattle, Washington

Smith, Sharon L., Geological Survey of Canada, Natural Resources Canada, Ottawa, Canada

Soden, Brian J., University of Miami, Miami, Florida

Sofieva, Viktoria, Finnish Meteorological Institute, Helsinki, Finland

Soldo, Logan, Cooperative Institute for Research in Environmental Sciences, University of Colorado Boulder, Boulder, Colorado; NOAA Global Monitoring Laboratory, Boulder, Colorado

Souza, Everaldo, Federal University of Pará (UFPA), Belém, Pará, Brazil

Spence-Hemmings, Jacqueline, Meteorological Service, Jamaica

Spillane, Sandra, Met Éireann, Dublin, Ireland

Sreejith, O. P., India Meteorological Department, Pune, India

Srivastava, A. K., India Meteorological Department, Pune, India

Stackhouse, Jr., NASA Langley Research Center, Hampton, Virginia

Stackhouse, Paul W., NASA Langley Research Center, Hampton, Virginia

Stammerjohn, Sharon, Institute of Arctic and Alpine Research, University of Colorado Boulder, Boulder, Colorado

Stauffer, Ryan M., Atmospheric Chemistry and Dynamics Laboratory, NASA Goddard Space Flight Center, Greenbelt, Maryland

Steinberg, Jacob M., NOAA/OAR Geophysical Fluid Dynamics Laboratory, Princeton, New Jersey

Steinbrecht, Wolfgang, Deutscher Wetterdienst, Hohenpeissenberg, Germany

Steiner, Andrea K., Wegener Center for Climate and Global Change, University of Graz, Graz, Austria

Stella, Jose L., Servicio Meteorológico Nacional, Buenos Aires, Argentina

Stephenson, Tannecia S., Department of Physics, The University of the West Indies, Kingston, Jamaica

Stevens, Laura, North Carolina Institute for Climate Studies, North Carolina State University, Asheville, North Carolina

Stoy, Paul, University of Wisconsin–Madison, Madison, Wisconsin

Streletskiy, Dmitry A., George Washington University, Washington, District of Columbia

Sun, Qiaohong, State Key Laboratory of Climate System Prediction and Risk Management, Nanjing University of Information Science and Technology, Nanjing, China

Svendby, Tove, The Climate and Environmental Research Institute NILU, Kjeller, Norway

Sweet, William, NOAA/NOS Center for Operational Oceanographic Products and Services, Silver Spring, Maryland

Taha, Ghassan, Morgan State University, Baltimore, Maryland; NASA Goddard Space Flight Center, Greenbelt, Maryland

Takemura, Kazuto, Tokyo Climate Center, Japan Meteorological Agency, Tokyo, Japan

Taylor, Michael A., Department of Physics, The University of the West Indies, Kingston, Jamaica

Thackeray, Stephen J., United Kingdom Centre for Ecology & Hydrology, Lancaster, United Kingdom

Thiaw, W. M., NOAA/NWS National Centers for Environmental Prediction Climate Prediction Center, College Park, Maryland

Thomalla, Sandy, Marine and Antarctic Research Centre for Innovation and Sustainability, Department of Oceanography, University of Cape Town, Cape Town, South Africa; Southern Ocean Carbon-Climate Observatory, Council for Scientific and Industrial Research (CSIR), Cape Town, South Africa

Thoman, Richard L., International Arctic Research Center, University of Alaska Fairbanks, Fairbanks, Alaska

Thompson, Philip R., Cooperative Institute for Marine and Atmospheric Research, Department of Oceanography, University of Hawaii, Honolulu, Hawaii

Thomson, L., Queen's University, Kingston, Ontario, Canada

Thorsteinsson, T., Icelandic Meteorological Office, Reykjavík, Iceland

Tian-Kunze, Xiangshan, Alfred Wegener Institute, Helmholtz Centre for Polar and Marine Research, Bremerhaven, Germany

Timmermans, Mary-Louise, Department of Earth and Planetary Sciences, Yale University, New Haven, Connecticut

Timofeyev, Maxim A., Irkutsk State University, Institute of Lake Baikal Biology, Irkutsk, Russia

Tourpali, Kleareti, Aristotle University, Thessaloniki, Greece

Tran, Harrison, NOAA National Weather Service Austin/San Antonio Office, New Braunfels, Texas

Trewin, Blair C., Bureau of Meteorology, Melbourne, Australia

Trinanes, Joaquin, Department of Electronics and Computer Science, Universidade de Santiago de Compostela, Santiago de Compostela, Spain

Trotman, Adrian, Caribbean Institute for Meteorology and Hydrology, Bridgetown, Barbados

Truchelut, Ryan E., WeatherTiger, Tallahassee, Florida

Trusel, Luke, Department of Geography, Pennsylvania State University, State College, Pennsylvania

Tuchen, Franz Philip, Rosenstiel School of Marine, Atmospheric, and Earth Science, University of Miami, Miami, Florida

Turňa, Maroš, Slovak Hydrometeorological Institute, Bratislava, Slovakia

Tømmervik, Hans, FRAM – High North Research Centre for Climate and the Environment, Tromsø, Norway; Norwegian Institute for Nature Research, Trondheim, Norway

Uehling, John, Cooperative Institute for Satellite Earth System Studies, North Carolina Institute for Climate Studies, North Carolina State University, Asheville, North Carolina

Umezu, Hironori, Tokyo Climate Center, Japan Meteorological Agency, Tokyo, Japan

Urraca, Ruben, European Commission Joint Research Centre, Ispra, Italy

Valdivieso, Cristina, Instituto Nacional de Meteorología e Hidrología de Ecuador (INAMHI), Quito, Ecuador

van der A, Ronald, Royal Netherlands Meteorological Institute (KNMI), De Bilt, The Netherlands

van der Linden, Roderick, Deutscher Wetterdienst, Offenbach, Germany

van der Schrier, Gerard, Royal Netherlands Meteorological Institute, De Bilt, The Netherlands

Van Meerbeeck, Cédric J., Caribbean Institute for Meteorology and Hydrology, Bridgetown, Barbados

Vazifeh, Ahad, Iran National Climate and Drought Crisis Management Center, Iran National Meteorological Organization, Tehran, Iran

Vázquez Romaña, Fabián, Servicio Meteorológico Nacional, Mexico City, Mexico

Veal, Karen, National Centre for Earth Observation (NCEO), University of Leicester, Leicester, United Kingdom; School of Physics and Astronomy, University of Leicester, Leicester, United Kingdom

Verburg, Piet, School of Geography, Environment and Earth Sciences, Victoria University of Wellington, Wellington, New Zealand

Vernier, Jean-Paul, NASA Langley Research Center, Hampton, Virginia

Vicencio, José, University of Cologne, Cologne, Germany

Vimont, Isaac J., NOAA Global Monitoring Laboratory, Boulder, Colorado

Virts, Katrina, University of Alabama in Huntsville, Huntsville, Alabama

Volkov, Denis L., Cooperative Institute for Marine and Atmospheric Studies, Rosenstiel School of Marine, Atmospheric, and Earth Science, University of Miami, Miami, Florida; NOAA/OAR Atlantic Oceanographic and Meteorological Laboratory, Miami, Florida

Vömel, Holger, National Center for Atmospheric Research, Boulder, Colorado

Vose, Russell S., NOAA/NESDIS National Centers for Environmental Information, Asheville, North Carolina

Waigl, Christine F., Geophysical Institute, University of Alaska Fairbanks, Fairbanks, Alaska

Walker, Donald (Skip) A., Institute of Arctic Biology, University of Alaska Fairbanks, Fairbanks, Alaska

Walsh, John E., International Arctic Research Center, University of Alaska Fairbanks, Fairbanks, Alaska

Wang, Bin, School of Ocean and Earth Science and Technology, Department of Meteorology, University of Hawaii at Manoa, Honolulu, Hawaii; International Pacific Research Center, Honolulu, Hawaii

Wang, Hui, NOAA/NWS National Centers for Environmental Prediction Climate Prediction Center, College Park, Maryland

Wang, Muyin, NOAA/OAR Pacific Marine Environmental Laboratory, Seattle, Washington; Cooperative Institute for Climate, Ocean, and Ecosystem Studies, University of Washington, Seattle, Washington

Wang, Ray H. J., Georgia Institute of Technology, Atlanta, Georgia

Wang, Zhankun, NOAA/NESDIS National Centers for Environmental Information, Dickinson, Texas

Wanninkhof, Rik, NOAA/OAR Atlantic Oceanographic and Meteorological Laboratory, Miami, Florida

Waring, Abigail Marie, National Centre for Earth Observation (NCEO), University of Leicester, Leicester, United Kingdom; School of Physics and Astronomy, University of Leicester, Leicester, United Kingdom

Warnock, Taran, University of Saskatchewan, Saskatoon, Canada

Weber, Mark, University of Bremen, Bremen, Germany

Webster, Melinda, Polar Science Center, Applied Physics Laboratory, University of Washington, Seattle, Washington

Wei, Zigang, Science and Technology Corporation (STC), College Park, Maryland

Weiss, Philipp, European Centre for Medium-Range Weather Forecasts, Bonn, Germany

Weller, Robert A., Department of Physical Oceanography, Woods Hole Oceanographic Institution, Woods Hole, Massachusetts

Westberry, Toby K., Oregon State University, Corvallis, Oregon

Widlansky, Matthew J., Cooperative Institute for Marine and Atmospheric Research, Department of Oceanography, University of Hawaii, Honolulu, Hawaii

Wiese, David N., Jet Propulsion Laboratory, California Institute of Technology, Pasadena, California

Wijffels, Susan E., Department of Physical Oceanography, Woods Hole Oceanographic Institution, Woods Hole, Massachusetts

Wild, Jeannette D., Earth System Science Interdisciplinary Center, University of Maryland, College Park, Maryland; NOAA/NESDIS Center for Satellite Applications and Research, College Park, Maryland; Retired, College Park, Maryland

Wille, Jonathan D., Institute for Atmospheric and Climate Science, ETH Zürich, Zürich, Switzerland; Institut des Géosciences de l'Environnement, IRD, CNRS, Grenoble INP, Saint Martin d'Hères, France

Willems, An, Royal Meteorological Institute of Belgium, Brussels, Belgium

Willett, Kate M., Met Office Hadley Centre, Exeter, United Kingdom

Williams, Earle, Massachusetts Institute of Technology, Cambridge, Massachusetts

Williams, Matthew, Department of Physics, The University of the West Indies, Kingston, Jamaica

Willis, Joshua K., Jet Propulsion Laboratory, California Institute of Technology, Pasadena, California

Wolken, G., University of Alaska Fairbanks, Fairbanks, Alaska; Alaska Division of Geological & Geophysical Surveys, Fairbanks, Alaska

Wood, Kimberly M., Department of Hydrology and Atmospheric Sciences, University of Arizona, Tucson, Arizona

Wood, Tom, King's College London, United Kingdom

Woolway, Richard Iestyn, School of Ocean Sciences, Bangor University, Bangor, United Kingdom

Wouters, B., Department of Geoscience and Remote Sensing, TU Delft, Delft, The Netherlands

Xin, Yi, School of Information Science and Electronic Engineering, Shanghai Jiao Tong University, Shanghai, China

Xu, Kuan-Man, NASA Langley Research Center, Hampton, Virginia

Xu, L., Entarian, Greenbelt, Maryland; NOAA/NWS National Centers for Environmental Prediction, Climate Prediction Center, College Park, Maryland

Yang, Dedi, Environmental Sciences Division, Oak Ridge National Laboratory, Oak Ridge, Tennessee

Yang, Kai, Department of Atmospheric and Oceanic Sciences, University of Maryland, College Park, Maryland

Yin, Xungang, NOAA/NESDIS National Centers for Environmental Information, Asheville, North Carolina

Yu, Lisan, Department of Physical Oceanography, Woods Hole Oceanographic Institution, Woods Hole, Massachusetts

Zeng, Zhenzhong, School of Environmental Science and Engineering, Southern University of Science and Technology, Shenzhen, China

Zhang, Peiqun, Beijing Climate Center, China Meteorological Administration, Beijing, China

Zhang, Wenxia, School of Atmospheric Sciences, Nanjing University, Nanjing, China

Zhao, Lin, School of Geographical Sciences, Nanjing University of Information Science and Technology, Nanjing, China

Editor and Author Affiliations (continued)

Zhou, Yuntao, School of Oceanography, Shanghai Jiao Tong University, Shanghai, China

Zhu, Zhiwei, Nanjing University of Information Science and Technology, Nanjing, China

Ziegler, Taylor, Antarctic Meteorological Research and Data Center, Space Science and Engineering Center, University of Wisconsin-Madison, Madison, Wisconsin

Ziemke, Jerry R., Goddard Earth Sciences Technology and Research, Morgan State University, Baltimore, Maryland; NASA Goddard Space Flight Center, Greenbelt, Maryland

Ziese, Markus, Global Precipitation Climatology Centre, Deutscher Wetterdienst, Offenbach, Germany

Zotta, Ruxandra-Maria, TU Wien, Vienna, Austria

Zou, Cheng-Zhi, George Mason University, Fairfax, Virginia

Zubler, Elias, Federal Office of Meteorology and Climatology MeteoSwiss, Zurich, Switzerland

Editorial and Production Team

Allen, Jessicca, Graphics Support, Cooperative Institute for Satellite Earth System Studies, North Carolina State University, Asheville, North Carolina

Camper, Amy V., Graphics Support, Innovative Consulting and Management Services, LLC, NOAA/NESDIS National Centers for Environmental Information, Asheville, North Carolina

Carroll, Lauren, Content Team Lead, Communications and Outreach, NOAA/NESDIS National Centers for Environmental Information, Asheville, North Carolina

Crossman, Jacquelyn, NCEI Librarian, MPF-ZAI, NOAA/NESDIS National Centers for Environmental Information, Asheville, North Carolina

Haley, Bridgette O., Graphics Support, NOAA/NESDIS National Centers for Environmental Information, Asheville, North Carolina

Noguchi, Lukas, Technical Editor, Innovative Consulting and Management Services, LLC, NOAA/NESDIS National Centers for Environmental Information, Asheville, North Carolina

Ohlmann, Laura, Technical Editor, Innovative Consulting and Management Services, LLC, NOAA/NESDIS National Centers for Environmental Information, Asheville, North Carolina

Veasey, Sara W., Visual Communications Team Lead, Communications and Outreach, NOAA/NESDIS National Centers for Environmental Information, Asheville, North Carolina

STATE OF THE CLIMATE IN 2025

INTRODUCTION

J. Reagan, J. Blunden, and R. J. H. Dunn

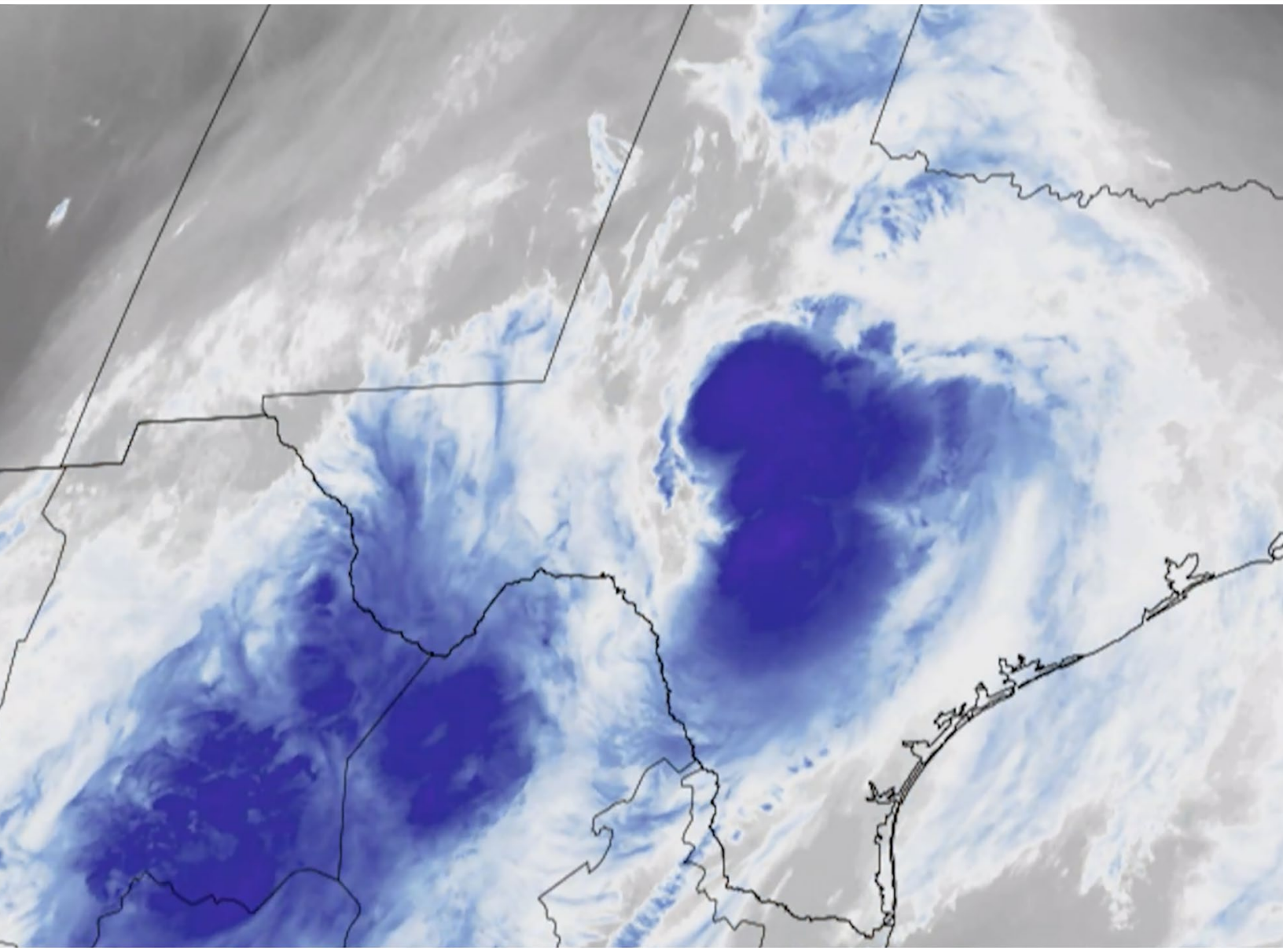

Special Online Supplement to the *Bulletin of the American Meteorological Society* Vol. 107, No. 8, August, 2026

https://doi.org/10.1175/2026BAMSStateoftheClimate_Intro.1
Corresponding author: Jessica Blunden / jessica.blunden@noaa.gov
©2026 American Meteorological Society
For information regarding reuse of this content and general copyright information, consult the AMS Copyright Policy.

STATE OF THE CLIMATE IN 2025
Introduction

Editors

Jessica Blunden
James Reagan

Chapter Editors

Anthony Arguez
Josh Blannin
Peter Bissolli
Kyle R. Clem
Howard J. Diamond
Matthew L. Druckenmiller
Robert J. H. Dunn
Catherine Ganter
Nadine Gobron
Rodney Martinez
Twila A. Moon
Gary A. Morris
Marilyn N. Raphael
Renellys C. Perez
Carl J. Schreck III
Zewdu Segele
Laura Stevens
Richard L. Thoman
Denis L. Volkov
Zhiwei Zhu

Technical Editors

Lukas Noguchi
Laura Ohlmann

BAMS Special Editor for Climate

Timothy DelSole

American Meteorological Society

Cover Credit:
NOAA GOES-19 water vapor satellite imagery of historic rainfall across Central Texas on 4 July 2025. (Credit: Cooperative Institute for Research in the Atmosphere at Colorado State University and the National Oceanic and Atmospheric Administration.)

How to cite this document:
Introduction is one chapter from the *State of the Climate in 2025* annual report and is available from https://doi.org10.1175/2026BAMSStateoftheClimate_Intro.1. Compiled by NOAA's National Centers for Environmental Information, *State of the Climate in 2025* is based on contributions from scientists from around the world. It provides a detailed update on global climate indicators, notable weather events, and other data collected by environmental monitoring stations and instruments located on land, water, ice, and in space. The full report is available from https://doi.org/10.1175/2026BAMSStateoftheClimate.1.

Citing the complete report:
Blunden, J. and J. Reagan, Eds., 2026: "State of the Climate in 2025". Bull. Amer. Meteor. Soc., 107 (8), Si–S512, https://doi.org/10.1175/2026BAMSStateoftheClimate.1.

Citing this chapter:
Reagan, J., J. Blunden, and R. J. H. Dunn, 2026: Introduction [in "State of the Climate in 2025"]. Bull. Amer. Meteor. Soc., 107 (8), S1–S11, https://doi.org/10.1175/2026BAMSStateoftheClimate_Intro.1.

Editor and Author Affiliations (alphabetical by name)

Blunden, Jessica, NOAA/NESDIS National Centers for Environmental Information, Asheville, North Carolina

Dunn, Robert J. H., Met Office Hadley Centre, Exeter, United Kingdom

Reagan, James, NOAA/NESDIS National Centers for Environmental Information, Silver Spring, Maryland

Editorial and Production Team

Allen, Jessicca, Graphics Support, Cooperative Institute for Satellite Earth System Studies, North Carolina State University, Asheville, North Carolina

Camper, Amy V., Graphics Support, Innovative Consulting and Management Services, LLC, NOAA/NESDIS National Centers for Environmental Information, Asheville, North Carolina

Carroll, Lauren, Content Team Lead, Communications and Outreach, NOAA/NESDIS National Centers for Environmental Information, Asheville, North Carolina

Crossman, Jacquelyn, NCEI Librarian, MPF-ZAI, NOAA/NESDIS National Centers for Environmental Information, Asheville, North Carolina

Haley, Bridgette O., Graphics Support, NOAA/NESDIS National Centers for Environmental Information, Asheville, North Carolina

Noguchi, Lukas, Technical Editor, Innovative Consulting and Management Services, LLC, NOAA/NESDIS National Centers for Environmental Information, Asheville, North Carolina

Ohlmann, Laura, Technical Editor, Innovative Consulting and Management Services, LLC, NOAA/NESDIS National Centers for Environmental Information, Asheville, North Carolina

Veasey, Sara W., Visual Communications Team Lead, Communications and Outreach, NOAA/NESDIS National Centers for Environmental Information, Asheville, North Carolina

1. INTRODUCTION

J. Reagan, J. Blunden, and R. J. H. Dunn

This is the 36th issuance of the annual assessment, now known as the *State of the Climate*, published in the Bulletin of the American Meteorological Society since 1996. The report provides a comprehensive, observation-based assessment of Earth's climate system that not only documents what happened during a given year (e.g., 2025), but also how that year compares to previous years in the observational record. Thus, it is critical to have continuous, long-term observations of various components of the Earth system to document variability and change over time. Many of these observations, both current and historical, are also assimilated into various reanalysis products (e.g., ERA5 and MERRA-2), which are physically constrained representations of the Earth system and are used extensively throughout the *State of the Climate* report. Reanalyses are particularly useful in regions where in situ and satellite observations are sparse.

The cover for the *State of the Climate* in 2025 report depicts the Geostationary Operational Environmental Satellite (GOES)-19 satellite, operated by the National Oceanic and Atmospheric Administration (NOAA). The GOES program recently celebrated its 50th anniversary of providing continuous satellite observations of Earth's atmosphere and environment. GOES is part of a much larger global observing system. This observing system, in which measurements are made from satellites orbiting thousands of miles above Earth to Argo diving deep into the abyssal ocean, allows for annual assessments to be conducted for dozens of variables that comprise the Earth's climate system. The continuity of these observations helps identify variability, extremes, and long-term changes within the atmosphere, ocean, cryosphere, and other elements of the Earth system that may impact society now and in the future. The findings within this report are a direct reflection of the breadth of accurate and sustained observations from a variety of platforms and highlight the value of long-term climate records.

All global surface temperature datasets in this report indicate that 2025 was among the three warmest years in the instrumental record, which spans more than 175 years. This warmth occurred despite the year being dominated by cool ENSO-neutral and weak La Niña conditions. Furthermore, the 11 warmest years on record all occurred in the past 11 years. The extreme warmth extended to the polar regions, with Antarctica experiencing its warmest year in the record that began in 1979, and the Arctic experiencing its second-warmest year since the start of its record in 1900. The Arctic continues to warm at a rate of roughly three times the global average. The warmth was also notable in the tropics where the combined land-ocean temperature was 0.27°C above the 1991–2020 average, making it the seventh-warmest year in the 176-year record. Above Earth's surface, the lower troposphere observed its second-warmest year on record.

The record and near-record warmth were not isolated to the atmosphere, as 2025 was a year of extreme warmth for the ocean too. The current in situ global ocean observing system is dominated by autonomous platforms, most notably those of the Argo program. Since the turn of the twenty-first century, Argo has enabled unprecedented monitoring of the subsurface ocean. Analyses of both in situ and remotely sensed observations indicate that global ocean heat content reached a record high in 2025, and marine heatwaves impacted approximately 87% of the global surface ocean. Global mean sea level reached 111.2 mm above the 1993 baseline, also a new record. The 2025 report also includes a new section documenting changes in dissolved oxygen, made possible through historical in situ measurements, mainly from bottle samples and CTD (Conductivity, Temperature, Depth) sensors, and more recently from biogeochemical

sensors deployed on some Argo profiling floats. The total amount of dissolved oxygen in the upper 1800 meters of the ocean has declined by approximately 0.45% per decade since 1965.

As was the case with the ocean and atmosphere, the cryosphere also experienced numerous impacts from the anomalously high temperatures. The cryosphere monitoring system uses remote sensing to detect changes in sea ice and ice-sheet extent, gravity measurements from missions such as Gravity Recovery and Climate Experiment (GRACE) to detect changes in ice mass, glacier monitoring programs, and in situ measurements such as permafrost boreholes. In Chapter 6, the Antarctica and the Southern Ocean cover photo captured from NASA Landsat imagery reveals meltwater ponds on the Amery Ice Shelf during the melt season in late 2024. Annual daily maxima and minima of Antarctic sea ice extent in 2025 were the third and fourth lowest on record, respectively. In the Arctic, the annual maximum sea ice extent was the lowest maximum extent observed in the 47-year satellite record. Across the globe, 2025 also marked the 38th consecutive year of land-based glacier mass loss, with 41% of the total glacier ice mass lost since 1976 occurring during just the last decade.

Satellite observations also captured many consequential weather-related events. In Chapter 4, the Tropics cover photo was taken from GOES-19 and is an infrared image of Hurricane Melissa as it approached Jamaica in October 2025. Hurricane Melissa was a Category 5 storm that impacted more than eight million people across the Caribbean. In total, the North Atlantic had three Category 5 storms in 2025, tying for the second-highest number on record for the basin. Overall, global tropical cyclone activity was above average, with 97 named tropical cyclones compared to the 1991–2020 average of 87.

The near-record global warmth of 2025 manifested differently in various regions around the world. Europe experienced its warmest year in the record dating as far back as 1900, with a mean temperature anomaly of +1.3°C, while North America experienced its third-warmest year in its 176-year record, with a mean temperature anomaly of +1.06°C relative to 1991–2020. The impacts of the record warmth were also evident throughout the global and regional hydrological cycles. Despite above-average precipitation over land areas globally, global cloud area fraction was the second lowest on record at 68.5%, and global average surface soil moisture reached its lowest value since 1991. Among other areas, drought conditions were notable across parts of Europe, the Danube basin, the Amazon, and portions of central Asia in 2025. The particularly hot and dry summer in southwest Europe contributed to unprecedented fire activity over the Iberian Peninsula, contributing to a record amount of fire emissions in Europe. The Chapter 7 Regional Climates cover image, captured by the Moderate Resolution Imaging Spectroradiometer (MODIS) aboard NASA's Terra satellite, depicts one of these major fires in August 2025.

The compilation of the *State of the Climate* is possible due to the dedication of the 626 authors and editors from 60 countries. It would be an impossible feat for one country to perform this sort of comprehensive analysis on the state of today's climate, and we express our sincere appreciation to those who volunteer their time and expertise to provide a well-rounded and scientifically-sound view of our climate system as well as to those who provide thoughtful feedback and peer review. The sequence of the *State of the Climate* in 2025 is similar to previous years: Chapter 1—Introduction (i.e., this chapter); Chapter 2—Global Climate; Chapter 3—Global Oceans; Chapter 4—The Tropics; Chapter 5—The Arctic; Chapter 6—Antarctica and the Southern Ocean; and Chapter 7—Regional Climates, which covers the seven regions of North America, Central America and the Caribbean, South America, Africa, Europe and the Middle East, Asia, and Oceania.

Essential Climate Variables

J. REAGAN, J. BLUNDEN, AND R. J. H. DUNN

The following variables are considered fully monitored in this report, in that there are sufficient spatial and temporal data, with peer-reviewed documentation to characterize them on a global scale:

- Surface atmosphere: air pressure, precipitation, temperature, water vapor, wind speed and direction
- Upper atmosphere: Earth radiation budget, temperature, water vapor, wind speed and direction
- Atmospheric composition: carbon dioxide, methane and other greenhouse gases, ozone
- Ocean physics: ocean surface heat flux, sea ice, sea level, surface salinity, sea surface temperature, subsurface salinity, subsurface temperature, surface currents, surface stress
- Ocean biogeochemistry: ocean color
- Ocean biogeosystems: plankton
- Land: albedo, river discharge, snow

The following variables are considered partially monitored, in that there is systematic, rigorous measurement found in this report, but some coverage of the variable in time and space is lacking due to observing limitations or limited availability of data or authors:

- Atmospheric composition: aerosols properties, cloud properties, precursors of aerosol and ozone
- Upper atmosphere: lightning
- Ocean physics: subsurface currents
- Ocean biogeochemistry: inorganic carbon
- Land: above-ground biomass, anthropogenic greenhouse gas fluxes, fire, fraction of absorbed photosynthetically active radiation, glaciers, groundwater, ice sheets and ice shelves, lakes, permafrost, soil moisture, land surface temperature
- Surface atmosphere: surface radiation budget

The following variables are not yet covered in this report, or are outside the scope of it.

- Ocean physics: sea state
- Ocean biogeochemistry: nitrous oxide, nutrients, oxygen, transient tracers
- Ocean biogeosystems: marine habitat properties
- Land: anthropogenic water use, land cover, latent and sensible heat fluxes, leaf area index, soil carbon

Selected Significant Climate Anomalies and Events: Annual 2025

GLOBAL AVERAGE TEMPERATURE
The Jan–Dec 2025 global surface temperature was among the three highest since global records began in 1850.

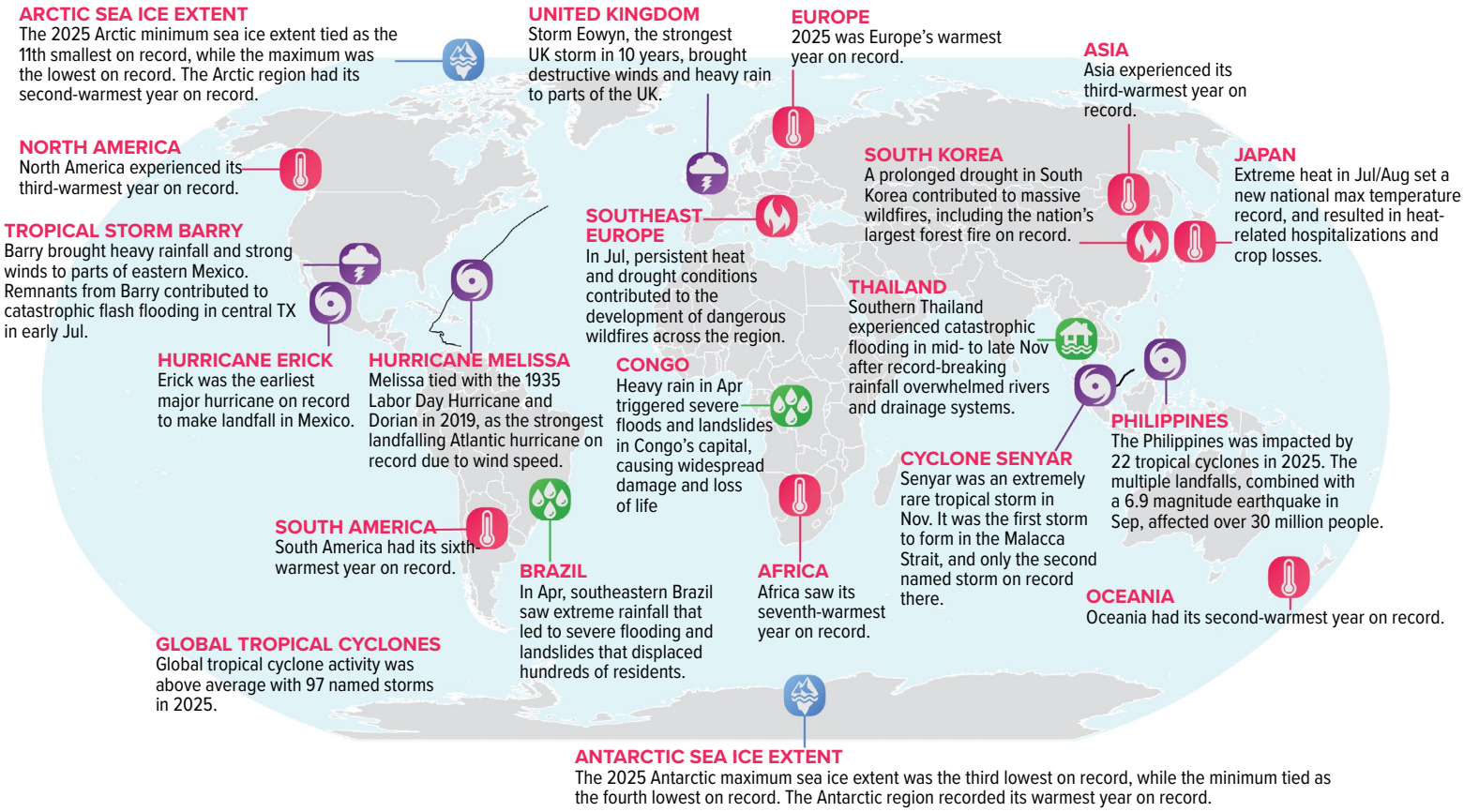

Please note: Material provided in this map was compiled from NOAA's State of the Climate Reports. For more information please visit: https://www.ncei.noaa.gov/access/monitoring/monthly-report/global/

Fig. 1.1. Geographical distribution of selected notable climate anomalies and events in 2025.

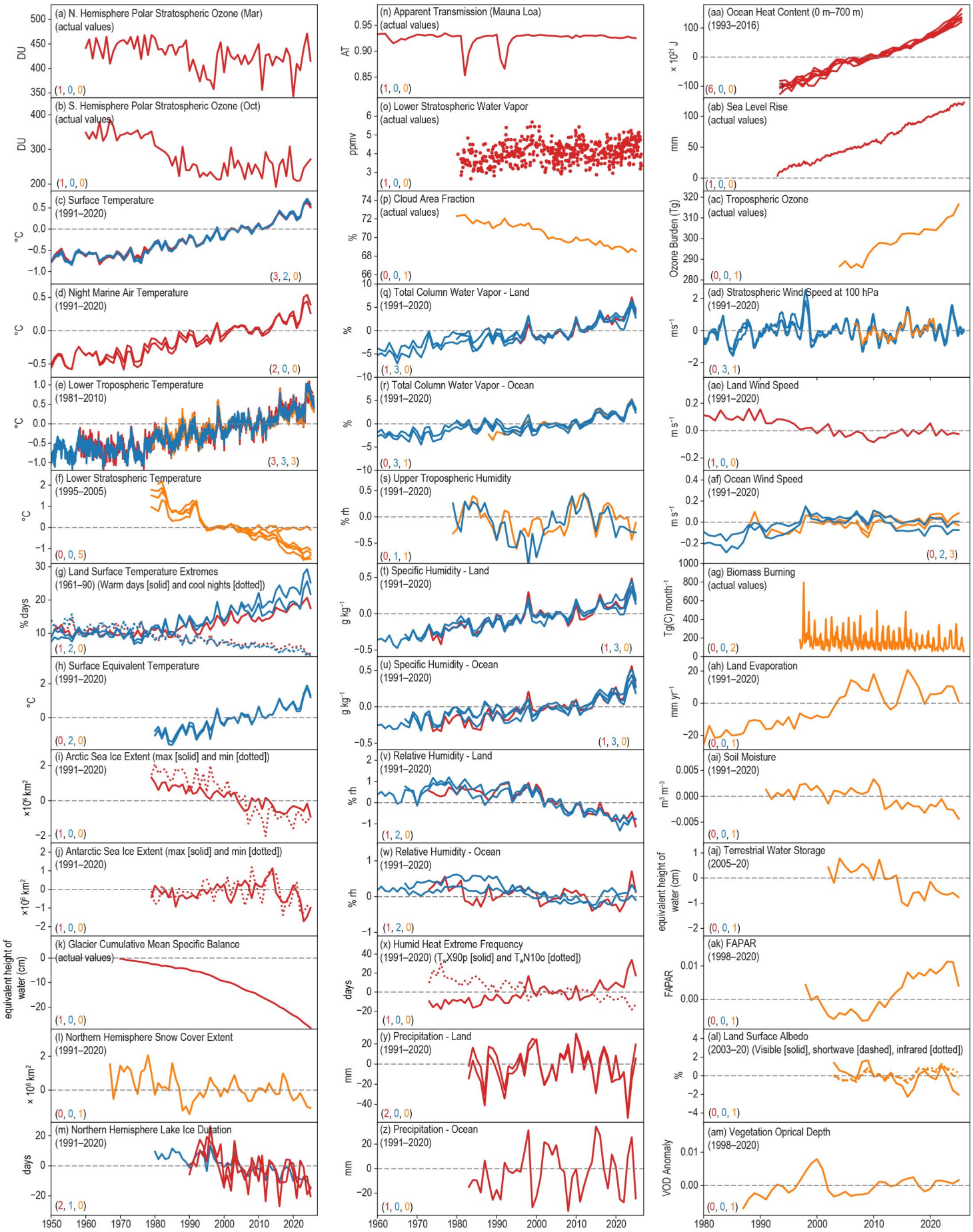
(a) N. Hemisphere Polar Stratospheric Ozone (Mar) (actual values)
(1, 0, 0)
(b) S. Hemisphere Polar Stratospheric Ozone (Oct) (actual values)
(1, 0, 0)
(c) Surface Temperature (1991–2020)
(3, 2, 0)
(d) Night Marine Air Temperature (1991–2020)
(2, 0, 0)
(e) Lower Tropospheric Temperature (1981–2010)
(3, 3, 3)
(f) Lower Stratospheric Temperature (1995–2005)
(0, 0, 5)
(g) Land Surface Temperature Extremes (1961–90) (Warm days [solid] and cool nights [dotted])
(1, 2, 0)
(h) Surface Equivalent Temperature (1991–2020)
(0, 2, 0)
(i) Arctic Sea Ice Extent (max [solid] and min [dotted]) (1991–2020)
(1, 0, 0)
(j) Antarctic Sea Ice Extent (max [solid] and min [dotted]) (1991–2020)
(1, 0, 0)
(k) Glacier Cumulative Mean Specific Balance (actual values)
(1, 0, 0)
(l) Northern Hemisphere Snow Cover Extent (1991–2020)
(0, 0, 1)
(m) Northern Hemisphere Lake Ice Duration (1991–2020)
(2, 1, 0)
(n) Apparent Transmission (Mauna Loa) (actual values)
(1, 0, 0)
(o) Lower Stratospheric Water Vapor (actual values)
(1, 0, 0)
(p) Cloud Area Fraction (actual values)
(0, 0, 1)
(q) Total Column Water Vapor - Land (1991–2020)
(1, 3, 0)
(r) Total Column Water Vapor - Ocean (1991–2020)
(0, 3, 1)
(s) Upper Tropospheric Humidity (1991–2020)
(0, 1, 1)
(t) Specific Humidity - Land (1991–2020)
(1, 3, 0)
(u) Specific Humidity - Ocean (1991–2020)
(1, 3, 0)
(v) Relative Humidity - Land (1991–2020)
(1, 2, 0)
(w) Relative Humidity - Ocean (1991–2020)
(1, 2, 0)
(x) Humid Heat Extreme Frequency (1991–2020) (T_wX90p [solid] and T_wN10o [dotted])
(1, 0, 0)
(y) Precipitation - Land (1991–2020)
(2, 0, 0)
(z) Precipitation - Ocean (1991–2020)
(1, 0, 0)
(aa) Ocean Heat Content (0 m–700 m) (1993–2016)
(6, 0, 0)
(ab) Sea Level Rise (actual values)
(1, 0, 0)
(ac) Tropospheric Ozone (actual values)
(0, 0, 1)
(ad) Stratospheric Wind Speed at 100 hPa (1991–2020)
(0, 3, 1)
(ae) Land Wind Speed (1991–2020)
(1, 0, 0)
(af) Ocean Wind Speed (1991–2020)
(0, 2, 3)
(ag) Biomass Burning (actual values)
(0, 0, 2)
(ah) Land Evaporation (1991–2020)
(0, 0, 1)
(ai) Soil Moisture (1991–2020)
(0, 0, 1)
(aj) Terrestrial Water Storage (2005–20)
(0, 0, 1)
(ak) FAPAR (1998–2020)
(0, 0, 1)
(al) Land Surface Albedo (2003–20) (Visible [solid], shortwave [dashed], infrared [dotted])
(0, 0, 1)
(am) Vegetation Oprical Depth (1998–2020)
(0, 0, 1)
Numbers of (In Situ, Reanalysis, Satellite) datasets shown in bottom left or right of each panel

Plate 1.1. Global (or representative) average time series for essential climate variables through 2025. Anomalies are shown relative to the base period in parentheses, although base periods used in other sections of the report may differ. The numbers in the parentheses in the lower left or right side of each panel indicate how many in situ (red), reanalysis (blue), and satellite (orange) datasets are used to create each time series, in that order. (a) Northern Hemisphere (NH) polar stratospheric ozone (Mar); (b) Southern Hemisphere polar stratospheric ozone (Oct); (c) surface temperature; (d) night marine air temperature; (e) lower tropospheric temperature; (f) lower stratospheric temperature; (g) land surface temperature extremes (warm days [TX90p, solid] and cool nights [TN10p, dotted]); (h) surface equivalent temperature; (i) Arctic sea ice extent (max [solid] and min [dotted]); (j) Antarctic sea ice extent (max [solid] and min [dotted]); (k) glacier cumulative mean specific balance; (l) NH snow cover extent; (m) NH lake ice duration; (n) Mauna Loa apparent transmission; (o) lower stratospheric water vapor; (p) cloud area fraction; (q) total column water vapor—land; (r) total column water vapor—ocean; (s) upper tropospheric humidity; (t) specific humidity—land; (u) specific humidity—ocean; (v) relative humidity—land; (w) relative humidity—ocean; (x) humid heat extreme frequency (days per year exceeding the 90th percentile of the climatological daily maximum wet-bulb temperature [TwX90p; solid] and days per year below the 10th percentile of the climatological daily-minimum wet-bulb temperature [TwN10p [dotted]); (y) precipitation—land; (z) precipitation—ocean; (aa) ocean heat content (0 m–700 m); (ab) sea level rise; (ac) tropospheric ozone; (ad) tropospheric wind speed at 850 hPa; (ae) land wind speed; (af) ocean wind speed; (ag) biomass burning; (ah) land evaporation; (ai) soil moisture; (aj) terrestrial groundwater storage; (ak) fraction of absorbed photosynthetically active radiation (FAPAR); (al) land surface albedo—visible (solid) and infrared (dotted); (am) vegetation optical depth.

Acknowledgments

The editors thank the BAMS editorial staff, in particular Bryan Hanssen, who provided technical guidance and oversaw publication of the report; Colleen Gaffney, who provided peer review support; Jess LaPointe, who oversaw the hundreds of citations and references this year; and the NCEI Graphics team for facilitating the construction of the report and executing the countless number of technical edits needed. We thank our technical editors Lukas Noguchi and Laura Ohlmann for their dedication and attention to detail. We also express our gratitude to Dr. Timothy DelSole, who served as the AMS special editor for this report. Finally, we thank all of the authors and chapter editors who provide these valuable contributions each year, always with an aim to improve and expand their analyses for the readers, as well as the many peer reviewers who dedicate their time and expertise to provide thoughtful feedback that continually helps evolve the report. Several authors and chapter editors retired prematurely and unexpectedly this year, many with multiple decades of contributions to this report. We thank them for their unwavering dedication to expanding our scientific knowledge and for sharing their work with us.

STATE OF THE CLIMATE IN 2025

GLOBAL CLIMATE

R. J. H. Dunn, J. Blannin, N. Gobron, and G. Morris, Eds.

Special Online Supplement to the *Bulletin of the American Meteorological Society* Vol. 107, No. 8, August, 2026

https://doi.org/10.1175/BAMS-D-26-0141.1
Corresponding author: Robert Dunn / robert.dunn@metoffice.gov.uk
©2026 American Meteorological Society
For information regarding reuse of this content and general copyright information, consult the AMS Copyright Policy.

STATE OF THE CLIMATE IN 2025
Global Climate

Editors

Jessica Blunden
James Reagan

Chapter Editors

Anthony Arguez
Josh Blannin
Peter Bissolli
Kyle R. Clem
Howard J. Diamond
Matthew L. Druckenmiller
Robert J. H. Dunn
Catherine Ganter
Nadine Gobron
Rodney Martinez
Twila A. Moon
Gary A. Morris
Marilyn N. Raphael
Renellys C. Perez
Carl J. Schreck III
Zewdu Segele
Laura Stevens
Richard L. Thoman
Denis L. Volkov
Zhiwei Zhu

Technical Editors

Lukas Noguchi
Laura Ohlmann

BAMS Special Editor for Climate

Timothy DelSole

American Meteorological Society

Cover Credit:
Image of the aftermath of a rockfall from the Kleines Nesthorn and Birch Glacier which destroyed large parts of the village of Blatten, Valais, Switzerland on 28th May 2025. A round callout image portrays a closeup view of the rockslide covering most of Blatten. Credit: Swisstopo Rapid Mapping.

How to cite this document:
Global Climate is one chapter from the *State of the Climate in 2025* annual report and is available from https://doi.org/10.1175/BAMS-D-26-0141.1. Compiled by NOAA's National Centers for Environmental Information, *State of the Climate in 2025* is based on contributions from scientists from around the world. It provides a detailed update on global climate indicators, notable weather events, and other data collected by environmental monitoring stations and instruments located on land, water, ice, and in space. The full report is available from https://doi.org/10.1175/2026BAMSStateoftheClimate.1.

Citing the complete report:
Blunden, J. and J. Reagan, Eds., 2026: "State of the Climate in 2025". Bull. Amer. Meteor. Soc., 107 (8), Si–S512, https://doi.org/10.1175/2026BAMSStateoftheClimate.1.

Citing this chapter:
Dunn, R. J. H., J. Blannin, N. Gobron, and G. Morris, Eds., 2026: Global Climate [in "State of the Climate in 2025"]. Bull. Amer. Meteor. Soc., 107 (8), S12–S152, https://doi.org/10.1175/BAMS-D-26-0141.1.

Citing a section (example):
Carrea, L., C. J. Merchant, L. McNamara, J.-F. Creatux, T. M. Dokulil, H. Dugan, A. Laas, E. Leibensperger, S.-I. Matsuzaki, D. Pierson, M. Pulkkanen, A. Räike, O. O. Rusanovskaya, R. Shinohara, S. V. Shimaraeva, E. A. Silow, M. Schmid, M. A. Timofeyev, P. Verburg, and R. I. Woolway, 2026: Lake surface water temperature [in "State of the Climate in 2025"]. Bull. Amer. Meteor. Soc., 107 (8), S30–S30, https://doi.org/10.1175/BAMS-D-26-0141.1.

Editor and Author Affiliations (alphabetical by name)

Ades, Melanie, European Centre for Medium-Range Weather Forecasts, Reading, United Kingdom

Adler, Robert, Earth System Science Interdisciplinary Center, University of Maryland, College Park, Maryland

Allan, Richard P., National Centre for Earth Observation (NCEO), University of Leicester, Leicester, United Kingdom; University of Reading, Reading, United Kingdom

Anneville, Orlane, Université Savoie Mont Blanc, INRAE, CARRTEL, Thonon-les-Bains, France

Aono, Yasuyuki, Graduate School of Agriculture, Osaka Metropolitan University, Sakai, Japan

Arguez, Anthony, NOAA/NESDIS National Centers for Environmental Information, Asheville, North Carolina

Armenteras, Dolors, Instituto de Ciencias Forestales (ICIFOR-INIA), Consejo Superior De Investigaciones Científicas (CSIC), Madrid, Spain; Science Faculty, Universidad Nacional de Colombia, Bogotá, Colombia

Arosio, Carlo, University of Bremen, Bremen, Germany

Asher, Elizabeth, Cooperative Institute for Research in Environmental Sciences, University of Colorado Boulder, Boulder, Colorado; NOAA Global Monitoring Laboratory, Boulder, Colorado

Augustine, John A., NOAA Global Monitoring Laboratory, Retired, Boulder, Colorado

Azorin-Molina, Cesar, Centro de Investigaciones sobre Desertificación – Spanish National Research Council (CSIC-UV-GVA), Valencia, Spain

Baez-Villanueva, Oscar M., Hydro-Climate Extremes Lab (H-CEL), Ghent University, Ghent, Belgium

Barichivich, Jonathan, Laboratoire des Sciences du Climat et de l'Environnement (LSCE), LSCE/IPSL, CEA-CNRS-UVSQ, Gif-sur-Yvette, France

Beck, Hylke E., Physical Science and Engineering Division, King Abdullah University of Science and Technology, Thuwal, Saudi Arabia

Bellouin, Nicolas, University of Reading, Reading, United Kingdom; Institute Pierre Simon Laplace (IPSL), Guyancourt, France

Blannin, Josh, Met Office Hadley Centre, Exeter, United Kingdom

Bock, Olivier, Univ Gustave Eiffel, Géodata Paris, IGN, Paris, France; Université Paris Cité, Institut de physique du globe de Paris, CNRS, IGN, Paris, France

Bonte, Olivier, Hydro-Climate Extremes Lab (H-CEL), Ghent University, Ghent, Belgium

Bosilovich, Michael G., Global Modeling and Assimilation Office, NASA Goddard Space Flight Center, Greenbelt, Maryland

Bowman, Kevin, Jet Propulsion Laboratory, California Institute of Technology, Pasadena, California

Buehler, Stefan, Universität Hamburg, Hamburg, Germany

Bunno, Ayaka, Japan Meteorological Agency, Tokyo, Japan

Byrne, Michael P., University of St Andrews, St Andrews, Fife, United Kingdom

Campos, Diego, Barcelona Supercomputing Centre, Barcelona, Spain

Cappucci, Fabrizio, European Commission Joint Research Centre, Ispra, Italy

Carere, Francesco, Hydro-Climate Extremes Lab (H-CEL), Ghent University, Ghent, Belgium

Carrea, Laura, University of Reading, Reading, United Kingdom

Casado-Rodríguez, Jesús, KAjO Services, Bytča, Slovakia

Chan, Steven, National Oceanography Centre, Southampton, United Kingdom

Chang, Kai-Lan, Cooperative Institute for Research in Environmental Sciences, University of Colorado Boulder, Boulder, Colorado; NOAA Chemical Sciences Laboratory, Boulder, Colorado

Christiansen, Hanne H., Department of Environmental Science, Aarhus University, Roskilde, Denmark

Chung, Eui-Seok, Korea Polar Research Institute, Incheon, South Korea

Ciasto, Laura M., NOAA/NWS National Centers for Environmental Prediction Climate Prediction Center, College Park, Maryland

Clingan, Scott, Cooperative Institute for Research in Earth Science, University of Colorado, Boulder, Colorado

Coldewey-Egbers, Melanie, German Aerospace Center (DLR), Oberpfaffenhofen, Germany

Cooper, Owen R., NOAA Chemical Sciences Laboratory, Boulder, Colorado

Cornes, Richard C., National Oceanography Centre, Southampton, United Kingdom

Covey, Curt, Lawrence Livermore National Laboratory, Livermore, California

Crimmins, Theresa, USA National Phenology Network, School of Natural Resources and the Environment, University of Arizona, Tucson, Arizona

Crotwell, Molly, Cooperative Institute for Research in Environmental Sciences, University of Colorado, Boulder, Boulder, Colorado

Crétaux, Jean-Francois, LEGOS (CNES/CNRS/IRD/UPS), Université de Toulouse, Toulouse, France

Culpepper, Joshua, Department of Biology, York University, Toronto, Ontario, Canada

Danzer, Julia, Wegener Center for Climate and Global Change, University of Graz, Graz, Austria

Davis, Sean M., NOAA Chemical Sciences Laboratory, Boulder, Colorado

de Jeu, Richard A. M., Transmissivity B.V., Alphen aan den Rijn, The Netherlands

de Laat, Jos, Royal Netherlands Meteorological Institute (KNMI), De Bilt, The Netherlands

Degenstein, Doug, University of Saskatchewan, Saskatoon, Canada

Delbare, Kwint, Hydro-Climate Extremes Lab (H-CEL), Ghent University, Ghent, Belgium

Di Tomaso, Enza, European Centre for Medium-Range Weather Forecasts, Bonn, Germany

DiGangi, Elizabeth, AEM R&D, Germantown, Maryland

Dokulil, Martin T., Research Institute for Limnology, University of Innsbruck, Mondsee, Austria

Donat, Markus G., Barcelona Supercomputing Centre, Barcelona, Spain; Catalan Institution for Research and Advanced Studies (ICREA), Barcelona, Spain

Dorigo, Wouter A., Department of Geodesy and Geoinformation, TU Wien, Vienna, Austria

Dostalova, Alena, EODC GmbH, Vienna, Austria

Duchemin, Diane, CESBIO, Université de Toulouse, CNES/CNRS/INRAe/IRD/UPS, Toulouse, France

Dugan, Hilary, Center of Limnology, University of Wisconsin-Madison, Madison, Wisconsin

Dunn, Robert J. H., Met Office Hadley Centre, Exeter, United Kingdom

Dutton, Geoff, Cooperative Institute for Research in Environmental Sciences, University of Colorado, Boulder, Boulder, Colorado

Effertz, Peter, Cooperative Institute for Research in Environmental Sciences, University of Colorado Boulder, Boulder, Colorado; NOAA Global Monitoring Laboratory, Boulder, Colorado

Estilow, Thomas W., Rutgers University, Piscataway, New Jersey

Estrella, Nicole, Ecoclimatology, Department of Life Science Systems, TUM School of Life Sciences, Technical University of Munich, Freising, Germany

Fereday, David, Met Office Hadley Centre, Exeter, United Kingdom

Fioletov, Vitali E., Environment and Climate Change Canada, Toronto, Ontario, Canada

Flemming, Johannes, European Centre for Medium-Range Weather Forecasts, Bonn, Germany

Flynn, Lawrence E., NOAA/NESDIS Center for Satellite Applications and Research, College Park, Maryland

Formanek, Maud, Department of Geodesy and Geoinformation, TU Wien, Vienna, Austria

Foster, Michael J., Cooperative Institute for Meteorological Satellite Studies, Space Science and Engineering Center, University of Wisconsin-Madison, Madison, Wisconsin

Frederikse, Thomas, Planet Labs, Haarlem, The Netherlands

Editor and Author Affiliations (continued)

Friedman, A. R., Climatic Research Unit, School of Environmental Sciences, University of East Anglia, Norwich, United Kingdom; National Centre for Atmospheric Science (NCAS), University of East Anglia, Norwich, United Kingdom

Frith, Stacey M., Adnet Systems, Inc., Lanham, Maryland; NASA Goddard Space Flight Center, Greenbelt, Maryland

Froidevaux, Lucien, Jet Propulsion Laboratory, California Institute of Technology, Pasadena, California; Retired, Pasadena, California

Füllekrug, Martin, University of Bath, Bath, United Kingdom

Gallemann, Thomas, Bavarian Environment Agency, Augsburg, Germany

Ghent, Darren, National Centre for Earth Observation (NCEO), University of Leicester, Leicester, United Kingdom; School of Physics and Astronomy, University of Leicester, Leicester, United Kingdom

Gobron, Nadine, European Commission Joint Research Centre, Ispra, Italy

Godin-Beekmann, Sophie, LATMOS/IPSL, Sorbonne Universite, Paris, France

Good, Elizabeth, Met Office Hadley Centre, Exeter, United Kingdom

Goodman, Steven, Thunderbolt Global Analytics, Huntsville, Alabama

Goto, Atsushi, Japan Meteorological Agency, Tokyo, Japan

Grimaldi, Stefania, European Commission Joint Research Centre, Ispra, Italy

Gruber, Alexander, Department of Geodesy and Geoinformation, TU Wien, Vienna, Austria

Gu, Guojun, Earth System Science Interdisciplinary Center, University of Maryland, College Park, Maryland

Guglielmin, Mauro, Department of Theoretical and Applied Sciences, Insubria University, Varese, Italy

Hahn, Sebastian, Department of Geodesy and Geoinformation, TU Wien, Vienna, Austria

Haimberger, Leopold, Department of Meteorology and Geophysics, University of Vienna, Vienna, Austria

Harder, Paula, European Centre for Medium-Range Weather Forecasts, Bonn, Germany

Harlan, Merritt E., U.S. Geological Survey, Denver, Colorado

Harris, Bethan L., National Centre for Earth Observation, UK Centre for Ecology & Hydrology, Wallingford, United Kingdom

Harris, Ian, Climatic Research Unit, School of Environmental Sciences, University of East Anglia, Norwich, United Kingdom

Hemming, Deborah L., Met Office Hadley Centre, Exeter, United Kingdom

Holliday, Rebecca, Met Office, Exeter, United Kingdom

Holzworth, Robert, University of Washington, Seattle, Washington

Horton, Radley M., Columbia Climate School, Columbia University, New York, New York; Lamont-Doherty Earth Observatory, Columbia University, Palisades, New York

Hrbáček, Filip, Department of Geography, Masaryk University, Brno, Czech Republic

Hu, Guojie, Cryosphere Research Station on Qinghai-Tibet Plateau, Northwestern Institute of Eco-Environment and Resources, CAS, Beijing, China

Hutchins, Benjamin W., University of Reading, Reading, United Kingdom

Inness, Antje, European Centre for Medium-Range Weather Forecasts, Reading, United Kingdom

Isaksen, Ketil, Climate and Environment Department, Norwegian Meteorological Institute, Oslo, Norway

Ishibumi, Nozomi, Japan Meteorological Agency, Tokyo, Japan

John, Viju O., EUMETSAT, Darmstadt, Germany

Jones, Philip D., Climatic Research Unit, School of Environmental Sciences, University of East Anglia, Norwich, United Kingdom

Junod, Robert, Earth System Science Center, University of Alabama in Huntsville, Huntsville, Alabama

Kaiser, Johannes W., NILU, Kjeller, Norway

Kalluri, Satya, NOAA Office of Low Earth Observations, Greenbelt, Maryland

Kent, Elizabeth C., National Oceanography Centre, Southampton, United Kingdom

Khaykin, Sergey, Laboratoire Atmosphères, Observations Spatiales (LATMOS), UVSQ, Sorbonne Université, CNRS, IPSL, Guyancourt, France

Kirchner, Nina, Department of Physical Geography, Stockholm University, Stockholm, Sweden; Tarfala Research Station, Stockholm University, Stockholm, Sweden

Kondragunta, Shobha, NOAA/NESDIS Center for Satellite Applications and Research, College Park, Maryland

Kovács, Dávid D., U.S. Geological Survey, Portland, Oregon

Kraemer, Benjamin M., University of Freiburg, Freiburg, Germany

Kuniyuki, Darryl T., NOAA/OAR Global Monitoring Laboratory, Hilo, Hawaii

Laas, Alo, Institute of Agricultural and Environmental Sciences, Estonian University of Life Sciences, Tartu, Estonia

Lan, Xin, Cooperative Institute for Research in Environmental Sciences, University of Colorado Boulder, Boulder, Colorado; NOAA Global Monitoring Laboratory, Boulder, Colorado

Lapierre, Jeff, AEM R&D, Germantown, Maryland

Laughner, Joshua L., Jet Propulsion Laboratory, California Institute of Technology, Pasadena, California

Leblanc, Thierry, JPL Table Mountain Facility, Wrightwood, California

Leibensperger, Eric, Department of Physics and Astronomy, Ithaca College, Ithaca, New York

Lems, Johanna, Department of Geodesy and Geoinformation, TU Wien, Vienna, Austria

Liley, Ben, New Zealand Institute for Earth Science Limited, Lauder, New Zealand

Lo, Y. T. Eunice, Cabot Institute for the Environment, University of Bristol, Bristol, United Kingdom

Loeb, Norman G., NASA Langley Research Center, Hampton, Virginia

Loyola, Diego, German Aerospace Center (DLR), Oberpfaffenhofen, Germany

Magnin, Florence, Laboratoire EDYTEM, CNRS/Université Savoie Mont-Blanc, Le Bourget-du-Lac, France

Maillard-Barras, Eliane, MeteoSwiss, Payerne, Switzerland

Marshall, Alex, Woodland Trust, Grantham, United Kingdom

Massant, Joppe, Hydro-Climate Extremes Lab (H-CEL), Ghent University, Ghent, Belgium

Matsuzaki, Shin-Ichiro, National Institute for Environmental Studies, Tsukuba, Ibaraki, Japan

Matthews, Jessica L., NOAA/NESDIS National Centers for Environmental Information, Asheville, North Carolina

Matthews, Tom, King's College London, United Kingdom

Mayer, Michael, U.S. Geological Survey, Portland, Oregon

McNamara, Laura, University of Reading, Reading, United Kingdom

McVicar, Tim R., CSIRO Environment, Canberra, Australia

Mears, Carl A., Remote Sensing Systems, Santa Rosa, California

Menzel, Annette, Ecoclimatology, Department of Life Science Systems, TUM School of Life Sciences, Technical University of Munich, Freising, Germany; Institute for Advanced Study, Technical University of Munich, Garching, Germany

Merchant, Christopher J., University of Reading, Reading, United Kingdom

Meyer, Michael F., U.S. Geological Survey, Portland, Oregon

Miralles, Diego G., Hydro-Climate Extremes Lab (H-CEL), Ghent University, Ghent, Belgium

Moldenhauer, Colin, Department of Geodesy and Geoinformation, TU Wien, Vienna, Austria

Monerie, Paul-Arthur, National Centre for Atmospheric Science, Reading, United Kingdom

Montzka, Stephen A., NOAA Global Monitoring Laboratory, Boulder, Colorado

Morice, Colin P., Met Office Hadley Centre, Exeter, United Kingdom

Editor and Author Affiliations (continued)

Morino, Isamu, National Institute for Environmental Studies, Tsukuba, Ibaraki, Japan

Morris, Gary, NOAA Global Monitoring Laboratory, Boulder, Colorado

Mrekaj, Ivan, Technical University in Zvolen, Zvolen, Slovakia

Mühle, Jens, Scripps Institution of Oceanography, San Diego, California

Nance, David, Cooperative Institute for Research in Environmental Sciences, University of Colorado, Boulder, Boulder, Colorado

Nicolas, Julien P., European Centre for Medium-Range Weather Forecasts, Bonn, Germany

Noetzli, Jeannette, Climate Change, Extremes and Natural Hazards in Alpine Regions Research Centre (CERC), Davos Dorf, Switzerland; WSL Institute for Snow and Avalanche Research SLF, Davos Dorf, Switzerland

Osborn, Timothy J., Climatic Research Unit, School of Environmental Sciences, University of East Anglia, Norwich, United Kingdom

O'Keefe, John, The Harvard Forest, Harvard University, Petersham, Massachusetts

Parrington, Mark, European Centre for Medium-Range Weather Forecasts, Bonn, Germany

Payne, Vivienne H., Jet Propulsion Laboratory, California Institute of Technology, Pasadena, California

Pelto, Mauri, Nichols College, Dudley, Massachusetts

Petersen, Kyle, Cooperative Institute for Research in Environmental Sciences, University of Colorado, Boulder, Boulder, Colorado

Petropavlovskikh, Irina, Cooperative Institute for Research in Environmental Sciences, University of Colorado Boulder, Boulder, Colorado; NOAA Global Monitoring Laboratory, Boulder, Colorado

Phillips, Coda, Cooperative Institute for Meteorological Satellite Studies, Space Science and Engineering Center, University of Wisconsin-Madison, Madison, Wisconsin

Pierson, Don, Department of Ecology and Genetics, Uppsala University, Uppsala, Sweden

Pilch-Kedzierski, Robin, Department of Meteorology and Geophysics, University of Vienna, Vienna, Austria

Po-Chedley, Stephen, Lawrence Livermore National Laboratory, Livermore, California

Pogliotti, Paolo, Environmental Protection Agency of Valle d'Aosta, Saint Christophe, Italy

Polvani, Lorenzo, Columbia University, New York, New York

Prajapati, Richa, CESBIO, Université de Toulouse, CNES/CNRS/INRAe/IRD/UPS, Toulouse, France

Preimesberger, Wolfgang, Department of Geodesy and Geoinformation, TU Wien, Vienna, Austria

Price, Colin, Tel Aviv University, Tel Aviv, Israel

Pulkkanen, Merja, Finnish Environment Institute (SYKE), Helsinki, Finland

Quagraine, Kwesi A., National Center for Atmospheric Research, Boulder, Colorado

Querel, Richard, Earth Sciences New Zealand, Lauder, New Zealand

Randel, William J., NSF National Center for Atmospheric Research, Boulder, Colorado

Raymond, Colin, Joint Institute for Regional Earth System Science and Engineering, University of California, Los Angeles, Los Angeles, California

Reiter, Annika, Wegener Center for Climate and Global Change, University of Graz, Graz, Austria

Remy, Samuel, HYGEOS, Lille, France

Ricciardulli, Lucrezia, Remote Sensing Systems, Santa Rosa, California

Richardson, Andrew D., Center for Ecosystem Science and Society, Northern Arizona University, Flagstaff, Arizona; School of Informatics, Computing, and Cyber Systems, Northern Arizona University, Flagstaff, Arizona

Riedl, Claudia, GeoSphere Austria, Salzburg, Austria

Riihimaki, Laura D., Cooperative Institute for Research in Environmental Sciences, University of Colorado Boulder, Boulder, Colorado; NOAA Global Monitoring Laboratory, Boulder, Colorado

Robinson, David A., Rutgers University, Piscataway, New Jersey

Rodell, Matthew, NASA Goddard Space Flight Center, Greenbelt, Maryland

Rodriguez-Fernandez, Nemesio, CESBIO, Université de Toulouse, CNES/CNRS/INRAe/IRD/UPS, Toulouse, France

Rogers, Cassandra D. W., Bureau of Meteorology, Melbourne, Australia

Rohini, P., India Meteorological Department, Pune, India

Rosenlof, Karen H., NOAA Chemical Sciences Laboratory, Boulder, Colorado; Retired, Boulder, Colorado

Rozanov, Alexei, University of Bremen, Bremen, Germany

Rozkošný, Jozef, Slovak Hydrometeorological Institute, Bratislava, Slovakia

Rusanovskaya, Olga O., Irkutsk State University, Institute of Lake Baikal Biology, Irkutsk, Russia

Russo, Emmanuele, European Centre for Medium-Range Weather Forecasts, Bonn, Germany

Rutishauser, This, Swiss Academy of Sciences (SCNAT), Bern, Switzerland

Räike, Antti, Finnish Environment Institute (SYKE), Helsinki, Finland

Said, Ryan, Vaisala R&D, Louisville, Colorado

Sakai, Tetsu, Meteorological Research Institute, Japan Meteorological Agency, Tsukuba, Ibaraki, Japan

Salamon, Peter, European Commission Joint Research Centre, Ispra, Italy

Sánchez-Lugo, Ahira, NOAA/NESDIS National Centers for Environmental Information, Asheville, North Carolina

Santee, Michelle L., Jet Propulsion Laboratory, California Institute of Technology, Pasadena, California

Sawaengphokhai, Parnchai, ADNET Systems, Inc., Hampton, Virginia

Schaffhauser, Timo, European Commission Joint Research Centre, Ispra, Italy

Schenzinger, Verena, India Meteorological Department, Pune, India

Schmid, Martin, Eawag, Department Surface Waters - Research and Management, Kastanienbaum, Switzerland

Sharma, Sapna, Department of Biology, York University, Toronto, Ontario, Canada

Shimaraeva, Svetlana V., Irkutsk State University, Institute of Lake Baikal Biology, Irkutsk, Russia

Shinohara, Ryuichiro, Regional Environment Conservation Division, National Institute for Environmental Studies, Tsukuba, Ibaraki, Japan

Shinohara, Ryuichiro, National Institute for Environmental Studies, Tsukuba, Ibaraki, Japan

Siddons, Joseph, National Oceanography Centre, Southampton, United Kingdom

Silow, Eugene A., Irkutsk State University, Institute of Lake Baikal Biology, Irkutsk, Russia

Simmons, Adrian J., European Centre for Medium-Range Weather Forecasts, Reading, United Kingdom

Smith, Sharon L., Geological Survey of Canada, Natural Resources Canada, Ottawa, Canada

Soden, Brian J., University of Miami, Miami, Florida

Sofieva, Viktoria, Finnish Meteorological Institute, Helsinki, Finland

Soldo, Logan, Cooperative Institute for Research in Environmental Sciences, University of Colorado Boulder, Boulder, Colorado; NOAA Global Monitoring Laboratory, Boulder, Colorado

Sreejith, O. P., India Meteorological Department, Pune, India

Stackhouse, Jr., NASA Langley Research Center, Hampton, Virginia

Stauffer, Ryan M., Atmospheric Chemistry and Dynamics Laboratory, NASA Goddard Space Flight Center, Greenbelt, Maryland

Steinbrecht, Wolfgang, Deutscher Wetterdienst, Hohenpeissenberg, Germany

Steiner, Andrea K., Wegener Center for Climate and Global Change, University of Graz, Graz, Austria

Stoy, Paul, University of Wisconsin–Madison, Madison, Wisconsin

Streletskiy, Dmitry A., George Washington University, Washington, District of Columbia

Editor and Author Affiliations (continued)

Sun, Qiaohong, State Key Laboratory of Climate System Prediction and Risk Management, Nanjing University of Information Science and Technology, Nanjing, China

Taha, Ghassan, Morgan State University, Baltimore, Maryland; NASA Goddard Space Flight Center, Greenbelt, Maryland

Thackeray, Stephen J., United Kingdom Centre for Ecology & Hydrology, Lancaster, United Kingdom

Timofeyev, Maxim A., Irkutsk State University, Institute of Lake Baikal Biology, Irkutsk, Russia

Tourpali, Kleareti, Aristotle University, Thessaloniki, Greece

Urraca, Ruben, European Commission Joint Research Centre, Ispra, Italy

van der A, Ronald, Royal Netherlands Meteorological Institute (KNMI), De Bilt, The Netherlands

van der Schrier, Gerard, Royal Netherlands Meteorological Institute, De Bilt, The Netherlands

Veal, Karen, National Centre for Earth Observation (NCEO), University of Leicester, Leicester, United Kingdom; School of Physics and Astronomy, University of Leicester, Leicester, United Kingdom

Verburg, Piet, School of Geography, Environment and Earth Sciences, Victoria University of Wellington, Wellington, New Zealand

Vernier, Jean-Paul, NASA Langley Research Center, Hampton, Virginia

Vicencio, José, University of Cologne, Cologne, Germany

Vimont, Isaac J., NOAA Global Monitoring Laboratory, Boulder, Colorado

Virts, Katrina, University of Alabama in Huntsville, Huntsville, Alabama

Vose, Russell S., NOAA/NESDIS National Centers for Environmental Information, Asheville, North Carolina

Vömel, Holger, National Center for Atmospheric Research, Boulder, Colorado

Wang, Ray H. J., Georgia Institute of Technology, Atlanta, Georgia

Waring, Abigail Marie, National Centre for Earth Observation (NCEO), University of Leicester, Leicester, United Kingdom; School of Physics and Astronomy, University of Leicester, Leicester, United Kingdom

Warnock, Taran, University of Saskatchewan, Saskatoon, Canada

Weber, Mark, University of Bremen, Bremen, Germany

Wei, Zigang, Science and Technology Corporation (STC), College Park, Maryland

Weiss, Philipp, European Centre for Medium-Range Weather Forecasts, Bonn, Germany

Wiese, David N., Jet Propulsion Laboratory, California Institute of Technology, Pasadena, California

Wild, Jeannette D., Earth System Science Interdisciplinary Center, University of Maryland, College Park, Maryland; NOAA/NESDIS Center for Satellite Applications and Research, College Park, Maryland; Retired, College Park, Maryland

Willett, Kate M., Met Office Hadley Centre, Exeter, United Kingdom

Williams, Earle, Massachusetts Institute of Technology, Cambridge, Massachusetts

Wood, Tom, King's College London, United Kingdom

Woolway, Richard Iestyn, School of Ocean Sciences, Bangor University, Bangor, United Kingdom

Xu, Kuan-Man, NASA Langley Research Center, Hampton, Virginia

Yang, Kai, Department of Atmospheric and Oceanic Sciences, University of Maryland, College Park, Maryland

Yin, Xungang, NOAA/NESDIS National Centers for Environmental Information, Asheville, North Carolina

Zeng, Zhenzhong, School of Environmental Science and Engineering, Southern University of Science and Technology, Shenzhen, China

Zhang, Wenxia, School of Atmospheric Sciences, Nanjing University, Nanjing, China

Zhao, Lin, School of Geographical Sciences, Nanjing University of Information Science and Technology, Nanjing, China

Ziemke, Jerry R., Goddard Earth Sciences Technology and Research, Morgan State University, Baltimore, Maryland; NASA Goddard Space Flight Center, Greenbelt, Maryland

Ziese, Markus, Global Precipitation Climatology Centre, Deutscher Wetterdienst, Offenbach, Germany

Zotta, Ruxandra-Maria, TU Wien, Vienna, Austria

Zou, Cheng-Zhi, George Mason University, Fairfax, Virginia

Editorial and Production Team

Allen, Jessicca, Graphics Support, Cooperative Institute for Satellite Earth System Studies, North Carolina State University, Asheville, North Carolina

Camper, Amy V., Graphics Support, Innovative Consulting and Management Services, LLC, NOAA/NESDIS National Centers for Environmental Information, Asheville, North Carolina

Carroll, Lauren, Content Team Lead, Communications and Outreach, NOAA/NESDIS National Centers for Environmental Information, Asheville, North Carolina

Crossman, Jacquelyn, NCEI Librarian, MPF-ZAI, NOAA/NESDIS National Centers for Environmental Information, Asheville, North Carolina

Haley, Bridgette O., Graphics Support, NOAA/NESDIS National Centers for Environmental Information, Asheville, North Carolina

Noguchi, Lukas, Technical Editor, Innovative Consulting and Management Services, LLC, NOAA/NESDIS National Centers for Environmental Information, Asheville, North Carolina

Ohlmann, Laura, Technical Editor, Innovative Consulting and Management Services, LLC, NOAA/NESDIS National Centers for Environmental Information, Asheville, North Carolina

Veasey, Sara W., Visual Communications Team Lead, Communications and Outreach, NOAA/NESDIS National Centers for Environmental Information, Asheville, North Carolina

2. Table of Contents

List of authors and affiliations S15

a. Overview S21

b. Temperature S29

1. Surface temperature S29
2. Lake surface water temperature S30
3. Night marine air temperature S32
4. Land surface temperature extremes S34
5. Tropospheric temperature S37
6. Stratospheric temperature S39
7. Equivalent temperature S39
8. Maximum land surface temperature S42

c. Cryosphere S44

1. Permafrost temperature and active layer thickness S44
2. Alpine glaciers S46
3. Lake ice S47
4. Northern Hemisphere continental snow cover extent S49

d. Hydrological cycle (atmosphere) S51

1. Near-surface humidity S51
2. Humid-heat extremes over land S53
3. Total column water vapor S56
4. Upper tropospheric humidity S58
5. Precipitation S59
6. Land surface precipitation extremes S60
7. Cloudiness S62

d. Hydrological cycle (land) S64

8. Lake water storage and level S64
9. River discharge and runoff S65
10. Groundwater and terrestrial water storage S68
11. Soil moisture S70
12. Monitoring global drought using the self-calibrating Palmer Drought Severity Index S71
13. Land evaporation S72

e. Atmospheric circulation S75

1. Mean sea level pressure and related modes of variability S75
2. Land and ocean surface winds S76
3. Upper air winds S79
4. Lightning S81

f. Earth radiation budget S83

1. Earth radiation budget at top-of-atmosphere S83
2. Mauna Loa apparent transmission record update for 2025 ..... S84

2. Table of Contents

g. Atmospheric composition S87
1. Long-lived greenhouse gases S87
2. Ozone-depleting gases S90
3. Tropospheric aerosols S91
4. Tropospheric ozone S94
5. Stratospheric aerosols S97
6. Stratospheric ozone S100
7. Stratospheric water vapor S103
8. Carbon monoxide S105

h. Land Surface Properties S107
1. Terrestrial surface albedo dynamics S107
2. Terrestrial vegetation dynamics S108
3. Biomass burning S110
4. Phenology of primary producers S112
5. Vegetation optical depth S115

Acknowledgments S117
Appendix 1: Acronyms S122
Appendix 2: Dataset Tables S127
Appendix 3: Supplemental Materials S140
References S153

2. GLOBAL CLIMATE

R. J. H. Dunn, J. Blannin, N. Gobron, and G. Morris, Eds.

a. Overview

—R. J. H. Dunn, J. Blannin, N. Gobron, and G. Morris

In a year without El Niño conditions, global average surface temperatures still placed 2025 in the top three years in the instrumental record (since at least 1850). This was higher than all other years except 2023 and 2024, which were affected by El Niño conditions. The last 11 years (2015–25) were also the warmest 11 years in the record, according to all five assessed datasets. Annual nighttime marine air temperature and equivalent temperature were both third highest for their respective records. Globally averaged temperature extremes over land had the third largest number of warm days, behind 2023 and 2024, and the second lowest number of cool days. Temperatures in the lower troposphere were elevated, with 2025 being the second warmest year on record. And high humidity heat extremes occurred with near-record frequency and intensity in 2025, with many measures second only to 2024.

Across the frozen parts of the globe, the effects of warming continued, with ongoing increases in permafrost temperatures and active layer (the seasonally thawed portion) thickness growth. Although the mass balance of mountain glaciers was similar to the previous two years, 2025 marked the 38th consecutive year of ice loss, and the fourth consecutive year of ice loss of more than 1-meter water equivalent. Forty-one percent of the loss experienced by glaciers since 1976 has occurred in the last decade. In 2025, most lakes froze later, thawed earlier, and had shorter durations of ice cover than normal. The annually averaged snow cover area in the Northern Hemisphere (NH) was the third lowest in the 55-plus year record; only 1990 and 1988 had lower extents.

In contrast to the strong warm-phase El Niño seen during 2023/24, the El Niño–Southern Oscillation (ENSO) was in a near-neutral, or weak cool-phase La Niña pattern during 2025, and influenced conditions for many of the hydrological variables. Both surface specific humidity and total column water vapor fell in 2025 from record values in 2024 but remained above average. The global mean cloud area fraction was the second lowest since records began in 1980. Precipitation was below normal over the oceans but above normal over land, typical for La Niña. Intense precipitation, as measured by the maximum one-day rainfall averaged across the globe, was the fourth highest in 2025, though substantially below the record years of 2020 and 2024. The most extreme precipitation occurred in southeastern Asia; in the latter part of the year, rainfall from five landfalling tropical cyclones was superimposed on enhanced monsoon rainfall, both of which contributed to above-average runoff and river discharge in these regions.

The increased rainfall over land led to above-average lake water storage, with over 70% of monitored lakes in the Northern Hemisphere having higher storage levels in 2025 compared to the 2000–20 average, though the Caspian Sea and Large Aral Sea were two notable examples with reduced levels.

Despite the increase in precipitation and near-normal evaporation levels over land globally, surface soil moisture was lower in 2025 than in any other year since 1991. Drier-than-usual conditions in the Northern Hemisphere was the major driver, with many areas experiencing above-average evaporation in contrast to global average conditions. Globally, terrestrial water storage anomalies also remained in their lower, post-2015 range.

Over the Amazon, drought conditions continued with reduced precipitation, and below-average runoff and river discharge. Globally, the area of the land surface experiencing drought remained elevated compared to conditions before 2019, with substantial increases in eastern Europe, the

Danube basin, and central Asia. However, drought conditions eased in southern Africa and central and northern South America.

In the upper atmosphere, stratospheric ozone levels in 2025 were comparable to values seen in recent years, and the 2025 and 2024 Antarctic ozone holes were less pronounced compared to previous years. Tropical lowermost stratospheric water vapor concentrations returned to anomalously high values in 2025, and lingering effects of the Hunga volcano eruption in 2022 were apparent elsewhere in the stratosphere. Monthly tropical water vapor anomalies at the 82-hPa level (near the cold point tropopause) were among the three highest in the record from January through October 2025, but dropped to record negative in December.

Nitrogen oxide (NO_x) species (NO and NO_2) and carbon monoxide (CO) are important to the tropospheric ozone budget. Satellite-observed NO_2 anomalies in 2025 generally reflected known long-term trends of NO_x emissions, with decreases across North America, Western Europe, northern China, South Korea, and Japan, and increases across the Middle East and India. Satellite records of the tropospheric ozone burden (60°S–60°N) indicate an increase of approximately 9% over the past two decades, with slightly stronger trends in the tropics.

The atmospheric burdens of the three most important long-lived greenhouse gases (carbon dioxide [CO_2], methane [CH_4], and nitrous oxide [N_2O]) continued to increase and hence reached new records in 2025, with fossil fuel emissions also setting a record. While the annual increase of CO_2 from 2024 to 2025 was lower than the prior year, it remained significantly higher than the mean increase during the period 2011–20. The annual increase in CH_4 from 2024 to 2025 was also slightly lower than the increase from 2023 to 2024.

Positive net imbalances in top-of-atmosphere radiation continued into 2025 despite the transition away from El Niño conditions. The global annual mean anomalies of the different radiative balance components (total incoming solar, reflected shortwave, and emitted longwave) are now near or even exceeding their historic 95% range of interannual variability. And although the radiative effect of clouds was close to average, this belied remarkable anticorrelations in the patterns of emitted longwave and reflected shortwave radiation, especially over Southeast Asia.

Canada experienced its third consecutive year with extreme fire activity, which contributed to positive aerosol optical depth (AOD) and PM2.5 anomalies in this region and also to a pronounced annual positive carbon monoxide anomaly that extended across the Atlantic and reached into Europe. The Iberian Peninsula had unprecedented fire activity, which drove a record for overall fire emissions in Europe. Nevertheless, at the global scale, 2025 had the lowest overall fire activity in the record (starting in 2003), driven by low activity in South America and Africa. This was also reflected in the globally averaged anomalies of AOD at 550 nm which were the lowest in the 23-year record. However, the trend of increased severity of biomass burning episodes in forested regions continued.

On average, the land surface continued to darken during 2025, driven by heatwaves, wildfires and low snow cover, all of which are associated with the continued above-average temperatures. The persistent warmer-than-average conditions also affected plant growth, with early start-of-season dates, including the earliest on record for the United Kingdom. However, the end-of-season was also earlier than the baseline, and the global greening trend seen around 2010 in the fraction of absorbed photosynthetically active radiation (FAPAR) has slowed since 2023.

In this chapter, Plate 2.1 shows maps of global annual anomalies for many of the variables and metrics presented here. Many of these variables are also presented as time series in Plate 1.1. Although most sections use the 1991–2020 climatological reference period, in line with the World Meteorological Organization (WMO) recommendations, alternate reference periods are used with some datasets due to their length or legacy processing methods.

We dedicate this report to Dr. Yasuyuki Aono, who passed away in 2025, in recognition of his remarkable legacy. For many years, he made invaluable contributions through the collection and preservation of Japan's cherry blossom records.

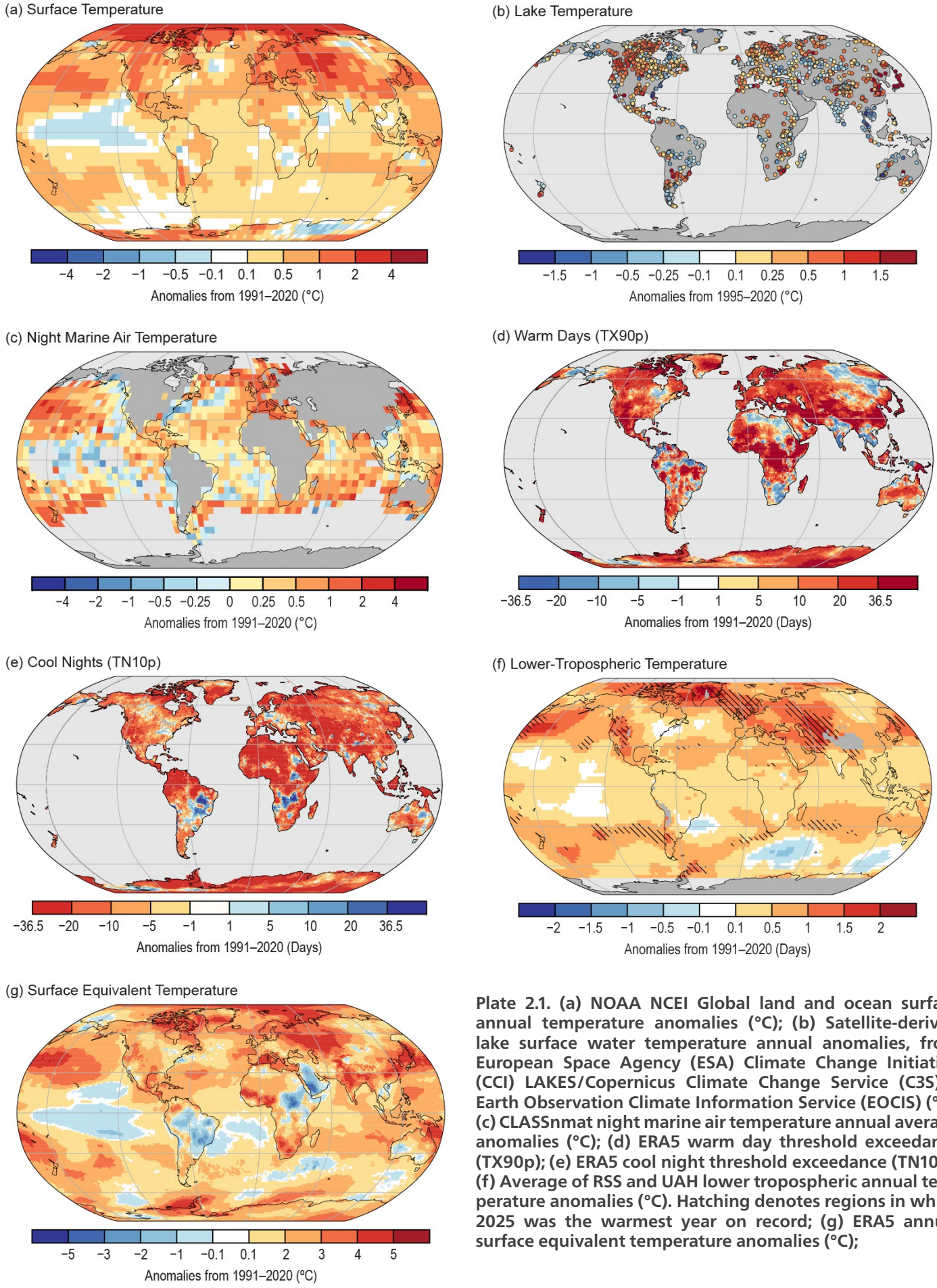

Plate 2.1. (a) NOAA NCEI Global land and ocean surface annual temperature anomalies (°C); (b) Satellite-derived lake surface water temperature annual anomalies, from European Space Agency (ESA) Climate Change Initiative (CCI) LAKES/Copernicus Climate Change Service (C3S) / Earth Observation Climate Information Service (EOCIS) (°C); (c) CLASSnmat night marine air temperature annual average anomalies (°C); (d) ERA5 warm day threshold exceedance (TX90p); (e) ERA5 cool night threshold exceedance (TN10p); (f) Average of RSS and UAH lower tropospheric annual temperature anomalies (°C). Hatching denotes regions in which 2025 was the warmest year on record; (g) ERA5 annual surface equivalent temperature anomalies (°C);

(h) Surface Specific Humidity

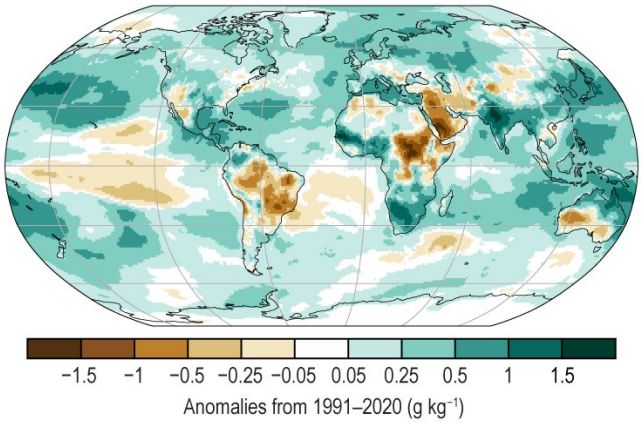

(i) Surface Relative Humidity

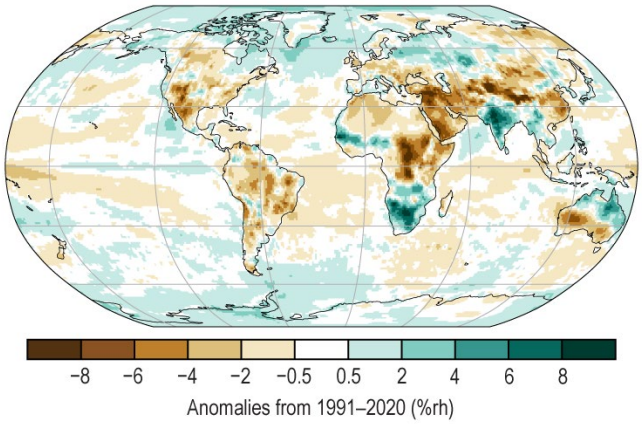

(j) Maximum Humid-Heat Intensity (T_wXX)

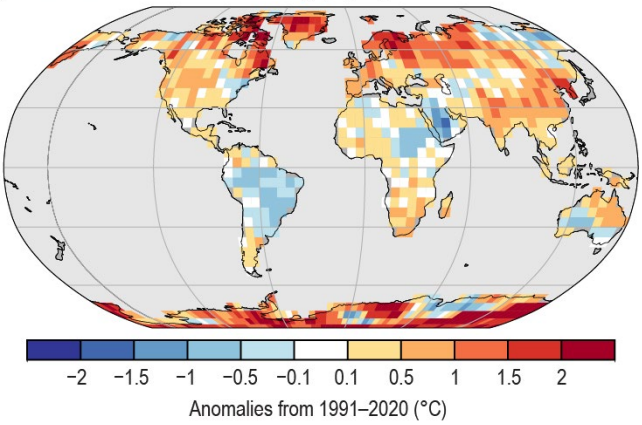

(k) High Maximum Humid-Heat Frequency (T_wX90p)

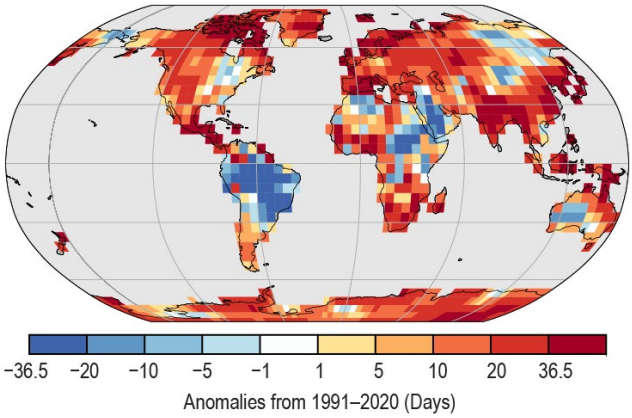

(l) Total Column Water Vapor

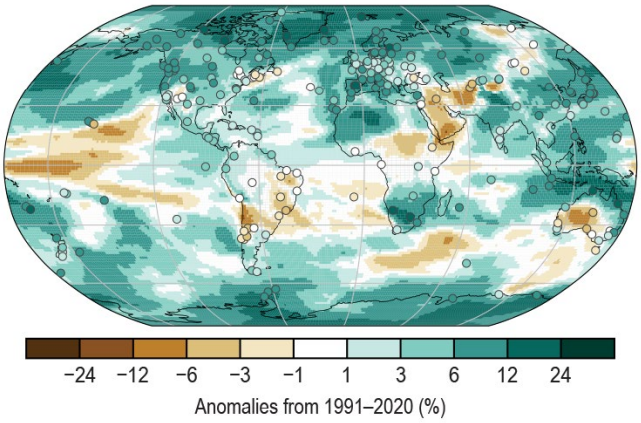

(m) Upper-Tropospheric Humidity

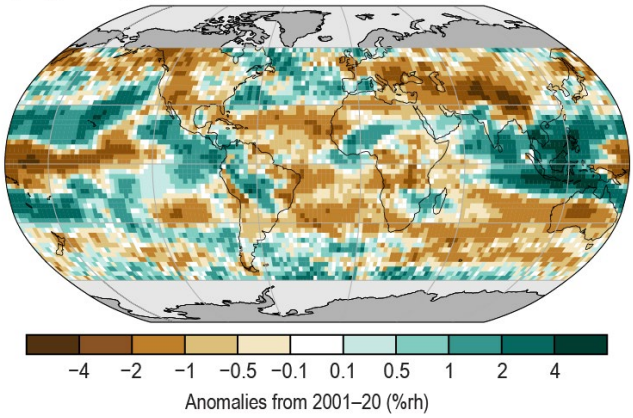

(n) Precipitation

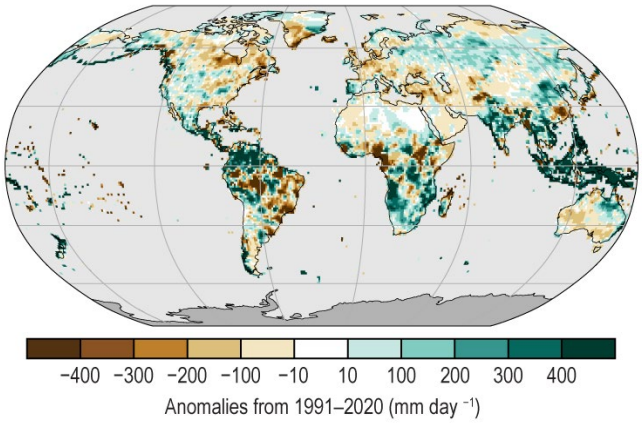

Plate 2.1 (cont.) (h) ERA5 surface specific humidity anomalies (g kg^{-1}); (i) ERA5 surface relative humidity anomalies (%rh); (j) ERA5 daily maximum humid heat intensity (T_wXX), measured by the monthly maximum daily maximum wet-bulb temperature (°C); (k) ERA5 high daily maximum humid heat frequency anomalies (T_wX90p), measured by the number of days where the maximum wet-bulb temperature exceeds the local daily 90th percentile (days); (l) ERA5 total column water vapor anomalies (%). Data from GNSS stations are plotted as filled circles; (m) Annual upper tropospheric humidity (UTH) anomalies (%rh); (n) GPCC annual mean precipitation anomalies (mm);

(o) Maximum 1-day (Rx1day) Precipitation

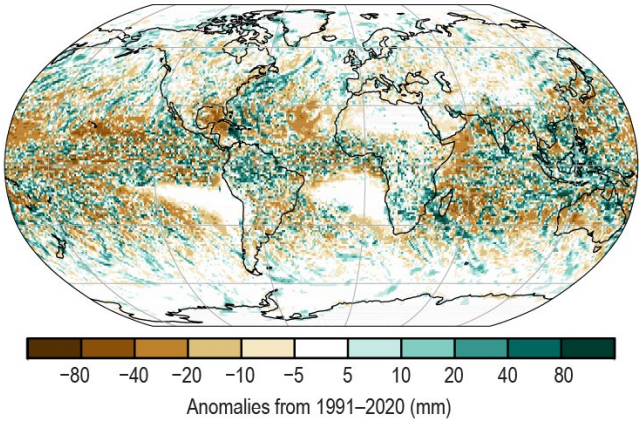

(p) Cloudiness

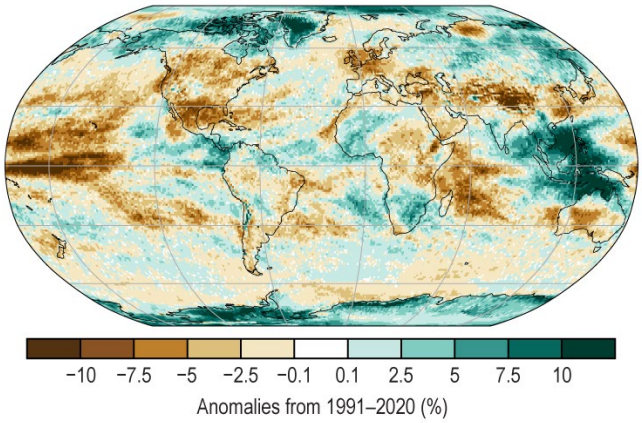

(q) Lake Water Storage

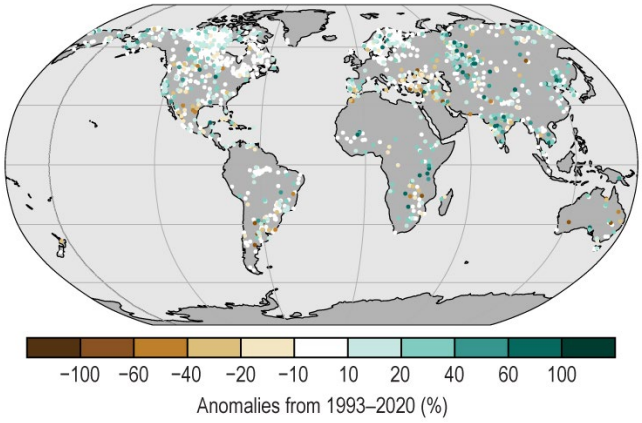

(r) Runoff

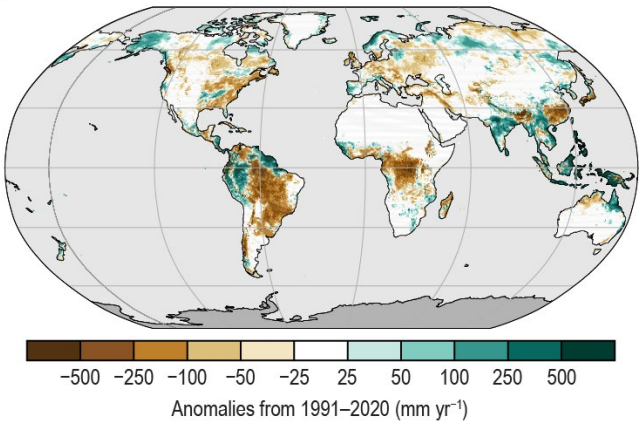

(s) River Discharge

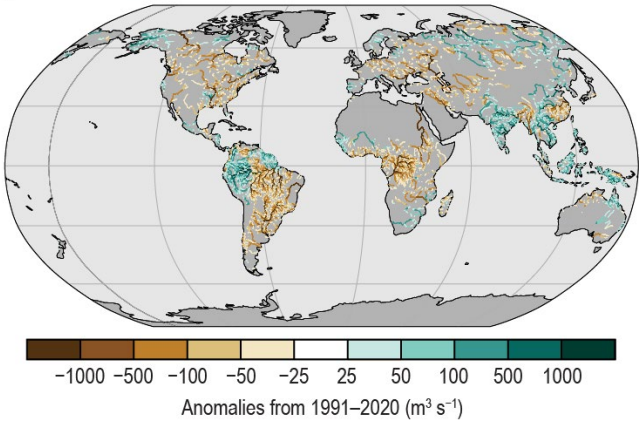

(t) Terrestrial Water Storage Difference

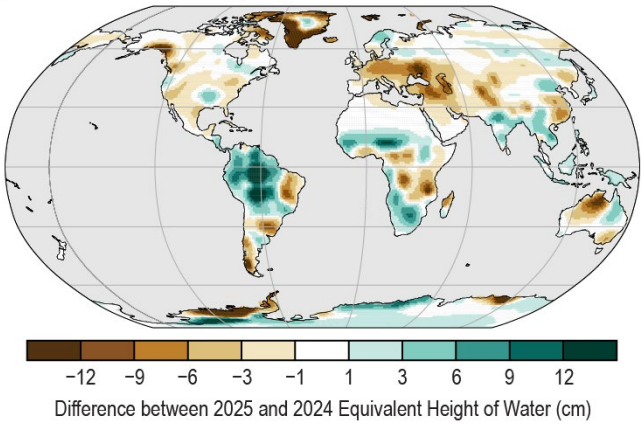

(u) Terrestrial Water Storage

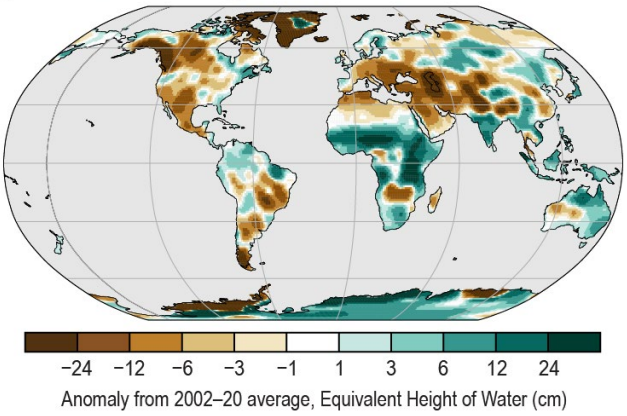

Plate 2.1 (cont.) (o) ERA5 maximum 1-day (Rx1day) annual precipitation anomalies (mm); (p) PATMOS-x 6.0 cloud fraction annual anomalies (%); (q) GloLakes lake water storage anomalies (%); (r) GloFASv4 runoff anomalies (mm yr^{-1}); (s) GloFASv4 river discharge anomalies (m^3 s^{-1}); (t) GRACE-FO difference in annual-mean terrestrial water storage between 2024 and 2025 (cm); (u) GRACE-FO terrestrial water storage anomalies (cm);

(v) Soil Moisture

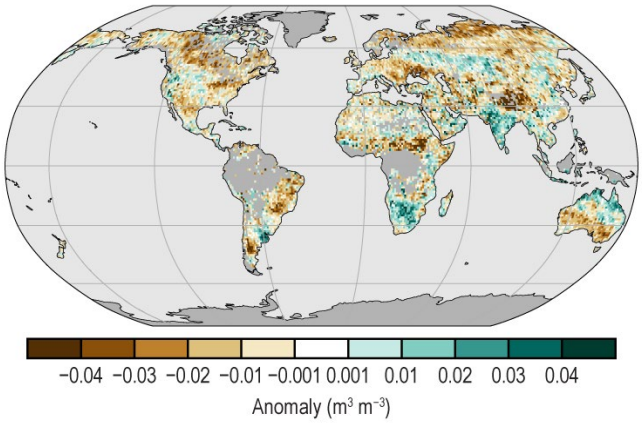

(w) Drought (self-calibrating PDSI)

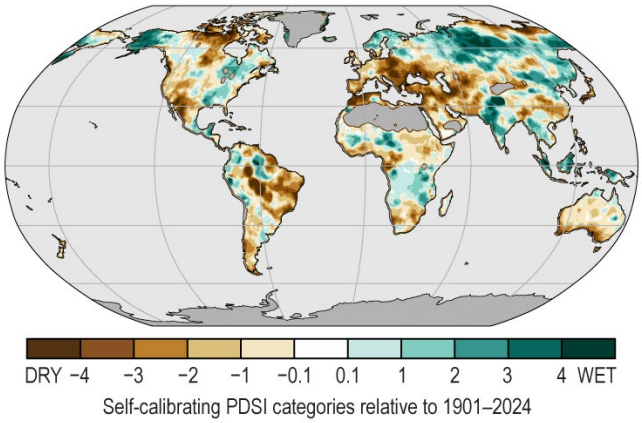

(x) Land Evaporation

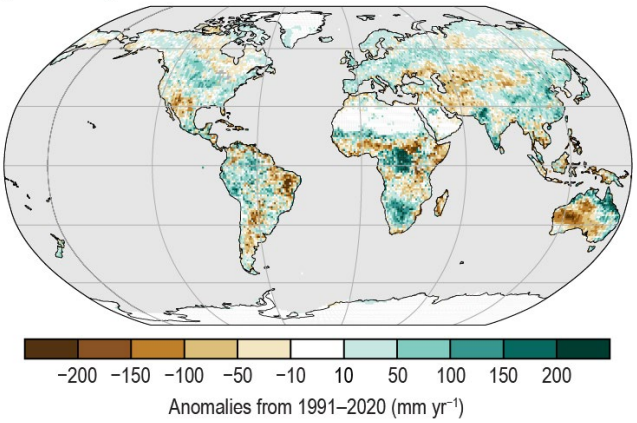

(y) Sea Level Pressure

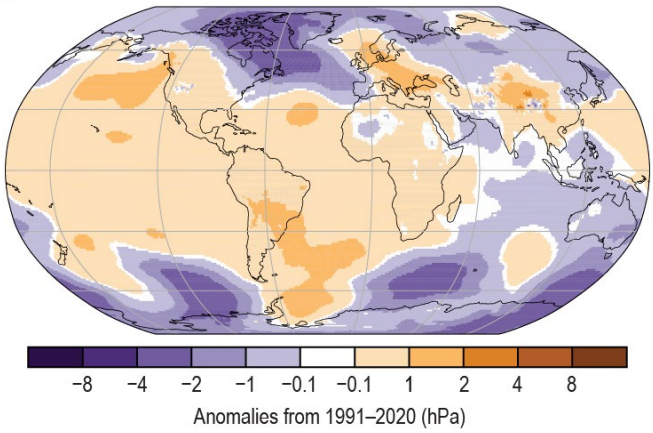

(z) Surface Winds

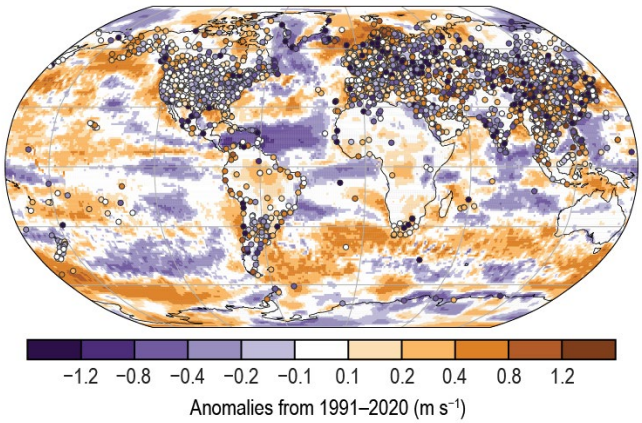

(aa) Lightning

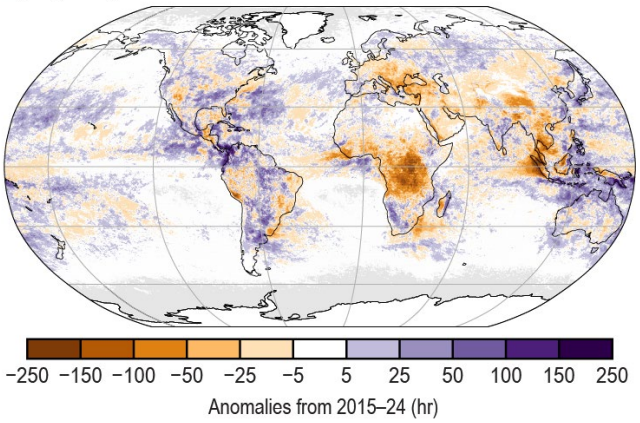

(ab) Total Aerosol Optical Depth

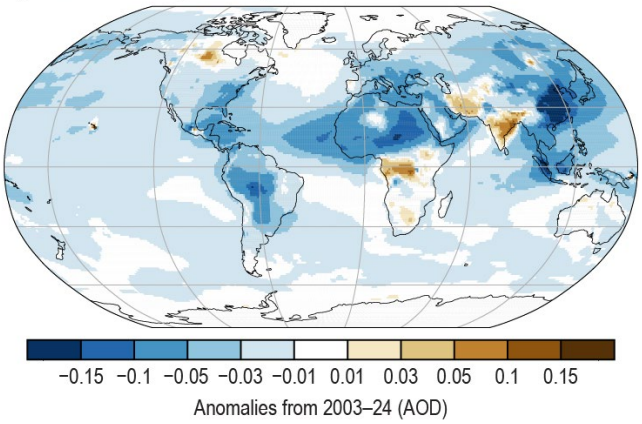

Plate 2.1 (cont.) (v) C3S average surface soil moisture anomalies (m^3 m^{-3}). Data are masked where no retrieval is possible or where the quality is not assured and flagged, for example due to dense vegetation, frozen soil, or radio frequency interference; (w) Mean self-calibrating Palmer Drought Severity Index (scPDSI) for 2025. Droughts are indicated by negative values (brown), wet episodes by positive values (green). No calculation is made where a drought index is meaningless (gray areas: ice sheets or deserts with approximately zero mean precipitation); (x) GLEAM land evaporation anomalies (mm yr^{-1}); (y) ERA5 mean sea level pressure anomalies (hPa); (z) Surface wind speed anomalies (m s^{-1}) from the observational GHCNh dataset (land, circles), the ERA5 reanalysis output (land, shaded areas), and RSS satellite observations (ocean, shaded areas); (aa) Lightning anomalies from merged ENTLN, GLD360, and WWLLN data (hr); (ab) CAMS reanalysis total aerosol optical depth (AOD) anomalies at 550 nm;

(ac) PM2.5

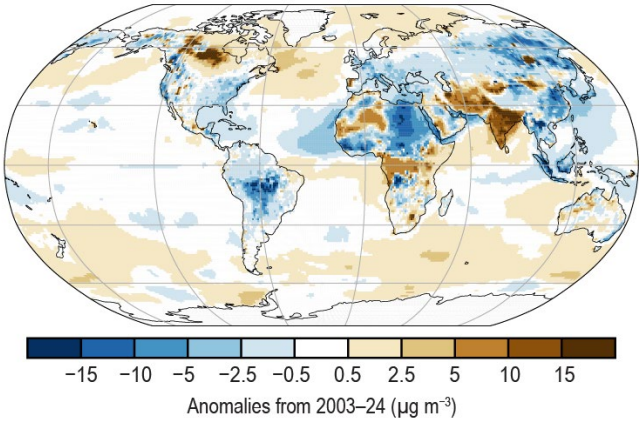

(ad) Extreme Aerosol Days

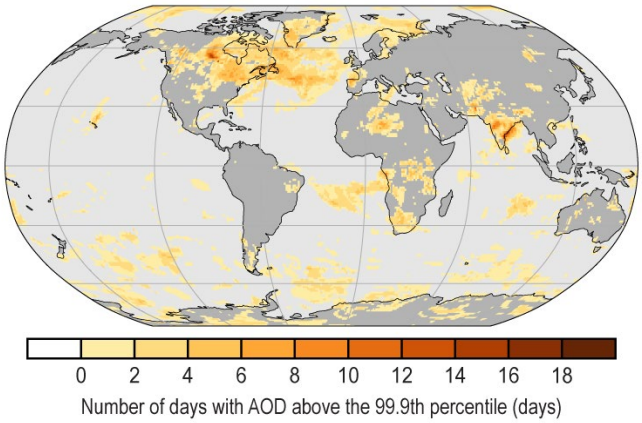

(ae) Extreme PM2.5 Days

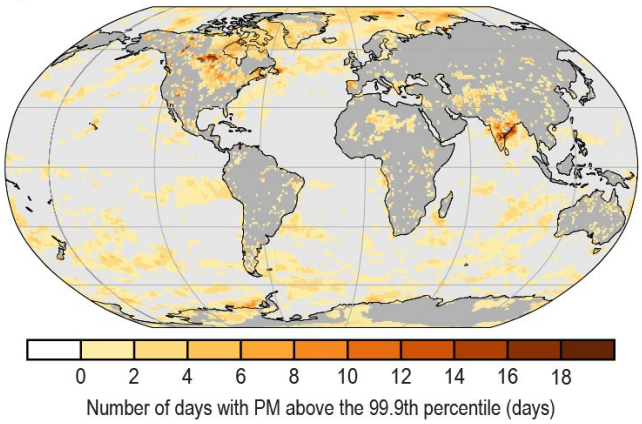

(af) Tropospheric Column Ozone

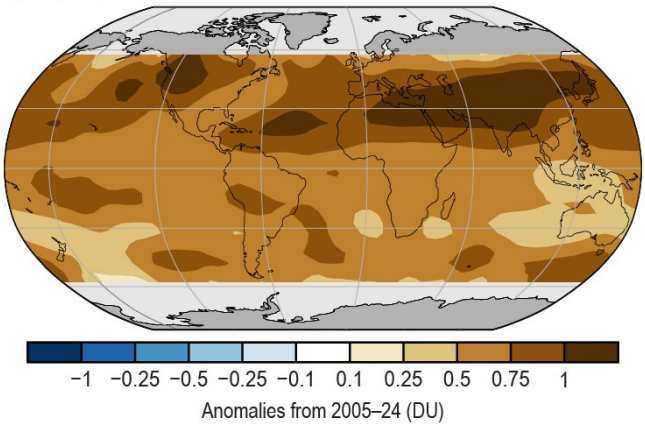

(ag) Tropospheric Column NO_2

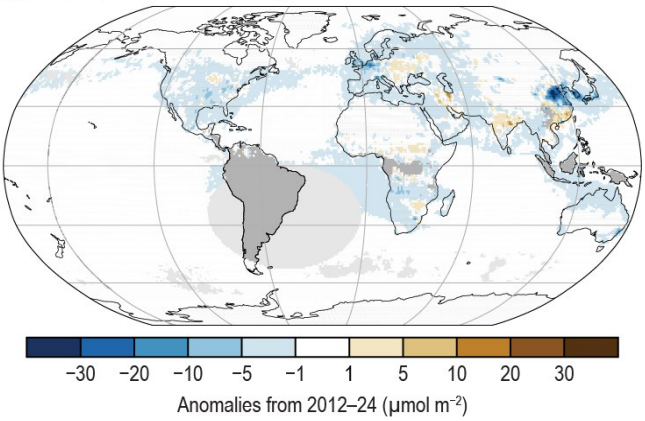

(ah) Stratospheric (Total Column) Ozone

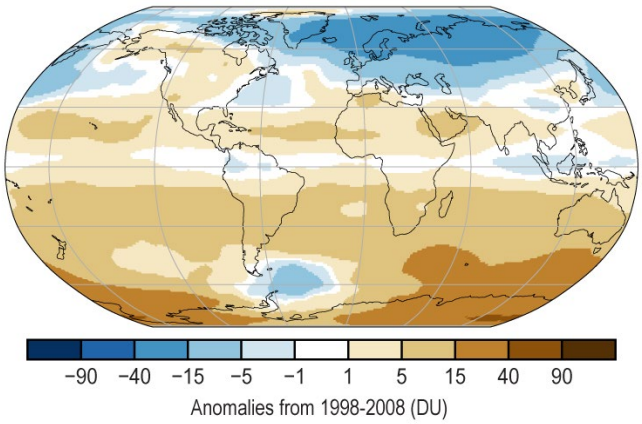

(ai) Carbon Monoxide

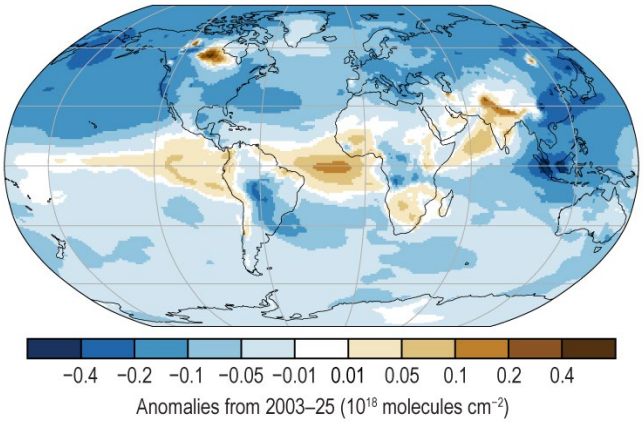

Plate 2.1 (cont.) (ac) CAMS reanalysis PM2.5 anomalies (μg m^{-3}); (ad) Number of days with AOD above the 99.9th percentile from CAMS reanalysis; (ae) Number of days with PM2.5 above the 99.9th percentile from CAMS reanalysis; (af) OMI/MLS tropospheric ozone column anomalies for 60°S–60°N (DU); (ag) OMPS tropospheric column nitrogen dioxide anomalies (μmol m^{-2}). Gray areas indicate regions with low data availability, and portions of South America and the South Atlantic are omitted due to instrument interference caused by the South Atlantic Anomaly; (ah) total column ozone anomalies from the merged GOME / SCIAMACHY / GOME-2 multi-satellite data record (DU); (ai) CAMS reanalysis total column carbon monoxide anomalies (× 10^{18} molecules cm^{-2});

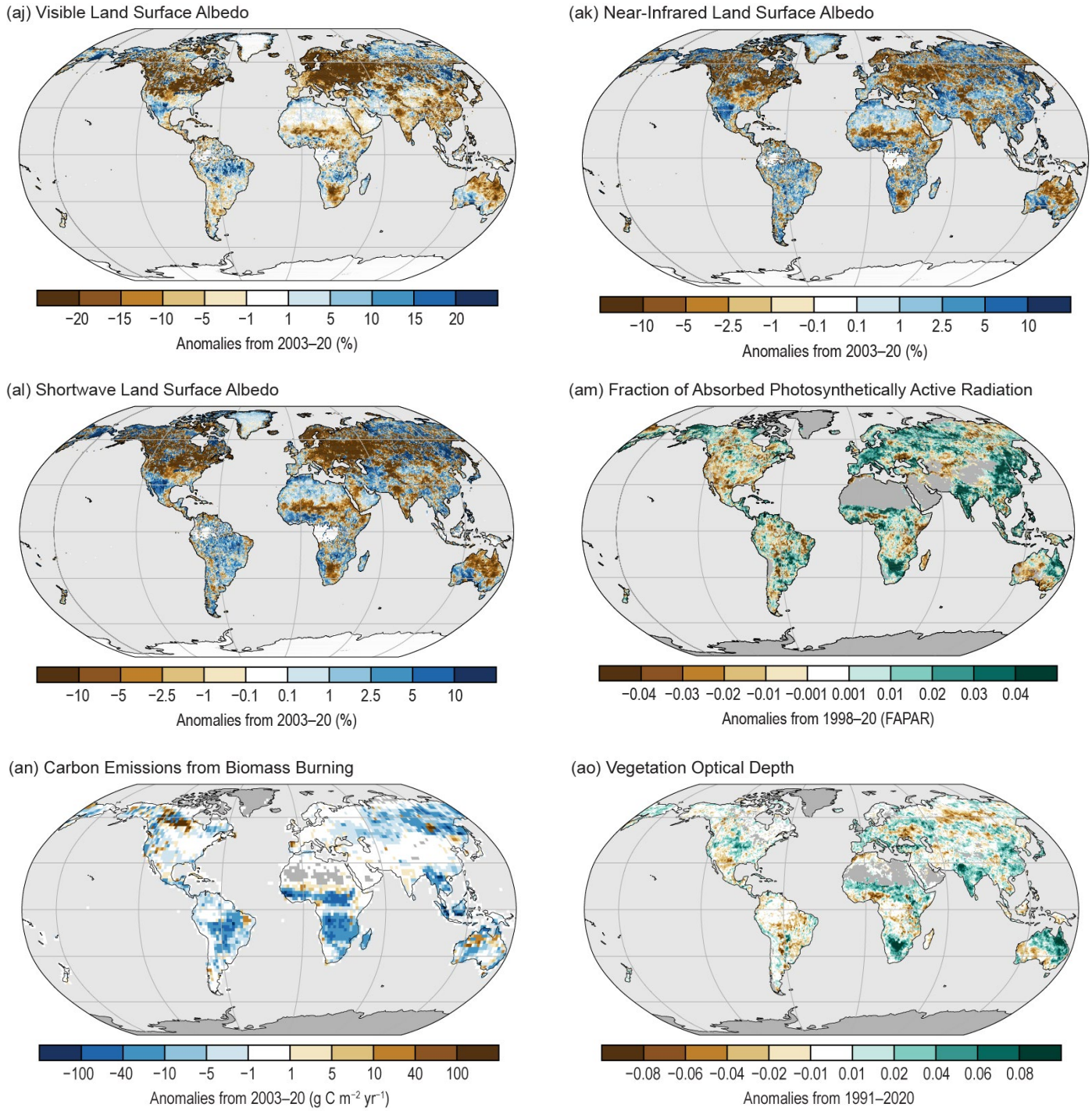

Plate 2.1 (cont.) (aj) VIIRS land surface visible broadband albedo anomalies (%); (ak) VIIRS land surface near-infrared albedo anomalies (%); (al) VIIRS land surface shortwave broadband albedo anomalies (%); (am) FAPAR anomalies; (an) GFASv1.4 carbonaceous emission anomalies (g C m^{-2} yr^{-1}) from biomass burning; (ao) VODCA CXKu-band VOD anomalies.

b. Temperature

1. SURFACE TEMPERATURE

—A. Sánchez-Lugo, A. Argüez, A. Bunno, A. Goto, N. Ishibumi, C. P. Morice, and J. P. Nicolas

The annual global surface temperature for 2025 ranked as the second or third highest on record, with a temperature departure of 0.51°C–0.59°C above the 1991–2020 average, according to the five global temperature datasets assessed herein (Table 2.1; Fig. 2.1). The datasets consist of three global in situ surface temperature analyses (GISTEMP, Lenssen et al. 2019; HadCRUT5, Morice et al. 2021; NOAAGlobalTemp, Huang B. et al. 2022) and two global atmospheric reanalyses (ERA5, Hersbach et al. 2020; Soci et al. 2024; JRA-3Q, Kosaka et al. 2024). Specifically, four of the five global datasets placed 2025 as the third-warmest year on record, trailing 2024 (by 0.11°C–0.13°C) and 2023 (by 0.01°C–0.06°C), while the GISTEMP dataset had 2025 as the second-warmest year on record, behind 2024 (by 0.09°C). According to all five global datasets, the last 11 years (2015–25) were the 11 warmest years on record, with the last three years (2023–25) ranking as the three warmest years on record.

The year 2025 began with La Niña conditions present in the tropical Pacific Ocean, followed by cool ENSO-neutral conditions from March to August. La Niña conditions re-emerged in September and persisted through the end of the year. This pattern distinguishes 2025 from the previous two years since 2023 also began with La Niña in the tropical Pacific Ocean but concluded with the onset of a strong El Niño that dominated the start of 2024. Notably, 2025 was the warmest year on record without an El Niño episode present in the tropical Pacific Ocean.

The global surface temperature for 2025 was also 1.33°C–1.41°C above the 1850–1900 average (a period commonly used to represent pre-industrial conditions). The pre-industrial temperature anomaly range was computed using the two datasets that extend back to 1850 (NOAAGlobalTemp and HadCRUT5) using each dataset's own 1850–1900 baseline.

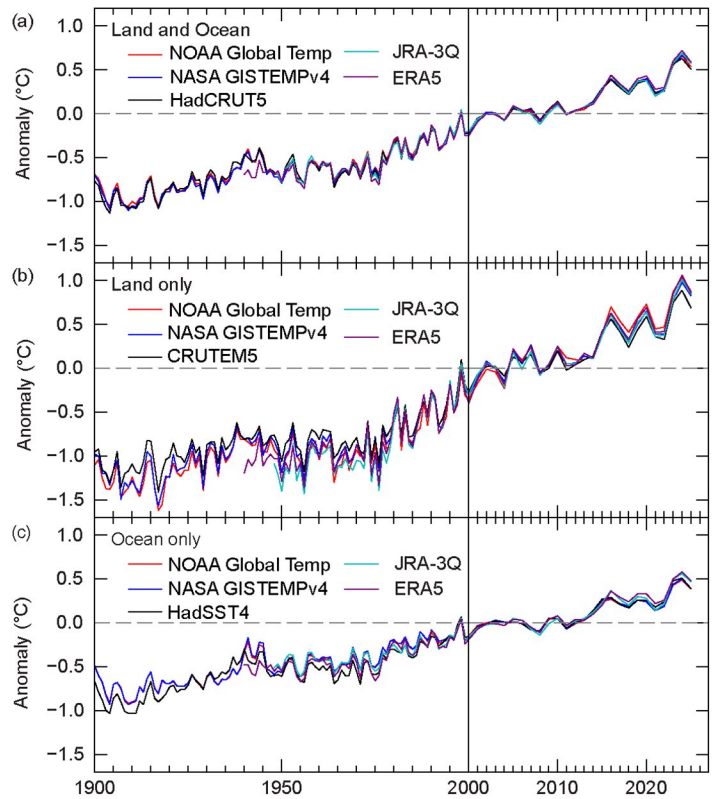

Fig. 2.1. Global average surface air temperature anomalies (°C; 1991–2020 base period). In situ estimates are shown from the NOAA Merged Land Ocean Global Surface Temperature Analysis (NOAAGlobalTemp; Huang et al. 2022), NASA Goddard Institute for Space Studies Surface Temperature Analysis version 4 (GISTEMPv4; Lenssen et al. 2019), Hadley Centre/Climatic Research Unit Temperature version 5 (HadCRUT5; Morice et al. 2021), Climatic Research Unit temperature version 5 (CRUTEM5; Osborn et al. 2021), and Hadley Centre Sea Surface Temperature Dataset version 4 (HadSST4; Kennedy et al. 2019). Reanalysis estimates are shown from ERA5 (Hersbach et al. 2020; Soci et al. 2024) and the Japanese Reanalysis for Three Quarters of a Century (JRA-3Q; Kosaka et al. 2024).

Table 2.1. Global temperature anomalies (°C; 1991–2020 base period) for 2025. Note that for the HadCRUT5 column, land values were computed using the Climatic Research Unit Temperature version 5 (CRUTEM.5.1.0.0) dataset (Osborn et al. 2021), ocean values were computed using the Hadley Centre Sea Surface Temperature Dataset version 4 (HadSST.4.2.0.0) dataset (Kennedy et al. 2019), and global land and ocean values were computed using the HadCRUT.5.1.0.0 dataset (Morice et al. 2021).

Global	NASA-GISTEMPv4	HadCRUT5	NOAA GlobalTemp	ERA5	JRA-3Q
Land	+0.83	+0.69	+0.88	+0.86	+0.85
Ocean	+0.39	+0.39	+0.39	+0.48	+0.47
Land and Ocean	+0.58	+0.51	+0.54	+0.59	+0.58

Therefore, the global temperature anomaly for 2025 remained below +1.5°C, the most ambitious limit set by the Paris Agreement (Paris Agreement 2015). It follows the first year (2024) to exceed this limit, according to several datasets. However, it is important to note that exceeding +1.5°C in a single year does not constitute a breach of the Paris Agreement limit, as the limit refers to a long-term average.

Since 1880, the global annual temperature has increased at an average rate of 0.08°C–0.09°C decade^{-1}. However, the rate of increase has nearly tripled during the most recent 30-year period (1996–2025) with an average rate of 0.24°C–0.27°C decade^{-1}. Using the trend-adjusted approach of Argüez et al. (2020), 2025 was 0.08°C–0.14°C above the 51-year linear trend (1975–2025), placing 2025 between the 79th and 91st percentiles. This marks three consecutive years (2023–25) with detrended anomaly percentiles above the 75th percentile across all datasets. The only comparable streak in the historical record occurred from 1979 to 1981, when anomalies exceeded the 70th percentile for three consecutive years. Notably, the last three years were 0.93°C–1.00°C warmer than 1979–81 on average, in accordance with the significant increase in global temperatures observed in recent decades. Typically, years that exceed the 79th percentile on a trend-adjusted basis are influenced by El Niño events, often strong events. However, this was not the case in 2025, making it a rare exception along with the years 1981 and 1990, and made even more remarkable by the fact that a weak La Niña dominated for most of the year.

The annual global land-only surface air temperature was 0.69°C–0.88°C above the 1991–2020 average, ranking second highest on record for most datasets, with one dataset (CRUTEM) ranking it as third highest. The ocean-only sea surface temperature ranked third highest on record, at 0.39°C–0.48°C above the 1991–2020 average (Table 2.1; see section 3b for details). The year was characterized by much-warmer-than-average conditions across most of the world (Plate 2.1a; Appendix Figs. A2.1–A2.4), with widespread record-high annual temperatures across parts of the Arctic, Europe, Asia, Antarctica, and the western Pacific Ocean and the central Pacific regions outside the tropics. In contrast, below-average annual temperatures were observed across the northern North Atlantic Ocean (see sections 3b and 3h for details), the central and eastern tropical Pacific Ocean (driven by the presence of La Niña; see section 4b for details), southern Africa, and parts of India, the northwestern Indian Ocean, and East Antarctica. Despite some areas experiencing below-average conditions, no land or ocean areas experienced record-cold annual average temperatures.

During the year, most months ranked among the top three warmest for their respective months globally, with only December ranking as the fifth-warmest December on record. According to all datasets, January 2025 was the warmest January on record.

2. LAKE SURFACE WATER TEMPERATURE

—L. Carrea, C. J. Merchant, L. McNamara, J.-F. Creatux, T. M. Dokulil, H. Dugan, A. Laas, E. Leibensperger, S.-I. Matsuzaki, D. Pierson, M. Pulkkanen, A. Räike, O. O. Rusanovskaya, R. Shinohara, S. V. Shimaraeva, E. A. Silow, M. Schmid, M. A. Timofeyev, P. Verburg, and R. I. Woolway

In 2025, satellite observations show that the global average lake surface water temperature (LSWT) anomaly was +0.31°C with respect to the 1995–2020 baseline. This is lower than the record-high anomaly of +0.51°C observed in 2024 and the fourth largest anomaly since records began. Over the period 1995–2025, the mean LSWT increased at a rate of 0.22±0.01°C decade^{-1}. This trend is broadly consistent with earlier studies even though the number of lakes analyzed has doubled since 2022 (e.g., Carrea et al. 2020, 2024; Fig. 2.2). Warm-season, lake-average LSWT anomalies for individual lakes are presented in Plate 2.1b where 75% of the 1912 lakes analyzed showed positive anomalies, while 25% exhibited negative anomalies.

In 2025, 34% of monitored lakes recorded LSWT anomalies >+0.5°C, with large regions showing persistently elevated anomalies (Plate 2.1b). The strongest positive anomalies were observed in lakes across Canada, China, Japan, the Tibetan area, Finland, northwest Russia (Karelia), and part of Argentina. By contrast, negative LSWT anomalies were recorded in Patagonia, part of tropical South America, India, Southeast Asia, Greenland, Alaska, and central Russia.

Four regions were examined in detail: Europe (number of lakes, n = 267, Figs. 2.2b, 2.3a), Africa (n = 143, Figs. 2.2c, 2.3b), Canada (n = 495), Figs. 2.2d, 2.3c), and Tibet (n = 144, Figs. 2.2e, 2.3d). Across

these regions, warm-season LSWT anomalies largely (but not closely) mirror air temperature anomalies reported by NASA GISS (Hansen et al. 2010; GISTEMP Team 2024).

In all four regions, the 2025 mean anomaly was below the respective record-high value observed in 2024, yet all four remained among the highest recorded since 1995: 10th highest for Europe and Canada and 7th and 4th for Africa and Tibet, respectively (Figs. 2.2b–e). Table 2.2 shows trends, anomalies in 2025, and the proportion of lakes experiencing positive and negative anomalies.

Single-point (as opposed to lake-average) in situ observations from 38 lakes (selecting from the data available considering timeseries length, frequency, and spatial distribution) were used to assess warm season temperature anomalies (Fig. 2.4). In general, because in situ measurements represent conditions at specific sampling locations, they may differ from satellite-derived estimations data, which provide an average temperature across the whole lake. For example, for Lake Nipissing in Canada, the satellite and in situ anomalies are similar in 2025 (+0.17°C and +0.19°C, respectively), but for Lake of the Woods (Canada/United States), the difference is substantial (+0.54°C and +2.5°C, respectively). The average anomaly in 2025 for the 19 lakes (with both data types) was +0.35°C for satellite data and +0.78°C for in situ data.

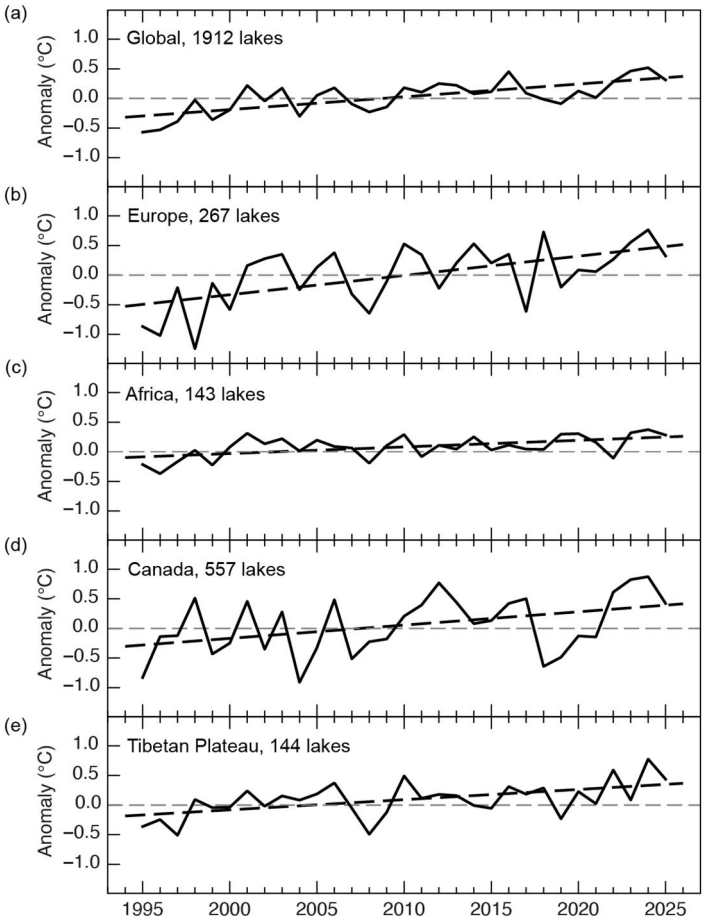

Fig. 2.2. Annual time series of satellite-derived warm-season lake surface water temperature anomalies (°C; 1995–2020 base period) from 1995 to 2025 lakes distributed (a) globally, and regionally in (b) Europe, (c) Africa, (d) Canada, and (e) the Tibetan Plateau.

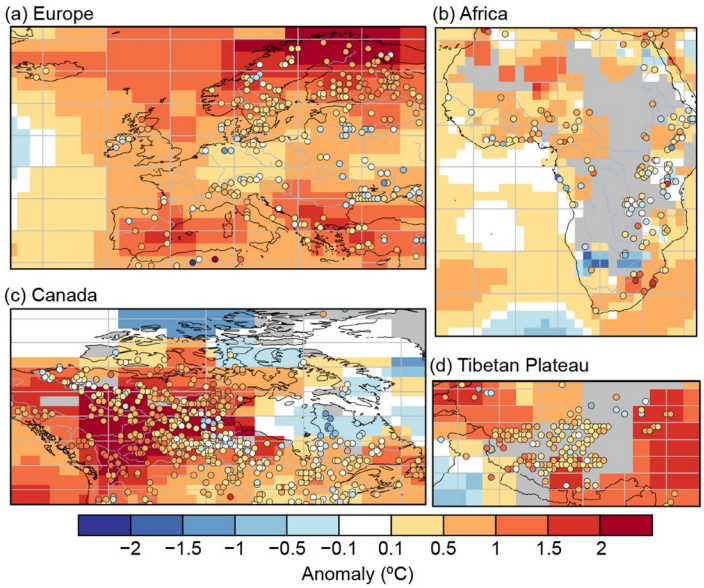

Fig. 2.3. Lake temperature anomalies (°C, colored dots) and 2-m air temperature anomalies (°C; NASA Goddard Institute for Space Studies [GISS]; Hansen et al. 2010, GISS Surface Temperature Analysis [GISTEMP] Team 2024) in 2025 for lakes in (a) Europe, (b) Africa, (c) Canada, and (d) the Tibetan Plateau. These values were calculated for the warm season (Jul–Sep in the extratropical Northern Hemisphere; Jan–Mar in the extratropical Southern Hemisphere; Jan–Dec in the tropics) with reference to the 1995–2020 base period.

Table 2.2. Lake temperature decadal trends (°C decade^{-1}), anomalies (°C) in 2025, and the proportion of lakes experiencing positive/negative anomalies in 2025 for Europe, Canada, Tibet, and Africa.

Region	Europe	Canada	Tibet	Africa
Trend (°C decade^{-1})	+0.33±0.03	+0.22±0.03	+0.17±0.02	+0.11±0.01
2025 Anomaly (°C)	+0.32	+0.42	+0.44	+0.28
Proportion of lakes experiencing positive anomalies in 2025	82%	84%	95%	75%
Proportion of lakes experiencing negative anomalies in 2025	18%	16%	5%	25%

In 2025, in situ data were available only for 25 of the 38 lakes, and their mean anomaly was +0.70°C. Twenty-one lakes exhibited positive anomalies (mean: +0.88°C), while only four lakes recorded negative anomalies (mean: −0.22°C). Figure 2.4 clearly indicates a pronounced warming trend, particularly since the year 2000.

For lakes with sufficient data, the baseline for calculating anomalies for both in situ and satellite temperature was computed using data from 1995 to 2020, otherwise only the available data were used. For mid- and high-latitude lakes, warm-season means were calculated for summer months (July–September in the Northern Hemisphere and January–March in the Southern Hemisphere) while annual averages were used for tropical lakes (within 23.5° of the equator).

LSWT timeseries were obtained from the European Space Agency Climate Change Initiative (ESA CCI) LAKES/Copernicus C3S/EOCIS climate data record (Carrea et al. 2022b, 2023a). For 2025, satellite observations from Sea and Land Surface Temperature Radiometers (SLSTR) on Sentinel-3A and -3B were used. LSWT was retrieved using the method of MacCallum and Merchant (2012), applied on image pixels identified as water based on both the inland water dataset of Carrea et al. (2015) and a reflectance-based water detection approach (Carrea et al. 2023a).

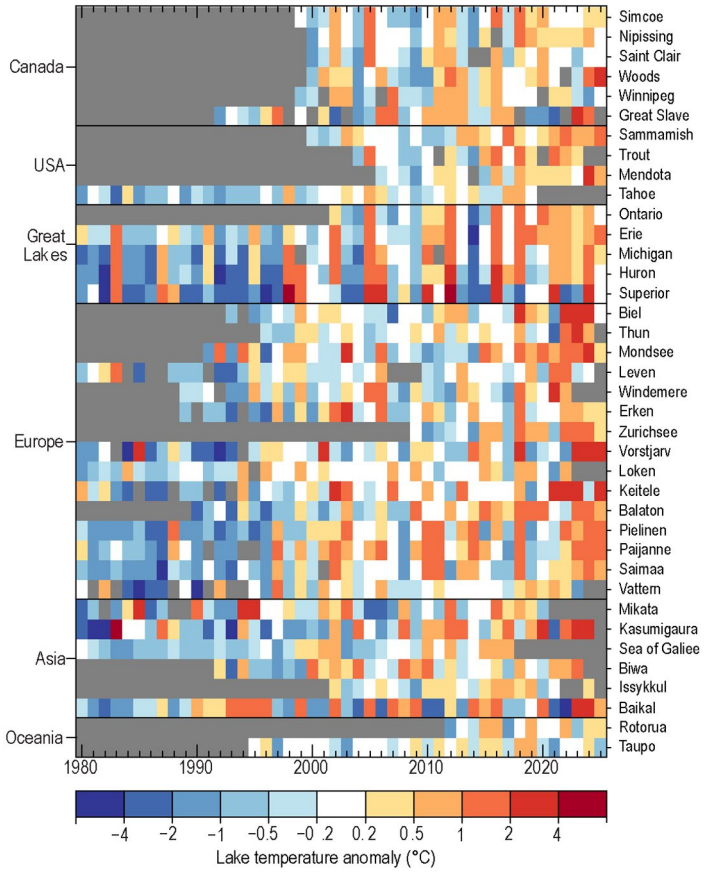

Fig. 2.4. In situ lake surface water temperature (LSWT) observations from 38 globally distributed lakes show the annually averaged warm season (Jul–Sep in the Northern Hemisphere; Jan–Mar in the Southern Hemisphere) anomalies (°C; 1995–2020 base period when available).

The satellite-derived LSWT values represent spatial averages for the 1912 lakes analyzed. These data were validated against in situ measurements using robust statistics with a robust standard deviation of the satellite minus in situ temperature discrepancy of about 0.5°C (Carrea et al. 2023a). Previous work has shown that lake-wide average surface temperatures provide a more representative assessment of LSWT responses to climate change than single-point observations (Woolway and Merchant 2018).

The averaged surface air temperature was calculated from the Global Historical Climatology Network version 4 (GHCN v4; 250-km smoothing radius) data of the NASA GISS surface temperature analysis (Hansen et al. 2010; GISTEMP Team 2024).

3. NIGHT MARINE AIR TEMPERATURE

—R. C. Cornes, R. Junod, J. Siddons, S. Chan, and E. C. Kent

The quasi-global annual average night marine air temperature (NMAT) in 2025 was the third highest in the record since 1900, with a value of 0.39°C above the 1991–2020 baseline in the Climate Linked Atlantic Sector Science Night Marine Air Temperature (CLASSnmat) dataset (Cornes et al. 2020) and 0.27°C in the University of Alabama in Huntsville Night Marine Air Temperature (UAHNMAT; Junod and Christy 2020). These values represent a drop of around 0.16°C from the record temperature seen in 2024 (see Cornes et al. 2025). Compared to the interannual variation of global average NMAT since 1900, this represents a moderate drop in annual average temperature.

The two NMAT datasets analyzed in this section (CLASSnmat and UAHNMAT) were both constructed using air temperature measurements made onboard ships; however, the datasets differ in how the height adjustment is applied to the temperature data (from respective observing height to 10 m), how the underlying ship data are quality-controlled, and how point values are

aggregated to grid-cell values (see Cornes et al. 2021). Evaluation of these two datasets therefore provides an estimate of structural uncertainty in gridded air temperature estimates over the ocean. Over the period 1900–2025, the quasi-global average NMAT increased at a rate of 0.08°C decade^{-1} in CLASSnmat, and 0.07°C decade^{-1} in UAHNMAT. Since 1981, the rate of warming has increased, with trends over the period 1981–2025 being 0.13°C decade^{-1} and 0.10°C decade^{-1} for the respective datasets. However, substantial regional differences are evident (Fig. 2.5). The strongest warming trends occur in the northern extratropics (0.26°C decade^{-1} for CLASSnmat and 0.25°C decade^{-1} for UAHNMAT), while the weakest trends are observed in the tropics (0.09°C decade^{-1} for CLASSnmat and 0.06°C decade^{-1} for UAHNMAT).

From December 2024 to April 2025, a weak La Niña event occurred (see section 4b for details). However, sea surface temperature anomalies in the Niño-3.4 region were modest and insufficient to meet NOAA's historical criterion of five overlapping seasons. Throughout the boreal summer, ENSO-neutral conditions prevailed, and then weak La Niña conditions resumed during the August–October period and continued for the rest of the year. The global pattern of annual average NMAT anomalies (Fig. 2.6) reflect this pattern, with positive temperature anomalies across the northwest and southwest Pacific, and weak negative anomalies across the tropical Pacific. Particularly warm temperature anomalies (>+1.5°C relative to 1991–2020 averages) occurred across the North Pacific. This pattern is also seen in sea surface temperature anomalies, depicted here by the

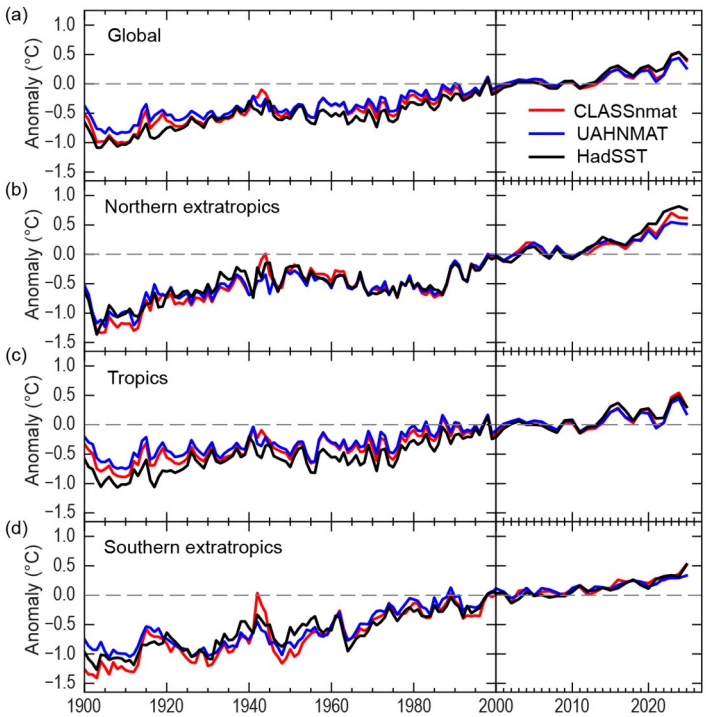

Fig. 2.5. Annual average marine temperature anomalies (°C; 1991–2020 base period) calculated from the Climate Linked Atlantic Sector Science Night Marine Air Temperature (CLASSnmat), University of Alabama in Huntsville Night Marine Air Temperature (UAHNMAT), and Hadley Centre Sea Surface Temperature Dataset version 4 (HadSST4) datasets averaged over the (a) globe, (b) northern extratropics, (c) tropics, and (d) southern extratropics. The tropics is defined as the latitude range 30°S–30°N and the northern (southern) extratropics as >30°N (<30°S). The averages only include values for grid boxes that are filled in all three datasets for a given year; since UAHNMAT starts in 1900, only values for the period 1900–2025 are plotted.

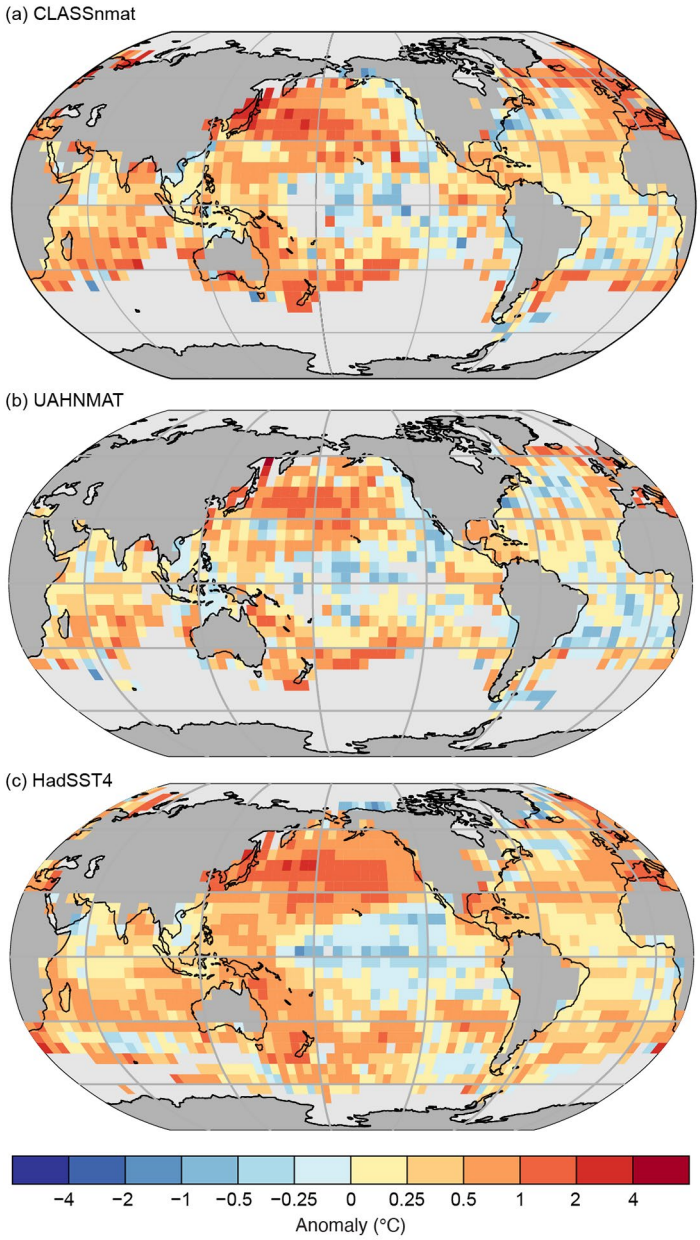

Fig. 2.6. Annual mean temperature anomalies for 2025 (°C; 1991–2020 base period) from the (a) Climate Linked Atlantic Sector Science Night Marine Air Temperature (CLASSnmat), (b) University of Alabama in Huntsville Night Marine Air Temperature (UAHNMAT), and (c) Hadley Centre Sea Surface Temperature Dataset version 4 (HadSST4) datasets.

Hadley Centre Sea Surface Temperature dataset version 4 (HadSST4; Kennedy et al. 2019; Sandford and Rayner 2026), which provide independently generated evidence of basin-scale warming, although sea surface temperature (SST) and NMAT are closely linked through air–sea heat exchange.

Another area of note is the northeast Atlantic region and the Mediterranean Sea, where NMAT anomalies in 2025 were also substantially above the 1991–2020 average. This warmth corresponds to a marine heatwave event that occurred across the region during June and July. While CLASSnmat and HadSST4 both show anomalies above +1.5°C, the UAHNMAT dataset shows comparatively weaker anomalies. Differences between the NMAT datasets reflect their varied treatments of ship metadata, quality control, height adjustments, and averaging procedures. More broadly, UAHNMAT generally reported cooler anomaly values in 2025; for example, in the tropical belt, the UAHNMAT anomaly is +0.19°C—ranking 2025 as the seventh-warmest year—compared with +0.31°C and third warmest in CLASSnmat.

In the Southern Hemisphere extratropics, 2025 ranked as the warmest year in each of the respective series. However, observational coverage in this region (especially south of 40°S) remains sparse, dominated by shipping routes concentrated around southern midlatitudes. As a result, while the available observations indicate a strong warming signal, definitive conclusions cannot be reached using these datasets.

4. LAND SURFACE TEMPERATURE EXTREMES

—R. J. H. Dunn, M. G. Donat, and M. Bosilovich

Along with other temperature metrics presented in this chapter, land surface high temperature extremes in 2025 were not as exceptional as in 2023 and 2024. However, global average numbers of warm days (TX90p; Table 2.3) were still above all years prior to 2023 for three of the four datasets assessed here (going back to between 1940 and 1980), and numbers of cool nights (TN10p; Table 2.3) were second lowest in the record for all datasets (Fig. 2.7).

As in previous reports (e.g., Dunn et al. 2025b), data are shown from three reanalyses (ERA5, Hersbach et al. 2020; Bell et al. 2021; Soci et al. 2024; MERRA-2, Gelaro et al. 2017; JRA-3Q, Kosaka et al. 2024) and from an in situ-based product (Global Historical Climatology Network Daily Extremes [GHCNDEX], Donat et al. 2013). The three reanalyses have complete global coverage, but results are shown here for the land surface only; all three indicate that 2025 had the third highest number of warm days (TX90p, 54–60 days using 1991–2020 as reference period to

Table 2.3. Definitions of indices used for land surface temperature extremes, their globally averaged values (days for Warm Days and Cool Nights and °C for Warmest T-max) for 2025, and ranks from the four datasets. Coverage uncertainties are shown for GHCNDEX.

Index	Name	Definition	GHCNDEX (1951–2025) Value, [rank] Ref. Period 1961–90	ERA5 (1940–2025) Value, [rank] Ref. Period 1961–90	JRA-3Q (1948–2025) Value, [rank] Ref. Period 1961–90	ERA5 (1940–2025) Value, [rank] Ref. Period 1991–2020	MERRA-2 (1980–2025) Value, [rank] Ref. Period 1991–2020	JRA-3Q (1948–2025) Value, [rank] Ref. Period 1991–2020
TX90p	Warm days (days)	The annual count of days when the daily maximum temperature exceeds the 90th percentile	64±7 [eighth highest]	92 [third highest]	60 [third highest]	60 [third highest]	60 [third highest]	54 [third highest]
TN10p	Cool nights (days)	The annual count of nights when the daily minimum temperature falls below the 10th percentile	14±7 [second lowest]	15 [second lowest]	13 [second lowest]	23 [second lowest]	21 [second lowest]	21 [second lowest]
TXx	Warmest T-max (°C)	Annual maximum of the daily maximum temperature	36.2±0.2 [eighth highest]	30.8 [fourth highest]	30.1 [fourth highest]	—	31.4 [third highest]	—

calculate the 90th percentile threshold), following 2024 and 2023, and the second-lowest number of cool nights (TN10p, 21–23 days using 1991–2020 as the reference period to calculate the 10th percentile threshold) following 2024. The annual values were substantially above (TX90p) or below (TN10p) the average number expected during the reference period (36.5 days by definition). GHCNDEX, with a lower spatial coverage for recent years especially in the Global South (post 2017; Figs. 2.7a,b; Appendix Fig. A2.5), only had the eighth-highest number of warm days in 2025, but the second-lowest number of cool nights (also following 2024), as in the reanalyses.

Most of the land surface experienced more warm days than expected on average during the percentile reference period (36.5 days), but some larger areas were slightly below the expected number, including parts of South America, southern and northern Africa, northeastern Asia, and Southeast Asia and the Indian peninsula (Plate 2.1d; Appendix Figs. A2.5–A2.7). Much of Europe experienced several heatwaves throughout the summer half-year (April–September), and record-high temperatures were set in eastern Asia. For the cool nights, the pattern was much more uniform (which may be partially the result of the zero-bound nature of this index affecting the statistics), with most areas experiencing a below-average number; however, parts of eastern South America and central Africa had more cool nights than average (Plate 2.1e).

The fraction of land area experiencing record numbers of warm days, cool nights, and record maximum temperatures also fell compared to 2023 and 2024 (Figs. 2.8b,d,f) for all three indices (TX90p, TN10p, and TXx). In each year, the fraction of land area setting new records relative to all previous years on record is calculated. In an unchanging climate, which is clearly not the case in recent decades, record-breaking values should become rarer over time (e.g., Fischer et al. 2025; Benestad 2003). As the first year will set a record everywhere, and the probability to set new records remains high in the first several years, values are not shown for the first 20 years of each reanalysis. Only a small fraction of land area set record maximum temperatures in 2025 (Figs. 2.8e,f), but for TX90p and TN10p, substantial areas set (near) record-high or record-low, respectively, values in a swathe from northern Europe through to East Asia, as well as southern Africa for TN10p (Figs. 2.8a,c). The area fractions for these two indices, although returning to much lower levels than

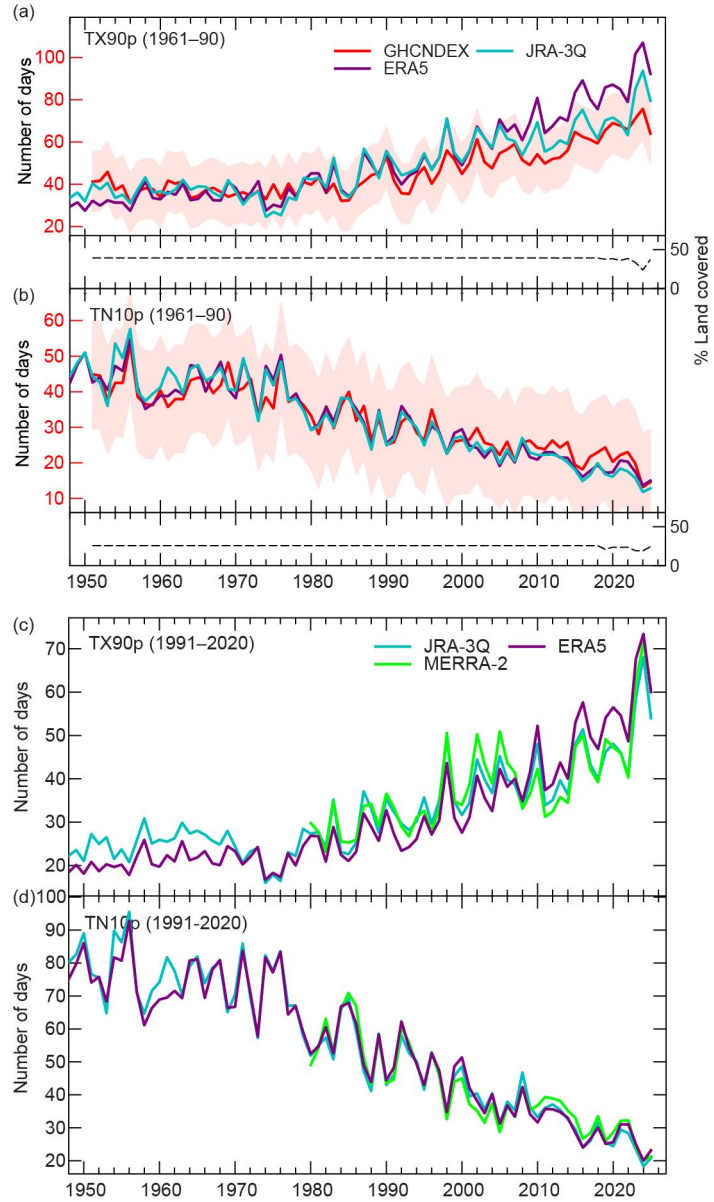

Fig. 2.7. (a),(b) Time series of the (a) annual number of warm days (TX90p) and (b) cool nights (TN10p) averaged over global land regions based on gridded station data from Global Historical Climatology Network Daily Extremes dataset (GHCNDEX; red line), ERA5 (purple line), and the Japanese Reanalysis for Three Quarters of a Century (JRA-3Q; blue line) reanalysis using 1961–90 as the reference period. The spatial coverage in GHCNDEX is limited; the black dashed lines show the percentage of land area covered in GHCNDEX (lower panels, right y-axis). The 2-σ coverage uncertainty for GHCNDEX (following Brohan et al. 2006; Dunn et al. 2020) is shown by the light red bands in (a),(b). (c),(d) As in (a),(b), for three atmospheric reanalyses (ERA5 [purple line], MERRA-2 [green line], and JRA-3Q [blue line]) using 1991–2020 as the reference period.

in 2023 and 2024, were still elevated compared to other years which follow ones with high records (e.g., 2022, 2017, 2018; Figs. 2.8b,d).

A number of indices have been recommended by the World Meteorological Organization to characterize temperature and precipitation extremes (Zhang et al. 2011; Dunn et al. 2024), of which three are presented here (Table 2.3). Dunn et al. (2022b) shows there is good agreement between the observation-based and reanalysis products, especially for the two percentile-based indices used in this section. See Donat et al. (2013) and Dunn et al. (2020, 2022b) for details of indices from the observation-based and reanalyses datasets, respectively.

The indices shown here use fixed reference periods for the calculation of the percentile thresholds, and an intercomparison between these is not trivial (Dunn et al. 2020; Yosef et al. 2021; Dunn and Morice 2022); we show versions using both 1961–90 (for GHCNDEX, ERA5, and JRA-3Q) and 1991–2020 (for ERA5, MERRA-2, and JRA-3Q) as reference periods for percentile calculation.

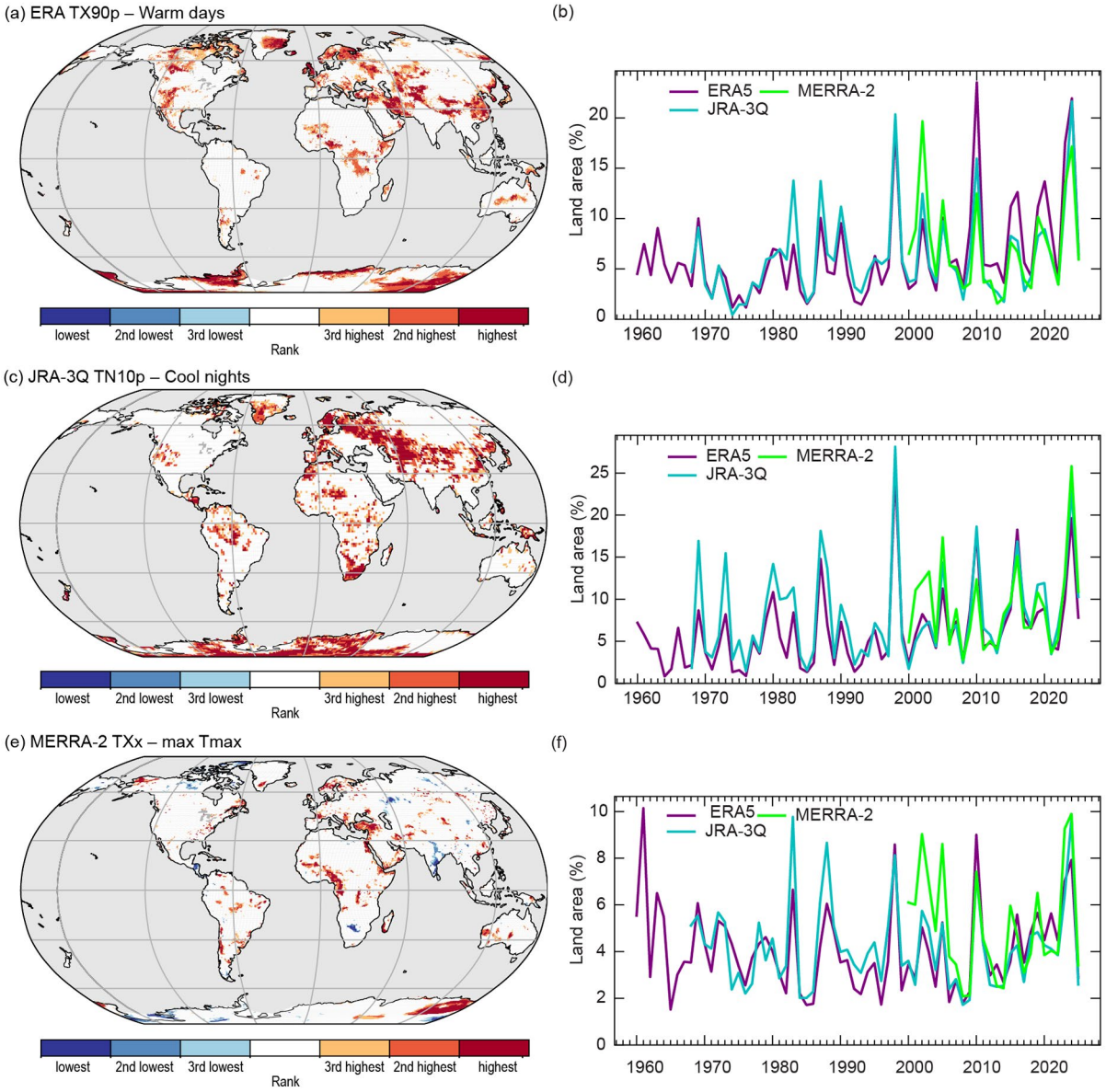

Fig. 2.8. Maps indicating grid cells where (a) the warm day index (TX90p) from ERA5 (since 1940), (c) the cool night index (TN10p) from the Japanese Reanalysis for Three Quarters of a Century (JRA-3Q; since 1948), and (e) the annual maximum temperature (TXx) from MERRA-2 (since 1980) for 2025 ranked in the three highest (orange to red) or three lowest (blue) values within their record. Time series of the percent of land area ranked as setting a new record value in each year; highest for (b) TX90p and (f) TXx and lowest for (d) TN10p, for ERA5 (shown from 1960), JRA-3Q (shown from 1968), and (f) MERRA-2 (shown from 2000). The ranks from the first 20 years of each reanalysis are not calculated.

5. TROPOSPHERIC TEMPERATURE

—S. Po-Chedley, C. Mears, C.-Z. Zou, R. Junod, and L. Haimberger

Following record-high temperatures in 2023 and 2024, the annual global mean lower tropospheric temperature (LTT) moderated in 2025—remaining anomalously warm but not record-setting. The evolution of LTT is largely a product of long-term tropospheric warming and interannual variability that is primarily driven by the El Niño–Southern Oscillation (ENSO). Depending on the dataset, eight or nine of the warmest years on record for this region of the atmosphere occurred in the last 10 years.

Above-average LTT over the last three years was driven in part by the persistent, decades-long warming of the climate that is evident across observing systems and individual datasets (Fig. 2.9; Table 2.4; section 2b1). On shorter timescales, both tropical and global average tropospheric temperature tend to follow variations in ENSO with a lag of three to five months (e.g., Yulaeva and Wallace 1994). The lag between ENSO and heat accumulation in the atmosphere affects the evolution of other geophysical quantities, such as the phasing of moisture and top-of-atmosphere radiation anomalies with respect to El Niño events (Mayer et al. 2026; sections 2d3, 2f1). Persistent La Niña conditions from 2020 through early 2023 transitioned to a strong El Niño that peaked in the boreal winter of 2023/24. Tropical and global LTT followed this evolution, reaching record values in late-2023 and throughout much of 2024 (Fig. 2.10). Following peak El Niño conditions, the central Pacific cooled over 2024, resulting in ENSO-neutral and weak La Niña conditions throughout 2025. The troposphere also cooled,

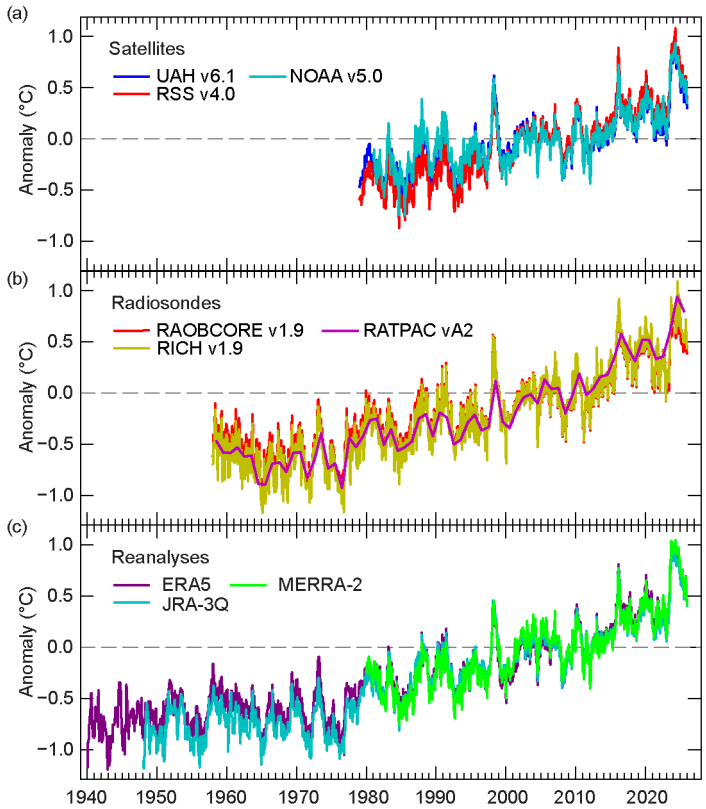

Fig. 2.9. Monthly average global lower tropospheric temperature (LTT) anomalies (°C; 1991–2020 base period) for (a) satellite, (b) radiosonde, and (c) reanalysis datasets. Annual averages are displayed only for the RATPAC vA2 dataset in panel (b).

Table 2.4. Temperature trends (°C decade^{-1}) for global lower-tropospheric temperature (LTT) and tropical (20°S–20°N) total tropospheric temperature (TTT) over the periods 1958–2025 and 1979–2025. NASA MERRA-2 data begin in 1980 and NOAA v5.0 LTT begins in 1981. Cells marked with a dash signify that the data do not extend back to 1958.

Observing System	Dataset	Global LTT (1958–present)	Global LTT (1979–present)	Tropical TTT (1958–present)	Tropical TTT (1979–present)
Radiosonde	NOAA RATPAC vA2 *(Free et al. 2005)*	0.19	0.24	0.18	0.20
Radiosonde	RAOBCORE v1.9 *(Haimberger et al. 2012)*	0.17	0.19	0.14	0.16
Radiosonde	RICH v1.9 *(Haimberger et al. 2012)*	0.19	0.22	0.19	0.21
Satellite	UAH v6.1 *(Spencer et al. 2017)*	—	0.16	—	0.15
Satellite	RSS v4.0 *(Mears and Wentz 2016)*	—	0.23	—	0.19
Satellite	NOAA v5.0 *(Zou et al. 2023)*	—	0.15	—	0.13
Reanalysis	ERA5 *(Hersbach et al. 2020)*	0.17	0.20	0.16	0.18
Reanalysis	JRA-3Q *(Kosaka et al. 2024)*	0.19	0.20	0.18	0.18
Reanalysis	NASA MERRA-2 *(Gelaro et al. 2017)*	—	0.22	—	0.20
Median	N/A	0.19	0.20	0.18	0.18

resulting in temperatures that were no longer record-breaking, but still above average. Following this multi-year evolution, all LTT datasets considered here rank 2024 as the warmest year on record. Global annual average LTT values in 2025 and 2023 are similar, but with an average temperature anomaly of +0.58°C, most datasets (six of nine) rank 2025 as the second-warmest year on record (with 2023 now generally ranked third warmest).

Spatially, 92.2% of the global troposphere exhibited LTT above the 1991–2020 climatological average, but only 6.0% experienced record-warmth in 2025 (Plate 2.1f). Regions of record warmth include the Southern Hemisphere subtropics, western Asia and Russia, and the North Atlantic Ocean and Greenland. Only 3.5% of the globe observed below-average lower tropospheric temperatures, and the remaining 4.3% of the surface area is not included in our observational estimate.

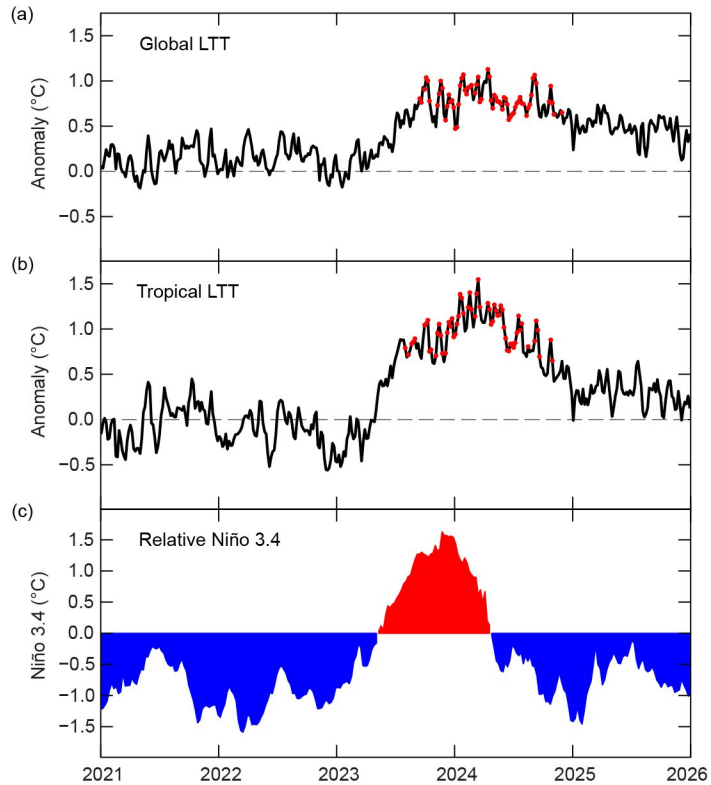

Fig. 2.10. Five-day average (a) global and (b) tropical (20°S–20°N) lower-tropospheric temperature (LTT) time series for the period 2021–25 (from the University of Alabama in Huntsville [UAH] dataset). Record LTT temperatures are denoted with a red dot. Panel (c) shows five-day averages of the relative Niño-3.4 index over this same period. The relative Niño-3.4 index is the traditional Niño-3.4 anomaly minus the average SST over the full tropics (van Oldenborgh et al. 2021; L'Heureux et al. 2024).

The principal tropospheric temperature metric used to represent LTT is derived from satellite-borne microwave sounders. LTT is a bulk-layer average measurement with atmospheric temperature values below 5 km weighted more heavily than upper tropospheric values (Appendix Fig. A2.8). Other metrics emphasize different layers, such as the total tropospheric temperature (TTT), which places more weight in the mid- and upper troposphere, where tropical warming and variability is expected to be largest. Satellite-based retrievals of tropospheric temperature have the advantage of near-global coverage and continuous temporal coverage since late-1978. Datasets are currently produced by three research groups (Table 2.4). In situ data are from balloon-borne radiosonde observations (a new comprehensive collection is available now at the Copernicus Data Store C3S CDS, 2025), which are homogenized into three additional datasets. To compare the radiosonde data with satellite observations, temperature data from the surface and discrete radiosonde levels are weighted and averaged to produce synthetic satellite brightness temperatures. Despite incomplete spatial coverage, radiosonde datasets are in reasonable agreement with global satellite-based observations (Fig. 2.9; Table 2.4). Reanalyses, which are models that ingest and assimilate many streams of geophysical data, produce spatially complete estimates of tropospheric temperature. As with the radiosonde datasets, atmospheric and surface temperature data are vertically weighted to produce layer-average temperatures that are comparable to satellite products. Three reanalysis products are included in this summary (Table 2.4) and show good agreement with satellite and radiosonde time series and trends. Uncertainty in tropospheric temperature trends from individual datasets is approximately ±0.04°C decade^{-1} (e.g., Mears et al. 2011). Furthermore, differences in retrieval decisions across satellite datasets affect vertical sampling, which produces trend differences of roughly ±0.01°C decade^{-1} (Spencer et al. 2017). Structural uncertainty across datasets stems in part from decisions about the treatment of inter-satellite drifts, which produces time series divergence over the early 1990s through the early 2000s and explains most of the trend differences across satellite datasets in Table 2.4 (Zou et al. 2023).

6. STRATOSPHERIC TEMPERATURE

—W. Randel, C. Covey, L. Polvani, and A. K. Steiner

In terms of climate variability, 2025 was an unremarkable year in the stratosphere. Global mean temperatures in the lower, middle, and upper stratosphere from satellite observations since 1979 show multi-decadal cooling of the stratosphere due primarily to anthropogenic carbon dioxide (CO_2) increases, in addition to ozone depletion prior to ~2000. Stratospheric cooling was enhanced over recent years due to the Hunga volcanic eruption in January 2022, and that transient cooling persisted through 2025. The Arctic stratospheric polar vortex was disturbed by a major stratospheric warming in March 2025. The Antarctic polar vortex was strong and persistent throughout the winter (section 2g6), but experienced a minor stratospheric warming event in September 2025 that led to an early transition to summer circulation in the lower stratosphere (section 2e3). The stratospheric quasi-biennial oscillation (QBO) progressed normally in 2025, with equatorial easterly zonal wind shears and cold temperature anomalies descending from the middle to lower stratosphere during the year.

Global stratospheric temperatures have been monitored from satellite observations for over four decades, and Fig. 2.11 shows time series of global monthly temperature anomalies for altitude levels spanning the lower to upper stratosphere and mesosphere from merged satellite data. The long-term cooling of the stratosphere is primarily due to the increase in CO_2 concentration. In addition, transient variations arise from the 11-year solar cycle and effects of large volcanic eruptions: El Chichón (1982), Pinatubo (1991), and Hunga (2022). The impacts of these volcanic eruptions are highlighted in Fig. 2.11 (solid vertical lines) by comparison to the time series fit with trend and solar cycle regression components (gray dashed lines). This comparison reveals that while the stratosphere warmed following the El Chichón (1982) and Pinatubo (1991) eruptions, it cooled following the Hunga (2022) eruption. That cooling resulted from the radiative and chemical impacts of large amounts of water vapor (H_2O) injected directly into the stratosphere by Hunga (Stocker et al. 2024; Randel et al. 2024; APARC 2025), whereas the El Chichón and Pinatubo warmings were caused by absorption of longwave radiation by sulfate aerosol. Interestingly, most of the Hunga H_2O remains in the stratosphere four years after the eruption (section 2g7), accounting for the persistent cold temperature anomalies seen in Fig. 2.11.

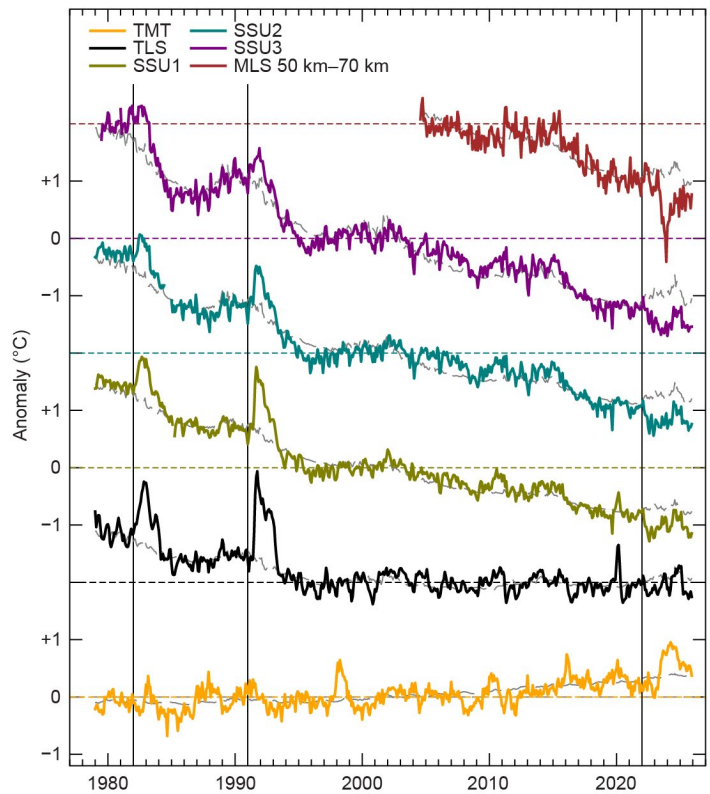

Fig. 2.11. Time series of monthly global average temperature anomalies (°C) for thick-layer averages spanning the middle troposphere, lower to upper stratosphere and mesosphere (bottom to top). Middle and upper stratosphere data are from the Stratospheric Sounding Unit (SSU) updated with Microwave Limb Sounder (MLS) measurements, representing thick-layer averages centered near 30 km, 38 km, and 45 km (SSU1, SSU2, and SSU3, respectively). Temperatures of the lower stratosphere (TLS) are ~13 km–22 km layer averages from satellite microwave measurements. Time series of middle troposphere temperature (TMT, 0 km–10 km) are included for comparison to the stratospheric data. These datasets are described in Steiner et al. (2020). Mesosphere temperatures are 50 km–70 km averages from MLS data. The dashed gray lines show piecewise linear trend and solar cycle regression fits to the time series at each level. The vertical lines denote the volcanic eruptions of El Chichon (1982), Pinatubo (1991), and Hunga (2022).

7. EQUIVALENT TEMPERATURE

—T. Wood, T. Matthews, M. P. Byrne, and P. Stoy

Equivalent temperature (*Teq*) tracks atmospheric heat accumulation:

$$Teq = T + q\frac{L}{Cp}$$

where T is dry-bulb air temperature, q is specific humidity (g kg^{-1}), L is the latent heat of vaporization, and Cp is the specific heat capacity of the air. L and Cp are treated

as constants in this analysis because they change trivially over small temperature ranges (Matthews and National Center for Atmospheric Research Staff 2025a).

Tracking *Teq* is critical because around one-third of recent heat accumulation globally, and over three-quarters in some tropical regions, has occurred through the latent term ($Tq = q\frac{L}{Cp}$), which rises exponentially with air temperature under fixed relative humidity. Extreme humid heat events and intense precipitation are sensitive to latent heat content and hence tied more closely to *Teq* than *T* (Song et al. 2022; Matthews et al. 2022; Stoy et al. 2022). *Teq* is similar to the wet-bulb temperature (section 2d2) but benefits from a linear relationship with moist enthalpy and is hence a more convenient metric to track near-surface heat accumulation in the atmosphere.

Global-mean *Teq* fell from its 2024 record high—driven mostly by cooling and drying in the tropics—to third highest (since 1979), according to ERA5 and JRA-3Q reanalyses (Table 2.5). This *Teq* cooling was broadly consistent with La Niña-type negative sea surface temperature (SST) anomalies present for much of the year and associated with a greater reduction in *Tq* (proportional to specific humidity) than in *T* (−0.69°C and −0.30°C, respectively) compared to 2024. The amplified *Tq* response is consistent with the greater sensitivity of latent heat accumulation to temperature variations within the tropics—which is predictable due to the Clausius Clapeyron relationship (Matthews et al. 2022).

Despite falling from the 2024 record high, global-mean *Teq* anomalies (Δ*Teq*) remained substantially above the 1991–2020 average (Fig. 2.12). While the smaller anomaly in 2025 compared to 2024 was broadly consistent between datasets (Fig. 2.12), important discrepancies were present (Table 2.5). For instance, JRA-3Q global-mean latent heat anomalies (Δ*Tq*) were around 20% larger than ERA5 (+0.58°C and +0.47°C, respectively), growing to 40% larger over land (+0.46°C and +0.32°C, respectively). Differences in zonal-mean Δ*Tq* were also evident (Fig. 2.13j): JRA-3Q indicates a near-uniform Δ*Tq* across latitudes, while ERA5 suggests relatively suppressed tropical Δ*Tq*.

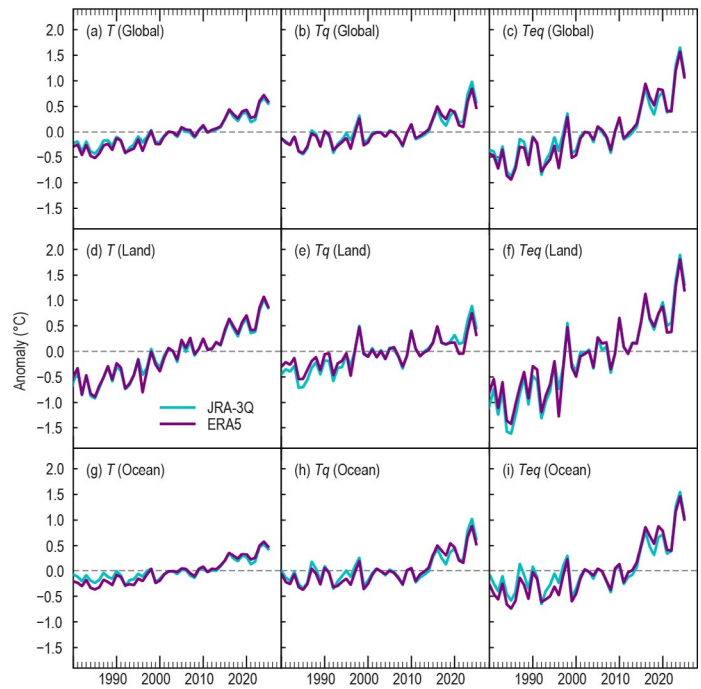

Fig. 2.12. (a),(d),(g) 2-m air temperature (*T*), (b),(e),(h) latent temperature (*Tq*), and (c),(f),(i) equivalent temperature (*Teq*) for (a)–(c) ocean + land, (d)–(f) land-only, and (g)–(i) ocean-only spatial mean anomalies (°C; 1991–2020 baseline). Each dataset is shown by colored lines: ERA5 (purple) and the Japanese Reanalysis for Three Quarters of a Century (JRA-3Q; blue), with the dataset-mean trend shown by horizontal dashed gray lines.

Table 2.5. Global equivalent temperature (*Teq*) anomalies and their constituent parts (*T, Tq*) in °C (1991–2020 base period) for 2025 and [rank] since 1979 (the earliest year common to all datasets). The uncertainty in the ensemble mean column represents one standard deviation. Cells marked with a dash signify that the data are not available.

Dataset	ERA5 *Teq*	ERA5 *T*	ERA5 *Tq*	JRA-3Q *Teq*	JRA-3Q *T*	JRA-3Q *Tq*	Ensemble Mean *Teq*	Ensemble Mean *T*	Ensemble Mean *Tq*
Land and Ocean	1.07 [3]	0.59 [3]	0.47 [4]	1.13 [3]	0.56 [3]	0.58 [3]	1.10±0.03	0.57±0.02	0.53±0.05
Land only	1.19 [3]	0.87 [2]	0.32 [6]	1.30 [3]	0.85 [2]	0.46 [5]	1.25±0.06	0.86±0.01	0.39±0.07
Ocean only	1.01 [3]	0.48 [3]	0.53 [4]	1.06 [3]	0.44 [3]	0.63 [3]	1.04±0.03	0.46±0.02	0.58±0.05

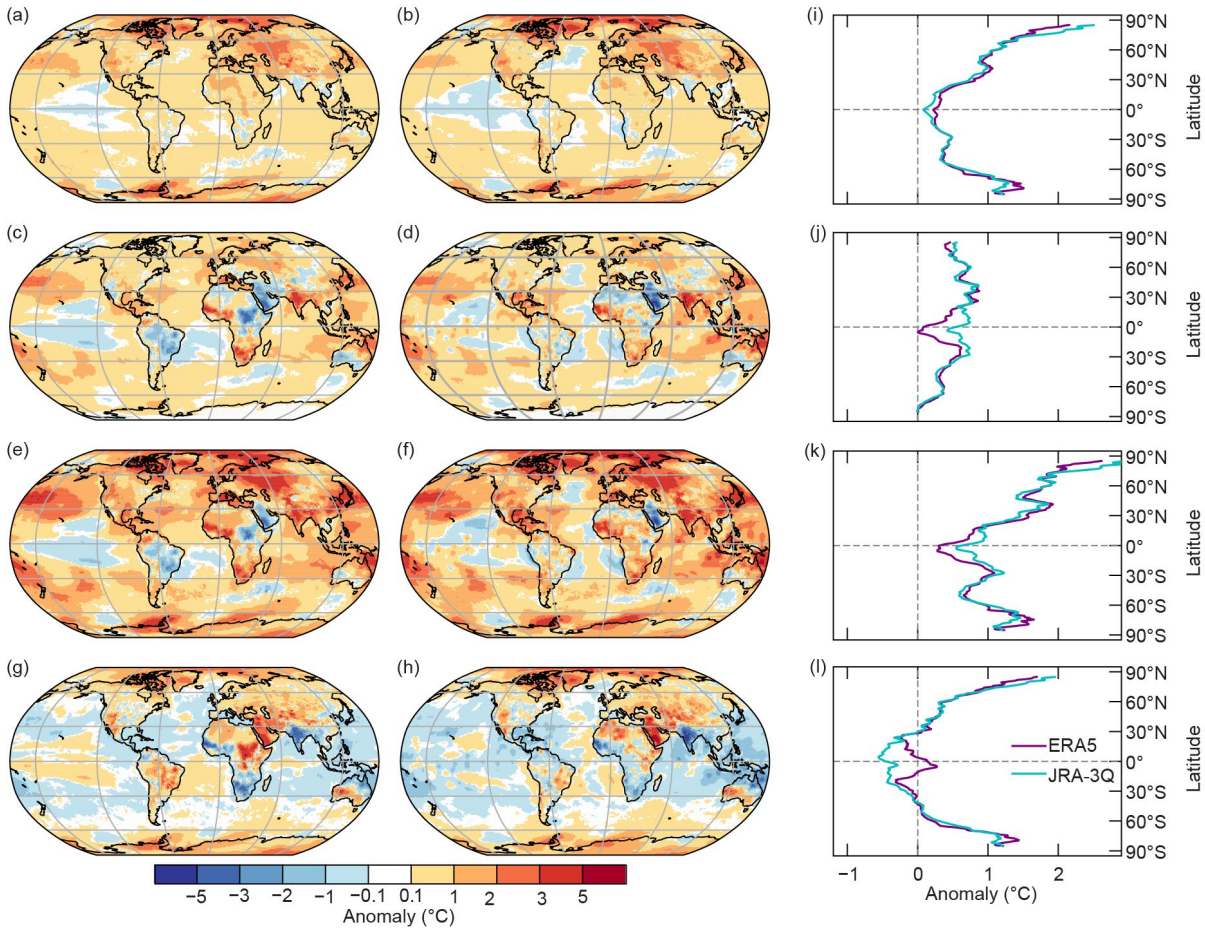

Fig. 2.13. Anomalies of (a),(b) 2-m air temperature (*T*), (c),(d) latent temperature (*Tq*), (e),(f) equivalent temperature (*Teq*), and (g),(h) *T* – *Tq* according to ERA5 (left; [a],[c],[e],[g]) and the Japanese Reanalysis for Three Quarters of a Century (JRA-3Q) (middle; [b],[d],[f],[h]) global (land and ocean). Zonal mean anomalies for each variable are shown in the right column (i)–(l) restricted to 85°S–85°N. Blue regions in the bottom row (*T* – *Tq*) experienced a larger 2025 anomaly in the latent heat term (*Tq*); red regions had a larger *T* anomaly. All units are in °C and the base period is 1991–2020.

Compared to 2024, Δ*Teq* diverged in tropical and polar regions. The tropics cooled and dried, with the tropical/subtropical mean (30°S–30°N) Δ*Tq* across datasets falling from the record-shattering +1.23°C in 2024—which was ~50% higher than the next highest year (2023)—to +0.54°C (ranked fifth). Tropical Δ*T* fell from a record +0.62°C in 2024 to +0.32°C (fifth), resulting in Δ*Teq* falling from a record +1.85°C in 2024 to +0.86°C (fifth). Conversely, in high northern latitudes (60°N–90°N), anomalies were the most humid (highest Δ*Tq*) and second warmest (second highest Δ*T*) on record, resulting in the second highest Δ*Teq*—breaching +2°C for the first time since the exceptional 2016 anomaly (Overland and Wang 2016; Appendix Table A2.1).

Regionally, ERA5 indicated notable drying (negative Δ*Tq*) relative to the baseline in central Africa and tropical South America, suppressing zonal-mean tropical anomalies compared to JRA-3Q. This dry anomaly overlaps with Amazon and Congo rainforests and was also observed last year (Matthews et al. 2025b).

Another continuity from 2024 was the strong dry anomalies over the Arabian Peninsula and moistening over the Indian subcontinent (Matthews et al. 2025b). By contrast, the widespread positive Δ*Tq* across northern Africa in 2024 was restricted to a region north of the Gulf of Guinea in 2025. In the northern mid- and high latitudes, *Tq* exhibited near-uniform positive anomalies in 2025.

The impact of the La Niña-type sea surface temperature (SST) anomalies during 2025 on precipitation and related regional drying were evident in unusual patterns in the Southern Hemisphere, including a high positive Δ*Tq* in South Africa (stronger in ERA5; de Oliveira et al. 2018; Nicholson and Selato 2000) and absent tropical Δ*Tq* amplification, contrasting with 2024 and longer-term trends (Song et al. 2022; Matthews et al. 2022).

In general, the discrepancy between reanalysis products is larger for *Teq* than for *T* because humidity (*Tq*) is more uncertain (Table 2.5). Indeed, NCEP/NCAR reanalyses are excluded here due to known deficiencies in tracking tropospheric moisture (Dessler and Davis 2010). However, humidity observations from critical tropical regions characterized by high *Tq* and *Teq* uncertainty (e.g., the Congo and Amazon rainforests) are sparse (Schröder et al. 2019).

8. MAXIMUM LAND SURFACE TEMPERATURE

—J. Blannin, A. M. Waring, E. Good, K. Veal, and D. Ghent

Maximum land surface temperature has a large range, shown in both the 2025 values (Fig. 2.14a) and the 2019–24 climatology (Fig. 2.14b), with such temperatures below –30°C in Antarctica and exceeding 60°C in regions such as north Africa, Iraq, Iran, and the United Arab Emirates, as well as in north-east Australia.

Positive land surface temperature (LST) maximum anomalies (Fig. 2.14c) for 2025 relative to the 2019–24 baseline period (Fig. 2.14b) can be seen in northern Alaska, eastern South America, parts of Europe, equatorial Africa, southern Russia, northern China, Japan, and much of central and southern Australia. The 95th percentile of maximum LST anomalies is +5.1°C for 2025, with anomalies exceeding this on the northeast coast of the Black Sea, in Russia to the east of Lake Baikal, and across parts of western Antarctica. Very high anomalies (>+10°C), were observed near Mongolia and on the southern coasts of Iran and Pakistan, and in eastern Antarctica. There is considerable geographical agreement between the 2025 anomalies (Fig. 2.14c) and the annual ranking patterns (Fig. 2.14d). Many of these warm-anomaly regions correspond to the highest or second-highest maximum LST in the 2019–25 series. Regions that experienced the highest ranking maximum LSTs in 2025 include much of Antarctica, almost half of the landmass of Türkiye (in line with record high air temperatures, see section 7f9), and some smaller areas within all continents.

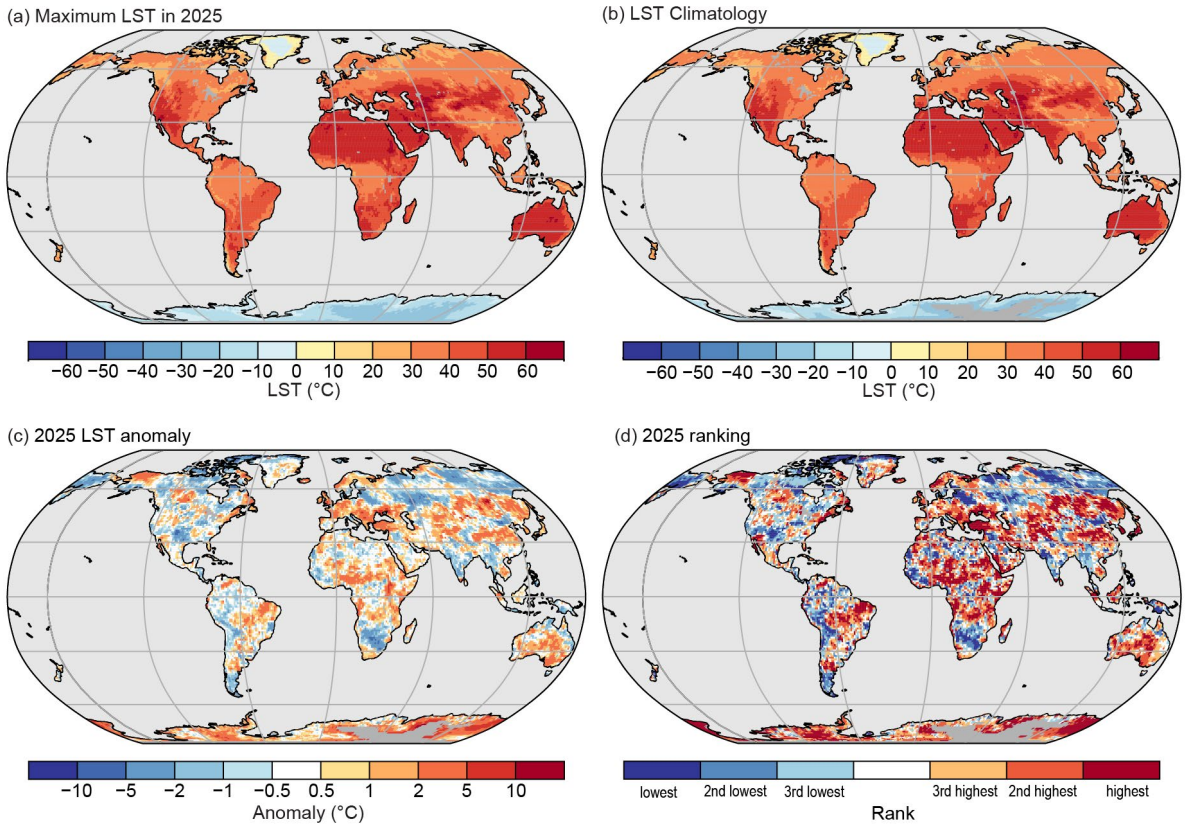

Fig. 2.14. (a) Maximum land surface temperature (LST) recorded in 2025, (b) maximum LST climatology (2019–24 base period), (c) 2025 maximum LST anomalies with respect to the LST climatology (2019–24), and (d) ranking of 2025 maximum LST over the period 2019–25. The data shown have been aggregated from the SLSTR-B native 0.01° latitude/longitude product to 1° latitude/longitude. Units for (a)–(c) are °C.

In contrast, negative LST maximum anomalies (Fig. 2.14c) occurred in northern Canada, the southern United States, western South America, along the northwest coast and across southeastern Africa, much of Russia, and parts of India and Thailand. The 5th percentile of maximum LST anomalies was –3.5°C for 2025, and anomalies less than this were observed across South Africa and Lesotho, the southern central United States, and northern Kazakhstan. As for the positive LST anomalies, the LST rankings demonstrate a high degree of consistency with the negative LST anomalies. Correspondingly, some of these regions saw their lowest LST maximums in the seven-year record (Fig. 2.14d), e.g., parts of Siberia, South Africa, and the southern United States.

As the climatology and annual ranking include only six and seven years of data, respectively, they should be interpreted with great care given the few years available, especially as a prolonged La Niña occurred between 2020 and 2023. In addition, the limited data results in the annual ranking displaying both record positive and negative anomalies, leading to a large degree of noise. As the record extends, the noise will decrease.

LST is an essential climate variable (WMO et al. 2025), and it should be noted that differences between LST and the corresponding near-surface air temperature (NSAT) can often reach several °C and may exceed 20°C in some conditions (Good 2016). Nevertheless, there are similarities between 2025 maximum LST anomalies (Fig. 2.14c) and NSAT TX90p (section 2b4) anomalies (Plate 2.1d), such as on the southeastern tip of Africa and across India. Similarly, dry regions across Europe and much of Australia (section 2d12) correspond with positive LST anomalies, and negative LST anomalies over northwestern South America may be associated with the enhanced precipitation in this region (section 2d5).

Satellite-observed LST, which is a measure of the aggregated surface skin or sub-skin temperature of the scene (e.g., bare ground, urban areas, forest canopies) visible within the field of view of the satellite instrument, was introduced in last year's report (Good et al. 2025). The LST data used in this section are from the Sea and Land Surface Temperature Radiometer B (SLSTR-B) between 2019 and 2025. Good et al. (2025) also highlighted the importance of temporal stability in satellite data and confirmed this dataset to be sufficiently free from non-climatic discontinuities to be used for temporal analysis of LST. LST from SLSTR-B is not measured directly; instead, it is derived from infrared radiance measurements and modeling of the atmosphere to account for attenuation effects, and for the non-unity effects of surface emissivity. LST from infrared measurements are only valid under cloud-free conditions, and can be cold-biased if cloud is undetected. For that reason, this section focuses on the maximum LST, which is less likely to be affected by undetected cloud contamination and is also highly relevant for human, plant, and animal heat stress.

c. Cryosphere

1. PERMAFROST TEMPERATURE AND ACTIVE LAYER THICKNESS

—J. Noetzli, H. H. Christiansen, T. Galleman, M. Guglielmin, F. Hrbáček, G. Hu, K. Isaksen, N. Kirchner, F. Magnin, P. Pogliotti, C. Riedl, S. L. Smith, L. Zhao, and D. A. Streletskiy

Permafrost is ground with temperatures not exceeding 0°C for at least two years and underlies polar or cold high mountain regions. Recent observed trends continued in 2025, with permafrost warming, active layer (the seasonally thawed layer) thickening, and ground ice loss (Streletskiy et al. 2025). New record levels for both permafrost temperature and active layer thickness (ALT) were reached across much of the permafrost region for many sites reporting, underscoring the rapid impact of climate change on polar and mountain permafrost with potentially important consequences for landscape, ecosystems, infrastructure, or natural hazards (Burn et al. 2025; Hjort et al. 2022; Ravanel and Deline 2011; Young et al. 2025).

Permafrost warming in continuous permafrost in the high Arctic and in cold high-elevation bedrock is up to 1°C decade^{-1} at 10-m to 20-m depth, comparable to surface air temperature (SAT) increase (Biskaborn et al. 2019; Noetzli et al. 2024; Smith et al. 2022). Warming is reduced in warmer ice-bearing permafrost—discontinuous permafrost in the polar areas or ice-bearing debris slopes in mountain regions—due to latent heat effects during ground ice melt (0.2°C–0.3°C decade^{-1}). Temperature changes at the surface take time to reach greater depths: e.g., in European mountains recent warming at 20-m depth was about half of that observed at 10-m depth (Noetzli et al. 2024).

In the Arctic, permafrost temperatures were higher in 2025 than in 2024 at 21 of 24 reporting sites across North America, Svalbard, and Scandinavia, and at record values at 15 sites (see also section 5j). In northern Alaska and the northern Mackenzie Valley, the higher permafrost temperatures reflect higher SAT in 2023/24, which followed a short cool period. In Antarctica, permafrost temperature shows relative warming in 2025 compared to 2024 in continental Antarctica (Oasi), while conditions were stable on the Antarctic Peninsula (Rothera). Near-surface temperatures in 2025 on James Ross Island were 1.4°C above the 2014–23 average (Hrbáček et al. 2025).

In Europe, permafrost warming continued in 2025 from the Alps to the Scandinavian mountains and high Arctic Svalbard (Fig. 2.15). Annual mean permafrost temperatures at ~10-m depth exceeded values from 2024 at 10 of 16 reported sites, with nine reaching new records since the start of the time series. Positive changes occurred mainly at bedrock sites, while other sites recorded slightly lower permafrost temperatures than in 2024. Absolute changes compared to 2024 were up

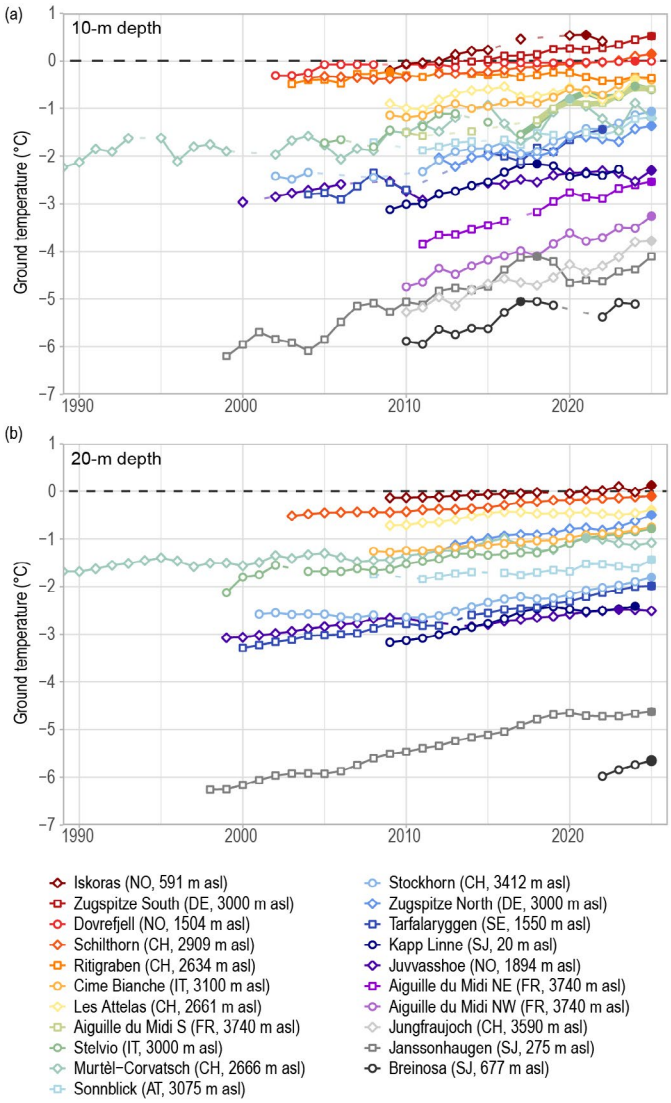

Fig. 2.15. Mean annual ground temperature (°C) measured in European permafrost boreholes in the Alps, Scandinavia, and Svalbard at (a) 10-m and (b) 20-m depth. Maximum values for each time series are indicated with a filled circle. (Sources: Austria: GeoSphere Austria; France: updated from Magnin et al. [2023]; Germany: Bavarian Environment Agency; Italy: updated from Pogliotti et al. [2023] and Guglielmin, M.: updated from Noetzli et al. [2024]; Norway and Svalbard: Norwegian Meteorological Institute and the University Centre in Svalbard UNIS; Sweden: Stockholm University; Switzerland: [PERMOS 2026].)

to 0.3°C. At ~20-m depth, permafrost temperatures increased by ca. 0.1°C at 11 of 12 sites (0.2°C at Sonnblick, Austria) and reached records at 10 sites. Widespread evidence of permafrost degradation was reported at observation sites: a supra-permafrost talik (year-round unfrozen ground) formed at Schilthorn, Switzerland, with positive temperatures at 10-m depth since 2023 and warm permafrost remaining below ~15-m depth (PERMOS 2025). The ALT in a borehole near Juvvasshoe, Norway (e.g., Noetzli et al. 2024), has increased from about 6-m to 13-m depth since 2008. Permafrost at 10-m depth has warmed by nearly 2°C since 1998 at Janssonhaugen, Svalbard, and by around 1.5°C since 2010 in high-elevation bedrock at Jungfraujoch, Switzerland, and Aiguille du Midi, France. Recent decadal warming for Svalbard was up to 0.9°C at 20-m depth (Strand and Christiansen 2025).

In the central Asian Qinghai Tibet Plateau (QTP), long-term permafrost warming rates at 10-m depth since 2000 are 0.04°C–0.4°C decade^{-1} (Fig. 2.16), matching those of ice-bearing ground reported from other regions. Permafrost temperatures in 2024 (the latest available year) at five sites were higher than in 2023. Simulations reveal that ground ice melt absorbs 88% of the total energy under future scenarios, far exceeding that for ground warming (Hu et al. 2025).

Decadal increases in ALT range from centimeters in continuous permafrost in Arctic sediments to decimeters in discontinuous bedrock permafrost in polar regions, southern Scandinavia, and the QTP, and to meters in bedrock or talus slopes in the European Alps (PERMOS 2025; Magnin et al. 2024). ALT in 2025 reached new records in the Alaskan Interior (IAK_CMV, Fig. 2.17), 4 cm–7 cm above the 2024 values, while it was on average 2 cm lower and below the 2000–24 mean on the Alaskan North Slope and Seward Peninsula (BCS; Fig. 2.17). In the Nordic Arctic and Greenland and Russian Northwest (BAR_WS), ALT in 2025 was above average but similar to the previous seven years. In Svalbard, ALT was close to record levels in bedrock and below 2024 values in fine grained sediments. In the Russian Arctic, ALT increase continued in central Siberia (CENT_SIB) with values slightly above 2023/24. In eastern Siberia and

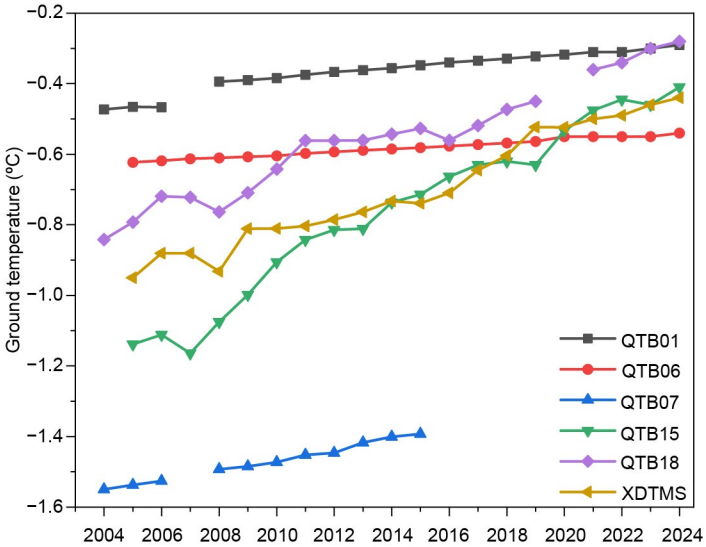

Fig. 2.16. Ground temperature (°C) measured at 10-m depth in the Qinghai-Tibet Plateau during the period 2005–24. (Source: Cryosphere Research Station on the Qinghai-Tibet Plateau, Northwest Institute of Eco-Environment and Resources, Chinese Academy of Sciences.)

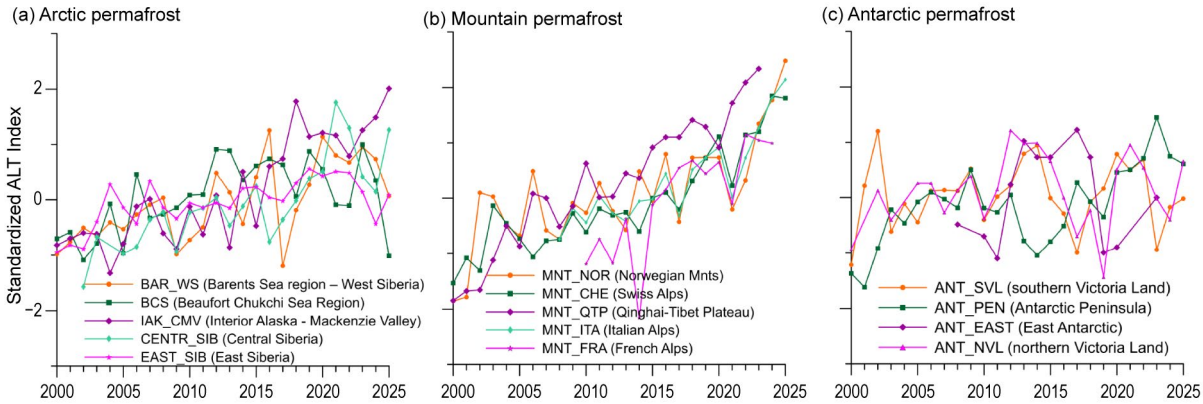

Fig. 2.17. Standardized index of active layer thickness (ALT) relative to the 2000–20 base period. (a) Arctic regions: Beaufort-Chukchi Sea (BCS)–Arctic Alaska and Mackenzie Delta region, Interior Alaska and Central Mackenzie Valley–Northwest Territories (IAK_CMV), Barents Sea region–West Siberia (BAR_WS), Central Siberia (CENT_SIB), and East Siberia (EAST_SIB); (b) Mountain regions: Norwegian mountains (MNT_NOR), Swiss Alps (MNT_CHE), Italian Alps (MNT_ITA), French Alps (MNT_FRA), and Qinghai-Tibet Plateau (MNT_QTP); and (c) Antarctic regions: Antarctic Southern Victoria Land (ANT_SVL), Antarctic Peninsula (ANT_PEN), and Antarctic East (ANT_EAST). Note that only data from 30% of the Russian sites are reported. (Source: Circumpolar Active Layer Monitoring [CALM].)

Chukotka (EAST_SIB), ALTs were close to the long-term mean (2000–24). In continental Antarctica, ALT was close to 2024 and the long-term mean in Southern Victoria Land, but above the mean in Northern Victoria Land (+18%). Except for two sites, ALT on the Antarctic Peninsula was 18% above average.

In European mountains, rapid increase in ALT continues with records in 2025 in the Norwegian Mountains. In the Alps, maxima were mostly reached between 2022 and 2024. In 2025, ALT was generally lower than in 2024, but close to record levels and above the 2000–24 mean. Decadal ALT increase at 10 sites along the Qinghai-Tibet highway during 1981–2024 was 20.8 cm (Zhao et al. 2021; Hu et al. 2024).

2. ALPINE GLACIERS

—M. Pelto

The 2025 World Glacier Monitoring Service (WGMS) dataset of annual glaciological mass balance observations includes 162 glaciers from six continents and 26 nations; 158 with a negative balance and four with a positive balance. In 2025, the mean annual mass balance of the 59 reporting global reference glaciers was –1.34 m water equivalent (w.e.), and also –1.34 m w.e. for all 162 reporting glaciers. The 2025 regionalized global average annual balance of –1.09 m w.e. marked the fourth consecutive year with mass balance loss exceeding 1.0 m w.e., with 2023 having the most negative at –1.23 m w.e. and 2024 at –1.04 m w.e. (Fig. 2.18). Since 1976, mountain glaciers and ice caps have lost 9179±621 gigatons (Gt) of water, contributing 25.3±1.7 mm to global mean sea level rise, with 41% of this loss occurring in the last decade (Dussaillant et al. 2025).

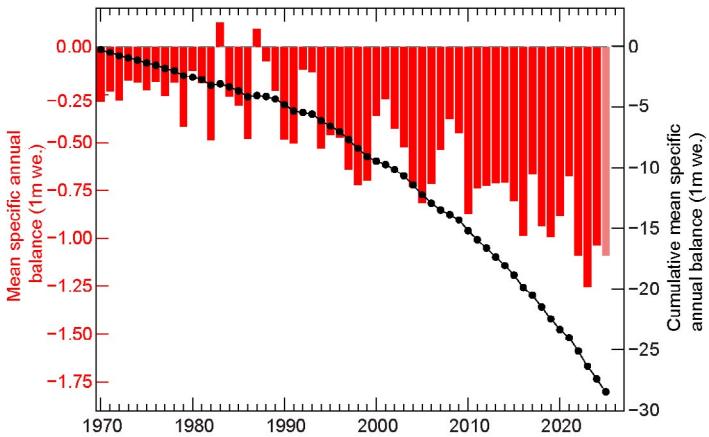

Fig. 2.18. Time series of regionalized average global mean annual glacier mass balance of alpine glaciers for the period 1970–2025 in meters of water equivalent (m w.e.) as determined by the World Glacier Monitoring Service. Annual mass balance is shown in red bars and annual cumulative mass balance is indicated by black dots.

The mean annual balance of global reference glaciers in 2025 was –1.34 m w.e., similar to 2023 and 2024, which had a mean annual balance of –1.60 m w.e. and –1.37 m w.e., respectively. This makes 2025 the 38th consecutive year with a global alpine mass balance loss, and the 16th consecutive year with a regionalized global mass balance below –0.5 m w.e. The significant acceleration of mass balance loss is evident in glaciological observations, geodetic observations, altimetry observations, and gravimetric observations (The GlaMBIE Team 2025). The acceleration of mass balance loss indicates glaciers are not approaching equilibrium and instead are increasingly disappearing. The Global Land Ice Measurement from Space inventory of global glaciers has added an extinct glacier layer to record glaciers that have disappeared; it is now populated by 181 glaciers that had existed in a previous inventory (Raup et al. 2025). In conjunction with 2025 being the United Nations International Year for Glaciers' Preservation, the Global Glacier Casualty List has been created to chronicle the story of specific glaciers being lost from each glaciated region (Boyer and Howe 2025).

For 2025, in the European Alps, all 54 glaciers observed had negative balances, with 45 of the glaciers losing over 1.0 m w.e. All glaciers in Iceland (six) and Svalbard (nine) observed loss of over 1.0 m w.e. In Norway, 8 of 10 glaciers had a negative balance, with two glaciers having a positive balance. In Sweden, three of four glaciers had a negative balance.

In Asia, all 23 glaciers across seven nations had negative balances that averaged –0.97 m w.e. In New Zealand, the two glaciers observed also had a negative mass balance. In the Andes Mountains of South America, 9 of 10 glaciers, reporting from four nations, had negative balances, with an average balance of –0.92 m w.e. All 14 glaciers in western North America, outside of Alaska, had mass balance below –1.0 m w.e. with an average of –2.24 m w.e. In Alaska, three of four glaciers had negative balances. The five glaciers reported in Arctic Canada all had small negative balances averaging –0.16 m w.e. Peyto Glacier in Canada exemplifies the limited

retained snow cover on alpine glaciers in western North America in 2025 at around 10%. A glacier should be 50%–60% snow covered at the end of summer to be in equilibrium (Fig. 2.19). It is evident that Peyto Glacier is representative of adjacent glaciers that also have limited retained snow cover.

Alpine annual mass balance glaciological observations are reported to the WGMS by national representatives with a 1 December annual submission deadline. WGMS reference glaciers (60) have at least 30 continuous years of mass balance observation. Benchmark glaciers (23) have at least a 10-year mass balance record and are in regions that lack sufficient reference glaciers. The combination of benchmark and reference glaciers are used to generate regional averages (WGMS 2023). Global values are calculated using a single averaged value for each of 19 mountain regions, limiting bias from the geographical variability of observation density (WGMS 2023). Expansion of this dataset leads to reanalysis and updated values.

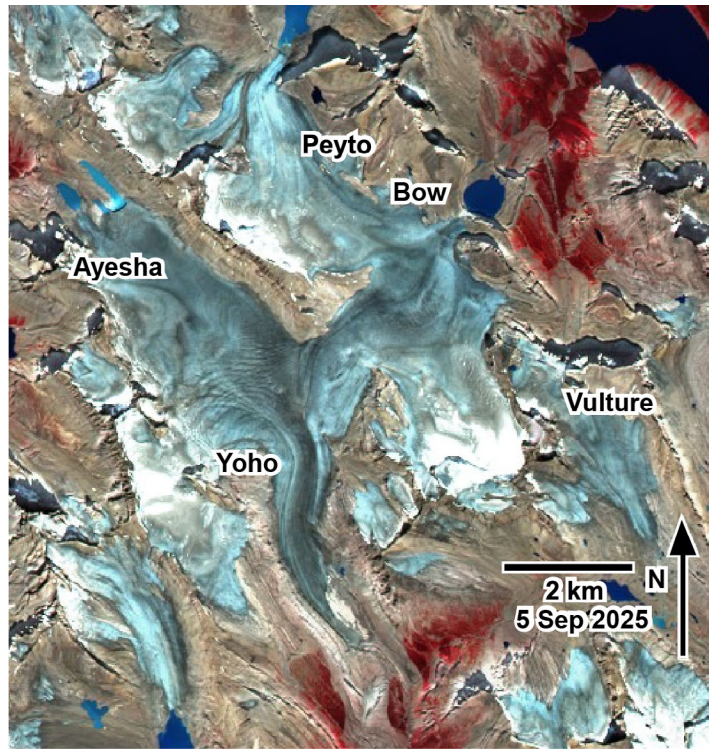

Fig. 2.19. Peyto Glacier in Canada: a global reference glacier that was less than 10% snow covered in Sep 2025. Snow cover is limited on all of the neighboring glaciers.

3. LAKE ICE

—S. Sharma, R. I. Woolway, and J. A. Culpepper

Northern Hemisphere (NH) lakes continued to exhibit later ice formation, earlier ice breakup, and reduced ice duration during the winter of 2024/25, consistent with long-term trends. On average, NH lakes froze 7.8 days later, experienced ice breakup 6.7 days earlier, and had ice durations that were 15.0 days shorter, based on ERA5 reanalysis data relative to the 1991–2020 base period (Fig. 2.20). Most regions showed shorter ice duration, with Scandinavia and parts of Canada experiencing considerable declines in duration, likely reflecting stronger positive winter air temperature anomalies across these regions. A slight increase in ice duration was observed in some regions, including in the United States south of the Laurentian Great Lakes, which experienced below-average air temperatures during the winter season.

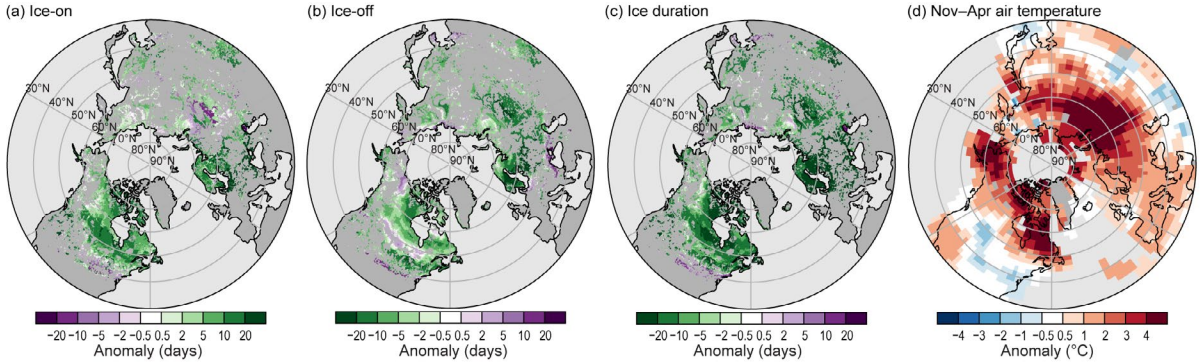

Fig. 2.20. Anomalies (days) compared to the 1991–2020 base period in lake ice cover across the Northern Hemisphere during the winter of 2024/25. Generally, green values indicate less ice, whereas purple depicts lakes with more ice. More specifically for the (a) ice formation period (ice-on; positive values indicate later ice formation), (b) ice breakup period (ice-off; negative values indicate earlier ice breakup), and (c) ice duration period. For duration, (c) negative (positive) values indicate shorter (longer) ice cover. (d) Average surface temperature anomalies (°C) for Nov 2024–Apr 2025, where negative (positive) values are colder (warmer) temperatures. (Sources: ERA5, GISTEMP.)

In situ lake ice observations from 139 lakes across the NH revealed that ice-on was 5.6 days later, ice-off was 11.3 days earlier, and ice duration was over 16 days shorter on average during the 2024/25 winter (defined here as the months in which lakes are ice covered, generally between November 2024 and April 2025) relative to the 1991–2020 base period. Lake Suwa, Japan, did not freeze in 2025.

The average ice duration in mountain lakes (a subset of in situ lakes >1000 m a.s.l.) during the winter of 2024/25 was 20.2 days shorter than the 20-year average (2000–19; Fig. 2.21), due to a combination of later ice-on (5.2 days) and earlier ice-off (13.4 days). Mountain lakes in Norway showed a particularly strong loss of ice duration (29.3 days) compared to the North American lakes (13.7 days). Extremely high temperatures in the Arctic likely explain the high anomalies in the Norwegian mountain lakes, as the months of January, February, and March of 2025 were the second warmest on record since 1900 (Ballinger et al. 2025).

During the 2024/25 winter, Lakes Erie (+19.8%) and Huron (+11.2%) had higher maximal ice cover anomalies, whereas Lakes Superior (–8.9%), Michigan (–2.9%), and Ontario (–0.1%) had lower maximal ice cover anomalies relative to 1991–2020 (Fig. 2.22). Taken as a whole, the Great Lakes reached their maximal ice coverage on 21 February 2025, three days earlier than the average of the 1991–2020 winters.

Ice-on and ice-off dates, in addition to ice duration, were calculated for lakes across the NH using ice simulations guided by the ECMWF ERA5 reanalysis product (Hersbach et al. 2020), following the methodology of Grant et al. (2021). We obtained in situ observations for 139 lakes across Canada, the United States, Norway, Finland, and Japan from community scientists and established monitoring networks. We also obtained in situ ice phenology for eight mountain lakes in the United States and five alpine lakes in Europe (Caine et al. 2025; Chandra et al. 2022; L'Abée-Lund et al. 2021). Updated ice data from Chandra et al. (2022) were amended through personal correspondence with the data authors. Moreover, we acquired annual maximum ice coverage (%) data for each of the Laurentian Great Lakes from 1973 to 2025 (https://www.glerl.noaa.gov/data/ice/). Finally, surface air temperature data for the NH cold season (November–April average) were downloaded from the NASA GISS surface temperature analysis (GISTEMP Team 2024; Lenssen et al. 2024).

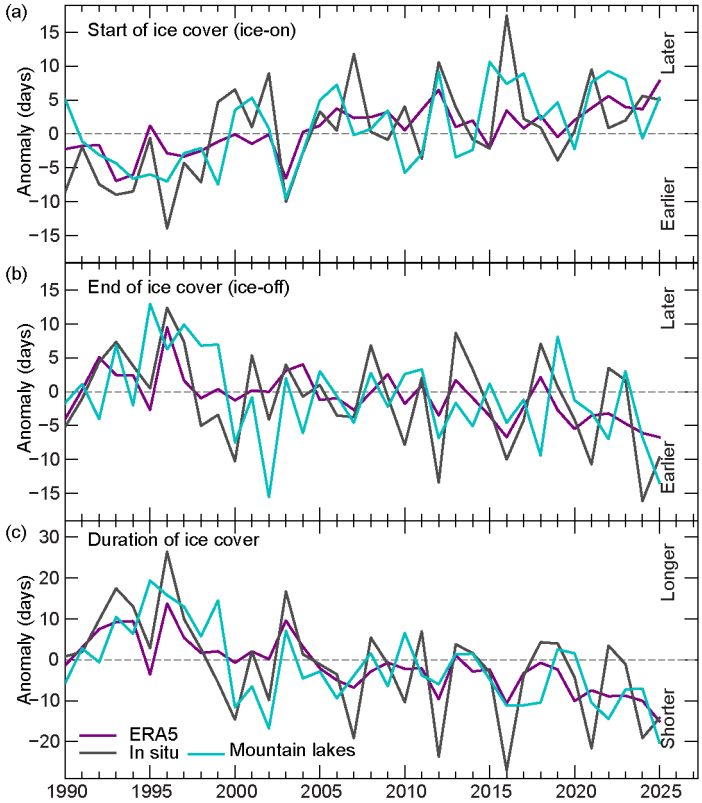

Fig. 2.21. The (a) ice-on, (b) ice-off, and (c) ice duration anomalies (days) for Northern Hemisphere lakes from 1990 to 2024 compared to the 1991–2020 base period for all in situ observations (dark gray), mountain lake subset of in situ observations (blue), and ERA5 (purple). Negative (positive) values indicate earlier (later) ice-on, earlier (later) ice-off, and shorter (longer) ice duration.

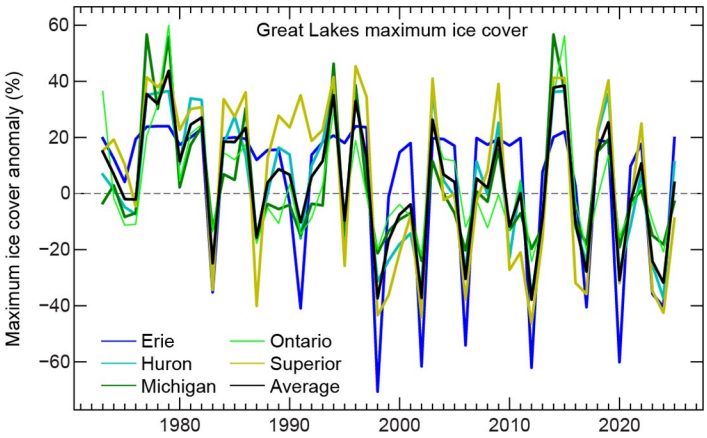

Fig. 2.22. Maximum ice cover extent anomalies (%) of the Laurentian Great Lakes for the period 1973–2025 with respect to the 1991–2020 base period. The colored lines indicate individual lake anomalies (e.g., Erie anomaly in blue), while the black line shows the average anomaly for the five lakes. Negative (positive) values indicate less (more) maximum ice cover extent.

4. NORTHERN HEMISPHERE CONTINENTAL SNOW COVER EXTENT

—D. A. Robinson and T. W. Estilow

Annual snow cover extent (SCE) over Northern Hemisphere (NH) lands averaged 23.7 million km² in 2025. This was 1.2 million km² less than the 1991–2020 mean and 1.3 million km² below the mean of the full 56-year record (Table 2.6). Overall, 2025 had the third least extensive annual cover on record, slightly less than 2024, but larger than 1990 and 1988. Monthly SCE in 2025 ranged from 45.5 million km² in February to 2.9 million km² in both July and August. Twelve-month running mean SCE departures at the end of 2025 across all NH lands were the lowest since July 1990 (Fig. 2.23a). Annual mean SCE in Eurasia was the fourth least extensive on record in 2025 and North America (NA) the eighth least extensive. Weekly NH SCE in 2025 was below the respective long-term means for a large majority of weeks throughout the year (Fig. 2.23b). Exceptions included near-normal SCE in the summer low period, when cover is mainly confined to the Greenland ice sheet, and during the onset of the snow season in autumn. The last three weeks of winter (February) were above normal.

In January, the NH SCE was the fourth least extensive in the 59-year record, with Europe (EUR) observing its second lowest extent for the month on record while North America (NA) had its 22nd most extensive January. April

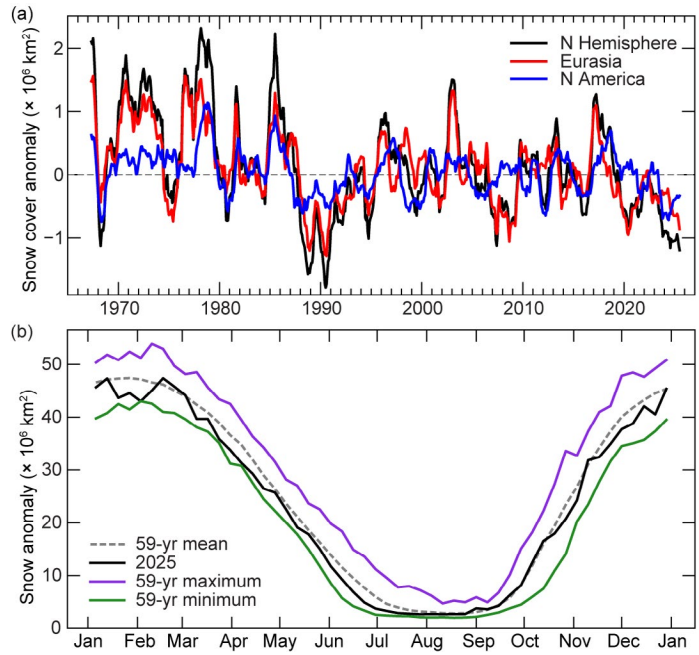

Fig. 2.23. (a) Twelve-month running anomalies (× 10⁶ [million] km²) of monthly snow cover extent (SCE) over Northern Hemisphere (NH) lands as a whole and Europe (EUR) and North America (NA) separately plotted on the seventh month using values from Nov 1966 to Dec 2025. Anomalies are calculated from NOAA snow maps. Mean NH SCE is 25.1 million km² for the full period of record. Monthly means for the period of record are used for nine missing months during 1968, 1969, and 1971 to create a continuous series of running means. Missing months fall between Jun and Oct. (b) Weekly NH SCE for 2025 (black) plotted with the mean (gray dashed line), maximum (purple), and minimum (green) SCE for each week. Mean weekly SCE and extremes are calculated using the 59-year record from Jan 1967 to Dec 2025. Weekly means for the period of record are used for 4, 21, and 12 missing weeks during 1968, 1969, and 1971, respectively. Weekly data granules represent SCE for each seven-day period ending on Monday.

Table 2.6. Monthly and annual climatological information on Northern Hemisphere (NH), Eurasia (EUR), and North America (NA) snow cover extent (SCE) between Nov 1966 and Dec 2025. Included are the numbers of years with data used in the calculations, 2025 NH anomalies, NH means, NH std. dev., and ranks. Units are millions of square kilometers. The years 1968, 1969, and 1971 have one, five, and three missing months respectively, thus are not included in the annual (Ann) calculations. NA includes Greenland. Ranks are from most to least extensive (least to most in parentheses).

Time Period	Yrs	2025 NH Anomaly	NH Mean	NH Std. Dev.	2025 NH Rank	2025 EUR Rank	2025 NA Rank
Jan	59	–2.1	47.1	1.5	56 (4)	58 (2)	22 (38)
Feb	59	–0.4	45.9	1.8	35 (25)	31 (29)	31 (29)
Mar	59	–2.4	40.3	1.8	53 (7)	52 (8)	42 (18)
Apr	59	–2.6	30.4	1.7	59 (1)	58 (2)	37 (23)
May	59	–1.7	19.0	2.0	45 (15)	44 (16)	50 (10)
Jun	58	–2.6	9.2	2.5	47 (12)	45 (14)	48 (11)
Jul	56	–0.9	3.8	1.2	42 (15)	47 (10)	34 (23)
Aug	57	0.0	2.9	0.7	22 (36)	49 (9)	11 (47)
Sep	57	+0.3	5.4	0.9	21 (37)	12 (46)	43 (15)
Oct	58	–0.6	18.6	2.6	32 (27)	22 (37)	54 (5)
Nov	60	–1.2	34.3	2.1	46 (15)	45 (16)	32 (29)
Dec	60	–1.8	43.7	1.8	56 (5)	56 (5)	35 (26)
Ann	56	–1.3	25.1	0.8	54 (3)	53 (4)	49 (8)
Ann vs 1991-2020	30	–1.2	24.9	0.5	N/A	N/A	N/A

SCE for the NH was the least extensive for the month on record, surpassing the record set the previous year in 2024. As in January, this was driven by the second least extensive April SCE for Eurasia (NA was 23rd least extensive). Below-normal SCE continued through May and June for both Eurasia and NA.

The new snow season began with September and October NH SCE each ranking in the middle tercile due to a combination of above-average Eurasia SCE and below-average NA. Low SCE extent for the NH in November (15th least extensive) and December (fifth least) were mostly due to low EUR SCE, with NA SCE in the middle tercile.

The contiguous United States SCE ranked in the middle tercile in January and February 2025. Spring months ranked from 10th (April) to second (May) least extensive. Over Canada, the year started with above-average SCE in January and February before declining to the middle tercile in March and April. May and June had the 13th and sixth least extensive SCE, respectively, in conjunction with early snow melt. Canada SCE during autumn was in the lower tercile in September and October, increasing to the third largest extent for December.

SCE is calculated at the Rutgers Global Snow Lab (GSL) from daily SCE maps produced by meteorologists at the U.S. National Ice Center, who rely primarily on visible satellite imagery to construct the maps (Estilow et al. 2015). Maps depicting daily, weekly, and monthly conditions, anomalies, and climatology's may be viewed at the GSL website (https://snowcover.org).

In recent years, the contrast between sharply declining spring SCE and steadier autumn SCE (with EUR above average and NA below average early in the 2025 onset season) reflects the differing seasonal behavior of the record. A recent analysis indicates that part of the long-term increase in autumn SCE in the NH record arises from a gradual increase in the sensitivity of the operational snow charts to thin and ephemeral snow cover over the period of record, an effect most pronounced from September through November (Chereque et al. 2025), consistent with earlier comparisons against independent satellite and modeled products (Brown and Derksen 2013). A distinct regional increase in autumn SCE over central EUR, which contributed to the above-average EUR onset in 2025 and other post-2000 years, has an independent physical basis in changing atmospheric circulation, including enhanced moisture transport linked to reduced Arctic sea ice and a strengthened Siberian high (Allchin and Déry 2020; Li et al. 2025). Quantifying the relative roles of evolving map sensitivity and circulation-driven change in onset-season SCE trends remains an active area of investigation.

d. Hydrological cycle (atmosphere)

1. NEAR-SURFACE HUMIDITY

—K. M. Willett, M. Bosilovich, and A. J. Simmons

Near-surface humidity dropped substantially in all measures in 2025, compared to the record highs of 2024. Nevertheless, near-surface specific humidity (q), a measure of atmospheric water vapor, remained high in 2025 and was 0.14 g kg^{-1} to 0.24 g kg^{-1} above the 1991–2020 average over land (Fig. 2.24; Table 2.7), and 0.19 g kg^{-1} to 0.36 g kg^{-1} above average over ocean. Relative humidity (RH) is a measure of saturation or how much water vapor is in the air compared to the maximum that could be. Over land, RH anomalies were below average, −0.21 %rh to −1.12 %rh, continuing a decreasing trend that has been apparent since at least 2000. According to the Met Office Hadley Centre Integrated Surface Dataset of Humidity over land (HadISDH.land), 2025 was the driest year on record but fourth to ninth driest for the other datasets. Over ocean, all datasets except for MERRA-2 show that 2025 was drier than 2024. The 2025 anomalies ranged from −0.09 %rh (ERA5) to +0.44 %rh (MERRA-2). While there is good consensus between the datasets for q globally, uncertainties are larger for RH, especially over oceans, where observation coverage remains challenging.

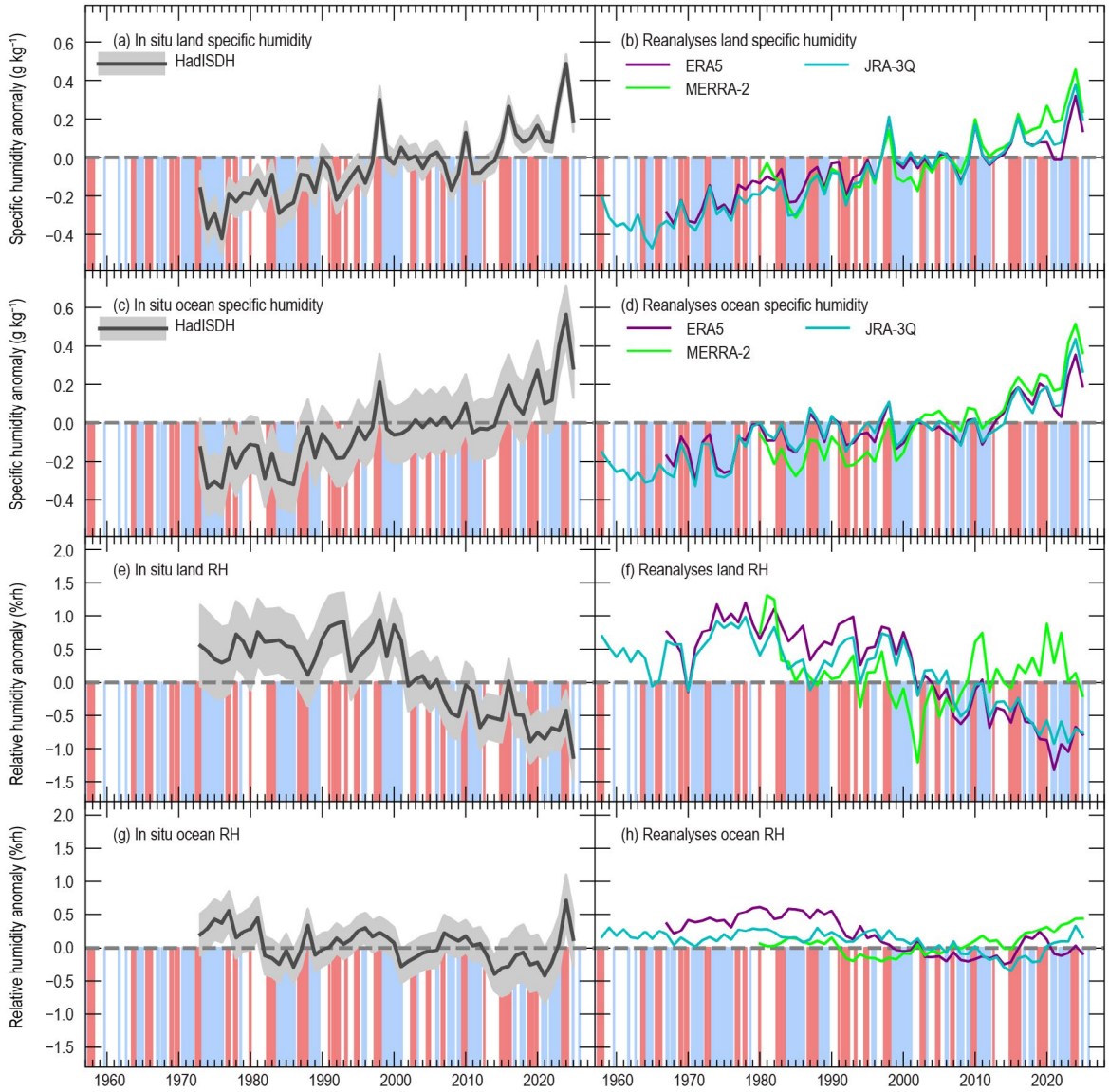

Fig. 2.24. Global average surface humidity annual anomalies (g kg^{-1} for [a]–[d] and %rh for [e]–[h]; 1991–2020 base period). For the in situ datasets, 2-m surface humidity is used over land and ~10-m surface humidity over the oceans. For the reanalysis, 2-m humidity is used over the whole globe. For ERA5, ocean-series-only points over open sea are selected. 2-sigma uncertainty is shown for HadISDH capturing the observation, gridbox sampling, and spatial coverage uncertainty. Pink and blue shading highlights El Niño and La Niña years, respectively, as identified by the NOAA Physical Sciences Laboratory Niño-3.4 index using the ±0.5°C threshold. (Sources: HadISDH [Willett et al. 2013, 2014, 2020]; ERA5 [Hersbach et al. 2020]; JRA-3Q [Kosaka et al. 2024]; MERRA-2 [Gelaro et al. 2017].)

Table 2.7. Global mean near-surface specific humidity (*q*) and relative humidity (RH) anomalies (g kg^{-1} and %rh, respectively) for 2025 and comparison with previous record values. Note that no previous record is reported for ocean RH because a long-term trend has not yet been robustly established. Values with an asterisk (*) identify new record-high values and year of previous record. Note that record highs/lows have low importance for marine RH where there is no consensus on long-term trend direction. Cells marked with a dash signify that the data are not available.

Dataset	2025 Global Mean Anomaly (rank highest) *q* (g kg^{-1}) specific humidity	Record High Global Mean Anomaly (year) *q* (g kg^{-1}) specific humidity	2025 Global Mean Anomaly (rank lowest, land only) RH (%rh) relative humidity	Record low (land) and Global Mean Anomaly (year) RH (%rh) relative humidity
HadISDH.land	0.19 (5th)	0.49 (2024)	–1.12 * (1st, previous record 2019)	—
ERA5 Over Land	0.14 (6th)	0.32 (2024)	–0.79 (6th)	–1.32 (2021)
MERRA-2 Over Land	0.24 (4th)	0.46 (2024)	–0.21 (9th)	–1.21 (2002)
JRA-3Q Over Land	0.20 (5th)	0.38 (2024)	–0.76 (4th)	–0.93 (2021)
HadISDH.marine	0.29 (3rd)	0.57 (2024)	0.13	—
ERA5 Over Ocean	0.19 (4th)	0.35 (2024)	–0.09	—
MERRA-2 Over Ocean	0.36 (3rd)	0.52 (2024)	0.44	—
JRA-3Q Over Ocean	0.27 (3rd)	0.44 (2024)	0.16	—

In 2025, *q* anomalies were well above average, yet only around half of the record-high values in 2024 (all datasets; land and ocean). El Niño conditions generally enhance evaporation and water holding capacity, whereas cooler La Niña conditions do the opposite. So, the 2025 decrease relative to 2024 was expected given the weak La Niña-to-neutral conditions following a strong 2023/24 El Niño. Pacific Ocean spatial patterns (Plate 2.1h; Appendix Figs. A2.9, A2.11) were consistent with typical C-shaped moister-than-average anomalies around a central Pacific tongue of drier-than-average anomalies. Despite this, *q* was still fourth to sixth highest on record over land and third to fourth highest over ocean.

Relative humidity is more complicated than specific humidity; the global mean can peak during El Niño events (Figs. 2.24e–h) but often its large variability masks this. Furthermore, RH compounds errors and biases from air temperature and humidity measurements. With the exception of MERRA-2, all datasets show decreasing RH over land since at least 2000. Changes from manual wet-bulb thermometers to automated electronic sensors are often associated with drier measurements. These have occurred across entire countries over short time periods, making related inhomogeneities difficult to detect (e.g., Li et al. 2020; Yin et al. 2025), potentially contributing to the decreasing land RH signal. Over ocean, there is little consensus between the datasets in annual and multi-decadal variability. The magnitude of the 2024/25 spike and drop in HadISDH over ocean (HadISDH.marine) is unusual compared to the earlier record, and other products. Various differences are apparent in the 2025 annual anomaly patterns (Plate 2.1i; Appendix Figs. A2.10, A2.12). Note that HadISDH.marine, MERRA-2, and JRA-3Q incorporate air and dewpoint temperature observations from ships; ERA5 does not.

Annual anomaly patterns (Plates 2.1h,i Appendix Figs. A2.9–A2.12) broadly match wet and dry anomalies across the hydrological cycle variables. Drier-than-average land RH aligned more closely to precipitation, cloudiness, and drought anomalies (Plates 2.1n,p,w, respectively) than *q*, particularly over Southern Europe and North America. To understand long-term trends, we note that, theoretically, near-surface ocean mean RH should remain near-constant or increase very slightly (Shakespeare and Roderick 2024), while near-surface mean *q* tends to scale close to

7% over oceans and slower over land (O'Gorman and Muller 2010; Bosilovich et al. 2017). This follows the Clausius-Clapeyron relation. HadISDH (Fig. 2.25) shows a wide range of scaling and, although this is broadly related to water availability, it is also influenced by circulation. Between 1973 and 2025, ocean *q* increased at 5%–7% per °C and over land at 1%–5% per °C, with negative scaling in some arid regions. Increases were highest in the tropics, where heat, water, and convergence are all prominent. This helps to explain the observed land and ocean changes in RH. Rising land and ocean air temperatures (see Fig. 2.1) mean that the air can hold more water vapor. Consequently, over the water-abundant oceans, *q* increased closer to ~7% per °C, and RH changed very little. Over land, two processes are particularly important. First, water availability is lower and so the temperature-driven *q* increase was slower than the increase in water vapor carrying capacity. Second, the air over land warmed faster than over oceans. Water evaporated from the oceans and advected over land was driven by the rate of warming over oceans, which was insufficient to keep pace with the greater increase in water holding capacity over the faster warming land (Simmons et al. 2010; Joshi et al. 2008). Hence, the scaling in *q* over land was generally lower, or even negative, and RH decreased.

This year, HadISDH.land.5.0.0.2025f and HadISDH.marine.1.8.0.2025f were used, in addition to three reanalyses: ERA5, MERRA-2, and JRA-3Q. Reliable observational records began in 1973. A significant update to HadISDH has changed its underlying hourly source data to NOAA NCEI's GHCNh v1.1/C3S 3.0.0 (based on Release 8.1; https://www.ncei.noaa.gov/products/global-historical-climatology-network-hourly; Menne et al. 2025; C3S CDS 2026). This is a new archive of historical in situ land surface observations, where substantial effort has gone into harmonizing disparate data sources and quality control flags, in addition to running a further comprehensive automated quality control. At present, although providing some improved Southern Hemisphere coverage, HadISDH.land.5.0.0.2025f has reduced coverage compared to HadISDH.land.4.6.1.2024f, particularly over South America, India, and Russia. Despite this, the versions are near-identical in global and hemispheric means (not shown). Given the greater sensitivity of RH compared to *q*, the HadISDH.land record-low RH this year may be influenced by this reduced coverage. Regardless, 2025 land RH is highly likely to be below the long-term mean.

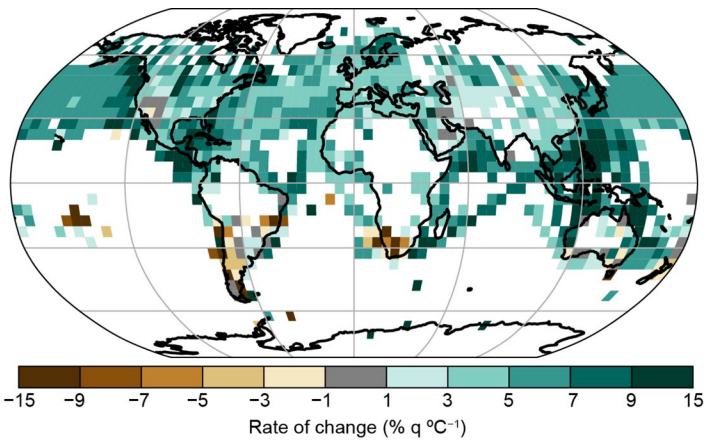

Fig. 2.25. Linear rate of change of specific humidity per 1°C of air temperature (% *q* °C^{-1}) over the 1973–2025 period. (Source: Hadley Centre Integrated Surface Dataset of Humidity [HadISDH.blend.2.0.0.2025f].)

2. HUMID-HEAT EXTREMES OVER LAND

—C. Raymond, K. M. Willett, R. M. Horton, Y. T. E. Lo, and C. D. W. Rogers

High humid heat intensity and frequency were substantially higher than average in 2025, with several measures trailing only the records of 2024. The 2025 high-humid-heat intensity (T_wXX; Figs. 2.26a,b Table 2.8) was 0.3°C higher than the 1991–2020 mean, and the fourth-highest since at least 1973, according to ERA5 and the gridded Met Office Hadley Centre Integrated Surface Dataset of Humidity Extremes (HadISDH.extremes). The analogous anomaly in humid-heat monthly minima (T_wNN) was 0.6°C, the third highest.

The number of days with high daily maximum humid heat (T_wX90p; Figs. 2.26c,d; Table 2.8) was 16–18 days above average, the sixth highest on record for ERA5 and third highest for HadISDH.extremes. The frequency of high daily-minimum wet-bulb temperature (T_wN90p; Figs. 2.26c,d; Table 2.8) agrees closely with that of daily maxima over the time series, including for 2025. Cool-dry extremes (T_wX10p, T_wN10p; Figs. 2.26e,f; Table 2.8) only slightly increased in frequency from 2024's record-low numbers.

Anomalies in exceedances of high T_wX thresholds (25°C, 27°C, 29°C, and 31°C) in 2025 fell close to the mean of the last 10 years, but remained above or at the 1991–2020 average (Figs. 2.26g,h, Table 2.8). For both datasets, 2025 frequencies for T_wX25 ranked among the top 10 years over the 1973–2025 period, as did HadISDH.extremes for T_wX27 and ERA5 for T_wX29 (Figs. 2.26g,h; Table 2.8).

Table 2.8. Definitions of 10 humid-heat indices and their respective recent global land annual anomalies (1991–2020 base period), based on ERA5 with HadISDH.extremes in brackets. The global (70°S–70°N) monthly mean anomalies are calculated for all indices weighted by the cosine of the latitude of each gridbox center. The annual anomalies for the exceedance indices (not T_wXX and T_wNN) are the sum of the monthly values whereas T_wXX and T_wNN are computed as medians of the monthly values.

Index	Description	Meaning	2022 Global Anomaly	2023 Global Anomaly	2024 Global Anomaly	2025 Global Anomaly
T_wXX	Gridbox median of monthly maximum daily maximum wet-bulb temperature	Intensity of daily maximum humid heat	0.0°C [0.0°C]	0.3°C [0.5°C]	0.5°C [0.7°C]	0.3°C [0.3°C]
T_wNN	Gridbox median of monthly minimum daily minimum wet-bulb temperature	Intensity of daily minimum humid heat	0.3°C [0.2°C]	0.7°C [0.7°C]	0.9°C [1.0°C]	0.6°C [0.6°C]
T_wX90p	Days per year exceeding the 90th percentile of the climatological daily maximum wet-bulb temperature (seasonally varying)	Frequency of high daily maximum humid-heat days relative to local climatology	2.1 days [4.8 days]	22.5 days [24.6 days]	33.8 days [33.9 days]	15.7 days [17.5 days]
T_wX10p	Days per year below the 10th percentile of the climatological daily maximum wet-bulb temperature (seasonally varying)	Frequency of low daily maximum humid-heat days relative to local climatology	–3.8 days [–3.9 days]	–12.7 days [–14.5 days]	–18.4 days [–18.5 days]	–12.8 days [–12.3 days]
T_wN90p	Days per year exceeding the 90th percentile of the climatological daily minimum wet-bulb temperature (seasonally varying)	Frequency of high daily minimum humid-heat days relative to local climatology	5.2 days [5.9 days]	28.3 days [22.6 days]	45.4 days [33.8 days]	20.5 days [16.9 days]
T_wN10p	Days per year below the 10th percentile of the climatological daily minimum wet-bulb temperature (seasonally varying)	Frequency of low daily minimum humid-heat days relative to local climatology	–5.5 days [–4.2 days]	–13.8 days [–12.1 days]	–19.1 days [–18.5 days]	–13.9 days [–12.8 days]
T_wX25	Days per year where the daily maximum wet-bulb temperature was ≥25°C	Frequency of moderately extreme humid-heat days	–0.5 days [2.4 days]	5.9 days [6.4 days]	12.0 days [10.3 days]	4.9 days [6.4 days]
T_wX27	Days per year where the daily maximum wet-bulb temperature was ≥27°C	Frequency of extreme humid-heat days	–0.8 days [2.3 days]	1.7 days [8.4 days]	4.5 days [11.7 days]	0.5 days [5.0 days]
T_wX29	Days per year where the daily maximum wet-bulb temperature was ≥29°C	Frequency of very extreme humid-heat days	0.1 days [0.5 days]	0.3 days [1.3 days]	0.6 days [1.5 days]	0.1 days [0.0 days]
T_wX31	Days per year where the daily maximum wet-bulb temperature was ≥31°C	Frequency of severe humid-heat days	0.0 days [–0.1 days]	0.0 days [0.2 days]	0.0 days [0.3 days]	0.0 days [0.0 days]

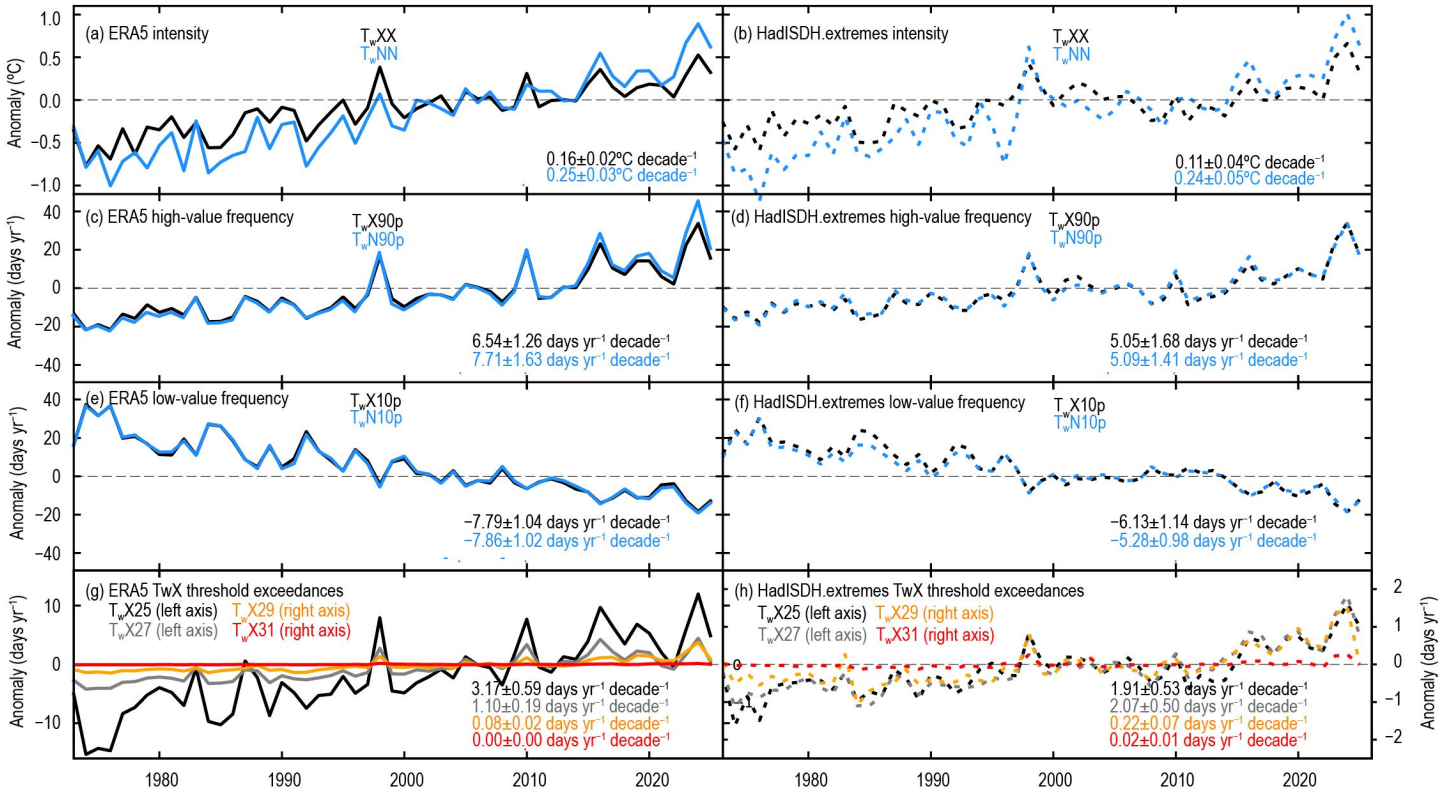

Fig. 2.26. Global land mean annual anomaly time series of various daily maximum and minimum wet-bulb temperature indices, relative to a 1991–2020 base period. Decadal trends are also shown. Trends were fitted using an ordinary least-squares linear regression with an autoregressive (1) correction following Santer et al. (2008). (a) Anomaly of the annual median of the monthly maximum daily-maximum (T_wXX; black) and minimum daily-minimum (T_wNN; blue) wet-bulb temperature (°C) from ERA5. (b) As in (a) but for Hadley Centre Integrated Surface Dataset of Humidity (HadISDH.extremes). (c) Anomaly of the annual sum of days where daily maximum (T_wX90p; black) and daily minimum (T_wN90p; blue) wet-bulb temperature exceeds the locally defined daily 90th percentile for ERA5. (d) As in (c) but for HadISDH.extremes. (e) Anomaly of the annual sum of days where daily maximum (T_wX10p; black) and daily minimum (T_wN10p; blue) wet-bulb temperature is lower than the locally defined daily 10th percentile for ERA5. (f) As in (e) but for HadISDH.extremes. (g) Anomalies of the annual sums of days where the daily maximum wet-bulb temperature ≥25°C (T_wX25; black), 27°C (T_wX27; gray), 29°C (T_wX29; orange), and 31°C (T_wX31; red) thresholds for ERA5. (h) As in (g) but for HadISDH.extremes. Note that coverage is skewed towards the northern extratropical latitudes with large data gaps over Africa and considerable gaps over South America, Australia, and parts of Central Asia.

Regionally, unusually high numbers of days with T_wX≥25°C occurred across East Asia, South Asia, the Maritime Continent, southeast Africa, West Africa, and the Caribbean and Central America (Fig. 2.27a), agreeing well with in situ data where available (Appendix Fig. A2.13). East Asia stands out with a large contiguous area of 'very unusually frequent' T_wX≥25°C occurrences, coinciding with the record-warmest summer in China, South Korea, and Japan (see section 7g3; WMO 2026). Central Australia, the Sahel, and eastern Brazil saw lower-than-normal T_wX≥25°C frequencies. For 27°C (Fig.2.27b), high humid heat was anomalously infrequent for African and South American tropical regions likely due to La Niña's net cooling and drying effects. Globally, compared to the climatological "normal" over 1991–2020, there was approximately 1% more land area than usual that reached 25°C at least once, 3% more that reached 27°C, 10% more that reached 29°C, and 180% more that reached 31°C in 2025.

The spatial anomalies of intensity (T_wXX; Plate 2.1j; Appendix Fig. A2.14), using the median of monthly maxima, spotlight high humid heat in eastern Canada and Northern Europe (>+2°C) and over parts of Asia (>+1°C). Conversely, anomalies near –1°C occurred across much of South America, Arabia, and portions of eastern Africa.

Substantial swathes of the Maritime Continent, Japan, northern South Asia, and the Caribbean experienced daily maximum humid heat exceeding the local 90th percentile (T_wX90p) on >50 additional days relative to the climatological mean, more than a doubling of climatological "normal" (1991–2020) occurrences (Plate 2.1k; Appendix Fig. A2.15). Numerous other locations saw more than 20 additional such days. The Amazon region, Arabia, and east-central Africa had

notably fewer T_wX90p events than normal, a tropical signature of the predominantly La Niña-like conditions in 2025. Positive anomalies in high daily-minimum humid heat (T_wN90p; Appendix Fig. A2.16) were slightly larger than for T_wX90p, with similar spatial patterns.

Humid heat is assessed here using gridded daily wet-bulb temperature indices, computed from hourly air temperature, specific humidity, and surface pressure (Warren 2025). Statistics are based on the entire calendar year and available land area from ERA5 reanalysis (Hersbach et al. 2020) and the HadISDH.extremes in situ-based dataset version 2.0.0.2025f (Willett et al. 2023a,b), both aggregated to a 5° × 5° grid. The two datasets differ primarily in spatial coverage, although there are some systematic humidity differences (Simpson et al. 2023; Willett et al. 2024). Due to ongoing dataset upgrades, at the time of writing HadISDH.extremes had additional, temporary geographic gaps (see section 2d1). The inclusion of ERA5 is thus intended to provide a complete spatial view, despite its considerable biases and uncertainties, especially for less-well-observed regions. Where available, observational HadISDH.extremes results generally support those from ERA5.

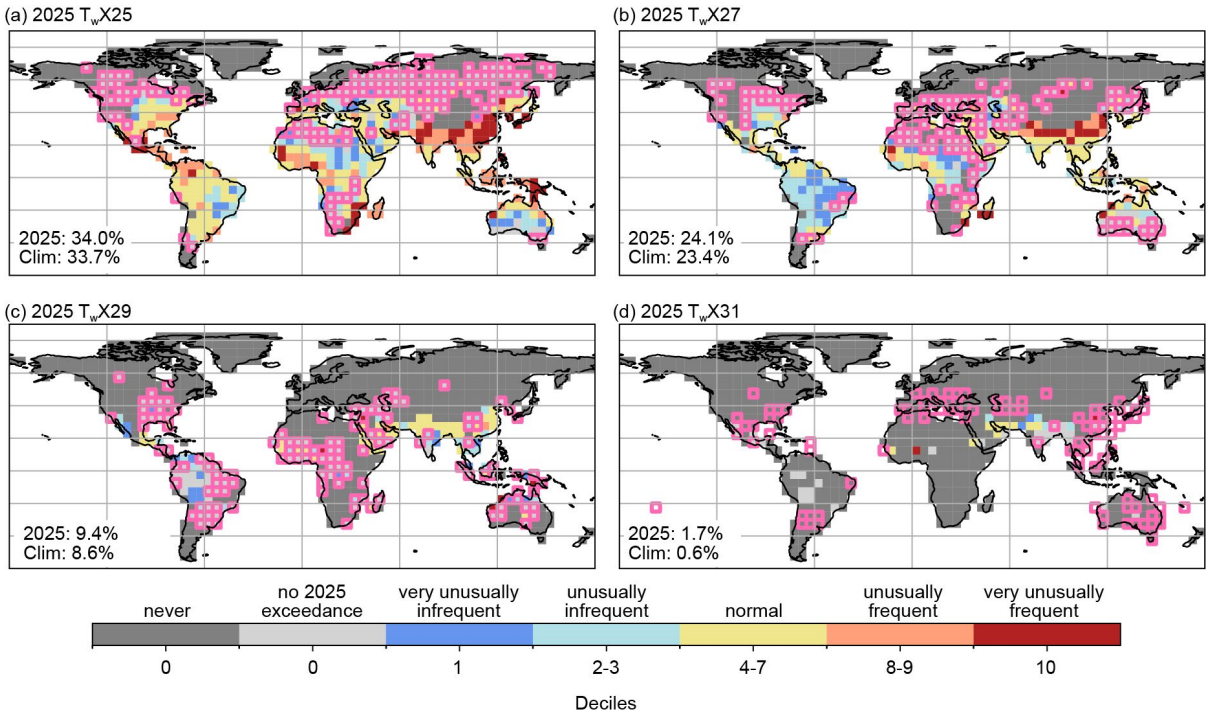

Fig. 2.27. High humid-heat extremes of 2025 as deciles over the period 1973–2025, ranking the number of days with maximum wet-bulb temperature (T_w) ≥ (a) 25°C (T_wX25), (b) 27°C (T_wX27), (c) 29°C (T_wX29), and (d) 31°C (T_wX31). Gridboxes bounded in pink indicate <15 years within the 1991–2020 period when exceedances occur. These panels are annotated with the percentage of observed gridbox area where an exceedance occurred in 2025 and climatologically (including only gridboxes with at least one exceedance between 1991 and 2020). (Source: ERA5.)

3. TOTAL COLUMN WATER VAPOR

—C. A. Mears and O. Bock

In 2025, the quasi-global (60°S–60°N) mean total column water vapor (TCWV) was approximately 3% above the 1991–2020 climatological average (27 kg m^{-2}; Table 2.9), with the land percentage slightly exceeding the ocean percentage, according to three global reanalyses (ERA5, MERRA-2, and JRA-3Q) and two observational datasets (Microwave Radiometer [MWR], ground-based Global Navigation Satellite System [GNSS]). The various vapor estimates have similar overall features (positive trends over the study period, modulated by ENSO cycles), but have significant spreads in trends over 1991–2025 (Table 2.9) and individual annual anomalies, especially over land (Fig. 2.28), suggesting substantial structural uncertainty. Noticeably, the large-scale wet anomalies persisted into 2025 despite the appearance of weak La Niña conditions for part of 2025 (Fig. 2.28; see section 4b for details). La Niña usually causes lower temperatures and a drier atmosphere. Compared to record values reached in 2024, the atmosphere was colder and drier in 2025, although both temperature (sections 2b1, 2b5) and water vapor anomalies (also see section 2d1) remained largely above the 1990–2020 baseline. The

ongoing rising decadal trends in TCWV as expected, given global warming, are also shown in Table 2.9.

The spatial distribution of TCWV percent anomalies in 2025 (Plate 2.1l) was dominated by large wet anomalies over the polar regions. There were also wet areas over the Maritime Continent, southern Africa, the western Saharan desert, and over most of the northern midlatitudes. There was a pronounced dry anomaly in the central tropical Pacific associated with the weak La Niña conditions. This dry area extended to the northeast and to the southeast over the Pacific Ocean. There were smaller dry anomalies over the Arabian Peninsula and western Australia. In the southern midlatitudes, the TCWV values were closer to the 1991–2020 climatology than in the northern midlatitudes.

This assessment is based on observations from satellite-borne MWRs over the oceans (Remote Sensing Systems [RSS] satellite; Mears et al. 2018), as well as homogenized ground-based GNSS observations over land and islands (Quarello et al. 2022; Bock 2025; Nguyen et al. 2026). Three global reanalysis products were used: ERA5 (Hersbach et al. 2020), MERRA-2 (Gelaro et al. 2017), and JRA-3Q (Kosaka et al. 2024). All three reanalyses assimilate satellite microwave radiometer data (as radiances) but not ground-based GNSS measurements, which serve as an independent validation dataset.

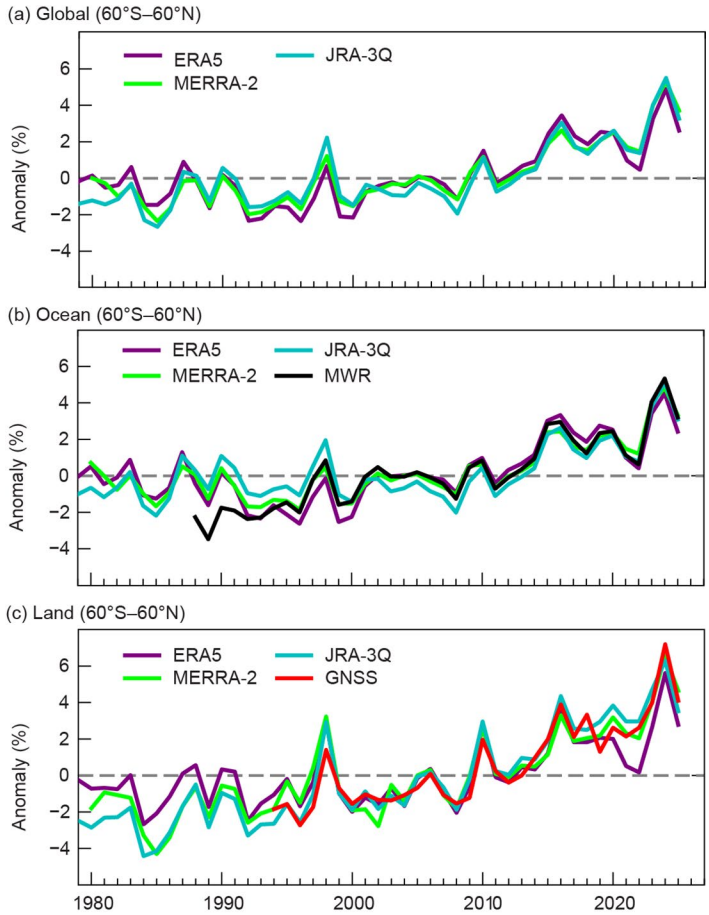

Fig. 2.28. Global mean (60°S–60°N) total column water vapor annual anomalies (%; 1991–2020 base period) over (a) land and ocean, (b) ocean-only, and (c) land-only from observations and reanalyses. The time series from the Global Navigation Satellite System (GNSS) observations have been adjusted, so there is zero mean difference relative to the ERA5 results during their respective periods of record.

Table 2.9. Global mean (60°S–60°N) total column water vapor (TCWV) anomalies (kg m^{-2} [%]; 1991–2020 base period) for 2025, and linear trends (kg m^{-2} decade^{-1}) over the period 1991–2025 for reanalyses and Microwave Radiometer (MWR), (*) 1995–2024 for ground-based Global Navigation Satellite System (GNSS; including 166 stations over land). Cells marked with a dash signify that the data are not available.

TCWV Anomalies in 2024, Units in kg m^{-2} (%) rank					
Dataset	ERA5	MERRA-2	JRA-3Q	MWR	GNSS*
Global	0.709 (2.61) [fourth]	0.915 (3.70) [third]	0.895 (3.27) [third]	—	—
Ocean	0.702 (2.42) [seventh]	0.945 (3.33) [third]	0.915 (3.09) [third]	0.954 (3.20) [third]	—
Land	0.640 (2.78) [fourth]	0.805 (4.64) [third]	0.785 (3.52) [fifth]	—	0.893 (4.02) [second]
Trends over 1991–2024, Units in kg m^{-2} (% decade^{-1})					
Dataset	ERA5	MERRA-2	JRA-3Q	MWR	GNSS*
Global	0.415±0.045 (1.52±0.17)	0.408±0.043 (1.48±0.16)	0.366±0.055 (1.34±0.20)	—	—
Ocean	0.458±0.047 (1.58±0.16)	0.418±0.044 (1.41±0.15)	0.320±0.061 (1.0±0.21)	0.458±0.050 (1.54±0.17)	—
Land	0.282±0.055 (1.23±0.24)	0.389±0.057 (1.70±0.24)	0.463±0.049 (2.08±0.22)	—	0.437±0.054 (2.01±0.25)

4. UPPER TROPOSPHERIC HUMIDITY

—V. O. John, E.-S. Chung, R. P. Allan, S. A. Buehler, B. J. Soden, and J. L. Matthews

Monitoring upper tropospheric humidity is important for many reasons: 1) it strongly controls Earth's greenhouse effect, and a very small increase in the amount of water vapor at these altitudes can substantially reduce Earth's ability to lose heat to space; 2) it determines the formation and lifetime of clouds, especially high cirrus clouds, and how saturated the upper troposphere is determines whether aircraft condensation trails (contrails) will be formed and sustained, which is a major climate impact from the aviation industry (Johansson et al. 2025); 3) it can affect weather patterns through its bearing on the formation of convection which can be suppressed by a drier mid- and upper troposphere; and 4) it reveals large-scale circulation patterns, so it can be used for monitoring changes in the atmospheric dynamics.

Plate 2.1m shows annual mean anomalies of upper tropospheric humidity (UTH) using the High-Resolution Infrared Radiation Sounder (HIRS; Shi and Bates 2011). The spatial distribution of the anomalies resembles precipitation anomalies in 2025 (section 2d5). Evident in the anomaly pattern is the large and intense positive area centered over the Maritime Continent with a negative feature to the east. These correlations of UTH with precipitation and SST illustrate that the distribution of UTH is driven by convection and large-scale weather/circulation features, with positive anomalies associated with wetter conditions and negative anomalies associated with drier conditions at the surface. During 2025, multiple severe flooding events in Pakistan (between May and September) and Southeast Asia are clearly associated with positive UTH anomalies. The anomaly patterns are linked to weak La Niña conditions (see section 4b), with positive anomalies over the Maritime Continent and a strong dry signal in the western equatorial Pacific. Drier conditions over the western United States and western China are reflected in lower-than-average UTH and coincide also with a deficit in snowfall over the Himalayas. The anomaly patterns also show negative Indian Ocean dipole (IOD) conditions characterized by warmer-than-average sea surface temperatures in the eastern Indian Ocean (near Indonesia) and cooler-than-average waters in the west (near Africa).

Figure 2.29a shows time series of UTH since 1979 for two datasets—one from satellite infrared-based measurements (HIRS; Shi and Bates 2011) and the other from model-based reanalysis (ERA5; Hersbach et al. 2020). The average value of UTH in 2025 was slightly below normal for both ERA5 (−0.27±0.41 %rh) and HIRS (−0.09±0.78 %rh). However, the time series of UTH from the satellite infrared-based measurements (HIRS) shows slightly-above-average UTH for part of 2025. During an El Niño event, the infrared dataset tends to have a smaller magnitude of UTH anomalies compared to other datasets, and the opposite occurs during a La Niña event (Shi et al. 2022).

Figure 2.29b shows a proxy time series for absolute water vapor, which is constructed by differencing the mid- to upper-tropospheric temperature measurements by satellite microwave sounding unit (MSU) and advanced microwave sounding unit (AMSU) instruments (Zou et al. 2023) and the HIRS upper-tropospheric water vapor measurements. The MSU instruments measure the radiation emitted by oxygen molecules in the atmosphere. As the concentration of oxygen is not significantly changing, the emission levels of those measurements remain unchanged. In contrast, the emission levels of the water vapor channel are increasing as the amount of water vapor is increasing in the atmosphere. Differencing the two time series removes the effect of the temperature increase and shows

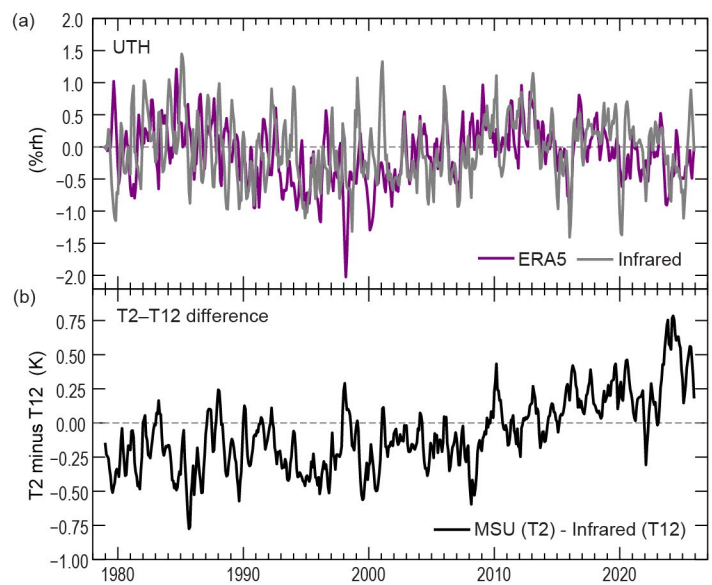

Fig. 2.29. Time series of 60°S–60°N monthly mean anomalies of (a) upper-tropospheric relative humidity (%rh) for the two datasets (see text for details) and (b) the difference between mid- to upper-tropospheric temperature (MSU T2) and water vapor channel (HIRS T12) brightness temperatures (K).

only the impact of the water vapor changes (e.g., see Soden et al. 2005; Chung et al. 2014). Peak values in 2024 show elevated water vapor amounts that are driven by the record global atmospheric temperatures, rather than higher UTH. A significant positive trend of 0.13±0.01°C decade^{-1} denotes a moistening of the upper troposphere, significantly contributing to the water vapor feedback that is strongly amplifying the warming of climate driven by rising greenhouse gases.

5. PRECIPITATION

—M. Ziese, R. S. Vose, R. Adler, G. Gu, and X. Yin

Precipitation is the primary source of fresh water needed for human consumption, agriculture, and hydropower over land, and its deviations over both ocean and land are important components of Earth's climate. On a global average (land and ocean), 2025 was drier than normal (Fig. 2.30). This was caused by the below-average precipitation amounts over ocean, which were not fully balanced by the above-normal totals over land, typical of a La Niña anomaly pattern.

Weak La Niña conditions were present in the first and last months of 2025 (see section 4b for details). Usually, both global mean temperature and global mean precipitation are lower in La Niña years. While the global mean temperature was high (section 2b1), and even above the long-term warming trend, the global mean precipitation was slightly below normal in 2025 (Fig. 2.30c). The ocean–land divide was typical of La Niña, with land having a positive anomaly and the ocean a negative one (Figs. 2.30a,b).

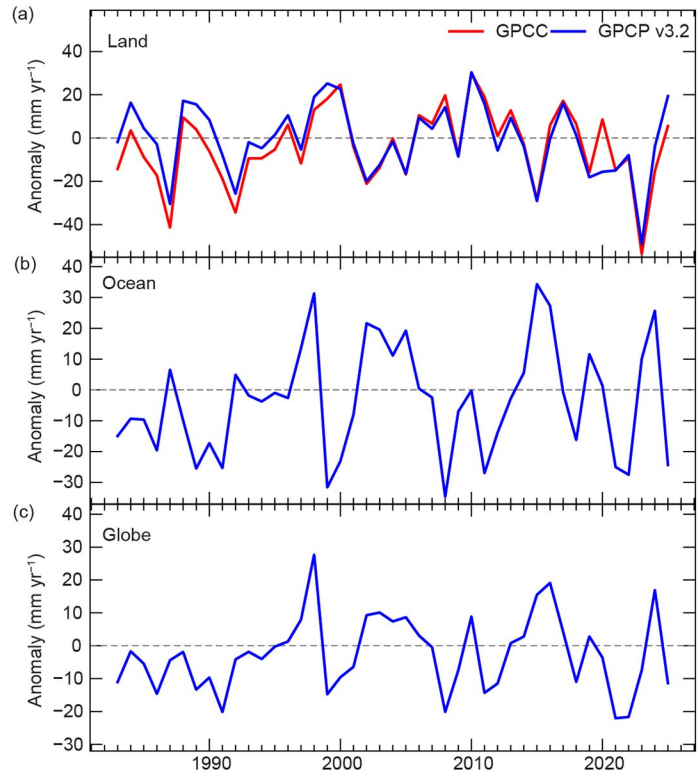

Fig. 2.30. Globally averaged annual precipitation anomalies (mm; 1991–2020 base period) for (a) land areas, (b) ocean areas, and (c) the globe (land and ocean).

The effect of La Niña is evident across most of the tropics. The anomalies (Fig. 2.31; Plate 2.1n) show a strikingly intense and large positive region centered over the Maritime Continent, with tendrils extending outward in multiple directions, including parts of southern Asia and mainland Southeast Asia. To the east of this region, over the Pacific Ocean, there is an intense drier feature with a core near the equator at 160°E with attached extensions stretching to the east and southeast. The western Indian Ocean was mainly dry in 2025 (section 2d4); the dryness extended to the southeast and also across the Horn of Africa and the Middle East.

Most of northern Asia received more precipitation than usual. Large parts of southern and central Africa were wetter than normal, as were some locations around the western Upper Guinea Rise. The drought situation in southwestern Africa, causing food insecurity in the previous year, was eased. Near- and regionally above-normal annual precipitation eased the prolonged drought situation in northwestern North Africa. Wetter-than-normal conditions were observed in northern South America, large portions of Central America, southern and central North America, and Alaska. The central Andes, northern Pampas, the southern Pacific coast of Patagonia, as well as some parts of the Brazilian Highlands, also received above-normal precipitation. Above-normal rainfall was received in northeastern Australia, parts of New Zealand, and over Pacific Ocean islands west of the dateline. In Europe, wetter-than-normal conditions were recorded in the western Mediterranean region, eastern East Europe (extending to the above-mentioned wet conditions in northern Asia), and the northern and northwestern coast of Northern Europe.

A precipitation deficit occurred over northern North America (around the Hudson Bay, Labrador, and Newfoundland), around the Gulf of Alaska, around the Gulf of America/ Gulf of Mexico, and in the Caribbean.

Central and southeastern South America, along with much of Patagonia, was drier than normal. Drought conditions in much of the Amazon basin have prevailed for around the last four years. Some regions in Africa received below-normal rainfall amounts, e.g., around the Gulf of Guinea and the Horn of Africa. Also, the East African Islands were drier than usual, except southwestern Madagascar, which was wetter than usual. Less precipitation than normal fell in Western, Central and Southeast Europe. Another region with below-normal precipitation spanned from the eastern Mediterranean region over southwestern Asia to western Central Asia. Furthermore, parts of East Asia and the region around the Laptev Sea were drier than usual. Much of central and southern Australia and the islands east of the dateline in the Pacific Ocean received below-normal rainfall.

The analyses presented here are based on data from two data centers: in situ based on the Global Precipitation Climatology Centre (GPCC; Becker et al. 2013) and gauge-adjusted satellite data from the Global Precipitation Climatology Project (GPCP version 3.2; Huffman et al. 2023). Gauge adjustment is the process by which precipitation rates from satellite retrievals are calibrated with in situ gauge measurements to increase the reliability of the data. The GPCC data are part of the input to the global GPCP analyses.

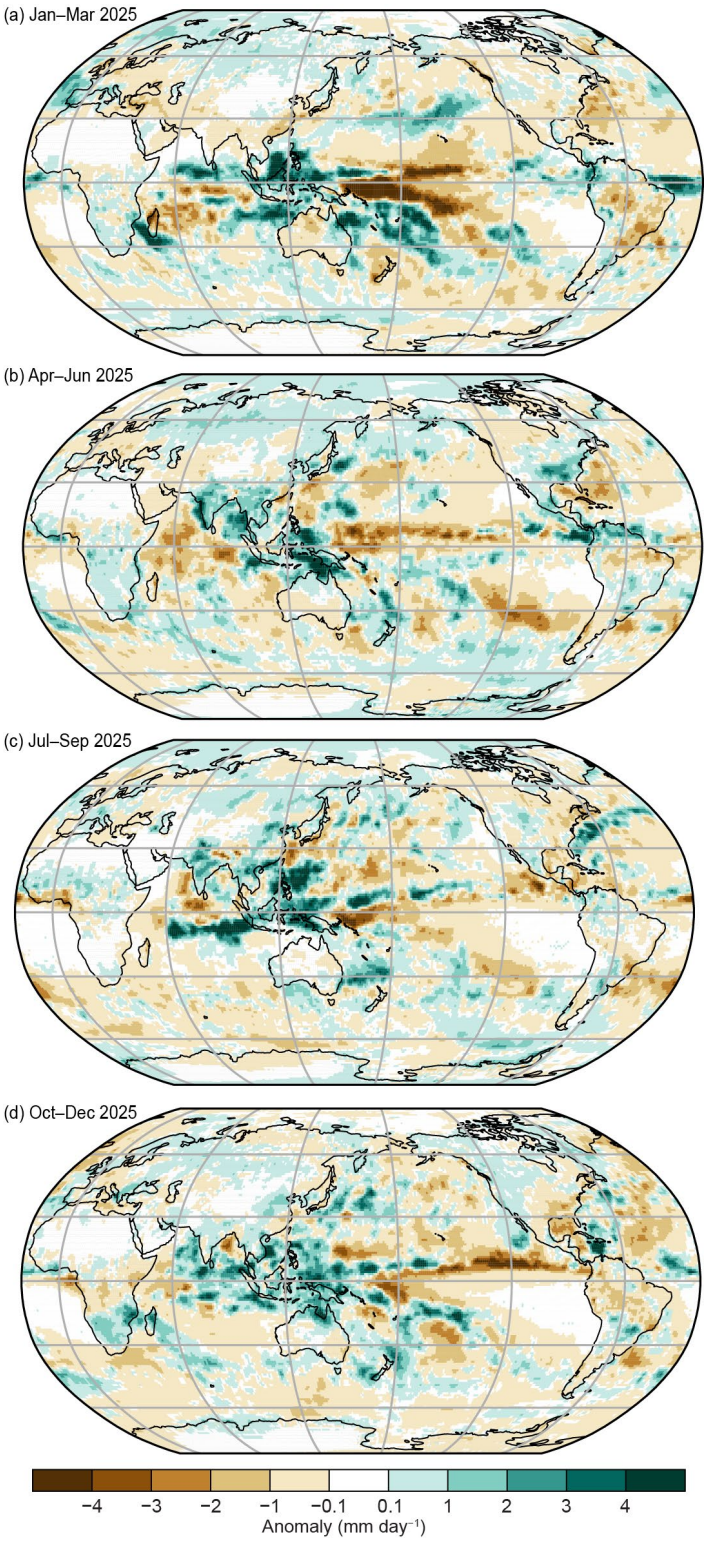

Fig. 2.31. Seasonal precipitation anomalies (mm day^{-1}; 1991–2020 base period) for (a) Jan–Mar (JFM) 2025, (b) Apr–Jun (AMJ) 2025, (c) Jul–Sep (JAS) 2025, and (d) Oct–Dec (OND) 2025. (Source: Global Precipitation Climatology Project [GPCP].)

6. LAND SURFACE PRECIPITATION EXTREMES

—K. A. Quagraine, M. Ziese, A. Simmons, S. Qiaohong, and W. Zhang

Global mean annual maximum one-day precipitation (Rx1day) over land in 2025 was slightly above the 1991–2020 average, according to ERA5 reanalysis (+2.20 mm), marking the fourth-highest daily precipitation extreme on record, well below the record year of 2024 (+5.80 mm; Fig. 2.32). The Rx1day and five-day maximum (Rx5day) are derived from station-based (Global Historical Climatology Network Daily Extremes [GHCNDEX], Donat et al. 2013, with the Met Office Hadley Centre Extremes dataset version 3 [HadEX3], Dunn et al. 2020, shown to 2018 for longer-term context), gauge-based (Global Precipitation Climatology Centre [GPCC], Ziese et al. 2022), and reanalysis (ERA5, Hersbach et al. 2020; MERRA-2, Gelaro et al.

2017; JRA-3Q, Kosaka et al. 2024) data. These datasets consistently place 2025 as a positive anomaly year (Fig. 2.32), though notable differences arise in data-sparse regions and over complex terrain. Despite this only modestly positive global mean, 2025 was marked by devastating regional extremes, with several of the most destructive events striking regions already stressed by prolonged drought.

Weak La Niña conditions emerged in December 2024, returned to ENSO-neutral by March 2025 and persisted much of the year. La Niña re-emerged in boreal autumn and continued as a weak event through the year's end (see section 4b for details). A concurrent negative Indian Ocean dipole (IOD) reinforced wetter-than-average conditions across Southeast Asia and northeastern Australia while suppressing precipitation over the central and eastern tropical Pacific, the western Indian Ocean, and the East Africa (Fig. 2.33).

Precipitation extremes across Southeast Asia were well above average in 2025, driven by an above-average number of named storms in the western North Pacific, though the accumulated cyclone energy (ACE) remained below average (see section 4g4 for details). These frequent landfalls, superimposed on enhanced monsoon rainfall, concentrated moisture into short-duration extreme events across the region. Tropical Storm Wipha and Typhoon Co-May amplified southwest monsoon rains, driving severe flooding across the northern Philippines in July (see section 4g4). From September through November, five tropical cyclones struck the region in rapid succession, including multiple major typhoons and the rare near-equatorial Cyclonic Storm Senyar (section 4g4). These storms, combined with an anomalously active northeast monsoon (section 4e), triggered widespread flooding across Indonesia, Vietnam, Thailand, Malaysia, and Sri Lanka. ERA5 shows prominent positive Rx1day and Rx5day anomalies across the region, extending into northeastern Australia (Plate 2.1o; Fig. 2.33b), while GPCC data confirmed increased precipitation-day frequency but with more spatially heterogeneous intensity anomalies over the data-sparse Maritime Continent (Fig. 2.33a).

The differences between ERA5 and GPCC Rx1day fields are most pronounced over gauge-sparse regions and areas affected by

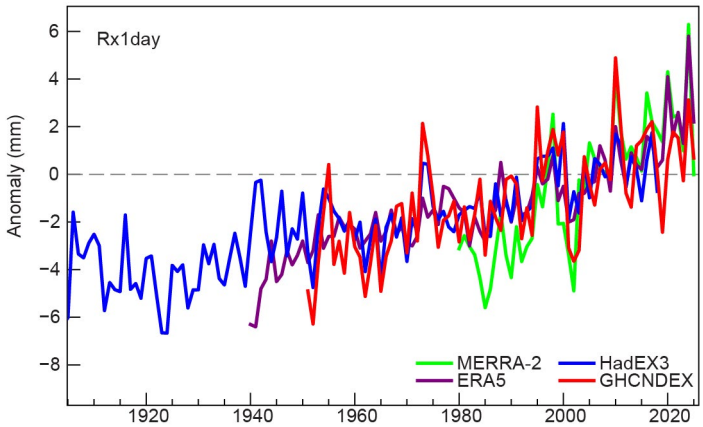

Fig. 2.32. Global mean anomaly (mm; 1991–2020 base period) time series of annual maximum one-day precipitation (Rx1day) over land in 2025 from station-based datasets (the Met Office Hadley Centre Extremes dataset version 3 [HadEX3; Dunn et al. 2020], and Global Historical Climatology Network Daily Extremes dataset [GHCNDEX; Donat et al. 2013]), and reanalyses (ERA5 [Hersbach et al. 2020] and MERRA-2 [Gelaro et al. 2017]).

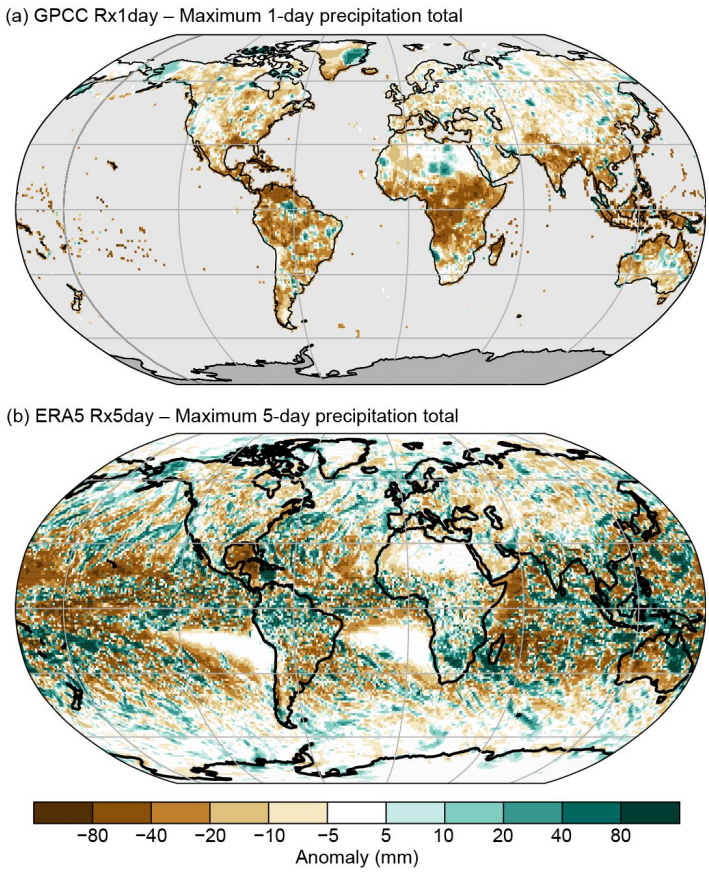

Fig. 2.33. Maps of (a) maximum one-day precipitation (Rx1day) anomalies (mm; 1991–2020 base period) for 2025 from Global Precipitation Climatology Centre (GPCP; Ziese et al. 2022), and (b) maximum five-day accumulated precipitation (Rx5day) anomalies (mm; 1991–2020 base period) for 2025 from ERA5 (Hersbach et al. 2020).

tropical cyclone rainfall, where reanalysis products capture broader precipitation footprints through model physics and data assimilation than the gauge network can resolve due to limited coverage; however, ERA5 can overestimate precipitation in tropical oceanic regions (Hersbach et al. 2020). Furthermore, there may be a dry bias in the GPCC near-real-time Rx1day anomalies, which are under further investigation.

In the Atlantic, Hurricane Melissa, which intensified to Category 5 status on the Saffir-Simpson Hurricane Wind Scale, produced extreme rainfall over Hispaniola during its developmental stage, with substantial impacts in the Dominican Republic and Haiti, although gauge coverage of Haiti is very limited. Melissa subsequently made landfall in Jamaica on 28 October, where satellite-based rainfall estimates indicate totals of 450 mm–600 mm based and a localized but intense positive Rx1day/Rx5day anomaly visible in ERA5 (Plate 2.1o; Fig. 2.33b; see Sidebars 4.1 and 7.2).

Central and southern Africa recorded wetter-than-average conditions throughout 2025 (see section 2d5). In terms of extremes, Rx1day and Rx5day anomalies were also positive across the region (Plate 2.1o; Fig. 2.33). In February, heavy rainfall triggered flooding across southern Botswana and eastern South Africa. In June, a powerful cold front produced record rainfall over South Africa's Eastern Cape, with Mthatha recording 129 mm in 24 hours. Late in the year, La Niña-enhanced rains produced 10-day rainfall accumulations exceeding the average annual total in parts of Mozambique, South Africa, Eswatini, and Zimbabwe, an event estimated at approximately a 1-in-50-year occurrence under current climate conditions (WWA 2026).

Over the Indian subcontinent, Rx1day and Rx5day anomalies from ERA5 remained near the 1991–2020 climatology (Plate 2.1o; Fig. 2.33). India's southwest monsoon delivered 108% of the long-term average (about one standard deviation [std. dev.] above normal, see section 7g4), while Pakistan's Punjab province experienced its worst flooding since 1988 (OCHA 2025). This near-climatological Rx1day signal across India reflects the persistent—rather than intense—character of the 2025 Indian monsoon over India itself, where enhanced seasonal totals were distributed across more rain days rather than concentrated synoptic systems which are better captured by longer-duration indices (Zhang et al. 2026). The Pakistan flooding represents a distinct regional extreme superimposed on this pattern.

Several notable Rx1day and Rx5day events occurred in otherwise arid or drought-affected regions. Along the west coast of North America, a series of atmospheric river landfalls brought exceptional multi-day rainfall—these began in February 2025 over northern California and continued to November and December across Washington State and California with record totals and widespread flooding. ERA5 Rx5day anomalies show positive values along the Pacific coast of North America, consistent with repeated atmospheric river activity (Fig. 2.33b). Iran experienced devastating flash floods in November and December following five consecutive years of extreme drought, with heavy rainfall affecting several provinces. ERA5 shows positive Rx5day anomalies over western Iran (Fig. 2.33b), although sparse gauge coverage over Iran in late 2025 limits independent verification of the magnitude. The weaker Rx1day signal in ERA5 and GPCC (Plate 2.1o; Fig. 2.33a) is consistent with multi-day rather than single-day rainfall.

7. CLOUDINESS

—C. Phillips and M. Foster

Global mean cloud area fraction (CF) decreased moderately in 2025 (–0.28%) compared to 2024, according to Pathfinder Atmospheres-Extended (PATMOS-x) version 6.0 observations (Foster et al. 2023). Averaged over the year, the Earth was 68.5% cloud covered in 2025, which is well below (–1.7%) the 1991–2020 mean and was the second lowest CF since the record began in 1980. A decrease in global CF suggests that clouds were less effective in their roles of reflecting incoming solar radiation and trapping outgoing longwave radiation. By comparing the observed top-of-atmosphere (TOA) radiation to the counterfactual cloud-free TOA radiation, we can estimate the strength of these effects. The shortwave cloud radiative effect (SWCRE) quantifies the cooling effect of clouds by reflecting sunlight, while the longwave cloud radiative effect (LWCRE) quantifies the warming effect of clouds by trapping outgoing infrared radiation. An analysis of the Clouds and the Earth's Radiant Energy System (CERES) Energy Balanced and

Filled Top-of-Atmosphere (EBAF-TOA Ed4.2.1) product shows the LWCRE had a record-weakest warming effect in 2025 (−0.73 W m^{-2} relative to the 2000–20 average) and was entirely offset by weaker reflection in SWCRE (0.88 W m^{-2}). The net cloud radiative cooling effect slightly weakened (−0.13W m^{-2}) compared to 2024 but remained stable at only 0.15 W m^{-2} weaker than the 2000–20 average. This stability is surprising given the large observed trends in the shortwave (SWCRE: 0.46 W m^{-2} decade^{-1}) and longwave (LWCRE: −0.41 W m^{-2} decade^{-1}) cloud radiative effect components.

The 2025 SWCRE and LWCRE anomalies are remarkably anti-correlated, spatially (Fig. 2.34), as well as temporally. For instance, over the Maritime Continent, we observed more warming from LWCRE coupled with more cooling from SWCRE, which is consistent with the observed increase in CF in this region (Plate 2.1p). Increased precipitation (Plate 2.1n) and upper-tropospheric humidity (Plate 2.1m) are also linked to this region. The opposite is true in the central Pacific, where a decrease in CF is observed, and the LWCRE is less warming while the SWCRE is less cooling. In both regions, the shortwave and longwave effects cancel out so that the net cloud radiative effect is close to the average (Fig. 2.34c). At annual/regional spatiotemporal scales (e.g., Fig. 2.34), the largest anomalies in the cloud radiative effect components, and even TOA radiation components (see Fig. 2.58), are driven by cloud variability. To what degree the longer trends in global mean SWCRE and LWCRE are attributable to cloud changes or to changes in the clear-sky environment (such as aerosol or greenhouse gas forcing) remains an open question (Loeb et al. 2024; Raghuraman et al. 2023).

The PATMOS-x v6.0 observations were analyzed using the same methodology as in the 2024 report (Phillips and Foster 2025). This processing included corrections for satellite drift using the observed diurnal cycle from geostationary satellites (Heidinger et al. 2026). In mid-2025, the NOAA-15, NOAA-18, and NOAA-19 satellites were decommissioned, leaving only MetOp-B and MetOp-C to complete the year. The 2024–2025 CF difference was checked against a difference derived from the Suomi National Polar-orbiting Partnership (SNPP) Visible Infrared Imaging Radiometer Suite (VIIRS) Cloud Properties (CLDPROP) dataset and was consistent.

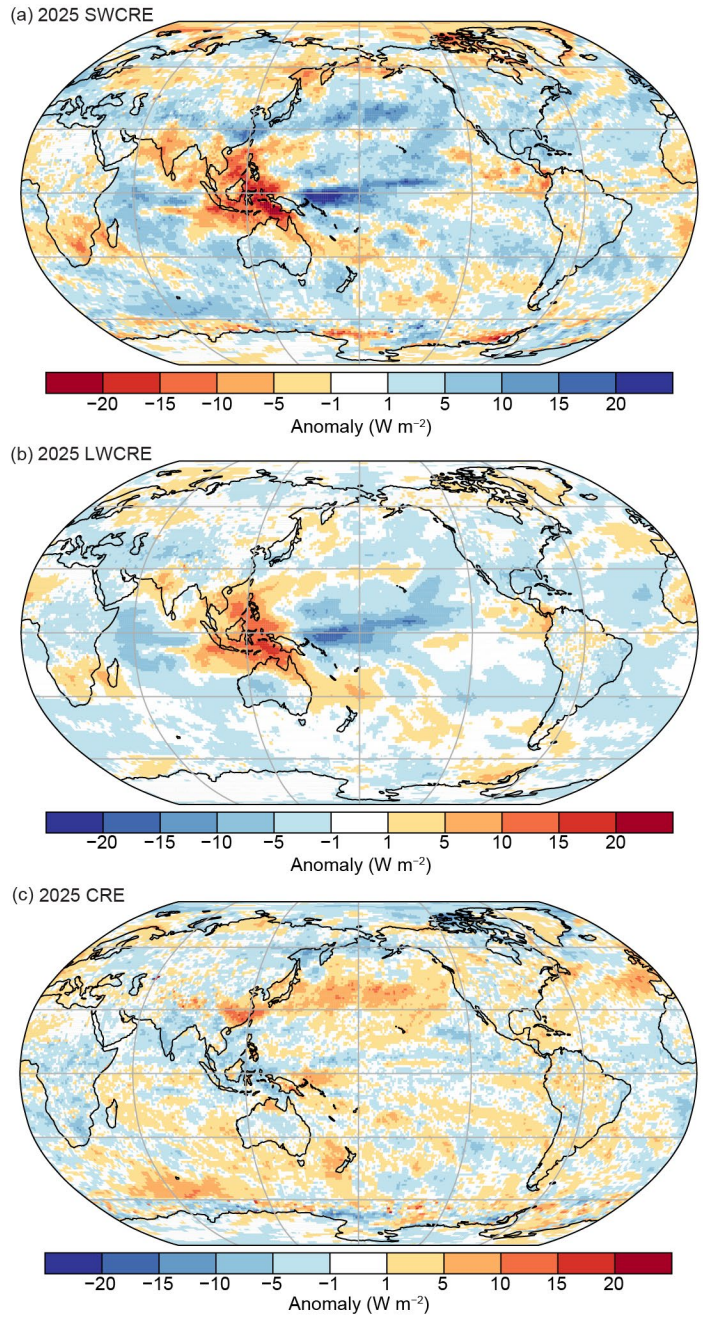

Fig. 2.34. The 2025 anomalies (W m^{-2}; 2000–20 base period) for the global-mean shortwave cloud radiative effect (SWCRE), longwave, global-mean cloud radiative effect (LWCRE), and net CRE from Clouds and the Earth's Radiant Energy System (CERES) EBAF-TOA Ed4.2.1. Positive (negative) values indicate more (less) warming. Note the inverted color scale for SWCRE to align with the LWCRE and cloud area fraction anomalies.

d. Hydrological cycle (land)

8. LAKE WATER STORAGE AND LEVEL

—M. E. Harlan, M. F. Meyer, and B. M. Kraemer

In 2025, water storage and levels across 2508 lakes were slightly above the long-term mean (2000–20) based on data from three global datasets. We evaluated lake storage from the GloLakes dataset (Hou et al. 2024; 2015 lakes, median area 9 km^2) and the MODIS Global Reservoir Product, hereafter referred to as MODIS (Gao 2021; 109 lakes, median area 360 km^2). For lake levels, the Global Reservoirs and Lakes Monitor (GREALM) dataset (Birkett et al. 2011; 384 lakes, median area 283 km^2) was used. Median storage in the 2025 was 6% higher than storage for the baseline mean. In aggregate, lakes in these two storage datasets exhibited a cumulative increase of 35,620 million cubic meters (MCM), equivalent to roughly three times the volume of Lake Superior in North America. The median lake level from lakes within the GREALM dataset was 0.05 m above the baseline, with individual 2025 median anomalies ranging between −43.6 m and +16.6 m. When combining storage and lake level datasets, 73% of lakes were above the respective respective baseline mean and 27% were below, with 84% agreement in the 2025 anomaly direction between the 124 shared GloLakes and GREALM lakes, and 44% agreement in anomaly direction between the 70 shared MODIS and GREALM lakes (no overlap between GloLakes and MODIS). Anomaly differences between datasets may stem from temporal differences. Welch's t-tests (Levene 1960) comparing 2025 lake level and storage observations to baseline conditions indicated that 39% of lakes were significantly above and 9% significantly below the baseline; $p < 0.05$. When considering these trends in lake storage relative compared with other components of the hydrosphere, global trends in soil moisture, river discharge, and terrestrial water storage broadly suggest drier conditions, whereas our results suggest accumulation of water in lakes (sections 2d9, 2d10, 2d11). These diverging trends could stem from regional differences in climate that tend to co-occur with lakes' global distribution, but regardless, our analyses indicate that lakes worldwide may be changing differently than the global hydrosphere.

Median lake storage and lake level anomalies across all lakes in the respective datasets support that, on average, lakes reported higher storage values and levels in 2025 relative to 2000–20 averages (Fig. 2.35). However, these median-level trends may obscure total water storage trends within the total lake cumulative storage (Fig. 2.36). Annual cumulative storage was computed as the sum of all lake storage from both GloLakes and MODIS for a given year. Lake level-area composites were computed for GREALM lakes from multiplying the anomaly level by the lake area. Lake level trends scaled by lake area as shown here highlight decreasing cumulative lake trends in recent years, particularly among large lakes, whereas cumulative lake storage over time from the GloLakes and MODIS datasets are relatively stable (Fig. 2.36). Among the lakes with available lake level data from GREALM, waterbodies with decreases in lake level include the Caspian Sea (Kazakhstan, Russia, Turkmenistan, Azerbaijan, and Iran), Aral Sea (Kazakhstan), Cahora Bassa Reservoir (Mozambique), Kariba Reservoir (Zambia), Zakhovka Reservoir (Ukraine), Buhayrat ath Tharthar (Iraq), Balqash (Kazakhstan), and Lake Winnipeg (Canada). Lakes with increases in lake level include Lake Victoria (Uganda,

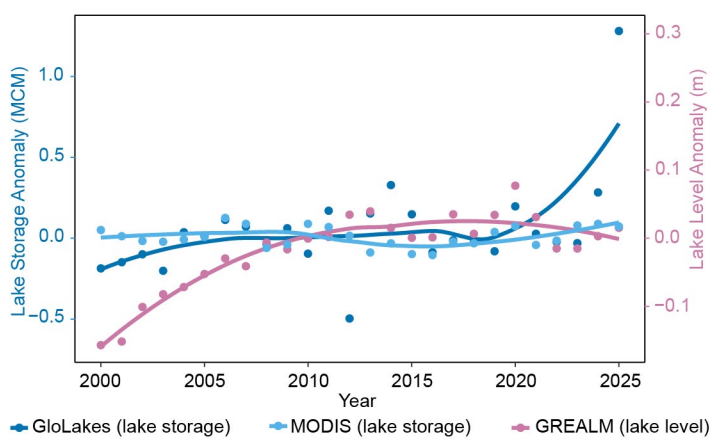

Fig. 2.35. Annual median lake water storage and level anomalies for the period 2000–25 relative to a 2000–20 base period. Yearly median water storage (GloLakes [dark blue] and the MODIS Global Reservoir Product [light blue]) and level (Global Reservoirs and Lakes Monitor [pink]) anomalies averaged across each water body are shown on dual y axes, expressed in million cubic meters (MCM) for lake water storage anomalies and meters (m) for lake water level anomalies. Local regression (loess) smoothing is applied to the annual median anomalies represented by the three lines. Notably, GloLakes data suggest a dramatic increase in lake water storage anomalies in 2025; however, much of this increase is attributed to higher storage in numerically abundant, small lakes. When considered amongst all lakes worldwide, these small lakes make up a marginal percentage of terrestrial lake storage relative to world's largest lakes.

Tanzania, Kenya), Tanganyika, Turkana Hāyk' (Kenya, Ethiopia), Rukwa-See (Tanzania), Lake Malawi (Malawi, Mozambique, and Tanzania), Volta (Ghana), Nasser (Egypt), and Bratsk Reservoir (Russia). Although many of these lakes with increasing storage exist within arid basins, previous evidence corroborates these trends and suggests that they are driven by local precipitation change (Papa et al. 2023). Collectively, these 16 waterbodies account for 57% of lake volume worldwide reported in similar lake volume datasets, such as HydroLAKES (Messager et al. 2016), and the Caspian Sea alone accounts for 40%. Thus, even marginal changes in lake level distributed across these lakes, especially the Caspian Sea, can drive global cumulative trends. Continuous monitoring of lake anomalies, both in near-real time and over multi-decadal scales, can strengthen water availability forecasts, support ecosystem resilience, and improve drought and flood risk management (Cheng et al. 2025; Woolway et al. 2025).

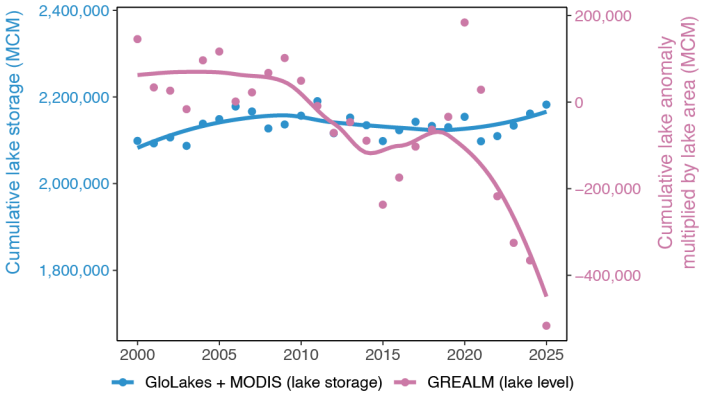

Fig. 2.36. Cumulative lake storage (left axis; blue; million cubic meters [MCM]) for the period 2000–25 summed from both GloLakes and the MODIS Global Reservoir Product with years linearly interpolated. Lake level anomalies (right axis; pink; MCM) from the Global Reservoirs and Lakes Monitor (GREALM) dataset are multiplied by lake area to represent a scaled volumetric change. These lake level-area composites do not represent lake storage, but rather a cumulative loss or gain in lake level scaled by area (storage change would only be appropriate if each lake was cylindrical in shape).

Lake datasets analyzed incorporate remote sensing data to estimate storage (GloLakes; MODIS) or level (GREALM). GloLakes combines Ice, Cloud, and land Elevation Satellite 2 (ICESat2) laser altimetry (Jasinski et al. 2023), GREALM radar altimetry data, and optical imagery from Landsat and Sentinel-2. The 2015 GloLakes lakes included in this study represent just 1% of global lake volume estimates in HydroLAKES—to improve volume coverage, lake storage from the MODIS Global Reservoir Product (Gao 2021) and GREALM lake level data (Birkett et al. 2011) are incorporated, adding an additional 493 lakes covering 90% of HydroLAKES volume. We refined each dataset by selecting lakes with at least 15 years of data, no data gaps longer than three years, and at least three observations in 2025.

Several limitations exist: datasets are limited in both geospatial and spatiotemporal coverage globally, with overrepresentation in North America (Plate 2.1q) relative to tropical regions, and underrepresentation of small (<1 km^2) lakes, which dominate global lake area and storage variability (Pi et al. 2022; Xu et al. 2024). Further, these satellite-based estimates of storage levels may not capture fine-scale temporal dynamics, including lake dynamics from seasonality (Li et al. 2025). Future integration of data across multiple satellite missions, such as the fusion of MODIS and Landsat data, or from incorporating the OPERA Dynamic Surface Water Extent (DSWx) data may help increase spatiotemporal coverage.

Disclaimer: any use of trade, firm, or product names is for descriptive purposes only and does not imply endorsement by the U.S. Government.

9. RIVER DISCHARGE AND RUNOFF

—T. Schaffhauser, J. Casado Rodriguez, S. Grimaldi, and P. Salamon

In line with recent years, 2025 was another dry year for the globe—runoff (Fig. 2.37) and discharge anomalies (Fig. 2.38) remained below normal relative to the 1991–2020 baseline. Although negative, the anomalies were less pronounced than in 2024 or the exceptionally dry year 2023 (Blunden and Reagan 2025), suggesting a gradual return towards normal conditions. However, in 2025, both discharge and runoff anomalies exhibited large spatial variability: different oceans experienced distinct total discharge anomalies, and within each ocean, individual outlet discharges and the corresponding land areas showed considerable positive and negative runoff anomalies (Fig. 2.39). While the above average land precipitation in 2025 (see Fig. 2.30) did not fully translate into a positive runoff anomaly, it reduced the deficit. The persistent negative runoff anomaly is consistent with below-normal terrestrial water storage (TWS) and

soil moisture (sections 2d10, 2d11), reflecting the slow recovery of the hydrological system from preceding dry years.

Monthly runoff anomalies weakened steadily over the course of 2025 (black line in Fig. 2.37b), likely reflecting the decay of the El Niño signal that was still partly evident in 2024. In contrast, the Oceanic Niño Index (ONI) in 2025 fluctuated around slightly negative values within the neutral ENSO range. The Pacific Decadal Oscillation (PDO) reached a new negative record since 1980, surpassing the already low values of 2024 and thereby extending the persistent cool-phase trend that has been ongoing since around 2020. Regionally, dry conditions were particularly notable in the Paraná, central Amazon, Yangtze, and Congo basins, as well as in several major European catchments such as the Danube and parts of the eastern United States (see Fig. 2.39). Large parts of Europe showed notable coherence across variables, with precipitation, soil moisture, and total water storage all remaining below normal in 2025 (see sections 2d5, 2d10, and 2d11 for more details). The Paraná faced consistent dry conditions over nearly its entire catchment area, similar to those found for the Congo basin. In contrast, above-average runoff occurred in northwestern South America and the upper Amazon, central and southwestern India, and the Mekong basin, and were especially pronounced in Indonesia and the Philippines, consistent with the wet precipitation anomalies reported in section 2d5. The spatial heterogeneity of runoff is, for example, evident in the Amazon basin, where headwater catchments experienced pronounced positive anomalies, while the central Amazon was characterized by drier conditions. These opposing signals largely compensated for each other, resulting in near-normal discharge at the basin outlet.

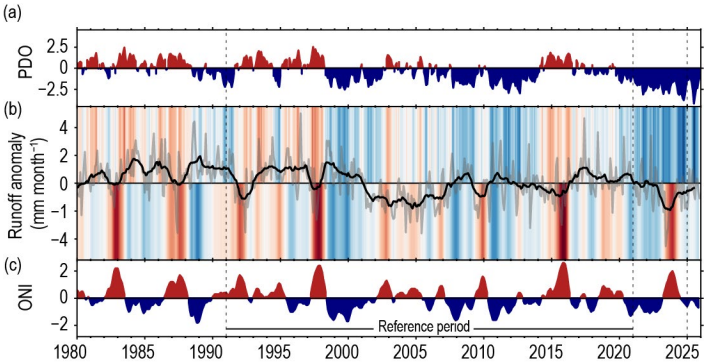

Fig. 2.37. Interannual variability of (b) global runoff and its connections with the (a) Pacific Decadal Oscillation (PDO) and (c) Oceanic Niño Index (ONI). In panel (b), the gray line represents the monthly time series of anomalies (mm month^{-1}; 1991–2020 base period), the black line represents the 12-month moving average, and the shading indicates the phase of the two indices (PDO in the upper part and ONI in the lower part). Negative phases are illustrated in blue and positive modes in red.

Freshwater discharge into the oceans remained generally below normal for all months (except June) at the global scale in 2025, by roughly one standard deviation relative to the 1991–2020 baseline (Fig. 2.38a). This negative anomaly was largely driven by persistently reduced discharge from rivers draining into the Atlantic Ocean, where anomalies were around two standard deviations below normal. In contrast, discharge into all other ocean basins ranged from near-to slightly-above normal. For the Atlantic basin, 2025 continued the recent sequence of dry years, although the magnitude of the anomaly was reduced compared to 2024. The Pacific Ocean exhibited several months with notably positive discharge anomalies, particularly during September and November. Overall, discharge conditions across all ocean basins in 2025 tended to be closer to normal than in 2024. Several major rivers draining into the Atlantic, including the São Francisco, Congo, Nelson, and Danube Rivers, exhibited below-normal discharge, while the Colorado River showed reduced flows among rivers draining into the Pacific. In contrast, major Arctic rivers such as the Ob, Yenisei, Lena, and Amur displayed near-normal discharge throughout the year.

A similar near-neutral pattern was observed for rivers discharging into the Indian Ocean. Despite wetter-than-usual conditions across large parts of India, e.g., reflected in positive discharge anomalies for the Krishna, albeit major systems such as the Ganges–Brahmaputra and Indus recorded near-normal discharge in 2025. For the Ganges–Brahmaputra, this reflects compensating effects between a wet Ganges and a dry Brahmaputra, consistent with total Indian Ocean discharge remaining close to the climatological mean.

The river discharge and runoff data used in this analysis are derived from the historical simulation of the Global Flood Awareness System version 4 (GloFASv4) of the Copernicus Emergency Management Service (Joint Research Centre–European Commission 2025). GloFASv4 employs the LISFLOOD-OS hydrological model (Burek et al. 2013), incorporating surface fields that represent land characteristics (Choulga et al. 2024) and parameters calibrated against discharge

records from nearly 2000 stations, or regionalized where necessary. The historical simulation spans from 1979 to the present, utilizing a 0.05° grid and a daily temporal resolution. ERA5 (Hersbach et al. 2020) served as the meteorological forcing input.

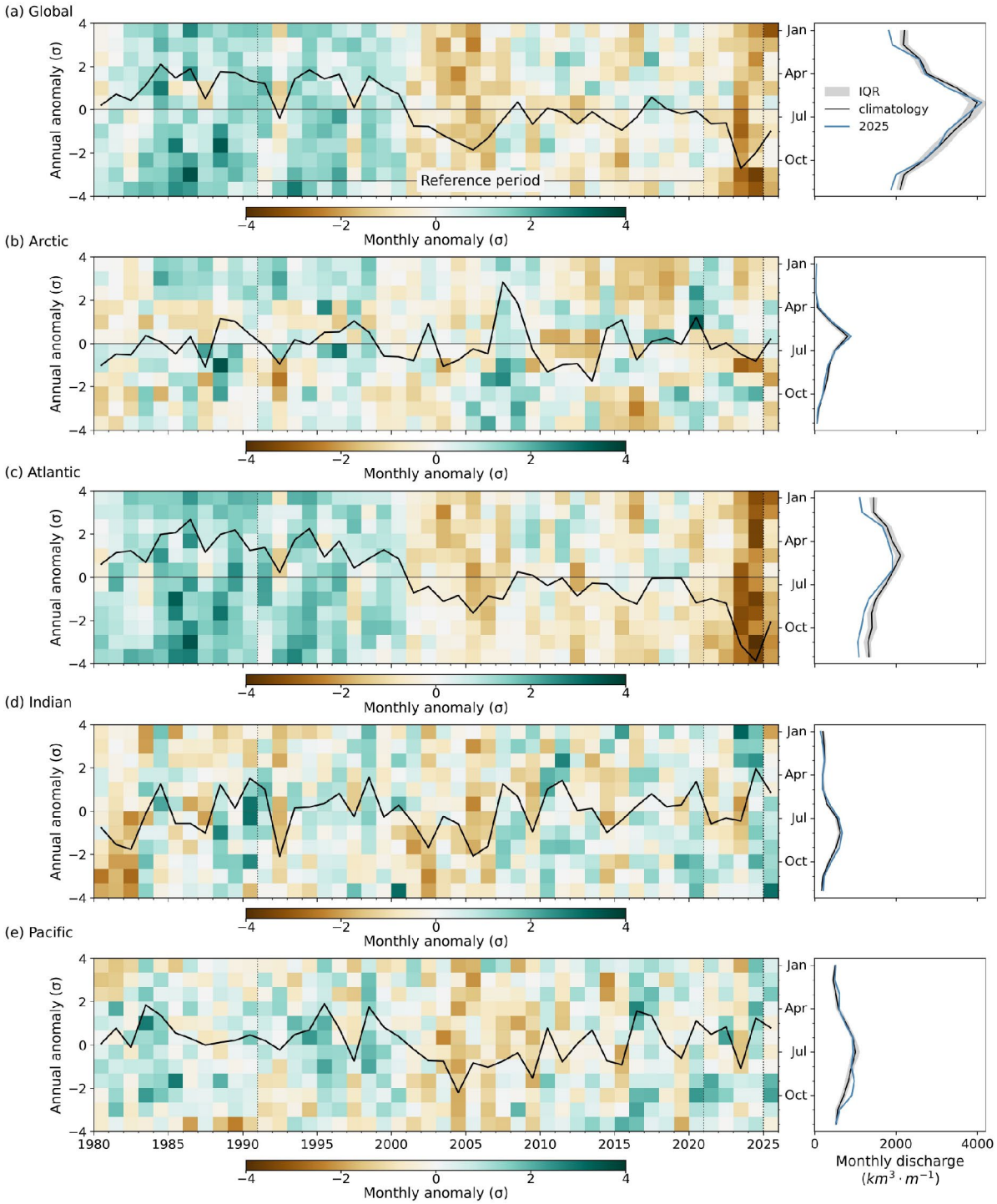

Fig. 2.38. Standardized interannual and monthly variability (left panels) and absolute seasonal freshwater discharge (km^3 $month^{-1}$; right panels) into the (a) global, (b) Arctic, (c) Atlantic, (d) Indian, and (e) Pacific Ocean basins. In the left panels, the black line represents the standardized annual discharge anomaly, and the background color array shows the standardized monthly anomalies with respect to the reference seasonality. The right panels exhibit the absolute seasonal discharge, where the black line represents the climatological mean, the gray shading indicates the interquartile range (IQR) in the climatology, and the blue line shows the seasonal variation in 2025.

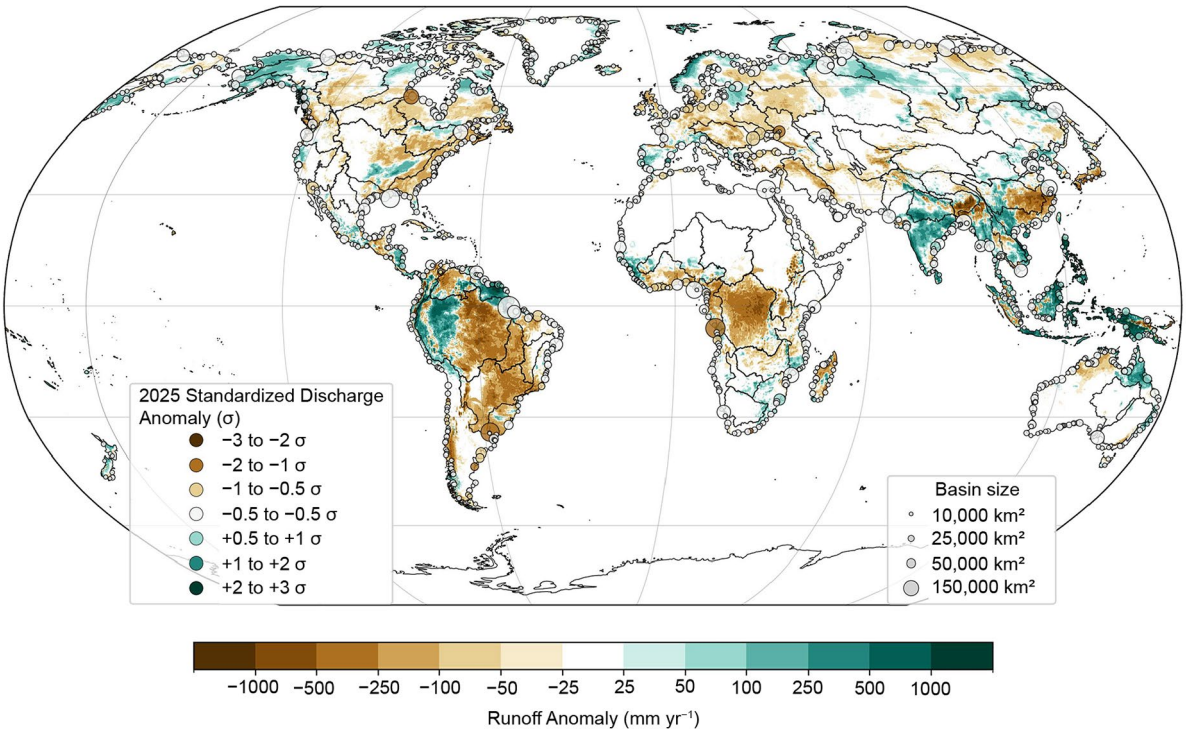

Fig. 2.39. Map of 2025 runoff anomalies and standardized outlet discharge anomalies relative to the 1991–2020 base period. Colored land areas show runoff anomalies (mm yr^{-1}), and the scattered circles along the coastlines represent standardized discharge anomalies (σ) at river outlets. Circle size is proportional to the upstream catchment area, with larger circles indicating larger basins, and the minimum catchment area considered is 5000 km^2. Black lines indicate outlines of major global river basins with catchment sizes >50,000 km^2. Discharge and runoff data are derived from the historical simulation of the Global Flood Awareness System version 4 (GloFASv4) of the Copernicus Emergency Management Service (Joint Research Centre–European Commission 2026).

10. GROUNDWATER AND TERRESTRIAL WATER STORAGE

—M. Rodell and D. N. Wiese

Global mean terrestrial water storage (TWS), excluding ice sheets and glaciers, remained squarely within its post-2015 range during 2025, about 0.9 cm equivalent height of water below its 2002–14 range (Rodell et al. 2024). Relative to the 2002–20 mean, TWS was notably elevated in central Africa, central Russia, southern India, and northern and eastern Australia, and levels were relatively low in much of western North America, southeastern South America, Europe, and the Middle East (Plate 2.1u). Following a characteristic precipitation regime change during an El Niño to La Niña transition, on a year-over-year basis (Plate 2.1t), most of northern South America gained a substantial amount of water (3 cm–20 cm) as it recovered from drought. In Europe and the Middle East, drought deepened. In many parts of the world, including South America, central and southern Africa, northern Australia, and much of Eurasia, the patterns of 2024 to 2025 changes were the reverse of those seen in 2023 to 2024. TWS record highs occurred in a swath of north central Russia, parts of South Africa, and scattered locations elsewhere, while record lows occurred over a much larger fraction of the land surface, including along the entire United States–Mexico border, parts of central and western Canada, and a large region stretching from Eastern Europe across the Middle East to Mongolia and south into the Arabian Peninsula.

As seen in Plate 2.1u, TWS levels remained depressed across most of North America, especially in the regions noted above, but year-to-year TWS changes in North America were muted (mostly <5 cm) compared with other parts of the world (Plate 2.1t). Though California enjoyed some TWS gains towards the end of 2025 that made the state completely drought-free for the first time in 25 years, its 2025-mean TWS was still lower than that in 2024. In contrast, northern South America, excluding eastern Brazil, gained a huge amount of water (>15 cm in the central Amazon) as it snapped back from record drought (in terms of 2002–25 TWS) during the prior two years, with flooding and landslides reported in parts of Bolivia, Brazil, Argentina, and

Venezuela. Central Africa, which has been experiencing a massive, multi-year pluvial event (Rodell and Li 2023), finally saw a TWS decline (mostly in the top of the soil column; see section 2d11). The exception was a zone south of the Sahara and north of the equator, where TWS continued to increase, including some record highs (>25 cm above the 2002–20 mean). South Africa also broke some records with a second consecutive year of TWS gains. Record-wet conditions also occurred in central Russia, southern India, and northeastern China near Beijing. Australia's Northern Territory shed more than 12 cm of water in some parts between 2024 and 2025, yet it remained very wet relative to normal. A multi-year drought persisted across Central Europe in what was the continent's hottest year on record, despite short episodes of extreme rainfall and flash flooding (section 7f). The same drought extended all the way to western Mongolia in the east and Saudi Arabia to the south (see Plate 2.1t). The lowest TWS levels (<–25 cm) were seen in eastern China and Kazakhstan and encircling the Black Sea. Another region of deep drought extended from Bangladesh to central China.

Time series of monthly zonal mean and global mean TWS anomalies are plotted in Figs. 2.40 and 2.41. Gaps occur when observations were not made. The averages excluded regions where TWS declines tend to be dominated by ice sheet and glacier losses: Antarctica, Greenland, the Gulf Coast of Alaska, polar islands, High Mountain Asia, alpine western Canada, and the southern Andes. A 20°-wide zone of TWS losses in the northern midlatitudes became even drier in 2025. Wetting in a 23°-wide equatorial zone, which had lessened in 2024, resumed in 2025 as northern South America recovered from drought, southern India and southeast Asia gained water, and TWS in central Africa remained elevated. Boreal latitudes remained dry on average, continuing a long-term trend, due to ongoing drought in northern Canada, and pockets of drought in northern Russia despite wet conditions in central Russia. During 2025, global mean non-ice TWS (Fig. 2.41) varied within its lower, post-2015 range (Rodell et al. 2024). It approached its record minimum in March but rebounded to the middle of that range just two months later.

TWS anomaly data were derived from Gravity Recovery and Climate Experiment (GRACE) and GRACE Follow-On (GRACE-FO) satellite observations of Earth's time-varying gravity field (Tapley et al. 2004; Landerer et al. 2020). In situ networks do not have adequate density to observe the components of TWS (groundwater, soil moisture, surface waters, snow, and ice) needed to estimate large-scale changes. At midlatitudes, the monthly TWS anomalies are believed to be accurate to within about 1 cm–2 cm equivalent height of water

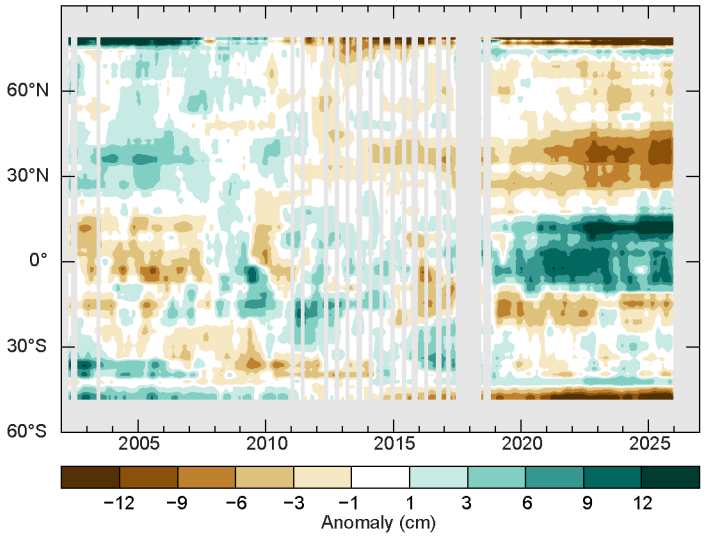

Fig. 2.40. Zonal means of monthly terrestrial water storage anomalies—excluding those in Antarctica, Greenland, the Gulf Coast of Alaska, polar islands, High Mountain Asia, alpine western Canada, and the southern Andes—in cm equivalent height of water (cm; 2002–20 base period), based on gravity observations from the Gravity Recovery and Climate Experiment (GRACE) and GRACE Follow-On (GRACE-FO).

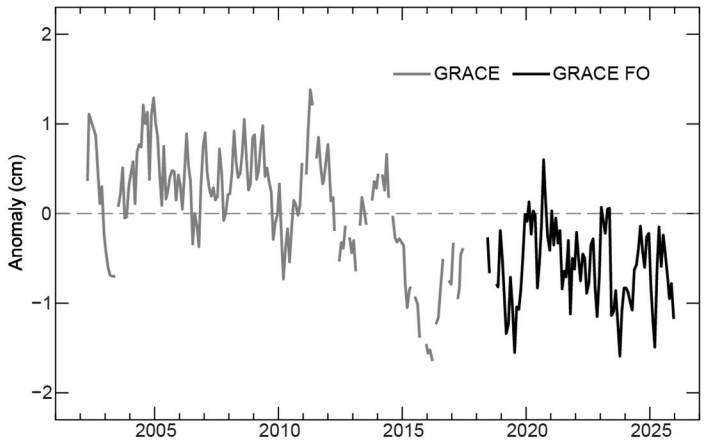

Fig. 2.41. Global average terrestrial water storage anomalies (cm equivalent height of water [cm]; 2002–20 base period) from Gravity Recovery and Climate Experiment (GRACE; gray) and GRACE Follow-On (GRACE-FO; black)—excluding those in Antarctica, Greenland, the gulf coast of Alaska, polar islands, High Mountain Asia, alpine western Canada, and the southern Andes.

averaged over a 500,000 km² region (Wiese et al. 2016). Groundwater tends to dominate TWS interannual variability except in the humid tropics (surface water dominant) and high-latitude and alpine regions (ice and snow dominant), while soil moisture (section 2d11) often dominates on seasonal timescales (Getirana et al. 2017).

11. SOIL MOISTURE

—B. L. Harris, J. Lems, W. Preimesberger, D. D. Kovács, C. Moldenhauer, S. Hahn, A. Gruber, M. Formanek, N. Rodríguez-Fernández, D. Duchemin, R. Prajapati, T. Frederikse, A. Dostalova, R. A. M. de Jeu, and W. A. Dorigo

Soil moisture plays a crucial role in the water, energy, and carbon cycles. It influences vegetation growth and land–atmosphere interactions, with impacts on surface air temperature, precipitation, and extreme weather events including heatwaves and wildfires (Seneviratne et al. 2010). Global soil moisture conditions were drier on average in 2025 than in any other year over the 1991–2025 period (Fig. 2.42), although the global anomaly became less dry as the year progressed. These unprecedented dry conditions were mostly driven by below-average soil moisture in the Northern Hemisphere, with particularly dry anomalies observed at latitudes above 55°N (Fig. 2.43). The Southern Hemisphere transitioned from drier-than-average soil moisture into near-normal conditions by the end of 2025.

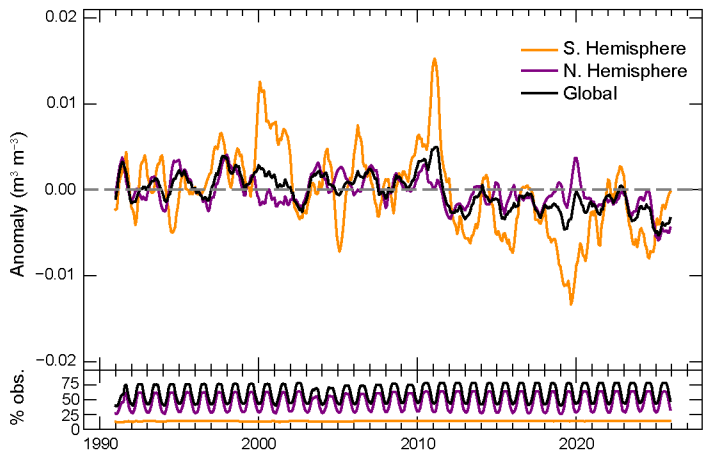

Fig. 2.42. (top) Time series of global (black), Northern Hemisphere (purple), and Southern Hemisphere (orange) monthly surface soil moisture anomalies (m^3 m^{-3}; 1991–2020 base period) for the period 1991–2025, and (bottom) the valid observations as a percentage (%) of total global land surface. Data are masked where no retrieval is possible or where the quality is not assured and flagged, for example due to dense vegetation, frozen soil, permanent ice cover, or radio frequency interference. (Source: Copernicus Climate Change Service [C3S] Soil Moisture.)

The high-latitude regions contributing to the unusually dry soil moisture conditions include the Siberian boreal forest and tundra, with the dry anomaly extending west into Fennoscandia (Plate 2.1v). The dry anomaly over Siberia is consistent with low observed precipitation rates in this region (section 2d5). Dry conditions were also evident over the Canadian prairies and boreal forest and across the Tibetan Plateau.

The United States and Mexico began 2025 with drier-than-usual soil moisture across all regions (Appendix Fig. A2.17), compared to the 1991–2020 average. The northeastern United States remained drier than average throughout the year, while the southeastern United States and Mexico saw these conditions alleviated during spring and summer, before returning to dry anomalies by October. In the western United States, above-average precipitation from September onwards helped to relieve drought conditions in some areas (NOAA NCEI 2026).

Northeastern Brazil experienced dry conditions from February onwards, associated with extreme drought (section 2d12), with the location of the strongest dry anomalies moving southward over the course of the year (Appendix Fig. A2.17). Drier-than-usual soil

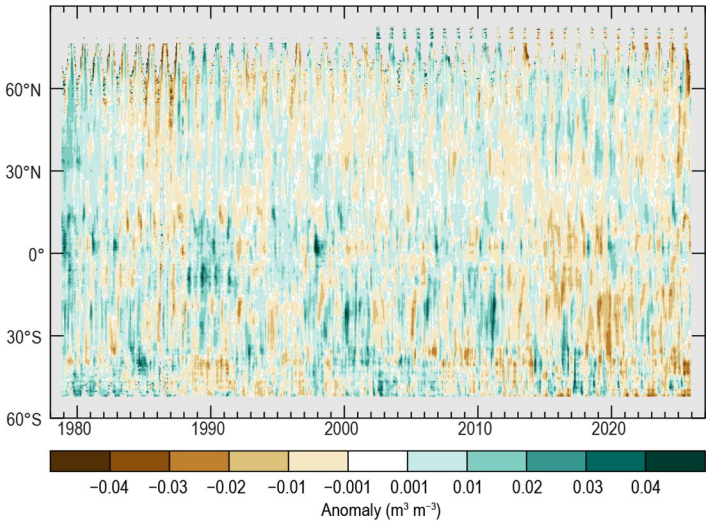

Fig. 2.43. Time–latitude diagram of monthly surface soil moisture anomalies (m^3 m^{-3}; 1991–2020 base period). Data are masked where no retrieval is possible or where the quality is not assured and flagged, for example due to dense vegetation, frozen soil, permanent ice cover, or radio frequency interference. (Source: Copernicus Climate Change Service [C3S] Soil Moisture.)

moisture was also observed in northern Patagonia throughout the year. This contrasted with the southern River Plate basin, which experienced extensive heavy rainfall and associated flooding in March and early April, leading to wet soil moisture anomalies that persisted for the rest of 2025.

Soil moisture in eastern Europe was drier than average from February to September, before transitioning to a wet anomaly for the rest of the year. Western Europe experienced more moderate anomalies, with dry conditions extending farther to the west during boreal summer.

The southern border of the Sahel was drier than average during the early part of the rainy season (May–August), with a particularly pronounced negative soil moisture anomaly in Sudan. Drought conditions returned to the Horn of Africa in November, after wet anomalies in previous years had ended the prolonged drought of 2020–22 (Anderson et al. 2023; Hirschi et al. 2024). However, wetter-than-usual soil moisture conditions were observed across Kenya for most of the year, particularly during the long rains from March to May. Southern Africa was also notably wetter than usual, with large parts of Botswana exhibiting soil moisture anomalies exceeding 30% above average. These wet conditions were likely linked to increased rainfall due to the weak La Niña conditions at the beginning and end of the year—a marked contrast to 2024, when southern Africa was in drought following a strong El Niño event (Lems et al. 2025). La Niña was also associated with wetter-than-average soil moisture conditions in northern Australia, while southern Australia was drier than usual (Plate 2.1v). As in 2024, wet soil moisture anomalies were widespread across India, with the wettest anomalies occurring in the northwest of the country.

Soil moisture was observed by microwave satellite remote sensing of the upper few centimeters of soil, as provided by the COMBINED product of the Copernicus Climate Change Service (C3S) version v202505 (Dorigo et al. 2025). C3S combines multi-sensor data in the 1978–2025 period through statistical merging (Gruber et al. 2017, 2019). Version v202505 includes EUMETSAT H SAF H121 Advanced Scatterometer (ASCAT) data that corrects previous artificial wetting trends (Hahn et al. 2026). Wet and dry anomalies here are based on the 1991–2020 climatological normal. Note that changes in spatiotemporal coverage (both between season and periods, e.g., resulting from the inclusion of additional sensors) can introduce uncertainties in the domain-averaged soil moisture time series (e.g., Bessenbacher et al. 2023).

12. MONITORING GLOBAL DROUGHT USING THE SELF-CALIBRATING PALMER DROUGHT SEVERITY INDEX

—J. Barichivich, T. J. Osborn, A. R. Friedman, I. Harris, G. van der Schrier, and P. D. Jones

The 2025 update of the self-calibrating Palmer Drought Severity Index (scPDSI) indicates that the global extent of drought conditions (Fig. 2.44) during 2025 was notably above the long-term 1950–2025 average. Nevertheless, global drought area declined slightly compared with 2024 and remained below the preceding peak observed during the second half of 2023 (Barichivich et al. 2025). Global drought area expanded rapidly after mid-2019, and since then it has remained above the long-term 1950–2025 mean (Fig. 2.44). During 2025, drought conditions of at least moderate intensity (scPDSI ≤–2) affected 22%–25% of the global land area during the year, while severe or worse drought (≤–3) and extreme drought (≤–4) affected approximately 10%–12% and 3%–5% of the land area, respectively (Fig. 2.44).

The global distribution of drought during 2025 (Plate 2.1w) shows several large dry regions across the Northern Hemisphere mid-latitudes and parts of South America and Africa. Severe to extreme drought conditions occurred across the Mediterranean basin, central and southeastern Europe, northern

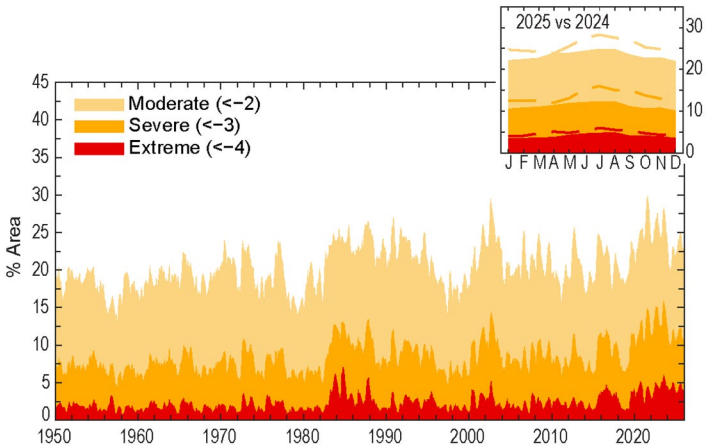

Fig. 2.44. Percentage of global land area (excluding ice sheets and deserts) with self-calibrating Palmer Drought Severity Index (scPDSI) indicating moderate (<–2), severe (<–3), and extreme (<–4) drought for each month of 1950–2025. Inset: each month of 2025 (shading) compared with 2024 (dashed lines).

parts of the Middle East and Central Asia, northeastern South America, western North America, and portions of west and southern Africa and Australia (Plate 2.1w). Notable drought relief occurred across southern Africa, Central America, and parts of northwestern South America (Fig. 2.45).

In the Americas, drought eased in Mexico and persisted across northern North America while autumn rain eased the drought in the western United States (sections 2d5, 2d11), but this was too late for the 2025 annual scPDSI to move out of drought conditions. Across South America, widespread extreme drought conditions affected most of central and northern Amazonia and parts of northeastern Brazil, reflecting the continuation of regional precipitation deficits following the severe drought of 2023/24 that led to critically low river levels in the dry season of 2024 (Barichivich et al. 2025). In contrast, parts of northwestern Amazonia, southern Brazil, and the La Plata basin experienced near-normal to relatively wetter conditions.

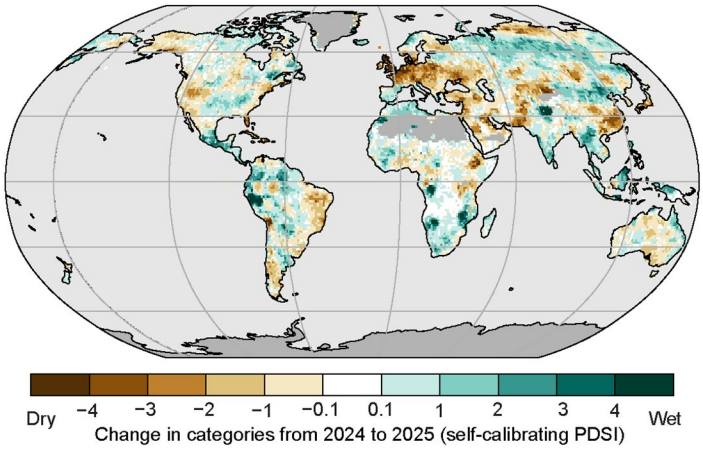

Fig. 2.45. Change in drought from 2024 to 2025 (mean self-calibrating Palmer Drought Severity Index [scPDSI]) for 2025 minus mean scPDSI for 2024). Increases in drought severity are indicated by negative values (brown) and decreases by positive values (green). No calculation is made where a drought index is meaningless (gray areas: ice sheets or deserts with near-zero mean precipitation).

Across Europe and the Mediterranean, drought conditions were among the most pronounced globally (Plate 2.1w) due to a combination of precedent moisture deficits (Barichivich et al. 2025), above-average temperatures (section 2b4), and rainfall deficits (section 2d5; Toreti et al. 2025). The scPDSI pattern shows severe to extreme drought extending across eastern, southern, and southeastern Europe, including the Balkans, Greece, and parts of Türkiye. Compared to conditions in 2024, central Europe experienced stronger intensification of drought in 2025 than any other region (Fig. 2.45). This was fueled by a very dry spring and coincided with more-than-usual sunshine amounts throughout the year. In North Africa, severe-to-extreme drought persisted along the Mediterranean coast from Morocco to Tunisia, though its intensity decreased relative to 2024. Severe drought also affected parts of the Middle East during 2025, including Syria where it contributed to major agricultural losses (FAO 2025).

Across Asia, extensive dry anomalies stretched from the Caspian region through Kazakhstan into Mongolia and northern China (Plate 2.1w). In contrast, parts of South and Southeast Asia experienced relatively wetter conditions associated with regional monsoon variability. In Australia, moderate drought persisted along the western and southern coastal zones, although drought conditions were less extensive than in recent years.

Hydrological drought results from periods of abnormally low precipitation, sometimes amplified by increased evapotranspiration associated with higher temperatures. Here, global drought conditions are estimated using the self-calibrating Palmer Drought Severity Index (scPDSI; Wells et al. 2004; van der Schrier et al. 2013) derived from precipitation and Penman-Monteith potential evapotranspiration from the Climatic Research Unit gridded Terrestrial Series (CRU-TS 4.10) dataset (Harris et al. 2020).

13. LAND EVAPORATION

—D. G. Miralles, O. M. Baez-Villanueva, O. Bonte, J. Massant, K. Delbare, F. Carere, and H. E. Beck

Land evaporation is a major component of the continental water cycle and a primary mechanism through which land regulates climate variability and change. Its sensitivity to both water availability and atmospheric demand makes evaporation an effective diagnostic of these climate anomalies. The global mean land evaporation anomaly in 2025 was close to the 1991–2020 average (Fig. 2.46). It aligned below the multi-decadal upward trend of approximately +0.7 mm yr^{-1} since

the early 1980s. This trend has been attributed to rising near-surface air temperatures, increasing atmospheric evaporative demand, and widespread terrestrial greening (Miralles et al. 2014; Brutsaert 2017; Yang et al. 2023). Estimates of this trend vary, however, largely depending on the evaporation dataset, as recently reported (Ruan et al. 2025).

The Northern Hemisphere extratropical regions maintained above-average evaporation during much of the year, whereas the Southern Hemisphere exhibited stronger seasonal and regional variability, including pronounced negative anomalies during parts of the year, particularly in tropical and subtropical latitudes (Fig. 2.47). This asymmetry reflects differences in land fraction, drought exposure, and the spatial heterogeneity of temperature and precipitation anomalies between both hemispheres, and it has been a recurrent feature of recent decades (Miralles et al. 2014; Martens et al. 2018).

In terms of regional patterns, positive anomalies persisted for much of the year across North America, Europe, and eastern Asia (Plate 2.1x), coinciding with sustained warm conditions (section 2b1). Since cool ENSO-neutral conditions dominated much of 2025, with a weak return toward La Niña tendencies later in the year, ENSO-induced modulation of evaporation was secondary, and the characteristic global signature of ENSO on terrestrial evaporation patterns (Miralles et al. 2014; Martens et al. 2018) was not present in 2025. Instead, Plate 2.1x reveals contrasts between regions that often show synchronized behavior, such as Australia and southern Africa. Negative anomalies were observed across the west and central parts of Australia, especially in semiarid regions, consistent with prevailing precipitation deficits, reduced soil water availability, and drought conditions in 2025 (Van Dijk et al. 2026; section 2d12). In northeastern Brazil, particularly across the Caatinga region, persistent precipitation deficits also led to reduced soil moisture availability (section 2d11) and suppressed evaporation. In addition, extensive areas of tropical Africa exhibited lower-than-usual evaporation, mostly reflecting precipitation deficits that constrained evaporation despite high temperatures (section 2d5).

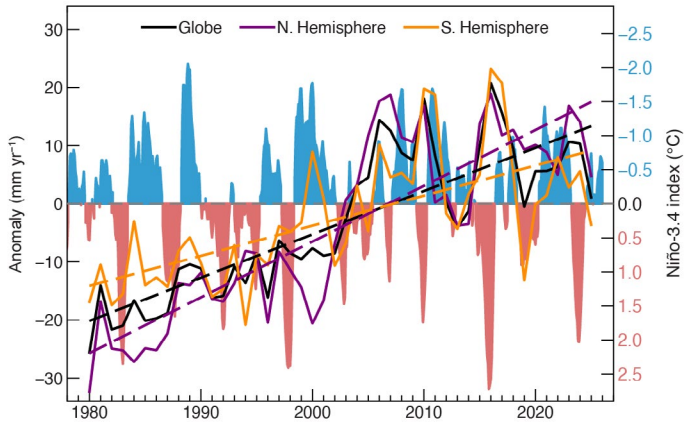

Fig. 2.46. Land evaporation anomaly (left axis; mm yr^{-1}; 1991–2020 base period) for the Northern Hemisphere, Southern Hemisphere, and the entire globe (purple, orange, and black solid lines, respectively). Linear trends in evaporation (dashed lines) and the Niño-3.4 index (right axis; °C; red and blue shaded areas) are also shown. (Source: Global Land Evaporation Amsterdam Model [GLEAM] version 4.3a and NOAA Physical Sciences Laboratory [PSL].)

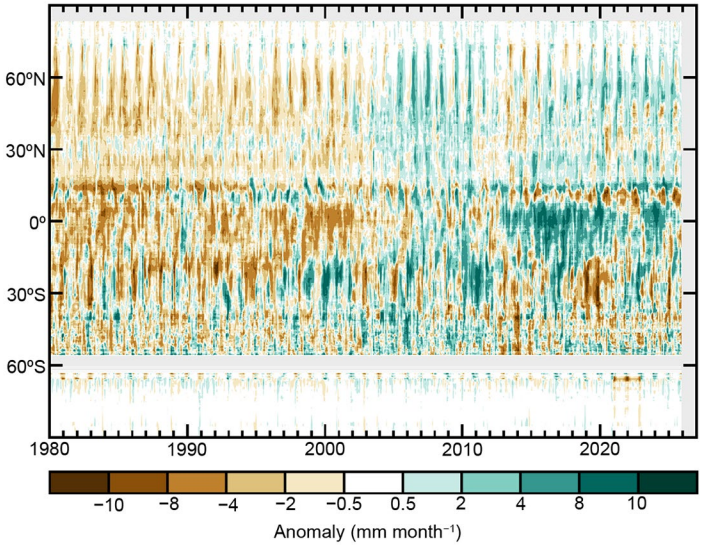

Fig. 2.47. Zonal mean terrestrial evaporation anomalies (mm month^{-1}; 1991–2020 base period). (Source: Global Land Evaporation Amsterdam Model version 4.3a [GLEAM v4.3a].)

In contrast, positive evaporation anomalies spread across southern and central Africa, northern Australia, and India (Plate 2.1x). These higher-than-usual values are consistent with enhanced precipitation during 2025, which increased soil moisture availability and supported high evaporation rates across the region (sections 2d5, 2d11). The pattern of negative anomalies in the Caatinga in northeastern Brazil, western Australia, and tropical Africa with positive anomalies in southern Africa, India, and northern Australia, highlights the strong regional control of

precipitation on evaporation at intra-annual and inter-annual scales, despite the dominant role of temperature trends over decadal time scales (Miralles et al. 2014).

The evaporation estimates used are based on the Global Land Evaporation Amsterdam Model (GLEAM) version 4.3a (Miralles et al. 2011, 2025). GLEAM combines satellite observations of soil moisture and vegetation characteristics with precipitation and meteorological forcing to estimate terrestrial evaporation and its main components, including soil evaporation, transpiration, interception loss, and sublimation. New GLEAM versions are routinely evaluated against in situ eddy-covariance measurements, with reported correlations around 0.7 to 0.8 and unbiased root mean square errors on the order of 0.7 to 0.9 mm day^{-1} (Miralles et al. 2025; Martens et al. 2017). Despite ongoing advances, uncertainties remain, particularly in regions with sparse observational constraints. Continued progress is expected in the field of evaporation retrievals for climate monitoring, both from the employment of new thermal missions and high-resolution optical observations, which can better constrain surface energy partitioning and vegetation water use (McCabe et al. 2017; Fisher et al. 2020; Lagouarde et al. 2018), as well as from initiatives aiming to consolidate long-term multi-satellite records, like the new Climate Change Initiative (CCI) Land Evaporation from the European Space Agency (ESA).

e. Atmospheric circulation

1. MEAN SEA LEVEL PRESSURE AND RELATED MODES OF VARIABILITY

—D. Campos, D. Fereday, and J. Vicencio

Mean sea level pressure (MSLP) variability is driven by large-scale modes of atmospheric circulation that influence regional weather, climate anomalies, and extremes across the globe (Kaplan 2011). In the Southern Hemisphere (SH), the Antarctic Oscillation (AAO), also known as the Southern Annular Mode (SAM), dominates extratropical variability through fluctuations in the strength and latitude of the circumpolar westerly winds. In the Northern Hemisphere (NH), the North Atlantic Oscillation (NAO), and Pacific North American (PNA) patterns have important impacts on the European and North American sectors.

The El Niño–Southern Oscillation (ENSO) is an important driver of global atmospheric circulation (Capotondi et al. 2015; Yeh et al. 2018). It impacts the tropics via the Walker circulation, an overturning tropical atmospheric mode driven by zonal surface temperature gradients (Bjerknes 1969). ENSO also drives planetary-scale atmospheric Rossby waves that propagate into the extratropics and influence midlatitude circulation (Sardeshmukh and Hoskins 1988; Scaife et al. 2017).

In the Northern Hemisphere, the PNA was strongly positive during winter (December 2024–February 2025) with low pressure in the Aleutian region and high pressure over the United States (Fig. 2.48a). Observed North American temperature anomalies were broadly consistent with the positive PNA (NCEI synoptic discussion [Leathers et al. 1991; Loikith and Broccoli 2014]). Although the positive PNA is associated with El Niño (Livezey et al. 1997), weak La Niña conditions were seen at this time. While ENSO has important atmospheric teleconnections to the extratropics (Yeh et al. 2018), these may have been less evident in 2025 due to the lack of strong ENSO anomalies throughout the year.

In the European region, the winter NAO fluctuated between positive and negative phases during winter 2024/25, and was neutral overall (Fig. 2.48e). The summer NAO (Folland et al. 2009) was positive during July/August (Figs. 2.48c,f) with a low-pressure anomaly over Iceland and Greenland, consistent with warm temperature anomalies over northwestern Europe (see section 7f for details). In December 2025, the winter NAO was again neutral, while the PNA was negative.

During austral summer (DJF 2024/25), despite the long-term positive trend in SAM (Fogt and Marshall 2020), the mode was predominantly negative, with negative AAO values occurring on 64.4% of days. This behavior was consistent with the seasonal MSLP anomaly pattern (Fig. 2.49a) and the development of a positive Pacific–South American (PSA) pattern (O'Kane and Franzke 2025), despite the weak La Niña conditions in the tropical Pacific (Fogt et al. 2011).

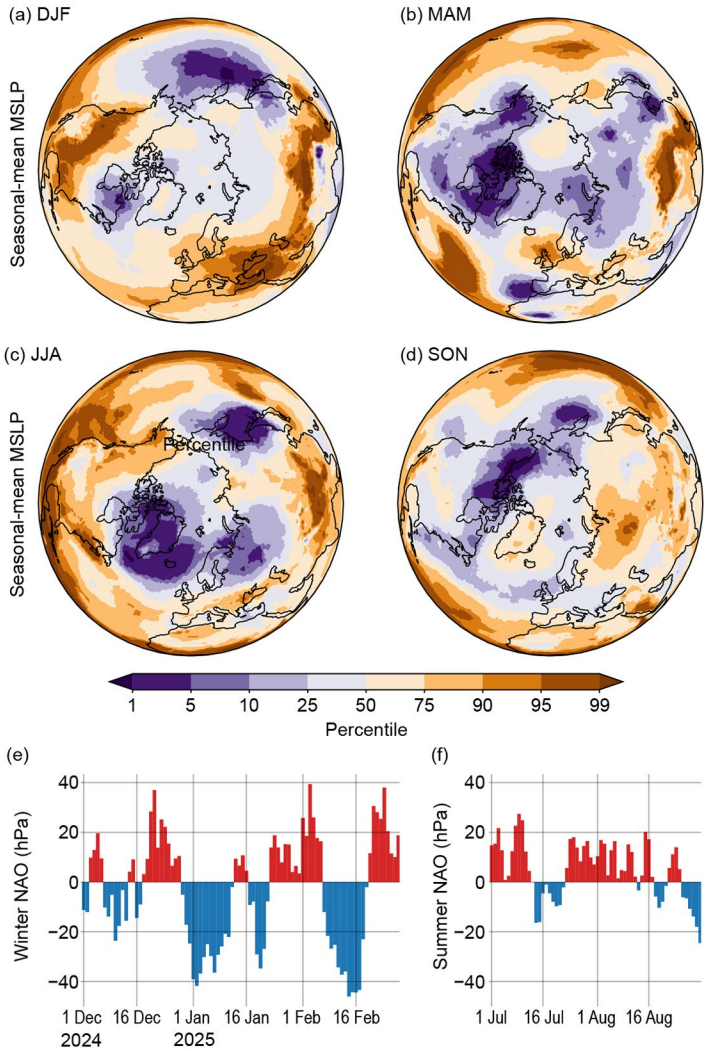

Fig. 2.48. Northern Hemisphere mean sea level pressure (MSLP) for 2024/25. Panels (a)–(d): seasonal mean sea level pressure (MSLP) for Dec 2024 to Nov 2025. Fields are anomalies with respect to a 1991–2020 climatology, expressed as percentiles. (e) Daily North Atlantic Oscillation (NAO) index for Dec 2024 to Feb 2025 defined as Azores minus Iceland MSLP. (f) Daily Summer North Atlantic Oscillation (SNAO) index for Jul–Aug 2025 defined as United Kingdom (UK) minus Greenland MSLP. (Source: ERA5.)

During austral autumn (MAM), the SAM shifted decisively to a positive phase, with 84.8% of days exhibiting positive AAO values, and remained predominantly positive through winter (JJA), when 64.1% of days were positive. This period saw lower-than-average MSLP over Antarctica and enhanced midlatitude and subtropical high-pressure centers (Figs. 2.49b,c), consistent with a strengthened annular circulation. These circulation anomalies modulated regional hydroclimate across the Southern Hemisphere, particularly during austral winter. In JJA, enhanced anticyclonic conditions near New Zealand allowed frequent intrusions of tropical moisture from the north, i.e., atmospheric rivers, contributing to heavy rainfall and flooding between late May and mid-July (Reid et al. 2021; see section 7h5). In contrast, persistent positive MSLP anomalies over the southern tip of South America were associated with suppressed precipitation during austral winter in central-southern Chile and central-southern Argentina, contributing to negative annual rainfall anomalies, potentially preconditioning the region for the highly active 2025/26 austral summer wildfire season (see Fig. 2.31; also see section 7d3; https://www.worldweatherattribution.org/climate-change-fuels-the-destruction-of-worlds-oldest-trees).

From September onward, the SAM was again negative, with 94.5% of days characterized by negative AAO values during the SON season, coincident with the development of a weak La Niña (Fig. 2.49d; see section 4b for details). The SON-mean SAM index was the second-most negative on record (since 1979), exceeded only by 2002. Particularly strong negative MSLP anomalies were observed over the Australia-New Zealand sector during this period, coincident with exceptionally warm and wet spring conditions across parts of New Zealand (see section 7h5; NIWA 2025). This late-year negative SAM contrasts with the canonical La Niña response, which typically favors positive SAM phases, and likely reflects the weak amplitude of the La Niña event and the influence of competing internal atmospheric variability (Fogt and Bromwich 2006).

The Southern Oscillation Index (SOI), which represents the atmospheric component of ENSO (McPhaden et al. 2020), closely tracked the evolution of La Niña conditions in 2025. During the austral summer (DJF 2024/25), the SOI was predominantly positive, consistent with an enhanced Walker circulation. As La Niña weakened, the SOI returned to near-neutral values during austral autumn and early winter, before becoming positive again toward the end of the year in association with the re-emergence of weak La Niña conditions.

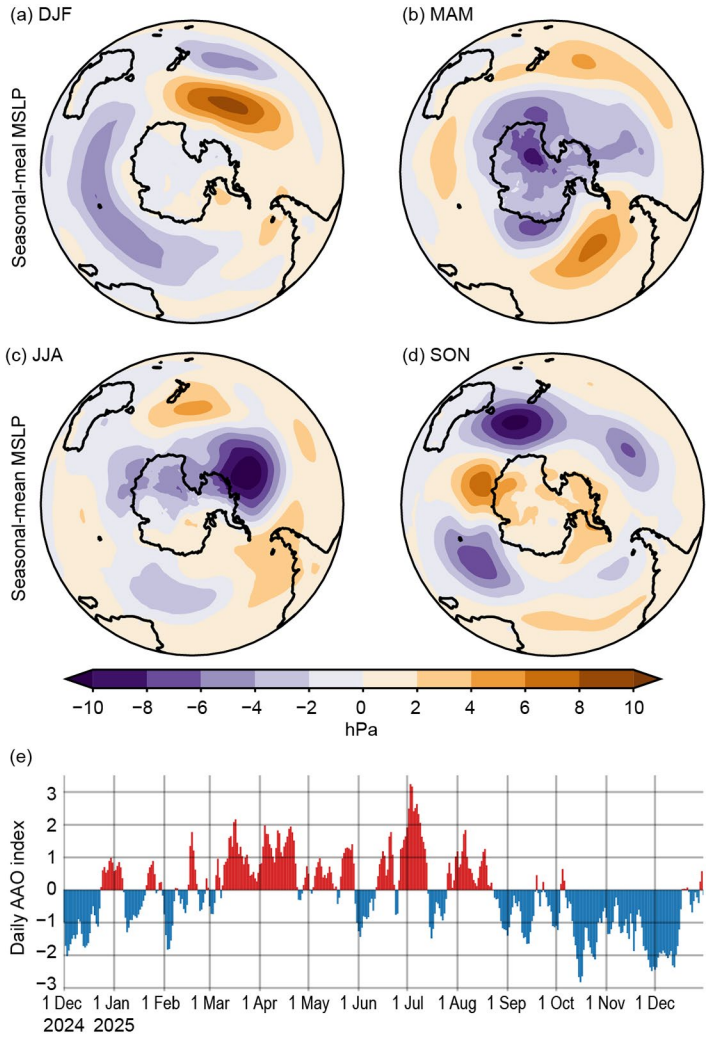

Fig. 2.49. Southern Hemisphere mean sea level pressure (MSLP) for 2024/25. Panels (a)–(d): seasonal-mean MSLP (hPa) for Dec 2024 to Nov 2025. Fields are anomalies with respect to a 1991–2020 climatology. (Source: ERA5.) Panel (e) Daily Antarctic Oscillation (AAO) index for Jan–Dec 2025. (Source: NOAA National Centers for Environmental Prediction.)

2. LAND AND OCEAN SURFACE WINDS

—C. Azorin-Molina, R. J. H. Dunn, L. Ricciardulli, T. R. McVicar, J. P. Nicolas, C. A. Mears, Z. Zeng, M. G. Bosilovich, P. A. Monerie, and B. W. Hutchins

Terrestrial surface wind speeds at ~10 m above ground were generally below the 1991–2020 climatological baseline (Plate 2.1z), with a 2025 anomaly of −0.041 m s^{-1} in the Northern Hemisphere from the Global Historical Climatology Network hourly (GHCNh) observational dataset (Table

2.10). Negative anomalies were primarily confined to North America and Europe, contrasting with positive departures over Asia and a pronounced interhemispheric asymmetry driven by the strongest positive anomaly recorded over South America (Fig. 2.50a; Table 2.10). The wind speed "reversal" that emerged around the 2010s (Zeng et al. 2019), following several decades of "stilling" (McVicar et al. 2012), appears to be weaker in GHCNh than in previous in situ datasets (Fig. 2.50a; Azorin-Molina et al. 2024).

Surface land winds are evaluated through comparisons between observations and reanalysis products, including the new GHCNh observational dataset (1973–2025; Menne et al. 2025, in collaboration with C3S 2025) and the ERA5 (1979–2025; Hersbach et al. 2020; Bell et al. 2021), MERRA-2 (1980–2025; Gelaro et al. 2017), and JRA-3Q (1970–2025; Kosaka et al. 2024) reanalysis products. While atmospheric reanalyses broadly capture the climatological characteristics of station-based wind observations and year-to-year variability, they generally underestimate the amplitude of observed anomalies and fail to fully reproduce their multidecadal variability and trends for continental-scale averages (Monerie et al. 2026); the exception is JRA-3Q, which shows the closest agreement with observations, although there are known issues in the assimilation in the mid-1990s (Ayaka Bunno, pers. communication). This underscores the importance of exercising caution when relying solely on (a single) reanalysis data for wind assessments. Despite these limitations, the representation of surface winds in reanalyses more closely match the station-based observations since the mid-1990s than before (Fig. 2.50b; e.g., Torralba et al. 2017; Wohland et al. 2019; Monerie et al. 2026).

Observed long-term trends in terrestrial wind speed over 1979–2025 reveal a broad hemispheric-scale deceleration, with Northern Hemisphere land regions declining at an overall rate of –0.041 m s^{-1} decade^{-1} (Table 2.10). Central Asia stands as the sole exception

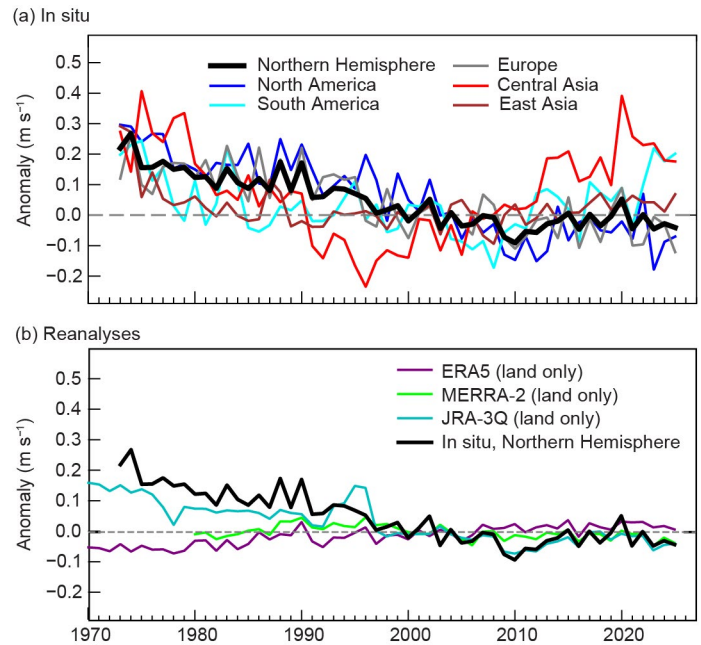

Fig. 2.50. Land surface Northern Hemisphere (20°N–70°N) and regional surface wind speed anomaly time series (m s^{-1}; 1991–2020 base period). Panel (a) shows the Global Historical Climatology Network hourly (GHCNh) observational dataset (1973–2025) across various regions, and (b) shows ERA5 (1970–2025; purple line), MERRA-2 (1980–2025; green), and JRA-3Q (1970–2025; blue) reanalyses for the globe, along with GHCNh (black) for the Northern Hemisphere.

Table 2.10. Northern Hemisphere (20°N–70°N) and regional statistics for land surface wind speed (m s^{-1}) using the observational Global Historical Climatology Network hourly (GHCNh) dataset for the period 1979–2025. Trend and confidence range from median of pairwise slopes method (Lanzante 1996; Sen 1968; Thiel 1950).

Region	Mean Wind Speed 1991–2020 (m s^{-1})	Wind Speed Anomaly 2025 (m s^{-1})	Wind Speed Trend 1979–2025 (m s^{-1} decade^{-1}) and 5th → 95th percentile confidence range	Number of Stations
Northern Hemisphere	3.390	–0.041	–0.041 (–0.050 → –0.033)	2891
North America	3.569	–0.070	–0.067 (–0.084 → –0.052)	940
Europe	3.521	–0.121	–0.052 (–0.069 → –0.037)	1223
Central Asia	2.742	+0.176	+0.045 (+0.009 → +0.083)	129
East Asia	2.877	+0.068	–0.006 (–0.002 → +0.015)	369
South America	3.748	+0.201	+0.014 (–0.007 → +0.032)	92

(+0.045 m s^{-1} decade^{-1}), while the magnitude of the decline varies substantially by region, ranging from −0.067 m s^{-1} decade^{-1} in North America to just −0.006 m s^{-1} decade^{-1} in East Asia. In contrast, available observations from South America recorded a weak positive trend of +0.014 m s^{-1} decade^{-1} (Zha et al. 2021). This north–south dipole in trend direction is partially reproduced by the ERA5 reanalysis (Fig. 2.51a), although discrepancies remain, particularly where Southern Hemisphere land observations are sparse.

Ocean wind speed anomalies in 2025 (relative to 1988–2025) displayed an opposite pattern compared to land surfaces. The Remote Sensing Systems (RSS) merged radiometers recorded a positive anomaly of +0.084 m s^{-1}, exceeding the value observed in 2024 (Fig. 2.52). In contrast, both scatterometer measurements (ASCAT; −0.028 m s^{-1}) and the ERA5 reanalysis (+0.006 m s^{-1}) remained near zero (see Fig. 2.52). Satellite wind datasets from RSS include the merged radiometers (Special Sensor Microwave/Imager series [SSM/I], Special Sensor Microwave Imager/Sounder series [SSMIS], Advanced Microwave Scanning Radiometer [AMSRE and AMSR2], TMI, WindSat, and GMI) and the QuickSCAT and ASCAT scatterometers (Wentz 1997, 2015; Wentz et al. 2007, 2024; Ricciardulli and Wentz 2015; Ricciardulli and Manaster 2021). The spatial distribution of ocean wind anomalies in 2025 (Plate 2.1z) reveals predominantly positive anomalies with distinct regional patterns. The tropical central Pacific showed a strong positive anomaly (~+1 m s^{-1}), consistent with La Niña conditions but weaker than in the La Niña of 2022. The tropical and midlatitude Atlantic also exhibited positive anomalies, reversing the strongly negative values of 2024, while the tropical Indian Ocean showed mostly weak negative anomalies. The Southern Ocean exhibited a strong positive anomaly. Regional patterns were generally consistent across RSS radiometers, ASCAT, and ERA5, although the reanalysis showed central Pacific anomalies approximately 20% higher, likely reflecting calibration changes in the TAO buoy network (section 2e3; Ricciardulli et al. 2025). Between 1988 and 2025, global ocean wind trends (60°S–60°N) remained small and not significant, with RSS and ERA5 both at +0.03 m s^{-1} decade^{-1} (Figs. 2.51a, 2.52). Positive trends continued in the central Pacific, likely linked to multiple La Niña years,

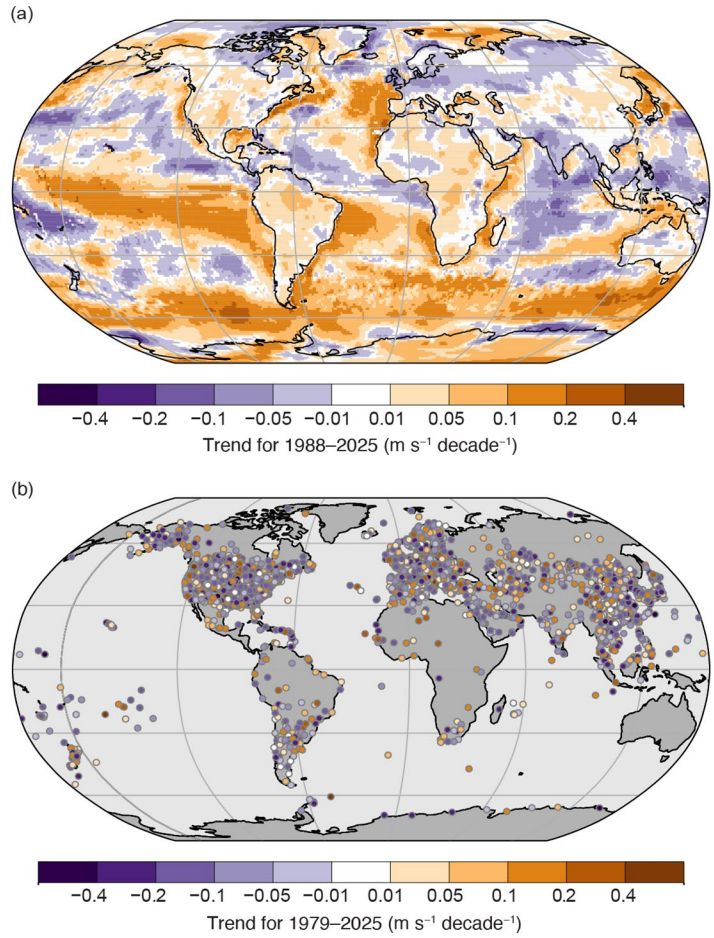

Fig. 2.51. Wind speed trends (m s^{-1} decade^{-1}) from the (a) ERA5 reanalysis output over land/ice and Remote Sensing Systems (RSS) satellite radiometers (Special Sensor Microwave/Imager [SSM/I], Special Sensor Microwave Imager/Sounder [SSMIS], Tropical Rainfall Measuring Mission Microwave Imager [TMI], AMSR2 [Advanced Microwave Scanning Radiometer 2], ASMR-E [Advanced Microwave Scanning Radiometer for the Earth Observing System], WindSat, and Global Precipitation Measurement Microwave Imager [GMI]) over ocean for the period 1988–2025 (shaded areas), and (b) observational Global Historical Climatology Network hourly (GHCNh) dataset over land (circles) for 1979–2025.

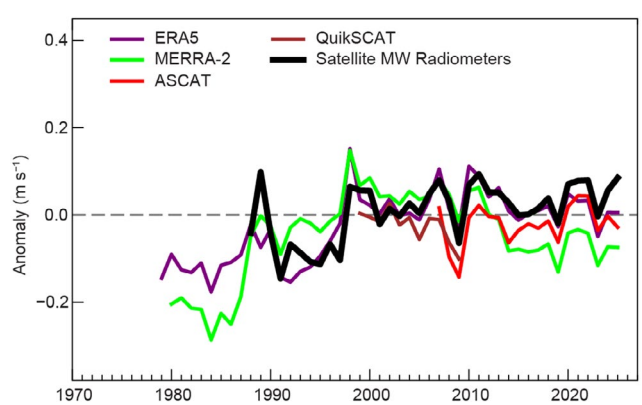

Fig. 2.52. Annual global mean wind speed anomalies (m s^{-1}; 1991–2020 base period) over the ocean from merged satellite radiometers, the Quick Scatterometer (QuickSCAT) and Advanced Scatterometer (ASCAT), and ERA5 and MERRA-2 reanalyses.

and strengthened over the Southern Ocean. ERA5 displayed stronger central Pacific trends but weaker signals elsewhere (Appendix Fig. A2.18).

The physical mechanisms driving surface wind variability remain only partly known. Decadal ocean–atmosphere oscillations are recognized as the primary driver of multidecadal variability, including the "stilling" and "reversal" phenomena (Zeng et al. 2019). Anthropogenic warming likely contributes to the observed interhemispheric asymmetry (e.g., Zha et al. 2021; Shen et al. 2022), with negative trends in the Northern Hemisphere and positive in the Southern Hemisphere, potentially through modifications to large-scale pressure gradients (Zha et al. 2021; Zhang et al. 2021; Deng et al. 2021). Additional factors such as land use changes (Vautard et al. 2010; Zhang et al. 2019; Minola et al. 2022), polar amplification (Deng et al. 2021), data encoding and processing inconsistencies (Dunn et al. 2022a; Zhang and Wang 2025), and systematic anemometer biases (Azorin-Molina et al. 2023; Liu et al. 2024) may further modulate the observed signal.

3. UPPER AIR WINDS

—L. Haimberger, M. Mayer, J. Danzer, R. Pilch-Kedzierski, A. Reiter, C. T. Sabeerali, O. P. Sreejith, P. Rohini, and V. Schenzinger

The global 100-hPa eastward wind time series in Fig. 2.53 compares the ERA5 (Hersbach et al. 2020), the Japanese Reanalysis for Three Quarters of a Century (JRA-3Q; Kosaka et al. 2024), and MERRA-2 (Gelaro et al. 2017) reanalyses together with a new global wind product derived from GPS-RO data (Danzer et al. 2024; Nimac et al. 2025). This metric is impacted by both tropical tropospheric phenomena, leading to the strong eastward anomalies during the 1997/98 and 2015/16 El Niños, and the 100-hPa level is reached by relatively many early upper air balloons. Yet those measurements appear not sufficient to constrain discrepancies between the ERA5 and JRA-3Q reanalyses prior to 1970, particularly in the Southern Hemisphere and the tropics. In the satellite era from 1979 onward, there is good agreement, except for some clearly higher values in MERRA-2 in the 1990s. The zonal wind time series, derived from highly accurate and temporally stable GPS-RO-derived geopotential height data using dynamical constraints (Danzer et al. 2024; Nimac et al. 2025; Unegg et al. 2026), also shows good agreement. While currently available only up to 2020, timely updates up to recent months can be expected later in 2026.

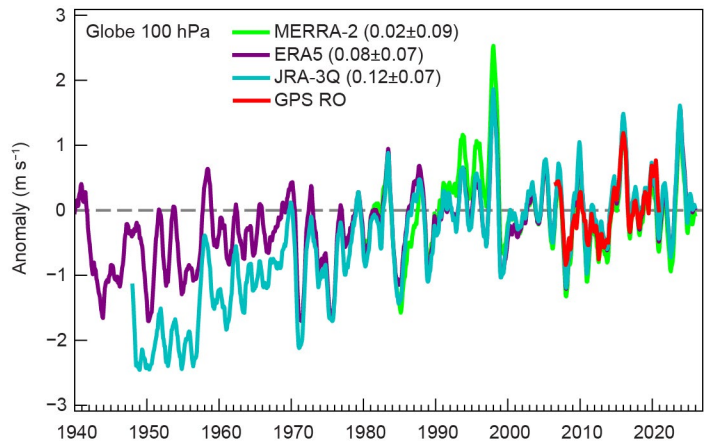

Fig. 2.53. Globally averaged 100-hPa eastward wind speed anomalies (m s^{-1}; 2006–20 base period) as depicted from three reanalyses: MERRA-2 (Gelaro et al. 2017), the Japanese Reanalysis for Three Quarters of a Century [JRA-3Q Kosaka et al. 2024]), and ERA5 (Hersbach et al. 2020). The GPS-RO derived winds are based on Danzer et al. (2024) and Unegg et al. (2026), using the Wegener Center OPSv5.6 record (Angerer et al. 2017).

At lower levels (850 hPa), there are considerable decadal (1980–2025) eastward wind trends across many regions (Figs. 2.54a–c), including easterly trends in the tropical Pacific (e.g., Seager et al. 2022; Lee et al. 2022; Mayer et al. 2025), but there are also discrepancies in trend patterns between products. Eastward wind trends over the Indian Ocean are relatively weak in ERA5 compared to MERRA-2 and JRA-3Q, and insignificant when taking the trend spread across the three reanalyses into account (Fig. 2.54d). The spread in wind trends in the tropical oceans across different reanalyses underscore the importance of a multi-product approach for diagnostic studies as well as the continuity of high quality and temporally consistent observational records to constrain reanalyses (e.g., Riccardiulli et al. 2025). In contrast, strengthening westerly trends in the Southern Ocean, a critical feature related to ocean heat uptake and redistribution (Trenberth et al. 2025), are similar across the three considered reanalyses, at least for the period considered here. Furthermore, nowhere are trends over land significant if reanalysis spread is considered (Fig. 2.54d).

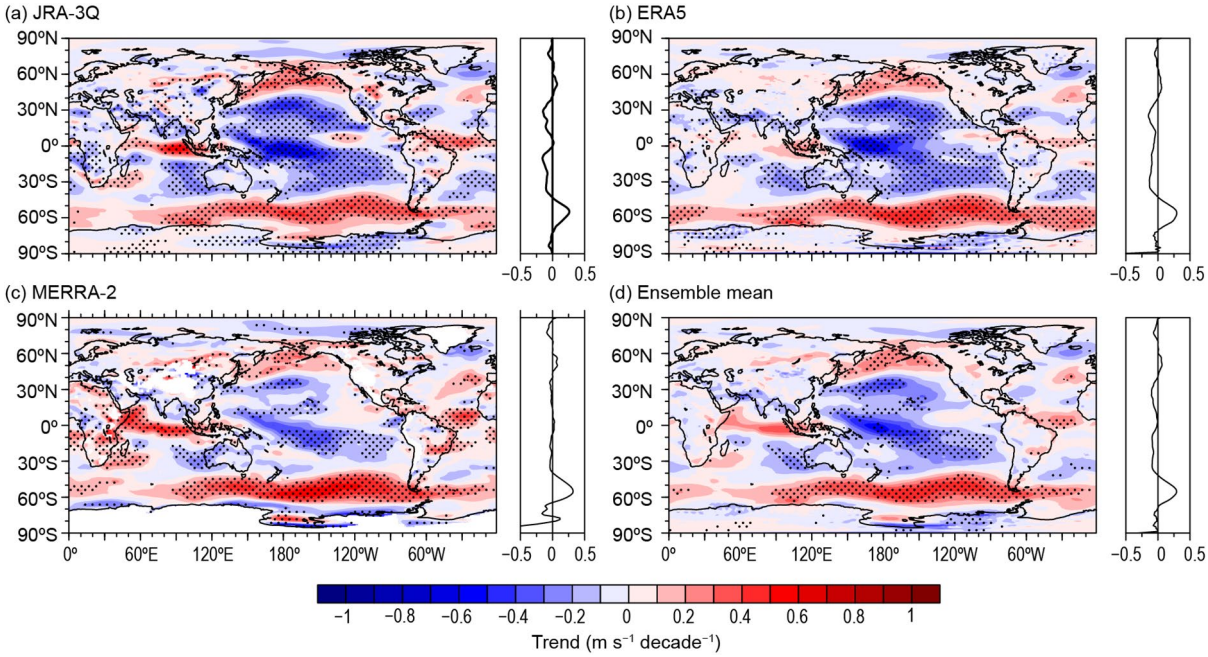

Fig. 2.54. 850-hPa eastward wind trends (m s^{-1} $decade^{-1}$) for the period 1980–2025 for (a) JRA-3Q, (b) ERA5, and (c) MERRA-2 reanalyses, and (d) the ensemble mean. Stippling in (a)–(c) indicates statistically significant trends at the 90% confidence level (based on standard error of regression taking temporal autocorrelation into account). Stippling in (d) additionally takes trend spread across the three reanalyses into account (by adding it in quadrature to standard error of regression, as in Mayer et al. 2022). Zonal averages are shown to the right of each map.

In the tropical stratosphere, 2025 was dominated by an easterly shear zone of the quasi-biennial oscillation (QBO), with a maximum amplitude of –35.50 m s^{-1} at 15 hPa in September, which is strong in the historical record. It descended at a rather slow rate of 0.22 km $month^{-1}$. Hence autumn and winter months saw easterly winds between 10 hPa and 50 hPa. At the same time, the newly formed Northern Hemisphere (NH) polar vortex was consistently weaker than normal through September and October, and in late November a rare minor sudden stratospheric warming (SSW) event was observed, which was only a couple of tenths of m s^{-1} shy of becoming the earliest major SSW on record. This can be seen as a manifestation of the Holton-Tan (Holton and Tan 1980) effect, a well-observed QBO teleconnection believed to be due to the influence of the QBO state on the propagation of planetary waves (Labitzke 1982; Anstey et al. 2022).

In the Southern Hemisphere (SH), the polar vortex westerlies remained slightly, but consistently, above average through June and July. A minor SSW event took place in early September, after which the vortex remained in a quite disrupted state until mid-October. Below-average westerlies remained until an early transition into summer circulation in early November. Weakened westerlies were also consistently present in the lower stratosphere (70 hPa) after September. This weaker SH vortex with a shorter lifespan is also typical for the E-QBO phase that had settled in the second half of the year. It is also consistent with the near-surface circulation anomalies reported in section 2e1.

The El Niño–Southern Oscillation (ENSO) was in a weak La Niña or neutral state during 2025, characterized by modestly negative Niño-3.4 SST anomalies (see section 4b for details), and consequently the associated upper-tropospheric wind anomalies were relatively weak. A marked region of anomalous subsidence in October–December (OND) 2025 over 10°S–10°N dominated the central to eastern equatorial Pacific (170°E–80°W; Fig. 2.55), extending

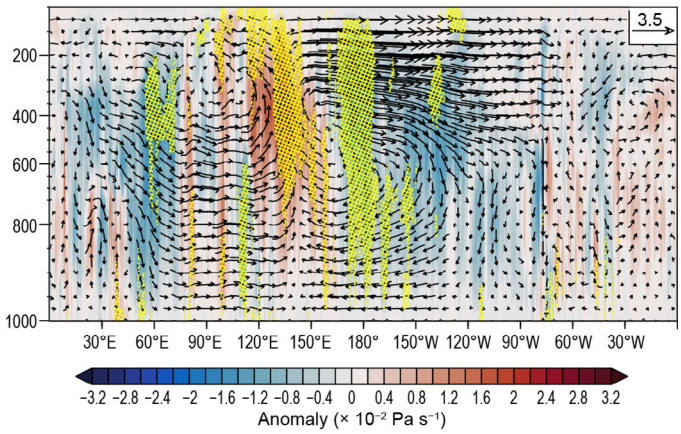

Fig. 2.55. Oct–Dec (OND) 2025 pressure vertical velocity anomalies (shaded; × 10^{-2} Pa s^{-1}) and u/w anomalies (arrows) averaged over the region 10°S–10°N (zonal [divergent + rotational] wind anomaly [u], m s^{-1}; pressure vertical velocity anomaly [w], × 10^{-2} Pa s^{-1}). Yellow hatched regions show vertical velocity anomalies stronger than 90% of the OND anomaly time series (1991–2025).

through much of the troposphere, consistent with a strengthened Walker circulation and a La Niña-like pattern. Low-level easterly and upper-level westerly anomalies further indicate enhanced zonal overturning. In contrast, strong ascent over the Indo-Pacific Warm Pool (110°E–150°E) suggests intensified convection, while subsidence over the western Indian Ocean indicates suppressed convective activity, together implying an east–west convective contrast across the Indian Ocean characteristic of a negative Indian Ocean dipole during OND 2025. Overall, the pattern reflects a mature La Niña-type atmospheric response.

The AAO, the NAO, and the AO indices (section 2e1) showed little imprint in the wind patterns in 2025.

4. LIGHTNING

—M. Füllekrug, E. Williams, C. Price, S. Goodman, R. Holzworth, K. Virts, R. Said, J. Lapierre, and E. DiGangi

The lightning anomalies in 2025 are generally characterized by an increase of lightning in North America, central South America, and parts of Oceania, in contrast with a decrease of lightning in Southeast Asia and central Africa when compared to the preceding reference decade of 2015–24. Lightning is an essential climate variable (ECV) that is often used as a proxy measure for some difficult-to-quantify meteorological parameters associated with deep convection. One specific example in relation to lightning variability in extreme and high impact weather is presented for Hurricane Melissa, a Category 5 tropical storm that made landfall in Jamaica on 28 October 2025 (see Sidebars 4.1 and 7.2 for details).

For climate studies of lightning, the occurrence of at least two lighting flashes within one hour and 15 km from a given location results in global binary maps of lightning reported by merging Earth Networks Total Lightning Network (ENTLN), Vaisala's Global Lightning Detection Network (GLD360), and the University of Washington's World-Wide Lightning Location Network (WWLLN; Fullekrug et al. 2024; DiGangi et al. 2022 and references therein). These global maps are accumulated over each month from 2015 to 2025 to effectively count the number of hours that lightning was present during that month. Monthly lightning anomalies are calculated in percent deviation from the decadal mean of the reference period (2015–24). A reference period of 10 years is chosen to average the lightning hours over two El Niño cycles and thereby reduce the influence of strong El Niño years. An extension of lightning climatologies to several decades requires merging data from different measurement systems into one quality-controlled lightning record, which is currently ongoing research.

Geographically, the largest negative anomalies are in Africa and Southeast Asia, whereas positive anomalies occur mainly in North America, central South America, and parts of Oceania (Plate 2.1aa). The monthly anomalies exhibit an annual variation ±30%–40%, with minima in February and maxima in July/August (Fig. 2.56; e.g., Christian et al. 2003). During Northern Hemisphere summer, maximum monthly global lightning anomalies occur about one to two months after the summer solstices, when lightning mainly occurs over the larger land masses in the Northern Hemisphere (~68% of Earth's land mass), whereas during Northern Hemisphere winter, minimum monthly global lightning anomalies occur about one to two months after the winter solstices when lightning mainly occurs over the smaller land masses in the Southern Hemisphere. The annual anomalies, calculated from the averages of the monthly anomalies, vary by ±5%–10%, and overall, the 2025 anomaly was close to zero (red star at 2025 in Fig. 2.56). The reduction of lightning in 2020 is attributed to

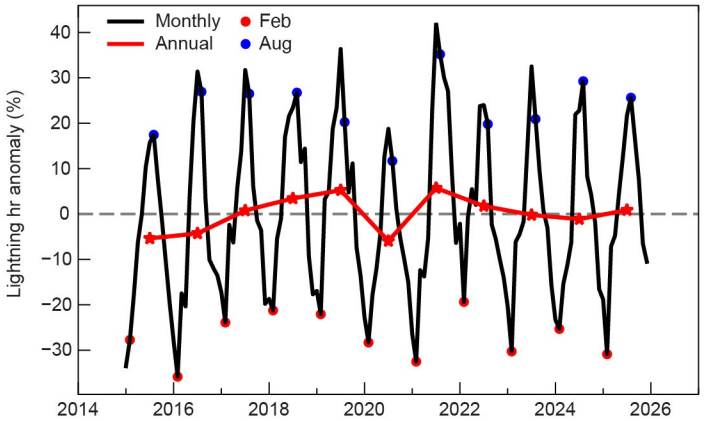

Fig. 2.56. Monthly (black line) and annual (red line with red stars) global lightning hour anomalies, measured in % with respect to the decadal year-round mean of 2015–24. The monthly anomalies are ±30%–40% with consistent minima in Feb (red dots) and consistent maxima around Aug (blue dots). Lightning is more common over land, so this variation reflects the larger land masses in the Northern Hemisphere. Annual anomalies vary within ±5%–10%.

diminished global aerosol induced by the COVID pandemic (Liu et al. 2025; Fig. SB2.1b in Füllekrug et al. 2022).

Although the reference period of one decade used here is relatively short when compared to other climate variables spanning three or more decades, the overall results are similar to those obtained from ~25 year-long synoptic lightning observations from low Earth orbit (Fullekrug et al. 2022, Fig. SB2.1b). The stability of the lightning record is expected to increase as more data are collected and ground- and space-based data sources are harmonized in future studies.

(i) Lightning during Hurricane Melissa

Hurricane Melissa was accompanied by abundant lightning, both in the eyewall convection and the rainbands (Fig. 2.57). Globally, Melissa was the strongest tropical cyclone in 2025 and was among the strongest Atlantic hurricanes ever recorded (see Sidebar 4.1). Tropical Storm Melissa formed in the Caribbean Sea on 21 October, gained Category 1 status on the 25th, intensified rapidly to Category 5 on the 27th, made landfall in Jamaica on the 28th, continued north over Cuba, and dissipated by 4 November in the western Atlantic Ocean (Fig. 2.57a). Melissa-related lightning strokes, which produce illuminated groups of pixels seen on satellite images, were recorded with the Geostationary Lightning Mapper (GLM) on board the NOAA GOES-19 geostationary satellite (Rudlosky and Virts 2021), and individual lightning strikes are reported by WWLLN (Holzworth et al. 2021). The temporal evolution of these lightning stroke densities inferred from optical measurements in space and from electromagnetic wave measurements on the ground agree well (Figs. 2.57b–d). Lightning stroke densities in the eyewall and the inner rain band, i.e., <100 km from the center, show a significant increase during the initial growth phase of Melissa and during its maximum intensity (Fig. 2.57b; Stevenson et al. 2014; Fierro et al. 2018), demonstrating that lightning can be a suitable aid in operational forecasting (Slocum et al. 2023). Lightning stroke densities 100 km–500 km from the center were lower and exhibited a quasi-diurnal variation with relative maxima during local nighttime (Fig. 2.57c; Wu et al. 2015). Lightning stroke densities 500 km–1000 km from the center were lower still, where the diurnal variation was still present in this area, but was somewhat less pronounced (Fig. 2.57d). The agreement between optical observations from space and electromagnetic wave measurements from the ground confirms that the diurnal variation represents nocturnal deep convection over the ocean.

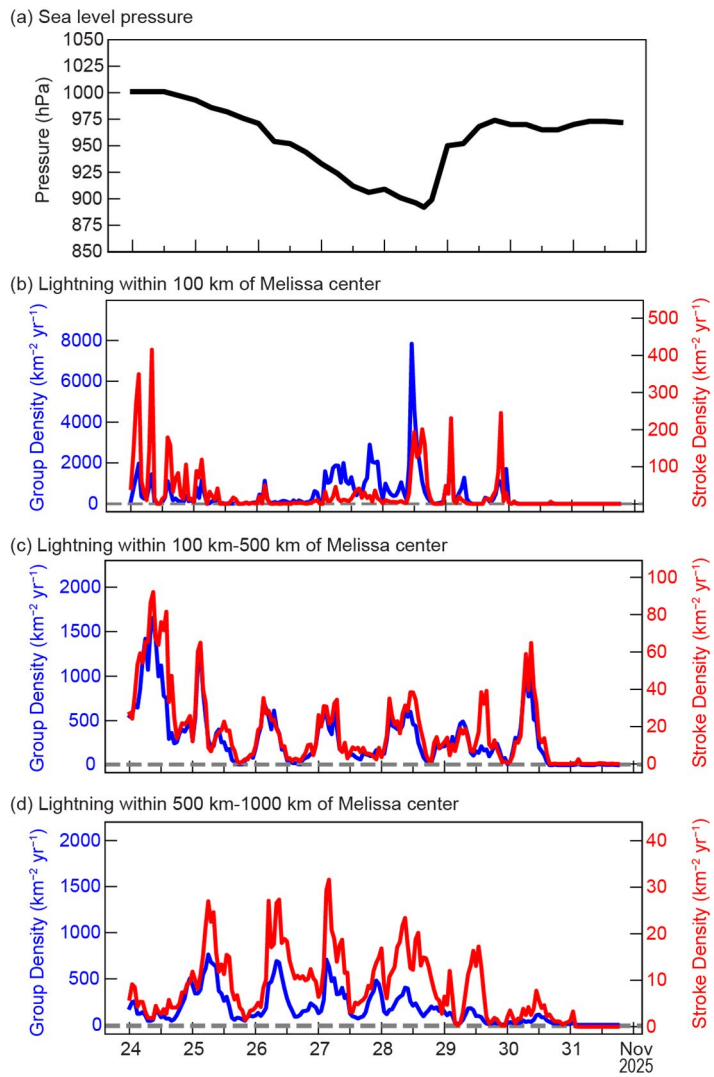

Fig. 2.57. Hurricane Melissa is associated with an abundance of lightning. Time series shown for (a) sea level pressure (hPa) in Melissa's eye with minimum (892 hPa) reached on 28 Oct at landfall over Jamaica. (b)–(d) Lightning group, and equivalent stroke densities are observed by the Geostationary Lightning Mapper (GLM) and the University of Washington's World-Wide Lightning Location Network (WWLLN; measured in group density [left axis] and stroke density [km^{-2} yr^{-1}; right axis]), (b) within the eyewall and inner rainband (<100 km from the center), (c) 100 km–500 km from the center, and (d) 500 km–1000 km from the center.

f. Earth radiation budget

1. EARTH RADIATION BUDGET AT TOP-OF-ATMOSPHERE

—P. W. Stackhouse Jr., P. Sawaengphokhai, K.-M. Xu, and N. G. Loeb

The Earth radiation budget (ERB) at top-of-atmosphere (TOA) represents the balance between incoming total solar irradiance (TSI) and outgoing radiation, which consists of reflected shortwave (RSW) and emitted (outgoing) longwave radiation (OLR). This balance is fundamental to understanding Earth's climate system and global temperature variations. Over the past two decades, observations show a growing net positive imbalance—more energy entering the system than leaving it—indicating an energy surplus within the Earth–atmosphere system (Loeb et al. 2021, 2022; von Schuckmann et al. 2023). This positive imbalance persisted in 2025 with a global annual mean anomaly of +0.70 W m^{-2} relative to the 2001–20 climatology.

An analysis of Clouds and the Earth's Radiant Energy System (CERES) TOA ERB measurements (Table 2.11) shows that, relative to 2024, the global annual-mean net TOA flux increased by 0.65 W m^{-2} in 2025. This year-over-year increase was driven primarily by a reduction in RSW (–0.45 W m^{-2}), implying decreased planetary albedo (see section 2h1). A smaller but reinforcing contribution came from a modest decrease in OLR (–0.25 W m^{-2}), indicating reduced heat loss to space, while TSI remained effectively unchanged. Relative to the 2001–20 climatology, 2025 exhibited substantial anomalies in OLR (+1.00 W m^{-2}), RSW (–1.45 W m^{-2}), and absorbed solar radiation (ASR; +1.70 W m^{-2}), resulting in a net TOA flux anomaly of +0.70 W m^{-2}. These departures from climatology are substantially larger than the 2024–2025 year-over-year changes and exceed their respective 2σ interannual anomaly ranges in the modern CERES record, except for the net TOA flux.

Regional flux differences between 2024 and 2025 reveal that the global-mean changes arise from coherent adjustments in tropical circulation accompanying the transition from El Niño toward weak La Niña conditions (see section 4b for details). As shown in Fig. 2.58a, OLR

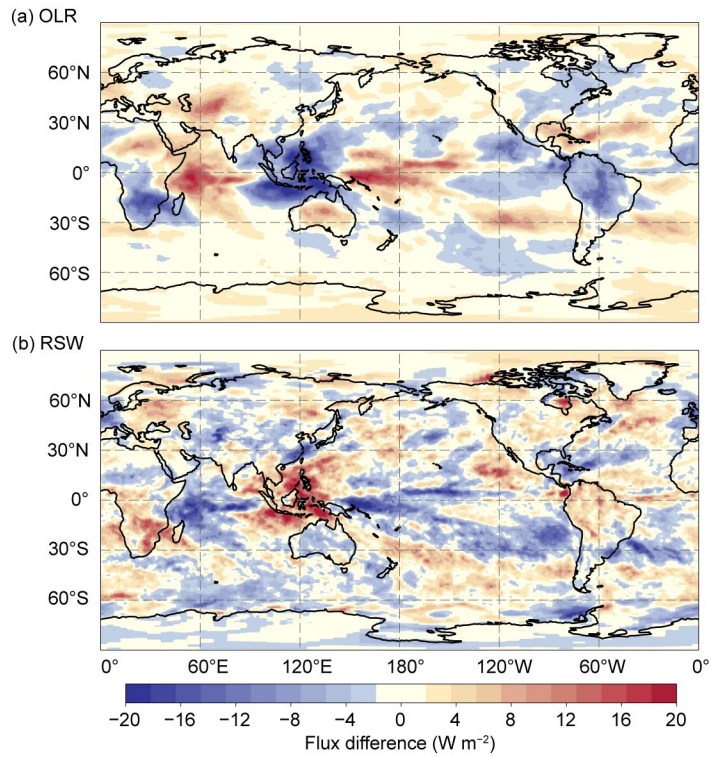

Fig. 2.58. Annual average top-of-atmosphere flux differences (W m^{-2}) between 2024 and 2025 for (a) outgoing longwave radiation (OLR) and (b) reflected shortwave radiation (RSW). The annual mean maps for 2024 and 2025 were derived using the Clouds and the Earth's Radiant Energy System (CERES) EBAF (Energy Balanced and Filled) Ed4.2.1.

Table 2.11. Global annual mean top-of-atmosphere (TOA) radiative flux changes between 2024 and 2025, the 2025 global annual mean radiative flux anomalies relative to their corresponding 2001–20 mean climatological values, the mean 2001–20 climatological values, and the 2-sigma interannual variabilities of the 2001–20 global annual mean fluxes (all units in W m^{-2}) for the outgoing longwave radiation (OLR), total solar irradiance (TSI), reflected shortwave (RSW), absorbed solar radiation (ASR, determined from TSI – RSW), and total net fluxes (Net). All flux values have been rounded to the nearest 0.05 W m^{-2} and only balance to that level of significance.

Global	One Year Change (2025 minus 2024) (W m^{-2})	2025 Anomaly (Relative to 2001–20) (W m^{-2})	Climatological Mean (2001–20) (W m^{-2})	Interannual Variability (2001–20) (W m^{-2})
OLR	–0.25	+1.00	240.35	±0.65
TSI	–0.05	+0.25	340.15	±0.15
RSW	–0.45	–1.45	99.05	±0.95
ASR	+0.40	+1.70	241.10	±0.90
Net	+0.65	+0.70	0.75	±0.80

decreases are evident across portions of the Maritime Continent and western Pacific, southern Africa, and Amazonia, while increases occurred over parts of the central equatorial Pacific, the southeast Pacific subtropics, and the tropical western Indian Ocean. Weaker but discernible responses extended into the extratropics. These patterns are consistent with a redistribution of large-scale convective organization across the tropics associated with the El Niño–Southern Oscillation (ENSO) evolution, rather than spatially uniform, temperature-driven emission changes (Trenberth et al. 2002). Interestingly, the resumption of convection in the Maritime Continent region corresponds to a precipitation anomaly in that region (section 2d5). However, the OLR change over South America is indicative of a recovery of the severe drought of 2024, restoring rainfall closer to its climatological values. Reductions in RSW were spatially widespread across tropical ocean basins, particularly within convective regions of the Indo-Pacific (Fig. 2.58b). Features that appear more pronounced in RSW than in the OLR field include a westward displacement of the South Pacific Convergence Zone and strengthening/weakening of the stratocumulus decks off the coasts of North and South America. The RSW patterns point to systematic cloud radiative adjustments linked to circulation changes rather than isolated or purely local cloud thinning/thickening and associated cloud radiative effects (section 2d7). They also highlight the importance of regional variability of cloud regimes in shaping the shortwave component of the ERB.

The time series of global monthly-mean TOA OLR anomalies from 2000 through 2025 (Fig. 2.59) indicates that the pronounced variability associated with the 2023/24 El Niño diminished somewhat in 2025. However, anomalies remained positive but systematically dropped throughout the year relative to the climatological baseline. Global monthly mean ASR anomalies recovered from a large decrease early in the year, ending at a peak positive anomaly. Thus, 2025 continued to exhibit the gradual upward tendency seen over the past decade, reflecting sustained reductions in annual averaged RSW radiation. The 2025 ASR anomaly remained elevated relative to the early-2000s baseline and lies within the upper range established during recent peak years, indicating that enhanced solar absorption persisted despite the moderation of El Niño-related variability. Net TOA anomalies exhibit pronounced interannual variability, with excursions approaching +2 W m^{-2} and a well-documented trend of about 0.48±0.16 W m^{-2} (Loeb et al. 2024). The +0.65 W m^{-2} year-over-year increase in net TOA flux reflects interannual variability superimposed on the longer-term positive imbalance evident in the CERES record.

TSI is taken from the Community-Consensus TSI Composite (Dudok de Wit et al. 2017). TOA, RSW, and OLR are derived from CERES datasets. Data from March 2000 through December 2025 use the CERES EBAF (Energy Balanced and Filled) Ed4.2.1 product (Loeb et al. 2009, 2012, 2018), based on measurements from CERES instruments aboard Terra, Aqua, and NOAA-20 spacecraft (Wielicki et al. 1996, 1998).

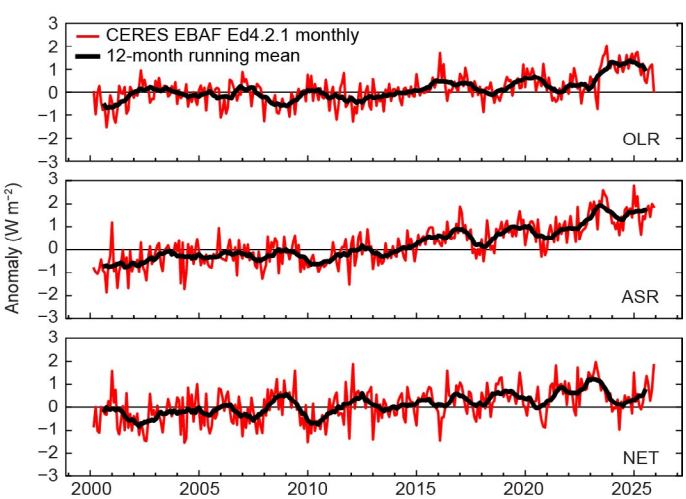

Fig. 2.59. Time series of global monthly mean deseasonalized anomalies (W m^{-2}) of top-of-atmosphere Earth radiation budget (red lines) for (top) outgoing longwave radiation (OLR), (middle) absorbed solar radiation (ASR, determined from total solar irradiance [TSI] minus reflected shortwave [RSW]), and (bottom) total net (TSI–RSW–OLR) from Mar 2000 to Dec 2025. Anomalies are relative to their calendar month climatology (2001–20) and a 12-month running mean is plotted for illustration (black line). Time series are from the Clouds and the Earth's Radiant Energy (CERES) Energy Balanced and Filled (EBAF) Ed4.2.1 1-Deg data (Mar 2000–Dec 2025) in solid red line. (Source: CERES EBAF tool at https://ceres-tool.larc.nasa.gov/ord-tool/jsp/EBAFTOA421Selection.jsp.)

2. MAUNA LOA APPARENT TRANSMISSION RECORD UPDATE FOR 2025

—L. Soldo, J. A. Augustine, E. Asher, D. T. Kuniyuki, J.-P. Vernier, and L. D. Riihimaki

The NOAA observatory near the summit of the Mauna Loa volcano (MLO) on Hawaii's Big Island (19.536°N, 155.576°W) is well positioned to measure atmospheric transmission with

minimal contamination from external influences. Its high elevation (3397 m a.s.l.), combined with its low-atmospheric moisture, minimal tropospheric aerosols, and predominantly cloud-free weather, makes atmospheric transmission estimates there a good proxy for the level of stratospheric aerosols and their impact on incoming solar radiation. Apparent daily transmission is calculated from morning pyrheliometer measurements using a unique method devised by Ellis and Pueschel (1971). Monthly averages of the apparent transmission at Mauna Loa have been compiled since 1958.

The updated time series through 2025 is shown in Fig. 2.60. An interesting feature in recent years is the period of relatively low transmission that began in 2018 and has continued through 2025. This extended period of decreased transmission, or overabundance of stratospheric aerosols, was caused by successive volcanic and wildfire events (Khaykin et al. 2026). The Global Space-based Stratospheric Aerosol Climatology (GloSSAC) compilation of several sensors (Kovilakam et al. 2020) through August 2025 shown in Khaykin et al. (2026) indicates that the remnants of the 2022 Hunga and 2024 Ruang eruptions account for most of that trend. Model calculations by Dutton et al. (1985) indicate that the water vapor excess in the stratosphere from Hunga as of 2025, about half of the 146 Tg originally injected in 2022 (section 2g7), accounts for 0.001 of the transmission diminution in 2025.

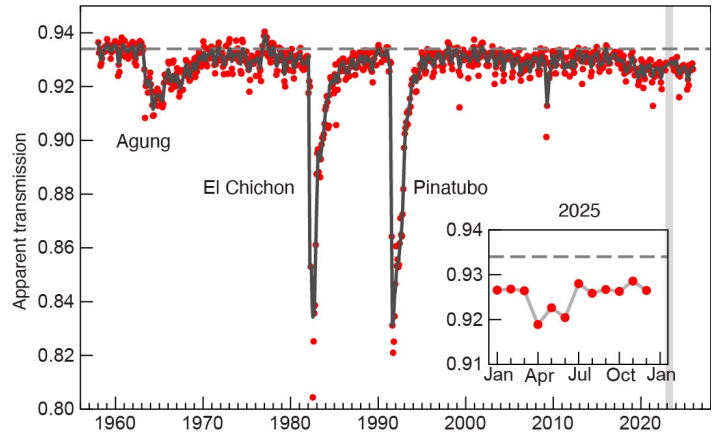

Fig. 2.60. Apparent transmission at Mauna Loa, Hawaii, from 1958 through 2025. Red dots are monthly averages of morning transmission, and the gray curve is a locally weighted scatterplot smoothing (LOWESS) fit with a six-month smoother applied. Inset shows monthly averages for 2025. Gray horizontal dashed lines represent the average transmission of the clean period before the eruption of Agung that resulted from nearly 20 years of insignificant explosive volcano activity. The vertical shaded area represents the period from Dec 2022 through Jun 2023 when the station was down due to the eruption of Mauna Loa in late Nov 2022.

The average transmission and monthly variability for 2025 was 0.9253 (±0.003), well below that of the "clean period" (0.934) from 1958 to 1964 (Ammann et al. 2003; Sato et al. 1993). Discounting the effects of three major explosive eruptions shown, the transmission from 1964 to 2017 hovers around ~0.93. The inset of Fig. 2.60 shows a transmission of ~0.927 (±0.004 uncertainty) from January through March 2025, followed by a marked decrease in April, a slight recovery in May, and another minimum in June. After June, the transmission stabilized to levels observed in the first few months of the year.

Minima in April and May are likely due to the perennial passage of Asian dust, which is almost always detected in the time series (Bodhaine et al. 1981; Augustine et al. 2025). Supporting this, balloon-borne aerosol profiles over Hilo, Hawaii, suggest elevated aerosol extinction in the upper troposphere in April 2025. From February to June, balloon-borne measurements show tropospheric enhancements in aerosol extinction below 6-km altitude. Monthly aerosol optical depth (AOD) from NASA's Moderate Resolution Imaging Spectroradiometer (https://earthobservatory.nasa.gov/global-maps/MODAL2_M_AER_OD) shows relatively high AOD over Hawaii in March, April, and May, after which AOD over the central Pacific fell dramatically, leaving unclear an explanation of the low transmission in June.

However, balloon measurements indicate that the ongoing eruption of Kilauea in Hawaii likely contributed to observed transmission minima in 2025, with effects persisting from February through June. This period also featured high-volume fountaining, particularly in June, which accounted for 6 of the 27 eruptive episodes in 2025. These were especially intense during 20–24 June. On 11 June, an eight-hour episode produced 305-m lava fountains and plumes of thick black smoke that were well documented by measurements and an eyewitness, who noted the smoke tracking toward MLO, 34 km to the west-northwest. Signals from a Portable Optical Particle Spectrometer (POPS; Gao et al. 2016) aboard a balloon sonde at Hilo, Hawaii (~60 km east of MLO), on 12 June show high aerosol concentration of probable volcanic origin between 15 km and 17 km a.s.l. While a 10-day back trajectory shows the air at that level came from Vanuatu

(5660 km to the southwest), no volcanic activity was occurring there. Conversely, isentropic back trajectories from MLO, modeled for the level near the top of the observed lava fountains and at 5000 m a.s.l., track to the southeast near Kilauea, making its plumes a probable contributor to the June transmission minimum.

According to the Smithsonian Institution's annual compilation of volcanoes (https://volcano.si.edu/faq/index.cfm?question=eruptionsbyyear), 2025 was moderately active with regard to volcano number and intensity. No eruption exceeded a Volcanic Explosivity Index of two (Newhall and Self 1982). Explosive eruptions of note in 2025 were Etna (Italy) on 2 June, Ruang (Indonesia) on 25 June, and Hayli Gubbi (Ethiopia) on 23 November. However, none of these reached the stratosphere, and trajectory analyses indicate their plumes did not track near Hawaii.

g. Atmospheric composition

1. LONG-LIVED GREENHOUSE GASES

—X. Lan, G. Dutton, and I. Vimont

In 2025 the atmospheric burdens of the three most important long-lived greenhouse gases (LLGHGs), carbon dioxide (CO_2), methane (CH_4), and nitrous oxide (N_2O), continued their increases and reached new records. The global average CO_2 level at the earth's surface in 2025—as derived from remote marine boundary layer measurements made by NOAA's Global Monitoring Laboratory—reached 425.6±0.1 ppm (parts per million by moles in dry air) (Fig. 2.61a; Table 2.12; uncertainties are reported as one sigma in this section), a 53% increase from the pre-industrial level of ~278 ppm (Etheridge et al. 1996). Global average CH_4 and N_2O levels reached 1935.7±0.6 ppb (parts per billion by moles in dry air) and 338.9±0.1 ppb in 2025, respectively.

Carbon dioxide is the most abundant anthropogenic LLGHG and the dominant greenhouse gas driving global climate change (IPCC 2013; Forster et al. 2025). Its rate of increase in the atmosphere from 2023 to 2024 reached 3.4 ppm, a record high since modern measurements began in late 1950s. While the rate of increase from 2024 to 2025 moderated slightly at 2.9 ppm, it remains substantially higher than the average increase during 2011–20. Increasing emissions of CO_2 from fossil fuels have driven a roughly monotonic increase in the long-term CO_2 trend, with the average rate increasing from 0.6±0.1 ppm yr^{-1} in the early 1960s to 2.4 ppm yr^{-1} during 2011–20 (Lan et al. 2026a). Fossil fuel emissions, including cement production, increased from 3.0±0.2 Pg C yr^{-1} in the 1960s to 9.8±0.5 Pg C yr^{-1} in the past decade (2015–24; Friedlingstein et al. 2026). Fossil fuel emissions in 2025 are estimated to be a record high of 10.3±0.5 Pg C yr^{-1} (Friedlingstein et al. 2026). The high CO_2 increase in 2023–25 is also associated with a strong El Niño in 2023/24 and record-high global temperatures. The El Niño–Southern Oscillation (ENSO), which changes regional temperature and precipitation patterns, influences photosynthetic CO_2 uptake, respiratory release, and fires. It is the main driver of CO_2 interannual variability (std. dev. = 0.4 ppm in 2015–24) above the long-term monotonic increase (Keeling and Revelle 1985; Betts et al. 2016). In 2023–25 the El Niño weather pattern likely contributed to a large fire-carbon emission and reduced terrestrial CO_2 uptake, accelerating the atmospheric CO_2 increase. In 2025, as El Niño conditions ended, the atmospheric CO_2 growth became more moderate.

Atmospheric CH_4 is the second most important LLGHG, and in 2025 its globally averaged abundance at Earth's surface reached 1935.7±0.6 ppb (Lan et al. 2026b), about 266% of its pre-industrial level of 729±9 ppb (Mitchell et al. 2013). Global CH_4 rose rapidly during the 1980s at an average rate of 11.5±1.4 ppb yr^{-1}, driven by rapid increase in fossil fuel CH_4 emissions (Nisbet et al. 2023), but this CH_4 increase flattened to near zero (0.7±3.0 ppb yr^{-1}) between 1999 and 2006 when CH_4 emitted to the atmosphere equaled the amount being removed by chemical reactions. Atmospheric CH_4 growth restarted in 2007 and has accelerated since 2014, with further acceleration in 2020–22 leading to an increase of 14.8±2.0 ppb yr^{-1}, a record-high average rate since modern measurement record started in 1980s (Fig. 2.61b). Atmospheric CH_4 increased by 6.3±0.4 ppb from 2024 to 2025, slightly less than the 8.0±0.4 ppb increase from 2023 to 2024.

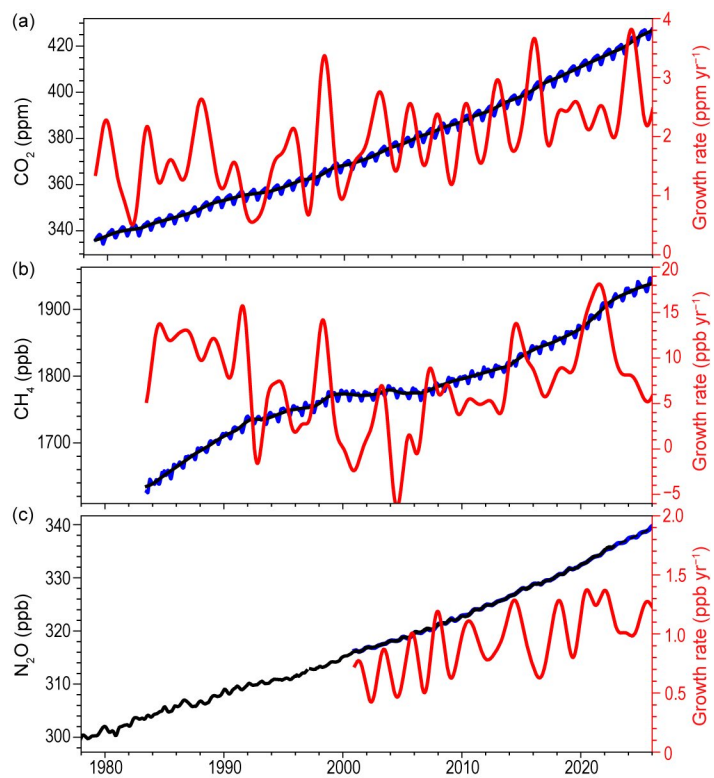

Fig. 2.61. Global mean dry-air remote surface mole fractions (approximately weekly data in blue and deseasonalized trend in black (see Dlugokencky et al. 1994 for methods); left axis) and instantaneous growth rate (red; right axis) of (a) CO_2, (b) CH_4, and (c) N_2O derived from marine boundary layer measurements from the NOAA Global Monitoring Laboratory's Global Greenhouse Gases Reference Network (Lan et al. 2024). N_2O data prior to 2000 are insufficient and noisy, hindering the calculation of a growth rate.

Emissions of CH_4 to the atmosphere are from both anthropogenic (such as fossil fuel exploitation, livestock, waste and landfills, and rice cultivation) and natural sources (such as wetlands and shallow lakes). The reduction in atmospheric δ13C-CH_4 (defined by the ratio of stable carbon isotopes in CH_4) from 2008 to 2023 (Michel et al. 2024) indicates increased emissions from microbial sources (Basu et al. 2022), including emissions from livestock as well as natural wetlands and lakes, which have more negative δ13C-CH_4 signatures. Small increases in fossil fuel emissions may also play a role in the post-2006 global CH_4 increase (Lan et al. 2019; Oh et al. 2023). The contribution of the hydroxyl radical, the main removal for CH_4, is still uncertain. However, it is less likely to be a major factor in the long-term increase since 2007 (Zhao et al. 2019; Lan et al. 2021; Morgenstern et al. 2025), while its influence on recent CH_4 interannual variabilities can be more prominent (Ciais et al. 2026; Peng et al. 2022). Recent studies suggest a dominant role of increased tropical wetland emissions in the 2020–22 CH_4 surge (Feng et al. 2022; Peng et al. 2022; Lin et al. 2024) coinciding with a three-year La Niña that provided wet conditions over the tropics. Sustained increases in wetland CH_4 emissions may be an indication of an emerging carbon climate feedback (Nisbet et al. 2023; Zhang et al. 2023).

Nitrous oxide (N_2O) is a potent greenhouse gas with an atmospheric lifetime of 120 years (Tian et al. 2024). Atmospheric N_2O abundance shows a long-term increase with significant accelerations in the past decade. The average global atmospheric abundance of N_2O in 2025 was 338.9±0.1 ppb (Lan et al. 2026b), a 26% increase over its pre-industrial level of 270 ppb (Rubino et al. 2019). The source of atmospheric N_2O are microbes that rely on nitrogen from natural and agricultural soils, animal manure, and the oceans (Davidson 2009). Increased agricultural emissions related to fertilizer usage are the major source of its long-term increase (Tian et al. 2023). The average rate of increase reached 1.3±0.1 ppb yr^{-1} from 2020 to 2022 (Fig. 2.61c), larger than the average rate between 2010 and 2019 (1.0±0.2 ppb yr^{-1}), strongly suggesting increased emissions (Tian et al. 2023). Atmospheric N_2O continued its large annual increase in 2024/25 at 1.2±0.1 ppb.

The impacts of LLGHGs on global climate can be estimated using their effective radiative forcing (ERF), the change of radiative energy caused by added LLGHGs to the atmosphere, following the approach used in the Intergovernmental Panel on Climate Change's Sixth Assessment Report (Forster et al. 2021). Increased atmospheric abundances of LLGHGs are largely responsible for increasing global temperatures (Forster et al. 2025; IPCC 2013). Since the industrial era (1750), increasing atmospheric CO_2 has accounted for 64% of the increase in ERF by LLGHGs, reaching 2.37 W m^{-2} in 2025 (Fig. 2.62). The increase in CH_4 contributed a 0.57 W m^{-2} increase in ERF, while CH_4-related production of tropospheric ozone and stratospheric water vapor contributes to ~0.30 W m^{-2} of indirect radiative forcing (Myhre et al. 2014). The increase in atmospheric N_2O abundance contributed to a 0.23 W m^{-2} increase in ERF between 1750 and 2025. The atmospheric abundances and the ERF of other industrial gases reduced substantially in the 1990s due to the implementation of the Montreal Protocol.

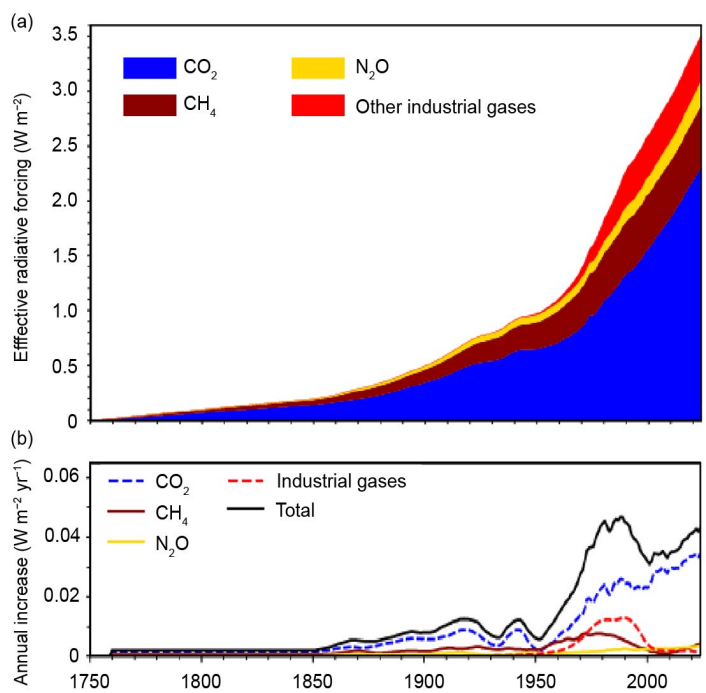

Fig. 2.62. (a) Effective radiative forcing (W m^{-2}) due to long-lived greenhouse gases (LLGHGs; see Table 2.12 for details on industrial gases). (b) Annual increase in effective radiative forcing (W m^{-2} yr^{-1}) smoothed by 10-year running averages.

Table 2.12. Summary table of long-lived greenhouse gases for 2025 (CO_2 mixing ratios are in ppm, N_2O and CH_4 in ppb, and all others in ppt).

Compound Class	Industrial Designation or Common Name	Chemical Formula	ERF[a]	Effective Rad. Efficiency ($W\ m^{-2}\ ppb^{-1}$)[b]	Effective Rad. Forcing[a] (ERF or SARF) ($W\ m^{-2}$)	Mean Surface Mole Fraction 2025, [Change from Prior Year][c]	Lifetime (yrs)[b]
Acidic Oxide	Carbon Dioxide	CO_2	Y	1.33×10^{-5}	2.37	425.6 [2.9]	—
Alkane	Methane	CH_4	Y	3.88×10^{-4}	0.57	1935.7 [6.3]	9.1
Nitride	Nitrous Oxide	N_2O	Y	3.20×10^{-3}	0.23	338.9 [1.2]	123
Chlorofluorocarbons	CFC-11	CCl_3F	N(Y)[e]	0.26	0.057 (0.064)	211.7 [–2.8][d]	52
Chlorofluorocarbons	CFC-12	CCl_2F_2	N(Y)[e]	0.32	0.156 (0.174)	477.0 [–4.5][d]	102
Chlorofluorocarbons	CFC-113	CCl_2FCClF_2	N	0.30	0.020	65.7 [–0.6][f]	93
Hydrochlorofluorocarbons	HCFC-22	$CHClF_2$	N	0.21	0.052	242.2 [–2.8]	11.9
Hydrochlorofluorocarbons	HCFC-141b	CH_3CCl_2F	N	0.16	0.004	24.3 [–0.1]	9.4
Hydrochlorofluorocarbons	HCFC-142b	CH_3CClF_2	N	0.19	0.004	20.4 [–0.3]	18
Hydrofluorocarbons	HFC-134a	CH_2FCF_3	N	0.17	0.021	138.7 [4.9]	14
Hydrofluorocarbons	HFC-152a	CH_3CHF_2	N	0.10	<0.001	7.95 [0.2]	1.6
Hydrofluorocarbons	HFC-143a	CH_3CF_3	N	0.17	0.005	34.3 [1.8]	51
Hydrofluorocarbons	HFC-125	CHF_2CF_3	N	0.23	0.009	51.4 [4.0]	30
Hydrofluorocarbons	HFC-32	CH_2F_2	N	0.11	0.002	43.3 [5.1]	5.4
Hydrofluorocarbons	HFC-23	CHF_3	N	0.18	0.007	38.7 [0.9]	228
Hydrofluorocarbons	HFC-365mfc	$CH_3CF_2CH_2CF_3$	N	0.22	<0.001	0.96 [–0.1]	8.9
Hydrofluorocarbons	HFC-227ea	CF_3CHFCF_3	N	0.26	<0.001	2.58 [0.2]	36
Chlorocarbons	Methyl Chloroform	CH_3CCl_3	N	0.07	<0.001	0.77 [–0.1]	5.0
Chlorocarbons	Carbon Tetrachloride	CCl_4	N	0.17	0.013	72.0 [–1.1] [d]	32
Chlorocarbons	Methyl Chloride	CH_3Cl	N	0.01	<0.001	554.0 [4.3]	0.9
Bromocarbons	Methyl Bromide	CH_3Br	N	0.004	<0.001	6.57 [0.06]	0.8
Bromocarbons	Halon 1211	$CBrClF_2$	N	0.29	0.001	2.65 [–0.10]	16
Bromocarbons	Halon 1301	$CBrF_3$	N	0.30	0.001	3.33 [0.0]	72
Bromocarbons	Halon 2402	$CBrF_2CBrF_2$	N	0.31	<0.001	0.382 [–0.008]	28
Fully Fluorinated Species	Sulfur Hexafluoride	SF_6	N	0.57	0.007	12.2 [0.4]	>600
Fully Fluorinated Species	PFC-14	CF_4	N	0.09	0.005	91.3 [0.9]	~50,000
Fully Fluorinated Species	PFC-116	C_2F_6	N	0.25	0.001	5.42 [0.09]	~10,000
Fully Fluorinated Species	PFC-218	C_3F_8	N	0.28	<0.001	0.796 [0.010]	~2600
Fully Fluorinated Species	PFC-318	$c\text{-}C_4F_8$	N	0.32	<0.001	2.28 [0.09]	~3200

[a] Effective radiative forcing (ERF) calculated by multiplying the stratospheric-temperature adjusted radiative efficiency (SARF) by the global mole fraction (in ppb) and then applying a tropospheric adjustment factor for the species indicated based on recommended values from chapters 6 and 7 in the IPCC AR6 WGI Report. The Radiative Forcing column is either ERF (where indicated) or SARF. The adjustments to the SARF are CO_2: 5%±5%, CH_4: –14%±15%, N_2O: 7%±13%–16%.

[b] Radiative efficiencies and lifetimes were taken from Appendix A in WMO (2018) and Hodnebrog et al. (2020a), except for SF6 lifetime from Ray et al. (2017) and CH_4 lifetime from Prather et al. (2012). For CO_2, numerous removal processes complicate the derivation of a global lifetime. AGGI = Annual Greenhouse Gas Index. For radiative forcing, see https://www.esrl.noaa.gov/gmd/aggi/aggi.html.

[c] Mole fractions are global, annual, and midyear surface means determined from the NOAA cooperative global air sampling network (Hofmann et al. 2006), except for PFC-14, PFC-116, PFC-218, PFC-318, and HFC-23, which were measured by AGAGE (Mühle et al. 2010; Miller et al. 2010, Prinn et al. 2018, Prinn et al. 2025). Changes indicated in brackets are the differences between the 2025 and 2024 means, the relevant quantities for calculating radiative forcing. These changes are somewhat different from the 2025 annual increases reported in section 2g1, which are determined as the difference between 1 Jan 2024 and 1 Jan 2025. All values are preliminary and subject to minor updates.

[d] Global mean estimates derived from multiple NOAA measurement programs ("Combined Dataset").

[e] ERF calculated values for CFC-11 and CFC-12 are highly uncertain but recommended by the IPCC AR6 WGI Report. Thus, they are included in parentheses here as the lower confidence value. The adjustment to the SARF for these values is 12%±13% (Hodnebrog et al. [2020b]).

[f] Values provided for CFC-113 do not include biases related to co-elution of CFC-113a, unlike in past years.

2. OZONE-DEPLETING GASES

—I. J. Vimont, S. A. Montzka, G. Dutton, J. Mühle, M. Crotwell, K. Petersen, S. Clingan, and D. Nance

Ozone depleting substances (ODSs) and their replacements have been controlled internationally through the Montreal Protocol on Substances that Deplete the Ozone Layer and subsequent amendments (hereinafter referred to as The Protocol) since 1987. The initial motivation for The Protocol was to limit, and eventually reverse, the damage to the stratospheric ozone layer caused by many industrial chemicals. Simultaneously, The Protocol reduced the impact of these same species on the global radiation budget. The Protocol and its subsequent amendments in the 1990s placed controls on the production for dispersive end uses of long-lived chlorine- and bromine-containing gases that deplete ozone, such as chlorofluorocarbons (CFCs), carbon tetrachloride (CCl_4), methyl chloride (CH_3Cl), methyl bromide (CH_3Br), methyl chloroform (CH_3CCl_3), halons, and the first generation of CFC replacement chemicals, the hydrochlorofluorocarbons (HCFCs). While the HCFCs have lower ozone depletion potentials (ODPs) than their predecessors, they nonetheless pose a threat to the recovery of the stratospheric ozone layer. In addition to their ability to deplete stratospheric ozone, many ODSs are also powerful greenhouse gases (GHGs). In response to the phase-down and eventual phase-out of HCFCs for end use, hydrofluorocarbons (HFCs) were developed and put into use as they do not chemically affect ozone. However, similar to their ozone depleting precursors, many HFCs are exceptionally strong GHGs, and in 2016 the Kigali Amendment to The Protocol was adopted. The Kigali amendment initiated the phase-down of 18 HFCs for dispersive end uses, although HFC-23 has additional constraints. The intention of this amendment was not to protect the ozone layer, but to limit the HFC impact on Earth's climate.

The global phase-out of CFC production for dispersive end use was completed in 2010. Since that time, with the exception of CFC-11 (Montzka et al. 2018; Rigby et al. 2019) and CCl_4 (SPARC 2016), most CFCs and other controlled chemicals have steadily decreased in the atmosphere at rates generally consistent with their respective lifetimes and emissions from preexisting reservoirs, or banks, like insulating foams and equipment produced prior to the final phase-out. As has been reported in previous *State of the Climate* reports, atmospheric concentrations of CFC-11 continued declining at an expected rate after a brief period in the 2010s, but by 2015 the rate of decrease slowed due to increased emissions from apparent violations of The Protocol that subsequently diminished (Montzka et al. 2021; Park et al. 2021). It is important to note that the Protocol places carefully defined controls on ODSs, but production for some uses remains exempt from control. The main exemptions include production for feedstock or intermediary use in the synthesis of other compounds and polymers, such as the HFCs, hydrofluoroolefins (HFOs) and polytetrafluoroethylene (PTFE). Hypothetically, exempted production was thought to result in minimal emissions. Recent studies have suggested that exempt production can result in substantially larger emissions and may explain the increasing concentrations and emissions of CFC-13, CFC-112a, CFC-113a, CFC-114a, and CFC-115 derived for recent years from atmospheric measurements (Western et al. 2023). Recently, a new technique to separate the isomers CFC-113 (Fig. 2.63) and CFC-113a

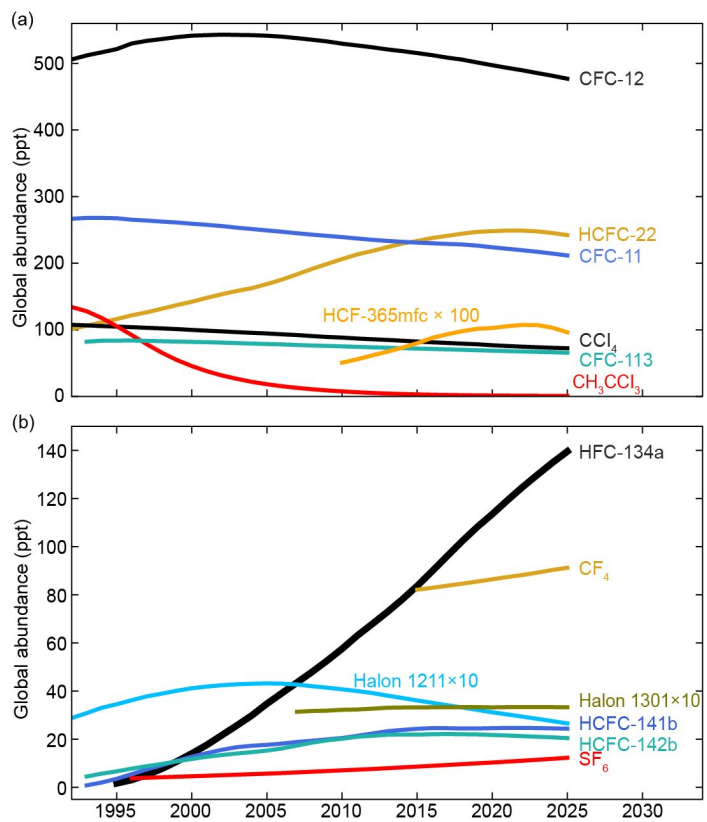

Fig. 2.63. Global mean abundances (mole fractions) at Earth's surface (ppt = pmol mol^{-1} in dry air) for several halogenated gases, many of which deplete stratospheric ozone. See Table 2.12 for the 2025 global mean mole fractions of these and other gases.

(not shown) has been developed, and a new record of global CFC-113a is available for the first time (Montzka 2025). This minor CFC is currently increasing rapidly in the atmosphere (Fig. 2.63).

Global mean mole fractions of HCFC-22 and HCFC-142b have continued to decline since 2024, and HCFC-141b has remained relatively stable (Fig. 2.63). These are the three most abundant HCFCs in the atmosphere, and their combined abundance peaked in 2021 and has been declining since (Western et al. 2024). The mole fractions of the most abundant HFCs, including HFC-134a (Fig. 2.63) and HFC-32, HFC-125, and HFC-23 (not shown), have continued to increase significantly in the atmosphere, in spite of the Kigali Amendment controls (Fig. 2.63). One less abundant HFC, HFC-365mfc, began declining around 2023 (Fig. 2.63). There is increasing interest in the emission of HFC-23 due to its extremely high global warming potential (GWP) and its emission as a byproduct in the production of HCFC-22, which in turn is used as a feedstock in the creation of PTFE (UNEP 2024).

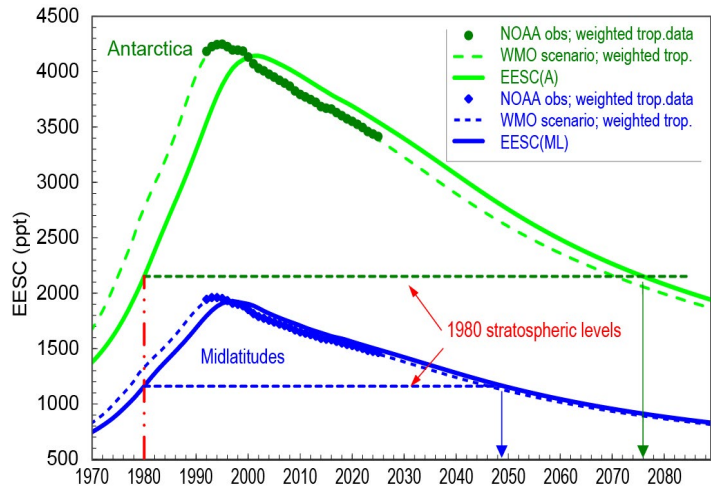

Fig. 2.64. Equivalent effective stratospheric chlorine (EESC; ppt) calculated for air representative of the Antarctic (green) and midlatitude (blue) stratosphere (EESC[A] and EESC[ML], respectively). Dashed lines represent tropospheric measurement-derived scenarios, based on past measurements and full adherence to all controls from The Protocol based on the World Meteorological Organization (WMO)/United Nations Environment Programme 2018 Ozone Assessment. Solid blue and green arrows indicate currently predicted dates for the return of EESC to 1980s levels in midlatitudes (year 2048) and over the Antarctic (year 2076), respectively. Solid lines depict inferred stratospheric changes based on the measured tropospheric curves.

Ground-based measurements provide information about the halogen loading in the troposphere, which differs from the amount of halogen available for reacting with ozone in the stratosphere. Therefore, equivalent effective stratospheric chlorine (EESC) is examined, which uses atmospheric transport and chemical reactivity in combination with global surface measurements, to estimate stratospheric halogen loading (Daniel et al. 1995; Newman et al. 2007). EESC provides a measure of total reactive stratospheric halogen in ppt. To put the EESC in the context of ozone layer recovery, NOAA's Ozone Depleting Gas Index (ODGI) is used (Hofmann and Montzka 2009; https://gml.noaa.gov/odgi/). The ODGI tracks the progress of reductions in the stratospheric abundance of ozone-depleting halogen. An ODGI value of 0 represents 1980 levels of EESC, while an ODGI of 100 represents peak, or maximum, EESC levels. We report two different regions for EESC, and therefore ODGI: one at midlatitudes and one for Antarctica (i.e., where the ozone hole forms). The ODGI reached 100 in 1996/97 for the midlatitudes and 2001/02 in the Antarctic. In 2025, EESC was 1498 ppt in the mid-latitudes and 3556 ppt in the Antarctic, with ODGI being 43.6 and 70.2, respectively, which translates to 56% and 30% recovery of the ozone layer back to 1980 values (Fig. 2.64).

3. TROPOSPHERIC AEROSOLS

—S. Rémy, N. Bellouin, M. Parrington, M. Ades, E. Di Tomaso, P. Weiss, and E. Russo

Aerosols represent a serious public health issue in many countries, and hence are subject to monitoring and forecasting as part of air quality policies. They also significantly impact continental and maritime ecosystems and play an important role in the climate system by scattering and absorbing radiation, and by affecting the life cycle, optical properties, and precipitation activity of clouds (IPCC AR6, chapter 6; Szopa et al. 2021).

The Copernicus Atmosphere Monitoring Service (CAMS; https://atmosphere.copernicus.eu) runs near-real-time (NRT) global analyses and forecasts of aerosols and trace gases. CAMS also produces a reanalysis of global aerosols and trace gases that covers the years 2003–25, the CAMS reanalysis (CAMSRA; Inness et al. 2019), by combining state of the art numerical modeling

and aerosol remote sensing retrievals from the Moderate Resolution Imaging Spectroradiometer (MODIS; Levy et al. 2013) and the Advanced Along Track Scanning Radiometer (AATSR; Popp et al. 2016). This section uses data exclusively from the CAMS reanalysis, focusing on aerosol optical depth at 550 nm, in the middle of the visible spectrum and comparable to many remote sensing products, and surface PM2.5 concentrations, as broad measure of the air quality and optical impact of aerosols. Other factors that impact the radiative impact of aerosols, such as the composition and number concentration, are not discussed in this section.

AOD at 550 nm and PM2.5 in 2025 (Figs. 2.65a,b) show maxima over the polluted regions of India and China, as well as from dust over the Sahara and the Middle East. High values also arise from seasonal vegetation fires in equatorial Africa and Indonesia, and occasional extreme fires, most notably across large parts of high-latitude North America (Alaska and central Canada) and eastern Siberia. Figure 2.65c shows the time series of monthly and yearly globally averaged total AOD during 2003–25. For all years, there is a strong seasonality in AOD, driven mainly by dust episodes between March and July in the Sahara, Middle East, and Taklimakan/Gobi desert regions, and seasonal biomass burning in tropical regions of Africa, South America, and Indonesia. Globally averaged AOD in 2025 was the lowest of the time series, which started in 2003.

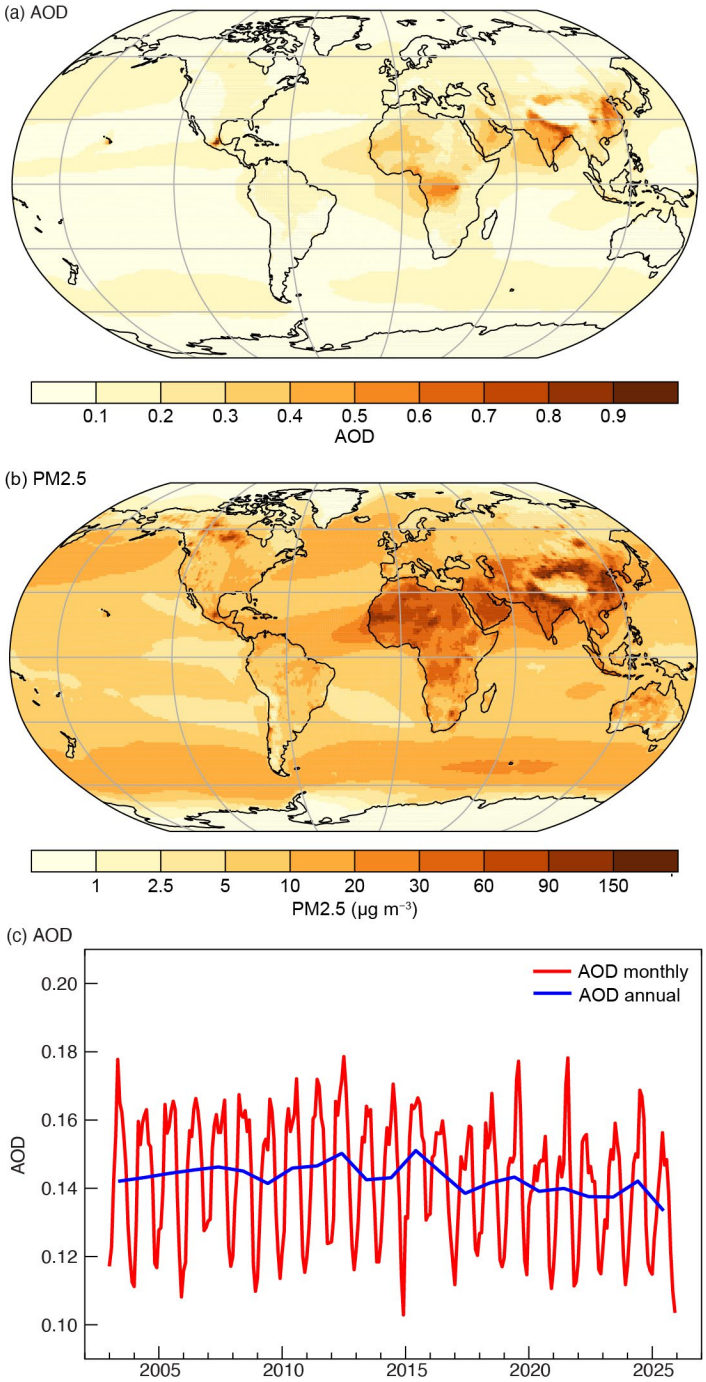

Fig. 2.65. (a) Global aerosol optical depth (AOD) at 550 nm in 2025. (b) Global surface particulate matter (PM2.5) concentrations (μg m^{-3}) in 2025. (c) Global average of total AOD at 550 nm averaged over monthly (red) and annual (blue) periods for 2003–25.

The AOD at 550 nm and PM2.5 anomalies (Plates 2.1ab,ac) are dominated by negative values, particularly for AOD. Positive anomalies of AOD and PM2.5 occurred over parts of Canada and equatorial Africa from biomass burning aerosols, and over India and Iran from mostly anthropogenic sources. Elsewhere, the fires in 2025 were less active than average, except for northwest Iberia and eastern Siberia. Desert dust emissions were also lower in 2025 than usual over the eastern Sahara and most of the Middle East. The negative anomalies of AOD and PM2.5 over East Asia, Europe, and the Amazon basin (positive anomalies over India and Iran) can be explained by ongoing decreasing (increasing) long-term trends in these regions and by the exceptional drought in Iran in 2025. In terms of exceptional events as measured by the number of days with AOD above the 99.9th percentile (Plates 2.1ad,ae), the very large fires that occurred in late spring and summer 2025 over Canada are prominent, with also extreme AOD values over parts of the North Atlantic

from the transport of the fire plumes, as well as over most of India, with high values from anthropogenic emissions.

Trends in the AOD at 550 nm and PM2.5 from 2003–25 and 2012–25 are shown in Figs. 2.66a–d, respectively. The trends in AOD and PM2.5 are generally collocated, although discrepancies can occur, particularly for regions mainly affected by fires and desert dust. Between 2003 and 2025, there is a significant negative trend over most of United States, Europe, East Asia, and the eastern Sahara. The first three can be attributed to a decrease in anthropogenic emissions while the last is caused mainly by a decrease of desert dust emissions over the region. Positive trends are noted over India and Iran, driven by an increase in anthropogenic emissions for India (Soulié et al. 2024). Between 2012 and 2025, the picture is slightly different: the small decreasing trend over parts of the Amazon basin between 2003 and 2025 disappears in the 2012–25 trend, showing that most of the decrease took place before 2012. The 2012–25 negative trend over Europe and the eastern United States is smaller than the 2003–25 trend, while over East Asia this is the reverse, which is consistent with the observed decrease of most of anthropogenic emissions that started there since around 2012 (Quaas et al. 2022). Interestingly, the positive trend in AOD over Iran and the Indian subcontinent is not matched by a corresponding positive trend in PM2.5, which could be a data assimilation artifact.

Anthropogenic AOD and radiative forcing resulting from aerosol–radiation (RFari) and aerosol–cloud interactions (RFaci) are shown in Fig. 2.67 for 2025 and the period 2003–25. The corresponding aerosol radiative forcing was weak in 2025.

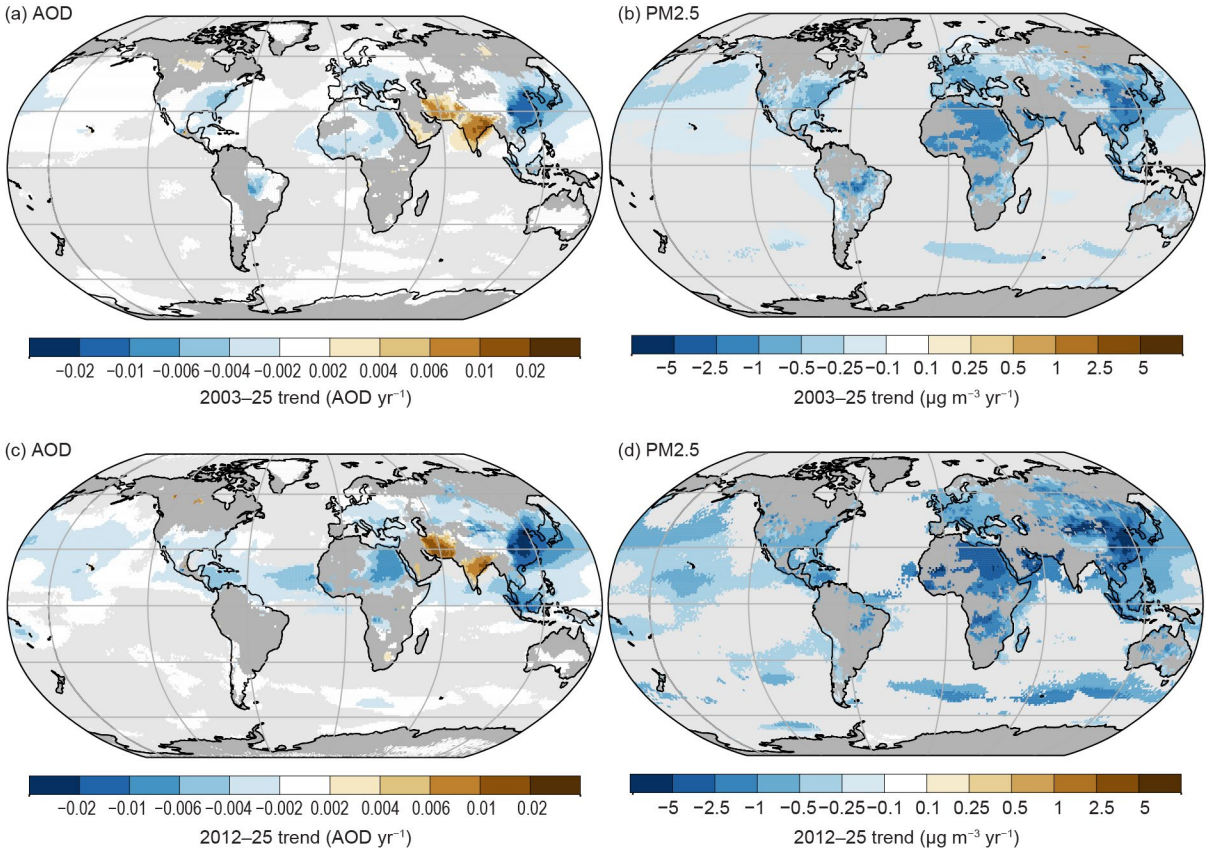

Fig. 2.66. (a),(b) Linear trends of total aerosol optical depth (AOD yr^{-1}) and particulate matter (PM2.5; μg m^{-3} yr^{-1}) for the period 2003–25. (c),(d) as in (a),(b) but for the period 2012–25. Only trends that are statistically significant (95% confidence level) are shown.

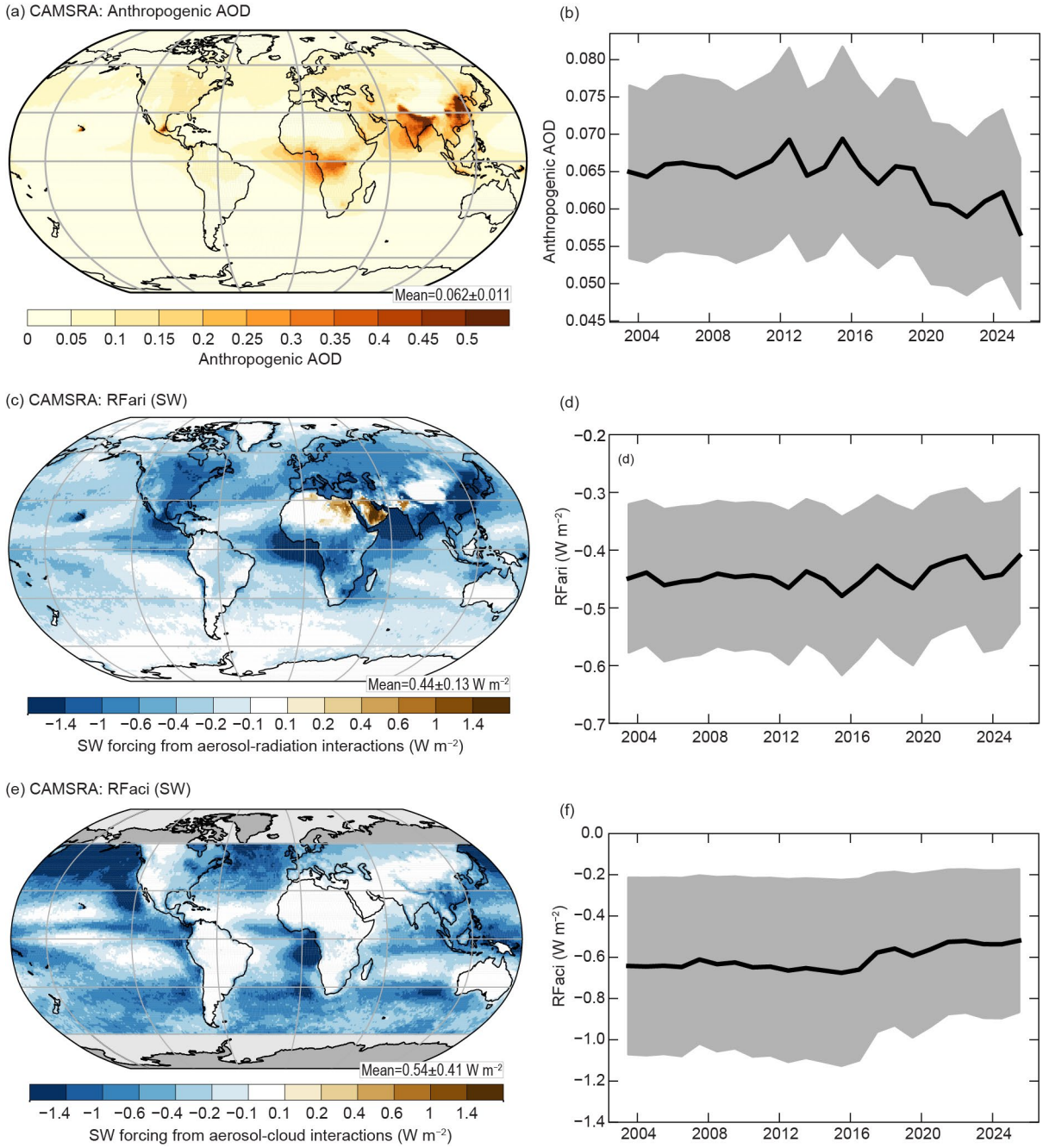

Fig. 2.67. The Copernicus Atmosphere Monitoring Service reanalysis (CAMSRA) (a) 2025 average of anthropogenic aerosol optical depth (AOD); (b) global annual average of anthropogenic AOD for the period 2003–25. Radiative forcing in the shortwave (SW) spectrum due to (c),(d) aerosol-radiation (RFari) and (e),(f) aerosol-cloud interactions (RFaci). The left column shows the distributions for the year 2025. The right column shows time series of global averages for the period 2003–25, with the 1-σ uncertainties of these estimates shown in gray.

4. TROPOSPHERIC OZONE

—O. R. Cooper, J. R. Ziemke, K.-L. Chang, P. Effertz, S. Kondragunta, K. Yang, Z. Wei, S. Kalluri, K. W. Bowman, J. L. Laughner, and V. H. Payne

Tropospheric ozone is a direct short-lived climate forcer (Szopa et al. 2021; Forster et al. 2025) with a global distribution that varies regionally, vertically, and on seasonal and interannual time scales, posing a challenge for accurate trend detection (Fiore et al. 2022; Chang et al. 2024). The present-day tropospheric ozone burden is approximately 40% greater than in pre-industrial times (Archibald et al. 2020), due to photochemical production from anthropogenic emissions of ozone precursor gases, classified as either direct (methane [CH_4]) or indirect (nitrogen dioxide [NO_2], non-methane volatile organic compounds [NMVOCs], and carbon monoxide [CO]) short-lived climate forcers (IPCC 2021). Several ozone precursors can be monitored from

space, as presented in last year's *State of the Climate* report (Cooper et al. 2025a). To track global changes in key ozone precursors, this edition of *State of the Climate* provides updates on the global distributions of tropospheric column NO_2, as detected by the Ozone Mapping and Profiler Suite (OMPS), onboard three NOAA operational polar-orbiting satellites (Yang 2017; Huang X. et al. 2022), and free tropospheric mixing ratios of acyl peroxynitrates (PANs), as retrieved from the Cross-Track Infrared Sounder (CrIS), onboard the same satellites as OMPS (Bowman 2021).

Since 2013, *State of the Climate* has provided annual updates on the tropospheric ozone burden, based on the Ozone Monitoring Instrument and the Microwave Limb Sounder onboard the Aura satellite (OMI/MLS) (Ziemke et al. 2019; Cooper et al. 2025b). Figure 2.68a shows OMI/MLS annual mean tropospheric column ozone for 2025, with large-scale features similar to previous years (Gaudel et al. 2018). The greater tropospheric ozone burden in the Northern Hemisphere is due to stronger anthropogenic emissions than in the Southern Hemisphere (SH; Griffiths et al. 2021), and the enhancement above the South Atlantic Ocean is largely due to biomass burning emissions (Bourgeois et al. 2021). The OMI/MLS product provides a continuous record of the tropospheric ozone burden (60°S–60°N) from 2004 to 2025, indicating an increase of approximately 9% over the past two decades (Fig. 2.69), with slightly stronger trends in the tropics (30°S–30°N) than midlatitudes. The largest region with positive trends stretches from northern Africa in the tropics and subtropics to East Asia in the midlatitudes (Fig. 2.68b); this is also the region with the strongest positive ozone anomalies in 2025 (Plate 2.1af). The positive

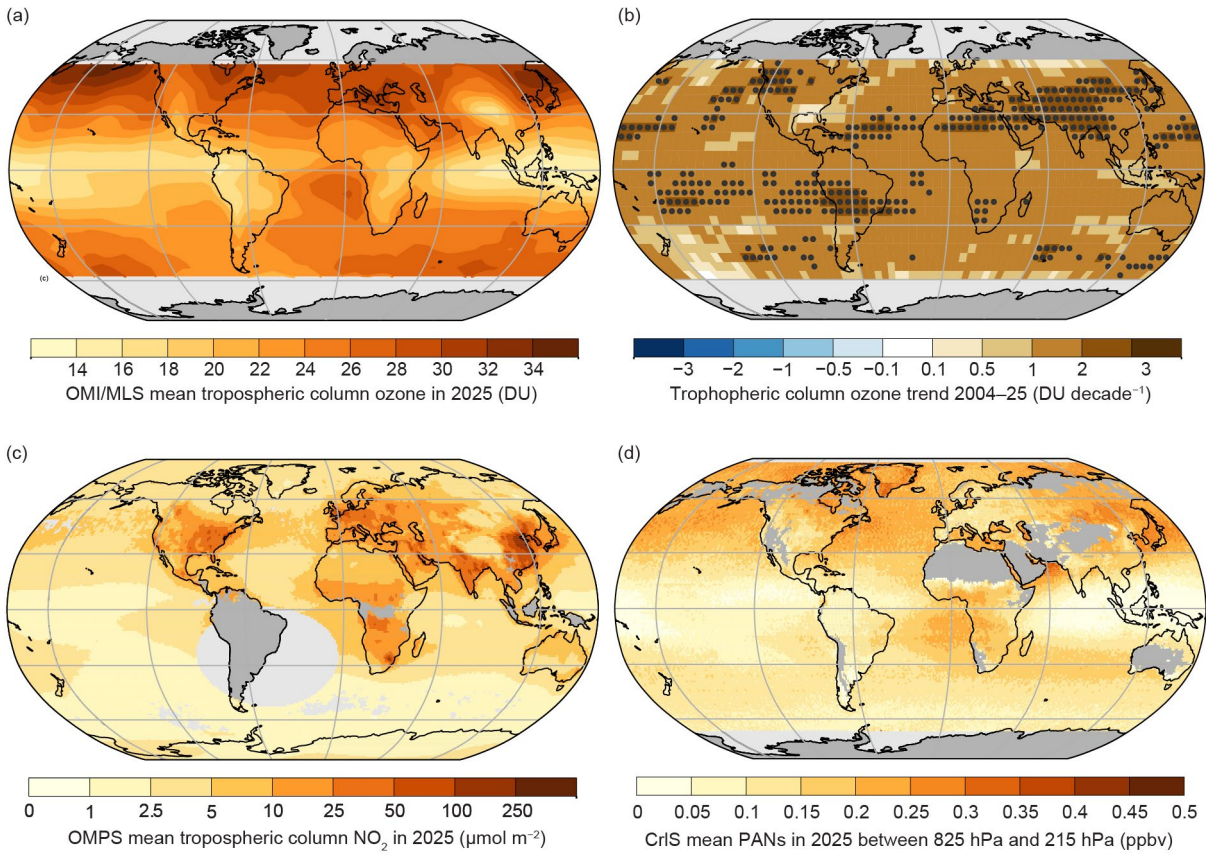

Fig. 2.68. (a) Ozone Monitoring Instrument (OMI)/Microwave Limb Sounder (MLS) tropospheric column ozone averaged over 2025 (5° × 5°; DU). (b) Linear trends in OMI/MLS tropospheric column ozone from Oct 2004 through Dec 2025 (DU decade^{-1}). Circles denote trends with p-values <0.05. Trends were calculated using a multivariate linear regression model (Randel and Cobb 1994) that includes a seasonal cycle fit and the Niño-3.4 index as an El Niño–Southern Oscillation proxy; trend uncertainties include an autoregressive adjustment (Weatherhead et al. 1998). (c) Ozone Mapping and Profiler Suite (OMPS) tropospheric column nitrogen dioxide (NO_2) averaged over 2025 (0.25° × 0.25°; μmol m^{-2}); gray areas indicate regions with low data availability, and portions of South America and the South Atlantic are omitted due to instrument interference caused by the South Atlantic Anomaly (Finlay et al. 2020). (d) Cross-Track Infrared Sounder (CrIS) peroxyacetal nitrates (PANs) averaged over 2025 (1° × 1°; ppbv). The product is most sensitive for the atmospheric layer between 825 hPa and 215 hPa. Gray indicates areas with no data. Areas north of 60°S are classified as "bare soil and rocks" or "open shrubland" by an International Geosphere–Biosphere Programme (IGBP) land cover map; such areas were removed due to likely interference in those regions. The area south of 60°S was not included in the retrieval domain.

OMI/MLS ozone trend has been more or less continuous since 2004, although it shows a period of no increase during 2020–22 in the Northern Hemisphere and in the midlatitudes of the Southern Hemisphere (Fig. 2.69). The product does not show an ozone decrease in 2020–23 as reported by several other satellite ozone products, generally attributed to emissions reductions during the COVID-19 pandemic (Miyazaki et al. 2021; Ziemke et al. 2022, 2025; Boynard et al. 2025; Pimlott et al. 2025). An ongoing synthesis analysis of multiple satellite ozone products conducted by the second phase of the Troposphere Ozone Assessment Report is expected to reconcile the differences among satellite products in the 2020–22 post-COVID period, and those findings will be summarized in next year's *State of the Climate* report.

Regions with intense fossil fuel and biomass burning emissions release high levels of nitric oxide (NO), which can be rapidly converted to NO_2. The sum of NO and NO_2 is referred to as NO_x, and satellite-detected NO_2 is a good indicator of NO_x emissions regions. The OMPS tropospheric column NO_2 product (Fig. 2.68c), shows that the strongest NO_x emissions are found in the Northern Hemisphere, especially in eastern North America, Europe, the Middle East, South Asia, and East Asia. In the Southern Hemisphere, strong emissions occur in industrialized regions of South Africa and across regions of southern Africa with frequent biomass burning. Strong NO_x emissions also occur above the populated regions of South America (Crippa et al. 2024), but these regions cannot be monitored by OMPS due to interference from the geomagnetic South Atlantic Anomaly (Finlay et al. 2020). The NO_2 anomalies in 2025 (Plate 2.1ag) generally reflect known long-term trends of NO_x emissions (Elshorbany et al. 2024; Huber et al. 2026), with decreases across North America, Western Europe, northern China, South Korea, and Japan, and increases across the Middle East and India. The positive 2025 anomalies across Eastern Europe and southern China are opposed to the recent declining trends across these regions and warrant further investigation.

NO_2 has a relatively short lifetime (typically less than a day in the boundary layer), and the OMPS product highlights regions where rapid boundary layer ozone production is most likely. In contrast, PANs are a class of hydrocarbon that act as a reservoir for NO_x—they are most stable in the cooler regions of the atmosphere, especially above the boundary layer, and contribute to long-range transport of pollution (Jiang et al. 2016; Zhai et al. 2024). Figure 2.68d shows the regions of the atmosphere where longer-lived PANs have been transported away from surface emissions regions, with the highest mixing ratios downwind of North America, South Asia, and East Asia. Elevated mixing ratios are also found above the South Atlantic Ocean, central Africa, and in a band stretching from southern Africa to Australia, with biomass burning (Bourgeois et al. 2021) and the combination of lightning NO_x and biogenic VOC emissions (Payne et al. 2017) being major contributors to PANs formation. These enhancements indicate pollution pathways where PANs can thermally decompose, release NO_2, and produce ozone far downwind of the emissions sources. Comparison of Fig. 2.68a to Fig. 2.68d demonstrates the similarity between enhancements

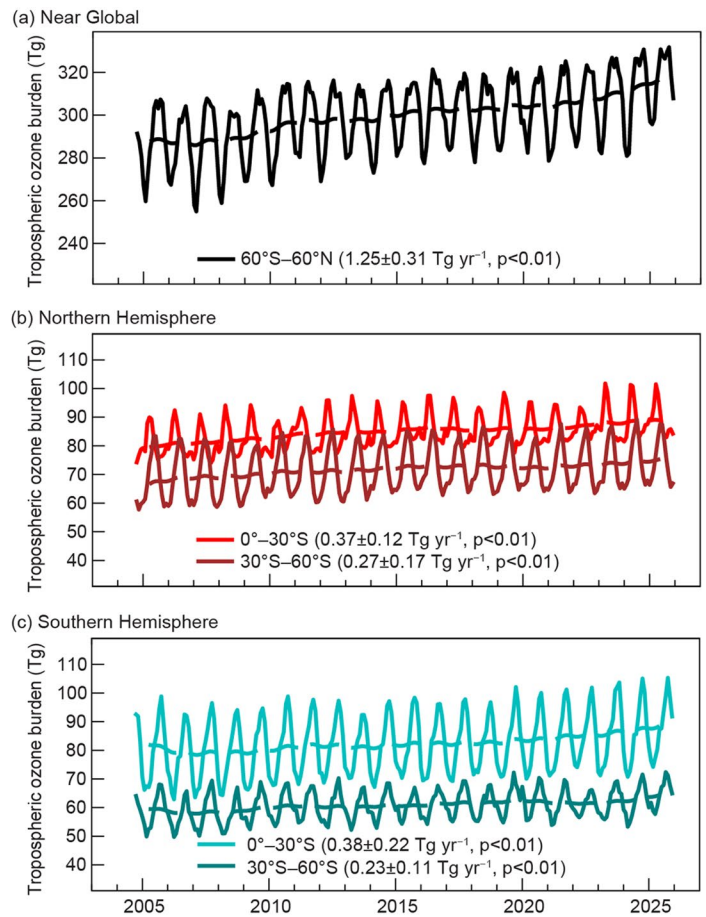

Fig. 2.69. Monthly averages (solid lines) and 12-month running means (dashed lines) of Ozone Monitoring Instrument (OMI)/Microwave Limb Sounder (MLS) tropospheric ozone burdens (Tg) from Oct 2004 through Dec 2025 for (a) 60°S–60°N (black), (b) the Northern Hemisphere tropics (red) and midlatitudes (dark red), and (c) the Southern Hemisphere tropics (aqua) and midlatitudes (green). Slopes of linear fits to the data are presented with their 95% confidence-level uncertainties.

of PANs and tropospheric column ozone. Continued long-term monitoring of PANs is expected to reveal changes in the transport and accumulation of key tropospheric ozone precursors.

Ozone trends from six remote surface sites are reported here, with records 25–50 years in length (Fig. 2.70; Table 2.13). While these sites are too sparse to be representative of global average surface ozone trends, they are suitable for evaluating coarse resolution global models. In the Arctic, Barrow Atmospheric Observatory (at sea level) reported a weak positive trend of 0.41±0.29 ppbv decade^{-1} for the years 1973–2025, while the high-elevation site of Summit, Greenland, showed decreasing ozone since 2000 (–1.60±0.82 ppbv decade^{-1}). In the remote North Atlantic, Bermuda (sea level) reported high interannual variability and a weak negative trend (–0.74±1.12 ppbv decade^{-1}), while Mauna Loa (3400 m a.s.l.) in the tropical North Pacific showed a clear ozone increase since 1974 (1.20±0.29 ppbv decade^{-1}). The Antarctic site of Arrival Heights showed no trend since 1996, while ozone has increased slightly at South Pole (0.35±0.32 ppbv decade^{-1}).

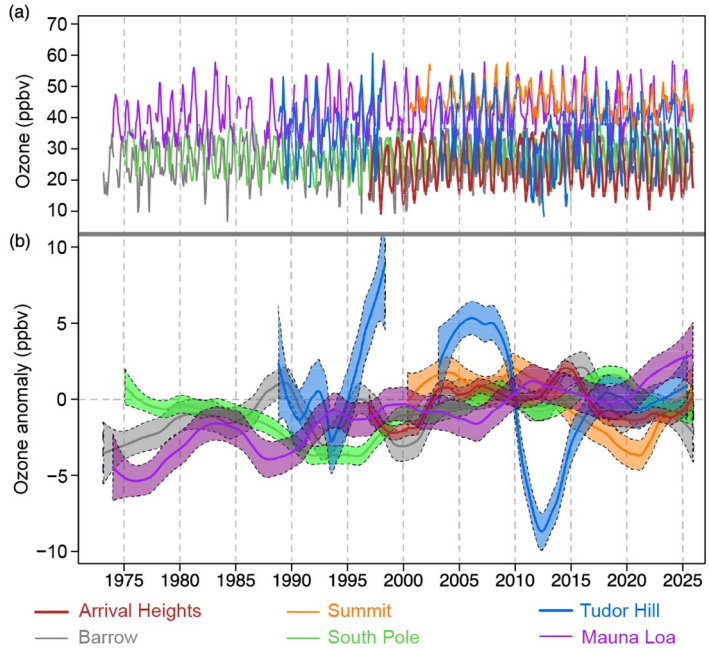

Fig. 2.70. (a) Monthly mean surface ozone (ppbv) at Barrow Observatory, Alaska (gray), Summit, Greenland (orange), Tudor Hill, Bermuda (blue), Mauna Loa, Hawaii (purple), Arrival Heights, Antarctica (red), and South Pole (green). Monthly means are produced for months with at least 50% data availability using observations from all 24 hours of the day, except for Mauna Loa, which is based on nighttime data (Price and Pales 1963). The locations of each site are listed in Table 2.13. (b) The same time series after conversion to monthly anomalies referenced to the monthly climatological values over 2000–20 and smoothed using locally weighted scatterplot smoothing (LOWESS) regression (Chang et al. 2021).

Table 2.13. Ozone trends at the six baseline monitoring sites shown in Fig. 2.70. Trends are estimated by the generalized least-squares method, based on monthly anomalies referenced to the monthly 2000–20 base period (Chang et al. 2021), and reported with 95% confidence intervals and *p*-values. The trends at the Mauna Loa Observatory (MLO) were adjusted to account for interannual meteorological variability following the methods of Chang et al. (2024), spanning the period 1974–2025.

Site Name — Latitude, Longitude, Elevation (m)	Years With Data	Trend, ppbv decade^{-1}	*p*-value
Summit, Greenland — 72.6°N, 38.5°W, 3238 m	2000–present	–1.60±0.82	p<0.01
Barrow Atmospheric Observatory, Alaska — 71.3°N, 156.6°W, 11 m	1973–present	0.41±0.29	p=0.01
Tudor Hill, Bermuda — 32.3°N, 64.9°W, 30 m	1988–98, 2003–present	–0.74±1.12	p=0.19
Mauna Loa Observatory (MLO), Hawaii — 19.5°N, 155.6°W, 3397 m	1974–present	1.20±0.29	p<0.01
Arrival Heights, Antarctica — 77.8°S, 166.8°W, 50 m	1996–present	0.08±0.48	p=0.73
South Pole, Antarctica — 90.0°S, 59.0°E, 2840 m	1975–present	0.35±0.32	p=0.03

5. STRATOSPHERIC AEROSOLS

—S. Khaykin, G. Taha, T. Sakai, I. Morino, and B. Liley

Stratospheric aerosols influence atmospheric chemistry and the radiative balance (Kremser et al. 2016). Major volcanic eruptions can inject sulfur dioxide (SO_2) and ash into the stratosphere, elevating aerosol loading from hemispheric to global scales for months to years, while intense wildfires can loft smoke into the stratosphere via pyrocumulonimbus (pyroCb) storms that overshoot the tropopause (Peterson et al. 2021).

Following the April 2024 Mt. Ruang (Indonesia, 2.3°N) eruptive sequence that injected a total of ~0.4 Tg SO_2 into the stratosphere with eruptive columns reaching ~19 km–25 km (Khaykin et al. 2026), the stratospheric aerosol optical depth (SAOD) remained globally elevated through 2025. The Ozone Mapping and Profiler Suite-Limb Profiler (OMPS-LP) onboard the NOAA-21 satellite shows enhanced SAOD in the tropics and southern extratropics persisting into early 2025 (Fig. 2.71a). By January 2025, the sulfate aerosols from Ruang spread across almost the entire

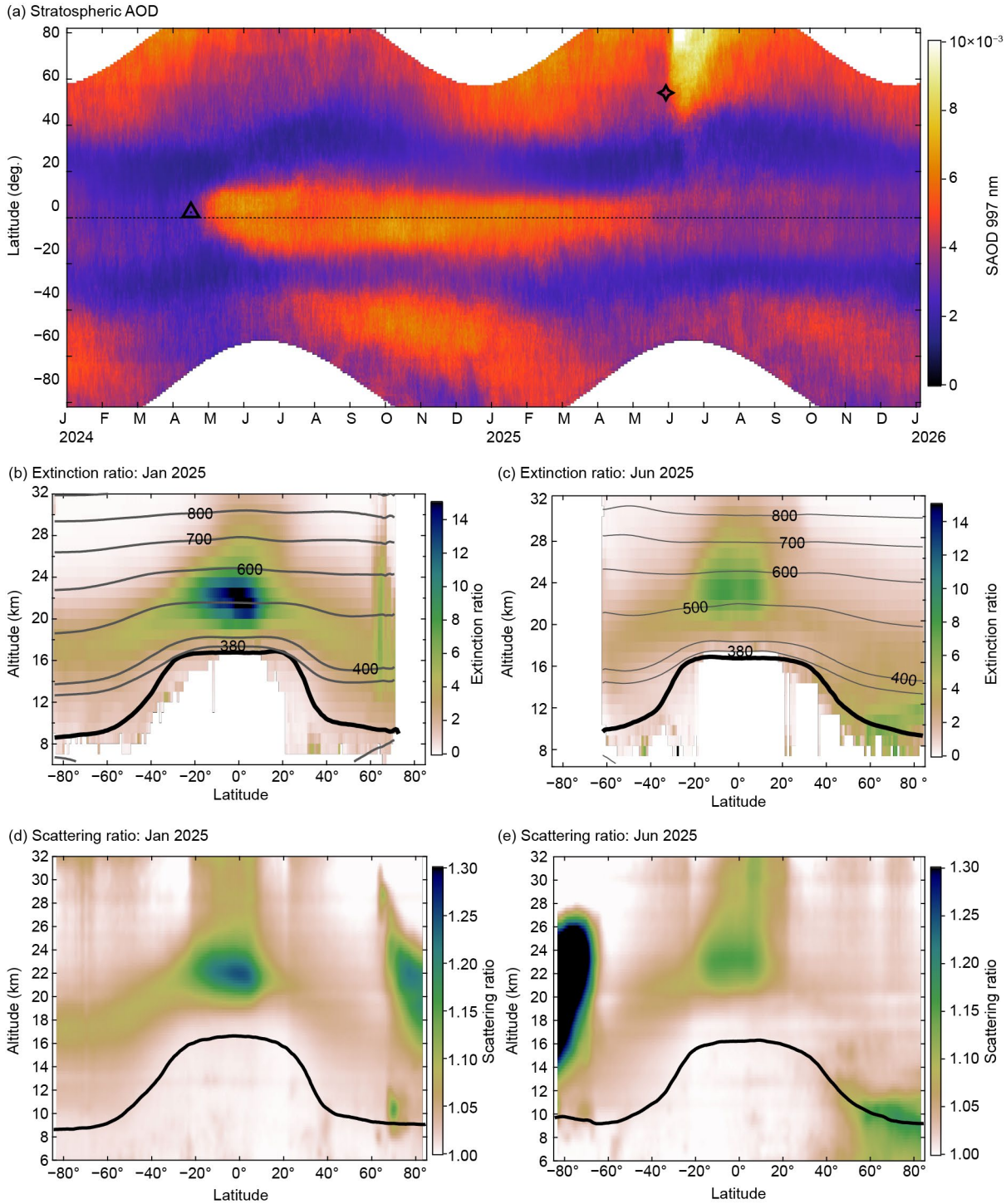

Fig. 2.71. Global evolution of the stratospheric aerosol from the NOAA-21 Ozone Mapping and Profiler Suite–Limb Profile (OMPS-LP) observations at 997 nm during 2024/25. (a) Zonal-mean stratospheric aerosol optical depth (SAOD). The triangle indicates the eruption of Ruang (Ru) volcano in Apr 2024, and the star indicates the Panboreal Wildfire Outbreak (PWO) in May 2025. (b),(c) NOAA-21 OMPS-LP zonal/monthly mean latitude–altitude section of the aerosol-to-molecular extinction ratio (ER) at 997 nm during Jan and Jun 2025. The black thick line is the tropopause altitude, and the black thin lines are the potential temperature levels in Kelvin (K). (d),(e) EarthCARE Atmospheric Lidar (ATLID) zonal/monthly tropospheric cloud-cleared scattering ratio at 355 nm. Note that the aerosol enhancements in the Arctic (panels [b],[d]) and in the Antarctic (panel [e]) are caused by incomplete polar stratospheric clouds clearing.

Southern Hemisphere and were most probably entrained by the 2025 Antarctic polar vortex, potentially enhancing the polar stratospheric cloud occurrence through the increased sulfate aerosol surface area (e.g., Kremser et al. 2016). Elevated SAOD in the northern extratropics during January–March can be associated with the poleward transport of Ruang aerosols during boreal winter 2024/25. By May 2025, the enhanced tropical SAOD shifted into the northern tropics, which is likely linked to the quasi-biennial oscillation (QBO) phase change around that time. The lower SAOD in the subtropics (appearing as a relative discontinuity between the tropical reservoir and midlatitudes in Fig. 2.71a) is a common feature in both hemispheres following tropical eruptions. It is particularly evident in the SH in 2024 and likely reflects rapid meridional redistribution across the subtropical "surf zone". In this region, wave breaking and mixing near the subtropical jet efficiently transport aerosols out of the subtropical band toward midlatitudes (Plumb 2002).

A distinct SAOD increase in the northern extratropics during June–July 2025 is attributed to the late-May 2025 Panboreal Wildfire Outbreak (PWO), when widespread fires and pyroCb activity across Canada and in Siberia injected smoke into the lower stratosphere. OMPS-LP indicates that the SAOD enhancement spans a broad latitude band—from the North Pole to about 15°S—where wildfire smoke merges with the residual Ruang sulfate aerosols.

To understand the changes in the vertical distribution of aerosols, we use complementary profile measurements from both OMPS-LP and the Atmospheric Lidar (ATLID), a high-spectral-resolution lidar onboard the EarthCARE mission launched in May 2024. ATLID provides high-resolution cloud/aerosol profiling, complementing OMPS-LP's established limb record. Here we used ATLID Level-1 data processed using the method described by Khaykin et al. (2026) and cloud-cleared using Level-2 tropospheric cloud mask. The latitude–altitude distributions of zonal-mean mean extinction ratio (ER; aerosol-to-molecular extinction ratio) from OMPS-LP and scattering ratio (total to molecular backscatter ratio) from ATLID for January and June 2025 are shown in Figs. 2.71b–e.

The January latitude–altitude cross-sections place the tropical aerosol maximum between ~19 km and 24 km and show enhanced aerosol signal extending to higher altitudes in the upwelling branch of Brewer–Dobson circulation, as well as to the southern and northern midlatitudes, associated with the isentropic transport towards the poles. ATLID observations, covering the polar night regions, reveal a notable enhancement in scattering ratio in the Arctic, associated with polar stratospheric clouds (PSCs) in January 2025. In June, the tropical aerosol layer is higher and weaker, reflecting ongoing upwelling and dispersion, whereas the northern extratropical upper troposphere/lower stratosphere (UTLS) exhibits a notable enhancement in aerosol abundance, associated with the pyroCb injections during PWO-2025.

Figure 2.72 shows SAOD time series from ground-based Network for the Detection of Atmospheric Composition Change (NDACC) lidars at Observatoire de Haute Provence (OHP; 43.9°N) and Lauder observatory (45.0°S), representing northern and southern midlatitudes, respectively, together with the corresponding zonally averaged satellite data from the International Space Station Stratospheric Aerosol and Gas Experiment III (ISS/SAGE III) instrument and the Global Space-based Stratospheric Aerosol Climatology (GloSSAC). In 2025, both OHP and Lauder SAOD exhibit significant enhancements, although with different origins. In the northern midlatitudes (Fig. 2.72a), a sharp SAOD enhancement is associated with the boreal wildfires (PWO) and to a lesser extent with the waning Ruang aerosols, whereas the southern stratosphere is polluted by the remaining Ruang aerosols, whose abundance at the southern midlatitudes is modulated by the seasonally varying transport (as can be inferred from Fig. 2.71a).

In November 2025, Ethiopia's Hayli Gubbi volcano (13.5°N) erupted, sending 0.22 Tg of SO_2 mostly into the upper troposphere at 10 km–15 km (NASA Earth Observatory 2025). However, OMPS LP and ATLID instruments detected only a small portion of the volcanic plume in the lower stratosphere between 17 km and 18 km, just above the tropopause (not shown).

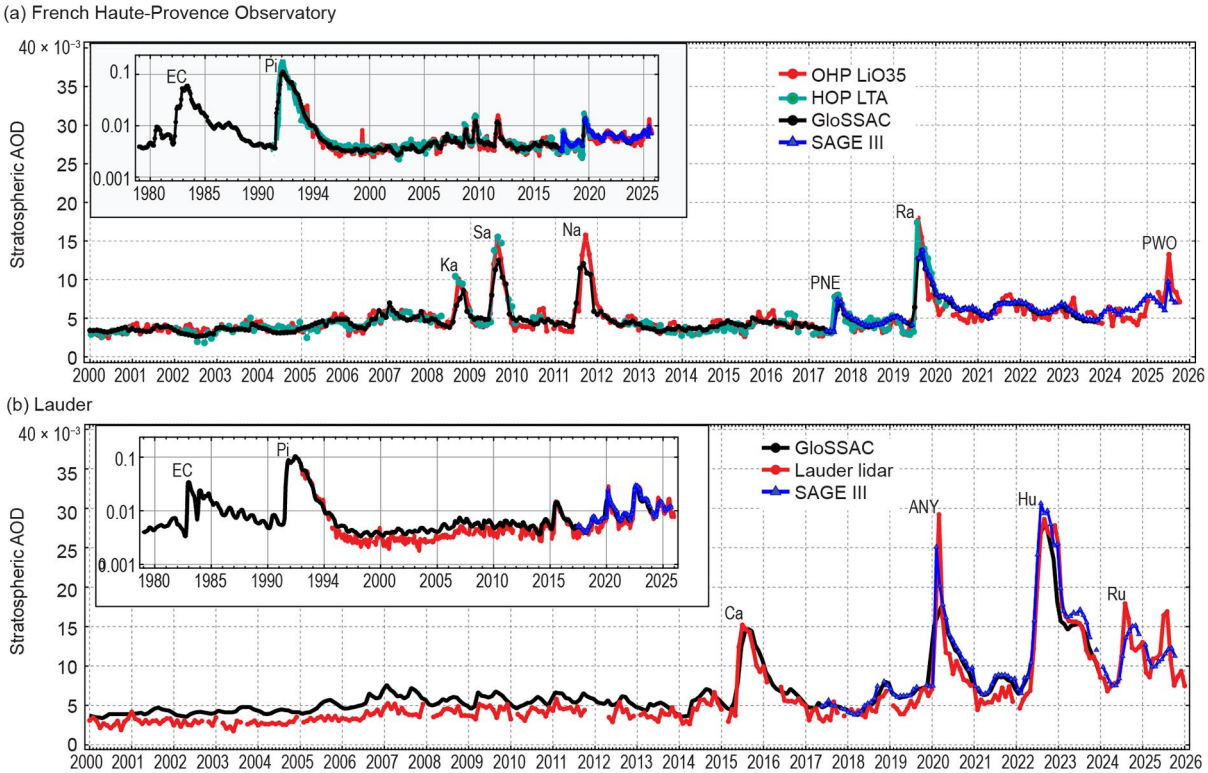

Fig. 2.72. Time series of monthly mean aerosol optical depth at 532 nm of the stratospheric overworld (380 K; 33 km) from ground-based lidars at (a) French Observatoire de Haute Provence (OHP, 43.9°N, 5.7°E, Stratospheric Ozone Lidar [LiO3S] and the Lidar Temperature Aerosol [LTA] instruments) and (b) New Zealand's Lauder station (45°S, 179°E, Lauder aerosol lidar) and the corresponding monthly/zonal-mean values from satellite observations within 40°N–50°N and 50°S–40°S latitude bands from ISS's Stratospheric Aerosol and Gas Experiment III (SAGE III) instrument and Global Space-based Stratospheric Aerosol Climatology (GloSSAC) merged satellite record. The embedded panels display the log-scaled time series from the beginning of the GloSSAC record. The literal notations indicate the most significant volcanic eruptions: El Chichon (EC), Pinatubo (Pi), Kasatochi (Ka), Sarychev (Sa), Nabro (Na), Raikoke (Ra), Calbuco (Ca), Hunga (Hu), and Ruang (Ru); and wildfire events: Pacific Northwest Event (PNE) in British Columbia, Canada and Australian New Year (ANY) super outbreak; Panboreal Wildfire Outbreak (PWO).

6. STRATOSPHERIC OZONE

—W. Steinbrecht, M. Weber, C. Arosio, R. van der A, L. M. Ciasto, M. Coldewey-Egbers, S. Davis, D. Degenstein, P. Effertz, V. E. Fioletov, L. Flynn, S. M. Frith, L. Froidevaux, S. Godin-Beekmann, J. de Laat, T. Leblanc, D. Loyola, E. Maillard Barras, I. Petropavlovskikh, R. Querel, A. Rozanov, M. L. Santee, V. Sofieva, K. Tourpali, R. Wang, T. Warnock, and J. D. Wild

Almost all ozone in the atmosphere, about 90% of the total column, resides in the stratosphere. On timescales shorter than a year, transport processes in the lower stratosphere are the most important source of total column ozone variations (e.g., Chipperfield et al. 2018). Chemical ozone loss due to anthropogenic ozone-depleting substances is important for springtime polar "ozone holes" and for decadal ozone changes (WMO 2022). The international Montreal Protocol has successfully banned production and consumption of ozone-depleting substances. Their atmospheric concentrations have been declining slowly since about 2000, but year-to-year variations of ozone are relatively unaffected. Full recovery of the ozone layer is not expected for another few decades (WMO 2022).

For the year 2025, Plate 2.1ah shows that total column ozone values over much of the North Hemisphere (NH) were up to 30 Dobson Units (DU) below the 1998–2008 average. This was due to weak planetary wave activity in the NH 2024/25 winter stratosphere (e.g., https://ozonewatch.gsfc.nasa.gov/meteorology/NH.html), resulting in weak poleward transport of ozone in the NH and a strong Arctic winter vortex in January and February, with significant chemical ozone depletion and very low total column ozone in February and March over Eurasia. This low ozone signature from January to March remained in the annual mean anomaly shown in Plate 2.1ah.

While total column ozone over the NH mid- and high latitudes changed from above normal in 2024 (Newman et al. 2024) to below normal in 2025, total column ozone over the

SH mid- and high latitudes was above normal in both 2024 and 2025, by up to 60 DU in 2025 (Plate 2.1ah). The low values near 60°S, 45°W were due to an unusual shift of the remainder of the Antarctic ozone hole towards South America in November and December 2025 (e.g., https://woudc.org/en/data/products/ozone-maps/archive). Overall, planetary wave activity and poleward ozone transport in the SH were above normal in 2025 (and in 2024), and the 2025 and 2024 Antarctic ozone holes were less pronounced than in previous years (see section 6h for details).

Between 30°S and 30°N, total column ozone in 2025 was affected by the easterly shear phase of the quasi-biennial oscillation of equatorial winds (QBO) and by a weak La Niña (cool phase; section 2e3). The situation was almost the opposite of 2024, which had a westerly shear QBO phase and an El Niño (warm phase) in the first months of the year. The QBO-induced residual circulation (Baldwin et al. 2001) resulted in reduced (up to 2 DU below normal) total column ozone over the equator in 2025 and enhanced (by up to 10 DU) values around 20°N and 20°S. These alternating bands of high and low total ozone are visible in Plate 2.1ah. La Niña, with cooler sea surface temperatures in the equatorial Pacific, weakly counteracted the QBO-induced anomalies (Oman et al. 2013; Domeisen et al. 2019), as seen in slightly higher total ozone columns above the equatorial Pacific and slightly lower columns above Indonesia and Australia (Plate 2.1ah).

The long-term evolution of total column ozone is plotted in Fig. 2.73. The data clearly show the depletion of ozone from the 1970s to the mid-1990s, caused by increasing concentrations of anthropogenic ozone-depleting substances, and the beginning of a slow recovery since about 2000 (WMO 2022). Compared to 2024 and other recent years, the 2025 total column ozone values were similar for four of the six latitude bands (near-global 60°S–60°N, tropical 20°S–20°N, Southern Hemisphere (SH) 35°S–60°S, and the SH polar 60°S–90°S). For the NH midlatitude and polar bands, total column ozone in 2025 was much lower than that in 2024 (as explained above) and slightly higher compared to 2021 to 2023.

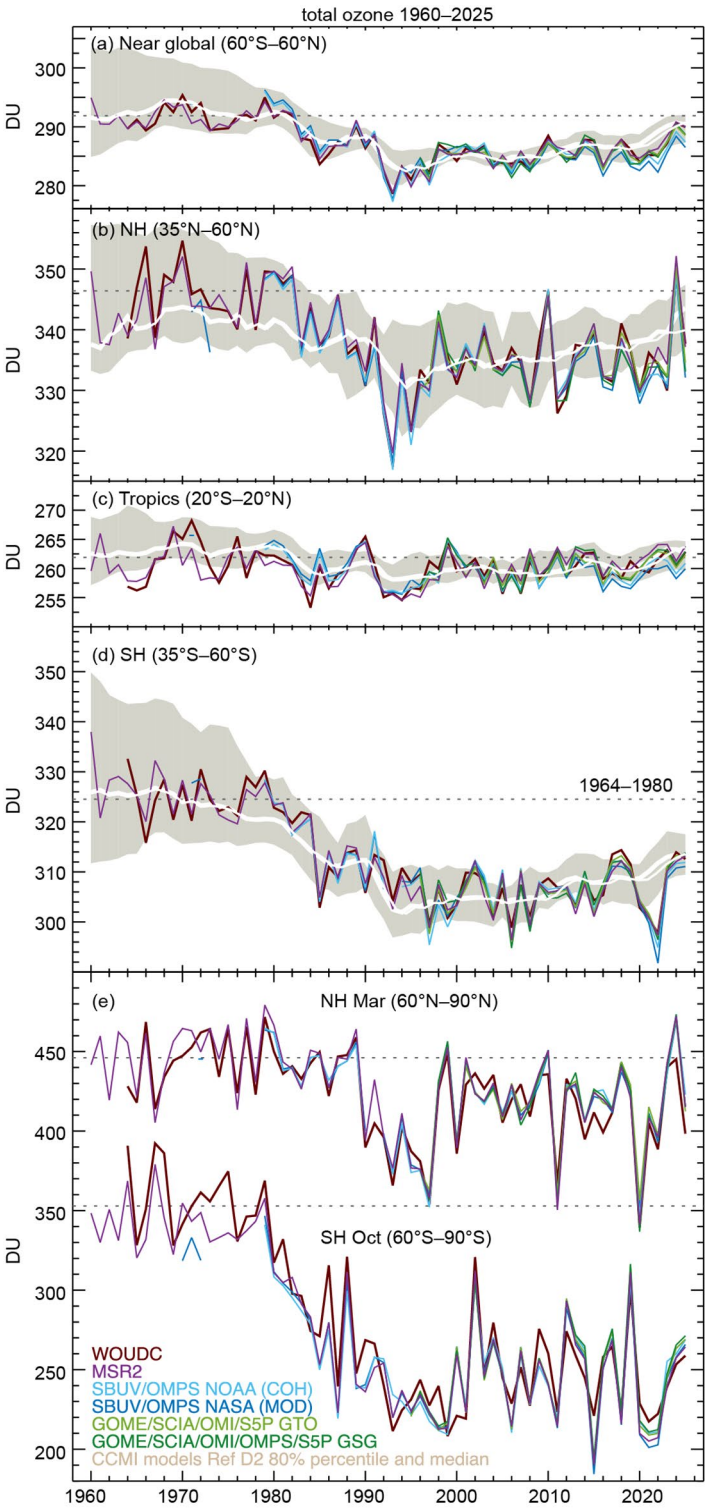

Fig. 2.73. Time series of annual mean total column ozone (DU) in four zonal bands: (a) near global (60°S–60°N), (b) Northern Hemisphere (35°N–60°N), (c) tropics (20°S–20°N), and (d) Southern Hemisphere (35°S–60°S). Panel (e), time series of polar total column ozone (60°S–90°S; DU) for the Northern Hemisphere (NH) and the Southern Hemisphere (SH) in Mar and Oct, respectively, the months when polar ozone losses are largest. The dotted gray lines in each panel show the average for 1964–1980, calculated from the World Ozone and Ultraviolet Radiation Data Centre's (WOUDC) data. The observational data for 2025 are preliminary. The thick white lines and gray shading in (a)–(d) show the median and 80th percentile range from model simulations by the Chemistry-Climate Model Initiative CCMI-2022 (refD2 simulations; Abalos et al. 2026). All datasets are shifted to the same average value over the reference period 1998–2008 as the multi-instrument mean.

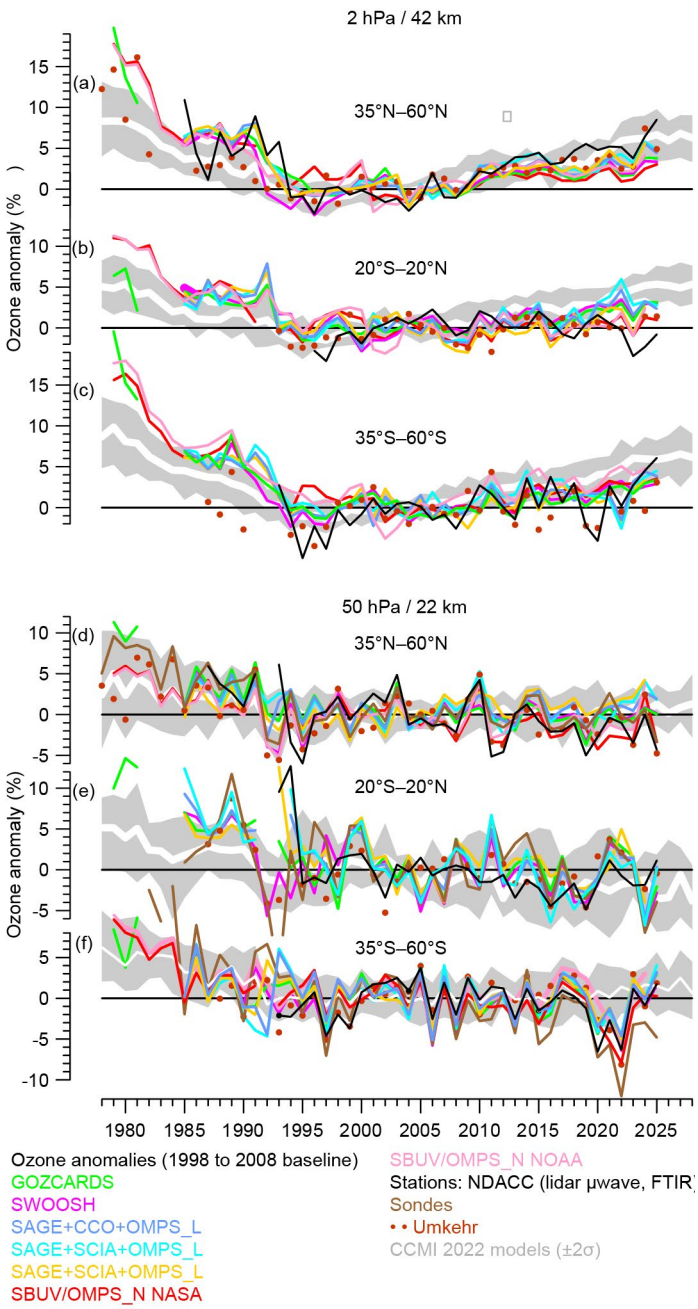

Using ozone profile data, Fig. 2.74 shows the long-term behavior of ozone at two levels in the stratosphere (Steinbrecht et al. 2017; WMO 2022). At the 2-hPa level in the upper stratosphere (about 42-km altitude), chlorine from anthropogenic ozone-depleting substances and atmospheric temperature have the largest influence, while the transport processes that also influence total column ozone are most important at the 50-hPa level in the lower stratosphere (about 22 km).

Consistent with total column ozone in Fig. 2.73, lower stratospheric ozone anomalies in 2025 in Figs. 2.74d–f show values similar to those in recent years, higher than in 2024 in the tropical 20°S–20°N band and in the SH 35°S–60°S band, and lower than in 2024 in the NH 35°N–60°N band. For all three bands, the observed long-term evolution is generally consistent with the range of ozone values (gray) simulated by the CCMI-2022 modeling experiments (Abalos et al. 2026), although the observed data in the NH (Fig. 2.74d) are often lower in recent years. The observed low values from 2020 to 2023 in the SH (Fig. 2.74f) were due to extreme events not accounted for in the model simulations—among them the Australian New Year wildfires in 2020 and the Hunga Tonga volcanic eruption in 2022.

In the upper stratosphere, 2025 ozone anomalies in Figs. 2.74a–c are comparable to or higher than anomalies in the last couple of years. The sparse station data (e.g., NDACC, black lines) do not always agree with the zonal mean data from the satellites. Compared to the CCMI-2022 model simulations (gray), the observed anomalies in recent years lie at the lower end of the simulated range. These simulations account for the expected evolution of

Fig. 2.74. Annual mean anomalies of ozone (%) in the (a)–(c) upper stratosphere near 42-km altitude or 2-hPa pressure, and in the (d)–(f) lower stratosphere near 22 km or 50 hPa for three zonal bands: (a),(d) 35°N–60°N, (b),(e) 20°S–20°N (tropics), and (c),(f) 35°S–60°S, respectively. Anomalies are referenced to the 1998–2008 baseline. Annual means are plotted at the tick marks of the start of each year. Colored lines are long-term records obtained by merging different limb (Global Ozone Chemistry and Related Trace Gas Data Records for the Stratosphere [GOZCARDS], Stratospheric Water and Ozone Satellite Homogenized [SWOOSH], Stratospheric Aerosol and Gas Experiment [SAGE]+Climate Change Initiative [CCI]+Ozone Mapping and Profiler Suite Limb Profiler [OMPS-LP], SAGE+Scanning Imaging Absorption Spectrometer for Atmospheric Chartography [SCIAMACHY]+OMPS-LP, SAGE+Optical Spectrograph and InfraRed Imaging System [OSIRIS]+OMPS-LP) and nadir-viewing (Solar Backscatter Ultraviolet Radiometer [SBUV], OMPS Nadir Profile [OMPS-NP]) satellite instruments. The nadir-viewing instruments have a much coarser altitude resolution than the limb-viewing instruments. This can cause differences in some years, especially at 50 hPa. Red dots are results from ground-based Umkehr data (Petropavlovskikh et al. 2025). The black line is from merging ground-based ozone records at seven Network for the Detection of Atmospheric Composition Change (NDACC) stations employing differential absorption lidars and microwave radiometers. See Steinbrecht et al. (2017), WMO (2022), and Arosio et al. (2019) for details on the various datasets. The gray shaded areas show the range of chemistry-climate model simulations from the Chemistry-Climate Model Initiative (CCMI-2022, refD2 simulations; Abalos et al. 2026), with the white line showing the multi-model median. Ozone data for 2025 are still preliminary.

chlorine (and bromine) from anthropogenic ozone-depleting substances and for stratospheric cooling due to increasing greenhouse gas concentrations; however, stratospheric chlorine abundances might be underestimated (Lickley et al. 2024).

Overall, stratospheric ozone in 2025 was comparable to values seen in recent years, and consistent with understanding and expectations summarized in WMO (2022).

7. STRATOSPHERIC WATER VAPOR

—S. M. Davis, E. A. Asher, H. Vömel, R. M. Stauffer, E. G. Hall, and K. H. Rosenlof

In 2025, tropical lowermost stratospheric water vapor (WV) concentrations returned to anomalously high values following a year (2024) in which the values were relatively low. The lingering effects of the January 2022 eruption of the Hunga volcano (Millán et al. 2022; Vömel et al. 2022) were evident in other regions of the stratosphere. Deseasonalized tropical lower-stratospheric WV anomalies (using a climatological base period of 2004–21 to exclude the effects of the large Hunga perturbation) of air entering the stratosphere (near the tropopause at 82 hPa) were positive for all but the final months of the year (Figs. 2.75a,c, 2.76, 2.77), consistent with the anomalously positive values observed in the last five years.

Although the cause of the recent positive "trend" remains an active area of research, there are potential contributions from surface warming, volcanoes (including moderate eruptions in addition to Hunga), wildfires, and natural interannual to decadal-scale variability (Konopka et al. 2022; Peng et al. submitted; Tao et al. 2023; Zolghadrshojaee et al. 2024).

Zonal-mean WV calculated from satellite measurements shows that lingering positive anomalies from Hunga were evident in 2025 in the tropical upper stratosphere (above 10 hPa, Figs. 2.75a, 2.76) and middle stratosphere (particularly the SH; Figs. 2.75b, 2.76), with some of these WV anomalies being most positive in the extratropics and high latitudes (see hatched regions, Fig. 2.76). Positive WV anomalies, including many record-high values, were also present in the lower stratosphere throughout most of 2025 (Fig. 2.76). These lower stratospheric record-high anomalies were most geographically coherent from May through the end of the year, spanning from nearly pole to pole a few kilometers above the tropopause, and ascending over this time in the tropics in a manner that appears consistent with the yearly progression of the so-called "tropical tape recorder" (Mote et al. 1996).

Attribution of these lower-stratosphere anomalies is subject to ongoing research, but they are plausibly explained as some combination of Hunga-impacted air and anomalously moist air entering the stratosphere in the tropics. The tropical WV anomalies are expected to be primarily caused by anomalies in tropical tropopause temperatures, which affect freeze-drying of air ascending into the stratosphere. Indeed, lower-stratospheric

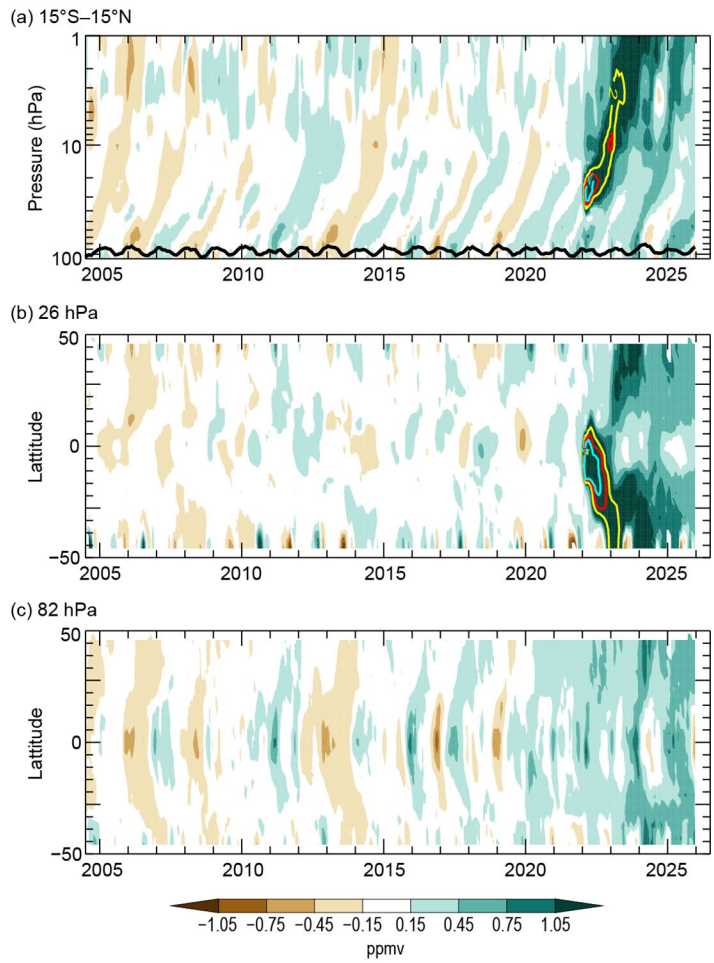

Fig. 2.75. (a) Pressure–time contour of tropical (15°S–15°N) lower-stratospheric water vapor (WV) anomalies. (b),(c) Latitude–time contour of WV anomalies at (b) 26 hPa (middle stratosphere) and (c) 82 hPa (lower stratosphere). Yellow, red, and cyan contour lines represent values of +2, +3, and +4 ppmv, respectively (no values in [c] exceed +2 ppmv). The black line in (a) shows the MERRA-2 tropical cold point pressure. All panels are based on merged satellite data from the Stratospheric Water and Ozone Satellite Homogenized version 2.72 (SWOOSH v2.72). Anomalies are differences from the mean 2004–21 water vapor mixing ratios (ppmv) for each month. Tick marks denote the beginning of each year.

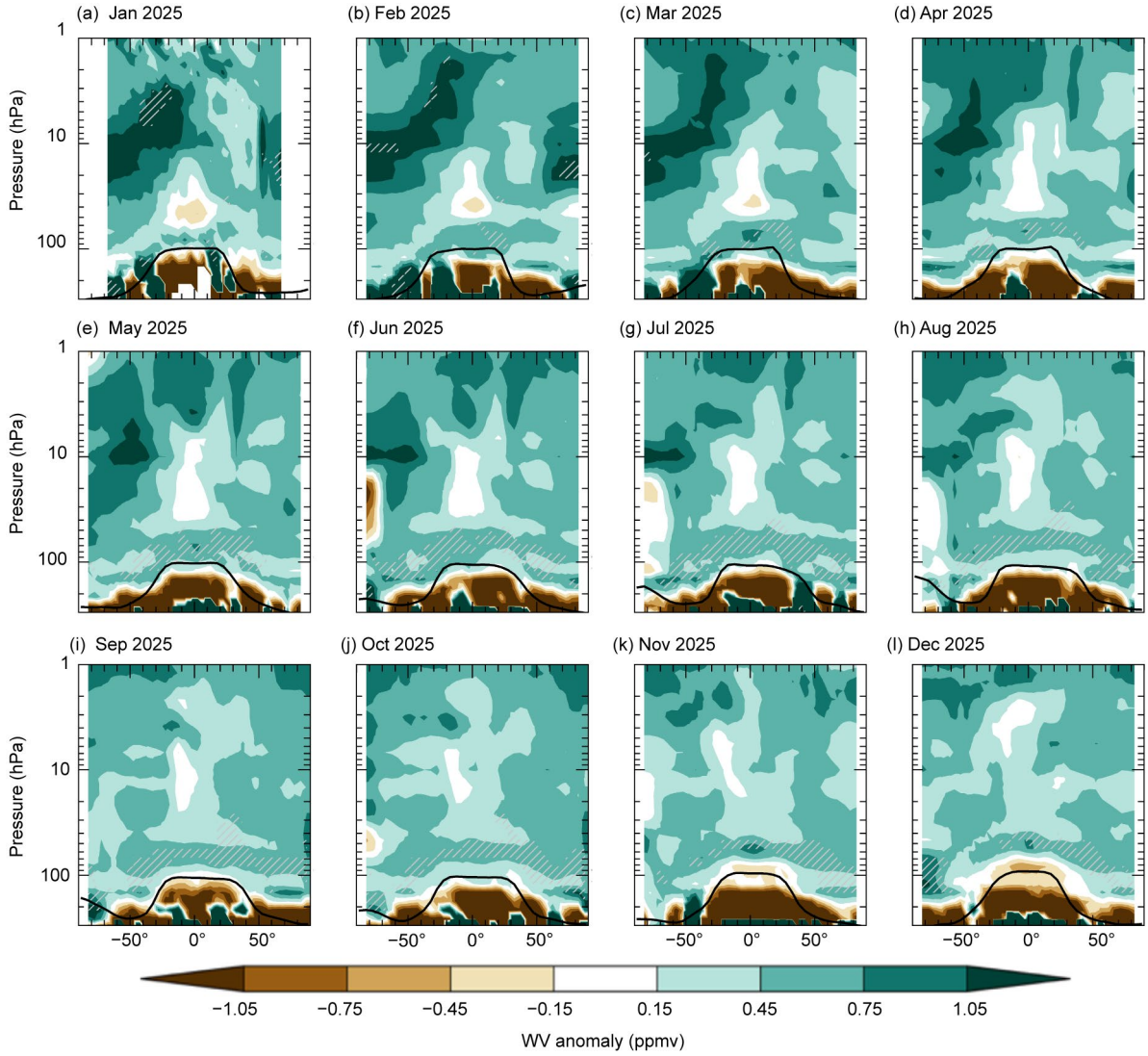

Fig. 2.76. Latitude–pressure cross-sections of zonally averaged water vapor (WV) anomalies (ppmv; 2004–21 base period). Hatching shows where the zonal-mean WV was at record-high values for the given month over the 2005–25 time period for which complete sampling is provided by Aura Microwave Limb Sounder (MLS). Black lines show the monthly mean tropopause pressure from the MERRA-2 reanalysis.

satellite WV anomalies are well correlated with tropical (15°S–15°N) cold-point tropopause temperature (CPTT) anomalies (Figs. 2.77b,c). While the annual mean 2024 CPTT anomaly was slightly colder than average (−0.24K, ranking 15th since 2004 when Aura MLS began), monthly CPTT anomalies ended 2024 and began 2025 in a positive (warm) state. CPTT monthly anomalies then transitioned from being strongly warm (among the three warmest for their respective months for the period 2004–25, over January–May 2025, including the warmest on record in April and May) to strongly negative and the coldest on record by December 2025. The net effect of this large swing in CPTT led to the annual average CPTT being +0.20K, or sixth since 2004. Consistent with these CPTT changes, monthly tropical (15°S–15°N) WV anomalies at the 82-hPa level (near the cold point) in the Stratospheric Water and Ozone Satellite Homogenized (SWOOSH) combined WV record (Davis et al. 2016) were also in the top three from January through October, after which they precipitously dropped and were record negative in December. For the annual average in 2025, tropical WV anomalies were eighth highest out of the 22 years since 2004, with an anomaly of +0.39 parts per million by volume (ppmv; i.e., μmol mol^{-1}).

As is typical, the tropical lower-stratosphere WV anomalies propagate both upward and to higher latitudes, becoming evident at other frost-point measurement stations with a lag of up to several months at subtropical and midlatitude stations (Hurst et al. 2011). Consistent with this pattern, the sharp drop in tropical lower-stratosphere WV anomalies in November 2025 became apparent at both Hilo (20°N) and Lauder (45°S) in December 2025 (Fig. 2.77).

To place the 2025 stratospheric WV in context, it is worth considering some of the known drivers of interannual variations in CPTT and hence WV concentrations entering the stratosphere: El Niño–Southern Oscillation (ENSO) and the quasi-biennial oscillation (QBO) in equatorial stratospheric winds. According to the Multivariate ENSO index (MEI.v2), La Niña-like conditions existed for all two-month periods of the year except for March–April and April–May when conditions were briefly neutral. During boreal winter, La Niña conditions are associated with a wetter tropical lowermost stratosphere (e.g., Garfinkel et al. 2021), which is consistent with conditions at the beginning, but not the end of 2025. However, the transition from warm to cold CPTTs at the end of 2025 can be explained by the QBO-related transition from westerly to easterly wind shear in 2025 in the equatorial 100-hPa–70-hPa layer. In this layer, wind shear was westerly during the first part of the year (January–May), and then easterly afterwards (section 2e3), which is consistent with stronger upwelling, anomalously cold CPTT, and anomalously dry conditions in the tropical lower stratosphere at the end of 2025.

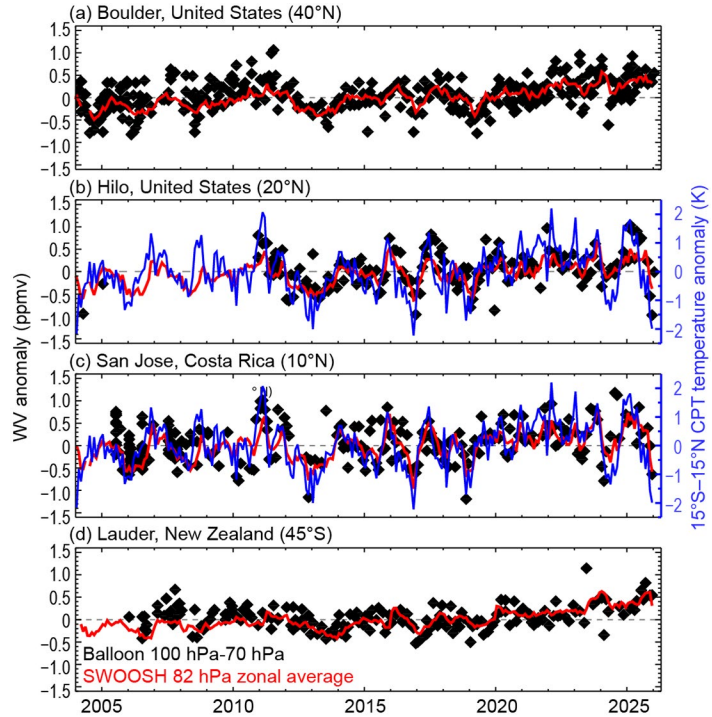

Fig. 2.77. Lower-stratospheric water vapor (WV) anomalies over four balloon-borne frost point (FP) hygrometer stations. Each panel shows the lower-stratospheric anomalies (relative to that specific station) of individual FP soundings (black diamonds) and of monthly zonal averages from Stratospheric Water and Ozone Satellite Homogenized (SWOOSH) version 2.72 data at 82 hPa in the 5° latitude band containing the FP station (red lines). High-resolution FP vertical profile measurements were averaged between 70 hPa and 100 hPa for comparison with the SWOOSH 82-hPa level. Anomalies for SWOOSH and FP data are calculated relative to the 2004–21 period for all sites except Hilo (2011–21). Tropical cold-point tropopause temperature anomalies based on the MERRA-2 reanalysis ([b],[c], blue lines) are generally well correlated with the tropical lower-stratospheric WV anomalies.

8. CARBON MONOXIDE

—J. Flemming, A. Inness, and P. Harder

The global burden of carbon monoxide (CO) in 2025 was dominated by the long-term negative trend in the Northern Hemisphere, driven by declining anthropogenic emissions. Intense wildfires in Canada during summer 2025 generated a pronounced, local, positive anomaly (Plate 2.1ai). On the seasonal scale (JJA), this anomaly extended across the Atlantic and reached Western and Central Europe (Fig. 2.78), a result of long-range smoke transport. The enhanced CO burden resulting from the intense South American fires of 2024 persisted, leading to elevated CO levels over the tropical oceans well into early 2025.

CO is emitted into the atmosphere by incomplete combustion processes from anthropogenic sources such as motor vehicles and energy production facilities, as well as from wildfires. Secondary production of CO in the atmosphere—primarily from formaldehyde as part of the oxidation chains of methane (CH_4), isoprene, and other volatile organic compounds—is of similar magnitude to direct emissions (Zheng et al. 2019). Oxidation by the hydroxyl radical (OH) is the only chemical CO

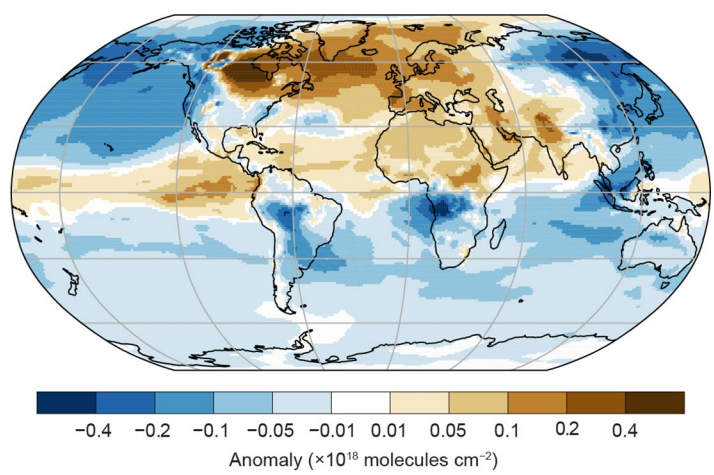

Fig. 2.78. Jun–Aug (JJA) 2025 anomalies of the total column of carbon monoxide (×10^{18} molecules cm^{-2}) compared to the reference period 2003–25 as derived from the CAMS reanalysis and a machine-learning based prediction for 2025.

loss, while soil uptake constitutes the remaining CO sink, resulting in an atmospheric lifetime of 1–3 months (Mirrezaei et al. 2026). CO is a key contributor to tropospheric ozone production.

Global monitoring of CO has previously relied on the ECMWF Atmospheric Composition reanalysis version 4 (EAC4) of the Copernicus Atmosphere Monitoring Service (Inness et al. 2019). EAC4 assimilates CO satellite observations exclusively from the MOPITT instrument (Deeter et al. 2014, 2017, 2019). Although reliable CO retrievals from other instruments (e.g. IASI since 2008, TROPOMI/S_5P since 2018) exist, they were not assimilated in EAC4 because inter-instrument biases (Inness et al. 2022) would have introduced discontinuities that reduce the suitability of EAC4 for trend and anomaly assessments. The discontinuation of MOPITT in January 2025 caused a shift in the EAC4 total column CO (TCCO) record, limiting its usefulness for analyzing anomalies or trends in 2025. To maintain consistency, Harder and Flemming (2026, submitted) generated monthly mean total column CO data for 2025 using a machine learning extension of EAC4, referred to as EAC4P. A neural network model was developed with data from 2003 to 2024 to reproduce monthly-mean EAC4 TCCO data using monthly mean TCCO and total columns of formaldehyde from a control run (CR) as predictors. The applied neural network model was then trained on the five prior years, i.e., 2020–24, to produce values for 2025. The CR does not assimilate atmospheric composition observations but uses the same model, emissions, and meteorology as EAC4. In particular, CO wildfire emissions, the main driver of CO anomalies in EAC4 (Flemming and Inness 2025), are used in both CR and EAC4. These were taken from the Global Fire Assimilation System (GFAS v1.2; Kaiser et al. 2012). The anthropogenic emissions for EAC4 and CR were taken from the MACCity inventory (Granier et al. 2011), which incorporates projected emission trends following the RCP8.5 scenario.

According to EAC4, the global CO burden (Fig. 2.79) has decreased since 2003 due to declining anthropogenic emissions in most regions and a strong reduction in fire activity in South America during the period 2003–13. In recent years, positive global and regional CO anomalies have occurred due to intensified wildfires associated with exceptional meteorological conditions, such as the extensive peat fires in Indonesia in 2015 and the severe wildfires in South America in 2024. The predicted EAC4P variability of the global burden agrees closely with the original EAC4 dataset, supporting the use of EAC4P as a substitute for EAC4 in 2025. As in previous years, though less intensely than in 2023 and 2024, boreal wildfires in Canada produced regional positive CO anomalies against the background of a decreasing Northern Hemisphere CO burden. Other wildfire-affected regions, such as South America and Central Africa, showed only small negative anomalies in 2025 relative to the 2003–25 EAC4 reference. However, the pronounced wildfires in 2024 resulted in increased CO burdens over the tropical Pacific into the first quarter of 2025. A pronounced negative CO anomaly occurred over East Asia and the adjacent Pacific in 2025, driven by reduced anthropogenic emissions in China and lower fire activity under the prevailing La Niña conditions.

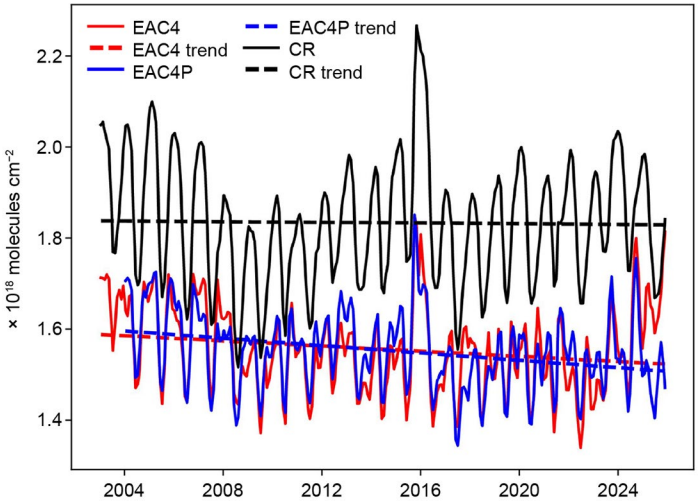

Fig. 2.79. Global monthly mean of total column carbon monoxide from the CAMS re-analysis (EAC4), the control run (CR), and a machine learning prediction (EAC4P) of EAC4 using CR as an input/feature. The EAC4P data of 2025 have been used to extend the CAMS reanalysis as a result of the discontinuation of the MOPITT data record in Jan 2025. The linear trend for each time series is shown as a dashed line.

h. Land Surface Properties

1. TERRESTRIAL SURFACE ALBEDO DYNAMICS

—F. Cappucci, R. Urraca, and N. Gobron

The terrestrial surface albedo is an important variable controlling the partitioning of incoming solar radiation between reflection and absorption at the Earth's surface. Defined as the nondimensional ratio of reflected-to-incident irradiance, surface albedo is modulated by a variety of biophysical and cryospheric factors. Enhanced vegetation density induces a "darkening" effect (negative anomalies) in the visible spectral range (0.3 μm–0.7 μm) due to increased absorption, while in tandem elevating near-infrared albedo (0.7 μm–5.0 μm) owing to the high reflectivity of healthy foliage (positive anomalies). Conversely, processes such as desertification or snow accumulation led to an increase in integrated shortwave albedo (0.3 μm–5.0 μm), known as brightening.

The 2025 anomaly (2003–20 reference period) of white-sky albedo in the visible domain (Plate 2.1aj) indicates a continued tendency toward surface darkening across widespread land areas. This pattern is consistent with recent years and reflects the combined effects of global warming, which drives both vegetation activity through carbon dioxide fertilization and the retreat of global snow cover (Cappucci et al. 2025). The darkening across the visible spectrum, near-infrared (Plate 2.1ak), and shortwave spectrum (Plate 2.1al) over Canada and the northern United States was mainly driven by above-average temperatures that affected the region during the winter and late spring of 2025 and contributed to earlier snowmelt and reduced snow cover duration (section 2c5). Widespread wildfires from late spring to late autumn, with the most extensive fire activity reported in Manitoba, Ontario, and Saskatchewan, further enhanced this tendency (section 2h3). The albedo darkening (negative anomaly) in the visible and near-infrared spectra over Eastern Europe (mainly Poland, Baltic republics, Romania, Ukraine, and western Russia) can be linked to early snowmelt that occurred during the first half of the year, associated with above-average temperatures (sections 2c5, 2b1). The brightening of near-infrared albedo, accompanied by a decrease in the visible spectrum over sub-Saharan Africa, eastern China, and western India, can be linked to increased vegetation activity driven by above-normal precipitation during the mid-year period, often combined with warmer-than-average conditions throughout the year (section 2h2). In the Amazon basin, the increased visible and near-infrared surface brightness can be correlated to vegetation stress resulting from severe drought conditions, partly associated with deforestation-driven reductions in regional precipitation (Qin et al. 2025).

The zonally averaged shortwave albedo anomaly patterns (Fig. 2.80c) during 2025 exhibit a decline in albedo at high latitudes (60°N), most evident during spring and primarily driven by early snowmelt. The darkening in visible surface albedo anomaly

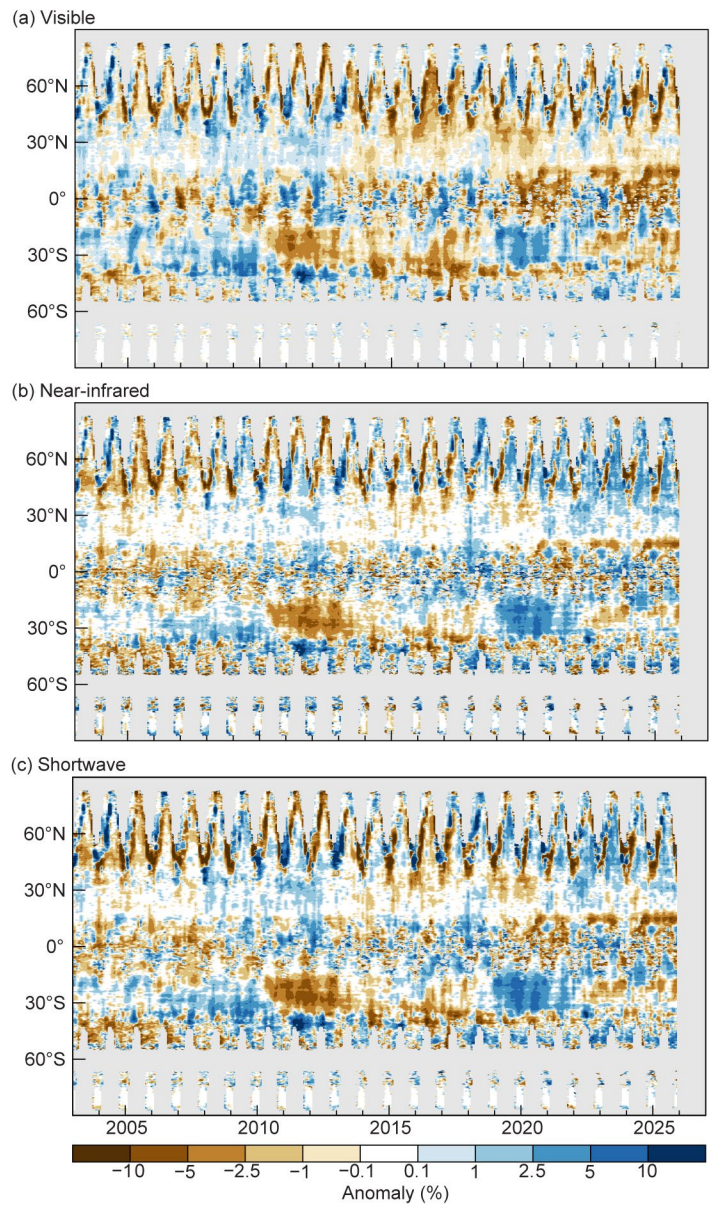

Fig. 2.80. Zonally averaged white-sky (a) visible, (b) near-infrared, and (c) shortwave broadband land surface albedo anomalies (%) for the period 2003–25 (2003–20 base period).

(Fig. 2.80a), detected over Europe and northern America, is pronounced between 40°N and 50°N, especially during the first and the last quarter of the year. The decline in the visible albedo anomaly pattern (negative anomaly) between 10°N and 20°N is primarily associated with vegetation intensification over China, India, and the sub-Saharan Africa, a tendency that emerged in 2023 and consolidated throughout 2025. The brightening (positive anomaly) of visible, near-infrared and shortwave albedo anomalies in the Amazon basin, correlated to vegetation stress and associated bare soil exposure, is particularly evident during spring and summer between 0° and 15°S. Surface near-infrared darkening (Fig. 2.80b), accompanied by visible-spectrum darkening between 15°S and 30°S, evident during the second and fourth quarters of 2025, is linked with above-average precipitation and associated soil moisture increase, particularly over northern Australia and southern Africa.

The globally smoothed average anomaly (solid black lines) from 2003 to 2025 exhibits fluctuations within ±3% in the visible domain (Fig. 2.81a) and ±2% in the near-infrared (Fig. 2.81b) and shortwave domains (Fig. 2.81c). Both Northern and Southern Hemisphere smoothed average albedo anomalies in the visible spectrum exhibit a decreasing trend during 2025. While the Northern Hemisphere trend was already under way in 2023, the negative trend in the Southern Hemisphere emerged in the last quarter of 2024 and continued during 2025. This tendency is possibly linked to vegetation growth over the Australian interior, particularly inland Queensland, enhanced by the exceptional wet conditions that occurred during 2024/25.

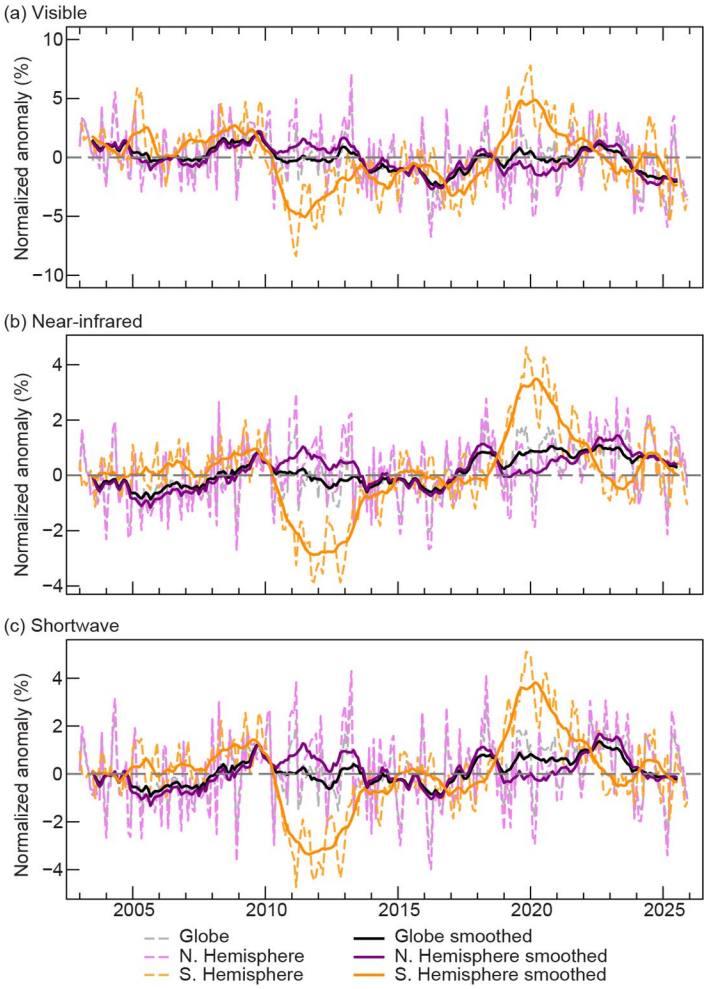

Fig. 2.81. Global (black lines), Northern Hemisphere (purple), and Southern Hemisphere (orange) land surface (a) visible, (b) near-infrared, and (c) shortwave broadband albedo normalized anomalies (%; 2003–20 base period) for the period 2003–25. Dotted lines denote each monthly period; solid lines indicate the 12-month running averaged mean.

This analysis is based on satellite products derived from the Visible Infrared Imaging Radiometer Suite (VIIRS) Collection 2 aboard the Suomi NPP, NOAA-20, and NOAA-21 satellites, providing data from 2012 to the present. For this study, the Visible Infrared Imaging Radiometer Suite (VIIRS) time series was restricted to the period 2013–25 and was complemented with data from the Moderate Resolution Imaging Spectroradiometer (MODIS) Collection 6.1 aboard the Aqua and Terra satellites (Schaaf et al. 2002) for the period 2003–12. Despite the good temporal consistency between the MODIS and VIIRS land products (Liu et al. 2017; Román et al. 2024), a small difference in surface albedo values was identified. Therefore, the MODIS data were bias-corrected to harmonize them with the VIIRS reference.

2. TERRESTRIAL VEGETATION DYNAMICS

—N. Gobron and F. Cappucci

The fraction of photosynthetically active radiation absorbed (FAPAR) is an essential climate variable that quantifies the amount of radiation absorbed by plant canopies (GCOS 2022). FAPAR is a key indicator of vegetation density, health, and productivity, and it plays a crucial role in assessing how efficiently plants take up carbon dioxide from the atmosphere.

In 2025, the extreme deviations from the 1998–2020 average (above +0.04 or below −0.04) represented 9% of the land surfaces, with 6% showing a positive anomaly, almost half of the area observed the previous year, while 3% showed a negative anomaly (decrease in productivity).

The greening of Earth's surfaces in 2025 was less pronounced compared to 2024. Many regions reverted to normal or even negative conditions over all continents (Plate 2.1am). In particular, several boreal areas in North America and eastern Russia were impacted by wildfires (section 2h3). Although the North American Arctic has experienced an exceptional level of tundra greenness in recent years (Frost et al. 2024), this signal was weaker in 2025.

There were strong negative anomaly patterns over both the North and South American continents. The Northwest Territories, British Columbia, and Alberta in Canada were affected by a series of severe wildfires and longer fire seasons (section 2h3; see also section 7b1), driven by drier conditions.

A large part of the western United States experienced drought conditions ranging from severe to exceptional, with California and Nevada among the most affected states. These drought conditions stressed vegetation and depleted soil moisture, significantly reducing moisture content and amplifying wildfire severity over extensive areas. Heatwaves that produced droughts in South America, from Peru to Brazil and northern Bolivia, impacted the Amazon rainforest, which suffered in 2025.

Western European countries recorded a net positive greening signal, although weaker than in the previous year. The grassy steppes of Central Asia experienced below-average rainfall and above-average temperatures during spring and summer, resulting in significant vegetation decline compared to previous years. In contrast, China, India, and Pakistan continued to exhibit strong annual greening, driven by agricultural intensification (Park et al. 2023; Zhu et al. 2016), despite occasional heatwaves and flooding affecting the regions.

Vegetation in eastern Africa (Somalia, Kenya, Ethiopia) suffered throughout most of the year due to below-average rainfall and warmer-than-average conditions, except for a brief improvement in spring. The Sahel savannah zone, spanning from Senegal to Ivory Coast, recovered from the decline in 2024, but experienced record-high temperatures (section 2b8). Southern Africa, especially Botswana, rebounded from the previous year's drought, with improved vegetation condition reflected in a positive anomaly.

In Australia, all states except Queensland experienced heatwaves and significant wildfire activity during austral summer, substantially affecting land surface conditions. Monthly anomalies of longitude-averaged FAPAR from 1998 to 2025 (Fig. 2.82) show that mainly positive values observed from 2019 to 2024 across Northern Hemisphere (NH) high latitudes shifted to near-zero or negative values in 2025. The Southern Hemisphere (SH) experienced a significant reduction in vegetation productivity (below −0.04) between 2002 and 2013, and in 2025 a strong negative pattern occurred south of the equator.

The global and hemispheric seasonal variability illustrates how terrestrial productivity has evolved over the past 28 years (Fig. 2.83). SH FAPAR smoothed monthly anomalies were positive before 2002, in 2011, and after 2014 (with the exception of 2019), while in 2025 the values returned to near-normal conditions. In the NH, the FAPAR anomaly was positive in 1998, negative from 1999 to 2013, and positive thereafter, reaching a maximum above +0.014 in spring 2024. Since then, anomalies have decreased to wards baseline conditions during 2025.

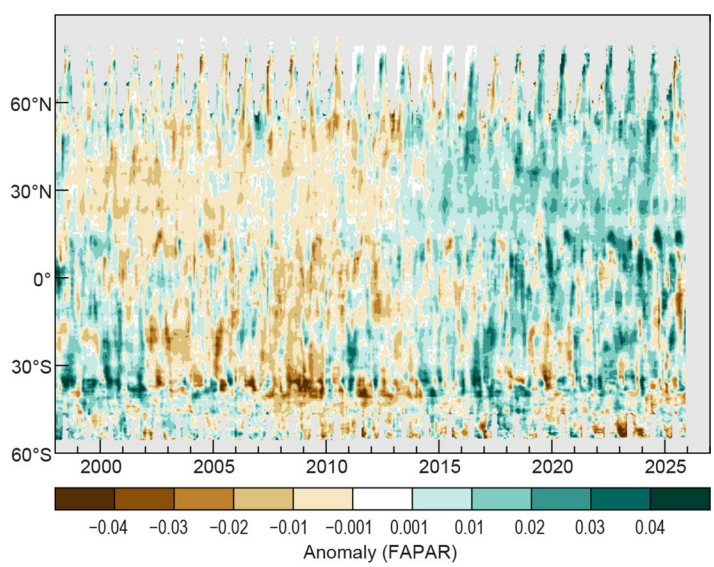

Fig. 2.82. Zonally averaged fraction of absorbed photosynthetically active radiation (FAPAR) anomalies for the period 1998–2025 (1998–2020 base period).

The current analysis combines 28 years of global satellite observations derived from four optical sensors: Sea-Viewing Wide Field-of-View Sensor (SeaWiFS; 1998–2002); Envisat/MERIS (2003–10), Terra-Aqua/MODIS (2011–16), and EU Copernicus Sentinel-3/Ocean and Land Colour Instrument (OLCI; 2017–25; Gobron et al. 2010, 2022; Gobron 2024). Intrinsic sensor characteristics introduce small differences between satellite generations; a bias-correction procedure was therefore implemented to harmonize the various contributions. Uncertainties were estimated through error propagation techniques and validated against multiple proxies, including ground-based measurements (Bai et al. 2022) and radiative transfer simulations. These assessments provide an overall average uncertainty of ~5%–10% for the long-term FAPAR record.

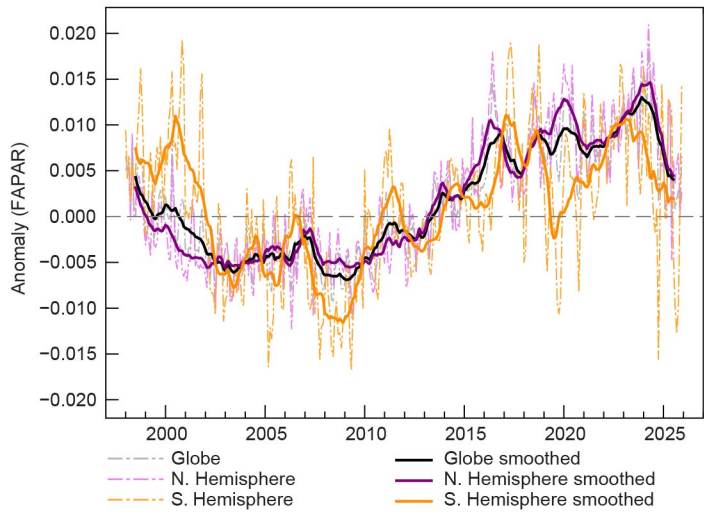

Fig. 2.83. Global (black line), Northern Hemisphere (purple), and Southern Hemisphere (orange) fraction of absorbed photosynthetically active radiation (FAPAR) anomalies for the period 1998–2025 (1998–2020 base period). Dotted lines denote each monthly period; solid lines indicate the six-month running averaged mean.

3. BIOMASS BURNING

—J. W. Kaiser, M. Parrington, and D. Armenteras

The year 2025 continued to illustrate the two distinct trends that have emerged in global biomass burning over the last decade: 1) a declining trend in many savanna and grassland regions strongly influenced by agricultural expansion, and 2) an increasing trend in many forested regions where climate change- induced severe droughts increase flammability (Fig. 2.84; Plate 2.1an). We characterize the amount of open biomass burning (also referred to here as "fire activity" or "landscape fires") with the amount of carbon that is consumed by fire—this includes wildfires and controlled agricultural fires. About 80%–95% of carbon is emitted as carbon dioxide, depending on fire type (smoldering vs. flaming), 1%–2% is emitted as particulate matter and subject to deposition within a few days, and the remainder (carbon monoxide, methane, and others) is further oxidized to carbon dioxide in the atmosphere. In a stable ecosystem, all this carbon dioxide is virtually assimilated again on time scales of years by regrowth of vegetation. However, 20% is estimated to contribute to the long-term build-up of atmospheric carbon dioxide (Zheng et al. 2023).

Global annual total estimated fire emissions in 2025 were the lowest in the Global Fire Assimilation System (GFAS) data record, which begins in 2003 (Table 2.14). Relative to 2024, which was one of the highest annual totals since 2015, it decreased by 26%.

Despite the lowest global annual total, North America, especially Canada, experienced its third consecutive year of extreme fire activity, with an annual total similar to 2024 and second only to the record fires of 2023 (Fig. 2.85). In contrast to Canada, the United States experienced slightly-below-average total fire emissions despite the widely reported fires that burned in and around Los Angeles in January. In Europe, a widespread decline of landscape fires in the east of the European Union (EU) was balanced by a sharp

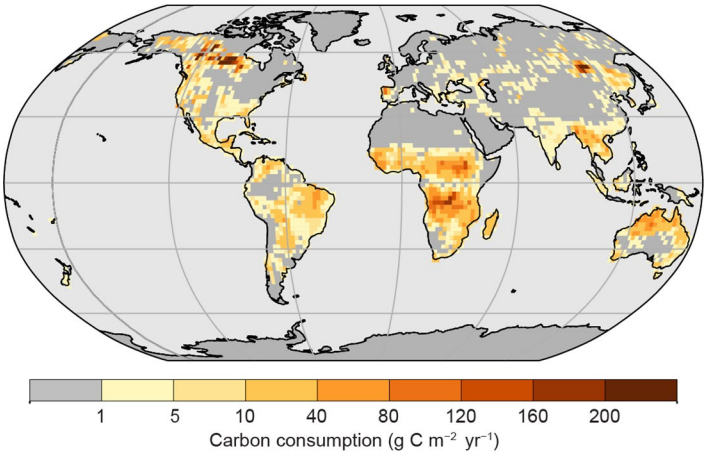

Fig. 2.84. Global map of fire activity in 2025 in terms of carbon consumption (g C m^{-2} yr^{-1}). (Source: GFAS4 Hemispheric Transport of Air Pollution [GFAS4HTAP] based on Copernicus Atmosphere Monitoring Service Global Fire Assimilation System version 1.2 [CAMS-GFASv1.2].)

increase in wildfire emissions from within the EU, which reached its highest annual total with intense fires in northwestern Spain and northern Portugal contributing more than half in just a two-week period in mid-August; the wildfire activity on the Iberian Peninsula was unprecedented, reaching ~328% of its 2003–20 average (Fig. 2.85; Table 2.14). The United Kingdom and Cyprus experienced notable increases, albeit at lower absolute levels.

Global fire emissions are dominated by savanna burning except for rare episodes of extreme tropical peat burning during El Niño conditions. African fire emissions accounted for ~40% of the total fire carbon emissions of 2025. Consistent with the decline in savanna burned area over the past two decades (Chen et al. 2023), both Northern and Southern Hemisphere Africa reached their lowest level of fire activity since 2003. Likewise, South America experienced a year-over-year drop of fire emissions by ~65%, resulting in its lowest emissions on record (Fig. 2.85). This continues the broader pattern of declining anthropogenic wildfires in several South American savanna regions, even as forest-related fires in Amazonia remain highly variable and sensitive to drought and land-use change (Lou et al. 2026).

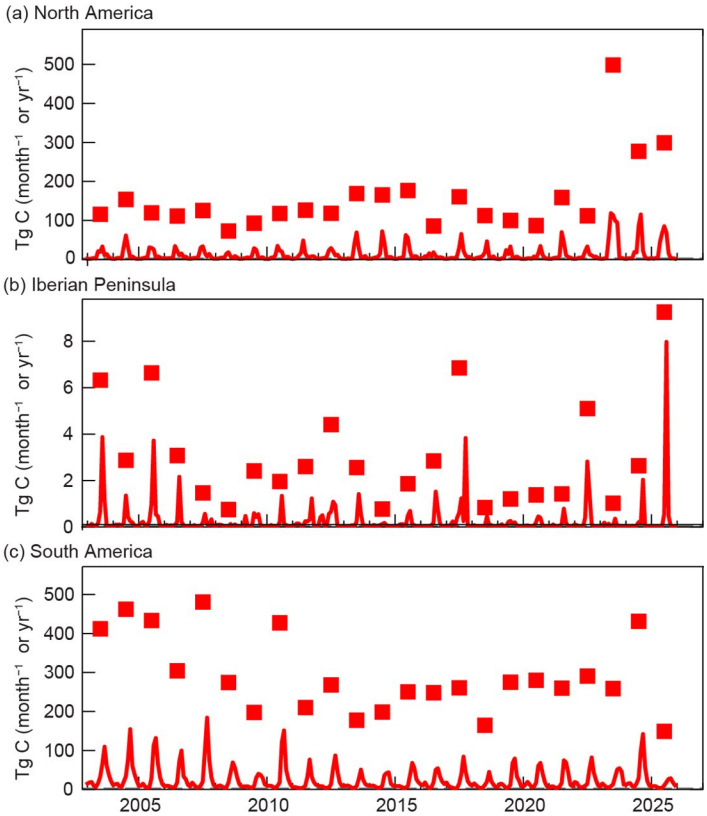

Fig. 2.85. Regional time series of monthly (lines in Tg C month^{-1}) and annual (squares in Tg C yr^{-1}) biomass burning activity in (a) North America, (b) the Iberian Peninsula, and (c) South America.

The fire activities in Asia were close to their previous lowest levels. The large range of activity in northern Asia, including Siberia, illustrates the influence of regional wildfire–climate interactions in combination with large-scale trends (He et al. 2025).

Table 2.14. Annual continental-scale biomass burning budgets in terms of carbon emission (Tg C yr^{-1}) from GFAS4HTAP based on Copernicus Atmosphere Monitoring Service Global Fire Assimilation System version 1.2 (CAMS-GFASv1.2).

Region	Area	2003–20 Mean value (Range) [Tg C yr^{-1}]	2025 Value [Tg C yr^{-1}]	2025 Anomaly (%) [Tg C yr^{-1} (%)]
Global	90°N–90°S, 0°–360°E	1878 (1414–2274)	1310	–569 (–30%)
North America	75°N–30°N, 190°E–330°E	123 (73–177)	299	+177 (+144%)
Central America	30°N–13°N, 190°E–330°E	31 (20–52)	23	–7 (–24%)
South America	13°N–60°S, 190°E–330°E	296 (165–481)	149	–147 (–50%)
Europe and the Mediterranean	75°N–30°N, 330°E–60E	26 (13–47)	24	–2 (–6%)
Northern Hemisphere Africa	30°N–0°, 330°E–60°E	365 (249–446)	215	–150 (–41%)
Southern Hemisphere Africa	0°–35°S, 330°E–60°E	481 (326–558)	305	–176 (–37%)
Northern Asia	75°N–30°N, 60°E–190°E	207 (104–468)	107	–100 (–48%)
Southern Asia	30°N–10°N, 60°E–190°E	115 (66–159)	57	–58 (–50%)
Tropical Asia	10°N–10°S, 60°E–190°E	92 (9–347)	10	–83 (–90%)
Australia	10°S–50°S, 60°E–190°E	142 (58–291)	120	–22 (–16%)
Iberian Peninsula	43°N–35°N, 350°E–2°E	3 (1–7)	9	+6 (+228%)

Generally decreased fire activity in Australia led to an overall decrease by ~16% compared to 2003–20, although notably increased wildfire emissions occurred in some tropical regions of the country between September and November.

GFAS is operated by the Copernicus Atmosphere Monitoring Service (CAMS) to produce global fire emission estimates in near-real time (Kaiser et al. 2012). It is based on the MODIS Fire Radiative Power products (Giglio et al. 2016). Here, we use the biomass combustion rate of Version 1.2 with custom processing of 9–14 August 2024 and December 2025, and subsequent carbon emission calculation for Whaley et al. 2025 (Kaiser et al. 2025). The time series in Plate 1.1b also puts GFAS in the context of GFED4s, which is primarily based on burnt area observation and dates to 1997 (van der Werf et al. 2017).

4. PHENOLOGY OF PRIMARY PRODUCERS

—D. L. Hemming, O. Anneville, Y. Aono, T. Crimmins, N. Estrella, R. Holliday, S.-I. Matsuzaki, A. Menzel, I. Mrekaj, J. O'Keefe, A. D. Richardson, J. Rozkošný, T. Rutishauser, R. Shinohara, S. J. Thackeray, and A. Marshall

Vegetation phenology, "the rhythm of the seasons", is a prominent dynamic process in Earth's bioclimate system (Hassan et al. 2024). While climate is a major driver of many phenological events, different species, ecosystems and phenology metrics vary greatly in their response to climate. Some records in this section show coherent regional responses consistent with climate variations, while others indicate more complex interactions.

PhenoCam (http://phenocam.nau.edu/) is a network of over 900 automated digital cameras monitoring phenological changes in various ecosystems around the world (Richardson 2019; Seyednasrollah et al. 2019). PhenoCam indicators of start of season (SOSPC) and end of season (EOSPC) were estimated (Table 2.15) along with ground observations of red oak (SOSGO, EOSGO) in Harvard Forest, a deciduous forest in Massachusetts in the United States (Richardson and O'Keefe 2009; O'Keefe and VanScoy 2024), and from red oak observations across the northeastern United States contributed to Nature's Notebook (SOSNN, EOSNN), the USA-National Phenology Network (USA-NPN) monitoring platform (Rosemartin et al. 2014; Crimmins et al. 2022). Interannual variations in the start and end of season at Harvard Forest are broadly consistent with larger-scale data from USA-NPN's Nature's Notebook program (Figs. 2.86a,b; Table 2.15).

Table 2.15. Day of year (DOY, equivalent to Julian day) and date of start of season (SOS), end of season (EOS) and full bloom date (FBD; cherry tree observations only) for land phenology records in USA (Harvard; PhenoCam, red oak, and USA National Phenology Network (USA-NPN, mean covering northeastern USA), Europe oak records (Germany, Slovakia, and United Kingdom), and Japan (native cherry tree observations in Japan). The baseline period is 2000–20 for all records except Harvard (PhenoCam, red oak), and USA-NPN, which have baseline periods of 2011–20. The growing season length for 2025 and the baseline are calculated as EOS minus SOS or FBD as appropriate for the record. Negative/positive values represent earlier/later dates for 2025 relative to the baseline. Cells marked with a dash signify that the data are not available.

Location / Record	SOS/FBD 2025 (doy, date)	SOS/FBD Baseline (doy, date)	SOS/FBD Difference 2025 – Baseline (days)	EOS 2025 (doy, date)	EOS Baseline (doy, date)	EOS Difference 2025 – Baseline (days)	Growing Season EOS – SOS 2025 (days)	Growing Season EOS – SOS Baseline Mean (days)
Harvard PhenoCam	118 28 Apr	126 5 May	–8	291 18 Oct	294 20 Oct	–3	173	168
Harvard Red oak	124 4 May	128 7 May	–4	292 19 Oct	293 19 Oct	–1	168	165
USA-NPN	117 27 Apr	125 4 May	–8	256 13 Sep	276 2 Oct	–20	139	151
Germany	111 21 Apr	118 28 Apr	–7	309 8 Nov	310 6 Nov	–1	198	192
Slovakia	113 23 Apr	116 26 Apr	–3	291 18 Oct	291 18 Oct	0	178	175
UK	102 12 Apr	114 24 Apr	–12	332 28 Nov	334 30 Nov	–2	230	220
Japan	95 4 Apr	97 6 Apr	–2	—	—	—	—	—

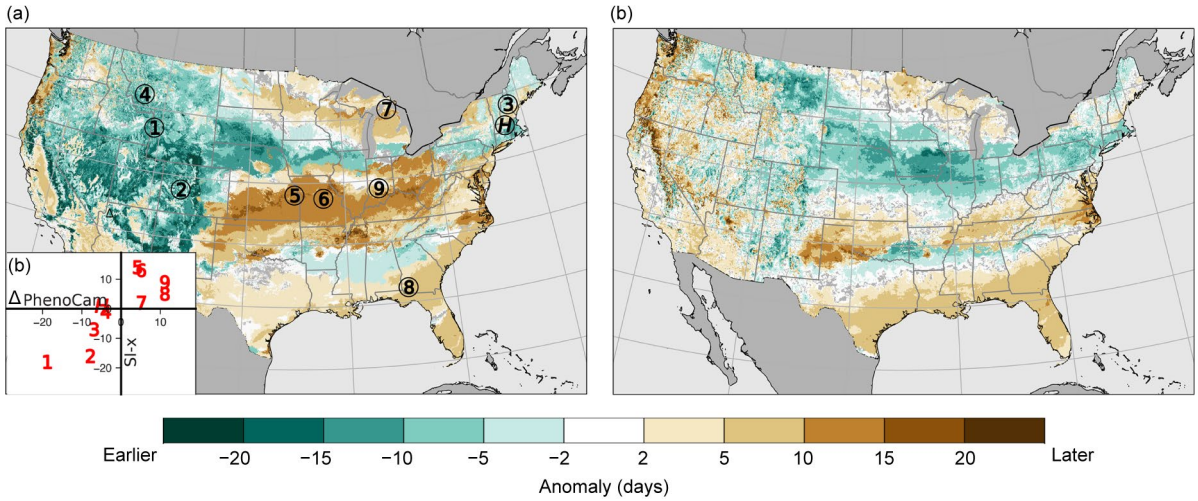

Fig. 2.86. 2025 "first leaf" date anomalies across the United States for 2025 relative to (a) 2024 and (c) the 2011–20 baseline, estimated using the USA National Phenological Network (USA-NPN) extended Spring Index (SI-x) model. (Source: USA-NPN data; https://www.usanpn.org/data.) Negative (green) values show earlier first leaf and positive (brown) values are later estimates for 2025. First leaf SI-x anomalies are generally consistent with start of season PhenoCam (SOSPC) anomalies at the 10 selected sites highlighted in (a): 1) National Elk Refuge, Wyoming, grassland; 2) Snodgrass Mountain, Colorado, deciduous forest; 3) Bartlett Experimental Forest, New Hampshire, deciduous forest; 4) Butte, Montana, grassland; 5) University of Kansas Field Station, prairie; 6) Missouri Ozarks AmeriFlux Site; mixed forest; 7) University of Michigan Biological Station, deciduous forest; 8) Flint River, Georgia, deciduous forest; 9) Morgan Monroe State Forest, Indiana; 10) Harvard Forest, Massachusetts, deciduous forest. The scatter plot (b, inset in [a]) shows PhenoCam date anomalies on the x axis, and first leaf SI-x date anomalies on the y axis (Deming regression, y = 1.2±0.3x + 0.8±2.3, r^2 = 0.71).

In 2025, SOSPC (EOSPC), SOSGO (EOSGO) and SOSNN (EOSNN) were 8 (3), 4 (2), and 8 (20) days earlier, respectively than the 2011–20 baseline (Table 2.15). The growing season length (GSL) for USA-NPN was 139 days, 12 days shorter than the baseline, and a few days later in 2025 for the other two records. There is generally a strong agreement between the dates of SOS and EOS for the PhenoCam and ground observations (Fig. 2.87).

The USA-NPN's extended Spring Index (SI-x) predicts the first leaf of lilac and honeysuckle (Schwartz et al. 2013; Crimmins et al. 2017) driven by air temperature, with anomalously warm winter/spring weather leading to earlier predicted onset dates, and vice versa. The first half of 2025 experienced an early-January extreme cold arctic blast and heavy snow across the southeastern United States, a warm February across southwestern states, and record-warm March temperatures across the midwestern and northeastern United States. The alternating warm and cold in early spring led to a "stop-start" progression towards first leaf, manifesting as horizontal banding in spring on "first leaf" maps (Figs. 2.86a,b). First leaf in 2025 was later across eastern and central USA and earlier across the west compared with 2024. In contrast, compared with the baseline, first leaf in 2025 was early across most of north central and northeastern United States, and late across the south central and southeastern portion of the country (Figs. 2.86a,b).

Start- and end-of-season indicators for native oak trees (*Quercus robur* or *Quercus petraea*) at European sites in Germany, Netherlands (note 2025 is missing), Slovakia, and the United Kingdom are represented by observations of first leaf (SOS) and leaf fall or bare tree (EOS; Table 2.15; Figs. 2.87c,d). They are strongly influenced by spring and autumn/winter temperatures (Menzel et al. 2020). Compared to the 2000–20 baseline, 2025 SOS (EOS) dates in Germany, Slovakia, and the United Kingdom were earlier (later) by 7 (1), 3 (0), and 12 (2) days, respectively (Table 2.15). The earlier SOS (earliest on record for United Kingdom) dates resulted from generally warmer-than-normal temperatures across Europe (see section 7f), EOS dates and climate conditions were similar to the baseline, except for a severe October frost event in Slovakia. These records showed 3–10 days longer GSL than the baseline.

In Kyoto, Japan, full bloom dates (FBD) for native cherry tree (*Prunus jamasakura*) in 2025 were the same as in 2024; two days earlier than the baseline (2000–20 mean; Table 2.15; Fig. 2.87e). Annual FBDs have been recorded since 812 AD (Aono and Kazui 2008), and for the Arashiyama district of Kyoto, they are recorded in newspapers and on websites from daily observations by railway passengers at train stations.

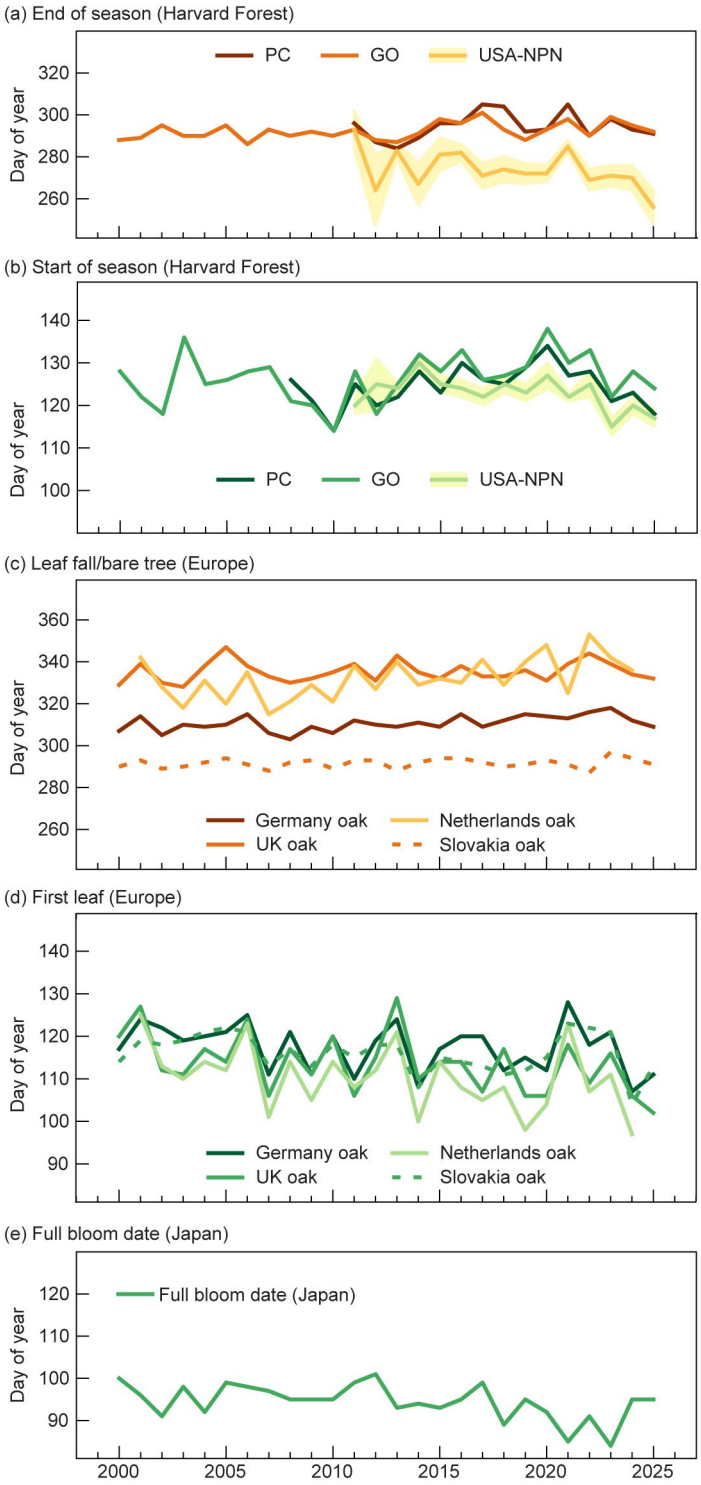

Fig. 2.87. Day of year of spring (green shades) and autumn (orange and yellow) vegetation phenology indicators for: (a),(b) Harvard Forest, Massachusetts, derived from PhenoCam (PC), ground observations (GO) of red oak (*Quercus rubra*), and the USA-National Phenology Network (USA-NPN) regional-scale means of red oak observations (calculated across the northeastern states of Pennsylvania, New Jersey, New York, Connecticut, Rhode Island, Massachusetts, Vermont, New Hampshire, and Maine, with ±1 std. dev. error shaded); (c),(d) Germany, United Kingdom, Netherlands (no data for 2025), and Slovakia mean of native oak observations (*Quercus robur* or *Quercus petraea*), and (e) full bloom date observations of native cherry trees (*Prunus jamasakura*) in Kyoto (Arashiyama district), Japan.

Lake water concentrations of the photosynthetic pigment chlorophyll-*a* were available to estimate spring phytoplankton phenology, in eight Northern Hemisphere lakes in 2025 (Fig. 2.88). The seasonal timing was estimated

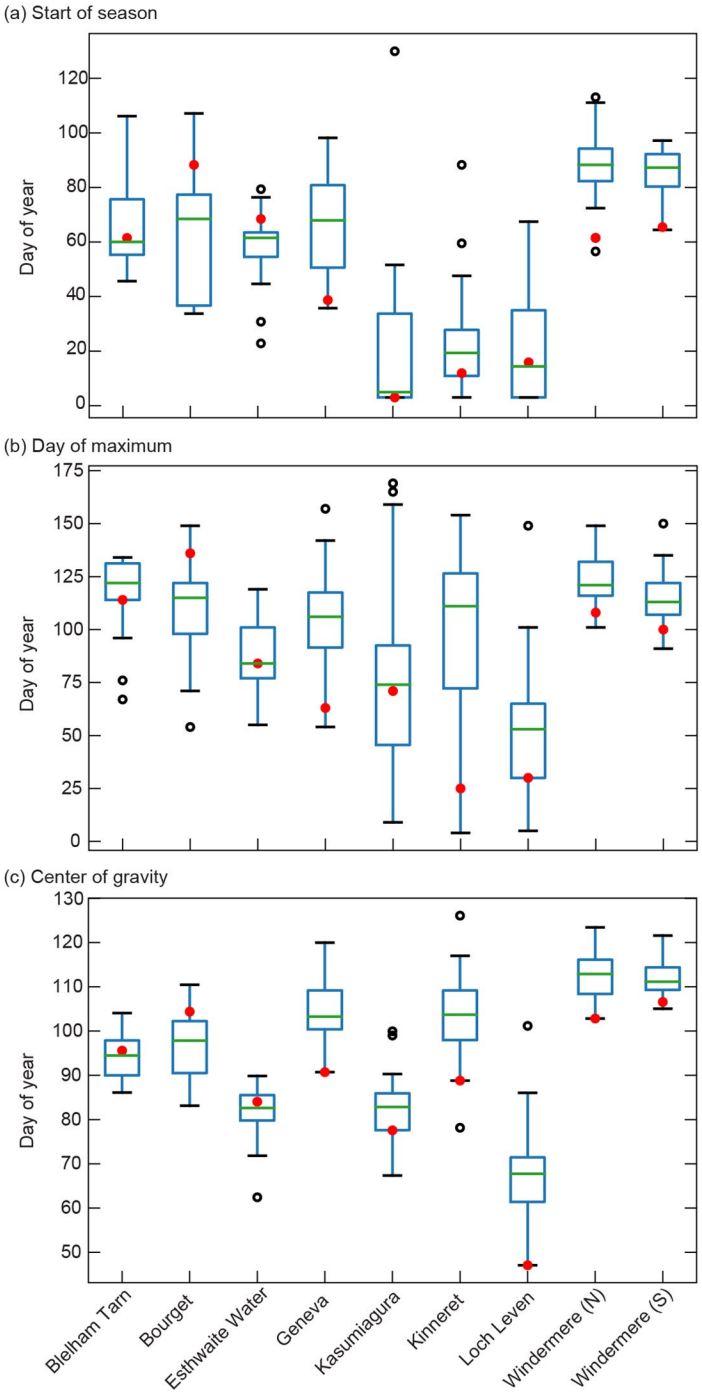

Fig. 2.88. Phenological metrics based on lake chlorophyll-*a* concentrations, as a proxy of phytoplankton biomass: (a) start of season, (b) day of maximum, and (c) center of gravity. Boxplots show variation during the 2000–20 baseline period, and red dots show 2025 values. The nine lakes are in the Northern Hemisphere (Blelham Tarn, United Kingdom; Bourget, France; Esthwaite Water, United Kingdom; Geneva, France/Switzerland; Kasumigaura, Japan; Kinneret, Israel; Loch Leven, United Kingdom; and the north and south basins of Windermere, United Kingdom).

for SOS lakes (SOSL; Park et al. 2016), day of maximum concentration (DOML), and center of gravity (COGL), which estimates the mid-point of the plankton bloom (Edwards and Richardson 2004). The lake basins showed great interannual variation and mixed phenological behavior in 2025 relative to the 2000–20 baseline. The DOML and COGL occurred earlier than the baseline median for over half of the lakes—six and five of eight, respectively—whereas no consistent pattern was observed for SOSL (four earlier and four later than the baseline median).

5. VEGETATION OPTICAL DEPTH

—R.-M. Zotta, D. D. Kovács, R. De Jeu, and W. Dorigo

Vegetation optical depth (VOD) is estimated from satellite-based passive microwave observations and describes how strongly vegetation attenuates radiation emitted or reflected by the Earth's surface. Because this attenuation depends on both plant water status and canopy structure, VOD is used as a proxy for vegetation water content (VWC) and vegetation density. VOD is useful for a range of applications, including monitoring vegetation condition (Moesinger et al. 2022; Feldman et al. 2024). Positive VOD anomalies generally reflect above-average vegetation growth or development. Negative anomalies indicate stressed or less developed vegetation, with reduced VWC relative to typical conditions, due to physiological stress, lower biomass, or both.

In 2025, the Northern Hemisphere VOD anomalies were comparable to those in 2024 (Fig. 2.92 from Zotta et al. 2025; Figs. 2.89, 2.90). By contrast, in the Southern Hemisphere, where the El Niño–Southern Oscillation (ENSO) strongly modulates vegetation dynamics (Bastos et al. 2013; Martens et al. 2017), VOD increased relative to 2024 (Figs. 2.90, 2.91), reflecting the transition from cool neutral ENSO conditions to a weak La Niña in August–October.

Long-term patterns linked to land-use change remained evident in 2025 (Plate 2.1ao; Zotta et al. 2025). Below-average VOD persisted in regions including northern Mongolia, Bolivia, Paraguay, and Brazil, consistent with the effects of deforestation and land degradation (Song et al. 2018). In contrast, above-average VOD in parts of India and northeastern China is consistent with intensified agricultural activity and reforestation efforts, respectively (Song et al. 2018).

Higher VOD relative to 2024 was seen across several regions, including southern Africa, parts of the Sahel, Europe, and sections of the central and northern Plains in North America (Fig. 2.91). The most prominent positive patterns are seen in southern Africa, consistent with observed precipitation increase patterns (section 2d5). VOD also increased across parts of the Sahel (Fig. 2.91), which is consistent with above-normal rainfall (section 2d5) and

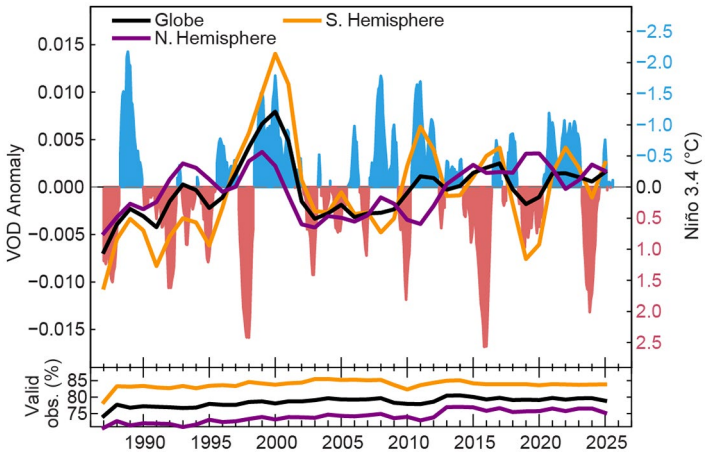

Fig. 2.89. Yearly vegetation optical depth (VOD) anomaly averages computed from the 1991–2020 climatology and Niño-3.4 index. The Niño-3.4 index tracks the state of the El Niño–Southern oscillation (ENSO). A negative Niño-3.4 index corresponds to a negative ENSO phase. (Source: VOD Climate Archive version 2 [VODCA v2]; NOAA Physical Sciences laboratory [https://psl.noaa.gov/data/timeseries/month/DS/Nino34].)

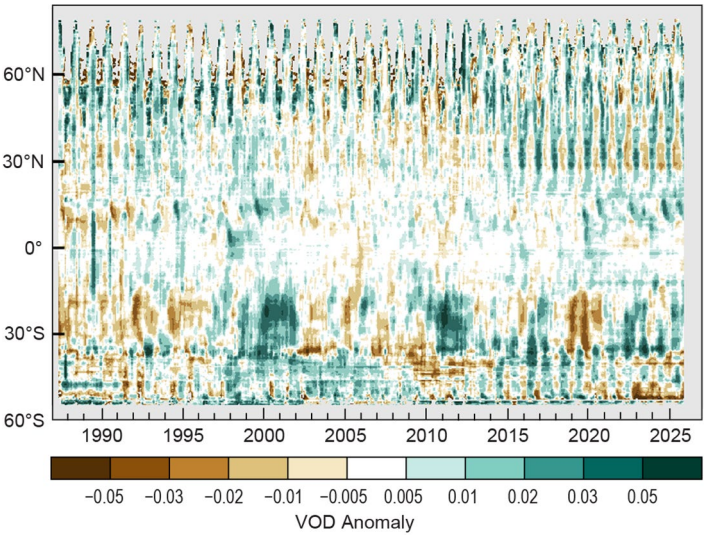

Fig. 2.90. Time–latitude diagram of monthly vegetation optical depth (VOD) anomalies (1991–2020 base period). Data are masked where no retrieval is possible or where the quality of the retrieval is not assured and flagged due to frozen soil, radio frequency interference, etc. (Source: VOD Climate Archive version 2 [VODCA v2].)

supported by regional monitoring indicating above-average biomass production across large areas of the Sahel in 2025 (AGRHYMET RCC-WAS 2025; European Commission 2025a).

In Europe, monthly VOD anomalies were largely positive through June (Appendix Fig. A2.19) but shifted negative in July–September, consistent with drought monitoring reports indicating a transition from favorable spring vegetation conditions to more widespread summer vegetation stress (Ben Aoun et al. 2025; European Commission 2025b). In North America, above-average VOD is evident across much of the central and northern Plains (Plate 2.1ao), consistent with wetter-than-average conditions in this region during 2025 (section 2d5; see also section 7b).

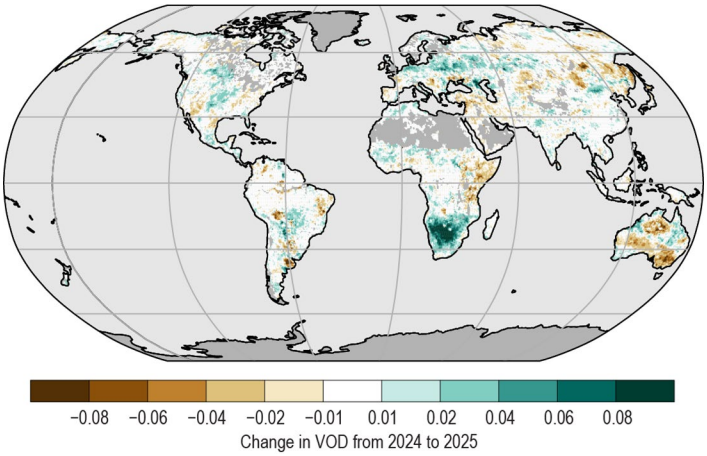

Fig. 2.91. Difference in average CXKu vegetation optical depth (VOD) from 2024 to 2025. Brown (green) colors indicate areas where VOD in 2025 were lower (higher) than in 2024. (Source: Vegetation Optical Depth Climate Archive version 2 [VODCAv2].)

Compared to 2024, prominent decreases in VOD can be observed in the eastern Horn of Africa, southern Australia, and parts of the Russian Far East, Korean Peninsula, and Ukraine (Fig. 2.91). Negative VOD anomalies across the eastern Horn of Africa (Fig. 2.91) are consistent with the failure of the October–December short rains across much of Somalia, eastern Kenya, and southern Ethiopia (section 2d5) and with above-average temperatures (section 2b1). Drought alerts reported widespread negative impacts of lacking precipitation on vegetation conditions (section 2d12; ICPAC 2025). Similarly, VOD decreases over southern Australia in 2025 (Fig. 2.91) align with below-average rainfall across much of the temperate south and below-average soil moisture over large parts of southern Australia (section 2d11; BOM 2026), conditions that would reduce VWC and, hence, VOD, while northeastern Australia showed contrasting positive anomalies consistent with above-average rainfall (section 2d5). Negative VOD changes over the Russian Far East and the Korean Peninsula (Fig. 2.91) coincide with arid, windy, spring conditions and extensive wildfire activity in 2025 (Copernicus 2026; section 2h3). Negative VOD anomalies over Ukraine are consistent with rainfall-driven soil-moisture shortages (section 2d11; European Commission 2025c).

The VOD data are from the Vegetation Optical Depth Climate Archive version 2 (VODCA v2; Zotta et al. 2024a,b). VODCA harmonizes VOD estimates retrieved with the Land Parameter Retrieval Model (Meesters et al. 2005; van der Schalie et al. 2017; Zotta et al. 2026) from multiple space-borne microwave radiometers, including the Special Sensor Microwave/Imager (SSM/I), Tropical Rainfall Measuring Mission (TRMM), WindSat, Advanced Microwave Scanning Radiometer for the Earth Observing System (AMSR-E), and Advanced Microwave Scanning Radiometer 2 (AMSR2), into a consistent long-term record. Here, we used the VODCA CXKu product, which merges C-, X-, and Ku-band observations and provides daily data at 0.25° spatial resolution.

Acknowledgments

a Introduction

R. J. H. D. and J. B. were supported by the Met Office Hadley Centre Climate Programme funded by U.K. Department for Science, Innovation and Technology (DSIT). GM is supported by funding from NOAA's Climate Program Office. The statements, findings, conclusions, and recommendations are those of the author(s) and do not necessarily reflect the views of NOAA or the U.S. Department of Commerce. We thank six anonymous reviews, and Emily Carlisle, John Kennedy, David Parker, Jessica Poulton, and Reuben Urraca for their detailed and insightful comments which helped improve this chapter. We also thank Ayaka Bunno, Atsushi Goto, and Ishibumi Nozomi (Japanese Meteorological Association [JMA]), Mike Bosilovich (NASA), and Julien Nicolas (European Centre for Medium-Range Weather Forecasts [ECMWF]), for their assistance with the reanalysis data used in this chapter. Many of the figures in this chapter were produced with the help of the Matplotlib v3.7.2 (Hunter et al. 2007), Iris v3.7.0 (Hattersley et al. 2023), and Cartopy v0.21.1 (Elson et al. 2022) packages.

b2 Lake Surface Temperature

Lake surface water temperatures from satellite data have been generated within the Climate Change Initiative Lakes project funded by the European Space Agency (ESA) (4000125030/18/I-NB) with adaptation funded by the E.U. Copernicus Climate Change Service (C3S) programme and extensions by the U.K. Earth Observation Climate Information Service (EOCIS) project (NE/X019071/1). Part of the in-situ data used for the validation of the satellite data and for this report have kindly been made publicly available by the Fisheries and Oceans Canada (FOC), the National Data Buoy Center from NOAA, the Hungarian Meteorological Office, the Upper Great Lakes Observing System (UGLOS), the North Temperate Lakes Long-Term Ecological Research (NTL-LTER). The authors gratefully acknowledge the late Alon Rimmer for always supplying data for Lake Kinneret.

b3 Night Marine Air Temperature

R. C., J. S., S. C., and E. K. were supported by the Natural Environmental Research Council through National Capability funding (AtlantiS: NE/Y005589/1).

b4 Surface Temperature Extremes

R. J. H. D. was supported by the Met Office Hadley Centre Climate Programme funded by DSIT.

b5 Tropospheric Temperature

Work performed by Stephen Po-Chedley at Lawrence Livermore National Laboratory (LLNL) was performed under the auspices of the DOE under Contract DE-AC52-07NA27344 (IM LLNL-JRNL-2016371).

b7 Equivalent Temperature

T. M. and T. W. were supported by grant MR/X03450X/1. M. B. was supported by grant EP/Y027868/1.

c1 Permafrost Temperature and Active-Layer Thickness

The Circumpolar Active Layer Monitoring (CALM) program is funded by the NSF project (2412865). Northern Canadian data collection and analysis is supported by Natural Resources Canada. The Svalbard permafrost data is part of SIOS, the Svalbard Integrated Earth Observing System. The Swiss Permafrost Monitoring Network (PERMOS) is financially supported by MeteoSwiss (in the framework of the Global Climate Observing System [GCOS] Switzerland), the Federal Office for the Environment and the Swiss Academy of Sciences and acknowledges the contribution of its partner institutions. The French PermaFRANCE network is financially supported by the Observatoire des Sciences de l'Univers Grenoble and the French Research Infrastructure OZCAR. The Chinese Permafrost Monitoring Network is financially supported by the Chinese National Science Foundation (41931180) and the Cryosphere Research Station on Qinghai-Xizang

Plateau (CAS). Research on James Ross Island was supported by the Czech Antarctic Research Programme and MEYS project (LL2505).

c2 Alpine Glaciers

The World Glacier Monitoring Service mass balance data set is the primary data used in the section.

c3 Lake Ice Cover

We thank Al and Sue Stangel, Alexander Mills, Ann LaLiberte, Beth Kohlman, BJ Bauer, Bob Katzenberger, Bonny Pederson, Brendan Wiltse, Brian D. Neill, Brian Vlach, John Barten, Rick Brascke, Calvin Maurer, Carl C. Nelson, Carol Wendorf, Cheryl and Dorothy Zingler, Clare and Dan Shirley, Craig Hillman, Dale Robertson, Dan Brumm, Daniel L. Anderson, Dave & Lynda J. Urshan, David Kahan, Don Pierson, Don McClanathan, Donald & Mureil Fornasiere, Doug Fitzgerald, Douglas Pierzina, Dr. Neal D. Mundahl, Duane Williams & Edie Evarts, Duncan A. Brown, Earl Cook, Facundo Scordo, Fred Buckley, Gary Teigen, Gay Alberts Ruby, Gene Cooper, George Grevich, Greg Sass, Holly Waterfield, Huaxia Yao, James and Sharon Fenner, James W. Danielson, Jan Henning L'Abée-Lund, Jeff Goelzer, Jeffrey G. Lowe, Jerry Evans, Jerry Sondreal, Jim and Judy Daugherty, Joe Jenkins, Joel Rasmussen, John and Catherine Bart, John Maier, Jonathan Ross, Dan Drumm, Martin Kainz, Joy Krubsack, Kay and Rich Rezanka, Kay Olson, Kay Wepfer, Kay Wepfer, Ken Blumenfeld, Larry & Marlene Lotto, Larry Peterson, Lars Rudstam, Lolita Olson, Lowell Dague, Marge Kellor, Mark Biller, Mark Holland, Mark J. and Rosie Peters, Mary Jane Dillingham, Mary Lou Fry, Randell Fry, Merja Pulkkanen, Michael Allen, Michael Bradley, Michael Kolecheck, Michael Traufler, Mickey and Dennis Chick, Mike, Jeff, and Thomm Backus, Molly Hibbard, Morris & Doris Whiting, Mr. & Mrs. Jay R. Mackie, Mr. & Mrs. William Bergersen, Mrs. Gale Wheeler, Mrs. Kathy Elhard, Mrs. Margery Armstrong, Myron Hagelstrom, Nancy Putnam, Nancy Steenport, Patricia Bebak, Patrick Collins, Paulette Janssen, Pete Boulay, Peter Bearup, Rachel Dahlke, Raymond (Joe) Jenkins, Richard L. Tamke, Rock Anderson, Ron Pabich, Ronald Jones, Ross Swain, Sally Ketchen, Sandra Anderson, Scott Schoepp, Sogee Spinner, Sharon Natzel, Shin-Ichiro Matsuzaki, Susan Reineking, Susan Verhaalen, Tana McNutt, Theodore (Ted) Peters, Thomas Sommerfeldt, Tom Stangl, Travis Campbell, Virgil Luehrs, Walt & Nancy Quillinan, Walter R. Brown, Water Dahlke III, William and Brenda Jones, and William Hanson, for their dedication and efforts to collect and share in situ ice phenological records with us.

c4 Northern Hemisphere Continental Snow Cover Extent

This work is funded in part by NOAA's Climate Data Record (CDR) Program at the National Centers for Environmental Information (NCEI).

d1 Surface Humidity

Kate Willett was supported by the Met Office Hadley Centre Climate Programme funded by DSIT.

d2 Humid-Heat Extremes

Kate Willett was funded by the U.K.–China Research & Innovation Partnership Fund through the Met Office Climate Science for Service Partnership (CSSP) China under the International Science Partnerships Fund (ISPF). Cassandra Rogers is supported by funding from the Australian Climate Service.

d6 Land surface Precipitation Extremes

Kwesi A. Quagraine is supported by the National Center for Atmospheric Research, which is a major facility sponsored by the U.S. National Science Foundation (NSF) under Cooperative Agreement No. 1852977.

d7 Cloudiness

Clouds and the Earth's Radiant Energy System (CERES) Energy Balanced and Filled (EBAF) data were obtained from the NASA Langley Research Center CERES ordering tool at https://ceres.larc.nasa.gov/data/.

d9 River Discharge

The Global Flood Awareness System (GloFAS) is part of the Copernicus Emergency Management Service, which is funded by the European Union Space Program.

d10 Groundwater and Terrestrial Water Storage

Work on the Groundwater and Terrestrial Water Storage section was funded by NASA's Gravity Recovery and Climate Experiment Follow-On (GRACE-FO) Science Team. GRACE and GRACE-FO were jointly developed and operated by NASA, German Aerospace Center (DLR), and the Geo-Research (GFZ) Helmholtz Centre for Geosciences. A portion of this research was carried out at the Jet Propulsion Laboratory, California Institute of Technology, under a contract with the National Aeronautics and Space Administration (80NM0018D0004).

d11 Soil Moisture

This study uses satellite soil moisture observations from the Copernicus Climate Change Service (C3S) Climate Data Store (CDS): Dorigo, W., Preimesberger, W., Lems, J., Frederikse, T., Dostalova, A. (2026): Soil moisture gridded data from 1978 to present, v202505.
https://cds.climate.copernicus.eu/dataset/satellite-soil-moisture?tab=overview, doi:10.24381/cds.d7782f18.

d12 Monitoring Drought using the Self Calibrating Palmer Drought Severity Index

Jonathan Barichivich was supported by the European Research Council (ERC) under the Horizon Europe research and innovation programme (ERC-starting grant CATES, No. 101043214). Andrew Friedman received funding from U.K. National Centre for Atmospheric Science (NCAS).

d13 Global Land Evaporation

D. G. M. acknowledges support from the European Research Council (ERC) under grant agreement No. 101088405 (HEAT). H. E. B. is supported by the King Abdullah University of Science and Technology (KAUST).

e2 Surface Winds

C. A. M. was supported by Spanish National Research Council (CSIC), University of Valencia (UV), Generalitat Valenciana (GVA) and funded by PROMETEO Grant International Global Change Laboratory (LINCGLOBAL)-CSIC ref. LINCG24042, and Interdisciplinary Thematic Platform for Climate and Climate Services (PTI-CLIMA).

R. J. H. D. was supported by the Met Office Hadley Centre Climate Programme funded by U.K. Department for Science, Innovation and Technology (DSIT). L.R. was supported by NASA Ocean Vector Wind Science Team (grant 80NSSC23K0984). Z. Z. was supported by the National Natural Science Foundation of China (grant 42071022). P. A. M. is supported by the WISTERA (Wind Stilling and Energy in Europe and Asia) project under the umbrella of the Climate Science for Service Partnership China (CSSP China), as part of the International Science Partnerships Fund (ISPF), delivered by the Met Office.

e4 Lightning

The work of M. F. was sponsored by the Royal Society (U.K.) grant NMG/R1/180252 and the Natural Environment Research Council (NERC; U.K.) under grants NE/L012669/1 and NE/H024921/1. E. W. is supported for studies on global circuit response to climate change from the Physical and Dynamic Meteorology Program at the National Science Foundation (NSF) on grant no. 6942679. C. P. was supported in his lightning research by the Israel Science Foundation (ISF) grant 2701/17, and the Ministry of Energy grant No. 220-17-002. S. G. is retired and contributed in-kind. The authors wish to thank Stephanie Stevenson from the NOAA Ocean Prediction Center, in College Park, Maryland, U.S., for information on Hurricane Melissa, and Peter Thorne at Maynooth University in Ireland and the European Centre for Medium Range Weather Forecast (ECMWF) for suggesting and initiating this work and for recommending that lightning be made an essential climate variable. Thunder hour data provided by Earth Networks, in collaboration with WWLLN, are available at http://thunderhours.earthnetworks.com. GLM data are available from https://www.earthdata.nasa.gov/data/instruments/glm/data-access-tools. Robbie Berg of the National Hurricane Center provided surface pressure observations for Hurricane Melissa.

f1 Earth Radiation Budget at Top-of-Atmosphere

This research has been supported by the NASA CERES project supported under the Earth Radiation Budget Continuity (ERBC) program with Dr. David Considine (NASA HQ) serving as the program scientist. The resources of the NASA Langley Atmospheric Sciences Data Center are utilized in collaboration with ERBC to process the various data products required as input to EBAF Ed4.2.1. We further acknowledge the efforts of Walt Miller and Pam Mlynczak of the CERES team who monitor CERES data production and make the data available via the CERES subsetter tool.

g2 Ozone-Depleting Gases

This research was supported in part by NOAA cooperative agreement NA22OAR4320151, for the Cooperative Institute for Earth System Research and Data Science (CIESRDS). The statements, findings, conclusions, and recommendations are those of the author(s) and do not necessarily reflect the views of NOAA or the U.S. Department of Commerce.

g4 Tropospheric Ozone

The NOAA NESDIS LEO Innovation Program supported the contributions by O. R. Cooper and K.-L. Chang. K.-L. Chang was also supported by NOAA cooperative agreement NA22OAR4320151. P. Effertz was supported by NOAA cooperative agreement NA22OAR4320151. Funding for J. Ziemke for this research was provided in part by NASA NNH14ZDA001N-DSCOVR, NASA NASA Suomi National Polar-orbiting Partnership (SNPP) and Joint Polar Satellite System (JPSS) Satellites Standard Products. A portion of this research was carried out at the Jet Propulsion Laboratory (JPL), California Institute of Technology, under a contract with NASA (80NM0018D0004).

g5 Stratospheric Aerosols

Lidar observations at the Haute-Provence Observatory (OHP) are funded by the French National Centre for Scientific Research/National Institute of Sciences of the Universe (CNRS/INSU) and the National Centre for Space Studies (CNES). S. Khaykin's work is supported by National Agency for Research (ANR) PyroStrat 21-CE01- 335 0007-01 project. We thank Christine David, Alain Hauchecorne, S. Godin-Beekmann, Julien Jumelet, Philippe Keckhut (LATMOS) and the lidar station operators for their contributions to long-term monitoring of stratospheric aerosol at OHP. Lidar observations at Lauder are funded in part by the GOSAT (Greenhouse gases Observing SATellite) project. We thank Richard Querel (ESNZ), Ben Liley (ESNZ), Osamu Uchino (MRI), Tomohiro Nagai (MRI), and Yushitaka Jin (NIES) for their contributions to long-term monitoring of stratospheric aerosol at Lauder. G. Taha's work is supported by the National Aeronautics and Space Administration, Earth Science Division grant 80NSSC23K1037.

g6 Stratospheric Ozone

The OSIRIS Team would like to thank the Canadian Space Agency for their generous support over the past thirty years. Without their commitment the OSIRIS data record would not exist.

Michelle Santee's work at the Jet Propulsion Laboratory, California Institute of Technology, was carried out under a contract with the National Aeronautics and Space Administration (80NM0018D0004).

Mark Weber, Carlo Arosio, Alexei Rozanov, and Victoria Sofieva are grateful for financial support from the European Space Agency (ESA) via the OREGANO Project (Ozone Recovery from Merged Observational Data and Model Analysis; Contract No. 4000137112/22/I-AG). Lidar and ozone sondes observations at OHP are funded by CNRS/INSU and CNES. The work of S. Godin-Beekmann and Gerard Ancellet (ozone sondes) is supported by ANR ALPHA-O3 ANR-22-CE01-0007-02. Stacey Frith is supported by NASA programmatic fund "Longterm ozone trends" (project no. WBS 479717).

g7 Stratospheric Water Vapor

Inclusion of SAGE III/ISS products into SWOOSH are supported by NASA grant 80NSSC26K0049.

g8 Carbon Monoxide

The Copernicus Atmosphere Monitoring Service is funded by the European Union.

h2 Terrestrial Vegetation Dynamics

The authors thank the providers of the remote sensing dataset needed to perform this analysis and the Joint Research Centre's (JRC) Big Data Analytics Platform (BDAP) (https://doi.org/10.5281/zenodo.10214201).

h3 Biomass Burning

This work was funded by the E.U.'s Copernicus programme through contract CAMS2_64_bis_NILU.

h4 Phenology of Primary Producers

Debbie Hemming and Rebecca Holliday acknowledge support from the Met Office Hadley Centre Climate Programme funded by DSIT. Andrew Richardson acknowledges support from the National Science Foundation LTER (award 1832210) and John O'Keefe also acknowledges support from the National Science Foundation (NSF) through the LTER (award 1832210) program. Nature's Calendar (Woodland Trust) in the UK thanks all its volunteer recorders and support from players of People's Postcode Lottery. Theresa Crimmins and the USA-NPN acknowledge support from the National Science Foundation through the Division of Biological Infrastructure (award 2404760), the U.S. Fish and Wildlife Service (agreements F16AC01075 and F19AC00168) and the U.S. Geological Survey (G14AC00405 and G18AC00135). The U.S. National Phenology Network thanks the many participants contributing phenology observations to Nature's Notebook. De Natuurkalender (Nature's Calendar) program in the Netherlands thanks all the volunteers and school children in the GLOBE program for their many observations. Slovak Hydrometeorological Institute thanks all its volunteer observers for participating in the phenological observation program. De Natuurkalender (Nature's Calendar) program in the Netherlands thanks all the volunteers and school children in the GLOBE program for their many observations, these data were provided by A. J. H. van Vliet up to 2024. Orlane Anneville acknowledges support from INRAE. Stephen Thackeray thanks Oded Liran, Heidrun Feuchtmayr, Shin-Ichiro Matsuzaki, Ryuichiro Shinohara, Jan-Erik Thrane, Linda May and all field and lab workers associated with the provision of the lake chlorophyll-*a* data. We acknowledge funding from Vassdragsforbundet for Mjøsa med tilløpselver (https://www.vassdragsforbundet.no/om-oss/). Windermere, Blelham Tarn, Esthwaite Water, and Loch Leven monitoring were supported by Natural Environment Research Council award numbers NE/R016429/1 and NE/Y006208/1 as part of the U.K. Status, Change and Projections of the Environment and U.K. Challenges Programmes delivering National Capability. Data for Lakes Geneva and Bourget were contributed by the Observatory of LAkes (OLA), © Observation and Experimentation System for Environmental Research (SOERE) OLA-IS, AnaEE-France, INRAE of Thonon-les-Bains, International Commission for the Protection of the Waters of Lake Geneva (CIPEL), Intercommunity Committee for the Sanitation of Lake Bourget (CISALB).

h5 Vegetation Optical Depth

R. M. Zotta and W. Dorigo acknowledge the TU Wien Wissenschaftspreis 2015, a personal grant awarded to W. Dorigo. We also acknowledge support from the ESA CCI and the C3S programmes.

Appendix 1: Acronyms

AAO	Antarctic Oscillation
AATSR	Advanced Along Track Scanning Radiometer
ACE	accumulated cyclone energy
ALT	active-layer thickness
AMSR-E	Advanced Microwave Scanning Radiometer for the Earth Observing System
AMSR2	Advanced Microwave Scanning Radiometer 2
AMSU	advanced microwave sounding unit
ANY	Australian New Year
AOD	aerosol optical depth
ASCAT	Advanced Scatterometer
ASR	absorbed solar radiation
C3S	Copernicus Climate Change Service
CALM	Circumpolar Active Layer Monitoring
CAMS	Copernicus Atmosphere Monitoring Service
CAMSRA	Copernicus Atmosphere Monitoring Service reanalysis
CAS	Chinese Academy of Sciences
CCI	Climate Change Initiative
CCMI	Chemistry-Climate Model Initiative
CDR	climate data record
CDS	Climate Data Store
CERES	Clouds and the Earth's Radiant Energy System
CFC	chlorofluorocarbon
CH_3CCl_3	methyl chloroform
CH_4	methane
CLASSnmat	Climate Linked Atlantic Sector Science Night Marine Air Temperature
CO	carbon monoxide
CO_2	carbon dioxide
COGL	center of gravity
Cp	specific heat capacity of air
CPTT	cold-point tropopause temperature
CR	control run
CrIS	Cross-Track Infrared Sounder
CRUTEM5	Climatic Research Unit temperature version 5
DOE	U.S. Department of Energy
DOML	day of maximum concentration
DU	Dobson unit
EBAF	Energy Balanced and Filled
ECMWF	European Center for Medium-Range Weather Forecasts
ECV	essential climate variable
EESC	equivalent effective stratospheric chlorine
ENSO	El Niño–Southern Oscillation
ENTLN	Earth Networks Total Lightning Network
EOCIS	Earth Observation Climate Information Service
EOS	end of season
ER	extinction ratio
ERB	Earth radiation budget
ERBC	Earth Radiation Budget Continuity
ERC	European Research Council
ERF	effective radiative forcing

ESA	European Space Agency
ESSIC	Earth System Science Interdisciplinary Center
EUMETSAT	European Organisation for the Exploitation of Meteorological Satellites
FAPAR	fraction of absorbed photosynthetically active radiation
FBD	full bloom date
FP	frost point
GCOS	Global Climate Observing System
GFAS	Global Fire Assimilation System
GFED4S	Global Fire Emissions Database version 4.1
GHCN	Global Historical Climatology Network
GHCNDEX	Global Historical Climatology Network Daily Extremes
GHCNh	Global Historical Climatology Network hourly
GHG	greenhouse gas
GISS	Goddard Institute for Space Studies
GISTEMP	Goddard Institute for Space Studies Surface Temperature Analysis
GLEAM	Global Land Evaporation Amsterdam Model
GLM	Geostationary Lightning Mapper
GloFASv4	Global Flood Awareness System version 4
GloSSAC	Global Space-based Stratospheric Aerosol Climatology
GMI	Global Precipitation Measurement Microwave Imager
GNSS	Global Navigation Satellite System
GO	ground observation
GOES	Geostationary Operational Environmental Satellite
GOSAT	Greenhouse gases Observing SATellite
GOZCARDS	Global Ozone Chemistry and Related Trace Gas Data records for the Stratosphere
GPCC	Global Precipitation Climatology Centre
GPCP	Global Precipitation Climatology Project
GRACE	Gravity Recovery and Climate Experiment
GRACE-FO	Gravity Recovery and Climate Experiment Follow-On
GREALM	Global Reservoirs and Lakes Monitor
GSL	Global Snow Lab
GWP	global warming potential
HadCRUT5	Met Office Hadley Centre/Climatic Research Unit Temperature version 5
HadEX3	Met Office Hadley Centre Extremes Dataset version 3
HadISDH	Met Office Hadley Centre Integrated Surface Dataset of Humidity
HadISDH.blend	Met Office Hadley Centre Integrated Surface Dataset of Humidity over Land and Ocean
HadISDH.extremes	Met Office Hadley Centre Integrated Surface Dataset of Humidity Extremes
HadISDH.land	Met Office Hadley Centre Integrated Surface Dataset of Humidity over Land
HadISDH.marine	Met Office Hadley Centre Integrated Surface Dataset of Humidity over Ocean
HadSST4	Met Office Hadley Centre Sea Surface Temperature Dataset version 4
HCFC	hydrochlorofluorocarbon
HFC	hydrofluorocarbon
HIRS	High-resolution Infrared Radiation Sounder
ICESat-2	Ice, Cloud, and land Elevation Satellite 2
IGBP	International Geosphere Biosphere Programme
IOD	Indian Ocean dipole
ISS	International Space Station
JMA	Japanese Meteorological Agency
JPL	Jet Propulsion Laboratory
JPSS	Joint Polar Satellite System
JRA-3Q	Japanese Reanalysis for Three Quarters of a Century
JRC	Joint Research Centre

LEO	Office of Low Earth Orbit
LINCGLOBAL	International Global Change Laboratory
LiO3s	Stratospheric Ozone Lidar at Haute-Provence Observatory
LLGHG	long-lived greenhouse gases
LOWESS	locally weighted scatterplot smoothing
LST	land surface temperature
LSWT	lake surface water temperature
LTA	Lidar Temperature Aerosol
LTT	lower-tropospheric temperature
LWCRE	longwave cloud radiative effect
MACCity	Monitoring Atmospheric Composition and Climate and CityZen
MCM	million cubic meters
MERIS	Medium Resolution Imaging Spectrometer
MetOp	Meteorological Operational satellite
MLO	Mauna Loa Observatory
MLS	Microwave Limb Sounder
MODIS	Moderate Resolution Imaging Spectroradiometer
MOPITT	Measurement of Pollution in the Troposphere
MSLP	mean sea-level pressure
MSU	Microwave Sounding Unit
MWR	Microwave Radiometer
N_2O	nitrous oxide
NA	North America
NAO	North Atlantic Oscillation
NCEI	National Centers for Environmental Information
NCEP	National Centers for Environmental Prediction
NDACC	Network for the Detection for Stratospheric Change
NERC	Natural Environmental Research Council
NH	Northern Hemisphere
NIWA	National Institute of Water and Atmospheric Research
NMAT	night marine air temperature
NO_2	nitrogen dioxide
NOAAGlobalTemp	NOAA Merged Land Ocean Global Surface Temperature Analysis
NOx	nitrogen oxides
NRT	near-real-time
NSAT	near-surface air temperature
NTL-LTER	North Temperate Lakes Long-Term Ecological Research
ODGI	Ozone Depleting Gas Index
ODS	ozone-depleting substance
OH	hydroxyl radical
OHP	Haute-Provence Observatory
OLA	Observatory of alpine LAkes
OLCI	Ocean and Land Colour Instrument
OLR	outgoing longwave radiation
OMI	Ozone Monitoring Instrument
OMPS	Ozone Mapping and Profiler Suite
OMPS-LP	Ozone Mapping and Profiler Suite Limb Profiler
OMPS-NP	Ozone Mapping and Profiler Suite Nadir Profile
ONI	Oceanic Niño Index
OZCAR	Critical Zone Observatories: Research and Application
PANs	Acyl peroxynitrates
PC	PhenoCam

PDO	Pacific Decadal Oscillation
PERMOS	Swiss Permafrost Monitoring Network
PM2.5	particulate matter
PNA	Pacific–North American
PNE	Pacific Northwest Event
POPS	Portable Optical Particle Spectrometer
PSA	Pacific–South American
PWO	Panboreal Wildfire Outbreak
pyroCb	pyrocumulonimbus
QBO	quasi-biennial oscillation
QTP	Qinghai–Tibet Plateau
QuickSCAT	Quick Scatterometer
RATPAC	Radiosonde Atmospheric Temperature Products for Assessing Climate
RCP	Representation Concentration Pathways
RFaci	aerosol–cloud interactions
RFari	aerosol–radiation interactions
RH	relative humidity
RSS	Remote Sensing Systems
RSW	reflected shortwave
Rx1day	one-day precipitation maximum
Rx5day	accumulated five-day precipitation maximum
SAGE III	Stratospheric Aerosol and Gas Experiment III
SAM	Southern Annular Mode
SAOD	stratospheric aerosol optical depth
SAT	surface air temperature
SBUV	Solar Backscatter Ultraviolet Radiometer
SCE	snow cover extent
SCIAMACHY	Scanning Imaging Absorption Spectrometer for Atmospheric Chartography
scPDSI	self-calibrating Palmer Drought Severity Index
SeaWiFS	Sea-Viewing Wide Field-of-View Sensor
SH	Southern Hemisphere
SI-x	Spring Index
SLSTR	Sea and Land Surface Temperature Radiometers
SLSTR-A	Sea and Land Surface Temperature Radiometer onboard the Sentinel 3A platform
SLSTR-B	Sea and Land Surface Temperature Radiometer onboard the Sentinel 3B platform
SNAO	Summer North Atlantic Oscillation
SNPP	Suomi National Polar-orbiting Partnership
SO_2	sulfur dioxide
SOI	Southern Oscillation Index
SOS	start of season
SSM/I	Special Sensor Microwave/Imager
SSMIS	Special Sensor Microwave Imager/Sounder
SST	sea surface temperature
SSU	Stratospheric Sounding Unit
SSW	sudden stratospheric warming
SW	shortwave
SWCRE	shortwave cloud radiative effect
SWOOSH	Stratospheric Water and OzOne Satellite Homogenized
T12	water vapor channel
T2	upper-tropospheric temperature
TCWV	total column water vapor
Teq	equivalent temperature

TLS	Lower-stratosphere temperatures
TMI	Tropical Rainfall Measuring Mission Microwave Imager
TOA	top-of-atmosphere
Tq	latent temperature
TRMM	Tropical Rainfall Measuring Mission
TROPOMI	Tropospheric Monitoring Instrument
TSI	total solar irradiance
TTT	tropical tropospheric temperatures
Tw	wet-bulb temperature
T_wN	minimum humid-heat intensity
TWS	terrestrial water storage
T_wX	maximum humid-heat intensity
TXx	highest annual maximum temperature
UAHNMAT	University of Alabama in Huntsville Night Marine Air Temperature
USA–NPN	USA National Phenology Network
UTH	upper tropospheric humidity
UTLS	upper troposphere/lower stratosphere
UV	University of Valencia
VIIRS	Visible Infrared Imaging Radiometer Suite
VOC	volatile organic compound
VOD	vegetation optical depth
VODCA	Vegetation Optical Depth Climate Archive
VWC	vegetation water content
WGMS	World Glacier Monitoring Service
WMO	World Meteorological Organization
WOUDC	World Ozone and Ultraviolet Radiation Data Centre
WV	water vapor

Appendix 2: Dataset Tables

Section 2b Temperature

Sub-section	General Variable or Phenomenon	Specific Dataset or Variable	Source
2b1, 2b4, 2b7	Temperature, [Near] Surface	ERA5	https://cds.climate.copernicus.eu/datasets/reanalysis-era5-single-levels-monthly-means
2b1	Temperature, [Near] Surface	HadCRUT5	https://www.metoffice.gov.uk/hadobs/hadcrut5/
2b1	Temperature, [Near] Surface	Climatic Research Unit Temperature Version 5 (CRUTEM5)	https://www.metoffice.gov.uk/hadobs/crutem5/
2b1, 2b3	Temperature, [Near] Surface	Met Office Hadley Centre Sea Surface Temperature Dataset (HadSST) Version 4	https://www.metoffice.gov.uk/hadobs/hadsst4/
2b1, 2b4, 2b7	Temperature, [Near] Surface	Japanese Reanalysis for Three Quarters of a Century (JRA-3Q)	https://www.data.jma.go.jp/jra/html/JRA-3Q/index_en.html; http://rda.ucar.edu/datasets/d640000/
2b1, 2b2	Temperature, [Near] Surface	NASA/Goddard Institute for Space Studies (GISS) Global Temperature Version 4	https://data.giss.nasa.gov/gistemp/
2b1	Temperature, [Near] Surface	NOAA/NCEI NOAAGlobalTemp	https://www.ncei.noaa.gov/products/land-based-station/noaa-global-temp
2b2	Lake Temperature	Full Lake Surface Temperature Water Dataset	https://cds.climate.copernicus.eu/datasets/satellite-lake-water-temperature
2b2	Lake Temperature	National Buoy Data Center Great Lakes Buoys	https://www.ndbc.noaa.gov/mobile/region.php?reg=great_lakes
2b2	Lake Temperature	Balaton Lakes	https://odp.met.hu/climate/observations_hungary/hourly/historical/
2b2	Lake Temperature	Canadian Lakes	https://www.meds-sdmm.dfo-mpo.gc.ca/isdm-gdsi/waves-vagues/data-donnees/index-eng.asp
2b2	Lake Temperature	Biel and Thun Lakes (Switzerland); Biwa and Mikata Lakes (Japan)	https://portal.gemstat.org/applications/public.html?publicuser=PublicUser
2b2	Lake Temperature	Trout Lake	https://doi.org/10.6073/pasta/767e476fca7bedf46d4905517854c8f7
2b2	Lake Temperature	European Space Agency (ESA) Climate Change Initiative (CCI) LAKES Lake Surface Water Temperature (LSWT) Version 2.0.2	https://catalogue.ceda.ac.uk/uuid/a07deacaffb8453e93d57ee214676304

Sub-section	General Variable or Phenomenon	Specific Dataset or Variable	Source
2b3	Nighttime Marine Air Temperature	Climate Linked Atlantic Sector Science Night Marine Air Temperature (CLASSnmat)	https://catalogue.ceda.ac.uk/uuid/5bbf48b128bd488dbb10a56111feb36a
2b3	Nighttime Marine Air Temperature	University of Alabama in Huntsville Night Marine Air Temperature (UAHNMAT) Version 1	https://www.nsstc.uah.edu/climate/; https://doi.org/10.1002/joc.6354
2b4	Temperature, [Near] Surface	MERRA-2	https://gmao.gsfc.nasa.gov/gmao-products/merra-2/
2b4	Temperature, [Near] Surface	Global Historical Climatology Network Daily Extremes (GHCNDEX)	https://www.climdex.org/
2b5	Temperature, Upper Atmosphere	ERA5	https://cds.climate.copernicus.eu/datasets/reanalysis-era5-pressure-levels-monthly-means
2b5	Temperature, Upper Atmosphere	MERRA-2	https://gmao.gsfc.nasa.gov/gmao-products/merra-2/
2b5	Temperature, Upper Atmosphere	JRA-3Q	https://www.data.jma.go.jp/jra/html/JRA-3Q/index_en.html
2b5	Temperature, Upper Atmosphere	NOAA National Environmental Satellite, Data, and Information Service (NESDIS) Center for Satellite Applications and Research (STAR) Microwave Sounding Unit (MSU) Version 5	https://www.ncei.noaa.gov/data/mean-layer-temperature-noaa/access/
2b5	Temperature, Upper Atmosphere	Radiosone Observation Correction Using Reanalyses (RAOBCORE) Radiosonde Innovation Composite Homogenization (RICH) Version 1.9	https://webdata.wolke.img.univie.ac.at/haimberger/v1.9/
2b5	Temperature, Upper Atmosphere	Radiosonde Atmospheric Temperature Products for Assessing Climate (RATPAC) A2	https://www1.ncdc.noaa.gov/pub/data/ratpac/
2b5	Temperature, Upper Atmosphere	Remote Sensing Systems (RSS) Version 4.0	https://www.remss.com/measurements/upper-air-temperature/
2b5	Temperature, Upper Atmosphere	University of Alabama in Huntsville (UAH) Microwave Sounding Unit (MSU) Version 6.1	https://www.nsstc.uah.edu/data/msu/v6.1/
2b5	Sea Surface Temperature	Pentad Relative Niño 3.4	https://psl.noaa.gov/data/timeseries/month/DS/Nino34_CPC/

Sub-section	General Variable or Phenomenon	Specific Dataset or Variable	Source
2b6	Temperature, Upper Atmosphere	Aura Microwave Limb Sounder (MLS)	https://discnrt1.gesdisc.eosdis.nasa.gov/data/Aura_MLS_NRT/ML2T_NRT.005/
2b6	Temperature, Upper Atmosphere	MLS derived Stratospheric Sounding Unit (SSU)	https://doi.org/10.5281/zenodo.17087209
2b6	Temperature, Upper Atmosphere	SSU	https://www.star.nesdis.noaa.gov/data/mscat/SSU/SSU_V2/SSU_Monthly_V2/
2b6	Temperature, Upper Atmosphere	Lower stratosphere temperature (TLS)/middle troposphere temperature (TMT)	http://wamis.gmu.edu/cdr/products.html
2b7	Equivalent Temperature, [Near] Surface	JRA-3Q	https://gdex.ucar.edu/datasets/d640002/dataaccess/
2b7	Equivalent Temperature, [Near] Surface	ERA5	https://www.ecmwf.int/en/forecasts/dataset/ecmwf-reanalysis-v5
2b8	Temperature, [Near] Surface	Centre for Environmental Data Analysis (CEDA) Archive, European Space Agency (ESA) Land Surface Temperature Climate Change Initiative (LST_cci)—Sea and Land Surface Temperature Radiometer Onboard the Sentinel-3B Platform (SLSTR-B)	https://catalogue.ceda.ac.uk/uuid/5f66a881adf846bfaad58b0e6068f0ea/
2b8	Temperature, [Near] Surface	CEDA Archive, Earth Observation Climate Information Service (EOCIS)—SLSTR-B	https://catalogue.ceda.ac.uk/uuid/fc0bc3d5887d441296091a8025f8f45d/

Section 2c Cryosphere

Sub-section	General Variable or Phenomenon	Specific Dataset or Variable	Source
2c1	Permafrost	Global Terrestrial Network for Permafrost (GTN-P)	http://gtnpdatabase.org/
2c1	Permafrost	GTN-P Global Mean Annual Ground Temperature Data for Permafrost	https://doi.org/10.1594/PANGAEA.884711
2c1	Permafrost	Permafrost Temperature at Chinese Qinghai–Tibet Plateau (QTP) Sites	https://nsidc.org/data/GGD700/versions/1

Sub-section	General Variable or Phenomenon	Specific Dataset or Variable	Source
2c1	Permafrost	Permafrost Temperature in European Mountains	https://zenodo.org/records/13628540
2c1	Permafrost	Permafrost Temperature at French Sites	https://permafrance.osug.fr
2c1	Permafrost	Permafrost Temperature at Norwegian Sites	https://cryo.met.no/
2c1	Permafrost	Permafrost Temperature at Swiss Sites (Swiss Permafrost Monitoring Network [PERMOS])	https://www.permos.ch; https://www.permos.ch/doi/permos-dataset-2026-1
2c1	Active Layer Depth	Circumpolar Active Layer Monitoring (CALM)	https://www.gwu.edu/~calm/
2c2	Glacier Mass, Area or Volume	World Glacier Monitoring Service	https://doi.org/10.5904/wgms-amce-2025-02b
2c3	Lake Ice	ERA5	https://www.ecmwf.int/en/forecasts/dataset/ecmwf-reanalysis-v5
2c3	Lake Ice	Lake Ice Clearance and Formation Data for Green Lakes Valley, 1968—Ongoing. Version 6. Environmental Data Initiative	https://doi.org/10.6073/pasta/e89a9a6984ebbcdbbc85c16d65298dd2
2c3	Lake Ice	Global Lake and River Ice Phenology Database, Version 1	https://doi.org/10.7265/N5W66HP8
2c3	Lake Ice	Mountain Lake Biology, Chemistry, Physics, and Climate Data Since 1959 at Castle Lake Version 1. Environmental Data Initiative	https://doi.org/10.6073/pasta/a8e3b81cfe5864731b29ad42506c65d7
2c3	Lake Ice	Great Lakes Annual Maximum Ice Cover (%)	https://www.glerl.noaa.gov/data/ice/
2c3	Lake Ice	Great Lakes Ice	https://www.glerl.noaa.gov/data/ice
2c3	Lake Ice	Geographic Variation and Temporal Trends in Ice Phenology in Norwegian Lakes During a Century, Dryad	https://datadryad.org/stash/dataset/doi:10.5061/dryad.bk3j9kd9x
2c3	Temperature, [Near] Surface	NASA/Goddard Institute for Space Studies (GISS) Global Temperature	https://data.giss.nasa.gov/gistemp/
2c4	Snow Properties	Northern Hemisphere (NH) Snow Cover Extent (SCE) Version 1	https://doi.org/10.7289/V5N014G9; https://www.snowcover.org

Section 2d Hydrological cycle			
Sub-section	**General Variable or Phenomenon**	**Specific Dataset or Variable**	**Source**
2d1, 2d2	Humidity, [Near] Surface	ERA5	https://www.ecmwf.int/en/forecasts/dataset/ecmwf-reanalysis-v5
2d1, 2d2	Humidity, [Near] Surface	Met Office Hadley Centre Integrated Surface Dataset of Humidity over Land (HadISDH.land.4.6.1.2024f), Met Office HadISDH over Ocean (HadISDH.marine.1.6.1.2024), Met Office HadISDH over Land and Ocean (HadISDH.blend.1.5.1.2024f), Met Office HadISDH of Humidity Extremes (HadISDH.extremes.1.2.0.2024f)	https://www.metoffice.gov.uk/hadobs/hadisdh
2d1	Humidity, [Near] Surface	Japanese Reanalysis for Three Quarters of a Century (JRA-3Q)	https://www.data.jma.go.jp/jra/html/JRA-3Q/index_en.html
2d1	Humidity, [Near] Surface	MERRA-2	https://disc.gsfc.nasa.gov/datasets/M2T1NXSLV_5.12.4/summary
2d3	Water Vapor, Total Column	ERA5	https://www.ecmwf.int/en/forecasts/dataset/ecmwf-reanalysis-v5
2d3	Water Vapor, Total Column	Global Navigation Satellite System (GNSS) Ground-Based Total Column Water Vapor	https://doi.org/10.25326/68
2d3	Water Vapor, Total Column	JRA-3Q	https://www.data.jma.go.jp/jra/html/JRA-3Q/index_en.html
2d3	Water Vapor, Total Column	MERRA-2	https://gmao.gsfc.nasa.gov/gmao-products/merra-2/
2d3	Water Vapor, Total Column	Special Sensor Microwave Imager (SSM/I)–Advanced Microwave Scanning Radiometer for Earth Observing System (AMSR-E) Ocean Total Column Water Vapor	https://www.remss.com
2d4	Humidity, Upper Atmosphere	ERA5	https://www.ecmwf.int/en/forecasts/dataset/ecmwf-reanalysis-v5
2d4	Humidity, Upper Atmosphere	High Resolution Infrared Sounder (HIRS)	https://www.ncei.noaa.gov/products/climate-data-records/ir-sounder-uth-brightness-temperature

Sub-section	General Variable or Phenomenon	Specific Dataset or Variable	Source
2d4	Temperature, Upper Atmosphere	NOAA National Environmental Satellite, Data, and Information Service (NESDIS) Center for Satellite Applications and Research (STAR) Microwave Sounding Unit (MSU) Version 5	http://wamis.gmu.edu/cdr/products.html
2d5, 2d6	Precipitation	Global Precipitation Climatology Centre (GPCC)	https://www.dwd.de/EN/ourservices/gpcc/gpcc.html
2d5	Precipitation	GPCPv3.2	https://www.ncei.noaa.gov/products/global-precipitation-climatology-project; https://rda.ucar.edu/datasets/d728008/dataaccess/
2d6	Precipitation	Met Office Hadley Centre Dataset of Extreme Indices (HadEX3) Version 3	https://www.metoffice.gov.uk/hadobs/hadex3/
2d6	Precipitation	ERA5	https://cds.climate.copernicus.eu/datasets/reanalysis-era5-single-levels
2d6	Precipitation	Global Historical Climatology Network Daily Extremes (GHCNDEX)	https://www.climdex.org
2d6	Precipitation	MERRA-2	https://gmao.gsfc.nasa.gov/gmao-products/merra-2/; https://disc.gsfc.nasa.gov/datasets/M2SMNXEDI_2/summary
2d7	Cloud properties	PATMOS-xv6.0	https://www.ncei.noaa.gov/products/climate-data-records/avhrr-hirs-cloud-properties-patmos
2d7	Cloud properties	Suomi National Polar-orbiting Partnership (SNPP) Visible Infrared Imaging Radiometer Suite (VIIRS) Cloud Properties (CLDPROP)	https://ladsweb.modaps.eosdis.nasa.gov/missions-and-measurements/products/CLDPROP_M3_VIIRS_SNPP
2d7	Cloud Properties	Clouds and the Earth's Radiant Energy System Energy Balance and Filled (CERES EBAF) Version 4.2	https://ceres.larc.nasa.gov/data/
2d8	Lake Water Storage and Level	'GloLakes' Lake and Reservoir Storage	https://doi.org/10.5194/essd-16-201-2024
2d8	Lake Water Storage and Level	Global Lakes and Reservoir Monitor (GREALM) Lake Level	https://ipad.fas.usda.gov/cropexplorer/global_reservoir/
2d8	Lake Water Storage and Level	Moderate Resolution Imaging Spectroradiometer (MODIS) Global Reservoirs and Lakes	https://modis-land.gsfc.nasa.gov/modgwr.html
2d9	River Discharge	Global Flood Awareness System Version (GloFAS) 4	https://ewds.climate.copernicus.eu/datasets/cems-glofas-historical; https://data.jrc.ec.europa.eu/dataset/68050d73-9c06-499c-a441-dc5053cb0c86

Sub-section	General Variable or Phenomenon	Specific Dataset or Variable	Source
2d9	River Discharge	ERA5	https://cds.climate.copernicus.eu/datasets/reanalysis-era5-single-levels
2d10	Groundwater and Terrestrial Water Storage	Gravity Recovery and Climate Experiment (GRACE)/GRACE Follow-On (GRACE-FO)	https://podaac.jpl.nasa.gov/dataset/TELLUS_GRAC-GRFO_MASCON_CRI_GRID_RL06.3_V4
2d11	Soil Moisture	Copernicus Climate Change Service (C3S) Version 202505 product based on the ESA Climate Change Initiative for Soil Moisture (ESA CCI SM) Version 9 Merging Algorithm	https://cds.climate.copernicus.eu/datasets/satellite-soil-moisture
2d12	Drought	Climatic Research Unit Gridded Time Series (CRU TS) 4.09	https://crudata.uea.ac.uk/cru/data/drought/
2d13	Land Evaporation	Global Land Evaporation Amsterdam Model (GLEAM)	https://www.gleam.eu/
2d13	Modes of Variability	Niño 3.4 index	https://psl.noaa.gov/data/timeseries/month/DS/Nino34

Section 2e Atmospheric circulation

Sub-section	General Variable or Phenomenon	Specific Dataset or Variable	Source
2e1, 2e3	Modes of Variability	Antarctic Oscillation (AAO)	https://www.cpc.ncep.noaa.gov/products/precip/CWlink/daily_ao_index/aao/aao.shtml
2e1	Pressure, Sea Level or Near-Surface	ERA5	https://www.ecmwf.int/en/forecasts/dataset/ecmwf-reanalysis-v5
2e2	Wind, [Near] Surface	ERA5	https://www.ecmwf.int/en/forecasts/dataset/ecmwf-reanalysis-v5
2e2	Wind, [Near] Surface	Japanese Reanalysis for Three-Quarters of a Century (JRA-3Q)	https://www.data.jma.go.jp/jra/html/JRA-3Q/index_en.html
2e2	Wind, [Near] Surface	Global Historical Climate Network hourly (GHCNh)	https://www.ncei.noaa.gov/products/global-historical-climatology-network-hourly
2e2	Wind, [Near] Surface	MERRA-2	https://gmao.gsfc.nasa.gov/gmao-products/merra-2/
2e2	Wind, [Near] Surface	Remote Sensing Systems (RSS) Merged 1-Degree Monthly Radiometer Winds	https://www.remss.com/measurements/wind/

Sub-section	General Variable or Phenomenon	Specific Dataset or Variable	Source
2e2	Wind, [Near] Surface	Remote Sensing Systems (RSS) Advanced Scatterometer (ASCAT)	https://www.remss.com/missions/ascat/
2e2	Wind, [Near] Surface	Remote Sensing Systems (RSS) QuickScat4	https://www.remss.com/missions/qscat/
2e3	Wind, [Upper Atmosphere]	Quasi-biennial Oscillation (QBO)	https://www.atmohub.kit.edu/data/singapore2024.dat; https://www.atmohub.kit.edu/807.php
2e3	Wind, [Upper Atmosphere]	ERA5 Hourly Data on Pressure Levels from 1940 to Present. Copernicus Climate Change Service (C3S) Climate Data Store (CDS)	https://cds.climate.copernicus.eu/datasets/reanalysis-era5-single-levels
2e3	Wind, [Upper Atmosphere]	MERRA-2	https://gmao.gsfc.nasa.gov/gmao-products/merra-2/
2e3	Wind, [Upper Atmosphere]	GPS Radio Occultation (GPSRO)	https://wegcwww.uni-graz.at/data-store/WEGC/OPS5.6:2021.1/
2e3	Wind, [Upper Atmosphere]	Japanese Reanalysis for Three-Quarters of a Century (JRA-3Q)	https://www.data.jma.go.jp/jra/html/JRA-3Q/index_en.html
2e4	Lightning	Earth Networks Total Lightning Network (ENTLN)	https://www.earthnetworks.com/product/lightning-data/
2e4	Lighting	Vaisala's Global Lightning Detection Network (GLD360)	https://www.vaisala.com/en/products/systems/lightning/gld360
2e4	Lighting	University of Washington's World-Wide Lightning Location Network (WWLLN)	https://wwlln.net/

Section 2f Earth's radiation budget

Sub-section	General Variable or Phenomenon	Specific Dataset or Variable	Source
2f1	TOA Earth Radiation Budget	Clouds and the Earth's Radiant Energy System (CERES) Energy Balanced and Filled (EBAF) Version 4.2.1	https://ceres-tool.larc.nasa.gov/ord-tool/jsp/EBAFTOA421Selection.jsp
2f1	TOA Earth Radiation Budget	CERES Fast Longwave And Shortwave Radiative Fluxes (FLASHflux) Version 4C	https://ceres-tool.larc.nasa.gov/ord-tool/jsp/FLASH_TISASelection.jsp

Sub-section	General Variable or Phenomenon	Specific Dataset or Variable	Source
2f1	TOA Earth Radiation Budget	Community-Consensus Total Solar Irradiance (TSI) Composit	https://spot.colorado.edu/~koppg/TSI/TSI_Composite-SIST.txt
2f2	Solar Transmission, Apparent	Mauna Loa Observatory	https://www.esrl.noaa.gov/gmd/webdata/grad/mloapt/mauna_loa_transmission.dat
2f2	Aerosol Optical Depth	NASA's Moderate Resolution Imaging Spectroradiometer (MODIS)	https://earthobservatory.nasa.gov/global-maps/MODAL2_M_AER_OD
2f2	Stratospheric Aerosol Loadings	Balloon Network for Stratospheric Aerosol Observations (BalNeO)	https://science.larc.nasa.gov/balneo/
2f2	Stratospheric Aerosol Loadings	Balloon Baseline Stratospheric Aerosol Profiles (B2SAP)	https://csl.noaa.gov/projects/b2sap/pops.php?loc=HIH

Section 2g Atmospheric composition

Sub-section	General Variable or Phenomenon	Specific Dataset or Variable	Source
2g1	Trace Gases	Atmospheric Gas Trends	https://gml.noaa.gov/ccgg/trends/
2g1	Trace Gases	Global Greenhouse Gas Reference Network	https://gml.noaa.gov/ccgg/about.html
2g1	Trace Gases	Atmospheric Greenhouse Gas Index (AGGI)	https://gml.noaa.gov/ccgg/trends/
2g2	Trace Gases	Halocarbons and Other Atmospheric Trace Species	https://gml.noaa.gov/hats/data.html
2g2	Trace Gases	Ozone-Depleting Gas Index (ODGI)	https://gml.noaa.gov/odgi/
2g3	Aerosols	Copernicus Atmosphere Monitoring Service Reanalysis (CAMSRA)	https://www.ecmwf.int/en/research/climate-reanalysis/cams-reanalysis
2g4	Ozone, Surface	NOAA Global Monitoring Laboratory	https://gml.noaa.gov/aftp/data/ozwv/SurfaceOzone/
2g4	Ozone, Tropospheric	Ozone Monitoring Instrument (OMI)/ Microwave Limb Sounder (MLS)	https://acdb-ext.gsfc.nasa.gov/Data_services/cloud_slice/; https://avdc.gsfc.nasa.gov/

Sub-section	General Variable or Phenomenon	Specific Dataset or Variable	Source
2g5	Stratospheric Aerosols	Haute-Provence Observatory (OHP) Lidar Temperature Aerosol (LTA) Lidar	https://www-air.larc.nasa.gov/missions/ndacc/data.html?station=haute.provence/ames/lidar/
2g5	Stratospheric Aerosols	Stratospheric Ozone Lidar at Haute-Provence Observatory (LiO3S)	https://www-air.larc.nasa.gov/missions/ndacc/data.html?station=haute.provence/ames/lidar/
2g5	Stratospheric Aerosols	Lauder Aerosol Lidar	https://www-air.larc.nasa.gov/missions/ndacc/data.html?station=lauder/ames/lidar/
2g5	Stratospheric Aerosols	Stratospheric Aerosol and Gas Experiment III (SAGE III) Version 6	https://asdc.larc.nasa.gov/project/SAGE%20III-ISS/g3bssp_6.0
2g5	Stratospheric Aerosols	Global Space-based Stratospheric Aerosol Climatology (GloSSAC) Version 2	https://asdc.larc.nasa.gov/project/GloSSAC
2g5	Stratospheric Aerosols	Ozone Mapping and Profiler Suite Limb Profiler (OMPS-LP) Version 2.1	https://snpp-omps.gesdisc.eosdis.nasa.gov/data/NOAA21_OMPS_Level2/OMPS_N21_LP_L2_AER_DAILY.1.0/2024
2g6	Ozone, Total Column and Stratospheric	Atmospheric Composition Satellite Application Facility (AC-SAF) GOME-2 gridded ozone profiles	https://acsaf.org/datarecords/ohp.php
2g6	Ozone, Total Column and Stratospheric	Chemistry-Climate Model Initiative (CCMI)-2022 Model Runs	https://blogs.reading.ac.uk/ccmi/ccmi-2022/
2g6	Ozone, Total Column and Stratospheric	Global Ozone Chemistry and Related Trace Gas Data Records (GOZCARDS) Ozone Profiles	https://disc.gsfc.nasa.gov/datasets/GozMmlpO3_1/summary
2g6	Ozone, Total Column and Stratospheric	Global Ozone Monitoring Experiment (GOME)/Scanning Imaging Absorption Spectrometer for Atmospheric Cartography (SCIAMACHY)/GOME2 (GSG) Merged Total Ozone	https://www.iup.uni-bremen.de/UVSAT/data/wfdoas/
2g6	Ozone, Total Column and Stratospheric	GOME/SCIAMACHY/GOME2 (GTO) Merged Total Ozone	https://atmos.eoc.dlr.de/app/products/gto-ecv
2g6	Ozone, Total Column and Stratospheric	Multi Sensor Reanalysis (MSR-2) of Total Ozone	https://www.temis.nl/protocols/O3global.html

Sub-section	General Variable or Phenomenon	Specific Dataset or Variable	Source
2g6	Ozone, Total Column and Stratospheric	NASA Backscatter Ultraviolet Radiometer (BUV)/Solar Backscatter Ultraviolet Radiometer (SBUV)/Ozone Mapping and Profiler Suite (OMPS) Version 8.7 (MOD) Merged Ozone	https://acd-ext.gsfc.nasa.gov/Data_services/merged/
2g6	Ozone, Total Column and Stratospheric	Network for the Detection of Atmospheric Composition Change (NDACC) Lidar, Microwave, and Fourier Transform Infrared Spectroscopy (FTIR)	https://www-air.larc.nasa.gov/missions/ndacc
2g6	Ozone, Total Column and Stratospheric	NOAA ozone sondes	https://www.temis.nl/protocols/O3global.html
2g6	Ozone, Total Column and Stratospheric	NOAA SBUV V8.6 OMPS V4r1 Cohesive Dataset (COH)	https://ftp.cpc.ncep.noaa.gov/SBUV_CDR/
2g6	Ozone, Total Column and Stratospheric	SAGE-Climate Change Initiative (CCI)-OMPS	https://climate.esa.int/en/projects/ozone/data
2g6	Ozone, Total Column and Stratospheric	SAGE/Origins, Spectral Interpretation, Resource Identification, and Security (OSIRIS)	https://doi.org/10.5194/amt-11-489-2018; https://research-groups.usask.ca/osiris/
2g6	Ozone, Total Column and Stratospheric	SAGE-SCIA-OMPS	https://doi.org/10.5194/amt-2018-275; https://www.iup.uni-bremen.de/DataRequest/
2g6	Ozone, Total Column and Stratospheric	Southern Hemisphere Additional Ozone Sondes (SHADOZ)	https://tropo.gsfc.nasa.gov/shadoz/
2g6	Ozone, Total Column and Stratospheric	Stratospheric Water and Ozone Satellite Homogenized (SWOOSH)	https://csl.noaa.gov/groups/csl8/swoosh/
2g6	Ozone, Total Column and Stratospheric	UMKEHR ground-based ozone profiles	https://gml.noaa.gov/aftp/ozwv/DobsonUmkehr/Optimized/Monthly_Means/
2g7	Stratospheric Water Vapor	The Aura Microwave Limb Sounder Version 5.0 Data, as Merged Into SWOOSH	https://csl.noaa.gov/groups/csl8/swoosh/
2g7	Tropopause Temperature	MERRA-2	https://gmao.gsfc.nasa.gov/gmao-products/merra-2/

Sub-section	General Variable or Phenomenon	Specific Dataset or Variable	Source
2g7	Stratospheric Water Vapor	NOAA Frostpoint Hygrometer (FPH)	https://gml.noaa.gov/aftp/data/ozwv/WaterVapor/
2g8	Trace Gases	Copernicus Atmosphere Monitoring Service Reanalysis (CAMSRA) for Carbon Monoxide	https://ads.atmosphere.copernicus.eu/datasets/cams-global-radiative-forcing-auxilliary-variables

Section 2h Land surface properties

Sub-section	General Variable or Phenomenon	Specific Dataset or Variable	Source
2h1	Albedo	Moderate Resolution Imaging Spectroradiometer (MODIS)/Terra+Aqua Bidirectional Reflectance Distribution Function (BDRF)/Albedo Albedo Daily L3 Global 0.05 Deg Climate Modeling Grid (CMG) Version 061	https://www.earthdata.nasa.gov/data/catalog/lpcloud-mcd43c3-061
2h1	Albedo	VIIRS VNP43C3 Collection 1.0	https://www.earthdata.nasa.gov/data/catalog/lpcloud-vnp09cmg-002
2h2	Fraction of Absorbed Photosynthetically Active Radiation (FAPAR)	Joint Research Centre (JRC) Two-Stream Inversion Package (TIP) MODIS	https://fapar.jrc.ec.europa.eu
2h2	FAPAR	Medium Resolution Imaging Spectrometer (MERIS)	https://doi.org/10.5270/EN1-vqoj1gs
2h2	FAPAR	Sea-Viewing Wide Field-of-View Sensor (SeaWIFS) FAPAR	https://fapar.jrc.ec.europa.eu/
2h2	FAPAR	Ocean and Land Colour Instrument (OLCI)	https://dataspace.copernicus.eu/
2h3	Biomass, Greenness or Burning	Global Fire Assimilation System Version (GFAS) 1.2	https://ads.atmosphere.copernicus.eu/cdsapp#!/dataset/cams-global-fire-emissions-gfas v1.4, available upon request
2h3	Biomass, Greenness or Burning	GFAS4HTAP	https://doi.org/10.5281/zenodo.13753451
2h4	Phenology	USA-National Phenology Network (NPN) Phenology Data	https://www.usanpn.org/data/observational

Sub-section	General Variable or Phenomenon	Specific Dataset or Variable	Source
2h4	Phenology	USA-National Phenology Network (NPN) Spring Index Raster Data Products	https://data.usanpn.org/geoserver-request-builder/
2h4	Phenology	German Oak Phenology Data	https://opendata.dwd.de/
2h4	Phenology	Harvard Forest	https://harvardforest1.fas.harvard.edu/exist/apps/datasets/showData.html?id=hf003
2h4	Phenology	Natures Calendar	https://naturescalendar.woodlandtrust.org.uk/
2h4	Phenology	PhenoCam	https://phenocam.sr.unh.edu
2h4	Phenology	UK Cumbrian Lakes Data	https://catalogue.ceh.ac.uk/documents/bf30d6aa-345a-4771-8417-ffbcf8c08c28/
2h4	Phenology	UK Loch Leven	https://catalogue.ceh.ac.uk/documents/ac973b0d-2c99-4e00-8931-22aa0881006d
2h4	Phenology	Dutch Oak Phenology Data	https://www.natuurkalender.nl/
2h4	Phenology	Lakes Geneva and Bourget Data	https://si-ola.inrae.fr/si_lacs/login.jsf
2h5	Vegetation Optical Depth	Global Long-term Microwave Vegetation Optical Depth Climate Archive Version 2 (VODCAv2)	https://researchdata.tuwien.ac.at/records/t74ty-tcx62
2h5	Modes of Variability	Niño 3.4 Index	https://psl.noaa.gov/data/timeseries/month/DS/Nino34

Appendix 3: Supplemental Materials

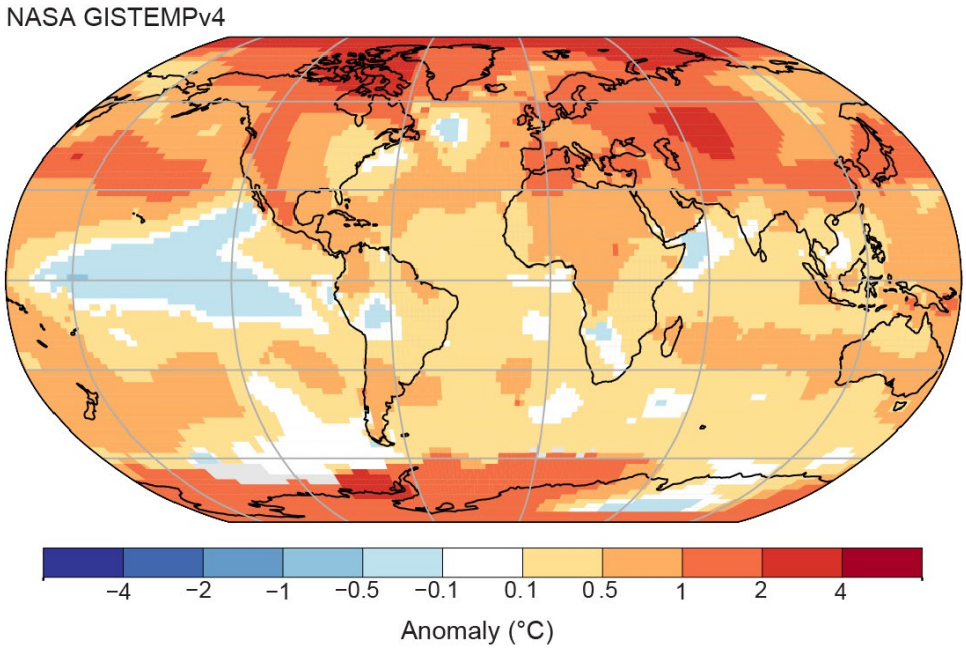

Fig. A2.1. Global surface temperature anomalies in 2025 (°C). (Source: NASA Goddard Institute for Space Studies Surface Temperature Analysis version 4 [GISTEMPv4].)

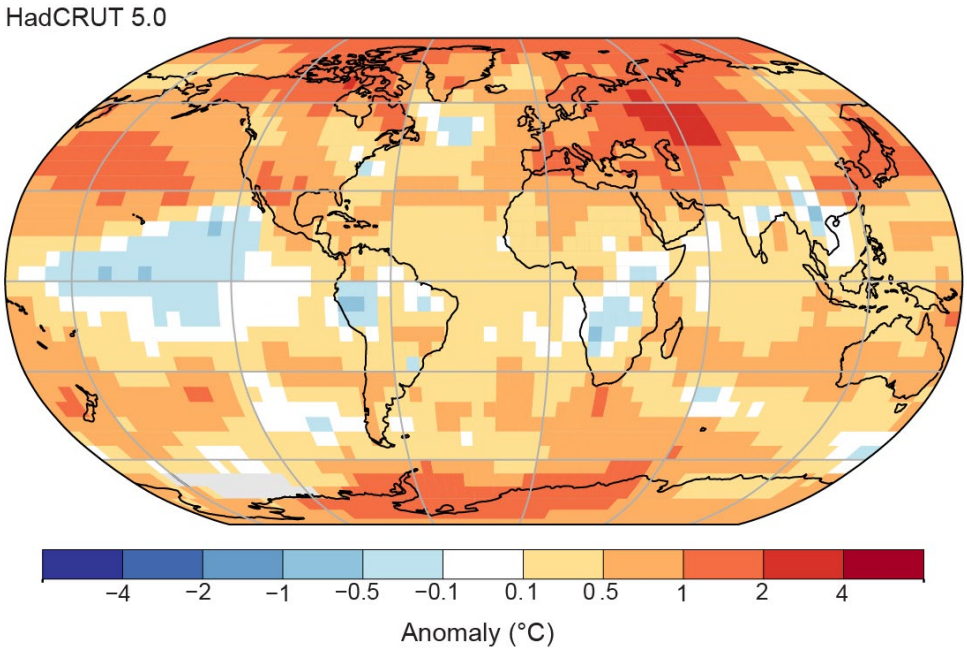

Fig. A2.2. Global surface temperature anomalies in 2025 (°C). (Source: HadCRUT5.0.)

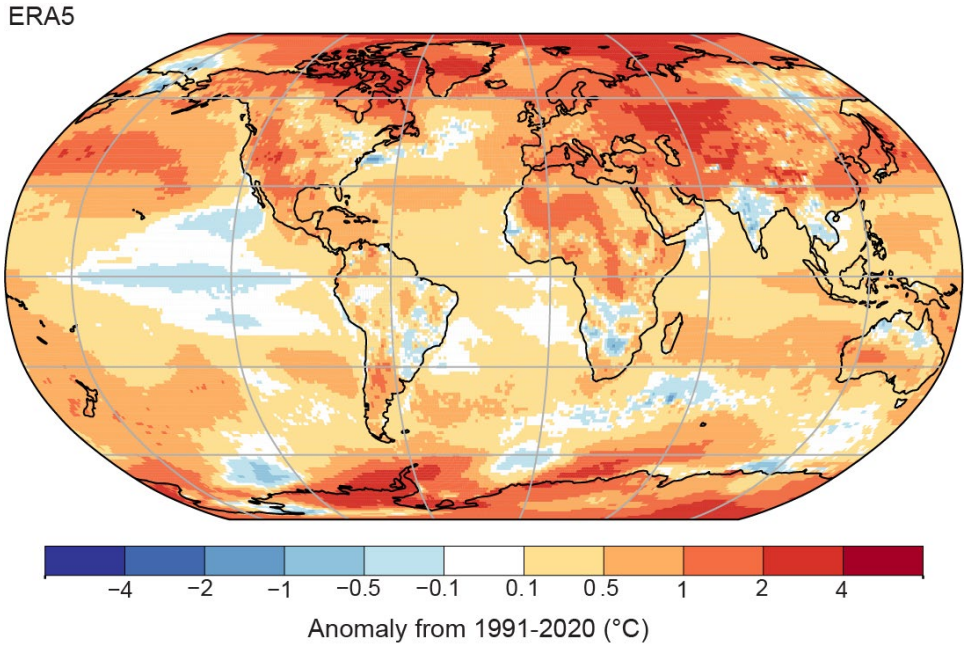

Fig. A2.3. Global surface temperature anomalies in 2025 (°C). (Source: ERA5.)

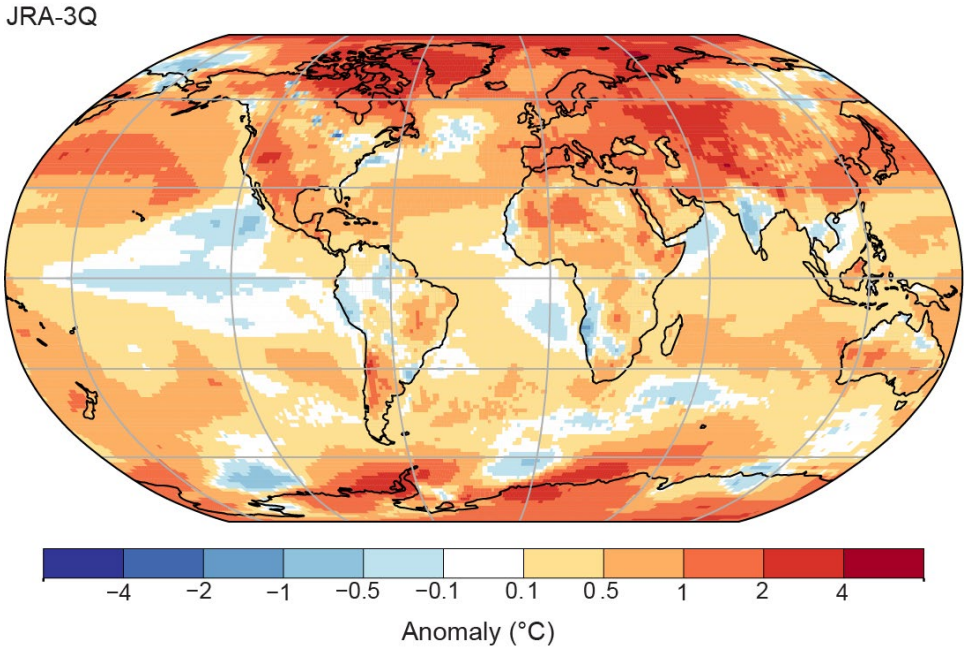

Fig. A2.4. Global surface temperature anomalies in 2025 (°C). (Source: Japanese Reanalysis for Three Quarters of a Century [JRA-3Q].)

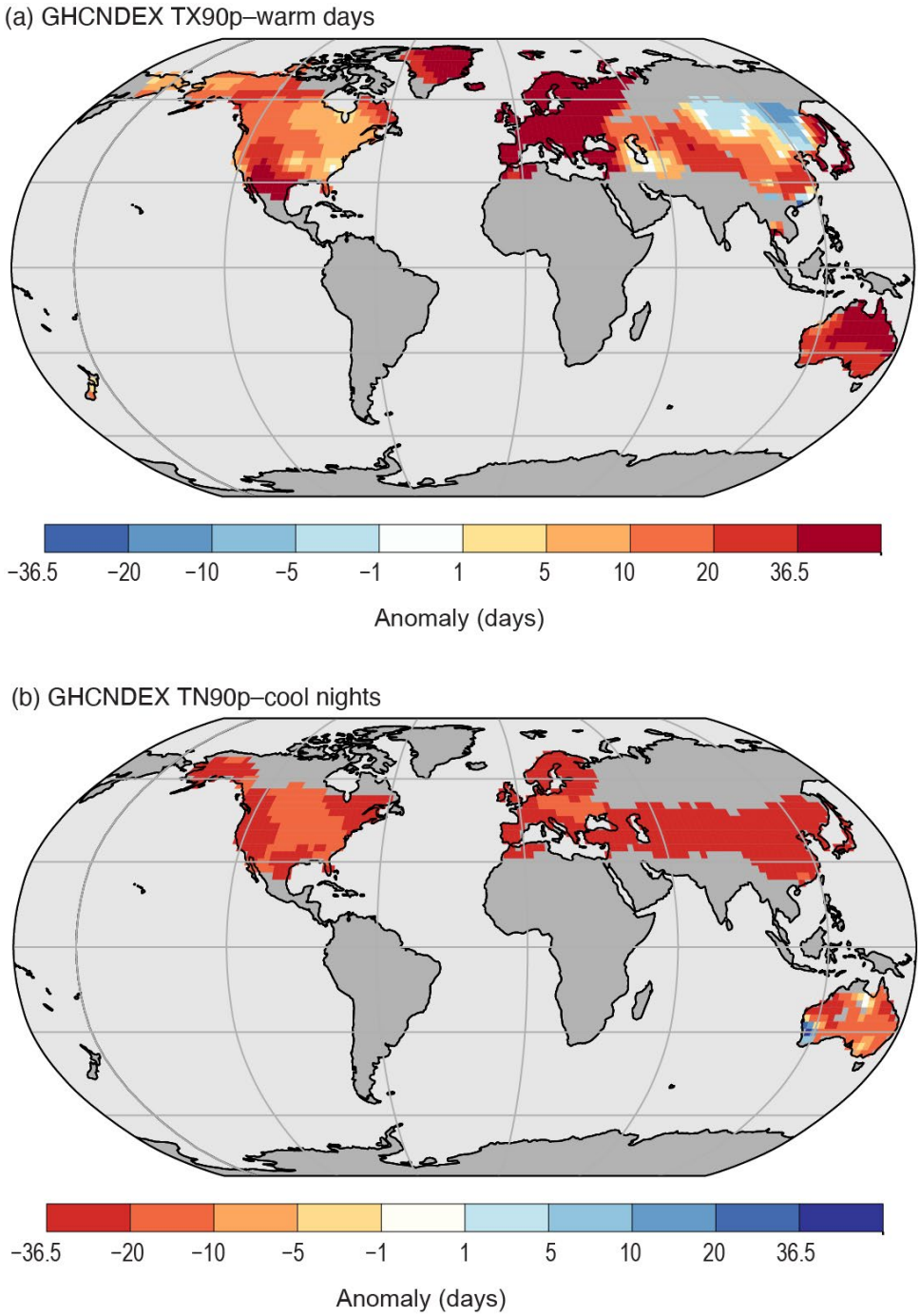

Fig. A2.5. (a) Warm day threshold exceedance (TX90p), (b) cool night threshold exceedance (TN10p) in 2025. (Source: Global Historical Climatology Network Daily Extremes [GHCNDEX].)

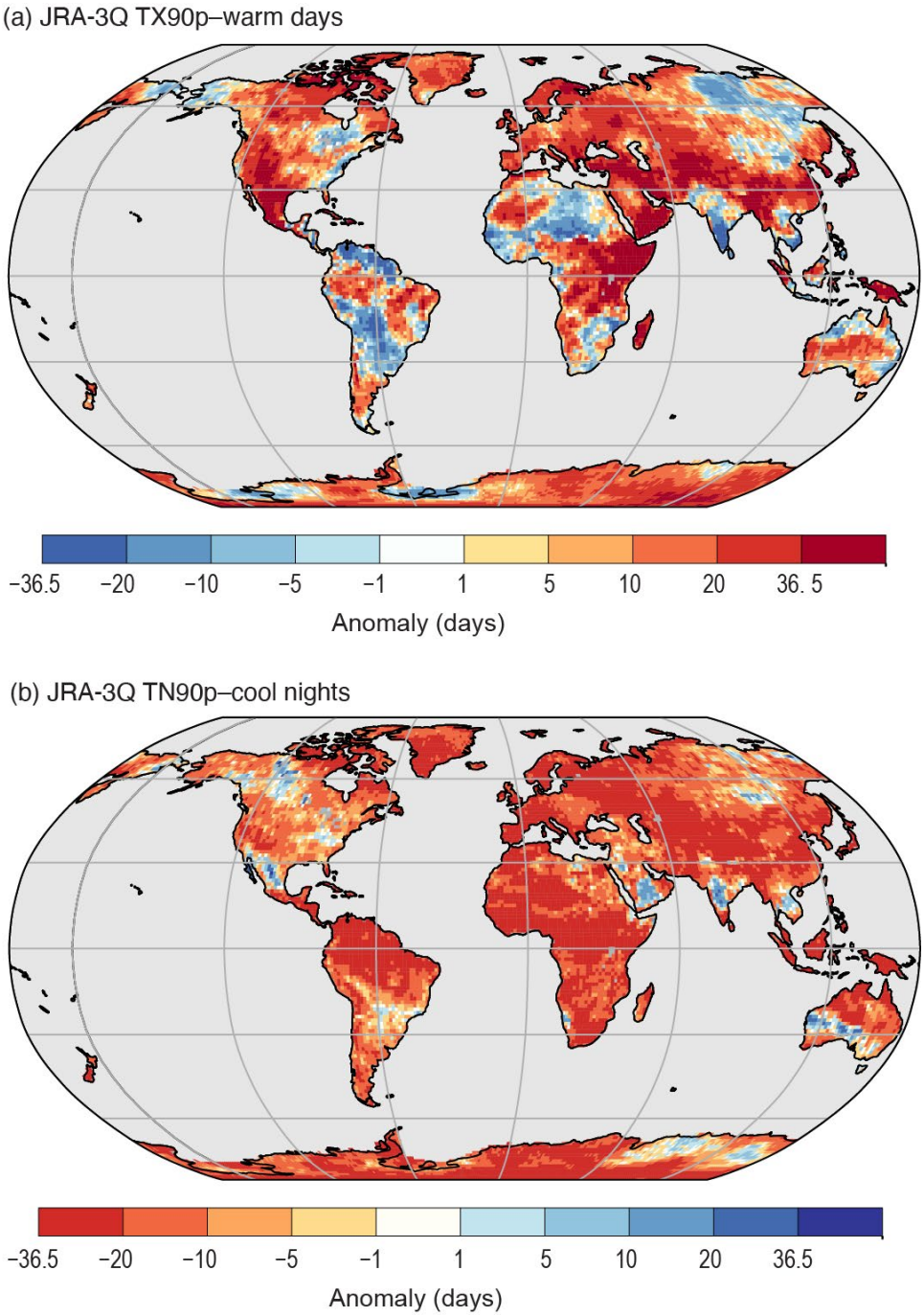

Fig. A2.6. (a) Warm day threshold exceedance (TX90p), (b) cool night threshold exceedance (TN10p) in 2025. (Source: Japanese Reanalysis for Three Quarters of a Century [JRA-3Q].)

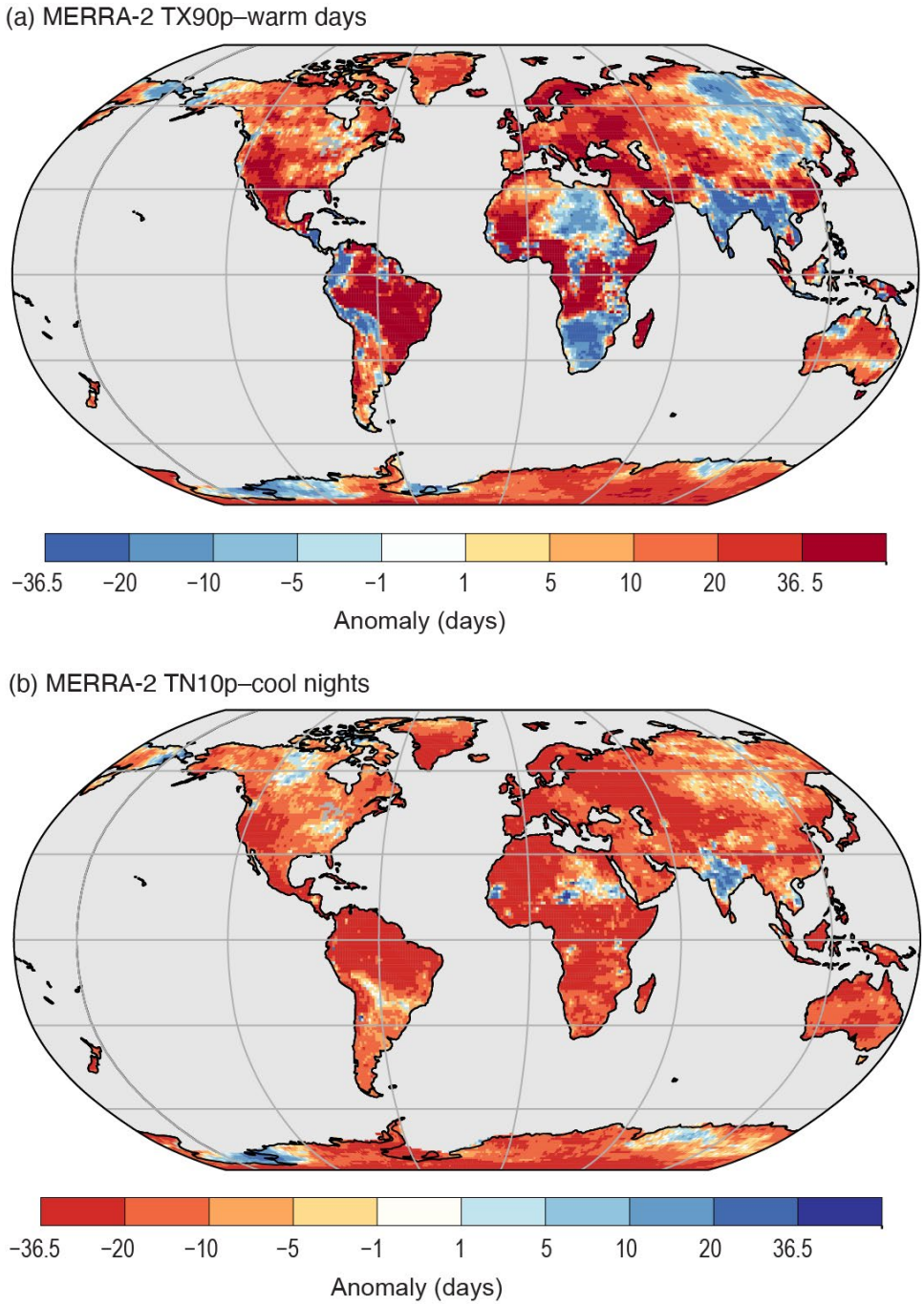

Fig. A2.7. (a) Warm day threshold exceedance (TX90p), (b) cool night threshold exceedance (TN10p) in 2025. (Source: MERRA-2.)

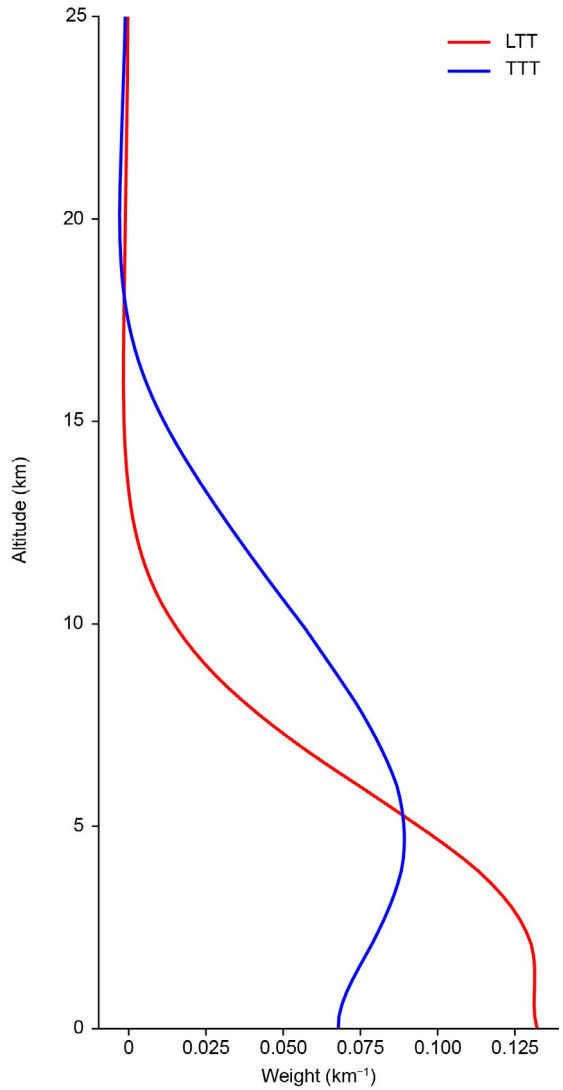

Fig. A2.8. Atmospheric weighting functions (km^{-1}) for global lower-tropospheric temperature (LTT; red line) and total tropospheric temperature (TTT; blue line). The vertical weighting function describes the relative contribution that microwave radiation emitted by a layer in the atmosphere makes to the total intensity measured above the atmosphere by the satellite. Weighting functions were obtained from https://www.remss.com/measurements/upper-air-temperature/.

Appendix Table A2.1. Arctic (>60°N) and tropical (30°S–30°N) annual mean temperature (*T*) and equivalent temperature (*Teq*) anomalies for 2025 and their rank from ERA5 and Japanese Reanalysis for Three Quarters of a Century [JRA-3Q] re-analyses. Units are °C.

Region	Variable	ERA5	Rank	JRA-3Q	Rank	Dataset Mean	Rank
Arctic (>60°N)	*T*	1.40	2	1.52	2	1.46	2
Arctic (>60°N)	*Teq*	1.96	2	2.10	2	2.03	2
Arctic (>60°N)	*Tq*	0.56	1	0.58	1	0.57	1
Tropics (30°S–30°N)	*T*	0.36	5	0.29	6	0.32	5
Tropics (30°S–30°N)	*Teq*	0.78	5	0.94	4	0.86	5
Tropics (30°S–30°N)	*Tq*	0.43	9	0.66	4	0.54	5

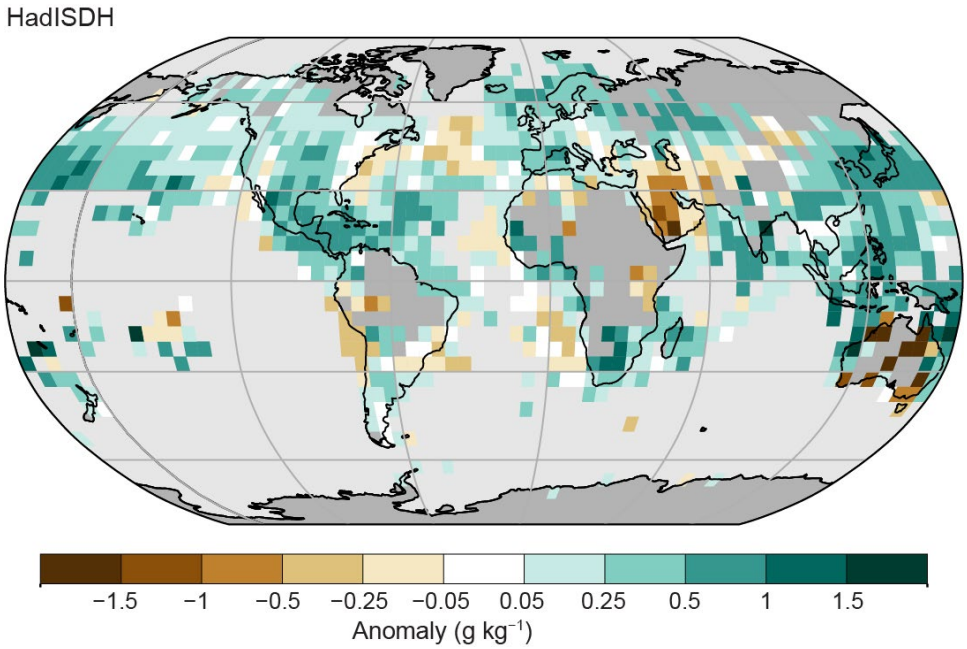

Fig. A2.9. Surface specific humidity anomaly (g kg^{-1}) relative to 1991–2020. (Source: Met Office Hadley Centre Integrated Surface Dataset of Humidity Blend [HadISDH.blend.1.5.1.2024f].)

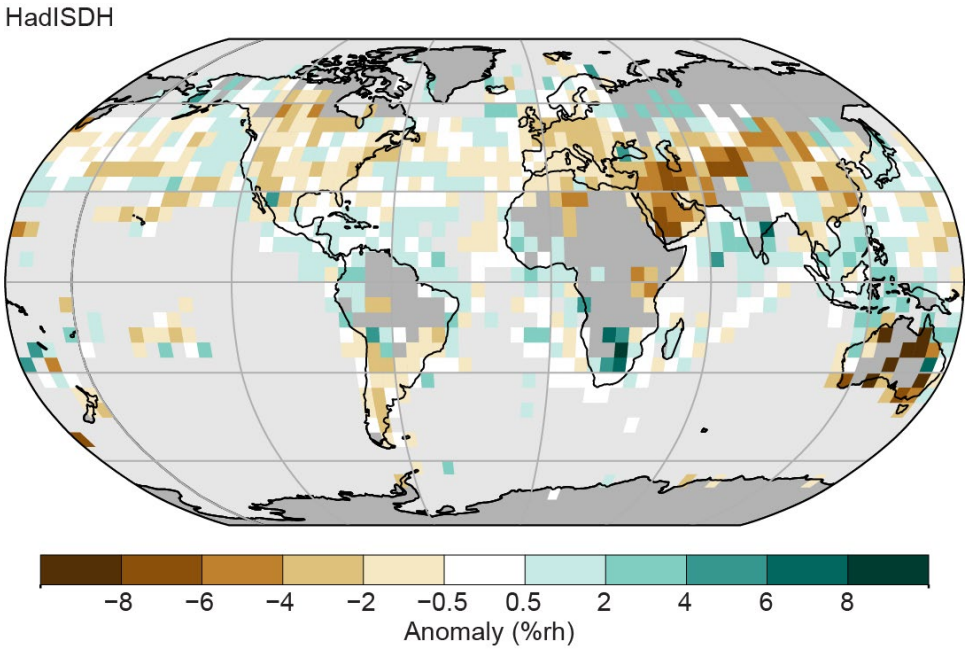

Fig. A2.10. Surface relative humidity anomaly (%rh) relative to 1991–2020. (Source: Met Office Hadley Centre Integrated Surface Dataset of Humidity over Land and Ocean [HadISDH.blend.1.5.1.2024f].)

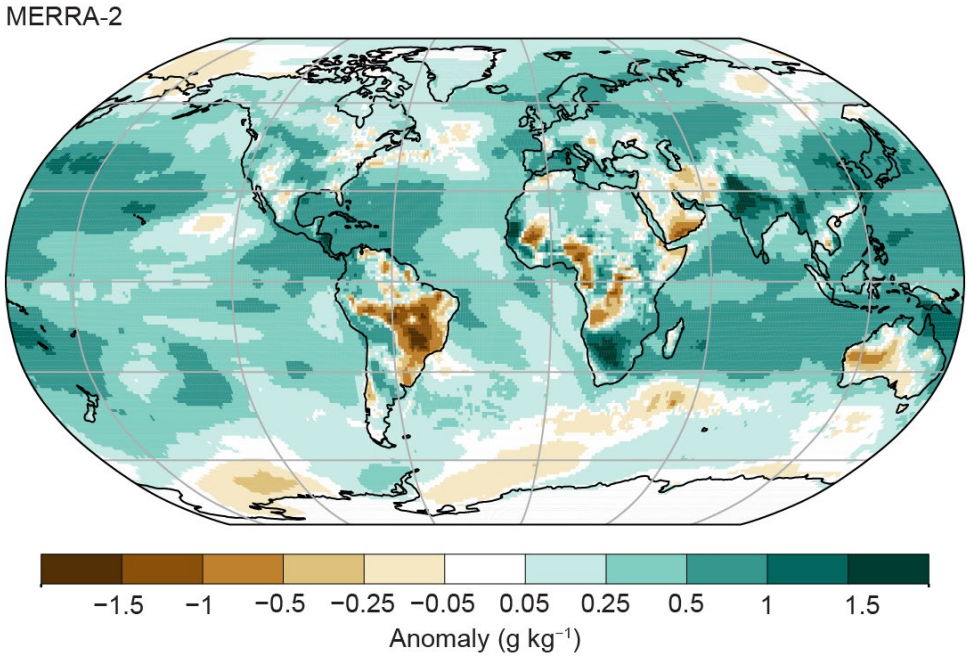

Fig. A2.11. Surface specific humidity anomaly (g kg^{-1}) relative to 1991–2020. (Source: MERRA-2.)

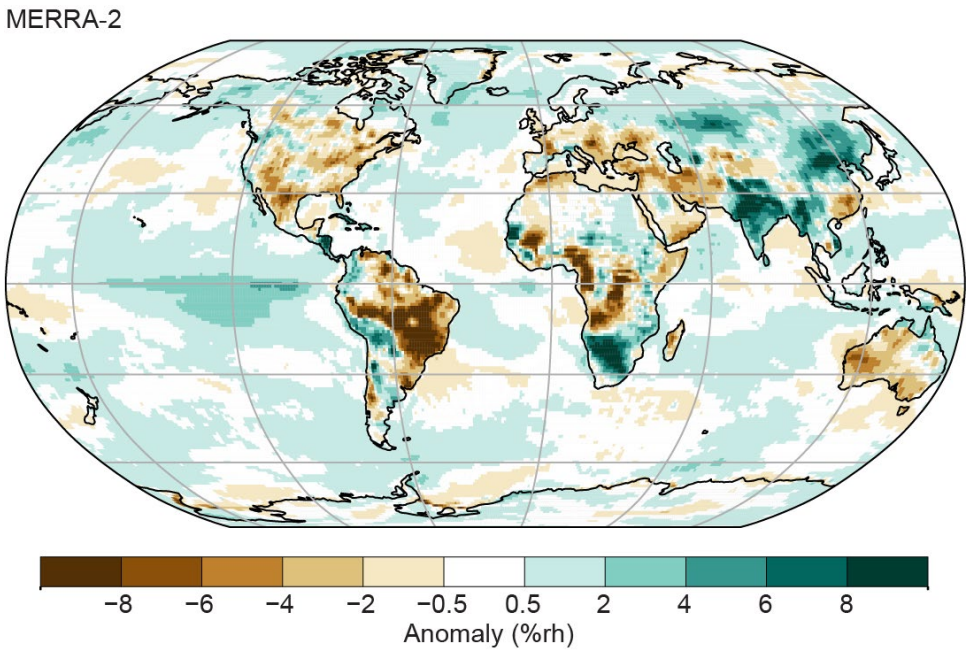

Fig A2.12. Surface relative humidity (%rh) anomaly relative to 1991–2020. (Source: MERRA-2.)

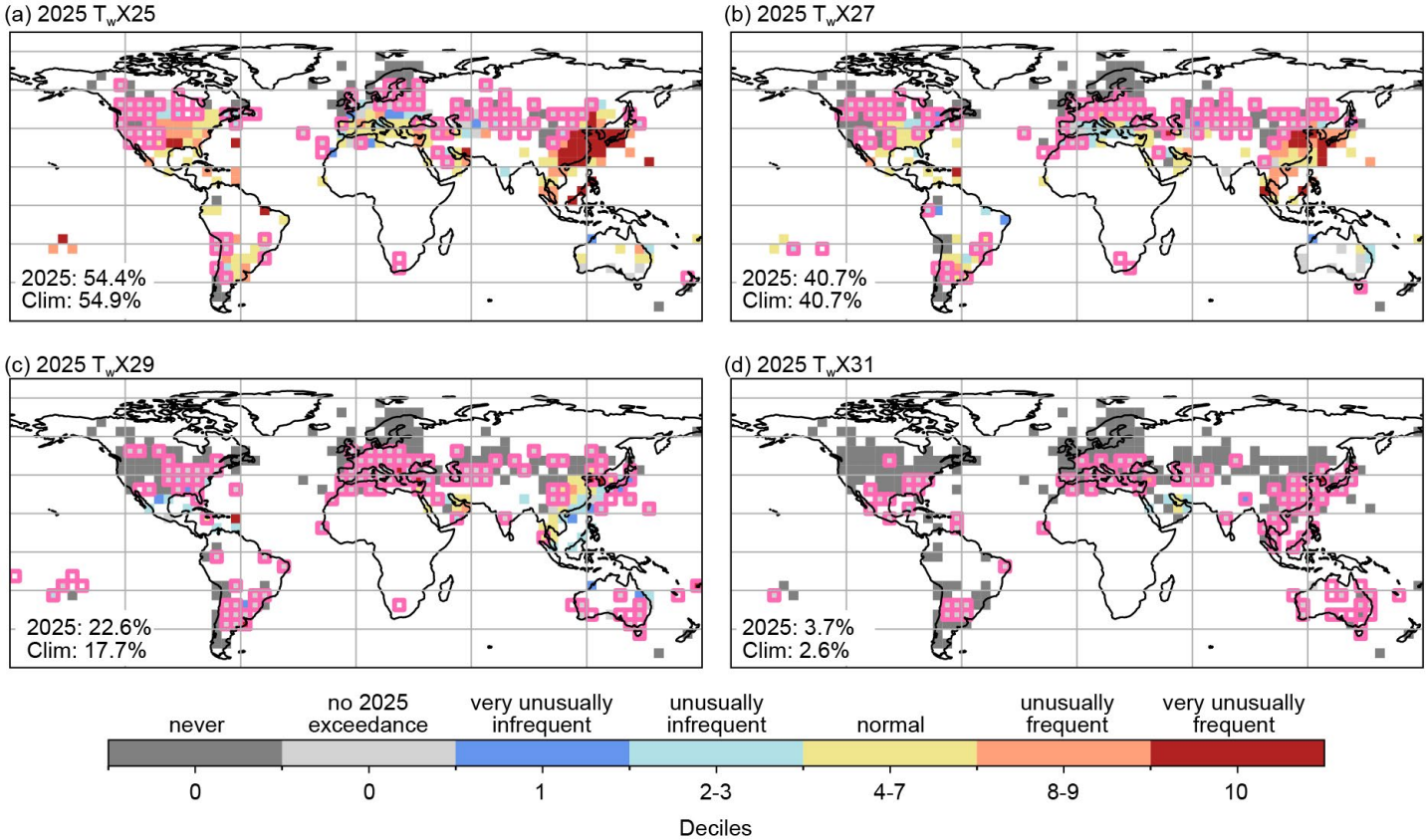

Fig. A2.13. High humid-heat extremes in 2025 shown as deciles over the period 1973–2025, ranking the number of days with maximum wet-bulb temperature (T_w) ≥ (a) 25°C (T_wX25), (b) 27°C (T_wX27), (c) 29°C (T_wX29), and (d) 31°C (T_wX31). Gridboxes bounded in pink indicate that exceedances occurred in <15 years within the 1991–2020 period. Annotations state the percentage of observed gridboxes where an exceedance occurred in 2025 and climatologically (including only those with at least one exceedance between 1991–2020). Data have been screened to remove gridboxes where annual temporal completeness is less than 70% with whole years removed if any months are missing (Source: The Met Office Hadley Centre Integrated Surface Dataset of Humidity Extremes [HadISDH. extremes].)

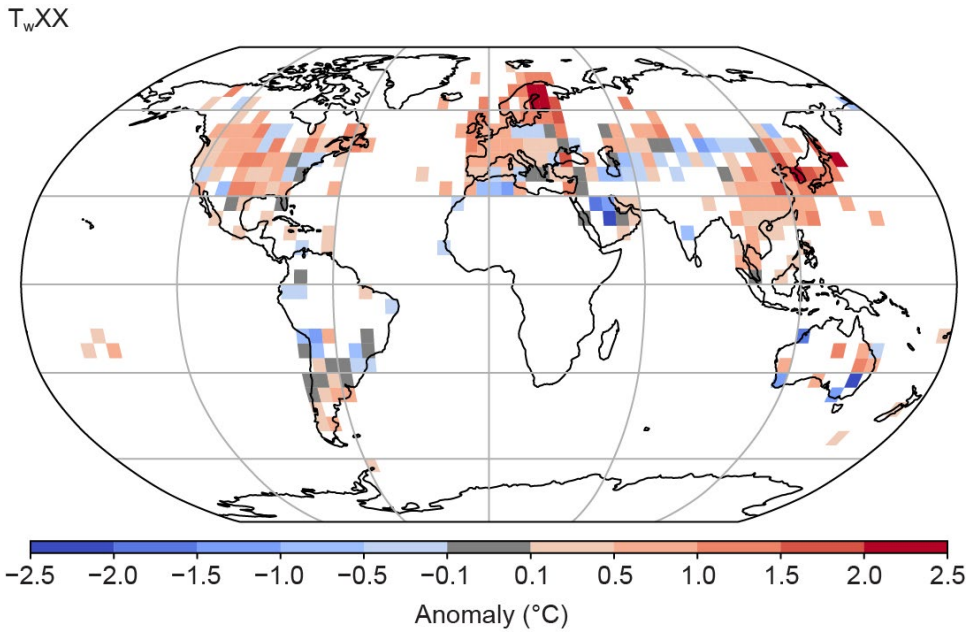

Fig. A2.14. Daily maximum humid-heat intensity anomalies in 2025 as measured by the annual median of monthly maximum daily maximum wet-bulb temperature (T_wXX; °C) from the Met Office Hadley Centre Integrated Surface Dataset of Humidity Extremes (HadISDH.extremes). White gridboxes over land represent regions with insufficient data.

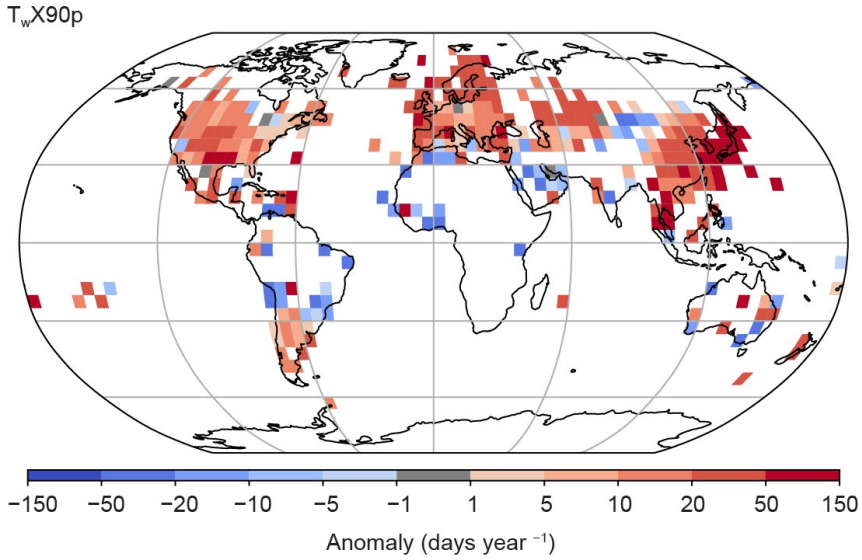

Fig. A2.15. High daily maximum humid-heat frequency anomalies in 2025 as measured by the number of days where the maximum wet-bulb temperature exceeds the local daily 90th percentile (T_wX90p; days yr^{-1}; calculated over the 1991–2020 period) from the Met Office Hadley Centre Integrated Surface Dataset of Humidity Extremes (HadISDH.extremes). White gridboxes over land represent regions with insufficient data.

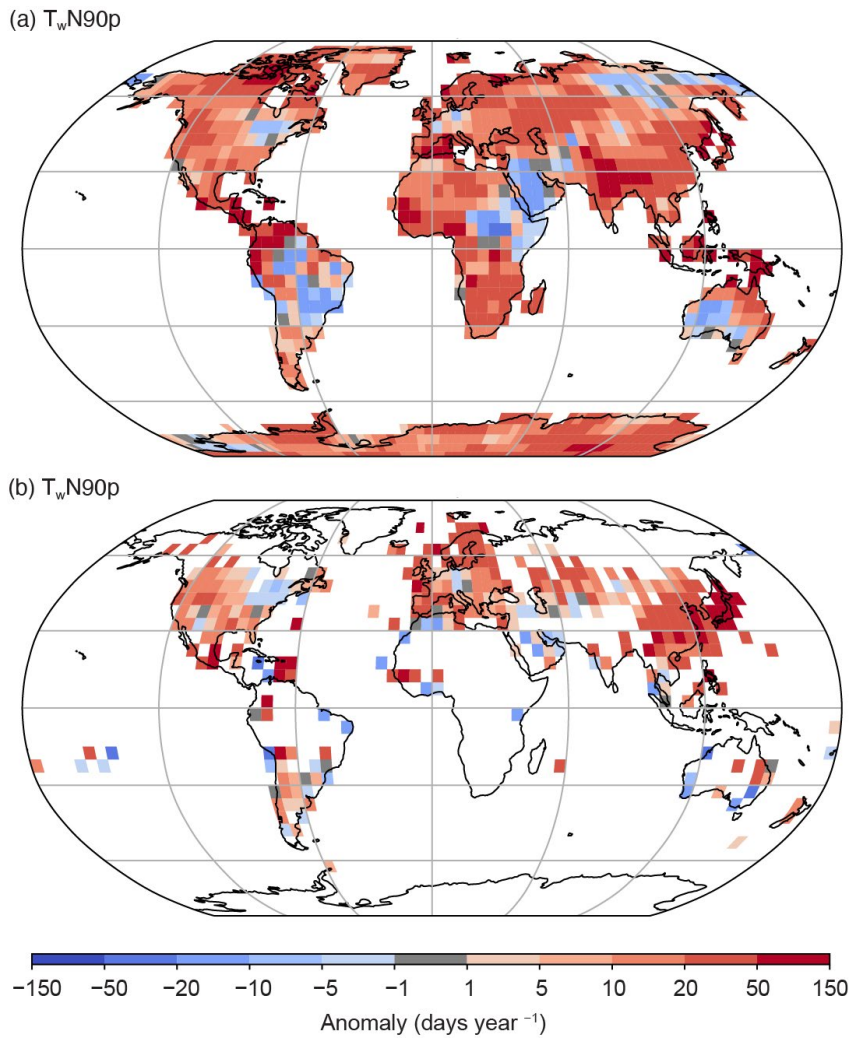

Fig. A2.16. High daily minimum humid-heat frequency anomalies in 2025 as measured by the number of days where the daily minimum wet-bulb temperature exceeds the local daily 90th percentile (T_wN90p; days yr^{-1}; calculated over the 1991–2020 period) from (a) ERA5 and (b) the Met Office Hadley Centre Integrated Surface Dataset of Humidity Extremes (HadISDH.extremes). White gridboxes over land represent regions with insufficient data.

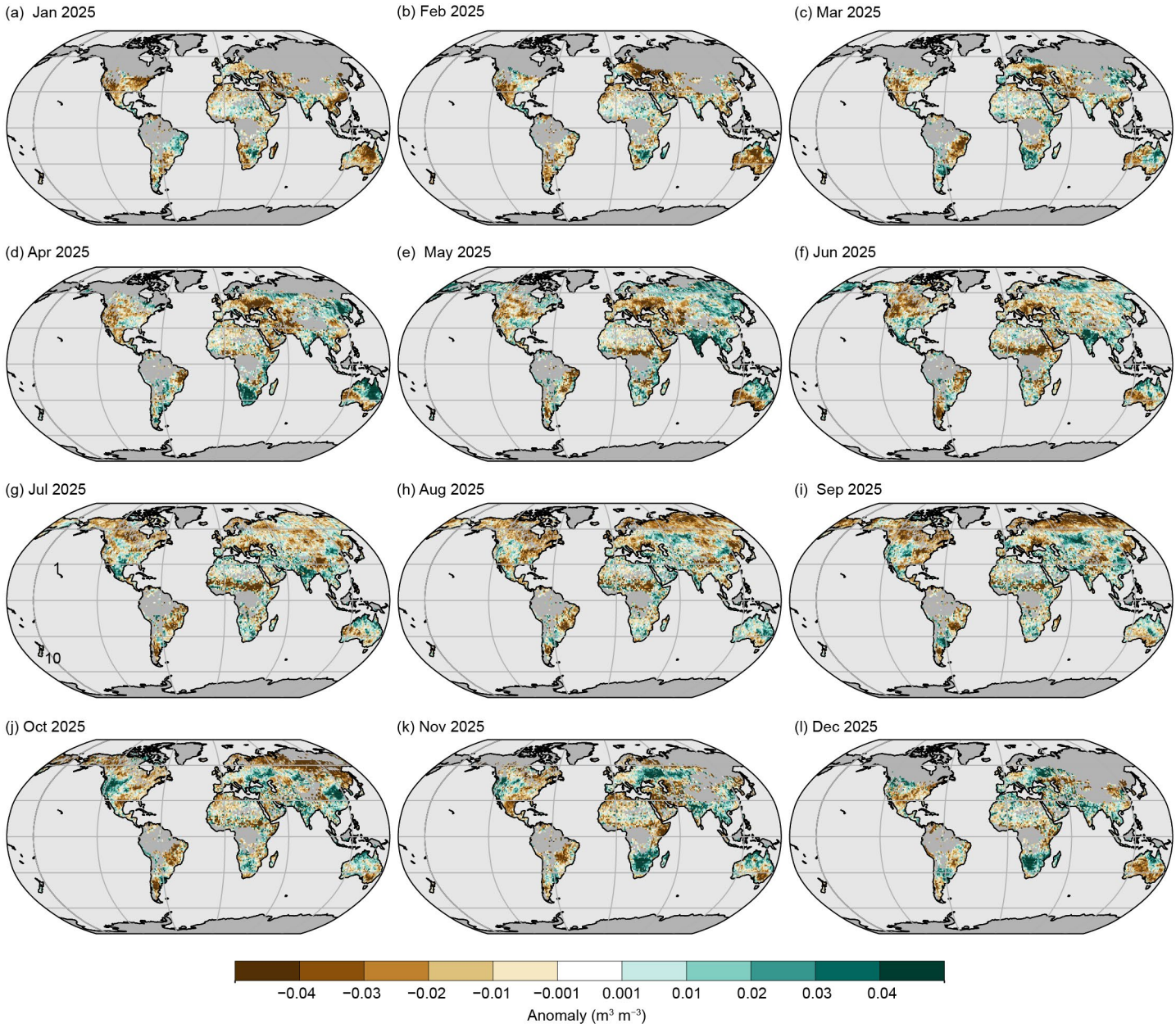

Fig. A2.17. Monthly average surface soil moisture anomalies ($m^3\ m^{-3}$; 1991–2020 base period) for 2025. Data are masked where no retrieval is possible or where the quality is not assured and flagged, for example due to dense vegetation, frozen soil, permanent ice cover, or radio frequency interference. (Source: Copernicus Climate Change Service [C3S] Soil Moisture.)

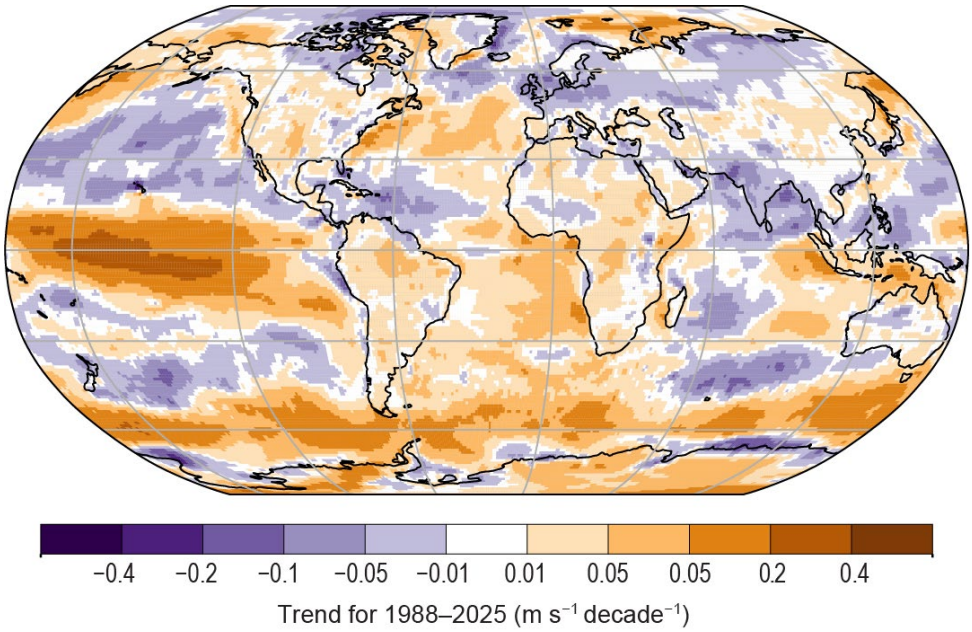

Fig. A2.18. Wind speed trends (m s^{-1} $decade^{-1}$) over land/ice and ocean for the period 1988–2025. (Source: ERA5.)

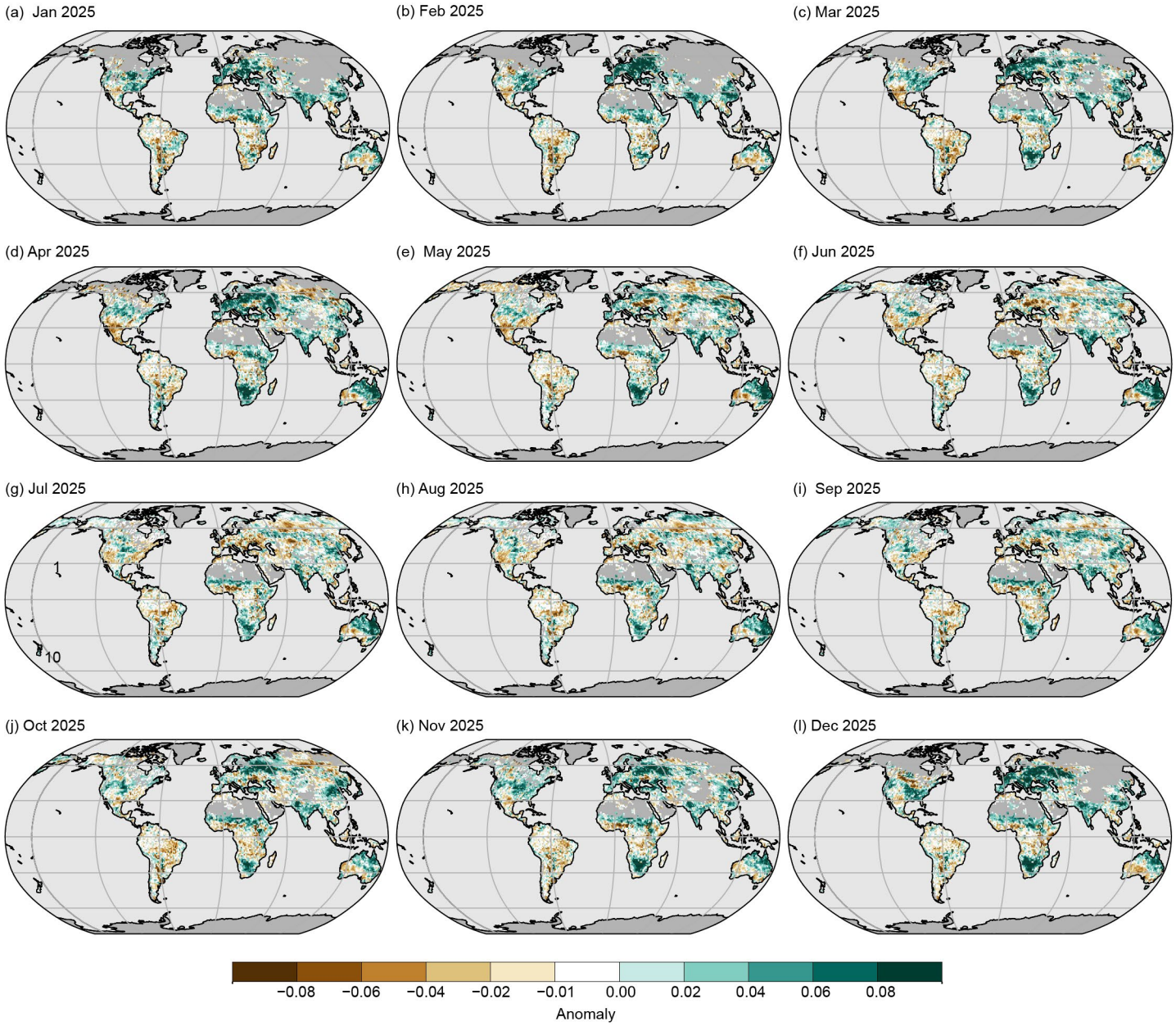

Fig. A2.19. Vegetation Optical Depth Climate Archive (VODCA) monthly CXKu vegetation optical depth (VOD) anomalies in 2025 (1991–2020 base period). VOD cannot be retrieved under frozen or snow-covered areas, which is why they are masked in winter. (Source: VOD Climate Archive version 2 [VODCA v2].)

References

Abalos, M., and Coauthors, 2026: Evaluation of stratospheric transport in three generations of chemistry-climate models. *Atmos. Chem. Phys.*, **26**, 5249–5291, https://doi.org/10.5194/acp-26-5249-2026.

AGRHYMET RCC-WAS, 2025: Special Bulletin PRESASS 04/2025: Seasonal forecast of agro-hydro-climatic characteristics of the rainy season for the Sudanian and Sahelian zones of West Africa and the Sahel [PDF]. Permanent Inter-State Committee for Drought Control in the Sahel (CILSS), 14 pp., accessed 2 February 2026, https://agrhymet.cilss.int/wp-content/uploads/2025/06/Bulletin_PRESASS042025_En-1.pdf.

Ammann, C. M., G. A. Meehl, W. M. Washington, and C. S. Zender, 2003: A monthly and latitudinally varying volcanic forcing dataset in simulations of 20th century climate. *Geophys. Res. Lett.*, **30**, 1657, https://doi.org/10.1029/2003GL016875.

Anderson, W., B. I. Cook, K. Slinski, K. Schwarzwald, A. McNally, and C. Funk, 2023: Multiyear La Niña events and multiseason drought in the Horn of Africa. *J. Hydrometeor.*, **24**, 119–131, https://doi.org/10.1175/JHM-D-22-0043.1.

Angerer, B., F. Ladstädter, B. Scherllin-Pirscher, M. Schwärz, A. K. Steiner, U. Foelsche, and G. Kirchengast, 2017: Quality aspects of the Wegener Center multi-satellite GPS radio occultation record OPSv5.6. *Atmos. Meas. Tech.*, **10**, 4845–4863, https://doi.org/10.5194/amt-10-4845-2017.

Anstey, J. A., and Coauthors, 2022: Teleconnections of the quasi-biennial oscillation in a multi-model ensemble of QBO-resolving models. *Quart. J. Roy. Meteor. Soc.*, **148**, 1568–1592, https://doi.org/10.1002/qj.4048.

Aono, Y., and K. Kazui, 2008: Phenological data series of cherry tree flowering in Kyoto, Japan, and its application to reconstruction of springtime temperatures since the 9th century. *Int. J. Climatol.*, **28**, 905–914, https://doi.org/10.1002/joc.1594.

APARC, 2025: The Hunga volcanic eruption atmospheric impacts report. Y. Zhu et al., Eds., Rep. 11, WCRP Rep. 10/2025, 382 pp., https://aparc-climate.org/publications/aparc-report-no-11/.

Archibald, A. T., and Coauthors, 2020: Tropospheric ozone assessment report: A critical review of changes in the tropospheric ozone burden and budget from 1850 to 2100. *Elementa*, **8**, 034, https://doi.org/10.1525/elementa.2020.034.

Arguez, A., and Coauthors, 2020: Should we expect each year in the next decade (2019–28) to be ranked among the top 10 warmest years globally? *Bull. Amer. Meteor. Soc.*, **101**, E655–E663, https://doi.org/10.1175/BAMS-D-19-0215.1.

Arosio, C., A. Rozanov, E. Malinina, M. Weber, and J. P. Burrows, 2019: Merging of ozone profiles from SCIAMACHY, OMPS and SAGE II observations to study stratospheric ozone changes. *Atmos. Meas. Tech.*, **12**, 2423–2444, https://doi.org/10.5194/amt-12-2423-2019.

Augustine, J. A., L. Soldo, K. O. Lantz, A. Baron, K. Smith, E. Asher, and J.-P. Vernier, 2025: Mauna Loa apparent transmission record update for 2024 [in "State of the Climate in 2024"]. *Bull. Amer. Meteor. Soc.*, **106** (8), S89–S90, https://doi.org/10.1175/2025BAMSStateoftheClimate.1.

Australian Bureau of Meteorology, 2026: Bureau releases summary of Australia's climate in 2025. Accessed 2 February 2026, https://www.bom.gov.au/news-and-media/bureau-releases-summary-of-australias-climate-in-2025.

Azorin-Molina, C., and Coauthors, 2023: Biases in wind speed measurements due to anemometer changes. *Atmos. Res.*, **289**, 106771, https://doi.org/10.1016/j.atmosres.2023.106771.

——, R. J. H. Dunn, L. Ricciardulli, C. A. Mears, J. P. Nicolas, T. R. McVicar, Z. Zeng, and M. G. Bosilovich, 2024: Land and ocean surface winds [in "State of the Climate in 2023"]. *Bull. Amer. Meteor. Soc.*, **105** (8), S76–S79, https://doi.org/10.1175/BAMS-D-24-0116.1.

Bai, G., and Coauthors, 2022: GBOV (Ground-Based Observation for Validation): A Copernicus service for validation of land products. *IGARSS 2022 - 2022 IEEE Int. Geoscience and Remote Sensing Symp.*, Kuala Lumpur, Malaysia, Institute of Electrical and Electronics Engineers, 4304–4307, https://doi.org/10.1109/IGARSS46834.2022.9883162.

Baldwin, M. P., and Coauthors, 2001: The quasi-biennial oscillation. *Rev. Geophys.*, **39**, 179–299, https://doi.org/10.1029/1999RG000073.

Ballinger, T. J., and Coauthors, 2025: Surface air temperature. Arctic Report Card 2025, NOAA Tech. Rep. OAR ARC 25-02, 7 pp., https://doi.org/10.25923/cj60-9s07.

Barichivich, J., T. J. Osborn, I. Harris, G. van der Schrier, and P. D. Jones, 2025: Monitoring global drought using the self-calibrating Palmer drought severity index [in "State of the Climate in 2024"]. *Bull. Amer. Meteor. Soc.*, **106** (8), S77–S78, https://doi.org/10.1175/2025BAMSStateoftheClimate.1.

Bastos, A., S. W. Running, C. Gouveia, and R. M. Trigo, 2013: The global NPP dependence on ENSO: La Niña and the extraordinary year of 2011. *J. Geophys. Res. Biogeosci.*, **118**, 1247–1255, https://doi.org/10.1002/jgrg.20100.

Basu, S., and Coauthors, 2022: Estimating emissions of methane consistent with atmospheric measurements of methane and $\delta^{13}C$ of methane. *Atmos. Chem. Phys.*, **22**, 15 351–15 377, https://doi.org/10.5194/acp-22-15351-2022.

Becker, A., P. Finger, A. Meyer-Christoffer, B. Rudolf, K. Schamm, U. Schneider, and M. A. Ziese, 2013: A description of the global land-surface precipitation data products of the Global Precipitation Climatology Centre with sample applications including centennial (trend) analysis from 1901–present. *Earth Syst. Sci. Data*, **5**, 71–99, https://doi.org/10.5194/essd-5-71-2013.

Bell, B., and Coauthors, 2021: The ERA5 global reanalysis: Preliminary extension to 1950. *Quart. J. Roy. Meteor. Soc.*, **147**, 4186–4227, https://doi.org/10.1002/qj.4174.

Ben Aoun, W., and Coauthors, 2025: Above-average winter crop yield expectations. *JRC MARS Bull.*, Vol. 33, No. 6, JRC Tech. Rep. 141589, 38 pp., https://data.europa.eu/doi/10.2760/4130848.

Benestad, R. E., 2003: How often can we expect a record event? *Climate Res.*, **25**, 3–13, https://doi.org/10.3354/cr025003.

Bessenbacher, V., D. L. Schumacher, M. Hirschi, S. I. Seneviratne, and L. Gudmundsson, 2023: Gap-filled multivariate observations of global land–climate interactions. *J. Geophys. Res. Atmos.*, **128**, e2023JD039099, https://doi.org/10.1029/2023JD039099.

Betts, R. A., C. D. Jones, J. R. Knight, R. F. Keeling, and J. J. Kennedy, 2016: El Niño and a record CO_2 rise. *Nat. Climate Change*, **6**, 806–810, https://doi.org/10.1038/nclimate3063.

Birkett, C., C. Reynolds, B. Beckley, and B. Doorn, 2011: From research to operations: The USDA Global Reservoir and Lake Monitor. *Coastal Altimetry*, S. Vignudelli et al., Eds., Springer, 19–50, https://doi.org/10.1007/978-3-642-12796-0_2.

Biskaborn, B. K., and Coauthors, 2019: Permafrost is warming at a global scale. *Nat. Commun.*, **10**, 264, https://doi.org/10.1038/s41467-018-08240-4]

Bjerknes, J., 1969: Atmospheric teleconnections from the equatorial Pacific. *Mon. Wea. Rev.*, **97**, 163–172, https://doi.org/10.1175/1520-0493(1969)097<0163:ATFTEP>2.3.CO;2.

Blunden, J., J. Reagan, and R. J. H. Dunn, Eds., 2025: State of the Climate in 2024. *Bull. Amer. Meteor. Soc.*, **106** (8), Si–S513, https://doi.org/10.1175/2025BAMSStateoftheClimate.1.

Bock, O., 2025: Global GNSS integrated water vapour data, 1994-2024. AERIS, accessed 15 February 2026, https://doi.org/10.25326/68.

Bodhaine, B. A., B. G. Mendonca, J. M. Harris, and J. M. Miller, 1981: Seasonal variations in aerosols and atmospheric transmission at Mauna Loa Observatory. *J. Geophys. Res.*, **86**, 7395–7398, https://doi.org/10.1029/JC086iC08p07395.

Bosilovich, M. G., F. R. Robertson, L. Takacs, A. Molod, and D. Mocko, 2017: Atmospheric water balance and variability in the MERRA-2 reanalysis. *J. Climate*, **30**, 1177–1196, https://doi.org/10.1175/JCLI-D-16-0338.1.

Bourgeois, I., and Coauthors, 2021: Large contribution of biomass burning emissions to ozone throughout the global remote troposphere. *Proc. Natl. Acad. Sci. USA*, **118**, e2109628118, https://doi.org/10.1073/pnas.2109628118]

Bowman, K. W., 2021: TROPESS CrIS-JPSS1 L2 peroxyacetyl nitrate for forward stream, standard product V. GES DISC, accessed 31 January 2025, https://doi.org/10.5067/W0W6L8M6J85X.

Boyer, D., and C. Howe, 2025: Communication efforts to educate the public about vanishing glaciers, 1958–2025. *Ann. Glaciol.*, **67**, e2, https://doi.org/10.1017/aog.2025.10033.

Boynard, A., and Coauthors, 2025: Assessment of 16-year tropospheric ozone trends from the IASI climate data record. *Atmos. Chem. Phys.*, **25**, 11 719–11 755, https://doi.org/10.5194/acp-25-11719-2025.

Brohan, P., J. J. Kennedy, I. Harris, S. F. Tett, and P. D. Jones, 2006: Uncertainty estimates in regional and global observed temperature changes: A new data set from 1850. *J. Geophys. Res.*, **111**, D12106, https://doi.org/10.1029/2005JD006548.

Brutsaert, W., 2017: Global land surface evaporation trend during the past half century: Corroboration by Clausius-Clapeyron scaling. *Adv. Water Resour.*, **106**, 3–5, https://doi.org/10.1016/j.advwatres.2016.08.014.

Burek, P., J. van der Knijff, and A. de Roo, 2013: LISFLOOD, distributed water balance and flood simulation model. Revised User Manual 2013, Publications Office of the European Union, 139 pp., https://doi.org/10.2788/24719.

Burn, C. R., and Coauthors, 2025: Developments in permafrost science and engineering in response to climate warming in circumpolar and high mountain regions, 2019–2024. *Permafrost Periglacial*, **36**, 167–188, https://doi.org/10.1002/ppp.2261.

C3S CDS, 2025: Comprehensive upper-air observation network from 1901 to present. Copernicus Climate Change Service (C3S) Climate Data Store (CDS), accessed 1 January 2026, https://doi.org/10.24381/ba504f7a.

——, 2026: Global land surface atmospheric variables from 1755 to present from comprehensive in-situ observations. Copernicus Climate Change Service (C3S) Climate Data Store (CDS), accessed 28 May 2026, https://doi.org/10.24381/cds.cf5f3bac.

Caine, T., J. Morse, and Niwot Ridge LTER, 2025: Lake ice clearance and formation data for Green Lakes Valley, 1968–ongoing, version 8. Environmental Data Initiative, accessed 23 January 2026, https://doi.org/10.6073/pasta/49e45fe9be26dab91bb20927972bb342

Capotondi, A., and Coauthors, 2015: Understanding ENSO diversity. *Bull. Amer. Meteor. Soc.*, **96**, 921–938, https://doi.org/10.1175/BAMS-D-13-00117.1.

Cappucci, F., R. Urraca, and N. Gobron, 2025: Terrestrial surface albedo dynamics [in "State of the Climate in 2024"]. *Bull. Amer. Meteor. Soc.*, **106** (8), S111–S112, https://doi.org/10.1175/BAMS-D-25-0102.1.

Carrea, L., O. Embury, and C. J. Merchant, 2015: Datasets related to in-land water for limnology and remote sensing applications: Distance-to-land, distance-to-water, water-body identifier and lake-centre co-ordinates. *Geosci. Data J.*, **2**, 83–97, https://doi.org/10.1002/gdj3.32.

——, and Coauthors, 2020: Lake surface temperature [in "State of the Climate in 2019"]. *Bull. Amer. Meteor. Soc.*, **101** (8), S26–S28, https://doi.org/10.1175/2020BAMSStateoftheClimate.1.

——, and Coauthors, 2022: ESA lakes climate change initiative (Lakes_cci): Lake products, version 2.0.2. NERC EDS Centre for Environmental Data Analysis, accessed 2 February 2026, https://doi.org/10.5285/a07deacaffb8453e93d57ee214676304.

——, and Coauthors, 2023: Satellite-derived multivariate worldwide lake physical variable timeseries for climate studies. *Sci. Data*, **10**, 30, https://doi.org/10.1038/s41597-022-01889-z.

——, and Coauthors, 2024: Lake surface water temperature [in "State of the Climate in 2023"]. *Bull. Amer. Meteor. Soc.*, **105** (8), S3–S35, https://doi.org/10.1175/2024BAMSStateoftheClimate.1.

Chandra, S., E. K. Suenaga, F. Scordo, and T. A. Daniel, 2022: Mountain lake biology, chemistry, physics, and climate data since 1959 at Castle Lake, version 1. Environmental Data Initiative, accessed 23 January 2026, https://doi.org/10.6073/pasta/a8e3b81cfe5864731b29ad42506c65d7.

Chang, K. L., M. G. Schultz, X. Lan, A. McClure-Begley, I. Petropavlovskikh, X. Xu, and J. R. Ziemke, 2021: Trend detection of atmospheric time series: Incorporating appropriate uncertainty estimates and handling extreme events. *Elementa*, **9**, 00035, https://doi.org/10.1525/elementa.2021.00035.

——, O. R. Cooper, A. Gaudel, I. Petropavlovskikh, P. Effertz, G. Morris, and B. C. McDonald, 2024: Technical note: Challenges in detecting free tropospheric ozone trends in a sparsely sampled environment. *Atmos. Chem. Phys.*, **24**, 6197–6218, https://doi.org/10.5194/acp-24-6197-2024.

Chen, Y., and Coauthors, 2023: Multi-decadal trends and variability in burned area from the fifth version of the Global Fire Emissions Database (GFED5). *Earth Syst. Sci. Data*, **15**, 5227–5259, https://doi.org/10.5194/essd-15-5227-2023.

Cheng, X., S. Wang, J. Chen, and A. AghaKouchak, 2025: Global assessment and hotspots of lake drought. *Commun. Earth Environ.*, **6**, 308, https://doi.org/10.1038/s43247-025-02285-2.

Chipperfield, M. P., and Coauthors, 2018: On the cause of recent variations in lower stratospheric ozone. *Geophys. Res. Lett.*, **45**, 5718–5726, https://doi.org/10.1029/2018GL078071.

Choulga, M., F. Moschini, C. Mazzetti, S. Grimaldi, J. Disperati, H. Beck, P. Salamon, and C. Prudhomme, 2024: Technical note: Surface fields for global environmental modelling. *Hydrol. Earth Syst. Sci.*, **28**, 2991–3036, https://doi.org/10.5194/hess-28-2991-2024.

Christian, H., and Coauthors, 2003: Global frequency and distribution of lightning as observed from space by the optical transient detector. *J. Geophys. Res.*, **108**, 4005, https://doi.org/10.1029/2002JD002347.

Chung, E.-S., B. Soden, B. J. Sohn, and L. Shi, 2014: Upper-tropospheric moistening in response to anthropogenic warming. *Proc. Natl. Acad. Sci. USA*, **111**, 11 636–11 641, https://doi.org/10.1073/pnas.1409659111.

Ciais, P., and Coauthors, 2026: Why methane surged in the atmosphere during the early 2020s. *Science*, **391**, eadx8262, https://doi.org/10.1126/science.adx8262.

Cooper, O. R., E. Pennington, J. Worden, K. Bowman, S. Kondragunta, Z. Wei, and K. Yang, 2025a: Operational satellite instruments monitor a range of indirect short-lived climate forcers [in "State of the Climate in 2024"]. *Bull. Amer. Meteor. Soc.*, **106** (8), S108–S110, https://doi.org/10.1175/BAMS-D-25-0102.1.

——, J. R. Ziemke, K.-L. Chang, and P. Effertz, 2025b: Tropospheric ozone [in "State of the Climate in 2024"]. *Bull. Amer. Meteor. Soc.*, **106** (8), S97–S99, https://doi.org/10.1175/BAMS-D-25-0102.1.

Copernicus, 2025: CAMS tracks intense global wildfire activity in first six months of 2025. Accessed 4 February 2026, https://www.copernicus.eu/en/news/news/observer-cams-tracks-intense-global-wildfire-activity-first-six-months-2025.

Cornes, R. C., E. C. Kent, D. I. Berry, and J. J. Kennedy, 2020: CLASSnmat: A global night marine air temperature data set, 1880–2019. *Geosci. Data J.*, **7**, 170–184, https://doi.org/10.1002/gdj3.100.

——, D. I. Berry, R. Junod, E. C. Kent, and N. A. Rayner, 2021: Night marine air temperature [in "State of the Climate in 2020"]. *Bull. Amer. Meteor. Soc.*, **102** (8), S39–S41, https://doi.org/10.1175/2021BAMSStateoftheClimate.1.

——, R. Junod, and E. C. Kent, 2025: Night marine air temperature [in "State of the Climate in 2024"]. *Bull. Amer. Meteor. Soc.*, **106** (8), S31–S32, https://doi.org/10.1175/2025BAMSStateoftheClimate.1.

Crimmins, T. M., R. L. Marsh, J. Switzer, M. A. Crimmins, K. L. Gerst, A. H. Rosemartin, and J. F. Weltzin, 2017: USA National Phenology Network gridded products documentation. USGS Open-File Rep. 2017-1003, 27 pp., https://doi.org/10.3133/ofr20171003.

——, E. G. Denny, E. E. Posthumus, A. H. Rosemartin, R. Croll, M. Montano, and H. Panci, 2022: Science and management advancements made possible by the USA National Phenology Network's nature's notebook platform. *BioScience*, **72**, 908–920, https://doi.org/10.1093/biosci/biac061.

Crippa, M., and Coauthors, 2024: Insights into the spatial distribution of global, national, and subnational greenhouse gas emissions in the Emissions Database for Global Atmospheric Research (EDGAR v8.0). *Earth Syst. Sci. Data*, **16**, 2811–2830, https://doi.org/10.5194/essd-16-2811-2024.

Daniel, J. S., S. Solomon, and D. L. Albritton, 1995: On the evaluation of halocarbon radiative forcing and global warming potentials. *J. Geophys. Res.*, **100**, 1271–1285, https://doi.org/10.1029/94JD02516.

Danzer, J., M. Pieler, and G. Kirchengast, 2024: Closing the gap in the tropics: The added value of radio-occultation data for wind field monitoring across the equator. *Atmos. Meas. Tech.*, **17**, 4979–4995, https://doi.org/10.5194/amt-17-4979-2024.

Davidson, E. A., 2009: The contribution of manure and fertilizer nitrogen to atmospheric nitrous oxide since 1860. *Nat. Geosci.*, **2**, 659–662, https://doi.org/10.1038/ngeo608.

Davis, S. M., and Coauthors, 2016: The Stratospheric Water and Ozone Satellite Homogenized (SWOOSH) database: A long-term database for climate studies. *Earth Syst. Sci. Data*, **8**, 461–490, https://doi.org/10.5194/essd-8-461-2016.

Deeter, M. N., and Coauthors, 2014: The MOPITT version 6 product: Algorithm enhancements and validation. *Atmos. Meas. Tech.*, **7**, 3623–3632, https://doi.org/10.5194/amt-7-3623-2014.

——, D. P. Edwards, G. L. Francis, J. C. Gille, S. Martínez-Alonso, H. M. Worden, and C. Sweeney, 2017: A climate-scale satellite record for carbon monoxide: The MOPITT version 7 product. *Atmos. Meas. Tech.*, **10**, 2533–2555, https://doi.org/10.5194/amt-10-2533-2017.

——, and Coauthors, 2019: Radiance-based retrieval bias mitigation for the MOPITT instrument: The version 8 product. *Atmos. Meas. Tech.*, **12**, 4561–4580, https://doi.org/10.5194/amt-12-4561-2019.

Deng, K., C. Azorin-Molina, L. Minola, G. Zhang, and D. Chen, 2021: Global near-surface wind speed changes over the last decades revealed by reanalyses and CMIP6 model simulations. *J. Climate*, **34**, 2219–2234, https://doi.org/10.1175/JCLI-D-20-0310.1.

de Oliveira, C. P., L. Aímola, T. Ambrizzi, and A. C. V. Freitas, 2018: The influence of the regional Hadley and Walker circulations on precipitation patterns over Africa in El Niño, La Niña, and neutral years. *Pure Appl. Geophys.*, **175**, 2293–2306, https://doi.org/10.1007/s00024-018-1782-4.

Dessler, A. E., and S. M. Davis, 2010: Trends in tropospheric humidity from reanalysis systems. *J. Geophys. Res.*, **115**, D19127, https://doi.org/10.1029/2010JD014192.

DiGangi, E. A., M. Stock, and J. Lapierre, 2022: Thunder hours: How old methods offer new insights into thunderstorm climatology. *Bull. Amer. Meteor. Soc.*, **103**, E548–E569, https://doi.org/10.1175/BAMS-D-20-0198.1.

Dlugokencky, E. J., L. P. Steele, P. M. Lang, and K. A. Masarie, 1994: The growth rate and distribution of atmospheric methane. *J. Geophys. Res.*, **99**, 17 021–17 043, https://doi.org/10.1029/94JD01245.

Domeisen, D. I. V., C. I. Garfinkel, and A. H. Butler, 2019: The teleconnection of El Niño Southern Oscillation to the stratosphere. *Rev. Geophys.*, **57**, 5–47, https://doi.org/10.1029/2018RG000596.

Donat, M. G., L. V. Alexander, H. Yang, I. Durre, R. Vose, and J. Caesar, 2013: Global land-based datasets for monitoring climatic extremes. *Bull. Amer. Meteor. Soc.*, **94**, 997–1006, https://doi.org/10.1175/BAMS-D-12-00109.1.

Dorigo, W., W. Preimesberger, J. Lems, T. Frederikse, and A. Dostalova, 2025: Soil moisture gridded data from 1978 to present, v202505.0.0. Copernicus Climate Change Service (C3S) Climate Data Store (CDS), accessed 29 January 2026, https://doi.org/10.24381/cds.d7782f18.

Dudok de Wit, T., G. Kopp, C. Fröhlich, and M. Schöll, 2017: Methodology to create a new total solar irradiance record: Making a composite out of multiple data records. *Geophys. Res. Lett.*, **44**, 1196–1203, https://doi.org/10.1002/2016GL071866.

Dunn, R. J. H., and C. P. Morice, 2022: On the effect of reference periods on trends in percentile-based extreme temperature indices. *Environ. Res. Lett.*, **17**, 034026, https://doi.org/10.1088/1748-9326/ac52c8.

——, and Coauthors, 2020: Development of an updated global land in situ–based data set of temperature and precipitation extremes: HadEX3. *J. Geophys. Res. Atmos.*, **125**, 2098–2118, https://doi.org/10.1029/2019JD032263.

——, C. Azorin-Molina, M. J. Menne, Z. Zeng, N. W. Casey, and C. Shen, 2022a: Reduction in reversal of global stilling arising from correction to encoding of calm periods. *Environ. Res. Commun.*, **4**, 061003, https://doi.org/10.1088/2515-7620/ac770a.

—— , M. G. Donat, and L. V. Alexander, 2022b: Comparing extremes indices in recent observational and reanalysis products. *Front. Climate*, **4**, 183, https://doi.org/10.3389/fclim.2022.989505.

—— , and Coauthors, 2024: Observed global changes in sector-relevant climate extremes indices—An extension to HadEX3. *Earth Space Sci.*, **11**, e2023EA003279, https://doi.org/10.1029/2023EA003279.

—— , J. Blannin, K. M. Willett, N. Gobron, and G. A. Morris, Eds., 2025a: Global climate [in "State of the Climate in 2024"]. *Bull. Amer. Meteor. Soc.*, **106** (8), S11–S172, https://doi.org/10.1175/BAMS-D-25-0102.1.

—— , M. G. Donat, S. Kirkpatrick, and M. G. Bosilovich, 2025b: Surface temperature extremes [in "State of the Climate in 2024"]. *Bull. Amer. Meteor. Soc.*, **106** (8), S32–S35, https://doi.org/10.1175/BAMS-D-25-0102.1.

Dussaillant, I., R. Hugonnet, M. Huss, E. Berthier, J. Bannwart, F. Paul, and M. Zemp, 2025: Annual mass change of the world's glaciers from 1976 to 2024 by temporal downscaling of satellite data with in situ observations. *Earth Syst. Sci. Data*, **17**, 1977–2006, https://doi.org/10.5194/essd-17-1977-2025.

Dutton, E. G., J. J. DeLuisi, and A. P. Austring, 1985: Interpretation of Mauna Loa atmospheric transmission relative to aerosols, using photometric precipitable water amounts. *J. Atmos. Chem.*, **3**, 53–68, https://doi.org/10.1007/BF00049368.

Edwards, M., and A. Richardson, 2004: Impact of climate change on marine pelagic phenology and trophic mismatch. *Nature*, **430**, 881–884, https://doi.org/10.1038/nature02808.

Ellis, H. T., and R. F. Pueschel, 1971: Solar radiation: Absence of air pollution trends at Mauna Loa. *Science*, **172**, 845–846, https://doi.org/10.1126/science.172.3985.845.

Elshorbany, Y., and Coauthors, 2024: Tropospheric ozone precursors: Global and regional distributions, trends, and variability. *Atmos. Chem. Phys.*, **24**, 12 225–12 257, https://doi.org/10.5194/acp-24-12225-2024.

Estilow, T. W., A. H. Young, and D. A. Robinson, 2015: A long-term Northern Hemisphere snow cover extent data record for climate studies and monitoring. *Earth Syst. Sci. Data*, **7**, 137–142, https://doi.org/10.5194/essd-7-137-2015.

Etheridge, D. M., L. P. Steele, R. L. Langenfelds, R. J. Francey, J. M. Barnola, and V. I. Morgan, 1996: Natural and anthropogenic changes in atmospheric CO2 over the last 1000 years from air in Antarctic ice and firn. *J. Geophys. Res.*, **101**, 4115–4128, https://doi.org/10.1029/95JD03410.

European Commission, 2025a: Drought in Africa – April 2025 – GDO analytical report. Publications Office of the European Union, accessed 4 February 2026, https://data.europa.eu/doi/10.2760/2135988.

—— , 2025b: Drought in Europe – April 2025 – GDO analytical report. Publications Office of the European Union, accessed 4 February 2026, https://data.europa.eu/doi/10.2760/7964287.

—— , 2025c: Drought in Europe – June 2025 – GDO analytical report. Publications Office of the European Union, accessed 4 February 2026, https://data.europa.eu/doi/10.2760/1544910.

FAO, 2025: Drought alert: Widespread crop failure to impact the food security of millions of people due to failed 2024/2025 winter rains. 14 pp., https://openknowledge.fao.org/handle/20.500.14283/cd5629en.

Feldman, A. F., and Coauthors, 2024: Large global-scale vegetation sensitivity to daily rainfall variability. *Nature*, **636**, 380–384, https://doi.org/10.1038/s41586-024-08232-z.

Feng, L., P. I. Palmer, S. Zhu, R. J. Parker, and Y. Liu, 2022: Tropical methane emissions explain large fraction of recent changes in global atmospheric methane growth rate. *Nat. Commun.*, **13**, 1378, https://doi.org/10.1038/s41467-022-28989-z.

Fierro, A. O., S. Stevenson, and R. M. Rabin, 2018: Evolution of GLM-observed total lightning in Hurricane Maria (2017) during the period of maximum intensity. *Mon. Wea. Rev.*, **146**, 1641–1666, https://doi.org/10.1175/MWR-D-18-0066.1.

Finlay, C. C., C. Kloss, N. Olsen, M. D. Hammer, L. Tøffner-Clausen, A. Grayver, and A. Kuvshinov, 2020: The CHAOS-7 geomagnetic field model and observed changes in the South Atlantic anomaly. *Earth Planets Space*, **72**, 156, https://doi.org/10.1186/s40623-020-01252-9.

Fiore, A. M., and Coauthors, 2022: Understanding recent tropospheric ozone trends in the context of large internal variability: A new perspective from chemistry-climate model ensembles. *Environ. Res Climate*, **1**, 025008, https://doi.org/10.1088/2752-5295/ac9cc2.

Fischer, E. M., M. Bador, R. Huser, E. J. Kendon, A. Robinson, and S. Sippel, 2025: Record-breaking extremes in a warming climate. *Nat. Rev. Earth Environ.*, **6**, 456–470, https://doi.org/10.1038/s43017-025-00681-y.

Fisher, J. B., and Coauthors, 2020: ECOSTRESS: NASA's next generation mission to measure evapotranspiration from the international space station. *Water Resour. Res.*, **56**, e2019WR026058, https://doi.org/10.1029/2019WR026058.

Flemming, J., and A. Inness, 2025: Carbon monoxide [in "State of the Climate in 2024"]. *Bull. Amer. Meteor. Soc.*, **106** (8), S106–S107, https://doi.org/10.1175/BAMS-D-25-0102.1.

Fogt, R. L., and D. H. Bromwich, 2006: Decadal variability of the ENSO teleconnection to the high-latitude South Pacific governed by coupling with the Southern Annular Mode. *J. Climate*, **19**, 979–997, https://doi.org/10.1175/JCLI3671.1.

—— , and G. J. Marshall, 2020: The Southern Annular Mode: Variability, trends, and climate impacts across the Southern Hemisphere. *Wiley Interdiscip. Rev.: Climate Change*, **11**, e652, https://doi.org/10.1002/wcc.652.

—— , D. H. Bromwich, and K. M. Hines, 2011: Understanding the SAM influence on the South Pacific ENSO teleconnection. *Climate Dyn.*, **36**, 1555–1576, https://doi.org/10.1007/s00382-010-0905-0.

Folland, R. L., J. Knight, H. W. Linderholm, D. Fereday, S. Ineson, and J. W. Hurrelland, 2009: The summer North Atlantic oscillation: Past, present, and future. *J. Climate*, **22**, 1082–1103, https://doi.org/10.1175/2008JCLI2459.1.

Forster, P., and Coauthors, 2021: The Earth's energy budget, climate feedbacks, and climate sensitivity. *Climate Change 2021: The Physical Science Basis*, V. Masson-Delmotte et al., Eds., Cambridge University Press, 923–1054, https://doi.org/10.1017/9781009157896.009.

—— , and Coauthors, 2025: Indicators of global climate change 2024: Annual update of key indicators of the state of the climate system and human influence. *Earth Syst. Sci. Data*, **17**, 2641–2680, https://doi.org/10.5194/essd-17-2641-2025.

Foster, M. J., C. Phillips, A. K. Heidinger, E. E. Borbas, Y. Li, W. P. Menzel, A. Walther, and E. Weisz, 2023: PATMOS-x version 6.0: 40 years of merged AVHRR and HIRS global cloud data. *J. Climate*, **36**, 1143–1160, https://doi.org/10.1175/JCLI-D-22-0147.1.

Free, M., D. J. Seidel, J. K. Angel, J. Lanzante, I. Durre, and T. C. Peterson, 2005: Radiosonde atmospheric temperature products for assessing climate (RATPAC): A new data set of large-area anomaly time series. *J. Geophys. Res.*, **110**, D22101, https://doi.org/10.1029/2005JD006169.

Friedlingstein, P., and Coauthors, 2026: Global carbon budget 2025. *Earth Syst. Sci. Data*, **18**, 3211–3288, https://doi.org/10.5194/essd-18-3211-2026.

Frost, G. V., and Coauthors, 2024: NOAA Arctic Report Card 2024: Tundra greenness. https://doi.org/10.25923/5t2g-fm41.

Füllekrug, M., E. Williams, C. Price, S. Goodman, R. Holzworth, K. Virts, and D. Buechler, 2022: Lightning [in "State of the Climate in 2021"]. *Bull. Amer. Meteor. Soc.*, **103** (8), S79–S81, https://doi.org/10.1175/2022BAMSStateoftheClimate.1.

——, and Coauthors, 2024: Thunder hours [in "State of the Climate in 2023"]. *Bull. Amer. Meteor. Soc.*, **105** (8), S81–S82, https://doi.org/10.1175/2024BAMSStateoftheClimate.1.

Gao, H., 2021: MODIS/Terra water reservoir monthly L3 Global V061. NASA Land Processes Distributed Active Archive Center, accessed 25 February 2026, https://doi.org/10.5067/MODIS/MOD28C3.061.

Gao, R. S., and Coauthors, 2016: A light-weight, high-sensitivity particle spectrometer for PM2.5 aerosol measurements. *Aerosol Sci. Technol.*, **50**, 88–99, https://doi.org/10.1080/02786826.2015.1131809.

Garfinkel, C. I., and Coauthors, 2021: Influence of the El Niño–Southern Oscillation on entry stratospheric water vapor in coupled chemistry–ocean CCMI and CMIP6 models. *Atmos. Chem. Phys.*, **21**, 3725–3740, https://doi.org/10.5194/acp-21-3725-2021.

Gaudel, A., and Coauthors, 2018: Tropospheric ozone assessment report: Present-day distribution and trends of tropospheric ozone relevant to climate and global atmospheric chemistry model evaluation. *Elementa*, **6**, 39, https://doi.org/10.1525/elementa.291.

GCOS, 2022: The 2022 Global Climate Observing System (GCOS) implementation plan. GCOS-244, WMO, 98 pp., https://gcos.wmo.int/en/publications/gcos-implementation-plan2022.

Gelaro, R., and Coauthors, 2017: The Modern-Era Retrospective Analysis for Research and Applications, version 2 (MERRA-2). *J. Climate*, **30**, 5419–5454, https://doi.org/10.1175/JCLI-D-16-0758.1.

Getirana, A., S. Kumar, M. Girotto, and M. Rodell, 2017: Rivers and floodplains as key components of global terrestrial water storage variability. *Geophys. Res. Lett.*, **44**, 10 359–10 368, https://doi.org/10.1002/2017GL074684.

Giglio, L., W. Schroeder, and C. O. Justice, 2016: The Collection 6 MODIS active fire detection algorithm and fire products. *Remote Sens. Environ.*, **178**, 31–41, https://doi.org/10.1016/j.rse.2016.02.054.

GISTEMP Team, 2024: GISS Surface Temperature Analysis (GISTEMP), version 4. NASA Goddard Institute for Space Studies, accessed 2 February 2026, data.giss.nasa.gov/gistemp/.

Gobron, N., 2024: Sentinel-3 OLCI GI-FAPAR and rectified channels in O10, **O11**, O12 and O17 bands with uncertainties. Publications Office of the European Union, JRC Tech. Rep. 138238, 57 pp., https://doi.org/10.2760/5540982.

——, A. Belward, B. Pinty, and W. Knorr, 2010: Monitoring biosphere vegetation 1998–2009. *Geophys. Res. Lett.*, **37**, L15402, https://doi.org/10.1029/2010GL043870.

——, and Coauthors, 2022: Evaluation of Sentinel-3A and Sentinel-3B ocean land colour instrument green instantaneous fraction of absorbed photosynthetically active radiation. *Remote Sens. Environ.*, **270**, 112850, https://doi.org/10.1016/j.rse.2021.112850.

Good, E. J., 2016: An in situ–based analysis of the relationship between land surface "skin" and screen-level air temperatures. *J. Geophys. Res. Atmos.*, **121**, 8801–8819, https://doi.org/10.1002/2016JD025318.

——, J. Blannin, A. Waring, K. Veal, and D. Ghent, 2025: Super extreme land surface temperature hotspots [in "State of the Climate in 2024"]. *Bull. Amer. Meteor. Soc.*, **106** (8), S36–S38, https://doi.org/10.1175/BAMS-D-25-0102.1.

Granier, C., and Coauthors, 2011: Evolution of anthropogenic and biomass burning emissions of air pollutants at global and regional scales during the 1980–2010 period. *Climatic Change*, **109**, 163, https://doi.org/10.1007/s10584-011-0154-1.

Grant, L., and Coauthors, 2021: Attribution of global lake systems change to anthropogenic forcing. *Nature Geosci.*, **14**, 849–854, https://doi.org/10.1038/s41561-021-00833-x.

Griffiths, P. T., and Coauthors, 2021: Tropospheric ozone in CMIP6 simulations. *Atmos. Chem. Phys.*, **21**, 4187–4218, https://doi.org/10.5194/acp-21-4187-2021.

Gruber, A., W. A. Dorigo, W. Crow, and W. Wagner, 2017: Triple collocation-based merging of satellite soil moisture retrievals. *IEEE Trans. Geosci. Remote Sens.*, **55**, 6780–6792, https://doi.org/10.1109/TGRS.2017.2734070.

——, T. Scanlon, R. van der Schalie, W. Wagner, and W. Dorigo, 2019: Evolution of the ESA CCI soil moisture climate data records and their underlying merging methodology. *Earth Syst. Sci. Data*, **11**, 717–739, https://doi.org/10.5194/essd-11-717-2019.

Hahn, S., T. Melzer, and W. Wagner, 2026: Next-generation Metop ASCAT surface soil moisture datasets from EUMETSAT H SAF. *Earth Syst. Sci. Data*, **18**, 4393–4423, https://doi.org/10.5194/essd-18-4393-2026.

Haimberger, L., C. Tavolato, and S. Sperka, 2012: Homogenization of the global radiosonde temperature dataset through combined comparison with reanalysis background series and neighboring stations. *J. Climate*, **25**, 8108–8131, https://doi.org/10.1175/JCLI-D-11-00668.1.

Hansen, J., R. Ruedy, M. Sato, and K. Lo, 2010: Global surface temperature change. *Rev. Geophys.*, **48**, RG4004, https://doi.org/10.1029/2010RG000345.

Harder, P., and J. Flemming, 2026: Reconstructing carbon monoxide reanalysis with machine learning. arXiv, 2602.15056v1, https://doi.org/10.48550/arXiv.2602.15056.

Harris, I., T. J. Osborn, P. D. Jones, and D. H. Lister, 2020: Version 4 of the CRU TS monthly high-resolution gridded multivariate climate dataset. *Sci. Data*, **7**, 109, https://doi.org/10.1038/s41597-020-0453-3.

Hassan, T., R. Gulzar, M. Hamid, R. Ahmad, S. A. Waza, and A. A. Khuroo, 2024: Plant phenology shifts under climate warming: A systematic review of recent scientific literature. *Environ. Monit. Assess.*, **196**, 36, https://doi.org/10.1007/s10661-023-12190-w.

He, K., X. Shen, and E. Anagnostou, 2025: Global burn severity in forest ecoregions: Trends, climate drivers, and predictive insights. *npj Nat. Hazards*, **2**, 61, https://doi.org/10.1038/s44304-025-00113-3.

Heidinger, A., and Coauthors, 2026: A GEO-Ring of spectral radiances: Toward a next generation of the International Satellite Cloud Climatology Project (ISCCP-NG). *Bull. Amer. Meteor. Soc.*, **107**, E291–E308, https://doi.org/10.1175/BAMS-D-24-0161.1.

Hersbach, H., and Coauthors, 2020: The ERA5 global reanalysis. *Quart. J. Roy. Meteor. Soc.*, **146**, 1999–2049, https://doi.org/10.1002/qj.3803.

Hirschi, M., and Coauthors, 2024: Soil moisture [in "State of the Climate in 2023"]. *Bull. Amer. Meteor. Soc.*, **105** (8), S69–S70, https://doi.org/10.1175/2024BAMSStateoftheClimate.1.

Hjort, J., D. Streletskiy, G. Doré, Q. Wu, K. Bjella, and M. Luoto, 2022: Impacts of permafrost degradation on infrastructure. *Nat. Rev. Earth Environ.*, **3**, 24–38, https://doi.org/10.1038/s43017-021-00247-8.

Hodnebrog, Ø., and Coauthors, 2020a: Updated global warming potentials and radiative efficiencies of halocarbons and other weak atmospheric absorbers. *Rev. Geophys.*, **58**, e2019RG000691, https://doi.org/10.1029/2019RG000691.

——, and Coauthors, 2020b: The effect of rapid adjustments to halocarbons and N_2O on radiative forcing. *npj Climate Atmos. Sci.*, **3**, 43, https://doi.org/10.1038/s41612-020-00150-x.

Hofmann, D. J., and S. A. Montzka, 2009: Recovery of the ozone layer: The ozone depleting gas index. *Eos, Trans. Amer. Geophys. Union*, **90** (1), 1–2, https://doi.org/10.1029/2009EO010001.

——, J. H. Butler, E. J. Dlugokencky, J. W. Elkins, K. Masarie, S. A. Montzka, and P. Tans, 2006: The role of carbon dioxide in climate forcing from 1979 to 2004: Introduction of the annual greenhouse gas index. *Tellus*, **58**, 614–619, https://doi.org/10.1111/j.1600-0889.2006.00201.x.

Holton, J. R., and H. C. Tan, 1980: The influence of the equatorial quasi-biennial oscillation on the global circulation at 50 mb. *J. Atmos. Sci.*, **37**, 2200–2208, https://doi.org/10.1175/1520-0469(1980)037<2200:TIOTEQ>2.0.CO;2.

Holzworth, R. H., J. B. Brundell, M. P. McCarthy, A. R. Jacobson, C. J. Rodger, and T. S. Anderson, 2021: Lightning in the Arctic. *Geophys. Res. Lett.*, **48**, e2020GL091366, https://doi.org/10.1029/2020GL091366.

Hou, J., A. I. J. M. Van Dijk, L. J. Renzullo, and P. R. Larraondo, 2024: GloLakes: Water storage dynamics for 27 000 Lakes globally from 1984 to present derived from satellite altimetry and optical imaging. *Earth Syst. Sci. Data*, **16**, 201–218, https://doi.org/10.5194/essd-16-201-2024.

Hrbáček, F., M. Kňažková, K. Láska, and L. K. Pastíriková, 2025: Active layer warming and thickening on CALM-S JGM, James Ross Island, in the period 2013/14–2022/23. *Permafrost Periglacial Processes*, **36**, 378–389, https://doi.org/10.1002/ppp.2274.

Hu, G., and Coauthors, 2024: Spatiotemporal characteristics and variability in the thermal state of permafrost on the Qinghai–Tibet Plateau. *Permafrost Periglacical Processes*, **35**, 143–156, https://doi.org/10.1002/ppp.2219.

——, and Coauthors, 2025: The crucial role of ground ice in slowing permafrost degradation. *Sci. Bull.*, **71**, 1641–1644, https://doi.org/10.1016/j.scib.2025.11.042.

Huang, B., X. Yin, M. J. Menne, R. Vose, and H.-M. Zhang, 2022: Improvements to the land surface air temperature reconstruction in NOAAGlobalTemp: An artificial neural network approach. *Artif. Intell. Earth Syst.*, **1**, e220032, https://doi.org/10.1175/AIES-D-22-0032.1.

Huang, X., K. Yang, S. Kondragunta, Z. Wei, L. Valin, J. Szykman, and M. Goldberg, 2022: NO_2 retrievals from NOAA-20 OMPS: Algorithm, evaluation, and observations of drastic changes during COVID-19. *Atmos. Environ.*, **290**, 119367, https://doi.org/10.1016/j.atmosenv.2022.119367.

Huber, D. E., G. H. Kerr, M. O. Nawaz, S. Runkel, S. C. Anenberg, and D. L. Goldberg, 2026: Global NO2 changes between 2019 and 2024 as observed by TROPOMI in urban areas and emerging hotspots. *Atmos. Chem. Phys.*, **26**, 3783–3803, https://doi.org/10.5194/acp-26-3783-2026.

Huffman, G. J., R. Adler, A. Behrangi, D. Bolvin, E. Nelkin, G. Gu, and M. Ehsani, 2023: The new version 3.2 Global Precipitation Climatology Project (GPCP) monthly and daily precipitation products. *J. Climate*, **36**, 7635–7655, https://doi.org/10.1175/JCLI-D-23-0123.1.

Hurst, D. F., S. J. Oltmans, H. Vömel, K. H. Rosenlof, S. M. Davis, E. A. Ray, E. G. Hall, and A. F. Jordan, 2011: Stratospheric water vapor trends over Boulder, Colorado: Analysis of the 30 year Boulder record. *J. Geophys. Res.*, **116**, D02306, https://doi.org/10.1029/2010JD015065.

IGAD Climate Prediction and Applications Centre, 2025: An extremely poor October to December 2025 rainfall season in the Horn of Africa: Urgent action needed now to address severe food security risks. Drought Alert, 5 pp., https://www.icpac.net/documents/1026/FSNWG_Drought_Alert_Dec_16_2025.pdf.

Inness, A., and Coauthors, 2019: The CAMS reanalysis of atmospheric composition. *Atmos. Chem. Phys.*, **19**, 3515–3556, https://doi.org/10.5194/acp-19-3515-2019.

——, and Coauthors, 2022: Assimilation of S5P/TROPOMI carbon monoxide data with the global CAMS near-real-time system. *Atmos. Chem. Phys.*, **22**, 14 355–14 376, https://doi.org/10.5194/acp-22-14355-2022.

IPCC, 2013: *Climate Change 2013: The Physical Science Basis.* Cambridge University Press, 1535 pp.

——: Annex VII: Glossary. *Climate Change 2021: The Physical Science Basis*, V. Masson-Delmotte et al., Eds., Cambridge University Press, 2215–2256, https://doi.org/10.1017/9781009157896.022.

Jasinski, M. F., and Coauthors, 2023: ATLAS/ICESat-2 L3A along track inland surface water data, version 6. NASA National Snow and Ice Data Center Distributed Active Archive Center, accessed 25 February 2026, https://doi.org/10.5067/ATLAS/ATL13.006.

Jiang, Z., J. R. Worden, V. H. Payne, L. Zhu, E. Fischer, T. Walker, and D. B. Jones, 2016: Ozone export from East Asia: The role of PAN. *J. Geophys. Res. Atmos.*, **121**, 6555–6563, https://doi.org/10.1002/2016JD024952.

Johansson, D. J. A., C. Azar, S. Pettersson, T. Sterner, M. E. J. Stettler, and R. Teoh, 2025: The social costs of aviation CO_2 and contrail cirrus. *Nat. Commun.*, **16**, 8558, https://doi.org/10.1038/s41467-025-64355-5.

Joint Research Centre–European Commission, 2025: Global flood awareness system. Accessed 10 January 2026, https://global-flood.emergency.copernicus.eu/.

Joshi, M. M., J. M. Gregory, M. J. Webb, D. M. H. Sexton, and T. C. Johns, 2008: Mechanisms for the land/sea warming contrast exhibited by simulations of climate change. *Climate Dyn.*, **30**, 455–465, https://doi.org/10.1007/s00382-007-0306-1.

Junod, R. A., and J. R. Christy, 2020: A new compilation of globally gridded night-time marine air temperatures: The UAHNMATv1 dataset. *Int. J. Climatol.*, **40**, 2609–2623, https://doi.org/10.1002/joc.6354.

Kaiser, J. W., and Coauthors, 2012: Biomass burning emissions estimated with a global fire assimilation system based on observed fire radiative power. *Biogeosciences*, **9**, 527–554, https://doi.org/10.5194/bg-9-527-2012.

——, D. G. Holmedal, M. A. Ytre-Eide, and M. de Jong, 2025: GFAS4HTAP vegetation fire emissions 2003-2023. Zenodo, accessed 15 January 2026, https://doi.org/10.5281/zenodo.15721463.

Kaplan, A., 2011: Patterns and indices of climate variability [in "State of the Climate 2020"]. *Bull. Amer. Meteor. Soc.*, **92** (6), S20–S25, https://doi.org/10.1175/1520-0477-92.6.S1.

Keeling, C. D., and R. Revelle, 1985: Effects of El Niño/Southern Oscillation on the atmospheric content of carbon dioxide. *Meteoritics*, **20**, 437–450.

Kennedy, J. J., N. A. Rayner, C. P. Atkinson, and R. E. Killick, 2019: An ensemble data set of sea surface temperature change from 1850: The Met Office Hadley Centre HadSST.4.0.0.0 data set. *J. Geophys. Res. Atmos.*, **124**, 7719–7763, https://doi.org/10.1029/2018JD029867.

Khaykin, S., and Coauthors, 2026: Global transport of stratospheric aerosol produced by Ruang eruption from EarthCARE ATLID, limb-viewing satellites and ground-based lidar observations. *Atmos. Chem. Phys.*, **26**, 607–622, https://doi.org/10.5194/acp-26-607-2026.

Konopka, P., M. Tao, F. Ploeger, D. F. Hurst, M. L. Santee, J. S. Wright, and M. Riese, 2022: Stratospheric moistening after 2000. *Geophys. Res. Lett.*, **49**, e2021GL097609, https://doi.org/10.1029/2021GL097609.

Kosaka, Y., and Coauthors, 2024: The JRA-3Q reanalysis. *J. Meteor. Soc. Japan*, **102**, 49–109, https://doi.org/10.2151/jmsj.2024-004.

Kovilakam, M., L. W. Thomason, N. Ernest, L. Rieger, A. Bourassa, and L. Millán, 2020: The Global Space-Based Stratospheric Aerosol Climatology (version 2.0): 1979–2018. *Earth Syst. Sci. Data*, **12**, 2607–2634, https://doi.org/10.5194/essd-12-2607-2020.

Kremser, S., and Coauthors, 2016: Stratospheric aerosol-observations, processes, and impact on climate. *Rev. Geophys.*, **54**, 278–335, https://doi.org/10.1002/2015RG000511.

L'Abée-Lund, J. H., L. A. Vøllestad, J. E. Brittain, Å. S. Kvambekk, and T. Solvang, 2021: Geographic variation and temporal trends in ice phenology in Norwegian lakes during the period 1890–2020. *Cryosphere*, **15**, 2333–2356. https://doi.org/10.5194/tc-15-2333-2021.

Labitzke, K., 1982: On the interannual variability of the middle stratosphere during the northern winters. *J. Meteor. Soc. Japan*, **60**, 124–139, https://doi.org/10.2151/jmsj1965.60.1_124.

Lagouarde, J.-P., and Coauthors, 2018: The Indian–French TRISHNA mission: Earth observation in the thermal infrared with high spatio-temporal resolution. *IGARSS 2018 - 2018 IEEE Int. Geoscience and Remote Sensing Symp.*, Valencia, Spain, IEEE, 4078–4081, https://doi.org/10.1109/IGARSS.2018.8518720.

Lan, X., and Coauthors, 2019: Long-term measurements show little evidence for large increases in total U.S. methane emissions over the past decade. *Geophys. Res. Lett.*, **46**, 4991–4999, https://doi.org/10.1029/2018GL081731.

——, and Coauthors, 2021: Improved constraints on global methane emissions and sinks using $\delta^{13}C$-CH_4. *Global Biogeochem. Cycles*, **35**, e2021GB007000, https://doi.org/10.1029/2021GB007000.

——, P. Tans, K. Thoning, and NOAA Global Monitoring Laboratory, 2024: NOAA Greenhouse Gas Marine Boundary Layer Reference - CO2. NOAA GML, accessed 6 February 2026, https://doi.org/10.15138/DVNP-F961.

——, ——, and ——, 2026a: Trends in globally-averaged CO_2 determined from NOAA Global Monitoring Laboratory measurements. Version 2026-02. Accessed 6 February 2026, https://doi.org/10.15138/9N0H-ZH07.

——, K. W. Thoning, and E. J. Dlugokencky, 2026b: Trends in globally-averaged CH_4, N_2O, and SF_6 determined from NOAA Global Monitoring Laboratory measurements. Version 2026-02. Accessed 6 February 2026, https://doi.org/10.15138/P8XG-AA10.

Landerer, F. W., and Coauthors, 2020: Extending the global mass change data record: GRACE follow-on instrument and science data performance. *Geophys. Res. Lett.*, **47**, e2020GL088306, https://doi.org/10.1029/2020GL088306.

Lanzante, J. R., 1996: Resistant, robust and non-parametric techniques for the analysis of climate data: Theory and examples, including applications to historical radiosonde station data. *Int. J. Climatol.*, **16**, 1197–1226, https://doi.org/10.1002/(SICI)1097-0088(199611)16:11<1197::AID-JOC89>3.0.CO;2-L.

Leathers, D. J., B. Yarnal, and M. A. Palecki, 1991: The Pacific/North American teleconnection pattern and United States climate. Part I: Regional temperature and precipitation associations. *J. Climate*, **4**, 517–528, https://doi.org/10.1175/1520-0442(1991)004<0517:TPATPA>2.0.CO;2.

Lee, S., M. L'Heureux, A. T. Wittenberg, R. Seager, P. A. O'Gorman, and N. C. Johnson, 2022: On the future zonal contrasts of equatorial Pacific climate: Perspectives from observations, simulations, and theories. *npj Climate Atmos. Sci.*, **5**, 82, https://doi.org/10.1038/s41612-022-00301-2.

Lems, J., and Coauthors, 2025: Soil moisture [in "State of the Climate in 2024"]. *Bull. Amer. Meteor. Soc.*, **106** (8), S75–S76, https://doi.org/10.1175/2025BAMSStateoftheClimate.1.

Lenssen, N. J. L., G. A. Schmidt, J. E. Hansen, M. J. Menne, A. Persin, R. Ruedy, and D. Zyss, 2019: Improvements in the GISTEMP uncertainty model. *J. Geophys. Res. Atmos.*, **124**, 6307–6326, https://doi.org/10.1029/2018JD029522.

——, ——, M. Hendrickson, P. Jacobs, M. Menne, and R. Ruedy, 2024: A GISTEMPv4 observational uncertainty ensemble. *J. Geophys. Res. Atmos.*, **129**, e2023JD040179. https://doi.org/10.1029/2023JD040179.

Levene, H., 1960: Robust tests for equality of variances. *Contributions to Probability and Statistics: Essays in Honor of Harold Hotelling*, I. Olkin et al., Eds., Stanford University Press, 278–292.

Levy, R. C., S. Mattoo, L. A. Munchak, L. A. Remer, A. M. Sayer, F. Patadia, and N. C. Hsu, 2013: The Collection 6 MODIS aerosol products over land and ocean. *Atmos. Meas. Tech.*, **6**, 2989–3034, https://doi.org/10.5194/amt-6-2989-2013.

L'Heureux, M. L., and Coauthors, 2024: A relative sea surface temperature index for classifying ENSO events in a changing climate. *J. Climate*, **37**, 1197–1211, https://doi.org/10.1175/JCLI-D-23-0406.1.

Li, L., D. Long, Y. Wang, and R. I. Woolway, 2025: Global dominance of seasonality in shaping lake-surface-extent dynamics. *Nature*, **642**, 361–368, https://doi.org/10.1038/s41586-025-09046-3.

Li, Z., Z. Yan, Y. Zhu, N. Freychet, and S. Tett, 2020: Homogenized daily relative humidity series in China during 1960–2017. *Adv. Atmos. Sci.*, **37**, 318–327, https://doi.org/10.1007/s00376-020-9180-0.

Lickley, M. J., J. S. Daniel, L. A. McBride, R. J. Salawitch, and G. J. M. Velders, 2024: The return to 1980 stratospheric halogen levels: A moving target in ozone assessments from 2006 to 2022. *Atmos. Chem. Phys.*, **24**, 13081–13099, https://doi.org/10.5194/acp-24-13081-2024.

Lin, X., and Coauthors, 2024: Recent methane surges reveal heightened emissions from tropical inundated areas. *Nat. Commun.*, **15**, 10894, https://doi.org/10.1038/s41467-024-55266-y.

Liu, Y., and Coauthors, 2017: Evaluation of the VIIRS BRDF, albedo and NBAR products suite and an assessment of continuity with the long term MODIS record. *Remote Sens. Environ.*, **201**, 256–274, https://doi.org/10.1016/j.rse.2017.09.020.

——, L. Zhou, Y. Qin, C. Azorin-Molina, C. Shen, R. Xu, and Z. Zeng, 2024: Impacts of anemometer changes, site relocations and processing methods on wind speed trends in China. *Atmos. Meas. Tech.*, **17**, 1123–1131, https://doi.org/10.5194/amt-17-1123-2024.

——, and Coauthors, 2025: Reduction in global lightning activity during the COVID pandemic. *J. Geophys. Res. Atmos.*, **130**, e2024JD042319, https://doi.org/10.1029/2024JD042319.

Livezey, R. E., M. Masutani, A. Leetmaa, H. Rui, M. Ji, and A. Kumar, 1997: Teleconnective response of the Pacific–North American region atmosphere to large central equatorial Pacific SST anomalies. *J. Climate*, **10**, 1787–1820, https://doi.org/10.1175/1520-0442(1997)010<1787:TROTPN>2.0.CO;2.

Loeb, N. G., B. A. Wielicki, D. R. Doelling, G. L. Smith, D. F. Keyes, S. Kato, N. Manalo-Smith, and T. Wong, 2009: Toward optimal closure of the Earth's top-of-atmosphere radiation budget. *J. Climate*, **22**, 748–766, https://doi.org/10.1175/2008JCLI2637.1.

——, S. Kato, W. Su, T. Wong, F. G. Rose, D. R. Doelling, J. R. Norris, and X. Huang, 2012: Advances in understanding top-of-atmosphere radiation variability from satellite observations. *Surv. Geophys.*, **33**, 359–385, https://doi.org/10.1007/s10712-012-9175-1.

——, and Coauthors, 2018: Clouds and the Earth's Radiant Energy System (CERES) Energy Balanced and Filled (EBAF) top-of-atmosphere (TOA) edition-4.0 data product. *J. Climate*, **31**, 895–918, https://doi.org/10.1175/JCLI-D-17-0208.1.

——, G. C. Johnson, T. J. Thorsen, J. M. Lyman, F. G. Rose, and S. Kato, 2021: Satellite and ocean data reveal marked increase in Earth's heating rate. *Geophys. Res. Lett.*, **48**, e2021GL093047, https://doi.org/10.1029/2021GL093047.

——, and Coauthors, 2022: Evaluating twenty-year trends in Earth's energy flows from observations and reanalyses. *J. Geophys. Res. Atmos.*, **127**, e2022JD036686, https://doi.org/10.1029/2022JD036686.

——, S.-H. Ham, R. P. Allan, T. J. Thorsen, B. Meyssignac, S. Kato, G. C. Johnson, and J. M. Lyman, 2024: Observational assessment of changes in Earth's energy imbalance since 2000. *Surv. Geophys.*, **45**, 1757–1783, https://doi.org/10.1007/s10712-024-09838-8.

Loikith, P. C., and A. J. Broccoli, 2014: The influence of recurrent modes of climate variability on the occurrence of winter and summer extreme temperatures over North America. *J. Climate*, **27**, 1600–1618, https://doi.org/10.1175/JCLI-D-13-00068.1.

Lou, Y., Q. Zhang, Y. Jiang, C. Gao, and C. Shi, 2026: Declining anthropogenic wildfires in South American savannas. *Global Planet. Change*, **258**, 105305, https://doi.org/10.1016/j.gloplacha.2026.105305.

MacCallum, S. N., and C. J. Merchant, 2012: Surface water temperature observations of large lakes by optimal estimation. *Can. J. Remote Sens.*, **38**, 25–45, https://doi.org/10.5589/m12-010.

Magnin, F., L. Ravanel, X. Bodin, P. Deline, E. Malet, J. Krysiecki, and P. Schoeneich, 2024: Main results of permafrost monitoring in the French Alps through the *PermaFrance* network over the period 2010–2022. *Permaforest Periglacial Processess*, **35**, 3–23, https://doi.org/10.1002/ppp.2209.

Martens, B., and Coauthors, 2017: GLEAM v3: Satellite-based land evaporation and root-zone soil moisture. *Geosci. Model Dev.*, **10**, 1903–1925, https://doi.org/10.5194/gmd-10-1903-2017.

——, W. Waegeman, W. A. Dorigo, N. E. C. Verhoest, and D. G. Miralles, 2018: Terrestrial evaporation response to modes of climate variability. *npj Climate Atmos. Sci.*, **1**, 43, https://doi.org/10.1038/s41612-018-0053-5.

Matthews, T., and National Center for Atmospheric Research Staff, Eds., 2025: The climate data guide: Equivalent temperature: HadISDH.land and ERA5. Accessed 13 February 2026, https://climatedataguide.ucar.edu/climate-data/equivalent-temperature-hadisdhland-and-era5.

——, M. Byrne, R. Horton, C. Murphy, R. Pielke Sr., C. Raymond, P. Thorne, and R. L. Wilby, 2022: Latent heat must be visible in climate communications. *Wiley Interdiscip. Rev.: Climate Change*, **13**, e779, https://doi.org/10.1002/wcc.779.

——, T. Wood, M. Byrne, and P. Stoy, 2025: Equivalent temperature [in "State of the Climate in 2024"]. *Bull. Amer. Meteor. Soc.*, **106** (8), S80–S81, https://doi.org/10.1175/BAMS-D-25-0102.1

Mayer, M., T. Tsubouchi, K. von Schuckmann, V. Seitner, S. Winkelbauer, and L. Haimberger, 2022: Atmospheric and oceanic contributions to observed Nordic seas and Arctic Ocean heat content variations 1993-2020. *J. Oper. Oceanogr.*, **15** (Suppl. 1), s119–s126, https://doi.org/10.1080/1755876X.2022.2095169.

——, M. A. Balmaseda, F. Vitart, and S. Tietsche, 2025: Tropical Pacific trends in the ECMWF seasonal system and implications for predictions of the 2020–22 triple-dip La Niña. *J. Climate*, **38**, 2989–3003, https://doi.org/10.1175/JCLI-D-24-0467.1.

——, N. G. Loeb, J. M. Lyman, G. C. Johnson, and S. Winkelbauer, 2026: The atmosphere's substantial role in interannual variability of Earth's energy imbalance. *Geophys. Res. Lett.*, **53**, e2025GL119833, https://doi.org/10.1029/2025GL119833.

McCabe, M. F., B. Aragon, R. Houborg, and J. Mascaro, 2017: CubeSats in hydrology: Ultrahigh-resolution insights into vegetation dynamics and terrestrial evaporation. *Water Resour. Res.*, **53**, 10017–10024, https://doi.org/10.1002/2017WR022240.

McPhaden, M. J., A. Santoso, and W. Cai, 2020: Introduction to El Niño Southern Oscillation in a Changing Climate. *El Niño Southern Oscillation in a Changing Climate, Geophys. Monogr.*, Vol. 253, Amer. Geophys. Union, 1–19, https://doi.org/10.1002/9781119548164.ch1.

McVicar, T. R., and Coauthors, 2012: Global review and synthesis of trends in observed terrestrial near-surface wind speeds: Implications for evaporation. *J. Hydrol.*, **416–417**, 182–205, https://doi.org/10.1016/j.jhydrol.2011.10.024.

Mears, C. A., and F. J. Wentz, 2016: Sensitivity of satellite-derived tropospheric temperature trends to the diurnal cycle adjustment. *J. Climate*, **29**, 3629–3646, https://doi.org/10.1175/JCLI-D-15-0744.1.

—— , —— , P. Thorne, and D. Bernie, 2011: Assessing uncertainty in estimates of atmospheric temperature changes from MSU and AMSU using a Monte-Carlo estimation technique. *J. Geophys. Res.*, **116**, D08112, https://doi.org/10.1029/2010JD014954.

—— , A. K. Smith, L. Ricciardulli, J. Wang, H. Huelsing, and F. J. Wentz, 2018: Construction and uncertainty estimation of a satellite-derived total precipitable water data record over the world's oceans. *Earth Space Sci.*, **5**, 197–210, https://doi.org/10.1002/2018EA000363.

Meesters, A. G., R. A. M. De Jeu, and M. Owe, 2005: Analytical derivation of the vegetation optical depth from the microwave polarization difference index. *IEEE Geosci. Remote Sens. Lett.*, **2**, 121–123, https://doi.org/10.1109/LGRS.2005.843983.

Menne, M. J., and Coauthors, 2025: The Global Historical Climatology Network hourly (GHCNh) dataset. *29th Conf. of Applied Climatology*, New Orleans, LA, Amer. Meteor. Soc., 9.1, https://ams.confex.com/ams/105ANNUAL/meetingapp.cgi/Paper/446924.

Menzel, A., Y. Yuan, M. Matiu, T. Sparks, H. Scheifinger, R. Gehrig, and N. Estrella, 2020: Climate change fingerprints in recent European plant phenology. *Global Change Biol.*, **26**, 2599–2612, https://doi.org/10.1111/gcb.15000.

Messager, M. L., B. Lehner, G. Grill, I. Nedeva, and O. Schmitt, 2016: Estimating the volume and age of water stored in global lakes using a geo-statistical approach. *Nat. Commun.*, **7**, 13603, https://doi.org/10.1038/ncomms13603.

Michel, S. E., and Coauthors, 2024: Rapid shift in methane carbon isotopes suggests microbial emissions drove record high atmospheric methane growth in 2020-2022. *Proc. Natl. Acad. Sci. USA*, **121**, e2411212121, https://doi.org/10.1073/pnas.2411212121.

Millán, L., and Coauthors, 2022: The Hunga Tonga-Hunga Ha'apai hydration of the stratosphere. *Geophys. Res. Lett.*, **49**, e2022GL099381, https://doi.org/10.1029/2022GL099381.

Miller, B. R., and Coauthors, 2010: HFC-23 (CHF_3) emission trend response to HCFC-22 ($CHClF_2$) production and recent HFC-23 emission abatement measures. *Atmos. Chem. Phys.*, **10**, 7875–7890, https://doi.org/10.5194/acp-10-7875-2010.

Minola, L., H. Reese, H. W. Lai, C. Azorin-Molina, J. A. Guijarro, S. W. Son, and D. Chen, 2022: Wind stilling-reversal across Sweden: The impact of land-use and large-scale atmospheric circulation changes. *Int. J. Climatol.*, **42**, 1049–1071, https://doi.org/10.1002/joc.7289.

Miralles, D. G., T. R. H. Holmes, R. A. M. De Jeu, J. H. Gash, A. G. C. A. Meesters, and A. J. Dolman, 2011: Global land-surface evaporation estimated from satellite-based observations. *Hydrol. Earth Syst. Sci.*, **15**, 453–469, https://doi.org/10.5194/hess-15-453-2011.

—— , and Coauthors, 2014: El Niño–La Niña cycle and recent trends in continental evaporation. *Nat. Climate Change*, **4**, 122–126, https://doi.org/10.1038/nclimate2068.

—— , and Coauthors, 2025: GLEAM4: Global land evaporation and soil moisture dataset at 0.1 resolution from 1980 to near present. *Sci. Data*, **12**, 416, https://doi.org/10.1038/s41597-025-04610-y.

Mirrezaei, M. A., and Coauthors, 2026: Toward realistic prognostic modeling of the methane chemical loss. *J. Geophys. Res. Atmos.*, **131**, e2025JD045079, https://doi.org/10.1029/2025JD045079.

Mitchell, L., E. Brook, J. E. Lee, C. Buizert, and T. Sowers, 2013: Constraints on the late Holocene anthropogenic contribution to the atmospheric methane budget. *Science*, **342**, 964–966, https://doi.org/10.1126/science.1238920.

Miyazaki, K., K. Bowman, T. Sekiya, M. Takigawa, J. L. Neu, K. Sudo, G. Osterman, and H. Eskes, 2021: Global tropospheric ozone responses to reduced NO_x emissions linked to the COVID-19 worldwide lockdowns. *Sci. Adv.*, **7**, eabf7460, https://doi.org/10.1126/sciadv.abf7460.

Moesinger, L., R.-M. Zotta, R. van Der Schalie, T. Scanlon, R. de Jeu, and W. Dorigo, 2022: Monitoring vegetation condition using microwave remote sensing: The standardized vegetation optical depth index (SVODI). *Biogeosciences*, **19**, 5107–5123, https://doi.org/10.5194/bg-19-5107-2022.

Monerie, P.-A., R. Shiemann, D. J. Brayshaw, and J. I. Robson, 2026: Global wind stilling and the role of sub-monthly variability in explaining deficiencies in atmospheric reanalyses. *Climate Dyn.*, **64**, 179, https://doi.org/10.1007/s00382-026-08163-7.

Montreal Protocol, 1989: Montreal protocol on substances that deplete the ozone layer Final Act 1987. *J. Environ. Law*, **1**, 128–136, https://doi.org/10.1093/jel/1.1.128.

Montzka, S. A., 2025: Method for quantifying overlapping chemical signals. US Patent Application US20250329422A1, filed 16 April 2025, https://patents.google.com/patent/US20250329422A1.

—— , and Coauthors, 2018: An unexpected and persistent increase in global emissions of ozone-depleting CFC-11. *Nature*, **557**, 413–417, https://doi.org/10.1038/s41586-018-0106-2.

—— , and Coauthors, 2021: A decline in global CFC-11 emissions during 2018-2019. *Nature*, **590**, 428–432, https://doi.org/10.1038/s41586-021-03260-5.

Morgenstern, O., and Coauthors, 2025: Radiocarbon monoxide indicates increasing atmospheric oxidizing capacity. *Nat. Commun.*, **16**, 249, https://doi.org/10.1038/s41467-024-55603-1.

Morice, C. P., and Coauthors, 2021: An updated assessment of near-surface temperature change from 1850: The HadCRUT5 data set. *J. Geophys. Res. Atmos.*, **126**, e2019JD032361, https://doi.org/10.1029/2019JD032361.

Mote, P. W., and Coauthors, 1996: An atmospheric tape recorder: The imprint of tropical tropopause temperatures on stratospheric water vapor. *J. Geophys. Res.*, **101**, 3989–4006, https://doi.org/10.1029/95JD03422.

Mühle, J., and Coauthors, 2010: Perfluorocarbons in the global atmosphere: Tetrafluoromethane, hexafluoroethane, and octafluoropropane. *Atmos. Chem. Phys.*, **10**, 5145–5164, https://doi.org/10.5194/acp-10-5145-2010.

Myhre, G., and Coauthors, 2014: Anthropogenic and natural radiative forcing. *Climate Change 2013: The Physical Science Basis*, T. F. Stocker et al., Eds., Cambridge University Press, 659–740.

NASA Earth Observatory, 2025: Hayli Gubbi's explosive first impression. Accessed 4 December 2025, https://science.nasa.gov/earth/earth-observatory/hayli-gubbis-explosive-first-impression/.

NCEI, 2026: Synoptic discussion. Accessed 11 February 2026, www.ncei.noaa.gov/access/monitoring/monthly-report/synoptic.

Newhall, C. G., and S. Self, 1982: The volcanic explosivity index (VEI) an estimate of explosive magnitude for historical volcanism. *J. Geophys. Res.*, **87**, 1231–1238, https://doi.org/10.1029/JC087iC02p01231.

Newman, P. A., J. S. Daniel, D. W. Waugh, and E. R. Nash, 2007: A new formulation of equivalent effective stratospheric chlorine (EESC). *Atmos. Chem. Phys.*, **7**, 4537–4552, https://doi.org/10.5194/acp-7-4537-2007.

—— , L. R. Lait, N. A. Kramarova, L. Coy, S. M. Frith, L. D. Oman, and S. S. Dhomse, 2024: Record high March 2024 Arctic total column ozone. *Geophys. Res. Lett.*, **51**, e2024GL110924, https://doi.org/10.1029/2024GL110924.

Nguyen, N. K., O. Bock, and E. Lebarbier, 2026: PMLseg, a R package for the segmentation of univariate time series based on Penalized Maximum Likelihood. Accessed 15 February 2026, https://github.com/khanhninhnguyen/PMLSeg.

Nicholson, S. E., and J. C. Selato, 2000: The influence of La Niña on African rainfall. *Int. J. Climatol.*, **20**, 1761–1776, https://doi.org/10.1002/1097-0088(20001130)20:14<1761::AID-JOC580>3.0.CO;2-W.

Nimac, I., J. Danzer, and G. Kirchengast, 2025: The added value and potential of long-term radio occultation data for climatological wind field monitoring. *Atmos. Meas. Tech.*, **18**, 265–286, https://doi.org/10.5194/amt-18-265-2025.

Nisbet, E. G., and Coauthors, 2023: Atmospheric methane: Comparison between methane's record in 2006–2022 and during glacial terminations. *Global Biogeochem. Cycles*, **37**, e2023GB007875, https://doi.org/10.1029/2023GB007875.

NIWA, 2025: Spring 2025 climate summary. National Institute of Water and Atmospheric Research, accessed 25 May 2026, https://niwa.co.nz/climate-and-weather/seasonal/spring-2025.

NOAA/NCEI, 2026: Monthly drought report for annual 2025. Accessed 11 February 2025, https://www.ncei.noaa.gov/access/monitoring/monthly-report/drought/202513.

Noetzli, J., and Coauthors, 2024: Enhanced warming of European mountain permafrost in the early 21st century. *Nat. Commun.*, **15**, 10508, https://doi.org/10.1038/s41467-024-54831-9.

OCHA, 2025: Pakistan: Monsoon floods 2025 flash update #4 (as of 30 August 2025). United Nations Office for the Coordination of Humanitarian Affairs, accessed 18 February 2026, https://www.unocha.org/publications/report/pakistan/pakistan-monsoon-floods-2025-flash-update-4-30-august-2025.

O'Gorman, P. A., and C. J. Muller, 2010: How closely do changes in surface and column water vapor follow Clausius-Clapeyron scaling in climate change simulations? *Environ. Res. Lett.*, **5**, 025207, https://doi.org/10.1088/1748-9326/5/2/025207.

Oh, Y., and Coauthors, 2023: CarbonTracker CH_4 2023. Accessed 2 February 2026, https://doi.org/10.25925/40jt-qd67.

O'Kane, T. J., and C. L. Franzke, 2025: Pacific–South American pattern. *Atmospheric Oscillations*, Elsevier, 171–181.

O'Keefe, J., and G. VanScoy, 2024: Phenology of woody species at Harvard Forest since 1990. Harvard Forest Data Archive: HF003. Accessed 3 July 2026, https://harvardforest1.fas.harvard.edu/exist/apps/datasets/showData.html?id=HF003.

Oman, L. D., A. R. Douglass, J. R. Ziemke, J. M. Rodriguez, D. W. Waugh, and J. E. Nielsen, 2013: The ozone response to ENSO in Aura satellite measurements and a chemistry-climate simulation. *J. Geophys. Res. Atmos.*, **118**, 965–976, https://doi.org/10.1029/2012JD018546.

Osborn, T. J., and Coauthors, 2021: Land surface air temperature variations across the globe updated to 2019: The CRUTEM5 data set. *J. Geophys. Res. Atmos.*, **126**, e2019JD032352, https://doi.org/10.1029/2019JD032352.

Overland, J. E., and M. Wang, 2016: Recent extreme Arctic temperatures are due to a split polar vortex. *J. Climate*, **29**, 5609–5616, https://doi.org/10.1175/JCLI-D-16-0320.1.

Papa, F., and Coauthors, 2023: Water resources in Africa under global change: Monitoring surface waters from space. *Surv. Geophys.*, **44**, 43–93, https://doi.org/10.1007/s10712-022-09700-9.

Park, S., and Coauthors, 2021: A decline in emissions of CFC-11 and related chemicals from eastern China. *Nature*, **590**, 433–437, https://doi.org/10.1038/s41586-021-03277-w.

Park, T., and Coauthors, 2016: Changes in growing season duration and productivity of northern vegetation inferred from long-term remote sensing data. *Environ. Res. Lett.*, **11**, 084001, https://doi.org/10.1088/1748-9326/11/8/084001.

—— , M. K. Gumma, W. Wang, P. Panjala, S. K. Dubey, and R. R. Nemani, 2023: Greening of human-dominated ecosystems in India. *Commun. Earth Environ.*, **4**, 419, https://doi.org/10.1038/s43247-023-01078-9.

Payne, V. H., E. V. Fischer, J. R. Worden, Z. Jiang, L. Zhu, T. P. Kurosu, and S. S. Kulawik, 2017: Spatial variability in tropospheric peroxyacetyl nitrate in the tropics from infrared satellite observations in 2005 and 2006. *Atmos. Chem. Phys.*, **17**, 6341–6351, https://doi.org/10.5194/acp-17-6341-2017.

Peng, S., and Coauthors, 2022: Wetland emission and atmospheric sink changes explain methane growth in 2020. *Nature*, **612**, 477–482, https://doi.org/10.1038/s41586-022-05447-w.

Peng, Y., W. Randel, O. B. Toon, X. Wang, K. Qie, S. M. Davis, K. H. Rosenlof, and P. Yu, 2026: Moderate volcanic eruptions and extreme wildfires humidify the stratosphere. Research Square, https://www.researchsquare.com/article/rs-8624912/v1.

PERMOS, 2025: *Swiss Permafrost Bulletin 2024* (Annual Report of the Swiss Permafrost Monitoring Network PERMOS No. 6). Swiss Permafrost Monitoring Network PERMOS, https://doi.org/10.13093/permos-bull-2025.

—— , 2026: Swiss permafrost monitoring network database (PERMOS database). Swiss Permafrost Monitoring Network, accessed 2 July 2026, https://doi.org/10.13093/permos-2026-01.

Peterson, D. A., and Coauthors, 2021: Australia's black summer pyrocumulonimbus super outbreak reveals potential for increasingly extreme stratospheric smoke events. *npj Climate Atmos. Sci.*, **4**, 38, https://doi.org/10.1038/s41612-021-00192-9.

Petropavlovskikh, I., and Coauthors, 2025: Ozone trends in homogenized Umkehr, ozonesonde, and COH overpass records. *Atmos. Chem. Phys.*, **25**, 2895–2936, https://doi.org/10.5194/acp-25-2895-2025.

Phillips, C., and M., Foster, 2025: Cloudiness [in "State of the Climate in 2024"]. *Bull. Amer. Meteor. Soc.*, **106** (8), S67–S69, https://doi.org/10.1175/2025BAMSStateoftheClimate.1.

Pi, X., and Coauthors, 2022: Mapping global lake dynamics reveals the emerging roles of small lakes. *Nat. Commun.*, **13**, 5777, https://doi.org/10.1038/s41467-022-33239-3.

Pimlott, M. A., R. J. Pope, B. J. Kerridge, R. Siddans, B. G. Latter, L. J. Ventress, W. Feng, and M. P. Chipperfield, 2025: Large reductions in satellite-derived and modelled European lower-tropospheric ozone during and after the COVID-19 pandemic (2020–2022). *Atmos. Chem. Phys.*, **25**, 4391–4401, https://doi.org/10.5194/acp-25-4391-2025.

Plumb, R. A., 2002: Stratospheric transport. *J. Meteor. Soc. Japan*, **80**, 793–809, https://doi.org/10.2151/jmsj.80.793.

Pogliotti, P., E. Cremonese, and U. M. D. Cella, 2023: Warming permafrost in the western Alps: A further evidence of elevation dependent warming. *J. Alp. Res.*, **111–2**, https://doi.org/10.4000/rga.11784.

Popp, T., and Coauthors, 2016: Development, production and evaluation of aerosol climate data records from European satellite observations (Aerosol_cci). *Remote Sens.*, **8**, 421, https://doi.org/10.3390/rs8050421.

Prather, M. J., C. D. Holmes, and J. Hsu, 2012: Reactive greenhouse gas scenarios: Systematic exploration of uncertainties and the role of atmospheric chemistry. *Geophys. Res. Lett.*, **39**, L09803, https://doi.org/10.1029/2012GL051440.

Price, S., and J. C. Pales, 1963: Mauna Loa Observatory: The first five years. *Mon. Wea. Rev.*, **91**, 665–680, https://doi.org/10.1175/1520-0493(1963)091<0665:MLOTFF>2.3.CO;2.

Prinn, R. G., and Coauthors, 2018: History of chemically and radiatively important atmospheric gases from the Advanced Global Atmospheric Gases Experiment (AGAGE). *Earth Syst. Sci. Data*, **10**, 985–1018, https://doi.org/10.5194/essd-10-985-2018.

——, and Coauthors, 2025: The dataset of in-situ measurements of chemically and radiatively important atmospheric gases from the Advanced Global Atmospheric Gas Experiment (AGAGE) and affiliated stations, version 20251230, NASA Langley Research Center (LaRC) Data Host Facility (DHF), accessed XX XXXX XXXX, https://doi.org/10.60718/2zet-cn22.

Qin, Y., D. Wang, A. D. Ziegler, B. Fu, and Z. Zeng, 2025: Impact of amazonian deforestation on precipitation reverses between seasons. *Nature*, **639**, 102–108, https://doi.org/10.1038/s41586-024-08570-y.

Quaas, J., and Coauthors, 2022: Robust evidence for reversal of the trend in aerosol effective climate forcing. *Atmos. Chem. Phys.*, **22**, 12 221–12 239, https://doi.org/10.5194/acp-22-12221-2022.

Quarello, A., O. Bock, and E. Lebarbier, 2022: GNSSseg, a statistical method for the segmentation of daily GNSS IWV time series. *Remote Sens.*, **14**, 3379, https://doi.org/10.3390/rs14143379.

Raghuraman, S. P., D. Paynter, R. Menzel, and V. Ramaswamy, 2023: Forcing, cloud feedbacks, cloud masking, and internal variability in the cloud radiative effect satellite record. *J. Climate*, **36**, 4151–4167, https://doi.org/10.1175/JCLI-D-22-0555.1.

Randel, W. J., and J. B. Cobb, 1994: Coherent variations of monthly mean total ozone and lower stratospheric temperature. *J. Geophys. Res.*, **99**, 5433–5447, https://doi.org/10.1029/93JD03454.

——, X. Wang, J. Starr, R. R. Garcia, and D. Kinnison, 2024: Long-term temperature impacts of the Hunga volcanic eruption in the stratosphere and above. *Geophys. Res. Lett.*, **51**, e2024GL111500, https://doi.org/10.1029/2024GL111500.

Raup, B., L. Andreassen, D. Boyer, C. Howe, M. Pelto, and A. Rabatel, 2025: Tracking extinct glaciers in GLIMS. *Ann. Glaciol.*, **66**, e35, https://doi.org/10.1017/aog.2025.10027.

Ravanel, L., and P. Deline, 2011: Climate influence on rockfalls in high-Alpine steep rockwalls: The north side of the Aiguilles de Chamonix (Mont Blanc massif) since the end of the 'Little Ice Age'. *Holocene*, **21**, 357–365, https://doi.org/10.1177/0959683610374887.

Ray, E. A., F. L. Moore, J. W. Elkins, K. H. Rosenlof, J. C. Laube, T. Röckmann, D. R. Marsh, and A. E. Andrews, 2017: Quantification of the SF6 lifetime based on mesospheric loss measured in the stratospheric polar vortex. *J. Geophys. Res. Atmos.*, **122**, 4626–4638, https://doi.org/10.1002/2016JD026198.

Reid, K. J., S. M. Rosier, L. J. Harrington, A. D. King, and T. P. Lane, 2021: Extreme rainfall in New Zealand and its association with atmospheric rivers. *Environ. Res. Lett.*, **16**, 044012, https://doi.org/10.1088/1748-9326/abeae0.

Ricciardulli, L., and F. J. Wentz, 2015: A scatterometer geophysical model function for climate-quality winds: QuikSCAT Ku-2011. *J. Atmos. Oceanic Technol.*, **32**, 1829–1846, https://doi.org/10.1175/JTECH-D-15-0008.1.

——, and A. Manaster, 2021: Intercalibration of ASCAT scatterometer winds from MetOp-A, -B, and -C, for a stable climate data record. *Remote Sens.*, **13**, 3678, https://doi.org/10.3390/rs13183678.

——, ——, and R. Lindsley, 2025: Investigation of a calibration change in the ocean surface wind measurements from the TAO buoy array. *Bull. Amer. Meteor. Soc.*, **106**, E242–E260, https://doi.org/10.1175/BAMS-D-24-0072.1.

Richardson, A. D., 2019: Tracking seasonal rhythms of plants in diverse ecosystems with digital camera imagery. *New Phytol.*, **222**, 1742–1750, https://doi.org/10.1111/nph.15591.

——, and J. O'Keefe, 2009: Phenological differences between understory and overstory. Phenology of Ecosystem Processes, A. Noormets, Ed., Springer, 87–117, https://doi.org/10.1007/978-1-4419-0026-5_4.

Rigby, M., and Coauthors, 2019: Increase in CFC-11 emissions from eastern China based on atmospheric observations. *Nature*, **569**, 546–550, https://doi.org/10.1038/s41586-019-1193-4.

Rodell, M., and B. Li, 2023: Changing intensity of hydroclimatic extreme events revealed by GRACE and GRACE-FO. *Nat. Water*, **1**, 241–248, https://doi.org/10.1038/s44221-023-00040-5.

——, and Coauthors, 2024: An abrupt decline in global terrestrial water storage and its relationship with sea level change. *Surv. Geophys.*, **45**, 1875–1902, https://doi.org/10.1007/s10712-024-09860-w.

Román, M. O., and Coauthors, 2024: Continuity between NASA MODIS Collection 6.1 and VIIRS Collection 2 land products. *Remote Sens. Environ.*, **302**, 113963, https://doi.org/10.1016/j.rse.2023.113963.

Rosemartin, A. H., and Coauthors, 2014: Organizing phenological data resources to inform natural resource conservation. *Biol. Conserv.*, **173**, 90–97, https://doi.org/10.1016/j.biocon.2013.07.003.

Ruan, F., Y. Yang, Z. Tu, J. Xiong, and H. Guo, 2025: Global evaluation of terrestrial evaporation trend from diagnostic products. *J. Hydrol.*, **655**, 132979, https://doi.org/10.1016/j.jhydrol.2025.132979.

Rubino, M., and Coauthors, 2019: Revised records of atmospheric trace gases CO_2, CH_4, N_2O, and $\delta^{13}C$-CO_2 over the last 2000 years from Law Dome Antarctica. *Earth Syst. Sci. Data*, **11**, 473–492, https://doi.org/10.5194/essd-11-473-2019.

Rudlosky, S. D., and K. S. Virts, 2021: Dual geostationary lightning mapper observations. *Mon. Wea. Rev.*, **149**, 979–998, https://doi.org/10.1175/MWR-D-20-0242.1.

Sandford, C., and N. Rayner, 2026: Addressing the World War 2 warm anomaly in HadSST.4.2.0.0 (Version 1). arXiv, 2602.03347v1, https://doi.org/10.48550/arXiv.2602.03347.

Santer, B. D., and Coauthors, 2008: Consistency of modelled and observed temperature trends in the tropical troposphere. *Int. J. Climatol.*, **28**, 1703–1722, https://doi.org/10.1002/joc.1756.

Sardeshmukh, P. D., and B. J. Hoskins, 1988: The generation of global rotational flow by steady idealized tropical divergence. *J. Atmos. Sci.*, **45**, 1228–1251, https://doi.org/10.1175/1520-0469(1988)045<1228:TGOGRF>2.0.CO;2.

Sato, M., J. E. Hansen, M. P. McCormick, and J. B. Pollack, 1993: Stratospheric aerosol optical depths, 1890-1990. *J. Geophys. Res.*, **98**, 22 987–22 994, https://doi.org/10.1029/93JD02553.

Scaife, A. A., and Coauthors, 2017: Tropical rainfall, Rossby waves and regional winter climate predictions. *Quart. J. Roy. Meteor. Soc.*, **143** (702), 1–11, https://doi.org/10.1002/qj.2910.

Schaaf, C. B., and Coauthors, 2002: First operational BRDF, albedo nadir reflectance products from MODIS. *Remote Sens. Environ.*, **83**, 135–148, https://doi.org/10.1016/S0034-4257(02)00091-3.

Schröder, M., and Coauthors, 2019: The GEWEX water vapor assessment: Overview and introduction to results and recommendations. *Remote Sens.*, **11**, 251, https://doi.org/10.3390/rs11030251.

Schwartz, M. D., T. R. Ault, and J. L. Betancourt, 2013: Spring onset variations and trends in the continental United States: Past and regional assessment using temperature-based indices. *Int. J. Climatol.*, **33**, 2917–2922, https://doi.org/10.1002/joc.3625.

Seager, R., N. Henderson, and M. Cane, 2022: Persistent discrepancies between observed and modeled trends in the tropical Pacific Ocean. *J. Climate*, **35**, 4571–4584, https://doi.org/10.1175/JCLI-D-21-0648.1.

Sen, P. K., 1968: Estimates of the regression coefficient based on Kendall's tau. *J. Amer. Stat. Assoc.*, **63**, 1379–1389, https://doi.org/10.1080/01621459.1968.10480934.

Seneviratne, S. I., T. Corti, E. L. Davin, M. Hirschi, E. B. Jaeger, I. Lehner, B. Orlowsky, and A. J. Teuling, 2010: Investigating soil moisture–climate interactions in a changing climate: A review. *Earth-Sci. Rev.*, **99**, 125–161, https://doi.org/10.1016/j.earscirev.2010.02.004.

Seyednasrollah, B., A. M. Young, K. Hufkens, T. Milliman, M. A. Friedl, S. Frolking, and A. D. Richardson, 2019: Tracking vegetation phenology across diverse biomes using version 2.0 of the PhenoCam dataset. *Sci. Data*, **6**, 222, https://doi.org/10.1038/s41597-019-0229-9.

Shakespeare, C. J., and M. L. Roderick, 2024: What controls near-surface relative humidity over the ocean. *J. Adv. Model. Earth Syst.*, **16**, e2023MS004168, https://doi.org/10.1029/2023MS004168.

Shen, C., J. Zha, Z. Li, C. Azorin-Molina, K. Deng, L. Minola, and D. Chen, 2022: Evaluation of global terrestrial near-surface wind speed simulated by CMIP6 models and their future projections. *Ann. N. Y. Acad. Sci.*, **1518**, 249–263, https://doi.org/10.1111/nyas.14910.

Shi, L., and J. J. Bates, 2011: Three decades of intersatellite-calibrated high-resolution infrared radiation sounder upper tropospheric water vapor. *J. Geophys. Res.*, **116**, D04108, https://doi.org/10.1029/2010JD014847.

——, C. J. Schreck III, V. O. John, E.-S. Chung, T. Lang, S. A. Buehler, and B. J. Soden, 2022: Assessing the consistency of satellite-derived upper tropospheric humidity measurements. *Atmos. Meas. Tech.*, **15**, 6949–6963, https://doi.org/10.5194/amt-15-6949-2022.

Simmons, A. J., K. M. Willett, P. D. Jones, P. W. Thorne, and D. P. Dee, 2010: Low-frequency variations in surface atmospheric humidity, temperature, and precipitation: Inferences from reanalyses and monthly gridded observational data sets. *J. Geophys. Res.*, **115**, D01110, https://doi.org/10.1029/2009JD012442.

Simpson, I. R., K. A. McKinnon, D. Kennedy, D. M. Lawrence, F. Lehner, and R. Seager, 2024: Observed humidity trends in dry regions contradict climate models. *Proc. Natl. Acad. Sci. USA*, **121**, e2302480120, https://doi.org/10.1073/pnas.2302480120.

Slocum, C., J. A. Knaff, and S. N. Stevenson, 2023: Lightning-based tropical cyclone rapid intensification guidance. *Wea. Forecasting*, **38**, 1209–1227, https://doi.org/10.1175/WAF-D-22-0157.1.

Smith, S. L., H. B. O'Neill, K. Isaksen, J. Noetzli, and V. E. Romanovsky, 2022: The changing thermal state of permafrost. *Nat. Rev. Earth Environ.*, **3**, 10–23, https://doi.org/10.1038/s43017-021-00240-1.

Soci, C., and Coauthors, 2024: The ERA5 global reanalysis from 1940 to 2022. *Quart. J. Roy. Meteor. Soc.*, **150**, 4014–4048, https://doi.org/10.1002/qj.4803.

Soden, B. J., and Coauthors, 2005: The radiative signature of upper tropospheric moistening. *Science*, **310**, 841–844, https://doi.org/10.1126/science.1115602.

Song, F., G. J. Zhang, V. Ramanathan, and L. R. Leung, 2022: Trends in surface equivalent potential temperature: A more comprehensive metric for global warming and weather extremes. *Proc. Natl. Acad. Sci. USA*, **119**, e2117832119, https://doi.org/10.1073/pnas.2117832119.

Song, X.-P., M. C. Hansen, S. V. Stehman, P. V. Potapov, A. Tyukavina, E. F. Vermote, and J. R. Townshend, 2018: Global land change from 1982 to 2016. *Nature*, **560**, 639–643, https://doi.org/10.1038/s41586-018-0411-9.

Soulie, A., and Coauthors, 2024: Global anthropogenic emissions (CAMS-GLOB-ANT) for the Copernicus Atmosphere Monitoring Service simulations of air quality forecasts and reanalyses. *Earth Syst. Sci. Data*, **16**, 2261–2279, https://doi.org/10.5194/essd-16-2261-2024.

SPARC, 2016: SPARC report on the mystery of carbon tetrachloride. Q. Liang, P. A. Newman, and S. Reimann, Eds., SPARC Rep. 7, WCRP-13/2016, 68 pp., https://doi.org/10.3929/ethz-a-010690647.

Spencer, R. W., J. R. Christy, and W. D. Braswell, 2017: UAH version 6 global satellite temperature products: Methodology and results. *Asia-Pac. J. Atmos. Sci.*, **53**, 121–130, https://doi.org/10.1007/s13143-017-0010-y.

Steinbrecht, W., and Coauthors, 2017: An update on ozone profile trends for the period 2000 to 2016. *Atmos. Chem. Phys.*, **17**, 10 675–10 690, https://doi.org/10.5194/acp-17-10675-2017.

Steiner, A. K., and Coauthors, 2020: Observed temperature changes in the troposphere and stratosphere from 1979 to 2018. *J. Climate*, **33**, 8165–8194, https://doi.org/10.1175/JCLI-D-19-0998.1.

Stevenson, S. N., K. L. Corbosiero, and J. Molinari, 2014: The convective evolution and rapid intensification of Hurricane Earl (2010). *Mon. Wea. Rev.*, **142**, 4364–4380, https://doi.org/10.1175/MWR-D-14-00078.1.

Stocker, M., A. K. Steiner, F. Ladstädter, U. Foelsche, and W. J. Randel, 2024: Observed impacts of the Hunga eruption on stratospheric temperature. *Commun. Earth Environ.*, **5**, 450, https://doi.org/10.1038/s43247-024-01620-3.

Stoy, P. C., J. Roh, and G. T. Bromley, 2022: It's the heat and the humidity: The complementary roles of temperature and specific humidity to recent changes in the energy content of the near-surface atmosphere. *Geophys. Res. Lett.*, **49**, e2021GL096628, https://doi.org/10.1029/2021GL096628.

Strand, S. M., and H. H. Christiansen, 2025: Permafrost thermal regime and active layer dynamics across periglacial landforms in Svalbard's Nordenskiöld Land Permafrost Observatory, 2008–2023. *Arct. Sci*, **11**, 1–19, https://doi.org/10.1139/as-2024-0027.

Streletskiy, D. A., and Coauthors, 2025: Thawing permafrost is subsiding in the Northern Hemisphere—Review and perspectives. *Environ. Res. Lett.*, **20**, 013006, https://doi.org/10.1088/1748-9326/ada2ff.

Szopa, S., and Coauthors, 2021: Short-lived climate forcers. *Climate Change 2021: The Physical Science Basis*, V. Masson-Delmotte et al., Eds., Cambridge University Press, 817–922, https://doi.org/10.1017/9781009157896.008.

Tao, M., P. Konopka, J. S. Wright, Y. Liu, J. Bian, S. M. Davis, Y. Jia, and F. Ploeger, 2023: Multi-decadal variability controls short-term stratospheric water vapor trends. *Commun. Earth Environ.*, **4**, 441, https://doi.org/10.1038/s43247-023-01094-9.

Tapley, B. D., S. Bettadpur, J. C. Ries, P. F. Thompson, and M. M. Watkins, 2004: GRACE measurements of mass variability in the earth system. *Science*, **305**, 503–505, https://doi.org/10.1126/science.1099192.

The GlaMBIE Team, 2025: Community estimate of global glacier mass changes from 2000 to 2023. *Nature*, **639**, 382–388, https://doi.org/10.1038/s41586-024-08545-z.

Thiel, H., 1950: A rank-invariant method of linear and polynomial regression analysis, Parts 1–3. *Proc. K. Ned. Akad. Wet.*, **53**, 386–392.

Tian, H., and Coauthors, 2024: Global nitrous oxide budget 1980–2020. *Earth Syst. Sci. Data*, **16**, 2543–2604, https://doi.org/10.5194/essd-16-2543-2024.

Toreti, A., and Coauthors, 2025: Drought in South-eastern Europe October 2025—GDO analytical report. Publications Office of the European Union, JRC Tech. Rep. 144234, 37 pp., https://data.europa.eu/doi/10.2760/7855749.

Torralba, V., F. J. Doblas-Reyes, and N. Gonzalez-Reviriegol, 2017: Uncertainty in recent near-surface wind speed trends: A global reanalysis intercomparison. *Environ. Res. Lett.*, **12**, 114019, https://doi.org/10.1088/1748-9326/aa8a58.

Trenberth, K. E., D. P. Stepaniak, and J. M. Caron, 2002: Interannual variations in the atmospheric heat budget. *J. Geophys. Res.*, **107**, AAC 4-1–AAC 4-15, https://doi.org/10.1029/2000JD000297.

——, L. Cheng, Y. Pan, J. Fasullo, and M. Mayer, 2025: Distinctive pattern of global warming in ocean heat content. *J. Climate*, **38**, 2155–2168, https://doi.org/10.1175/JCLI-D-24-0609.1.

Unegg, J., I. Nimac, and J. Danzer, 2026: Beyond geostrophic and gradient wind: Enhancing the estimation of climatic wind fields from radio occultation. *Earth Space Sci.*, **13**, e2025EA004579, https://doi.org/10.1029/2025EA004579.

UNEP, 2024: Report of the Scientific Assessment Panel in response to Decision XXXV/7: Emissions of HFC-23. 35 pp., https://ozone.unep.org/science/assessment/sap.

van der Schalie, R., and Coauthors, 2017: The merging of radiative transfer based surface soil moisture data from SMOS and AMSR-E. *Remote Sens. Environ.*, **189**, 180–193, https://doi.org/10.1016/j.rse.2016.11.026.

van der Schrier, G., J. Barichivich, K. R. Briffa, and P. D. Jones, 2013: A scPDSI-based global dataset of dry and wet spells for 1901-2009. *J. Geophys. Res. Atmos.*, **118**, 4025–4048, https://doi.org/10.1002/jgrd.50355.

van der Werf, G. R., and Coauthors, 2017: Global fire emissions estimates during 1997–2016. *Earth Syst. Sci. Data*, **9**, 697–720, https://doi.org/10.5194/essd-9-697-2017.

Van Dijk, A. I. J. M., and Coauthors, 2026: Global Water Monitor, 2025 report. Global Water Monitor Consortium, accessed 27 January 2026, www.globalwater.online.

van Oldenborgh, G. J., H. Hendon, T. Stockdale, M. L'Heureux, E. Coughlan de Perez, R. Singh, and M. van Aalst, 2021: Defining El Niño indices in a warming climate. *Environ. Res. Lett.*, **16**, 044003, https://doi.org/10.1088/1748-9326/abe9ed.

Vautard, R., J. Cattiaux, P. Yiou, J.-N. Thépaut, and P. Ciais, 2010: Northern Hemisphere atmospheric stilling partly attributed to an increase in surface roughness. *Nat. Geosci.*, **3**, 756–761, https://doi.org/10.1038/ngeo979.

Vömel, H., S. Evan, and M. Tully, 2022: Water vapor injection into the stratosphere by Hunga Tonga-Hunga Ha'apai. *Science*, **377**, 1444–1447, https://doi.org/10.1126/science.abq2299.

von Schuckmann, K., and Coauthors, 2023: Heat stored in the earth system 1960–2020: Where does the energy go? *Earth Syst. Sci. Data*, **15**, 1675–1709, https://doi.org/10.5194/essd-15-1675-2023.

Warren, R., 2025: A consistent treatment of mixed-phase saturation for atmospheric thermodynamics. *Quart. J. Roy. Meteor. Soc.*, **151**, e4866, https://doi.org/10.1002/qj.4866.

Weatherhead, E. C., and Coauthors, 1998: Factors affecting the detection of trends: Statistical considerations and applications to environmental data. *J. Geophys. Res.*, **103**, 17 149–17 161, https://doi.org/10.1029/98JD00995.

Weber, M., and Coauthors, 2022: Global total ozone recovery trends attributed to ozone-depleting substance (ODS) changes derived from five merged ozone datasets. *Atmos. Chem. Phys.*, **22**, 6843–6859, https://doi.org/10.5194/acp-22-6843-2022.

Wells, N., S. Goddard, and M. J. Hayes, 2004: A self-calibrating palmer drought severity index. *J. Climate*, **17**, 2335–2351, https://doi.org/10.1175/1520-0442(2004)017<2335:ASPDSI>2.0.CO;2.

Wentz, F. J., 1997: A well-calibrated ocean algorithm for special sensor microwave/imager. *J. Geophys. Res.*, **102**, 8703–8718, https://doi.org/10.1029/96JC01751.

——, 2015: A 17-yr climate record of environmental parameters derived from the Tropical Rainfall Measuring Mission (TRMM) microwave imager. *J. Climate*, **28**, 6882–6902, https://doi.org/10.1175/JCLI-D-15-0155.1.

——, L. Ricciardulli, K. Hilburn, and C. Mears, 2007: How much more rain will global warming bring. *Science*, **317**, 233–235, https://doi.org/10.1126/science.1140746.

Wentz, K., T. Meissner, F. Wentz, and A. Manaster, 2024: Absolute intercalibration of spaceborne microwave radiometers. *J. Atmos. Oceanic Technol.*, **41**, 1121–1138, https://doi.org/10.1175/JTECH-D-24-0024.1.

Western, L. M., and Coauthors, 2023: Author correction: Global increase of ozone-depleting chlorofluorocarbons from 2010 to 2020. *Nat. Geosci.*, **16**, 546–546, https://doi.org/10.1038/s41561-023-01205-3.

——, and Coauthors, 2024: A decrease in radiative forcing and equivalent effective chlorine from hydrochlorofluorocarbons. *Nat. Climate Change*, **14**, 805–807, https://doi.org/10.1038/s41558-024-02038-7.

WGMS, 2023: Global Glacier Change Bulletin No. 5 (2020–2021). M. Zemp et al., Eds., ISC(WDS)/IUGG(IACS)/UNEP/UNESCO/WMO, World Glacier Monitoring Service, 134 pp., https://doi.org/10.5904/wgms-fog-2023-09.

Whaley, C. H., and Coauthors, 2025: HTAP3 fires: Towards a multi-model, multi-pollutant study of fire impacts. *Geosci. Model Dev.*, **18**, 3265–3309, https://doi.org/10.5194/gmd-18-3265-2025.

Wielicki, B. A., B. R. Barkstrom, E. F. Harrison, R. B. Lee III, G. L. Smith, and J. E. Cooper, 1996: Clouds and the Earth's Radiant Energy System (CERES): An earth observing system experiment. *Bull. Amer. Meteor. Soc.*, **77**, 853–868, https://doi.org/10.1175/1520-0477(1996)077<0853:CATERE>2.0.CO;2.

——, and Coauthors, 1998: Clouds and the Earth's Radiant Energy System (CERES): Algorithm overview. *IEEE Trans. Geosci. Remote Sens.*, **36**, 1127–1141, https://doi.org/10.1109/36.701020.

Wiese, D. N., F. W. Landerer, and M. M. Watkins, 2016: Quantifying and reducing leakage errors in the JPL RL05M GRACE mascon solution. *Water Resour. Res.*, **52**, 7490–7502, https://doi.org/10.1002/2016WR019344.

Willett, K. M., 2023a: HadISDH.extremes Part I: A gridded wet bulb temperature extremes index product for climate monitoring. *Adv. Atmos. Sci.*, **40**, 1952–1967, https://doi.org/10.1007/s00376-023-2347-8.

——, 2023b: HadISDH.extremes Part II: Exploring humid heat extremes using wet bulb temperature indices. *Adv. Atmos. Sci.*, **40**, 1968–1985, https://doi.org/10.1007/s00376-023-2348-7.

——, C. N. Williams Jr., R. J. H. Dunn, P. W. Thorne, S. Bell, M. de Podesta, P. D. Jones, and D. E. Parker, 2013: HadISDH: An updateable land surface specific humidity product for climate monitoring. *Climate Past*, **9**, 657–677, https://doi.org/10.5194/cp-9-657-2013.

——, R. J. H. Dunn, P. W. Thorne, S. Bell, M. de Podesta, D. E. Parker, P. D. Jones, and C. N. Williams Jr., 2014: HadISDH land surface multi-variable humidity and temperature record for climate monitoring. *Climate Past*, **10**, 1983–2006, https://doi.org/10.5194/cp-10-1983-2014.

——, ——, J. Kennedy, and D. Berry, 2020: Development of the HadISDH.marine humidity climate monitoring dataset. *Earth Syst. Sci. Data*, **12**, 2853–2880, https://doi.org/10.5194/essd-12-2853-2020.

——, A. J. Simmons, M. Bosilovich, and D. A. Lavers, 2024: Surface humidity [in "State of the Climate in 2023"]. *Bull. Amer. Meteor. Soc.*, **105** (8), S52–S54, https://doi.org/10.1175/bams-d-24-0116.1.

WMO, 2018: Scientific assessment of ozone depletion: 2018. Global Ozone Research and Monitoring Project Rep. 58, 588 pp., https://csl.noaa.gov/assessments/ozone/2018.

——: World Meteorological Organization (WMO). Scientific Assessment of Ozone Depletion: 2022, GAW Rep. 278, WMO, 509 pp.

——, 2026: State of the global climate 2025. WMO-1391, 46 pp., https://doi.org/10.59327/WMO/S/CRI/SOC/1.

——, IOC-UNESCO, ISC, UNEP, and C3S, 2025: The 2022 GCOS ECVs requirements (2022 edition – Updated in 2025, GCOS-245). 250 pp., https://library.wmo.int/idurl/4/58111.

Wohland, J., N.-E. Omrani, D. Witthaut, and N.-S. Keenlyside, 2019: Inconsistent wind speed trends in current twentieth century reanalyses. *J. Geophys. Res. Atmos.*, **124**, 1931–1940, https://doi.org/10.1029/2018JD030083.

Woolway, R. I., and C. J. Merchant, 2018: Intralake heterogeneity of thermal responses to climate change: A study of large Northern Hemisphere lakes. *J. Geophys. Res. Atmos.*, **123**, 3087–3098, https://doi.org/10.1002/2017JD027661.

——, and Coauthors, 2025: Extreme and compound events in lakes. *Nat. Rev. Earth Environ.*, **6**, 593–611, https://doi.org/10.1038/s43017-025-00710-w.

Wu, Q., Z. Ruan, D. Chen, and T. Lian, 2015: Diurnal variations of tropical cyclone precipitation in the inner and outer rainbands. *J. Geophys. Res. Atmos.*, **120**, 1–11, https://doi.org/10.1002/2014JD022190.

WWA, 2026: La Niña, climate change, high exposure and vulnerability combined led to devastating floods in parts of southern Africa. World Weather Attribution, accessed 29 January 2026, https://www.worldweatherattribution.org/la-nina-climate-change-high-exposure-and-vulnerability-combined-led-to-devastating-floods-in-parts-of-southern-africa/.

Xu, N., H. Lu, W. Li, and P. Gong, 2024: Natural lakes dominate global water storage variability. *Sci. Bull.*, **69**, 1016–1019, https://doi.org/10.1016/j.scib.2024.02.023.

Yang, K., 2017: OMPS-NPP L2 NM Nitrogen Dioxide (NO2) Total and Tropospheric Column swath orbital V2. GES DISC, accessed 29 January 2026, https://doi.org/10.5067/N0XVLE2QAVR3.

Yang, Y., and Coauthors, 2023: Evapotranspiration on a greening Earth. *Nat. Rev. Earth Environ.*, **4**, 626–641, https://doi.org/10.1038/s43017-023-00464-3.

Yeh, S., and Coauthors, 2018: ENSO atmospheric teleconnections and their response to greenhouse gas forcing. *Rev. Geophys.*, **56**, 185–206, https://doi.org/10.1002/2017RG000568.

Yin, C., K. Wang, R. Li, and Z. Zhang, 2025: Homogenization of the observed surface relative humidity from 1959 to 2020 in China. *J. Geophys. Res. Atmos.*, **130**, e2024JD042644, https://doi.org/10.1029/2024JD042644.

Yosef, Y., E. Aguilar, and P. Alpert, 2021: Is it possible to fit extreme climate change indices together seamlessly in the era of accelerated warming. *Int. J. Climatol.*, **41**, E952–E963, https://doi.org/10.1002/joc.6740.

Young, J. M., L. Farquharson, J. Luo, N. Nesterova, J. Van Der Sluijs, and S. V. Kokelj, 2025: Permafrost mass wasting in ice-rich landscapes: Recent advances (2013 to 2024) on mechanisms, dynamics and impacts. *Permafrost Periglacal Processes*, **37**, 284–304, https://doi.org/10.1002/ppp.70015.

Yulaeva, E., and J. M. Wallace, 1994: The signature of ENSO in global temperature and precipitation fields derived from the microwave sounding unit. *J. Climate*, **7**, 1719–1736, https://doi.org/10.1175/1520-0442(1994)007<1719:TSOEIG>2.0.CO;2.

Zeng, Z., and Coauthors, 2019: A reversal in global terrestrial stilling and its implications for wind energy production. *Nat. Climate Change*, **9**, 979–985, https://doi.org/10.1038/s41558-019-0622-6.

Zha, J., and Coauthors, 2021: Projected changes in global terrestrial near-surface wind speed in 1.5°C–4.0°C global warming levels. *Environ. Res. Lett.*, **16**, 114016, https://doi.org/10.1088/1748-9326/ac2fdd.

Zhai, S., and Coauthors, 2024: Transpacific transport of Asian peroxyacetyl nitrate (PAN) observed from satellite: Implications for ozone. *Environ. Sci. Technol.*, **58**, 9760–9769, https://doi.org/10.1021/acs.est.4c01980.

Zhang, G. F., and Coauthors, 2021: Uneven warming likely contributed to declining near-surface wind speeds in northern China between 1961 and 2016. *J. Geophys. Res. Atmos.*, **126**, e2020JD033637, https://doi.org/10.1029/2020JD033637.

Zhang, W., and Coauthors, 2026: Weather and climate extremes in populated global monsoon regions in 2025. *Adv. Atmos. Sci.*, **43**, 1752–1762, https://doi.org/10.1007/s00376-026-5905-z.

Zhang, X., L. Alexander, G. C. Hegerl, P. Jones, A. K. Tank, T. C. Peterson, B. Trewin, and F. W. Zwiers, 2011: Indices for monitoring changes in extremes based on daily temperature and precipitation data. *Wiley Interdiscip. Rev.: Climate Change*, **2**, 851–870, https://doi.org/10.1002/wcc.147.

Zhang, Z., and K. Wang, 2025: Homogenization of surface wind speed over global land from 1973 to 2022. *J. Geophys. Res. Atmos.*, **130**, e2024JD042939, https://doi.org/10.1029/2024JD042939.

——, ——, D. Chen, J. Li, and R. Dickinson, 2019: Increase in surface friction dominates the observed surface wind speed decline during 1973–2014 in the Northern Hemisphere lands. *J. Climate*, **32**, 7421–7435, https://doi.org/10.1175/JCLI-D-18-0691.1.

——, B. Poulter, A. F. Feldman, Q. Ying, P. Ciais, S. Peng, and X. Li, 2023: Recent intensification of wetland methane feedback. *Nat. Climate Change*, **13**, 430–433, https://doi.org/10.1038/s41558-023-01629-0.

Zhao, L., and Coauthors, 2021: A synthesis dataset of permafrost thermal state for the Qinghai–Tibet (Xizang) Plateau, China. *Earth Syst. Sci. Data*, **13**, 4207–4218, https://doi.org/10.5194/essd-13-4207-2021.

Zhao, Y., and Coauthors, 2019: Inter-model comparison of global hydroxyl radical (OH) distributions and their impact on atmospheric methane over the 2000–2016 period. *Atmos. Chem. Phys.*, **19**, 13 701–13 723, https://doi.org/10.5194/acp-19-13701-2019.

Zheng, B., and Coauthors, 2019: Global atmospheric carbon monoxide budget 2000–2017 inferred from multi-species atmospheric inversions. *Earth Syst. Sci. Data*, **11**, 1411–1436, https://doi.org/10.5194/essd-11-1411-2019.

——, and Coauthors, 2023: Record-high CO_2 emissions from boreal fires in 2021. *Science*, **379**, 912–917, https://doi.org/10.1126/science.ade0805.

Zhu, Z., and Coauthors, 2016: Greening of the earth and its drivers. *Nat. Climate Change*, **6**, 791–795, https://doi.org/10.1038/nclimate3004.

Ziemke, J. R., and Coauthors, 2019: Trends in global tropospheric ozone inferred from a composite record of TOMS/OMI/MLS/OMPS satellite measurements and the MERRA-2 GMI simulation. *Atmos. Chem. Phys.*, **19**, 3257–3269, https://doi.org/10.5194/acp-19-3257-2019.

——, and Coauthors, 2022: NASA satellite measurements show global-scale reductions in free tropospheric ozone in 2020 and again in 2021 during COVID-19. *Geophys. Res. Lett.*, **49**, e2022GL098712, https://doi.org/10.1029/2022GL098712.

——, N. A. Kramarova, S. M. Frith, K.-L. Huang, K. Baek, and J. R. Herman, 2025: Ten years of tropospheric ozone from DSCOVR EPIC: Science and applications. *Front. Remote Sens.*, **6**, 1634922, https://doi.org/10.3389/frsen.2025.1634922.

Ziese, M., A. Rauthe-Schoch, A. Becker, P. Finger, E. Rustemeier, S. Hansel, and U. Schneider, 2022: GPCC Full Data Daily Version 2022 at 1.0 degrees: Daily land-surface precipitation from rain-gauges built on GTS-based and historic data. DWD, accessed 18 February 2026, https://doi.org/10.5676/DWD_GPCC/FD_D_V2022_100.

Zolghadrshojaee, M., S. Tegtmeier, S. M. Davis, and R. Pilch Kedzierski, 2024: Variability and long-term changes in tropical cold-point temperature and water vapor. *Atmos. Chem. Phys.*, **24**, 7405–7419, https://doi.org/10.5194/acp-24-7405-2024.

Zotta, R.-M., L. Moesinger, R. van der Schalie, M. Vreugdenhil, W. Preimesberger, T. Frederikse, R. De Jeu, and W. Dorigo, 2024a: VODCA v2: Multi-sensor, multi-frequency vegetation optical depth data for long-term canopy dynamics and biomass monitoring (1.0.0). TU Wien, accessed 12 January 2026, https://doi.org/10.48436/t74ty-tcx62.

——, ——, ——, ——, ——, ——, ——, and ——, 2024b: VODCA v2: Multi-sensor, multi-frequency vegetation optical depth data for long-term canopy dynamics and biomass monitoring. *Earth Syst. Sci. Data*, **16**, 4573–4617, https://doi.org/10.5194/essd-16-4573-2024.

——, W. Preimesberger, R. De Jeu, T. Frederikse, and W. Dorigo, 2025: Vegetation optical depth [in "State of the Climate in 2024"]. *Bull. Amer. Meteor. Soc.*, **106** (8), S120–S121, https://doi.org/10.1175/2025BAMSStateoftheClimate.1.

——, R. de Jeu, N. F. Bader, T. Frederikse, and W. Dorigo, 2026: Improving AMSR2 vegetation optical depth retrievals via land parameter retrieval model parameter optimisation. *Remote Sens. Environ.*, **335**, 115286, https://doi.org/10.1016/j.rse.2026.115286.

Zou, C.-Z., H. Xu, X. Hao, and Q. Liu, 2023: Mid-tropospheric layer temperature record derived from satellite microwave sounder observations with backward merging approach. *J. Geophys. Res. Atmos.*, **128**, e2022JD037472, https://doi.org/10.1029/2022JD037472]

STATE OF THE CLIMATE IN 2025

GLOBAL OCEANS

D. L. Volkov and R. C. Perez, Eds.

Special Online Supplement to the *Bulletin of the American Meteorological Society* Vol. 107, No. 8, August, 2026

https://doi.org/10.1175/BAMS-D-26-0100.1
Corresponding author: Denis L. Volkov / denis.volkov@noaa.gov
©2026 American Meteorological Society
For information regarding reuse of this content and general copyright information, consult the AMS Copyright Policy.

STATE OF THE CLIMATE IN 2025
Global Oceans

Editors

Jessica Blunden
James Reagan

Chapter Editors

Anthony Arguez
Josh Blannin
Peter Bissolli
Kyle R. Clem
Howard J. Diamond
Matthew L. Druckenmiller
Robert J. H. Dunn
Catherine Ganter
Nadine Gobron
Rodney Martinez
Twila A. Moon
Gary A. Morris
Marilyn N. Raphael
Renellys C. Perez
Carl J. Schreck III
Zewdu Segele
Laura Stevens
Richard L. Thoman
Denis L. Volkov
Zhiwei Zhu

Technical Editors

Lukas Noguchi
Laura Ohlmann

BAMS Special Editor for Climate

Timothy DelSole

American Meteorological Society

Cover Credit:
Skyline view from a research cruise in the Florida Straits, between Florida and the Bahamas, in September 2025. Photo credit: Denis L. Volkov.

How to cite this document:
Global Oceans is one chapter from the *State of the Climate in 2025* annual report and is available from https://doi.org/10.1175/BAMS-D-26-0100.1. Compiled by NOAA's National Centers for Environmental Information, *State of the Climate in 2025* is based on contributions from scientists from around the world. It provides a detailed update on global climate indicators, notable weather events, and other data collected by environmental monitoring stations and instruments located on land, water, ice, and in space. The full report is available from https://doi.org/10.1175/2026BAMSStateoftheClimate.1.

Citing the complete report:
Blunden, J.and J. Reagan, Eds., 2026: "State of the Climate in 2025". Bull. Amer. Meteor. Soc., 107 (8), Si–S512, https://doi.org/10.1175/2026BAMSStateoftheClimate.1.

Citing this chapter:
Volkov, D. L. and R. C. Perez, Eds., 2026: Global Oceans [in "State of the Climate in 2025"]. Bull. Amer. Meteor. Soc., 107 (8), S168–S227, https://doi.org/10.1175/BAMS-D-26-0100.1.

Citing a section (example):
Sharp, J. D., Z. Wang, T. Ito, S. Minobe, L. Cheng, J. Du, H. Garcia, C. J. Roach, B. Lu, Y. Xin, M. Han, Y. Zhou, and G. G. Navarra, 2026: Global ocean dissolved oxygen [in "State of the Climate in 2025"]. Bull. Amer. Meteor. Soc., 107 (8), S215–S219, https://doi.org/10.1175/BAMS-D-26-0100.1.

Editor and Author Affiliations (alphabetical by name)

Atkinson, Christopher P., Met Office Hadley Centre, Exeter, United Kingdom

Beckley, Brian, Earth Resources Technology, Inc., Greenbelt, Maryland

Carter, Brendan R., NOAA/OAR Pacific Marine Environmental Laboratory, Seattle, Washington

Cetinić, Ivona, NASA Goddard Space Flight Center, Greenbelt, Maryland; Universities Space Research Association, Columbia, Maryland

Chan, Duo, School of Ocean and Earth Science, University of Southampton, Southampton, United Kingdom

Cheng, Lijing, State Key Laboratory of Earth System Numerical Modeling and Application, Institute of Atmospheric Physics, Chinese Academy of Sciences, Beijing, China

Domingues, Catia M., Global Climate, National Oceanography Centre, Southampton, United Kingdom

Dong, Shenfu, NOAA/OAR Atlantic Oceanographic and Meteorological Laboratory, Miami, Florida

Du, Juan, International Center for Climate and Environment Sciences, Institute of Atmospheric Physics, Chinese Academy of Sciences, Beijing, China

Elipot, Shane, Rosenstiel School of Marine, Atmospheric, and Earth Science, University of Miami, Miami, Florida

Feely, Richard A., NOAA/OAR Pacific Marine Environmental Laboratory, Seattle, Washington

Franz, Bryan A., NASA Goddard Space Flight Center, Greenbelt, Maryland

Fu, Yao, College of Marine Science, University of South Florida, St. Petersburg, Florida

Gao, Meng, NASA Goddard Space Flight Center, Greenbelt, Maryland; Science Systems and Applications, Inc., Lanham, Maryland

Garcia, Hernan, NOAA/NESDIS National Centers for Environmental Information, Silver Spring, Maryland

Graham, Garrett, North Carolina Institute for Climate Studies, North Carolina State University, Asheville, North Carolina

Hamlington, Benjamin D., Jet Propulsion Laboratory, California Institute of Technology, Pasadena, California

Han, Mingyu, School of Oceanography, Shanghai Jiao Tong University, Shanghai, China

Hobbs, Will, Australian Antarctic Program Partnership (AAPP), Hobart, Tasmania, Australia; Institute for Marine and Antarctic Studies, University of Tasmania, Hobart, Tasmania, Australia

Hu, Zeng-Zhen, NOAA/NWS National Centers for Environmental Prediction Climate Prediction Center, College Park, Maryland

Huang, Boyin, NOAA/NESDIS National Centers for Environmental Information, Asheville, North Carolina

Ito, Takamitsu, School of Earth and Atmospheric Sciences, Georgia Institute of Technology, Atlanta, Georgia

Jersild, Annika, Earth System Science Interdisciplinary Center/Cooperative Institute for Satellite Earth System Studies, University of Maryland, College Park, Maryland

Jevrejeva, Svetlana, National Oceanography Centre, Liverpool, United Kingdom

Johnson, Gregory C., NOAA/OAR Pacific Marine Environmental Laboratory, Seattle, Washington; School of Oceanography, University of Washington, Seattle, Washington

Killick, Rachel. E., Met Office Hadley Centre, Exeter, United Kingdom

Landerer, Felix W., Jet Propulsion Laboratory, California Institute of Technology, Pasadena, California

Landschützer, Peter, Flanders Marine Institute, InnovOcean Campus, Ostend, Belgium

Le Hénaff, Matthieu, NOAA/OAR Atlantic Oceanographic and Meteorological Laboratory, Miami, Florida

Leuliette, Eric, NOAA/NWS NCWCP Laboratory for Satellite Altimetry, College Park, Maryland

Locarnini, Ricardo, NOAA/NESDIS National Centers for Environmental Information, Silver Spring, Maryland

Lozier, M. Susan, School of Earth and Atmospheric Sciences, Georgia Institute of Technology, Atlanta, Georgia

Lu, Bin, School of Information Science and Electronic Engineering, Shanghai Jiao Tong University, Shanghai, China

Lyman, John M., Cooperative Institute for Marine and Atmospheric Research, University of Hawaii, Honolulu, Hawaii; NOAA/OAR Pacific Marine Environmental Laboratory, Seattle, Washington

Minobe, Shoshiro, Faculty of Science, Hokkaido University, Sapporo, Japan

Mishonov, Alexey, Earth System Science Interdisciplinary Center/Cooperative Institute for Satellite Earth System Studies, University of Maryland, College Park, Maryland; NOAA/NESDIS National Centers for Environmental Information, Silver Spring, Maryland

Mitchum, Gary T., College of Marine Science, University of South Florida, St. Petersburg, Florida

Miyamoto, Masatoshi, Japan Meteorological Agency, Tokyo, Japan

Moat, Ben I., National Oceanography Centre, Southampton, United Kingdom

Monselesan, Didier P., CSIRO, Environment Research Unit, Climate Intelligence, Climate Variability and Hazards, Hobart, Tasmania, Australia

Navarra, Gian G., Atmospheric and Oceanic Sciences, Princeton University, Princeton, New Jersey

Nerem, R. Steven, Colorado Center for Astrodynamics Research, Cooperative Institute for Research in Environmental Sciences, University of Colorado Boulder, Boulder, Colorado

Perez, Renellys C., NOAA/OAR Atlantic Oceanographic and Meteorological Laboratory, Miami, Florida

Petit, Tyllis, National Oceanography Centre, Southampton, United Kingdom

Reagan, James, NOAA/NESDIS National Centers for Environmental Information, Silver Spring, Maryland

Roach, Christopher J., Institute for Marine and Antarctic Studies, University of Tasmania, Hobart, Tasmania, Australia

Savita, Abhishek, Centre for Atmospheric Sciences, Indian Institute of Technology Delhi, Delhi, India

Schlegel, Robert W., Laboratoire d'Océanographie de Villefranche, Sorbonne Université, Villefranche-sur-mer, France

Sharp, Jonathan D., Cooperative Institute for Climate, Ocean, and Ecosystem Studies, University of Washington, Seattle, Washington; NOAA/OAR Pacific Marine Environmental Laboratory, Seattle, Washington

Smeed, David A., National Oceanography Centre, Southampton, United Kingdom

Stackhouse, Paul W., NASA Langley Research Center, Hampton, Virginia

Steinberg, Jacob M., NOAA/OAR Geophysical Fluid Dynamics Laboratory, Princeton, New Jersey

Sweet, William, NOAA/NOS Center for Operational Oceanographic Products and Services, Silver Spring, Maryland

Thompson, Philip R., Cooperative Institute for Marine and Atmospheric Research, Department of Oceanography, University of Hawaii, Honolulu, Hawaii

Trinanes, Joaquin, Department of Electronics and Computer Science, Universidad de Santiago de Compostela, Santiago, Spain

Tuchen, Franz Philip, Rosenstiel School of Marine, Atmospheric, and Earth Science, University of Miami, Miami, Florida

Volkov, Denis L., Cooperative Institute for Marine and Atmospheric Studies, Rosenstiel School of Marine, Atmospheric, and Earth Science, University of Miami, Miami, Florida; NOAA/OAR Atlantic Oceanographic and Meteorological Laboratory, Miami, Florida

Wang, Zhankun, NOAA/NESDIS National Centers for Environmental Information, Dickinson, Texas

Wanninkhof, Rik, NOAA/OAR Atlantic Oceanographic and Meteorological Laboratory, Miami, Florida

Weller, Robert A., Department of Physical Oceanography, Woods Hole Oceanographic Institution, Woods Hole, Massachusetts

Westberry, Toby K., Oregon State University, Corvallis, Oregon

Editor and Author Affiliations (continued)

Widlansky, Matthew J., Cooperative Institute for Marine and Atmospheric Research, Department of Oceanography, University of Hawaii, Honolulu, Hawaii

Wijffels, Susan E., Department of Physical Oceanography, Woods Hole Oceanographic Institution, Woods Hole, Massachusetts

Willis, Joshua K., Jet Propulsion Laboratory, California Institute of Technology, Pasadena, California

Xin, Yi, School of Information Science and Electronic Engineering, Shanghai Jiao Tong University, Shanghai, China

Yin, Xungang, NOAA/NESDIS National Centers for Environmental Information, Asheville, North Carolina

Yu, Lisan, Department of Physical Oceanography, Woods Hole Oceanographic Institution, Woods Hole, Massachusetts

Zhou, Yuntao, School of Oceanography, Shanghai Jiao Tong University, Shanghai, China

Editorial and Production Team

Allen, Jessicca, Graphics Support, Cooperative Institute for Satellite Earth System Studies, North Carolina State University, Asheville, North Carolina

Camper, Amy V., Graphics Support, Innovative Consulting and Management Services, LLC, NOAA/NESDIS National Centers for Environmental Information, Asheville, North Carolina

Carroll, Lauren, Content Team Lead, Communications and Outreach, NOAA/NESDIS National Centers for Environmental Information, Asheville, North Carolina

Crossman, Jacquelyn, NCEI Librarian, MPF-ZAI, NOAA/NESDIS National Centers for Environmental Information, Asheville, North Carolina

Haley, Bridgette O., Graphics Support, NOAA/NESDIS National Centers for Environmental Information, Asheville, North Carolina

Noguchi, Lukas, Technical Editor, Innovative Consulting and Management Services, LLC, NOAA/NESDIS National Centers for Environmental Information, Asheville, North Carolina

Ohlmann, Laura, Technical Editor, Innovative Consulting and Management Services, LLC, NOAA/NESDIS National Centers for Environmental Information, Asheville, North Carolina

Veasey, Sara W., Visual Communications Team Lead, Communications and Outreach, NOAA/NESDIS National Centers for Environmental Information, Asheville, North Carolina

3. Table of Contents

List of authors and affiliations S171
a. Overview S174
b. Sea surface temperature S176
1. Introduction S176
2. Sea surface temperatures in 2025 S176
3. Marine heatwaves and cold spells S178
4. Sea surface temperature trends S179
c. Ocean temperature and heat content S182
d. Salinity S186
1. Introduction S186
2. Sea surface salinity S186
3. Subsurface salinity S188
e. Global ocean heat, freshwater, and momentum fluxes S191
1. Surface heat fluxes S191
2. Surface freshwater fluxes S192
3. Wind stress S193
4. Long-term perspective S194
f. Sea level variability and change S196
g. Surface currents S200
1. Pacific Ocean S200
2. Indian Ocean S202
3. Atlantic Ocean S202
4. Methodological advances S202
h. Atlantic meridional overturning circulation and heat transport S203
i. Global ocean phytoplankton S207
j. Global ocean carbon cycle S211
1. Introduction S211
2. Air–sea carbon dioxide fluxes S211
3. Ocean interior inventory estimates S213
k. Global ocean dissolved oxygen S215
Appendix 1: Acronyms S220
Appendix 2: Dataset Tables S222
References S228

3. GLOBAL OCEANS

D. L. Volkov and R. C. Perez, Eds.

a. Overview

—D. L. Volkov and R. C. Perez

This chapter synthesizes changes in the ocean's physical state and key biogeochemical indicators during 2025, highlighting the persistence of exceptional warmth following the record-breaking years of 2023 and 2024 and the continued influence of large-scale climate variability, particularly the El Niño–Southern Oscillation (ENSO). The strong El Niño that developed in 2023 and weakened through the spring of 2024, transitioned towards La Niña conditions by the second half of 2024 (see section 4b). Weak La Niña was prevalent for most of 2025 except later spring/summer when neutral conditions dominated. This transition influenced ocean–atmosphere exchanges, the redistribution of heat, freshwater, and momentum across ocean basins while the long-term warming trend continued.

Air–sea fluxes in 2025 reflected ongoing ocean heat uptake and ENSO-related variability. Compared to 2024, heat gain increased notably in the tropics and subtropics. Freshwater flux patterns were shaped by the developing La Niña conditions, with increased precipitation and freshening near the Maritime Continent and western tropical Pacific and enhanced freshwater loss and salinification across the central and eastern equatorial Pacific. These changes were driven mainly by precipitation anomalies rather than evaporation. Wind stress anomalies were generally weak in the tropics but showed strengthened westerlies in the Southern Ocean and North Atlantic and weaker winds over parts of the North Pacific, influencing regional circulation and wind-driven vertical velocity.

Global sea surface temperatures (SSTs) remained exceptionally high in 2025, marking the third consecutive year of extreme ocean warmth. Long-term warming has accelerated, increasing from approximately 0.12°C per decade over 1950–2025 to about 0.21°C per decade since 2000. Although the shift toward neutral and weak La Niña conditions produced some cooling in the tropical Pacific compared to the peak warmth of 2023/24, global SSTs remained elevated due to the continued accumulation of heat in the climate system. Marine heatwaves remained widespread, affecting about 87% of the ocean surface. While heatwave occurrence declined slightly relative to 2024, 2025 remained among the highest occurrence years on record. In contrast, marine cold spells became even less frequent, reaching their lowest occurrence in the observational record and highlighting the continued shift toward warmer ocean conditions.

Ocean heat content also remained at record highs, with continued warming in the upper 2000 m and detectable warming extending into deeper layers. The transition from El Niño to weak La Niña conditions redistributed heat within the tropical Pacific, reducing heat content in the eastern equatorial Pacific and increasing it in the western and central equatorial Pacific, but did not offset the long-term warming trend. Most ocean basins remained warmer than average. The Atlantic Ocean continued to exhibit widespread warm anomalies, though slightly cooler than the extreme conditions of 2024. The Indian Ocean remained warmer than the climatological average despite localized cooling in the southwestern Indian Ocean compared to 2024. The sustained heat uptake by the oceans contributes to accelerated sea level rise, enhanced tropical cyclone activity, amplified stratification, and increased marine heatwaves.

Ocean salinity patterns reflected both interannual variability and long-term hydrological changes. The equatorial Pacific generally became saltier under La Niña-related precipitation shifts, while high-latitude regions of the Atlantic experienced freshening that may influence deep water formation and overturning circulation. The Indian Ocean exhibited mixed salinity

changes, with both freshening and salinification depending on location, and shifted from anomalously fresh to slightly salty relative to climatology. Subsurface salinity changes were most pronounced in the upper few hundred meters and varied by basin. Despite these interannual fluctuations, long-term trends remain consistent with an intensifying global hydrological cycle, in which salty regions become saltier and fresh regions fresher.

Global mean sea level reached a new record high in 2025, rising to 111.2 mm above the 1993 baseline and continuing a long-term increase of about 3.5 mm per year, with clear acceleration over recent decades. Although ocean warming drove a substantial thermosteric increase, the total annual rise from 2024 to 2025 was relatively modest, likely due to La Niña-related redistribution of water between the ocean and land. Regional patterns reflected ENSO-driven circulation changes, with lower sea levels in the central and eastern tropical Pacific and higher levels in the Indo–western Pacific. Long-term sea level rise continues to increase the frequency and severity of coastal flooding and extreme sea level events.

Ocean circulation patterns in 2025 showed strong regional variability linked to ENSO and atmospheric forcing. Surface currents in the equatorial Pacific exhibited enhanced westward flow associated with developing La Niña conditions, while the Kuroshio Extension remained displaced northward of its long-term mean position. Seasonal monsoon forcing drove pronounced circulation changes in the Indian Ocean, and variability in the Atlantic reflected regional climate modes. The Atlantic meridional overturning circulation continued to exhibit strong interannual variability, with some evidence of localized weakening in the subtropical North Atlantic and strengthening in the subtropical South Atlantic, but limited evidence of a long-term basin-wide decline.

The global ocean continues to play a major role in the global carbon cycle by absorbing approximately 29% of anthropogenic carbon dioxide emissions and helping slow its atmospheric accumulation, while contributing to ocean acidification. The oceanic uptake of carbon dioxide in 2025 increased compared to the prior decade. Despite regional variability and observational uncertainties, the ocean carbon sink remains strong and continues to increase. Satellite observations showed that global phytoplankton biomass and distribution in 2025 remained largely within historical ranges, with modest productivity increases in the tropical Pacific associated with weak La Niña conditions.

This year's report features a new section on dissolved oxygen, which is an essential climate variable, especially for marine ecosystems and biogeochemical cycling. In 2025, global ocean dissolved oxygen continued to decline, with inventories decreasing by about 0.45% per decade since 1965 due to warming, reduced ventilation, ocean circulation changes, and enhanced biological respiration. An ensemble of statistical and machine-learning analyses confirms widespread deoxygenation, especially in the North Pacific and Southern Oceans, with broadly negative oxygen anomalies in 2025 consistent with elevated ocean heat content and ENSO-driven variability.

Overall, the ocean in 2025 remained in a state of persistent change. Record-high global sea level, high SSTs and heat content, widespread marine heatwaves, and continued carbon uptake and deoxygenation highlight the ocean's central role in regulating Earth's climate.

b. Sea surface temperature

—X. Yin, R. W. Schlegel, B. Huang, D. Chan, G. Graham, and Z.-Z. Hu

1. INTRODUCTION

The state of sea surface temperatures (SSTs) in global oceans and seas in 2025 was analyzed using four gridded SST datasets: Daily Optimum Interpolation SST version 2.1 (DOISSTv2.1; Huang et al. 2021), Extended Reconstructed SST version 5 (ERSSTv5; Huang et al. 2017), Hadley Centre SST version 4 (HadSST.4.2.0.0; Kennedy et al. 2019), and Dynamically Consistent ENsemble of Temperature version 1.1.0.0 (DCENT-Iv1.1.0.0; Chan et al. 2026). DOISSTv2.1 is a blended product from in situ observations and satellite measurements, covering the period since late 1981, when satellite-retrieved SSTs became available. It provides daily mean SSTs and is analyzed on 0.25° latitude–longitude grids. The latter three datasets are in situ observation-based products, providing the longest available global SST records with monthly mean values extending back to preindustrial times, beginning in 1854 for ERSSTv5, 1850 for HadSST.4.2.0.0 and DCENT-Iv1.1.0.0, to present, when shipborne instrumental measurements of water temperature were deemed sufficiently extensive and reliable to support global SST analyses. The horizontal resolution is 2° for ERSSTv5 and 5° for HadSST.4.2.0.0 and DCENT-Iv1.1.0.0.

Marine heatwaves (MHWs) are defined as periods of five or more consecutive days with SSTs above the 90th percentile daily climatological values (Hobday et al. 2016). A MHW is categorized as Moderate (Category 1) when the greatest SST anomaly (SSTA) during the event is between one and two times the difference between the 90th percentile and the seasonal climatology. When this value is more than two, three, or four times of the difference, the MHW is categorized as Strong (Category 2), Severe (Category 3), or Extreme (Category 4), respectively (Hobday et al. 2018). The direct inverse of MHWs (i.e., days below the 10th percentile) is used to define and categorize marine cold spells (MCSs), with an additional 'ice' category for days when the daily climatology is below –1.7°C (Schlegel et al. 2021). An interactive visualization of global MHW and MCS coverage from 1982 to the present with DOISSTv2.1 is available at https://www.marineheatwaves.org/tracker.html.

In this report, the higher-resolution dataset DOISSTv2.1 is primarily used to examine daily SST variations and evaluate MHW/MCS occurrences, while the coarser-resolution but long-term datasets ERSSTv5, HadSST.4.0.1.0, and DCENT-Iv1.1.0.0 are used for large-scale SST pattern analysis and decadal-to-centennial SST trend assessment. The base period for computing SSTAs and analyzing MHWs/MCSs is 1991–2020, the current standard reference period for SST climate normals (Yin et al. 2024).

2. SEA SURFACE TEMPERATURES IN 2025

For the global ocean, recent strong warming manifested as historically high SSTs that began in March 2023 have persisted, making 2025 the third consecutive exceptionally warm year. Figure 3.1 shows the daily global-mean SST for each year since 1981 in DOISSTv2.1. The 1991–2020 normal SSTs and the corresponding ±1.96-standard deviation (std. dev.) envelope (Yin et al. 2024) are also shown for reference. The envelope represents the 95% confidence interval of the normal SSTs, corresponding to a 5% significance level when assessing departures of observed SSTs from normal conditions.

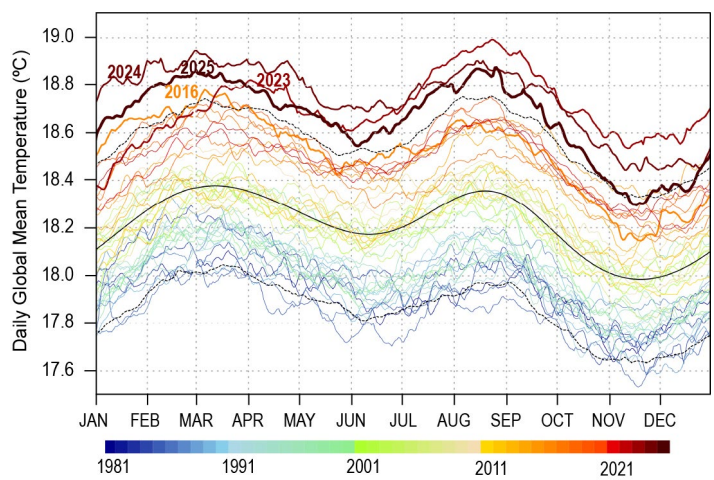

Fig. 3.1. Daily global-mean sea surface temperatures (SST) since 1981. Individual years are shown in different colors, as indicated by the color bar, plotted over a common 366-day Julian calendar year. The current year and the recent record-setting years (2016, 2023, and 2024) are highlighted with thicker lines and labeled. The solid and dashed black lines denote the 1991–2020 normal SST and the ±1.96-std. dev. envelope (95% confidence interval), respectively. (Source: Daily OISST [DOISSTv2.1].)

Although the daily global-mean SST in 2025 did not set new records as in the previous two years, it remained remarkable, ranking as the second or third highest during most

of the year. Consistent with the climatological seasonal cycle, daily global-mean SST reached maxima in early March and late August and minima in early June and mid-November. From January through late March, the 2025 global-mean SST was second only to the 2024 mean and remained substantially higher than in all other previous years, including the record-breaking years of 2016 and 2023. Between April and May, global-mean SSTs in 2025 and 2023 were comparable, alternating between the second- and third-highest positions for that time of year. Since early June, global-mean SSTs in 2025 were lower than in the previous two years for nearly the remainder of the year. During most of November and December, 2025 SSTs fell outside the top three highest for the time of year.

In 2025, the highest daily global-mean SST was 18.87°C, recorded on 26 August, ranking as the second highest for that time of year after 2024. The lowest daily global-mean SST, 18.30°C, was observed on 17 November, ranking as the fourth highest for that time of year, following 2023, 2024, and 2016. Figure 3.1 also shows that SSTs during the last three years were distinct from those in earlier years. With the exception of a few intermittent periods in November and December, the 2025 global-mean SST lay outside the ±1.96-std. dev. envelope of the 1991–2020 normal. Indeed, global-mean SST remained continuously more than 1.96 std. devs. above the 1991–2020 normal from mid-March 2023 through early November 2025, indicating an unusually warm global ocean for three consecutive years.

In the centennial record of ERSSTv5, the annual-average global-mean SST for 2025 was 18.68°C, which was 0.87°C higher than the 1854–1900 pre-industrial level and 0.38°C above the 1991–2020 reference level. Within the 172-year SST record beginning 1854, 2025 ranked as the third warmest year, 0.03°C cooler than 2023 and 0.09°C cooler than 2024, but 0.10°C warmer than 2016, the fourth warmest year. Moreover, the most recent decade (2016–25) was the warmest on record, with an average SST of 18.57°C, 0.77°C above the pre-industrial level and 0.27°C above the 1991–2020 reference level.

Changes of global SST in 2025 relative to the 1991–2020 reference period are shown in Fig. 3.2. On the annual mean (Fig. 3.2a), 2025 SSTs were characterized by ENSO-related patterns in the tropics, enhanced SST contrasts in the Northern Hemisphere, and comparatively lower variability in the Southern Hemisphere. In the equatorial Pacific, SSTs were lower than the reference period by less than 0.5°C between 170°E and 90°W and slightly higher than the reference period off the western coast of the Americas, consistent with the evolution from ENSO-neutral to La Niña-like conditions during 2025 (see section 4b; Tan et al. 2025). Across the remaining ocean basins, warm anomalies predominated, with scattered pockets of cold anomalies. Particularly large positive SSTAs (>+1.0°C) occurred in the midlatitude eastern and central North Pacific, the western Mediterranean Sea, the central Maritime Continent, the North Sea, and the Barents Sea. The seasonal evolution of global SST patterns is further illustrated using seasonal-mean SSTs (Figs. 3.2b–e). Here, the four seasons are defined as boreal winter (January–March), spring (April–June), summer (July–September), and autumn (October–December), corresponding to austral summer, autumn, winter, and spring, respectively.

As shown in Fig. 3.2, cooling in the central equatorial Pacific was most pronounced in boreal winter and autumn, with large areas exhibiting SSTs more than 0.5°C below the 1991–2020 average, suggesting that La Niña conditions briefly developed during these two seasons (see section 4b; Tan et al. 2025). Cooling in the Arabian Sea was observed in all seasons and was strongest in autumn, when negative SSTAs extended across nearly the entire basin. The Arctic Ocean exhibited relatively minor variability in winter and spring because of extensive ice coverage. However, SSTAs in the Barents Sea remained above normal throughout the year, while cooling occurred across much of the Beaufort Sea in summer and subsequently extended into the East Siberian Sea in autumn. Globally, ocean warming peaked in the Northern Hemisphere during summer (Fig. 3.2d). In contrast, the Southern Hemisphere exhibited comparatively weaker seasonal variability, with stronger warming during austral summer (Fig. 3.2b). Meanwhile, persistent positive SSTAs in the midlatitude North Pacific indicated that the Pacific Decadal Oscillation (PDO) maintained a five-year negative phase since 2020 (NOAA National Centers for Environmental Information 2026). In addition, the seasonal SSTA pattern in the Indian Ocean suggests that the

Indian Ocean dipole (IOD) was in a negative phase during boreal summer and autumn of 2025 (see section 4f for details; NOAA Climate Prediction Center 2026). For most of the year, the equatorial Atlantic was warm, with weak cooling associated with a short-lived Atlantic Niña event from June to August 2025.

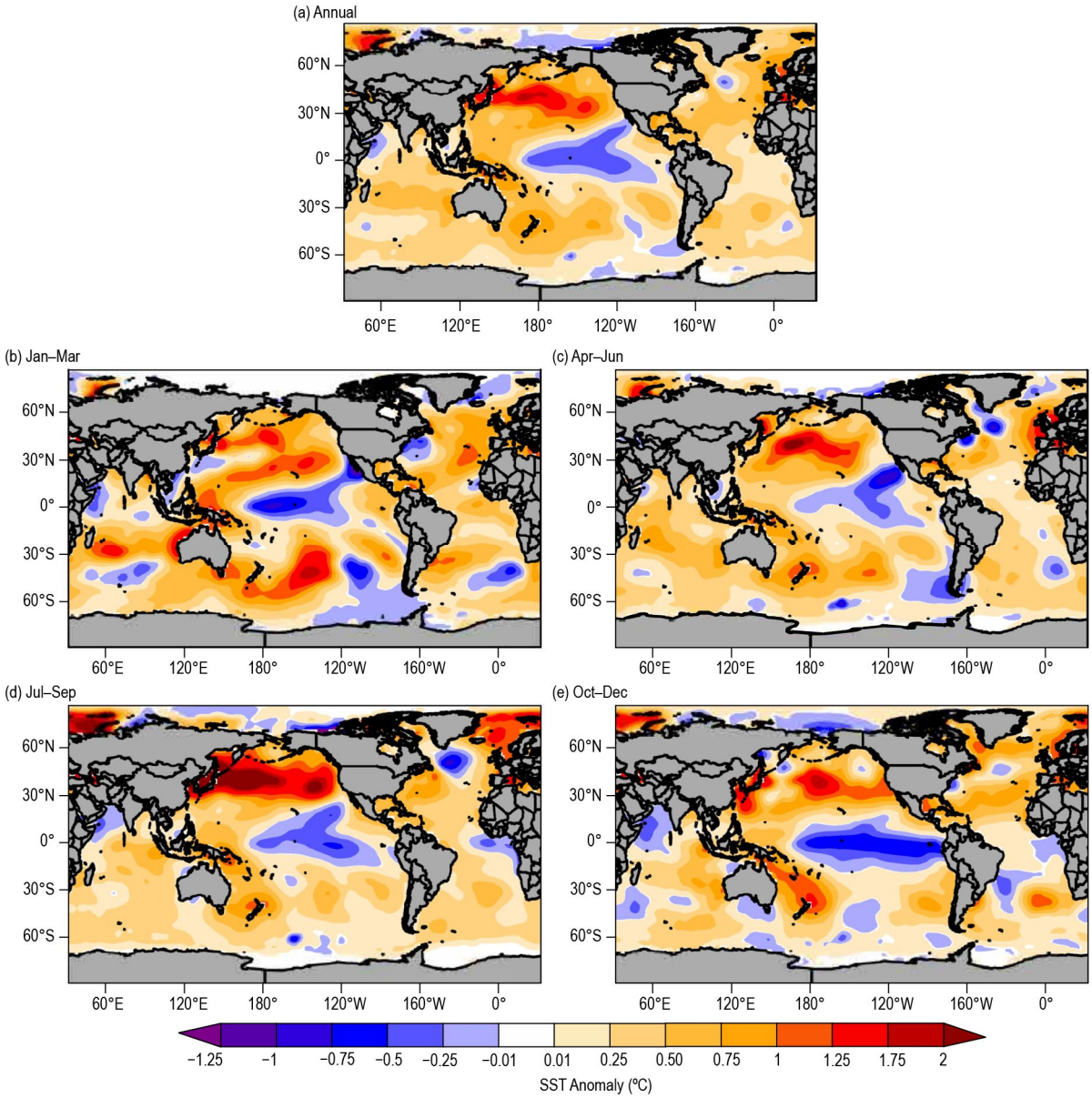

Fig. 3.2. Annual and seasonal mean sea surface temperature anomalies (SSTAs; °C) for 2025 relative to the 1991–2020 reference period. (a) Annual; (b) boreal winter (Jan–Mar); (c) spring (Apr–Jun); (d) summer (Jul–Sep); and (e) autumn (Oct–Dec). (Source: ERSSTv5.)

3. MARINE HEATWAVES AND COLD SPELLS

The 2025 analysis of DOISSTv2.1 indicates that 87% of the ocean surface experienced at least one marine heatwave (MHW; Hobday et al. 2016; Figs. 3.3a,b), while 26% experienced at least one marine cold spell (MCS; Figs. 3.3c,d). The most common MHW category in 2025 was Category 1 (Moderate), accounting for 40% of the total coverage, followed by Category 2 (Strong) events at 39%, with Category 3 (Severe) and Category 4 (Extreme) MHWs accounting for 6% and 2% of the total coverage, respectively. Category 1 (Moderate) MCSs remained the most prevalent cool events (17% in 2025), as has been the case since 2001. Globally, the ocean experienced an average of 73 MHW days and 5 MCS days in 2025. Although this is below the record high 100 MHW days observed in 2024 (and the MCS record high of 57 days in 1985; Figs. 3.3a,c), 2025 conditions correspond to a daily mean MHW coverage of 20% of the ocean surface, compared to about 1% for MCSs (Figs. 3.3a,c), making 2025 the new record-low year for MCSs.

With the transition from El Niño conditions in 2023/24 to La Niña conditions in 2024/25 (see section 4b; Tan et al. 2025), all MHW occurrences declined from 2024 to 2025. Nevertheless, 2025 still experienced more MHW activity than the previous record-setting year of 2016, ranking as the third highest year for daily MHW coverage after 2023 and 2024 (Fig. 3.3a).

While much of the Arctic experienced Category 4 MHW conditions during the first two months of the year, the absolute SST anomaly relative to the historical record was about +0.5°C. A recurring pattern of large MHWs with central cores reaching Category 4 affected the southwest coast of New Zealand from mid-February to mid-March. The northeastern region of the archipelago experienced another extensive MHW in November, again featuring a Category 4 core. As in 2024, waters surrounding Ireland and the United Kingdom were affected by Category 1 and 2 MHWs for much of the year.

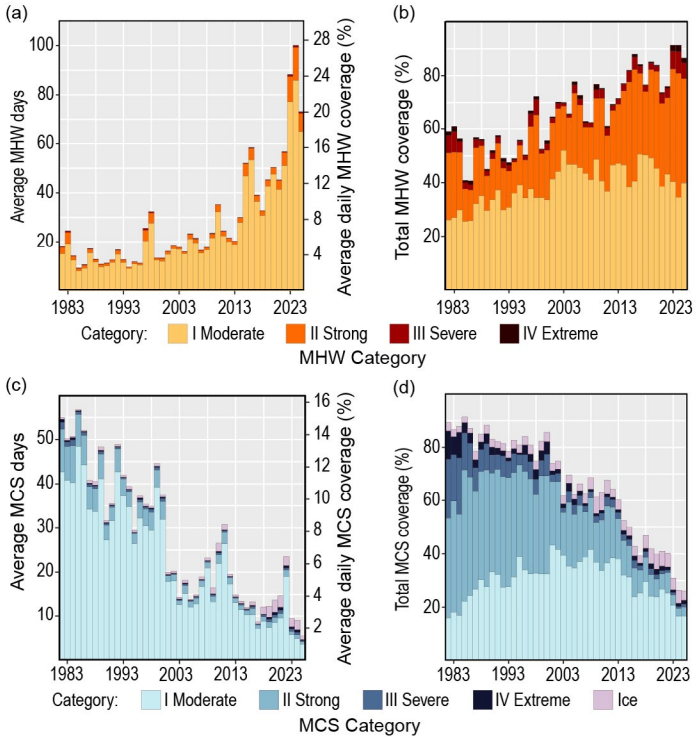

Fig. 3.3. Annual global occurrence (a),(b) of marine heatwaves (MHW) and (c),(d) marine cold spells (MCS) relative to the 1991–2020 base period. (a) Average count of MHW days experienced over the surface of the ocean each year (left y-axis), also expressed as the percent of the surface of the ocean experiencing a MHW on any given day (right y-axis) of that year; (b) total percent of the surface area of the ocean that experienced a MHW at some point during the year; (c) same as (a) but for MCS; and (d) same as (b) but for MCS. Values shown are for the highest category of MHW/MCS experienced at any point. (Source: Daily OISST [DOISSTv2.1].)

The spatial extent of this event affected much of the Atlantic coastline of Spain and France. Although short-lived, this otherwise mild MHW intensified in mid-May, with uninterrupted Category 3 conditions extending from the north of Iceland to the southern tip of Ireland. In 2025, the western Mediterranean experienced record-breaking warming during the first half of boreal summer (surpassing the previous record set in 2022). In contrast, the eastern Mediterranean was less warm in summer 2025 than in previous summers, although Category 3 MHW conditions occurred during the first two months of the year. Waters east and west of the Japanese archipelago reached Category 3 intensity beginning in July, persisting mainly as Category 2 and 3 events through October. This feature would occasionally connect across the Pacific to the 'blob-like' MHW that occurred along the west coast of North America (a now semi-permanent feature), whose most intense point was reached in mid-September with a near-basin scale core of Category 3 MHW coverage. In late July, the majority of the waters from Norway to the Arctic ice edge experienced a Category 2 MHW lasting one month. Meanwhile, the recurring summer Category 4 MHW across the Barents and Kara Seas reached its highest intensity since its annual reappearance began in 2015.

Although many other MHWs in 2025 would have been considered noteworthy a decade ago, none were as pronounced as those highlighted here. While the ocean experienced less extreme heat events in 2025 than in 2024, it did not experience correspondingly more extreme cold spells. All occurrences of MCSs declined relative to the previous year, indicating an upward shift in the overall SST envelope of the global ocean. No notable MCSs occurred in 2025; all Category 3 or 4 events were associated with cyclonic or anticyclonic eddy activity in western boundary currents or potential ice-edge-related artefacts.

4. SEA SURFACE TEMPERATURE TRENDS

Time series of global- and regional-mean annual SSTAs for the periods 1880–2025 and 1950–2025 are shown in Fig. 3.4. Uncertainty estimates derived from the ERSSTv5 ensemble analysis (Huang et al. 2015, 2020) are included for reference. Across all domains, the four SST datasets exhibit similar temporal variability and comparable trends; however, both variability

and trends differ substantially among regions. Notably, North Atlantic SSTAs display pronounced interdecadal variability over the full record since 1880 (Fig. 3.4f), largely associated with the Atlantic Multidecadal Variability (Schlesinger and Ramankutty 1994).

Uncertainties are largest during the early part of the record, with substantial spreads among datasets, as illustrated for the global ocean (Fig. 3.4b) and the North Atlantic (Fig. 3.4f). This is because in situ observations were scarce in the early years, and different data reconstruction algorithms based on limited observations led to higher uncertainties in each SST reconstruction.

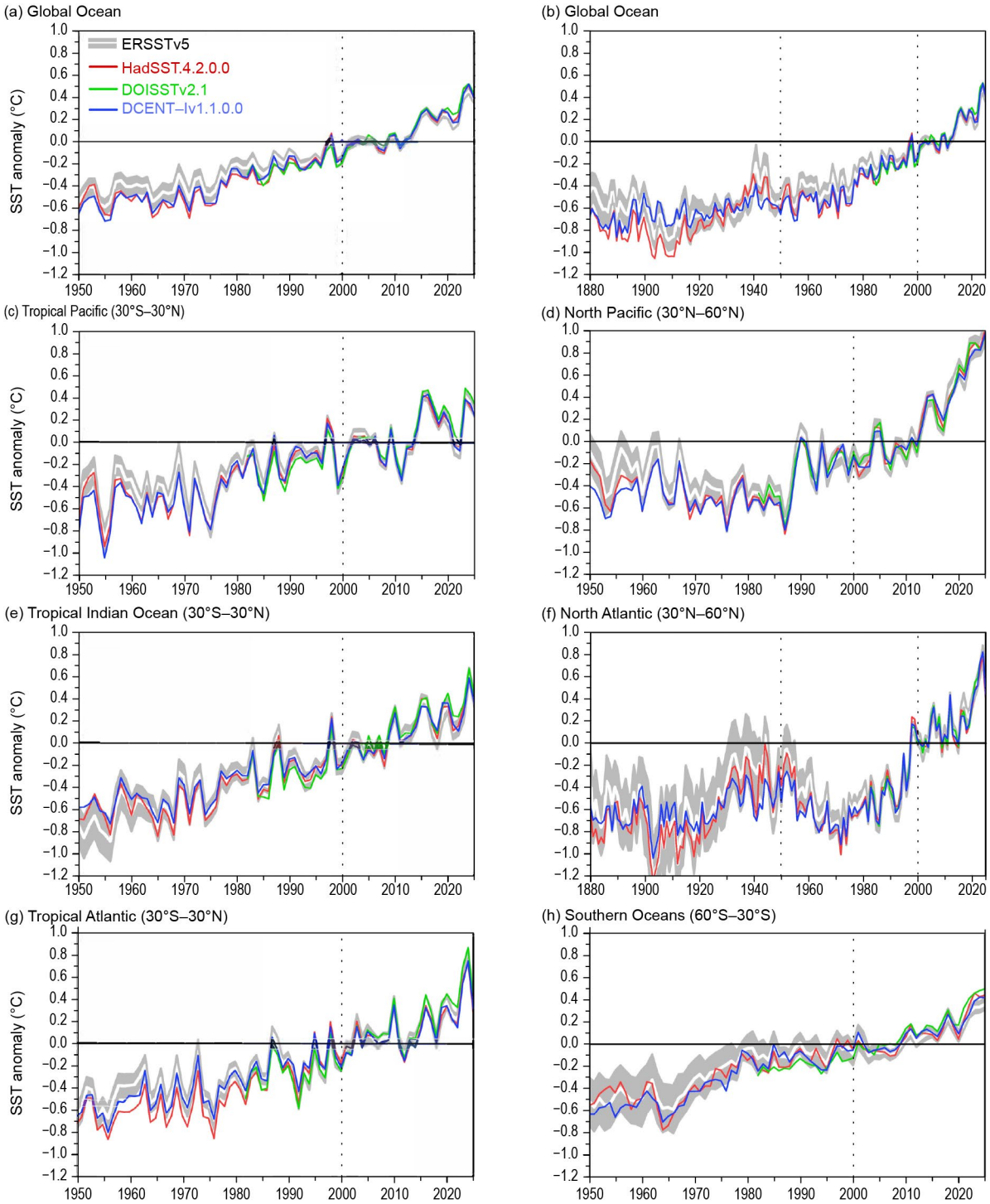

Fig. 3.4. Regional mean annual average sea surface temperature anomalies (SSTAs; °C) of ERSSTv5 (solid white), Hadley Centre Sea Surface Temperature dataset (HadSST.4.2.0.0; solid red), Daily OISST (DOISSTv2.1; solid green), and Dynamically Consistent ENsemble of Temperature (DCENT-Iv1.1.0.0; solid blue) for the period 1950–2025 except for (b) and (f). (a) Global Ocean; (b) Global Ocean for 1880–2025; (c) Tropical Pacific; (d) North Pacific; (e) Tropical Indian; (f) North Atlantic for 1880–2025; (g) Tropical Atlantic; and (h) Southern Oceans. Shadings provide the 2-std. dev. envelope derived from a 500-member ensemble analysis based on ERSSTv5 and centered on the SSTAs of ERSSTv5. The starting years of the two periods for trend assessment, 1950 and 2000, are indicated by vertical dotted black lines.

The gradual improvement of the observing network since World War II, and especially the widespread use of buoy data since the 1980s, greatly reduced SST uncertainties and narrowed the differences among datasets.

Trends in global-mean SST were evaluated for a longer period (1950–2025) and a shorter period (2000–25) using the four datasets (Table 3.1). For both periods, the estimated trends are consistent across datasets. During 1950–2025 (excluding DOISSTv2.1, which began in 1981), global trends range from 0.11°C to 0.13°C decade^{-1}, with small uncertainties between 0.01°C and 0.02°C decade^{-1}. During 2000–25, trends increased to 0.19°C–0.22°C decade^{-1} in all four products, with larger uncertainties of 0.05°C–0.06°C decade^{-1}. Accounting for uncertainties, all datasets show statistically the same trends for the two periods, with average trends of 0.12°C decade^{-1} in 1950–2025 and 0.21°C decade^{-1} for 2000–25.

Regional trends were also assessed for the six domains shown in Fig. 3.4 using ERSSTv5 (Table 3.1). For 1950–2025, trends are broadly similar across regions, ranging from 0.10°C to 0.14°C decade^{-1}, consistent with the global trends in the four datasets (0.11°C–0.13°C decade^{-1}) over the same period. In contrast, trends for 2000–25 show pronounced regional differences, spanning from 0.15°C decade^{-1} in the tropical Pacific and 0.16°C decade^{-1} in the Southern Ocean to 0.46°C decade^{-1} in the North Pacific, consistent with accelerated warming in that basin since 2013 (Hu et al. 2024). Trends in the tropical Indian Ocean (0.20°C decade^{-1}), North Atlantic (0.24°C decade^{-1}), and tropical Atlantic (0.21°C decade^{-1}) are close to the global trends (0.19°C–0.22°C decade^{-1}). Although all regional trends are statistically significant, their relative uncertainties are generally larger than those of global trends. Notably, the tropical Pacific exhibits both the weakest trend (0.15°C decade^{-1}) among all regions but the highest uncertainty (0.12°C decade^{-1}), reflecting comparatively weak warming and higher variability in the region, which is associated with the weak La Niña conditions that appeared at the beginning and end of the year (see section 4b).

Table 3.1. Linear trends (°C decade^{-1}) of global and regional mean annual sea surface temperature anomalies (SSTAs; °C) from ERSSTv5, the Hadley Centre Sea Surface Temperature Dataset version 4 (HadSST.4.2.0.0), the Dynamically Consistent ENsemble of Temperature (DCENT-Iv1.1.0.0), and the Daily OISST (DOISSTv2.1). The uncertainties at a 95% confidence level, expressed as ± values, are estimated by accounting for the effective sampling number quantified by lag–1 autocorrelation on the degrees of freedom of annual mean SSTAs.

Product	Region	1950–2025	2000–25
DCENT-Iv1.1.0.0	Global	0.13±0.01	0.20±0.06
HadSST.4.2.0.0	Global	0.13±0.02	0.21±0.06
DOISSTv2.1	Global	N/A	0.22±0.05
ERSSTv5	Global	0.11±0.01	0.19±0.06
ERSSTv5	Tropical Pacific (30°S–30°N)	0.10±0.02	0.15±0.12
ERSSTv5	North Pacific (30°N–60°N)	0.12±0.05	0.46±0.11
ERSSTv5	Tropical Indian (30°S–30°N)	0.14±0.02	0.20±0.07
ERSSTv5	North Atlantic (30°N–60°N)	0.13±0.05	0.24±0.10
ERSSTv5	Tropical Atlantic (30°S–30°N)	0.12±0.02	0.21±0.09
ERSSTv5	Southern oceans (30°S–60°S)	0.10±0.01	0.16±0.05

c. Ocean temperature and heat content

—G. C. Johnson, J. M. Lyman, C. P. Atkinson, L. Cheng, C. M. Domingues, R. E. Killick, R. Locarnini, A. Mishonov, D. P. Monselesan, M. Miyamoto, J. Reagan, A. Savita, and S. E. Wijffels

The oceans transport substantial amounts of heat within Earth's climate system (e.g., Donohoe et al. 2024) and act as the dominant heat sink, absorbing ~89% of the excess energy associated with Earth's top-of-atmosphere energy imbalance from 1971 to 2020 (e.g., von Schuckmann et al. 2023). This imbalance, driven by increasing greenhouse gas concentrations and the large thermal inertia of the oceans, substantially delays global warming (e.g., Forster et al. 2025). Surface-intensified ocean warming has increased the strength and duration of marine heatwaves (MHWs; e.g., Oliver et al. 2021) and enhanced upper ocean stratification (e.g., Li et al. 2020). This substantial upper ocean warming provides additional energy to fuel stronger tropical cyclones (e.g., Walsh et al. 2016), accelerates ice loss where the cryosphere interacts with the ocean (von Schuckmann et al. 2023), and exacerbates coral bleaching (e.g., Hughes et al. 2017). Subsurface ocean warming also contributes to sea level rise (section 3f).

Here, we discuss ocean temperature and heat content anomalies in 2025 relative to both 2024 and a 30-year climatology (1993–2022). We focus primarily on the upper 2 km of the ocean, but also update an estimate of decadal temperature trends for the deep (2 km–4 km) and abyssal (4 km–6 km) layers, where warming is also detected. To do this, we generated weekly maps of ocean heat content anomaly (OHCA) relative to a 1993–2022 baseline mean as well as temperature fields on 58 pressure layers from 0 dbar to 2000 dbar using Random Forest regression following Lyman and Johnson (2023), with V2.2 methodological improvements (https://www.pmel.noaa.gov/rfrom/). In situ ocean temperature profiles, including Argo data downloaded from an Argo Global Data Assembly Centre in January 2026 (http://doi.org/10.17882/42182#125185), were used for training data for these maps, and prediction variables included satellite sea surface height and SST, location, and time. Multidecadal time series of annual global estimates of OHCA using primarily in situ data for two depth layers (0 m–700 m and 700 m–2000 m) from multiple research groups are also discussed. Finally, a deep subset of these same Argo data is used along with shipboard conductivity, temperature, and depth (CTD) data downloaded from the World Ocean Database (Mishonov et al. 2024; https://www.ncei.noaa.gov/products/world-ocean-database) in January 2026 to update a 2000 dbar–6000 dbar multidecadal estimate of deep and abyssal ocean temperature trends following Johnson and Purkey (2024).

The boreal winter of 2023/24 marked an El Niño year, but the winters of 2024/25 and marginally 2025/26 both exhibited weak La Niña conditions (see section 4b). Consistent with this history, the 2025-minus-2024 difference of 0-m–2000-m OHCA (Fig. 3.5b) generally shows a decrease in the eastern tropical Pacific and an increase in the west, with ocean heat content anomalies for 2025 (Fig. 3.5a) being above the 30-year climatological conditions in the western tropical Pacific and below that climatology in much of the eastern tropical Pacific. As in 2020 through 2024, the centers of the North and South Pacific continued to be anomalously warm in 2025, with less warm conditions around the edges, consistent with a continued negative Interdecadal Pacific Oscillation index (Henley et al. 2015). As in 2022 through 2024, cold anomalies just south of the Kuroshio Extension and warm anomalies within that current in 2025 are associated with a long-lasting northward shift of that current (see section 3g). Pacific marginal seas remained warmer than climatological means in 2025, as they were in 2024.

In the Indian Ocean, the 2025-minus-2024 difference of OHCA (Fig. 3.5b) shows a strong decrease from about 15°S to about 5°S in the western two-thirds of the basin, with a smaller magnitude increase almost everywhere else. The 2025 OHCA anomalies (Fig. 3.5a) were mostly positive, except around some of the outer edges of the aforementioned strong decrease.

The 2025-minus-2024 difference of OHCA (Fig. 3.5b) in the Atlantic Ocean was heterogeneous, with broad regions of relatively weak cooling and warming in the interior, and smaller scale but stronger eddy signatures of warming and cooling in western boundary current extensions and the Antarctic Circumpolar Current (ACC). Much of the Atlantic Ocean exhibited OHCA well above the 1993–2022 average (Fig. 3.5a), with anomalies in the Gulf of America/Gulf of Mexico being especially high. The north side of the Gulf Stream extension remained cool as it was in 2024, suggesting a continued southward shift in the axis of that current. The cooler-than-average conditions southeast of Greenland that have persisted for several years were less apparent in 2025.

As expected, the large-scale statistically significant regional patterns in the 1993–2025 local linear trends of 0-m–2000-m OHCA (Fig. 3.5c) are similar to those from 1993–2024 (Johnson et al. 2025), and earlier reports for 0-m–700-m OHCA.

Near-global average seasonal temperature anomalies in the upper 2000 dbar of the ocean since 1993 (Fig. 3.6) show signatures of past strong El Niño events: Subsurface cold anomalies with maximum amplitude around 140 dbar–150 dbar and warm near-surface anomalies with maximum amplitude around 40 dbar–50 dbar peak in boreal winters of El Niño years. The opposite pattern is observed during La Niña years (Fig. 3.6a). Boreal winter 2023/24 shows a typical El Niño signature, with a near-surface warm anomaly and a relatively cool (compared to surrounding years) subsurface anomaly centered at about 160 dbar. The record-warm near-surface anomalies reached during winter 2023/24 have slowly diminished over the past two years, with two subsequent winters that have exhibited weak La Niña conditions. However, the ocean below 100 dbar has exhibited an overall warming trend over this period. The 33-year record length warming trend (Fig. 3.6b) is strongest near the surface (0.19°C decade^{-1} at 30 dbar), diminishing steadily with increasing pressure to reach 0.04°C decade^{-1} by 420 dbar, and then diminishing more gradually with increasing pressure to about 0.01°C decade^{-1} around 2000 dbar.

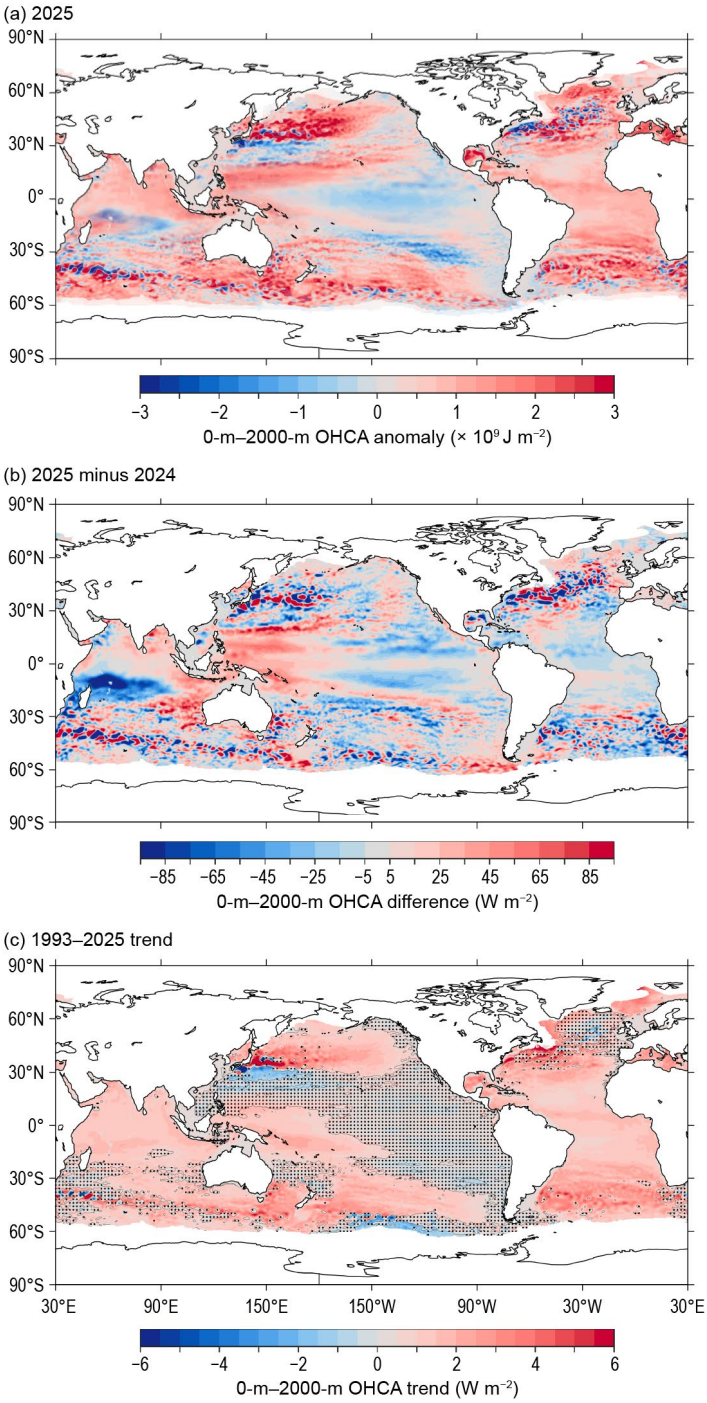

Fig. 3.5. (a) Random Forest Regression Ocean Maps (RFROM) v2 estimate of 0-m–2000-m ocean heat content anomaly (OHCA; × 10^9 J m^{-2}) for 2025 analyzed following Lyman and Johnson (2023) with v2.2 improvements as in https://www.pmel.noaa.gov/rfrom/. Values are displayed relative to a 1993–2022 baseline. (b) 2025-minus-2024 of 0-m–2000-m OHCA expressed as a local surface heat flux equivalent (W m^{-2}). For (a) and (b) comparisons, note that 95 W m^{-2} applied over one-year results in a 3 × 10^9 J m^{-2} change of OHCA. (c) Linear trend for 1993–2025 0-m–2000-m annual OHCA (W m^{-2}). Areas with statistically insignificant trends at 5%–95% confidence (taking into account the decorrelation time scale of the residuals when estimating effective degrees of freedom) are stippled.

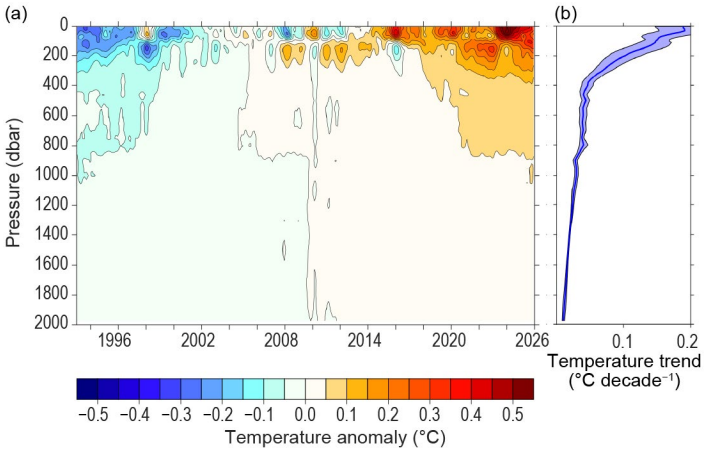

Fig. 3.6. (a) Near-global (66.5°S–81.5°N, but excluding seasonally ice-covered regions within that latitude range) average monthly ocean temperature anomalies (°C; from Random Forest Regression Ocean Maps [RFROM] v2.2, Lyman and Johnson [2023]) relative to a 1993–2022 seasonal cycle and mean, smoothed with a five-month Hanning filter and contoured at 0.05°C intervals (see color bar) vs. pressure and time. (b) Linear trend of temperature anomalies over the period 1993–2025 in (a) plotted vs. pressure in °C decade^{-1} (blue line) with 5%–95% confidence intervals (blue shading).

Nearly global integrated annually averaged OHCA estimates from 0 m–700 m and 700 m–2000 m from six and five research groups, respectively, are presented (Fig. 3.7). As noted in previous reports, year-round, near-global sampling in both of those layers commenced around 2005 from Argo, making estimates relatively certain after that date. Deep expendable bathythermographs sampling to 700 m were deployed extensively over much of the globe (with the exception of the high southern latitudes) starting in the early 1990s (Lyman and Johnson 2014), hence the upper layer results may be fairly robust back to 1993. Results for the 700-m–2000-m layer, which is quite sparsely sampled prior to about 2005, should be interpreted with caution in earlier years.

The various estimates of annual globally integrated 0-m–700-m OHCA (Fig. 3.7a) consistently show large increases since 1993, with all six analyses reporting 2025 as a record high. The 700-m–2000-m OHCA annual analyses (Fig. 3.7b) show a smaller, but still distinct, long-term warming trend, and again all five analyses report 2025 as a record high in that deeper layer. The water column from 0 m to 700 m gained 13±5 ZJ and from 700 m to 2000 m gained 8.0±1.1 ZJ (means and standard deviations given) from 2024 to 2025. Causes of differences among estimates are discussed in Johnson et al. (2014, 2015).

The estimated linear rates of heat gain for each of the six global integral estimates of 0-m–700-m OHCA that extended from 1993 through 2025 (Fig. 3.7a) range from 0.39 (±0.05) W m^{-2} to 0.48 (±0.07) W m^{-2}. These estimates are applied over the surface area of Earth (Table 3.2) rather than the surface area of the ocean, to relate directly to the top-of-atmosphere energy imbalance (e.g., Loeb et al. 2021; see section 2f for details). Linear trends for the 700-m–2000-m layer from five groups over the same time period range from 0.18 (±0.03) W m^{-2} to 0.24 (±0.03) W m^{-2}. Trends from all groups agree within 5%–95% uncertainties in both layers. Using shipboard and Deep Argo CTD data collected from 1968 through 2025 to update the OHCA estimates of Johnson and Purkey (2024) for the 2000-dbar–6000-dbar layer, the linear trend is 0.07 (±0.02) W m^{-2} from February 1988 to June 2015. These dates are the global volume-average times of the first and last sampling used in the local trend calculations.

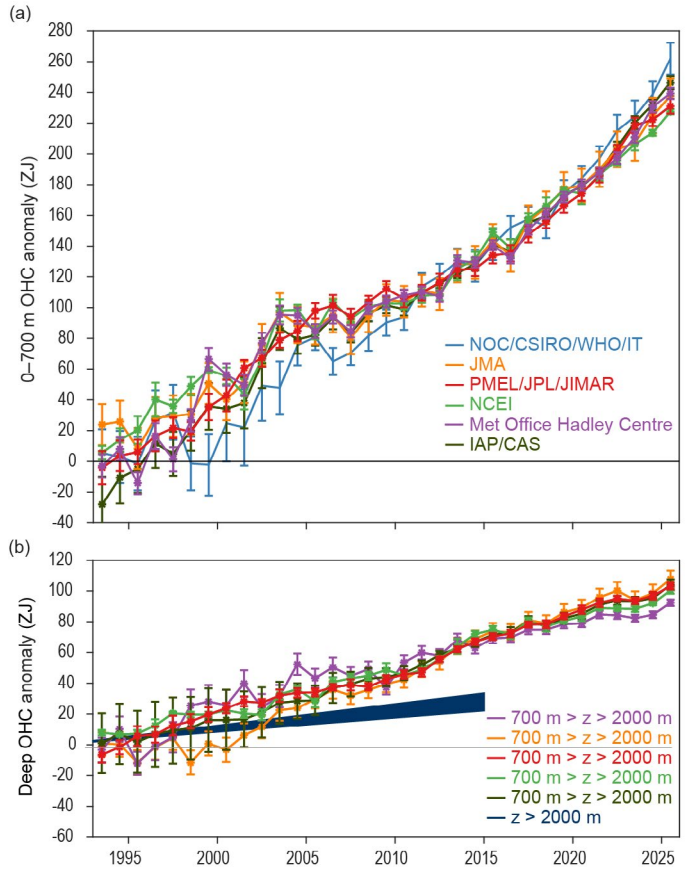

Fig. 3.7. (a) Annually averaged global integrals of in situ estimates of upper (0 m–700 m) ocean heat content anomaly (OHCA; ZJ; 1 ZJ = 10^{21} J) for the period 1993–2025 with standard errors of the mean. The Meteorological Research Institute (MRI)/Japan Meteorological Agency (JMA estimate is an update of Ishii et al. (2017). The Pacific Marine Environmental Laboratory (PMEL)/Jet Propulsion Laboratory (JPL)/Cooperative Institute for Marine and Atmospheric Research (CIMAR) estimate is from Random Forest Regression Ocean Maps (RFROM) v2.2 after Lyman and Johnson (2023). The Met Office Hadley Centre estimate is computed from gridded monthly temperature anomalies following Palmer et al. (2007) and Good et al. (2013). Both the PMEL and Met Office estimates use Cheng et al. (2014) eXpendable BathyThermograph (XBT) corrections and Gouretski and Cheng (2020) mechanical bathythermograph corrections (MBT) corrections. The NCEI estimate follows Levitus et al. (2012). The Institute of Atmospheric Physics (IAP)/Chinese Academy of Sciences (CAS) estimate was reported in Pan et al. (2026). The National Oceanography Centre (NOC)/Commonwealth Scientific and Industrial Research Organisation (CSIRO)/Woods Hole Oceanographic Institution (WHOI)/Indian Institutes of Technology (IIT) estimate is an update of Domingues et al. (2008). See Johnson et al. (2015, 2024) for details on uncertainties, methods, and datasets. For comparison, all estimates have been individually offset (vertically on the plot), first to their individual 2005–25 means (the best sampled time period) and then to their collective 1993 mean. (b) Annual average global integrals of in situ estimates of intermediate (700 m–2000 m) OHCA for 1993–2025 (ZJ) with standard errors of the mean and a long-term trend with one standard error uncertainty shown from February 1988 to June 2015 for deep and abyssal (2000 dbar–6000 dbar) OHCA following Johnson and Purkey (2024) but updated as detailed in the text.

This result is consistent with previously reported decadal deep and abyssal warming trends (e.g., Purkey and Johnson 2010), though it features smaller uncertainties than earlier estimates due to inclusion of more recent and historical data. Summing the three layers (despite their different time periods as given above), the full-depth ocean heat gain rate applied to Earth's entire surface ranges from 0.65 W m^{-2} to 0.74 W m^{-2}. While in situ observations of long-term rates of heat uptake by the ocean and other components of Earth's climate system are used to calibrate top-of-atmosphere satellite measurements of Earth's energy imbalance (e.g., Loeb et al. 2024), the precision and stability of those satellite measurements allows closer tracking of year-to-year variations in that quantity (see section 2f).

Table 3.2. Trends of ocean heat content increase (in W m^{-2} applied over the 5.1×10^{14} m^2 surface area of Earth) from seven different research groups over three depth ranges (see Fig. 3.7 for details). For the upper (0-m–700-m) and intermediate (700-m–2000-m) depth ranges, estimates cover 1993–2025, with 5%–95% uncertainties based on the residuals taking their temporal correlation into account when estimating degrees of freedom (Von Storch and Zwiers 1999). The 2000-dbar–6000-dbar depth range estimate, an update of Johnson and Purkey (2024), uses data from 1970 to 2025, having a global average start and end date of February 1988 to June 2015, again with 5%–95% uncertainty.

Research group	0 m–700 m Global ocean heat content trends (W m^{-2})	700 m–2000 m Global ocean heat content trends (W m^{-2})	2000 dbar–6000 dbar Global ocean heat content trends (W m^{-2})
MRI/JMA	0.40±0.06	0.24±0.03	—
PMEL/JPL/CIMAR	0.42±0.08	0.20±0.03	—
NCEI	0.39±0.05	0.19±0.02	—
Met Office Hadley Centre	0.43±0.08	0.18±0.03	—
IAP/CAS	0.47±0.07	0.21±0.02	—
NOC/CSIRO/WHOI/IIT	0.48±0.07	—	—
Johnson and Purkey	—	—	0.07±0.02

d. Salinity

—J. Reagan, J. M. Lyman, and R. Locarnini

1. INTRODUCTION

Ocean salinity is the concentration of dissolved salts in seawater. Surface freshwater fluxes such as precipitation and evaporation, river run-off, ice melt, and ice freezing can alter local salinity, with advection and mixing redistributing these anomalies at both the surface and subsurface (Ren et al. 2011; Yu 2011). Salinity is a conservative tracer and as it is subducted into the subsurface, it retains its surface footprint (in the absence of mixing), allowing water masses to be tracked over large distances. Ocean salinity also plays a major role in ocean stratification and ultimately deep-ocean circulation by stabilizing (destabilizing) the water column leading to reduced (enhanced) mixing. Additionally, changes in ocean salinity can act as a proxy for estimating the strength of the global hydrological cycle (Schmitt 1995; Durack et al. 2012; Skliris et al. 2014), while the integration of salinity anomalies provides estimates of freshwater content. Finally, ocean salinity anomalies have been shown to improve subseasonal to seasonal precipitation forecasts (Li et al. 2016; Arcodia et al. 2025).

The sea surface salinity (SSS) analysis relies on Argo data downloaded in January 2026, with annual anomaly maps relative to a seasonal climatology generated following Johnson and Lyman (2012) updated using World Ocean Atlas 2023 (Reagan et al. 2024) as well as monthly maps of bulk (as opposed to skin) SSS data from the Blended Analysis of Surface Salinity (BASS; Xie et al. 2014). BASS blends in situ SSS data with data from the Aquarius (Le Vine et al. 2014; mission ended in June 2015), Soil Moisture and Ocean Salinity (SMOS; Font et al. 2013), and the Soil Moisture Active Passive (SMAP; Fore et al. 2016) satellite missions. Despite the larger uncertainties of satellite data relative to Argo data, their higher spatial and temporal sampling allows higher spatial and temporal resolution maps than are possible using in situ data alone at present. To investigate interannual changes of subsurface salinity, all available salinity profile data within the World Ocean Database (Mishonov et al. 2024; WOD Team 2025) are quality controlled following Garcia et al. (2024b) and then used to derive 1° monthly mean gridded salinity anomalies relative to a long-term monthly mean for the years 1955–2022 from World Ocean Atlas 2023 at standard depths from the surface to 2000 m. Note that all salinity values used in this section are reported on the dimensionless Practical Salinity Scale-78 (PSS-78; Fofonoff and Lewis 1979).

Since ~2005, profiling floats of the Argo program (Riser et al. 2016) have dominated the ocean salinity observing system and have provided unprecedented spatial and temporal coverage of salinity. These data are a mix of real-time (preliminary) and delayed-mode (scientific quality controlled) observations. Hence, the estimates presented here may be subject to instrument biases such as the positive salinity drift identified in a subset of Argo floats (Wong et al. 2023), and will be refined after all data are subjected to scientific quality control.

2. SEA SURFACE SALINITY

Sea surface salinity anomalies, unlike SST anomalies, are generally quite persistent since salinity has no direct feedback to the atmosphere. Regions dominated by evaporation, such as the subtropics, tend to exhibit higher salinity values, while areas where precipitation prevails, like the Intertropical Convergence Zone (ITCZ) and high latitudes, usually have fresher water (e.g., Wüst 1936; Schmitt 1995).

The equatorial Pacific generally became saltier from 2024 to 2025 (Fig. 3.8b). This includes both the western equatorial Pacific fresh pool and the ITCZ. However, the South Pacific Convergence Zone (SPCZ) freshened and shifted south after moving north in 2024 (see section 3e). Also, a strong patch of anomalously fresh water just east of the Galápagos Islands became even fresher. The Philippine Sea, which had become saltier in 2024, became anomalously fresh (Fig. 3.8a).

The North Atlantic experienced regions of SSS freshening in the Davis Strait, the Greenland Sea, and the Labrador Sea (Fig. 3.8b). This sea surface freshening at high latitudes is potentially important in that it could affect thermohaline circulation by making surface waters less dense (Gordon 1986; Broecker 1991). A fresh region off Venezuela also developed in 2025, presumably from an increase in river runoff from the Orinoco and possibly the Amazon Rivers (see section 2d). The ITCZ in the Atlantic remained anomalously fresh in 2025 (Fig. 3.8a).

The equatorial Indian Ocean, which had become relatively fresh in 2024, became saltier in 2025, shifting from anomalously fresh to slightly salty (Figs. 3.8a,b). While the region west of Australia became anomalously fresh, reversing the pattern of SSS change that was observed last year. As would be expected in the weak La Niña conditions, a freshening occurred over the maritime continent as precipitation increased over this region (see section 3e).

Sea surface salinity trends from 2005 to 2025 are essentially unchanged compared to those previously reported in Johnson and Lyman (2025). While most regions have statistically insignificant trends, there has been, and continues to be, statistically significant freshening in some climatologically fresh areas such as parts of the Pacific ITCZ, the Gulf of Alaska, the northeastern portions of the North Atlantic Ocean, the Greenland-Iceland-Norwegian Seas, the western Bay of Bengal, and the Gulf of Guinea (Fig. 3.8c). Likewise, climatologically salty regions have become increasingly salty, as evidenced by portions of the subtropics across all ocean basins. This overall "salty gets saltier and fresh gets fresher" trend, which has been evident to varying degrees and discussed in *State of the Climate* reports since 2006, is expected on a warming Earth. As the atmosphere warms, it can hold more moisture, enabling an increased hydrological cycle over the ocean (Held and Soden 2006; Durack and Wijffels 2010; Durack et al. 2012, Skliris et al. 2014).

The seasonal progression in the surface salinity features shown in Argo data can be traced in BASS SSS anomalies, which have higher spatial and temporal resolution but less accuracy (Fig. 3.9). In the equatorial Pacific, the freshening east of the Galápagos Islands is relatively episodic, occurring primarily during the March–May season, when precipitation is generally high. The Amazon/Orinoco River plume region is salty during December–February when river runoff is low, and becomes fresher in the subsequent seasons as flow increases. In the Indian Ocean, the region of anomalous freshwater west of Australia starts off fresh in December–February, and becomes progressively fresher each season, reaching its freshest in September–November.

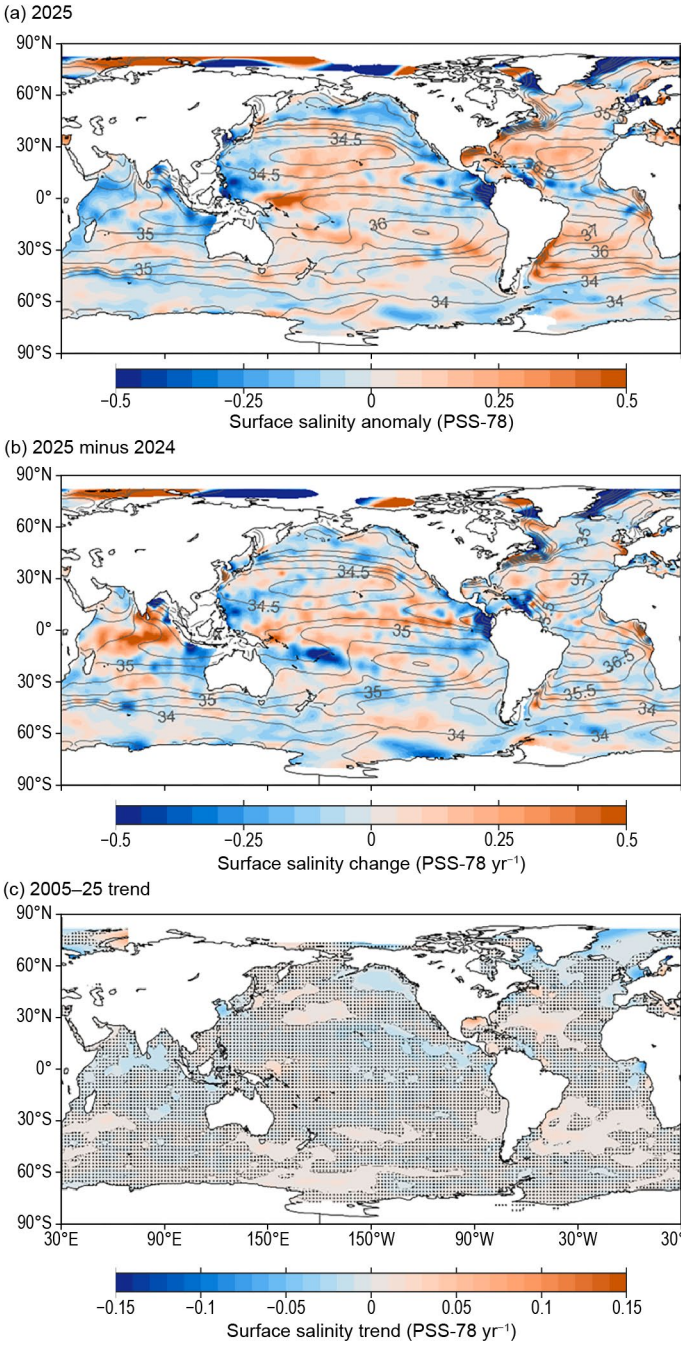

Fig. 3.8. (a) Map of the 2025 annual surface salinity anomaly (colors, Practical Salinity Scale-78 [PSS-78]) with respect to monthly climatological 1955–2022 salinity fields from World Ocean Atlas 2023 (yearly average; gray contours at 0.5 intervals, PSS-78). (b) Difference of 2025 and 2024 surface salinity maps (colors, PSS-78 yr^{-1}). White ocean areas are too data-poor (retaining <80% of a large-scale signal) to map. (c) Map of local linear trends estimated from annual surface salinity anomalies for 2005–25 (colors, PSS-78 yr^{-1}). Areas with statistically insignificant trends at 5%–95% confidence (taking into account the decorrelation time scale of the residuals when estimating effective degrees of freedom) are stippled. All maps are made using Argo data.

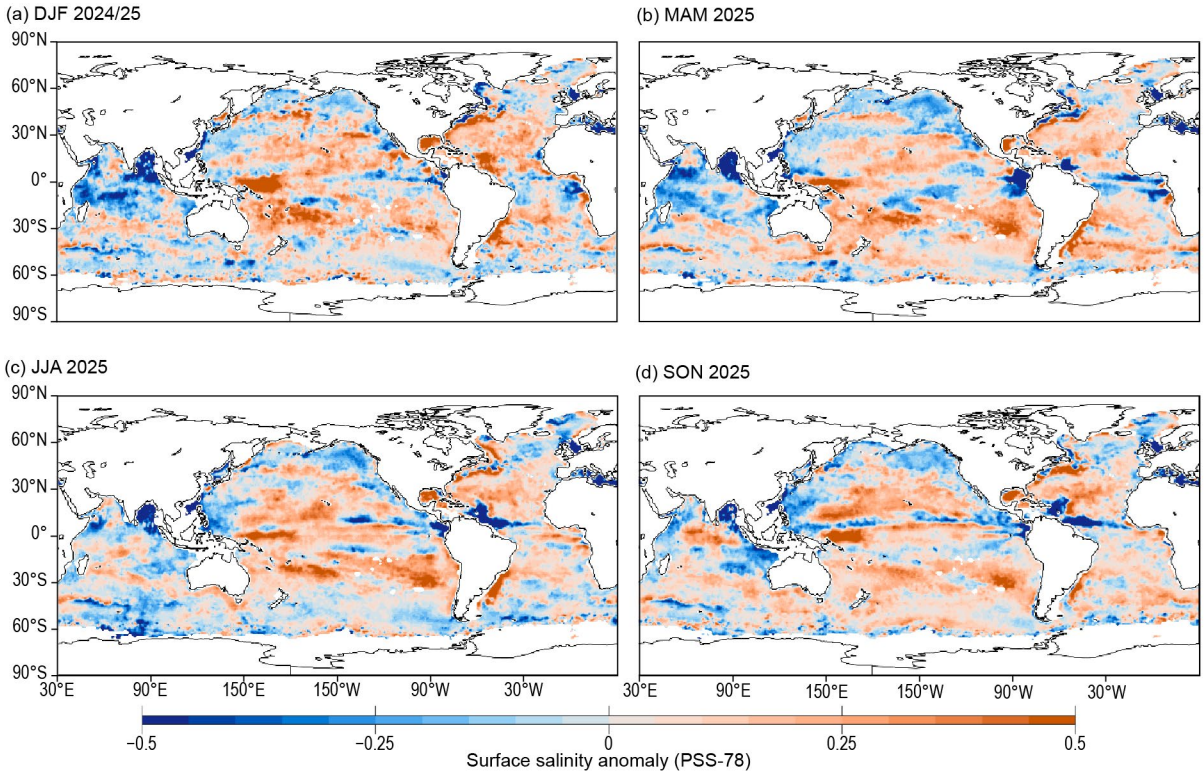

Fig. 3.9. Seasonal maps of surface salinity anomalies (colors) from monthly blended maps of satellite and in situ salinity data (Blended Analysis of Surface Salinity [BASS]; Xie et al. 2014) relative to monthly climatological 1955–2022 salinity fields from World Ocean Atlas 2023 for (a) Dec 2024–Feb 2025, (b) Mar–May 2025, (c) Jun–Aug 2025, and (d) Sep–Nov 2025.

3. SUBSURFACE SALINITY

Subduction (downward movement along isopycnals) and convection (vertical mixing) are the two primary pathways for surface water to reach the ocean interior. The propagation of surface salinity anomalies into the ocean's interior enables water masses to be tracked, changes in freshwater content to be estimated, and potential impacts on ocean dynamics to be assessed.

The 2025 Atlantic basin-averaged salinity anomalies continued the multiyear pattern that has been evident since ~2020, with nearly the entire 0-m–1000-m layer saltier than the long-term mean, and the greatest anomalies (>0.06) observed in the upper 100 m, decreasing with depth (Fig. 3.10a). Unlike the strong (>0.02) near-surface increase in the Atlantic basin-averaged salinity from 2023 to 2024 (Reagan et al. 2025), the 2024 to 2025 changes are within ±0.01 in the upper 1000 m (Fig. 3.10b). The weak salinity changes in the Atlantic between 2024 and 2025 are reflected in the interannual change in zonally averaged salinity, where significant changes are mostly localized and shallow (Fig. 3.10c).

The basin-averaged Pacific salinity anomalies, unlike the Atlantic, have exhibited vertical decoupling over the past decade with recent near-surface salinification deepening in 2025 (Fig. 3.10d). The deepening of the near-surface salinification is more evident in the basin-averaged salinity difference between 2024 and 2025 where there is slight (~−0.008) freshening in the upper 30 m and salinification extending from ~30 m to 600 m with a peak (~0.012) at 100 m (Fig. 3.10e). The slight freshening at the surface is influenced by shallow freshening between 10°S and 20°S (Figs. 3.10e,f.), which may be due to enhanced precipitation in the SPCZ (Section 3e). The maximum salinification at 100 m is a reflection of the positive changes in both the northern and southern Pacific subduction zones (20°S–30°S and 20°N–30°N) and large changes (>0.03) near 50°N.

Similar to the Pacific, the Indian Ocean basin-averaged salinity anomalies have exhibited vertical decoupling since mid-2019 with fresh anomalies (<−0.01) in the upper 100 m and weak (≤0.01) salty anomalies in a 100-m–200-m thick layer beneath (Fig. 3.10g). From 2024 to 2025, the fresh anomalies near the surface deepened with the −0.02 contour moving from 50 m to 100 m.

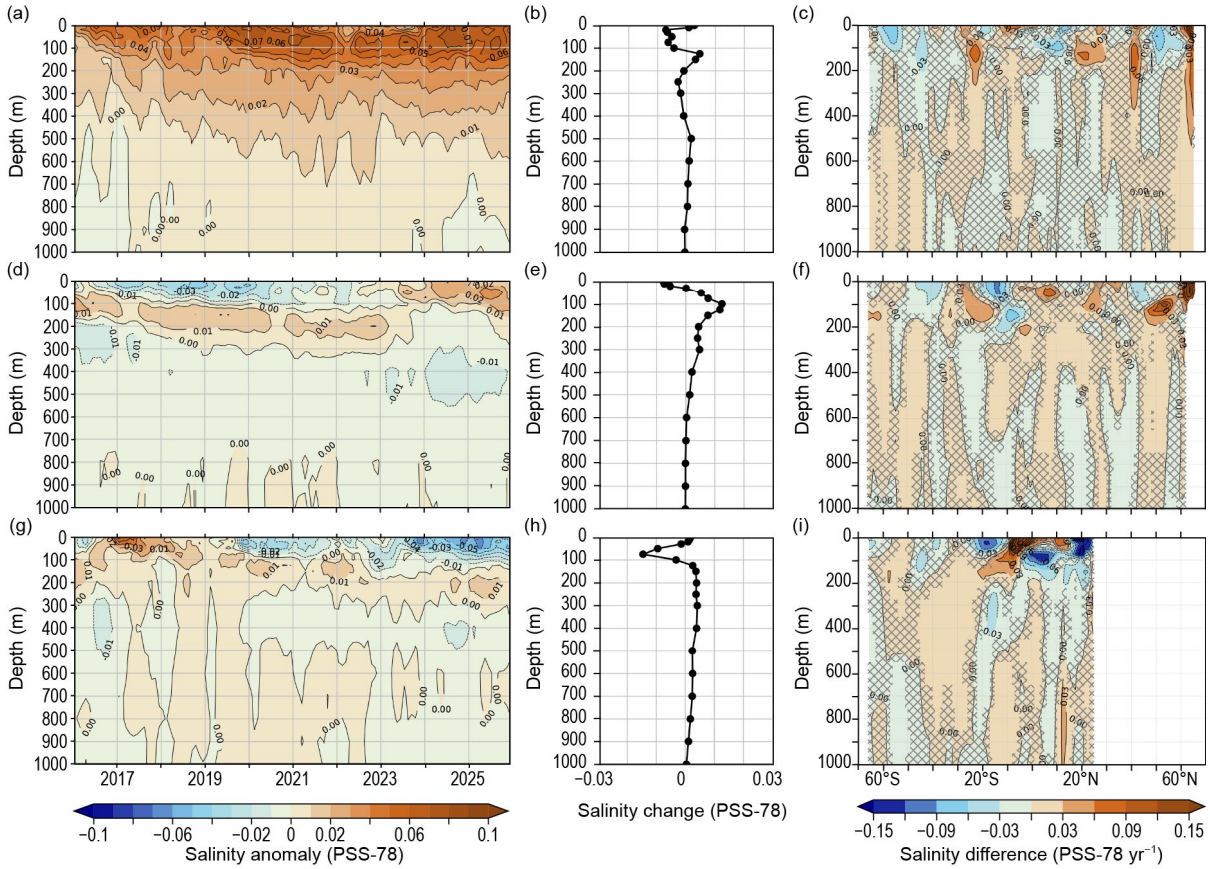

Fig. 3.10. Average monthly salinity anomalies (Practical Salinity Scale-78 [PSS-78]) vs. depth for the (a) Atlantic, (d) Pacific, and (g) Indian basins from 2016 through 2025. Change in salinity from 2024 to 2025 vs. depth for the (b) Atlantic, (e) Pacific, and (h) Indian basins. Change in the 0-m–1000-m zonal-average salinity from 2024 to 2025 vs. latitude and depth in the (c) Atlantic, (f) Pacific, and (i) Indian Ocean. Areas of statistically insignificant change, defined as <±1 std. dev. and calculated from all year-to-year changes between 2005 and 2024, are stippled in gray. Data are smoothed using a three-month running mean. Anomalies are relative to the long-term (1955–2022) World Ocean Atlas 2023 monthly salinity climatology (Reagan et al. 2024).

This freshening is even more evident in the basin-averaged change where there was peak freshening at 75 m (~−0.015), with very weak salinification below (<0.005) (Fig. 3.10h). The most significant changes between 2024 and 2025 occurred within the tropics and in the upper 200 m, which is consistent with freshwater fluxes playing a large role in this interannual change (Fig. 3.10i).

Surface salinity anomalies reflect changes in freshwater fluxes and are redistributed both horizontally and vertically through ocean circulation. The 2005–25 zonally averaged salinity trends highlight common large-scale changes, but also reveal basin-specific contrasts (Fig. 3.11). As documented in prior *State of the Climate* reports (e.g., Reagan et al. 2025), the large-scale trends, particularly near the surface (Fig. 3.8c), reflect the "wet gets wetter, dry gets drier" paradigm (Held and Soden 2006) that has been recognized in multiple studies (e.g., Durack and Wijffels 2010; Durack et al. 2012; Skliris et al. 2014).

The 2005–25 Atlantic zonally averaged salinity trends (Fig. 3.11a) remain largely unchanged from prior *State of the Climate* reports, as there were few significant changes between 2024 and 2025 (Fig. 3.10c). Unlike the Atlantic, the 2005–25 Pacific salinity trends do not exhibit coherent significant trends from the upper ocean to deeper depths outside of the 55°S–65°S salinification band that extends from the surface to >900 m (Fig. 3.11b). While there were some significant changes in the upper 200 m in the Pacific between 2024 and 2025 (Figs. 3.10e,f), these changes do not substantially alter the significant 2005–25 trends. The 2005–25 zonally averaged Indian Ocean basin trends are dominated by significant subsurface changes, with much of the surface

characterized by insignificant trends outside of freshening in the upper 50 m between the equator and 15°N. The salinification changes in 2025 (Fig. 3.10i) may have modestly strengthened the subsurface salinification region in the South Indian Ocean basin between 125 m and 550 m and 35°S–50°S (Fig. 3.11c) when compared to the 2005–24 trends (see Fig. 3.11c in Reagan et al. 2025). Overall, the 2025 basin-scale changes in subsurface salinity did not significantly impact the long-term trends.

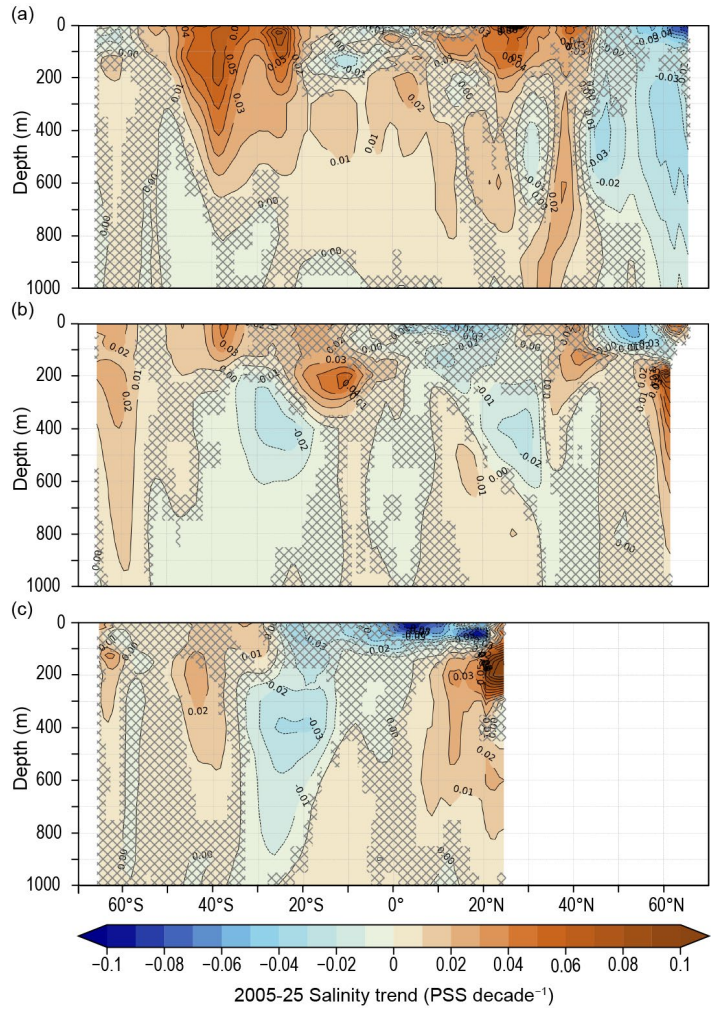

Fig. 3.11. Linear trends of zonally averaged salinity (Practical Salinity Scale-78 [PSS-78], psu decade^{-1}) for the period 2005–25 vs. latitude and depth for the (a) Atlantic, (b) Pacific, and (c) Indian Ocean computed using least squares regression. Areas stippled in gray are not significant at the 95% confidence interval.

e. Global ocean heat, freshwater, and momentum fluxes

—L. Yu, P. W. Stackhouse, and R. A. Weller

The ocean and the atmosphere interact through the exchange of heat, freshwater, and momentum across their interface. These air–sea fluxes are key to maintaining the global climate system's equilibrium in response to incoming solar radiation. The ocean absorbs the majority of shortwave radiation reaching the Earth's surface and returns energy to the atmosphere through longwave radiation, evaporation (latent heat flux), and conduction (sensible heat flux). Any remaining heat is stored in the ocean and redistributed by currents, driven largely by wind stress. Evaporation not only mediates heat but also moisture transfer, the latter of which, together with precipitation, determines the surface freshwater flux across the open ocean. Variations in these air–sea fluxes are key drivers of changes in ocean circulation, influencing the global distribution of heat and salt from the tropics to the poles.

Here, we present surface heat flux, freshwater flux, and wind stress for 2025, along with their changes relative to 2024. The net surface heat flux (Q_{net}) comprises four components: shortwave (SW), longwave (LW), latent heat (LH), and sensible heat (SH). We calculate the net surface freshwater flux into the ocean, excluding inputs from rivers and glaciers, as the difference between precipitation (P) and evaporation (E), referred to as the $P–E$ flux. Data from multiple research groups are synthesized to produce global maps of Q_{net}, $P–E$, and wind stress (Figs. 3.12–3.14) and provide a long-term view over time (Fig. 3.15). SW and LW in 2024 were sourced from the Fast Longwave And Shortwave Radiative Fluxes (FLASHFlux) version 4A product (Stackhouse et al. 2006), which have been radiometrically scaled to the SW and LW products from the Clouds and the Earth's Radiant Energy Systems (CERES) Surface Energy Balanced and Filled (EBAF) Edition 4.2 (Loeb et al. 2018; Kato et al. 2018). SW and LW in 2024 and 2025 were also sourced from the ERA5 reanalysis (Hersbach et al. 2020), which provides comparable surface radiation fields. P was derived from the Global Precipitation Climatology Project (GPCP) version 2.3 products (Adler et al. 2018). Estimates for LH, SH, E, and wind stress were produced by the second generation of the Objectively Analyzed Air–Sea Heat Fluxes (OAFlux2; Yu and Weller 2007; Yu 2019), computed from satellite retrievals and the bulk parameterization COARE version 3.6 (Fairall et al. 2003). The Q_{net} time series begins in 2001, aligning with the availability of CERES EBAF 4.2.1 products, while the $P–E$ and wind stress time series extend back 38 years, starting in 1988.

1. SURFACE HEAT FLUXES

The 2025 Q_{net} anomalies relative to 2001–15 (Fig. 3.12a) are predominantly positive, indicating enhanced ocean heat gain over much of the global ocean. The largest positive anomalies (~10 W m^{-2}–20 W m^{-2}) occur in the tropical Indian Ocean, tropical Atlantic, and across much of the tropical and subtropical Pacific. Negative anomalies, indicating enhanced ocean heat loss, are concentrated in the central North Pacific (30°N–50°N), parts of the subtropical North Atlantic, the South Indian Ocean, and portions of the Southern Ocean. The central North Pacific heat-loss feature is consistent with the Pacific Decadal Oscillation (PDO)-like pattern evident in recent years, although it is weaker than in 2024. The 2025 Q_{net} anomalies are consistent with corresponding sea surface temperature anomalies (see Fig. 3.2a).

The 2025–2024 Q_{net} differences (Fig. 3.12b) are positive across broad regions, implying greater ocean heat gain in 2025 than in 2024. The largest increases (~10 W m^{-2}–20 W m^{-2}) occur in the North Atlantic (20°N–40°N and the subpolar gyre poleward of 55°N), the midlatitude North Pacific, and the subtropical South Pacific and South Atlantic. Notably, the Kuroshio Extension region exhibits positive differences of ~10 W m^{-2}–15 W m^{-2}, reversing the pronounced negative Q_{net} anomalies (~20 W m^{-2}) observed in 2024. The North Atlantic (20°N–40°N) also shows widespread positive differences of ~15 W m^{-2}–20 W m^{-2}. In contrast, the South Indian Ocean displays a more heterogeneous pattern, with alternating bands of positive and negative Q_{net} differences.

These year-to-year Q_{net} changes are driven primarily by differences in turbulent heat fluxes (LH+SH; Fig. 3.12d), with a smaller contribution from net surface radiation (SW–LW; Fig. 3.12c). Radiative differences are generally weak over most basins, with modest positive anomalies (~5 W m^{-2}) in many midlatitude regions. The clearest radiative feature is a dipole over the far western Pacific/Maritime Continent, with negative anomalies to the west and positive anomalies to the east, consistent with a shift in convection under weak La Niña conditions.

For Fig. 3.12d, red (negative) LH+SH differences indicate reduced turbulent heat loss from the ocean (therefore greater ocean heat gain in 2025), whereas blue (positive) differences indicate enhanced turbulent heat loss. The LH+SH differences show widespread negative (red) anomalies (~10 W m^{-2}–20 W m^{-2}) over the North Atlantic (20°N–40°N and the subpolar gyre), the midlatitude North Pacific, and the subtropical South Pacific and South Atlantic, consistent with reduced turbulent cooling in 2025. Positive (blue) differences (locally ~15 W m^{-2}–25 W m^{-2}) indicate enhanced turbulent heat loss over parts of the tropical Indian Ocean (15°S–30°S), with weaker positive anomalies in portions of the subtropical North Atlantic and North Pacific (10°S–25°N).

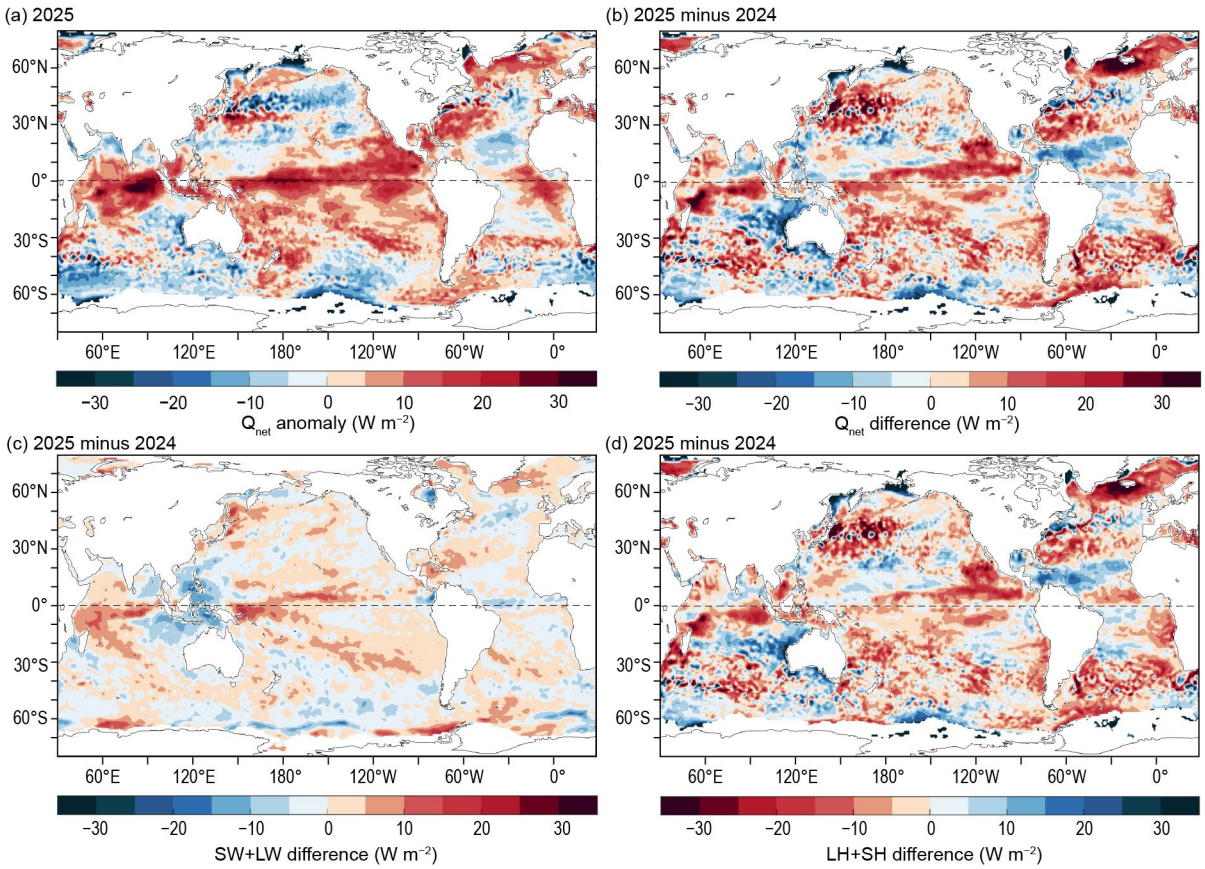

Fig. 3.12. (a) Surface heat flux (Q_{net}) anomalies (W m^{-2}) for 2025 relative to the 2001–15 climatology. Positive (negative) values denote ocean heat gain (loss). (b) 2025-minus-2024 difference for (b) Q_{net}, (c) net surface radiation (shortwave [SW] – longwave [LW]), and (d) turbulent heat fluxes (latent heat [LH] + sensible heat [SH]), respectively. Positive tendencies denote more ocean heat gain in 2025 than in 2024. LH+SH are from Woods Hole Oceanographic Institution (WHOI) OAFlux2, and SW–LW from ERA5. Net radiative fluxes defined as the difference between the incoming and outgoing radiation (positive indicates radiative flux into the ocean).

2. SURFACE FRESHWATER FLUXES

The 2025 *P–E* anomalies relative to the 2001–15 climatological mean (Fig. 3.13a) show widespread positive *P–E* (green colors), indicating anomalous net freshwater gain and a freshening tendency over much of the tropical ocean. The strongest freshening anomalies occur over the western tropical Pacific/Maritime Continent, with weaker positive anomalies (~10 cm yr^{-1}) in parts of the tropical Indian and tropical Atlantic Oceans. In contrast, negative *P–E* anomalies (brown colors) across the central equatorial Pacific indicate anomalous net freshwater loss and a salinification tendency (see Fig. 3.8a), locally exceeding ~60 cm yr^{-1}. Additional salinification anomalies appear in patches of the midlatitude North Pacific and in parts of the Southern Ocean (south of 40°S). Freshwater loss anomalies remained notable in the central North Pacific (~20 cm yr^{-1}), consistent with the continued negative PDO-like background state.

The 2025–2024 *P–E* differences (Fig. 3.13b) are dominated by tropical Pacific changes consistent with the shift from ENSO-neutral conditions in 2024 to weak La Niña in 2025. Relative to

2024, $P–E$ decreased sharply across the central/eastern equatorial Pacific, indicating enhanced freshwater loss and a stronger salinification tendency (locally >60 cm yr^{-1}), while $P–E$ increased over the far western Pacific/Maritime Continent and parts of the southwest Pacific/South Pacific Convergence Zone (SPCZ), indicating enhanced freshwater gain and a stronger freshening tendency in 2025. In contrast, the western tropical Indian Ocean and portions of the subtropical North and South Atlantic Ocean show reduced $P–E$ in 2025, implying a shift toward greater freshwater loss (salinification) relative to 2024. These year-to-year $P–E$ changes are driven primarily by precipitation (Fig. 3.13d), with rainfall decreasing over the central/eastern equatorial Pacific and increasing over the far western Pacific/Maritime Continent and parts of the SPCZ. Evaporation differences (Fig. 3.13c) are comparatively weak, including a modest decrease over the eastern equatorial Pacific cold tongue consistent with cooler SSTs during weak La Niña conditions, confirming that precipitation dominates the 2025–2024 $P–E$ changes.

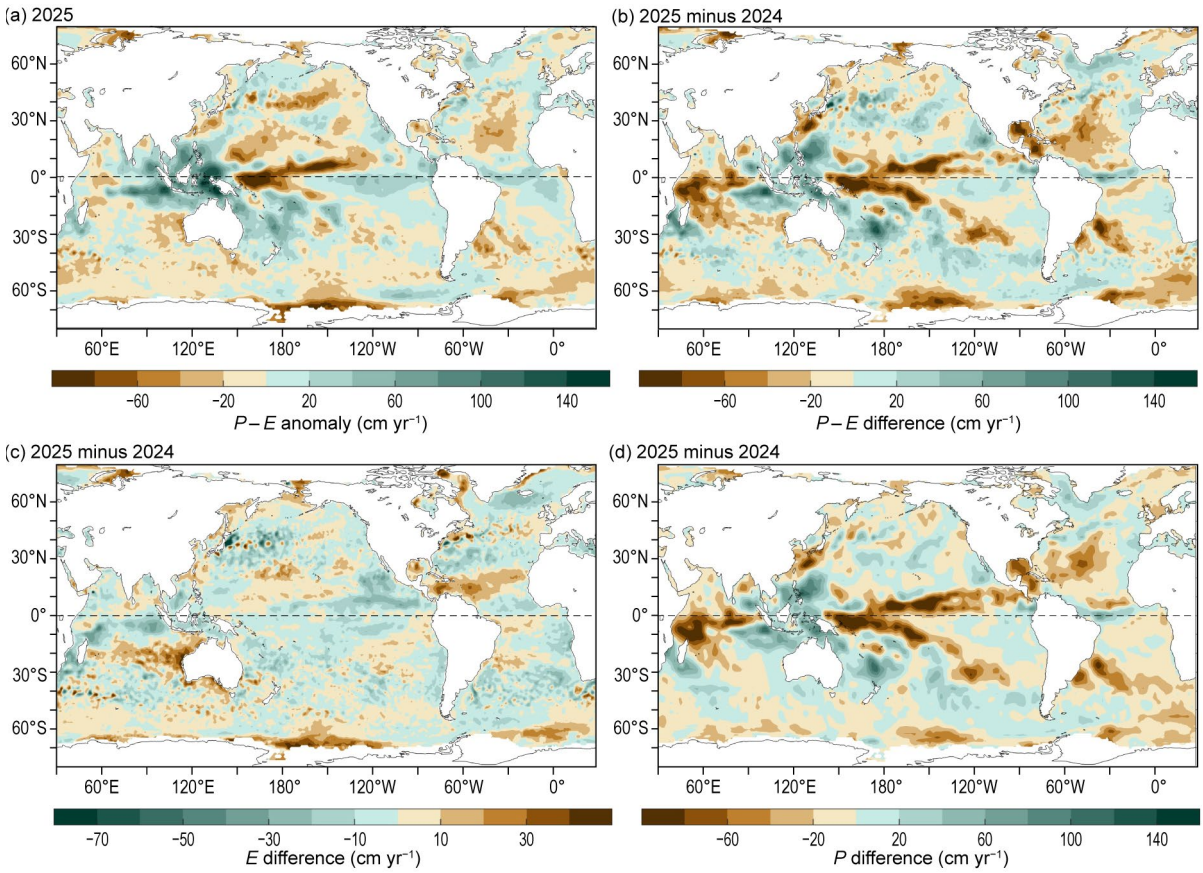

Fig. 3.13. (a) Surface freshwater precipitation (*P*)–evaporation (*E*) flux anomalies (cm yr^{-1}) for 2025 relative to the 2001–15 climatology. Positive values denote ocean freshwater gain. 2025-minus-2024 differences for (b) *P–E*, (c) evaporation (*E*), and (d) precipitation (*P*). Positive (negative) values denote ocean freshwater gain (loss). *P* is the GPCP version 2.3 product, and *E* is from Woods Hole Oceanographic Institution (WHOI) OAFlux2.

3. WIND STRESS

In 2025, wind stress magnitude anomalies were generally weak and negative across much of the tropics (Fig. 3.14a), indicating slightly weaker near-surface winds overall, with the clearest negative anomalies over the tropical Pacific and eastern tropical Indian Ocean. Vector anomalies nevertheless indicate a modest enhancement of the easterly (trade-wind) component in the western/central equatorial Pacific, consistent with weak La Niña conditions, while winds weaken in parts of the eastern tropical Indian Ocean. The tropical Atlantic exhibits a mixed pattern, with localized strengthening in the tropical North Atlantic. In the extratropics, anomalies are larger and more coherent. Over the Antarctic Circumpolar Current (ACC) belt (~40°S–60°S), wind stress exhibits mixed signs, with locally positive anomalies exceeding ~0.02 N m^{-2} (Fig. 3.14a). The North Atlantic also shows strengthened mid- to high-latitude wind stress, whereas the central North Pacific is characterized by negative anomalies (~0.02 N m^{-2}), indicating weaker westerlies there.

The 2025–2024 differences (Fig. 3.14b) underscore these changes, with marked strengthening of westerlies across the Southern Ocean and the North Atlantic, contrasted by weaker wind stress over the central North Pacific midlatitudes. The strengthening of westerlies in the North Atlantic likely contributed to the reduction of meridional overturning circulation at 41°N (see section 3h). In the tropics, the most prominent features are enhanced easterly wind anomalies in the western equatorial Pacific and the tropical North Atlantic.

Wind stress curl drives divergence/convergence of Ekman transport and the associated Ekman pumping velocity, W_{EK}, at the base of the Ekman layer. Here W_{EK} is computed as $W_{EK} = 1/\rho\nabla\times(\tau/f)$, where ρ is seawater density, τ is wind stress, and f the Coriolis parameter. The ±2° band is not calculated to avoid the Coriolis singularity (f=0). The 2025 W_{EK} anomalies (Fig. 3.14c) are predominantly negative (downwelling) over much of the tropical/subtropical ocean, with the strongest signal expressed as a narrow, intense negative band along the equatorial Pacific. Positive (upwelling) anomalies are more spatially confined, occurring in localized equatorial and coastal bands. The 2025–2024 W_{EK} differences (Fig. 3.14d) show enhanced downwelling over the equatorial Pacific and broad subtropical regions, while upwelling differences appear in patches of the Southern Ocean and the subpolar North Atlantic, consistent with the regional wind-stress changes in Fig. 3.14b.

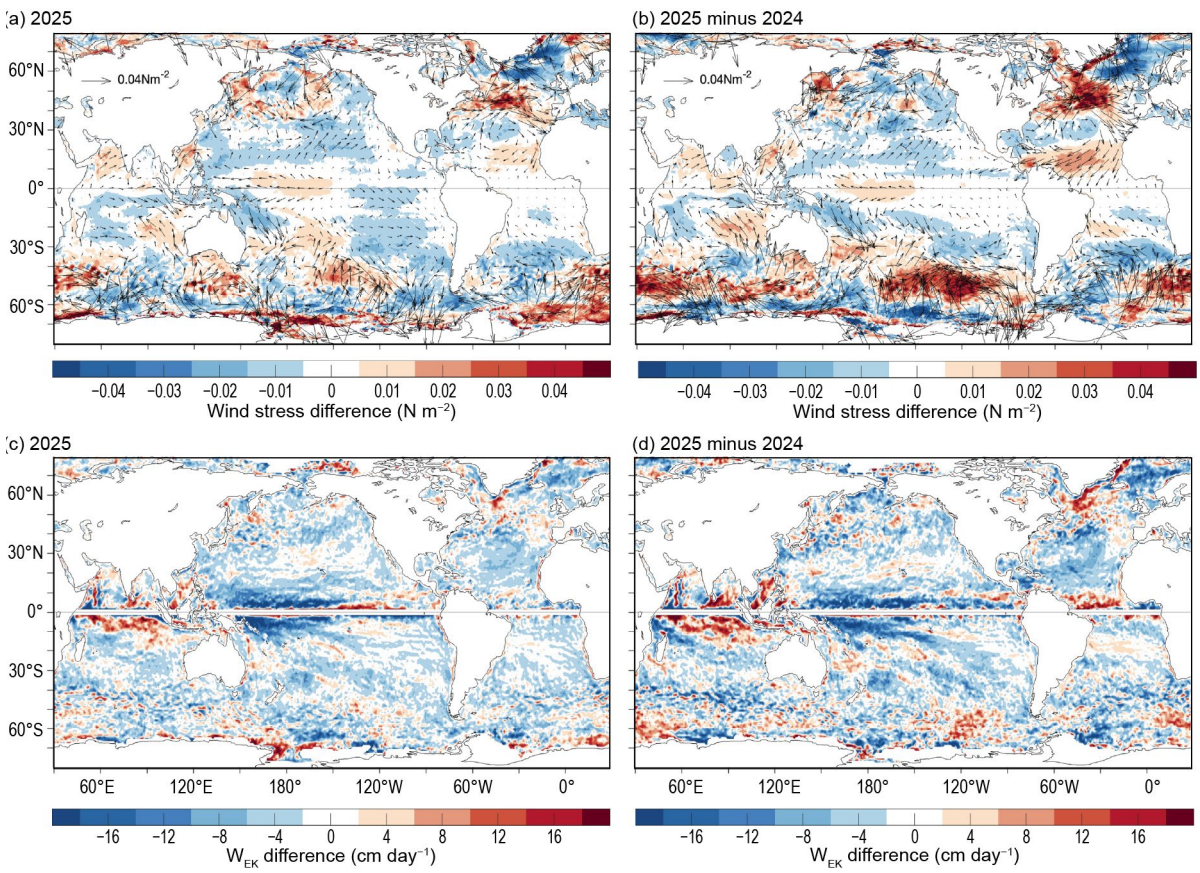

Fig. 3.14. (a) Wind stress magnitude (shaded) and vector anomalies (N m^{-2}) for 2025 relative to a 2001–15 climatology. (b) 2025-minus-2024 differences in wind stress. (c) Ekman vertical velocity (W_{EK}; cm day^{-1}) anomalies for 2025 relative to a 2001–15 climatology. Positive (negative) values denote upwelling (downwelling). (d) 2025-minus-2024 differences of W_{EK}. Wind stress and W_{EK} fields are from Woods Hole Oceanographic Institution (WHOI) OAFlux2.

4. LONG-TERM PERSPECTIVE

A long-term perspective on ocean surface forcing in 2025 is shown using annual-mean time series of Q_{net}, $P–E$, and wind stress anomalies averaged over the global ice-free ocean (Figs. 3.15a–c). All variables are referenced to the 2001–15 climatological mean. Positive (negative) Q_{net} anomalies indicate increased (reduced) net downward heat flux into the ocean, positive (negative) $P–E$ anomalies indicate increased (reduced) freshwater input, and positive (negative) wind stress anomalies indicate stronger (weaker) surface momentum forcing. Error bars denote one standard deviation of interannual variability.

Annual-mean Q_{net} was relatively stable in the early 2000s, and then rose by ~3±1 W m^{-2} from the 2011 La Niña to a peak greater than 2 W m^{-2} during the strong 2016 El Niño (Fig. 3.15a). Q_{net} declined thereafter during the 2017/18 La Niña and remained reduced through the 2020/23 triple-dip La Niña. By 2025, Q_{net} had recovered and remained slightly negative (~ −0.1 W m^{-2}) relative to the 2001–15 mean state. The *P*–*E* record exhibits pronounced decadal and interannual variability (Fig. 3.15b). After peaking in 2015/16, *P*–*E* reached a minimum around 2021 of approximately −4±2 cm yr^{-1}. In 2025, *P*–*E* remained slightly negative (≈ −1 cm yr^{-1} to −2 cm yr^{-1}), indicating a weak residual salinification tendency relative to the climatological mean. The wind stress time series shows a regime shift in the late 1990s followed by relatively stable behavior since 2000 (Fig. 3.15c). After modest strengthening around 2020/21, wind stress weakened again. In 2025, wind stress anomalies were negative, remaining below the climatological mean and consistent with relatively weak global-mean surface momentum forcing. Together, changes in Q_{net}, *P*–*E*, and wind stress represent variability in air–sea exchanges that both force the ocean and influence the atmosphere through two-way ocean–atmosphere coupling.

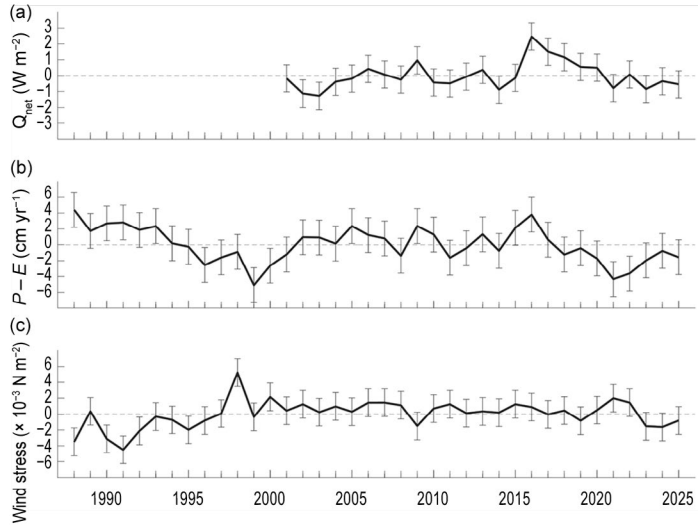

Fig. 3.15. Annual mean time series of global ocean surface (a) net surface heat flux anomalies (Q_{net}; W m^{-2}) from a combination of Clouds and the Earth's Radiant Energy System (CERES) EBAF4.2 short wave (SW) + long wave (LW) and the Woods Hole Oceanographic Institution (WHOI) OAFlux2 latent heat (LH) + sensitive heat (SH). (b) Net freshwater flux anomaly (precipitation [*P*]–evaporation [*E*] cm yr^{-1}) from a combination of GPCP *P* and OAFlux2 *E*. (c) Wind stress magnitude anomalies (N m^{-2}) from OAFlux2. Error bars denote one std. dev. of annual-mean variability.

f. Sea level variability and change

—P. R. Thompson, M. J. Widlansky, B. Beckley, B. D. Hamlington, S. Jevrejeva, F. W. Landerer, E. Leuliette, G. T. Mitchum, R. S. Nerem, J. M. Steinberg, and W. Sweet

Annual average global mean sea level (GMSL) from satellite altimetry (1993–present; Willis et al. 2025) reached a new high in 2025, rising to 111.2 mm above the 1993 mean (Fig. 3.16a). This marks the 14th consecutive year (and 30th out of the last 32) that GMSL increased relative to the previous year, reflecting the combined effects of the ongoing trend and acceleration in GMSL. The average linear trend over the entire altimetry era is 3.5±0.4 mm yr^{-1} (Fig. 3.16a) when corrected for glacial isostatic adjustment (GIA; –0.25±0.1 mm yr^{-1}; Tamisea and Mitrovica 2011; Caron and Ivins 2020), with positive local trends from altimetry over 99% of the ice-free ocean (Fig. 3.16b). However, the global mean rate has increased during this time, and acceleration in GMSL, 0.071±0.06 mm yr^{-2}, has doubled the decadal rate of GMSL rise since 1993 (Hamlington et al. 2024). A quadratic fit with corrections for the eruption of Mt. Pinatubo (Fasullo et al. 2016) yields a climate-driven linear trend of 3.1±0.4 mm yr^{-1} and an acceleration of 0.092±0.025 mm yr^{-2} (updated from Nerem et al. 2018).

The thermosteric (i.e., ocean-warming) contribution to GMSL change over ±65° latitude was 1.6±0.3 mm yr^{-1} during 2005–25 (Fig. 3.16a), which primarily reflects warming of the upper 2000 m of the ocean based on Argo observations (Roemmich and Gilson 2009). The ocean below 2000 m contributes less than 10% of the thermosteric trend based on measurements made by deep Argo floats and ship-based observations (Johnson and Purkey 2024; section 3c). Mass concentration anomalies spanning ±65° latitude from the Gravity Recovery and Climate Experiment (GRACE) and GRACE Follow-On (GRACE-FO) missions (Wiese et al. 2022) show the average mass contribution to GMSL rise during the 2005–25 period was 2.0±0.4 mm yr^{-1} when corrected for GIA (–1.0±0.3 mm yr^{-1}; Caron and Ivins 2020; Fig. 3.16a). The trend in the sum of thermosteric and mass contributions, 3.6±0.5 mm yr^{-1}, agrees within uncertainty with the GMSL trend of 3.9±0.2 mm yr^{-1} measured by altimetry since 2005 (Leuliette and Willis 2011; Chambers et al. 2017), with the thermosteric component contributing to positive

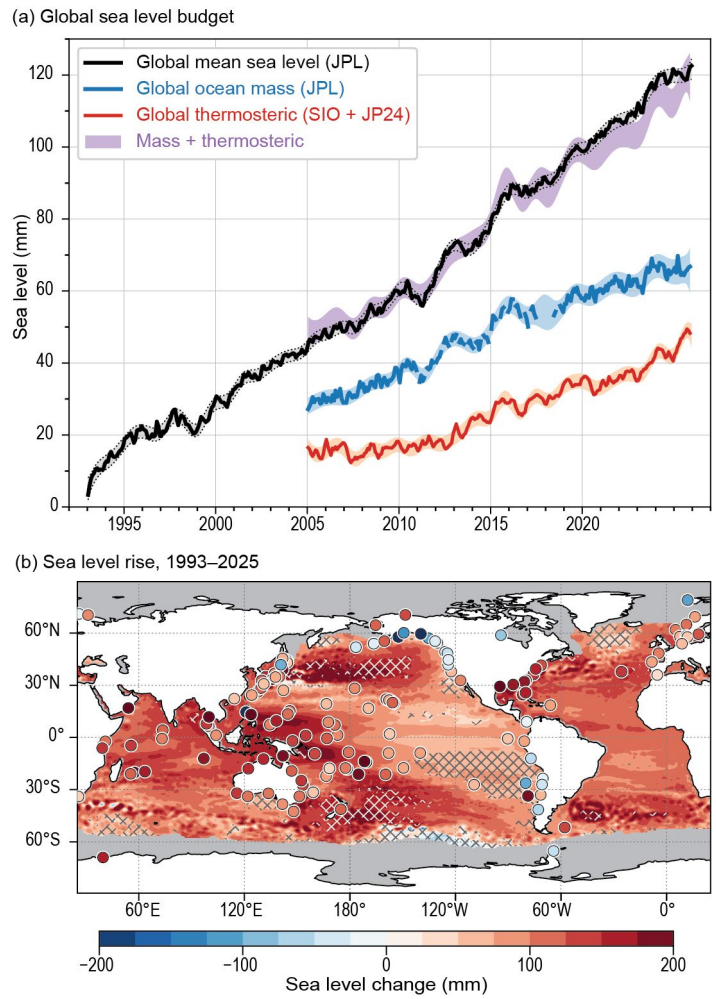

Fig. 3.16. (a) Monthly global mean sea level (GMSL) estimates from satellite altimetry (1993–2025) produced by NASA Jet Propulsion Laboratory (JPL) with support from the NASA Sea Level Change and Ocean Surface Topography Science Teams (black). Monthly global ocean mass (2005–25) from GRACE and GRACE Follow-On (GRACE-FO) calculated from mass concentrations produced by NASA JPL (blue). GRACE and GRACE-FO data within 300 km of land were excluded. Monthly global mean thermosteric sea level (2005–25) from Scripps Institute of Oceanography (SIO) for depths above 2000 m and from Johnson and Purkey (2024; JP24) for depths below 2000 m (red). Shading around the GMSL, mass, and thermosteric series represents a 95% confidence range for annual and longer variations, including glacial isostatic adjustment (GIA) uncertainty for the GMSL and mass time series. The confidence ranges for mass and thermosteric are used to produce a 95% confidence range for the sum of the contributions to GMSL (purple). (b) Total local sea level change during 1993–2025 as measured by satellite altimetry (contours) and tide gauges (circles). Hatching indicates local changes that differ from the change in GMSL by more than one standard deviation. The sea level change map was generated using gridded delayed-mode and near-real-time altimetry data produced by the Copernicus Climate Change Service and obtained from the Copernicus Marine Service. Tide-gauge observations were obtained from the University of Hawaii Sea Level Center Fast Delivery database.

acceleration during this time. Halosteric (salinity-related) contributions are small and typically excluded (Roemmich et al. 2019).

Annually averaged GMSL from altimetry, adjusted for GIA, rose just 1.0±0.5 mm from 2024 to 2025, which is well below the long-term rate of sea level rise (Figs. 3.17a,b). La Niña conditions during early 2025 likely suppressed global sea levels by redistributing fresh water from ocean to land (Figs. 3.13a,b; see Fig. 2.43; e.g., Fasullo et al. 2013), consistent with the modest 0.1±0.6 mm annual increase in global ocean mass from GRACE-FO, which also fell short of the long-term trend. By contrast, global mean thermosteric sea level from Argo rose 3.9±0.8 mm, well above the long-term trend and consistent with the unprecedented increase in ocean temperatures observed during 2025 (Pan et al. 2026).

Reconciling these annual increases in the context of the global sea level budget proves difficult, as the thermosteric increase, third largest in the Argo record, far outpaces the lower-than-expected increases in ocean mass and GMSL. One factor that may reduce the discrepancy is the halosteric contribution, as mentioned earlier. Nevertheless, Argo salinity data show a 1 mm–2 mm decrease in global mean halosteric sea level from 2024 to 2025, which would substantially narrow the gap. The decrease in halosteric sea level aligns with the salinification of the Pacific from 2024 to 2025 (see Fig. 3.10e), assuming it dominates the global average. Differences in spatial sampling may also contribute. For example, Argo undersamples continental shelves and shallow seas, including the southeast Asian seas around the Maritime Continent.

Local sea level anomalies averaged during 2025 were positive over most of the global ocean relative to the 1993–2022 baseline (Fig. 3.17a), consistent with the continuing rise in mean sea level onto which regional variability is superimposed. The anomaly pattern in altimetry observations exhibits pronounced spatial structure across the tropics and midlatitudes, with broad areas of above-normal sea level spanning much of the Indo-western Pacific and additional positive anomalies in almost all parts of the North Pacific and North Atlantic midlatitudes (Fig. 3.17a). In contrast, slightly below-normal sea level is evident across portions of the southern Indian Ocean and equatorial central-to-eastern Pacific, yielding a strong zonal contrast across the tropical Pacific that is more apparent in the seasonal averages when the long-term trend is removed (Figs. 3.17c,d). Tide gauges provide coastal examples of the elevated background sea levels relative to 1993–2022, while generally agreeing with the regional patterns evident in

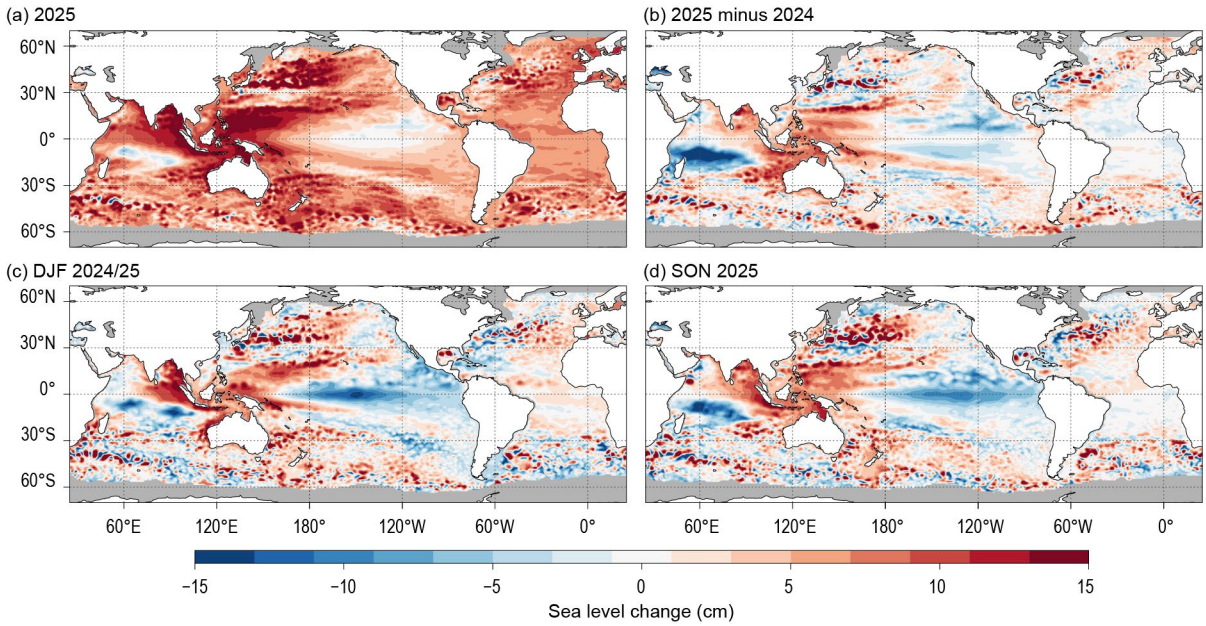

Fig. 3.17. (a) Annual average sea level anomaly during 2025 relative to average sea level at each location during 1993–2022. (b) Average 2025-minus-2024 sea level anomaly. (c) Average sea level anomaly during Dec–Feb (DJF) 2024/25 relative to the 1993–2022 DJF average. (d) Same as (c), but for Sep–Nov (SON). Units are given in cm. Global mean sea level was subtracted from panels (c),(d) to emphasize regional, non-secular change. These maps were generated using gridded delayed-mode and near-real-time altimetry data produced by the Copernicus Climate Change Service and obtained from the Copernicus Marine Service.

the altimetry data (e.g., Woodworth et al. 2019). Tide gauge data (Caldwell et al. 2015) confirm elevated sea levels globally, with especially large positive anomalies in parts of the western Pacific (Fig. 3.17a).

Year-over-year differences (2025 minus 2024) indicate that 2025 featured a substantial reorganization of sea level across the tropical Pacific, with lower sea level in 2025 in much of the tropical central/eastern Pacific and compensating increases elsewhere in the Indo–western Pacific (Fig. 3.17b). The December–February (DJF) and September–November (SON) seasonal maps emphasize a coherent band of negative sea level anomalies along the equator in the central-to-eastern Pacific, together with relatively higher sea level in the off-equatorial western tropical Pacific (Figs. 3.17c,d), consistent with wind-driven changes (Fig. 3.14) that redistribute upper-ocean heat and mass, deepen the thermocline, and alter the zonal sea level slope across the basin (e.g., Widlansky et al. 2014). The El Niño–Southern Oscillation (ENSO) conditions during 2025, as characterized by NOAA's Climate Prediction Center Relative Oceanic Niño Index (RONI), were consistent with two short-lived periods of La Niña conditions (e.g., DJF values near –1.1°C, near-neutral May–July means, and SON values near –0.9°C), supporting the observed tropical Pacific sea level zonal seesaw pattern (Fig. 3.17; Widlansky et al. 2015). Consistent with these basin-scale changes, tide gauges show regionally differing interannual tendencies: 2025 mean sea level (updated through November at the time of writing) increased since 2024 by about 6 cm and 10 cm at Guam and Yap, respectively, while Honolulu and neighboring stations in Hawaii decreased by about –2 cm over the same period. These changes illustrate how ENSO-related dynamic adjustment can produce opposing changes across the basin depending on location and time (e.g., Long et al. 2020).

Outside the Pacific, the 2025 sea level variability also reflects the influence of other climate modes and regional wind stress forcing, particularly in the Indian Ocean and the extratropical basins. The annual anomaly field shows above-normal sea levels in the northern and eastern Indian Ocean, whereas most of the southern Indian Ocean was well below normal (Figs. 3.17a,b). Consistent with this, the Indian Ocean dipole (IOD) index was negative on average in 2025 (see section 4f), a state often associated with wind and thermocline adjustments that can favor relatively higher sea level in the eastern Indian Ocean/Maritime Continent region relative to the western basin. More locally, interannual variability in the tropical Indian Ocean sea level includes contributions from wind forcing (e.g., Ekman suction in the southwestern tropics associated with wind stress curl that shoals the thermocline and reduces sea levels; Fig. 3.14) and covarying climate modes (e.g., IOD and ENSO interactions; Kumar et al. 2020). Along the U.S. West and East Coasts, tide gauges illustrate regionally differing year-over-year changes superimposed on a positive background relative to 1993–2022: year-to-date 2025 mean sea level at San Diego (West Coast) was approximately unchanged relative to 2024 (0 cm) while Charleston (East Coast) was lower by about 5 cm, even though both sites were elevated by about +3 cm to +6 cm relative to the 1993–2022 climatology (through 30 November 2025; Caldwell et al. 2015).

Ongoing trends, interannual variability, and seasonal changes in sea level increase the magnitude and frequency of extreme sea level events, contributing to coastal flooding and erosion (e.g., Wahl et al. 2014; Kendon et al. 2024; Li et al. 2022). Minor impacts occur when water levels exceed the 99th percentile of daily maxima (Sweet et al. 2014). Using 1993–2022 as the baseline, such extreme events have become more frequent in recent years (Sweet et al. 2024). Tide-gauge records with at least 80% completeness during 1993–2025 and in both 2024 and 2025 show that the median number of extreme events per year increased from one during 1993–97 to five during 2021–25, while the 90th percentile rose from six to 18 events per year.

Thirty-six of the 116 locations experienced more than 10 extreme sea level events during 2025 (Fig. 3.18a). These locations were distributed around the global ocean and were concentrated in areas where sea level trends and/or annual sea level anomalies were largest (Figs. 3.16a, 3.17b). The greatest number of extreme events occurred in the western Pacific, especially Guam and Yap, where annual 2025 sea level anomalies were especially high due to La Niña conditions. Relative to 2024, more locations experienced large decreases in the number of extremes during 2025 compared to large increases (Figs. 3.16b, 3.17d). The lone exception was the western Pacific, where the large number of extremes during 2025 in Guam and Yap represented substantial increases over the previous year (Fig. 3.18c).

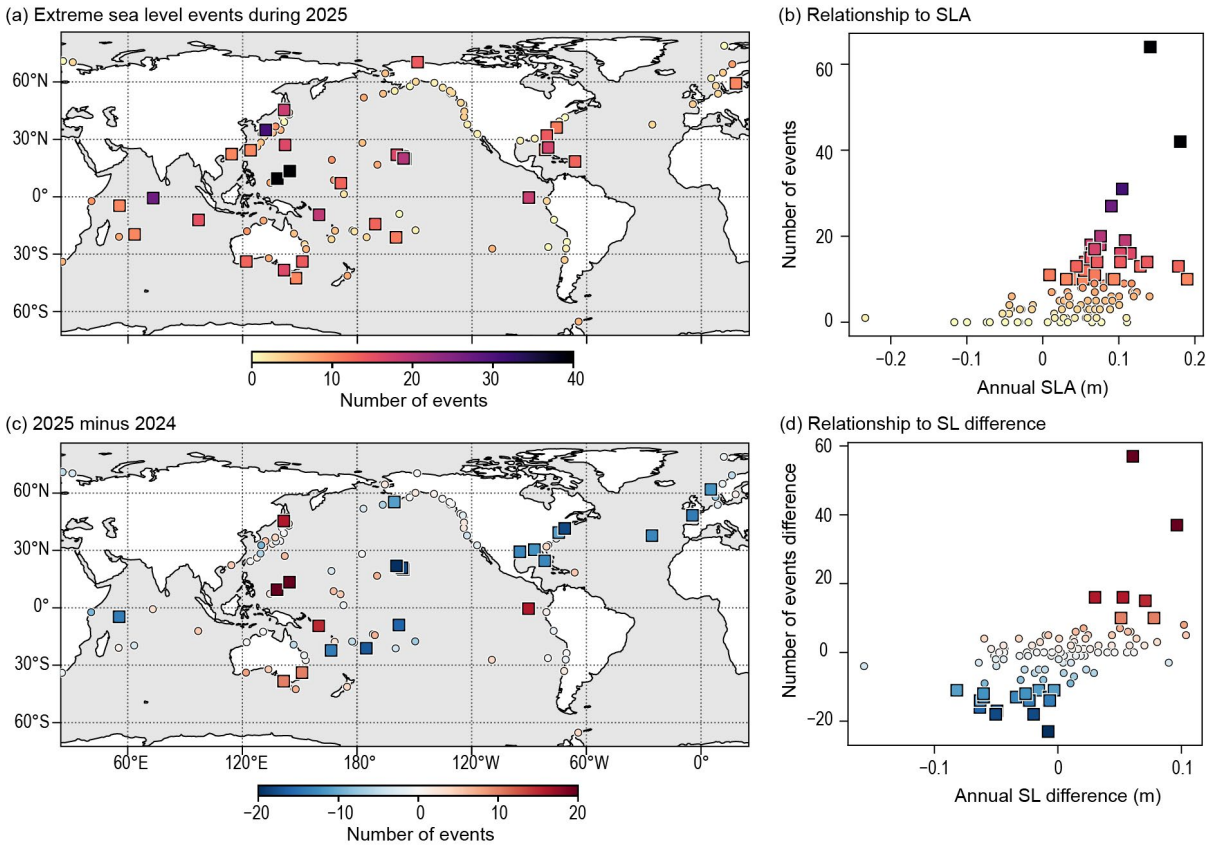

Fig. 3.18. (a) Number of extreme sea level (SL) events from tide gauges during 2025. (b) Counts in (a) as a function of annual sea level anomaly (SLA) during 2025. Square markers in (a) and (b) highlight locations with more than 10 extreme events. (c) Change in number of extreme sea level events from 2024 to 2025. (d) Counts in (c) as a function of the change in annual sea level from 2024 to 2025. Square markers in (c) and (d) highlight locations where the magnitudes of changes in counts of extreme events were greater than 10. Counts of extreme sea level events were calculated from hourly tide gauge observations obtained from the University of Hawai'i Sea Level Center Fast Delivery database.

g. Surface currents

—M. Le Hénaff, R. C. Perez, and F. P. Tuchen

This section describes variations of ocean surface currents, transports, and associated features, such as rings. Here, geostrophic surface current estimates are obtained from in situ and satellite observations. See Lumpkin et al. (2012) for details of these calculations. Zonal geostrophic current anomalies are calculated with respect to a 1993–2020 climatology and are discussed below for individual ocean basins.

Near-surface in situ measurements (12-m depth or shallower) are available from seven mooring sites in the tropical Atlantic, three sites along the equator in the tropical Pacific, and six sites along 65°E Indian Ocean, as part of the Global Tropical Moored Buoy Array (GTMBA; e.g., McPhaden et al. 2023). In August–September 2025, as part of the National Data Buoy Center (NBDC) recapitalization of the Tropical Atmosphere Ocean (TAO) array and a NBDC, Pacific Marine Environmental Laboratory (PMEL), and Atlantic Oceanographic and Meteorological Laboratory (AOML) collaboration, 17 acoustic current meters and six acoustic doppler current profilers (ADCPs) were deployed at TAO mooring locations between 165°E and 155°W and 2°S to 2°N as part of a Tropical Pacific Observing System (TPOS) field experiment to resolve the upper ocean jets in the western equatorial Pacific.

1. PACIFIC OCEAN

In 2025, zonal geostrophic currents in the equatorial Pacific (Fig. 3.19a) exhibited annual mean westward (negative) current anomalies exceeding –10 cm s^{-1} in the western portion of the equatorial band, between 2°S and 2°N and between 155°E and 170°E, with the strongest anomalies of –20 cm s^{-1} at 158°E and 0.5°S. The rest of the equatorial band in the Pacific does not show marked anomalies. Since 2024 presented intense negative anomalies across the whole basin (Lumpkin et al. 2025), the 2025-minus-2024 difference map (Fig. 3.19b) shows a weakening relative to the previous year with eastward anomalies of 10 cm s^{-1} covering most of the equatorial waveguide in the Pacific basin.

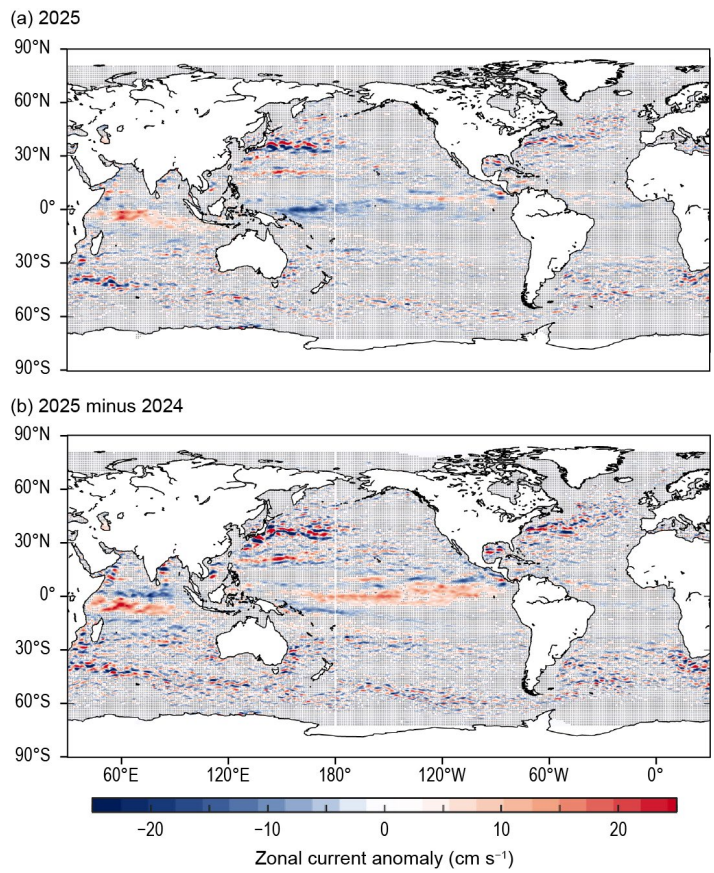

Fig. 3.19. Annually averaged geostrophic zonal current anomalies (cm s^{-1}) with respect to the 1993–2020 climatology for (a) 2025 and (b) 2025 minus 2024. Values are only shown where they are significantly different from zero.

Westward anomalies exceeding –20 cm s^{-1} were present in the western equatorial Pacific in December 2024–February 2025 (Fig. 3.20a) between 2°S and 1°N, and between 150°E and 160°W. Significant westward anomalies extended to 6°S between 160°E and 160°W, and to 6°N between 160°W and 140°W. These anomalies are consistent with the weak La Niña conditions observed at the end of 2024 (see section 4b). In March–May, eastward anomalies of 10 cm s^{-1}–20 cm s^{-1} developed in the central and eastern parts of the basin, between 160°W and 90°W, and between 1°S and 3°N, associated with more neutral ENSO conditions. The equatorial anomalies reversed again to westward anomalies in June–August in the central to eastern part of the basin, between 150°W and 105°W, and between the equator and 3°N, exceeding –10 cm s^{-1}, as weak La Niña conditions began to develop again. North of this pattern, eastward anomalies exceeding 20 cm s^{-1} between 140°W and 120°W were associated with an accelerated North Equatorial Countercurrent. The westward anomalies intensified in September–November, covering most of the equatorial band between 2°S and 4°N and exceeding –20 cm s^{-1} between 160°E and 180°E near the equator, and are associated with the development of more marked La Niña conditions.

In 2020–25, the annual-average latitude of the Kuroshio Extension in the region 141°E–153°E, 32°N–38°N was shifted north of its long-term (1993–2025) location of 35.5°N, to a maximum of 36.8°N in 2021 and to 36.5°N in 2025 (Fig. 3.21c). This can be seen as alternating eastward/westward current anomalies in Fig. 3.19a that persisted through the year (Fig. 3.20). This 2020–25 northward shift of the Kuroshio Extension corresponded with a multiyear increase in averaged eddy kinetic energy (EKE; Fig. 3.21d), associated with a large meander of the Kuroshio Current off the southern coast of Japan (Qiu et al. 2020). Initiated since 2017 (Qiu and Chen 2021), this large meander ended in 2025, as seen in the altimetry data (Fig. 3.21b).

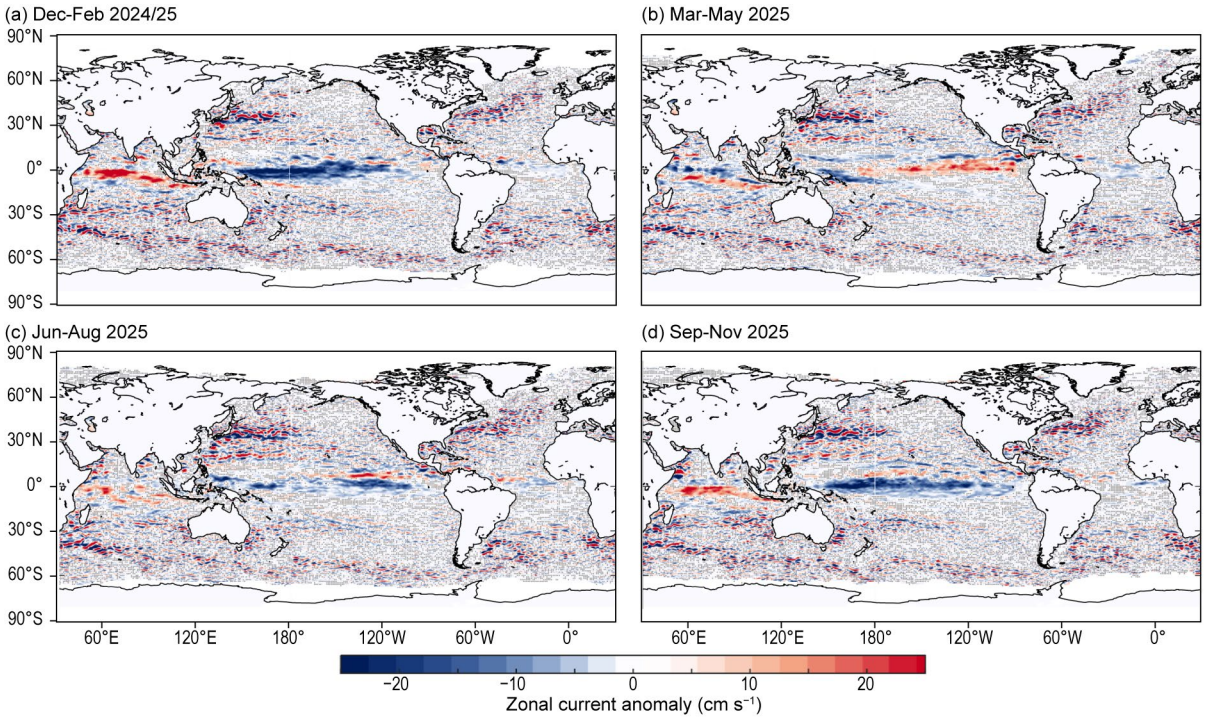

Fig. 3.20. Seasonally-averaged zonal geostrophic anomalies (cm s^{-1}) with respect to 1993–2020 seasonal climatology for (a) Dec–Feb 2024/25, (b) Mar–May 2025, (c) Jun–Aug 2025, and (d) Sep–Nov 2025. Values are only shown where they are significantly different from zero.

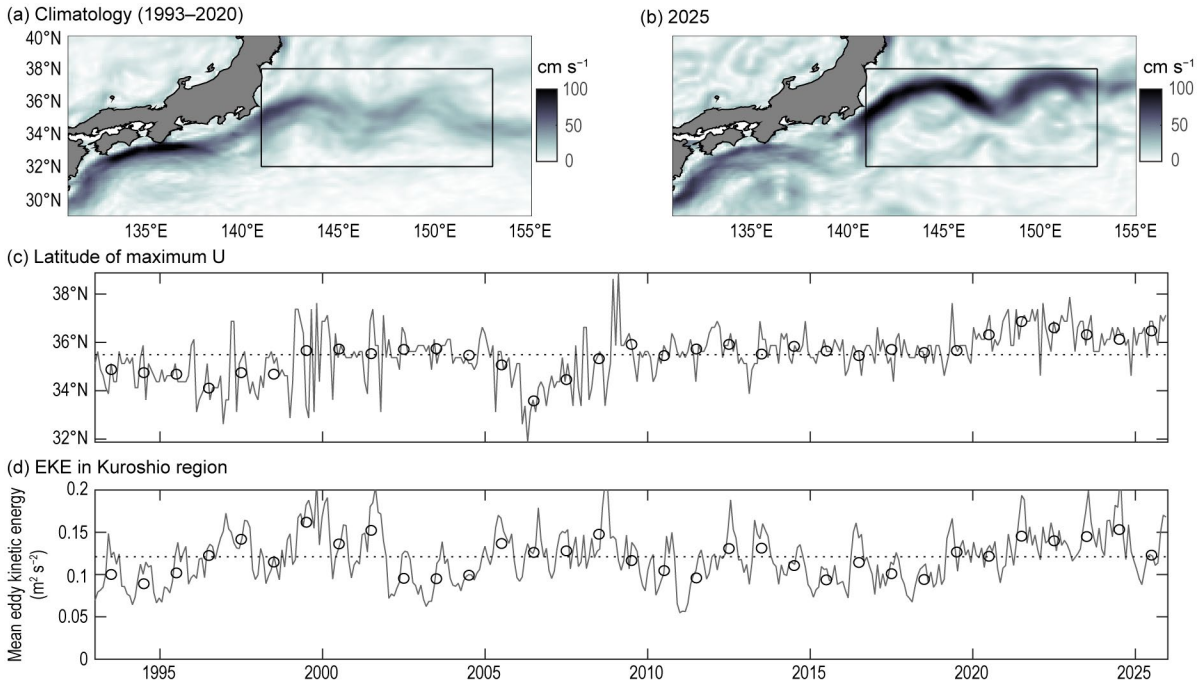

Fig. 3.21. (a) Climatological geostrophic surface current speed (cm s^{-1}) from Mulet et al. (2021) and (b) 2025 mean geostrophic currents from MDT13 Mean Dynamic Topography (Rio et al. 2014) and Copernicus near-real-time altimetry in the Kuroshio Current region (box) and surrounding regions. (c) Latitude of maximum zonal currents averaged in the Kuroshio Current region. (d) Mean eddy kinetic energy (EKE; m^2 s^{-2}) in the Kuroshio region.

2. INDIAN OCEAN

Annually averaged geostrophic zonal current anomalies in the Indian Ocean (Fig. 3.19a) exhibited eastward anomalies exceeding 10 cm s^{-1} between 6°S and the equator and between 55°E and 75°E, reaching 20 cm s^{-1}–25 cm s^{-1} locally. Because the equatorial currents presented eastward anomalies centered on the equator with westward anomalies south of that pattern, the 2025-minus-2024 difference map (Fig. 3.19b) shows a dipole pattern of negative anomalies between 1°S and 2°N, and positive anomalies south of it. During December 2024–February 2025 (Fig. 3.20a), eastward anomalies exceeding 25 cm s^{-1}–30 cm s^{-1} were present across the equatorial band. These were replaced by westward anomalies of up to 25 cm s^{-1} in March–May 2025 (Fig. 3.20b) near the equator, which disappeared in June–August (Fig. 3.20c). Eastward anomalies of 20 cm s^{-1}–30 cm s^{-1} developed in the central basin at 55°E–85°E, 3.5°S–0.5°N in September–November (Fig. 3.20d), with peak values of 35 cm s^{-1} at 80°E, 1°S reflecting an acceleration of the seasonal Southwest Monsoon Current.

3. ATLANTIC OCEAN

Annual mean geostrophic zonal current anomalies in the tropical Atlantic Ocean in 2025 did not exceed ±5 cm s^{-1} (Fig. 3.19a). Because a similar situation was observed in 2024, the 2025-minus-2024 difference map (Fig. 3.19b) is not remarkable. Westward –(5–10) cm s^{-1} anomalies were present between 1°S and 3°N in the central part of the basin in December 2024–February 2025 (Fig. 3.20a) and in March–May 2025 (Fig. 3.20b), before disappearing in June–November (Figs. 3.20c,d). During June–August 2025, the tropical Atlantic (20°W–0°, 3°S–3°N) exhibited an Atlantic Niña event with sea surface temperature anomalies below –0.5°C persisting for three consecutive months (Tuchen 2025). Such cold events are commonly associated with a seasonal intensification of easterly trade winds and westward surface currents. Accordingly, anomalous westward surface currents emerged during the onset phase of the cold sea surface temperature anomalies, resembling the evolution of the weaker but more rapidly developing cold event observed in 2024 (Tuchen et al. 2025).

In the subtropical North Atlantic, comparable to 2024, a band of strong positive and negative anomalies of magnitude 15 cm s^{-1}–20 cm s^{-1} east of Cape Hatteras (Fig. 3.19a) indicated that the Gulf Stream extension east of Cape Hatteras was shifted anomalously northward in 2025 compared to the long-term mean. This anomalous banding persisted throughout the year (Fig. 3.20b).

4. METHODOLOGICAL ADVANCES

In terms of ocean surface current retrieval methodologies, several approaches, all based on machine learning (ML), were developed in 2025. Sun et al. (2025), Shao et al. (2025), and Bai et al. (2025) applied various ML techniques to retrieve ocean current information from Sentinel-1 synthetic aperture radar (SAR) data, which has been a significant challenge since the inception of SAR imagery. Blending standard satellite altimetry, satellite wind estimates, and surface drifter data, Ge et al. (2025) implemented a deep learning approach to reconstruct near-surface currents. Also using deep learning, Garcia et al. (2025) used standard and Surface Water and Ocean Topography (SWOT) altimetry, together with surface drifters, to estimate geostrophic surface currents and forecast them over seven days. Finally, Ciani et al. (2025) developed a deep learning method to estimate surface currents from standard altimetry and high-resolution sea surface temperature images. These efforts illustrate how machine learning allows the retrieval of surface currents estimates from a wide range of platforms.

h. Atlantic meridional overturning circulation and heat transport

—D. L. Volkov, S. Dong, T. Petit, J. K. Willis, W. Hobbs, Y. Fu, R. C. Perez, B. Moat, D. Smeed, S. Elipot, and M. S. Lozier.

The upper limb of the meridional overturning circulation (MOC) transports large quantities of heat and seawater properties across the South and North Atlantic toward the North Pole and plays a key role in shaping regional and global climate, weather, and ocean variability patterns. The MOC volume transport and associated meridional heat transport (MHT) have been observed using moored arrays and synthetic estimates combining satellite altimetry and in situ data at selected latitudes (Fig. 3.22). Here, we present, from north to south, updated time series of the MOC and MHT from the Overturning in the Subpolar North Atlantic Program (OSNAP), RAPID-Meridional Overturning Circulation and Heat-flux Array-Western Boundary Time Series (RAPID-MOCHA-WBTS; hereafter, RAPID), and synthetic estimates at 41°N, 20°S, 25°S, 30°S, and 34.5°S. Updates from the Meridional Overturning Variability Experiment (MOVE), Tropical Atlantic Circulation and Overturning at 11°S (TRACOS), and South Atlantic Meridional overturning Basin-wide Array (SAMBA) moored arrays (black lines in Fig. 3.22) are pending. Due to logistical constraints, only the synthetic MOC and MHT estimates extend through 2025.

The recently extended OSNAP MOC and MHT time series spans August 2014 to July 2022 (Fig. 3.23a). Over this period, the time–mean MOC across the full OSNAP array, comprising OSNAP West between Labrador and West Greenland and OSNAP East between East Greenland and Scotland (Lozier et al. 2017), is 16.5±3.3 Sverdrup (Sv; mean±standard deviation). Mean overturning is 16.4±2.9 across OSNAP East and 2.7±1.3 Sv across OSNAP West, with OSNAP East dominating both the mean and variability, consistent with previous studies (e.g., Lozier et al. 2019). The full-array OSNAP MOC is defined as the maximum of the combined streamfunction, so it does not equal the sum of the individual East and West maxima, which occur at different density levels. The annual mean MOC in 2021 was near the record mean, while the January–July 2022 average was ~1 Sv lower but remained within uncertainty bounds. Using the extended record, Fu et al. (2025) showed that surface buoyancy-driven water-mass transformation explains up to 30% of interannual MOC variability in both subpolar basins. No statistically significant MOC and MHT trends are evident over the eight-year period.

Overturning at OSNAP East and OSNAP West is anti-correlated on interannual timescales, with a maximum correlation of −0.64 when OSNAP East leads by a few months (Fu et al. 2025), indicating partial compensation between the eastern and western segments. The time–mean MHT across the full OSNAP array is 0.51±0.06 PW, dominated by OSNAP East (0.42±0.06 PW) with a smaller fraction from OSNAP West (0.08±0.02 PW). The MOC–MHT correlation is 0.7, indicating that overturning variability largely controls heat transport, with important contributions from gyre circulation and temperature structure. Petit et al. (2025a) showed that variability in MOC strength measured at OSNAP does not directly reflect changes at midlatitudes; instead, the density at which maximum overturning occurs in the subpolar North Atlantic acts as a key precursor to midlatitude MOC variability. This underscores that OSNAP and

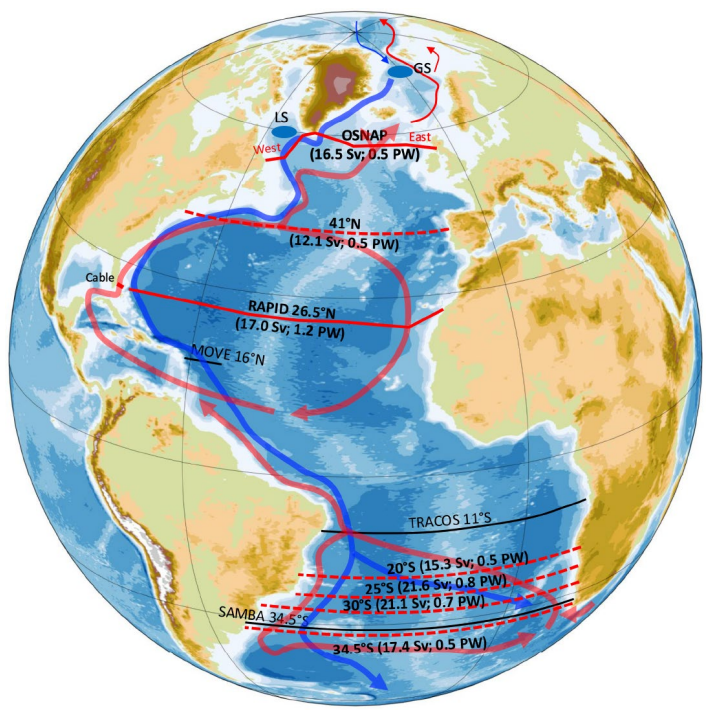

Fig. 3.22. The Atlantic meridional overturning circulation (MOC)/meridional heat transport (MHT) observing network: moored arrays (solid red and black lines) and sections across which the MOC/MHT is estimated by synthesizing in situ measurements (Argo, eXpendable BathyThermograph [XBT]) with satellite altimetry data (dashed red lines). The red lines show the sections that have updates covered in this report, while the black lines show the sections for which updates are pending. The updated record mean MOC/MHT values are shown in parentheses. Red arrows show flows associated with the upper limb of the MOC and blue arrows show deeper limb of the MOC.

subtropical and tropical observing systems farther south capture different aspects of MOC variability, and that OSNAP density structure may help interpret meridional MOC coherence in the North Atlantic.

The MOC estimates at 41°N (Fig. 3.23b), derived from satellite altimetry sea surface height (SSH) and Argo observations, are reproduced from Willis (2010) and Hobbs and Willis (2012) and extended from January 2002 through December 2025 (Willis and Hobbs 2026). Each estimate represents a three-month moving average, with uncertainties of 2.3 Sv for the MOC and 0.23 PW for the MHT. The time–mean MOC and MHT are 12.1 Sv and 0.47 PW, respectively. The smaller MOC at 41°N compared to OSNAP can reflect both methodological differences and a real northward increase in overturning due to subpolar water-mass transformation. The annual-mean MOC was 14.7 Sv in 2023, increased to 16.0 Sv in 2024, and declined to 13.0 Sv in 2025. Both MOC and MHT weakened in 2025, returning within the uncertainty range of the long-term mean; only the 2023 and 2024 values remain statistically distinct. The 2025 weakening was likely contributed to by the observed strengthening of the anticyclonic wind circulation in the subtropical North Atlantic (see Figs. 3.14a,b) through enhanced southward Ekman transport at 41°N and the corresponding geostrophic adjustment. A strong MOC-MHT correlation (0.9) indicates that large-scale overturning variability is the primary driver of meridional heat transport at this latitude. On interannual to decadal time scales, the 24-year record shows extended periods of positive (2004–08 and 2022–25) and negative (2009–21) anomalies. As quality control of Argo and altimeter data is continuously updated, refinements to the estimates are expected. Updates since the *State of the Climate* report in 2024 (Volkov et al. 2025a), including improved Argo quality control and higher-resolution altimetry grids, reduced the 2023 and 2024 annual-mean MOC estimates by 0.4 Sv and 0.2 Sv, respectively. These adjustments are smaller than the year-to-year uncertainty, and the elevated MOC values in 2023/24 remain unusually high relative to the previous two decades.

The RAPID array at 26.5°N has provided continuous, basin-wide observations of the Atlantic MOC since 2004, forming the longest observational record of the MOC, now extended through March 2024 (Fig. 3.23c; Moat et al. 2026). Florida Current transport—the primary contributor to northward flow in the upper limb of the MOC at this latitude—has historically been estimated from submarine cable measurements. Following a cable failure in November 2023, transport is now derived from cross-stream pressure gauges and altimetry (Volkov et al. 2025b). While the impact of this change on the MOC estimates is still under investigation, preliminary assessments indicate that low-frequency variability and trends remain unchanged. Petit et al. (2025b) evaluated the sensitivity of RAPID MOC estimates to the array design and showed that while moorings in the upper 3000 m and at the western boundary are essential, deep eastern boundary and Mid-Atlantic Ridge moorings can be replaced by repeat hydrographic sections with only a small additional error (~0.3 Sv).

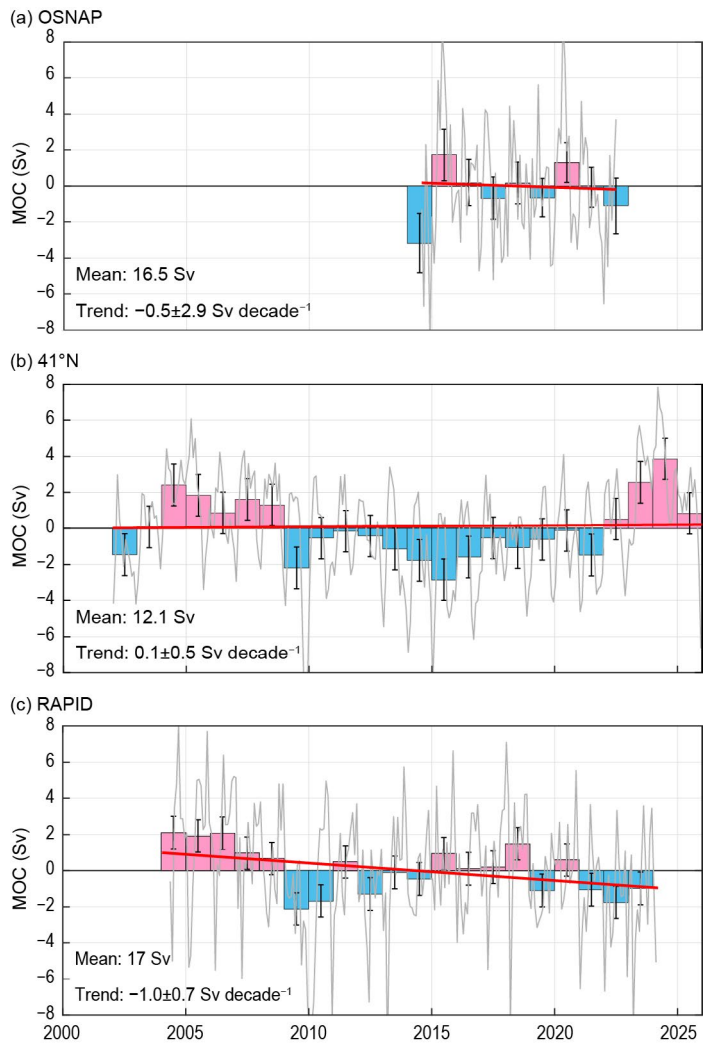

Fig. 3.23. Monthly (gray lines) and annual (bars) estimates of meridional overturning circulation (MOC) anomalies (Sverdrup [Sv]) in the North Atlantic: (a) Overturning in the Subpolar North Atlantic Program (OSNAP) array, (b) 41°N section, and (c) RAPID array. Error bars indicate uncertainties of annual mean values. Trends are shown by red lines.

The mean MOC at the RAPID array in 2023—the most recent full year in the currently available record—was ~1 Sv below the long-term mean of 16.9 Sv, but remained within uncertainty bounds (Fig. 3.23c), following statistically significant reductions in 2021 and 2022. In contrast to the positive anomalies observed at 41°N during 2022/23, this pattern indicates divergence within the subtropical gyre. Following a reassessment of Florida Current transport that reduced the previously inferred long-term MOC decline by ~40% (Volkov et al. 2024), a modest weakening trend of –1.0±0.7 Sv decade^{-1} remains. This rate is broadly consistent with climate model projections (Weijer et al. 2020) but inconsistent with collapse scenarios suggested by some statistical models (McCarthy et al. 2025). At 26.5°N, MOC and MHT are strongly correlated (r = 0.97), indicating that most poleward heat transport is carried by the overturning circulation (Johns et al. 2023). While the 2004–23 MOC trend is marginally significant, the corresponding MHT trend (–0.03±0.07 PW decade^{-1}) is not statistically significant. A recent study combining RAPID observations with repeated Florida Straits sections and Argo data estimated the overturning streamfunction at 26.5°N in density coordinates (Smeed et al. 2026). The density-based MOC in Smeed et al. (2026) was slightly stronger than the depth-based estimate and more clearly captured subtropical gyre overturning, although variability remained closely aligned with the depth-based MOC.

In the South Atlantic, synthetic estimates of the MOC and MHT at 20°S, 25°S, 30°S, and 34.5°S —reproduced from Dong et al. (2015, 2021)—have been extended through December 2025 (only MOC is shown in Fig. 3.24). The updated estimates incorporate a reprocessed relationship between satellite altimeter SSH anomalies and vertical temperature structure, based on more than a decade of additional hydrographic observations, and a higher-resolution (0.125°) SSH product for deriving temperature profiles. As in the North Atlantic, the MOC and MHT time series at these latitudes are strongly correlated (r = 0.84–0.97). In 2025, statistically significant positive MOC and MHT anomalies occurred only at 25°S and 30°S. On interannual time scales, variability is coherent between 25°S and 35°S, with significant increasing trends. Detrended annual MOC and MHT estimates at 20°S, 25°S, and 30°S are significantly correlated with one another at near-zero lag (r = 0.6–0.8), whereas correlations with 34.5°S are weaker, with statistically significant relationships only between 30°S and 34.5°S. The reduced coherence of MOC and MHT at 34.5°S relative to latitudes farther north likely reflects regional dynamics associated with Agulhas leakage and the Brazil–Malvinas Confluence. Regarding the robustness of the estimates, it should be noted that the standard deviation of the monthly synthetic MOC at 34.5°S (2.7 Sv) is substantially smaller than that derived from the SAMBA moored array (7.6 Sv; Volkov et al. 2025a), although their monthly anomalies are moderately correlated (r = 0.65). Ongoing community efforts are investigating discrepancies between synthetic and mooring-based estimates, potentially arising from differences in instrumentation, sampling, and methodology.

Together, these observations highlight the importance of sustained, basin-wide monitoring for characterizing Atlantic MOC variability and change. Variability across latitudes is dominated by short- to interannual

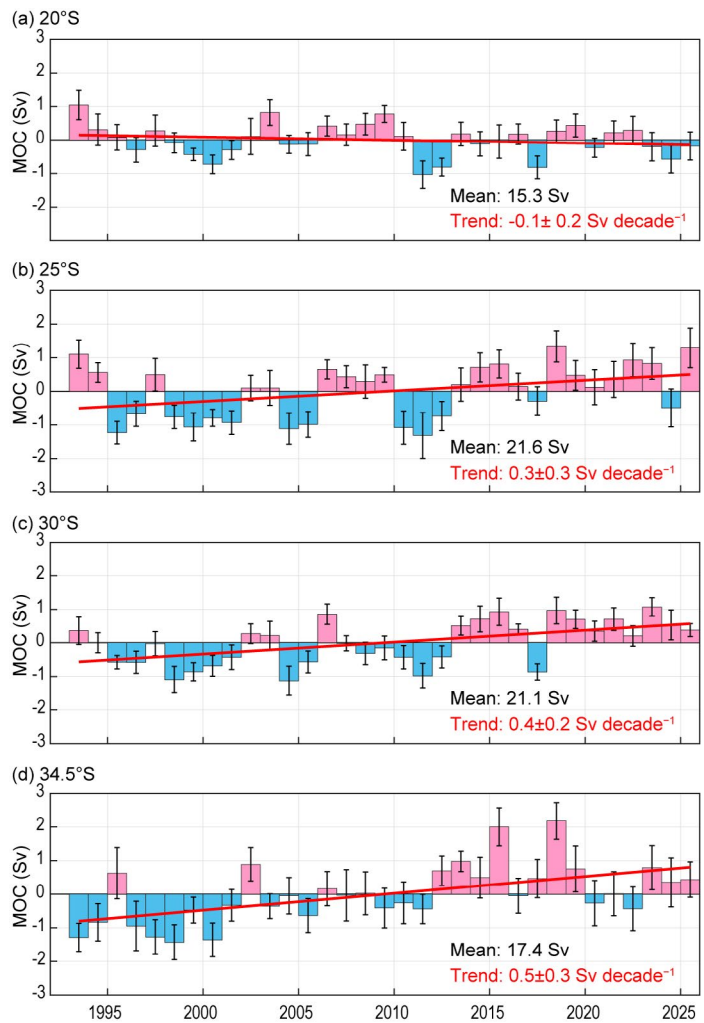

Fig. 3.24. Annual estimates of meridional overturning circulation (MOC) anomalies (Sverdrup [Sv]) and their associated standard errors (error bars) in the South Atlantic, at (a) 20°S, (b) 25°S, (c) 30°S, and (d) 34.5°S. Trends are shown by red lines.

time scales, with no statistically robust evidence of a persistent basin-wide weakening, despite a modest trend at 26.5°N, while positive trends persist in the subtropical South Atlantic. It is acknowledged that the observational time series may still be too short to detect a centennial MOC decline that is projected by climate models and proxy-based reconstructions (e.g., Weijer et al. 2020; Rahmstorf et al. 2015). There is, however, new observational evidence of a coherent multidecadal decline in the Deep Western Boundary Current transport across the tropical/subtropical North Atlantic, indicating a weakening of the lower limb of the Atlantic MOC (Xing et al. 2026). Meridional coherence of the MOC varies, with stronger coherence evident among subtropical latitudes in the South Atlantic and weaker or no coherence in regions influenced by distinct regional dynamics. The complementary use of moored arrays and the synthetic estimates based on satellite and in situ data provides a resilient observing system for detecting change and refining MOC assessments, which remains essential for advancing understanding of the Atlantic's role in the climate system.

i. Global ocean phytoplankton

—B. A. Franz, I. Cetinić, M. Gao, and T. K. Westberry

Marine phytoplankton are microscopic algae that perform a vital function in global ecosystems, generating approximately 50% of Earth's oxygen and newly synthesized organic matter through photosynthesis. In addition to supporting the oceanic food web as primary producers, phytoplankton are a crucial component of the biological pump, capturing carbon dioxide from the atmosphere and transporting it to the deep ocean for long-term storage (Field et al. 1998; Siegel et al. 2023). Phytoplankton distribution and abundance are shaped by multiple interacting factors. Biological factors such as predation by zooplankton and infection by viruses control population size, while environmental factors including nutrient concentrations, light availability, water temperature, ocean stratification, and circulation patterns determine rate of growth (Behrenfeld et al. 2006). Satellite-based ocean color sensors provide a global perspective on phytoplankton dynamics by measuring two key indicators in surface waters: chlorophyll-*a* (Chl *a*; mg m^{-3}) and phytoplankton carbon (C_{phy}; mg m^{-3}). Chlorophyll-*a* is the primary photosynthetic pigment and reflects both the abundance of phytoplankton present and their physiological condition. In contrast, phytoplankton carbon provides a direct measurement of biomass, independent of physiological changes. While Chl *a* and C_{phy} often covary, discrepancies between these two measurements provide valuable insights into phytoplankton community dynamics, such as shifting physiological or compositional makeup of phytoplankton communities (Geider et al. 1997; Cetinić et al. 2012; Siegel et al. 2013; Westberry et al. 2016, Stoer and Fennel 2024).

This report evaluates the global distribution of phytoplankton from October 2024 through September 2025. The assessment uses remotely-sensed Chl *a* and C_{phy} measurements from a continuous 28-year record (October 1997–September 2025) that combines observations from three satellite sensors: SeaWiFS (October 1997–September 2003), MODIS on *Aqua* (MODIS-A, October 2002–September 2018), and VIIRS on NOAA20 (VIIRS-N20, October 2018–September 2025). To provide context on the physical state of the oceans, daytime sea surface temperature (SST) from MODIS-A is also assessed over a common time period. The Chl *a* product was derived using the Ocean Color Index algorithm originally developed by Hu et al. (2012), but with updated algorithm coefficients (Hu et al. 2019; O'Reilly and Werdell 2019). The C_{phy} product was derived in two steps: first, calculating the particle backscattering coefficient (b_{bp}) at 443 nm using the Generalized Inherent Optical Properties algorithm (Werdell et al. 2013; McKinna et al. 2016), then applying a linear relationship between b_{bp} and C_{phy} (Graff et al. 2015).

Creating a seamless multisensor time series requires careful bias correction between the different instruments. To merge SeaWiFS and MODIS-A observations, differences between the sensors were assessed during their overlapping period from 2003 through 2008. A mean bias correction of −0.0021 mg m^{-3} for Chl *a* and -6.7×10^{-5} m^{-1} for b_{bp} (equivalent to −0.78 mg m^{-3} of C_{phy}) was derived and applied to the SeaWiFS time series. Similarly, the overlap period from 2018 to 2020 was used to assess differences between MODIS-A and VIIRS-N20, resulting in a bias correction of −0.0021 mg m^{-3} for Chl *a* and -3.1×10^{-4} m^{-1} for b_{bp} (equivalent to −3.6 mg m^{-3} of C_{phy}) that was applied to the VIIRS-N20 time series. It is important to note that the bias corrections between VIIRS-N20 and MODIS-A b_{bp} retrievals are relatively large, primarily due to residual sensor radiometric calibration errors and the sensitivity of b_{bp} retrievals to spectral sampling differences between the sensors (Werdell and McKinna 2019). While NASA efforts are underway to reduce this retrieval bias, some additional caution is warranted when interpreting C_{phy} anomalies from VIIRS-N20 relative to the climatological record, which is dominated by MODIS-A observations. Nevertheless, the VIIRS-N20 instrument demonstrates very good temporal stability (Twedt et al. 2022) and, therefore, provides the primary reference for assessing changes during the current analysis year.

Changes in the global distribution of phytoplankton were assessed by comparing current observations to historical baselines. For each month during the 2025 analysis year, VIIRS-N20 measurements of Chl *a* and C_{phy} were compared against VIIRS-N20 monthly means spanning October 2019 through September 2024. These monthly anomalies were then averaged to produce global annual mean anomaly maps for both Chl *a* and C_{phy} (Figs. 3.25a,b). The same approach and reference period was applied to MODIS-A SST data to generate an equivalent SST annual mean

anomaly map (Fig. 3.25c). The analyses presented in Figs. 3.25 and 3.26 utilize the full 28-year bias-corrected multisensor record, but focus specifically on the permanently stratified ocean (PSO), a region that encompasses the tropical and subtropical oceans. The PSO is defined by two key characteristics: annual average SST exceeding 15°C and surface mixed layers that are typically shallow and nutrient-depleted, remaining above the nutricline (the depth below which nutrient concentrations increase). This region extends roughly between 40°S and 40°N latitude, as indicated by the black lines in Figure 3.25 (Behrenfeld et al. 2006).

For the 2025 analysis year, the distribution of SST anomalies (Fig. 3.25c) is consistent with La Niña conditions over much of the analysis year, including a pronounced tongue of anomalously cool waters extending across the equatorial Pacific. Negative SST anomalies within the PSO are typically associated with a deeper surface mixed layer (Deser et al. 2010), which reduces phytoplankton light exposure rates leading to higher cellular Chl *a* and a decoupling between Chl *a* and C_{phy} variability (Behrenfeld et al. 2016; Graff et al. 2016; Stoer and Fennel 2024). Consistent with that expectation, Chl *a* anomalies were elevated for this analysis year (>30%) within the cooler water of the equatorial Pacific and depressed (<20%) in the anomalously warm waters of the subtropical and subpolar Pacific and the Indian Ocean (Fig. 3.25a). While C_{phy} and Chl *a* anomalies largely covary within the PSO, C_{phy} is elevated where Chl *a* is depressed in the subtropical western North Pacific, with the opposite relationship to the east. Patches of elevated and depressed Chl *a* are visible throughout the subpolar and polar regions above and below the PSO (Fig. 3.25a), and the C_{phy} anomalies show higher spatial variability and dynamic range (Fig. 3.25b). Observed heterogeneity in biomass indicators outside of the PSO are a result of the ephemeral nature of phytoplankton blooms in these waters, as well as poor spatial and temporal sampling due to clouds and low-light conditions and the confounding influence of wind-driven whitecaps (Randolf et al. 2014) that limit our ability to interpret interannual variability in higher latitude regions.

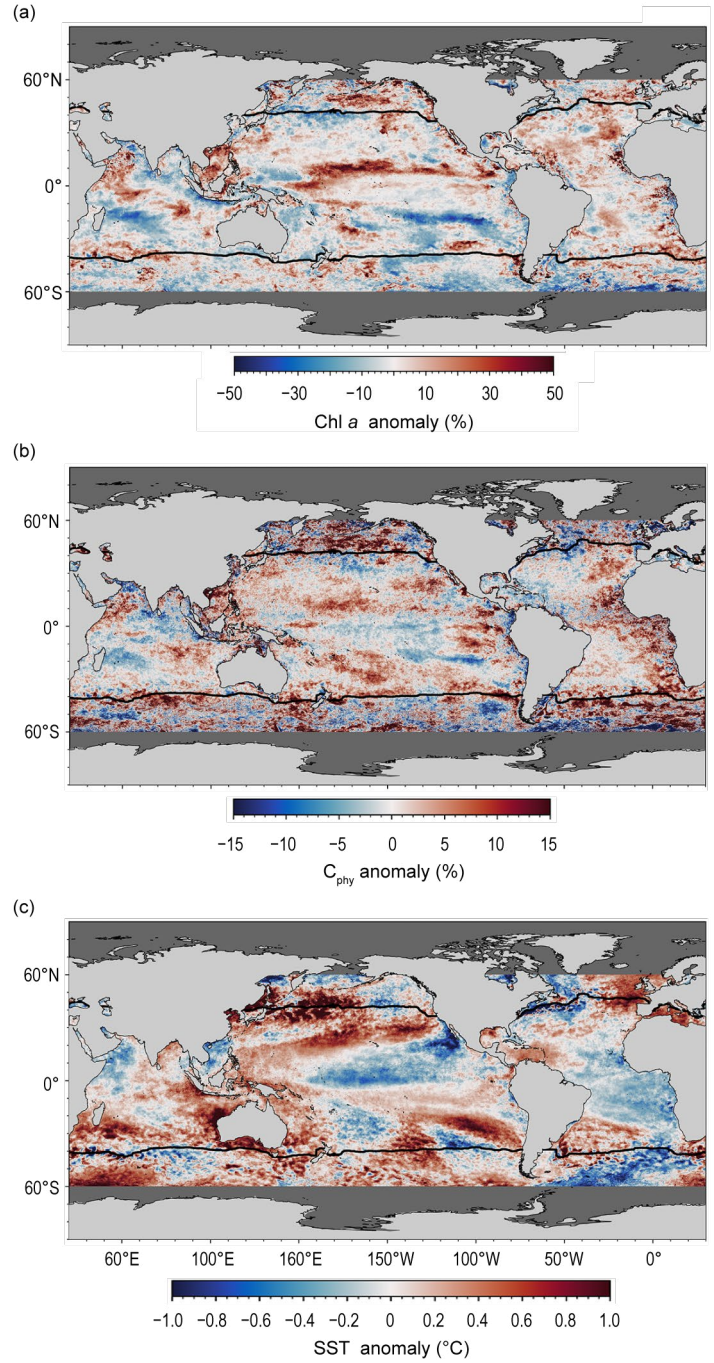

Fig. 3.25. Spatial distribution of average monthly (a) VIIRS-N20 Chl *a* anomalies (%), (b) VIIRS-N20 C_{phy} anomalies (%), and (c) Moderate Resolution Imaging Spectroradiometer on *Aqua* (MODIS-A) sea surface temperature (SST) anomalies (°C) for Oct 2024–Sep 2025, where monthly differences were derived relative to the VIIRS-N20 mission period (Oct 2019–Sep 2024). Chl *a* and C_{phy} are stated as % difference from climatology, while SST is shown as an absolute difference. Also shown in each panel is the location of the mean 15°C SST isotherm (black lines) delineating the permanently stratified ocean (PSO). Differences in the SST anomalies here vs. in Fig. 3.2a are owing to differences in climatological periods, smoothing, and data sources.

Annual variability of Chl *a* and C_{phy} within the permanently stratified ocean typically exhibits two distinct peaks (Figs. 3.26a,b), corresponding to springtime increases in phytoplankton biomass in the Northern Hemisphere (Figs. 3.26c,d) and Southern Hemisphere (Figs. 3.26g,h).

Notably, the timing of C_{phy} peaks lags two to three months behind those of Chl *a*. This lag reflects two important biological processes: the tight coupling between phytoplankton and its losses (mostly through zooplankton grazing) keep biomass in check long after nutrient-driven increases in growth give rise to corresponding increases in cellular Chl *a*, and subsequently the phytoplankton chlorophyll-to-carbon ratios decline as the seasonal bloom progresses (Westberry et al. 2016). The timing of seasonal peaks and troughs observed during the 2025 analysis year is consistent with the climatological record (averaged over the period of October 1997 to September 2024). In the equatorial region, Chl *a* was slightly elevated in February and again in July–August of 2025, consistent with weak La Niña conditions, but otherwise remained close to climatological monthly means (Figs. 3.26e,f). In the Northern Hemisphere, for both Chl *a* and C_{phy} (Figs. 3.26c,d), the magnitude of the spring peak was slightly depressed, while in the Southern Hemisphere the peak was elevated for C_{phy} but remained close to the historical mean for Chl *a* (Figs. 3.26g,h).

Over the 28-year time series of spatially averaged monthly mean Chl *a* within the PSO, concentrations vary by 5.7% (0.008 mg m^{-3}, standard deviation) around an average of 0.136 mg m^{-3} (Fig. 3.27a). C_{phy} over the same 28-year period varies by 3.1% (0.68 mg m^{-3}) around an average of 21.8 mg m^{-3} (Fig. 3.27c). Chl *a* monthly anomalies within the PSO (Fig. 3.27b) vary by 4.5%

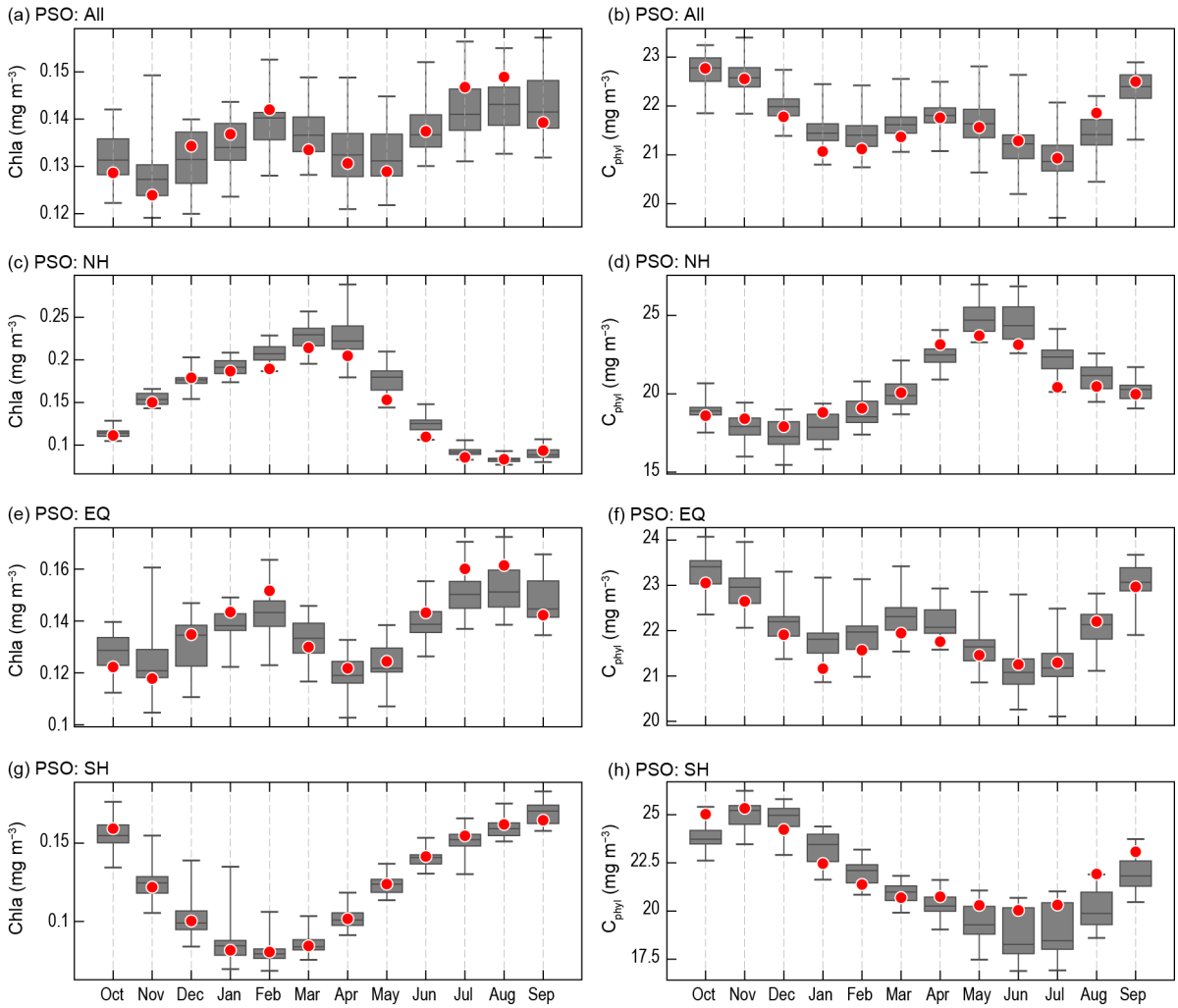

Fig. 3.26. Distribution of Oct 2024–Sep 2025 monthly means (red circles) for (a) VIIRS on NOAA-20 (VIIRS-N20) chlorophyll-*a* (Chl *a*) and (b) VIIRS-N20 phytoplankton carbon (C_{phy}) for the permanently stratified ocean (PSO) region (see Fig. 3.27), superimposed on the climatological values as derived from the combined time series of Sea-Viewing Wide Field-of-View Sensor (SeaWiFS), Moderate Resolution Imaging Spectroradiometer on Aqua (MODIS-A), and Visible Infrared Imaging Radiometer Suite on NOAA-20 (VIIRS-N20) over the period of Oct 1997–Sep 2024. Gray boxes show the interquartile range of the climatology, with a black line for the median value and whiskers extending to minimum and maximum values. Subsequent panels show latitudinally segregated subsets of the PSO for (c),(d) the Northern Hemisphere (above tropics)NH, (e),(f) tropical ±23.5° latitude subregion EQ, and (g),(h) Southern Hemipshere (below tropics). SH Units for (a), (c), (e), and (g) are Chl *a* (mg m^{-3}) and (b), (d), (f), and (h) are C_{phy} (mg m^{-3}).

(0.006 mg m^{-3}) over the multimission time series, with the largest interannual deviations generally associated with ENSO events (r = −0.38), as demonstrated by the correspondence of Chl *a* anomaly variations with the Multivariate ENSO Index (MEI; Wolter and Timlin 1998; presented in the inverse to illustrate the covariation). C_{phy} anomalies (Fig. 3.27d), which vary by 1.9% (0.42 mg m^{-3}), are less correlated with the MEI (r = −0.27) due to the inherent lag between environmental change, phytoplankton growth, and biomass accumulation. The monthly mean anomalies in 2025 for Chl *a* and C_{phy} within the PSO indicate modestly elevated concentrations in the early part of the analysis year and again in boreal summer, consistent with La Niña conditions that enhanced phytoplankton production.

Continuous ocean color monitoring enables us to track changes in the global distribution of marine phytoplankton, which play a critical role in driving biogeochemical processes, regulating the ocean's contribution to the global carbon cycle, and controlling marine ecosystems, food webs, and fisheries. By analyzing subtle variations in Chl *a* and C_{phy} distributions and seasonal cycles, we can distinguish between climate-driven changes in both phytoplankton biomass and shifts in their physiological state or community composition. The timing and distribution of phytoplankton biomass indicators for 2025 is consistent with the climatological record and the weak La Niña conditions that prevailed over much of the analysis year.

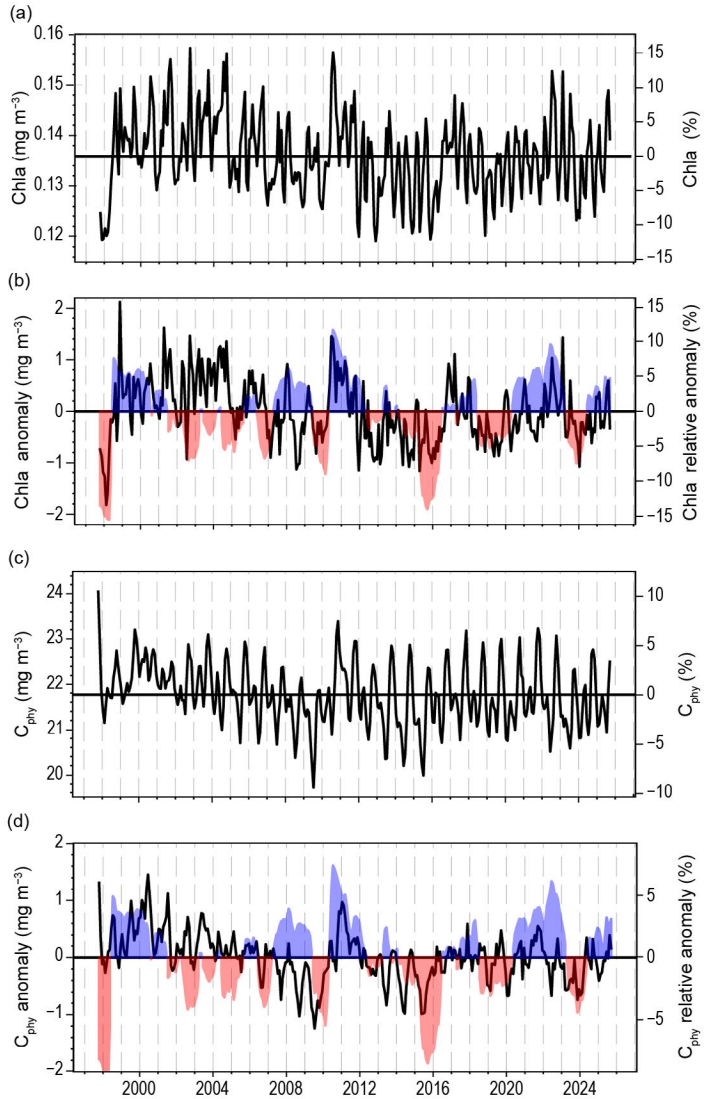

Fig. 3.27. Twenty-eight-year, multimission record of chlorophyll-*a* (Chl *a*; mg m^{-3}) and phytoplankton carbon (C_{phy}; mg m^{-3}) averaged over the permanently stratified ocean (PSO; Oct 1997 to Sep 2025). (a) Monthly Chl *a*, with the horizontal line indicating the multimission mean Chl *a* concentration for the entire PSO region. (b) Monthly Chl *a* anomalies after subtraction of the multimission climatological mean (Fig. 3.26a). (c) Monthly C_{phy}, with the horizontal line indicating the multimission mean C_{phy} concentration for the entire PSO region. (d) Monthly C_{phy} anomalies after subtraction of the multimission climatological mean (Fig. 3.26b). Shaded blue and red colors show the Multivariate El Niño–Southern Oscillation (ENSO) Index, inverted and scaled to match the range of the Chl *a* and C_{phy} anomalies, where blue indicates La Niña and red indicate El Niño conditions.

j. Global ocean carbon cycle

—A. Jersild, R. Wanninkhof, J. A. Triñanes, P. Landschützer, R. A. Feely, and B. R. Carter

1. INTRODUCTION

The oceans play a major role in the global carbon cycle by taking up a substantial fraction of the excess carbon dioxide (CO_2) that humans release into the atmosphere. As a consequence of these anthropogenic CO_2 (C_{ant}) emissions, the atmospheric CO_2 concentration has risen from pre-industrial levels of about 278 ppm (parts per million) to 425.7 ppm. Over the last decade the global ocean has continued to take up C_{ant} and is a major mediator of atmospheric CO_2 levels. Of the 11.2±0.9 Pg C yr^{-1} C_{ant} released during the period 2015–24, 3.2±0.4 Pg C yr^{-1} (29%) accumulated in the ocean, 2.4±0.8 Pg C yr^{-1} (21%) accumulated on land, and 5.6±0.02 Pg C yr^{-1} (50%) remained in the atmosphere (see Table 7 in Friedlingstein et al. 2026). This decadal C_{ant} uptake estimate by the ocean is a consensus view from a combination of measured ocean decadal CO_2 inventory changes, global ocean biogeochemical models, and global air–sea CO_2 flux estimates using data-based and machine learning systems, based on surface ocean fugacity of CO_2 (fCO_{2w})[1] measurements.

The ocean interior is more challenging to observe than the surface, leading to reduced temporal and spatial coverage than for surface ocean fCO_2. Machine-learning gap filling techniques are now being employed to provide increased resolution of interior C_{ant} estimates, with a 2025 mean inventory uptake of 3.7 Pg C yr^{-1} (Carter et al. 2025).

2. AIR–SEA CARBON DIOXIDE FLUXES

Ocean uptake of CO_2 is estimated from the net air–sea CO_2 flux derived from a bulk flux formula determined from the product of the difference of air and surface-seawater fCO_2 (ΔfCO_2) and gas transfer coefficients. Gas transfer is parameterized with wind, described in Wanninkhof (2014). This provides a net flux estimate. A river adjustment of 0.65 Pg C yr^{-1} is applied to uptake (Regnier et al. 2022), as recommended in the Global Carbon Budget (GCB) 2025. The data sources for fCO_{2w} are annual updates of observations from the Surface Ocean CO_2 Atlas (SOCAT) composed of moorings, autonomous surface vehicles, and ship-based observations (Bakker et al. 2016). The increased observations and improved mapping techniques, including machine learning methods summarized in Rödenbeck et al. (2015), provide global fCO_{2w} fields on a 1° × 1° grid at monthly time scales. For this report, we use a self-organizing maps feed-forward neural network (SOM-FNN) approach of Landschützer et al. (2013, 2014) and an extremely randomized trees (ET) machine learning technique (AOML-ET) described in Wanninkhof et al. (2025), both using SOCATv2025 for training. Predictor variables include: sea surface temperature (SST; Rayner et al. 2003); chlorophyll-*a* (Globcolour; Maritorena et al. 2010); mixed-layer depth (de Boyer Montégut et al. 2004 merged with Schmidtko et al. 2013), and salinity (Good et al. 2013). For atmospheric CO_2, the zonally resolved NOAA marine boundary layer atmospheric CO_2 product is used (Lan et al. 2023). Gas transfer coefficients are determined using European Centre for Medium-Range Weather Forecasts Reanalysis version 5 (ERA5) winds (Hersbach et al. 2018). The air–sea CO_2 flux for 2025 extrapolates the predictor variables for that year rather than having a year's latency.

The SOM-FNN and AOML-ET results (solid lines in Fig. 3.28) show a steady ocean CO_2 sink (S_{ocean}) from 1982 to the early 1990s, followed

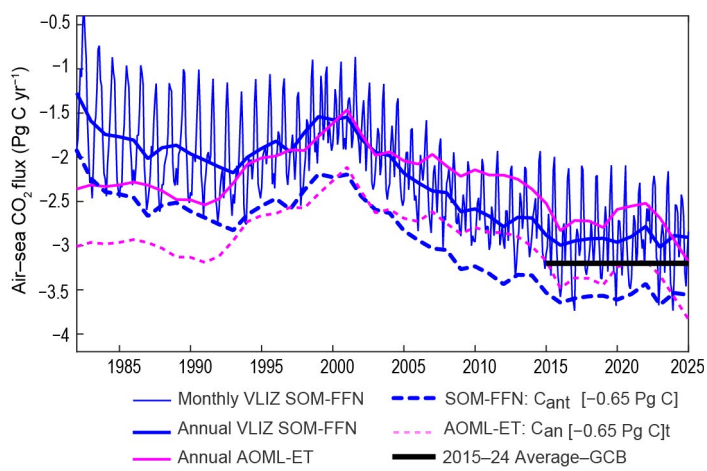

Fig. 3.28. Global annual (thick lines) and monthly (thin blue line) net air–sea carbon dioxide (CO_2) fluxes (Pg C yr^{-1}) for the period 1982–2025 using the Flanders Marine Institute (VLIZ) self-organizing maps feed-forward neural network (SOM-FFN) and the extremely randomized trees (ET) machine learning technique (AOML-ET) output. The annual anthropogenic CO_2 (C_{ant}) air–sea flux (dashed lines) includes the riverine adjustment of –0.65 Pg C. Negative values indicate CO_2 uptake by the ocean. The black line is the 2015–24 average from global carbon budget products (Friedlingstein et al. 2025).

[1] The fugacity is the partial pressure of CO_2 (pCO_2) corrected for non-ideality. They are numerically similar for surface waters with $fCO_2 \approx 0.994\ pCO_2$.

by a period of decreasing uptake to 2002. There is a strong increase in the ocean sink from 2002 onward that continues through 2016, after which the global uptake decreases until 2022. The 2025 S_{ocean} of 3.4 Pg C yr^{-1} (SOM-FFN) and 3.6 Pg C yr^{-1} (AOML-ET; dashed lines in Fig. 3.28) shows a ≈0.2 Pg C–0.4 Pg C increase in uptake above the 2015–24 GCB average of 3.2±0.4 Pg C yr^{-1} when the riverine adjustment is included. The amplitude of seasonal variability is ≈1.6 Pg C with a minimum uptake in June–September.

The annual average flux map for 2025 (Fig. 3.29a) shows the characteristic pattern of high effluxes (ocean-to-air CO_2 fluxes) in equatorial-tropical, coastal upwelling, and open-ocean upwelling regions. Coastal upwelling regions include those in the Arabian Sea and off the west coasts of North America, South America, and West Africa. The western Bering Sea continues to be a strong CO_2 source, a juxtaposition to the strong sink in surrounding regions. This regional source is hypothesized to result from a local outcropping of shallow isopycnals with high CO_2 values, but this has not been independently verified. Cumulatively, the regions of effluxes are substantial CO_2 sources to the atmosphere (≈1 Pg C). The primary CO_2 uptake regions are in the subtropical and subpolar regions. The largest sinks are poleward of the sub-tropical fronts. Generally, SST influences solubility (positive SST anomalies decrease solubility, increasing fCO_{2w}). However, in regions with high fCO_{2w} due to upwelling, warmer SST stemming from decreased upwelling of the cold CO_2-rich water leads to lower fCO_{2w}.

In the Northern Hemisphere, the North Atlantic is a large sink, while the North Pacific is punctuated by a substantial source of CO_2 in the western subpolar Pacific and the central Bering Sea (Fig. 3.29a). The Northern Hemisphere sinks are, in part, due to the position of the western boundary currents whose cooling waters, transported poleward, increase solubility and contribute to CO_2 uptake at high latitudes. The Gulf Stream/North Atlantic Drift in the Atlantic extends farther north than the Kuroshio in the Pacific, extending the region of a strong sink in the North Atlantic.

The ocean carbon uptake anomalies (Fig. 3.29c) in 2025 relative to the 1990–2020 average, adjusted for the 30-year trend, demonstrate the return to neutral El Niño–Southern Oscillation (ENSO) conditions over much of the summer, with some evidence of the weak La Niña returning in autumn 2025. The Southern Ocean (≈45°S–60°S) continues to show reduced uptake when compared to the 30-year trend, although it should be noted the regional average is still overall an ocean sink. This reduction of uptake of nearly 50% smaller

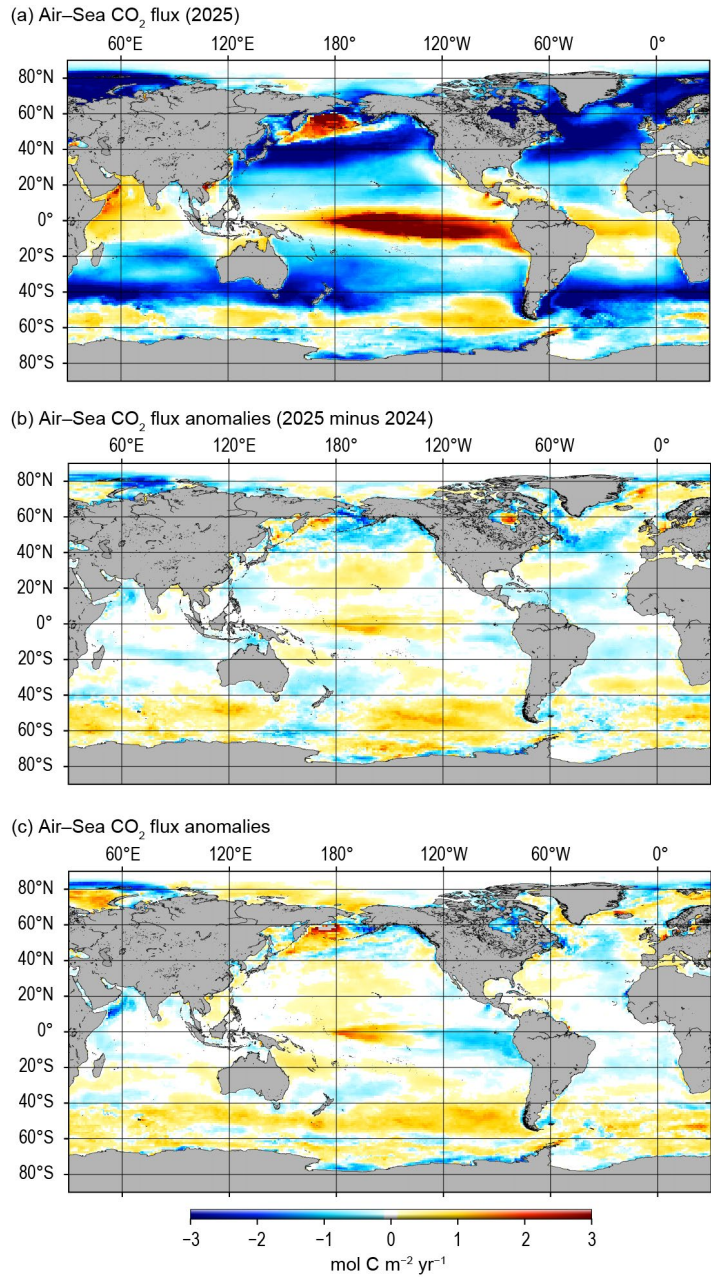

Fig. 3.29. Global map of (a) net air–sea carbon dioxide (CO_2) fluxes for 2025, (b) net air–sea CO_2 flux anomalies for 2025 minus 2024, and (c) net air–sea CO_2 flux anomalies for 2025 relative to 1990–2020 average values, adjusted for the 30-year trend using the Flanders Marine Institute (VLIZ) self-organizing maps feed-forward neural network (SOM-FNN) approach. Units are all mol C m^2 yr^{-1}. Ocean CO_2 uptake regions are shown in blue. For reference, a global ocean CO_2 uptake of 2.8 Pg C yr^{-1} equals a flux density of –0.65 mol C m^2 yr^{-1}.

than previous estimates is likely due to a combination of temporal variation, methodological improvements, and estimate uncertainty stemming from data sparsity in the region (Hauck et al. 2023).

The spatial differences in CO_2 fluxes between 2025 and 2024 (Fig. 3.29b) shows an increased influx (blue shading) in the Atlantic and polar regions, potentially a recovery of the anomalous reduced uptake observed in 2023/24 (Müller et al. 2025). In the Southern Ocean, we observe an increased efflux. This difference can mainly be attributed to shifting levels of observations in the Southern Ocean in the SOCAT dataset (Fay et al. 2025). The machine-learning methods and use of predictor values to complete the time series can be sensitive to data availability, and low-sampled regions can be highly responsive to individual observations (Jersild and Landschützer 2024; Hauck et al. 2023).

3. OCEAN INTERIOR INVENTORY ESTIMATES

The ocean inventory of dissolved inorganic carbon (DIC) varies over time due to surface CO_2 fluxes, interior ocean cycling of organic matter, riverine inputs, and sedimentary exchanges. Interior ocean observations are more expensive and challenging to obtain than surface observations, so their coverage tends to be more limited across time and space. For this reason, interior ocean DIC observations are primarily used in decadal retrospective analyses that quantify the accumulation of C_{ant} throughout the ocean.

As with fCO_{2w}, machine learning gap-filling techniques are now being used to map the available measurements onto data products that have better spatial and temporal resolution (e.g., Keppler et al. 2023). For example, Fig. 3.30 reflects machine learning estimates of DIC (Carter et al. 2021, centered on the year 2002) and C_{ant} (Carter et al. 2025) derived from the temperature and salinity climatology of Roemmich and Gilson (2009). These estimates collectively allow the total ocean inventory ($C_{inventory}$) estimates and their increases (Fig. 3.30, attributable primarily to S_{ocean}) to be separated into natural variations (ΔC_{nat}) and anthropogenic accumulation (ΔC_{ant}).

Meaningful interannual variability can be seen in the annually averaged rate of $C_{inventory}$ accumulation (Fig. 3.30). This variability is also attributable primarily to C_{nat} variability. The C_{ant} changes are mostly steady from year to year, and the variations generally oppose the much larger variations in the C_{nat}. This anticorrelation can result when increases in ocean overturning generate anomalous loss of deep carbon accumulated from organic matter respiration and anomalous uptake of C_{ant} with ventilation of older waters (DeVries et al. 2017). Surface ocean heat content variations also play a role; anomalously warm waters hold less DIC and more C_{ant} than anomalously cool waters when in air–sea gas exchange equilibrium with the atmosphere.

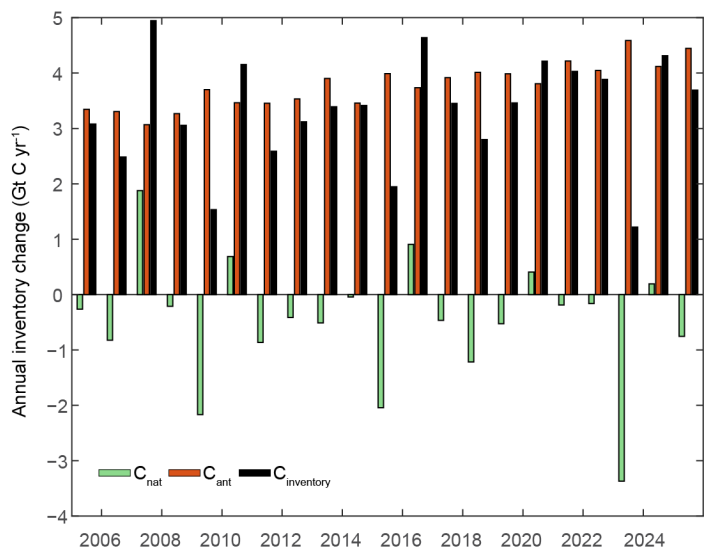

Fig. 3.30. Annual average accumulation rates (Gt C yr^{-1}) for the ocean inventories of total dissolved inorganic carbon ($C_{inventory}$; black), the portion attributable to anthropogenic carbon emissions (C_{ant}; red), and the portion attributable to natural processes (C_{nat}; green), which is estimated by residual.

The mean inventory increase rate over the 2015–24 period of 3.4 Pg C yr^{-1} is comparable to the 3.2±0.4 Pg C yr^{-1} estimate from air–sea fluxes. Both ways of estimating S_{ocean} imply larger increases in 2025: 3.7 Pg C yr^{-1} for the inventory estimate and 3.4 Pg C–3.6 Pg C yr^{-1} for the air–sea CO_2 flux estimate. Two differences in the estimates, that are well within their uncertainties, can be attributed to the fact that the interannual variations in the inventory estimates are greater and the inventory estimates do not show the recent (post 2016) relaxation of ocean CO_2 uptake.

Ocean interior inventory mapping can take advantage of regular updates to the underlying climatologies to provide timely and detailed information about ocean carbon inventory variations. However, as of yet, these estimates solely provide projections of expected patterns based on DIC measurements that predate 2024, and rely on the Argo-array-dominated temperature and salinity patterns from ~2004 onward to generate the estimates for the most recent years. Furthermore, the methodological uncertainties for this approach have yet to be quantified.

k. Global ocean dissolved oxygen

—J. D. Sharp, Z. Wang, T. Ito, S. Minobe, L. Cheng, J. Du, H. Garcia, C. J. Roach, B. Lu, Y. Xin, M. Han, Y. Zhou, and G. G. Navarra

Dissolved oxygen (O_2) is vital for aerobic marine organisms and plays a major role in shaping species distributions (Deutsch et al. 2024; Stramma et al. 2012), modulating elemental cycles (Gruber 2008), and regulating the production of natural greenhouse gases such as nitrous oxide and methane (Bianchi et al. 2012). A major consequence of climate warming is the widespread loss of dissolved O_2 from seawater (Gruber 2011; Keeling et al. 2010; Levin 2018; Long et al. 2016; Oschlies et al. 2017). Unlike the well-mixed atmosphere, oxygen is unevenly distributed in the ocean, and some regions contain levels too low to support most marine organisms (Breitburg et al. 2018). This variability arises because 1) oxygen supply from photosynthesis and air–sea exchange is limited to surface waters, 2) biological respiration, whereby heterotrophic organisms use oxygen to extract energy from organic carbon (OC), depletes oxygen in a spatiotemporally uneven way depending on the rate of OC supply, heterotrophic community composition, and additional environmental factors, and 3) ocean circulation and mixing redistribute oxygen throughout the ocean interior. Dissolved oxygen in seawater is declining; estimates have suggested the global ocean lost 0.5%–3.3% of its O_2 inventory (surface to 1000-m depth) from 1970 to 2010 (Bindoff et al. 2019; Helm et al. 2011; Ito et al. 2017; Schmidtko et al. 2017).

The ocean's oxygen inventory, the total amount of oxygen in the ocean, is difficult to track, as observations are scattered and the quality of O_2 observations is generally lower than that of temperature and salinity. Further, there has been an evolution over time in the data sources that contribute to the observational record for dissolved oxygen in the open ocean, with Winkler titrations from bottle samples being most prevalent from the 1960s through the 1980s, electrochemical sensors on shipboard CTDs contributing heavily to the record from the 1990s through the 2010s, and optical sensors on profiling floats becoming the dominant data source in the 2010s through the present (Fig. 3.31). This diversity of data sources means that discrepancies among measurement types and their spatial distribution must be carefully considered, especially when trying to extract a trend from the observational record using aggregated data from several sources. We analyze time-varying, three-dimensional, mapped fields of ocean oxygen from nine different approaches to evaluate the changing ocean oxygen inventory over the last 60 years and anomalies in 2025 relative to a 1990–2020 baseline.

The O_2 fields considered in this analysis include results from five statistical interpolation (SI) methods—objective analysis using weighted-averaging interpolation (NCEI; Garcia et al. 2024a), ensemble optimal interpolation (IAP; Cheng et al. 2020; Cheng ad Zhu 2016; Gouretski et al. 2024), Gaussian optimal interpolation (GT-OI; Ito 2022), data-interpolating variational analysis (UTAS; Roach and Bindof 2023), and geostatistical regression (SJTU-GR; Zhou et al. 2022)—and four machine-learning (ML) methods—Gaussian mixture models and shallow neural networks (GOBAI; Sharp et al. 2023), neural networks and random forest regressions (GT-ML; Ito et al. 2024), hybrid graph learning (Jingwei; Lu et al. 2024), and Bayesian ensemble machine learning (SJTU-HZ; Han et al. 2025).

The maps considered here may not correspond directly with the data products described in the references listed but are built using the methods described in those references. Eight are constructed using data extracted from the World Ocean Database 2023 (WOD23) updated through 2025 (Garcia et al. 2024a; Mishonov et al. 2024), and one (IAP) uses data from the IAP database (Gouretski et al. 2024). Because eight out of nine results use WOD23 with the same quality control, comparisons among the ensemble differ primarily in mapping methodology, not in their primary data sources and quality-control methods. However, previous work has demonstrated that mapping methods have a greater effect on variability among mapped climatological (annual mean) products than the small variations in the primary data sources and the quality-control methods (Ito et al. 2025), so we believe our results represent a robust ensemble. The SI maps use data binned into 1° × 1° annual bins and the ML maps use individual profile data to train models that are applied to temperature and salinity data mapped onto 1° × 1° monthly bins. Three of the ML maps (GOBAI, GT-ML, and Jingwei) use temperature and salinity data from the EN4.2.2 dataset (Good et al. 2013) and SJTU-HZ uses the ORAS5 dataset (Copernicus Climate Change Service 2021).

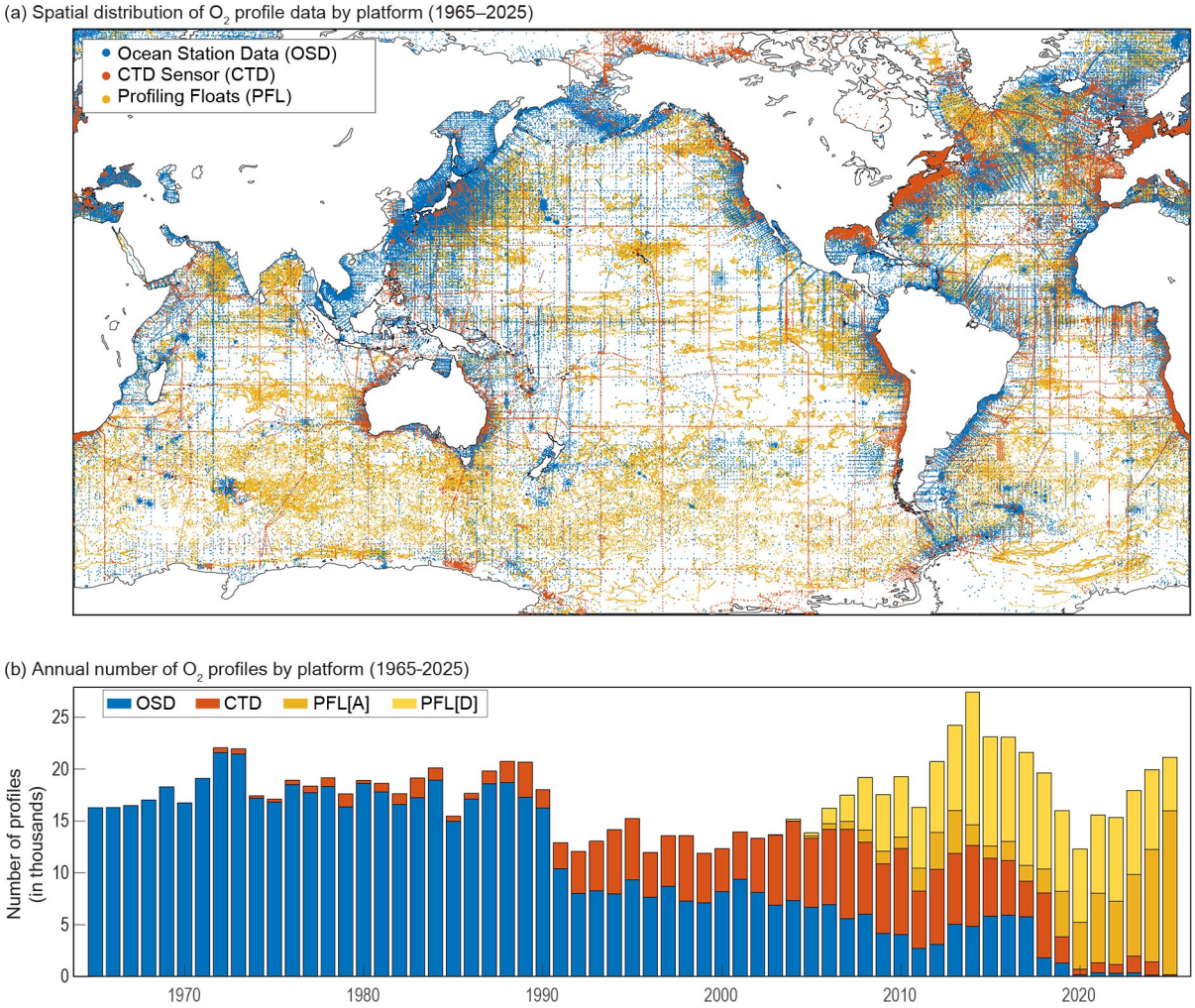

Fig. 3.31. (a) Spatial distribution and (b) annual number of profiles containing dissolved oxygen (O_2) observations contributed by different platforms to the dataset used to create the dissolved oxygen maps. Measurements were extracted from the World Ocean Database 2023, updated through 2025. Data from bottle measurements at ocean stations (OSD), conductivity-temperature-depth profiles (CTD), and profiling floats (PFL) are included, as they are the three most prevalent oxygen data sources. In (b), profiling float data are separated into data with real-time adjustments (PFL[A]) and data with delayed-mode quality-control (PFL[D]).

The ensemble long-term mean oxygen inventories show the effects of high O_2 solubility in cold, high-latitude waters compared to low O_2 solubility in warm, tropical waters in the 0-m–50-m depth layer (Fig. 3.32a). From 50 m to 1000 m, accumulated respiration and weak ventilation result in extremely low oxygen inventories in the subarctic North Pacific, eastern tropical Pacific, North Indian, and eastern tropical Atlantic (Fig. 3.32b). Conversely, strong ventilation forms highly oxygenated mode and intermediate waters in the North Atlantic and Southern Oceans, which extend equatorward.

Dissolved oxygen content in the ocean has generally decreased over at least the last 60 years (Fig. 3.32e). Negative trends in the 0-m–50-m depth layer (Fig. 3.32c) reveal the widespread influence of rising sea surface temperature (section 3b), which decreases O_2 solubility and increases upper ocean stratification (Oschlies et al. 2018). Negative trends from 50 m to 1000 m (Fig. 3.32d) reflect deoxygenation driven by additional factors, including reduced ventilation, changes in interior ocean circulation, and enhanced biological respiration. Bindoff et al. (2019) indicated that the North Pacific and Southern Oceans have seen the largest changes in oxygen inventory over the past few decades, which is supported by our results (Fig. 3.32d). Long et al. (2016) highlight the impact of reduced ventilation driving strong deoxygenation trends in the North Pacific, agreeing with our results as well as an analysis of oxygen trends at Ocean Station Papa (Cummins and Ross 2020) and recent global-scale work by Ito et al. (2026). The small area exhibiting an O_2 increase in the North Atlantic (Fig. 3.32d) is likely related to variability in the ventilation of Labrador Sea Water (Rhein et al. 2017) and in the Atlantic meridional overturning circulation

(section 3h). A weak O_2 increase in the western subtropical South Pacific (Fig. 3.32d) aligns with a feature pointed out by Ito et al. (2026) and corresponds with a cooling signal pointed out by Garcia-Soto et al. (2021).

Volume-integrated O_2 inventories from 0 m–1800 m (Fig. 3.32e) show an average trend from 1965 to 2025 of −0.45±0.10% decade^{-1} (mean±sample standard deviation across nine maps) relative to a climatological mean inventory (1965–2025) of 91.2±0.2 Pmol O_2 (in a volume equal to 565.96×10^6 km^3). All the maps show relatively weak trends until about the mid-1980s, after which stronger O_2 loss continues through 2025. This behavior was first reported by Garcia et al. (2005), who noted an O_2 increase from the 1950s to mid-1980s, followed by O_2 loss in the upper 100 m. This pattern has since been confirmed by more recent studies that include deeper levels (e.g., Ito et al. 2017). The ML maps tend to display greater interannual variability (IAV = 0.28±0.12%) and stronger trends (−0.52±0.08% decade^{-1}) compared to the SI maps (IAV = 0.24±0.07%; trend = −0.39±0.08 % decade^{-1}). IAV is calculated as the standard deviation of de-trended annual mean inventory values for each product, with the trend removed using a linear least-squares fit. For both IAV and trends, the mean (μ) and sample standard deviation (±σ) are reported across the SI maps (n = 5) and the ML maps (n = 4).

The differences in multidecadal trends and interannual variability between the two subsets of O_2 maps (SI and ML) could be partially explained by fundamental differences between the

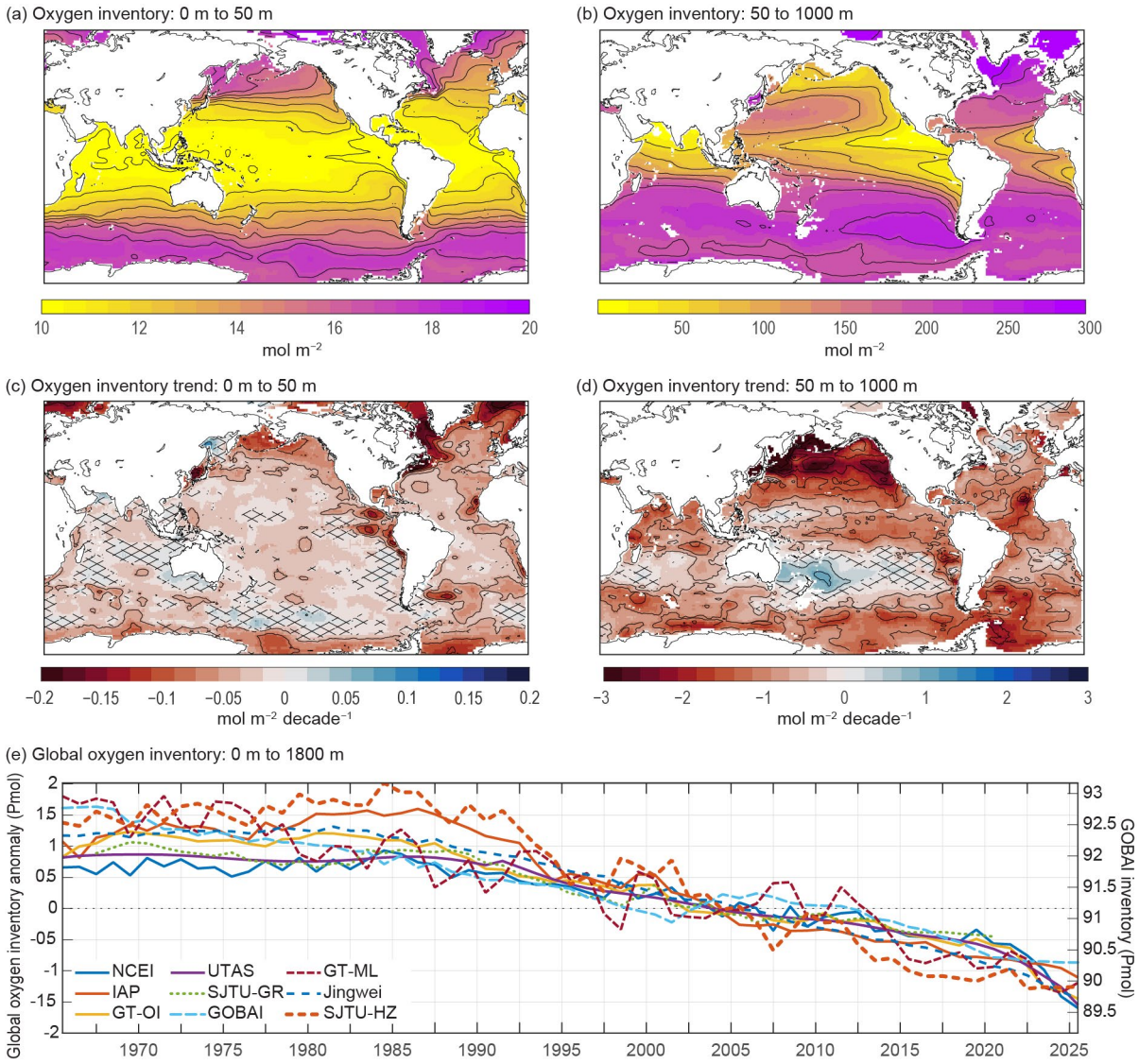

Fig. 3.32. (a),(b) Ensemble mean dissolved oxygen (O_2) inventories (mol m^{-2}) and (c),(d) trends (1965–2025; mol m^{-2} decade^{-1}) from (a),(c) 0 m to 50 m and (b),(d) 50 m to 1000 m across all nine mapping approaches. (e) Global O_2 inventory anomalies (Pmol; 1990–2020 baseline) integrated from 0 m to 1800 m for each individual approach. Areas in (c),(d) where fewer than seven out of the nine products agree on the sign of the trend are cross-hatched.

approaches. SI methods tend to relax toward the long-term mean in the absence of data, potentially contributing to weaker trends near the beginning of the time series (Fig. 3.32e) where the dominant bottle data are less widespread (Fig. 3.31b). ML approaches are inextricably tied to their predictors (e.g., gridded temperature and salinity) and have more variation in how they are implemented, potentially contributing to greater disagreement among these approaches (Fig. 3.32e). Another important consideration is the shift in observational sources toward profiling floats over time (Fig. 3.31b) and the correction applied to compensate for an apparent, global-mean negative bias (about –1.69 μmol kg^{-1}) in the profiling float dataset relative to colocated bottle and CTD measurements (Gouretski et al. 2024; Wang et al. 2025). Although the negative bias is adjusted for in the O_2 dataset, steep declines in some of the SI maps in recent years when float data are particularly dominant suggest that the +1.69 μmol kg^{-1} adjustment to the float dataset may be insufficient, or that the spatial variation in the float O_2 bias requires a more complex adjustment (Bittig and Körtzinger 2017; Maurer et al. 2021).

O_2 anomalies in 2025 (relative to 1990–2020) were broadly negative (Figs. 3.33a,b), consistent with the long-term deoxygenation trend (Figs. 3.33e,f). Strong negative anomalies from 0 m–50 m in the midlatitude western Pacific corresponded with strong positive SST, heat content, and sea level anomalies in the same region (sections 3b,c,f, respectively). Similarly, negative near-surface

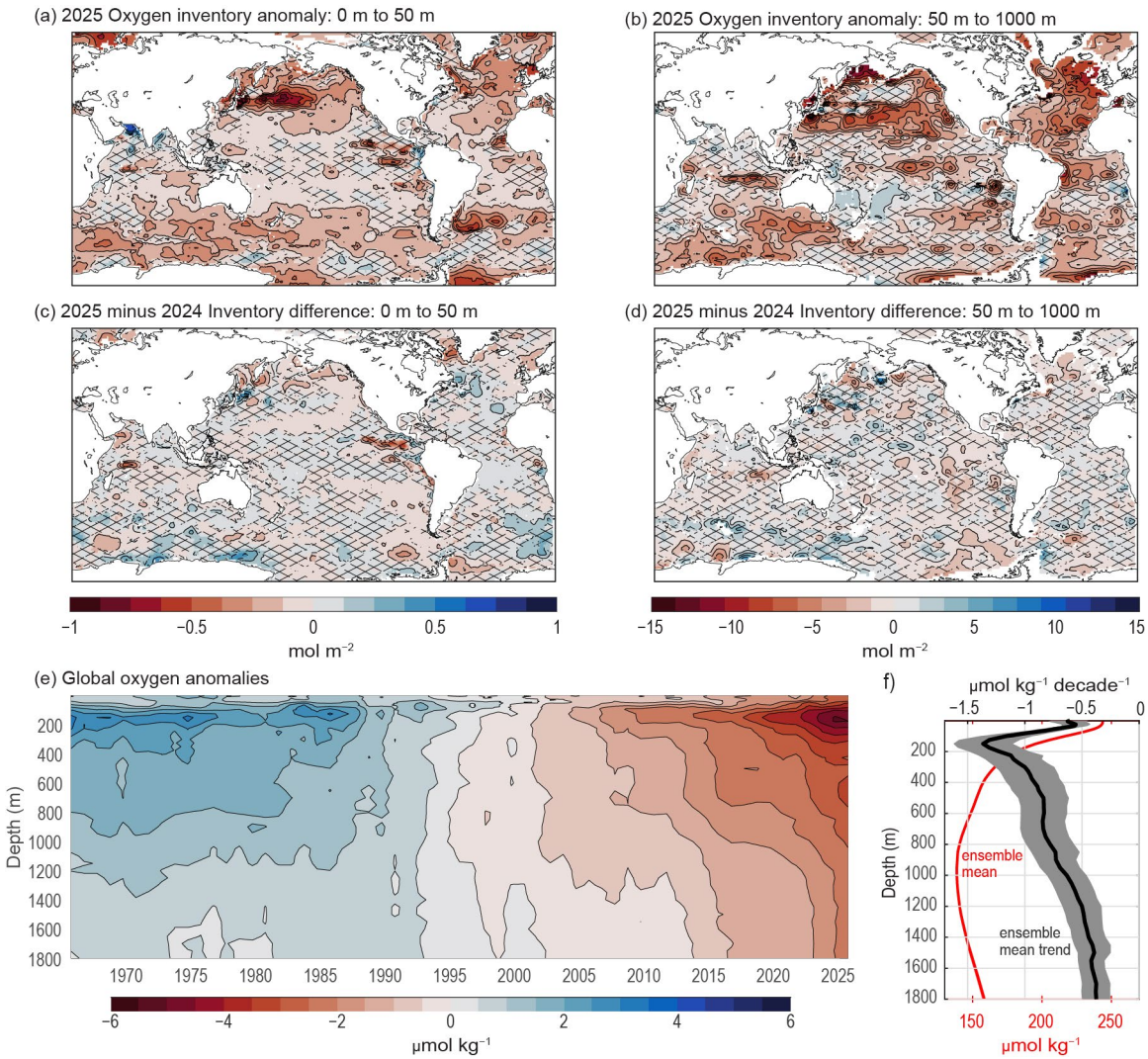

Fig. 3.33. Ensemble mean dissolved oxygen (O_2) inventory anomalies (mol m^{-2}) in 2025 compared to the 1990–2020 baseline from (a) 0 m to 50 m and (b) 50 m to 1000 m; the difference between the ensemble mean inventory in 2025 versus in 2024 (mol m^{-2}) from (c) 0 m to 50 m and (d) 50 m to 1000 m; (e) the global ensemble mean [O_2] anomaly as a function of depth over time (μmol kg^{-1}) ; and (f) the ensemble average profile of [O_2; μmol kg^{-1}; red] and decadal [O_2; μmol kg^{-1} decade^{-1}; black] trends (units for the x-axes are listed in the labels within the plot area). Each ensemble average map (a)–(d) is computed across eight of the nine mapping approaches (SJTU-GR excluded). Areas in the maps where fewer than six out of the eight products agree on the sign of the anomalies are cross-hatched.

anomalies are observed in the Southern Ocean from 45°S to 55°S as well as the Weddell and Ross Seas. On the contrary, near-zero O_2 anomalies from 0 m–50 m in much of the equatorial Pacific were associated with negative SST, heat content, and sea level anomalies, consistent with a weak intermittent La Niña in 2025 (see section 4b for details). From 50 m–1000 m, strong negative O_2 anomalies occurred in the North Pacific and North Atlantic, consistent with positive heat content anomalies in these regions (Fig. 3.4). Apparent positive O_2 anomalies in the subpolar North Pacific (Fig. 3.33b) surrounded by negative anomalies in both subtropical waters to the south and polar waters to the north is consistent with recent findings of a decadal northward displacement of the subtropical and subpolar gyre boundaries caused by the northward contraction of the Aleutian Low (e.g., Minobe 2025), which can be driven by the superposition of internal variability and anthropogenic trends (Abe and Minobe 2023; Long et al. 2016). A moderate positive anomaly is also observed in the western subtropical South Pacific.

Differences between the 2025 and 2024 anomalies were mostly small (Figs. 3.33c,d). The oxygen levels in the eastern equatorial Pacific are known to covary with the thermocline shoaling in the region with implications to the regional ecosystem and air–sea oxygen exchange (Eddebbar et al. 2017; Leung et al. 2019; Parouffe et al. 2025). The tropical Pacific Ocean is influenced by the interannual climate variability associated with ENSO, and the lower O_2 in the near-surface eastern equatorial Pacific in 2025 (Fig. 3.33c) may have been connected to the superposition of weak La Niña conditions with the long-term trends.

Appendix 1: Acronyms

ACC	Antarctic Circumpolar Current
ADCPs	acoustic doppler current profilers
AOML	Atlantic Oceanographic and Meteorological Laboratory
BASS	Blended Analysis of Surface Salinity
b_{bp}	particle backscattering coefficient
C_{ant}	anthropogenic CO_2
CAS	Chinese Academy of Sciences
CDS	Climate Data Store
Chl *a*	chlorophyll-*a*
CIMAR	Cooperative Institute for Marine and Atmospheric Research
Cinventory	changes in the total ocean inventory
CO_2	carbon dioxide
C_{phy}	phytoplankton carbon
CSIRO	Commonwealth Scientific and Industrial Research Organisation
CTD	conductivity temperature and depth
DCENT	Dynamically Consistent ENsemble of Temperature
DIC	dissolved inorganic carbon
DOISST	Daily OISST
EBAF	Energy Balanced and Filled
ENSO	El Niño–Southern Oscillation
fCO_{2w}	surface ocean fugacity of CO_2
FLASHFlux	Fast Longwave And Shortwave Radiative Fluxes
GCB	Global Carbon Budget
GIA	glacial isostatic adjustment
GMSL	global mean sea level
GPCP	Global Precipitation Climatology Project
GRACE	Gravity Recovery and Climate Experiment
GRACE-FO	GRACE Follow-On
HadSST	Hadley Centre Sea Surface Temperature
IAP	Institute of Atmospheric Physics
IIT	Indian Institutes of Technology
IOD	Indian Ocean dipole
ITCZ	Intertropical Convergence Zone
JPL	Jet Propulsion Laboratory
LH	latent heat flux
LW	longwave radiation
MBT	mechanical bathythermograph
MCS	marine cold spell
MHT	meridional heat transport
MHW	marine heatwave
ML	machine learning
MOC	meridional overturning circulation
MODIS-A	Moderate Resolution Imaging Spectroradiometer on Aqua
MOVE	Meridional Overturning Variability Experiment
MRI	Meteorological Research Institute
NDBC	National Data Buoy Center
NH	Northern Hemisphere
NOC	National Oceanography Centre
OC	organic carbon

OHCA	ocean heat content anomaly
ORAS5	Ocean ReAnalysis System 5
OSNAP	Overturning in the Subpolar North Atlantic Program
pCO_2	partial pressure of CO_2
PDO	Pacific Decadal Oscillation
PMEL	Pacific Marine Environmental Laboratory
PSO	permanently stratified ocean
PSS-78	Practical Salinity Scale-78
Q_{net}	net surface heat flux
RAPID	Rapid Climate Change
RFROM	Random Forest Regression Ocean Maps
SAMBA	South Atlantic MOC Basin-wide Array
SAR	synthetic aperture radar
SH	Southern Hemisphere
SI	statistical interpolation
SIO	Scripps Institution of Oceanography
SMAP	Soil Moisture Active Passive
SMOS	Soil Moisture and Ocean Salinity
SOCAT	Surface Ocean CO_2 Atlas
S_{ocean}	steady ocean CO_2 sink
SOM-FNN	self-organizing maps feed-forward neural network
SPCZ	South Pacific Convergence Zone
SSH	sea surface height
SSS	sea surface salinity
SST	sea surface temperature
SSTA	sea surface temperature anomaly
SSTAs	sea surface temperature anomalies
SSTs	sea surface temperatures
SW	shortwave radiation
SWOT	Surface Water and Ocean Topography
TAO	Tropical Atmosphere Ocean
TOA	Top-Of-Atmosphere
TPOS	Tropical Pacific Observing System
VIIRS-N20	Visible Infrared Imaging Radiometer Suite on NOAA20
VLIZ	Flanders Marine Institute
W_{EK}	Ekman vertical velocity
WHOI	Woods Hole Oceanographic Institution
XBT	Expendable Bathythermograph
ΔC_{ant}	anthropogenic accumulation
ΔC_{nat}	natural variations

Appendix 2: Dataset Tables

Section 3b Sea surface temperature

Sub-section	General Variable or Phenomenon	Specific Dataset or Variable	Source
3b	Sea Surface Temperature	Dynamically Consistent ENsemble of Temperature (DCENT) Version 1.1	https://doi.org/10.7910/DVN/ROG38Q
3b	Sea Surface Temperature	ERSSTv5	https://doi.org/10.7289/V5T72FNM
3b	Sea Surface Temperature	Hadley Centre Sea Surface Temperature Dataset (HadSST) Version 4	https://www.metoffice.gov.uk/hadobs/hadsst4/
3b	Sea Surface Temperature	NOAA Daily Optimum Interpolated Temperature (DOISST) Version 2.1	https://doi.org/10.25921/RE9P-PT57

Section 3c Ocean temperature and heat content

Sub-section	General Variable or Phenomenon	Specific Dataset or Variable	Source
3c	Ocean Heat Content	Argo	http://doi.org/10.17882/42182#125185
3c	Ocean Heat Content	Argo Monthly Climatology	https://sio-argo.ucsd.edu/RG_Climatology.html
3c	Ocean Heat Content	CLIVAR and Carbon Hydrographic Data Office	https://cchdo.ucsd.edu/
3c	Ocean Heat Content	Institute of Atmospheric Physics (IAP)/Chinese Academy of Sciences (CAS)	http://www.ocean.iap.ac.cn/pages/dataService/dataService.html
3c	Ocean Heat Content	Meteorological Research Institute (MRI)/Japan Meteorological Agency (JMA)	https://www.data.jma.go.jp/kaiyou/english/ohc/ohc_global_en.html
3c	Ocean Heat Content	NCEI	https://www.ncei.noaa.gov/access/global-ocean-heat-content/
3c	Ocean Heat Content	Pacific Marine Environmental Laboratory (PMEL)/Jet Propulsion Laboratory (JPL)/ Cooperative Institute for Marine and Atmospheric Research (CIMAR)	https://www.pmel.noaa.gov/rfrom/
3c	Ocean Heat Content	Random Forest Regression Ocean Maps (RFROM) Version 2.2	https://www.pmel.noaa.gov/rfrom/
3c	Ocean Heat Content	UK Met Office EN4.2.2	https://www.metoffice.gov.uk/hadobs/en4/download-en4-2-2.html

Sub-section	General Variable or Phenomenon	Specific Dataset or Variable	Source
3c	Ocean Heat Content	University of Colorado/ Carnegie Mellon University (CU/CMU)	https://doi.org/10.5281/zenodo.18187866
3c	Ocean Temperature	World Ocean Database	https://www.ncei.noaa.gov/products/world-ocean-database

Section 3d Salinity

Sub-section	General Variable or Phenomenon	Specific Dataset or Variable	Source
3d2	Ocean Salinity	Aquarius Version 3.0	http://podaac.jpl.nasa.gov/aquarius
3d2	Ocean Salinity	Argo	https://doi.org/10.17882/42182
3d2	Ocean Salinity	Blended Analysis for Surface Salinity	ftp://ftp.cpc.ncep.noaa.gov/precip/BASS
3d	Ocean Salinity	NCEI Salinity Anomaly	https://www.ncei.noaa.gov/access/global-ocean-heat-content/
3d2	Ocean Salinity	Soil Moisture Active Passive (SMAP)	https://podaac.jpl.nasa.gov/SMAP
3d2	Ocean Salinity	Soil Moisture Ocean Salinity (SMOS)	https://earth.esa.int/eogateway/missions/smos
3d	Ocean Salinity	World Ocean Atlas 2023	https://www.ncei.noaa.gov/products/world-ocean-atlas
3d	Ocean Salinity	World Ocean Database	https://www.ncei.noaa.gov/products/world-ocean-database

Section 3e Global ocean heat, freshwater, and momentum flux

Sub-section	General Variable or Phenomenon	Specific Dataset or Variable	Source
3e1	Air–Sea Fluxes (Shortwave/Longwave Radiation)	CERES FlashFlux	https://asdc.larc.nasa.gov/project/CERES/FLASH_SSF_NOAA20-FM6-VIIRS_Version1B
3e1	Air–Sea Fluxes (Shortwave/Longwave Radiation)	Clouds and the Earth's Radiant Energy System (CERES) Energy Balanced and Filled (EBAF) Version 4.2	https://asdc.larc.nasa.gov/project/CERES/CERES_EBAF_Edition4.2
3e1	Air–Sea Fluxes (Shortwave/Longwave Radiation)	ERA5	https://www.ecmwf.int/en/forecasts/dataset/ecmwf-reanalysis-v5
3e2	Precipitation	GPCPv2.3	https://psl.noaa.gov/data/gridded/data.gpcp.html
3e2	Evaporation	OAFLux2	https://oaflux.whoi.edu/

Sub-section	General Variable or Phenomenon	Specific Dataset or Variable	Source
3e3	Wind Stress	OAFlux2	https://oaflux.whoi.edu/
3e1	Air–Sea Fluxes (Latent Heat/Sensible Heat)	Objectively Analyzed Air–Sea Heat Fluxes (OAFlux2)	https://oaflux.whoi.edu/

Section 3f Sea Level variability and change

Sub-section	General Variable or Phenomenon	Specific Dataset or Variable	Source
3f	Sea Level / Sea Surface Height	Argo	https://sio-argo.ucsd.edu/RG_Climatology.html
3f	Ocean Heat Content	Argo Monthly Climatology	https://sio-argo.ucsd.edu/RG_Climatology.html
3f	Sea Level / Sea Surface Height	Copernicus Climate Change Service (C3S) Altimetry Data	Delayed mode: https://data.marine.copernicus.eu/product/SEALEVEL_GLO_PHY_L4_MY_008_047; Near real time: https://data.marine.copernicus.eu/product/SEALEVEL_GLO_PHY_L4_NRT_008_046
3f	Ocean Mass	Gravity Recovery and Climate Experiment (GRACE)/Grace Follow-On (GRACE-FO)	https://grace.jpl.nasa.gov/data/get-data
3f	Sea Level / Sea Surface Height	NASA Making Earth Science Data Records for Use in Research Environments (MEaSURES)	https://podaac.jpl.nasa.gov/dataset/SEA_SURFACE_HEIGHT_ALT_GRIDS_L4_2SATS_5DAY_6THDEG_V_JPL2205
3f	Sea Level / Sea Surface Height	Tide Gauge	http://uhslc.soest.Hawai'i.edu/

Section 3g Surface currents

Sub-section	General Variable or Phenomenon	Specific Dataset or Variable	Source
3g	Surface Velocity	Drifter/Altimetry/Wind Synthesis Product	1993-2024: https://www.aoml.noaa.gov/ftp/pub/phod/lumpkin/decomp/; 2025: https://www.aoml.noaa.gov/ftp/pub/phod/matthieu.lehenaff/decomp/
3g	Ocean Currents	Global Tropical Moored Buoy Array (GTMBA)	https://www.pmel.noaa.gov/gtmba/

Section 3h Meridional overturning circulation and heat transport			
Sub-section	**General Variable or Phenomenon**	**Specific Dataset or Variable**	**Source**
3h	Ocean Currents	Atlantic Ship of Opportunity Expendable Bathythermograph (XBT)	https://www.aoml.noaa.gov/phod/goos/xbt_network/; https://www.aoml.noaa.gov/phod/hdenxbt/index.php
3h	Ocean Currents	Argo	https://doi.org/10.17882/42182#116315; https://www.aoml.noaa.gov/argo/#argodata
3h	Ocean Currents	ERA5	https://cds.climate.copernicus.eu/datasets/reanalysis-era5-single-levels-monthly-means?tab=overview
3h	Ocean Currents	Florida Current Transport	https://www.aoml.noaa.gov/phod/floridacurrent/data_access.php
3h	Ocean Currents	Global Temperature and Salinity Profile Program (GTSPP)	https://www.ncei.noaa.gov/products/global-temperature-and-salinity-profile-programme
3h	Ocean Currents	Meridional Overturning Variability Experiment (MOVE) array	https://mooring.ucsd.edu/move/
3h	Ocean Currents	Overturning in the Subpolar North Atlantic Program (OSNAP)	https://www.o-snap.org/
3h	Ocean Currents	RAPID–Meridional Overturning Circulation and Heat-flux Array–Western Boundary Time Series (RAPID)	https://rapid.ac.uk/rapidmoc/
3h	Ocean Currents	Sea Level Anomalies	https://doi.org/10.48670/moi-00149; https://doi.org/10.48670/moi-00148
3h	Ocean Currents	Sea Surface Height (Delayed-mode)	https://data.marine.copernicus.eu/product/SEALEVEL_GLO_PHY_L4_MY_008_047/services
3h	Ocean Currents	Sea Surface Height (Near-real time)	https://data.marine.copernicus.eu/product/SEALEVEL_GLO_PHY_L4_NRT_008_046/services
3h	Ocean Currents	South Atlantic MOC Basin-wide Array (SAMBA)	https://www.aoml.noaa.gov/sam/

Section 3i Global ocean phytoplankton			
Sub-section	**General Variable or Phenomenon**	**Specific Dataset or Variable**	**Source**
3i	Daytime Sea Surface Temperature	Moderate Resolution Imaging Spectroradiometer on *Aqua* (MODIS-A) Version R2022.0	https://oceancolor.gsfc.nasa.gov/data/reprocessing/r2022/aqua/
3i	Phytoplankton Chlorophyll Particle Backscattering Coefficient	MODIS-A	https://modis.gsfc.nasa.gov/data/dataprod/chlor_a.php
3i	Phytoplankton Chlorophyll Particle Backscattering Coefficient	Sea-viewing Wide Field-of-view Sensor (SeaWiFS) Version R2022.0	https://oceancolor.gsfc.nasa.gov/data/reprocessing/r2022/seawifs/
3i	Phytoplankton Chlorophyll Particle Backscattering Coefficient	Visible Infrared Imaging Radiometer Suite (VIIRS)-NOAA20 Version R2022.0	https://data.nasa.gov/dataset/noaa-20-viirs-global-mapped-chlorophyll-chl-nrt-data-version-r2022-0

Section 3j Global ocean carbon cycle			
Sub-section	**General Variable or Phenomenon**	**Specific Dataset or Variable**	**Source**
3j3	Ocean Salinity	Argo Monthly Climatology	https://sio-argo.ucsd.edu/RG_Climatology.html
3j3	Ocean Temperature	Argo Monthly Climatology	https://sio-argo.ucsd.edu/RG_Climatology.html
3j2	Mixed Layer Depth	de Boyer Montegut (2004; 2023 update); Monthly Isopycnal & Mixed-layer Ocean Climatology (MMOC)	https://www.seanoe.org/data/00806/91774/; https://www.pmel.noaa.gov/mimoc/
3j2	Winds [Near] Surface	ERA5	https://www.ecmwf.int/en/forecasts/dataset/ecmwf-reanalysis-v5
3j2	Chlorophyll	GlobColour	https://hermes.acri.fr/index.php
3j2	Ocean Salinity	Hadley Center EN4	https://www.metoffice.gov.uk/hadobs/en4/
3j2	Atmospheric Carbon Dioxide	NOAA Greenhouse Gas Marine Boundary Layer Reference	https://gml.noaa.gov/ccgg/mbl/mbl.html
3j2	Sea Surface Temperature	NOAA OISST Version 2.1	https://www.ncei.noaa.gov/products/optimum-interpolation-sst
3j2	Ocean Carbon	Surface Ocean CO_2 Atlas (SOCAT) Version 2024	https://socat.info/index.php/version-2025/

3k Global ocean dissolved oxygen			
Sub-section	**General Variable or Phenomenon**	**Specific Dataset or Variable**	**Source**
3k	Ocean Temperature / Salinity / Oxygen	AP Global Ocean Oxygen	https://doi.org/10.12157/IOCAS.20231208.001
3k	Ocean Temperature / Salinity	EN4 Objective Analyses	https://www.metoffice.gov.uk/hadobs/en4/
3k	Ocean Oxygen	GODIP-DO Mapped Oxygen	https://doi.org/10.5281/zenodo.19892752
3k	Ocean Temperature / Salinity / Oxygen	World Ocean Database 2023	https://doi.org/10.25923/z885-h264

References

Abe, Y., and S. Minobe, 2023: Comparison of ocean deoxygenation between CMIP models and an observational dataset in the North Pacific from 1958 to 2005. *Front. Mar. Sci.*, **10**, 1161451, https://doi.org/10.3389/fmars.2023.1161451.

Adler, R. F., and Coauthors, 2018: The Global Precipitation Climatology Project (GPCP) monthly analysis (new version 2.3) and a review of 2017 global precipitation. *Atmosphere*, **9**, 138, https://doi.org/10.3390/atmos9040138.

Arcodia, M. C., E. A. Barnes, P. J. Durack, P. W. Keys, and J. Rocha, 2025: Sea surface salinity provides subseasonal predictability for forecasts of opportunity of U.S. summertime precipitation. *J. Geophys. Res. Atmos.*, **130**, e2024JD042402, https://doi.org/10.1029/2024JD042402.

Bai, Y., Y. Zhang, X. Zhang, and X. Li, 2025: A machine learning-based ocean current velocity inversion model using Sentinel-1 OCN observations. *IEEE J. Sel. Top. Appl. Earth Obs. Remote Sens.*, **18**, 9622–9635, https://doi.org/10.1109/JSTARS.2025.3554229.

Bakker, D. C. E., and Coauthors, 2016: A multi-decade record of high-quality fCO_2 data in version 3 of the Surface Ocean CO_2 Atlas (SOCAT). *Earth Syst. Sci. Data*, **8**, 383–413, https://doi.org/10.5194/essd-8-383-2016.

——, and Coauthors, 2025: Surface Ocean CO2 Atlas Database version 2025 (SOCATv2025) (NCEI Accession 0304549). NOAA NCEI, accessed 10 July 2025, https://doi.org/10.25921/648f-fv35.

Behrenfeld, M. J., and Coauthors, 2006: Climate-driven trends in contemporary ocean productivity. *Nature*, **444**, 752–755, https://doi.org/10.1038/nature05317.

——, and Coauthors, 2016: Reevaluating ocean warming impacts on global phytoplankton. *Nat. Climate Change*, **6**, 323–330, https://doi.org/10.1038/nclimate2838

Bianchi, D., J. P. Dunne, J. L. Sarmiento, and E. D. Galbraith, 2012: Data-based estimates of suboxia, denitrification, and N_2O production in the ocean and their sensitivities to dissolved O_2. *Global Biogeochem. Cycles*, **26**, GB2009, https://doi.org/10.1029/2011GB004209.

Bindoff, N. L., and Coauthors, 2019: Changing ocean, marine ecosystems, and dependent communities. *Ocean and Cryosphere in a Changing Climate*, H.-O. Pörtner et al., Eds., IPCC, 447–588.

Bittig, H. C., and A. Körtzinger, 2017: Technical note: Update on response times, in-air measurements, and in situ drift for oxygen optodes on profiling platforms. *Ocean Sci.*, **13** (1), 1–11, https://doi.org/10.5194/os-13-1-2017.

Breitburg, D., and Coauthors, 2018: Declining oxygen in the global ocean and coastal waters. *Science*, **359**, eaam7240, https://doi.org/10.1126/science.aam7240.

Broecker, W. S., 1991: The great ocean conveyor. *Oceanography*, **4**, 79–89, https://doi.org/10.5670/oceanog.1991.07.

Caldwell, P. C., M. A. Merrifield, and P. R. Thompson, 2015: Sea level measured by tide gauges from global oceans—The Joint Archive for Sea Level holdings (NCEI Accession 0019568), version 5.5. NOAA NCEI, accessed 9 February 2026, https://doi.org/10.7289/V5V40S7W.

Caron, L., and E. R. Ivins, 2020: A baseline Antarctic GIA correction for space gravimetry. *Earth Planet. Sci. Lett.*, **531**, 115957, https://doi.org/10.1016/j.epsl.2019.115957.

Carter, B. R., J. Schwinger, R. Sonnerup, A. J. Fassbender, J. D. Sharp, L. M. Dias, and D. E. Sandborn, 2025: Tracer-based Rapid Anthropogenic Carbon Estimation (TRACE). *Earth Syst. Sci. Data*, **17**, 3073–3088, https://doi.org/10.5194/essd-17-3073-2025.

——, and Coauthors, 2021: New and updated global empirical seawater property estimation routines. *Limnol. Oceanogr. Methods*, **19**, 785–809, https://doi.org/10.1002/lom3.10461.

Cetinić, I., M. J. Perry, N. T. Briggs, E. Kallin, E. A. D'Asaro, and C. M. Lee, 2012: Particulate organic carbon and inherent optical properties during 2008 North Atlantic bloom experiment. *J. Geophys. Res.*, **117**, C06028, https://doi.org/10.1029/2011JC007771.

Chambers, D. P., A. Cazenave, N. Champollion, H. Dieng, W. Llovel, R. Forsberg, K. von Schuckmann, and Y. Wada, 2017: Evaluation of the global mean sea level budget between 1993 and 2014. *Surv. Geophys.*, **38**, 309–327, https://doi.org/10.1007/s10712-016-9381-3.

Chan, D., and Coauthors, 2026: DCENT-I: A globally infilled extension of the Dynamically Consistent Ensemble of Temperature dataset. *Geosci. Data J.*, **13**, e70054, https://doi.org/10.1002/gdj3.70054.

Cheng, L., and J. Zhu, 2016: Benefits of CMIP5 multimodel ensemble in reconstructing historical ocean subsurface temperature variations. *J. Climate*, **29**, 5393–5416, https://doi.org/10.1175/JCLI-D-15-0730.1.

——, ——, R. Cowley, T. Boyer, and S. Wijffels, 2014: Time, probe type, and temperature variable bias corrections to historical expendable bathythermograph observations. *J. Atmos. Oceanic Technol.*, **31**, 1793–1825, https://doi.org/10.1175/JTECH-D-13-00197.1.

——, and Coauthors, 2020: Improved estimates of changes in upper ocean salinity and the hydrological cycle. *J. Climate*, **33**, 10 357–10 381, https://doi.org/10.1175/JCLI-D-20-0366.1.

Ciani, D., C. Fanelli, and B. Buongiorno Nardelli, 2025: Estimating ocean currents from the joint reconstruction of absolute dynamic topography and sea surface temperature through deep learning algorithms. *Ocean Sci.*, **21**, 199–216, https://doi.org/10.5194/os-21-199-2025.

Copernicus Climate Change Service, 2021: ORAS5 global ocean reanalysis monthly data from 1958 to present. ECMWF, accessed 1 July 2025, https://doi.org/10.24381/CDS.67E8EEB7.

Cummins, P. F., and T. Ross, 2020: Secular trends in water properties at Station P in the northeast Pacific: An updated analysis. *Prog. Oceanogr.*, **186**, 102329, https://doi.org/10.1016/j.pocean.2020.102329.

de Boyer Montégut, C., G. Madec, A. S. Fischer, A. Lazar, and D. Iudicone, 2004: Mixed layer depth over the global ocean: An examination of profile data and a profile-based climatology. *J. Geophys. Res.*, **109**, C12003, https://doi.org/10.1029/2004JC002378.

Deser, C., M. A. Alexander, S.-P. Xie, and A. S. Phillips, 2010: Sea surface temperature variability: Patterns and mechanisms. *Ann. Rev. Mar. Sci.*, **2**, 115–143, https://doi.org/10.1146/annurev-marine-120408-151453.

Deutsch, C., J. L. Penn, and N. Lucey, 2024: Climate, oxygen, and the future of marine biodiversity. *Ann. Rev. Mar. Sci.*, **16**, 217–245, https://doi.org/10.1146/annurev-marine-040323-095231.

DeVries, T., M. Holzer, and F. Primeau, 2017: Recent increase in oceanic carbon uptake driven by weaker upper-ocean overturning. *Nature*, **542**, 215–218, https://doi.org/10.1038/nature21068.

Domingues, C. M., J. A. Church, N. J. White, P. J. Gleckler, S. E. Wijffels, P. M. Barker, and J. R. Dunn, 2008: Improved estimates of upper-ocean warming and multi-decadal sea-level rise. *Nature*, **453**, 1090–1093. https://doi.org/10.1038/nature07080.

Dong, S., G. Goni, and F. Bringas, 2015: Temporal variability of the South Atlantic meridional overturning circulation between 20°S and 35°S. *Geophys. Res. Lett.*, **42**, 7655–7662, https://doi.org/10.1002/2015GL065603.

—— , —— , R. Domingues, F. Bringas, M. Goes, J. Christophersen, and M. Baringer, 2021: Synergy of in situ and satellite ocean observations in determining meridional heat transport in the Atlantic Ocean. *J. Geophys. Res. Oceans*, **126**, e2020JC017073, https://doi.org/10.1029/2020JC017073.

Donohoe, A., R. Fajber, T. Cox, K. C. Armour, D. S. Battisti, and G. H. Roe, 2024: Model biases in the atmosphere?ocean partitioning of poleward heat transport are persistent across three CMIP generations. *Geophys. Res. Lett.*, **51**, e2023GL106639, https://doi.org/10.1029/2023GL106639.

Durack, P. J., and S. E. Wijffels, 2010: Fifty-year trends in global ocean salinities and their relationship to broad-scale warming. *J. Climate*, **23**, 4342–4362, https://doi.org/10.1175/2010JCLI3377.1.

—— , —— , and R. J. Matear, 2012: Ocean salinities reveal strong global water cycle intensification during 1950 to 2000. *Science*, **336**, 455–458, https://doi.org/10.1126/science.1212222.

Eddebbar, Y. A., M. C. Long, L. Resplandy, C. Rödenbeck, K. B. Rodgers, M. Manizza, and R. F. Keeling, 2017: Impacts of ENSO on air-sea oxygen exchange: Observations and mechanisms. *Global Biogeochem. Cycles*, **31**, 901–921, https://doi.org/10.1002/2017GB005630.

Fairall, C. W., E. F. Bradley, J. E. Hare, A. A. Grachev, and J. B. Edson, 2003: Bulk parameterization of air–sea fluxes: Updates and verification for the COARE algorithm. *J. Climate*, **16**, 571–591, https://doi.org/10.1175/1520-0442(2003)016<0571:BPOASF>2.0.CO;2.

Fasullo, J. T., C. Boening, F. W. Landerer, and R. S. Nerem, 2013: Australia's unique influence on global sea level in 2010–2011. *Geophys. Res. Lett.*, **40**, 4368–4373, https://doi.org/10.1002/grl.50834.

—— , R. Nerem, and B. Hamlington, 2016: Is the detection of accelerated sea level rise imminent?. *Sci. Rep.*, **6**, 31245, https://doi.org/10.1038/srep31245.

Fay, A. R., T. H. Heimdal, V. Acquaviva, A. P. Shaum, and G. A. McKinley, 2025: Sensitivity of ocean carbon sink estimates to rare observations. *Geophys. Res. Lett.*, **52**, e2025GL117961, https://doi.org/10.1029/2025GL117961.

Field, C. B., M. J. Behrenfeld, J. T. Randerson, and P. Falkowski, 1998: Primary production of the biosphere: Integrating terrestrial and oceanic components. *Science*, **281**, 237–240, https://doi.org/10.1126/science.281.5374.237.

Fofonoff, N. P., and E. L. Lewis, 1979: A practical salinity scale. *J. Oceanogr. Soc. Japan*, **35**, 63–64, https://doi.org/10.1007/BF02108283.

Font, J., and Coauthors, 2013: SMOS first data analysis for sea surface salinity determination. *Int. J. Remote Sens.*, **34**, 3654–3670, https://doi.org/10.1080/01431161.2012.716541.

Fore, A. G., S. H. Yueh, W. Q. Tang, B. W. Stiles, and A. K. Hayashi, 2016: Combined active/passive retrievals of ocean vector wind and sea surface salinity with SMAP. IEEE Trans. *Geosci. Remote Sens.*, **54**, 7396–7404, https://doi.org/10.1109/TGRS.2016.2601486.

Forster, P. M., and Coauthors, 2025: Indicators of global climate change 2024: Annual update of key indicators of the state of the climate system and human influence. *Earth Syst. Sci. Data*, **17**, 2641–2680, https://doi.org/10.5194/essd-17-2641-2025.

Friedlingstein, P., and Coauthors, 2026: Global carbon budget 2025. *Earth Syst. Sci. Data*, **18**, 3211–3288, https://doi.org/10.5194/essd-2025-659.

Fu, Y., and Coauthors, 2025: Characterizing the interannual variability of North Atlantic subpolar overturning. *Geophys. Res. Lett.*, **52**, e2025GL114672, https://doi.org/10.1029/2025GL114672.

Garcia, H. E., T. P. Boyer, S. Levitus, R. A. Locarnini, and J. Antonov, 2005: On the variability of dissolved oxygen and apparent oxygen utilization content for the upper world ocean: 1955 to 1998. *Geophys. Res. Lett.*, **32**, L09604, https://doi.org/10.1029/2004GL022286.

—— ., and Coauthors, 2024a: *Dissolved Oxygen, Apparent Oxygen Utilization, and Dissolved Oxygen Saturation*. Vol. 3, *World Ocean Atlas 2023*, NOAA Atlas NESDIS 91, 110 pp., https://doi.org/10.25923/RB67-NS53.

—— , and Coauthors, 2024b: *User's Manual*. World Ocean Database 2023, A. V. Mishonov, Tech. Ed., NOAA Atlas NESDIS 98, 134 pp., https://doi.org/10.25923/j8gq-ee82.

Garcia, P., and Coauthors, 2025: ORCAst: Operational high-resolution current forecasts. *Artif. Intell. Earth Syst.*, **4**, e250002, https://doi.org/10.1175/AIES-D-25-0002.1.

Garcia-Soto, C., and Coauthors, 2021: An overview of ocean climate change indicators: Sea surface temperature, ocean heat content, ocean pH, dissolved oxygen concentration, Arctic sea ice extent, thickness and volume, sea level and strength of the AMOC (Atlantic meridional overturning circulation). *Front. Mar. Sci.*, **8**, 642372, https://doi.org/10.3389/fmars.2021.642372.

Ge, L., G. Chen, G. Wang, C. Cao, X. Chen, and B. Huang, 2025: Multiscale dynamics-informed deep learning reconstruction of global ocean offshore near-surface current. *GISci. Remote Sens.*, **62**, 2596455, https://doi.org/10.1080/15481603.2025.2596455.

Geider, R. J., H. L. MacIntyre, and T. M. Kana, 1997: Dynamic model of phytoplankton growth and acclimation: Responses of the balanced growth rate and the chlorophyll a: Carbon ratio to light, nutrient-limitation and temperature. *Mar. Ecol. Prog. Ser.*, **148**, 187–200, https://doi.org/10.3354/meps148187.

Good, S. A., M. J. Martin, and N. A. Rayner, 2013: EN4: Quality controlled ocean temperature and salinity profiles and monthly objective analyses with uncertainty estimates. *J. Geophys. Res. Oceans*, **118**, 6704–6716, https://doi.org/10.1002/2013JC009067.

Gordon, A. L., 1986: Interocean exchange of thermocline water. *J. Geophys. Res.*, **91**, 5037–5046, https://doi.org/10.1029/JC091iC04p05037.

Gouretski, V., and L. Cheng, 2020: Correction for systematic errors in the global dataset of temperature profiles from mechanical bathythermographs. *J. Atmos. Oceanic Technol.*, **37**, 841–855, https://doi.org/10.1175/JTECH-D-19-0205.1.

—— , —— , J. Du, X. Xing, F. Chai, and Z. Tan, 2024: A consistent ocean oxygen profile dataset with new quality control and bias assessment. *Earth Syst. Sci. Data*, **16**, 5503–5530, https://doi.org/10.5194/essd-16-5503-2024.

Graff, J. R., T. K. Westberry, A. J. Milligan, M. B. Brown, G. Dall'Olmo, V. V Dongen-Vogels, K. M. Reifel, and M. J. Behrenfeld, 2015: Analytical phytoplankton carbon measurements spanning diverse ecosystems. *Deep-Sea Res. I*, **102**, 16–25, https://doi.org/10.1016/j.dsr.2015.04.006.

—— , —— , —— , —— , —— , —— , —— , and —— , 2016: Photoacclimation of natural phytoplankton communities. *Mar. Ecol. Prog. Ser.*, **542**, 51–62, https://doi.org/10.3354/meps11539.

Gruber, N., 2008: The marine nitrogen cycle: Overview and challenges. *Nitrogen in the Marine Environment*, Vol. 2, Academic Press, 1–50.

——, 2011: Warming up, turning sour, losing breath: Ocean biogeochemistry under global change. *Philos. Trans. Roy. Soc.*, **A369**, 1980–1996, https://doi.org/10.1098/rsta.2011.0003.

Hamlington, B. D., and Coauthors, 2024: The rate of global sea level rise doubled during the past three decades. *Commun. Earth Environ.*, **5**, 601, https://doi.org/10.1038/s43247-024-01761-5.

Han, M., X. Xing, and Y. Zhou, 2025: Global Monthly Ocean Dissolved Oxygen (1960–2023) reconstructed to 5,902 m with BLENDR, a Bayesian-optimized ensemble learning framework. *Earth Syst. Sci. Data*, **18**, 3757–3777, https://doi.org/10.5194/essd-2025-781.

Hauck, J., and Coauthors, 2023: The Southern Ocean carbon cycle 1985–2018: Mean, seasonal cycle, trends, and storage. *Global Biogeochem. Cycles*, **37**, e2023GB007848, https://doi.org/10.1029/2023GB007848.

Held, I. M., and B. J. Soden, 2006: Robust responses of the hydrological cycle to global warming. *J. Climate*, **19**, 5686–5699, https://doi.org/10.1175/JCLI3990.1.

Helm, K. P., N. L. Bindoff, and J. A. Church, 2011: Observed decreases in oxygen content of the global ocean. *Geophys. Res. Lett.*, **38**, L23602, https://doi.org/10.1029/2011GL049513.

Henley, B. J., J. Gergis, D. J. Karoly, S. B. Power, J. Kennedy, and C. K. Folland, 2015: A tripole index for the interdecadal Pacific oscillation. *Climate Dyn.*, **45**, 3077–3090, https://doi.org/10.1007/s00382-015-2525-1.

Hersbach, H., and Coauthors, 2018: ERA5 hourly data on single levels from 1959 to present. Copernicus Climate Change Service (C3S) Climate Data Store (CDS), accessed 2 January 2024, https://doi.org/10.24381/cds.adbb2d47.

——, and Coauthors, 2020: The ERA5 global reanalysis. *Quart. J. Royal Meteor. Soc.*, **146**, 1999–2049. https://doi.org/10.1002/qj.3803.

Hobbs, W. R., and J. K. Willis, 2012: Midlatitude North Atlantic heat transport: A time series based on satellite and drifter data. *J. Geophys. Res.*, **117**, C01008, https://doi.org/10.1029/2011JC007039.

Hobday, A. J., and Coauthors, 2016: A hierarchical approach to defining marine heatwaves. *Prog. Oceanogr.*, **141**, 227–238, https://doi.org/10.1016/j.pocean.2015.12.014.

——, and Coauthors, 2018: Categorizing and naming marine heatwaves. *Oceanography*, **31** (2), 162–173, https://doi.org/10.5670/oceanog.2018.205.

Hu, C., Z. Lee, and B. Franz, 2012: Chlorophyll *a* algorithms for oligotrophic oceans: A novel approach based on three-band reflectance difference. *J. Geophys. Res.*, **117**, C01011, https://doi.org/10.1029/2011JC007395.

——, L. Feng, Z. Lee, B. A. Franz, S. W. Bailey, P. J. Werdell, and C. W. Proctor, 2019: Improving satellite global chlorophyll *a* data products through algorithm refinement and data recovery. *J. Geophys. Res. Oceans*, **124**, 1524–1543, https://doi.org/10.1029/2019JC014941.

Hu, Z.-Z., M. J. McPhaden, B. Huang, J. Zhu, and Y. Liu, 2024: Accelerated warming in the North Pacific since 2013. *Nat. Climate Change*, **14**, 929–931, https://doi.org/10.1038/s41558-024-02088-x.

Huang, B., and Coauthors, 2015: Extended reconstructed sea surface temperature version 4 (ERSST.v4). Part I: Upgrades and intercomparisons. *J. Climate*, **28**, 911–930, https://doi.org/10.1175/JCLI-D-14-00006.1.

——, and Coauthors, 2017: Extended reconstructed sea surface temperature, version 5 (ERSSTv5): Upgrades, validations, and intercomparisons. *J. Climate*, **30**, 8179–8205, https://doi.org/10.1175/JCLI-D-16-0836.1.

——, and Coauthors, 2020: Uncertainty estimates for sea surface temperature and land surface air temperature in NOAAGlobalTemp version 5. *J. Climate*, **33**, 1351–1379, https://doi.org/10.1175/JCLI-D-19-0395.1.

——, C. Liu, V. Banzon, E. Freeman, G. Graham, B. Hankins, T. Smith, and H.-M. Zhang, 2021: Improvements of the Daily Optimum Interpolation Sea Surface Temperature (DOISST) version 2.1. *J. Climate*, **34**, 2923–2939, https://doi.org/10.1175/JCLI-D-20-0166.1.

Hughes, T. P., and Coauthors, 2017: Global warming and recurrent mass bleaching of corals. *Nature*, **543**, 373–377, https://doi.org/10.1038/nature21707.

Ishii, M., Y. Fukuda, S. Hirahara, S. Yasui, T. Suzuki, and K. Sato, 2017: Accuracy of global upper ocean heat content estimation expected from present observational data sets. *SOLA*, **13**, 163–167, https://doi.org/10.2151/sola.2017-030.

Ito, T., 2022: Optimal interpolation of global dissolved oxygen: 1965–2015. *Geosci. Data J.*, **9**, 167–176, https://doi.org/10.1002/gdj3.130.

——, S. Minobe, M. C. Long, and C. Deutsch, 2017: Upper ocean O_2 trends: 1958–2015. *Geophys. Res. Lett.*, **44**, 4214–4223, https://doi.org/10.1002/2017GL073613.

——, A. Cervania, K. Cross, S. Ainchwar, and S. Delawalla, 2024: Mapping dissolved oxygen concentrations by combining shipboard and Argo observations using machine learning algorithms. *J. Geophys. Res. Mach. Learn. Comput.*, **1**, e2024JH000272, https://doi.org/10.1029/2024JH000272.

——, and Coauthors, 2025: Assessing the observational uncertainties of dissolved oxygen climatology and seasonal cycle through a coordinated intercomparison project. *Global Biogeochem. Cycles*, **39**, e2025GB008751, https://doi.org/10.1029/2025GB008751.

——, and Coauthors, 2026: Are simulated ocean deoxygenation rates consistent with the observational reconstructions? *Annu. Rev. Earth Planet. Sci.*, **54**, 239–267, https://doi.org/10.1146/annurev-earth-032524-123111.

Jersild, A. J., and P. Landschützer, 2024: A spatially explicit uncertainty analysis of the air-sea CO_2 flux from observations. *Geophys. Res. Lett.*, **51**, e2023GL106636, https://doi.org/10.1029/2023GL106636.

Johns, W. E., S. Elipot, D. A. Smeed, B. I. Moat, B. King, D. L. Volkov, and R. H. Smith, 2023: Towards two decades of Atlantic Ocean mass and heat transports at 26.5°N. Philos. *Trans. Roy. Soc.*, **A381**, 20220188, https://doi.org/10.1098/rsta.2022.0188.

Johnson, G. C., and J. M. Lyman, 2012: Sea surface salinity [in "State of the Climate in 2011"]. *Bull. Amer. Meteor. Soc.*, **93** (7), S68–S69, S72, https://doi.org/10.1175/2012BAMSStateofTheClimate.1.

——, and S. G. Purkey, 2024: Refined estimates of global ocean deep and abyssal decadal warming trends. *Geophys. Res. Lett.*, **51**, e2024GL111229, https://doi.org/10.1029/2024GL111229.

——, and J. M. Lyman, 2025: Sea surface salinity [in "State of the Climate in 2024"]. *Bull. Amer. Meteor. Soc.*, **106** (8), S190–S192, https://doi.org/10.1175/2025BAMSStateoftheClimate.1.

——, ——, J. K. Willis, T. Boyer, J. Antonov, S. A. Good, C. M. Domingues, and N. Bindoff, 2014: Ocean heat content [in "State of the Climate in 2013"]. *Bull. Amer. Meteor. Soc.*, **95** (7), S54–S57, https://doi.org/10.1175/2014BAMSStateoftheClimate.1.

—— , and Coauthors, 2015: Ocean heat content [in "State of the Climate in 2014"]. *Bull. Amer. Meteor. Soc.*, **96** (7), S64–S66, S68, https://doi.org/10.1175/2015BAMSStateoftheClimate.1.

—— , and Coauthors, 2025: Ocean heat content [in "State of the Climate in 2024"]. *Bull. Amer. Meteor. Soc.*, **106** (8), S186–S190, https://doi.org/10.1175/BAMS-D-25-0074.1.

Kato, S., and Coauthors, 2018: Surface irradiances of edition 4.0 clouds and the Earth's Radiant Energy System (CERES) Energy Balanced and Filled (EBAF) data product. *J. Climate*, **31**, 4501–4527, https://doi.org/10.1175/JCLI-D-17-0523.1.

Keeling, R. F., K. Arne, and N. Gruber, 2010: Ocean deoxygenation in a warming world. *Ann. Rev. Mar. Sci.*, **2**, 199–229, https://doi.org/10.1146/annurev.marine.010908.163855.

Kendon, M., and Coauthors, 2024: State of the UK climate 2023. *Int. J. Climatol.*, **44**, 1–117, https://doi.org/10.1002/joc.8553.

Kennedy, J. J., N. A. Rayner, C. P. Atkinson, and R. E. Killick, 2019: An ensemble data set of sea surface temperature change from 1850: The Met Office Hadley Centre HadSST.4.0.0.0 data set. *J. Geophys. Res. Atmos.*, **124**, 7719–7763, https://doi.org/10.1029/2018JD029867.

Keppler, L., P. Landschützer, S. K., and N. Gruber, 2023: Recent trends and variability in the oceanic storage of dissolved inorganic carbon. *Global Biogeochem. Cycles*, **37**, e2022GB007677, https://doi.org/10.1029/2022GB007677.

Kumar, P., B. Hamlington, S. Cheon, W. Han, and P. Thompson, 2020: 20th century multivariate Indian Ocean regional sea level reconstruction. *J. Geophys. Res. Oceans*, **125**, e2020JC016270, https://doi.org/10.1029/2020JC016270.

Lan, X., and Coauthors, 2023: NOAA greenhouse gas marine boundary layer reference–CO_2. NOAA GML, accessed 30 Jan 2026, https://doi.org/10.15138/DVNP-F961.

Landschützer, P., N. Gruber, D. C. E. Bakker, U. Schuster, S. Nakaoka, M. R. Payne, T. P. Sasse, and J. Zeng, 2013: A neural network-based estimate of the seasonal to inter-annual variability of the Atlantic Ocean carbon sink. *Biogeosciences*, **10**, 7793–7815, https://doi.org/10.5194/bg-10-7793-2013.

—— , N. Gruber, D. C. E. Bakker, and U. Schuster, 2014: Recent variability of the global ocean carbon sink. *Global Biogeochem. Cycles*, **28**, 927–949, https://doi.org/10.1002/2014GB004853.

Leuliette, E. W., and J. K. Willis, 2011: Balancing the sea level budget. *Oceanography*, **24** (2), 122–129, https://doi.org/10.5670/oceanog.2011.32.

Leung, S., L. Thompson, M. J. McPhaden, and K. A. S. Mislan, 2019: ENSO drives near-surface oxygen and vertical habitat variability in the tropical Pacific. *Environ. Res. Lett.*, **14**, 064020, https://doi.org/10.1088/1748-9326/ab1c13.

Levin, L. A., 2018: Manifestation, drivers, and emergence of open ocean deoxygenation. *Ann. Rev. Mar. Sci.*, **10**, 229–260, https://doi.org/10.1146/annurev-marine-121916-063359.

Le Vine, D. M., E. P. Dinnat, G. S. E. Lagerloef, P. de Matthaeis, S. Abraham, C. Utku, and H. Kao, 2014: Aquarius: Status and recent results. *Radio Sci.*, **49**, 709–720, https://doi.org/10.1002/2014RS005505.

Levitus, S., and Coauthors, 2012: World ocean heat content and thermosteric sea level change (0–2000 m), 1955–2010. *Geophys. Res. Lett.*, **39**, L10603, https://doi.org/10.1029/2012GL051106.

Li, G., L. Cheng, J. Zhu, K. E. Trenberth, M. E. Mann, and J. P. Abraham, 2020: Increasing ocean stratification over the past half-century. *Nat. Climate Change*, **10**, 1116–1123, https://doi.org/10.1038/s41558-020-00918-2.

Li, L., R. W. Schmitt, C. C. Ummenhofer, and K. B. Karnauskas, 2016: North Atlantic salinity as a predictor of Sahel rainfall. *Sci. Adv.*, **2**, e150158, https://doi.org/10.1126/sciadv.1501588.

Li, S., and Coauthors, 2022: Contributions of different sea-level processes to high-tide flooding along the U.S. Coastline. *J. Geophys. Res. Oceans*, **127**, e2021JC018276, https://doi.org/10.1029/2021JC018276.

Loeb, N. G., and Coauthors, 2018: Clouds and the Earth's Radiant Energy System (CERES) Energy Balanced and Filled (EBAF) Top-of-Atmosphere (TOA) edition-4.0 data product. *J. Climate*, **31**, 895–918, https://doi.org/10.1175/JCLI-D-17-0208.1.

—— , G. C. Johnson, T. J. Thorsen, J. M. Lyman, F. G. Rose, and S. Kato, 2021: Satellite and ocean data reveal marked increase in Earth's heating rate. *Geophys. Res. Lett.*, **48**, e2021GL093047, https://doi.org/10.1029/2021GL093047.

—— , D. R. Doelling, S. Kato, W. Su, P. E. Mlynczak, and J. C. Wilkins, 2024: Continuity in top-of-atmosphere Earth radiation budget observations. *J. Climate*, **37**, 6093–6108, https://doi.org/10.1175/JCLI-D-24-0180.1.

Long, M. C., C. Deutsch, and T. Ito, 2016: Finding forced trends in oceanic oxygen. *Global Biogeochem. Cycles*, **30**, 381–397, https://doi.org/10.1002/2015GB005310.

Long, X., M. J. Widlansky, F. Schloesser, P. R. Thompson, H. Annamalai, M. A. Merrifield, and H. Yoon, 2020: Higher sea levels at Hawaii caused by strong El Niño and weak trade winds. *J. Climate*, **33**, 3037–3059, https://doi.org/10.1175/JCLI-D-19-0221.1.

Lozier, M. S., and Coauthors, 2017: Overturning in the subpolar North Atlantic program: A new international ocean observing system. *Bull. Amer. Meteor. Soc.*, **98**, 737–752, https://doi.org/10.1175/BAMS-D-16-0057.1.

—— , and Coauthors, 2019: A sea change in our view of overturning in the subpolar North Atlantic. *Science*, **363**, 516–521, https://doi.org/10.1126/science.aau6592.

Lu, B., and Coauthors, 2024: OxyGenerator: Reconstructing global ocean deoxygenation over a century with deep learning. *Proceedings of Machine Learning Research*, Vol. 235, PMLR, 33 219–33 242.

Lumpkin, R., G. Goni, and K. Dohan, 2012: Surface currents [in "State of the Climate in 2011"]. *Bull. Amer. Meteor. Soc.*, **93** (7), S75–S78, https://doi.org/10.1175/2012BAMSStateoftheClimate.1.

—— , M. Le Hénaff, F. P. Tuchen, and R. C. Perez, 2025: Surface currents [in "State of the Climate in 2024"]. *Bull. Amer. Meteor. Soc.*, **106** (8), S204–S207, https://doi.org/10.1175/BAMS-D-25-0074.1.

Lyman, J. M., and G. C. Johnson, 2014: Estimating global ocean heat content changes in the upper 1800 m since 1950 and the influence of climatology choice. *J. Climate*, **27**, 1946–1958, https://doi.org/10.1175/JCLI-D-12-00752.1.

—— , and —— , 2023: Global high-resolution random forest regression maps of ocean heat content anomalies using in situ and satellite data. *J. Atmos. Oceanic Technol.*, **40**, 575–586, https://doi.org/10.1175/JTECH-D-22-0058.1.

Maritorena, S., O. H. F. d'Andon, A. Mangin, and D. A. Siegel, 2010: Merged satellite ocean color data products using a bio-optical model: Characteristics, benefits and issues. *Remote Sens. Environ.*, **114**, 1791–1804, https://doi.org/10.1016/j.rse.2010.04.002.

Maurer, T. L., J. N. Plant, and K. S. Johnson, 2021: Delayed-mode quality control of oxygen, nitrate, and pH data on SOCCOM biogeochemical profiling floats. *Front. Mar. Sci.*, **8**, 683207, https://doi.org/10.3389/fmars.2021.683207.

McCarthy, G. D., G. Hug, D. A. Smeed, K. J. Morris, and B. I. Moat, 2025: Signal and noise in the Atlantic meridional overturning circulation at 26°N. *Geophys. Res. Lett.*, **52**, e2025GL115055, https://doi.org/10.1029/2025GL115055.

McKinna, L. I. W., P. J. Werdell, and C. W. Proctor, 2016: Implementation of an analytical Raman scattering correction for satellite ocean-color processing. *Opt. Express*, **24**, A1123–A1137, https://doi.org/10.1364/OE.24.0A1123.

McPhaden, M. J., K. J. Connell, G. R. Foltz, R. C. Perez, and K. Grissom, 2023: Tropical ocean observations for weather and climate: A decadal overview of the global tropical moored buoy array. *Oceanography*, **36** (2–3), 32–43, https://doi.org/10.5670/oceanog.2023.211.

Minobe, S., 2025: Exceptional heat and basin-scale connections in the Kuroshio–Oyashio region in the early 2020s. *J. Oceanogr.*, **81**, 443–461, https://doi.org/10.1007/s10872-025-00764-w.

Mishonov, A. V., and Coauthors, 2024: World Ocean Database 2023. NOAA Atlas NESDIS 97, accessed 11 January 2026, https://doi.org/10.25923/Z885-H264.

Moat, B. I., and Coauthors, 2026: Atlantic meridional overturning circulation observed by the RAPID-MOCHA-WBTS (RAPID-Meridional Overturning Circulation and Heatflux Array-Western Boundary Time Series) array at 26N from 2004 to 2024 (v2024.1a). British Oceanographic Data Centre–Natural Environment Research Council, accessed 13 January 2026, https://doi.org/10.5285/48d0bf43-0598-ceb2-e063-7086abc062f1.

Mulet, S., and Coauthors, 2021: The new CNES-CLS18 global mean dynamic topography. *Ocean Sci.*, **17**, 789–808, https://doi.org/10.5194/os-17-789-2021.

Müller, J. D., and Coauthors, 2025: Unexpected decline in the ocean carbon sink under record-high sea surface temperatures in 2023. *Nat. Climate Change*, **15**, 978–985, https://doi.org/10.1038/s41558-025-02380-4.

Nerem, R. S., B. D. Beckley, J. T. Fasullo, B. D. Hamlington, D. Masters, and G. T. Mitchum, 2018: Climate-change–driven accelerated sea-level rise detected in the altimeter era. *Proc. Natl. Acad. Sci. USA*, **115**, 2022–2025, https://doi.org/10.1073/pnas.1717312115.

NOAA Climate Prediction Center, 2026: Indian Ocean monitoring and forecasting. Accessed 28 January 2026, https://www.cpc.ncep.noaa.gov/products/international/ocean_monitoring/indian/IO_monitoring_fcsts/io_index.shtml.

NOAA NCEI, 2026: Climate monitoring: Pacific Decadal Oscillation (PDO). Accessed 28 January 2026, https://www.ncei.noaa.gov/access/monitoring/pdo/.

Oliver, E. C. J., J. A. Benthuysen, S. Darmaraki, M. G. Donat, A. J. Hobday, N. J. Holbrook, R. W. Schlegel, and A. Sen Gupta, 2021: Marine heatwaves. *Ann. Rev. Mar. Sci.*, **13**, 313–342, https://doi.org/10.1146/annurev-marine-032720-095144.

O'Reilly, J. E., and P. J. Werdell, 2019: Chlorophyll algorithms for ocean color sensors–OC4, OC5 & OC6. *Remote Sens. Environ.*, **229**, 32–47, https://doi.org/10.1016/j.rse.2019.04.021.

Oschlies, A., O. Duteil, J. Getzlaff, W. Koeve, A. Landolfi, and S. Schmidtko, 2017: Patterns of deoxygenation: Sensitivity to natural and anthropogenic drivers. *Philos. Trans. Roy. Soc.*, **A375**, 20160325, https://doi.org/10.1098/rsta.2016.0325.

——, P. Brandt, L. Stramma, and S. Schmidtko, 2018: Drivers and mechanisms of ocean deoxygenation. *Nat. Geosci.*, **11**, 467–473, https://doi.org/10.1038/s41561-018-0152-2.

Palmer, M. D., K. Haines, S. F. B. Tett, and T. J. Ansell, 2007: Isolating the signal of ocean global warming. *Geophys. Res. Lett.*, **34**, L23610, https://doi.org/10.1029/2007GL031712.

Pan, Y., and Coauthors, 2026: Ocean heat content sets another record in 2025. *Adv. Atmos. Sci.*, https://doi.org/10.1007/s00376-026-5876-0, in press.

Parouffe, A., B. Dewitte, A. Paulmier, and V. Garçon, 2025: ENSO modulates aerobic habitat across varying hypoxia tolerance levels in the southeast Pacific throughout the twenty-first century. *Sci. Rep.*, **15**, 20670, https://doi.org/10.1038/s41598-025-06498-5.

Petit, T., J. Robson, D. Ferreira, S. Yeager, and D. G. Evans, 2025a: Coherence of the AMOC over the subpolar North Atlantic on interannual to multiannual time scales. *Geophys. Res. Lett.*, **52**, e2025GL115171, https://doi.org/10.1029/2025GL115171.

——, and Coauthors, 2025b: Evaluation of a reduced RAPID array for measuring the AMOC. *J. Geophys. Res. Oceans*, **130**, e2025JC023093, https://doi.org/10.1029/2025JC023093.

Purkey, S. G., and G. C. Johnson, 2010: Warming of global abyssal and deep Southern Ocean waters between the 1990s and 2000s: Contributions to global heat and sea level rise budgets. *J. Climate*, **23**, 6336–6351, https://doi.org/10.1175/2010JCLI3682.1.

Qiu, B., and S. Chen, 2021: Revisit of the occurrence of the Kuroshio large meander south of Japan. *J. Phys. Oceanogr.*, **51**, 3679–3694, https://doi.org/10.1175/JPO-D-21-0167.1.

——, S. Chen, N. Schneider, E. Oka, and S. Sugimoto, 2020: On the reset of the wind-forced decadal Kuroshio extension variability in late 2017. *J. Climate*, **33**, 10?813–10?828, https://doi.org/10.1175/JCLI-D-20-0237.1.

Rahmstorf, S., J. E. Box, G. Feulner, M. E. Mann, A. Robinson, S. Rutherford, and E. J. Schaffernicht, 2015: Exceptional twentieth-century slowdown in Atlantic Ocean overturning circulation. *Nat. Climate Change*, **5**, 475–480, https://doi.org/10.1038/nclimate2554.

Randolph, K., H. M. Dierssen, M. Twardowski, A. Cifuentes-Lorenzen, and C. J. Zappa, 2014: Optical measurements of small deeply penetrating bubble populations generated by breaking waves in the Southern Ocean. *J. Geophys. Res. Oceans*, **119**, 757–776, https://doi.org/10.1002/2013JC009227.

Rayner, N. A., and Coauthors, 2003: Global analyses of sea surface temperature, sea ice, and night marine air temperature since the late nineteenth century. *J. Geophys. Res.*, **108**, 4407, https://doi.org/10.1029/2002JD002670.

Reagan, J., C. Schmid, and R. Locarnini, 2025: Subsurface salinity [in "State of the Climate in 2024"]. *Bull. Amer. Meteor. Soc.*, **106** (8), S192–S194, https://doi.org/10.1175/BAMS-D-25-0074.1.

Reagan, J. R., and Coauthors, 2024: *Salinity*. Vol. 2, *World Ocean Atlas 2023*. A. Mishonov, Ed., NOAA Atlas NESDIS 90, 52 pp., https://doi.org/10.25923/70qt-9574.

——, and Coauthors, 2024: World Ocean Atlas 2023 (NCEI Accession 0270533). NOAA National Centers for Environmental Information, https://www.ncei.noaa.gov/archive/accession/0270533.

Regnier, P., L. Resplandy, R. G. Najjar, and P. Ciais, 2022: The land-to-ocean loops of the global carbon cycle. *Nature*, **603**, 401–410, https://doi.org/10.1038/s41586-021-04339-9.

Ren, L., K. Speer, and E. P. Chassignet, 2011: The mixed layer salinity budget and sea ice in the Southern Ocean. *J. Geophys. Res.*, **116**, C08031, https://doi.org/10.1029/2010JC006634.

Rhein, M., R. Steinfeldt, D. Kieke, I. Stendardo, and I. Yashayaev, 2017: Ventilation variability of Labrador Sea Water and its impact on oxygen and anthropogenic carbon: A review. *Philos. Trans. Roy. Soc.*, **A375**, 20160321, https://doi.org/10.1098/rsta.2016.0321.

Rio, M. H., S. Mulet, and N. Picot, 2014: Beyond GOCE for the ocean circulation estimate: Synergetic use of altimetry, gravimetry, and in situ data provides new insight into geostrophic and Ekman currents. *Geophys. Res. Lett.*, **41**, 8918–8925, https://doi.org/10.1002/2014GL061773.

Riser, S. C., and Coauthors, 2016: Fifteen years of ocean observations with the global Argo array. *Nat. Climate Change*, **6**, 145–153, https://doi.org/10.1038/nclimate2872.

Roach, C. J., and N. L. Bindoff, 2023: Developing a new oxygen atlas of the world's oceans using data interpolating variational analysis. *J. Atmos. Oceanic Technol.*, **40**, 1475–1491, https://doi.org/10.1175/JTECH-D-23-0007.1.

Rödenbeck, C., and Coauthors, 2015: Data-based estimates of the ocean carbon sink variability—First results of the Surface Ocean pCO_2 Mapping intercomparison (SOCOM). *Biogeosciences*, **12**, 7251–7278, https://doi.org/10.5194/bg-12-7251-2015.

Roemmich, D., and J. Gilson, 2009: The 2004–2008 mean and annual cycle of temperature, salinity, and steric height in the global ocean from the Argo program. *Prog. Oceanogr.*, **82**, 81–100, https://doi.org/10.1016/j.pocean.2009.03.004.

—— , and Coauthors, 2019: On the future of Argo: A global, full-depth, multi-disciplinary array. *Front. Mar. Sci.*, **6**, 439, https://doi.org/10.3389/fmars.2019.00439.

Schlegel, R. W., S. Darmaraki, J. A. Benthuysen, K. Filbee-Dexter, and E. C. Oliver, 2021: Marine cold-spells. *Prog. Oceanogr.*, **198**, 102684, https://doi.org/10.1016/j.pocean.2021.102684.

Schlesinger, M. E., and N. Ramankutty, 1994: An oscillation in the global climate system of period 65–70 years. *Nature*, **367**, 723–726, https://doi.org/10.1038/367723a0.

Schmidtko, S., G. C. Johnson, and J. M. Lyman, 2013: MIMOC: A global monthly isopycnal upper?ocean climatology with mixed layers. *J. Geophys. Res. Oceans*, **118**, 1658–1672, https://doi.org/10.1002/jgrc.20122.

—— , L. Stramma, and M. Visbeck, 2017: Decline in global oceanic oxygen content during the past five decades. *Nature*, **542**, 335–339, https://doi.org/10.1038/nature21399.

Schmitt, R. W., 1995: The ocean component of the global water cycle. *Rev. Geophys.*, **33**, 1395–1409, https://doi.org/10.1029/95RG00184.

Shao, W. Z., S. J. Leng, Q. Zhang, and X. W. Jiang, 2025: A potential technique for SAR ocean surface current speed retrieval based on machine learning. *Eur. J. Remote Sens.*, **58**, 2600152, https://doi.org/10.1080/22797254.2025.2600152.

Sharp, J. D., A. J. Fassbender, B. R. Carter, G. C. Johnson, C. Schultz, and J. P. Dunne, 2023: GOBAI-O 2: Temporally and spatially resolved fields of ocean interior dissolved oxygen over nearly 2 decades. *Earth Syst. Sci. Data*, **15**, 4481–4518, https://doi.org/10.5194/essd-15-4481-2023.

Siegel, D. A., and Coauthors, 2013: Regional to global assessments of phytoplankton dynamics from the SeaWiFS mission. *Remote Sens. Environ.*, **135**, 77–91, https://doi.org/10.1016/j.rse.2013.03.025.

—— , T. DeVries, I. Cetinić, and K. M. Bisson, 2023: Quantifying the ocean's biological pump and its carbon cycle impacts on global scales. *Ann. Rev. Mar. Sci.*, **15**, 329–356, https://doi.org/10.1146/annurev-marine-040722-115226.

Skliris, N., R. Marsh, S. A. Josey, S. A. Good, C. Liu, and R. P. Allan, 2014: Salinity changes in the world ocean since 1950 in relation to changing surface freshwater fluxes. *Climate Dyn.*, **43**, 709–736, https://doi.org/10.1007/s00382-014-2131-7.

Smeed, D. A., and Coauthors, 2026: Overturning circulation of the North Atlantic subtropical gyre computed in density coordinates at 26°N. *Geophys. Res. Lett.*, **53**, e2025GL118277, https://doi.org/10.1029/2025GL118277.

Stackhouse, P. W., D. P. Kratz, G. R. McGarragh, S. K. Gupta, and E. B. Geier, 2006: Fast Longwave and Shortwave Radiative Flux (FLASHFlux) products from CERES and MODIS measurements. *12th Conf. on Atmospheric Radiation*, Madison, WI, Amer. Meteor. Soc., P1.10, https://ntrs.nasa.gov/api/citations/20060028146/downloads/20060028146.pdf.

Stoer, A. C., and K. Fennel, 2024: Carbon-centric dynamics of Earth's marine phytoplankton. *Proc. Natl. Acad. Sci. USA*, **121**, e2405354121, https://doi.org/10.1073/pnas.2405354121.

Stramma, L., and Coauthors, 2012: Expansion of oxygen minimum zones may reduce available habitat for tropical pelagic fishes. *Nat. Climate Change*, **2**, 33–37, https://doi.org/10.1038/nclimate1304.

Sun, K., J. Liang, X. M. Li, and J. Pan, 2025: Retrieval of ocean surface currents by synergistic Sentinel-1 and SWOT data using deep learning. *Remote Sens.*, **17**, 2133, https://doi.org/10.3390/rs17132133.

Sweet, W. V., J. Park, J. J. Marra, C. Zervas, and S. Gill, 2014: Sea level rise and nuisance flood frequency changes around the United States. NOAA Tech. Rep. NOS CO-OPS 73, 66 pp.

—— , A. S. Genz, M. Menendez, J. J. Marra, and J. Obeysekera, 2024: Implications of variability and trends in coastal extreme water levels. *Geophys. Res. Lett.*, **51**, e2024GL108864, https://doi.org/10.1029/2024GL108864.

Tamisiea, M. E., and J. X. Mitrovica, 2011: The moving boundaries of sea level change: Understanding the origins of geographic variability. *Oceanography*, **24** (2), 24–39, https://doi.org/10.5670/oceanog.2011.25.

Tan, W., Z-Z Hu, Y. Liu, and M. J. McPhaden, 2025: Evolution and prediction of the La Niña conditions in 2024/25. *Environ. Res. Commun.*, **7**, 125031, https://doi.org/10.1088/2515-7620/ae2e97.

Tuchen, F. P., 2025: The return of equatorial Atlantic extreme events. *CLIVAR Exchanges*, No. 84, International CLIVAR Project Office, Southampton, United Kingdom, 26–30, https://doi.org/10.36071/clivar.84.2025.

—— , and Coauthors, 2025: Record warmth and unprecedented drop in equatorial Atlantic sea surface temperatures in 2024. *Geophys. Res. Lett.*, **52**, e2025GL115973, https://doi.org/10.1029/2025GL115973.

Twedt, K., N. Lei, X. Xiong, A. Angal, S. Li, T. Chang, and J. Sun, 2022: On-orbit calibration and performance of NOAA-20 VIIRS reflective solar bands. *IEEE Trans. Geosci. Remote Sens.*, **60**, 1–13, https://doi.org/10.1109/TGRS.2021.3108970.

Volkov, D. L., R. H. Smith, R. F. Garcia, D. A. Smeed, B. I. Moat, W. E. Johns, and M. O. Baringer, 2024: Florida current transport observations reveal four decades of steady state. *Nat. Commun.*, **15**, 7780, https://doi.org/10.1038/s41467-024-51879-5.

—— , and Coauthors, 2025a: Meridional overturning circulation and heat transport in the Atlantic Ocean [in "State of the Climate in 2024"]. *Bull. Amer. Meteor. Soc.*, **106** (8), S208–2010, https://doi.org/10.1175/BAMS-D-25-0074.1.

—— , R. H. Smith, and R. F. Garcia, 2025b: Pressure gauges and satellite altimetry ensure the continuity of Florida current transport observations. *Geophys. Res. Lett.*, **52**, e2025GL115897, https://doi.org/10.1029/2025GL115897.

von Schuckmann, K., and Coauthors, 2023: Heat stored in the Earth system 1960–2020: Where does the energy go? *Earth Syst. Sci. Data*, **15**, 1675–1709, https://doi.org/10.5194/essd-15-1675-2023.

Von Storch, H., and F. W. Zwiers, 1999: *Statistical Analysis in Climate Research*. Cambridge University Press, 484 pp.

Wahl, T., F. M. Calafat, and M. E. Luther, 2014: Rapid changes in the seasonal sea level cycle along the US Gulf Coast from the late 20th century. *Geophys. Res. Lett.*, **41**, 491–498, https://doi.org/10.1002/2013GL058777.

Walsh, K. J. E., and Coauthors, 2016: Tropical cyclones and climate change. *Wiley Interdiscip. Rev.: Climate Change*, **7**, 65–89, https://doi.org/10.1002/wcc.371.

Wang, Z., and Coauthors, 2025: Bias evaluation for sensor-based dissolved oxygen from CTD and profiling floats in the world ocean database. *J. Atmos. Oceanic Technol.*, **42**, 1263–1280, https://doi.org/10.1175/JTECH-D-25-0027.1.

Wanninkhof, R., 2014: Relationship between wind speed and gas exchange over the ocean revisited. *Limnol. Oceanogr. Methods*, **12**, 351–362, https://doi.org/10.4319/lom.2014.12.351.

——, J. Triñanes, D. Pierrot, D. R. Munro, C. Sweeney, and A. R. Fay, 2025: Trends in sea-air CO_2 fluxes and sensitivities to atmospheric forcing using an extremely randomized trees machine learning approach. *Global Biogeochem. Cycles*, **39**, e2024GB008315, https://doi.org/10.1029/2024GB008315.

Weijer, W., W. Cheng, O. A. Garuba, A. Hu, and B. T. Nadiga, 2020: CMIP6 models predict significant 21st century decline of the Atlantic meridional overturning circulation. *Geophys. Res. Lett.*, **47**, e2019GL086075, https://doi.org/10.1029/2019GL086075.

Werdell, P. J., and L. I. Mckinna, 2019: Sensitivity of inherent optical properties from ocean reflectance inversion models to satellite instrument wavelength suites. *Front. Earth Sci.*, **7**, 54, https://doi.org/10.3389/feart.2019.00054.

——, and Coauthors, 2013: Generalized ocean color inversion model for retrieving marine inherent optical properties. *Appl. Opt.*, **52**, 2019–2037, https://doi.org/10.1364/AO.52.002019.

Westberry, T. K., P. Schultz, M. J. Behrenfeld, J. P. Dunne, M. R. Hiscock, S. Maritorena, J. L. Sarmiento, and D. A. Siegel, 2016: Annual cycles of phytoplankton biomass in the subarctic Atlantic and Pacific Ocean. *Global Biogeochem. Cycles*, **30**, 175–190, https://doi.org/10.1002/2015GB005276.

Widlansky, M. J., A. Timmermann, S. McGregor, M. F. Stuecker, and W. Cai, 2014: An interhemispheric tropical sea level seesaw due to El Niño Taimasa. *J. Climate*, **27**, 1070–1081, https://doi.org/10.1175/JCLI-D-13-00276.1.

——, ——, and W. Cai, 2015: Future extreme sea level seesaws in the tropical Pacific. *Sci. Adv.*, **1**, e1500560, https://doi.org/10.1126/sciadv.1500560.

Wiese, D. N., D.-N. Yuan, C. Boening, F. W. Landerer, and M. M. Watkins, 2022: JPL GRACE and GRACE-FO Mascon Ocean, ice, and hydrology equivalent HDR water height RL06.1M CRI filtered version 3.0. PO.DAAC, accessed 13 February 2024, https://doi.org/10.5067/TEMSC-3MJ62.

Willis, J., and W. Hobbs, 2026: Atlantic meridional overturning circulation near 41N from altimetry and Argo observations. Zenodo, accessed 15 Mar 2026, https://zenodo.org/records/18238115.

Willis, J. K., 2010: Can in situ floats and satellite altimeters detect long-term changes in Atlantic Ocean overturning? *Geophys. Res. Lett.*, **37**, L06602, https://doi.org/10.1029/2010GL042372.

——, B. D. Hamlington, and S. Fournier, 2025: Global mean sea level time series, trajectory and extrapolation. Accessed 4 February 2026, https://doi.org/10.5281/zenodo.18649998.

WOD Team, 2025: World Ocean Database data product series. NOAA NCEI, accessed 15 January 2026, https://doi.org/10.25921/v92s-y066.

Wolter, K., and M. S. Timlin, 1998: Measuring the strength of ENSO events: How does 1997/98 rank? *Weather*, **53**, 315–324, https://doi.org/10.1002/j.1477-8696.1998.tb06408.x.

Wong, A. P. S., J. Gilson, and C. Cabanes, 2023: Argo salinity: Bias and uncertainty evaluation. *Earth Syst. Sci. Data*, **15**, 383–393, https://doi.org/10.5194/essd-15-383-2023.

Woodworth, P. L., and Coauthors, 2019: Forcing factors affecting sea level changes at the coast. *Surv. Geophys.*, **40**, 1351–1397, https://doi.org/10.1007/s10712-019-09531-1.

Wüst, G., 1936: Oberflächensalzgehalt, Verdunstung und Niederschlag auf dem Weltmeere. *Länderkundliche Forschung: Festschrift zur Vollendung des sechzigsten Lebensjahres Norbert Krebs*, J. Engelhorns, 347–359.

Xie, P., and Coauthors, 2014: An in situ-satellite blended analysis of global sea surface salinity. *J. Geophys. Res. Oceans*, **119**, 6140–6160, https://doi.org/10.1002/2014JC010046.

Xing, Q., S. Elipot, W. E. Johns, D. A. Smeed, B. I. Moat, and J. W. Loder, 2026: Meridionally consistent decline in the observed western boundary contribution to the Atlantic meridional overturning circulation. *Sci. Adv.*, **12**, eadz7738, https://doi.org/10.1126/sciadv.adz7738.

Yin, X., B. Huang, J. A. Carton, L. Chen, G. Graham, C. Liu, T. Smith, and H.-M. Zhang, 2024: The 1991–2020 sea surface temperature normals. *Int. J. Climatol.*, **44**, 668–685, https://doi.org/10.1002/joc.8350.

Yu, L., 2011: A global relationship between the ocean water cycle and near-surface salinity. *J. Geophys. Res.*, **116**, C10025, https://doi.org/10.1029/2010JC006937.

——, 2019: Global air–sea fluxes of heat, fresh water, and momentum: Energy budget closure and unanswered questions. *Annu. Rev. Mar. Sci.*, **11**, 227–248, https://doi.org/10.1146/annurev-marine-010816-060704.

——, and R. A. Weller, 2007: Objectively analyzed air–sea heat fluxes for the global ice-free oceans (1981–2005). *Bull. Amer. Meteor. Soc.*, **88**, 527–540, https://doi.org/10.1175/BAMS-88-4-527.

Zhou, Y., H. Gong, and F. Zhou, 2022: Responses of horizontally expanding oceanic oxygen minimum zones to climate change based on observations. *Geophys. Res. Lett.*, **49**, e2022GL097724, https://doi.org/10.1029/2022GL097724]

STATE OF THE CLIMATE IN 2025

THE TROPICS

H. J. Diamond and C. J. Schreck, Eds.

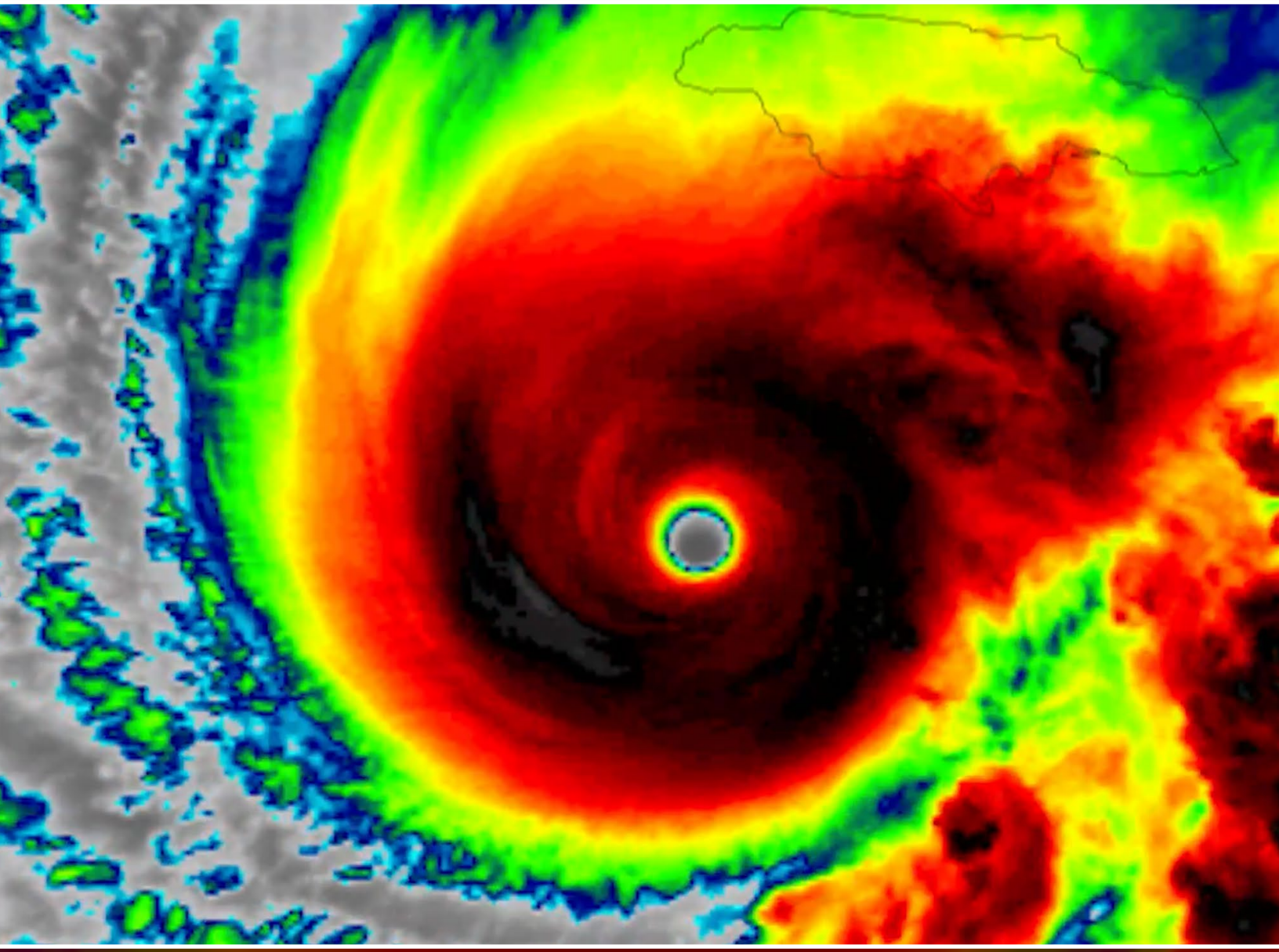

Special Online Supplement to the *Bulletin of the American Meteorological Society* Vol. 107, No. 8, August, 2026

https://doi.org/10.1175/BAMS-D-26-0101.1
Corresponding author: Howard J. Diamond / howard.diamond@noaa.gov
©2026 American Meteorological Society
For information regarding reuse of this content and general copyright information, consult the AMS Copyright Policy.

STATE OF THE CLIMATE IN 2025
The Tropics

Editors

Jessica Blunden
James Reagan

Chapter Editors

Anthony Arguez
Josh Blannin
Peter Bissolli
Kyle R. Clem
Howard J. Diamond
Matthew L. Druckenmiller
Robert J. H. Dunn
Catherine Ganter
Nadine Gobron
Rodney Martinez
Twila A. Moon
Gary A. Morris
Marilyn N. Raphael
Renellys C. Perez
Carl J. Schreck III
Zewdu Segele
Laura Stevens
Richard L. Thoman
Denis L. Volkov
Zhiwei Zhu

Technical Editors

Lukas Noguchi
Laura Ohlmann

BAMS Special Editor for Climate

Timothy DelSole

American Meteorological Society

Cover Credit:
GOES-19 satellite imagery of Category 5 Major Hurricane Melissa approaching Jamaica on 27–28 October 2025. (Credit: Cooperative Institute for Research in the Atmosphere [CIRA].)

How to cite this document:
The Tropics is one chapter from the *State of the Climate in 2025* annual report and is available from https://doi.org/10.1175/BAMS-D-26-0101.1. Compiled by NOAA's National Centers for Environmental Information, *State of the Climate in 2025* is based on contributions from scientists from around the world. It provides a detailed update on global climate indicators, notable weather events, and other data collected by environmental monitoring stations and instruments located on land, water, ice, and in space. The full report is available from https://doi.org/10.1175/2026BAMSStateoftheClimate.1.

Citing the complete report:
Blunden, J.and J. Reagan, Eds., 2026: "State of the Climate in 2025". Bull. Amer. Meteor. Soc., 107 (8), Si–S512, https://doi.org/10.1175/2026BAMSStateoftheClimate.1.

Citing this chapter:
Diamond, H.J. and C. J. Schreck, Eds., 2026: The Tropics [in "State of the Climate in 2025"]. Bull. Amer. Meteor. Soc., 107 (8), S235–S291, https://doi.org/10.1175/BAMS-D-26-0101.1.

Citing a section (example):
Trinanes, J., J. Knaff, and I-I. Lin, 2026: Tropical cyclone heat potential [in "State of the Climate in 2025"]. Bull. Amer. Meteor. Soc., 107 (8), S280–S282, https://doi.org/10.1175/BAMS-D-26-0101.1.

Editor and Author Affiliations (alphabetical by name)

Allgood, Adam, NOAA/NWS National Centers for Environmental Prediction Climate Prediction Center, College Park, Maryland

Becker, Emily J., Rosenstiel School of Marine, Atmospheric, and Earth Science, University of Miami, Miami, Florida

Blake, Eric S., NOAA/NWS National Hurricane Center, Miami, Florida

Camargo, Suzana J., Columbia Climate School, Columbia University, New York, New York

Chen, Lin, Institute for Climate and Application Research (ICAR)/KLME/ILCEC/CIC-FEMD, Nanjing University of Information Science and Technology, Nanjing, China

Coelho, Caio A. S., Centro de Previsão do Tempo e Estudos Climáticos/National Institute for Space Research, Center for Weather Forecasts and Climate Studies, Cachoeira Paulista, Brazil

Diamond, Howard J., NOAA/OAR Air Resources Laboratory, College Park, Maryland

Fauchereau, Nicolas, Earth Sciences New Zealand, Auckland, New Zealand

Fogarty, Chris, Canadian Hurricane Centre, Dartmouth, Canada

Goldenberg, Stanley B., NOAA/OAR Atlantic Oceanographic and Meteorological Laboratory, Miami, Florida

Harnos, Daniel S., NOAA/NWS National Centers for Environmental Prediction Climate Prediction Center, College Park, Maryland

He, Qiong, State Key Laboratory of Climate System Prediction and Risk Management/KLME/CIC-FEMD/School of Atmospheric Sciences, Nanjing University of Information Science and Technology, Nanjing, China

Hu, Zeng-Zhen, NOAA/NWS National Centers for Environmental Prediction Climate Prediction Center, College Park, Maryland

Klotzbach, Philip J., Department of Atmospheric Science, Colorado State University, Fort Collins, Colorado

Knaff, John A., NOAA/NESDIS Center for Satellite Applications and Research, Fort Collins, Colorado

L'Heureux, Michelle, NOAA/NWS National Centers for Environmental Prediction Climate Prediction Center, College Park, Maryland

Landsea, Chris W., NOAA/NWS National Hurricane Center, Miami, Florida

Li, Juan, State Key Laboratory of Climate System Prediction and Risk Management/KLME/CIC-FEMD/School of Atmospheric Sciences, Nanjing University of Information Science and Technology, Nanjing, China

Lin, I-I., National Taiwan University, Taipei, Taiwan

Long, Lindsey N., NOAA/NWS National Centers for Environmental Prediction Climate Prediction Center, College Park, Maryland

Lopez, Hosmay, NOAA/OAR Atlantic Oceanographic and Meteorological Laboratory, Miami, Florida

Lorrey, Andrew M., Earth Sciences New Zealand, Auckland, New Zealand

Luo, Jing-Jia, Institute for Climate and Application Research, Nanjing University of Information Science and Technology, Nanjing, China

Magee, Andrew D., JBA Global Resilience, Brisbane, Australia

Pasch, Richard J., NOAA/NWS National Hurricane Center, Miami, Florida

Pezza, Alexandre B., Greater Wellington Regional Council, Wellington, New Zealand

Rosencrans, Matthew, NOAA/NWS National Centers for Environmental Prediction Climate Prediction Center, College Park, Maryland

Schreck, Carl J., Cooperative Institute for Satellite Earth System Studies, North Carolina Institute for Climate Studies, North Carolina State University, Asheville, North Carolina

Trewin, Blair C., Bureau of Meteorology, Melbourne, Australia

Trinanes, Joaquin, Department of Electronics and Computer Science, Universidade de Santiago de Compostela, Santiago de Compostela, Spain

Truchelut, Ryan E., WeatherTiger, Tallahassee, Florida

Uehling, John, Cooperative Institute for Satellite Earth System Studies, North Carolina Institute for Climate Studies, North Carolina State University, Asheville, North Carolina

Wang, Bin, School of Ocean and Earth Science and Technology, Department of Meteorology, University of Hawaii at Manoa, Honolulu, Hawaii; International Pacific Research Center, Honolulu, Hawaii

Wang, Hui, NOAA/NWS National Centers for Environmental Prediction Climate Prediction Center, College Park, Maryland

Wood, Kimberly M., Department of Hydrology and Atmospheric Sciences, University of Arizona, Tucson, Arizona

Editorial and Production Team

Allen, Jessicca, Graphics Support, Cooperative Institute for Satellite Earth System Studies, North Carolina State University, Asheville, North Carolina

Camper, Amy V., Graphics Support, Innovative Consulting and Management Services, LLC, NOAA/NESDIS National Centers for Environmental Information, Asheville, North Carolina

Carroll, Lauren, Content Team Lead, Communications and Outreach, NOAA/NESDIS National Centers for Environmental Information, Asheville, North Carolina

Crossman, Jacquelyn, NCEI Librarian, MPF-ZAI, NOAA/NESDIS National Centers for Environmental Information, Asheville, North Carolina

Haley, Bridgette O., Graphics Support, NOAA/NESDIS National Centers for Environmental Information, Asheville, North Carolina

Noguchi, Lukas, Technical Editor, Innovative Consulting and Management Services, LLC, NOAA/NESDIS National Centers for Environmental Information, Asheville, North Carolina

Ohlmann, Laura, Technical Editor, Innovative Consulting and Management Services, LLC, NOAA/NESDIS National Centers for Environmental Information, Asheville, North Carolina

Veasey, Sara W., Visual Communications Team Lead, Communications and Outreach, NOAA/NESDIS National Centers for Environmental Information, Asheville, North Carolina

4. Table of Contents

List of authors and affiliations S238
a. Overview S240
b. ENSO and the tropical Pacific S241
1. Oceanic Conditions S241
2. Atmospheric circulation S243
3. Global Precipitation S244
c. Tropical intraseasonal activity S245
d. Intertropical convergence zones S248
1. Pacific S248
2. Atlantic S249
e. Global monsoon summary S251
1. Precipitation and Circulation Anomalies S251
2. Regional Monsoon Precipitation and Circulation S252
3. Land Monsoon Precipitation Anomalies S254
f. Indian Ocean dipole S255
g. Tropical cyclones S258
1. Overview S258
2. Atlantic Basin S259
3. Eastern North Pacific and central North Pacific basins S264
4. Western North Pacific S267
5. North Indian Ocean S271
6. South Indian Ocean S273
7. Australian basin S275
8. Southwest Pacific basin S277
h. Tropical cyclone heat potential S280
Sidebar 4.1: Hurricane Melissa: A record-breaking Caribbean hurricane S283
Appendix 1: Acronyms S285
Appendix 2: Dataset Tables S287
Appendix 3: Supplemental Materials S291
References S292

4. THE TROPICS

H. J. Diamond and C. J. Schreck, Eds.

a. Overview

—H. J. Diamond and C. J. Schreck

In 2025, the tropical climate was primarily characterized by cool neutral El Niño–Southern Oscillation (ENSO) conditions based on the Oceanic Niño Index (ONI; Fig. 4.1). The ONI was slightly cooler than the −0.5°C threshold for two overlapping seasons during the Northern Hemisphere winter of 2024/25, but the anomalies were weak and did not last long enough to be considered a La Niña episode by NOAA's historical definition (section 4b). For the global tropics (defined here as 20°S–20°N), the NOAA Merged Land Ocean Global Surface Temperature Analysis (NOAA GlobalTemp; Vose et al. 2021) dataset indicated that the combined average land and ocean surface temperature was 0.27°C above the 1991–2020 average, the seventh-warmest year for the tropics in the 176-year data record. Nine of the 10 warmest years in the tropics have all occurred since 2015. Data from the Global Precipitation Climatology Project (version 3.2) indicated a mean annual total precipitation value of 1466.5 mm across the tropics over land. This is 38.7 mm above the 1991–2020 average and was the 12th highest for the 1983–2025 period of record.

Globally, 97 named tropical cyclones (TCs; ≥34 kt or ≥17 m s^{-1}) occurred during the 2025 Northern Hemisphere season (January–December 2025) and the 2024/25 Southern Hemisphere season (July–June 2024/25; see Table 4.2), as documented by the National Hurricane Center and the Joint Typhoon Warning Center in the International Best Track Archive for Climate Stewardship Version 4.1 (Knapp et al. 2010). Overall, this number was above the 1991–2020 global average of 87 TCs as well as the 82 TCs reported during the 2024 season (Diamond and Schreck 2025). The record for most named storms in a single TC season is 104 in 1992, and the fewest since 1980 is 67 in 1985.

Of the 97 named storms, 50 reached hurricane strength (one-minute maximum sustained winds ≥64 kt), which was above the 1991–2020 average. A near-normal 25 reached major hurricane strength (one-minute maximum winds ≥96 kt; equivalent to Category 3+ on the Saffir–Simpson Hurricane Wind Scale). Global accumulated cyclone energy (ACE; an integrated metric of the strength, frequency, and duration of tropical storms and hurricanes; Bell et al. 2000) was also near normal in 2025. Of the seven TC basins, the western North Pacific and southwest Pacific basins each had below-normal ACE relative to 1991–2020, while the South Indian and Australian basins were above normal. Note that the North Atlantic has a longer period of reliable records than other basins, and it was above normal relative to 1951–2020. Globally, five storms reached Category 5 intensity on the Saffir–Simpson Hurricane Wind Scale (one-minute maximum sustained winds ≥137 kt) during 2025, compared with only three in 2022, seven in 2023, and four in 2024. Three basins—the North Atlantic, the western North Pacific and the Australian basin—had at least one Category 5 storm. The North Atlantic had three Category 5 storms, tying for the second most on record for that basin (2005 had four Category 5 North Atlantic storms).

The 2025 Atlantic hurricane season produced 13 named storms; of these, five became hurricanes, with four intensifying into major hurricanes. The season was less active than that of 2024, which had 18 named storms, 11 hurricanes, and 5 major hurricanes. One storm of particular note in 2025 was Hurricane Melissa in the North Atlantic. This system was a very extreme event that shattered records and is highlighted in the sidebar of this chapter with respect to its meteorological nature, as well as in section 7c of the Regional Climates chapter with respect to its effects in the Caribbean, particularly in Jamaica.

b. ENSO and the tropical Pacific

—M. L'Heureux, Z.-Z. Hu, D. Harnos, and E. Becker

The El Niño–Southern Oscillation (ENSO) is a coupled ocean–atmosphere climate phenomenon across the tropical Pacific Ocean, characterized by two distinct phases: El Niño and La Niña. For historical purposes, NOAA's Climate Prediction Center (CPC) classifies and assesses the strength and duration of El Niño and La Niña events using the Oceanic Niño Index (ONI; shown for mid-2024 through 2025 in Fig. 4.1). The ONI is the three-month (seasonal) running average of sea surface temperature (SST) anomalies in the Niño-3.4 region (5°S–5°N, 170°W–120°W), which was calculated as the departure from the 1991–2020 base period mean[1] during 2024/25. Beginning in 2026, NOAA will begin using the Relative Oceanic Niño Index (RONI; L'Heureux et al. 2024), which subtracts the tropical mean instead of using a moving base period. El Niño is classified when the ONI is at or greater than +0.5°C for at least five consecutive, overlapping seasons, while La Niña occurs when the ONI is at or less than −0.5°C for at least five consecutive, overlapping seasons.

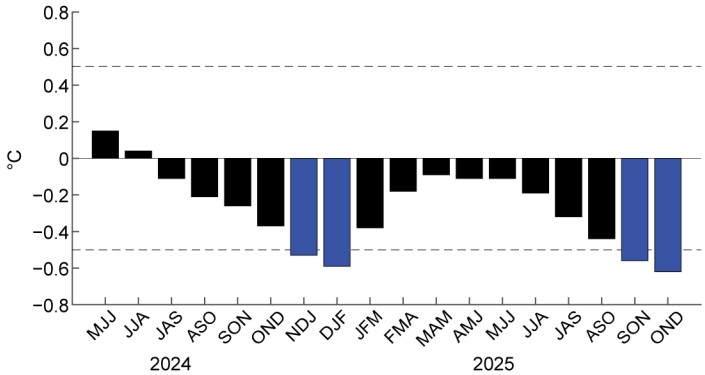

Fig. 4.1. Time series of the Oceanic Niño Index (ONI; °C) from mid-2024 through 2025. Overlapping three-month seasons are labeled on the x-axis, with initials indicating the first letter of each month in the season. Blue bars indicate negative values that are in excess of −0.5°C (La Niña conditions). Black bars indicate values that are within ±0.5 (El Niño–Southern Oscillation [ENSO] neutral). ONI values are derived from the ERSSTv5 dataset and are based on departures from the 1991–2020 period monthly means (Huang et al. 2017).

The ONI was slightly cooler than the −0.5°C threshold for two overlapping seasons during the Northern Hemisphere winter of 2024/25, but the anomalies were weak and did not last long enough to be considered a La Niña episode by NOAA's historical definition. At the time of writing, it is not yet clear whether the 2025/26 boreal winter will reach the duration required to be considered a La Niña episode. Despite the short period in the ONI, NOAA's CPC and other national meteorological services issued real-time La Niña Advisories (or Alerts) during boreal winter 2024/25 and again in late 2025. This was due to 1) real-time forecast uncertainty over whether the event would last enough to be retrospectively classified as a La Niña episode, and 2) the emergence of a robust atmospheric response over the tropical Pacific, which will be further discussed in this section.

The ONI remained between −0.1°C and −0.6°C from December–February (DJF) 2024/25 through October–December (OND) 2025. The minimum value of −0.6°C occurred in DJF 2024/25, September–November (SON) 2025, and OND 2025. The maximum value of −0.1°C was reached during March–May (MAM) 2025 through May–July (MJJ) 2025.

1. OCEANIC CONDITIONS

Figure 4.2 displays the mean SST (left column) and SST anomalies (right column) during DJF 2024/25 through September–November (SON) 2025. SST anomalies on the equator during DJF (Figs. 4.2a,b) were less than −1.0°C near the dateline, with anomalies less than −0.5°C extending eastward to 120°W. SST anomalies were either close to average or slightly above average east of 120°W. The western Pacific warm pool, and the extent of the 30°C isotherm, was retracted to 160°E on the equator. However, just south of the equator, the 30°C isotherm stretched to the dateline.

By MAM 2025, negative SST anomalies weakened in the equatorial central Pacific, and positive anomalies strengthened in the far eastern Pacific (Figs. 4.2c,d). SST anomalies also remained elevated in the far western equatorial Pacific, with the 30°C isotherm further extending to 160°W south of the equator in MAM. While remaining weak, near-to-below-average SSTs strengthened to the southwest of the Baja Peninsula. In boreal spring, negative anomalies in this region tend

[1] The ONI is an index measuring ENSO, and to highlight its seasonal-to-interannual component, the base period is updated every five years with a rolling 30-year climatology. SSTs in the Niño-3.4 region have multi-decadal and longer trends going back to 1950 or earlier, and the rolling climatology reduces the influence of trend on the state of ENSO.

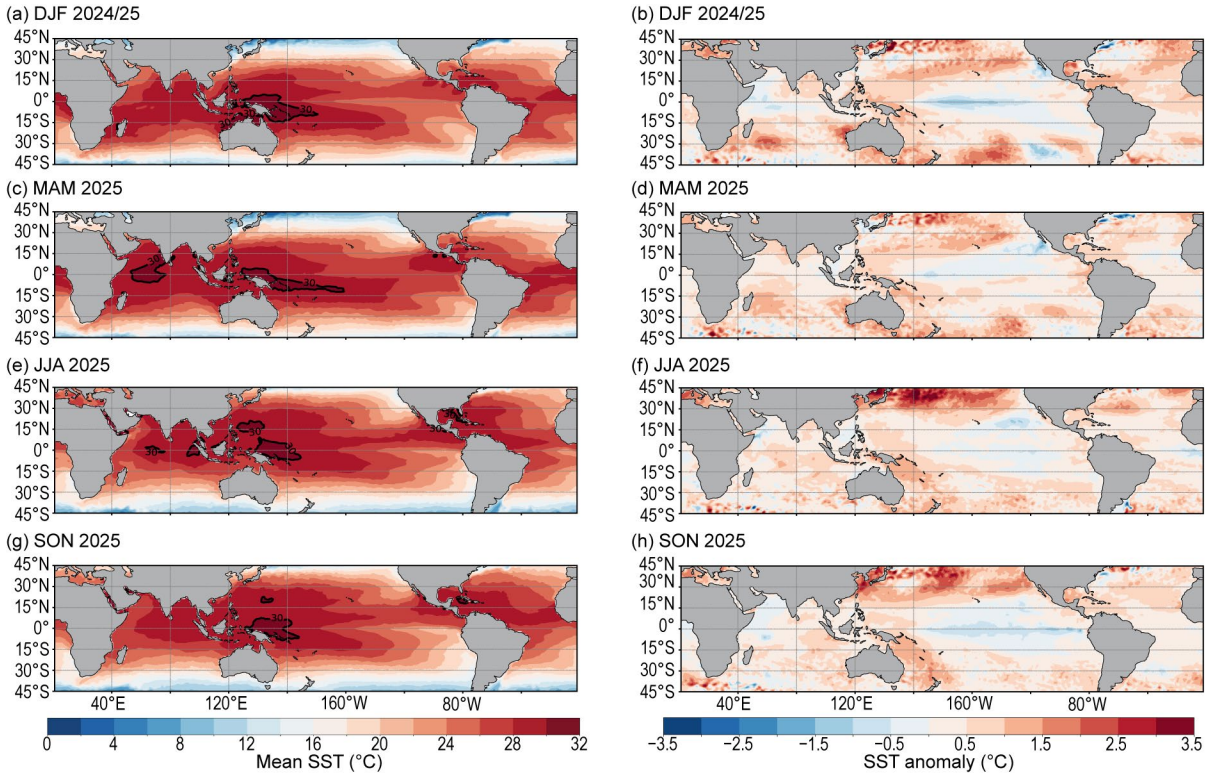

Fig. 4.2. Mean sea surface temperatures (SST; °C; left) and SST anomalies (°C; right) for (a),(b) Dec–Feb (DJF) 2024/25, (c),(d) Mar–May (MAM) 2025, (e),(f) Jun–Aug (JJA) 2025, and (g),(h) Sep–Nov (SON) 2025. The bold contour for the mean SST is 30°C. Anomalies are departures from the 1991–2020 seasonal adjusted OISSTv2.1 climatology (Huang et al. 2021).

to precede the development of La Niña the following winter (Penland and Sardeshmukh 1995), and by SON 2025, NOAA had declared a La Niña Advisory.

In June–August (JJA) 2025 (Figs. 4.2e,f), near-average equatorial SSTs prevailed across most of the Pacific, with slightly above-average equatorial SSTs persisting in the far western and eastern Pacific. By SON 2025 (Figs. 4.2g,h), negative SST anomalies had reemerged on the equator from the dateline to the South American coast. Equatorial SST anomalies were less than –1.0°C in small regions of the eastern Pacific, and the western Pacific warm pool was retracted to the west.

Despite near-average SSTs in the eastern equatorial Pacific during DJF 2024/25, equatorial subsurface temperatures were below average in the central and eastern Pacific (Fig. 4.3a). Temperature anomalies were less than –3.5°C along the mean position of the thermocline (gray dashed line) between 150°W and 100°W. The negative subsurface temperature anomalies weakened into MAM 2025 (Fig. 4.3b) and then began to strengthen again in JJA and SON 2025 (Figs. 4.3c,d, respectively).

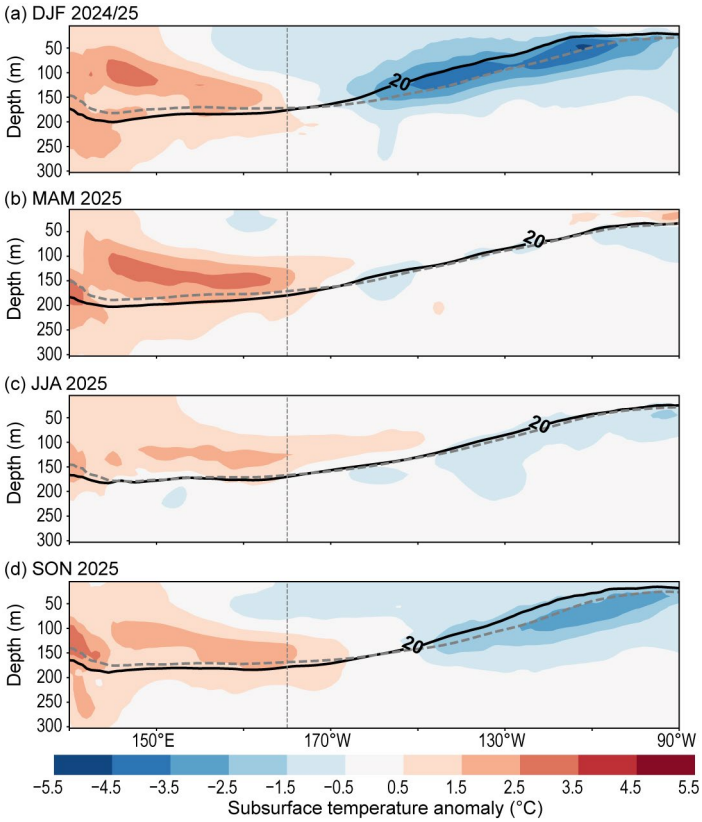

Fig. 4.3. Equatorial depth–longitude section of Pacific Ocean temperature anomalies (°C) averaged between 5°S and 5°N during (a) Dec–Feb (DJF) 2024/25, (b) Mar–May (MAM) 2025, (c) Jun–Aug (JJA) 2025, and (d) Sep–Nov (SON) 2025. The 20°C isotherm (thick solid line) approximates the center of the oceanic thermocline. The gray dashed line shows the 1991–2020 climatology of the 20°C isotherm. The data are derived from a reanalysis system that assimilates oceanic observations into an oceanic general circulation model (Behringer 2007). Anomalies are departures from the 1991–2020 period monthly means.

By SON 2025, below-average anomalies once again dominated the central and eastern equatorial Pacific, reflecting the shoaling of the equatorial thermocline and onset of conditions consistent with La Niña. Subsurface temperature anomalies were less than –3.5°C at ~25-m–100-m depth between 130°W and 90°W during SON 2025. Throughout the year, positive subsurface temperature anomalies were observed in the western equatorial Pacific and were restricted to depths greater than 100 m near the dateline.

2. ATMOSPHERIC CIRCULATION

Despite near-to-below-average SSTs across the central and east-central equatorial Pacific during most of the year, the overall pattern of convection and winds was generally consistent with La Niña (Figs. 4.4–4.6). The continuation of La Niña-like atmospheric anomalies was likely due to the enhanced east-to-west SST gradient in the equatorial Pacific, with relatively warmer (cooler) anomalies in the western (central and eastern) Pacific. In particular, tropical convection and rainfall (as measured by outgoing longwave radiation [OLR]) were below average near the dateline and above average near the Maritime Continent and Indonesia. The suppressed convection (brown shading) near the dateline was strongest during DJF 2024/25 and MAM 2025 (Figs. 4.4a,b), and weakened during JJA and SON 2025 (Figs. 4.4c,d). The enhanced convection (green shading) near Indonesia was remarkably persistent throughout all seasons.

In alignment with the tropical convection anomalies, a stronger Pacific Walker circulation was evident through most of the year (Figs. 4.5, 4.6). Low-level (850-hPa) wind anomalies were

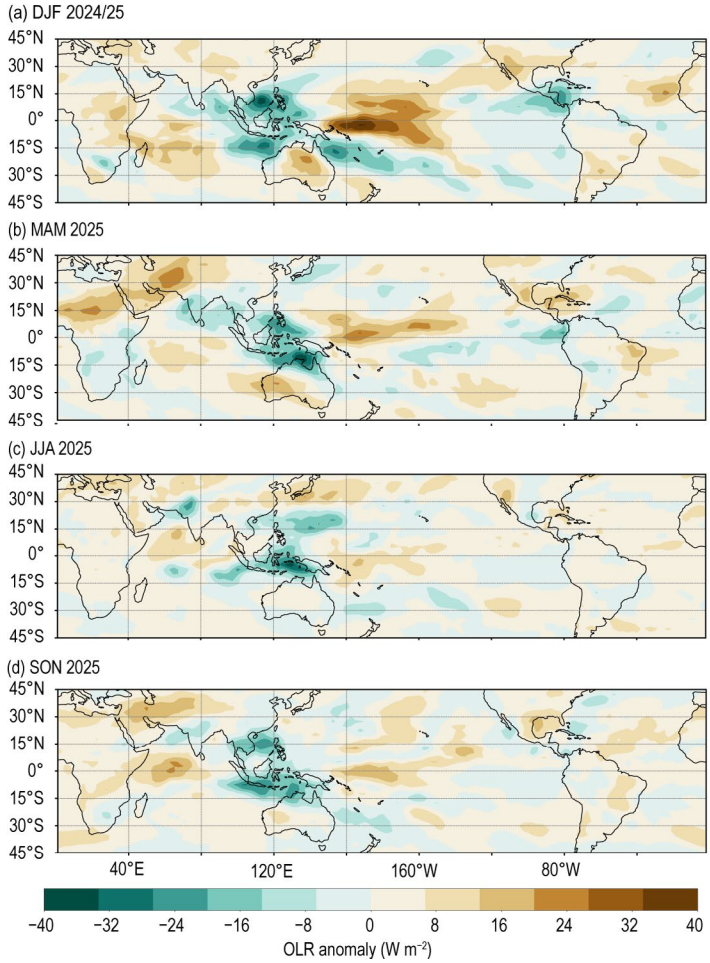

Fig. 4.4. Outgoing longwave radiation (OLR) anomalies (W m^{-2}) during (a) Dec–Feb (DJF) 2024/25, (b) Mar–May (MAM) 2025, (c) Jun–Aug (JJA) 2025, and (d) Sep–Nov (SON) 2025. Anomalies are departures from the 1991–2020 period monthly means. Data are from Guo et al. (2024).

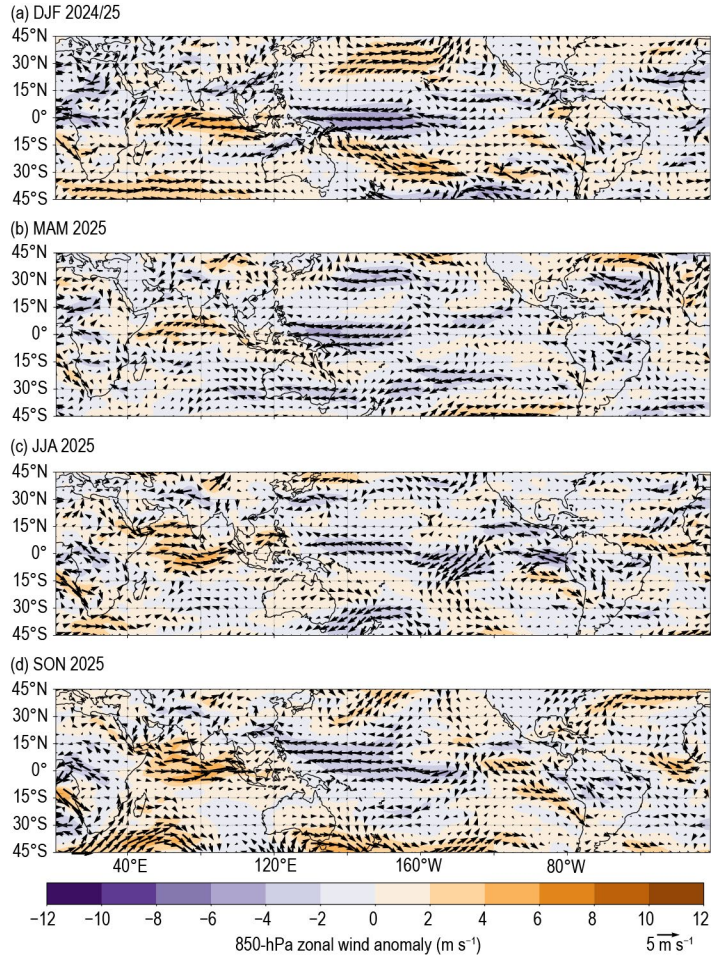

Fig. 4.5. Anomalous 850-hPa wind vectors and zonal wind speed (m s^{-1}; shading) during (a) Dec–Feb (DJF) 2024/25, (b) Mar–May (MAM) 2025, (c) Jun–Aug (JJA) 2025, and (d) Sep–Nov (SON) 2025. The reference wind vector is located at the bottom right. Anomalies are departures from the 1991–2020 period monthly means. Data are from the National Centers for Environmental Prediction (NCEP) National Center for Atmospheric Research (NCAR) reanalysis (Kalnay et al. 1996).

generally easterly over the equatorial Pacific, and upper-level (200-hPa) wind anomalies were mostly westerly. An anomalous upper-level cyclonic couplet straddled the equator during the year, with anomalous easterlies and a weaker upper-level jet stream (purple shading) located over the subtropics of the North and South Pacific Ocean (~15° to 30° degrees latitude). The anomalous cyclonic couplet was weakest during JJA 2025 (Fig. 4.6c), which also coincided with a weakening of the westerly wind anomalies and suppressed convection near the dateline. Low-level easterly wind anomalies were also strongest outside of JJA 2025, with the strongest zonal wind anomalies occurring during DJF 2024/25 over the western and central equatorial Pacific (Fig. 4.5a). Compared to the western and central Pacific, low-level wind anomalies were weaker over the eastern equatorial Pacific, with mostly northerly wind anomalies crossing the equator around ~120°W during JJA and SON 2025 (Figs. 4.5c,d). These meridional wind anomalies were opposite to the long-term trends over the eastern tropical Pacific (Hu and Fedorov 2018).

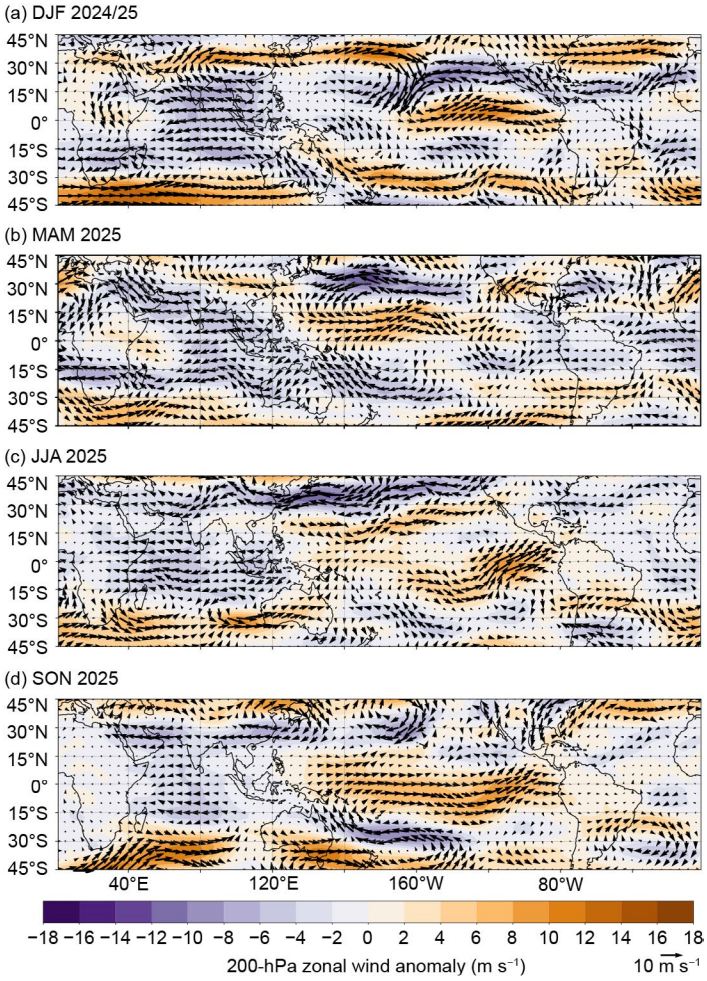

Fig. 4.6. Anomalous 200-hPa wind vectors and zonal wind speed (shading) during (a) Dec–Feb (DJF) 2024/25, (b) Mar–May (MAM) 2025, (c) Jun–Aug (JJA) 2025, and (d) Sep–Nov (SON) 2025. The reference wind vector is located at the bottom right. Units are m s^{-1} and anomalies are departures from the 1991–2020 period monthly means. Data are from the National Centers for Environmental Prediction (NCEP) National Center for Atmospheric Research (NCAR) reanalysis (Kalnay et al. 1996).

3. GLOBAL PRECIPITATION

ENSO-driven teleconnections can affect precipitation anomalies globally (Bjerknes 1969; Ropelewski and Halpert 1989). While a rigorous attribution is beyond the scope of this chapter, certain global precipitation anomalies during DJF 2024/25 were consistent with La Niña (Appendix Fig. A4.1). Precipitation was below average over most of the southern United States, central-eastern equatorial Africa, Iran, Pakistan, and the region stretching from eastern China to southern Japan. Over Indonesia, northwestern and northeastern Australia, and parts of southern Africa (e.g., Zimbabwe and Botswana), conditions were wetter than average. All of these precipitation anomalies are reminiscent of teleconnections typically associated with La Niña.

c. Tropical intraseasonal activity

—A. Allgood and C. J. Schreck

Organized tropical intraseasonal activity is modulated by several different modes of coherent atmospheric variability, most notably the Madden–Julian Oscillation (MJO; Madden and Julian 1971, 1972, 1994; Zhang 2005). The MJO is characterized by eastward-propagating envelopes of large-scale anomalous enhanced and suppressed convection that typically circumnavigate the globe in a 30-day to 60-day period. MJO-related convective anomalies are similar in spatial extent to those generated by the atmospheric response to El Niño–Southern Oscillation (ENSO), but the latter signal remains largely stationary and lasts for several months. MJO convective anomalies can influence the low-frequency base state of the tropics, including modulation of ENSO events (Moore and Kleeman 1999). Other impactful modes of variability include convectively coupled atmospheric waves, such as Kelvin waves—which exhibit a faster phase speed than the MJO—and westward propagating equatorial Rossby waves (Wheeler and Kiladis 1999; Kiladis et al. 2009). These waves are typically narrower (zonally) than the MJO and may not couple as well to the broader convective regime. The MJO can be identified through time–longitude analyses of various atmospheric fields, including anomalous 200-hPa velocity potential (Fig. 4.7b), anomalous zonal winds at 200 hPa (not shown) and 850 hPa (Fig. 4.8a), and anomalous outgoing longwave radiation (OLR; Fig. 4.7a). Another diagnostic tool frequently used to identify MJO activity is the Wheeler and Hendon (2004) Real-time Multivariate MJO (RMM) index. In RMM plots, robust atmospheric anomalies on a spatial scale resembling the MJO appear as a signal outside of the unit circle (Fig. 4.9). Eastward propagation is represented by counterclockwise looping of the index about the origin.

The 2025 calendar year opened with increasingly organized MJO activity. The enhanced convective phase amplified over the Western Hemisphere during mid-January, with eastward propagation evident across the Indian Ocean and Maritime Continent through the end of the

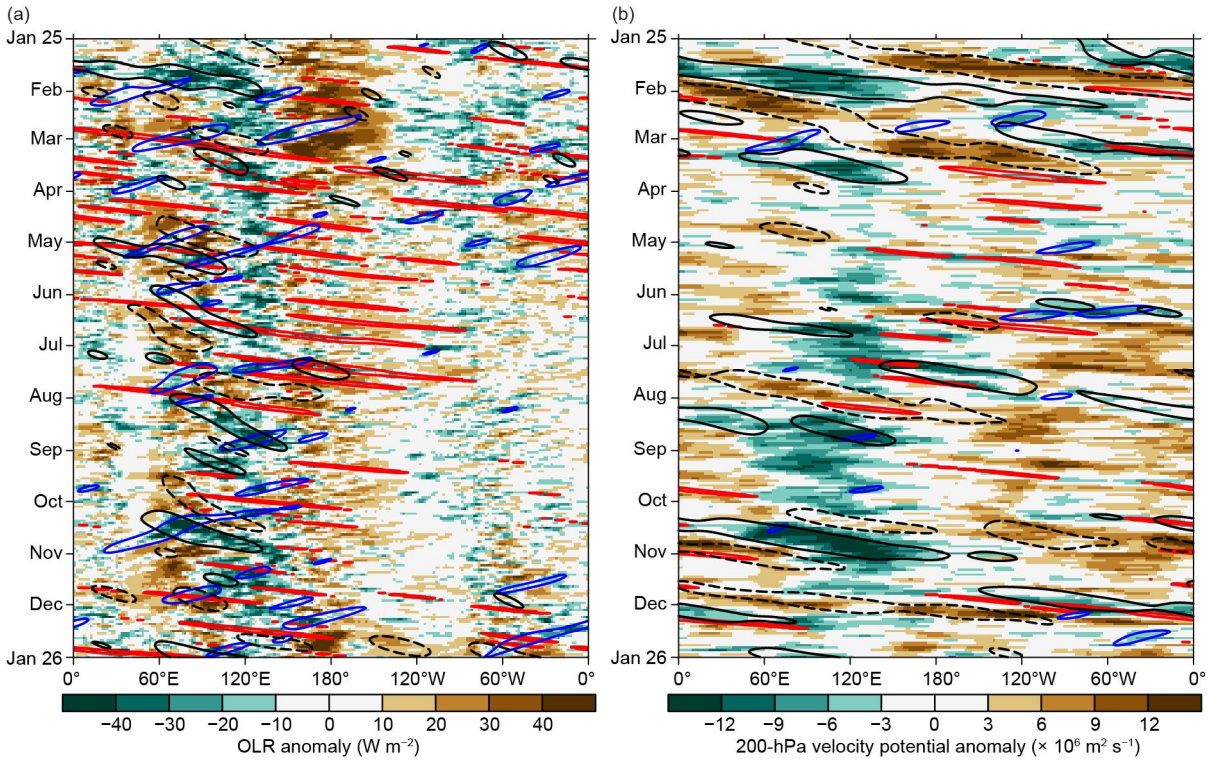

Fig. 4.7. Time–longitude section of (a) High Resolution Infrared Radiation Sounder (HIRS) outgoing longwave radiation (OLR; Schreck et al. 2018) anomalies (W m^{-2}) on the left and (b) 200-hPa velocity potential anomalies (× 10^6 m^2 s^{-1}) from the Climate Forecast System Reanalysis (Saha et al. 2014) on the right. Both variables are averaged for the region 10°S–10°N. Time increases downward on this graph, beginning with Jan 2025 at the top and ending with Jan 2026 at the bottom. Negative anomalies indicate enhanced convection, and positive anomalies indicate suppressed convection. Contours identify anomalies filtered for the Madden–Julian Oscillation (black), atmospheric Kelvin waves (red), and equatorial Rossby waves (blue). Contours are drawn at ±12 W m^{-2} and ±4 x 10^6 m^2 s^{-1} with the enhanced (suppressed) convective phase of these phenomena indicated by solid (dashed) contours. Anomalies are departures from the 1991–2020 base period daily means.

month (Fig. 4.9a). The suppressed phase of the MJO helped generate a strong trade wind surge across the equatorial Pacific, reinforcing the ongoing La Niña event at its peak amplitude (Fig. 4.8a). The MJO remained active through February and March, evident in the objective wave filtering of both the lower-level winds and upper-level velocity potential (Figs. 4.7b, 4.8a). During these time periods, however, other modes of intraseasonal variability periodically induced destructive interference with the MJO signal. Most notably, the MJO signal weakened in late February and mid-March due to a competing equatorial Rossby wave signal. These periods of interference appear as "loops" or brief retrogressions on the RMM-based MJO index (Fig. 4.9a). Additionally, the active MJO propagation continued to modulate the ENSO signal, with alternating periods of weakened and strengthened trade winds in mid-February and mid-March. By the end of March, the MJO signal began to weaken before reaching the Pacific, resulting in no substantial low-level westerly wind events across the equatorial Pacific, though warm water from the western Pacific warm pool began migrating eastward subsequent to this period.

Unlike the first three months of 2025, April, May, and June were characterized by weak and incoherent MJO activity. The incoherence of the MJO signal was apparent in the RMM index, with weak amplitudes that remained within the unit circle for much of these months. The time–longitude analyses of zonal winds and upper-level velocity potential anomalies also reflected the incoherent signal, with Kelvin waves (e.g., red contours in Fig. 4.7a) dominating the objective filtering. La Niña conditions waned during this period, with ENSO-neutral conditions returning by April. Despite the weakening ENSO signal, a low- frequency stationary pattern favoring enhanced convection over the Maritime Continent persisted through the boreal spring into the summer. A brief enhancement of the RMM index was noted in early May, but interference driven by Kelvin waves and a low-frequency enhanced convective signal over the Maritime Continent prevented a more substantive MJO evolution. A second period of brief activity was noted in early June, due to a confluence of a robust South Asian monsoon onset, equatorial Rossby wave activity, and Kelvin waves, but the signal broke down again by the middle of the month as these modes grew increasingly out of phase with each other.

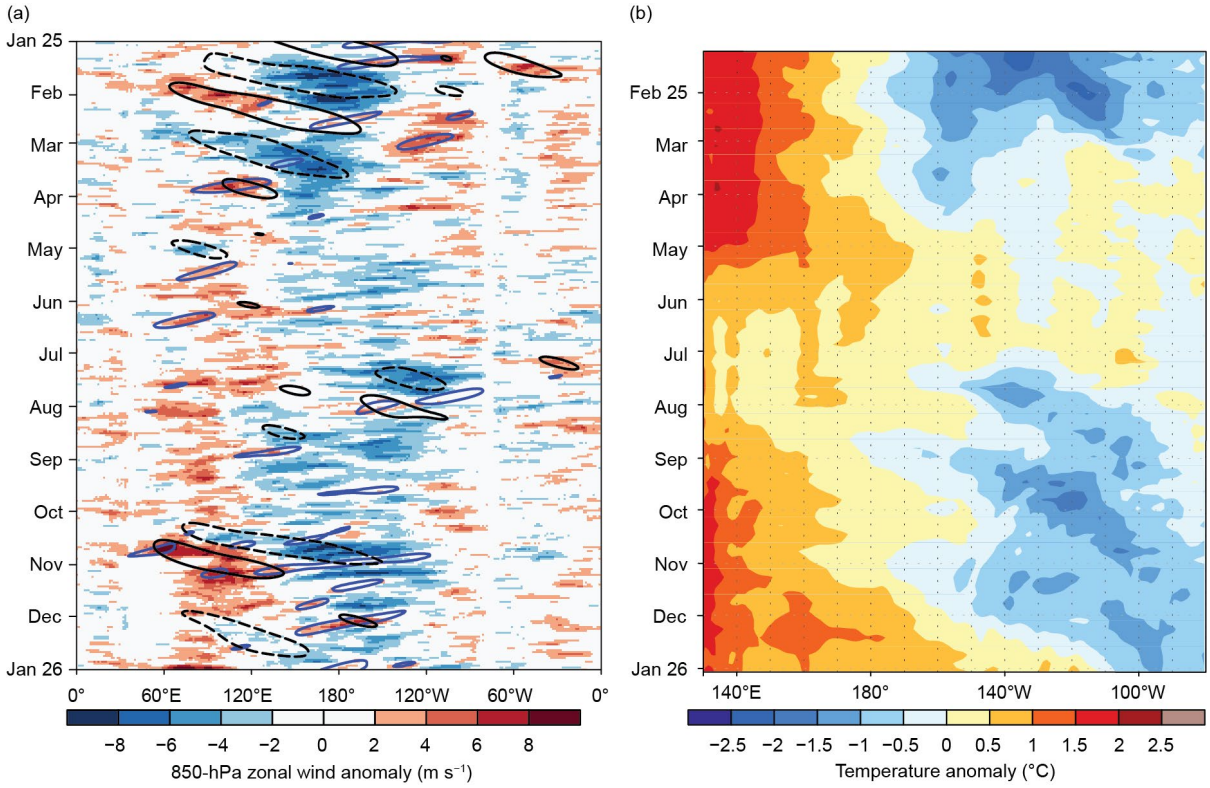

Fig. 4.8. (a) Time–longitude section for 2025 of anomalous 850-hPa zonal wind (m s^{-1}) averaged between 10°S and 10°N. Contours identify anomalies filtered for the Madden–Julian Oscillation (black) and equatorial Rossby waves (blue). (b) Time–longitude section for 2025 of the anomalous equatorial Pacific Ocean heat content, calculated as the mean temperature anomaly (°C) between 0-m and 300-m depth. Yellow/red (blue) shading indicates above- (below-) average heat content. Anomalies are departures from the 1991–2020 base period pentad means. Data in (b) are derived from an analysis system that assimilates oceanic observations into an oceanic general circulation model (Behringer et al. 1998).

A more active MJO signal emerged during July, with the enhanced convective phase propagating from the Maritime Continent, where it constructively interfered with the low-frequency base state, across the Pacific through the end of the month. The MJO propagation was evident on the RMM-based MJO index (Fig. 4.9c) but was less apparent in the objective wave filtering of the low-level wind anomalies (Fig. 4.8a), possibly due to the continued interference from the low-frequency state. By August, the MJO enhanced convective phase crossed the Western Hemisphere and Indian Ocean, becoming the dominant mode of intraseasonal variability in the tropics. The MJO progression resulted in a period of enhanced favorability for tropical cyclogenesis across the Atlantic basin ahead of the climatological peak of hurricane season, and may have aided in the formation and long duration of Hurricane Erin, which was one of three Category 5 hurricanes on the Saffir–Simpson Hurricane Wind scale to form during the 2025 Atlantic hurricane season. The MJO signal began to weaken towards the end of August, crashing inside the unit circle of the RMM index. A period of weak MJO activity returned through September.

Weak MJO activity continued into early October, with the low-frequency base state (an increasingly negative phase of the Indian Ocean dipole [IOD]) and Kelvin wave activity continuing to dominate the overall pattern. Cooling sea surface temperatures (SSTs) across the equatorial Pacific and strengthening trade winds resulted in renewed La Niña conditions, which constructively interfered with the peaking negative IOD to generate a strong enhanced convective signal over the eastern Indian Ocean and Maritime Continent. During the second half of October, however, robust MJO activity returned, with a coherent enhanced convective phase emerging over the Western Hemisphere and quickly propagating at high amplitude across the Indian Ocean and Maritime Continent. This MJO progression helped create renewed favorable conditions for tropical cyclone development across the Atlantic basin following a quiet peak of the hurricane season. Multiple cyclones formed during October, including devastating Category 5 Hurricane Melissa (see Sidebars 4.1 and 7.2 for details). MJO activity continued into November, though destructive interference with the low-frequency base state resulted in a looping of the RMM index over the Maritime Continent and West Pacific before eastward propagation resumed towards the end of the month. December began with a strong MJO projection on the RMM index over the Pacific, coinciding with a brief but potent westerly wind burst over the Pacific. This brief but strong enhancement may have also been due to constructive interference with an equatorial Rossby wave, and was sufficient to initiate a robust downwelling oceanic Kelvin wave in the Pacific, beginning to push down the upper-ocean thermocline from west to east (Fig. 4.8b). As the various modes went out of phase by mid-December, a rapid weakening of the MJO ensued, and the calendar year ended with incoherent MJO activity.

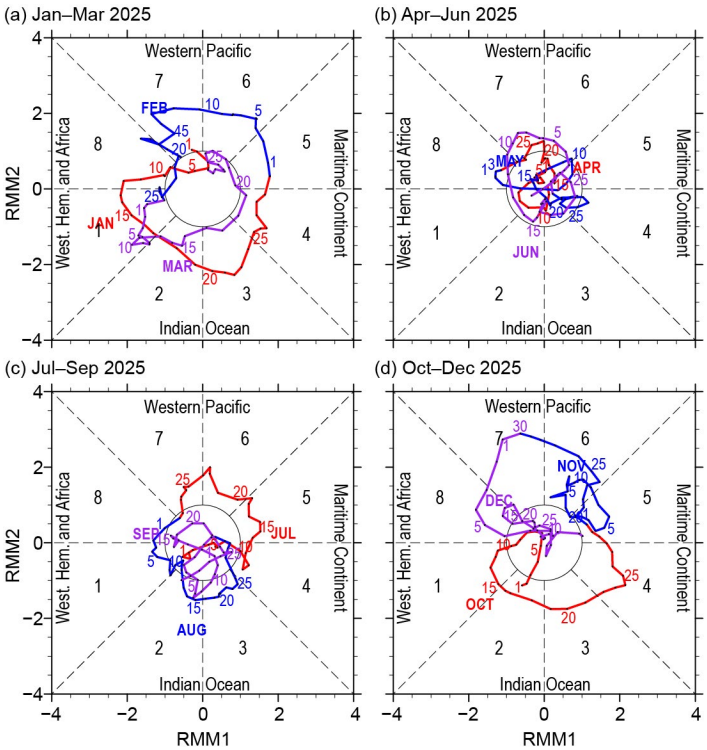

Fig. 4.9. Wheeler and Hendon (2004) Real-time Multivariate Madden–Julian Oscillation (RMM) index in 2025 for (a) Jan–Mar, (b) Apr–Jun, (c) Jul–Sep, and (d) Oct–Dec. Each point represents the Madden–Julian Oscillation (MJO) amplitude and location on a given day, and the connecting lines illustrate its propagation. Amplitude is indicated by distance from the origin, with points inside the circle representing weak or no MJO. The eight phases around the origin identify the region experiencing enhanced convection, and counter-clockwise movement is consistent with eastward propagation.

d. Intertropical convergence zones

1. PACIFIC

—N. Fauchereau

Tropical Pacific rainfall patterns are dominated by two convergence zones: the Intertropical Convergence Zone (ITCZ; Schneider et al. 2014) north of the equator, and the South Pacific Convergence Zone (SPCZ; Vincent 1994) in the southwest Pacific. The position and intensity of these convergence zones are highly sensitive to sea surface temperature (SST) anomalies, and therefore the state of El Niño–Southern Oscillation (ENSO; Trenberth 1984).

To a large extent, the rainfall anomalies recorded during January–March (JFM) 2025 (Fig. 4.10a) were consistent with the typical composite rainfall anomalies during La Niña for the same season (Fig. 4.10b). Large negative anomalies (suppressed rainfall and convection) extended eastward from about 160°E along the equator, while positive rainfall anomalies were recorded over the Maritime Continent. A wide band of negative rainfall anomalies also extended southeastward from Vanuatu to French Polynesia, while positive rainfall anomalies were present farther south, a pattern consistent with a SPCZ shifted southwest of its climatological position—another telltale La Niña pattern (Brown et al. 2020).

Later during the year, negative SST anomalies in the central and eastern Pacific weakened. However, rainfall patterns continued to exhibit signals at least partly consistent with La Niña, with a persistent "dipole" contrasting enhanced rainfall and convection over the Maritime Continent and decreased rainfall and convection farther east, centered roughly on the dateline. In August–October 2025, negative SST anomalies in the central and eastern equatorial Pacific strengthened and became more spatially coherent, signaling the return of weak La Niña conditions. Precipitation anomalies during the last quarter of 2025 again remained broadly consistent with the typical, composite rainfall anomalies observed during La Niña events.

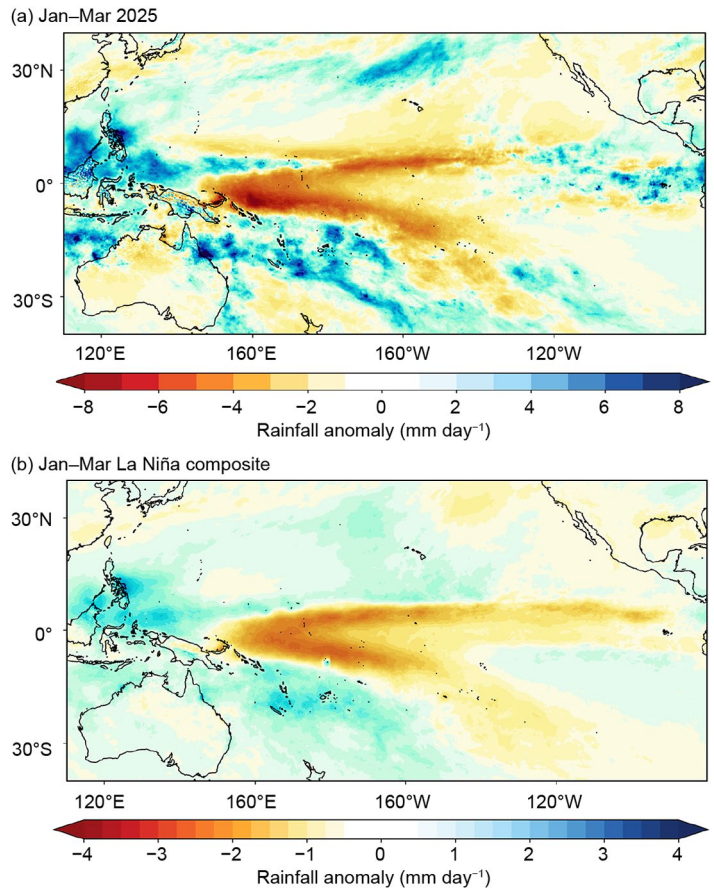

Fig. 4.10. (a) Rainfall anomalies (mm day^{-1}) for Jan–Mar 2025. The anomalies are calculated with respect to the 1991–2020 climatology. (b) Composite rainfall anomalies (mm day^{-1}) for Jan–Mar during La Niña phases (Relative Oceanic Niño Index values <–0.7°C, period 1979–2024). (Source: Multi-Source Weighted-Ensemble Precipitation [MSWEP] v2.8.0.)

Figure 4.11 summarizes the behavior for both convergence zones during 2025 using rainfall from the Multi-Source Weighted-Ensemble Precipitation (MSWEP) 2.8.0 dataset (Beck et al. 2019). Rainfall transects from 30°S to 20°N are presented for each quarter of the year, averaged across successive 30-degree longitude bands, starting in the western Pacific at 150°E–180°. The 2025 seasonal variation is compared against the longer-term 1991–2020 climatology.

The transects for January–March 2025 (Fig. 4.11a) for the western (150°E–180°) and central (180°–150°W) Pacific show that the SPCZ was shifted south and west of its climatological position, while rainfall rates within the ITCZ were reduced compared to climatology, a signature consistent with typical anomalies recorded during this season during La Niña.

Figure 4.12 shows a more detailed comparison of the western Pacific rainfall transect during January–March (Fig. 4.12a) and October–December (Fig. 4.12b), the two quarters in the year when La Niña conditions were the most established, relative to all other years in this dataset. Especially during JFM, the recorded rainfall (black line) closely corresponded to the rainfall rates recorded on average for all La Niña years (thick blue line).

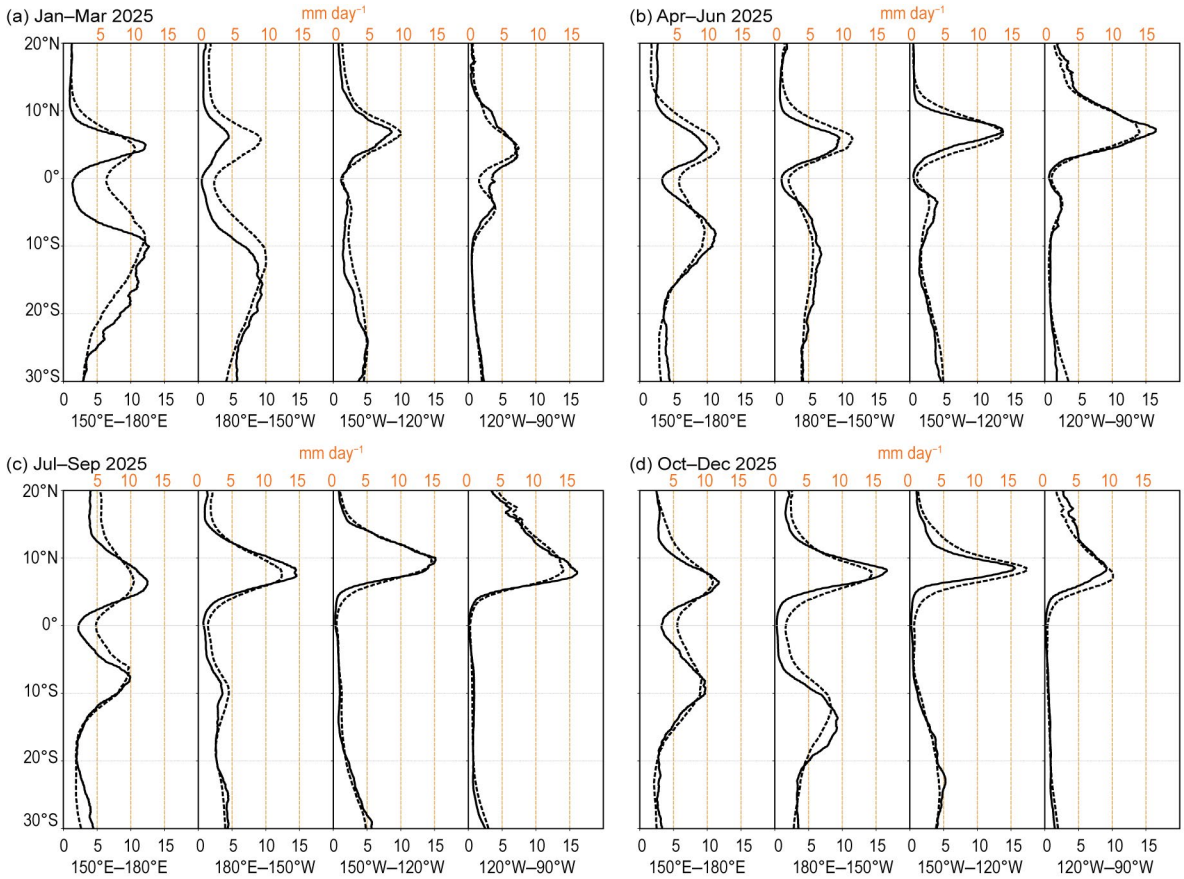

Fig. 4.11. Rainfall rate (mm day^{-1}) in 2025 for (a) Jan–Mar, (b) Apr–Jun, (c) Jul–Sep, and (d) Oct–Dec. The separate panels for each quarter show the 2025 rainfall cross-section between 30°S and 20°N (solid line) and the 1991–2020 climatology (dotted line), separately for four 30° sectors from 150°E–180° to 120°W–90°W. (Source: Multi-Source Weighted-Ensemble Precipitation [MSWEP] v2.8.0.)

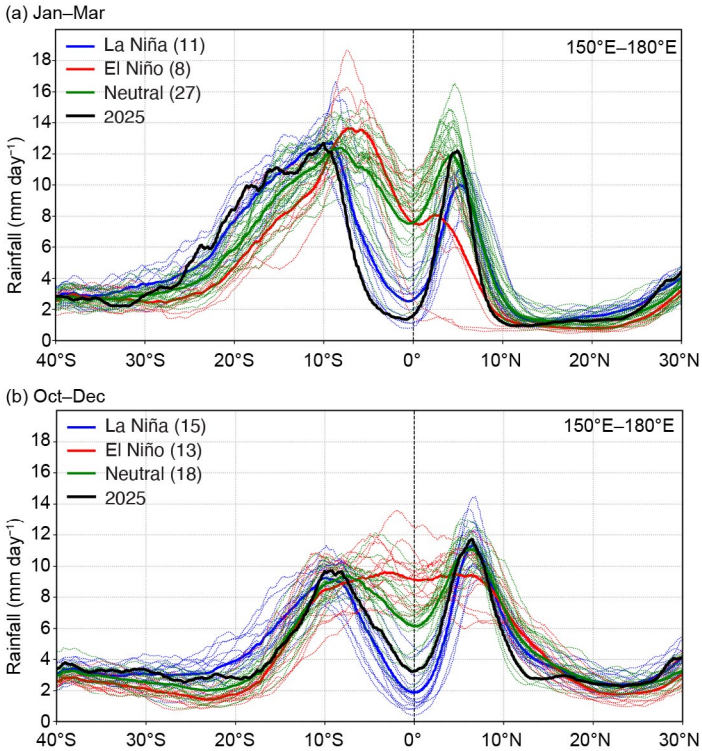

Fig. 4.12. Rainfall rate (mm day^{-1}) for (a) Jan–Mar and (b) Oct–Dec, for each year from 1979 to 2025, averaged over the longitude sector 150°E–180°. The cross-sections are color-coded according to NOAA's Relative Oceanic Niño Index (with a threshold of ±0.7°C), except 2025, which is shown in black. Dotted lines are individual years, and solid lines the average over all years in each El Niño–Southern Oscillation phase. The inset legend indicates how many years went into each composite. (Source: Multi-Source Weighted-Ensemble Precipitation [MSWEP] v2.8.0.)

2. ATLANTIC

—A. B. Pezza and C. A. S. Coelho

The Atlantic ITCZ is a well-organized convective band that oscillates between approximately 5°N–12°N during July–November and 5°S–5°N during January–May (Waliser and Gautier 1993; Nobre and Shukla 1996). Equatorial atmospheric Kelvin waves can modulate ITCZ intraseasonal variability (Guo et al. 2014). ENSO and the Southern Annular Mode (SAM) can also influence the ITCZ on interannual time scales (Münnich and Neelin 2005). The SAM, also known as the Antarctic Oscillation, describes the north–south movement of the westerly wind belt that circles Antarctica. A positive SAM event reflects a contraction of the westerly wind belt away from the equator, with stronger subtropical ridges and less precipitation in the midlatitudes (Ding et al. 2012; Liu et al. 2021; Moreno et al. 2018).

The South Atlantic responded to yet another borderline La Niña briefly developing at the beginning of 2025 and then re-emerging late in the year. Strong seasonal variability occurred, with the ITCZ sitting near its climatological position in March (Fig. 4.13a) before retreating far north of its climatological position towards the end of the year. The South Atlantic index remained negative but closer to neutral compared to the previous year (Fig. 4.13b), in concert with a more modest north–south temperature gradient compared to the vigorous Northern Hemisphere warming observed in 2024 (Figs. 4.13a,b).

In concert with the ITCZ southernmost displacement during the austral summer, positive precipitation anomalies in the South Atlantic affected parts of inland northern and northeastern Brazil during the rainy season (Fig. 4.14a). Sea level pressure anomalies over the South Atlantic (Fig. 4.14b) showed a weakened subtropical anticyclone and higher-than-normal pressures towards higher latitudes as part of a hemispheric pattern related to the SAM. Similar to 2024, this pattern was also associated with a well-developed South Atlantic Convergence Zone with some positive precipitation anomalies over southeastern Brazil (Fig. 4.14a). In essence, the combined La Niña signatures over the last two years helped bring some limited relief to a drought-stricken South American continent north of 25°S.

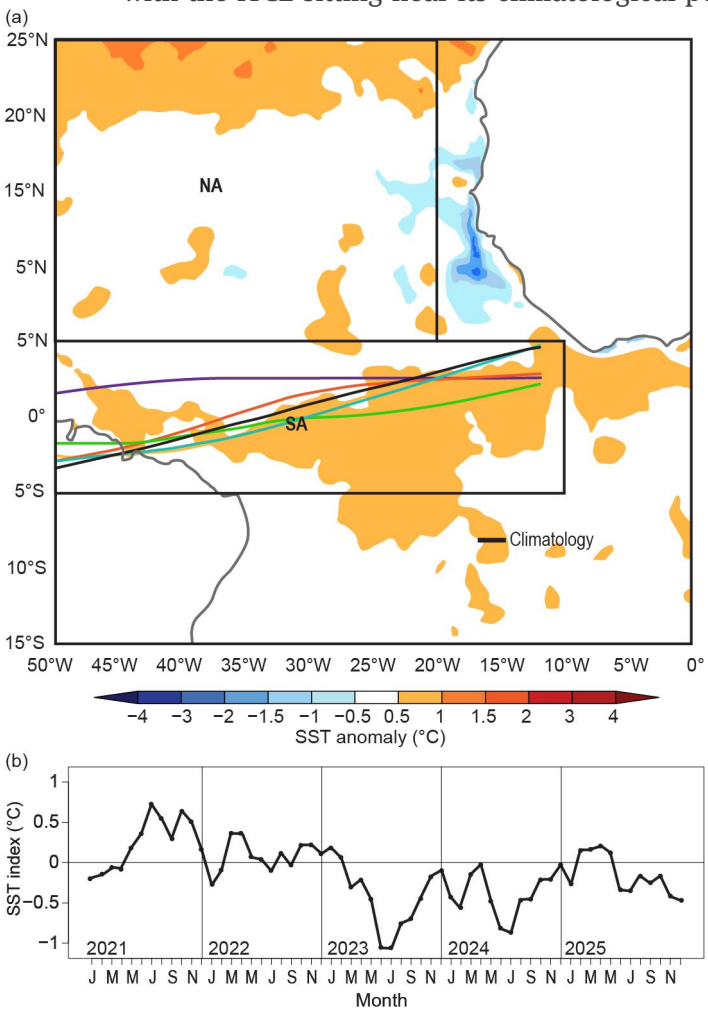

Fig. 4.13. (a) Atlantic Intertropical Convergence Zone (ITCZ) position inferred from outgoing longwave radiation (Liebmann and Smith 1996) during Mar 2025. The colored thin lines indicate the approximate position for the six pentads of the month. The thick black line indicates the Atlantic ITCZ climatological position for Mar. The sea surface temperature (SST) anomalies (°C) for Mar 2025, calculated with respect to the 1991–2020 climatology, are shaded. The two boxes indicate the areas used for the calculation of the Atlantic index in panel (b), which shows the monthly OISST (Huang et al. 2021) anomaly time series (°C) averaged over the South Atlantic (SA) sector (5°S–5°N, 10°W–50°W) minus the SST anomaly time series averaged over the North Atlantic (NA) sector (5°N–25°N, 20°W–50°W) for the period 2021–25, forming the Atlantic index. The positive phase of the index indicates favorable conditions for enhanced Atlantic ITCZ activity south of the equator.

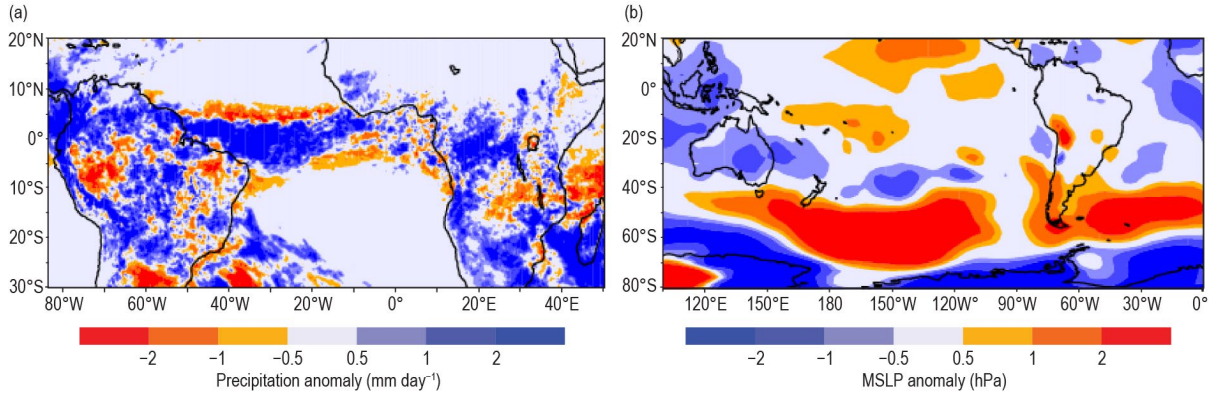

Fig. 4.14. Jan–Apr 2025 (a) precipitation anomalies (mm day^{-1}) over the Atlantic sector and (b) South American and high-latitude mean sea level pressure (MSLP; hPa) anomalies (Kalnay et al. 1996). Precipitation anomalies are calculated with respect to the 1998–2024 climatology and are derived from Global Precipitation Measurement (GPM) Integrated Multi-Satellite Retrievals for GPM (IMERG; Huffman et al. 2023). MSLP anomalies are calculated with respect to the 1991–2020 climatology and are derived from the National Centers for Environmental Prediction (NCEP) National Center for Atmospheric Research (NCAR) reanalysis (Kalnay et al. 1996).

e. Global monsoon summary

—B. Wang, J. Li, and Q. He

The global monsoon is the dominant mode of annual variations in tropical and subtropical precipitation and the atmospheric circulation (Wang and Ding 2008). Figure 4.15 shows the monsoon domain (purple lines) defined by rainfall characteristics (contrast between rainy summer and dry winter; Wang 1994), rather than the traditional definition based on winds (Ramage 1971). The Northern Hemisphere (NH) comprises five regional monsoons: northern Africa, India, East Asia, the western North Pacific, and North America. The Southern Hemisphere (SH) consists of three regional monsoons: southern Africa, Australia, and South America.

Here, precipitation and low-level circulation anomalies during the 2025 "monsoon year," are first reviewed, including the SH summer (November 2024–April 2025) and NH summer (May–October 2025) monsoons. Quantitative measures of regional and global monsoon anomalies are then presented using monsoon precipitation and circulation indices.

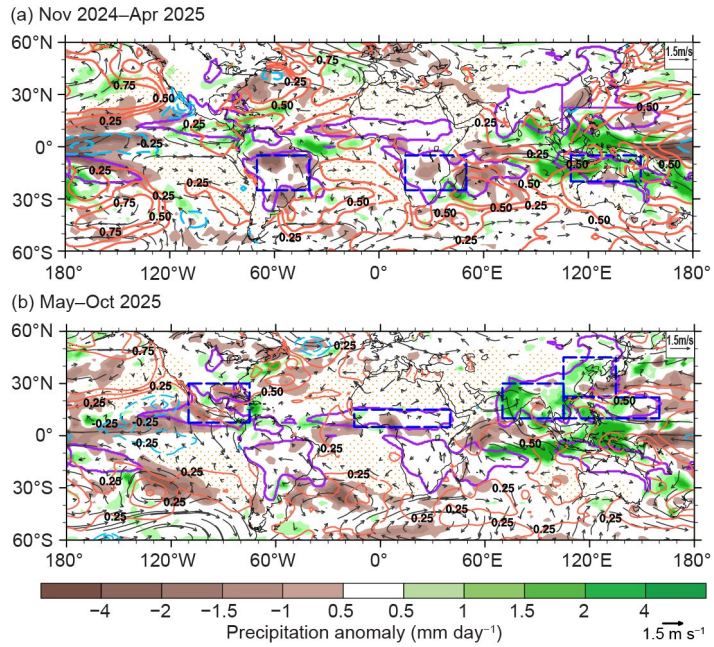

Fig. 4.15. Summer mean precipitation anomalies (mm day^{-1}, shading) and 850-hPa wind anomalies (m s^{-1}) for the (a) Southern Hemisphere (SH) summer monsoon season: Nov 2024–Apr 2025 and (b) Northern Hemisphere (NH) summer monsoon season: May–Oct 2025. Anomalies are departures from the 1991–2020 climatology. Purple lines in (a) and (b) outline the global monsoon precipitation domain. The orange (cyan) contours denote positive (negative) sea surface temperature anomalies with a contour interval of 0.25°C. The blue rectangular boxes denote the regions where the regional monsoon precipitation indices are measured. The dotted area represents the dry region, with local summer precipitation rates below 1 mm day^{-1}. Two criteria define the monsoon domains: 1) the annual precipitation range (summer-minus-winter mean) exceeds 300 mm, and 2) the summer precipitation is >55% of the total annual precipitation amount, where summer here refers to Nov–Mar for the SH and May–Sep for the NH (Wang and Ding 2008). (Source: Global Precipitation Climatology Project; Huffman et al. 2009.)

1. PRECIPITATION AND CIRCULATION ANOMALIES

During the SH summer from November 2024 to April 2025, a weak La Niña in the central Pacific strengthened the Walker circulation, leading to suppressed rainfall over the equatorial central Pacific (150°E–120°W) and enhanced rainfall across the Maritime Continent and the eastern equatorial Indian Ocean (80°E–120°E; Fig. 4.15a). Latent heating over the Maritime Continent generated a pair of low-level Rossby waves and low pressure over the eastern Indian Ocean, while also enhancing the anticyclonic circulation in the southwest Indian Ocean and southern Africa, suppressing southern African monsoon rainfall. Reduced precipitation over South America contradicted the typical rainfall enhancement during La Niña. This reduction was associated with enhanced convection over Central America and the adjacent oceans, which generated downward motion to its south and north via a local meridional circulation (Fig. 4.15a). Low-level wind divergence and downward motion across the southern Africa and South American monsoon regions reduces precipitation, leading to overall rainfall deficits across the SH monsoon region.

During the 2025 NH summer monsoon season (May–October), a La Niña-like cooling developed in the central-eastern equatorial Pacific (Fig. 4.15b). The Niño-3.4 sea surface temperature (SST) anomaly decreased from −0.1°C in May to −0.5°C in October. This cooling suppressed rainfall across the equatorial Pacific while increasing precipitation over the Maritime Continent and the eastern Indian Ocean (60°E–120°E; Fig. 4.15b). The increased rainfall anomaly over the Maritime Continent excited an atmospheric ascending Rossby wave low under the influence of easterly vertical shear associated with the Asian monsoon (Wang and Xie 1996), which enhanced Indian summer monsoon rainfall (Fig. 4.15b). Meanwhile, suppressed precipitation over the

central Pacific strengthened the western Pacific subtropical high through a descending Rossby wave high, resulting in increased East Asian monsoon rainfall to its northwest and western North Pacific monsoon rainfall to its southeast (Fig. 4.15b). The North American monsoon region was controlled by a low-level anticyclone due to eastward expansion of cool SST anomalies, resulting in divergent winds and reduced precipitation (Fig. 4.15b). Northern African monsoon precipitation was near normal, in line with near-average Atlantic SSTs (Fig. 4.15b).

2. REGIONAL MONSOON PRECIPITATION AND CIRCULATION

Regional monsoon precipitation and circulation indices are used to measure the integrated regional monsoon intensity. The regional monsoon precipitation indices are defined as the anomalous precipitation rate (mm day^{-1}) averaged over each of the blue rectangular box regions shown in Fig. 4.15. Precipitation averaged in each blue box can well represent the precipitation averaged over the corresponding, actual regional monsoon domain (Yim et al. 2014). The definitions of the circulation indices for each monsoon region are presented in Table 4.1. These circulation indices are generally defined by the meridional shear of the zonal winds at 850 hPa, which measures the intensity (relative vorticity) of the monsoon troughs, except for the northern African and East Asian monsoons. The northern African monsoon circulation index is defined by the westerly monsoon strength, reflecting the south–north thermal contrast across the northern African monsoon region. The East Asian summer monsoon circulation index is determined by the meridional wind strength, reflecting the east–west thermal contrast between the Asian continent and the western North Pacific.

Table 4.1 shows that precipitation and circulation indices are strongly correlated across most regional monsoons, with monthly mean correlation coefficients ranging from 0.70 to 0.88, except for the southern African monsoon, which has a lower correlation of 0.58. Therefore, the regional precipitation and circulation indices generally provide consistent measures of the strength of each regional monsoon system. Furthermore, the circulation indices faithfully represent land

Table 4.1. Definition of the regional summer monsoon circulation indices and their correlation coefficients with the corresponding regional summer monsoon precipitation indices for 1979/80–2024/25. The precipitation indices are defined by the areal mean precipitation anomalies over the blue box regions shown in Fig. 4.15. R (r) represents the correlation coefficient between the total (land) monsoon precipitation and the corresponding circulation index. Correlation coefficients were computed using monthly time series (184 summer months; Jun–Sep in the Northern Hemisphere [1980–2025] and Dec–Mar in the Southern Hemisphere [1979/80–2024/25]). All numbers are significant at the 99% confidence level.

Regional monsoon	Definition of the circulation index	R (r)
Indian (ISM)	U850 (5°N–15°N, 40°E–80°E) minus U850 (25°N–30°N, 60°E–90°E)	0.71 (0.59)
Western North Pacific (WNPSM)	U850 (5°N–15°N, 100°E–130°E) minus U850 (20°N–35°N, 110°E–140°E)	0.87 (0.71)
East Asian (EASM)	V850 (20°N–35°N, 120°E–140°E) plus V850 (10°N–25°N, 105°E–115°E)	0.72 (0.73)
North American (NASM)	U850 (5°N–15°N, 130°W–100°W) minus U850 (20°N–30°N, 110°W–80°W)	0.85 (0.79)
Northern African (NAFSM)	U850 (0°–10°N, 40°W–10°E)	0.70 (0.68)
South American (SASM)	U850 (20°S–5°S, 70°W–40°W) minus U850 (35°S–20°S, 70°W–40°W)	0.78 (0.79)
Southern African (SAFSM)	U850 (12°S–2°S, 10°W–30°E) minus U850 (30°S–10°S, 40°E–60°E)	0.58 (0.46)
Australian (AUSSM)	U850 (15°S–0°, 90°E–130°E) minus U850 (30°S–20°S, 100°E–140°E)	0.88 (0.79)

monsoon precipitation in each monsoon region, with correlation coefficients ranging from 0.68 to 0.79, except in the Indian and southern African land monsoon regions, where the leading modes of precipitation anomalies exhibit a dipolar pattern (Yim et al. 2014).

Figure 4.16 shows year-to-year variations in areal averaged summer monsoon precipitation and circulation intensities for each regional monsoon. Notably, the Indian and northern African summer monsoon rainfall shows an evident trend from 1979 to 2025. During boreal summer (May–October) 2025, the Indian, western North Pacific, and East Asian monsoon precipitation and circulation indices are all positive, exceeding one standard deviation (Figs. 4.16b–d). In particular, Indian monsoon rainfall exceeds the two standard deviation threshold. The northern

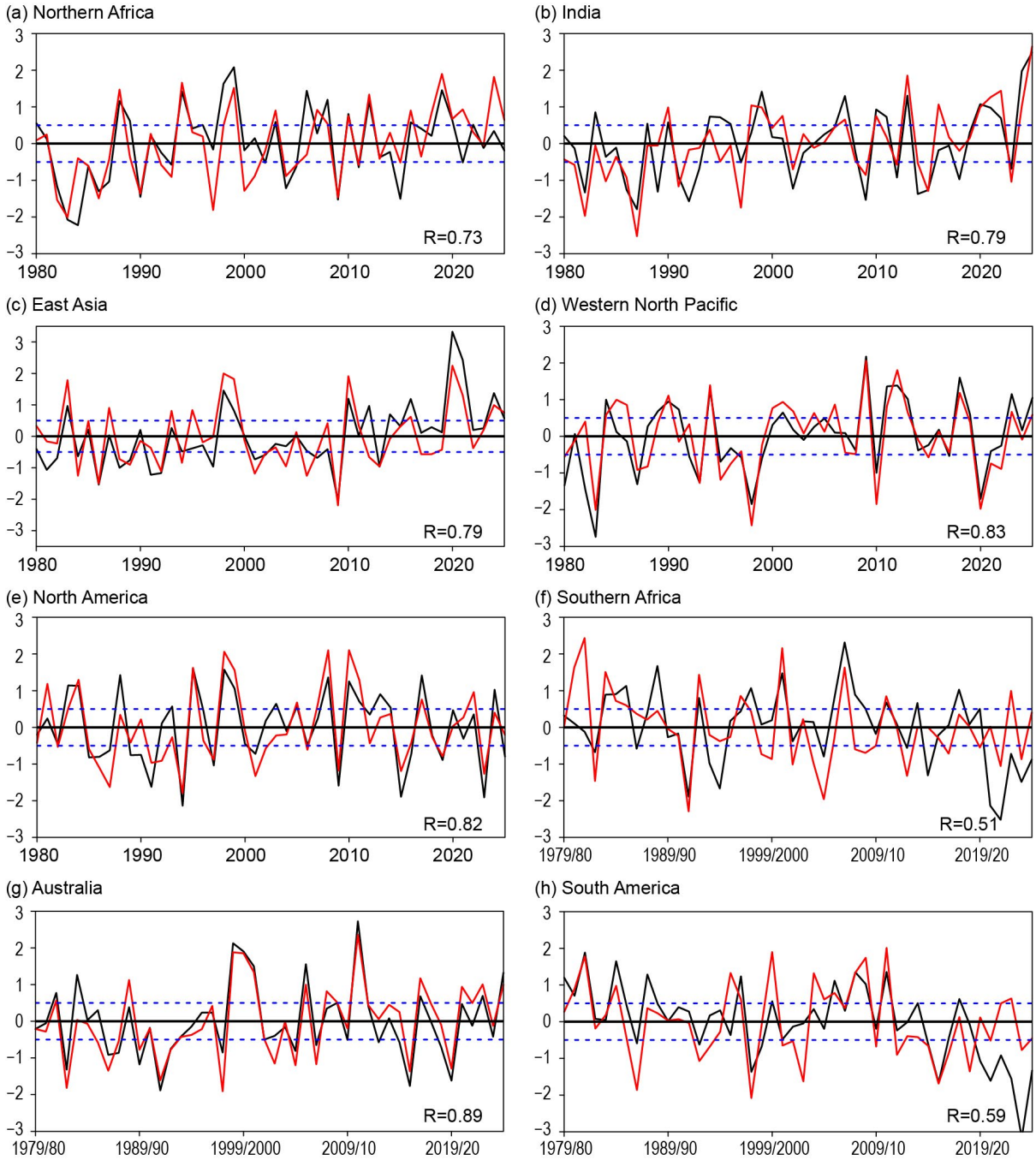

Fig. 4.16. (a)–(h) Temporal variations of summer monsoon precipitation (black lines) and low-level circulation (red lines) indices for eight regional monsoons. The precipitation indices represent the anomalous precipitation rate averaged over the blue rectangular box regions shown in Figure 4.15. The circulation indices are defined in Table 4.1. All indices were normalized by their corresponding standard deviations (ordinates) derived from the period 1979/80–2024/25. Numbers in the bottom right of each panel denote the correlation coefficient between the seasonal mean precipitation and circulation indices (sample size: 46). Dashed lines indicate ±0.5 std. dev. The summer monsoon seasons are May–Oct for the Northern Hemisphere and Nov–Apr for the Southern Hemisphere. (Source: GPCP for precipitation; ERA5 [Hersbach et al. 2020] for circulation.)

African monsoon circulation and rainfall indices reflect normal conditions (Fig. 4.16a). The North American monsoon circulation and rainfall indices indicate below-normal conditions (Fig. 4.16e). In summary, during the development of weak La Niña conditions during summer/autumn of 2025, the NH regional monsoon responses are similar to those observed during past La Niña events.

During the SH summer (November 2024 to April 2025), the Australian summer monsoon precipitation and circulation index were both positive (Fig. 4.16g). However, the South American summer monsoon had deficient rainfall (1.5 standard deviations below average) and a moderately weak circulation index (0.5 standard deviations below average; Fig. 4.16h). The southern African summer monsoon precipitation was deficient (one standard deviation below average) while the circulation intensity was 0.4 standard deviations above average (Fig. 4.16f). The severe drought-induced land surface conditions over the previous three years may have amplified the deficient rainfall when the monsoon circulation was weaker than normal.

3. LAND MONSOON PRECIPITATION ANOMALIES

Because monsoon rainfall over land has a greater socioeconomic impact than over the oceans, we examine land monsoon rainfall (LMR) in the NH (May–October) and the SH (November–April) seasons. We use the mean precipitation rate (mm day^{-1}) averaged over land areas within the NH and SH monsoon domains to measure NH and SH LMR intensity, respectively.

Year-to-year variations in the NH and SH LMR are primarily influenced by ENSO, as indicated by historical observations (Wang et al. 2012). Both NH and SH summer LMR show a significant anti-correlation with the concurrent Niño-3.4 index (Fig. 4.17). The NH LMR has a correlation of −0.72 for the period 1980–2025 (Fig. 4.17a). During the NH summer 2025, coinciding with the development of La Niña, the NH LMR increased by 1.9 std. dev., (~0.44 mm day^{-1} or ~79.4 mm over six months) in the NH land monsoon regions (Fig. 4.17a). The increased NH LMR under La Niña is consistent with the historically observed negative El Niño–NH LMR relationship.

Similarly, the SH LMR exhibits a negative correlation with the Niño-3.4 index. However, this negative correlation reversed in recent years. The SH land monsoon has experienced severe dry conditions for five consecutive years–2019/20 to 2024/25–despite four of those five years having La Niña events. As a result, the correlation coefficient for the entire period from 1979/80–2024/25 is −0.57 compared with −0.75 from the earlier 1979/80–2019/20 period (Fig. 4.17b). These differences are an area for future research.

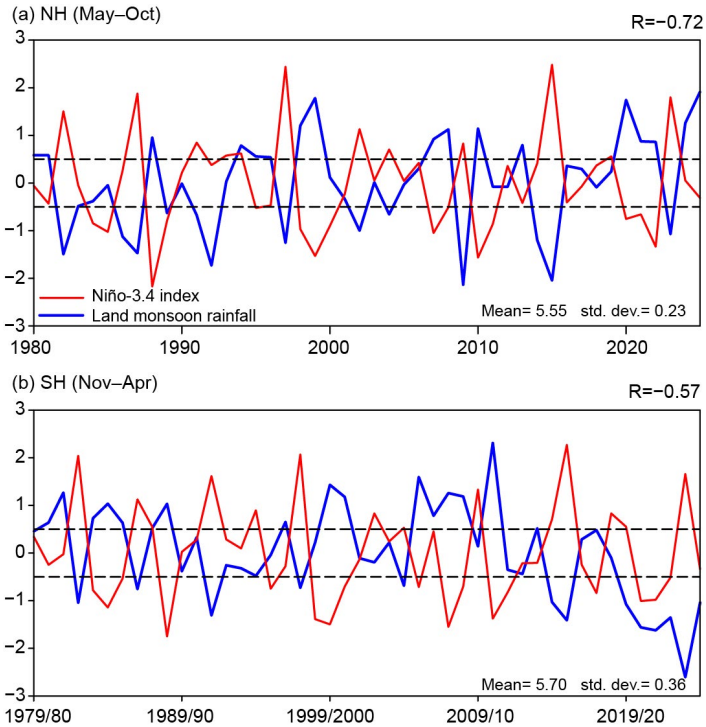

Fig. 4.17. Anticorrelation between El Niño–Southern Oscillation and the Northern Hemisphere (NH) and Southern Hemisphere (SH) land monsoon rainfall. (a) NH summer (May–Oct) land monsoon precipitation anomaly (blue line) normalized by its standard deviation (std. dev.) during the period 1980–2025. The climatological mean NH summer land monsoon precipitation (mean) and std. dev. are shown in the lower right panel (mm day^{-1}). The number at the top right of each panel denotes the correlation coefficient (R) between the seasonal mean precipitation anomaly and the simultaneous Niño-3.4 index (red line). Dashed lines indicate ±0.5 std. dev. (b) As in (a), except for the SH summer (Nov–Apr) during the period 1979/80–2024/25. The land monsoon precipitation excludes monsoon rainfall from the oceanic monsoon domain. (Source: GPCP for precipitation; HadISST and ERSSTv5 for sea surface temperature.)

f. Indian Ocean dipole

—L. Chen and J.-J. Luo

The Indian Ocean dipole (IOD) is the dominant mode of interannual variability in the tropical Indian Ocean (IO), characterized by a zonal dipole of sea surface temperature anomalies (SSTAs) along the equatorial IO (Saji et al. 1999; Webster et al. 1999; Luo et al. 2010, 2012). The IOD arises from local air–sea coupling within the tropical IO and/or remote forcing associated with the El Niño–Southern Oscillation (ENSO; Luo et al. 2007, 2010). Typically, IOD events develop during boreal spring and summer, mature in boreal autumn, and terminate rapidly in early winter. A negative IOD (nIOD) event features anomalous warming in the eastern IO and weak cooling in the western IO during boreal summer/autumn (with the opposite pattern for a positive IOD). The IOD also exhibits pronounced nonlinearity: positive IOD events are often stronger than nIOD events, reflecting asymmetric air–sea feedback strength between the two phases (Luo et al. 2007; Hong et al. 2008).

In 2025, the tropical IO experienced a strong nIOD event, with significant positive SSTAs in the eastern pole and negative SSTAs in the western pole (Fig. 4.18a). The IOD index reached –1.2°C in boreal autumn based on the OISST dataset (Fig. 4.18b). Since 1982, a total of 13 nIOD events have occurred, and the 2025 event was among the strongest over the past 44 years.

This nIOD began to develop in boreal summer 2025 and intensified into a strong nIOD in boreal autumn (Fig. 4.18b). Notably, a weak nIOD event occurred in boreal autumn 2024 (Chen and Luo 2025). This event peaked in October 2024 and decayed relatively slowly when compared with previous nIOD events, such that nIOD-like conditions persisted during the 2024/25 winter (Figs. 4.18a,b). Although the tropical-mean IO SSTA showed a weak negative Indian Ocean basin (IOB) mode from December 2024 to February 2025 (Fig. 4.18c), the equatorial zonal SSTA contrast and associated wind anomalies retained an nIOD-like structure during the 2024/25 winter (Fig. 4.20a).

This persistence was partly supported by remote forcing from the concurrent La Niña conditions. As indicated by the anomalous velocity potential field at the 200-hPa level (contours in Fig. 4.20a), the La Nina in 2024/25 winter (Fig. 4.18c) excited enhanced subsidence over the central equatorial Pacific and enhanced ascent over the Maritime Continent during the 2024/25 La Niña conditions (Fig. 4.20a), accompanied by an anomalous descending branch over eastern equatorial Africa and the western equatorial IO. These large-scale Walker circulation anomalies favored strong westerly surface wind anomalies over the central equatorial IO from December 2024 to January 2025 (black curve in Fig. 4.18b; vectors in Fig. 4.19a). As a result, positive upper-ocean heat content (OHC) anomalies accumulated in the eastern

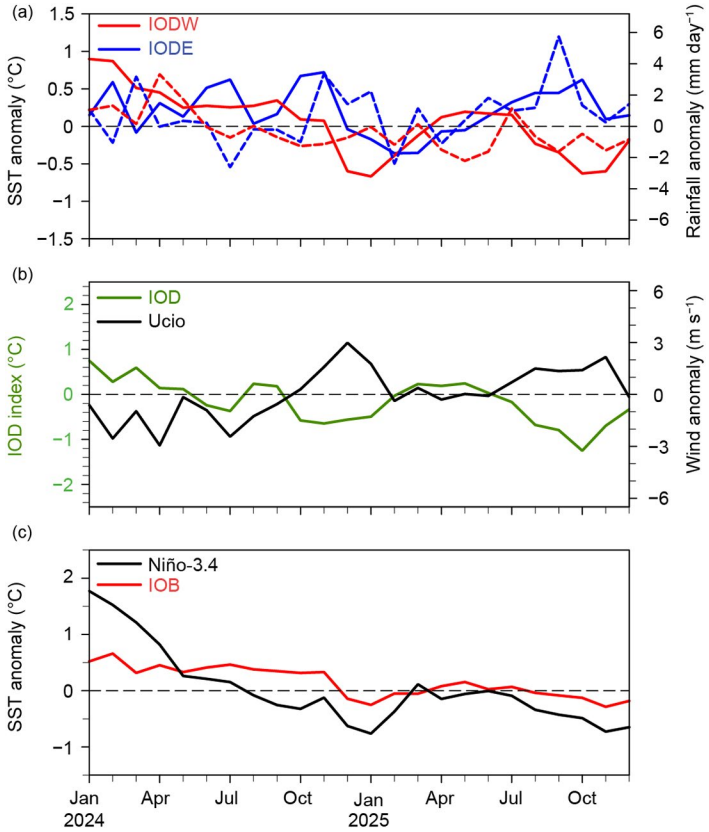

Fig. 4.18. (a) Monthly anomalies of sea surface temperature (SST; °C; solid lines) and precipitation (mm day⁻¹; dashed lines) in the eastern part of the Indian Ocean dipole (IODE; 10°S–0°, 90°E–110°E; blue lines) and the western part of the IOD (IODW; 10°S–10°N, 50°E–70°E; red lines). (b) As in (a), but for the IOD index (measured by the SST difference between IODW and IODE; green line) and surface zonal wind anomaly (m s⁻¹) in the central equatorial IO (Ucio; 5°S–5°N, 70°E–90°E; black line). (c) As in (a), but for the SST anomalies in the Niño-3.4 region (5°S–5°N, 170°W–120°W; black line) and the tropical IO (Indian Ocean basin [IOB]; 20°S–10°N, 40°E–120°E; red line). Anomalies are relative to the 1982–2025 base period. (Sources: NOAA OISST [Reynolds et al. 2002]; monthly CMAP precipitation analysis [available at https://psl.noaa.gov/data/gridded/data.cmap.html] and JRA-55 atmospheric reanalysis [Ebita et al. 2011].)

equatorial IO during the 2024/25 winter (Fig. 4.19a), even though SSTAs along the equatorial IO were negative (shading in Fig. 4.20a).

During boreal spring 2025, equatorial IO SSTAs weakened to near zero, and the tropical IO was characterized by anomalous cross-equatorial southerlies together with low-level westerly anomalies around the Indian Peninsula (Fig. 4.19b), consistent with the earlier onset of the Indian monsoon (see section 7g4 for details). Importantly, the positive OHC anomalies in the eastern equatorial IO did not fully dissipate; instead, a residual positive OHC signal persisted into spring (Fig. 4.19b). Although La Niña weakened during boreal spring 2025, the remaining negative SSTAs near the dateline continued to excite an anomalous Walker circulation across the equatorial Indo-Pacific (Fig. 4.20b). This remote forcing maintained weak westerly anomalies over the eastern equatorial IO and northwesterly anomalies along the west coast of Sumatra (Fig. 4.19b).

In boreal summer, La Niña fully dissipated (Fig. 4.18c). The residual positive OHC anomalies in spring 2025 preconditioned the eastern IO, allowing SSTAs in the eastern pole of the IOD to grow from late spring and emerge as clear warming by boreal summer (Figs. 4.18a, 4.20c). Subsequently, the Bjerknes feedback amplified the nIOD-related zonal SSTA contrast along the equatorial IO, and the associated westerly wind anomalies over the central equatorial

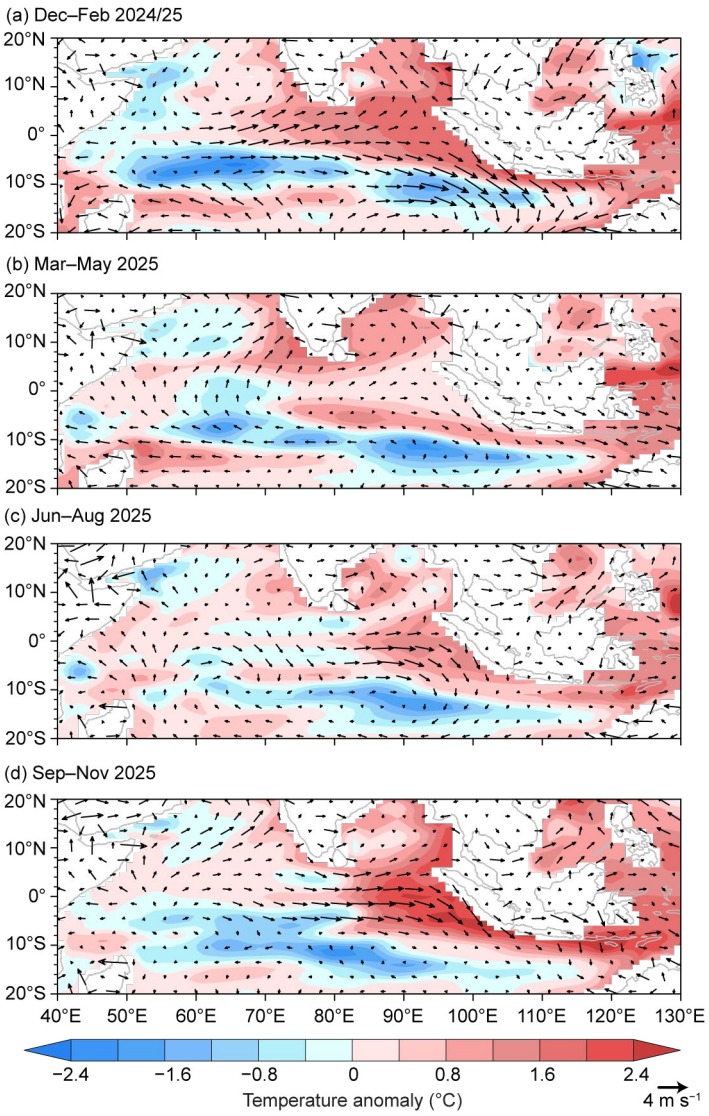

Fig. 4.19. Upper-ocean (0 m–300 m) mean temperature anomalies (°C, colored scale) and surface winds (m s^{-1}) anomalies (vectors) during (a) Dec 2024–Feb 2025, (b) Mar–May 2025, (c) Jun–Aug 2025, and (d) Sep–Nov 2025. (Sources: Monthly National Centers for Environmental Prediction GODAS data [available at https://psl.noaa.gov/data/gridded/data.godas.html Saha et al. 2006] and JRA-55 atmospheric reanalysis [Ebita et al. 2011].)

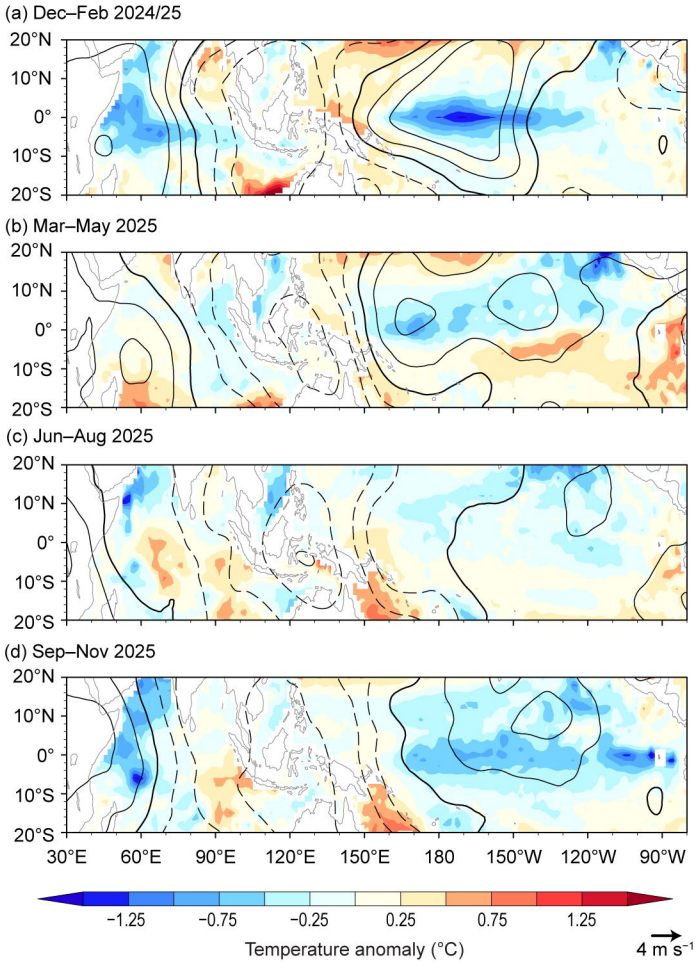

Fig. 4.20. Sea surface temperature anomalies (°C, colored scale) superposed by 200-hPa velocity potential (× 10^6 m^2 s^{-1}; contours with an interval of 1, and solid/dashed/bold curves denote positive/negative/zero values) during (a) Dec 2024–Feb 2025, (b) Mar–May 2025, (c) Jun–Aug 2025, and (d) Sep–Nov 2025. Anomalies were calculated relative to the climatology over the period 1982–2025. (Sources: NOAA OISST [Reynolds et al. 2002] and JRA-55 atmospheric reanalysis [Ebita et al. 2011].)

IO were also reinforced from boreal summer to boreal autumn (Figs. 4.18b, 4.20c,d). Here, the Bjerknes feedback refers to a positive air–sea coupling in which an initial sea surface temperature (SST) gradient anomaly modifies surface winds, the wind changes alter the upper-ocean conditions (e.g., thermocline depth and upwelling), and the resulting oceanic response further reinforces the original SST anomaly (Bjerknes 1969; Saji et al. 1999; and Li et al. 2003).

By boreal autumn, a weak La Niña began to redevelop in the Pacific (Figs. 4.18c, 4.20d). From an Indo-Pacific perspective, the renewed equatorial Pacific cooling reinvigorated the anomalous Walker circulation across the equatorial Indo-Pacific (Fig. 4.20d), thereby further strengthening the westerly wind anomalies over the central equatorial IO (Figs. 4.18b, 4.19d). Accordingly, the persistence of these westerly anomalies from boreal summer through autumn promoted continued oceanic heat buildup in the eastern IOD pole, allowing the positive OHC anomalies to peak in boreal autumn. Together, these processes contributed to the maturation of a strong nIOD in boreal autumn 2025.

A notable feature of the 2025 event was the prominent role of subsurface heat content in the eastern equatorial IO. Even when equatorial SSTAs weakened in boreal spring, the persistence of positive OHC provided a "memory" that bridged seasons and enabled a rapid surface re-emergence of warming in late spring–summer. This highlights the value of monitoring subsurface conditions (in addition to SST-based indices) for anticipating nIOD development. Additionally, the late springtime cross-equatorial flow and regional westerly wind anomalies due to the earlier onset of the Indian monsoon may have helped maintain eastern IO coastal wind anomalies (e.g., along Sumatra) that were conducive to anomalous coastal downwelling and the evolution of positive SST and OHC anomalies. This indicates that the monsoon seasonal transition may act as a "gatekeeper" for IOD evolution by shaping the background winds and coastal wind anomalies.

g. Tropical cyclones

1. OVERVIEW

—H. J. Diamond and C. J. Schreck

The International Best Track Archive for Climate Stewardship (IBTrACS) dataset comprises historical tropical cyclone (TC) best-track data from numerous sources around the globe, including all of the World Meteorological Organization (WMO) Regional Specialized Meteorological Centers (RSMCs; Knapp et al. 2010). This dataset represents the most complete compilation of global TC data. From these data, 1991–2020 climatological values of TC activity for each basin using statistics from both the WMO RSMCs and the Joint Typhoon Warning Center (JTWC) are calculated following Schreck et al. (2014). These values are referenced in each subsection. Tallying the global TC numbers is challenging and involves more than simply adding up basin totals, as some storms cross TC basin boundaries, some TC basins overlap, and multiple agencies track and categorize them. The Northern Hemisphere (NH) basins are typically measured from January to December, while Southern Hemisphere (SH) basins are typically measured from July to June. Global values here are the sum of NH for 2025 and SH for 2024/25. Unless otherwise noted, the statistics are based on preliminary data from NOAA's National Hurricane Center (NHC) and the JTWC. However, differences between the JTWC and the WMO RSMCs or other local agencies are noted as appropriate.

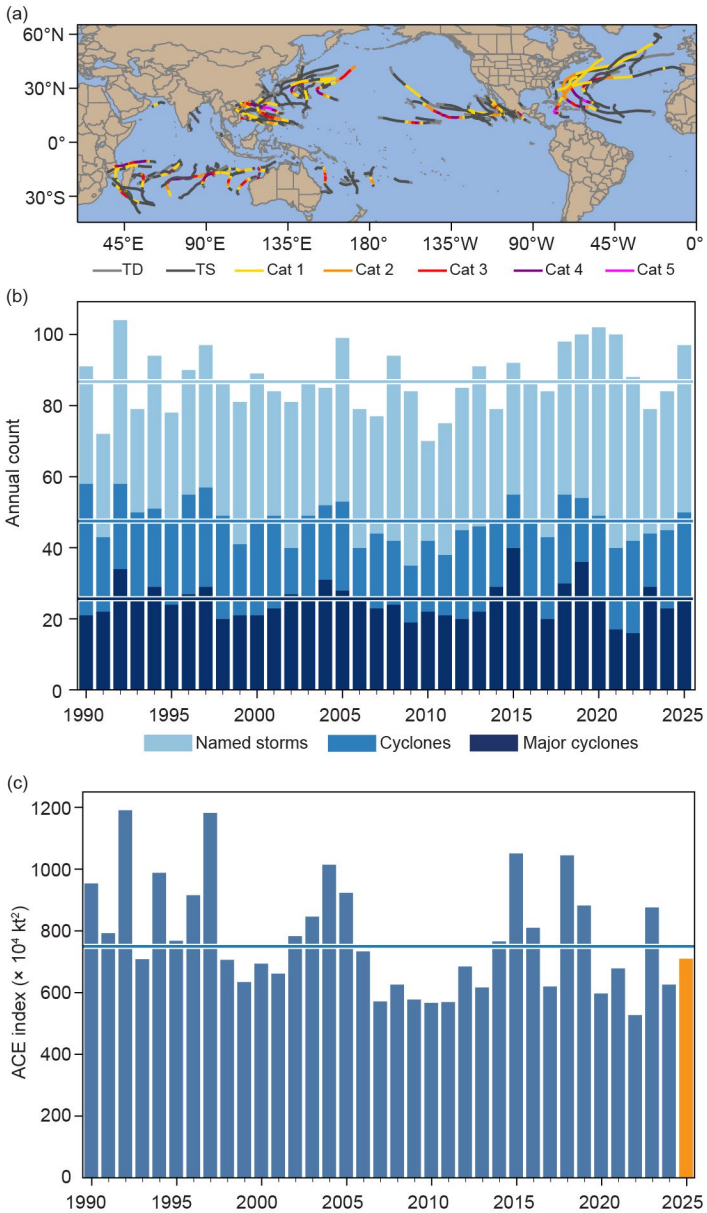

Fig. 4.21. (a) Global summary of tropical cyclone (TC) tracks for the 2025 Northern Hemisphere season (Jan–Dec) and 2024/25 Southern Hemisphere season (Jul–Jun) relative to the 1991–2020 base period; (b) global TC counts; and (c) global accumulated cyclone energy (ACE) values (× 10^4 kt^2). Horizontal lines on (b) and (c) represent the 1991–2020 climatology.

Based on preliminary data from the NHC and the JTWC as archived in IBTrACS (Fig. 4.21), the combined 2025 season had 97 named storms (sustained wind speeds ≥34 kt or 17 m s^{-1}), which is 15 greater than last season in 2024 (Diamond and Schreck 2025) and the most since 2021 (Diamond and Schreck 2022). There were 50 hurricanes/typhoons/cyclones (HTCs; sustained wind speeds ≥64 kt or 33 m s^{-1}), 25 of which reached major HTC status (sustained wind speeds ≥96 kt or 49 m s^{-1}), which was nearly equivalent to the number of major HTCs in 2024. The accumulated cyclone energy (ACE) for the season was 711 × 104 kt^2, ~14% more than in 2024 (Diamond and Schreck 2025).

In sections 4g2–4g8, 2024/25 SH and 2025 NH seasonal TC activities are described and compared to the historical record for each of the seven WMO-defined TC basins. For simplicity, all counts are broken down by the U.S. Saffir–Simpson Hurricane Wind Scale (SSHWS)[2]. The overall picture of global TCs during 2025 is depicted in Fig. 4.21 and counts by category and intensity are documented in Table 4.2.

The western North Pacific and southwest Pacific basins each had below-normal ACE relative to 1991–2020, while the South Indian and Australian basins were above normal. Table 4.2 uses

[2] SSHWS is based on one-minute averaged winds, and the categories are defined at: https://www.weather.gov/mfl/saffirsimpson; the Australian category scale is based on 10-minute averaged winds, and those categories are defined in Table 3 at: https://www.bom.gov.au/resources/learn-and-explore/tropical-cyclone-knowledge-centre/tropical-cyclone-categories

this climatological period to classify seasons for consistency amongst basins. However, NOAA uses the terciles from 1951–2020 to classify North Atlantic ACE owing to the longer record of data there. The 2025 seasonal totals for named storms, hurricanes, and major hurricanes were all close to long-term means, though the fraction of hurricanes that became major hurricanes was the highest since 1950. The 2025 seasonal ACE value was 135% of the 1951–2020 median of 96.7. In the North Atlantic, Hurricane Melissa was one of the strongest storms on record, achieving a lifetime maximum intensity of 165 kt (85 m s^{-1}) and a minimum central pressure of 892 hPa. Melissa made landfall in Jamaica at its peak intensity, causing devastation on the western part of the island. It made an additional landfall in Cuba as a Category 3 hurricane and brought significant impacts to the southeastern and central Bahamas. Two sidebar articles detail this storm: Sidebar 4.1 in this chapter focuses on the physical and meteorological aspects of the storm, and Sidebar 7.2 in the Regional Climates chapter examines the severe impacts of the storm on Jamaica and other Caribbean countries.

Table 4.2. Global counts of tropical cyclone (TC), hurricane/typhoon/cyclone (HTC), major HTC, and Category 5 storm activity by Global counts of tropical cyclone (TC), hurricane/typhoon/cyclone (HTC), major-HTC, and Category 5 storm activity by basin for 2025. "+" denotes top tercile; "++" is top 10%; "–" is bottom tercile; "––" is bottom 10% (all relative to 1991–2020). (Note that some inconsistencies between Table 4.2 and the text of the various basin analyses in section 4g exist and are unavoidable, as tallying global TC numbers is challenging and involves more than simply adding up basin totals, because some storms cross TC basin boundaries, some TC basins overlap, and multiple agencies are involved in tracking and categorizing TCs.)

Basin	TCs	HTCs	Major HTCs	Cat 5	ACE (× 10^4 kt^2)
North Atlantic	13	5 –	4 +	3 ++	133
Eastern N. Pacific	20 +	11 +	5	0	127
Western N. Pacific	28	17	5 –	1 –	186 –
North Indian	5	1	0	0	9 –
South Indian	13 +	9 ++	6 ++	0	139 +
Australia	14 +	8 ++	7 +++	1 ++	102 +
Southwest Pacific	7	2	0	0	14 – –
Northern Hemisphere	66 +	34	14 –	4	455 –
Southern Hemisphere	31 +	16 +	11 ++	1	256 +
Global	97 +	50 +	25	5	711

2. ATLANTIC BASIN

—M. Rosencrans, E. S. Blake, C. W. Landsea, H. Wang, S. B. Goldenberg, R. J. Pasch, D. S. Harnos, H. Lopez, and L. N. Long

(i) 2025 Seasonal activity

The 2025 Atlantic hurricane basin produced 13 named storms; of these, five became hurricanes, with four intensifying into major hurricanes (Fig. 4.22b). The HURDAT2 (Landsea and Franklin 2013) 1991–2020 seasonal averages (included in IBTrACS) are 14.4 named storms, 7.2 hurricanes, and 3.2 major hurricanes. The 2025 seasonal totals for named storms, hurricanes, and major hurricanes were all close to the 1991–2020 mean, though the fraction of hurricanes that became major hurricanes was the highest since 1950. Although the number of major hurricanes was above average, the number of named storms was below average—especially for a year of overall above-average activity.

The 2025 seasonal accumulated cyclone energy (ACE) value was 135% of the 1951–2020 median of 96.7 × 10^4 kt^2 (Fig. 4.22c). This value is above NOAA's threshold for an above-normal season (130% of median, or 126.1 × 10^4 kt^2). Consistent with recent decadal trends, nine of the previous 10 Atlantic hurricane seasons (2016–25) exhibited above-normal activity levels, with the 2022 season representing the sole near-normal outlier. Since the current Atlantic high-activity era began in 1995 (Goldenberg et al. 2001; Bell et al. 2019a,b, 2020; Bell and Chelliah 2006), there have been 22 above-normal seasons, with 11 being hyperactive (ACE above 159.6, or 165%). By comparison, the preceding 24-year low-activity era of 1971–94 had only two above-normal seasons, with none being hyperactive.

Three of the 13 named storms during 2025 were short-lived (<2 days). There has been a large artificial increase (approximately five per year) in these "shorties" since 2000 (Landsea et al. 2010). These increased counts primarily reflect new observational capabilities such as scatterometers, Advanced Microwave Sounding Units, and the Advanced Dvorak Technique, and have no association with any known climate variability (Villarini et al. 2011).

(ii) Storm formation times, regions, and landfalls

TC activity was highly variable during the core (peak) months of the season, August–October (ASO; Fig. 4.23b), with no activity outside of the official North Atlantic hurricane season (June–November). Activity started on 23 June with the development of Tropical Storm Andrea. During the Atlantic hurricane season, at least one named storm

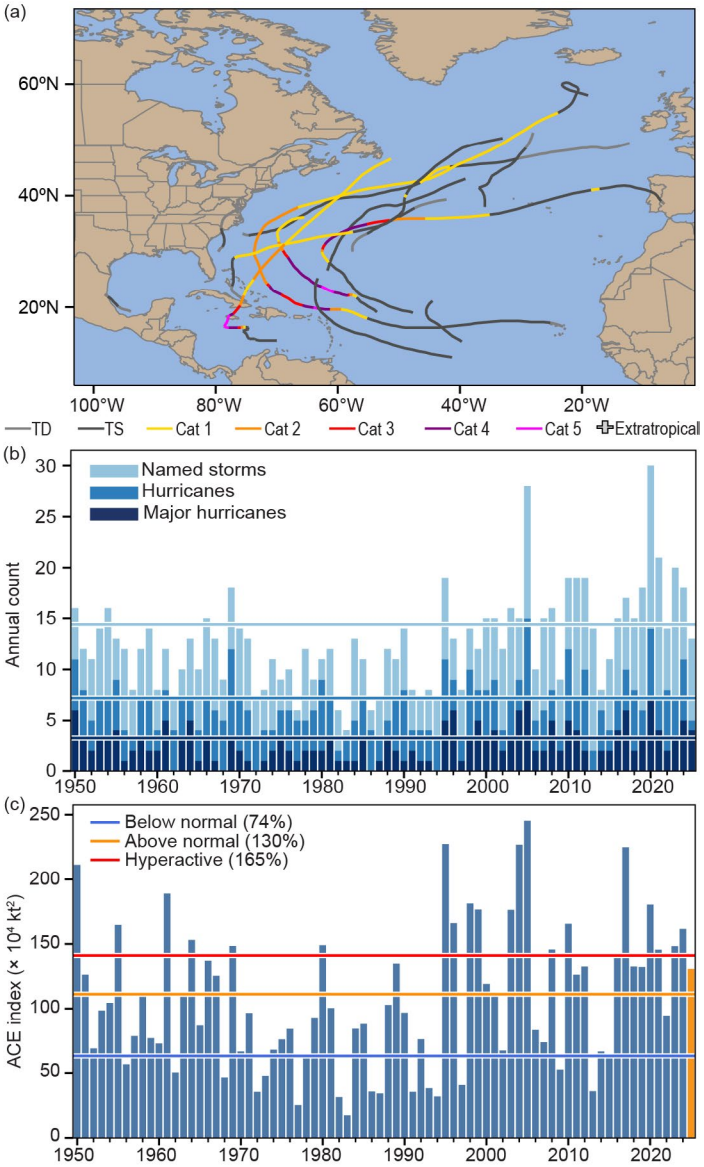

Fig. 4.22. Annual tropical cyclone statistics for the North Atlantic Ocean basin for the period 1950–2025: (a) storm tracks for 2025; (b) number of named storms, hurricanes, and major hurricanes; and (c) accumulated cyclone energy (ACE; × 10^4 kt^2; orange bar denotes 2025). Horizontal lines represent (b) the climatology for 1991–2020 and (c) the thresholds for below-normal, above-normal, and hyperactive seasons based on 1951–2020.

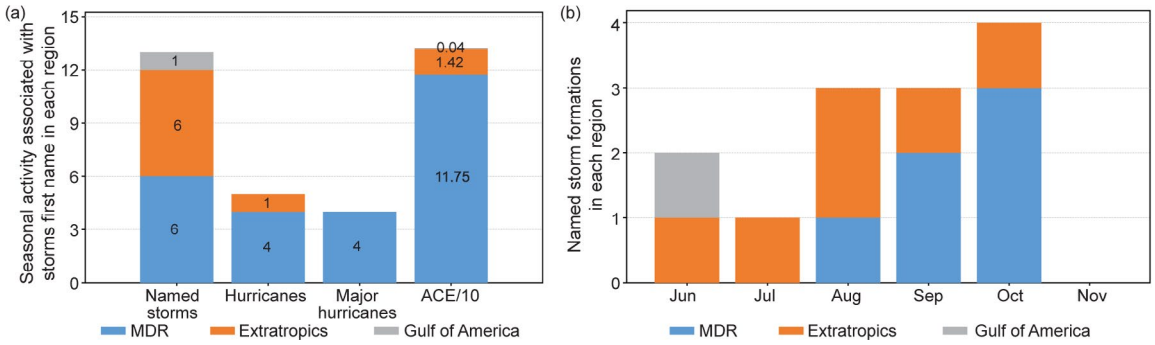

Fig. 4.23. Atlantic tropical cyclone (TC) activity in 2025. (a) Total seasonal counts for the three storm classifications and accumulated cyclone energy (ACE) for each region where the storm was first named and (b) named storm counts for the month and region where the storm was first named. ACE reflects the entire storm ACE and is attributed to the region in which the storm was first named. Regions in (a) and (b) are indicated by the color bar below each panel (main development region [MDR]: blue; extratropics: orange; Gulf of America: gray). (Source: National Hurricane Center HURDAT.)

developed during each month from June to October, including three named storm formations during September. Named storm formations in June were above normal, with activity during July through September being close to average. However, it was unusual that through 20 September, only one hurricane developed, and only one tropical storm formed between 12 August and 16 September. October had nearly double its climatological activity with four named storms (including one major hurricane). Similar to 2024, late August and early September were devoid of tropical cyclone activity, while October, in both years, had activity that was nearly double climatological levels. In contrast to 2024, no named storms developed during November 2025, while three named storms, including one major hurricane, developed in November of 2024. Historically, about 50% of the years experienced no storm formation in November.

Of the 13 named storms in 2025, 46% (six of 13) formed in the main development region (MDR; Fig. 4.22b). The MDR spans the tropical Atlantic Ocean and Caribbean Sea between 9.5°N and 21.5°N (Goldenberg and Shapiro 1996; Goldenberg et al. 2001). Since 1950, approximately 42% of named storms form in the MDR in any given year, with about 18% in the Gulf of America/Gulf of Mexico (hereafter referred to as the Gulf). The associated MDR-related ACE value of 118×10^4 kt^2 (ACE from named storms that developed in the MDR during 2025) was 171% of the median annual MDR ACE (69×10^4 kt^2). With only one tropical storm formation over the Gulf, ACE from named storms that formed over the region was 0.2 compared to the 1950–2024 median of 24.

Named storms and their tracks largely clustered over the open Atlantic, with Hurricane Melissa being the only hurricane over the Caribbean (Fig. 4.22a). Other than two tropical storms—Barry, which made landfall on the Mexican Gulf coast, and Chantal, which made landfall in South Carolina (bringing severe flooding to North Carolina)—all of the activity stayed farther east, with no other systems moving west of ~78°W. However, even though Hurricane Erin stayed more than 300 km offshore of the United States, its strong winds and high waves still destroyed some structures in the Outer Banks. Erin was also responsible for several rip current deaths along the U.S. East Coast. Despite the fairly limited impacts of the season for the United States, Hurricane Melissa made landfall as a Category 5 hurricane in Jamaica and then as a Category 3 hurricane in Cuba (see Sidebar 4.1), breaking records and bringing devastation to large portions of Jamaica (see Sidebar 7.2 for details) and causing extensive damage in Cuba.

(iii) Sea surface temperature

Sea surface temperatures (SSTs) were above average for most of the North Atlantic (Fig. 4.24a), with an ASO-area-averaged SST anomaly of +0.4°C (Fig. 4.24, red box), the fifth-highest value since 1950 (2024 was +1.0°C). The area-averaged SST anomaly in the MDR (Fig. 4.24a, green box) was 0.3°C higher than that of the remainder of the global tropics (Fig. 4.24b). The warm MDR signal combined with the above-normal SSTs farther north in the extratropical Atlantic is typical of the warm phase of the Atlantic Multidecadal Oscillation (Enfield and Mestas-Nuñez 1999; Bell and Chelliah 2006) and is characteristic of Atlantic high-activity eras such as 1950–70 and 1995–present (Goldenberg et al. 2001; Vecchi and Soden 2007; Bell et al. 2018). Despite these

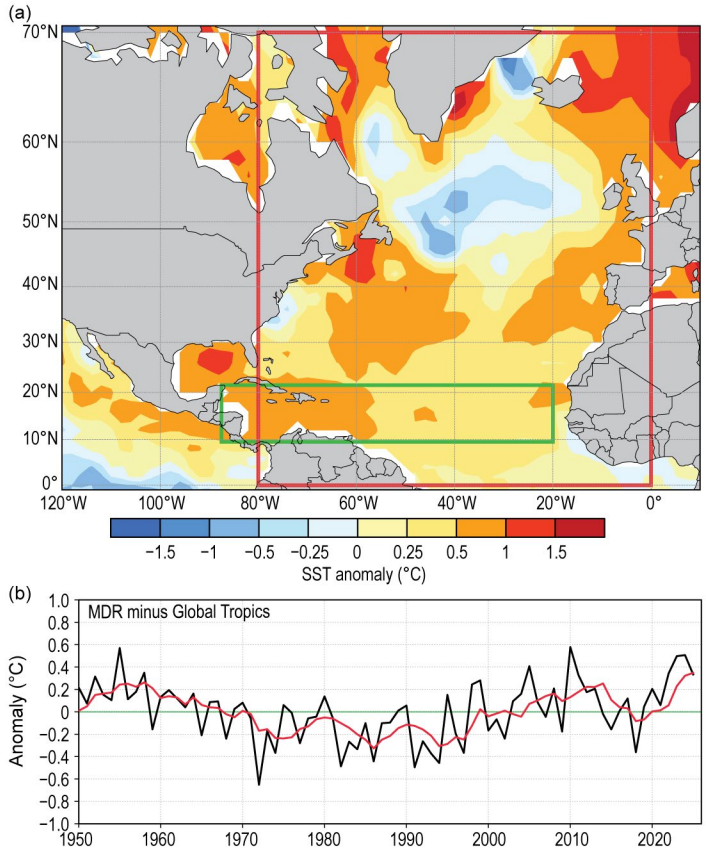

Fig. 4.24. (a) Aug–Oct 2025 sea surface temperature (SST) anomalies (°C). (b) Time series of Aug–Oct area-averaged SST anomalies (black) and five-point running mean of the time series (red) for the difference between the main development region (MDR, green box in [a] spanning 9.5°N–21.5°N and 20°W–87.5°W). Anomalies are departures from the 1991–2020 period means. (Source: ERSST-v6 [Huang et al. 2025].)

above-normal SSTs, overall activity was marginally above average with lower numbers of named storms and hurricanes.

In the Atlantic basin, the largest ASO SST anomalies (exceeding +1.0°C) occupied portions of the North Atlantic extratropics and the Gulf (red box, Fig. 4.24a). The area-averaged SST anomaly in the North Atlantic of +0.4°C reflects a continuation of exceptional warmth that began in 2022; however, the 2025 value does represent a considerable drop from 2024, when the anomaly was +0.7°C. A small area near the southeast coast of the United States exhibited near- or slightly below-normal SSTs. This area of below-normal SSTs was likely driven by the same troughing that increased 200-hPa–850-hPa vertical wind shear from the Gulf to the western Atlantic (discussed in the next section). ENSO-neutral conditions at the start of the North Atlantic hurricane season transitioned to La Niña conditions during ASO. The Oceanic Niño Index (ONI) values ranged from −0.1°C in June–August to −0.5°C in September–November.

(iv) Atmospheric conditions

Climatologically, the ASO peak in Atlantic hurricane activity largely reflects the June–September peak in the West African monsoon. The inter-related circulation features of an enhanced monsoon act to further increase hurricane activity, while those of an anomalously weak monsoon act to suppress it (Gray 1990; Hastenrath 1990; Landsea et al. 1992; Bell and Chelliah 2006; Bell et al. 2018, 2020). The association on multi-decadal time scales between Atlantic Multidecadal Variability (AMV) and Atlantic hurricane activity in part exists because of their common relationship to the West African monsoon (Bell and Chelliah 2006).

The West African monsoon was near average as a whole, with the intertropical front position in line with climatology, and the African easterly jet near its climatological latitudes. Outgoing longwave radiation (OLR) anomalies indicate rainfall west of 10°E was largely below normal for June–July, but above normal east of 10°E (Fig. 4.25a). During ASO, the OLR anomaly pattern indicates below-normal convection over the Gulf, the central portions of the MDR, and much of West Africa. Enhanced convection occurred over a small part of the MDR and northward from the Greater Antilles. The pattern in the OLR indicates an environment that was not largely conducive to tropical cyclone development over much of the MDR.

The 200-hPa velocity potential anomalies during ASO indicate enhanced divergence over the central Atlantic with strong convergence over the western North Atlantic and eastern North Pacific (Fig. 4.25b). Streamflow anomalies at 200 hPa (Fig. 4.25c) indicate anti-cyclonic flow over the Caribbean and the Gulf, with strong cyclonic flow from the East Coast of the United States to near Bermuda. Upstream of the trough over Bermuda is a strong anti-cyclonic anomaly, potentially indicating the influence of midlatitude flow into the western Atlantic. Analysis of 700-hPa–225-hPa layer average winds (Fig. 4.26a) also shows the presence of an anomalous trough extending southward along the east coast of North America, which probably contributed to the lack of storms developing near the coast and over the Gulf. The anomalous steering currents would have also directed storms away from the region, causing them to recurve before nearing the U.S. East Coast.

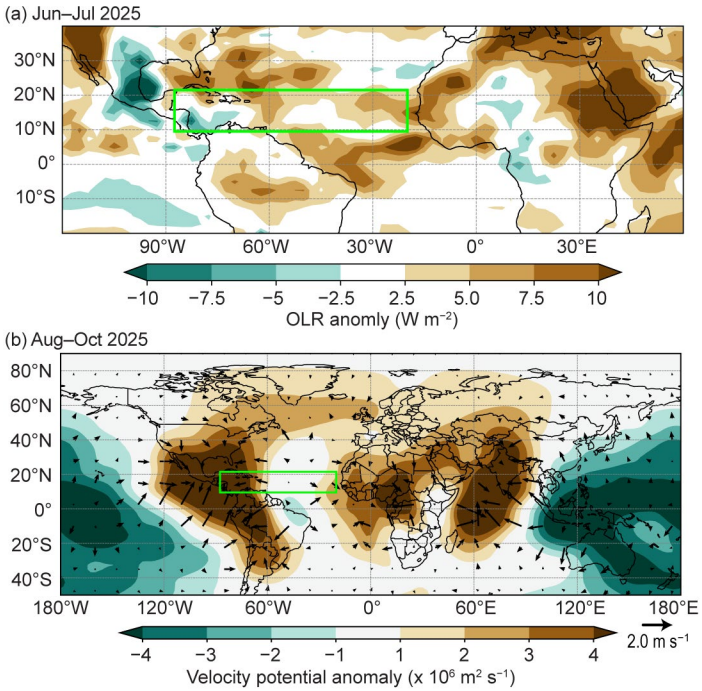

Fig. 4.25. (a) Jun–Jul 2025 anomalous outgoing longwave radiation (OLR; W m^{-2}), with negative (positive) values indicating enhanced (suppressed) convection. (b) Aug–Oct 2025 200-hPa velocity potential anomalies (shading; × 10^{6} m^{2} s^{-1}) and divergent wind (vectors; m s^{-1}). The green box denotes the Atlantic main development region. Anomalies are departures from the 1991–2020 means (Source: National Centers for Environmental Prediction [NCEP] National Center for Atmospheric Research [NCAR] reanalysis [Kalnay et al. 1996] and Climate Prediction Center OLR).

ASO 2025 200-hPa–850-hPa vertical wind shear was below average for much of the MDR and slightly above average for the Gulf (Fig. 4.26b). The area-averaged magnitude of the vertical wind shear was 5.4 m s^{-1} and 9.6 m s^{-1} for the entire MDR and the Gulf, respectively. The 200-hPa–850-hPa vertical wind shear over the Gulf was close to the upper threshold of 10 m s^{-1} considered conducive for hurricane formation on monthly time scales (Bell et al. 2017), and was particularly high during July, when formations in the western part of the Atlantic are climatologically favored compared to the MDR. Over the eastern MDR, vertical wind shear remained above normal through September, then subsided in October. Vertical wind shear over the Caribbean was at a local minimum during October, when Hurricane Melissa reached peak intensity. Note that the MDR shows strong multidecadal variability in vertical wind shear, which is correlated with multidecadal fluctuations in TC activity, whereas there is no such variability in the Gulf (Goldenberg et al. 2001).

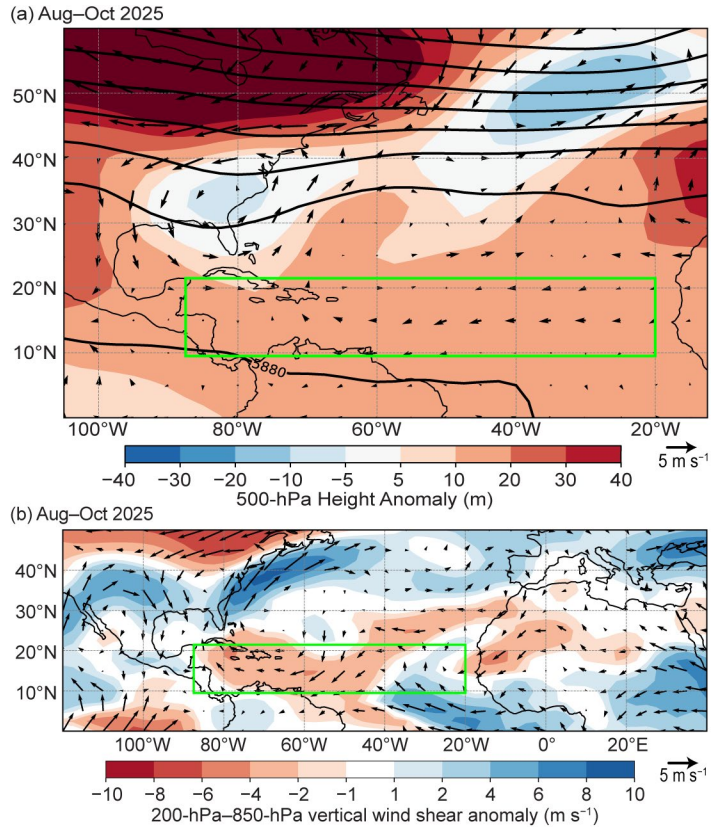

Fig. 4.26. (a) Aug–Oct 2025 500-hPa geopotential heights (contours, interval is 30 gpm) and anomalies (shaded) with 700-hPa–225-hPa layer mean winds (vector); (b) Aug–Oct 2025 magnitude of the 200-hPa–850-hPa vertical wind shear (m s^{-1}) anomalous magnitude and vector. Base period is 1991–2020. (Source: National Centers for Environmental Prediction [NCEP] National Center for Atmospheric Research [NCAR] reanalysis [Kalnay et al. 1996].)

(v) Unique aspects of the 2025 Atlantic hurricane season

The 2025 Atlantic hurricane season had several anomalous features. One was the low levels of tropical cyclone activity in the western half of the Atlantic basin, west of 78°W. Only one system developed over the Gulf, despite the above-normal SSTs. Large-scale subsidence and a relative lack of moisture likely played roles in keeping tropical development in the Gulf and western Atlantic to a relatively low level, while midlatitude influences in the steering flow forced almost every TC to recurve away from the region.

Despite the low levels of activity across most of the basin, all but one of the storms that became hurricanes reached major hurricane intensity, which was the highest percentage since 1950. Furthermore, the formation of three Category 5 hurricanes in a single season is the second highest number on record since the beginning of the satellite era when estimates for intensities of upper-end systems became more reliable. The propensity for storms to intensify quickly when the atmospheric conditions allow highlights the potential changes that increasing SSTs can provide when atmospheric conditions are, at a minimum, not prohibitive to TC development and intensification.

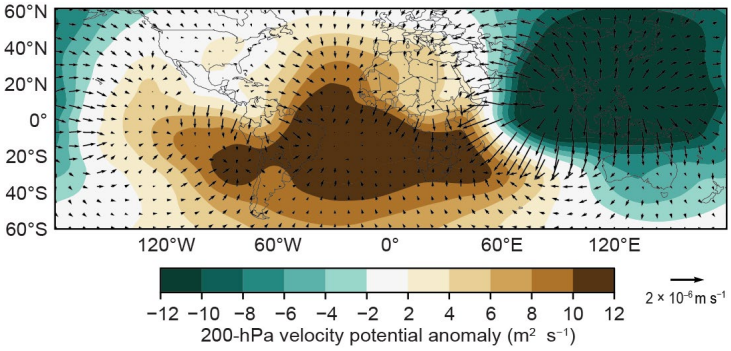

Fig. 4.27. The 31-day mean 200-hPa velocity potential anomalies (shading; m^2 s^{-1}) and divergent wind (vectors; m s^{-1}) ending on 9 Sep 2025. (Source: National Centers for Environmental Prediction [NCEP] National Center for Atmospheric Research [NCAR] reanalysis [Kalnay et al. 1996].)

Additionally, late August and early September featured no tropical storm formations, with several weeks during the peak of the hurricane season having no active storms for the second consecutive year. Vertical wind shear over much of the MDR was above normal during September in part due to a persistently strong tropical upper tropospheric trough. Positive 200-hPa velocity potential anomalies dominated over the tropical Atlantic from mid-August to mid-September (Fig. 4.27),

reflecting a hostile environment for waves emerging off of Africa. Following that lull, when these waves moved farther west in the basin, several encountered more favorable conditions and underwent rapid intensification to major hurricane intensity.

3. EASTERN NORTH PACIFIC AND CENTRAL NORTH PACIFIC BASINS

—K. M. Wood and C. J. Schreck

(i) Seasonal activity

Numbers reported in this section are combined from the two agencies responsible for issuing advisories and warnings in the eastern North Pacific (ENP) basin: NOAA's National Hurricane Center in Miami, Florida (spanning the Pacific coast of North America to 140°W), and NOAA's Central Pacific Hurricane Center in Honolulu, Hawaii (spanning 140°W to the dateline, the central North Pacific [CNP]).

A total of 20 named storms formed within the combined ENP/CNP basin in 2025, 11 of which became hurricanes and five of which became major hurricanes (Fig. 4.28a). All three metrics are above normal compared with the 1991–2020 averages of 16.9 named storms, 8.8 hurricanes, and 4.6 major hurricanes. All 20 TCs occurred between the official ENP hurricane season start date of 15 May and end date of 30 November. The first named storm of the season, Tropical Storm Alvin,

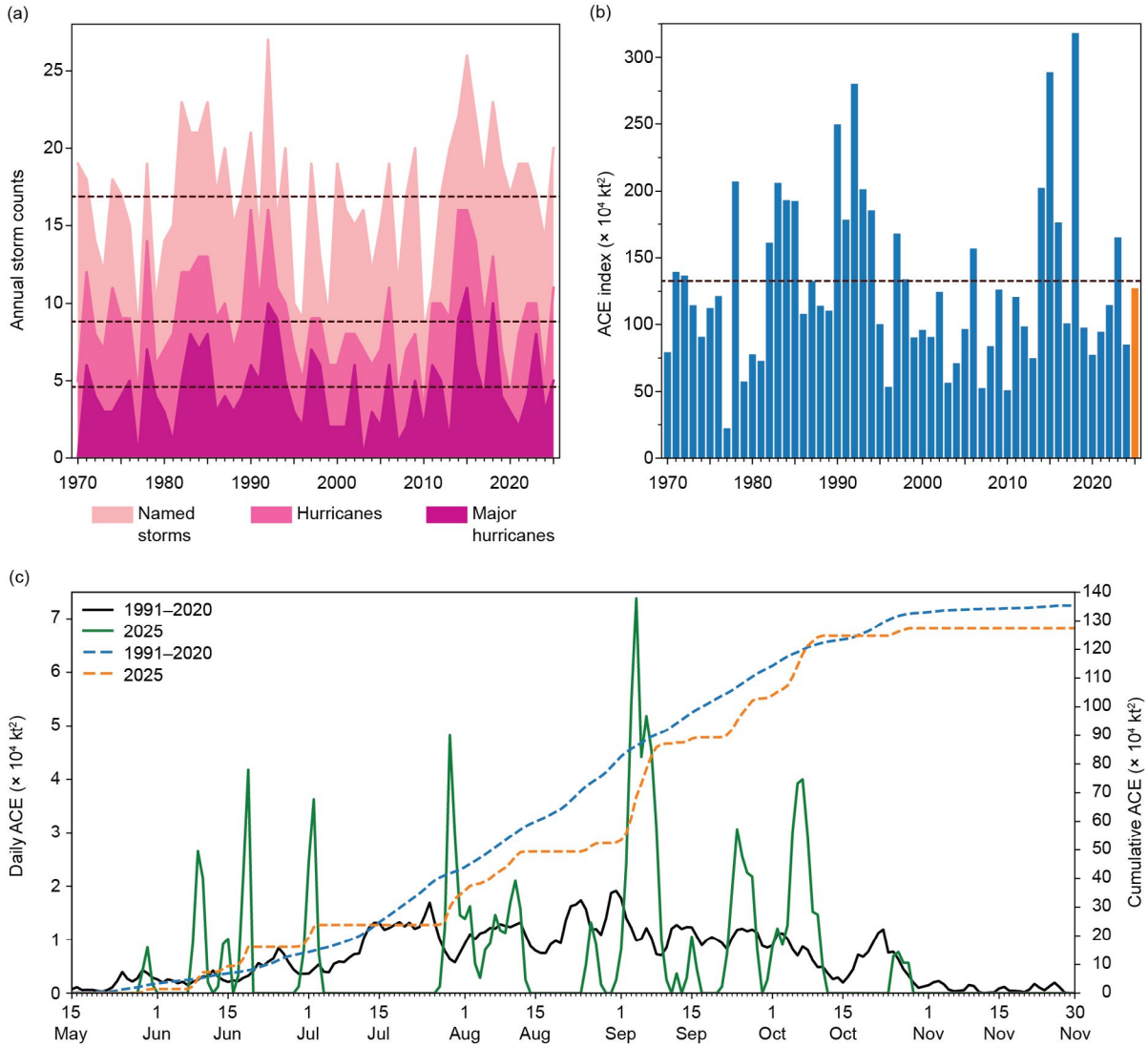

Fig. 4.28. (a) Annual eastern and central North Pacific storm counts by category for the period 1970–2025, with the 1991–2020 average by category denoted by each dashed line. (b) Annual accumulated cyclone energy (ACE; × 10^4 kt²) during 1970–2025, with 2025 highlighted in orange and the 1991–2020 average denoted by the dashed line. (c) Daily ACE for the 1991–2020 average (solid black) and for 2025 (solid green); accumulated daily ACE for the 1991–2020 average (dashed blue) and during 2025 (dashed orange).

developed on 28 May. The final named storm, Tropical Storm Sonia, dissipated on 29 October; no TC activity occurred in November. Two named storms developed within the CNP (Hurricane Iona and Tropical Storm Keli), and two ENP TCs crossed 140°W (Hurricanes Gil and Henriette) for a total of four TCs, which is above the 1991–2020 average of 3.4 for the CNP.

The 2025 seasonal ACE index was 127.3×10^4 kt^2, or 96% of the 1991–2020 mean of 132.8×10^4 kt^2 (Fig. 4.28b; Bell et al. 2000), making 2025 a near-normal season with respect to this metric despite above-average named storm and hurricane counts. The five TCs that achieved major hurricane intensity, or a maximum sustained wind speed greater than 96 kt (49 m s^{-1}), produced 50.7% of the season's ACE (Erick, Flossie, Kiko, Priscilla, and Iona). One hurricane (Barbara) and one major hurricane (Erick) occurred in June, followed by Major Hurricane Flossie in early July, though a subsequent lull spanned most of that month (Fig. 4.28c). August produced one major hurricane in the central Pacific (Iona) and two hurricanes (Gil and Henriette), both of which crossed from the eastern to the central North Pacific. September also resulted in one major hurricane (Kiko) and two hurricanes (Lorena and Narda). Finally, October produced one hurricane (Octave) and one major hurricane (Priscilla), the latter upgraded in post-season analysis (Bucci 2026). On a monthly basis, ACE was rarely typical in 2025: June produced 12% of the season's total (compared with an average of 8%), July was 14%, August ACE was 14% (compared with an average of 30%), September was 40% (compared with an average of 24%), and October was 19%.

(ii) Environmental influences on the 2025 season

Positive SST anomalies occurred near the North American coastline, and negative SST anomalies dominated lower latitudes farther westward during the 2025 ENP/CNP hurricane season (Fig. 4.29a). The region of warmer water was largely co-located with negative OLR anomalies (Fig. 4.29b) and near-normal vertical wind shear (Fig. 4.29c), likely contributing to much of the season's TC activity clustering in this area. Other than Hurricane Kiko, no TCs traversed the region of below-normal SSTs and above-normal OLR between 120°W and 150°W. Note that La Niña conditions are apparent in the negative SST anomalies and negative 850-hPa zonal wind anomalies at low latitudes (Figs. 4.29a,d), and steering flow anomalies associated with a La Niña event can increase the likelihood of near-coastal TC activity in this region (Gutzler et al. 2013). The confined distribution of comparatively favorable environmental conditions for TCs and proximity of those conditions to the coast may help explain the near-normal ACE but above-normal named storm count in 2025.

Both development and duration of ENP TCs can be influenced by intraseasonal tropical variability such as the Madden–Julian Oscillation (MJO) and convectively coupled equatorial Kelvin waves (e.g., Maloney and Hartmann 2001; Aiyyer and Molinari 2008; Schreck and Molinari 2011; Ventrice et al. 2012a,b; Schreck 2015, 2016). Enhanced convection likely associated with the MJO may

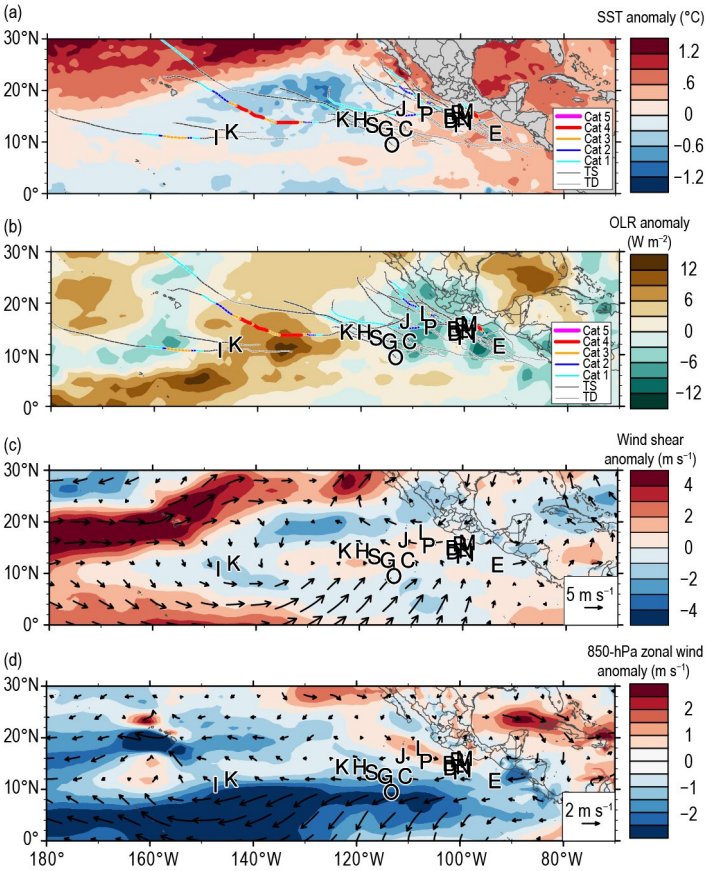

Fig. 4.29. 1 Jul–31 Oct 2025 anomaly maps of (a) sea surface temperature (SST; °C; Banzon and Reynolds 2013), (b) outgoing longwave radiation (OLR; W m^{-2}; Schreck et al. 2018), (c) 200-hP–850-hPa vertical wind shear (m s^{-1}) vector (arrows) and scalar (shading) anomalies, and (d) 850-hPa wind (m s^{-1}, arrows) and zonal wind (shading) anomalies. Anomalies are relative to the annual cycle from 1991–2020. Letters denote where each storm attained tropical storm intensity. The western I represents Iona (CP01), and the western K represents Keli (CP02). Wind data are obtained from CFSR (Saha et al. 2014).

have contributed to the burst of TC activity in June (Fig. 4.30), with signals indicating that easterly wave activity supported the development of some TCs during this time frame (red contours slanting downward from right to left). Positive OLR anomalies in conjunction with the suppressed phase of the MJO likely prevented TC development during the first half of July. The convective phase of the MJO entered the basin towards the end of July with two embedded Kelvin waves. No TCs formed in the CNP/ENP with the first Kelvin wave, but Iona and Keli in the CNP and Gil in the ENP formed in the wake of the second Kelvin wave. The subsequent suppressed MJO phase was likely related to the lull in activity during most of August. Later TC formation appears to have occurred without significant MJO or Kelvin wave influence.

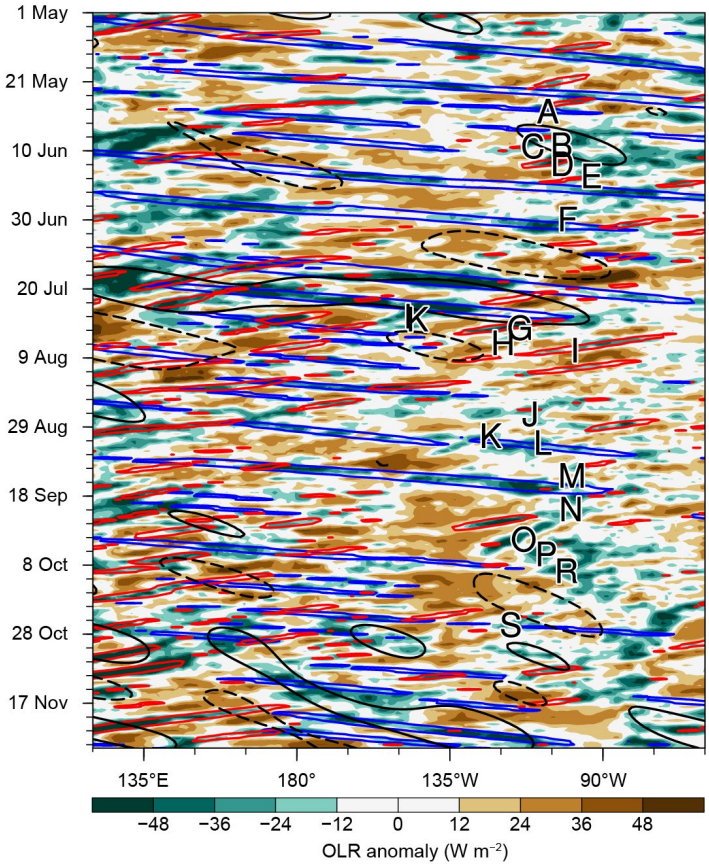

Fig. 4.30. Longitude–time Hovmöller diagram of 5°N–15°N average outgoing longwave radiation (OLR; W m^{-2}; Schreck et al. 2018) during 2025. Unfiltered anomalies from a daily climatology are shaded. Negative anomalies (green) indicate enhanced convection. Anomalies filtered for Kelvin waves are contoured in blue at 12 W m^{-2}, easterly waves are contoured in red at 18 W m^{-2}, and Madden–Julian Oscillation (MJO)-filtered anomalies are contoured in black at ±10 W m^{-2} (dashed for positive, solid for negative). Letters denote the longitude and time when each tropical cyclone attained tropical storm intensity. The western I represents Iona (CP01), and the western K represents Keli (CP02).

(iii) Notable TCs and impacts

Hurricane Erick made landfall in Oaxaca, Mexico, at 1130 UTC 19 June as a 110-kt (57 m s^{-1}) major hurricane, marking the earliest major hurricane landfall on record in Mexico from either the eastern North Pacific or North Atlantic basins (Cangialosi 2025). Erick underwent rapid intensification with a peak rate of 55 kt (28 m s^{-1}) in 24 hours before reaching its peak intensity of 120 kt (62 m s^{-1}), though its maximum intensity began decreasing prior to landfall. Homes and infrastructure sustained extensive damage, with widespread power outages and impacts to agriculture, and at least two related fatalities were confirmed (Jelsema 2025) with potentially more due to heavy rain and mudslides. Economic losses were estimated at $275 million (U.S. dollars; Gallagher Re 2026), and the Mexican government allocated over $1 billion (U.S. dollars) to recovery and reconstruction efforts (Jelsema 2025). One landfalling storm is below the long-term average for Mexico, which is 1.8 TCs per year (Raga et al. 2013); however, this single event resulted in wide-ranging impacts.

Other storms did not officially make landfall—defined as the TC center crossing a coastline—but still impacted land. Rainfall related to Tropical Storm Alvin's remnants affected parts of Mexico and the southwestern United States in late May. Hurricane Barbara and Tropical Storm Dalila dissipated offshore but contributed to heavy rainfall in coastal Mexico. In addition, many TCs moved parallel to the coastline without making landfall, leading to flooding and associated impacts from outer rainbands: these storms included Hurricane Flossie, Tropical Storm Ivo, Hurricane Lorena, Tropical Storm Mario, Hurricane Narda, Hurricane Priscilla, and Tropical Storm Raymond (Fig. 4.29).

All major hurricanes in 2025 exceeded the rapid intensification threshold of 30 kt (15 m s^{-1}) in 24 hours. Hurricane Iona reached a peak 24-hour intensification rate of 60 kt (31 m s^{-1}) and Erick a rate of 55 kt (28 m s^{-1}). The other two storms were less explosive: Hurricane Flossie intensified 40 kt (20 m s^{-1}) and Kiko 35 kt (18 m s^{-1}) in 24 hours. On the other end of the intensity change spectrum, all major hurricanes that did not make landfall underwent at least one rapid

weakening period while over open ocean (≤–30 kt or –15 m s^{-1} in 24 hours; Wood and Ritchie 2015): peak weakening rates were –55 kt for Flossie, –45 kt for Kiko, and –55 kt for Iona.

4. WESTERN NORTH PACIFIC

—S. J. Camargo

(i) Introduction

In 2025, 28 tropical cyclones were active in the western North Pacific (median: 26), according to the JTWC—the first year with the number of TCs above the median since 2019. Figure 4.31 compares the activity for 2025 as identified by both the JTWC and the Japan Meteorological Agency (JMA) with their climatologies for 1991–2020. There were 17 typhoons (median: 16), with four of those reaching Category 4 on the SSHWS and one reaching super typhoon status (≥130 kt, bottom quartile <3). While 61% of the TCs intensified into typhoons (median: 63%), only 6% reached super typhoon status (bottom quartile <17%). There were six tropical depressions that formed in the basin. In early August, Hurricane Iona, which formed in the central North Pacific and reached Category 4 intensity in that basin, crossed into the western North Pacific (WNP) as a tropical depression. Cyclone Senyar crossed into the WNP from the Bay of Bengal as a tropical depression in late November. Figure 4.31a shows the number of TCs identified by the JTWC for the period 1945–2025.

The JMA recorded 27 TCs (median: 25.5) in 2025, including seven tropical storms (median: 6), seven severe tropical storms (top quartile >6), and 13 typhoons (median: 13.5), with 48% reaching typhoon intensity (bottom quartile <48%). There were differences between the JTWC and JMA storm counts, intensities, and categories, as in previous years. Wutip, Wipha, Co-May, and Tapah were considered typhoons by the JTWC and severe tropical storms by the JMA. The JMA labeled Mun, Mitag, and Fengshen as severe tropical storms while the JTWC classified them as tropical storms. Unnamed storm 08W was a tropical storm according to the JTWC, but not by the JMA. The number of all TCs (from 1951 to 1976) and tropical storms, severe tropical storms, and typhoons (from 1977 to 2025) according to the JMA are shown in Fig. 4.31b. The Philippine Atmospheric, Geophysical, and Astronomical Services Administration (PAGASA) named 22 TCs that entered its area of responsibility, including Auring, Fabian, Salome, and Wilma, which were not numbered or named by either the JMA or the JTWC.

(ii) Seasonal activity

The cumulative monthly number of TCs and typhoons for 2025 are shown in Figs. 4.31c,e, respectively, with the number of TCs and typhoons per month displayed in Figs. 4.31d,f. In Figs. 4.31c,f, the 2025 values are compared with the climatological values, as well as the historical maxima and minima. As in 2023 and 2024, the 2025 typhoon season had a very late start. The first TC of the season was Typhoon Wutip (10–14 June), followed by Tropical Storm Sepat (22–26 June). Therefore, the early season (January–June) had a total of two TCs (bottom quartile <3), with only one reaching typhoon intensity (bottom quartile <1) matching exactly the number of TCs, tropical storms, and typhoons in the 2024 early season.

The typhoon season picked up in July, with the development of eight TCs (upper quartile >5) including four typhoons (upper quartile >4). This active period continued in August, with five TCs (median: 5) forming in the WNP, including two typhoons (bottom quartile <2). September had six TCs (upper quartile >6), including four typhoons (upper quartile >4). Ragasa (17–25 September) was the strongest typhoon of the 2025 season, reaching Category 5, while Neoguri (18–30 September) reached Category 4. October had four TCs (median: 3), with three typhoons (upper quartile >3). Halong (4–13 October) was the third major typhoon of the season (Category 3 or higher), reaching Category 4. The peak typhoon season (July–October) saw a total of 23 TCs (upper quartile >21), including 13 typhoons (median: 11.5). The 13 typhoons were slightly above normal, leading to a cumulative number of typhoons matching the climatological mean.

There were also two Category 4 typhoons in November: Kalmaegi (1–6 November) and Fung-Wong (4–13 November), of the total three typhoons that occurred that month (upper quartile >2). Typhoon Koto (24 November–1 December) was the last TC of the season. The late typhoon season (November–December) saw a total of three TCs (median: 3), all of them reaching typhoon intensity (upper quartile >3).

In summary, the total number of TCs in 2025 (28) was slightly above the climatology median (26), with no TCs forming until June, but with active middle and late parts of the season. Of the five major typhoons, four reached Category 4 (Neoguri, Halong, Kalmaegi, and Fung-Wong) and one reached Category 5 (Ragasa). All of these typhoons occurred during a busy period of the season from late September to mid-November.

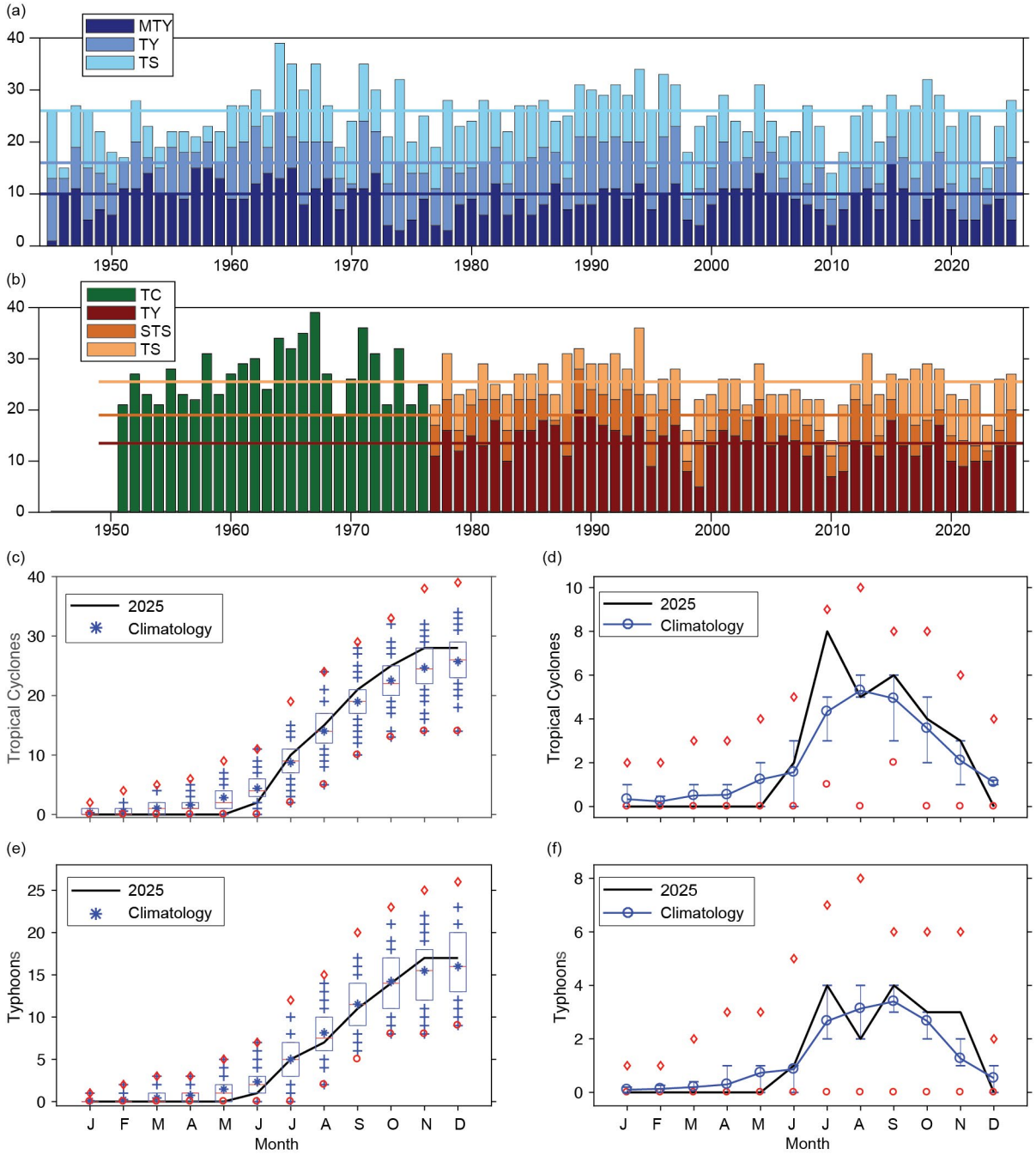

Fig. 4.31. (a) Number of tropical storms (TS), typhoons (TY), and major typhoons (MTY ≥96 kt) per year in the western North Pacific (WNP) for the period 1945–2025 based on the Joint Typhoon Warning Center (JTWC); horizontal lines are median values. (b) Number of tropical cyclones (TCs: all storms that reach TS intensity or higher) from 1951 to 1976; number of TSs, severe tropical storms (STS), and TYs from 1977 to 2025 based on the Japan Meteorological Agency (JMA). (c) Cumulative number of tropical cyclones with TS intensity or higher (named storms) per month in the WNP in 2025 (black line), and climatology (1991–2020) as box plots (interquartile range: box, median: red line, mean: blue asterisk, values in the top or bottom quartile: blue crosses, high [low] records in the 1945–2024 period: red diamonds [circles]). (e) As in (c) but for the number of typhoons. (d),(f) Number of tropical cyclones reaching TS intensity and typhoons, respectively, per month in 2025 (black line) and the climatological mean (blue line); the red diamonds and circles denote the maximum and minimum monthly historical records and the blue error bars show the climatological interquartile range for each month (in the case of no error bars, the upper and/or lower percentiles coincide with the median). (Sources: 1945–2024 JTWC best-track dataset; 2025 JTWC preliminary operational track data for [a], [c], [d], [e], and [f] [downloaded from IBTrACS]; 1951–2025 Regional Specialized Meteorological Center–Tokyo, JMA best-track dataset for [b].)

In contrast to the number of TCs, the total ACE in 2025 (Fig. 4.32a) was below normal, at 85% of the value of the bottom quartile threshold. This low value is despite the occurrence of five Category 4 and 5 typhoons. The ACE in 2025 was the 13th lowest out of the 81 years in the historical record. Typically, low ACE values are associated with La Niña events (Camargo and Sobel 2005). A short and weak La Niña event was present from December 2024 to April 2025. Weak La Niña conditions returned in August and continued throughout the 2025 peak typhoon season. ACE was zero for the months of January–May 2025 since there were no tropical cyclones during that period. The ACE value was in the bottom quartile for the months of August, October, and December, below-normal for June, close to normal for July and September, and above-normal for November (Fig. 4.32b). ACE was in the bottom quartile in the early and peak seasons and below normal in the late season. The high percentage contribution of ACE in September (fifth highest in the historical record) was due to the presence of Super Typhoon Ragasa and Category 4 Typhoon Neoguri. The presence of Category 4 Typhoons Kalmaegi and Fung-Wong in November led to an above-normal contribution to the total ACE that month. Two typhoons had ACE values per storm in the top quartile of the climatological distribution: Ragasa and Neoguri, contributing 14.6% and 14.4% of the total ACE of the season, respectively. The five Category 4/5 typhoons contributed to 52% of the total ACE for 2025.

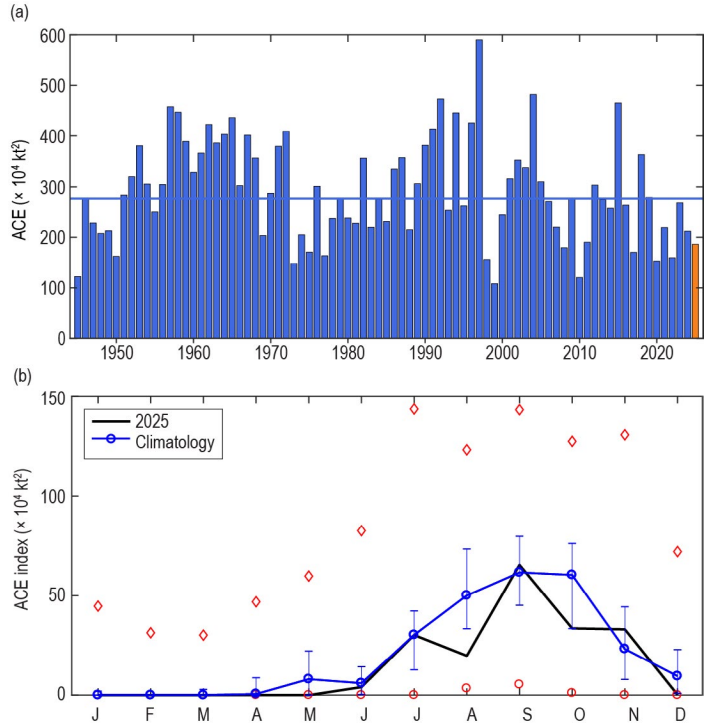

Fig. 4.32. (a) Accumulated cyclone energy (ACE; × 10^4 kt^2; orange bar denotes 2025) per year in the western North Pacific for the period 1945–2025. The solid blue line indicates the median for the climatology (1991–2020). (b) ACE per month in 2025 (black line) and the median during 1991–2020 (blue line), the blue error bars indicate the climatological interquartile range. In case of no error bars, the upper and/or lower percentiles coincide with the median. The red diamonds and circles denote the maximum and minimum values per month during the 1945–2024 period. (Source: 1945–2024 Joint Typhoon Warning Center [JTWC] best-track dataset, 2025 JTWC preliminary operational track data.)

During La Niña periods, the mean typhoon genesis location is typically shifted to the northwest part of the WNP basin (Chia and Ropelewski 2002; Camargo and Sobel 2005; Camargo et al. 2007a,b), and is associated with short tracks, weak storms, and low ACE values. The mean genesis position in 2025 was 19.2°N and 131.9°E, northwest of the climatological mean of 13.3°N and 140.5°E and the mean genesis position during La Niña periods in the period 1950–2024 (15.2°N, 136.8°E). These genesis values exclude both Hurricane Iona (central Pacific) and Cyclone Senyar (Bay of Bengal). The mean track position in 2025 was 21.6°N and 131.1°E, also northwest of the climatological mean of 17.8°N and 135.9°E.

There were 92.25 days with TCs in 2025 (mean: 105.12 days); of those, 32.5 days experienced active typhoons (bottom quartile <42.75 days) and 8.5 days saw major typhoons (Category 3–5; bottom quartile <15.75 days). Typhoons occurred on 28.6% of the active days (median: 36.6%), with only 7.5% of the active days seeing major typhoons (bottom quartile <10.7%). There were many short-lived TCs in 2025. The median lifetime of TCs was 4.9 days (bottom quartile <7 days), and the median lifetime of TYs was 6 days (bottom quartile <7.75 days). The typhoon with the longest lifetime was Krosa (11.5 days), followed by Neoguri (10.75 days) and Co-May (10 days), with only two typhoons being in the top of the quartile of the climatological distribution (>10 days). There were three TCs active simultaneously on 29 and 30 July (Co-May, Krosa, and Iona), as well as on 24 September (Ragasa, Neoguri, and Bualoi). The historical record is six active TCs in August 1996.

(iii) Environmental conditions

The 2024/25 La Niña event was short-lived and ended in early April 2025. ENSO-neutral conditions prevailed afterwards, before weak La Niña conditions returned in August and continued until the end of the year. Therefore, weak La Niña conditions were present during the peak typhoon season of July–October (JASO). Figure 4.33 shows the environmental conditions and tracks for JASO in 2025. SST anomalies (Fig. 4.33a) were slightly above normal in the western part of the basin south of 30°N. Strong positive SST anomalies were present in a zonal region between 30°N and 50°N extending from the Yellow Sea and the Sea of Japan through the central Pacific.

The typhoon tracks during JASO were concentrated in two regions. The first region included tracks affecting the Philippines and Taiwan. The second region consisted of tracks in more northern latitudes, east of Japan, where high SST anomalies were present. The potential intensity (PI) anomalies (Fig. 4.33c; Emanuel 1988) pattern was similar to the SST anomaly pattern, except that the zonal band of positive anomalies was narrower and extended to 40°N and west of the Philippines, where slightly below-normal PI anomalies were present. The genesis potential index (Fig. 4.33b; Emanuel and Nolan 2004; Camargo et al. 2007a,b) expresses the enhanced

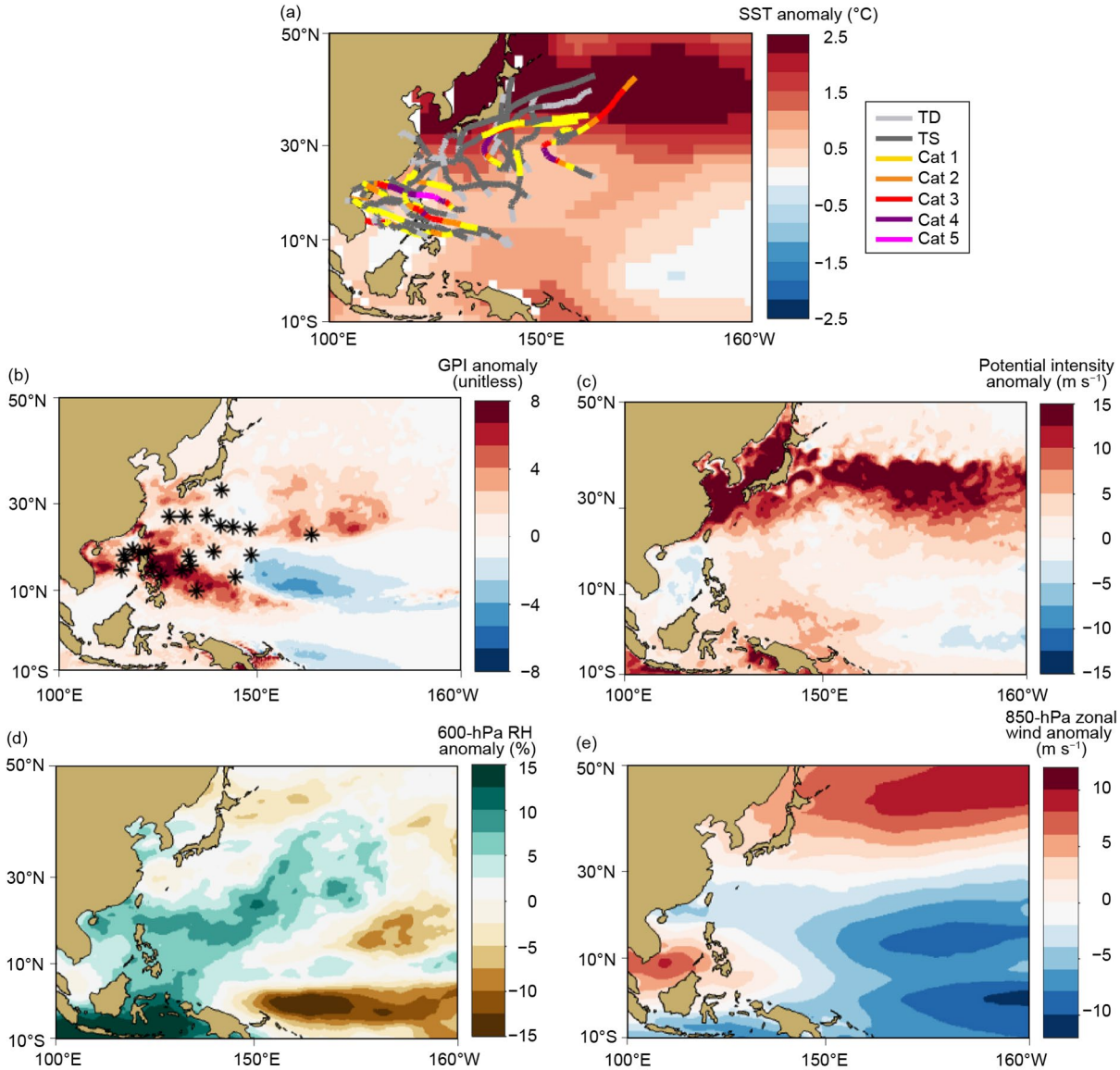

Fig. 4.33. Jul–Oct (JASO) 2025: (a) sea surface temperature (SST) anomalies (°C) and tracks of JASO 2025 storms (including tropical depressions [TD], tropical storms [TS], and typhoon-strength storms [Cat]), with colors denoting their intensity, (b) genesis potential index (GPI) anomalies and first position of JASO 2025 storms marked with an asterisk, (c) potential intensity anomalies (m s^{-1}), (d) relative humidity 600-hPa anomalies (%), and (e) 850-hPa zonal wind anomalies (m s^{-1}). (Data sources: SST: ERSSTv5 [Huang et al. 2017]; other environmental fields: ERA5 reanalysis [Hersbach et al. 2020]; tracks and first position: Joint Typhoon Warning Center preliminary operational track data.)

or reduced probability of TC formation through a nonlinear empirical combination of environmental factors known to affect TC genesis. In JASO, there was a region of high positive anomalies of the genesis potential index in a diagonal band crossing the South China Sea, the Philippines, and Taiwan, where many typhoons formed. A large number of typhoons also formed at subtropical latitudes (close to 30°N) south of Japan, where the genesis potential anomalies were near normal.

The 600-hPa relative humidity anomalies (Fig. 4.33d) in the equatorial region reflected the La Niña pattern with a strong drying region east of 150°E and strong wet anomalies near the Maritime Continent. These wet anomalies extended northward into the Philippines, Taiwan, and South China Sea area, as well as in the middle of the basin between 20°N and 40°N. The monsoon trough, which is defined by the 850-hPa zonal wind anomalies (Fig. 4.33e), tends to be restricted to the western part of the basin during La Niña events. This was indeed the case in 2025, with the edge of the monsoon trough occurring east of the Philippines. These environmental conditions match well the location of the typhoon activity in 2025, with many tracks near the Asian continent and at subtropical latitudes, leading to many short-lived typhoons.

(iv) Impacts

Twenty-three storms (including tropical depressions) made landfall in the western North Pacific in 2025 (top quartile >21, climatology 1961–2020): nine with TS intensity (top quartile >8.5), five as typhoons (median: 4), and three as major typhoons (top quartile >3). The three most intense landfalls in 2025 were associated with Typhoons Ragasa, Kalmaegi, and Fung-Wong. Super Typhoon Ragasa made landfall as a Category 5 storm over the Panuitan Island in the Luzon Strait before making a second landfall in China. Ragasa was followed shortly by Typhoon Bualoi, which made landfall in the central region of the Philippines, crossing multiple islands. In November, Typhoon Kalmaegi made multiple landfalls in the Philippines, before re-intensifying in the South China Sea and making landfall in Vietnam. Typhoon Fung-Wong also made landfall in the Philippines in November, but once it moved into the South China Sea, Fung-Wong recurved to the northwest and made landfall in Taiwan. Landfalls are defined as instances when the center of a storm that is over the ocean moves over land. The observed TC tracks were interpolated into 15-minute intervals, and a high-resolution land mask was used to determine the occurrence of landfall. In the statistics, only the highest-intensity landfall event for each storm was considered in cases of multiple landfalls.

The Philippines was severely impacted by multiple typhoons in 2025, with 22 TCs affecting that area. The September landfalls of Typhoons Ragasa and Buoloi were followed by a 6.9-magnitude earthquake, which struck offshore near Cebu City. This significantly complicated the recovery effort from these two typhoons, with two more strong typhoons (Kalmaegi and Fung-Wong) making landfall in November and causing 286 deaths. The multiple storm landfalls combined with the earthquake affected over 30 million people, with three million people displaced and an estimated 13 million people needing humanitarian assistance. More than one million houses were damaged following these compounding disasters. Vietnam was also affected by multiple typhoons in 2025. Heavy rainfall led to severe flooding that resulted in 85 deaths and substantial impacts on agriculture. Additionally, in October, the remnants of typhoon Halong re-intensified as an extratropical cyclone. The high winds and storm surge caused significant impacts in western Alaska, with record flooding recorded in multiple locations.

5. NORTH INDIAN OCEAN

—J. Uehling and C. J. Schreck

(i) Seasonal activity

The North Indian Ocean (NIO) TC season typically occurs between April and December, with peaks of activity in May–June and October–December, due to the presence of the monsoon trough over tropical waters of the NIO during these two periods. Tropical cyclone genesis typically occurs in the Arabian Sea and the Bay of Bengal between 8°N and 15°N. The Bay of Bengal, on average, experiences four times more TCs than the Arabian Sea (Dube et al. 1997).

The 2025 NIO TC season saw five named storms according to JTWC, which was slightly below the IBTrACS–JTWC 1991–2020 climatology of 5.4. One storm formed in the Arabian Sea, three formed in the Bay of Bengal, and one extremely rare storm formed in the Malacca Strait—only the second on record. Only one storm reached cyclone strength, and none reached major cyclone strength. These values were below the climatological average of 2.1 cyclones and 1.1 major cyclones (Fig. 4.34). The 2025 seasonal ACE index of 9.1×10^4 kt^2 was well below the 1991–2020 mean of 24.6×10^4 kt^2.

The only active part of the 2025 North Indian cyclone season occurred during the post-monsoon period from October to December, with all of the named storms forming during October and November. SSTs were above normal across the Bay of Bengal during this period (Fig. 4.35a).

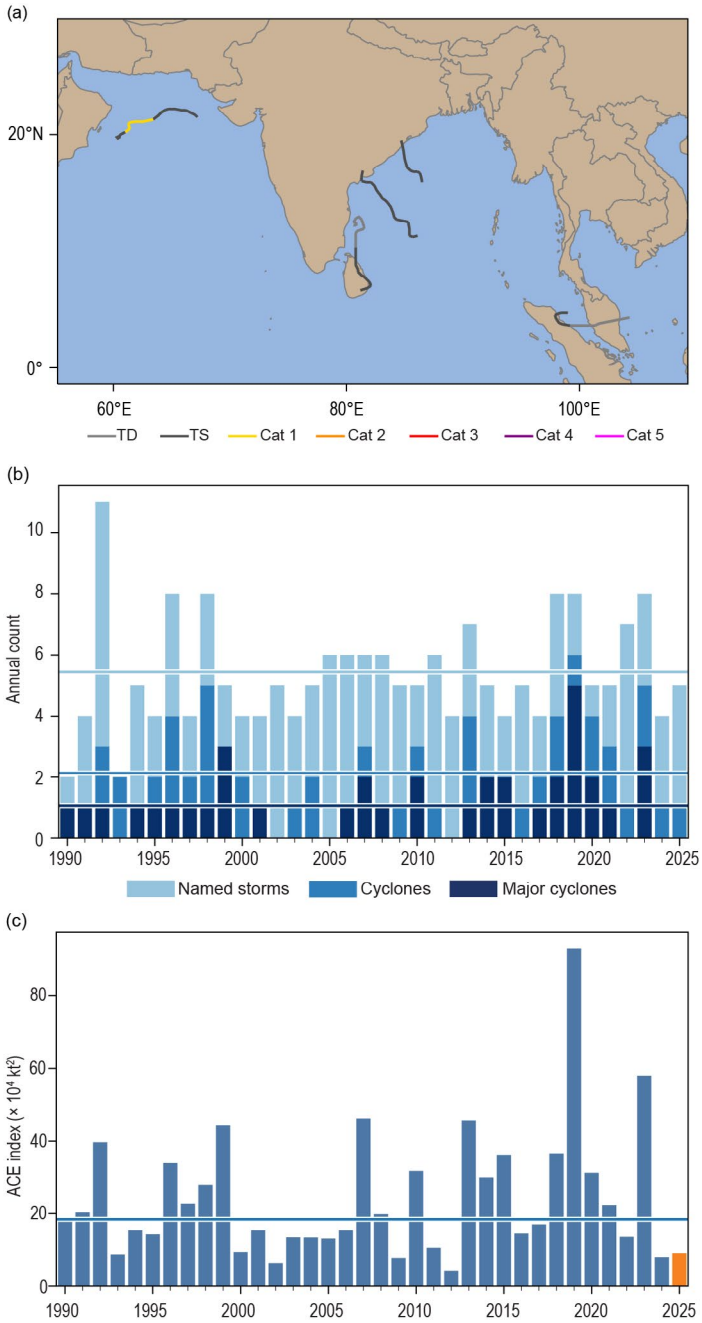

Fig. 4.34. (a) North Indian Ocean (NIO) tropical cyclone tracks in 2025. (b),(c) Annual tropical cyclone statistics in the NIO basin for the period 1990–2025: (b) number of named storms, cyclones, and major cyclones, and (c) accumulated cyclone energy (ACE; $\times 10^4$ kt^2; orange bar denotes 2025). Horizontal lines, representing the 1991–2020 climatology, are included in both (b) and (c).

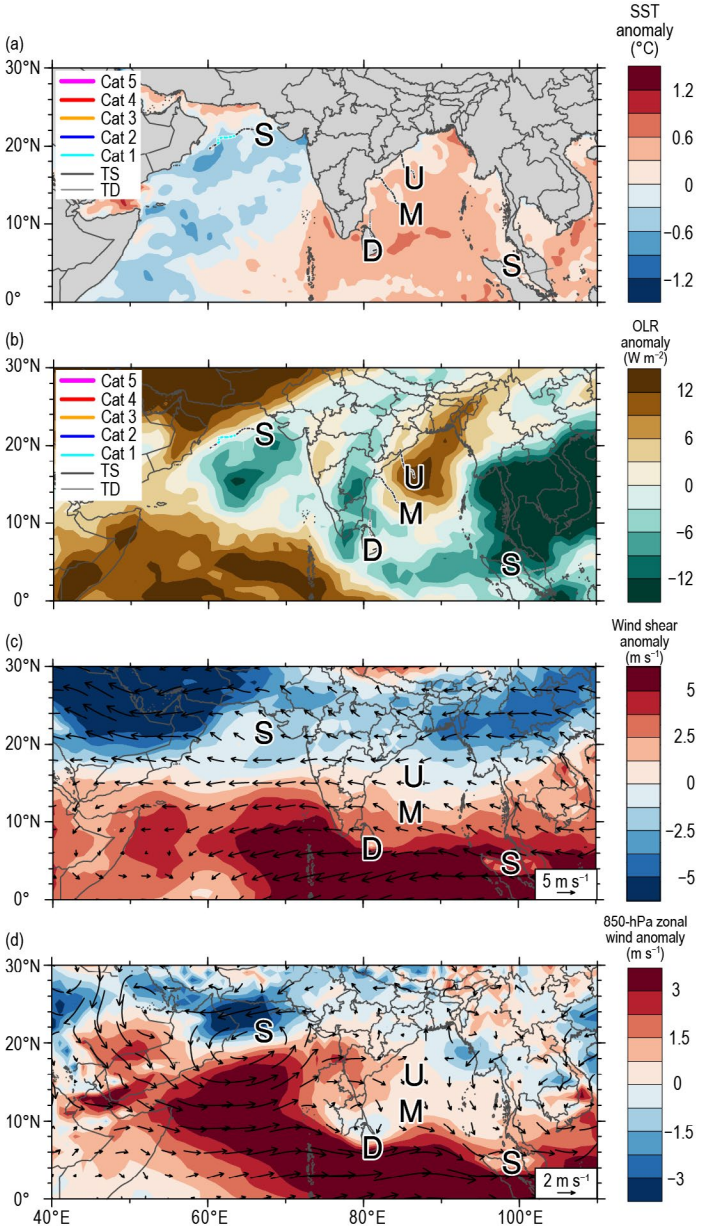

Fig. 4.35. Oct–Dec 2025 North Indian Ocean (NIO) anomaly maps of (a) sea surface temperature (SST; °C; Banzon and Reynolds 2013), (b) outgoing longwave radiation (OLR; W m^{-2}; Schreck et al. 2018); (c) 200-hPa–850-hPa vertical wind shear (m s^{-1}) vector (arrows) and scalar anomalies (shading), and (d) 850-hPa winds (m s^{-1}, arrows) and zonal wind anomalies (shading). Anomalies are relative to the annual cycle for 1991–2020. Letter symbols denote where each NIO tropical cyclone attained its initial tropical storm intensity. (Source: Wind data from CFSR [Saha et al. 2014].)

Convection was generally suppressed during this period over the Bay of Bengal, while some enhanced convection was observed over the Arabian Sea (Fig. 4.35b). The enhanced convective activity over the Arabian Sea likely contributed to Severe Cyclonic Storm Shakhti, which was the season's only tropical cyclone-strength storm. During the post-monsoon period, wind shear across the Arabian Sea was anomalously light, which also aided the intensification of Shakhti (Fig. 4.35c). Wind shear was light in the northern Bay of Bengal, but anomalously strong over the southern Bay of Bengal and most of the southern North Indian Ocean. Additionally, strong cyclonic low-level wind anomalies were present across the Arabian Sea, which likely also contributed to the season's only tropical cyclone forming there (Fig. 4.35d). The conditions for tropical cyclones overall were only marginally favorable for tropical cyclogenesis across the North Indian Ocean during the year. These conditions likely contributed to the below-average activity observed during the year.

(ii) Individual tropical cyclones and impacts

The first storm of the 2025 North Indian Ocean cyclone season formed during the post-monsoon period on 1 October. It was a short-lived unnamed tropical storm that made landfall along the central part of India's Bay of Bengal coastline. The storm brought heavy rainfall that led to significant flooding, damage, and loss of life. The second named storm was Severe Cyclonic Storm Shakhti. Shakhti peaked as a Category 1-equivalent tropical cyclone with maximum sustained winds of 74 kt (38 m s^{-1}) and a minimum central pressure of 976 hPa, making it the strongest storm of the season. Shakhti remained over the central Arabian Sea throughout its life, never making landfall. Towards the end of October, Cyclonic Storm Montha brought heavy rainfall and flooding to central India. Cyclonic Storm Montha peaked as a moderate-strength tropical storm, with maximum sustained winds of 43 kt (22 m s^{-1}) and a minimum central pressure of 995 hPa.

In November, two extremely destructive storms formed towards the end of the month. On 25 November, Cyclonic Storm Senyar formed in the Malacca Strait, becoming only the second storm ever observed in the strait. Senyar peaked as a moderate-strength TC with maximum sustained winds of 43 kt (22 m s^{-1}) and a minimum central pressure of 996 hPa. Senyar made landfall as a cyclonic storm on the island of Riau in Indonesia, bringing extremely heavy rainfall and catastrophic flooding. The storm's heavy precipitation also significantly affected parts of Malaysia and Thailand. The storm resulted in billions of dollars in damages and thousands of fatalities due to catastrophic flooding across the region, according to Reuters. The final storm of the year was Cyclonic Storm Ditwah, which peaked with maximum sustained winds of 35 kt (18 m s^{-1}) and a minimum central pressure of 1001 hPa. Ditwah brought heavy rainfall to Sri Lanka, causing significant flooding impacts, resulting in billions of dollars in damage (according to the World Bank Group) and hundreds of fatalities (according to the World Health Organization).

6. SOUTH INDIAN OCEAN

—A. D. Magee and C. J. Schreck

(i) Seasonal activity

The South Indian Ocean (SIO) TC basin extends south of the equator and from the East African coastline to 90°E. While TC activity can occur year-round, the peak season is typically between November and April when the Intertropical Convergence Zone is situated in the Southern Hemisphere. The 2024/25 season includes TCs that occurred from July 2024 to June 2025. Landfalling TCs typically impact Madagascar, Mozambique, and the Mascarene Islands, including Mauritius and La Réunion; however, impacts can be felt in other locations within the region.

The 2024/25 SIO TC season was above average and extremely destructive, and has been assessed as the costliest South Indian Ocean cyclone season on record, surpassing the previous record set in 2018/19. According to JTWC, 13 named storms occurred during the season, compared to the IBTrACS–JTWC 1991–2020 mean of 10.4 (Fig. 4.36). Of these, nine systems reached TC intensity, including six intense TCs (≥90 kt) and one very intense TC (≥115 kt). The six intense TCs tied as the third most in the basin since records began in 1967. Three named systems crossed into

the basin from the Australian region, contributing to the elevated storm count and accumulated impacts.

The 2024/25 seasonal ACE index was 139 × 10^4 kt^2, which is much higher than the 1991–2020 climatology of 94.3 × 10^4 kt^2. Cyclone-favorable conditions included anomalously high SSTs across the majority of the basin (Fig. 4.37a) and favorable wind shear anomalies (north of 20°S) across the main development region. These conditions supported frequent cyclogenesis and intensification (Fig. 4.37c). Strong cyclonic low-level wind anomalies were present across the northern portion of the basin, which likely also contributed to supporting cyclogenesis during the season (Fig. 4.37d).

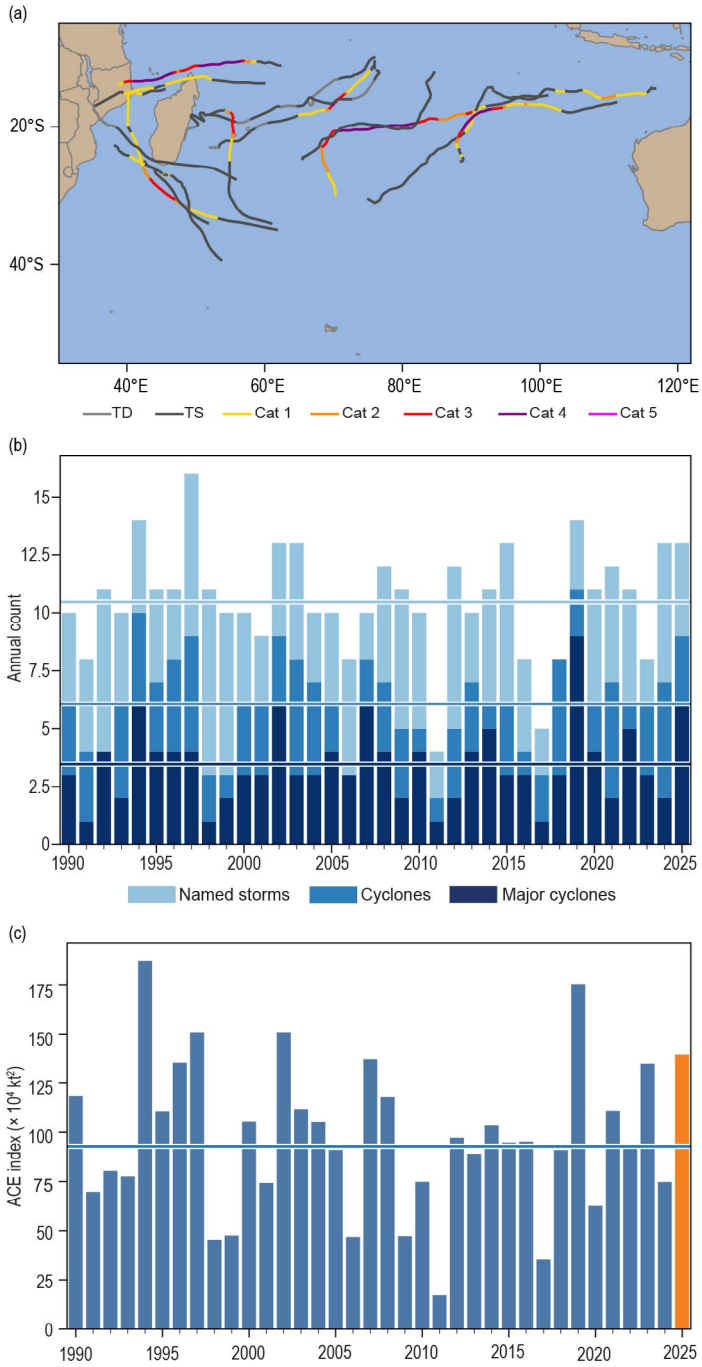

Fig. 4.36. (a) South Indian Ocean (SIO) tropical cyclone tracks in 2024/25. (b),(c) Annual tropical cyclone statistics for the SIO basin for the period 1990–2025: (b) number of named storms, cyclones, and major cyclones, and (c) accumulated cyclone energy (ACE; × 10^4 kt^2; orange bar denotes 2024/25). Horizontal lines, representing the 1991–2020 climatology, are included in both (b) and (c).

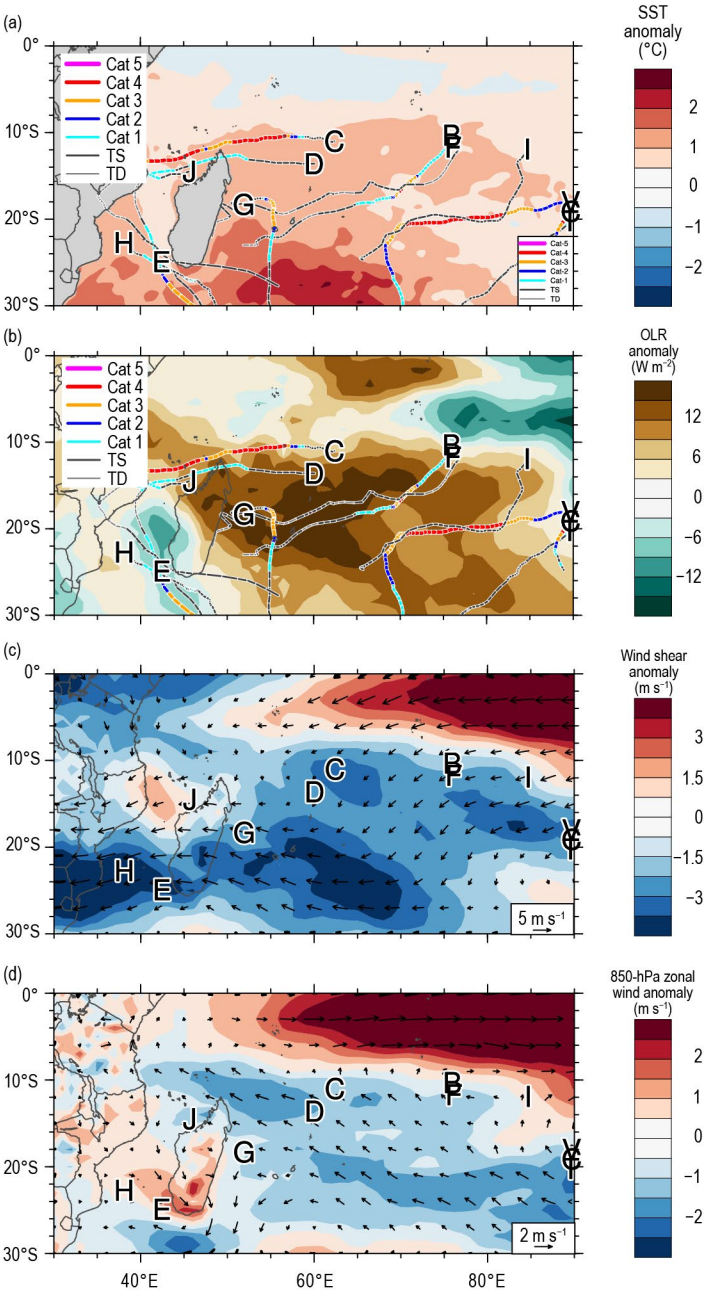

Fig. 4.37. Nov 2024–Apr 2025 South Indian Ocean (SIO) anomaly maps of: (a) sea surface temperature (SST; °C; Banzon and Reynolds 2013), (b) outgoing longwave radiation (OLR; W m^{-2}; Schreck et al. 2018); (c) 200-hPa–850-hPa vertical wind shear (m s^{-1}) vector (arrows) and scalar anomalies (shading), and (d) 850-hPa winds (m s^{-1}, arrows) and zonal wind anomalies (shading). Anomalies are relative to the annual cycle for 1991–2020. Letter symbols denote where each SIO tropical cyclone attained its initial tropical storm intensity. (Source: Wind data from CFSR [Saha et al. 2014].)

(ii) Noteworthy tropical cyclones and impacts

Very Intense Tropical Cyclone Chido (9–15 December) was the most impactful system of the season. Chido rapidly intensified to peak intensity on 12 December with sustained winds of 134 kt (69 m s^{-1}; SSHWS Category 4) and a minimum central pressure of 929 hPa, before making landfall on 15 December over northern Madagascar, with additional severe impacts across the Mascarene Islands (including Mauritius and La Réunion). Chido remained at major cyclone intensity for ~48 hours. Rainfall exceeded 300 mm–500 mm in 24 to 48 hours, producing severe riverine flooding, flash flooding, and landslides, while storm surge and coastal inundation affected low-lying communities. The cyclone caused over 170 fatalities, displaced tens of thousands of residents, and prompted a large-scale humanitarian response. Damage reached approximately $3.9 billion (U.S. dollars), making it the basin's costliest TC on record.

Cyclone Dikeledi developed in early January and intensified steadily before reaching peak intensity on 16 January, with sustained winds of 99 kt (51 m s^{-1}) and a minimum central pressure of ~950 hPa, making it a Category 3 strength cyclone on the SSHWS. The system made two landfalls on 11 and 13 January along the western and northern coasts of Madagascar, including regions bordering the Mozambique Channel. Dikeledi was slow-moving near landfall, producing widespread rainfall totals of 200 mm–400 mm over ~48 hours, which led to major flooding, river overflow, and landslides. Roads and bridges were washed out, isolating communities and delaying humanitarian access. The cyclone caused nine fatalities and $20 million (U.S. dollars) in insured damage. These impacts were compounded by already saturated soils and prior seasonal flooding.

Tropical Cyclone Honde (25 February–6 March) peaked as a Category 1 cyclone with sustained winds of 70 kt (36 m s^{-1}; SSHWS Category 1) and a minimum central pressure of 967 hPa. Honde affected southeastern Africa, including parts of Mozambique, producing prolonged heavy rainfall. Local totals exceeded 200 mm–300 mm, leading to riverine flooding and landslides. The cyclone caused flood-related fatalities, displaced thousands, and damaged housing, roads, and cropland.

Tropical Cyclone Jude (8–16 March) reached peak intensity on 9 March with sustained winds of 80 kt (41 m s^{-1}; SSHWS Category 1) and a minimum central pressure of 975 hPa. Jude made two landfalls (10 and 15 March), affecting eastern and northeastern Madagascar (including the Sava, Analanjirofo, and Atsinanana regions) before making a second landfall over northern and central Mozambique, with heavy rains and flooding extending inland into southern Malawi and parts of eastern Zimbabwe. Rainfall of 200 mm–400 mm led to widespread flooding, landslides, and river overflow, with multiple fatalities and large-scale displacement. Jude was a major contributor to cumulative seasonal impacts, particularly where recovery from earlier storms was ongoing.

Severe Tropical Cyclone Courtney (22 March–1 April) rapidly intensified to peak intensity on 29 March as it crossed from the Australian region with sustained winds of 128 kt (66 m s^{-1}; SSHWS Category 4) and a minimum central pressure of 932 hPa. Courtney generated severe marine hazards, coastal flooding, and storm surge, as well as producing damaging winds.

Other systems, including Intense Tropical Cyclone Bheki, Very Intense Tropical Cyclone Vince, Severe Tropical Cyclone Taliah, and Intense Tropical Cyclone Garance, largely remained offshore or caused localized impacts such as hazardous marine conditions and flooding, contributing to cumulative impacts but resulting in comparatively fewer fatalities and losses compared to the other storms discussed here.

7. AUSTRALIAN BASIN

—B. C. Trewin

(i) Seasonal activity

The 2024/25 TC season was more active than average in the broader Australian basin (areas south of the equator and between 90°E and 160°E[3], which includes Australian, Papua New Guinean, and Indonesian areas of responsibility). The season produced 12 TCs[4], above the

[3] The Australian Bureau of Meteorology's warning area overlaps both the southern Indian Ocean and southwest Pacific.

[4] This includes two TCs which were not named operationally but upgraded in post-season analysis.

1991–2020 average[5] of 9.5 and the highest number of TCs in a season since 2005/06 (Fig. 4.38). There were eight severe TCs (Australian Category 3 or above), which was also the most since 2005/06. The 1991–2020 IBTrACS seasonal averages for the basin are 10.2 named storms (NS), 5.0 TCs, and 2.5 major TCs, which compares with the 2024/25 IBTrACS-based counts of 14, 8, and 7 respectively.

Eleven of the 12 TCs during the 2024/25 season were in the western sector[6] of the broader Australian region, with Alfred being the only TC in the eastern sector. There were no TCs in the northern sector. Two TCs made landfall on mainland Australia as TCs (Zelia and Dianne); Alfred made landfall on near-coastal islands and Errol made landfall as a tropical low. Three of the 12 cyclones (Zelia, Courtney, and Errol) reached Category 5 intensity within the Australian basin.

(ii) Landfalling and other significant TCs

The most significant TCs of the season in terms of impact were Zelia and Alfred. Dianne also made landfall at cyclone intensity, while Sean had some impacts on land while remaining offshore.

Zelia was the most intense landfall of the season. It reached cyclone intensity at 1800 UTC on 11 February at 18.1°S, 119.0°E, about 280 km west of Broome. During 12 February, it became near-stationary over an area of very high sea surface temperatures (31°C–32°C, or 2°C–3°C above average) and intensified quickly, reaching Category 5 intensity by 1500 UTC on 12 February and a peak intensity (maximum sustained 10-minute winds of 115 kt [59 m s^{-1}], central pressure of 928 hPa) at 1200 UTC 13 February. It then moved south towards the coast while weakening slightly, crossing the coast as a Category 4 system at 0400 UTC on 14 February at the De Grey River mouth, northeast of Port Hedland. The system then moved inland while weakening.

Very heavy rain fell along the cyclone's path, with four-day totals from 12 to 15 February of 678 mm at De Grey (including 261 mm on the 14th) and 555 mm at Pardoo. Farther inland, 278 mm fell at Upper North Pole near Marble Bar. Flood heights at Marble Bar were nearly 2 m above previous records. There were major disruptions to offshore resource operations, and the Port Hedland port was closed for three days.

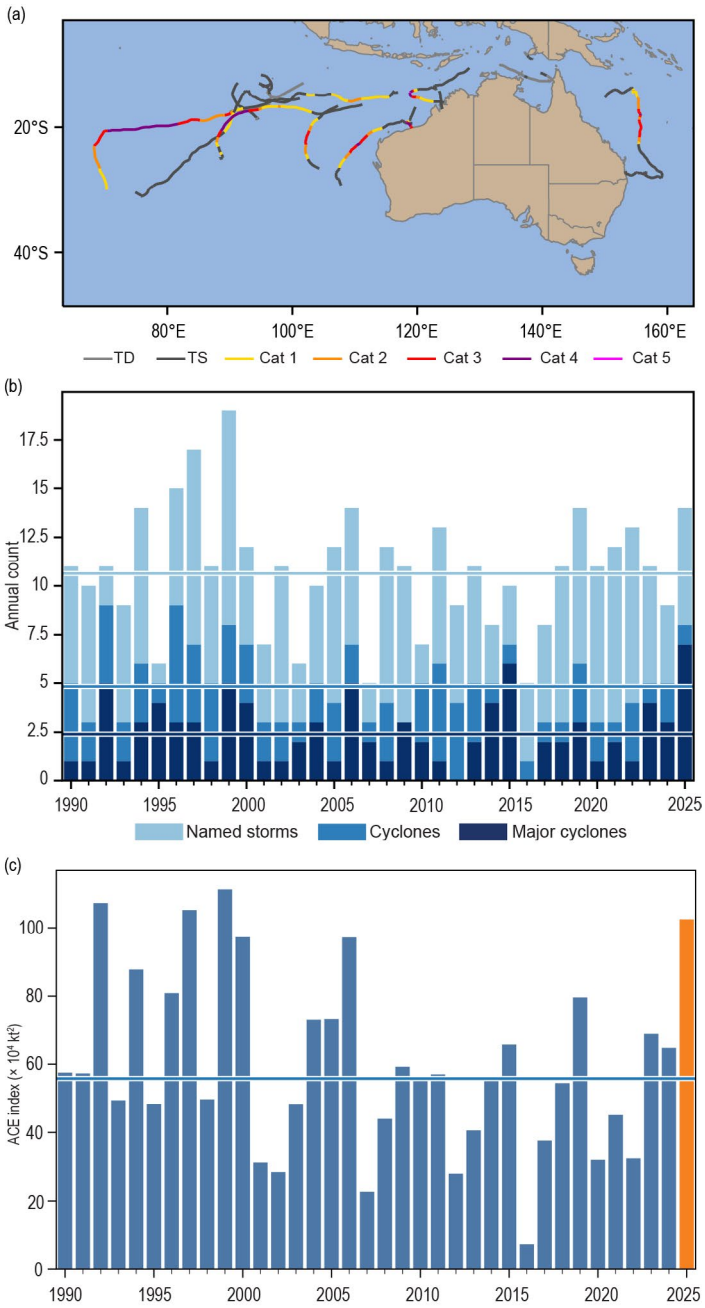

Fig. 4.38. (a) Australian tropical cyclone tracks in 2024/25. (b),(c) Annual tropical cyclone statistics for the Australian basin for the period 1990–2025: (b) number of named storms, cyclones, and major cyclones, and (c) accumulated cyclone energy (ACE; × 10^4 kt^2; orange bar denotes 2024/25). Horizontal lines, representing the 1991–2020 climatology, are included in both (b) and (c).

[5] References to cyclone category in this section are to the Australian system (https://www.bom.gov.au/resources/learn-and-explore/tropical-cyclone-knowledge-centre/tropical-cyclone-categories), which differs from the Saffir–Simpson Hurricane Wind Scale.

[6] The western sector covers areas between 90°E and 125°E. The eastern sector covers areas east of the eastern Australian coast to 160°E, as well as the eastern half of the Gulf of Carpentaria. The northern sector covers areas from 125°E east to the western half of the Gulf of Carpentaria. The western sector incorporates the Indonesian area of responsibility, while the Papua New Guinean area of responsibility is incorporated in the eastern sector.

Alfred, a long-lived cyclone, was the first cyclone to make landfall so far south in southeast Queensland since 1974. It was first named on 23 February at 14.0°S, 151.8°E, about 320 km northeast of Willis Island. Initially it moved east before turning south on 25 February, gradually intensifying and peaking on 27–28 February as a Category 4 system with maximum sustained winds of 90 kt (46 m s^{-1}). It weakened to Category 1 by 2 March as it moved south and was classified as a subtropical system from 3–5 March, before regaining tropical characteristics on 5 March and intensifying to Category 2 as it turned west towards the mainland, approaching Brisbane from the east. It made landfall as a Category 1 system on Moreton Island overnight on 7–8 March and then stalled, becoming subtropical before crossing the coast over Bribie Island on the evening of the 8th and moving over the mainland.

Heavy rainfall accompanied Alfred in many parts of southeast Queensland and northeast New South Wales. The heaviest precipitation occurred in the inland portion of the Gold Coast with a weekly total of 1146 mm at Upper Springbrook. Brisbane had its wettest day since 1974 with 275 mm on 10 March, with Nambour receiving a record 365 mm on the same day. At Hervey Bay, 189 mm fell in two hours on the morning of 9 March. Widespread main river and flash flooding occurred, with major flooding in the Bremer and Logan-Albert systems in Queensland and the Richmond, Clarence, and Bellinger systems in New South Wales. More than 500,000 properties lost power, and there was extensive coastal erosion. Insurance claims (per the Insurance Council of Australia) exceeded $1.5 billion Australian dollars ($1 billion U.S. dollars).

Sean tracked westward parallel to and 100 km north of the Pilbara coast of Western Australia in the third week of January, reaching a peak intensity of Category 4 (95 kt maximum sustained winds) 350 km west of Exmouth at 1200 UTC on 20 January. While it did not make landfall, heavy rain and strong winds associated with Sean affected parts of the coast, with Karratha having its wettest day on record (274 mm) on 20 January. There was some local flooding and building water ingress, along with tree damage in Karratha, and some disruption to mines and offshore resource operations.

Dianne, which peaked at Category 2 intensity, made landfall at near-peak intensity early on 29 March at Koolan Island, north of Derby. No major impacts were reported other than local flooding, with Derby receiving 99 mm in three hours early on 29 March. Errol was noteworthy for its rapid intensification. It was first named at 0600 UTC on 15 April near 13.8°S, 121.7°E, and within 30 hours reached Category 5 intensity, with maximum sustained winds of 110 kt (57 m s^{-1}) and gusts to 155 kt (80 m s^{-1}). It then weakened quickly as it turned southeast towards the west Kimberley coast, becoming a tropical low by the time it made landfall south of Kuri Bay on 18 April. The season's other Category 5 intensity system was Courtney, which followed an east-to-west track in the Indian Ocean well away from land areas and reached Category 5 intensity on 29 March near 19°S, 90°E just before leaving the Australian region.

8. SOUTHWEST PACIFIC BASIN

—A. D. Magee and A. M. Lorrey

(i) Seasonal activity

The 2024/25 southwest Pacific tropical cyclone season officially began on 1 November 2024 and ended on 30 April 2025. The data for the season were gathered from the Fiji Meteorological Service, Australian Bureau of Meteorology, and New Zealand MetService, Ltd. The southwest Pacific basin, defined by Diamond et al. (2012) as extending from 135°E–120°W, experienced a total of seven named TCs, including two severe storms. Compared with the 1991–2020 seasonal average of 9.8 named tropical cyclones, including 4.3 severe storms, as reported by the South Pacific Enhanced Archive for Tropical Cyclones (SPEArTC), the 2024/25 southwest Pacific tropical cyclone season was considered below normal.

Figure 4.39 illustrates the tropical cyclone activity in the basin, which spans the area 160°E–120°W to avoid overlap with the Australian basin and double counting of storms. It is important to note that the climatological definition of the southwest Pacific basin (Diamond et al. 2012) is used for this seasonal description and does not align with WMO-designated boundaries for Regional Specialized Meteorological Centre or Tropical Cyclone Warning Centre areas of responsibility. The section below describes events that both formed and passed into the southwest Pacific basin (135°E–120°W) and uses the Australian Tropical Cyclone Intensity Scale.

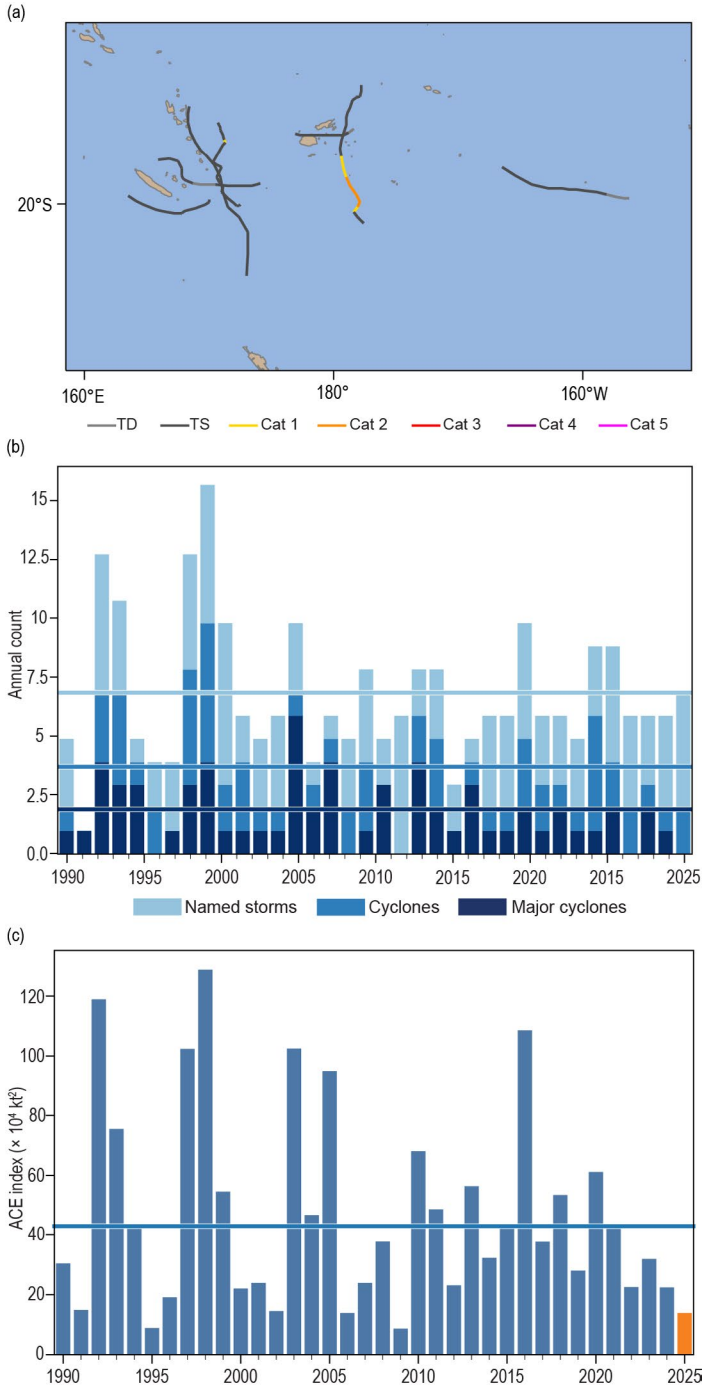

Fig. 4.39. (a) Southwest Pacific tropical cyclone tracks in 2024/25. (b),(c) Annual tropical cyclone statistics for the southwest Pacific basin for the period 1990–2025: (b) number of named storms, cyclones, and major cyclones, and (c) accumulated cyclone energy (ACE; × 10^4 kt^2; orange bar denotes 2024/25). Horizontal lines, representing the 1991–2020 climatology, are included in both (b) and (c).

(ii) Storm tracks, landfalls, and impacts

Tropical Cyclone Pita was a short-lived early-season system that developed early in 2025 (10–12 January). Pita reached peak intensity as a Category 1 tropical cyclone (Australian Tropical Cyclone Intensity Scale) of 39 kt (20 m s^{-1}) with a minimum central pressure of 993 hPa. The system passed near Niue and the Cook Islands, generating gale-force winds, heavy swell, and coastal inundation risk during high tides. Impacts were minor and no significant damage or loss of life was reported for those islands, although heavy rains and flooding did occur in relation to this storm in Fiji and Samoa.

Late February was the most active period of the season, with Tropical Cyclone Rae, Cyclone Seru, and Severe Tropical Cyclone Alfred occurring in close succession. Tropical Cyclone Rae developed north of Fiji on 22 February and intensified rapidly in a favorable environment characterized by warm sea surface temperatures (~30°C), low vertical wind shear, and strong upper-level outflow. Rae reached Category 2 intensity, with sustained winds of 89 kt (46 m s^{-1}) and a minimum central pressure of ~961 hPa, and affected Fiji during 23–25 February. Impacts included strong winds, heavy rainfall, flooding, and widespread disruption, with more than 1400 people displaced into evacuation centers. Rainfall totals exceeded 200 mm in 24 hours at several sites, contributing to localized flooding, road closures, uprooted trees, and damage to homes, farms, and public infrastructure. Some villages also reported food and water shortages from the weather impacts related to this system.

Tropical Cyclone Seru formed shortly thereafter (24–28 February) and peaked as a Category 2 system, with sustained winds of 64 kt (32 m s^{-1}) and a minimum central pressure near 980 hPa. Seru tracked to the southeast, passing east of Vanuatu, where warnings and red alerts were issued, particularly for Tafea Province. While the system largely remained offshore, its circulation produced periods of heavy rainfall, elevated seas, and localized flooding, including flash flooding in parts of Fiji during the system's extratropical phase.

Severe Tropical Cyclone Alfred was the strongest and most impactful system of the season, occurring from 21 February to 8 March. Alfred reached Category 4 intensity over the Coral Sea, with peak sustained winds of 115 kt (59 m s^{-1}) according to the JTWC, and a minimum central pressure near 943 hPa reported in multi-agency best-track datasets. Alfred was long-lived and complex, undergoing periods of weakening, re-intensification, and subtropical transition before approaching the Australian east coast. The cyclone produced widespread damaging winds, extreme rainfall, and severe coastal erosion across southeast Queensland and northeast New

South Wales, with seven-day rainfall totals exceeding 1000 mm at some locations and extensive flooding. More than 500,000 customers lost power, and insured losses exceeded $1.5 billion Australian dollars ($1.1 billion U.S. dollars), making Alfred one of the costliest weather events in Australia in 2025. One fatality was reported.

The final named storm of the season was Tropical Cyclone Tam (14–19 April), which peaked as a Category 1 cyclone, with sustained winds of 51 kt (26 m s^{-1}) and a minimum central pressure of ~977 hPa. Tam transitioned to an extratropical system as it moved southeastward, producing severe winds, heavy rainfall, flooding, and coastal erosion across northern New Zealand, including Northland, Auckland, the Coromandel Peninsula, and Bay of Plenty. Wind gusts exceeded 81 kt (42 m s^{-1}) at exposed sites, tens of thousands of properties lost power, and transport disruption was widespread.

h. Tropical cyclone heat potential

—J. Trinanes, J. Knaff, and I-I. Lin

Tropical cyclone heat potential (TCHP) is an indicator of the amount of heat stored in the upper ocean that can potentially promote TC intensification because, in addition to sea surface temperature (SST), subsurface thermal structure is also important for TC genesis and development (Shay et al. 2000; Goni and Trinanes 2003; Lin et al. 2008; Kang et al. 2024; Gao et al. 2025). TCHP is the ocean heat content calculated by integrating the ocean temperature between SST and the 26°C isotherm (D26), which has been reported as a useful predictor for TC intensification (Leipper and Volgenau 1972; Mainelli et al. 2008; Dare and McBride 2011; Knaff et al. 2018). TCs traveling over regions of high TCHP conditions experience higher enthalpy fluxes from the ocean into the atmosphere due to reduced SST cooling, favoring intensification (e.g., Lin et al. 2013). Areas in the ocean with TCHP values above 50 kJ cm^{-2} have been statistically linked with TC intensification, including rapid intensification when the maximum sustained wind speed increases by at least 30 kt in 24 hours, in situations in which atmospheric conditions are also favorable (e.g., Shay et al. 2000; Mainelli et al. 2008; Lin et al. 2021; Knaff et al. 2018, 2020). In addition to upper-ocean heat content, upper-ocean salinity conditions may also modulate TC intensification as storms traveling over areas of fresh-water-induced barrier layers may receive increased air–sea heat fluxes caused by reduced upper ocean mixing and cooling (e.g., Balaguru et al. 2012; Domingues et al. 2015).

In this section we present an assessment and analysis of the upper-ocean heat content conditions during 2025, based on estimates of two parameters: 1) TCHP (e.g., Goni et al. 2009, 2017) global anomalies with respect to their long-term mean (1993–2022), and 2) TCHP anomaly values differences in 2025 compared to conditions observed in 2024. TCHP anomalies during 2025 (Fig. 4.40) are computed for June–November in the Northern Hemisphere and November 2024–April 2025 in the Southern Hemisphere. The seven regions where TCs are known to form, travel, and intensify/weaken are highlighted in Fig. 4.40. In all these regions, TCHP values exhibit large temporal and spatial variability due to mesoscale features (e.g., surface currents and associated eddies and rings), and short- to long-term modes of climate variability (e.g., El Niño–Southern Oscillation, North Atlantic Oscillation, Pacific Decadal Oscillation). The differences in TCHP anomalies between 2025 and 2024 presented in Fig. 4.41 are computed for the primary months of TC activity in each hemisphere as described above.

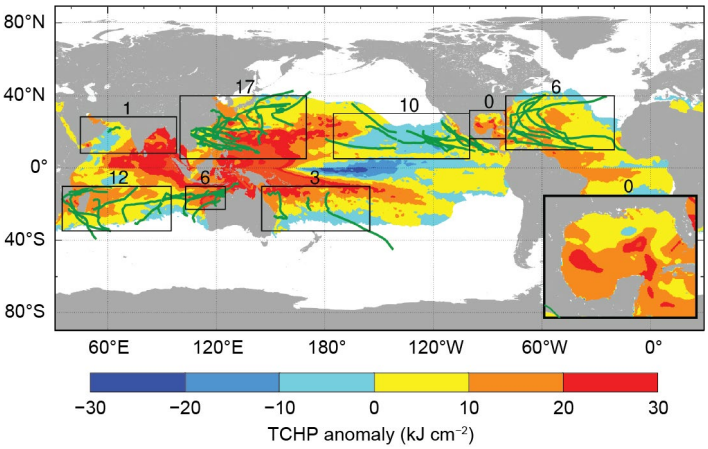

Fig. 4.40. Global anomalies of tropical cyclone heat potential (TCHP; kJ cm^{-2}) during 2025 computed as described in the text. The numbered boxes indicate the seven regions where tropical cyclones (TC) occur: from left to right, southwest Indian, North Indian, western North Pacific, southeast Indian, South Pacific, eastern North Pacific, and North Atlantic (shown as Gulf of America/Gulf of Mexico and tropical Atlantic separately). The green lines indicate the trajectories of all TCs reaching at least Category 1 (one-minute average wind ≥64 kt) and above during Nov 2024–Apr 2025 in the Southern Hemisphere and Jun–Nov 2025 in the Northern Hemisphere. The numbers above each box correspond to the number of Category 1 and above cyclones that traveled within each box. Gulf of America/Gulf of Mexico conditions are shown in the inset in the lower right corner.

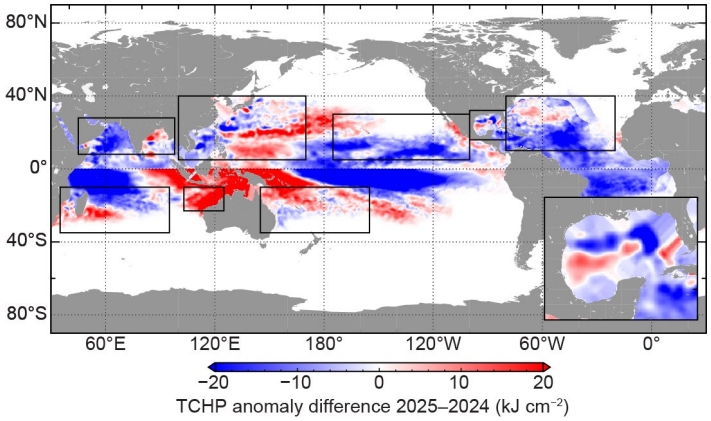

Fig. 4.41. Tropical cyclone heat potential (TCHP; kJ cm^{-2}) anomaly difference between the 2025 and 2024 tropical cyclone seasons (Jun–Nov in the Northern Hemisphere and Nov–Apr in the Southern Hemisphere). Gulf of America/Gulf of Mexico conditions are shown in the inset in the lower right corner.

TCHP anomalies during 2025 exhibited some above-average values in all TC regions and basins, with positive anomalies reaching 30 kJ cm^{-2}, showing favorable ocean conditions for TCs, although the anomalies are most pronounced in the regions north of Australia, large swaths of both the North and South Indian Oceans (including the Bay of Bengal), and both the southwest and western North Pacific basins (Fig. 4.40a). The TCHP difference between 2024 and 2025 shows positive differences over the central western North Pacific, while much of the eastern North Pacific and the North Atlantic have negative differences (Fig. 4.41). The difference pattern in the Pacific is understandable because during a La Niña year, eastern North Pacific SSTs were cooler as compared to the normal year (e.g., 2024). TCHP positive differences in 2025 (as compared to 2024) were also observed in the southeastern Indian and southwestern Pacific Oceans.

In terms of individual TCs, Hurricane Melissa (October 2025) was the most intense TC globally. It intensified to Category 5 in the western Caribbean south of Jamaica where TCHP exceeded 100 kJ cm^{-2} (Fig. 4.42), and while TCHP was lower than in 2024 (Fig. 4.41), it was still much higher than the climatological mean (Fig. 4.40). Melissa's rapid intensification was also associated with a warm ocean eddy where TCHP exceeded 120 kJ cm^{-2} (Fig. 4.42a). These favorable TCHP conditions enabled Melissa to intensify even while moving at a rather slow (<3 m s^{-1}) translation speed, ultimately achieving 150-kt intensity.

Another notable storm was Hurricane Erin (Fig. 4.42b), which intensified extremely rapidly: maximum winds increased by 45 kt (23 m s^{-1}) between 0600 and 1800 UTC 16 August and the pressure dropped by 4.5 hPa hr^{-1} (Pasch and Mahoney 2026). Erin represents an outlier among recent Atlantic storms in terms of the rate of intensification. During this period, the storm traversed a region characterized by moderately high ocean energy, with TCHP values along its track exceeding 100 kJ cm^{-2}, as well as SST anomalies of ~+1°C. These oceanic conditions along with Erin's small inner core/eyewall likely contributed to the storm's exceptional intensification, primarily by sustaining large air–sea heat fluxes. While the evolution of this hurricane also required favorable atmospheric conditions, the presence of high TCHP and SSTs along its trajectory highlights the critical role of the upper-ocean thermal structure in supporting extreme TC intensification events.

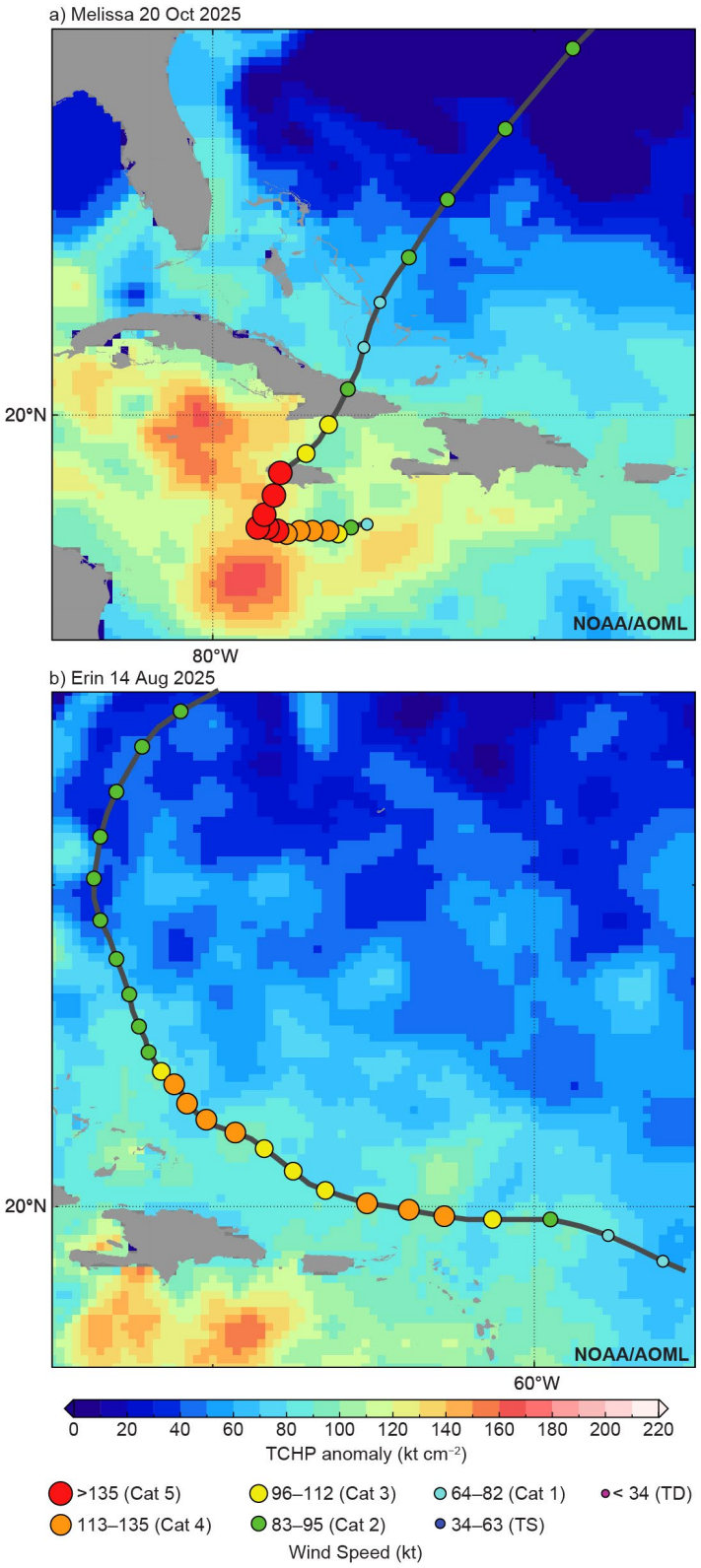

Fig. 4.42. Tropical cyclone heat potential (TCHP; kJ cm^{-2}) conditions for (a) Tropical Cyclone Melissa in Oct 2025; and (b) Tropical Cyclone Erin in Aug 2025.

In the 2024/25 season, above-normal TC activity in the South Indian Ocean was linked to elevated TCHP anomalies (Figs. 4.40, 4.41). These elevated anomalies helped fuel Tropical Cyclones Chido (135 kt; 69 m s^{-1}), Vince (135 kt; 69 m s^{-1}), Courtney (130 kt; 67 m s^{-1}), Errol (140 kt; 72m s^{-1}), and Zelia (130 kt; 67 m s^{-1}). Chido hit the island of Mayotte with an intensity of 105 kt (54 m s^{-1}) and destroyed 90% of the island's structures and then later made a second landfall in Mozambique (100 kt; 51 m s^{-1}) where it caused at least 120 deaths. Errol and Zelia both affected Western Australia. Despite Zelia making landfall in a relatively remote region (Bond 2025), it resulted in $733 million (U.S. dollars) in economic loss for this iron mining region.

Sidebar 4.1: **Hurricane Melissa: A record-breaking Caribbean hurricane**

—P. KLOTZBACH, C. FOGARTY, AND R. TRUCHELUT

Hurricane Melissa was one of the strongest Atlantic hurricanes on record, achieving a lifetime maximum intensity of 165 kt (85 m s^{-1}) and a minimum central pressure of 892 hPa on 28 October. Melissa made landfall in Jamaica with 160 kt (82 m s^{-1}) maximum sustained winds, causing devastation on the western part of the island. It made an additional landfall in Cuba as a Category 3 hurricane and two landfalls in the Bahamas as a Category 1 hurricane as it accelerated northeastward. Melissa also caused catastrophic flooding in Hispaniola, as well as in parts of Jamaica and eastern Cuba (Fig. SB4.1, inset). Overall, the storm was responsible for 95 fatalities and resulted in $8.8 billion (U.S. dollars) in damage in Jamaica, with significant damage reported elsewhere throughout the Caribbean. This sidebar focuses on the meteorological history of Melissa, highlights several records that the storm set, and discusses improvements in forecast modeling that resulted in highly skillful predictions for Melissa. Sidebar 7.2 (Regional Climates chapter) focuses on Melissa's societal impacts. Additional details on Melissa are available in the National Hurricane Center's (NHC) report on the system (Kelly et al. 2026).

When comparing Melissa with previous hurricanes, we use the NHC's North Atlantic (hereafter Atlantic) hurricane dataset from 1851 to 2025 (e.g., HURDAT2 (https://www.aoml.noaa.gov/hrd/hurdat/hurdat2.html); Landsea and Franklin 2013). All times are listed in UTC.

Melissa originated from a vigorous tropical wave that exited the African continent on 13 October. While the tropical wave produced consistent deep convection as it moved westward, its fast movement along with elevated vertical wind shear prevented development until the system slowed down upon reaching the eastern Caribbean. Melissa became a tropical storm on 21 October but intensified little over the next several days, battling significant westerly wind shear and dry air entrainment as weak steering flow caused slow, erratic motion. While the shear began to ease on 24 October, Melissa strengthened only slowly at first due to considerable residual displacement of the low- and mid-level vortices. The system began to become better organized late on 24 October, and by midday on 25 October, vortex tilt had substantially diminished as the shear weakened further. Melissa then began a period of rapid intensification from a 60 kt (31 m s^{-1}) tropical storm on 25 October at 1200 UTC to a 115 kt (59 m s^{-1}) Category

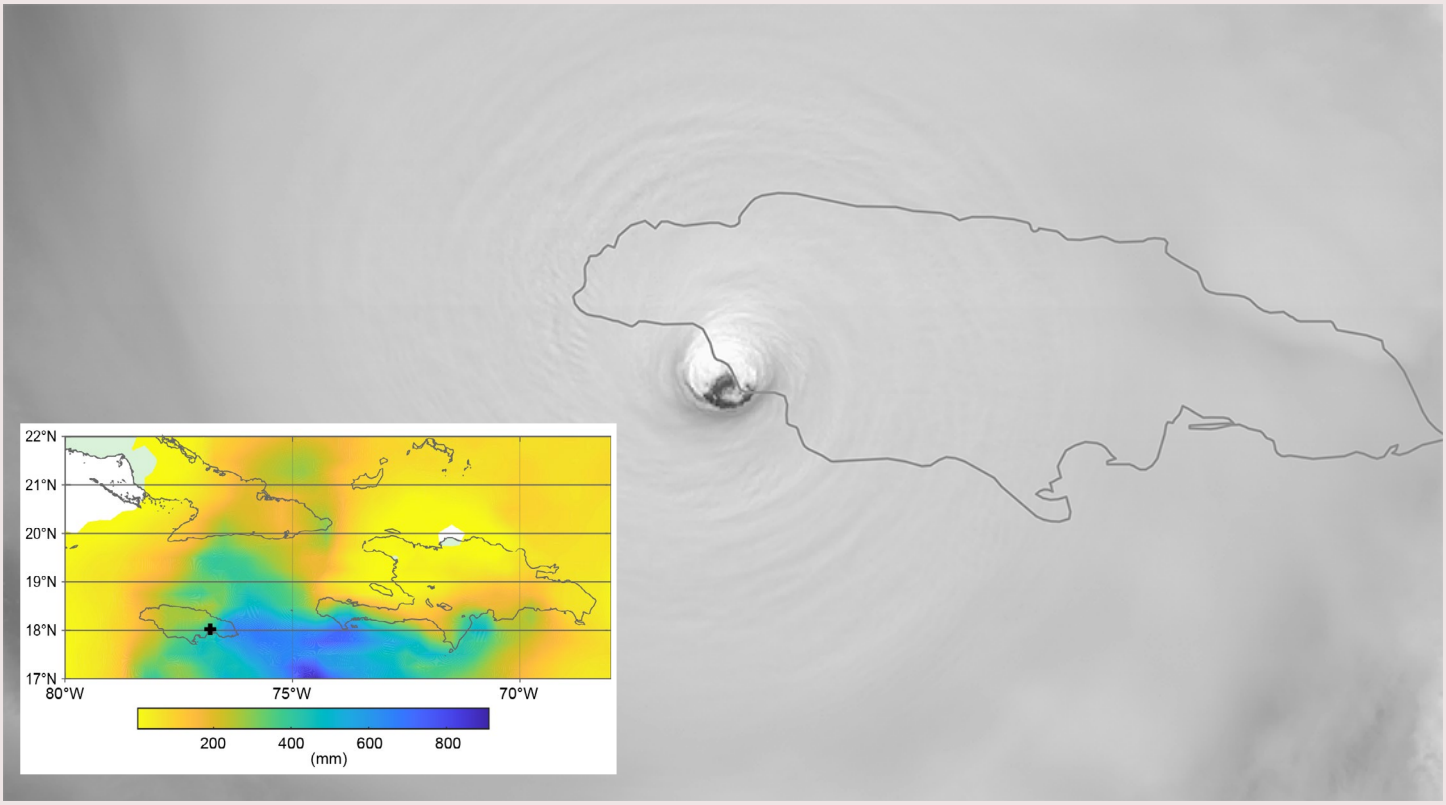

Fig. SB4.1. GOES-19 GeoColor satellite image of Hurricane Melissa at landfall in Jamaica at 1725 UTC on 28 Oct 2025. (Source: NOAA National Environmental Satellite, Data, and Information Service Center for Satellite Applications and Research.) Inset: ERA5-derived accumulated precipitation (mm) from 21 to 31 Oct 2025 (black plus sign indicates the location of Kingston, Jamaica).

4 hurricane on 26 October at 1200 UTC, fueled by extremely warm sea surface temperatures of ~30°C, copious mid-level moisture (60%–70% relative humidity) and low vertical wind shear (5 kt–10 kt; 3 m s^{-1}–5 m s^{-1}).

After a brief slowdown in its intensification early on 26 October, Melissa underwent another period of rapid intensification from 120 kt (62 m s^{-1}) to 155 kt (80 m s^{-1}) sustained winds between 1800 UTC on 26 October and 1800 UTC on 27 October. During this time, Melissa was stalled over a region of extremely high oceanic heat content, with Argo floats indicating a 30°C isotherm depth south of Jamaica of roughly 60 m prior to the hurricane. This reserve of heat potential slowed sea surface temperature cooling due to upwelling and evaporation (see section 4h for more discussion on the oceanic environment for Melissa). The storm continued to intensify as it approached western Jamaica (Fig. SB4.1), with sustained winds peaking at 165 kt (85 m s^{-1}) and the pressure dropping to 892 hPa. As Melissa began to interact with Jamaica, it weakened slightly before making landfall with sustained winds of 160 kt (82 m s^{-1}) and a pressure of 897 hPa.

Land interaction significantly weakened Melissa as it tracked slowly northeastward across Jamaica. After re-emerging in the Caribbean, Melissa became a bit better organized with its eye clearing out on satellite imagery before making landfall as a Category 3 hurricane in eastern Cuba with 100 kt (51 m s^{-1}) maximum winds (Fig. SB4.2). Later, on 29 October, Melissa expanded as it accelerated northeastward across the western Atlantic, passing through the central Bahamas as a Category 1 hurricane. Increasing vertical wind shear and cooler sea surface temperatures caused Melissa to slowly weaken and subsequently become post-tropical on 31 October.

Hurricane Melissa set several records during its traverse of the eastern and central Caribbean. Melissa's peak intensity of 165 kt (85 m s^{-1}) tied with Hurricane Allen in 1980 for the strongest on record for an Atlantic hurricane. Its minimum pressure of 892 hPa tied with the Labor Day Hurricane in 1935 for third lowest for an Atlantic hurricane on record—lagging only Wilma (2005; 882 hPa) and Gilbert (1988; 888 hPa). Melissa's maximum 24-hour intensification rate of 55 kt (28 m s^{-1}) from 25 October to 26 October was the third highest on record for an Atlantic hurricane that late in the calendar year, trailing only Hurricane Eta (2020; 70 kt [36 ms^{-1}]) and Hurricane Iota (2020; 65 kt [33 ms^{-1}]). It was a Category 5 hurricane until late on 28 October, becoming the latest calendar year Category 5 hurricane since Hattie on 31 October in 1961.

Melissa's sustained winds of 160 kt (72 m s^{-1}) at the time of its landfall in Jamaica are equal with the Labor Day Hurricane in 1935 in the Florida Keys and Dorian in 2019 in the northern Bahamas for the strongest Atlantic hurricane landfall intensity on record. Its Jamaican landfall pressure of 897 hPa trails only

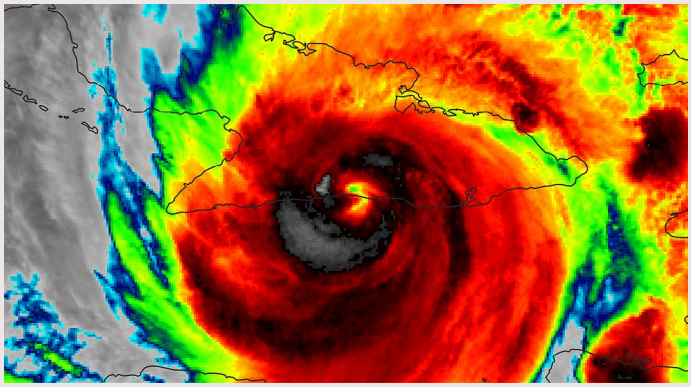

Fig. SB4.2. GOES-19 infrared satellite image of Hurricane Melissa making landfall in Cuba at 0720 UTC on 29 Oct 2025. (Source: NOAA National Environmental Satellite, Data, and Information Service Center for Satellite Applications and Research.)

the Labor Day Hurricane for the lowest pressure for an Atlantic landfall on record. Melissa also shattered the record for strongest Jamaican hurricane landfall, previously set by Gilbert in 1988 (115 kt; 59 m s^{-1}). These extreme intensity estimates are well supported by reconnaissance data, with a NOAA Hurricane Hunter dropsonde reporting a 219 kt (113 m s^{-1}) gust approximately 200 m above the ocean surface at 1350 UTC on 28 October. This is the strongest tropical cyclone wind on record, surpassing a 209 kt (108 m s^{-1}) dropsonde gust observed during western North Pacific's Typhoon Megi in 2010.

While Melissa caused devastating impacts across Jamaica as well as other Caribbean islands, the forecasts of Melissa's track and intensity from the NHC were extremely skillful. As noted in Cangialosi et al. (2025), Melissa's five-day track errors averaged ~185 km, which is ~50% of the average NHC five-day forecast error over the past five years. On 24 October (four days prior to landfall), the NHC was already forecasting Melissa to track over western Jamaica. The NHC first predicted Melissa to reach Category 5 intensity with its forecast issued on 25 October at 2100 UTC when the hurricane was still a Category 1. Per Cangialosi et al. (2025), this was the first time that the NHC had forecast a storm to reach Category 5 intensity from such a low initial intensity.

These decreases in error are due to more skillful model guidance. The aggregate performance of dynamical model track forecasts has continued to advance, while both statistical and dynamical models have demonstrated increased reliability in predicting rapid intensification. In addition to these more traditional forecasting tools, the NHC began adopting artificial intelligence models into its real-time forecasting in 2025. Notably, the Google DeepMind model was among the most skillful models at predicting Melissa's intensity and track, proving itself as a valuable new tool for NHC forecasters. While Melissa was an exceptionally powerful and damaging hurricane, the NHC's highly skillful, timely forecasts helped reduce loss of life and property damage.

Appendix 1: Acronyms

ACE	accumulated cyclone energy
AMV	Atlantic Multidecadal Variability
AUSSM	Australian summer monsoon
Cat	category
CMORPH	Climate Prediction Center Morphing technique
CNP	Central North Pacific
CoCoRaHS	Community Collaborative Rain, Hail and Snow Network
CPC	Climate Prediction Center
D26	26°C isotherm
DOISST	Daily Optimum Interpolation Sea Surface Temperature
EASM	East Asian summer monsoon
ENP	eastern North Pacific
ENSO	El Niño–Southern Oscillation
GODAS	Global Ocean Data Assimilation System
GPI	genesis potential index
GPM	Global Precipitation Measurement
HTC	hurricane/typhoon/cyclone
HTCs	hurricanes/typhoons/cyclones
ICAR	Institute for Climate and Application Research
IO	Indian Ocean
IOB	Indian Ocean basin
IOD	Indian Ocean dipole
IODE	eastern part of the Indian Ocean dipole
IODW	western part of the Indian Ocean dipole
ISM	Indian summer monsoon
ITCZ	Intertropical Convergence Zone
JMA	Japan Meteorological Agency
JTWC	Joint Typhoon Warning Center
LMR	land monsoon rainfall
MDR	main development region
MJO	Madden–Julian Oscillation
MSLP	mean sea level pressure
MSWEP	Multi-Source Weighted-Ensemble Precipitation
MTY	major typhoon
NAFSM	North African summer monsoon
NASM	North American summer monsoon
NCAR	National Centers for Atmospheric Research
NCEP	National Centers for Environmental Prediction
NH	Northern Hemisphere
NHC	National Hurricane Center
NIO	North Indian Ocean
nIOD	negative Indian Ocean dipole
NS	named storms
OHC	ocean heat content
OLR	outgoing longwave radiation
ONI	Oceanic Niño Index
PAGASA	Philippine Atmospheric, Geophysical and Astronomical Services Administration
PI	potential intensity
RMM	Real-time Multivariate Madden–Julian Oscillation

SA	South Atlantic
SAFSM	South African summer monsoon
SAM	Southern Annular Mode
SASM	South American summer monsoon
SH	Southern Hemisphere
SHIPS	statistical hurricane intensity prediction scheme
SIO	South Indian Ocean
SPCZ	South Pacific Convergence Zone
SPEArTC	Southwest Pacific Enhanced Archive for Tropical Cyclones
SSHWS	Saffir–Simpson Hurricane Wind Scale
SST	sea surface temperature
SSTAs	sea surface temperature anomalies
SSTs	Sea surface temperatures
STS	severe tropical storms
TC	tropical cyclone
TCHP	tropical cyclone heat potential
TCO-SP	Tropical Cyclone Outlook for the Southwest Pacific
TD	tropical depression
TS	tropical storm
TY	typhoon
WMO	World Meteorological Organization
WNP	western North Pacific
WNPSM	Western North Pacific summer monsoon

Appendix 2: Dataset Tables

Section 4b ENSO and the tropical Pacific

Sub-section	General Variable or Phenomenon	Specific Dataset or Variable	Source
4b2	Outgoing Longwave Radiation	National Centers for Environmental Prediction (NCEP) Climate Prediction Center (CPC) Outgoing Longwave Radiation (OLR) (Guo et al. 2004)	https://www.cpc.ncep.noaa.gov/products/global_precip/html/wpage.olr.html
4b	Sea Surface Temperature	ERSSTv5	https://doi.org/10.7289/V5T72FNM
4b1	Sea Surface Temperature	OISSTv2.1	https://www.ncei.noaa.gov/products/optimum-interpolation-sst
4b1	Subsurface Ocean Temperature	Global Ocean Data Assimilation System (GODAS, Behringer 2007)	https://psl.noaa.gov/data/gridded/data.godas.html
4b2	Wind Vectors/Wind Speed	NCEP National Center for Atmospheric Research Reanalysis 1	https://psl.noaa.gov/data/gridded/data.ncep.reanalysis.html
4b3	Precipitation	Global Historical Climatology Network monthly v4	https://ncei.noaa.gov/products/land-based-station/global-historical-climatology-network-monthly

Section 4c Tropical intraseasonal activity

Sub-section	General Variable or Phenomenon	Specific Dataset or Variable	Source
4c	Outgoing Longwave Radiation (OLR)	High Resolution Infrared Radiation Sounder (HIRS) OLR (Schreck et al. 2018)	https://www.ncei.noaa.gov/access/metadata/landing-page/bin/iso?id=gov.noaa.ncdc:C00875
4c	Subsurface Ocean Heat Content	Global Ocean Data Assimilation System (GODAS, Behringer et al. 1998)	https://www.cpc.ncep.noaa.gov/products/GODAS/
4c	Wind Velocity Potential Anomalies	Climate Forecast System Reanalysis (CFSR)	https://climatedataguide.ucar.edu/climate-data/climate-forecast-system-reanalysis-cfsr

Section 4d Intertropical convergence zones

Sub-section	General Variable or Phenomenon	Specific Dataset or Variable	Source
4d1	Precipitation	Multisource Weighted Ensemble Precipitation (MSWEP Version 2.8.0)	https://www.gloh2o.org/mswep/

Sub-section	General Variable or Phenomenon	Specific Dataset or Variable	Source
4d2	Precipitation	Global Precipitation Measurement (GPM) Integrated Multi-Satellite Retrievals for GPM (IMERG)	https://gpm.nasa.gov/data/imerg
4d2	Outgoing Longwave Radiation (OLR)	National Centers for Environmental Prediction (NCEP) Climate Prediction Center (CPC) OLR (Liebmann and Smith, 1996)	https://www.cpc.ncep.noaa.gov/products/global_precip/html/wpage.olr.html
4d2	Sea Level Pressure	NCEP National Center for Atmospheric Research (NCAR) Reanalysis 1	https://psl.noaa.gov/data/gridded/data.ncep.reanalysis.html
4d2	Sea Surface Temperature	OISSTv2.1	https://www.ncei.noaa.gov/products/optimum-interpolation-sst

Section 4e Global monsoon summary

Sub-section	General Variable or Phenomenon	Specific Dataset or Variable	Source
4e	Precipitation	GPCP	https://www.ncei.noaa.gov/products/climate-data-records/precipitation-gpcp-monthly
4e	Sea Surface Temperature	ERSSTv5	https://doi.org/10.7289/V5T72FNM
4e	Sea Surface Temperature	HadISST	https://www.metoffice.gov.uk/hadobs/hadisst/
4e	Wind, [Near] Surface	ERA5	https://www.ecmwf.int/en/forecasts/dataset/ecmwf-reanalysis-v5
4e	Wind, Upper Atmosphere	ERA5	https://www.ecmwf.int/en/forecasts/dataset/ecmwf-reanalysis-v5

Section 4f Indian Ocean dipole

Sub-section	General Variable or Phenomenon	Specific Dataset or Variable	Source
4f	Precipitation	Climate Prediction Center Merged Analysis of Precipitation (CMAP)	https://www.cpc.ncep.noaa.gov/products/global_precip/html/wpage.cmap.html
4f	Sea Surface Temperature	OISSTv2	https://www.ncei.noaa.gov/products/optimum-interpolation-sst
4f	Subsurface Ocean Temperature	Global Ocean Data Assimilation System (GODAS)	https://psl.noaa.gov/data/gridded/data.godas.html
4f	Wind, [Near] Surface	Japanese Reanalysis for Three Quarters of a Century (JRA-3Q)	https://www.data.jma.go.jp/jra/html/JRA-55/index_en.html
4f	Wind, [Near] Surface	ERA5	https://www.ecmwf.int/en/forecasts/dataset/ecmwf-reanalysis-v5

Section 4g Tropical cyclones			
Sub-section	**General Variable or Phenomenon**	**Specific Dataset or Variable**	**Source**
4g2	Outgoing Longwave Radiation	National Centers for Environmental Prediction (NCEP) Climate Prediction Center (CPC) Outgoing Longwave Radiation (OLR) (Liebmann and Smith, 1996)	https://www.cpc.ncep.noaa.gov/products/global_precip/html/wpage.olr.html
4g3, 4g5	Outgoing Longwave Radiation	High Resolution Infrared Radiation Sounder (HIRS) OLR (Schreck et al. 2018)	https://www.ncei.noaa.gov/access/metadata/landing-page/bin/iso?id=gov.noaa.ncdc:C00875
4g2	Sea Surface Temperature	ERSSTv6	https://ncei.noaa.gov/products/extended-reconstructed-sst
4g3, 4g5, 4g6	Sea Surface Temperature	NOAA OISST v2	https://www.ncei.noaa.gov/products/optimum-interpolation-sst
4g4	Sea Surface Temperature	ERSSTv5	https://doi.org/10.7289/V5T72FNM
4g1, 4g2, 4g3, 4g5, 4g6, 4g7, 4g8	Tropical Cyclone Data	International Best Track Archive for Climate Stewardship (IBTrACS)	https://www.ncei.noaa.gov/products/international-best-track-archive
4g2	Tropical Cyclone Data	HURDAT2	www.aoml.noaa.gov/hrd/hurdat/Data_Storm.html
4g4	Tropical Cyclone Data	Regional Specialized Meteorological Center (RSMC) Tokyo, Japanese Meteorological Agency (JMA) Best-Track Database	www.jma.go.jp/jma/jma-eng/jma-center/rsmc-hp-pub-eg/besttrack.html
4g4	Tropical Cyclone Data	Joint Typhoon Warning Center (JTWC) Best-Track Database	https://www.metoc.navy.mil/jtwc/jtwc.html?best-tracks
4g8	Tropical Cyclone Data	Southwest Pacific Enhanced Archive of Tropical Cyclones (SPEArTC)	https://apdrc.soest.hawaii.edu/projects/speartc/
4g2	Wind, [Near] Surface	NCEP National Center for Atmospheric Research (NCAR) Reanalysis 1	https://psl.noaa.gov/data/gridded/data.ncep.reanalysis.html
4g4	Wind, [Near] Surface	ERA5	https://www.ecmwf.int/en/forecasts/dataset/ecmwf-reanalysis-v5
4g3, 4g5, 4g6	Wind, [Near] Surface	Climate Forecast System Reanalysis (CFSR)	https://climatedataguide.ucar.edu/climate-data/climate-forecast-system-reanalysis-cfsr

Section 4h Tropical cyclone heat potential			
Sub-section	**General Variable or Phenomenon**	**Specific Dataset or Variable**	**Source**
4h	Ocean Heat Content	ECMWF Ocean Reanalysis System 4 (ORAS4)	https://www.ecmwf.int/en/forecasts/dataset/ocean-reanalysis-system-4

Sidebar 4.1 Hurricane Melissa: A Record-Breaking Caribbean Hurricane			
Sub-section	**General Variable or Phenomenon**	**Specific Dataset or Variable**	**Source**
SB4.1	Precipitation	ERA5	https://www.ecmwf.int/en/forecasts/dataset/ecmwf-reanalysis-v5
SB4.1	Tropical Cyclone Data	HURDAT2	www.aoml.noaa.gov/hrd/hurdat/Data_Storm.html

Appendix 3: Supplemental Materials

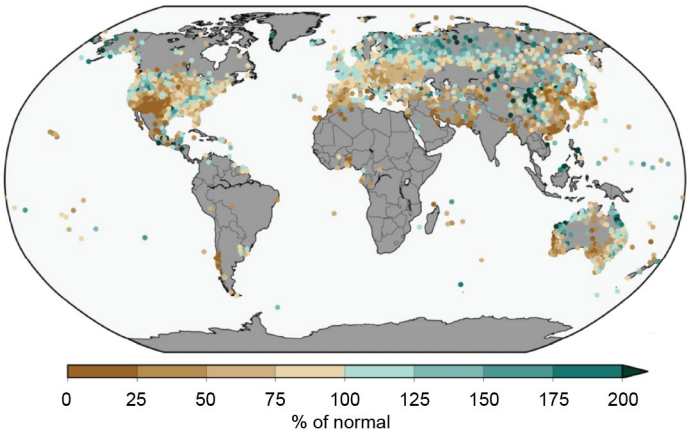

Appendix Fig. 4.1. Global precipitation over land areas during Dec 2024 to Feb 2025 (% of normal; 1961–90 base period). (Source: NOAA/NCEI Global Historical Climate Network monthly v4beta [Menne et al. 2017].)

References

Aiyyer, A., and J. Molinari, 2008: MJO and tropical cyclogenesis in the Gulf of Mexico and eastern Pacific: Case study and idealized numerical modeling. *J. Atmos. Sci.*, **65**, 2691–2704, https://doi.org/10.1175/2007JAS2348.1.

Balaguru, K., P. Chang, R. Saravanan, L. R. Leung, Z. Xu, M. Li, and J. S. Hsieh, 2012: Ocean barrier layers' effect on tropical cyclone intensification. *Proc. Natl. Acad. Sci. USA*, **109**, 14 343–14 347, https://doi.org/10.1073/pnas.1201364109.

Banzon, V. F., and R. W. Reynolds, 2013: Use of WindSat to extend a microwave-based daily optimum interpolation sea surface temperature time series. *J. Climate*, **26**, 2557–2562, https://doi.org/10.1175/JCLI-D-12-00628.1.

Baxter, S., C. Schreck, and G. D. Bell, 2019: Tropical intraseasonal activity [in "State of the Climate in 2018"]. *Bull. Amer. Meteor. Soc.*, **100** (9), S105–S107, https://doi.org/10.1175/2019BAMSStateoftheClimate.1.

Beck, H. E., E. F. Wood, M. Pan, C. K. Fisher, D. G. Miralles, A. I. J. M. van Dijk, T. R. McVicar, and R. F. Adler, 2019: MSWEP V2 global 3-hourly 0.1° precipitation: Methodology and quantitative assessment. *Bull. Amer. Meteor. Soc.*, **100**, 473–500, https://doi.org/10.1175/BAMS-D-17-0138.1.

Behringer, D. W., 2007: The Global Ocean Data Assimilation System (GODAS) at NCEP. Preprints, *11th Symp. on Integrated Observing and Assimilation Systems for Atmosphere, Oceans, and Land Surface*, San Antonio, TX, Amer. Meteor. Soc., 3.3, https://ams.confex.com/ams/87ANNUAL/techprogram/paper_119541.htm.

——, M. Ji, and A. Leetmaa, 1998: An improved coupled model for ENSO prediction and implications for ocean initialization. Part I: The ocean data assimilation system. *Mon. Wea. Rev.*, **126**, 1013–1021, https://doi.org/10.1175/1520-0493(1998)126<1013:AICMFE>2.0.CO;2.

Bell, G. D., and M. Chelliah, 2006: Leading tropical modes associated with interannual and multidecadal fluctuations in North Atlantic hurricane activity. *J. Climate*, **19**, 590–612, https://doi.org/10.1175/JCLI3659.1.

——, and Coauthors, 2000: The 1999 North Atlantic and eastern North Pacific hurricane seasons [in "Climate Assessment for 1999"]. *Bull. Amer. Meteor. Soc.*, **81** (6), S19–S22, https://doi.org/10.1175/1520-0477(2000)81[s1:CAF]2.0.CO;2.

——, and Coauthors, 2017: The 2016 North Atlantic hurricane season: A climate perspective [in "State of the Climate in 2016"]. *Bull. Amer. Meteor. Soc.*, **98** (8), S109–S112, https://doi.org/10.1175/2017BAMSStateoftheClimate.1.

——, and Coauthors, 2018: The 2017 North Atlantic hurricane season: A climate perspective [in "State of the Climate in 2017"]. *Bull. Amer. Meteor. Soc.*, **99** (8), S114–S118, https://doi.org/10.1175/2018BAMSStateoftheClimate.1.

——, and Coauthors, 2020: The 2019 North Atlantic hurricane season: A climate perspective [in "State of the Climate in 2019"]. *Bull. Amer. Meteor. Soc.*, **101** (8), S204–S212, https://doi.org/10.1175/2020BAMSStateoftheClimate.1.

Bjerknes, J., 1969: Atmospheric teleconnections from the equatorial Pacific. *Mon. Wea. Rev.*, **97**, 163–172, https://doi.org/10.1175/1520-0493(1969)097<0163:ATFTEP>2.3.CO;2.

Bond, S., 2025: Severe Tropical Cyclone Zelia (18U), 8–14 February 2025. Severe Weather Environmental Prediction Services, Bureau of Meteorology, 28 pp., https://www.bom.gov.au/cyclone/history/doc/Zelia2025_report.docx.

Brown, J. R., and Coauthors, 2020: South Pacific convergence zone dynamics, variability and impacts in a changing climate. *Nat. Rev. Earth Environ.*, **1**, 530–543, https://doi.org/10.1038/s43017-020-0078-2.

Bucci, L. R., 2026: Hurricane Priscilla. NHC Tropical Cyclone Rep., 17 pp., https://www.nhc.noaa.gov/data/tcr/EP162025_Priscilla.pdf.

Camargo, S. J., and A. H. Sobel, 2005: Western North Pacific tropical cyclone intensity and ENSO. *J. Climate*, **18**, 2996–3006, https://doi.org/10.1175/JCLI3457.1.

——, K. A. Emanuel, and A. H. Sobel, 2007a: Use of a genesis potential index to diagnose ENSO effects on tropical cyclone genesis. *J. Climate*, **20**, 4819–4834, https://doi.org/10.1175/JCLI4282.1.

——, A. W. Robertson, S. J. Gaffney, P. Smyth, and M. Ghil, 2007b: Cluster analysis of typhoon tracks. *Part II: Large-scale circulation and ENSO. J. Climate*, **20**, 3654–3676, https://doi.org/10.1175/JCLI4203.1.

Cangialosi, J., 2025: Hurricane Erick discussion number 13. NHC, https://www.nhc.noaa.gov/archive/2025/ep05/ep052025.discus.013.shtml.

——, J. Martinez, and P. Papin, 2025: 2025 NHC verification report preview. 8 pp., https://www.nhc.noaa.gov/pdf/NHC_Verification_Report_2025_Preview.pdf.

Chen, L., and J.-J. Luo, 2025: Indian Ocean dipole [in "State of the Climate in 2024"]. *Bull. Amer. Meteor. Soc.*, **106** (8), S255–S257, https://doi.org/10.1175/BAMS-D-25-0102.1.

Chia, H. H., and C. F. Ropelewski, 2002: The interannual variability in the genesis location of tropical cyclones in the northwest Pacific. *J. Climate*, **15**, 2934–2944, https://doi.org/10.1175/1520-0442(2002)015<2934:TIVITG>2.0.CO;2.

Dare, R. A., and J. L. McBride, 2011: Sea surface temperature response to tropical cyclones. *Mon. Wea. Rev.*, **139**, 3798–3808, https://doi.org/10.1175/MWR-D-10-05019.1.

Diamond, H. J., and C. J. Schreck, Eds., 2022: The tropics [in "State of the Climate in 2021"]. *Bull. Amer. Meteor. Soc.*, **103** (8), S193–S255, https://doi.org/10.1175/BAMS-D-22-0069.1.

——, and ——, Eds., 2024: [463155][h6]The tropics [in "State of the Climate in 2023"]. *Bull. Amer. Meteor. Soc.*, **105** (8), S1–S57, https://doi.org/10.1175/BAMS-D-24-0098.1.

——, and ——, Eds., 2025: The tropics [in "State of the Climate in 2024"]. *Bull. Amer. Meteor. Soc.*, **106** (8), S334–S395, https://doi.org/10.1175/BAMS-D-25-0086.1.

——, A. M. Lorrey, K. R. Knapp, and D. H. Levinson, 2012: Development of an enhanced tropical cyclone tracks database for the southwest Pacific from 1840 to 2010. *Int. J. Climatol.*, **32**, 2240–2250, https://doi.org/10.1002/joc.2412.

Ding, Q., E. J. Steig, D. S. Battisti, and J. M. Wallace, 2012: Influence of the tropics on the Southern Annular Mode. *J. Climate*, **25**, 6330–6348, https://doi.org/10.1175/JCLI-D-11-00523.1.

Domingues, R., and Coauthors, 2015: Upper ocean response to Hurricane Gonzalo (2014): Salinity effects revealed by targeted and sustained underwater glider observations. *Geophys. Res. Lett.*, **42**, 7131–7138, https://doi.org/10.1002/2015GL065378.

Dube, S. K., D. Rao, P. C. Sinha, T. S. Murty, and N. Bahuluyan, 1997: Storm surge in the Bay of Bengal and Arabian Sea: The problem and its prediction. *Mausam*, **48**, 283–304, https://doi.org/10.54302/mausam.v48i2.4012.

Ebita, A., and Coauthors, 2011: The Japanese 55-year reanalysis "JRA-55": An interim report. *SOLA*, **7**, 149–152, https://doi.org/10.2151/sola.2011-038.

Emanuel, K. A., 1988: The maximum intensity of hurricanes. *J. Atmos. Sci.*, **45**, 1143–1155, https://doi.org/10.1175/1520-0469(1988)045<1143:TMIOH>2.0.CO;2.

——, and D. S. Nolan, 2004: Tropical cyclone activity and the global climate system. *Proc. 26th Conf. on Hurricanes and Tropical Meteorology*, Miami, FL, Amer. Meteor. Soc., 10A.2, https://ams.confex.com/ams/26HURR/techprogram/paper_75463.htm.

Enfield, D. B., and A. M. Mestas-Nuñez, 1999: Multiscale variabilities in global sea surface temperatures and their relationships with tropospheric climate patterns. *J. Climate*, **12**, 2719–2733, https://doi.org/10.1175/1520-0442(1999)012<2719:MVIGSS>2.0.CO;2.

Gallagher Re, 2026: Natural catastrophe and climate report: 2025. 76 pp., https://www.ajg.com/gallagherre/-/media/files/gallagher/gallagherre/news-and-insights/2026/january/natural-catastrophe-and-climate-report-january-2026.pdf.

Gao, C., L. Zhou, I.-I. Lin, C. Wang, S. Guan, F.-F. Jin, and F. Murtugudde, 2025: Crucial role of subsurface ocean variability in tropical cyclone genesis. *Nat. Commun.*, **16**, 1050, https://doi.org/10.1038/s41467-025-56433-5.

Goldenberg, S. B., and L. J. Shapiro, 1996: Physical mechanisms for the association of El Niño and West African rainfall with Atlantic major hurricane activity. *J. Climate*, **9**, 1169–1187, https://doi.org/10.1175/1520-0442(1996)009<1169:PMFTAO>2.0.CO;2.

——, C. W. Landsea, A. M. Mestas-Nuñez, and W. M. Gray, 2001: The recent increase in Atlantic hurricane activity: Causes and implications. *Science*, **293**, 474–479, https://doi.org/10.1126/science.1060040.

Goni, G. J., and J. A. Trinanes, 2003: Ocean thermal structure monitoring could aid in the intensity forecast of tropical cyclones. *Eos, Trans. Amer. Geophys. Union*, **84**, 573–578, https://doi.org/10.1029/2003EO510001.

——, and Coauthors, 2009: Applications of satellite-derived ocean measurements to tropical cyclone intensity forecasting. *Oceanography*, **22** (3), 190–197, https://doi.org/10.5670/oceanog.2009.78.

——, and Coauthors, 2017: Autonomous and Lagrangian ocean observations for Atlantic tropical cyclone studies and forecasts. *Oceanography*, **30** (2), 92–103, https://doi.org/10.5670/oceanog.2017.227.

Gray, W. M., 1990: Strong association between West African rainfall and U.S. landfall of intense hurricanes. *Science*, **249**, 1251–1256, https://doi.org/10.1126/science.249.4974.1251.

Guo, Y., X. Jiang, and D. E. Waliser, 2014: Modulation of the convectively coupled Kelvin waves over South America and the tropical Atlantic Ocean in association with the Madden–Julian Oscillation. *J. Atmos. Sci.*, **71**, 1371–1388, https://doi.org/10.1175/JAS-D-13-0215.1.

——, S. Wu, H.-T. Lee, and P. Xie, 2024: CPC new OLR data set. *26th Conf. on Satellite Meteorology, Oceanography, and Climatology*, Baltimore, MD, Amer. Meteor. Soc., 85, https://ams.confex.com/ams/104ANNUAL/webprogram/Paper435981.html.

Gutzler, D. S, K. M. Wood, E. A. Ritchie, A.V. Douglas, M. D. Lewis, 2013: Interannual variability of tropical cyclone activity along the Pacific coast of North America, Atmósfera, 26(2), 149–162, https://doi.org/10.1016/S0187-6236(13)71069-5.

Hersbach, H., and Coauthors, 2020: The ERA5 global reanalysis. *Quart. J. Roy. Meteor. Soc.*, **146**, 1999–2049, https://doi.org/10.1002/qj.3803.

Hong, C.-C., T. Li, and J.-J. Luo, 2008: Asymmetry of the Indian Ocean dipole. Part II: Model diagnosis. *J. Climate*, **21**, 4849–4858, https://doi.org/10.1175/2008JCLI2223.1.

Hu, S., and A. V. Fedorov, 2018: Cross-equatorial winds control El Niño diversity and change. *Nat. Climate Change*, **8**, 798–802, https://doi.org/10.1038/s41558-018-0248-0.

Huang, B., and Coauthors, 2017: Extended Reconstructed Sea Surface Temperature, version 5 (ERSSTv5): Upgrades, validations, and intercomparisons. *J. Climate*, **30**, 8179–8205, https://doi.org/10.1175/JCLI-D-16-0836.1.

——, C. Liu, V. Banzon, E. Freeman, G. Graham, B. Hankins, T. Smith, and H.-M. Zhang, 2021: Improvements of the Daily Optimum Interpolation Sea Surface Temperature (DOISST) version 2.1. *J. Climate*, **34**, 2923–2939, https://doi.org/10.1175/JCLI-D-20-0166.1.

——, X. Yin, T. Boyer, C. Liu, M. Menne, Y. D. Rao, T. Smith, R. Vose, H.-M. Zhang, 2025: Extended Reconstructed Sea Surface Temperature version 6 (ERSSTv6): Part I. An artificial neural network approach. *J. Climate*, **38**, 1105–1121, https://doi.org/10.1175/JCLI-D-23-0707.1.

Huffman, G. J., R. F. Adler, D. T. Bolvin, and G. Gu, 2009: Improving the global precipitation record: GPCP version 2.1. *Geophys. Res. Lett.*, **36**, L17808, https://doi.org/10.1029/2009GL040000.

——, E. F. Stocker, D. T. Bolvin, E. J. Nelkin, J. Tan, 2023: GPM IMERG Final Precipitation L3 1 month 0.1 degree x 0.1 degree, version 07. Goddard Earth Sciences Data and Information Services Center (GES DISC), accessed December 2025, https://doi.org/10.5067/GPM/IMERG/3B-MONTH/07.

Jelsema, J., 2025: Hurricane Erick. NHC Tropical Cyclone Rep., 31 pp., https://www.nhc.noaa.gov/data/tcr/EP052025_Erick.pdf.

Kalnay, E., and Coauthors, 1996: The NCEP/NCAR 40-Year Reanalysis Project. *Bull. Amer. Meteor. Soc.*, **77**, 437–471, https://doi.org/10.1175/1520-0477(1996)077<0437:TNYRP>2.0.CO;2.

Kang, S. K., and Coauthors, 2024: The North Equatorial Current and rapid intensification of super typhoons. *Nat. Commun.*, **15**, 1742, https://doi.org/10.1038/s41467-024-45685-2.

Kelly, L. A., J. Alamo, and A. D. Mahoney, 2026: Tropical cyclone report: Hurricane Melissa (AL132025), 21–31 October 2025. NHC Tech. Rep., 87 pp., https://www.nhc.noaa.gov/data/tcr/AL132025_Melissa.pdf

Kiladis, G. N., M. C. Wheeler, P. T. Haertel, K. H. Straub, and P. E. Roundy, 2009: Convectively coupled equatorial waves. *Rev. Geophys.*, **47**, RG2003, https://doi.org/10.1029/2008RG000266.

Knaff, J. A., C. R. Sampson, and K. D. Musgrave, 2018: An operational rapid intensification prediction aid for the western North Pacific. *Wea. Forecasting*, **33**, 799–811, https://doi.org/10.1175/WAF-D-18-0012.1.

——, ——, and B. R. Strahl, 2020: A tropical cyclone rapid intensification prediction aid for the Joint Typhoon Warning Center's areas of responsibility. *Wea. Forecasting*, **35**, 1173–1185, https://doi.org/10.1175/WAF-D-19-0228.1.

Knapp, K. R., M. C. Kruk, D. H. Levinson, H. J. Diamond, and C. J. Neumann, 2010: The International Best Track Archive for Climate Stewardship (IBTrACS): Unifying tropical cyclone data. *Bull. Amer. Meteor. Soc.*, **91**, 363–376, https://doi.org/10.1175/2009BAMS2755.1.

Kruk, M. C., and C. J. Schreck, 2019: Eastern North Pacific basin [in "State of the Climate in 2018"]. *Bull. Amer. Meteor. Soc.*, **100** (9), S121–S124, https://doi.org/10.1175/2019BAMSStateoftheClimate.1.

Landsea, C. W., and J. L. Franklin, 2013: Atlantic hurricane database uncertainty and presentation of a new database format. *Mon. Wea. Rev.*, **141**, 3576–3592, https://doi.org/10.1175/MWR-D-12-00254.1.

——, W. M. Gray, P. W. Mielke, and K. J. Berry, 1992: Long-term variations of western Sahelian monsoon rainfall and intense U.S. landfalling hurricanes. *J. Climate*, **5**, 1528–1534, https://doi.org/10.1175/1520-0442(1992)005<1528:LTVOWS>2.0.CO;2.

——, G. A. Vecchi, L. Bengtsson, and T. R. Knutson, 2010: Impact of duration thresholds on Atlantic tropical cyclone counts. *J. Climate*, **23**, 2508–2519, https://doi.org/10.1175/2009JCLI3034.1.

Leipper, D. F., and D. Volgenau, 1972: Hurricane heat potential of the Gulf of Mexico. *J. Phys. Oceanogr.*, **2**, 218–224, https://doi.org/10.1175/1520-0485(1972)002<0218:HHPOTG>2.0.CO;2.

L'Heureux, M. L., and Coauthors, 2024: A relative sea surface temperature index for classifying ENSO events in a changing climate. *J. Climate*, **37**, 1197–1211, https://doi.org/10.1175/JCLI-D-23-0406.1.

Li, T., B. Wang, C.-P. Chang, and Y. Zhang, 2003: A theory for the Indian Ocean dipole zonal mode. *J. Atmos. Sci.*, **60**, 2119–2135, https://doi.org/10.1175/1520-0469(2003)060<2119:ATFTIO>2.0.CO;2.

Liebmann, B., and C. A. Smith, 1996: Description of a complete (interpolated) outgoing longwave radiation dataset. *Bull. Amer. Meteor. Soc.*, **77**, 1275–1277, https://doi.org/10.1175/1520-0477-77.6.1274.

Lin, I.-I., C.-C. Wu, I.-F. Pun, and D.-S. Ko, 2008: Upper-Ocean Thermal Structure and the Western North Pacific Category 5 Typhoons. Part I: Ocean Features and the Category 5 Typhoons' Intensification. *Mon. Wea. Rev.*, **136**, 3288–3306, https://doi.org/10.1175/2008MWR2277.1.

——, and Coauthors, 2013: An ocean coupling potential intensity index for tropical cyclones. *Geophys. Res. Lett.*, **40**, 1878–1882, https://doi.org/10.1002/grl.50091.

——, and Coauthors, 2021: A tale of two rapidly intensifying supertyphoons: Hagibis (2019) and Haiyan (2013). *Bull. Amer. Meteor. Soc.*, **102**, E1645–E1664, https://doi.org/10.1175/BAMS-D-20-0223.1.

Liu, T., J. Li, C. Sun, T. Lian, and Y. Zhang, 2021: Impact of the April–May SAM on central Pacific Ocean sea temperature over the following three seasons. *Climate Dyn.*, **57**, 775–786, https://doi.org/10.1007/s00382-021-05738-4.

Luo, J.-J., S. Masson, S. Behera, and T. Yamagata, 2007: Experimental forecasts of the Indian Ocean dipole using a coupled OAGCM. *J. Climate*, **20**, 2178–2190, https://doi.org/10.1175/JCLI4132.1.

——, R. Zhang, S. K. Behera, Y. Masumoto, F.-F. Jin, R. Lukas, and T. Yamagata, 2010: Interaction between El Niño and extreme Indian Ocean dipole. *J. Climate*, **23**, 726–742, https://doi.org/10.1175/2009JCLI3104.1.

——, W. Sasaki, and Y. Masumoto, 2012: Indian Ocean warming modulates Pacific climate change. *Proc. Natl. Acad. Sci. USA*, **109**, 18 701–18 706, https://doi.org/10.1073/pnas.1210239109.

Madden, R., and P. Julian, 1971: Detection of a 40–50 day oscillation in the zonal wind in the tropical Pacific. *J. Atmos. Sci.*, **28**, 702–708, https://doi.org/10.1175/1520-0469(1971)028<0702:DOADOI>2.0.CO;2.

——, and ——, 1972: Description of global-scale circulation cells in the tropics with a 40–50 day period. *J. Atmos. Sci.*, **29**, 1109–1123, https://doi.org/10.1175/1520-0469(1972)029<1109:DOGSCC>2.0.CO;2.

——, and ——, 1994: Observations of the 40–50-day tropical oscillation—A review. *Mon. Wea. Rev.*, **122**, 814–837, https://doi.org/10.1175/1520-0493(1994)122<0814:OOTDTO>2.0.CO;2.

Mainelli, M., M. DeMaria, L. Shay, and G. Goni, 2008: Application of oceanic heat content estimation to operational forecasting of recent Atlantic category 5 hurricanes. *Wea. Forecasting*, **23**, 3–16, https://doi.org/10.1175/2007WAF2006111.1.

Maloney, E. D., and D. L. Hartmann, 2001: The Madden–Julian Oscillation, barotropic dynamics, and North Pacific tropical cyclone formation. Part I: Observations. *J. Atmos. Sci.*, **58**, 2545–2558, https://doi.org/10.1175/1520-0469(2001)058<2545:TMJOBD>2.0.CO;2.

Moore, A. M., and R. Kleeman, 1999: Stochastic forcing of ENSO by the intraseasonal oscillation. *J. Climate*, **12**, 1199–1220, https://doi.org/10.1175/1520-0442(1999)012<1199:SFOEBT>2.0.CO;2.

Moreno, P. I., and Coauthors, 2018: Onset and evolution of Southern Annular Mode-like changes at centennial timescale. *Sci. Rep.*, **8**, 3458, https://doi.org/10.1038/s41598-018-21836-6.

Münnich, M., and J. D. Neelin, 2005: Seasonal influence of ENSO on the Atlantic ITCZ and equatorial South America. *Geophys. Res. Lett.*, **32**, L21709, https://doi.org/10.1029/2005GL023900.

Nobre, P., and J. Shukla, 1996: Variations of sea surface temperature, wind stress, and rainfall over the tropical Atlantic and South America. *J. Climate*, **9**, 2464–2479, https://doi.org/10.1175/1520-0442(1996)009<2464:VOSSTW>2.0.CO;2.

Pasch, R. J., and A. H. Mahoney, 2026: Tropical cyclone report: Hurricane Erin (AL052025), 11–22 August 2025. NHC Tech. Rep., 34 pp., https://www.nhc.noaa.gov/data/tcr/AL052025_Erin.pdf.

Penland, C., and P. D. Sardeshmukh, 1995: The optimal growth of tropical sea surface temperature anomalies. *J. Climate*, **8**, 1999–2024, https://doi.org/10.1175/1520-0442(1995)008<1999:TOGOTS>2.0.CO;2.

Raga, G. B., B. Bracamontes-Ceballos, L. Farfán, and R. Romero-Centeno, 2013: Landfalling tropical cyclones on the Pacific coast of Mexico: 1850-2010. *Atmósfera*, **26**, 209–220, https://doi.org/10.1016/S0187-6236(13)71072-5.

Ramage, C. S., 1971: *Monsoon Meteorology*. Academic Press, 296 pp.

Reynolds, R. W., N. A. Rayner, T. M. Smith, D. C. Stokes, and W. Wang, 2002: An improved in situ and satellite SST analysis for climate. *J. Climate*, **15**, 1609–1625, https://doi.org/10.1175/1520-0442(2002)015<1609:AIISAS>2.0.CO;2.

Ropelewski, C. F., and M. S. Halpert, 1989: Precipitation patterns associated with the high index phase of the Southern Oscillation. *J. Climate*, **2**, 268–284, https://doi.org/10.1175/1520-0442(1989)002<0268:PPAWTH>2.0.CO;2.

Saha, S., and Coauthors, 2006: The NCEP climate forecast system. *J. Climate*, **19**, 3483–3517, https://doi.org/10.1175/JCLI3812.1.

——, and Coauthors, 2014: The NCEP Climate Forecast System version 2. *J. Climate*, **27**, 2185–2208, https://doi.org/10.1175/JCLI-D-12-00823.1.

Saji, N. H., B. N. Goswami, P. N. Vinayachandran, and T. Yamagata, 1999: A dipole mode in the tropical Indian Ocean. *Nature*, **401**, 360–363, https://doi.org/10.1038/43854.

Schneider, T., T. Bischoff, and G. H. Haug, 2014: Migrations and dynamics of the intertropical convergence zone. *Nature*, **513**, 45–53, https://doi.org/10.1038/nature13636.

Schreck, C. J., 2015: Kelvin waves and tropical cyclogenesis: A global survey. *Mon. Wea. Rev.*, **143**, 3996–4011, https://doi.org/10.1175/MWR-D-15-0111.1.

——, 2016: Convectively coupled Kelvin waves and tropical cyclogenesis in a semi-Lagrangian framework. *Mon. Wea. Rev.*, **144**, 4131–4139, https://doi.org/10.1175/MWR-D-16-0237.1.

——, and J. Molinari, 2011: Tropical cyclogenesis associated with Kelvin waves and the Madden–Julian Oscillation. *Mon. Wea. Rev.*, **139**, 2723–2734, https://doi.org/10.1175/MWR-D-10-05060.1.

——, K. R. Knapp, and J. P. Kossin, 2014: The impact of best track discrepancies on global tropical cyclone climatologies using IBTrACS. *Mon. Wea. Rev.*, **142**, 3881–3899, https://doi.org/10.1175/MWR-D-14-00021.1.

——, H.-T. Lee, and K. R. Knapp, 2018: HIRS outgoing longwave radiation—Daily climate data record: Application toward identifying tropical subseasonal variability. *Remote Sens.*, **10**, 1325, https://doi.org/10.3390/rs10091325.

Shay, L. K., G. J. Goni, and P. G. Black, 2000: Effects of a warm oceanic feature on hurricane opal. *Mon. Wea. Rev.*, **128**, 1366–1383, https://doi.org/10.1175/1520-0493(2000)128<1366:EOAWOF>2.0.CO;2.

Trenberth, K. E., 1984: Signal versus noise in the Southern Oscillation. *Mon. Wea. Rev.*, **112**, 326–332, https://doi.org/10.1175/1520-0493(1984)112<0326:SVNITS>2.0.CO;2.

Vecchi, G. A., and B. J. Soden, 2007: Effect of remote sea surface temperature change on tropical cyclone potential intensity. *Science*, **450**, 1066–1070, https://doi.org/10.1038/nature06423.

Ventrice, M. J., C. D. Thorncroft, and M. A. Janiga, 2012a: Atlantic tropical cyclogenesis: A three-way interaction between an African easterly wave, diurnally varying convection, and a convectively coupled atmospheric Kelvin wave. *Mon. Wea. Rev.*, **140**, 1108–1124, https://doi.org/10.1175/MWR-D-11-00122.1.

——, C. D. Thorncroft, and C. J. Schreck, 2012b: Impacts of convectively coupled Kelvin waves on environmental conditions for Atlantic tropical cyclogenesis. *Mon. Wea. Rev.*, **140**, 2198–2214, https://doi.org/10.1175/MWR-D-11-00305.1.

Villarini, G., G. A. Vecchi, T. R. Knutson, and J. A. Smith, 2011: Is the recorded increase in short-duration North Atlantic tropical storms spurious? *J. Geophys. Res.*, **116**, D10114, https://doi.org/10.1029/2010JD015493.

Vincent, D. G., 1994: The South Pacific Convergence Zone (SPCZ): A review. *Mon. Wea. Rev.*, **122**, 1949–1970, https://doi.org/10.1175/1520-0493(1994)122<1949:TSPCZA>2.0.CO;2.

Vose, R. S., and Coauthors, 2021: Implementing full spatial coverage in NOAA's global temperature analysis. *Geophys. Res. Lett.*, **48**, e2020GL090873, https://doi.org/10.1029/2020GL090873.

Waliser, D. E., and C. Gautier, 1993: A satellite-derived climatology of the ITCZ. *J. Climate*, **6**, 2162–2174, https://doi.org/10.1175/1520-0442(1993)006<2162:ASDCOT>2.0.CO;2.

Wang, B., 1994: Climatic regimes of tropical convection and rainfall. *J. Climate*, **7**, 1109–1118, https://doi.org/10.1175/1520-0442(1994)007<1109:CROTCA>2.0.CO;2.

——, and Z. Xie, 1996: Low-frequency equatorial waves in vertically sheared zonal flow. Part I: Stable waves. *J. Atmos. Sci.*, **53**, 449–467, https://doi.org/10.1175/1520-0469(1996)053<0449:LFEWIV>2.0.CO;2.

——, and Q. Ding, 2008: Global monsoon: Dominant mode of annual variation in the tropics. *Dyn. Atmos. Ocean*, **44**, 165–183, https://doi.org/10.1016/j.dynatmoce.2007.05.002.

——, J. Liu, H. J. Kim, P. J. Webster, and S. Y. Yim, 2012: Recent change of the global monsoon precipitation (1979–2008). *Climate Dyn.*, **39**, 1123–1135, https://doi.org/10.1007/s00382-011-1266-z.

Webster, P. J., A. M. Moore, J. P. Loschnigg, and R. R. Leben, 1999: Coupled ocean-atmosphere dynamics in the Indian Ocean during 1997-98. *Nature*, **401**, 356–360, https://doi.org/10.1038/43848.

Wheeler, M., and G. N. Kiladis, 1999: Convectively coupled equatorial waves: Analysis of clouds and temperature in the wavenumber–frequency domain. *J. Atmos. Sci.*, **56**, 374–399, https://doi.org/10.1175/1520-0469(1999)056<0374:CCEWAO>2.0.CO;2.

——, and H. H. Hendon, 2004: An all-season real-time multivariate MJO index: Development of an index for monitoring and prediction. *Mon. Wea. Rev.*, **132**, 1917–1932, https://doi.org/10.1175/1520-0493(2004)132<1917:AARMMI>2.0.CO;2.

Wood, K. M., and E. A. Ritchie, 2015: A definition for rapid weakening in the North Atlantic and eastern North Pacific. *Geophys. Res. Lett.*, **42**, 10 091–10 097, https://doi.org/10.1002/2015GL066697.

Yim, S. Y., B. Wang, J. Liu, and Z. W. Wu, 2014: A comparison of regional monsoon variability using monsoon indices. *Climate Dyn.*, **43**, 1423–1437, https://doi.org/10.1007/s00382-013-1956-9.

Zhang, C., 2005: Madden–Julian Oscillation. *Rev. Geophys.*, **43**, RG2003, https://doi.org/10.1029/2004RG000158.

——, 2013: Madden–Julian Oscillation: Bridging weather and climate. *Bull. Amer. Meteor. Soc.*, **94**, 1849–1870, https://doi.org/10.1175/BAMS-D-12-00026.1.

——, and J. Gottschalck, 2002: SST anomalies of ENSO and the Madden–Julian Oscillation in the equatorial Pacific. *J. Climate*, **15**, 2429–2445, https://doi.org/10.1175/1520-0442(2002)015<2429:SAOEAT>2.0.CO;2.

Zheng, Z.-W., I.-I. Lin, B. Wang, H.-C. Huang, and C.-H. Chen, 2015: A long neglected damper in the El Niño–typhoon relationship: A 'Gaia-like' process. *Sci. Rep.*, **5**, 11103, https://doi.org/10.1038/srep11103.

STATE OF THE CLIMATE IN 2025

THE ARCTIC

T. A. Moon, M. L. Druckenmiller, and R. L. Thoman, Eds.

Special Online Supplement to the *Bulletin of the American Meteorological Society* Vol. 107, No. 8, August, 2026

https://doi.org/10.1175/BAMS-D-26-0123.1
Corresponding author: Twila A. Moon / Twila.Moon@colorado.edu
©2026 American Meteorological Society
For information regarding reuse of this content and general copyright information, consult the AMS Copyright Policy.

STATE OF THE CLIMATE IN 2025
The Arctic

Editors

Jessica Blunden
James Reagan

Chapter Editors

Anthony Arguez
Josh Blannin
Peter Bissolli
Kyle R. Clem
Howard J. Diamond
Matthew L. Druckenmiller
Robert J. H. Dunn
Catherine Ganter
Nadine Gobron
Rodney Martinez
Twila A. Moon
Gary A. Morris
Marilyn N. Raphael
Renellys C. Perez
Carl J. Schreck III
Zewdu Segele
Laura Stevens
Richard L. Thoman
Denis L. Volkov
Zhiwei Zhu

Technical Editors

Lukas Noguchi
Laura Ohlmann

BAMS Special Editor for Climate

Timothy DelSole

American Meteorological Society

Cover Credit:
Icebergs from the Greenland Ice Sheet shoal on the glacial outwash beach at Sermilik Station, on Ammassalik Island in East Greenland on 18 June 2025. Photo credit: Kristin Poinar

How to cite this document:
The Arctic is one chapter from the *State of the Climate in 2025* annual report and is available from https://doi.org/10.1175/BAMS-D-26-0123.1. Compiled by NOAA's National Centers for Environmental Information, *State of the Climate in 2025* is based on contributions from scientists from around the world. It provides a detailed update on global climate indicators, notable weather events, and other data collected by environmental monitoring stations and instruments located on land, water, ice, and in space. The full report is available from https://doi.org/10.1175/2026BAMSStateoftheClimate.1.

Citing the complete report:
Blunden, J. and J. Reagan, Eds., 2026: "State of the Climate in 2025". Bull. Amer. Meteor. Soc., 107 (8), Si–S512, https://doi.org/10.1175/2026BAMSStateoftheClimate.1.

Citing this chapter:
Moon, T. A., M. L. Druckenmiller, and R. L. Thoman, Eds., 2026: The Arctic [in "State of the Climate in 2025"]. Bull. Amer. Meteor. Soc., 107 (8), S296–S346, https://doi.org/10.1175/BAMS-D-26-0123.1.

Citing a section (example):
Ballinger, T. J., A. Crawford, A. H. Butler, M. C. Serreze, S. Bigalke, J. E. Walsh, B. Brettschneider, R. L. Thoman, U. S. Bhatt, E. Hanna, H. Motrøen Gjelten, S.-J. Kim, J. E. Overland, and M. Wang, 2026: Surface air temperature [in "State of the Climate in 2025"]. Bull. Amer. Meteor. Soc., 107 (8), S307–S309, https://doi.org/10.1175/BAMS-D-26-0123.1.

Editor and Author Affiliations (alphabetical by name)

Andreassen, Liss Marie, Section for Glaciers, Ice and Snow, Norwegian Water Resources and Energy Directorate, Oslo, Norway

Askjaer, Thomas G., Danish Meteorological Institute, Copenhagen, Denmark

Ballinger, Thomas J., International Arctic Research Center, University of Alaska Fairbanks, Fairbanks, Alaska

Berner, Logan T., School of Informatics, Computing, and Cyber Systems, Northern Arizona University, Flagstaff, Arizona

Bernhard, Germar H., Biospherical Instruments Inc., San Diego, California

Bhatt, Uma S., Geophysical Institute, University of Alaska Fairbanks, Fairbanks, Alaska

Bigalke, Siiri, Department of Geography, Portland State University, Portland, Oregon

Bjerke, Jarle W., FRAM – High North Research Centre for Climate and the Environment, Tromsø, Norway; Norwegian Institute for Nature Research, Trondheim, Norway

Bliss, Angela, NASA Goddard Space Flight Center, Greenbelt, Maryland

Box, Jason E., Geological Survey of Denmark and Greenland (GEUS), Copenhagen, Denmark

Brettschneider, Brian, NOAA/NWS Alaska Region, Anchorage, Alaska

Burgess, D., Geological Survey of Canada, Ottawa, Ontario, Canada

Butler, Amy H., NOAA Chemical Sciences Laboratory, Boulder, Colorado

Christiansen, Hanne H., University of the Arctic, Aarhus University, Aarhus, Denmark

Crawford, Alex, Department of Environment and Geography, University of Manitoba, Winnipeg, Manitoba, Canada

Decharme, Bertrand, Centre National de Recherches Météorologiques, Météo-France/CNRS, Toulouse, France

Derksen, Chris, Climate Research Division, Environment and Climate Change Canada, Toronto, Canada

Divine, Dmitry, Norwegian Polar Institute, Fram Centre, Tromsø, Norway

Druckenmiller, Matthew L., National Snow and Ice Data Center, Cooperative Institute for Research in Environmental Sciences, University of Colorado, Boulder, Colorado

Elias Chereque, Aleksandra, Department of Physics, University of Toronto, Toronto, Canada

Epstein, Howard E., Department of Environmental Sciences, University of Virginia, Charlottesville, Virginia

Farrell, Sinead, Department of Geographical Sciences, University of Maryland, College Park, Maryland

Fausto, Robert S., Geological Survey of Denmark and Greenland (GEUS), Copenhagen, Denmark

Fettweis, Xavier, SPHERES Research Unit, University of Liège, Liège, Belgium

Fioletov, Vitali E., Environment and Climate Change Canada, Toronto, Ontario, Canada

Florentine, Caitlyn, U.S. Geological Survey, Northern Rocky Mountain Science Center, Bozeman, Montana

Forbes, Bruce C., Arctic Centre, University of Lapland, Rovaniemi, Finland

Frost, Gerald V. (JJ), Alaska Biological Research, Inc., Fairbanks, Alaska

Gerland, Sebastian, Norwegian Polar Institute, Fram Centre, Tromsø, Norway

Grooß, Jens-Uwe, Forschungszentrum Jülich (ICE-4), Jülich, Germany

Hanna, Edward, Department of Geography and Lincoln Climate Research Group, Lincoln, United Kingdom

Hendricks, Stefan, Alfred Wegener Institute, Helmholtz Centre for Polar and Marine Research, Bremerhaven, Germany

Ialongo, Iolanda, Finnish Meteorological Institute, Helsinki, Finland

Isaksen, Ketil, Norwegian Meteorological Institute, Oslo, Norway

Jia, Gensuo, Institute of Atmospheric Physics, Chinese Academy of Sciences, Beijing, China

Johnsen, Bjørn, Norwegian Radiation and Nuclear Safety Authority, Østerås, Norway

Kaleschke, Lars, Alfred Wegener Institute, Helmholtz Centre for Polar and Marine Research, Bremerhaven, Germany

Kim, Seong-Joong, Korea Polar Research Institute, Incheon, South Korea

Kohler, J., Norwegian Polar Institute, Fram Centre, Tromsø, Norway

Labe, Zachary M., Climate Central, Princeton, New Jersey

Lader, Rick, International Arctic Research Center, University of Alaska Fairbanks, Fairbanks, Alaska

Lakkala, Kaisa, Finnish Meteorological Institute, Sodankylä, Finland

Lara, Mark J., Department of Plant Biology, University of Illinois, Urbana, Illinois; Department of Geography, University of Illinois, Urbana, Illinois

Lee, Simon H., School of Earth and Environmental Sciences, University of St Andrews, St Andrews, United Kingdom

Loomis, Bryant D., NASA Goddard Space Flight Center, Greenbelt, Maryland

Luks, B., Institute of Geophysics, Polish Academy of Sciences, Warsaw, Poland

Luojus, Kari, Arctic Research Centre, Finnish Meteorological Institute, Helsinki, Finland

López-Blanco, E., Department of Ecoscience, Arctic Research Center, Aarhus University, Roskilde, Denmark

Macander, Matthew J., Alaska Biological Research, Inc., Fairbanks, Alaska

Magnússon, Rúna Í., Plant Ecology and Nature Conservation Group, Wageningen University & Research, Wageningen, The Netherlands

Mankoff, Ken D., Business Integra, New York, New York; NASA Goddard Institute for Space Studies, New York, New York

Medley, Brooke, Cryospheric Sciences Laboratory, NASA Goddard Space Flight Center, Greenbelt, Maryland

Meier, Walter N., National Snow and Ice Data Center, Cooperative Institute for Research in Environmental Sciences, University of Colorado, Boulder, Colorado

Montesano, Paul M., NASA Goddard Space Flight Center, Greenbelt, Maryland

Moon, Twila A., National Snow and Ice Data Center, Cooperative Institute for Research in Environmental Sciences, University of Colorado, Boulder, Colorado

Mote, Thomas L., University of Georgia, Athens, Georgia

Motrøen Gjelten, Herdis, Norwegian Meteorological Institute, Oslo, Norway

Mudryk, Lawrence, Climate Research Division, Environment and Climate Change Canada, Toronto, Canada

Müller, Rolf, Forschungszentrum Jülich (ICE-4), Jülich, Germany

Natali, S. M., Woodwell Climate Research Center, Falmouth, Massachusetts

Neigh, Christopher S. R., NASA Goddard Space Flight Center, Greenbelt, Maryland

Nyland, Kelsey E., George Washington University, Washington, District of Columbia

Orndahl, K. M., School of Informatics, Computing, and Cyber Systems, Northern Arizona University, Flagstaff, Arizona

Overland, James E., NOAA/OAR Pacific Marine Environmental Laboratory, Seattle, Washington

Perovich, Donald K., Dartmouth College, Hanover, New Hampshire

Petty, Alek, NASA Goddard Space Flight Center, Greenbelt, Maryland

Phoenix, Gareth K., School of Biosciences, University of Sheffield, Sheffield, United Kingdom

Poinar, Kristin, University at Buffalo, Buffalo, New York

Pálsson, F., Institute of Earth Sciences, University of Iceland, Reykjavík, Iceland

Ricker, Robert, NORCE Norwegian Research Centre, Tromsø, Norway

Romanovsky, Vladimir E., Geophysical Institute, University of Alaska Fairbanks, Fairbanks, Alaska

Sass, L., U.S. Geological Survey, Alaska Science Center, Anchorage, Alaska

Schuur, E. A. G., Center for Ecosystem Science and Society, Northern Arizona University, Flagstaff, Arizona

Serreze, Mark C., National Snow and Ice Data Center, Cooperative Institute for Research in Environmental Sciences, University of Colorado, Boulder, Colorado

Smith, Benjamin E., Polar Science Center, Applied Physics Laboratory, University of Washington, Seattle, Washington

Editor and Author Affiliations (continued)

Smith, Sharon L., Geological Survey of Canada, Natural Resources Canada, Ottawa, Canada

Streletskiy, Dmitry A., George Washington University, Washington, District of Columbia

Svendby, Tove, The Climate and Environmental Research Institute NILU, Kjeller, Norway

Thoman, Richard L., International Arctic Research Center, University of Alaska Fairbanks, Fairbanks, Alaska

Thomson, L., Queen's University, Kingston, Ontario, Canada

Thorsteinsson, T., Icelandic Meteorological Office, Reykjavík, Iceland

Tian-Kunze, Xiangshan, Alfred Wegener Institute, Helmholtz Centre for Polar and Marine Research, Bremerhaven, Germany

Timmermans, Mary-Louise, Department of Earth and Planetary Sciences, Yale University, New Haven, Connecticut

Tømmervik, Hans, FRAM – High North Research Centre for Climate and the Environment, Tromsø, Norway; Norwegian Institute for Nature Research, Trondheim, Norway

Waigl, Christine F., Geophysical Institute, University of Alaska Fairbanks, Fairbanks, Alaska

Walker, Donald (Skip) A., Institute of Arctic Biology, University of Alaska Fairbanks, Fairbanks, Alaska

Walsh, John E., International Arctic Research Center, University of Alaska Fairbanks, Fairbanks, Alaska

Wang, Muyin, NOAA/OAR Pacific Marine Environmental Laboratory, Seattle, Washington; Cooperative Institute for Climate, Ocean, and Ecosystem Studies, University of Washington, Seattle, Washington

Webster, Melinda, Polar Science Center, Applied Physics Laboratory, University of Washington, Seattle, Washington

Wolken, G., University of Alaska Fairbanks, Fairbanks, Alaska; Alaska Division of Geological & Geophysical Surveys, Fairbanks, Alaska

Wouters, B., Department of Geoscience and Remote Sensing, TU Delft, Delft, The Netherlands

Yang, Dedi, Environmental Sciences Division, Oak Ridge National Laboratory, Oak Ridge, Tennessee

Editorial and Production Team

Allen, Jessicca, Graphics Support, Cooperative Institute for Satellite Earth System Studies, North Carolina State University, Asheville, North Carolina

Camper, Amy V., Graphics Support, Innovative Consulting and Management Services, LLC, NOAA/NESDIS National Centers for Environmental Information, Asheville, North Carolina

Carroll, Lauren, Content Team Lead, Communications and Outreach, NOAA/NESDIS National Centers for Environmental Information, Asheville, North Carolina

Crossman, Jacquelyn, NCEI Librarian, MPF-ZAI, NOAA/NESDIS National Centers for Environmental Information, Asheville, North Carolina

Haley, Bridgette O., Graphics Support, NOAA/NESDIS National Centers for Environmental Information, Asheville, North Carolina

Noguchi, Lukas, Technical Editor, Innovative Consulting and Management Services, LLC, NOAA/NESDIS National Centers for Environmental Information, Asheville, North Carolina

Ohlmann, Laura, Technical Editor, Innovative Consulting and Management Services, LLC, NOAA/NESDIS National Centers for Environmental Information, Asheville, North Carolina

Veasey, Sara W., Visual Communications Team Lead, Communications and Outreach, NOAA/NESDIS National Centers for Environmental Information, Asheville, North Carolina

5. Table of Contents

List of authors and affiliations S299
a. Overview S302
b. Atmosphere S304
1. Winter (January–March) S304
2. Spring (April–June) S306
3. Summer (July–September) S306
4. Autumn (October–December) S306
c. Surface air temperature S307
1. Overview S307
2. Historical context to 2025 air temperatures S307
3. Seasonal air temperature anomaly patterns in 2025 ..... S308
d. Precipitation S310
1. Introduction S310
2. Annual and seasonal Arctic precipitation S310
3. Regional anomalies S310
4. Heavy precipitation events S310
5. Historical perspective S311
Sidebar 5.1: Ex-typhoon Halong S313
e. Sea surface temperature S315
f. Sea ice cover S318
1. Sea ice extent and concentration S318
2. Sea ice age, thickness, and volume S319
g. Greenland Ice Sheet S321
h. Glaciers and ice caps outside Greenland S324
i. Terrestrial snow S328
j. Terrestrial permafrost S330
1. Permafrost temperature S330
2. Active layer thickness S333
Sidebar 5.2: The Arctic carbon cycle S334
k. Tundra greenness S337
Acknowledgments S341
Appendix 1: Acronyms S342
Appendix 2: Datasets and sources S343
References S347

5. THE ARCTIC

T. A. Moon, M. L. Druckenmiller, and R. L. Thoman, Eds.

a. Overview

—T. A. Moon, M. L. Druckenmiller, and R. L. Thoman

Environmental conditions across the Arctic, a vast area above 60°N, look today remarkably different than one or two decades ago. Modern satellite era measurements of Arctic annual surface air temperature (1979–2025) show that the region has, on average, warmed roughly three times faster than the rest of the planet. Human emissions of heat-trapping gases are driving the change globally with additional processes in the Arctic amplifying the heating (section 5c). The impacts touch every corner of the terrestrial and marine landscape, including serious compounding hazards for people in the Arctic. This chapter delves into these long-term trends and details 2025 observations across the Arctic system, including a section on 2023/24 observations on glaciers and ice caps outside of Greenland (section 5h, which alternates yearly with a section on Arctic river discharge).

Examining surface temperature in the Arctic, 2025 was the second warmest year since the observational record began in 1900 (section 5c). The surface temperature anomaly for the year was 1.38°C above the 1991–2020 mean, a reflection of warmer-than-usual temperatures occurring across seasons. Autumn and winter continue to show the strongest increases in surface warming as compared to global trends, and 2025 marked the 12th consecutive year that Arctic temperature anomalies were higher than global surface temperature anomalies. Temperature changes also occur from the Earth's surface up through the troposphere and stratosphere. The Arctic troposphere has warmed 0.3°C decade^{-1} since 1958, while the stratosphere has cooled by a similar amount, an expected pattern with human-caused climate change (section 5b). In 2025, polar tropospheric air temperatures were the second highest on record.

Overall warming in the Arctic is accompanied by increases in precipitation, including the potential for bigger rain and snow events. During the period 1950–2025, there was an upward trend in annual precipitation totals, including significant upward trends in all seasons (section 5d). Examining annual records, 2025 had the third highest annual precipitation total on record, and the largest precipitation anomalies with respect to 1991–2020 were in winter (112%), spring (108%; the highest spring anomaly on record), and autumn (104%). Snow cover extent is connected to these coupled changes in precipitation and temperature, with patterns of snowpack buildup and melt shifting over the last several decades. In 2025, Arctic snow cover extent was roughly normal in Eurasia and North America in May but dropped below normal in June with early loss of snow cover, a now common occurrence (section 5i).

Arctic landscapes both respond to and influence temperature and precipitation changes. With vast areas of tundra as well as permafrost, the Arctic is home to a unique physical system that is responding rapidly to overall warming. Changes in Arctic tundra plants and productivity, such as increases in the abundance, distribution, and height of shrubs, result in Arctic "greening", which has been detected since the late 1990s. Beginning in 2020, the Arctic has experienced a sequence of record- or near-record-high greenness values, to which 2025 is now added as the third highest value (section 5k). Local and regional variation is notable, however, with, for example, both greening and "browning" in the Eurasian Arctic. Vegetation changes in the Arctic are intrinsically connected to changes in permafrost as well. Since the 1980s, permafrost across the Arctic has seen a long-term warming trend, with the strongest trends in high-latitude, cold permafrost (section 5j). The active layer thickness, or the maximum depth of surface ground that seasonally thaws and freezes, has also increased, though at different regional rates.

Permafrost thaw is also a key player in Arctic terrestrial carbon dioxide and methane storage, though other important processes are also at play, such as wildfire, wetland development or loss, and river and lake outgassing. Examining tundra and boreal forest ecosystems in Arctic permafrost regions suggests that together carbon dioxide from these sources made the region a small net carbon dioxide source during the period 2000–20 (Sidebar 5.2). This is a serious and potentially long-term shift from Arctic permafrost regions acting as a carbon dioxide sink that dampens warming to a source that can enhance warming. Subannual records also show that the seasonal cycle of carbon storage and release is amplifying, reflecting both stronger winter emissions and stronger summer uptake (Sidebar 5.2).

Dramatic change continues for other frozen components of the Arctic system. On land, the Greenland Ice Sheet, which holds the second largest reservoir of frozen fresh water on the planet, had yet another year of overall ice loss (129±50 Gt based on gravity measurements; section 5g). Sixty percent of the planet's glaciers and ice caps outside of Greenland and Antarctic are also found in the Arctic, and ice loss across these areas has tripled since the mid-1990s. During 2023/24, both Arctic Scandinavia and Svalbard had record years of ice loss with melt 1473% above the 1991–2020 mean in Arctic Scandinavia and 482% above in Svalbard (section 5h).

Arctic sea ice records also continue to show very low extent and predominantly first-year ice. The maximum sea ice extent in March 2025 was the lowest in the 47-year record, continuing a downward trend of –2.5% per decade, while September 2025 minimum extent was the 11th lowest on record, adding to a trend of –13.6% per decade extent loss (section 5f). Ice older than four years old is now nearly absent, with only 95,000 km^2 of older ice in September 2025 as compared to 1.5 million km^2 in the 1980s. Without sea ice cover, Arctic Ocean surface waters are exposed to heating from solar radiation and the atmosphere. Examined annually in August, the 2025 sea surface temperature in most Arctic Ocean regions was the highest in the 1982–2025 record and the pan-Arctic mean was the second highest on record (section 5e).

Pervasive environmental changes have direct and indirect impacts on people within and beyond the Arctic (e.g., Meng et al. 2023; Moon et al. 2019). In many instances, communities experience the combined impacts of multiple rapidly changing systems. For example, permafrost thaw and glacier retreat are increasing hazards such as glacial lake outburst floods, landslides, and the reliability of water supplies. Extreme weather hazards are also increasing. A prime example is the devastating ex-typhoon Halong that hit the Alaska west coast on 11–12 October 2025 (Sidebar 5.1). The storm traveled across anomalously warm ocean surface temperatures, and peak storm surge arrival on shore coincided with the daily high tide. Storm impacts were intense and widespread, including substantial inland and coastal flooding, ferocious winds, infrastructure loss, and loss of life.

The pace of change and the seriousness of impacts across plants, animals, and people highlight the importance of maintaining and strengthening our environmental intelligence regarding the Arctic region. Real threats to our scientific monitoring ability exist, such as the loss of a long-term Arctic vegetation monitoring dataset due to funding cuts (section 5k). This chapter's observations show that the Arctic today is vastly different than the past, requiring close attention and increased action for hazard preparedness and response.

b. Atmosphere

—A. H. Butler, S. H. Lee, G. H. Bernhard, V. E. Fioletov, J.-U. Grooß, I. Ialongo, B. Johnsen, K. Lakkala, R. Müller, and T. Svendby

The Arctic atmosphere is changing rapidly due to increasing greenhouse gases and associated melting sea ice. Since 1958, the Arctic troposphere has warmed ~0.3°C decade^{-1}, with amplified warming at the surface, while the Arctic stratosphere has cooled by roughly the same amount (Fig. 5.1)—a fingerprint of human-caused carbon dioxide (CO_2) increases (e.g., Santer et al. 2023). The magnitude of these temperature trends varies by season, altitude, and time period over which the trend is calculated (Fig. 5.1; Riviere et al. 2024), reflecting year-to-year variability associated with the downward influence from the stratosphere, tropical to extratropical teleconnections, and high-latitude weather systems that drive moisture and heat transport into and out of the region.

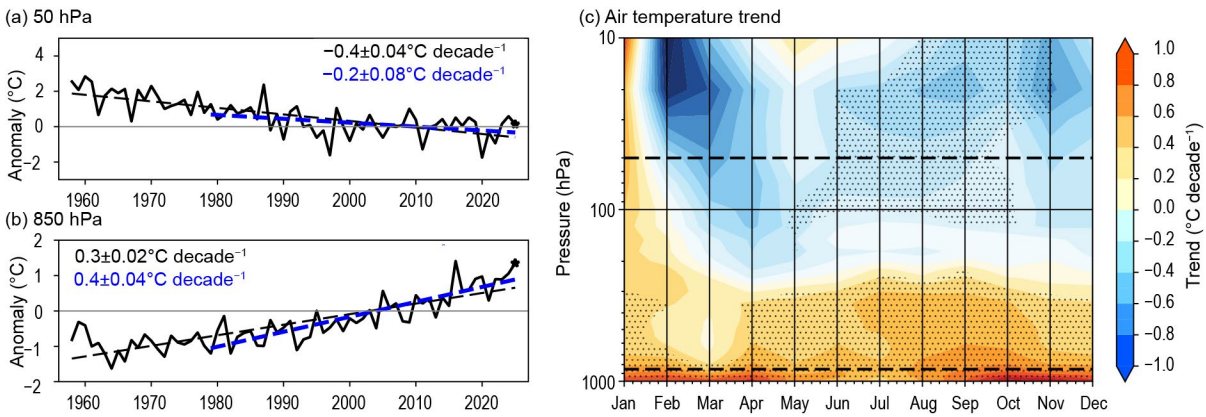

Fig. 5.1. Polar cap (60°N–90°N) air temperature trends from ERA5 reanalysis. Panels (a) and (b) show annual-mean temperature anomalies (°C; 1991–2020 climatology) at the 50-hPa and 850-hPa pressure level, respectively. Dashed black and blue lines in (a) and (b) show the least-squares linear fit to the data for the period 1958–2025 and 1979–2025 (satellite era), respectively, with corresponding trend values ± standard error. Panel (c) shows 1979–2025 linear trends in air temperature (°C decade^{-1}) by pressure level and month (adapted from Riviere et al. 2024). Stippling denotes p<0.025 significance (2-tailed Student's t-test). Horizontal dashed lines correspond to the pressure levels in (a) and (b).

In 2025, annual-mean polar tropospheric air temperatures at 850 hPa were the second highest on record (Fig. 5.1b; throughout this section, anomalies are defined relative to the 1991–2020 climatology over the 1958–2025 ERA5 reanalysis record, unless otherwise noted). Negative trends in lower polar stratospheric temperatures have slowed since the turn of the century, coincident with the recovery of the global ozone layer (Ferraro et al. 2015; Weber et al. 2022), and the 2025 value was near average (Fig. 5.1a). In addition to long-term changes, we highlight below the seasonal circulation and ozone variability in 2025.

1. WINTER (JANUARY–MARCH)

Winter Arctic tropospheric temperatures were above average, in agreement with widespread positive geopotential height anomalies at 500 hPa (Fig. 5.2a), with record warmth in February (Fig. 5.3b). In contrast, the Arctic lower stratosphere was

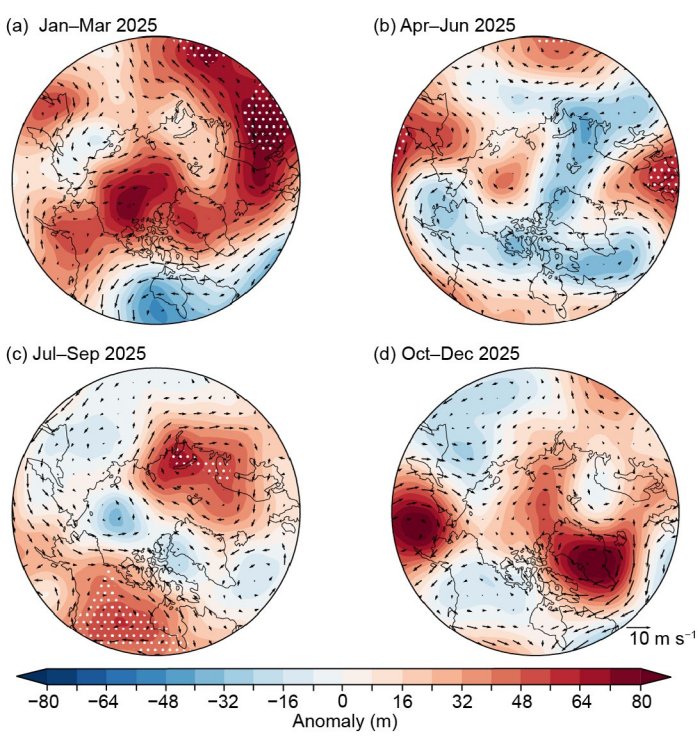

Fig. 5.2. Seasonal 500-hPa geopotential height (m; shading) and 200-hPa wind vector (m s^{-1}) anomalies for (a) winter (Jan–Mar; JFM), (b) spring (Apr–Jun; AMJ), (c) summer (Jul–Sep; JAS), and (d) autumn (Oct–Dec; OND). Higher geopotential heights generally indicate warmer air columns. Anomalies are relative to the 1991–2020 climatology; stippling denotes anomalies exceeding ±2 std. dev. (Source: ERA5 [Hersbach et al. 2020].)

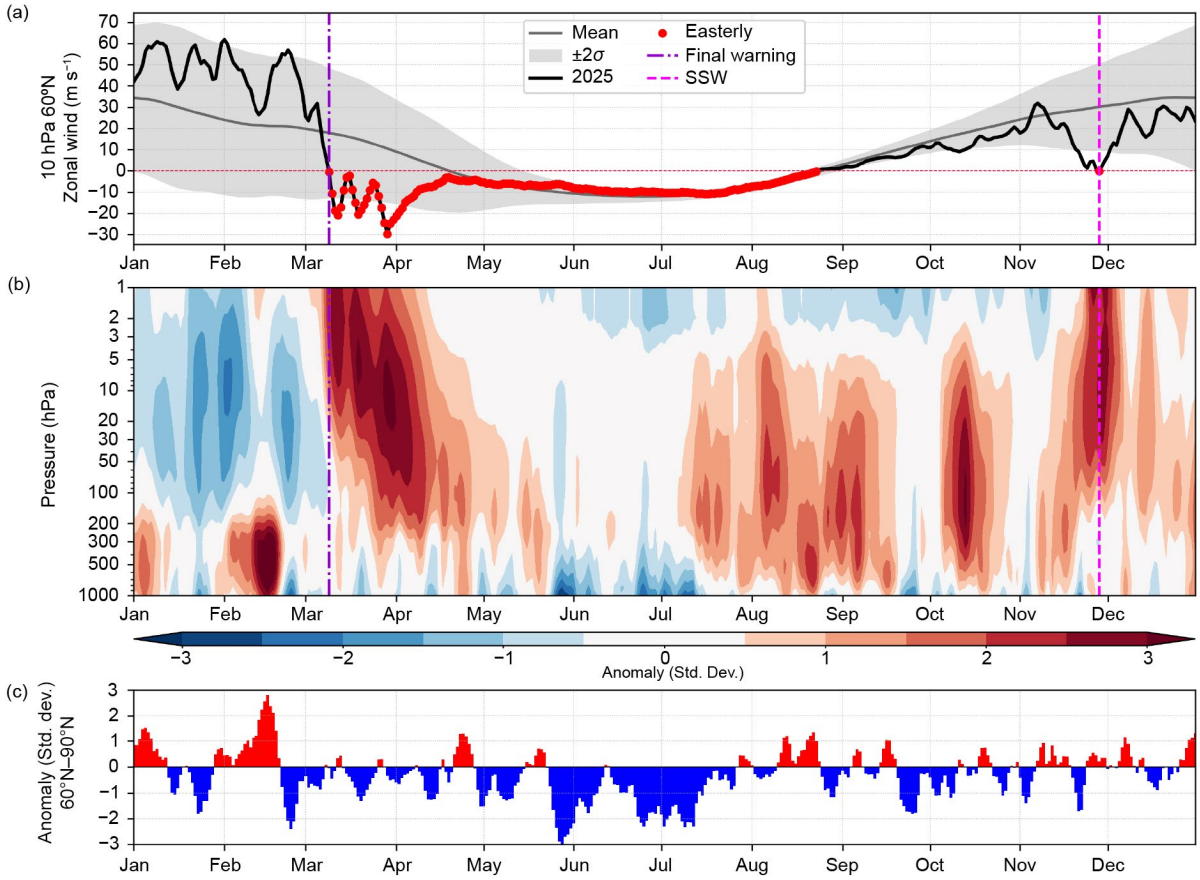

Fig. 5.3. 2025 Arctic atmosphere dynamics. (a) Daily stratospheric polar vortex winds (zonal-mean zonal winds at 10 hPa and 60°N) in black, with the 1991–2020 mean and ±2σ spread in gray. Red dots indicate easterly winds. (b) Vertical cross-section of daily polar cap-averaged (60°N–90°N) geopotential height anomalies in standard deviations. Purple dash-dot and pink dashed lines mark the 9 March final stratospheric warming and 28 November sudden stratospheric warming, respectively. (c) 1000-hPa polar cap-averaged (60°N–90°N) geopotential height anomalies. Anomalies are relative to 1991–2020. (Source: ERA5.)

extremely cold in January and February (the second coldest February on record at 50 hPa). This was associated with a stronger-than-normal polar vortex (Fig. 5.3a) and extremely low total column ozone anomalies stretching across the Arctic from eastern Canada to Asia (Fig. 5.4a). These regions of anomalously low ozone corresponded to broad increases (~30%) in ultraviolet (UV) radiation in February, according to satellite-based and ground-based measurements (though absolute values of UV in February are low due to partial polar darkness; Fig. 5.4c).

A strong Scandinavian anticyclone in February, concurrent with anomalously high pressure over Alaska, likely triggered a planetary-scale wave forcing that led to the second-earliest stratospheric final warming—the seasonal transition of the stratospheric polar vortex from a westerly to easterly state—on record, on 9 March 2025 (Fig. 5.3a). As the vortex broke down, it was displaced towards Europe, leading to a hemispheric dipole in the March total column ozone anomalies. Extremely low ozone remained in the vortex core; the minimum of March vortex total column ozone was 303 Dobson units (DU), which was the second lowest of the last four decades, after the year 2020. Conversely, strong positive anomalies formed over Alaska and the North Pacific, driven by accelerated stratospheric transport and enhanced mixing (Fig. 5.4b). Correspondingly, UV measurements showed strong surface UV radiation increases of ~30%–60% over Europe and Scandinavia but modest reductions over the Canadian archipelago and Canada (Fig. 5.4d). Some differences between ground- and satellite-based UV measurements are evident, particularly at Trondheim in March, which may be due to cloudiness conditions at that station, and climatologies used in the satellite retrievals, which do not always match the actual albedo (Bernhard et al. 2015).

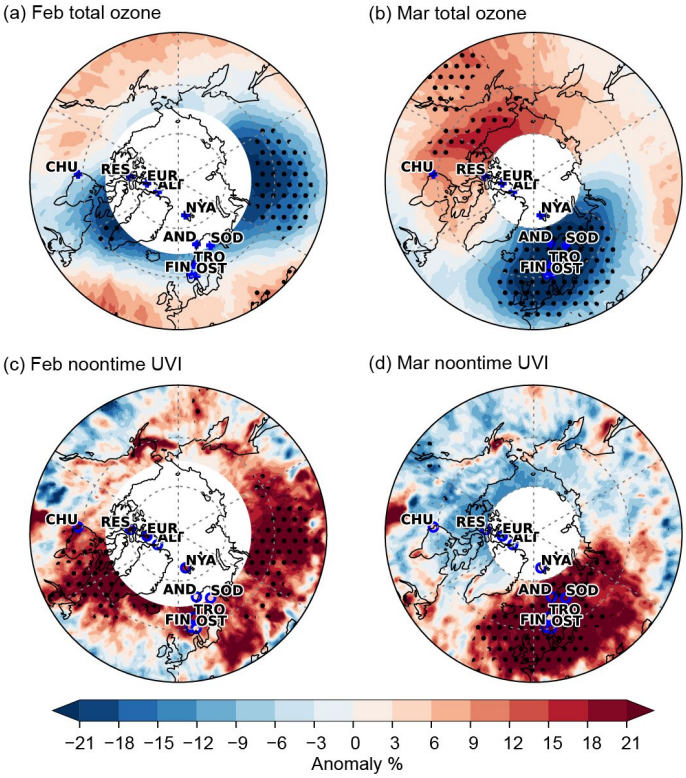

Base	Feb noontime UVI (satellite)	Feb noontime UVI (ground-based)	Mar noontime UVI (satellite)	Mar noontime UVI (ground-based)
ALT	N/A	N/A	N/A	−6%
EUR	N/A	28%	N/A	−11%
NYA	N/A	17%	N/A	4%
RES	N/A	31%	N/A	−6%
AND	N/A	3%	18%	19%
SOD	N/A	6%	27%	33%
TRO	20%	18%	29%	5%
FIN	15%	11%	44%	30%
OST	17%	3%	56%	40%
CHU	12%	25%	1%	5%

Fig. 5.4. Monthly ozone and ultraviolet (UV) anomalies. Panels (a),(b) show total ozone column (%) and (c),(d) noontime UV index (UVI; %) for Feb (a),(c) and Mar (b),(d) 2025 relative to 2005–24 means, using the Ozone Monitoring Instrument (OMI) Level-2 Total Column Ozone version 3 (OMTO3) product (Bhartia and Wellemeyer 2002). Stippling indicates anomalies exceeding ±2σ. Panels (c),(d) also show UVI anomalies (%) from ground-based measurements at 10 locations (shaded marker): Alert (ALT; 83°N); Eureka (EUR; 80°N); Ny-Ålesund (NYA; 79°N); Resolute (RES; 75°N); Andøya (AND; 69°N); Sodankylä (SOD; 67°N); Trondheim (TRO; 63°N); Finse (FIN; 61°N); Østerås (OST; 60°N); and Churchill (CHU; 59°N). White polar areas and values of N/A in the table indicate missing data due to polar darkness.

2. SPRING (APRIL–JUNE)

The early March dynamic final stratospheric warming led to a circulation perturbation that descended to the tropopause through June but only intermittently affected the troposphere (Figs. 5.3a,b). While an early final stratospheric warming tends to be followed by a negative Northern Annular Mode (NAM)/North Atlantic Oscillation (NAO)-like pattern—consisting of positive geopotential height anomalies over the polar cap—the mid-troposphere and surface instead showed broadly negative geopotential height anomalies across the polar region (Figs. 5.2b, 5.3b,c). Near the surface at 1000 hPa, polar cap-averaged height anomalies were persistently negative, especially in late May into June.

3. SUMMER (JULY–SEPTEMBER)

Summer featured cohesive positive polar geopotential height anomalies from the near-surface into the quiescent summer stratosphere (Fig. 5.3b). These positive height anomalies mainly arose due to two large anticyclones dominating the summertime mid-tropospheric flow: one over the Barents–Kara Sea region that peaked in strength in August and then retrograded towards Scandinavia in September, and another over Canada that was weakly present in August and amplified in September (Fig. 5.2c). This setup resulted in weak anomalous upper-tropospheric wind flow over the central Arctic and Baffin Bay.

4. AUTUMN (OCTOBER–DECEMBER)

The tropospheric circulation in autumn (Fig. 5.2d) showed two anticyclones over Greenland and the Bering Strait in the seasonal average, yet there was large month-to-month variability. For example, October was exceptionally warm in the troposphere, with record to near-record warmth from the surface (section 5c) to upper troposphere, potentially associated with two anticyclones over Canada and the Barents–Kara Seas region. On the other hand, December was extremely cold in eastern Alaska and the Yukon Territory, due to an exceptionally strong ridge over the Bering Strait supporting a downstream surface anticyclone, allowing for maximum surface cooling from northerly advection of Arctic air. In the stratosphere, the polar vortex was weaker than normal until November, when extended tropospheric wave forcing predominantly from the Greenland blocking high helped to displace the stratospheric polar vortex towards Asia, leading to one of the earliest major sudden stratospheric warmings in the ERA5 record (28 November, tied with 28 November 1968; Fig. 5.3a). The downward influence from this event just reached the Arctic troposphere by the end of December 2025 (Fig. 5.3b).

c. Surface air temperature

—T. J. Ballinger, A. Crawford, A. H. Butler, M. C. Serreze, S. Bigalke, J. E. Walsh, B. Brettschneider, R. L. Thoman, U. S. Bhatt, E. Hanna, H. Motrøen Gjelten, S.-J. Kim, J. E. Overland, and M. Wang

1. OVERVIEW

Arctic (60°N–90°N) surface air temperature (SAT) in 2025 continued to rise faster than the global (90°S–90°N) rate. Over the modern satellite era since 1979, the Arctic annual SAT has increased approximately three times faster than the global mean, a phenomenon often termed Arctic Amplification, due in large part to anthropogenic greenhouse gas emissions and amplifying feedbacks (Sweeney et al. 2023; Zhou et al. 2024).

Arctic Amplification has been linked to numerous physical and ecological changes that affect transportation, infrastructure, and subsistence livelihoods for people living in the North, with cascading impacts extending across lower latitudes (Moon et al. 2019; Walsh et al. 2020). Warming responses within the Arctic include increased annual precipitation (section 5d), persistent mass loss from the Greenland Ice Sheet (section 5g) and Arctic glaciers and ice caps (section 5h), and enhanced greening of tundra landscapes (section 5k). This section examines Arctic SAT in 2025 in historical context and highlights seasonal SAT and contemporaneous atmospheric circulation anomalies. Annual air temperatures follow the calendar year, with seasons defined as winter (January–March), spring (April–June), summer (July–September), and autumn (October–December).

2. HISTORICAL CONTEXT TO 2025 AIR TEMPERATURES

Time series of annual Arctic and global SAT anomalies from NASA's GISTEMP version 4 dataset (Lenssen et al. 2019) are shown in Fig. 5.5a. This past year was the second warmest on record since 1900 in the Arctic with an anomaly of 1.38°C above the 1991–2020 mean. This marks the 12th consecutive year that pan-Arctic temperature departures exceeded the global average (+0.58°C). Arctic and global seasonal anomalies over the past year were also above average (Figs. 5.5b–e). At both scales, all seasons ranked among their 10 warmest since 1900. However, annual and seasonal SAT anomalies and long-term trends continue to outpace global SAT trends, most notably in autumn and winter.

At the seasonal scale, Arctic Amplification is most pronounced during autumn and winter (Figs. 5.5b,e) when heat accumulated in the Arctic Ocean mixed layer from solar energy absorption in growing open water areas (section 5f) and northward advection of warm sub-Arctic water masses (e.g., Polyakov et al. 2025) is released to the overlying atmosphere. Arctic Amplification is strongest in the lower troposphere because the atmosphere is more stable in the Arctic than in lower latitudes, which inhibits vertical mixing and confines heating near the surface (Serreze et al. 2026). Spatial patterns of Arctic SAT anomalies, shown and discussed below, align with some of these processes.

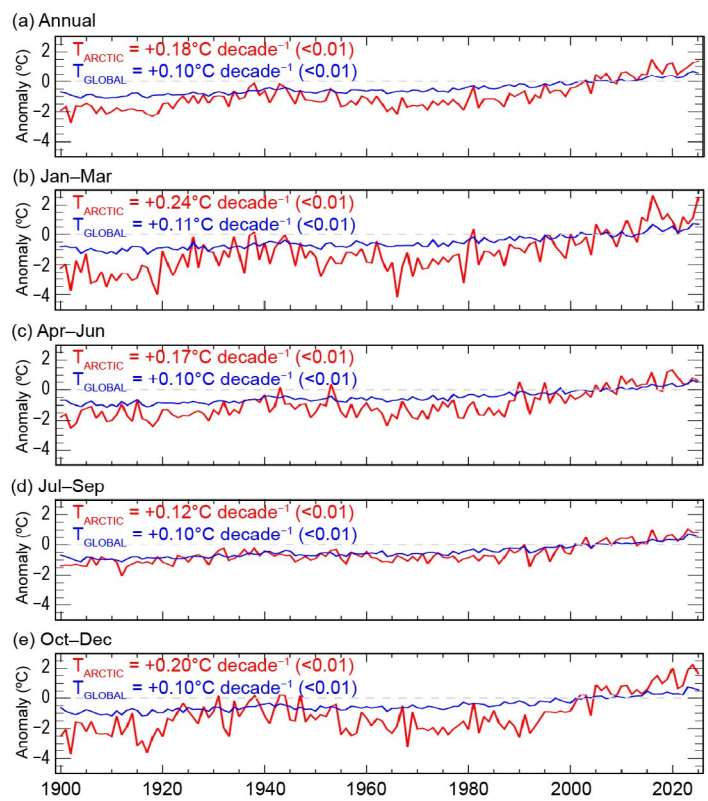

Fig. 5.5. Time series of (a) annual, (b) winter (Jan–Mar), (c) spring (Apr–Jun), (d) summer (Jul–Sep), and (e) autumn (Oct–Dec) surface air temperature anomalies (°C) averaged across Arctic (60°N–90°N) and global (90°S–90°N) land and ocean areas. The Arctic (T_{ARCTIC}) and global (T_{GLOBAL}) air temperature trends (°C decade^{-1}) for the 1900–2025 period are shown in each panel. All trends, based on linear least squares regression, are statistically significant ($p<0.01$). (Source: NASA GISTEMP v4.)

3. SEASONAL AIR TEMPERATURE ANOMALY PATTERNS IN 2025

Seasonal Arctic SAT anomaly patterns from ERA5 (Hersbach et al. 2020) are shown in Fig. 5.6. During winter (Fig. 5.6a), record-high temperatures were found over the Canadian Arctic Archipelago and the southern Barents Sea, with more modest anomalies over Alaska, the Bering Sea, Baffin Bay, the Lincoln Sea, the central Arctic Ocean, and east central Eurasia. The lone areas of below-average temperatures were eastern Siberia and north central Canada. Positive SAT anomalies in the North Atlantic Arctic sector are consistent with a relatively strong sea level pressure (SLP) dipole (Fig. 5.7a). This was characterized by below-average SLP (6 hPa–7 hPa below the 1991–2020 mean) indicative of an active storm track over eastern Canada promoting warm air advection west of Greenland.

During spring, near-average SAT characterized much of the Arctic Ocean and landmasses. Exceptions included record-high seasonal SATs over eastern Siberia and the Sea of Okhotsk, central Russia, and the Norwegian Sea (Fig. 5.6b). Central Greenland and the Kara Sea also saw above-average spring temperatures. Weak SLP anomalies covered much of the Arctic Ocean, except over the Kara Sea and the Canadian Arctic Archipelago. Below-average SLP also characterized Greenland and the Icelandic Low region to the south, which, along with slightly elevated SLP over western Europe, helped transport unseasonably warm air across the southern Norwegian Sea and drive record-high surface air temperatures in the region (Fig. 5.7b).

Summer saw average to above-average air temperatures over much of the Arctic with the exception of record warmth located over the North Atlantic Arctic, including central and eastern Greenland, the Norwegian Sea, northern Scandinavia, and areas northeast of Svalbard (Fig. 5.6c), associated with a large, blocking high pattern over the Barents Sea and Kara Sea (see Fig. 5.2c). Small anomalies over the Arctic Ocean are consistent with the cooling effects of a melting sea ice surface. Elevated SAT spanned much of the Kara Sea coastline and areas extending southward into central Eurasia, while on the North American side, north central Canada saw above-average SAT under anticyclonic conditions associated with higher-than-average SLP (Fig. 5.7c).

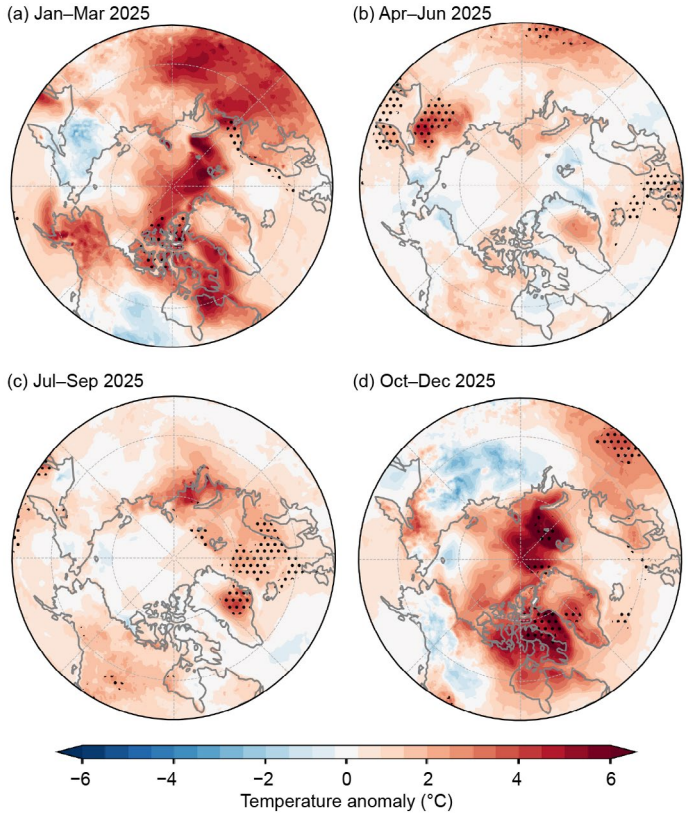

Fig. 5.6. Seasonal surface air temperature anomalies (°C) in 2025 for (a) winter (Jan–Mar), (b) spring (Apr–Jun), (c) summer (Jul–Sep), and (d) autumn (Oct–Dec). Temperature anomalies are shown relative to their 1991–2020 means. Stippled areas indicate record-high seasonal temperatures since 1940. (Source: ERA5.)

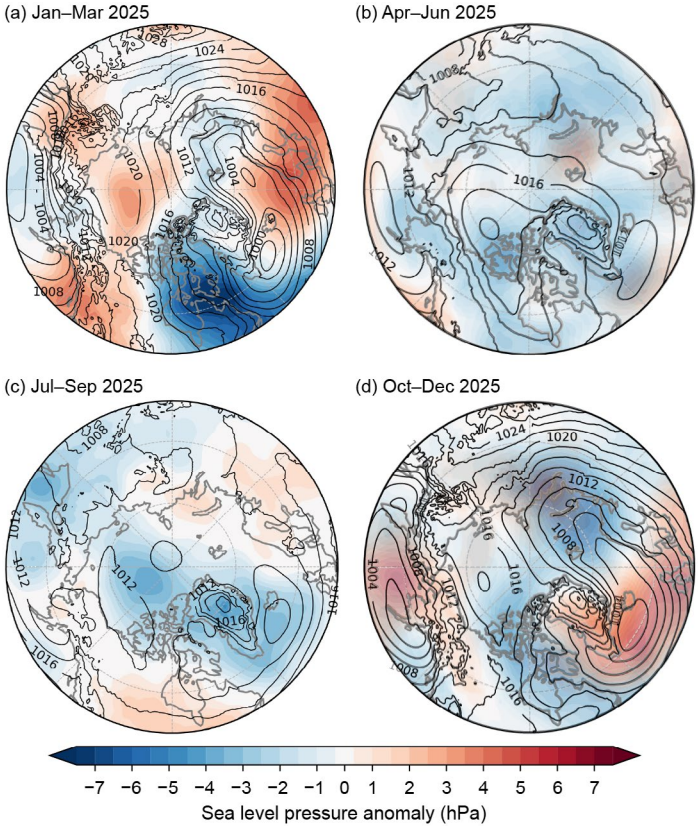

Fig. 5.7. Seasonal sea level pressure (SLP) anomalies (shading) and absolute values (isobars; both in hPa) in 2025 for (a) winter (Jan–Mar), (b) spring (Apr–Jun), (c) summer (Jul–Sep), and (d) autumn (Oct–Dec). SLP anomalies are shown relative to their 1991–2020 means. (Source: ERA5.)

Much of the North Atlantic Arctic was anomalously warm in autumn 2025 (Fig. 5.6d), with the magnitude of the anomalies relatively greater compared to other seasons across the calendar year. Record-high temperature anomalies of up to +6°C covered much of Baffin Bay, Baffin Island, and the Barents Sea while records were also set in the eastern Lincoln Sea and central Arctic Ocean. Portions of central Greenland, the Denmark Strait, and western Eurasia also saw record warmth, albeit with smaller SAT anomalies. Positive SLP anomalies around Greenland (Fig. 5.7d) coincided with a strong anticyclone aloft that produced flow from the southeast across Baffin Bay (see Fig. 5.2d). This pattern likely stunted sea ice advance across the region thereby shaping the pattern of record warmth west of Greenland. The two positive SLP anomaly centers over Greenland and the Bering Strait (Fig. 5.7d) were amplified at upper levels of the troposphere, suggesting a wavenumber-2 wave forcing may have contributed to one of the earliest sudden stratospheric warmings on record (section 5b).

d. Precipitation

—M. C. Serreze, S. Bigalke, R. Lader, A. Crawford, and T. J. Ballinger

1. INTRODUCTION

Annual precipitation over the Arctic region is characterized by high totals over the Atlantic sector (locally >2000 mm) due to open water and the frequent passage of storm systems, contrasting with polar desert (250 mm or less) over much of the Canadian Arctic Archipelago and central Arctic Ocean. Within these patterns, there is strong seasonality and local-to-regional variability. Obtaining accurate measurements of Arctic precipitation to assess anomalies and change is challenged by the sparse observation network—notably over the Arctic Ocean—and observation errors due to factors such as gauge undercatch of solid precipitation (Serreze et al. 2003).

To assess 2025 Arctic precipitation anomalies and historical trends, data from the ERA5 atmospheric reanalysis are utilized (Hersbach et al. 2020), which performs slightly better than other atmospheric reanalyses at matching observed precipitation (Barrett et al. 2020; Loeb et al. 2022), along with the gauge-based Global Precipitation Climatology Centre (GPCC) dataset (land-only measurements; Becker et al. 2013; Schneider et al. 2022). The Arctic is taken as the region poleward of 60°N. Winter, spring, summer, and autumn are defined as January–March, April–June, July–September, and October–December, respectively.

2. ANNUAL AND SEASONAL ARCTIC PRECIPITATION

For the Arctic as a whole, annual precipitation for 2025 based on ERA5 was 106.0% of the 1991–2020 average, the third highest total on record, reinforcing an upward trend as assessed over the period 1950–2025. Percent anomalies with respect to 1991–2020 by season were 111.8% (fourth highest on record) for winter, 108.3% for spring (record high), 99.7% for summer, and 104.3% for autumn (ninth highest). Summer was near the long-term average.

3. REGIONAL ANOMALIES

Figure 5.8 shows the spatial pattern of seasonal precipitation anomalies for 2025 based on ERA5. Regionally, above-to-slightly-above average precipitation over the Atlantic sector in winter contrasted with below-average precipitation over northern Europe and along the west coast of Canada. The dominant features of spring were above-average precipitation over coastal Alaska and the southeast coast of Greenland, both pointing to the effects of orographic uplift. Precipitation was somewhat low over most of Canada and northern Europe (with northern Norway as an exception), the latter continuing the pattern from winter. Summer dryness over most of Canada stands out, as does dry conditions over much of northern Eurasia. In autumn, the pattern shifted to above-average precipitation over Canada, while much of Arctic Eurasia remained dry.

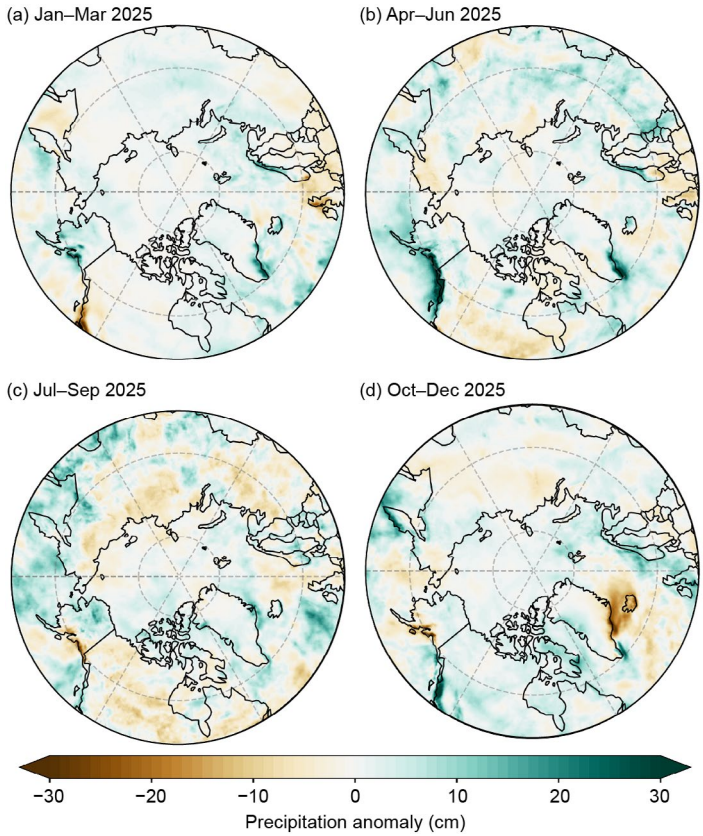

Fig. 5.8. Seasonal precipitation anomalies (cm; 1991–2020 baseline) in 2025 for (a) winter (Jan–Mar), (b) spring (Apr–Jun), (c) summer (Jul–Sep), and (d) autumn (Oct–Dec). Green shades denote above-average precipitation and brown shades denote below-average precipitation. (Source: ERA5.)

4. HEAVY PRECIPITATION EVENTS

Regionally heavy precipitation events in any year can approach or exceed previous records, even in a stable climate. Such events are important to track as they can result in flooding, loss of life, and damage to infrastructure. Figure 5.9 shows the pattern of heavy precipitation events by season in terms of

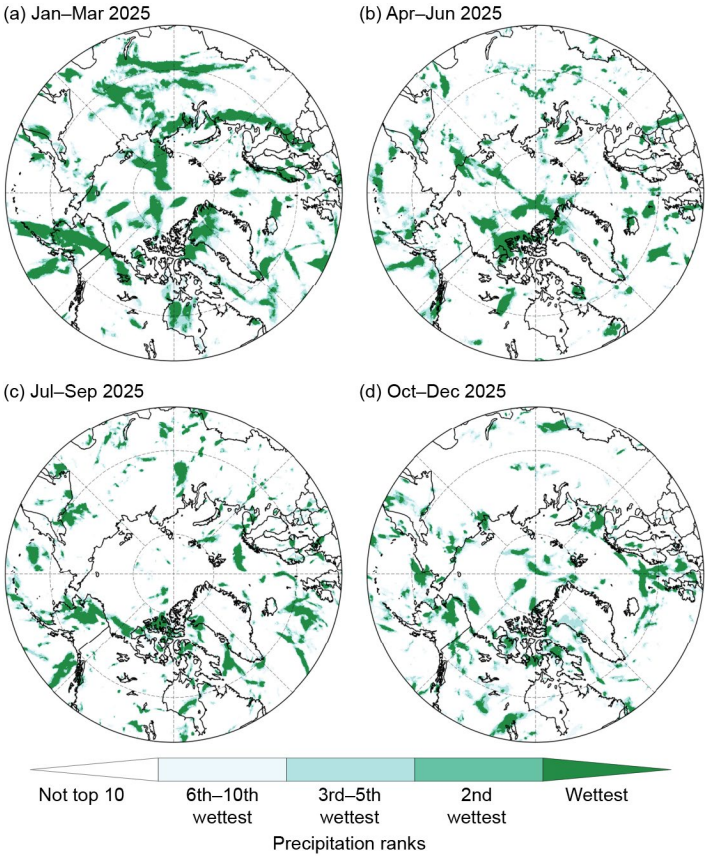

Fig. 5.9. Ranks of maximum five-day precipitation in 2025 for (a) winter (Jan–Mar), (b) spring (Apr–Jun), (c) summer (Jul–Sep), and (d) autumn (Oct–Dec) relative to the 1950–2024 period. (Source: ERA5.)

5. HISTORICAL PERSPECTIVE

Climate models project increased Arctic precipitation and more frequent heavy precipitation events as the climate warms, as well as an increase in the proportion of precipitation falling as rain. Previous studies addressing trends (Box et al. 2021; Yeh et al. 2021; Yu and Zhong 2021; Walsh et al. 2022a) emphasize interannual and multiyear variability and large regional variations in trends, as well as evidence of a transition from solid to liquid precipitation in the warmer parts of the Arctic (Box et al. 2021). However, as discussed in the Arctic precipitation section of the 2023 and 2024 *State of the Climate* reports and presented here with updates, pan-Arctic precipitation now has detectable upward trends in all seasons, as well as in the annual average.

Arctic precipitation time series from ERA5 (as a percentage of 1991–2020 averages for the region poleward of 60°N) are plotted in Fig. 5.10 along with the corresponding time series from the station-based GPCC dataset. While the percent anomaly time series from the two sources are generally similar, there are substantial differences for individual years ranks of the maximum five-day precipitation events (Rx5) in each season (relative to the 1950–2024 period). The standout feature is the comparatively higher density of heavy precipitation events across the Arctic in winter compared with the other seasons. Note especially the band of heavy precipitation events in winter stretching northward from south of the Aleutian Islands across Alaska. Much of that precipitation was related to a large northward pulse of moisture (an "atmospheric river") during 22–25 January. The associated southerly winds also contributed to above-average surface air temperatures across these areas (section 5c). As the water cycle intensifies and extreme precipitation events become more common (Yu and Zhong 2021; Dou et al. 2022), disruption to ecosystems (e.g., Christensen et al. 2020; Serreze et al. 2021) and human infrastructure (e.g., Hansen et al. 2014; Fox et al. 2023) will further impact Arctic communities.

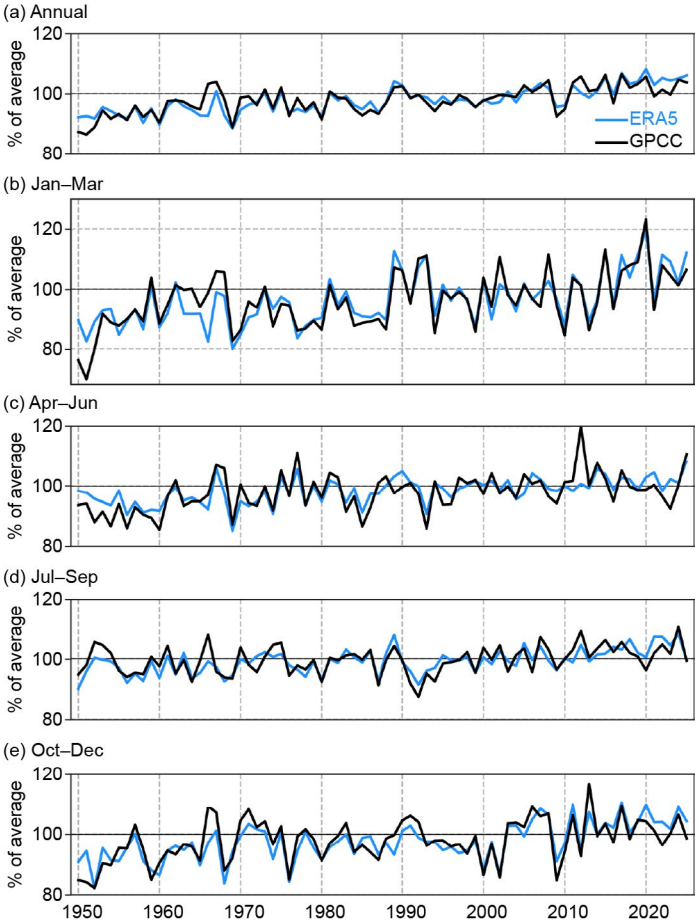

Fig. 5.10. Time series of Arctic (60°N–90°N) precipitation from 1950 through 2025 expressed as a percentage of the 1991–2020 average (%; shown by the horizontal black lines at 100%). (Source: ERA5 [blue lines] and Global Precipitation Climatology Centre [GPCC] 1.0° data [black lines].) GPCC values are for land only; ERA5 values are for land plus ocean.

due to the absence of coverage over the Arctic Ocean in GPCC and inherent uncertainties in each data source. The updated time series nevertheless reinforces the conclusion that precipitation for the Arctic region overall is increasing. Based on the ERA5 data from 1950–2025, the trend in annual mean precipitation stands at 0.75 cm decade^{-1}. Corresponding seasonal trends are 0.23 cm decade^{-1} for winter, 0.13 cm decade^{-1} for spring, 0.17 cm decade^{-1} for summer, and 0.23 cm decade^{-1} for autumn. Autumn and winter hence show the strongest seasonal trends. In terms of percent change relative to the 1991–2020 average, winter is strongest (2.25% decade^{-1}). Autumn is 1.7% decade^{-1}, summer is 1.01% decade^{-1}, spring is 1.11% decade^{-1}, and the year as a whole is 1.52% decade^{-1}.

The spatial pattern of annual trends for 1950–2025 is quite revealing (Fig. 5.11). Positive trends of up to 0.3 cm yr^{-1} are apparent over the North Atlantic sector of the Arctic and extending into the Barents Sea. The strong, positive trends along the Norwegian coast and parts of the southeast coast of Greenland point to orographic effects—forced uplift and cooling of moist air. Strong, positive trends along the Alaska coast are also consistent with orographic uplift. Pointing further to the spatial heterogeneity of trends, reductions in precipitation are seen in other areas, such as parts of Eurasia and Canada.

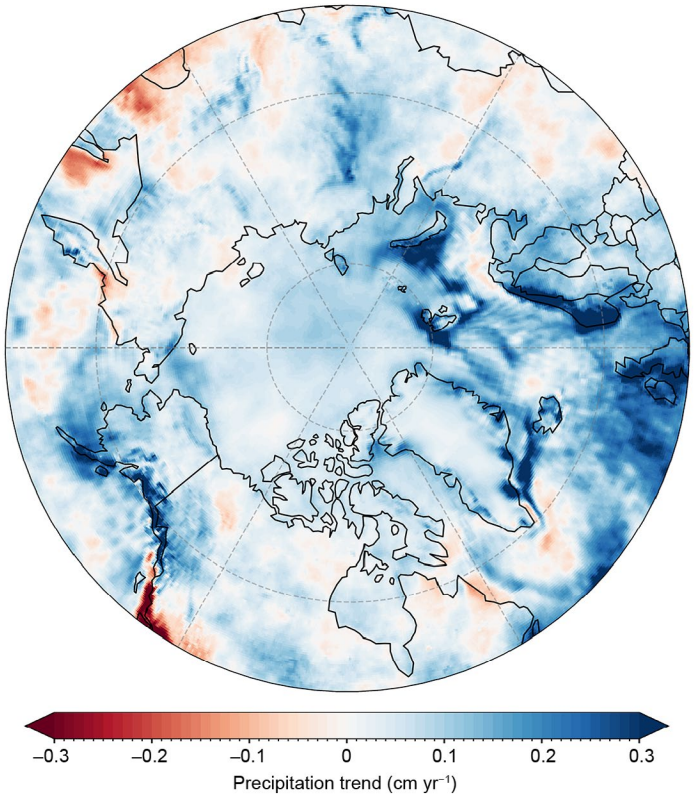

Fig. 5.11. Linear trends in annual precipitation (cm yr^{-1}) for the period 1950–2025. (Source: ERA5.)

Sidebar 5.1: **Ex-typhoon Halong**

—R. L. THOMAN

Southwest Alaska suffered widespread severe coastal flooding and wind damage during 11–12 October 2025 as ex-typhoon Halong tracked from the north-central Pacific Ocean northward through the eastern Bering Sea before moving into the Beaufort Sea north of Alaska. Dozens of primarily Yupik communities were adversely affected by the storm, with two communities almost entirely evacuated after the storm and over 1500 people relocated from across the region. Both the State of Alaska and the federal government issued disaster declarations in the aftermath of the storm. This was the latest in a series of high impact extreme weather events in Alaska in recent years, with the number of state-declared disasters about double since 2020 compared to 2014–19 (Thoman and McFarland 2024).

Hardest hit was the north shore of Kuskokwim Bay, a low-lying tundra region where thousands of square kilometers of land are at an elevation of five meters or less above mean sea level. The communities of Kipnuk (Fig. SB5.1) and Kwigillingok, located along rivers a few kilometers inland, suffered catastrophic flooding that damaged nearly all buildings and disabled most infrastructure, including electrical power and fresh and waste water systems. Homes with people inside were lifted off their foundations in the dead of night and floated several kilometers upriver, requiring helicopter rescue of those inside. One person from Kwigillingok died as a result of the storm, and two others remain unaccounted for. It was "the worst flooding in living memory", according to community members who have lived in the region for generations. The return timeline for both Kipnuk and Kwigillingok residents remains uncertain due to the extent of the damage, with many evacuees residing in the cities of Anchorage and Bethel, Alaska, many for an indefinite period of time.

Fig. SB5.1. Aerial view of Kipnuk, Alaska, on 12 October 2025 showing almost total inundation of the community. (Source: Alaska Air National Guard.)

Impacts from ex-Halong were not confined to coastal flooding. Strong winds caused municipal, tribal, and residential building and infrastructure damage and prolonged power outages in many coastal communities that were spared from storm surge. Additionally, communities as far as 200 kilometers inland experienced strong winds that downed many trees and caused power outages.

Typhoon Halong formed southeast of Japan on 5 October 2025 and rapidly intensified to a severe typhoon near Izu Island on 8 October (see section 4g4 for further detail on storm development). Thereafter, the storm turned northeast and transitioned to an extratropical cyclone (i.e., the primary energy for the storm changed from latent heat release to the horizontal temperature gradient) on 10 October. Ocean surface temperatures were above the 1991–2020 baseline average across virtually the entire track of Halong (Fig. SB5.2), from typhoon development southeast of Japan through the extratropical transition (ET) and across the eastern Bering Sea. After weakening rapidly prior to the ET, the lowest pressures in ex-Halong dropped significantly as the storm crossed the eastern Bering Sea, reaching a minimum pressure of 960 hPa at 1200 UTC on 12 October located between St. Lawrence Island and the Yukon River delta, whereafter the forward speed increased dramatically. Just 18 hours after reaching its minimum pressure, Halong was centered more than 1200 km to the northeast over the Beaufort Sea ice pack.

As the storm tracked northeastward, winds in the southeast quadrant of the storm were sustained at ~40 kt to 50 kt (21 m s^{-1} to 26 m s^{-1}), blowing onshore into the Kuskokwim delta coast. This produced a significant storm surge that unfortunately coincided in time with the daily high tide, making this a "worse-case" scenario. Had the timing of the storm surge corresponded with the daily low tide (e.g., 11 October evening instead of 12 October early morning), there would have been a prolonged "high tide" but little or no inundation (though wind damage would still have occurred).

Historical Context

Strong storms in the northern Bering Sea are common in the late summer and autumn. Based on the Crawford et al. (2021) storm track database, in the northern Bering Sea (north of 58°N, east of 180° longitude) between August and November during the 30-yr period of 1996–2025, there were 163 separate storms with a minimum pressure of 980 hPa or lower: only four were storms that originated as typhoons in the western Pacific. While Alaska's Aleutian Islands are occasionally impacted by ex-typhoons, historically it has been rare for such storms to

track from the North Pacific through the Bering Sea and into the Arctic prior to dissipating. Based on the Joint Typhoon Warning Center (JTWC) Western North Pacific Ocean Best Track Data and supplemented with MERRA-2 and ERA5 reanalysis when needed, between 1970 and 2021, only ex-Typhoon Carlo, in October 1996, followed such a path. Ex-Carlo produced stormy weather in the Bering Strait region but no significant coastal flooding was documented. Since 2022, three ex-typhoons followed such a path: ex-Merbok in September 2022, which caused widespread devastation on the northeast Bering Sea coast, ex-Amphil in August 2024, which caused wind damage in the Bering Strait region but did not cause coastal flooding, and now ex-Halong in October 2025.

The path of ex-Halong in the eastern Bering Sea was also unusual for storms of this intensity. Based on the Crawford et al. (2021) storm track database, since 1950, only one other autumn storm with a minimum pressure of 970 hPa or lower followed a track such that the center passed between St. Lawrence and the Yukon River delta. That storm occurred in October 1987 and produced some flooding in the Kuskokwim delta, though nothing comparable to ex-Halong.

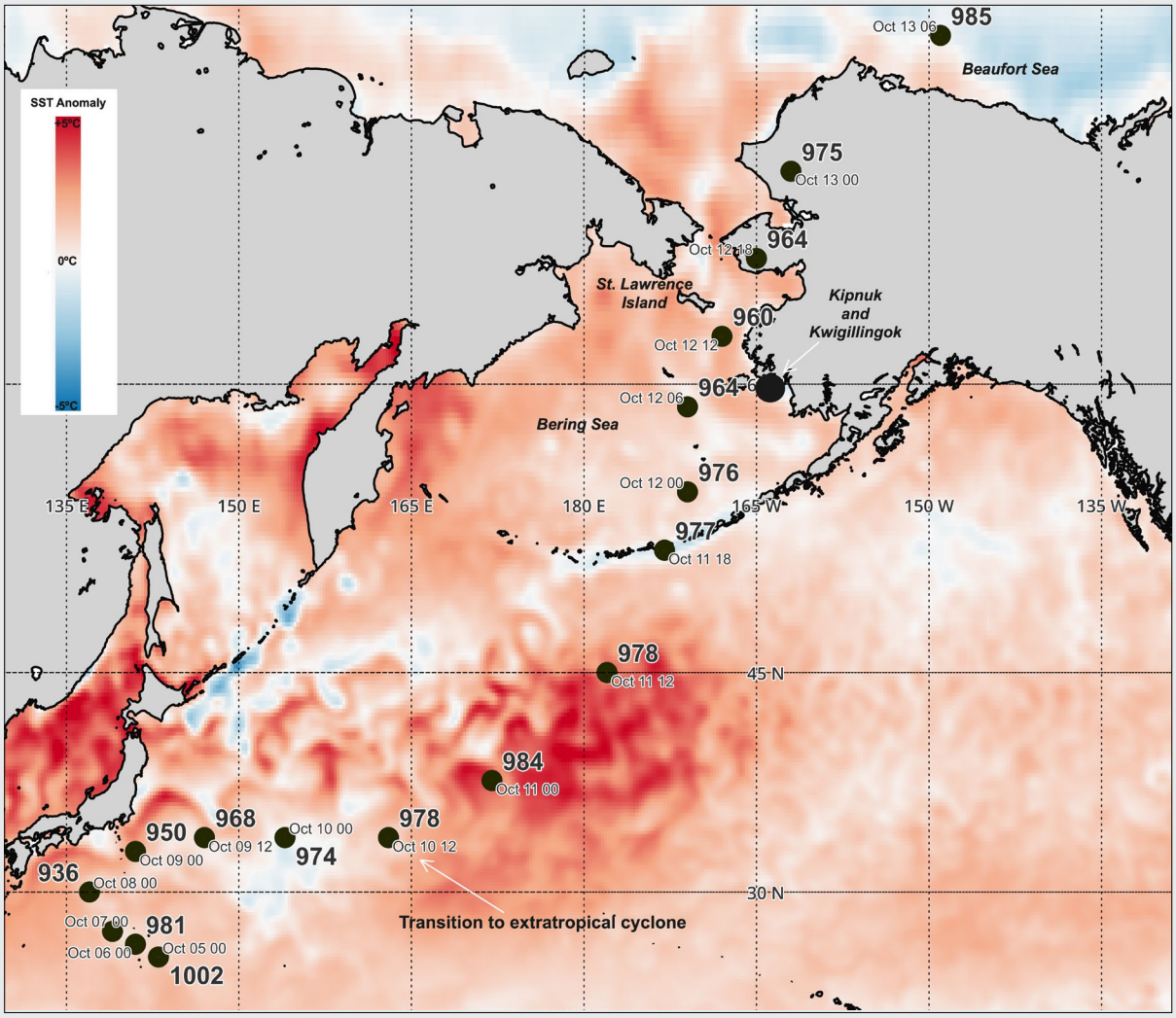

Fig. SB5.2. Track and intensity of ex-typhoon Halong during 5–13 October 2025. Positions (bold circle and date/time [UTC]) and minimum pressure (hPa) from the Joint Typhoon Warning Center (5–10 October) and the NWS Ocean Prediction Center (11–13 October) analyses. Color field is the 5–12 October 2025 average sea surface temperature anomalies (°C) relative to the 1991–2020 baseline based on NOAA Optimum Interpolated Sea Surface Temperature version 2.1 (OISSTv2.1).

e. Sea surface temperature

—M.-L. Timmermans and Z. M. Labe

Arctic Ocean sea surface temperatures (SSTs) in the summer are primarily influenced by the amount of incoming solar radiation absorbed by the sea surface and by the flow of warm waters into the Arctic from the North Atlantic and North Pacific Oceans. Solar warming of the Arctic Ocean surface is influenced by the sea ice distribution (with greater warming occurring in ice-free regions), cloud cover, and upper-ocean stratification. Inflows of relatively warm Arctic river waters can provide an additional heat source in coastal regions.

The SST data presented here are from the 0.25° × 0.25° NOAA Optimum Interpolation Sea Surface Temperature (OISST) Version 2.1 product (Huang et al. 2021). The analysis period spans June 1982 through September 2025, with 1991–2020 used as the climatological reference period. The analysis focuses most closely on August 2025 mean SSTs in context with the climatological record. August mean SSTs provide the most appropriate representation of Arctic Ocean summer SSTs because sea ice extent is near a seasonal low at this time of year, prior to the onset of surface cooling and subsequent sea ice growth that would otherwise influence SSTs later in September.

August 2025 mean SSTs were as high as ~12°C in parts of the Barents and Kara Seas (within the Arctic Ocean's Atlantic sector) with lower values of about –1°C to 7°C in other Arctic basin marginal regions (Figs. 5.12a,b). August 2025 mean SSTs were anomalously warm compared to the 1991–2020 August mean in the Barents, Kara, and Laptev Seas, with SST anomalies around +1°C to +4°C, and local SST anomalies as high as ~+7°C in the Kara Sea (Fig. 5.12c). In the Arctic's Pacific sector, the Beaufort and northern Chukchi Seas had anomalously cold SSTs (August 2025 mean values ~1°C–2°C lower than the 1991–2020 mean), while the southern Chukchi Sea and the Bering Sea were anomalously warm (SSTs ~1°C–2°C higher). This general pattern of August 2025 SST anomalies is consistent with regional patterns of anomalously warm surface air temperatures in the Kara and Laptev Sea regions and cold surface air temperatures in the Beaufort Sea region in summer 2025 (section 5c).

In most Arctic regions, August 2025 SSTs ranked among the warmest recorded in the 1982–2025 period (70th to 100th percentile; Fig. 5.12d), although regional SST anomalies differ significantly from year to year. The Kara and Chukchi Seas had considerably higher SSTs in August 2025 compared to August 2024, with differences of up to 9°C (Fig. 5.12e). By contrast, August 2025 SSTs were as much as a few degrees lower than 2024 SSTs in the Barents and southern Beaufort Seas.

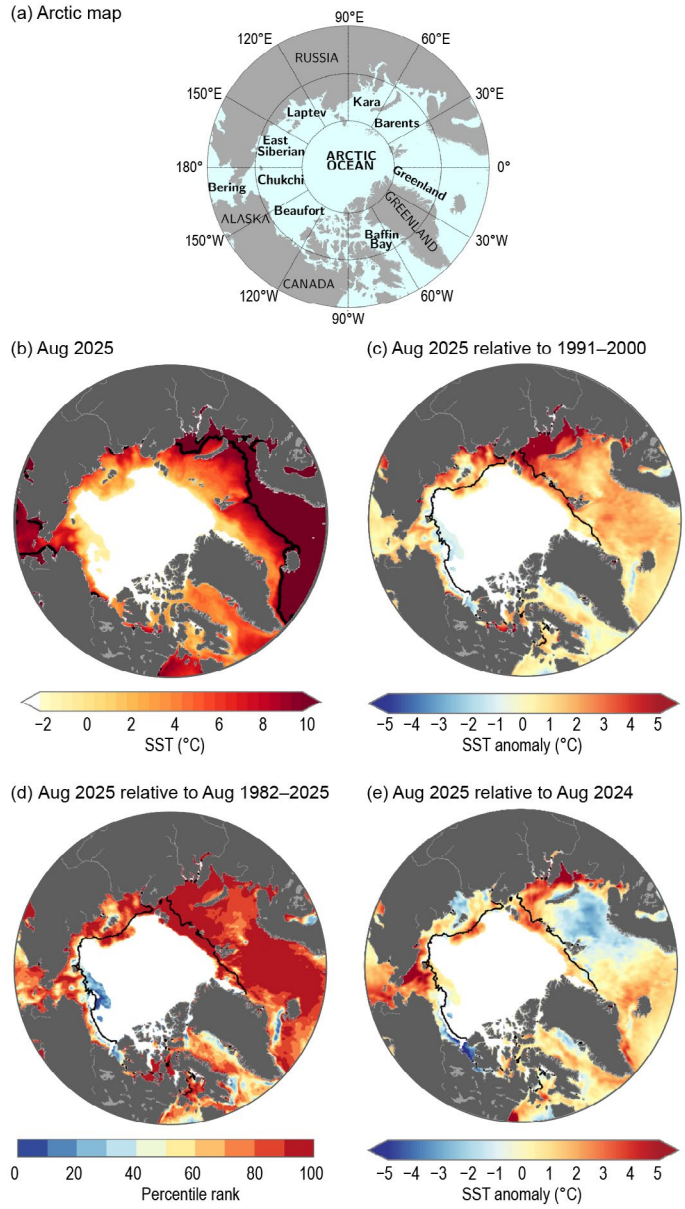

Fig. 5.12. (a) Arctic Ocean map showing relevant marginal sea locations and geographic features. (b) Mean sea surface temperature (SST; °C) in Aug 2025. Black contours indicate the 10°C-SST isotherm. (c) SST anomalies (°C) in Aug 2025 relative to the Aug 1991–2020 mean. (d) Aug 2025 SST percentile rank relative to the Aug values in 1982–2025. (e) Difference between Aug 2025 SSTs and Aug 2024 SSTs (negative values indicate where 2025 was cooler). White shading in all panels is the Aug 2025 mean sea ice extent. Black lines in (c)–(e) indicate the Aug 1991–2020 median ice edge. Sea ice concentration data are the (near-real-time) NOAA National Snow and Ice Data Center Climate Data Record of Passive Microwave Sea Ice Concentration, (version 4) version 6 (Meier et al. 2026a,b).

SST patterns in August 2025 followed developments in June and July. Above-normal SSTs in most of the Arctic's Atlantic sector were also observed in June and July 2025 (Figs. 5.13a,b). This is consistent with relatively warm summer 2025 surface air temperatures in the region (section 5c). Below-normal SSTs in the Bering Sea in June and July (Figs. 5.13a,b) were consistent with the relatively late sea ice retreat from the Pacific sector (section 5f). The transition from below-normal to above-normal SSTs from June to August in the Bering Strait region corresponded with the transition from anomalously cool surface air temperatures in spring to warm conditions in summer (section 5c). Anomalously cool SSTs across the Beaufort Sea sector in September (Fig. 5.13d) were consistent with the anomalously late ice retreat from the region (section 5f) and, consequently, a shorter duration of solar absorption by the surface ocean; surface air temperatures in September were near-normal or marginally above normal in the region (section 5c).

The Arctic Ocean has experienced significant mean August SST warming from 1982 to 2025, with statistically significant linear trends (95% confidence interval) in most regions (Fig. 5.14a). Mean August SSTs

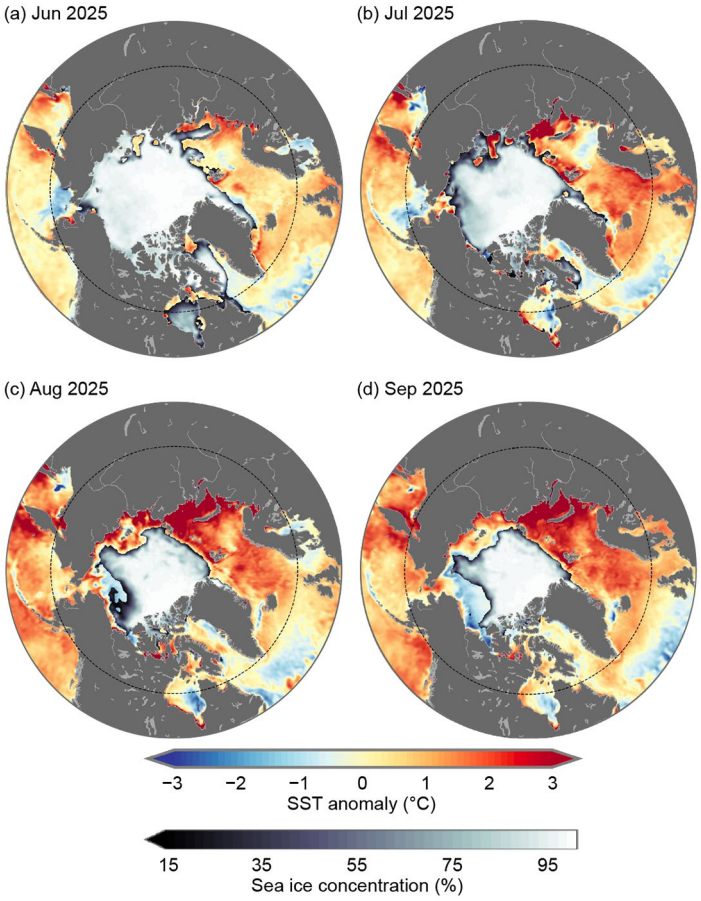

Fig. 5.13. Sea surface temperature (SST) anomalies (°C) in 2025 for (a) Jun, (b) Jul, (c) Aug, and (d) Sep relative to the 1991–2020 mean for their respective months. The dashed circle indicates the latitudinal bound of the maps in Fig. 5.12. Note a difference in the color bar scale compared to Figs. 5.12c,e. The mean sea ice concentration for the corresponding month is also shown. See Fig. 5.12 caption for sea ice dataset information.

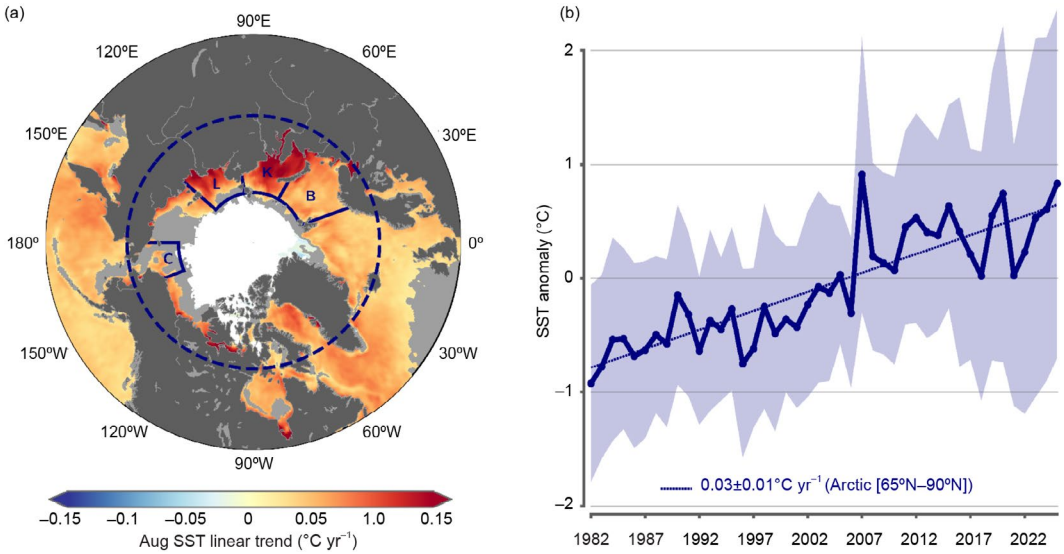

Fig. 5.14. (a) Linear sea surface temperature (SST) trend (°C yr^{-1}) for Aug of each year (1982–2025). The trend is only shown for values that are statistically significant at the 95% confidence interval; the region is shaded light gray otherwise. White shading indicates regions that are ice covered (>15% sea ice concentration) in all years. The dashed blue circle marks 65°N (the Arctic Ocean region), and solid blue line boundaries delineate the Barents (B; 66.5°N–80°N, 20°E–60°E), Kara (K; 70°N–80°N, 50°E–100°E), Laptev (L; 70°N–80°N, 100°E–139°E) and Chukchi (C; 65°N–75°N, 180°–202°E) Seas. (b) Area-averaged SST anomalies (°C) for Aug of each year from 1982 through 2025 relative to the 1991–2020 Aug mean for the Arctic Ocean north of 65°N (shading indicates ±1 std. dev. of the regional mean SST anomaly field). The dotted line shows the corresponding linear SST anomaly trend over the period 1982–2025, and numbers in the legend indicate the trend and 95% confidence interval.

for the entire Arctic Ocean region north of 65°N exhibit a linear warming trend of 0.3±0.1°C decade^{-1} (Fig. 5.14b). Within the long-term warming trend, the August 2025 mean Arctic Ocean SST was the second warmest on record, exceeded only by August 2007. Regionally, the Kara and Laptev Seas show the strongest warming trends in the Arctic Ocean (Fig. 5.14a), with August SST linear trends of 0.12±0.03°C yr^{-1} and 0.08±0.02°C yr^{-1}, respectively (Figs. 5.15a,b). In the Kara Sea, August 2025 mean SSTs were the highest on record. Statistically significant linear trends (0.06±0.02°C yr^{-1}) in August SST are also observed in the Barents Sea (Fig. 5.15c). On the other hand, there is no statistically significant trend in the Chukchi Sea (Fig. 5.15d). These regional differences in warming trends likely reflect varying sea ice loss patterns, ocean circulation, and atmospheric forcing across the Arctic basin.

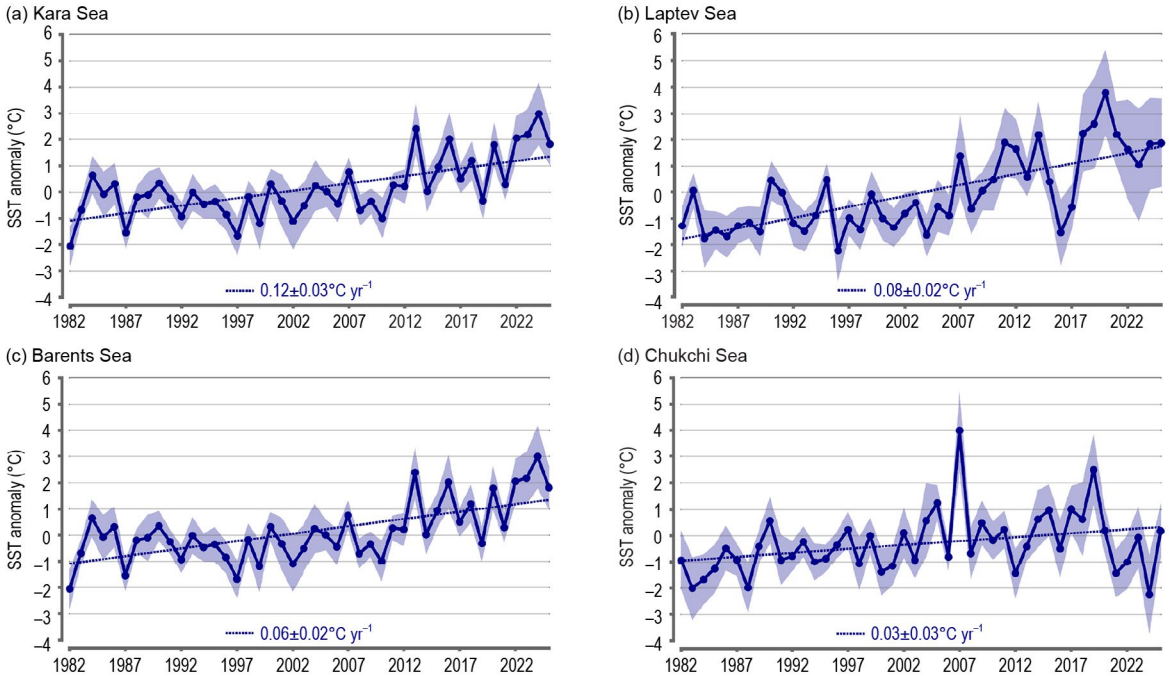

Fig. 5.15. Area averaged sea surface temperature (SST) anomalies (°C) for Aug of each year (1982–2025) relative to the 1991–2020 Aug mean for the (a) Kara Sea, (b) Laptev Sea, (c) Barents Sea, and (d) Chukchi Sea regions shown by the blue boundaries in Fig. 5.14a. The dotted lines show the linear SST anomaly trends over 1982–2025, and numbers in the legends indicate the trends in °C yr^{-1} (with 95% confidence intervals; trends that are not statistically significant are labeled in gray). Blue shading indicates ±1 std. dev. of the regional mean SST anomaly fields.

f. Sea ice cover

—W. N. Meier, S. Hendricks, A. Petty, D. Perovich, S. Farrell, M. Webster, D. Divine, S. Gerland, L. Kaleschke, R. Ricker, X. Tian-Kunze, and A. Bliss

Sea ice is the frozen interface between the ocean and atmosphere in the Arctic. It limits ocean–atmosphere exchanges of energy and moisture and plays a critical role in Arctic ecosystems and Earth's climate. The presence of sea ice affects human activities in the Arctic, including transportation, marine navigation, and Indigenous hunting. Arctic sea ice reached record monthly low extents during February, March, and December 2025. September sea ice extent, when the annual minimum usually occurs, has declined 46% over 1979–2025, though the trend over the past 20 years has been insignificant due to natural variability (England et al. 2025).

1. SEA ICE EXTENT AND CONCENTRATION

Arctic sea ice extent (defined as the total area covered by at least 15% ice concentration) in 2025 was generally on par with extents of the last 20 years but much lower than earlier decades within the observational record. For comparisons in this section, a climatological period of 1991–2020 is used. Extents during winter (January–March) 2025 were at record- or near-record-low levels (Fig. 5.16). Extent values are from the National Snow and Ice Data Center's Sea Ice Index (Fetterer et al. 2025), one of several extent products (Ivanova et al. 2014; Lavergne et al. 2019) derived from satellite-borne passive microwave sensors operating since 1979. Regionally, winter concentration was particularly below average in Hudson Bay (after a very slow freeze-up) and the Barents Sea, Bering Sea, Labrador Sea, and Sea of Okhotsk (Fig. 5.17).

By March, the month with the most extensive coverage, the total sea ice extent of 14.12×10^6 km^2 was 0.91×10^6 km^2 (6.1%) lower than average and the lowest March extent in the 47-year record. The March 2025 pan-Arctic extent continued the statistically significant downward trend of –2.5 % decade^{-1} over the 1979–2025 record.

After the record-low March extent, the seasonal retreat of sea ice began with much slower-than-normal ice loss through April. After April, ice loss increased and remained rapid through the rest of spring and early summer (mid-July). But after the beginning of August, the rate of sea ice loss slowed relative to 2024 and 2023 and was on par with the 1991–2010 average. As in 2024, Hudson Bay opened early in 2025, but it was not as extreme as in 2024. Summer ice loss was also particularly rapid in the Barents and Kara Seas.

In August, the Northern Sea Route, along the northern Russian coast, opened (<15% concentration in passive microwave data indicating the potential for safe navigation). Extent in the East Siberian Sea was near average, in contrast to the late opening that occurred in 2024. The Beaufort and Chukchi Seas were slow to open relative to 2024, but melted out

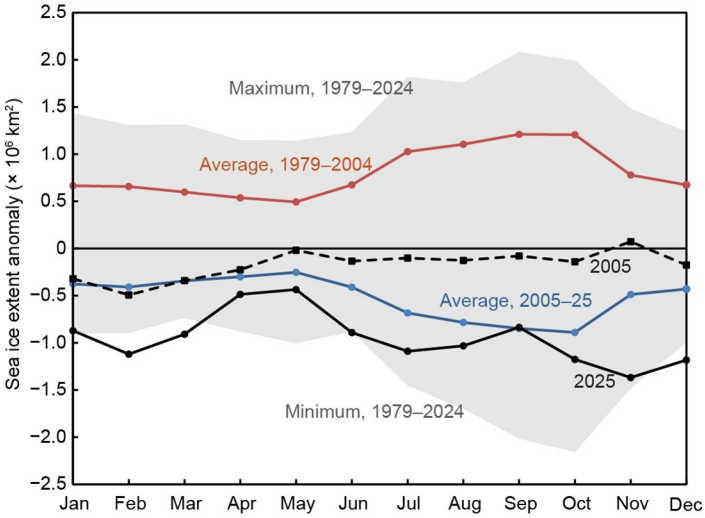

Fig. 5.16. Monthly average sea ice extent anomalies ($\times 10^6$ km^2) relative to 1991–2020 for: 2025 (black solid line), 2005 (black dashed line), 2005–24 average (blue), 1979–2004 average (red), and the maximum and minimum range (gray shading) for the period 1979–2024.

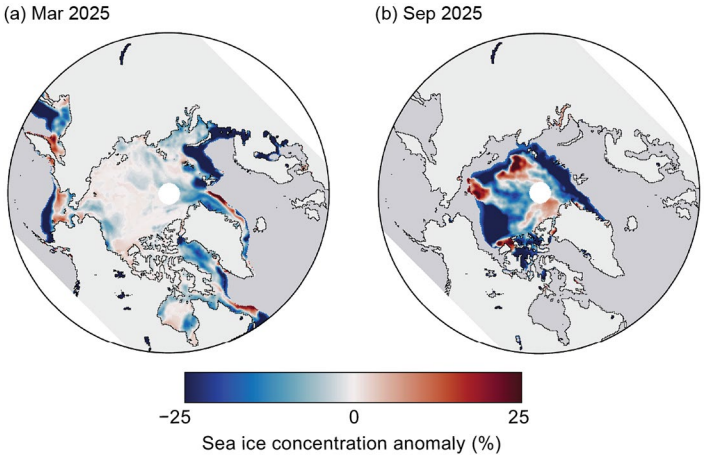

Fig. 5.17. Sea ice concentration anomalies (%) in 2025 for (a) Mar and (b) Sep relative to their 1991–2020 average. The extreme negative anomalies (darkest blue color, less than –25%) indicate regions where there is ice in the climatology, but no ice was present in 2025.

rapidly during August and September, yielding substantial open water that has been typical in nearly all years since 2007.

September, the month of the annual minimum sea ice extent, was characterized by below-average coverage in the Pacific sector with open water extending far northward from the coast in the Beaufort, Chukchi, and Siberian Seas (Fig. 5.17). The September 2025 sea ice extent of 4.75×10^6 km^2 was 0.83×10^6 km^2 (14.9%) lower than the 1991–2020 average and the 11th lowest September extent on record (Fig. 5.16). The September trend from 1979 through 2025 is –13.6% decade^{-1}, and like all other months, is statistically significant. The 19 lowest September extents in the satellite record have all occurred in the last 19 years (2007–25). The 2025 freeze-up period (October–December) was similar to 2024, with much lower-than-average extent in Hudson Bay and the Barents and Kara Seas.

2. SEA ICE AGE, THICKNESS, AND VOLUME

Sea ice drifts with winds and ocean currents while growing and melting thermodynamically. Ice divergence creates leads where, in freezing conditions, new ice forms while ice convergence leads to dynamic thickening. Sea ice thickness provides a record of the cumulative effect of dynamic and thermodynamic processes and thus is an important indicator of overall ice conditions. Sea ice age is a rough proxy for thickness as multiyear ice (ice that survives at least one summer melt season) grows thicker over successive winters. Age based on Tschudi et al. (2019a,b) covers the period 1984–2025, which is substantially longer than basin-wide thickness estimates, and shows that the amount of multiyear ice remaining in the Arctic continued to be far less than during the 1980s, with a substantial change even since 2005 (Fig. 5.18). Since 2012, the Arctic has been nearly devoid of the oldest ice (more than four years old); this continued in 2025, with an end-of-summer old ice extent of 95,000 km^2 compared to ~1.5×10^6 km^2 in the 1980s, a 95% reduction. In the 41 years since ice-age records began in 1984, the Arctic has changed from a region dominated by multiyear sea ice to one where first-year (seasonal) sea ice prevails. This much younger ice cover implies a thinner, less voluminous ice pack that is more sensitive to atmospheric and oceanic changes. For thickness estimates, the European Space Administration's (ESA) CryoSat-2/Soil Moisture Ocean Salinity (SMOS) satellites, in combination with the Copernicus Sentinel-3A/B satellites, have provided a record of seasonal (October–April) ice thickness and volume (Ricker et al. 2017; ESA 2023) since the 2010/11 winter. At the end of the winter growth season, the April 2025 thickness (Fig. 5.19a) in the Arctic had the typical pattern of thicker ice along the northern coast of Greenland and the Canadian Archipelago due to deformation and advection across the pole; this also corresponds to the region of older ice noted above. The thickness anomaly pattern for April 2025 shows a substantial amount of spatial variability (Fig. 5.19b). The 2024/25 sea ice growth season began with the Laptev, Kara, and Barents Seas having thicker ice than the 2010–21 average and other regions being thinner than average (Fig. 5.19c). Ice growth through the winter was robust, and by April 2025 all regions were either

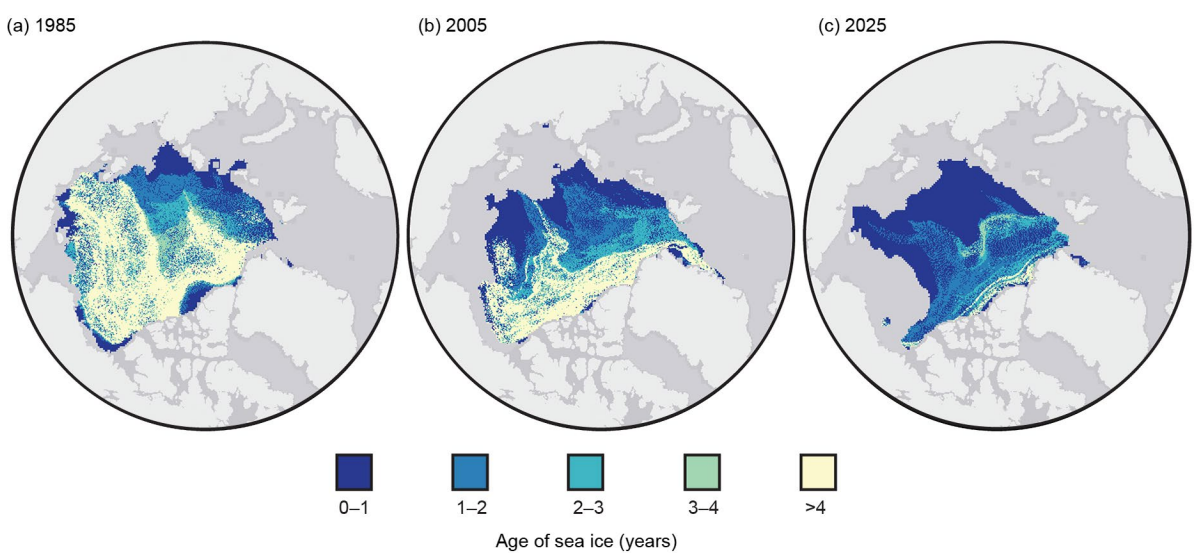

Fig. 5.18. Sea ice age during the week of the annual minimum ice extent in (a) 1985, (b) 2005, and (c) 2025.

average or thicker than the 2011–21 average; however, there were locations within some regions with thinner-than-average ice. By the start of the autumn freeze-up in October 2025, below-average thickness was prevalent in most regions, but by December 2025, most areas had thicker-than-average ice. Sea ice thickness from CryoSat-2/Sentinel-3/SMOS integrated with ice concentration shows no substantial trend in winter ice volume over the 15-year time series.

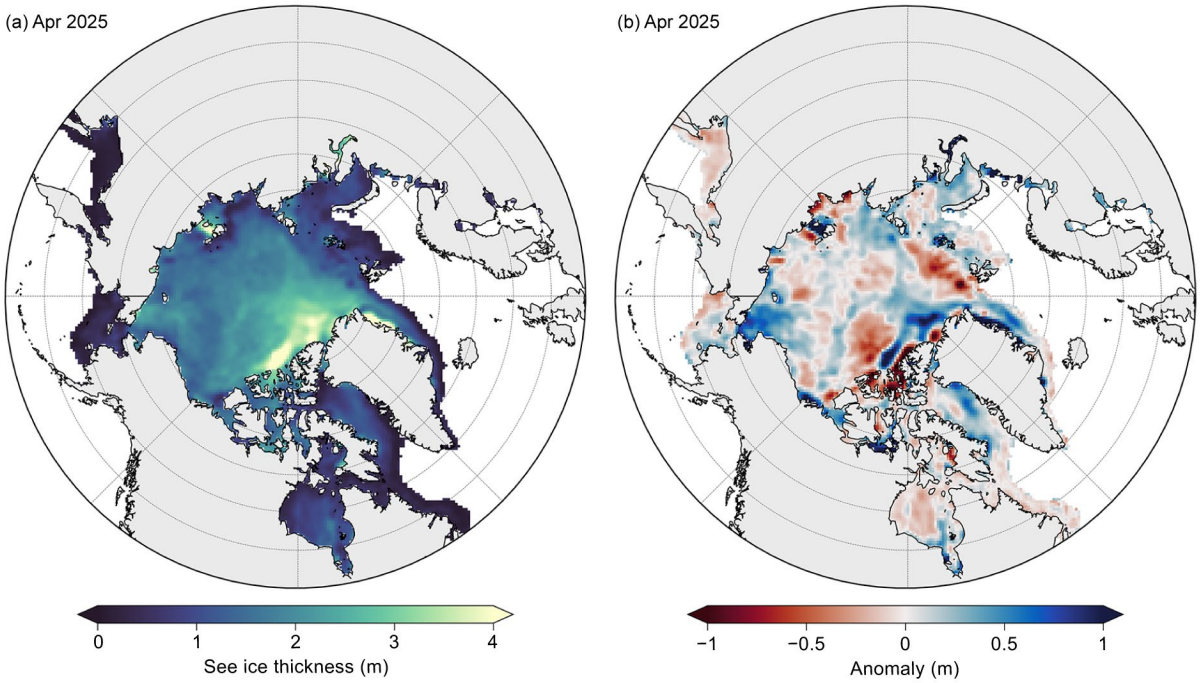

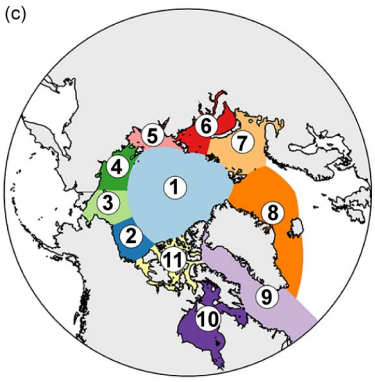

Location	Jan 2025	Feb 2025	Mar 2025	Apr 2025	Oct 2025	Nov 2025	Dec 2025
Central Arctic (1)	0.01 m	0.04 m	0.08 m	0.02 m	–0.06 m	–0.01 m	–0.04 m
Braufort Sea (2)	0.02 m	0.23 m	0.02 m	0.07 m	0.00 m	–0.01 m	0.07 m
Chukchi Sea (3)	0.06 m	0.30 m	0.45 m	0.32 m	0.17 m	0.14 m	0.13 m
East Siberian Sea (4)	–0.07 m	0.00 m	0.05 m	0.07 m	0.12 m	0.20 m	0.13 m
Laptev Sea (5)	0.00 m	0.08 m	0.11 m	0.03 m	0.02 m	0.03 m	0.11 m
Kara Sea (6)	0.09 m	0.18 m	0.21 m	0.28 m	0.22 m	0.08 m	0.07 m
Barents Sea (7)	0.21 m	0.27 m	0.29 m	0.20 m	0.42 m	0.44 m	0.33 m
East Greenland Sea (8)	–0.03 m	0.05 m	0.23 m	0.28 m	–0.05 m	0.03 m	0.13 m
Baffin Bay and Labrador Sea (9)	0.02 m	0.01 m	0.03 m	0.10 m	0.18 m	–0.03 m	–0.07 m
Hudson Bay (10)	–0.12 m	–0.05 m	0.00 m	0.00 m	0.02 m	–0.02 m	–0.03 m
Canadian Archipelago (11)	–0.10 m	–0.04 m	–0.02 m	0.00 m	–0.14 m	–0.11 m	–0.06 m

Fig. 5.19. Arctic sea ice in Apr 2025: (a) sea ice thickness (m), (b) sea ice thickness anomaly (m) relative to the Apr 2011–Apr 2021 average, and (c) regional monthly mean sea ice thickness anomalies (m) in 2025 relative to the Oct 2010–Apr 2021 average. (Source: European Space Administration's [ESA] CryoSat-2/Sentinel-3/Soil Moisture Ocean Salinity [SMOS].)

g. Greenland Ice Sheet

—K. Poinar, J. E. Box, T. L. Mote, X. Fettweis, B. D. Loomis, B. E. Smith, B. C. Medley, T. G. Askjaer, K. D. Mankoff, and R. S. Fausto

Net loss of ice from the Greenland Ice Sheet has occurred every year since the late 1990s (Mouginot et al. 2019; Mankoff et al. 2021), contributing to global sea level rise (see section 3f for details). Over the 2025 mass balance year (1 September 2024 to 31 August 2025), three independent estimates find that the ice sheet again lost mass, but at a rate ~30% less than the 1991–2020 average of roughly –200 Gt annually. These estimates are from input–output (–146±72 Gt), gravity (–129±50 Gt), and elevation (–143±36 Gt) methods; the values agree within measurement uncertainties.

The ice loss can be partitioned into ice discharge (iceberg calving) and surface mass balance (SMB). SMB is the sum of gain from snowfall and refrozen rainfall and loss from runoff, sublimation, and evaporation. Observations of air temperature, precipitation, snow cover, and albedo—key factors that influence SMB—over the 2025 mass balance year are summarized here.

Air temperatures were generally higher than the 1991–2020 average, especially in northern Greenland (Fig. 5.20a). Autumn (September–November 2024) and winter (December–February 2024/25) temperatures were above average, and spring (March–May 2025) brought pronounced warmth across Greenland, with record monthly highs set at 6 out of 34 stations. Summer (June–August 2025) was slightly cooler than average, except in mid-August, when a heatwave raised temperatures, primarily along the west coast.

Observations of rain and snowfall (hereafter, "precipitation") are reported for 11 coastal stations operated by the Danish Meteorological Institute (DMI) and 10 inland ice sheet stations operated by the Programme for Monitoring of the Greenland Ice Sheet (PROMICE). Precipitation at coastal stations was generally above the 1991–2020 average. Autumn 2024 precipitation was slightly below average at most stations, while winter precipitation was significantly above average at coastal stations but near-average at inland stations. Spring precipitation was close to average. Summer precipitation was above average, including notable snowfall at several inland

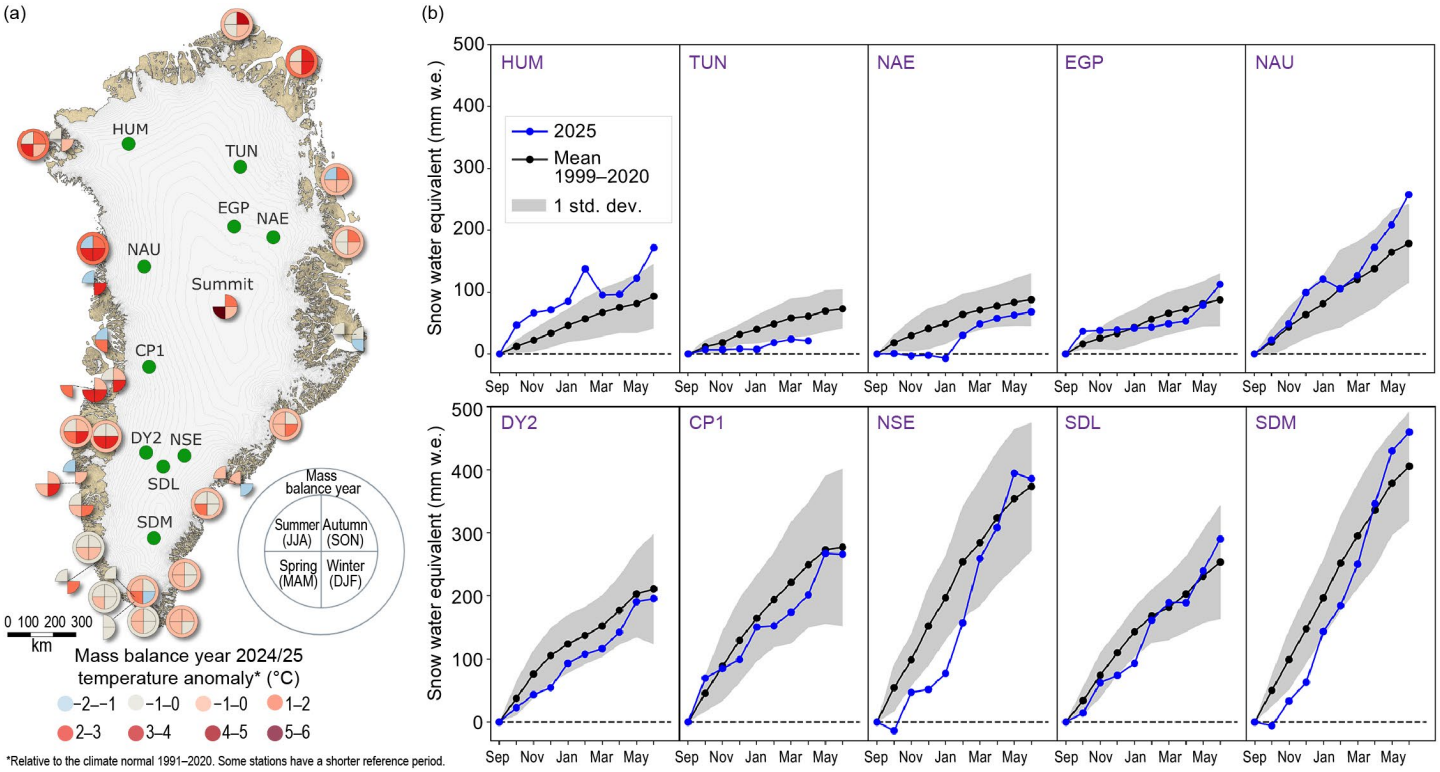

Fig. 5.20. (a) Map of Danish Meteorological Institute (DMI) coastal weather stations, colored by the temperature anomaly (°C) for each season (pie charts) and the full 2025 mass balance year (surrounding circles). Locations of inland weather stations operated by the Programme for Monitoring of the Greenland Ice Sheet (PROMICE) are indicated by green dots. (b) Snowfall (mm w.e.) at PROMICE stations from Sep 2024 through Jun 2025 (blue lines), compared to the 1991–2020 mean (black lines).

stations in June, July, and early August (Fig. 5.20b). Snow cover raises the albedo (surface reflectivity) of the ice sheet surface, so these events likely reduced ice melt by reflecting away sunlight.

Ice ablation (melt) was recorded across eight weather transects from PROMICE (Fausto et al. 2021) and also derived from daily Special Sensor Microwave Imager/Sounder (SSMIS) passive microwave radiometer satellite data (Mote 2007). Surface melt area was above average in mid-June and mid-July, and the 14–21 August heatwave caused widespread melt (Fig. 5.21a). While the number of observed melt days was slightly above average (Fig. 5.21b), the total mass of ice melt was below average, especially along the west coast, due to higher-than-normal albedo and cooler air temperatures there (Fig. 5.20).

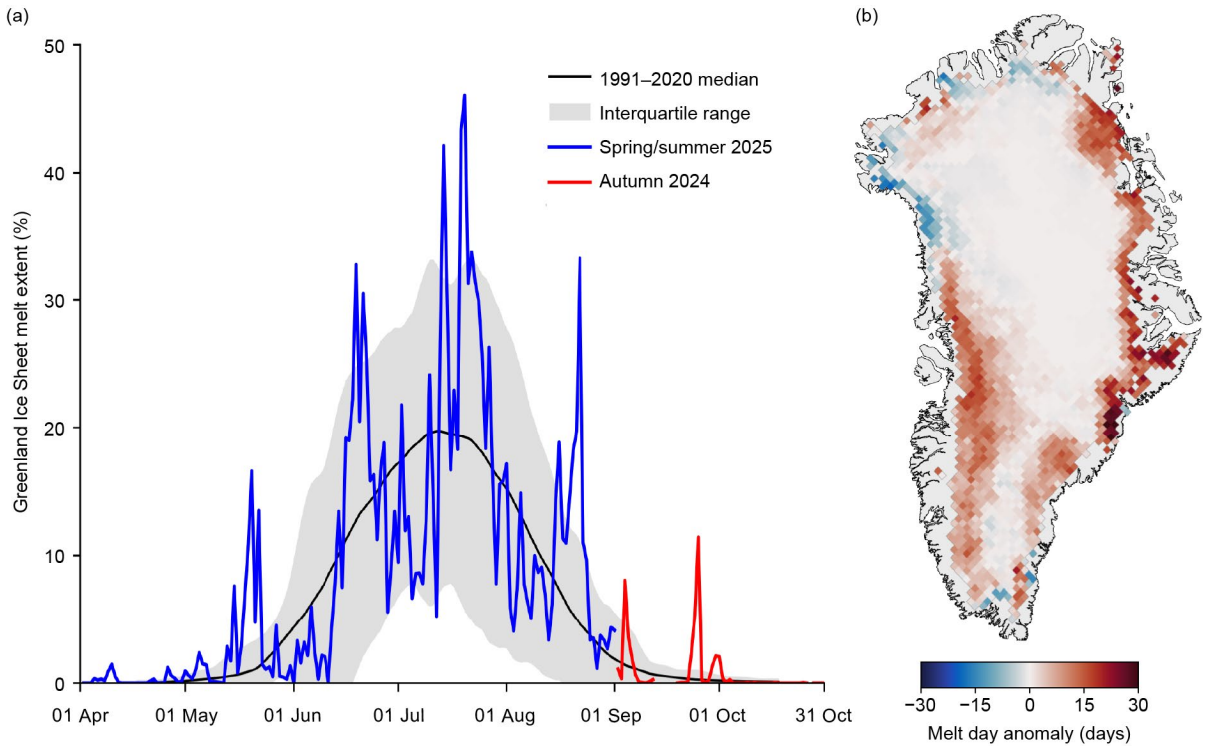

Fig. 5.21. (a) Daily surface melt extent as a percentage (%) of ice sheet area over the 2025 mass balance year, including autumn 2024 (red) and spring/summer 2025 (blue) but omitting Nov 2024–Mar 2025. (b) Number of surface melt days from 1 Apr to 31 Aug 2025 as an anomaly with respect to 1991–2020.

The ice-sheet-wide total SMB over the 2025 mass balance year was 365±55 Gt, which is consistent with the 1991–2020 annual mean of 366±106 Gt (mean ±1 st. dev), from the Modèle Atmosphérique Régionale version 3.14.1 regional climate model (MAR; Fettweis et al. 2020) forced by ERA5 (Hersbach et al. 2020), which provides SMB values at 5-km horizontal resolution.

The other term in ice-sheet mass balance is ice discharge, which is the mass flow rate out of glaciers at the ice–ocean boundary, where it calves off as icebergs or melts directly into the ocean. PROMICE estimates ice discharge from mass flow rate measurements collected near glacier fronts around the ice sheet (Mankoff et al. 2020). Total ice discharge over the 2025 mass balance year was 488±46 Gt, approximately 1 std. dev. above the 1991–2020 annual mean of 458±27 Gt (mean ±1 std. dev).

Ice discharge (488±46 Gt output) and basal melt (23±6 Gt output; Karlsson et al. 2021) are subtracted from the net SMB (365±55 Gt input) to obtain an input–output mass balance of –146±72 Gt over the 2025 mass balance year (Fig. 5.22). This is consistent with the average input–output-derived annual mass balance over 1991–2020 of –156±80 Gt (mean ±1 std. dev). While the input–output figure is close to the climatologic average, the other two methods find below-average mass loss in 2025.

The Gravity Recovery and Climate Experiment Follow-on (GRACE-FO) satellite mission detects gravity anomalies over time to measure changes in total ice mass (Tapley et al. 2019). After eliminating peripheral ice from these observations (Colgan et al. 2015), this gravity-based method

measures a 2025 mass balance of –129±50 Gt (Fig. 5.22). This is 50% less than the average annual mass balance measured by GRACE/GRACE-FO over 2002–24 of –256±135 Gt yr^{-1} (mean ±1 std. dev.).

The Ice, Cloud, and land Elevation Satellite-2 (ICESat-2) mission measures the surface elevation change of the ice sheet over time, which is converted to mass change (Smith et al. 2023; Medley et al. 2022; Smith 2023). This elevation-based method measured a 2025 mass balance of –143±36 Gt (Fig. 5.22), consistent with the ICESat-2 annual average over 2020–24 of –143±51 Gt (mean ±1 std. dev.).

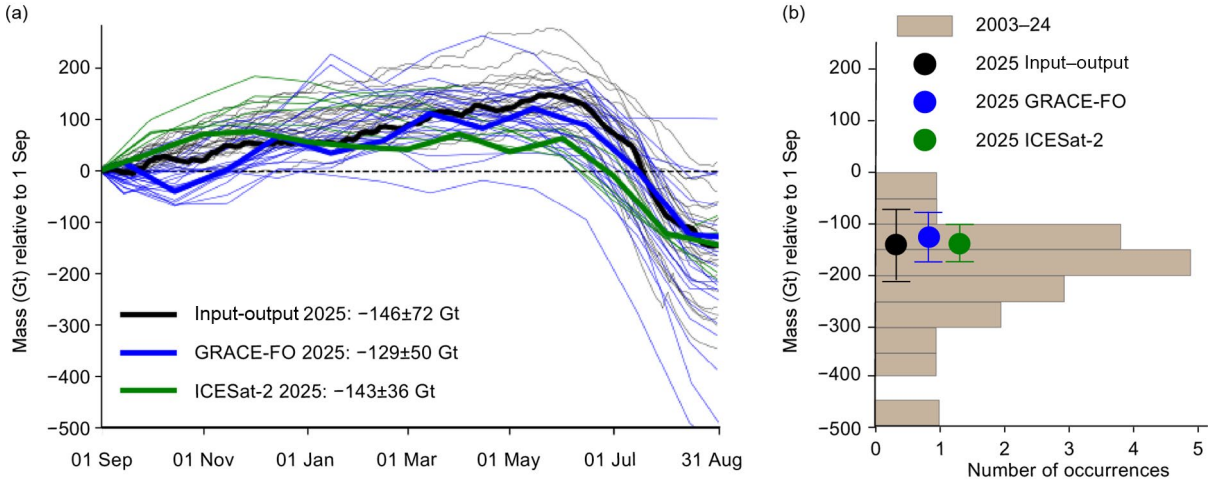

Fig. 5.22. (a) Mass balance (Gt) of the Greenland Ice Sheet over the 2025 mass balance year from the input–output method (thick black line), the Gravity Recovery and Climate Experiment Follow-On (GRACE-FO; thick blue line), and Ice, Cloud, and land Elevation Satellite-2 (ICESat-2; thick green line), with previous years (2003–24) in lighter thin lines. (b) Histogram of multi-method annual average mass balance in years from 2003 to 2024, with 2025 results from each method (by color) horizontally offset for visibility.

h. Glaciers and ice caps outside Greenland

—G. Wolken, D. Burgess, B. Wouters, L. M. Andreassen, C. Florentine, J. Kohler, B. Luks, F. Pálsson, L. Sass, L. Thomson, and T. Thorsteinsson

The Arctic represents approximately 60% of the global mountain glacier and ice cap area, excluding the Greenland and Antarctic ice sheets (RGI Consortium 2023; Fig. 5.23). Although their long-term sea level rise potential is smaller than that of the Greenland and Antarctic ice sheets, Arctic glaciers and ice caps respond more rapidly to climate variability and have been major contributors to recent sea level rise under sustained atmospheric warming (The GlaMBIE Team 2025).

Amid amplified warming at high northern latitudes (section 5c), annual mass loss from Arctic glaciers and ice caps has tripled since the mid-1990s (Zemp et al. 2019). While in situ data for the balance year 2024/25 (October 2024 to September 2025) are not yet available, observations from 2022/23 and 2023/24 reveal pronounced regional and interannual variability, even as the long-term trend continues with widespread and substantial ice loss.

Mass change in glaciers and ice caps reflects the balance between inputs, primarily snow accumulation, and outputs, including surface melt and runoff, as well as iceberg calving from tidewater- or lake-terminating glaciers. The net (total) mass balance is the difference between these processes. This assessment of 27 monitored Arctic glaciers excludes calving losses, which occur only at Kongsvegen, Hansbreen, and Devon Ice Cap (Table 5.1; Fig. 5.23). We therefore report climatic mass balance (B_{clim}): the difference between annual snow accumulation and annual runoff, expressed as mean annual thickness change (mm water equivalent, w.e.) averaged over the glacier or ice cap surface.

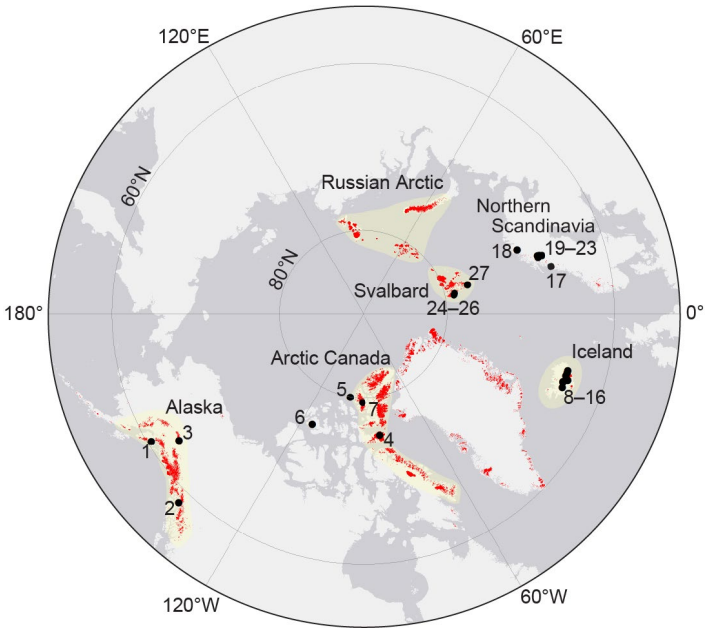

Fig. 5.23. Arctic glaciers and ice caps (red), including ice caps in Greenland that are separate from the ice sheet. Yellow shaded regions delineate the Gravity Recovery and Climate Experiment (GRACE)- and GRACE-Follow On (GRACE-FO)-derived mass anomaly domains used to estimate changes in annual glacier mass balance for heavily glacierized Arctic regions (Watkins et al. 2015; Landerer et al. 2020). Black dots indicate the 27 long-term Arctic glacier monitoring sites, with numbers linked to the glacier/ice cap names in Table 5.1. (Source: ESRI 2026.)

In balance year 2023/24, all 25 glaciers with available data (2 of the 27 lacked observations) registered negative mass balances, consistent with 2022/23 (Table 5.1; WGMS 2025). Although Alaska, Arctic Canada, and Iceland experienced negative anomalies in 2022/23, with melt increases of 27%, 112%, and 115%, respectively, melt was lower (positive anomalies) in 2023/24 relative to the 1991–2020 mean.

Losses were most extreme in Arctic Scandinavia and Svalbard, where land ice has declined sharply since 2021. Both regions recorded their most negative mass balance year on record in 2023/24 (Kjøllmoen et al. 2025; Schuler et al. 2025), with melt averaging 1473% above the 1991–2020 mean in Arctic Scandinavia and 472% above in Svalbard. This enhanced melt coincided with a persistent warm air mass over northern Scandinavia and the Barents Sea that produced record-high seasonal temperatures since the start of the record in 1950 (Ballinger et al. 2024).

The substantial scale of thinning is evident in individual glacier records. In Arctic Scandinavia, Langfjordjøkelen, and Engabreen saw their climatic mass balances decline from –1651 mm w.e. and –1101 mm w.e. in 2022/23 to –4060 mm w.e. and –3900 mm w.e. in 2023/24, respectively. In Svalbard, Midtre Lovénbreen and Austre Brøggerbreen shifted from –975 mm w.e. and –948 mm w.e. to –1968 mm w.e. and –2042 mm w.e. over the same period.

Table 5.1. Measured climatic mass balance (B_{clim}) for 27 glaciers in Alaska (3), Arctic Canada (4), Iceland (9), Arctic Scandinavia (7), and Svalbard (4): 1991–2020 mean value and standard deviation, 2022/23 value, and 2023/24 value, for each of the monitored glaciers (* indicates one or more years of data missing from the record; – indicates no data reported). Negative (positive) values for B_{clim} indicate mass loss (gain). Numbers listed in the Region column correspond to glacier locations in Fig. 5.23. Data were obtained from the World Glacier Monitoring Service (WGMS 2025) with updates from the Norwegian Water Resources and Energy Directorate (NVE) and Geological Survey of Canada. Bias corrections were applied to B_{clim} for Hofsjökull glaciers (N, E, and SW), Iceland using methods outlined in Jóhannesson et al. (2013). Regional climatic mass balances were derived as arithmetic means for all monitored glaciers within each region for each year, and these means were summed over the period of record and interpreted as cumulative mass balance changes in mm w.e.

Region	Glacier (record length, years)	B_{clim} Mean (w.e. yr^{-1}) *1991–2020*	B_{clim} Std. dev. (w.e. yr^{-1}) *1991–2020*	B_{clim} (w.e. yr^{-1}) *2022/23*	B_{clim} (w.e. yr^{-1}) *2023/24*
(1) Alaska	Wolverine (59)	–766	984	–1050	–650
(2) Alaska	Lemon Creek (72)	–1196	839	–2310	–1070
(3) Alaska	Gulkana (59)	–769	816	–400	–400
(4) Arctic Canada	Devon Ice Cap (64)	–257	215	–377	–290
(5) Arctic Canada	Meighen Ice Cap (65)	–326	432	–615	–198
(6) Arctic Canada	Melville S. Ice Cap (62)	–458	484	–1482	–300
(7) Arctic Canada	White (62)	–355	323	–653	–321
(8) Iceland	Langjökull S. Dome (28)	–1248	842*	–1430	–1005
(9) Iceland	Hofsjökull E (36)	–980	840	–1210	–580
(10) Iceland	Hofsjökull N (37)	–824	706	–1070	–730
(11) Iceland	Hofsjökull SW (36)	–956	951	–690	30
(12) Iceland	Köldukvislarjökull (33)	–467	708	–740	–80
(13) Iceland	Tungnaarjökull (33)	–1142	781*	–1529	–1370
(14) Iceland	Dyngjujökill (27)	–44	792*	–308	–50
(15) Iceland	Brúarjökull (32)	–238	622	–713	–60
(16) Iceland	Eyjabakkajökull (33)	–700	766*	–1417	–510
(17) Arctic Scandinavia	Engabreen (55)	–62	972	–1101	–3900
(18) Arctic Scandinavia	Langfjordjøkelen (34)	–953	771*	–1651	–4060
(19) Arctic Scandinavia	Marmaglaciaren (34)	–494	568*	–1256	–2573
(20) Arctic Scandinavia	Rabots (41)	–533	648*	–1565	–2804
(21) Arctic Scandinavia	Riukojietna (36)	–701	734*	–1347	–3458
(22) Arctic Scandinavia	Storglaciaren (79)	–235	747	–812	–2846
(23) Svalbard	Tarfalaglaciaren (20)	–331	1170*	–	–
(24) Svalbard	Midtre Lovénbreen (57)	–495	406	–975	–1968
(25) Svalbard	Austre Brøggerbreen (58)	–612	444	–948	–2042
(26) Svalbard	Kongsvegen (38)	–143	397	–673	–1410
(27) Svalbard	Hansbreen (33)	–419	470*	–	–

Data from 2023/24 further confirm the sustained, multi-decadal pattern of surface mass loss across the Arctic (Fig. 5.24). Since 1953, Alaska has seen the most significant cumulative thinning, with an area-averaged loss of –38 m w.e. It is followed by Arctic Scandinavia (1946) at –32 m w.e., while Iceland (1988) and Svalbard (1967) recorded losses of –29 m w.e and –27 m w.e., respectively. Arctic Canada (1960) follows with –16 m w.e. The persistence and scale of these mass losses emphasize the strong sensitivity of Arctic glaciers to climate warming and their ongoing contribution to sea level rise (Box et al. 2018).

Arctic glaciers and ice caps have been increasingly important contributors to global sea level rise since the early 1990s, but preliminary data for the 2024/25 balance year indicate that some Arctic glaciers may have shifted into net mass gain during that balance year (Fig. 5.25). Gravity anomalies from the combined The Gravity Recovery and Climate Experiment (GRACE; 2002–16) and GRACE Follow-On (GRACE-FO; 2018–25) missions indicate that Pan-Arctic glaciers and ice caps have lost mass at a rate of –178±21 Gt yr^{-1} over the full 2002–25 observational period, but mass gains in 2024/25 of 114.13±19 Gt break the pattern of sustained loss observed since 2011/12. This positive anomaly is driven primarily by regional mass gains in Alaska, Iceland, and Arctic Canada, which together outweigh the ongoing mass losses from Arctic Russia and Svalbard.

Although these initial findings remain subject to revision, Alaska was a key contributor to the 2024/25 Pan-Arctic mass gain, accounting for 97.84±37 Gt (~52.6%). This was followed by Arctic Canada at 74.32±20 Gt (~40.0%), and Iceland at 13.69±9 Gt (~7.4%). In contrast, Arctic Russia lost 52.36±17 Gt of mass (~73.0% of the Pan-Arctic mass loss), while Svalbard lost 19.36±12 Gt (~27.0%). These regional totals indicate that even during a year of overall Pan-Arctic mass gain, certain regions remain in a state of sustained retreat, reflecting the heterogeneous response of Arctic glacier systems to climate forcing.

Despite regional variability, glaciers in the Arctic are experiencing a consistent trend of cumulative mass loss. The continued loss of glacier and ice cap mass across the Arctic can be a primary indicator of climate change and societal risk (Wolken et al. 2021). The impacts of ice loss extend far beyond the cryosphere, ranging from diminishing late-season water

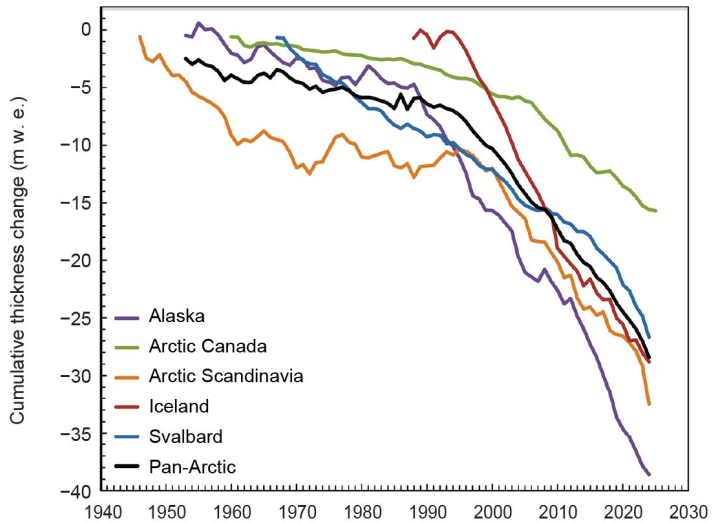

Fig. 5.24. Cumulative mass change (B_{clim}) expressed as thickness change in meters of water equivalent (m w.e.) for 27 monitored glaciers in five Arctic regions and for the Arctic as a whole (Pan-Arctic mean). Note the variable time periods over which cumulative changes are measured.

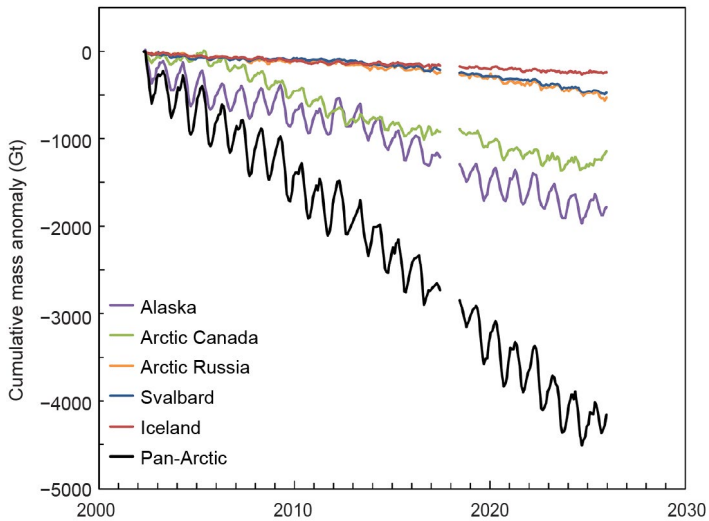

Fig. 5.25. Cumulative changes in regional total stored water (Gt) from 2002 to 2025 derived from Gravity Recovery and Climate Experiment (GRACE) and GRACE-Follow On (GRACE-FO) satellite gravimetry for the five regions shown in Fig. 5.23 and for the total of these five regions (Pan-Arctic). A Jul 2017–May 2018 data gap exists between retrieval periods. The data processing involved several steps. First, common post-corrections to the Level-2 data were applied, including the addition of degree-1 coefficients which are not directly observed by the satellites, and a correction for mass redistribution due to glacial isostatic adjustment (Wouters et al. 2019). A 150-km Gaussian smoothing filter was applied to the resulting Stokes coefficients for further noise reduction. Finally, to retrieve the mass changes for the glacier regions, the processed coefficients were converted into maps of equivalent water height anomalies using a mass concentration approach based on a global 0.5° × 0.5° grid.

supplies in communities like Ausuiktuq (Grise Fiord, Canada) to intensifying geohazards in Alaska. Examples of the latter include recurrent glacial lake outburst floods at Mendenhall Glacier and a large landslide at South Sawyer Glacier in Alaska's Tracy Arm fjord (Kienholz et al. 2020; USGS 2025). As Arctic warming persists, interconnected effects, from global sea level rise to local threats to infrastructure, public safety, and water security, highlight that these sustained observations can improve hazard assessment and support community-centered adaptation throughout the region.

i. Terrestrial snow

—L. Mudryk, A. Elias Chereque, C. Derksen, K. Luojus, and B. Decharme

Many components of the Arctic land surface are directly influenced by the presence and amount of snow cover. Reductions in snow cover directly contribute to amplified warming in the Arctic, while also affecting permafrost deterioration and ecosystem health (Brown et al. 2017; Meredith et al. 2019; Jones et al. 2011). Even following the snow cover season, the influence of spring snowmelt timing persists through impacts on river discharge timing and magnitude, surface water, soil moisture, vegetation phenology, and fire risk (Meredith et al. 2019).

Snow cover extent (SCE) anomalies from 1967 to 2025 are illustrated for both the North American and Eurasian sectors of the Arctic in Fig. 5.26 (relative to the 1991–2020 baseline; data from the NOAA Climate Data Record of Northern Hemisphere SCE; Robinson et al. 2012). In 2025, Arctic SCE was close to normal across both the Eurasian and North American sectors during May but dropped below normal by June (13th and 6th lowest by sector, respectively, in the 59-year record). Arctic snow cover extent during May and June has reduced by 15% and 50%, respectively, since 1967 (Mudryk et al. 2025), and these springtime reductions contribute substantially to an overall reduction in annual snow cover duration.

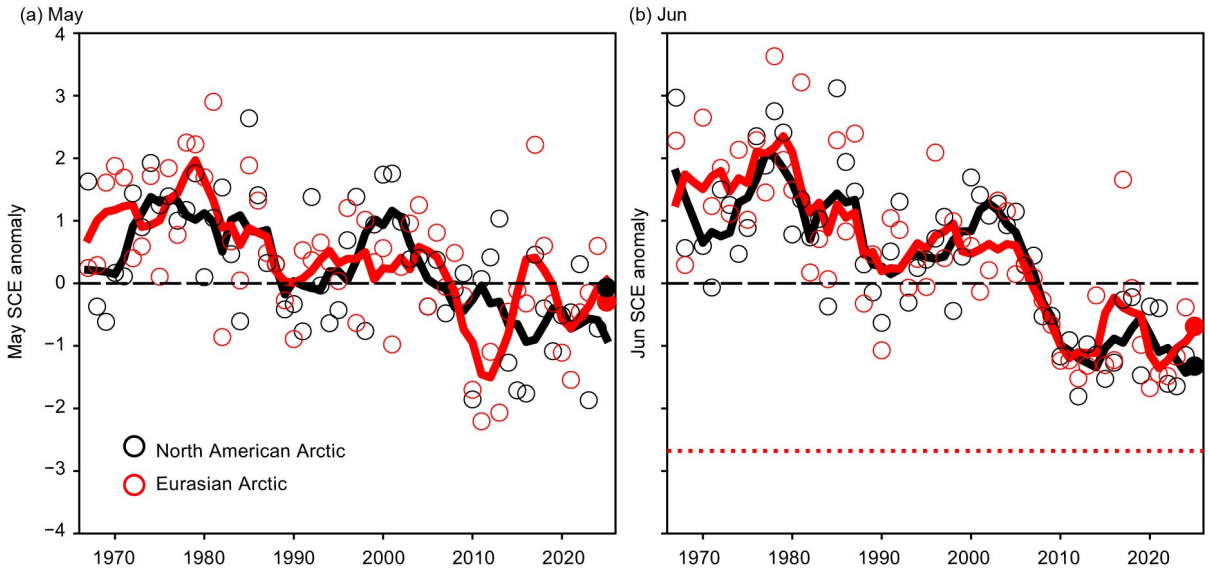

Fig. 5.26. Monthly Arctic snow cover extent anomalies for Arctic terrestrial land areas (poleward of 60°N) for (a) May and (b) Jun from 1967 to 2025 for the Eurasian (red circles) and North American (black circles) sectors. Filled circles highlight 2025 anomalies. Anomalies are relative to the 1991–2020 average and standardized (each observation differenced from the mean and divided by the standard deviation, and thus unitless). Solid black and red lines depict five-year running means for North America and Eurasia, respectively. The dotted red line illustrates the anomaly value representing zero SCE across Eurasia during Jun. The corresponding value for North America is below the plotted range at –5.4. (Source: Robinson et al. 2012.)

Snow cover duration (SCD) anomalies in 2025 are shown in Fig. 5.27 (data from the NOAA daily Interactive Multisensor Snow and Ice Mapping System [IMS] snow cover product; U.S. National Ice Center 2008). The maps illustrate the spring "melt period" at the end of the 2024/25 snow season (using data from February 2025 to July 2025; Fig. 5.27a) as well as the autumn "onset period" of the following 2025/26 snow season (using data from August 2025 to January 2026; Fig. 5.27b). Combining these periods describes the length of the snow-free period during summer 2025 (Fig. 5.27c). Snow melt timing in spring 2025 was earlier than normal over northern Europe and eastern Siberia, but later than normal over the intervening Arctic region (Ural and central Siberian regions). Across the North American Arctic, melt was later than normal over the western parts of the region but earlier than normal over the central and eastern parts. In autumn 2025, snow onset was later than normal in western Eurasia and earlier than normal in eastern Eurasia. Across North America, snow onset was earlier than normal in the northernmost Arctic and parts of Alaska but later than normal over the southern Canadian Arctic. For the regions of western Eurasia and the southern Canadian Arctic, earlier melt in spring and late onset in autumn combined to produce one of the longest summer snow-free periods in the available record (Fig. 5.27c).

Finally, snow water equivalent (SWE), a measure of snowpack amount, is used to characterize Arctic snow accumulation over the 2024/25 season. Maps of SWE anomalies are shown in Fig. 5.28 for April–June 2025. In April, the majority of Arctic land areas on both continents had positive SWE anomalies, indicating higher-than-normal snowfall accumulations since the preceding autumn (April is the approximate month that total snow mass across the terrestrial pan-Arctic region peaks before increasing temperatures in May and June lead to melt). The higher-than-normal SWE anomalies over much of the Arctic in May were aligned with near-normal SCE also seen during May. The exception to higher-than-normal SWE are the low values found in both April and May over parts of northern Europe and subarctic regions farther south, consistent with the earlier-than-normal spring melt timing across the same regions (Fig. 5.27a). By June, the SWE across much of the rest of Eurasia was also gone, consistent with lower-than-normal June SCE anomalies (Fig. 5.26). For North America during June, the western portion of the Canadian Arctic Archipelago had strongly above-normal SWE, while in the eastern portion and Baffin Island SWE was below normal.

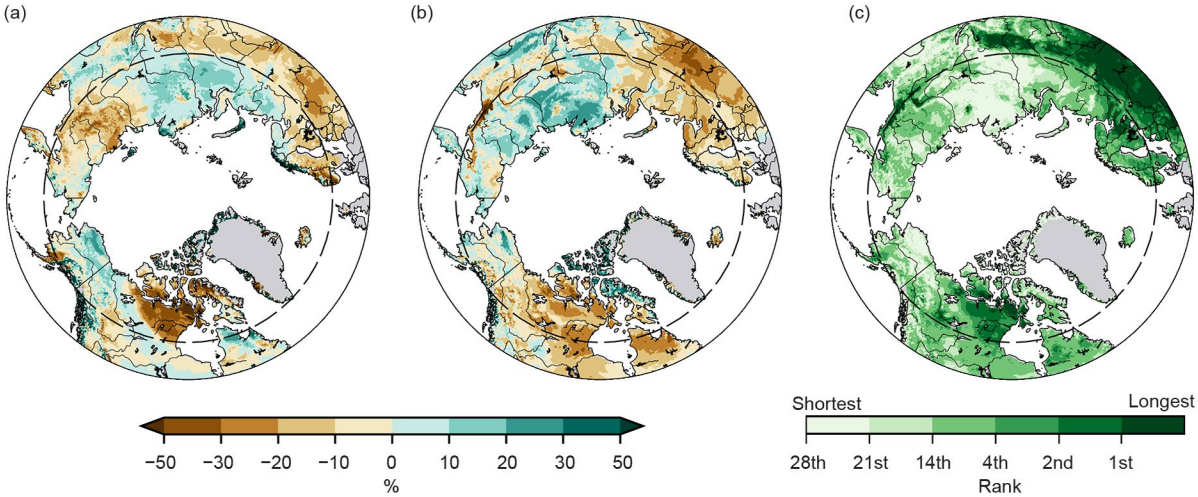

Fig. 5.27. Snow cover duration (SCD) anomalies (% difference relative to climatological number of snow-free days for the 1998/99–2022/23 baseline): (a) spring snow melt (Feb–Jul 2025) and (b) autumn snow onset (Aug 2025–Jan 2026). In both (a) and (b), brown (blue) indicates decreases (increases) in the number of days with snow cover. In (a) these changes are aligned with earlier (later) melt at the end of the snow season while in (b) these changes are aligned with a later (earlier) start to the snow season. Ranks in (c) illustrate how the duration of the summer 2025 snow-free period varied over the Arctic. The dashed circle marks the latitude 60°N. (Source: U.S. National Ice Center 2008.)

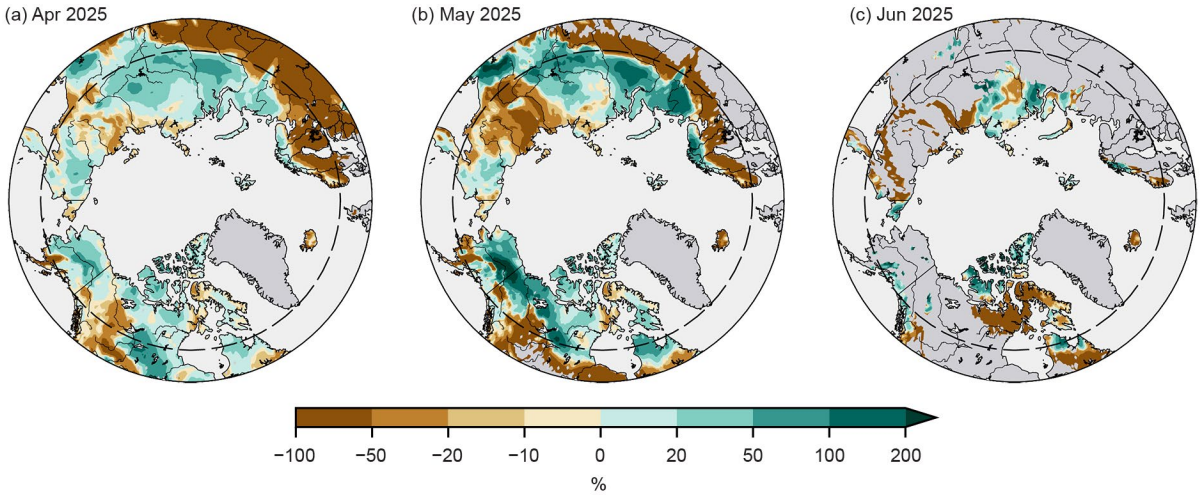

Fig. 5.28. Snow water equivalent (SWE) anomalies (% difference from the 1991–2020 baseline) in 2025 for (a) Apr, (b) May, and (c) Jun. Brown (green) indicates lower (higher) snow amounts than average. Latitude 60°N is marked by the black dashed circle. (Source: Selection of four SWE products from Snow Climate Change Initiative [CCI]; Luojus et al. 2022; MERRA-2 [GMAO 2015]; ERA5-Land [Muñoz Sabater 2019]; and Crocus-ERA5 [Decharme et al. 2024].)

j. Terrestrial permafrost

—S. L. Smith, V. E. Romanovsky, K. Isaksen, K. E. Nyland, D. A. Streletskiy, and H. H. Christiansen

Permafrost refers to earth materials (e.g., bedrock, mineral soil, organic matter) that remain at or below 0°C for at least two consecutive years, although most permafrost has existed for centuries to many millennia. Extensive regions of high-latitude landscapes are underlain by permafrost. The active layer, which thaws and refreezes annually, overlies the permafrost. Warming of permafrost, active layer thickening, and ground ice melt cause changes in surface topography, hydrology, and landscape stability, with implications for Arctic infrastructure, ecosystem integrity, and human livelihoods (Hjort et al. 2022; Smith et al. 2022; Burn et al. 2025). Changes in permafrost conditions also affect the rate of greenhouse gas release to the atmosphere, potentially accelerating global warming (Miner et al. 2022; Schuur et al. 2022).

Permafrost conditions respond to shifts in the surface energy balance through interrelated changes in ground temperature and active layer thickness (ALT). Ground temperatures fluctuate seasonally near the surface, while below the depth of seasonal temperature variation, they reflect longer-term climate. Long-term changes in permafrost temperatures are driven by changes in air temperature but also are influenced by local variability in snow cover, vegetation characteristics, and soil moisture (Romanovsky et al. 2017; Smith et al. 2022). Monitoring sites across the Arctic (Fig. 5.29) have recorded ground temperature in the upper 30 m for up to five decades, providing critical data on changes in permafrost conditions. Observed changes in ALT are more reflective of shorter-term (year-to-year) influences and are especially sensitive to changes in summer air temperature and precipitation.

Since the 1980s, permafrost temperatures have continued to increase on a decadal scale across the Arctic. Greater increases are generally observed in colder permafrost (temperature <–2°C) at higher latitudes (Smith et al. 2022, 2025; see also section 2c1), partly due to greater increases in air temperature (Figs. 5.29, 5.30). Positive ALT trends over the last 30 years (Fig. 5.31) are evident in all permafrost regions examined, but are more muted for the Alaskan North Slope, northwestern Canada, and East Siberia (Smith et al. 2025). However, the lack of permafrost temperature data and limited ALT measurements for the Russian Arctic since 2022 have resulted in a regional gap in the assessment of the current state and recent trends of Arctic permafrost.

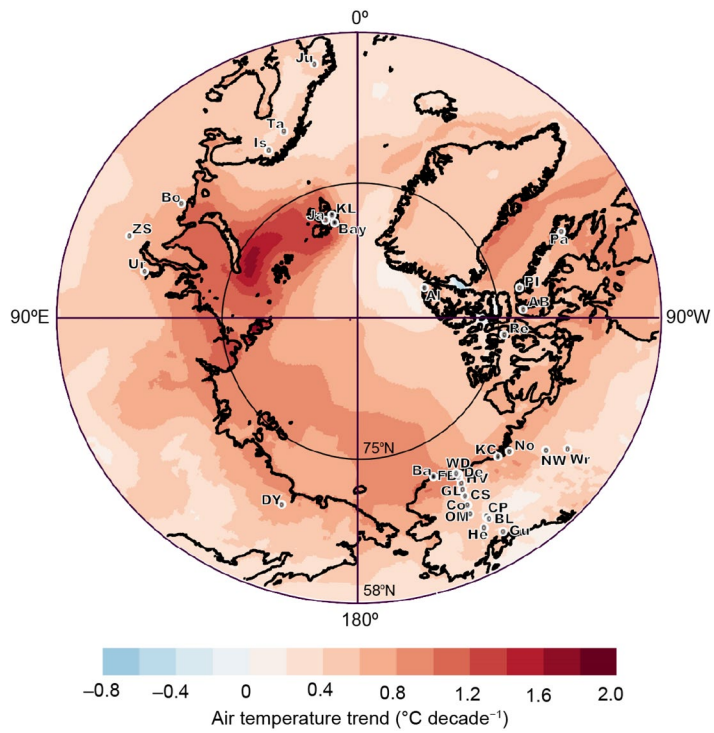

Fig. 5.29. Locations of the permafrost temperature monitoring sites (for which data are shown in Fig. 5.30) superimposed on annual average surface air temperature trends (°C decade^{-1}) for the period 1981–2025 from ERA5 (Hersbach et al. 2020; data available at https://cds.climate.copernicus.eu), which largely covers the period of record for permafrost monitoring. See Table 5.2 for site names. Information about these sites is available at http://gtnpdatabase.org/ and https://permafrost.gi.alaska.edu/sites_map.

1. PERMAFROST TEMPERATURE

Permafrost temperatures in 2025 were the highest on record at 15 of 24 sites reporting (Table 5.2). In North America, record temperatures were observed at 11 of 19 sites reporting. Seventeen of the North American sites, where there were sufficient data, had higher temperatures in 2025 compared to 2024, including all sites reporting for the Beaufort-Chukchi region, reflecting the higher air temperatures in 2023/24 following a short cooling period (Figs. 5.30a,b). For discontinuous permafrost in Alaska and northwestern Canada, permafrost in 2025 was warmer than in 2024 at all seven sites with sufficient data (Fig. 5.30b), with record temperatures at five sites. Record-high temperatures were observed at two of the four sites reporting in the eastern and high Canadian

Arctic (Fig. 5.30c). At the Nordic sites within the Barents region, permafrost temperatures in 2025 reached record highs at all reporting locations, except for one in southern Norway (Table 5.2; Fig. 5.30d).

Throughout the Arctic, warming of permafrost with temperatures near 0°C (temperatures >–2°C) is slower (generally <0.2°C decade^{-1}) than colder permafrost sites due to latent heat effects related to melting ground ice. At cold continuous permafrost sites in the Beaufort-Chukchi region, permafrost temperatures have increased by 0.4°C–0.8°C decade^{-1} with similar increases (up to 1°C decade^{-1}) for the four sites reporting in 2025 in the eastern and high Canadian Arctic (Figs. 5.30a,c; Table 5.2). In Svalbard, permafrost has warmed by up to 0.7°C decade^{-1} (Fig. 5.30d; Table 5.2) with significant warming detected down to a depth of 100 m (Isaksen et al. 2022). In Scandinavia's discontinuous permafrost regions, warming continues at rates of 0.2°C–0.5°C decade^{-1} (Fig. 5.30d; Table 5.2), with thawing observed to 22-m depth at Iskoras (Isaksen et al. 2022). Similar rates are observed in the discontinuous permafrost region of northwestern North America (Fig. 5.30b; Smith et al. 2024, 2025).

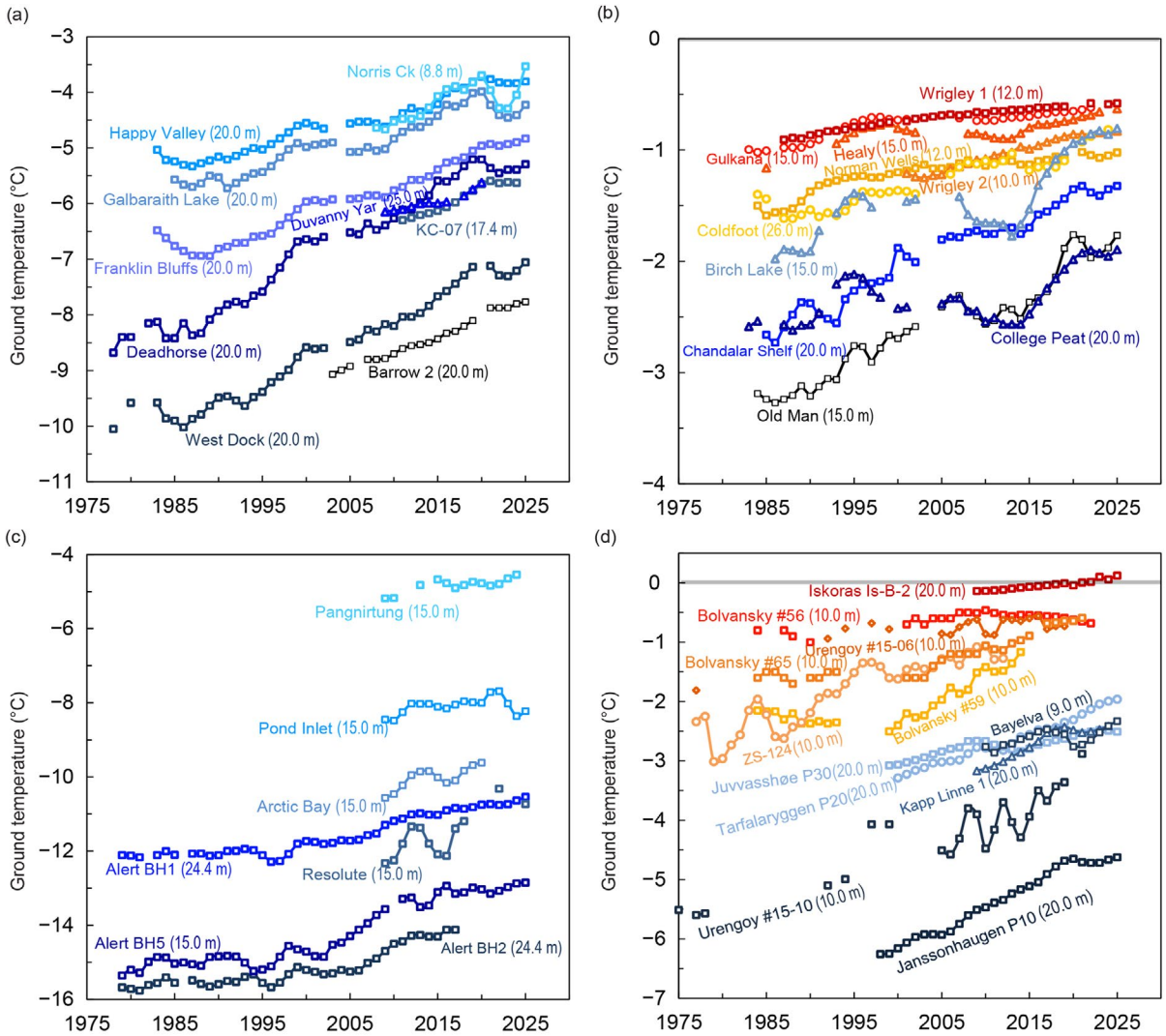

Fig. 5.30. Time series of mean annual ground temperature (°C) at depths of 9 m–25 m below the ground surface at selected measurement sites that fall roughly into the Adaptation Actions for a Changing Arctic priority regions (see Romanovsky et al. 2017): (a) cold continuous permafrost of northwestern North America and northeastern East Siberia (Beaufort–Chukchi region); (b) discontinuous permafrost in Alaska and northwestern Canada; (c) cold continuous permafrost in the eastern and high Arctic Canada (Baffin Davis Strait); and (d) continuous to discontinuous permafrost in Scandinavia, Svalbard, and Russia/Siberia (Barents regions). Temperatures are measured at or near the depth of zero annual amplitude, where the seasonal ground temperature variations are less than 0.1°C. Note differences in y-axis value ranges. Borehole locations are shown in Fig. 5.29 (data are updated from Smith et al. 2025).

Table 5.2. Rate of change in mean annual ground temperature (°C decade^{-1}) for permafrost monitoring sites shown in Fig. 5.29. The periods of record are shown in parentheses below the rates of change. For sites where measurements began prior to 2000, the rate of change for the entire available record and the period after 2000 are provided. Stations with record-high 2025 temperatures are indicated with a thermometer icon (🌡) and are underlined. Asterisks denote sites not reporting in 2025. Regions correspond to those shown in Fig. 5.29.

Region	Site	Entire Record	Since 2000
Northeast Siberia *(Beaufort–Chukchi Region)*	Duvany Yar (DY)*	NA	+0.4 (2009–20)
Alaskan Arctic plain *(Beaufort–Chukchi Region)*	West Dock (WD) 🌡, Deadhorse (De), Franklin Bluffs (FB) 🌡, Barrow (Ba) 🌡	+0.5 to +0.8 (1978–2025)	+0.5 to +0.7 (2000–25)
Northern foothills of the Brooks Range, Alaska *(Beaufort–Chukchi Region)*	Happy Valley (HV), Galbraith Lake (GL)	+0.4 (1983–2025)	+0.4 (2000–25)
Northern Mackenzie Valley *(Beaufort–Chukchi Region)*	Norris Ck (No) 🌡, KC-07 (KC)*	NA	+0.5 to +0.6 (2008–25)
Southern foothills of the Brooks Range, Alaska *(Discontinuous permafrost: Alaska and northwestern Canada)*	Coldfoot (Co)*, Chandalar Shelf (CS) 🌡, Old Man (OM)	+0.2 to +0.4 (1983–2025)	+0.2 to +0.4 (2000–25)
Interior Alaska *(Discontinuous Permafrost: Alaska and northwestern Canada)*	College Peat (CP) 🌡, Birch Lake (BL) 🌡, Gulkana (Gu)*, Healy (He) 🌡	+0.1 to +0.2 (1983–2025)	<+0.05 to +0.4 (2000–25)
Central Mackenzie Valley *(Discontinuous Permafrost: Alaska and northwestern Canada)*	Norman Wells (NW), Wrigley (Wr1, Wr2 🌡)	+0.1 (1984–2025)	+0.1 to +0.2 (2000–25)
Baffin Island *(Baffin Davis Strait region)*	Pangnirtung (Pa)*, Pond Inlet (PI)	NA	+0.2 to +0.3 (2009–25)
High Canadian Arctic *(Baffin Davis Strait region)*	Resolute (Re)	NA	+1.0 (2009–25)
High Canadian Arctic *(Baffin Davis Strait region)*	Alert (Al) @ 15 m 🌡, Alert (Al) @ 24 m 🌡	+0.6, +0.4 (1979–2025)	+0.8, +0.5 (2000–25)
Northwest Siberia *(Barents region)*	Urengoy 15-06* and 15-08* (Ur)	+0.2 to +0.5 (1974–2021)	+0.1 to +0.8 (2005–21)
Russian European North *(Barents region)*	Bolvansky 56* and 65* (Bo)	+0.1 to +0.3 (1984–2022)	0 to +0.5 (2001–22)
Svalbard *(Barents region)*	Janssonhaugen (Ja) 🌡, Bayelva (Bay) 🌡, Kapp Linne 1 (KL)*	+0.7 (1998–2025)	+0.1 to +0.7 (2000–25)
Northern Scandinavia *(Barents region)*	Tarfalarggen (Ta) 🌡, Iskoras Is-B-2 (Is) 🌡	NA	+0.1 to +0.5 (2000–25)
Southern Norway *(Barents region)*	Juvvasshøe (Ju)	+0.2 (1999–2025)	+0.2 (2000–25)

2. ACTIVE LAYER THICKNESS

Active layer thickness is measured directly using thaw tubes, inferred from mechanically probing at the end of the thaw season or by using interpolation of borehole temperatures to determine the maximum seasonal depth of the 0°C isotherm (Irrgang et al. 2025). Regional ALT trends presented (Fig. 5.31) are based primarily on spatially distributed mechanical probing across representative permafrost landscapes.

The highest long-term (1996–2025) rates of ALT increases are 0.19 m decade^{-1} and 0.15 m decade^{-1} observed in the Alaskan Interior and West Siberia, respectively. The 2025 data continue these trends with ALT values well above the 2009–18 mean for both regions. Record-high ALT anomalies were observed in 2025 in the Alaskan Interior and at bedrock sites in Svalbard.

ALT records from sites at the North Slope of Alaska, Greenland, northwest Canada, Russian European North, and East Siberia indicate no significant changes over the last five years. This can be partly attributed to subsidence associated with thaw propagation into ice-rich ground, therefore suggesting the underestimation of ice-rich permafrost thaw inferred from ALT records (O'Neill et al. 2023; Nyland et al. 2021; Streletskiy et al. 2025).

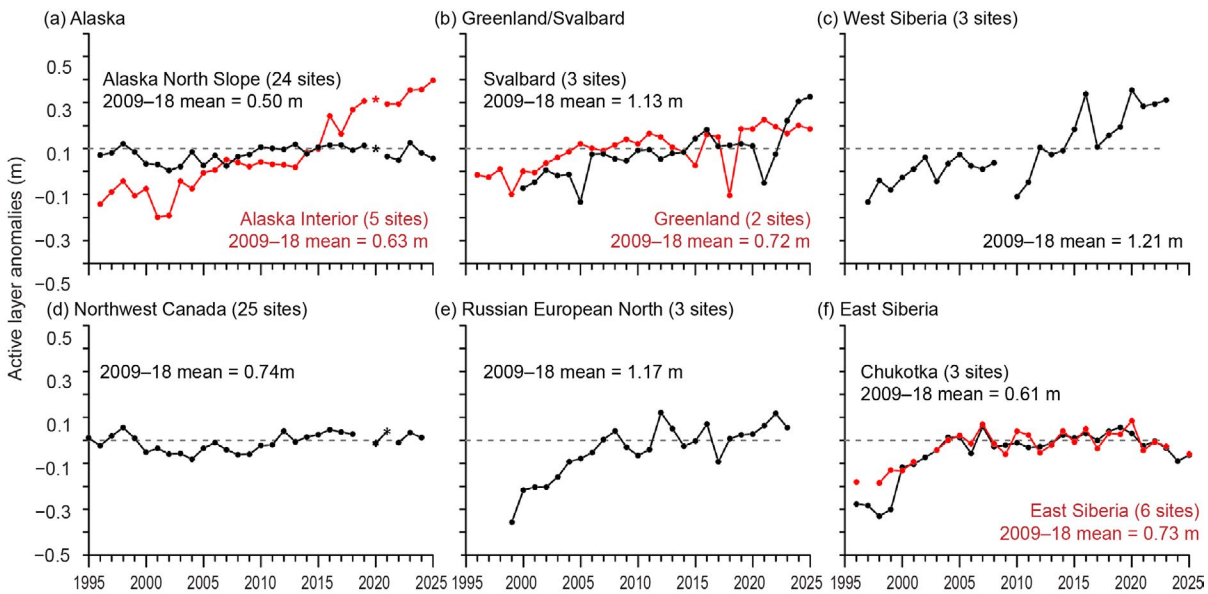

Fig. 5.31. Average annual active layer thickness (ALT) anomalies (m), relative to the 2009–18 mean, for six Arctic regions observed at the Circumpolar Active Layer Monitoring program sites with >20-years of continuous thaw depth observations from the end of the thaw season. Positive and negative anomalies indicate thicker or thinner ALT than the 10-yr reference, respectively. Asterisks represent atypical observations, for example, due to pandemic-related restrictions. Canadian ALT is derived from thaw tubes that record the maximum thaw depth over the previous year. Since Canadian sites were not visited in 2020 and 2021, the maximum thaw depth recorded during the 2022 visit could have occurred any summer from 2019 through 2021, although the data point is plotted in 2021. Only one site reported 2025 data from West and East Siberia, and none from the Russian European North. Additionally, 2023/24 measurements are based on only one Russian European North site. Site-specific data and metadata are available at www2.gwu.edu/~calm/.

Sidebar 5.2: **The Arctic carbon cycle**

—E. A. G. SCHUUR AND S. M. NATALI

The Arctic, in the broad sense of the term including the areas of northern continuous and discontinuous permafrost zones characterized by cryosphere elements (Meredith et al. 2019), has the potential to accelerate climate change by adding carbon dioxide (CO_2) and methane (CH_4) to the atmosphere in response to warming induced by human fossil fuel use and land use change (Schuur et al. 2015; Stroeve et al. 2025). A key research question is whether this climate feedback is already taking place and, if so, at what magnitude (Canadell et al. 2021). New evidence has been synthesized from networks of ground-based eddy covariance and chamber CO_2 and CH_4 exchange measurements (Vogt et al. 2025). Permafrost region soils contain organic carbon, the accumulated remains of past ecosystems that re-enters the modern carbon cycle when decomposed and emitted by microbes as CO_2 and CH_4 (Schuur et al. 2023). This can be offset, in part, by carbon uptake via increased plant growth that eventually ends up re-accumulating as surface soil organic matter (Frost et al. 2025a).

Carbon exchange measurements record the ecosystem carbon balance (net gain or loss of plant and soil carbon pools), which is the relatively small difference between large opposing fluxes: plant CO_2 uptake via plant photosynthesis and growth versus respiratory CO_2 loss via metabolism by most living organisms. In the case of net ecosystem CH_4 exchange, it is microbial CH_4 consumption in aerobic soil environments offsetting microbial CH_4 production in anaerobic environments typical of waterlogged soils, wetlands, and lake sediments (Parmentier et al. 2024; Saunois et al. 2025). Methane exchange is a much smaller amount by weight than CO_2 and consequently does not greatly alter ecosystem carbon balance at the landscape scale. But the larger warming potential of CH_4 means that changing emissions can affect climate at a similar magnitude as CO_2 (Schuur et al. 2022). While very few individual sites have monitored carbon exchange over long time periods, combining measurements across study sites has created a merged database and synthetic time series that can be analyzed for decadal-scale, site-based trends for CO_2 (See et al. 2024). Synthesized site-based carbon exchange measurements can also be scaled with environmental information to produce regional estimates for CO_2 and CH_4 (Ramage et al. 2024; Kuhn et al. 2025) and regional trends for CO_2 (Virkkala et al. 2025). When this is done, physical disturbances, such as fire and abrupt permafrost thaw that might occur away from carbon flux measurement sites, must also be considered as pathways of regional carbon exchange, as well as ecosystem types, such as inland waters that are sometimes less well represented by the ground-based measurement network.

New analyses of these merged databases suggest that tundra and boreal forest ecosystems in the northern permafrost region acted as an annual net CO_2 sink (–0.340 Pg C yr^{-1}; negative numbers indicate net ecosystem carbon accumulation), the balance of ecosystem carbon uptake and release averaged over the past several decades (2000–20) and scaled to the region (Ramage et al. 2024). When CO_2 outgassing from rivers and lakes are included into the budget along with fires, the region switches to a small net CO_2 source to the atmosphere (+0.012 Pg C yr^{-1}; positive numbers indicate net atmosphere carbon accumulation). This source strength is larger (+0.106 Pg C yr^{-1}) when lateral river carbon export is included, which is another source of carbon loss from the region. The effect of northern ecosystems on climate change is less about whether the region acts as a net carbon source/sink overall, but rather, on the change in source/sink strength over time that is induced by warming. At the same time, if this region was acting as a persistent net carbon source of CO_2 to the atmosphere over years to decades, it would be an unequivocal signal of departure from long-term patterns as a regional sink that served to accumulate and store permafrost carbon in the Arctic over the recent centuries to millennia (Lindgren et al. 2018).

A related analysis of the merged dataset supported the conclusion that tundra and boreal ecosystems scaled to the permafrost region acted as an annual net CO_2 sink (–0.249 Pg C yr^{-1}), and that this sink was almost entirely reversed when only fire emissions were added (–0.02 Pg C yr^{-1}), bringing these two components essentially to carbon neutral with respect to the atmosphere (Virkkala et al. 2025; Fig. SB5.3). Furthermore, the carbon sink trend over time of tundra and boreal forest that was shown to be increasing from 2000 to 2021 by an additional –0.009 Pg C yr^{-1} was erased when emissions by fires were included. This analysis also demonstrated a clear spatial pattern where the strongest net carbon sink ecosystems were farther south in the boreal biome whereas more than 30% of the tundra ecosystems to the north were acting as carbon sources, averaged over the 2001–20 period. The spatial covariance with fluxes means that the larger the northern land region considered, the larger the carbon sink strength as forests in the southern margin of the boreal biome responding to warming and CO_2 fertilization were masking carbon losses from tundra farther to the north. Indeed, the pattern of increasing growth and carbon sink strength in the summer growing season were found to be completely offset by increasing winter carbon emissions in ecosystems directly underlain by permafrost (See et al. 2024). This contrasted with non-permafrost ecosystems where trends of increasing annual net carbon sink over time matched summer patterns.

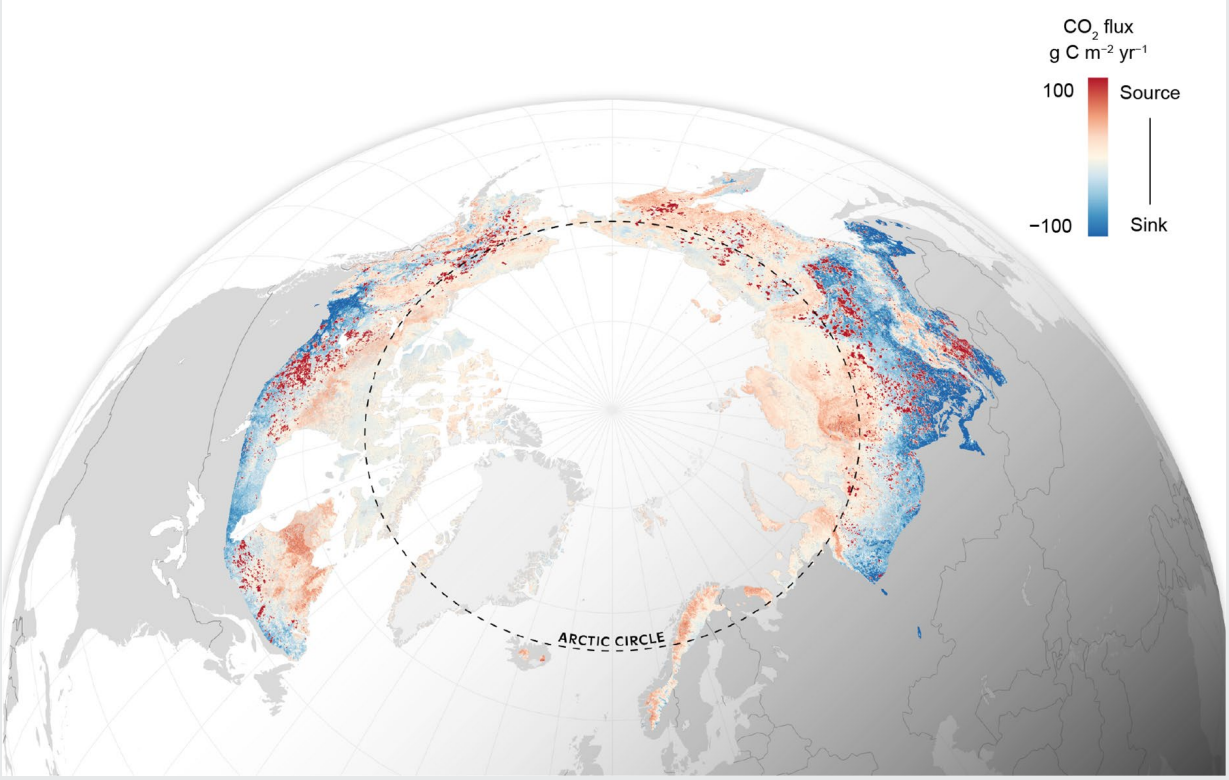

Fig. SB5.3. Terrestrial ecosystem carbon dioxide (CO_2) fluxes with direct fire emissions (red shading) for the northern permafrost region (2002–20 average). Areas that are CO_2 sources are shown in pink and red and CO_2 sinks are shown in blue (Natali et al. 2024).

These analyses have looked backwards at tundra and boreal ecosystem carbon fluxes over the past two decades. One of the grand challenges for Arctic carbon research has been to provide near real-time snapshots of carbon fluxes to understand how unprecedented environmental conditions observed right now in the region influence the carbon feedback to climate. Recent work has produced annual Arctic carbon updates for 2024 and 2025 by analyzing monthly carbon exchange across a snapshot of U.S. and European-based observatories that were able to provide near real-time carbon flux information in the year that it was collected (Falvo et al. 2025, 2026). Both 2024 and 2025 had record-warm winter conditions across the Arctic region, and dynamic patterns of precipitation. In 2024, a record number of monthly emission values were observed for CO_2 in the winter for both tundra and boreal sites, beyond the number expected by chance (Fig. SB5.4). CO_2 uptake was observed in the growing season for both tundra and boreal sites compensating for winter emissions, but uptake did not set more records than expected in 2024. The pattern of carbon cycle amplification, increased uptake and increased loss, has been observed in decadal-scale patterns from the merged dataset across the region (See et al. 2024). Methane observations from the near real-time analysis were from a more limited subset of sites as compared to CO_2 and there were more monthly emissions records than expected during winter in the 2024 analysis. Near real-time CO_2 and CH_4 measurements provide society immediate knowledge about the speed and strength of the Arctic carbon feedback to climate (Natali et al. 2021). Near real-time CO_2 and CH_4 measurements provide information about the speed and strength of Arctic carbon-cycle feedbacks to climate (Natali et al. 2021). These observations contribute to our understanding of how Arctic emissions affect the global carbon budget and influence projections associated with future temperature targets.

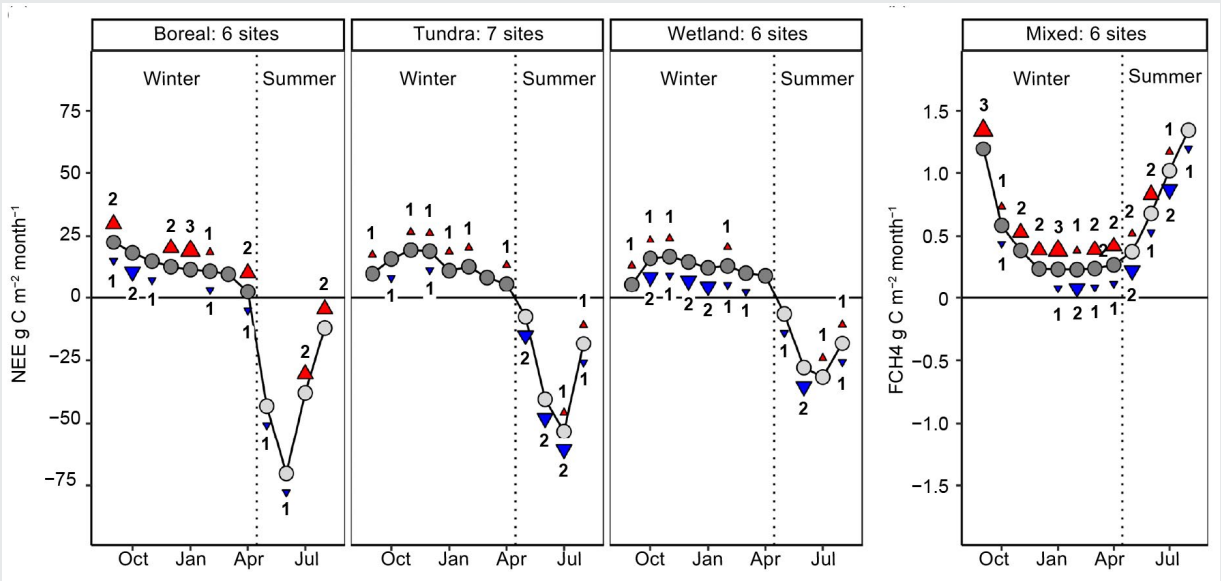

Fig. SB5.4. (a) Net carbon dioxide (NEE g C m^{-2} $month^{-1}$) and (b) methane fluxes (FCH_4 g C m^{-2} $month^{-1}$) and their records for Sep 2023–Aug 2024. Points denote the monthly mean flux grouped by ecosystem type (for carbon dioxide) or grouped across sites (for methane). Record-high and record-low observations of each month are highlighted with upward facing red triangles and downward facing blue triangles, respectively. The size of the triangles and the numbers denote the number of sites with a record flux observed in that month. Positive values indicate net release from the ecosystem to the atmosphere, and negative values indicate a net uptake from the atmosphere to the ecosystem (Falvo et al. 2026).

k. Tundra greenness

—G. V. Frost, M. J. Macander, U. S. Bhatt, L. T. Berner, J. W. Bjerke, H. E. Epstein, B. C. Forbes, G. Jia, M. J. Lara, E. López-Blanco, P. M. Montesano, R. Í. Magnússon, C. S. R. Neigh, K. M. Orndahl, G. K. Phoenix, H. Tømmervik, C. Waigl, D. A. Walker, and D. Yang

The Arctic tundra biome occupies Earth's northernmost lands, collectively encompassing a 5.1 million km^2 region bound by the Arctic Ocean to the north and the boreal forest biome to the south (Raynolds et al. 2019). While Arctic tundra ecosystems are treeless and lack the vertical structure of forests, they are very heterogeneous across multiple spatial scales, ranging from large-scale latitudinal climate gradients to local-scale gradients of soil, hydrological, and permafrost conditions (Fig. 5.32). In recent decades, the Arctic has warmed dramatically,

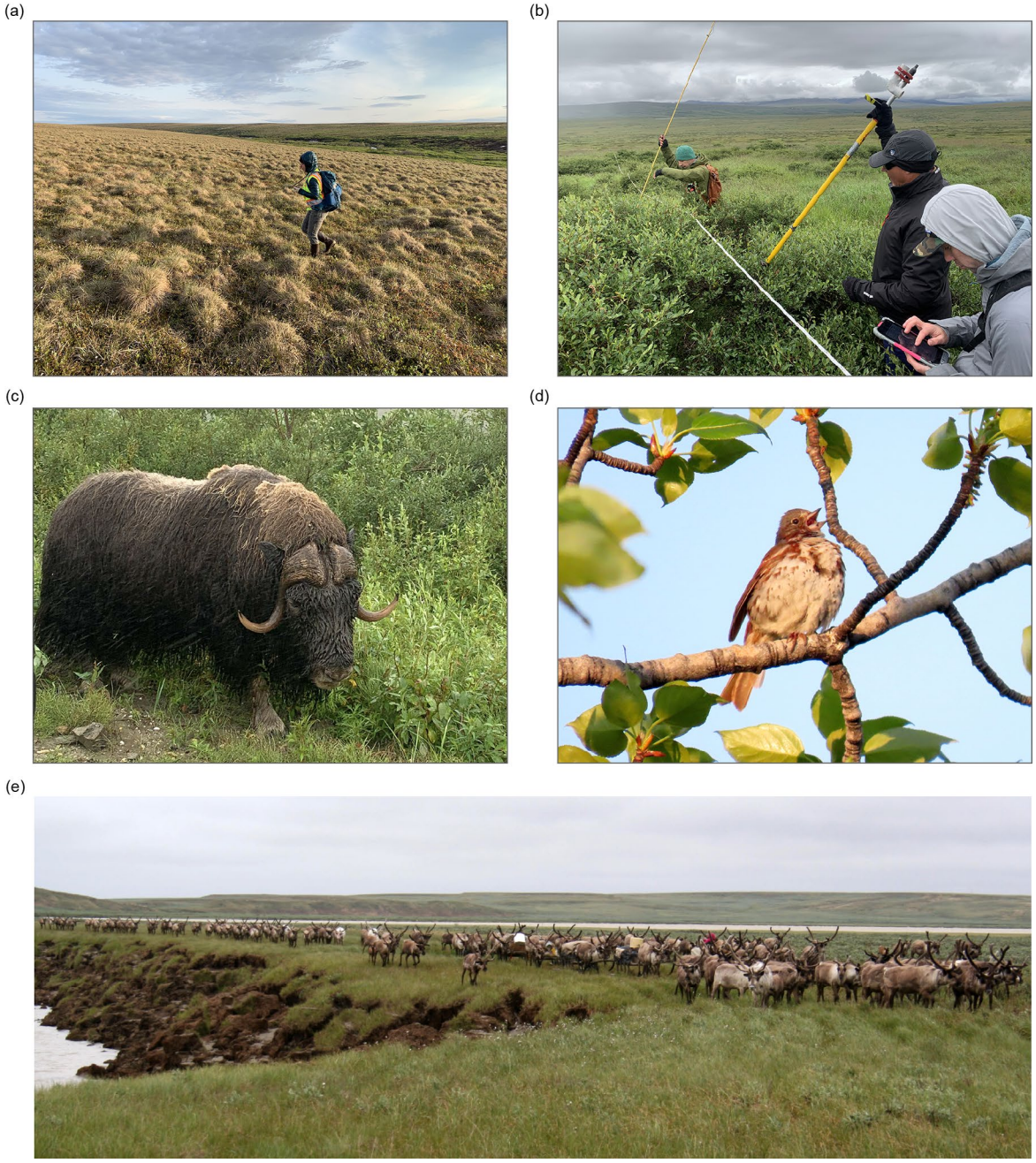

Fig. 5.32. Arctic tundra ecosystems are generally dominated by low-growing shrubs, herbs, and nonvascular plants, as seen in a tussock tundra community in northwestern Alaska (upper left). However, canopy-forming shrubs have been expanding in many Arctic regions and have become a focus of Arctic ecological research (upper right). Shrub increase has large implications for Arctic landscape processes, land–atmosphere interactions, permafrost dynamics, and wildlife including iconic Arctic mammals such as muskox (middle left). The increased vertical structure provided by shrubs has been a primary mechanism for "borealization," the northward expansion of boreal forest species such as Fox Sparrow (middle right). Interactions between changing Arctic ecosystems, traditional reindeer herding, and industrial development have led to complex changes in northwest Siberian tundra ecosystems (bottom).

far exceeding the global rate of warming (section 5c) and placing the circumpolar region at the forefront of global climate and environmental change (Rantanen et al. 2022). Today, the circumpolar region lies at the crossroads of multiple feedback mechanisms that connect the living Arctic with a warming climate, declining sea ice extent, changes in seasonal snow cover, permafrost thaw, and the global carbon cycle (Bartsch et al. 2025; Aalto et al. 2026; sections 5d,f,i,j; SB5.2). Some of the most compelling evidence of broad-scale changes in this expansive region comes from long-term satellite observations beginning in the early 1980s. By the late 1990s, Earth-observing satellites began to detect a sharp increase in the productivity of tundra vegetation, a phenomenon known today as "the greening of the Arctic."

The era of global spaceborne monitoring of vegetation began in late 1981 with a series of satellites equipped with the Advanced Very High Resolution Radiometer (AVHRR). Beginning in 2000, the circumpolar AVHRR record has been complemented by more modern sensors with improved calibration and spatial resolution, including the Moderate Resolution Imaging Spectroradiometer (MODIS) and the long-running series of Landsat satellites. Although AVHRR remains operational, the raw data require extensive processing, and the AVHRR-derived Global Inventory Modeling and Mapping Studies 3g V1.2 dataset (GIMMS-3g+) that long underpinned Arctic vegetation monitoring is no longer funded. MODIS is nearing the end of service, but continuity of this important record will be maintained by the Visible Infrared Imaging Radiometer Suite (VIIRS) sensor, first launched in 2011. Data from all of these sensors support monitoring of global vegetation greenness using the Normalized Difference Vegetation Index (NDVI), a spectral metric that exploits the unique way in which green vegetation absorbs and reflects visible and infrared light. Here, the ongoing phenomenon of Arctic greening and its pan-Arctic spatial variability are reported based on all four satellite records, with emphasis on the MODIS dataset.

Although the legacy GIMMS-3g+ dataset is no longer maintained, we include it here because of its longevity (1982–2024) with a spatial resolution of approximately 8 km (Pinzon et al. 2023). For MODIS, trends were computed by combining 16-day NDVI products from the *Terra* (MOD13A1, version 6.1) and *Aqua* (MYD13A1, version 6.1) satellites (Didan 2021a,b), referred to as MODIS MCD13A1, at a spatial resolution of 500 m. For VIIRS, the recently reprocessed VNP13A1 dataset (version 2; Román et al. 2024) was used. Landsat provides observations at a much higher spatial resolution (30 m); greenness time series from Landsat Collection 2 (Crawford et al. 2023) were calculated following the methods of Berner and Goetz (2022). All data were masked to the extent of the Circumpolar Arctic Vegetation Map (Raynolds et al. 2019), excluding permanent ice and water. For all records, the trends of annual Maximum NDVI (MaxNDVI), the peak greenness value observed in midsummer, are summarized. MaxNDVI is a strong indicator of aboveground biomass and is sensitive to disturbance, successional processes, and long-term shifts in vegetation structure.

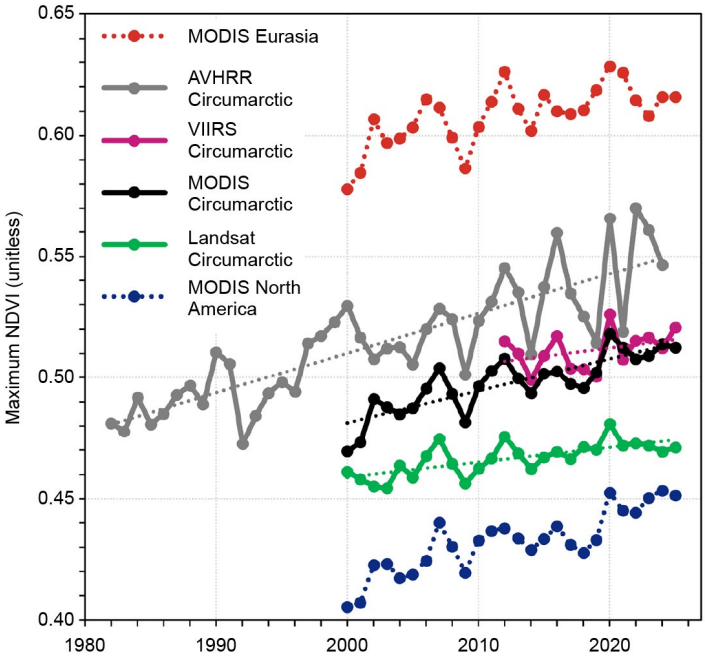

Fig. 5.33. Time series of circumpolar mean Maximum Normalized Difference Vegetation Index (MaxNDVI) from (now terminated) Advanced Very High-Resolution Radiometer (AVHRR) Global Inventory Modeling and Mapping Studies third generation (GIMMS-3g+; 1982–2024; gray), Moderate Resolution Imaging Spectroradiometer (MODIS) MCD13A1 (2000–25; black) Landsat Collection 2 (2000–25; green), and the Visible Infrared Imaging Radiometer Suite (VIIRS) VNP13A1 (2011–25; pink), with trendlines fitted using ordinary least squares linear regression. The MODIS record is further divided by continent for Arctic Eurasia (dotted red) and North America (dotted blue).

In 2025, the MODIS-observed circumpolar mean MaxNDVI was nearly identical to that in 2024 (−0.2%) and ranked as the third highest in the sensor's 26-year record. This continued a sequence of record- or near-record-high values that began in 2020, with the five highest MaxNDVI values occurring since that year (Fig. 5.33). Tundra greenness was much higher

than the 2000–25 mean value across most of the North American Arctic, particularly in northern Alaska, Quebec, and Labrador (Fig. 5.34). The Eurasian Arctic, however, featured a much greater mixture of positive and negative anomalies, a pattern that has recurred for the last several years. Nonetheless, the long-term trend in MODIS-observed tundra greenness is strongly positive (greening) for most of the circumpolar region (Fig. 5.35). Although no longer maintained, the GIMMS-3g+ dataset provides one of the clearest signals of long-term Arctic greening, with four of the five highest MaxNDVI values in the 43-year record occurring since 2020. The much shorter VIIRS record is generally consistent with the other records, especially MODIS; the circumpolar mean greenness in 2025 was the second highest in the 14-year record. Greening is least pronounced in the Landsat record, with very little variation in greenness following the record high value in 2020. Variations among the satellite records likely reflect differences in sensor bandpasses, radiometric spatial resolution, calibration, and frequency of observation (Frost et al. 2025b). Going forward, spaceborne monitoring of tundra greenness will rely solely on the VIIRS and Landsat records; continuity of these records is therefore essential to sustain current

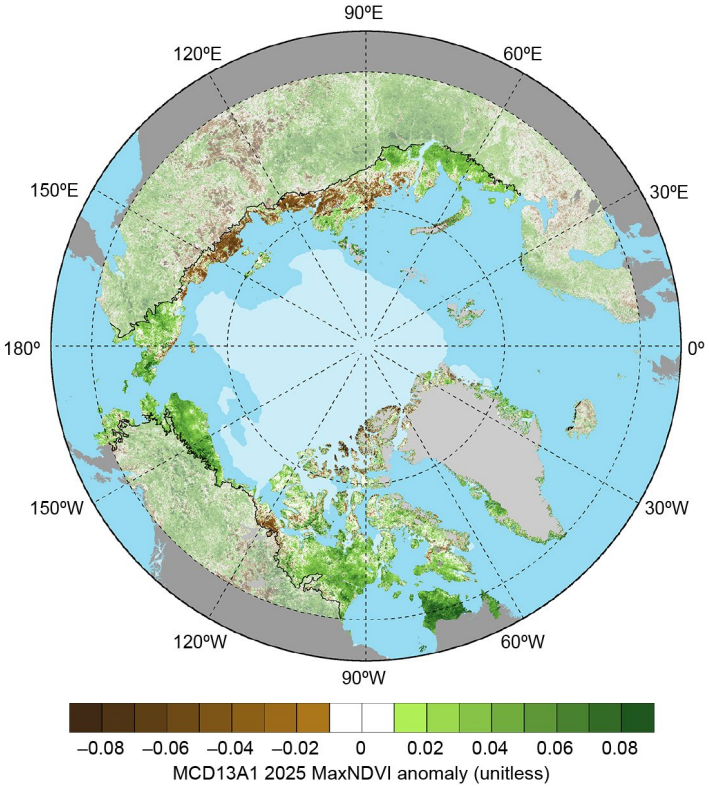

Fig. 5.34. Circumpolar Maximum Normalized Difference Vegetation Index (MaxNDVI) anomalies for the 2025 growing season relative to mean values (2000–25) for Arctic tundra (bold colors), and boreal forest (muted colors) north of 60° latitude from the Moderate Resolution Imaging Spectroradiometer (MODIS) MCD13A1 dataset. The circumpolar tree line is indicated by a black line, and the 2025 minimum sea ice extent is indicated by light shading.

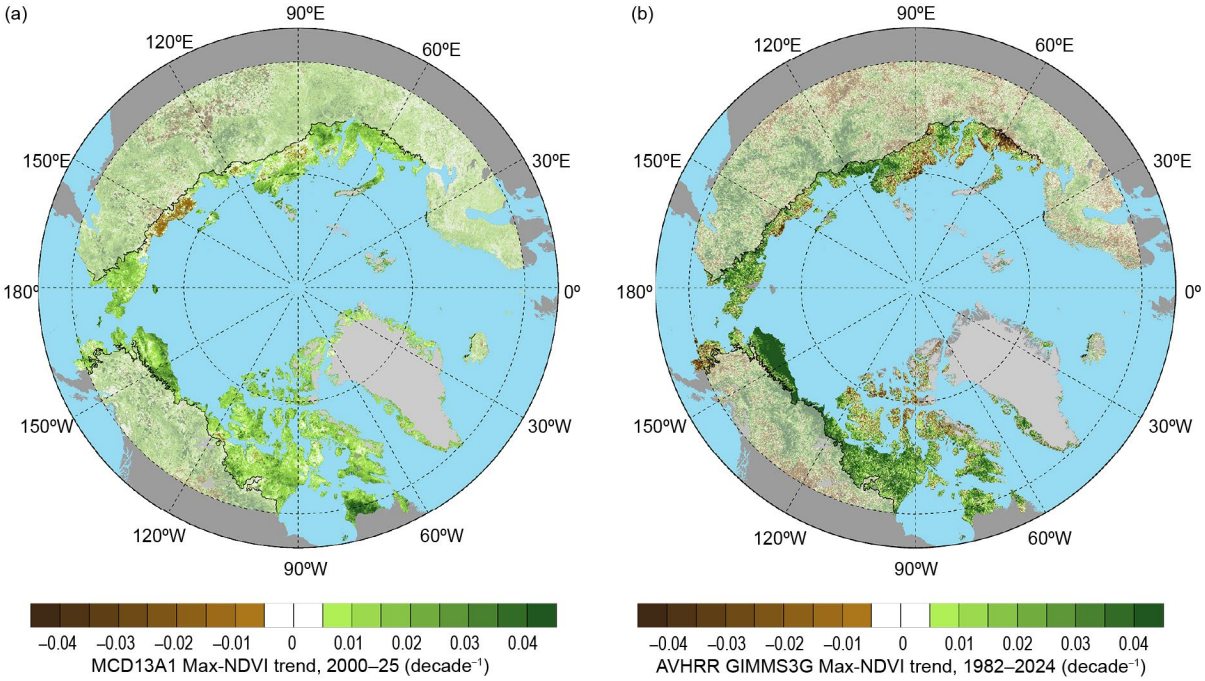

Fig. 5.35. Magnitude of the Maximum Normalized Difference Vegetation Index (MaxNDVI) trend calculated as the change decade^{-1} via ordinary least squares regression for Arctic tundra (bold colors), and boreal forest (muted colors) north of 60° latitude during (a) 2000–25 based on the Moderate Resolution Imaging Spectroradiometer (MODIS) MCD13A1 dataset, and (b) 1982–2024 based on the (now terminated) legacy Advanced Very High-Resolution Radiometer GIMMS 3-g+ dataset. The circumpolar tree line is indicated by a black line.

standards in monitoring Arctic vegetation dynamics and modeling their influence on the global carbon cycle.

Earth-observing satellites provide foundational datasets for monitoring Arctic changes and help overcome long-standing barriers to access posed by the remoteness of this region, and new ones arising from the cessation of international cooperation in the Russian Arctic and uncertainties in long-standing funding and logistical support for Arctic research in the United States and the European Union. Nonetheless, field studies provide crucial information needed to connect spaceborne observations with patterns of change (or stability) on the ground. Observed increases in the abundance, distribution, and height of Arctic shrubs are a major driver of Arctic greening, and have important impacts on biodiversity, wildlife habitat, surface energy balance, permafrost dynamics, and biogeochemical cycling, particularly in warmer, more southerly portions of the biome near the forest–tundra ecotone (Mekonnen et al. 2021; Fig. 5.32). However, trend attribution remains difficult in understudied regions, such as the Canadian Arctic Archipelago and much of the Russian Arctic. Furthermore, while changes to the Arctic climate have generally favored tundra greening, ecological disturbances, extreme events, and other causes of local declines in greenness ("browning") are increasing in frequency (Lechler et al. 2025; Phoenix et al. 2025), and major knowledge gaps remain concerning climate–carbon feedbacks in Arctic permafrost (Bao et al. 2025). Changes to Arctic land-use also contribute to the complexity in greening and browning trends. For example, the transition of nomadic reindeer herding from a non-monetary livelihood to a market economy has led to regional ecological changes in Eurasian tundra (Bjerke et al. 2024; Wallenius et al. 2025; Fig. 5.32). Understanding the regional variability of complex Arctic vegetation trends and determining their drivers continues to be an important focus of multi-disciplinary scientific research.

Acknowledgments

a. Overview

Authors/chapter editors appreciate support provided by NOAA's Global Ocean Monitoring & Observing Arctic Research Program, including content editing funded through the Cooperative Institute for Earth System Research and Data Science (CIESRDS) via NOAA Cooperative Agreement NA22OAR4320151 (M. Druckenmiller and T. Moon) and by the Cooperative Institute for Climate, Ocean, and Ecosystem Studies (CICOES) under NOAA Cooperative Agreement NA20OAR4320271 (R. Thoman).

e. Sea Surface Temperature

M.-L. Timmermans acknowledges support from the National Science Foundation Office of Polar Programs and the Office of Naval Research. We thank Dr. Kristina Dahl (Climate Central) for reviewing the section. NOAA OI SST V2 High Resolution Dataset data provided by the NOAA PSL, Boulder, Colorado, from their website at https://psl.noaa.gov.

Sidebar 5.2: The Arctic carbon cycle

This work was based on support provided by the following programs: The Arctic Carbon Warning Network (AWARE) funded by the Minderoo Foundation (EAGS, GF); Permafrost Pathways through TED Audacious (SMN).

Appendix 1: Acronyms

ALT	active layer thickness
AMAP	Arctic Monitoring and Assessment Programme
ATBD	Algorithm Theoretical Basis Document
AVHRR	Advanced Very High-Resolution Radiometer
CALM	Circumpolar Active Layer Monitoring
CAVM	Circumpolar Arctic Vegetation Map
CCI	Climate Change Initiative
CDR	Climate Data Record
CDS	Climate Data Store
CNECT	CEOS/NSIDC Extratropical Cyclone Tracking
CRDP	climate research data package
DMI	Danish Meteorological Institute
DOISST	Daily Optimum Interpolation Sea Surface Temperature
DU	Dobson units
ESA	European Space Administration
ET	extratropical transition
GIMMS-3g+	Global Inventory Modeling and Mapping Studies third generation
GPCC	Global Precipitation Climatology Centre
GRACE	Gravity Recovery and Climate Experiment
GRACE-FO	Gravity Recovery and Climate Experiment Follow-On
IMS	Interactive Multisensor Snow and Ice Mapping System
JTWC	Joint Typhoon Warning Center
MaxNDVI	Maximum Normalized Difference Vegetation Index
MODIS	Moderate Resolution Imaging Spectroradiometer
NAM	Northern Annular Mode
NAO	North Atlantic Oscillation
NDVI	Normalized Difference Vegetation Index
ODS	Ozone-Depleting Substance
OISST	Optimum Interpolation Sea Surface Temperature
OMI	Ozone Monitoring Instrument
OMTO3	Ozone Monitoring Instrument Level-2 Total Column Ozone version 3
PROMICE	Programme for Monitoring of the Greenland Ice Sheet
SAT	surface air temperature
SCD	snow cover duration
SCE	snow cover extent
SLP	sea level pressure
SMB	surface mass balance
SMOS	Soil Moisture Ocean Salinity
SSMIS	Special Sensor Microwave Imager/Sounder
SST	sea surface temperature
SWE	snow water equivalent
SWIPA	Snow Water Ice and Permafrost in the Arctic
UV	ultraviolet
VIIRS	Visible Infrared Imaging Radiometer Suite
WGMS	World Glacier Monitoring Service

Appendix 2: Datasets and sources

Section 5b Atmosphere

Sub-section	General Variable or Phenomenon	Specific Dataset or Variable	Source
5b	Geopotential Height	ERA5	https://www.ecmwf.int/en/forecasts/dataset/ecmwf-reanalysis-v5
5b	Temperature, Upper Atmosphere	ERA5	https://www.ecmwf.int/en/forecasts/dataset/ecmwf-reanalysis-v5
5b	Wind, Upper Atmosphere	ERA5	https://www.ecmwf.int/en/forecasts/dataset/ecmwf-reanalysis-v5
5b1	Ozone, Total Column and Stratospheric	Aura Ozone Monitoring Instrument (OMI)/Microwave Limb Sounder (MLS)	https://mls.jpl.nasa.gov/eos-aura-mls/data.php
5b1	Ozone, Total Column and Stratospheric	OMI/Aura Level-2 Total Column Ozone (OMTO3) Version 3	https://disc.gsfc.nasa.gov/datasets/OMTO3_003/summary

Section 5c Surface air temperature

Sub-section	General Variable or Phenomenon	Specific Dataset or Variable	Source
5c3	Pressure, Sea Level or Near-Surface	ERA5	https://www.ecmwf.int/en/forecasts/dataset/ecmwf-reanalysis-v5
5c2	Temperature, [Near] Surface	NASA GISTEMPv4	https://data.giss.nasa.gov/gistemp/
5c3	Temperature, [Near] Surface	ERA5	https://www.ecmwf.int/en/forecasts/dataset/ecmwf-reanalysis-v5

Section 5d Precipitation

Sub-section	General Variable or Phenomenon	Specific Dataset or Variable	Source
5d	Precipitation	ERA5	https://www.ecmwf.int/en/forecasts/dataset/ecmwf-reanalysis-v5
5d4	Precipitation	GPCC	https://opendata.dwd.de/climate_environment/GPCC/html/download_gate.html

Section 5e Sea surface temperature			
Sub-section	**General Variable or Phenomenon**	**Specific Dataset or Variable**	**Source**
5e	Sea Ice Extent	National Snow and Ice Data Center (NSIDC) Sea Ice Extent	https://nsidc.org/data/g02135
5e	Sea Surface Temperature	OISSTv2.1	https://www.ncei.noaa.gov/products/optimum-interpolation-sst

Section 5f Sea ice			
Sub-section	**General Variable or Phenomenon**	**Specific Dataset or Variable**	**Source**
5f1	Sea Ice Extent	National Snow and Ice Data Center (NSIDC) Sea Ice Extent	https://nsidc.org/data/g02135
5f2	Sea Ice Thickness	European Space Agency (ESA) Cryosat-2/ Soil Moisture and Ocean Salinity (SMOS)	https://earth.esa.int/eogateway/catalog/smos-cryosat-l4-sea-ice-thickness

Section 5g Greenland Ice Sheet			
Sub-section	**General Variable or Phenomenon**	**Specific Dataset or Variable**	**Source**
5g	Air Temperature	Danish Meteorological Institute (DMI)/ Programme for Monitoring the Greenland Ice Sheet (PROMICE) Weather	https://eng.geus.dk/products-services-facilities/data-and-maps/glaciological-data-from-greenland-promice
5g	Glacier Ablation	PROMICE Glacier Front Line (Greenland)	https://doi.org/10.22008/promice/data/calving_front_lines
5g	Glacier Mass, Area or Volume	Gravity Recovery and Climate Experiment (GRACE) /GRACE Follow-On (GRACE-FO)	https://grace.jpl.nasa.gov/data/get-data/
5g	Ice Sheet Albedo	Sentinel-3 Snow and Ice Products (SICE)	https://eo4society.esa.int/projects/pre-operational-sentinel-3-snow-and-ice-products-sice/
5g	Ice Sheet Discharge	Ice Discharge (Greenland)	https://doi.org/10.22008/promice/data/ice_discharge/d/v02
5g	Ice Sheet Melt	Special Sensor Microwave Imager/ Sounder (SSMIS)	https://nsidc.org/data/nsidc-0001
5g	Ice Sheet Surface Height	Ice, Cloud, and land Elevation Satellite 2 (ICESat-2)	https://icesat-2.gsfc.nasa.gov/icesat-2-data

Sub-section	General Variable or Phenomenon	Specific Dataset or Variable	Source
5g	Surface Mass Balance	Modèle Atmosphérique Régionale version 3.14.1 regional climate model (MAR)	https://zenodo.org/records/13151275
5g	Surface Mass Balance	ERA5	https://www.ecmwf.int/en/forecasts/dataset/ecmwf-reanalysis-v5

Section 5h Glaciers and ice caps outside Greenland

Sub-section	General Variable or Phenomenon	Specific Dataset or Variable	Source
5h	Glacier Mass, Area or Volume	World Glacier Monitoring Service	http://dx.doi.org/10.5904/wgms-fog-2022-09
5h	Glacier Mass, Area or Volume	Gravity Recovery and Climate Experiment Follow-on (GRACE/GRACE-FO)	https://grace.jpl.nasa.gov/data/get-data/

Section 5i Terrestrial snow cover

Sub-section	General Variable or Phenomenon	Specific Dataset or Variable	Source
5i	Snow Properties	Crocus Snowpack Model	https://egusphere.copernicus.org/preprints/2025/egusphere-2025-4540/
5i	Snow Properties	ERA5	https://www.ecmwf.int/en/forecasts/dataset/ecmwf-reanalysis-v5
5i	Snow Properties	MERRA-2	http://gmao.gsfc.nasa.gov/reanalysis/MERRA-2/
5i	Snow Properties	European Space Agency Snow Climate Change Initiative Snow Water Equivalent	https://snow-cci.enveo.at/
5i	Snow Properties	NOAA Interactive Multi-sensor Snow and Ice Mapping System (Snow Cover Duration)	https://usicecenter.gov/Products/ImsHome
5i	Snow Properties	NOAA Snow Chart Climate Data Record	https://www.ncei.noaa.gov/products/climate-data-records/snow-cover-extent

Section 5j Permafrost			
Sub-section	**General Variable or Phenomenon**	**Specific Dataset or Variable**	**Source**
5j1	Permafrost	Global Terrestrial Network for Permafrost (GTN-P)	http://gtnpdatabase.org/
5j1	Permafrost	Permafrost Site Map	http://permafrost.gi.alaska.edu/sites_map
5j1	Temperature, [Near] Surface	ERA5	https://www.ecmwf.int/en/forecasts/dataset/ecmwf-reanalysis-v5
5j2	Permafrost	Circumpolar Active Layer Monitoring Program (CALM) Active-Layer Thickness	www2.gwu.edu/~calm/

Section 5k Tundra greenness			
Sub-section	**General Variable or Phenomenon**	**Specific Dataset or Variable**	**Source**
5k	Vegetative Index	Global Inventory Modeling and Mapping Studies third generation (GIMMS-3g+) Version 1	https://daac.ornl.gov/VEGETATION/guides/Global_Veg_Greenness_GIMMS_3G.html
5k	Vegetative Index	MODIS MCD13A1 and MYD13A1 Normalized Difference Vegetative Index (NDVI)	https://lpdaac.usgs.gov/products/mod13a1v006/
5k	Vegetative Index	Landsat Collection 2 Normalized Difference Vegetative Index (NDVI)	https://www.usgs.gov/landsat-missions/landsat-collection-2
5k	Vegetative Index	Visible Infrared Imaging Radiometer Suite (VIIRS) VNP13A1	https://www.earthdata.nasa.gov/topics/biosphere/vegetation-index

Sidebar 5.1: Ex-typhoon Halong			
Sub-section	**General Variable or Phenomenon**	**Specific Dataset or Variable**	**Source**
SB5.1	Sea Surface Temperature	OISSTv2.1	https://www.ncei.noaa.gov/products/optimum-interpolation-sst

Sidebar 5.2: The Arctic carbon cycle			
Sub-section	**General Variable or Phenomenon**	**Specific Dataset or Variable**	**Source**
SB5.2	Carbon	Carbon emissions	https://iopscience.iop.org/article/10.1088/1748-9326/ae09bb#erlae09bbs5
SB5.2	Carbon dioxide (CO2)	Arctic-Boreal Vulnerability Experiment CO_2 fluxes	https://www.earthdata.nasa.gov/data/catalog/ornl-cloud-co2fluxes-arctic-boreal-domain-2377-1

References

Aalto, J., M. Kämäräinen, M. Rantanen, P. Niittynen, G. K. Phoenix, J. Lenoir, I. Maclean, and M. Luoto, 2026: A new era of bioclimatic extremes in the terrestrial Arctic. *Sci. Adv.*, **12**, eadw5698, https://doi.org/10.1126/sciadv.adw5698.

Ballinger, T. J., and Coauthors, 2024: Surface air temperature. NOAA Tech. Rep. OAR ARC 24-0, 8 pp., https://doi.org/10.25923/4bb3-3f87.

Bao, T., X. Xu, G. Jia, X. Zhu, W. J. Riley, and Y. Yang, 2025: Climate-carbon feedback tradeoff between Arctic and alpine permafrost under warming. *Sci. Adv.*, **11**, eadt8366, https://doi.org/10.1126/sciadv.adt8366.

Barrett, A. P., J. C. Stroeve, and M. C. Serreze, 2020: Arctic Ocean precipitation from atmospheric reanalyses and comparisons with North Pole drifting station records. *J. Geophys. Res. Oceans*, **125**, 1, https://doi.org/10.1029/2019JC015415.

Bartsch, A., and Coauthors, 2025: Similarities between sea ice area variations and satellite-derived terrestrial biosphere and cryosphere parameters across the Arctic. *Cryosphere*, **19**, 4929–4967, https://doi.org/10.5194/tc-19-4929-2025.

Becker, A., P. Finger, A. Meyer-Christoffer, B. Rudolf, K. Schamm, U. Schneider, and M. Ziese, 2013: A description of the global land-surface precipitation data products of the Global Precipitation Climatology Centre with sample applications including centennial (trend) analysis from 1901–present. *Earth Syst. Sci. Data*, **5**, 71–99, https://doi.org/10.5194/essd-5-71-2013.

Berner, L. T., and S. J. Goetz, 2022: Satellite observations document trends consistent with a boreal forest biome shift. *Global Change Biol.*, **28**, 3275–3292, https://doi.org/10.1111/gcb.16121.

Bernhard, G., and Coauthors, 2015: Comparison of OMI UV observations with ground-based measurements at high northern latitudes. *Atmos. Chem. Phys.*, **15**, 7391–7412, https://doi.org/10.5194/acp-15-7391-2015.

Bhartia, P. K., and C. W. Wellemeyer, 2002: TOMS-V8 total O3 algorithm. OMI Algorithm Theoretical Basis Doc. Volume II. NASA Goddard Space Flight Center Tech. Doc. ATBD-OMI-02, 91 pp., https://ozoneaq.gsfc.nasa.gov/content/public/OMI/ATBDs/ATBD-OMI-02.pdf.

Bjerke, J. W., K. Magnussen, R. M. Bright, S. Navrud, R. Erlandsson, E. A. Finne, and H. Tømmervik, 2024: Synergies and trade-offs between provisioning and climate-regulating ecosystem services in reindeer herding ecosystems. *Sci. Total Environ.*, **927**, 171914, https://doi.org/10.1016/j.scitotenv.2024.171914.

Box, J. E., W. Colgan, B. Wouters, D. Burgess, S. O'Neel, L. Thomson, and S. Mernild, 2018: Global sea-level contribution from Arctic land ice: 1971–2017. *Environ. Res. Lett.*, **13**, 125012, https://doi.org/10.1088/1748-9326/aaf2ed.

——, and Coauthors, 2021: Recent developments in Arctic climate observation indicators. AMAP Arctic Climate Change Update 2021: Key Trends and Impacts, Arctic Monitoring and Assessment Programme, 148 pp., https://www.amap.no/documents/doc/amap-arctic-climate-change-update-2021-key-trends-and-impacts/3594.

Brown, R., and Coauthors, 2017: Arctic terrestrial snow cover. *Snow, Water, Ice and Permafrost in the Arctic (SWIPA) 2017,* Arctic Monitoring and Assessment Programme, 25–64.

Burn, C. R., and Coauthors, 2025: Developments in permafrost science and engineering in response to climate warming in circumpolar and high mountain regions, 2019–2024. *Permafrost & Periglacial*, **36**, 167–188, https://doi.org/10.1002/ppp.2261.

Canadell, J. G., and Coauthors, 2021: Global carbon and other biogeochemical cycles and feedbacks. *Climate Change 2021: The Physical Science Basis*, V. Masson-Delmotte et al., Eds., Cambridge University Press, 673–816, https://doi.org/10.1017/9781009157896.007.

Christensen, T. R., and Coauthors, 2020: Multiple ecosystem effects of extreme weather events in the Arctic. *Ecosystems*, **24**, 122–136, https://doi.org/10.1007/s10021-020-00507-6.

Colgan, W., and Coauthors, 2015: Hybrid glacier Inventory, Gravimetry and Altimetry (HIGA) mass balance product for Greenland and the Canadian Arctic. *Remote Sens. Environ.*, **168**, 24–39, https://doi.org/10.1016/j.rse.2015.06.016.

Crawford, C. J., and Coauthors, 2023: The 50-year Landsat collection 2 archive. *Sci. Remote Sens.*, **8**, 100103, https://doi.org/10.1016/j.srs.2023.100103.

Crawford, A. D, M. C. Serreze, D. Barber, D. Dahl-Jensen, and J. Stroeve, 2021: "CEOS/NSIDC Extratropical Cyclone Tracking (CNECT)", 10.34992/ebnw-s681, CanWIN, Version 13.2, accessed 17 January 2026. https://doi.org/10.34992/ebnw-s681.

Decharme, B., A. Barbu, and S. Ramos Buarque, 2024: Crocus-ERA5 daily snow product over the Northern Hemisphere at 0.25° resolution, 2023v2. Zenodo, accessed 29 September 2025, https://doi.org/10.5281/zenodo.14513248.

Didan, K., 2021a: MODIS/Terra vegetation indices 16-day L3 global 500m SIN grid V061. NASA EOSDIS Land Processes Distributed Active Archive Center, accessed 20 March 2026, https://doi.org/10.5067/MODIS/MOD13A1.061.

——, 2021b: MODIS/Aqua vegetation indices 16-day L3 global 500m SIN grid V061. NASA EOSDIS Land Processes Distributed Active Archive Center, accessed 20 March 2026, https://doi.org/10.5067/MODIS/MYD13A1.061.

Dou, T. F., S. F. Pan, R. Bintanja, and C. D. Xiao, 2022: More frequent, intense, and extensive rainfall events in a strongly warming Arctic. *Earth's Future*, **10**, e2021EF002378, https://doi.org/10.1029/2021ef002378.

England, M. R., L. M. Polvani, J. Screen, and A. C. Chan, 2025: Minimal Arctic sea ice loss in the last 20 years, consistent with internal climate variability. *Geophys. Res. Lett.*, **52**, e2025GL116175, https://doi.org/10.1029/2025GL116175.

ESA, 2023: SMOS-CryoSat L4 sea ice thickness, version 206. ESA, accessed 1 September 2025, https://doi.org/10.57780/sm1-4f787c3.

ESRI, 2026: World Continents. Environmental Systems Research Institute, https://hub.arcgis.com/datasets/esri::world-continents/about.

Falvo, G., and Coauthors, 2025: Record 2024 winter carbon emissions coincide with record warmth across boreal forest, tundra, and wetland ecosystems. *Environ. Res. Lett.*, **20**, 114032, https://doi.org/10.1088/1748-9326/ae09bb.

——, and Coauthors, 2026: Reporting 2025 ecosystem CO_2 and CH_4 fluxes with near real-time data during back-to-back record warm Arctic-boreal winters. *Environ. Res. Lett.*, https://doi.org/10.1088/1748-9326/ae8711, in press.

Fausto, R. S., and Coauthors, 2021: Programme for monitoring of the Greenland ice sheet (PROMICE) automatic weather station data. *Earth Syst. Sci. Data*, **13**, 3819–3845, https://doi.org/10.5194/essd-13-3819-2021.

Ferraro, A. J., M. Collins, and F. H. Lambert, 2015: A hiatus in the stratosphere? *Nat. Climate Change*, **5**, 497–498, https://doi.org/10.1038/nclimate2624.

Fetterer, F., K. Knowles, W. N. Meier, M. Savoie, and A. K. Windnagel, 2025: Sea Ice Index, Version 4 (updated daily). National Snow and Ice Data Center, accessed 2 October 2025, https://doi.org/10.7265/a98x-0f50.

Fettweis, X., and Coauthors, 2020: GrSMBMIP: intercomparison of the modelled 1980–2012 surface mass balance over the Greenland Ice Sheet. *Cryosphere*, **14**, 3935–3958, https://doi.org/10.5194/tc-14-3935-2020.

Fox, S., A. Crawford, M. McCrystall, J. Stroeve, J. Lukovich, N. Loeb, J. Natanine, and M. Serreze, 2023: Extreme Arctic weather and community impacts in Nunavut: A case study of one winter's storms and lessons for local climate change preparedness. *Wea. Climate Soc.*, **15**, 881–892, https://doi.org/10.1175/WCAS-D-23-0006.1.

Frost, G. V., and Coauthors, 2025a: Tundra greenness. NOAA Tech. Rep. OAR ARC 25-09, 9 pp., https://doi.org/10.25923/0k84-kn78.

—— , and Coauthors, 2025b: The changing face of the Arctic: Four decades of greening and implications for tundra ecosystems. *Front. Environ. Sci.*, **13**, 1525574, https://doi.org/10.3389/fenvs.2025.1525574.

GMAO, 2015: MERRA-2tavg1_2d_lnd_Nx:2d, 1-hourly, time-averaged, single-level, assimilation, land surface diagnostics V5.12.4. Goddard Earth Sciences Data and Information Services Center, accessed 13 August 2025, https://doi.org/10.5067/RKPHT8KC1Y1T.

Hansen, B. B., and Coauthors, 2014: Warmer and wetter winters: Characteristics and implications of an extreme weather event in the high Arctic. *Environ. Res. Lett.*, **9**, 114021, https://doi.org/10.1088/1748-9326/9/11/114021.

Hersbach, H., and Coauthors, 2020: The ERA5 global reanalysis. *Quart. J. Roy. Meteor. Soc.*, **146**, 1999–2049, https://doi.org/10.1002/qj.3803.

Hjort, J., D. Streletskiy, G. Doré, Q. Wu, K. Bjella, and M. Luoto, 2022: Impacts of permafrost degradation on infrastructure. *Nat. Rev. Earth Environ.*, **3**, 24–38, https://doi.org/10.1038/s43017-021-00247-8.

Huang, B., C. Liu, V. Banzon, E. Freeman, G. Graham, B. Hankins, T. Smith, and H.-M. Zhang, 2021: Improvements of the Daily Optimum Interpolation Sea Surface Temperature (DOISST) version 2.1. *J. Climate*, **34**, 2923–2939, https://doi.org/10.1175/JCLI-D-20-0166.1.

Irrgang, A., and Coauthors, 2025: Measurement of permafrost. *Measurement of Cryospheric Variables*, Vol. 2, Guide to Instruments and Methods of Observation, WMO, 99–148, https://doi.org/10.59327/wmo/cimo/2.

Isaksen, K., J. Lutz, A. M. Sorensen, O. Godoy, L. Ferrighi, S. Eastwood, and S. Aaboe, 2022: Advances in operational permafrost monitoring on Svalbard and in Norway. *Environ. Res. Lett.*, **17**, 095012, https://doi.org/10.1088/1748-9326/ac8e1c.

Ivanova, N., O. M. Johannessen, L. T. Pedersen and R. T. Tonboe, 2014: Retrieval of Arctic sea ice parameters by satellite passive microwave sensors: A comparison of eleven sea ice concentration algorithms. *IEEE Trans. Geosci. and Rem. Sens.*, **52** (11), 7233-7246, https://doi.org/10.1109/TGRS.2014.2310136.

Jóhannesson, T., H. Björnsson, E. Magnússon, S. Guðmundsson, F. Pálsson, O. Sigurðsson, T. Thorsteinsson, and E. Berthier, 2013: Ice-volume changes, bias estimation of mass-balance measurements and changes in subglacial lakes derived by lidar mapping of the surface of Icelandic glaciers. *Ann. Glaciol.*, **54**, 63–74, https://doi.org/10.3189/2013AoG63A422.

Jones, H. G., J. W. Pomeroy, D. A. Walker, and R. W. Hoham, 2011: Snow ecology: An interdisciplinary examination of snow-covered ecosystems. Cambridge University Press, 400 pp., https://books.google.ca/books?id=7LhicgAACAAJ.

Karlsson, N. B., and Coauthors, 2021: A first constraint on basal melt-water production of the Greenland ice sheet. *Nat. Commun.*, **12**, 3461, https://doi.org/10.1038/s41467-021-23739-z.

Kienholz, C., and Coauthors, 2020: Deglacierization of a marginal basin and implications for outburst floods, Mendenhall Glacier, Alaska. *Front. Earth Sci.*, **8**, 137, https://doi.org/10.3389/feart.2020.00137.

Kjøllmoen, B., Ed., L. M. Andreassen, and H. Elvehøy, 2025: Glaciological investigations in Norway 2024, NVE Rapport 27-2025, 110 pp +app, Norwegian Water resources and Energy Directorate, Oslo, https://publikasjoner.nve.no/rapport/2025/rapport2025_27.pdf.

Kuhn, M., and Coauthors, 2025: Current and future methane emissions from boreal-Arctic wetlands and lakes. *Nat. Climate Change*, **15**, 986–991, https://doi.org/10.1038/s41558-025-02413-y.

Landerer, F. W., and Coauthors, 2020: Extending the global mass change data record: GRACE follow-on instrument and science data performance. *Geophys. Res. Lett.*, **47**, e2020GL088306, https://doi.org/10.1029/2020GL088306.

Lavergne, T., and Coauthors, 2019: Version 2 of the EUMETSAT OSI SAF and ESA CCI sea-ice concentration climate data records. *Cryosphere*, **13**, 49–78, https://doi.org/10.5194/tc-13-49-2019.

Lechler, L., Å. Ø. Pedersen, I. H. Myers-Smith, M. Le Moullec, L. E. Loe, B. B. Hansen, L. T. Beumer, and V. Ravolainen, 2025: Basal ice but not summer temperature affects land surface greenness in parts of the landscape in high Arctic tundra. *Environ. Res. Lett.*, **20**, 124058, https://doi.org/10.1088/1748-9326/ae2141.

Lenssen, N., G. Schmidt, J. Hansen, M. Menne, A. Persin, R. Ruedy, and D. Zyss, 2019: Improvements in the GISTEMP uncertainty model. *J. Geophys. Res. Atmos.*, **124**, 6307–6326, https://doi.org/10.1029/2018JD029522.

Lindgren, A., G. Hugelius, and P. Kuhry, 2018: Extensive loss of past permafrost carbon but a net accumulation into present-day soils. *Nature*, **560**, 219–222, https://doi.org/10.1038/s41586-018-0371-0.

Loeb, N. A., A. Crawford, J. C. Stroeve, and J. Hanesiak, 2022: Extreme precipitation in the eastern Canadian Arctic and Greenland: An evaluation of atmospheric reanalyses. *Front. Environ. Sci.*, **10**, 866929, https://doi.org/10.3389/fenvs.2022.866929.

Luojus, K., and Coauthors, 2022: ESA Snow Climate Change Initiative (Snow_cci): Snow Water Equivalent (SWE) level 3C daily global climate research data package (CRDP) (1979–2020), version 2.0. NERC EDS Centre for Environmental Data Analysis, accessed 13 August 2025, https://doi.org/10.5285/4647cc9ad3c044439d6c643208d3c494.

Mankoff, K. D., A. Solgaard, W. Colgan, A. P. Ahlstrøm, S. A. Khan, and R. S. Fausto, 2020: Greenland ice sheet solid ice discharge from 1986 through March 2020. *Earth Syst. Sci. Data*, **12**, 1367–1383, https://doi.org/10.5194/essd-12-1367-2020.

—— , and Coauthors, 2021: Greenland ice sheet mass balance from 1840 through next week. *Earth Syst. Sci. Data*, **13**, 5001–5025, https://doi.org/10.5194/essd-13-5001-2021.

Medley, B., T. A. Neumann, H. J. Zwally, B. E. Smith, and C. M. Stevens, 2022: Simulations of firn processes over the Greenland and Antarctic ice sheets: 1980–2021. *Cryosphere*, **16**, 3971–4011, https://doi.org/10.5194/tc-16-3971-2022.

Meier, W. N., F. Fetterer, A. K. Windnagel, J. S. Stewart, and T. Stafford, 2026a: Near-real-time NOAA/NSIDC climate data record of passive microwave sea ice concentration (G10016, Version 4). National Snow and Ice Data Center, accessed 6 February 2026, https://doi.org/10.7265/tm2n-1m33.

——, ——, ——, ——, and ——, 2026b: NOAA/NSIDC climate data record of passive microwave sea ice concentration (G02202, Version 6). National Snow and Ice Data Center, accessed 6 February 2026, https://doi.org/10.7265/b18j-z797.

Mekonnen, Z. A., and Coauthors, 2021: Arctic tundra shrubification: A review of mechanisms and impacts on ecosystem carbon balance. *Environ. Res. Lett.*, **16**, 053001, https://doi.org/10.1088/1748-9326/abf28b.

Meng, J., J. Fan, U. S. Bhatt, and J. Kurths, 2023: Arctic weather variability and connectivity. *Nat. Commun.*, **14**, 6574, https://doi.org/10.1038/s41467-023-42351-x.

Meredith, M., and Coauthors, 2019: Polar regions. *The Ocean and Cryosphere in a Changing Climate*, H.-O. Pörtner et al., Cambridge University Press, 203–320, https://doi.org/10.1017/9781009157964.005.

Miner, K. R., and Coauthors, 2022: Permafrost carbon emissions in a changing Arctic. *Nat. Rev. Earth Environ.*, **3**, 55–67, https://doi.org/10.1038/s43017-021-00230-3.

Moon, T. A., and Coauthors, 2019: The expanding footprint of rapid Arctic change. *Earth's Future*, **7**, 212–218, https://doi.org/10.1029/2018EF001088.

Mote, T., 2007: Greenland surface melt trends 1973–2007: Evidence of a large increase in 2007. *Geophys. Res. Lett.*, **34**, L22507, https://doi.org/10.1029/2007GL031976.

Mouginot, J., and Coauthors, 2019: Forty-six years of Greenland ice sheet mass balance from 1972 to 2018. *Proc. Natl. Acad. Sci. USA*, **116**, 9239–9244, https://doi.org/10.1073/pnas.1904242116.

Mudryk, L. R., A. Elias Chereque, C. Derksen, K. Luojus, and B. Decharme, 2025: Terrestrial snow cover. NOAA Tech. Rep. OAR ARC 25-04, 8 pp., https://doi.org/10.25923/cfhv-c239.

Muñoz Sabater, J., 2019: ERA5-Land hourly data from 1950 to present. Copernicus Climate Change Service Climate Data Store, accessed 18 July 2025, https://doi.org/10.24381/cds.e2161bac.

Natali, S. M., J. P. Holdren, B. M. Rogers, R. Treharne, P. B. Duffy, R. Pomerance, and E. MacDonald, 2021: Permafrost carbon feedbacks threaten global climate goals. *Proc. Natl. Acad. Sci. USA*, **118**, e2100163118, https://doi.org/10.1073/pnas.2100163118.

——, and Coauthors, 2024: Arctic terrestrial carbon cycling. NOAA Tech. Rep. OAR ARC 24-11, 8 pp., https://doi.org/10.25923/0gpp-mn10.

Nyland, K. E., N. I. Shiklomanov, D. A. Streletskiy, F. E. Nelson, A. E. Klene, and A. L. Kholodov, 2021: Long-term Circumpolar Active Layer Monitoring (CALM) program observations in northern Alaskan tundra. *Polar Geogr.*, **44**, 167–185, https://doi.org/10.1080/1088937X.2021.1988000.

O'Neill, H. B., S. L. Smith, C. R. Burn, C. Duchesne, and Y. Zhang, 2023: Widespread permafrost degradation and thaw subsidence in Northwest Canada. *J. Geophys. Res. Earth Surf.*, **128**, e2023JF007262, https://doi.org/10.1029/2023JF007262.

Parmentier, F.-J. W., B. F. Thornton, A. Silyakova, and T. R. Christensen, 2024: Vulnerability of Arctic-boreal methane emissions to climate change. *Front. Environ. Sci.*, **12**, 1460155, https://doi.org/10.3389/fenvs.2024.1460155.

Phoenix, G. K., and Coauthors, 2025: Browning events in Arctic ecosystems: Diverse causes with common consequences. *PLOS Climate*, **4**, e0000570, https://doi.org/10.1371/journal.pclm.0000570.

Pinzon, J. E., C. J. Tucker, U. S. Bhatt, G. V. Frost, and M. J. Macander, 2023: Global Vegetation Greenness (NDVI) from AVHRR GIMMS-3G+, 1981-2022. ORNL DAAC, accessed 31 March 2026, https://doi.org/10.3334/ORNLDAAC/2187.

Polyakov, I. V., and Coauthors, 2025: Atlantification advances into the Amerasian Basin of the Arctic Ocean. *Sci. Adv.*, **11**, eadq7580, https://doi.org/10.1126/sciadv.adq7580.

Ramage, J., and Coauthors, 2024: The net GHG balance and budget of the permafrost region (2000–2020) from ecosystem flux upscaling. *Global Biogeochem. Cycles*, **38**, e2023GB007953, https://doi.org/10.1029/2023GB007953.

Rantanen, M., A. Y. Karpechko, A. Lipponen, K. Nordling, O. Hyvärinen, K. Ruosteenoja, T. Vihma, and A. Laaksonen, 2022: The Arctic has warmed nearly four times faster than the globe since 1979. *Commun. Earth Environ.*, **3**, 168, https://doi.org/10.1038/s43247-022-00498-3.

Raynolds, M. K., and Coauthors, 2019: A raster version of the Circumpolar Arctic Vegetation Map (CAVM). *Remote Sens. Environ.*, **232**, 111297, https://doi.org/10.1016/j.rse.2019.111297.

RGI Consortium, 2023: Randolph Glacier Inventory - A dataset of global glacier outlines (NSIDC-0770, Version 7). National Snow and Ice Data Center, accessed 11 August 2023, https://doi.org/10.5067/f6jmovy5navz.

Ricker, R., S. Hendricks, L. Kaleschke, X. Tian-Kunze, J. King, and C. Haas, 2017: A weekly Arctic sea-ice thickness data record from merged CryoSat-2 and SMOS satellite data. *Cryosphere*, **11**, 1607–1623, https://doi.org/10.5194/tc-11-1607-2017.

Rivière, G., F. D'Andrea, D. I. V. Domeisen, and A. Portal, 2024: Opposite trends in the Northern Hemisphere stratosphere between mid?winter and early spring linked to surface temperature anomalies. *Geophys. Res. Lett.*, **51**, e2024GL109746, https://doi.org/10.1029/2024GL109746.

Robinson, D. A., T. W. Estilow, and NOAA CDR Program, 2012: NOAA Climate Data Record (CDR) of Northern Hemisphere (NH) Snow Cover Extent (SCE), Version 1 [r01]. NOAA National Centers for Environmental Information, accessed 12 August 2025, https://doi.org/10.7289/V5N014G9.

Román, M. O., and Coauthors, 2024: Continuity between NASA MODIS Collection 6.1 and VIIRS Collection 2 land products. *Remote Sens. Environ.*, **302**, 113963, https://doi.org/10.1016/j.rse.2023.113963.

Romanovsky, V. E., and Coauthors, 2017: Changing permafrost and its impacts. Snow, Water, Ice and Permafrost in the Arctic (SWIPA) 2017, Arctic Monitoring and Assessment Program, 65–102, https://www.amap.no/documents/doc/snow-water-ice-and-permafrost-in-the-arctic-swipa-2017/1610.

Santer, B. D., and Coauthors, 2023: Exceptional stratospheric contribution to human fingerprints on atmospheric temperature. *Proc. Natl. Acad. Sci. USA*, **120**, e2300758120, https://doi.org/10.1073/pnas.2300758120.

Saunois, M., and Coauthors, 2025: Global methane budget 2000–2020. *Earth Syst. Sci. Data*, **17**, 1873–1958, https://doi.org/10.5194/essd-17-1873-2025.

Schneider, U., P. Finger, E. Rustemeier, M. Ziese, and S. Hänsel, 2022: Global precipitation analysis products of the GPCC. Global Precipitation Climatology Centre, 17 pp., https://opendata.dwd.de/climate_environment/GPCC/PDF/GPCC_intro_products_v2022.pdf.

Schuler, T. V., R. E. Benestad, K. Isaksen, H. P. Kierulf, J. Kohler, G. Moholdt, and L. S. Schmidt, 2025: Svalbard's 2024 record summer: An early view of Arctic glacier meltdown? *Proc. Natl. Acad. Sci. USA*, **122**, e2503806122, https://doi.org/10.1073/pnas.2503806122.

Schuur, E. A. G., and Coauthors, 2015: Climate change and the permafrost carbon feedback. *Nature*, **520**, 171–179, https://doi.org/10.1038/nature14338.

——, and Coauthors, 2022: Permafrost and climate change: Carbon cycle feedbacks from the warming Arctic. *Annu. Rev. Environ. Resour.*, **47**, 343–371, https://doi.org/10.1146/annurev-environ-012220-011847.

——, C. Hicks Pries, M. Mauritz, E. Pegoraro, H. Rodenhizer, C. See, and C. Ebert, 2023: Ecosystem and soil respiration radiocarbon detects old carbon release as a fingerprint of warming and permafrost destabilization with climate change. *Philos. Trans. Roy. Soc.*, **A381**, 20220201, https://doi.org/10.1098/rsta.2022.0201.

See, C. R., and Coauthors, 2024: Decadal increases in carbon uptake offset by respiratory losses across northern permafrost ecosystems. *Nat. Climate Change*, **14**, 853–862, https://doi.org/10.1038/s41558-024-02057-4.

Serreze, M. C., and Coauthors, 2021: Arctic rain on snow events: Bridging observations to understand environmental and livelihood impacts. *Environ. Res. Lett.*, **16**, 105009, https://doi.org/10.1088/1748-9326/ac269b.

——., E. Cassano, A. Crawford, J. J. Cassano, and C. Zhang, 2026: The observed evolution of Arctic amplification over the past 45 years. *Cryosphere*, **20**, 411–425, https://doi.org/10.5194/tc-20-411-2026.

——, M. P. Clark, and D. H. Bromwich, 2003: Monitoring precipitation over the Arctic terrestrial drainage system: Data requirements, shortcomings, and applications of atmospheric reanalysis. *J. Hydrometeor.*, **4**, 387–407, https://doi.org/10.1175/1525-7541(2003)4<387:MPOTAT>2.0.CO;2.

Smith, B., 2023: Algorithm Theoretical Basis Document (ATBD) for Land-ice DEM (ATL14) and Land-ice height change (ATL15). Algorithm Theoretical Basis Doc., 71 pp., https://nsidc.org/sites/default/files/documents/technical-reference/icesat2_atl14_atl15_atbd_v003.pdf.

——, S. Dickinson, B. P. Jelley, T. A. Neumann, D. Hancock, J. Lee, and K. Harbeck, 2023: ATLAS/ICESat-2 L3B slope-corrected land ice height time series, Version 6. NASA National Snow and Ice Data Center Distributed Active Archive Center, accessed 25 January 2025, https://doi.org/10.5067/ATLAS/ATL11.006.

Smith, S. L., H. B. O'Neill, K. Isaksen, J. Noetzli, and V. E. Romanovsky, 2022: The changing thermal state of permafrost. *Nat. Rev. Earth Environ.*, **3**, 10–23, https://doi.org/10.1038/s43017-021-00240-1.

——, C. Duchesne, and H. B. O'Neill, 2024: Long-term permafrost monitoring in northern Canada – What have we learned? *12th Int. Conf. on Permafrost*, Whitehorse, YT, Canada, International Permafrost Association, 398–404, https://doi.org/10.52381/ICOP2024.84.1.

——, V. E. Romanovsky, K. Isaksen, K. E. Nyland, K. I. Shiklomanov, D. A. Streletskiy, and H. H. Christiansen, 2025: Permafrost [in "State of the Climate in 2024"]. *Bull. Amer. Meteor. Soc.*, **106** (8), S338–S341, https://doi.org/10.1175/BAMS-D-25-0104.1.

Streletskiy, D. A., and Coauthors, 2025: Thawing permafrost is subsiding in the Northern Hemisphere—Review and perspectives. *Environ. Res. Lett.*, **20**, 013006, https://doi.org/10.1088/1748-9326/ada2ff.

Stroeve, J. C., D. Notz, J. Dawson, E. A. G. Schuur, D. Dahl-Jensen, and C. Giesse, 2025: Disappearing landscapes: The Arctic at +2.7°C global warming. *Science*, **387**, 616–621, https://doi.org/10.1126/science.ads1549.

Sweeney, A. J., Q. Fu, S. Po-Chedley, H. Wang, and M. Wang, 2023: Internal variability increased Arctic amplification during 1980–2022. *Geophys. Res. Lett.*, **50**, e2023GL106060, https://doi.org/10.1029/2023GL106060.

Tapley, B. D., and Coauthors, 2019: Contributions of GRACE to understanding climate change. *Nat. Climate Change*, **5**, 358–369, https://doi.org/10.1038/s41558-019-0456-2.

The GlaMBIE Team, 2025: Community estimate of global glacier mass changes from 2000 to 2023. *Nature*, **639**, 382–388, https://doi.org/10.1038/s41586-024-08545-z.

Thoman, R., and H. R. McFarland, Eds., 2024: Alaska's Changing Environment 2.0. Alaska Center for Climate Assessment and Policy, International Arctic Research Center, University of Alaska Fairbanks, 32 pp., https://uaf-iarc.org/communicating-change.

Tschudi, M., W. N. Meier, J. S. Stewart, C. Fowler, and J. Maslanik, 2019a: EASE-grid sea ice age, Version 4. NASA National Snow and Ice Data Center Distributed Active Archive Center, accessed 5 September 2025, https://doi.org/10.5067/UTAV7490FEPB.

——, ——, and ——, 2019b: Quicklook Arctic weekly EASE-grid sea ice age, Version 1. NASA National Snow and Ice Data Center Distributed Active Archive Center, accessed 2 October 2025, https://doi.org/10.5067/2XXGZY3DUGNQ.

U.S. Geological Survey, 2025: 2025 Tracy Arm landslide-generated tsunami. U.S. Geological Survey, Landslide Hazards Program, accessed 14 August 2025, https://www.usgs.gov/programs/landslide-hazards/science/2025-tracy-arm-landslide-generated-tsunami#overview.

U.S. National Ice Center, 2008: IMS Daily Northern Hemisphere snow and ice analysis at 1 km, 4 km, and 24 km resolutions, Version 1. National Snow and Ice Data Center, accessed 31 January 2026, https://doi.org/10.7265/N52R3PMC.

Virkkala, A.-M., and Coauthors, 2025: Wildfires offset the increasing but spatially heterogeneous Arctic–boreal CO_2 uptake. *Nat. Climate Change*, **15**, 188–195, https://doi.org/10.1038/s41558-024-02234-5.

Vogt, J., and Coauthors, 2025: ARGO: ARctic greenhouse gas observation metadata version 1. *Earth Syst. Sci. Data*, **17**, 2553–2573, https://doi.org/10.5194/essd-17-2553-2025.

Wallenius, T., and Coauthors, 2025: Reconstructing the historical decline of lichen cover across the reindeer fence of the Finnish-Norwegian border. *Ambio*, **54**, 1683–1704, https://doi.org/10.1007/s13280-025-02171-3.

Walsh, J. E., T. J. Ballinger, E. S. Euskirchen, E. Hanna, J. Mård, J. E. Overland, H. Tangen, and T. Vihma, 2020: Extreme weather and climate events in northern areas: A review. *Earth Sci. Rev.*, **209**, 103324, https://doi.org/10.1016/j.earscirev.2020.103324.

——, S. Bigalke, S. A. McAfee, R. Lader, M. C. Serreze, and T. J. Ballinger, 2022: Precipitation. NOAA Tech. Rep. OAR ARC 22-03, 8 pp., https://doi.org/10.25923/yxs5-6c72.

Watkins, M. M., D. N. Wiese, D.-N. Yuan, C. Boening, and F. W. Landerer, 2015: Improved methods for observing Earth's time variable mass distribution with GRACE using spherical cap mascons. *J. Geophys. Res. Solid Earth*, **120**, 2648–2671, https://doi.org/10.1002/2014JB011547.

Weber, M., and Coauthors, 2022: Global total ozone recovery trends attributed to ozone-depleting substance (ODS) changes derived from five merged ozone datasets. *Atmos. Chem. Phys.*, **22**, 6843–6859, https://doi.org/10.5194/acp-22-6843-2022.

WGMS, 2025: Fluctuations of glaciers database. World Glacier Monitoring Service, accessed 3 June 2026, https://doi.org/10.5904/wgms-fog-2025-02b.

Wolken, G. J., and Coauthors, 2021: Glacier and permafrost hazards. NOAA Tech. Rep. OAR ARC 21-13, 9 pp., https://doi.org/10.25923/v40r-0956.

Wouters, B., A. Gardner, and G. Moholdt, 2019: Global glacier mass loss during the GRACE satellite mission (2002-2016). *Front. Earth Sci.*, **7**, 96, https://doi.org/10.3389/feart.2019.00096.

Ye, H., D. Yang, A. Behrangi, S. L. Stuefer, X. Pan, E. Mekis, Y. Dibike, and J. E. Walsh, 2021: Precipitation characteristics and changes. *Arctic Hydrology, Permafrost and Ecosystems*, D. Yang and D. L. Kane, Eds., Springer Nature, 25–59, https://doi.org/10.1007/978-3-030-50930-9_2.

Yu, L., and S. Zhong, 2021: Trends in Arctic seasonal and extreme precipitation in recent decades. *Theor. Appl. Climatol.*, **145**, 1541–1559, https://doi.org/10.1007/s00704-021-03717-7.

Zemp, M., and Coauthors, 2019: Global glacier mass changes and their contributions to sea-level rise from 1961 to 2016. *Nature*, **568**, 382–386, https://doi.org/10.1038/s41586-019-1071-0.

Zhou, W., L. R. Leung, and J. Lu, 2024: Steady threefold Arctic amplification of externally forced warming masked by natural variability. *Nat. Geosci.*, **17**, 508–515, https://doi.org/10.1038/s41561-024-01441-1.

STATE OF THE CLIMATE IN 2025

ANTARCTICA AND THE SOUTHERN OCEAN

M. N. Raphael and K. R. Clem, Eds.

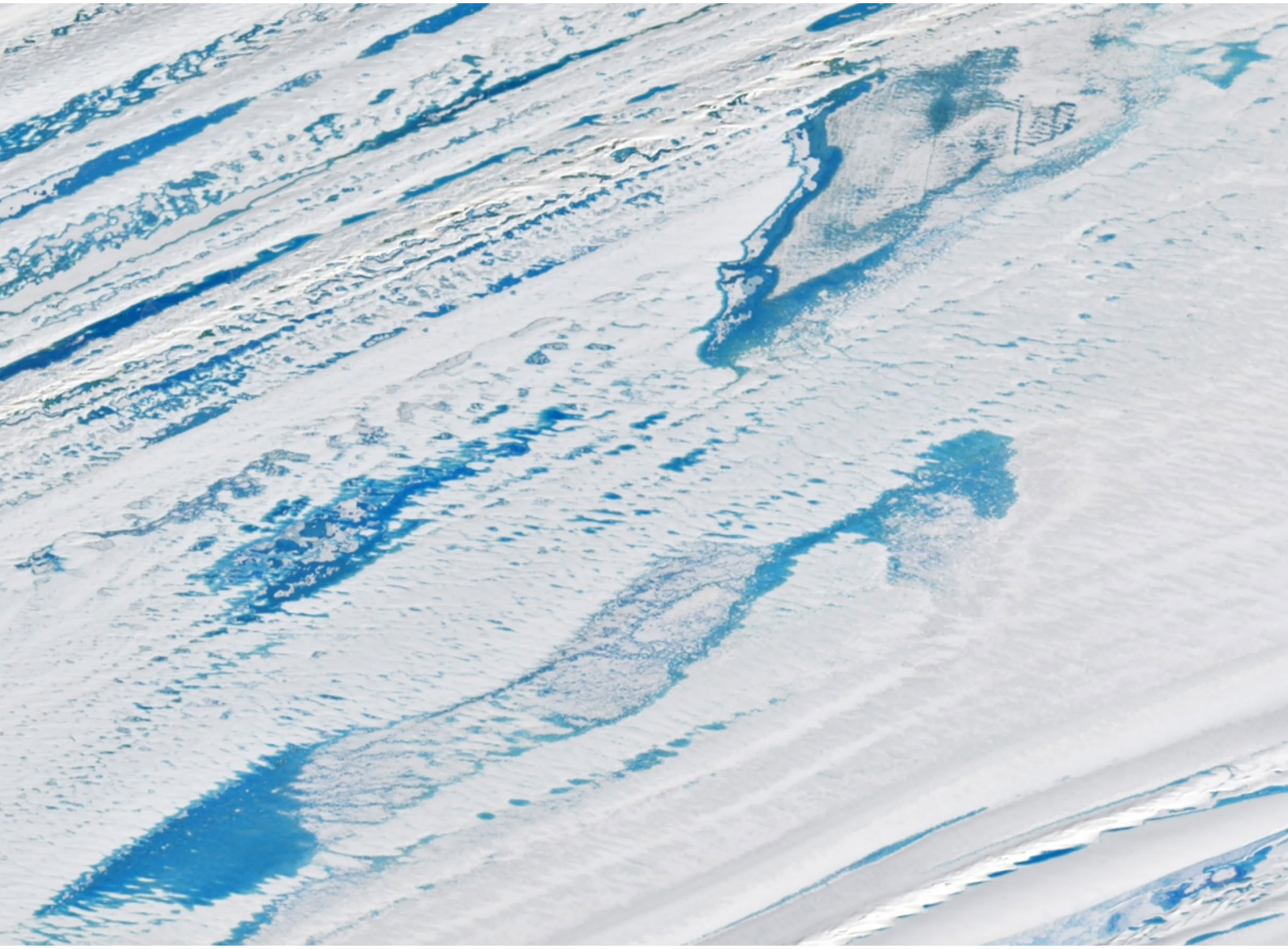

Special Online Supplement to the *Bulletin of the American Meteorological Society* Vol. 107, No. 8, August, 2026

https://doi.org/10.1175/BAMS-D-26-0127.1
Corresponding author: Marilyn N. Raphael / raphael@geog.ucla.edu
©2026 American Meteorological Society
For information regarding reuse of this content and general copyright information, consult the AMS Copyright Policy.

STATE OF THE CLIMATE IN 2025
Antarctica and the Southern Ocean

Editors

Jessica Blunden
James Reagan

Chapter Editors

Anthony Arguez
Josh Blannin
Peter Bissolli
Kyle R. Clem
Howard J. Diamond
Matthew L. Druckenmiller
Robert J. H. Dunn
Catherine Ganter
Nadine Gobron
Rodney Martinez
Twila A. Moon
Gary A. Morris
Marilyn N. Raphael
Renellys C. Perez
Carl J. Schreck III
Zewdu Segele
Laura Stevens
Richard L. Thoman
Denis L. Volkov
Zhiwei Zhu

Technical Editors

Lukas Noguchi
Laura Ohlmann

BAMS Special Editor for Climate

Timothy DelSole

American Meteorological Society

Cover Credit:
Meltwater ponds on the Amery ice shelf during the Antarctic melt season in late 2024. NASA Earth Observatory images by Wanmei Liang, using Landsat data from the U.S. Geological Survey.

How to cite this document:
Antarctica and the Southern Ocean is one chapter from the *State of the Climate in 2025* annual report and is available from https://doi.org/10.1175/BAMS-D-26-0127.1. Compiled by NOAA's National Centers for Environmental Information, *State of the Climate in 2025* is based on contributions from scientists from around the world. It provides a detailed update on global climate indicators, notable weather events, and other data collected by environmental monitoring stations and instruments located on land, water, ice, and in space. The full report is available from https://doi.org/10.1175/2026BAMSStateoftheClimate.1.

Citing the complete report:
Blunden, J. and J. Reagan, Eds., 2026: "State of the Climate in 2025". Bull. Amer. Meteor. Soc., 107 (8), Si–S512, https://doi.org/10.1175/2026BAMSStateoftheClimate.1.

Citing this chapter:
Raphael, M. N. and K. R. Clem, 2026: Antarctica and the Southern Ocean [in "State of the Climate in 2025"]. Bull. Amer. Meteor. Soc., 107 (8), S352–S396, https://doi.org/10.1175/BAMS-D-26-0127.1.

Citing a section (example):
Bahrami, M., E. Glen, L. D. Trusel, A. F. Banwell, P. Jackson, and R. L. Dell, 2026: The exceptional nature of supraglacial meltwater in 2024/25 [in "State of the Climate in 2025"]. Bull. Amer. Meteor. Soc., 107 (8), S372–S375, https://doi.org/10.1175/BAMS-D-26-0127.1.

Editor and Author Affiliations (alphabetical by name)

Adjou, Mohamed, ISEN Engineering School, LaBISEN, Knowledge Learning and Information Modeling (KLaIM), Brest, France; University of Brest, Institut Universitaire Européen de la Mer (IUEM) UAR3113, Plouzané, France

Adusumilli, Susheel, Department of Earth Sciences, University of Oregon, Eugene, Oregon

Amory, Charles, Université Grenoble Alpes, Institut des Géosciences de l'Environnement, IRD, CNRS, Grenoble INP, Grenoble, France

Bahrami, Mahsa, Department of Geography, Pennsylvania State University, State College, Pennsylvania

Baiman, Rebecca, Department of Atmospheric Science, Colorado State University, Fort Collins, Colorado

Banwell, Alison F., Centre for Polar Observation and Modelling, School of Geography and Natural Sciences, Northumbria University, Newcastle upon Tyne, United Kingdom; Cooperative Institute for Research in Environmental Sciences, University of Colorado Boulder, Boulder, Colorado

Barreira, Sandra, Argentine Naval Hydrographic Service, Buenos Aires, Argentina

Beadling, Rebecca L., Department of Earth and Environmental Science, Temple University, Philadelphia, Pennsylvania

Black, T., NASA Goddard Space Flight Center, Greenbelt, Maryland

Brown, Meghan, Department of Earth Sciences, University of Oregon, Eugene, Oregon

Clem, Kyle R., School of Geography, Environment and Earth Sciences, Victoria University of Wellington, Wellington, New Zealand

Colwell, Steve, British Antarctic Survey, Cambridge, United Kingdom

Coy, Lawrence, NASA Goddard Space Flight Center, Greenbelt, Maryland; Science Systems and Applications, Inc., Lanham, Maryland

Cullis, P., NOAA/OAR Earth System Research Laboratory, Global Monitoring Division, Boulder, Colorado; University of Colorado Boulder, Boulder, Colorado

Datta, Rajashree T., Department of Civil Engineering and Geosciences, TU Delft, Delft, The Netherlands

de Laat, Jos, Royal Netherlands Meteorological Institute (KNMI), De Bilt, The Netherlands

Dell, R. L., University of Cambridge, Cambridge, United Kingdom

du Plessis, Marcel, Department of Marine Sciences, University of Gothenburg, Gothenburg, Sweden

Fogt, Ryan L., Department of Geography, Ohio University, Athens, Ohio

Fricker, Helen A., Scripps Institution of Oceanography, University of California, San Diego, La Jolla, California

Glen, E., Department of Geography, Pennsylvania State University, State College, Pennsylvania

Hancock, Alyce M., Institute for Marine and Antarctic Studies, University of Tasmania, Hobart, Tasmania, Australia

Jackson, P., Scott Polar Research Institute, University of Cambridge, Cambridge, United Kingdom

Johnson, Bryan, NOAA/OAR Earth System Research Laboratory, Global Monitoring Division, Boulder, Colorado; University of Colorado Boulder, Boulder, Colorado

Josey, Simon A., National Oceanography Centre, Southampton, United Kingdom

Keller, Linda M., Antarctic Meteorological Research and Data Center, Space Science and Engineering Center, University of Wisconsin-Madison, Madison, Wisconsin

Kittel, Chri, Department of Geography, University of Liège, Liège, Belgium; Physical Geography Research Group, Department of Geography, Vrije Universiteit Brussel, Brussels, Belgium

Kramarova, Natalya A., NASA Goddard Space Flight Center, Greenbelt, Maryland

Lait, Leslie R., NASA Ames Research Center, Moffett Field, California

Lazzara, Matthew A., Antarctic Meteorological Research and Data Center, Space Science and Engineering Center, University of Wisconsin-Madison, Madison, Wisconsin; Department of Physical Sciences, School of Arts and Sciences, Madison Area Technical College, Madison, Wisconsin

Lieser, Jan L., Bureau of Meteorology, Hobart, Tasmania, Australia; Institute for Marine and Antarctic Studies, University of Tasmania, Hobart, Tasmania, Australia

MacFerrin, Michael, Earth Science and Observation Center, Cooperative Institute for Research in Environmental Sciences (ESOC/CIRES), University of Colorado Boulder, Boulder, Colorado

MacLennan, Michelle L., British Antarctic Survey, Cambridge, United Kingdom

Massom, Robert A., Australian Antarctic Division, Australian Antarctic Program Partnership (AAPP) and Australian Centre for Excellence in Antarctic Science (ACEAS), Hobart, Tasmania, Australia

Mikolajczyk, David E., Antarctic Meteorological Research and Data Center, Space Science and Engineering Center, University of Wisconsin-Madison, Madison, Wisconsin

Milward, James, Department of Earth and Environmental Science, Temple University, Philadelphia, Pennsylvania

Mote, Thomas L., Department of Geography, University of Georgia, Athens, Georgia

Newman, Paul A., NASA Goddard Space Flight Center, Greenbelt, Maryland; University of Maryland, Baltimore County, Baltimore, Maryland

Norton, Taylor, Antarctic Meteorological Research and Data Center, Space Science and Engineering Center, University of Wisconsin-Madison, Madison, Wisconsin

Petropavlovskikh, Irina, NOAA/OAR Earth System Research Laboratory, Global Monitoring Division, Boulder, Colorado; University of Colorado Boulder, Boulder, Colorado

Pezzi, Luciano P., Laboratory of Ocean and Atmosphere Studies (LOA), Earth Observation and Geoinformatics Division (DIOTG), National Institute for Space Research (INPE), São José dos Campos, São Paulo, Brazil

Raphael, Marilyn N., Department of Geography, University of California, Los Angeles, Los Angeles, California

Reid, Phillip, Australian Antarctic Program Partnership (AAPP), Hobart, Tasmania, Australia; Bureau of Meteorology, Hobart, Tasmania, Australia

Ryan-Keogh, Thomas J., Southern Ocean Carbon-Climate Observatory, Council for Scientific and Industrial Research (CSIR), Cape Town, South Africa

Santee, Michelle L., Jet Propulsion Laboratory, California Institute of Technology, Pasadena, California

Scambos, Theodore, Earth Science and Observation Center, Cooperative Institute for Research in Environmental Sciences (ESOC/CIRES), University of Colorado Boulder, Boulder, Colorado

Schulz, Cristina, Department of Marine and Environmental Sciences, Northeastern University, Boston, Massachusetts

Shi, Jia-Rui, Courant Institute of Mathematical Sciences, New York University, New York City, New York

Souza, Everaldo, Federal University of Pará (UFPA), Belém, Pará, Brazil

Stammerjohn, Sharon, Institute of Arctic and Alpine Research, University of Colorado Boulder, Boulder, Colorado

Thomalla, Sandy, Marine and Antarctic Research Centre for Innovation and Sustainability, Department of Oceanography, University of Cape Town, Cape Town, South Africa; Southern Ocean Carbon-Climate Observatory, Council for Scientific and Industrial Research (CSIR), Cape Town, South Africa

Trusel, Luke, Department of Geography, Pennsylvania State University, State College, Pennsylvania

Wille, Jonathan D., Institute for Atmospheric and Climate Science, ETH Zürich, Zürich, Switzerland; Institut des Géosciences de l'Environnement, IRD, CNRS, Grenoble INP, Saint Martin d'Hères, France

Ziegler, Taylor, Antarctic Meteorological Research and Data Center, Space Science and Engineering Center, University of Wisconsin-Madison, Madison, Wisconsin

Editorial and Production Team

Allen, Jessicca, Graphics Support, Cooperative Institute for Satellite Earth System Studies, North Carolina State University, Asheville, North Carolina

Camper, Amy V., Graphics Support, Innovative Consulting and Management Services, LLC, NOAA/NESDIS National Centers for Environmental Information, Asheville, North Carolina

Carroll, Lauren, Content Team Lead, Communications and Outreach, NOAA/NESDIS National Centers for Environmental Information, Asheville, North Carolina

Crossman, Jacquelyn, NCEI Librarian, MPF-ZAI, NOAA/NESDIS National Centers for Environmental Information, Asheville, North Carolina

Haley, Bridgette O., Graphics Support, NOAA/NESDIS National Centers for Environmental Information, Asheville, North Carolina

Noguchi, Lukas, Technical Editor, Innovative Consulting and Management Services, LLC, NOAA/NESDIS National Centers for Environmental Information, Asheville, North Carolina

Ohlmann, Laura, Technical Editor, Innovative Consulting and Management Services, LLC, NOAA/NESDIS National Centers for Environmental Information, Asheville, North Carolina

Veasey, Sara W., Visual Communications Team Lead, Communications and Outreach, NOAA/NESDIS National Centers for Environmental Information, Asheville, North Carolina

6. Table of Contents

List of authors and affiliations S355
a. Overview S358
b. Atmospheric circulation and surface observations S361
c. Ice sheet surface mass balance S365
d. Ice sheet seasonal melt extent and duration S369
Sidebar 6.1: The exceptional nature of supraglacial meltwater in 2024/25 ..... S372
e. Antarctic Ice Sheet mass balance S376
f. Sea ice extent, concentration, and seasonality S379
g. Southern Ocean S383
1. Sea surface temperature, salinity, and mixed-layer properties S383
2. Air–sea heat flux S383
3. Upper ocean heat content S385
4. Ocean biogeochemistry S386
h. 2025 Antarctic ozone hole S387
Acknowledgments S390
Appendix 1: Acronyms S391
Appendix 2: Datasets and sources S393
References S397

6. ANTARCTICA AND THE SOUTHERN OCEAN

M. N. Raphael and K. R. Clem, Eds.

a. Overview

—M. N. Raphael and K. R. Clem

In 2025, atmospheric conditions over Antarctica exhibited strong variability in pressure and temperature. Lower-than-average pressure over the continent in the early months of the year (January–March) was replaced by near-average conditions in late autumn (May–June) and winter (July–August). A strong positive Southern Annular Mode (SAM) and very strong westerlies accompanied the lower-than-average pressure in March and April, while a strong zonal wave three pattern dominated the circulation pattern offshore in winter. In spring and early summer (September–December), above-average surface pressure developed over the continent, supported by strong downward propagating positive geopotential heights from the stratosphere. This led to the development of a negative SAM supported by deep midlatitude lows over the Indian Ocean and southwest of New Zealand.

Numerous record-high monthly temperatures were set everywhere across the continent in 2025, and the polar cap saw its warmest year since the start of the record in 1979. There were no record-low monthly temperatures recorded at any station. Many regional record-high temperatures were linked to local northerly flow, predominantly associated with the zonal wave three pattern that dominated the winter circulation, influencing, for example, the Antarctic Peninsula and Dronning Maud Land where many monthly record-high temperatures were set. The most continent-wide anomalously high temperatures occurred with the above-average surface pressure that prevailed in spring.

The Antarctic Ice Sheet's surface mass balance (SMB) in 2025 saw positive anomalies, which were stronger over the grounded ice than over the floating ice shelves. The most significant anomaly occurred in April, when the Amundsen Sea Low paired with a blocking high east of the Peninsula, creating favorable conditions for sustained moisture transport, in association with a large number of atmospheric rivers into West Antarctica, some of which penetrated far inland. The resulting high snowfall rates led to the development of positive SMB anomalies both along the coast and in parts of the polar plateau.

Surface melt on the continent was above average on all the ice shelves (except the northeastern Ross Ice Shelf), particularly between mid-December 2024 and early January 2025, but was reduced to near-zero values by February. Melt on the Antarctic Peninsula approached record levels in early January. The total number of melt days generally exceeded that of the long-term average in many locations. Accompanying the melt was a record-high supraglacial meltwater presence. The strong melt was due to warmer air and ocean temperatures.

There was continued ice sheet mass loss in the West Antarctic Ice Sheet in 2025, with continued thinning of the ice sheet in the Amundsen Sea sector. The normally stable East Antarctic Ice Sheet decreased in height, with areas near the Totten ice shelf (unusually) experiencing the largest reductions. The most positive height and mass anomalies occurred along the coast of the East Antarctic Ice Sheet between March and September, while enhanced snowfall in some sectors such as the Bellingshausen Sea and Dronning Maud Land produced localized mass gains which offset the losses from the West Antarctic Ice Sheet. The anomalous snowfall in 2025 resulted in a net Antarctic mass gain of 153 Gt between January and November 2025, which was the fourth highest annual mass gain recorded by the Gravity Recovery and Climate Experiment (GRACE; since 2002).

Antarctic sea ice remained below average in 2025, with annual daily minima of sea ice extent and sea ice area recorded on 1 March, being the fourth and second lowest on record, respectively. The seasonal cycle was marked by late autumn-winter expansion and an early spring-summer retreat. This reduction in sea ice coverage led to record coastal exposure (50% more than the long-term average) throughout the year and was the net result of contrasting regional anomalies. Regionally, the Weddell Sea–Indian Ocean, Bellingshausen Sea, and central and western Ross Sea sectors experienced extremely low sea ice coverage. The opposite occurred in the eastern Ross Sea and western Amundsen Sea. The low sea ice coverage was associated with delayed sea ice advance, while higher sea ice coverage was associated with early ice advance. The net low sea ice coverage is a continuation of the trend in low sea ice extent and area seen since 2016, and in 2025 is attributed to both atmospheric and oceanic variability.

Across the Southern Ocean in 2025, sea surface temperatures exhibited positive anomalies. This continued the positive trend observed since 2005. The western Pacific region showed the greatest surface warming with peak warmth occurring in March. This was also the region with the largest positive salinity anomalies. Together with the sea surface temperatures, ocean heat content anomalies were also positive, reaching their highest level in 2025 and continuing a long-term warming trend. The increase in ocean heat content between 2024 and 2025 represents an acceleration of heat uptake by the ocean. As in 2024, chlorophyll, an important marker of ocean biogeochemistry, was at elevated levels during December 2024 and January 2025, particularly in the Atlantic. Dissolved oxygen anomalies were negative in all sectors, pointing to reduced solubility due to increased sea surface temperatures.

The 2025 Antarctic ozone hole was smaller than average, being the fourth or fifth weakest ozone hole, depending on the metric used, and among the weakest ozone holes observed since 1992. It began development in mid-July and reached its maximum size of 22.9 million km^2 on 9 September, earlier than in 2024. Further development was impeded by higher-than-average stratospheric temperatures associated with planetary scale wave events, which also contributed to the surface warming seen over the continent in spring. Observations of chlorine monoxide

Fig. 6.1. Map of weather stations and geographic regions discussed in this chapter. (Source: K. Marek, University of Wisconsin-Madison.)

were also lower than average in 2025, decreasing to near-zero by mid-October. The lower concentrations of this ozone depleting substance are part of the long-term trend of decline in ozone-depleting chlorine and bromine levels in the Antarctic stratosphere, and combined with the warm stratosphere, led to a weak ozone hole in October 2025. The ozone hole broke up on 30 November 2025, 11 days earlier than average, driven by multiple planetary-scale wave events, particularly one that began on 25 November.

More details on Antarctica's climate, weather, ice, ocean, and ozone are presented in this chapter for 2025. Unless otherwise stated, the 2025 anomalies and standard deviations are all based on the 1991–2020 climatology. Note that some sections use different climatology periods due to data availability, while others use non-traditional seasons centered around specific phenomena of interest, such as surface melt (October to April) and the Southern Ocean chlorophyll season (June to July); these details are stated at the beginning of each section. Common geographic regions and place names referenced throughout the chapter are shown in Fig. 6.1.

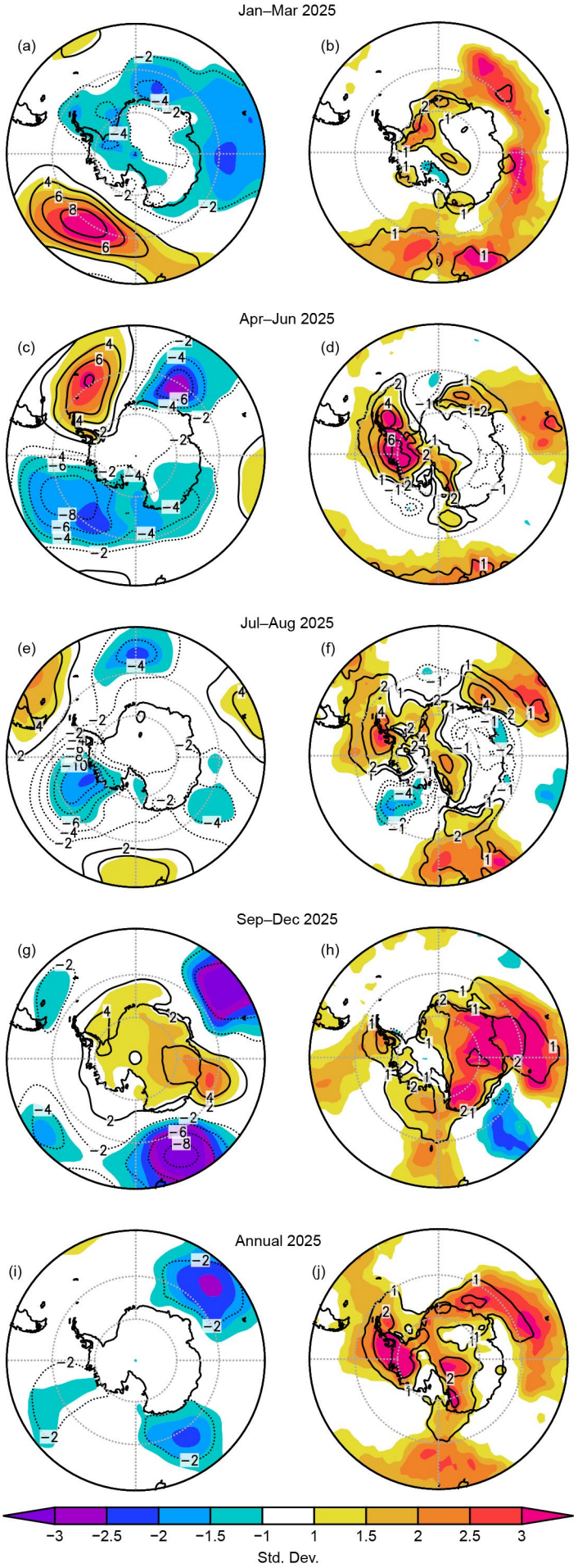

b. Atmospheric circulation and surface observations

—K. R. Clem, T. Ziegler, D. Mikolajczyk, L. M. Keller, M. A. Lazzara, S. Colwell, and R. L. Fogt

Here, the 2025 Antarctic atmospheric circulation and temperature anomalies are investigated using the European Centre for Medium-Range Weather Forecasts fifth generation atmospheric reanalysis (ERA5; Hersbach et al. 2020). Monthly surface temperature and pressure anomalies are also examined from staffed weather stations sourced from the Reference Antarctic Data for Environmental Research (READER) archive (Turner et al. 2004), and automatic weather station (AWS) data from the Antarctic Meteorological Research and Data Center (AMRDC) Data Repository (AMRDC 2022).

While various regions experienced large month-to-month variability (highlighted in the monthly anomaly plots), for brevity the ERA5 2-m temperature and surface pressure anomalies are shown grouped and averaged over four periods when the large-scale features were relatively persistent: January–March (Figs. 6.2a,b), April–June (Figs. 6.2c,d), July–August (Figs. 6.2e,f), and September–December (Figs. 6.2g,h). In addition, as reported in the Copernicus "Global Climate Highlights 2025" report based on ERA5 data (https://climate.copernicus.eu/copernicus-2025-was-third-hottest-year-record), the southern polar cap (60°S–90°S) experienced its warmest year on record in 2025 (since 1979). Thus, the 2025 annual mean anomalies are also shown in Figs. 6.2i,j. The vertical structure of the climate anomalies is examined in Fig. 6.3, showing the monthly geopotential height (Fig. 6.3a) and temperature (Fig. 6.3b) anomalies averaged over the polar cap (60°S–90°S) and the monthly circumpolar zonal wind anomalies (Fig. 6.3c) averaged over 50°S–70°S. Lastly, Fig. 6.4 shows the monthly temperature and pressure anomalies for select staffed and automated weather stations (see Fig. 6.1 for station locations and geographical references made in this section and throughout the chapter). All anomalies and standard deviations are based on the 1991–2020 climatology, with the exception of Relay Station AWS, whose

Fig. 6.2. (left) Surface pressure (hPa) and (right) 2-m temperature anomalies (°C) relative to 1991–2020 for (a),(b) Jan–Mar 2025, (c),(d) Apr–Jun 2025, (e),(f) Jul–Aug 2025, (g),(h) Sep–Dec 2025, and (i),(j) annual (Jan–Dec) 2025. Contour interval is 2 hPa for both fields with an additional ±1°C contour added for 2-m temperature; zero contours are omitted. Shading depicts standardized anomalies as indicated by the color bar at bottom. (Source: ERA5 reanalysis.)

observational record begins in 1995 (the starting year of each station's record is given in the Fig. 6.4 caption).

Continental Antarctica and the Atlantic-Indian sector of the Southern Ocean experienced generally below-average pressure during January–March, while the South Pacific was dominated by a strong ridge of high pressure (Fig. 6.2a). Locally higher cyclonic activity occurred in the southern Weddell Sea, producing strong regional warming from the coast stretching inland to parts of the plateau (Fig. 6.2b), including at Relay Station AWS, which experienced its warmest January on record (–24.9°C, 4.0°C above average; Fig. 6.4e). Enhanced cyclonic activity over much of the southern Indian Ocean was also accompanied by strong near-surface warming, but this remained offshore over the Southern Ocean. January had the strongest continent-wide warming, carrying over from December 2024 and persisting into February 2025 (Fig. 6.3b), reflecting a very warm 2024/25 austral summer over the polar cap. An intense spell of stronger-than-average circumpolar westerlies occurred during March and April (>2 m s^{-1} and 1.5 std. dev. to 2 std. dev. above average; Fig. 6.3c), accompanied by below-average tropospheric pressure over the continent (Fig. 6.3a) and strongly positive values of the Southern Annular Mode (SAM) index (bottom of Fig. 6.3); in April, Novolazarevskaya station in coastal Dronning Maud Land had its lowest April pressure on record (8.9 hPa below average; Fig. 6.4b), and the pressure at Dome C II AWS on the plateau was 10.5 hPa below average in April (Fig. 6.4d).

Over the period April–June, the atmospheric circulation became highly amplified over the Southern Ocean (Fig. 6.2c), while pressure over the continental interior returned to close to average during May–June (Fig. 6.3a). A strong ridge of high pressure developed over the South Atlantic extending westward to the Antarctic Peninsula (+6 to +8 hPa and >2 std. dev. above average), while below-average pressure formed over the South Pacific and also northeast of Dronning Maud Land. In the South Pacific-South Atlantic region, the warm, northerly flow in between the impressive low–high couplet brought record warmth to the Antarctic Peninsula extending inland to West Antarctica and the Ross Ice Shelf (Fig. 6.2d). Rothera station (on the western Antarctic Peninsula) and Marambio station (on the eastern Antarctic Peninsula) both experienced their warmest April on record (3.0°C and 8.8°C above average, respectively), and Rothera also had its warmest June on record (6.0°C above average; Fig. 6.4a). On the Ross Ice Shelf, Marble Point AWS recorded its warmest June (5.7°C above average; Fig. 6.4f). In interior West Antarctica, temperature anomalies at Byrd AWS ranged from +2.4°C in April to +4.8°C in June (not shown), but no records were set. In coastal Dronning Maud Land near the second prominent cyclonic circulation,

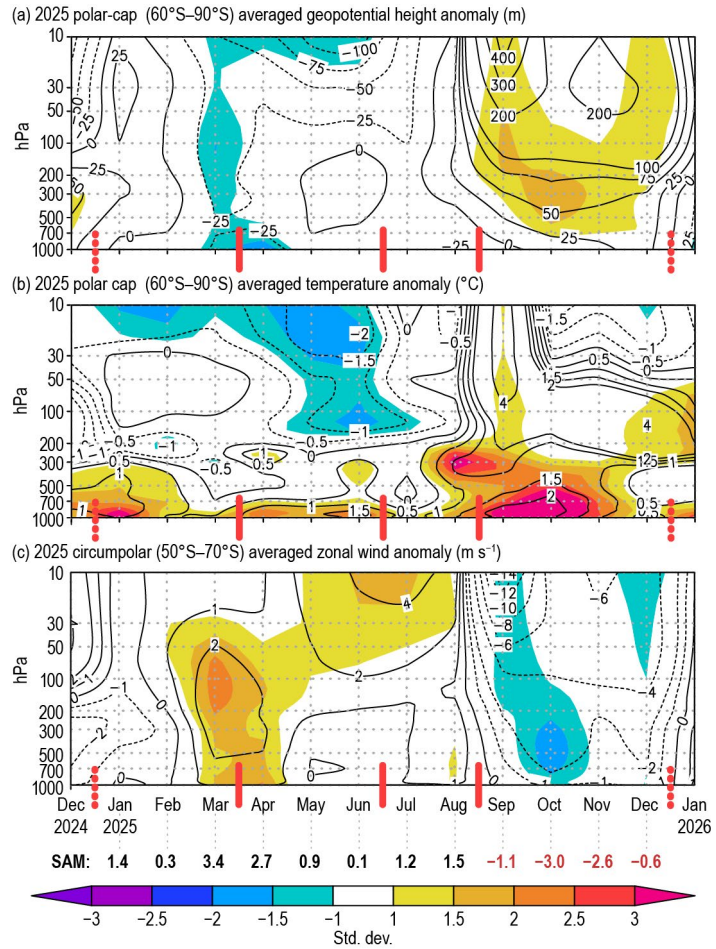

Fig. 6.3. Area-averaged (weighted by cosine of latitude) monthly anomalies over the southern polar region in 2025 relative to 1991–2020: (a) polar cap (60°S–90°S) averaged geopotential height anomalies (m; contour interval is 25 m up to ±100 m and 100 m after ±100 m); (b) polar cap averaged temperature anomalies (°C; contour interval is 0.5°C up to ±2°C and 2°C after ±2°C); (c) circumpolar (50°S–70°S) averaged zonal wind anomalies (m s^{-1}; contour interval is 2 m s^{-1} with an additional contour at ±1 m s^{-1}). Shading depicts standardized monthly anomalies as indicated by the color bar at bottom. (Source: ERA5 reanalysis.) Red vertical bars indicate the four climate periods used for compositing in Fig. 6.3; the dashed lines near Dec 2024 and Dec 2025 indicate circulation anomalies wrapping around the calendar year. Values from the Marshall (2003) Southern Annular Mode (SAM) index are shown below (c) in black (positive) and red (negative).

temperatures at Novolazarevskaya and Syowa stations ranged from 2.5°C to 4.0°C above average during April and May (Fig. 6.4b), with warm conditions persisting through July at Syowa.

During July–August, a more prominent zonal wave 3 structure developed (an offshore circumpolar band of three highs and three lows; Fig. 6.2e) while pressure over the interior continent remained close to average (Fig. 6.3a). The key regional changes were that the ridge in the South Atlantic shifted northward, and the low in the South Pacific shifted southward into the Amundsen Sea. This produced a more classic dipole temperature anomaly across West Antarctica, with strong warming over the Antarctic Peninsula and Bellingshausen Sea (a continuation of the warm conditions that began in April; Fig. 6.4a) and below-average temperatures in the Ross Sea (Fig. 6.2f). Despite the dipole, the northerly flow to the east of the cyclone channeled warmer air from the South Atlantic poleward onto the plateau (temperatures at the South Pole-Amundsen Scott station were 5.7°C above average in August; Fig. 6.4d) and down onto the Ross Ice Shelf (Marble Point AWS recorded its warmest August on record; 5.9°C above average).

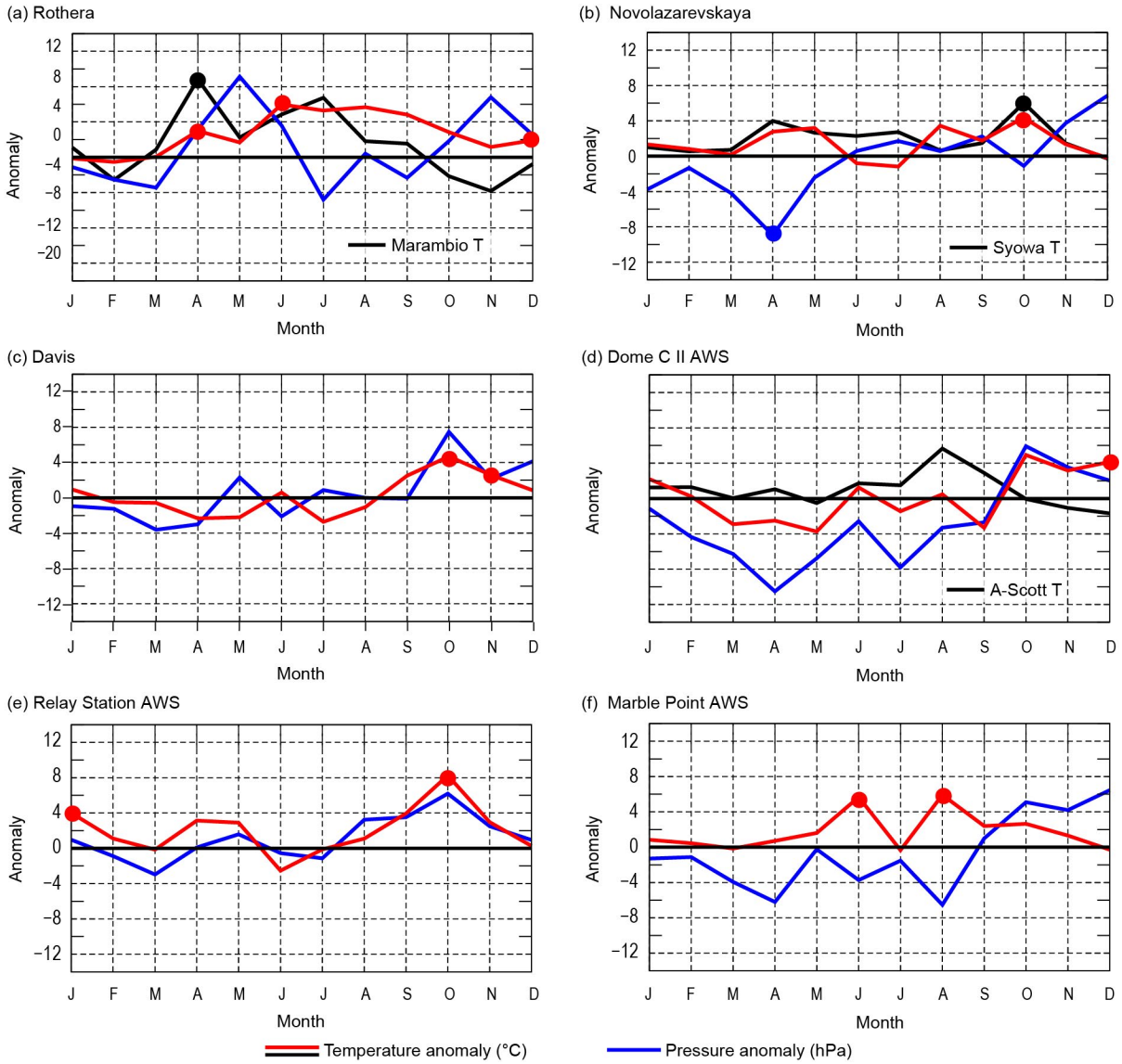

Fig. 6.4. Observed monthly Antarctic surface air temperature and station pressure anomalies during 2025 from nine representative stations [six staffed (a)–(d), and three automatic (d)–(f)]. Anomalies for temperature (°C) are shown in red and black and mean sea level pressure/surface pressure (hPa) is shown in blue. The station with both temperature (red) and pressure (blue) anomalies plotted is labeled at the top of each panel, while select complementary temperature anomalies (black) for nearby stations are labeled in the panel insets in (a),(b), and (d). Filled circles denote monthly-mean records set in 2025. The station records start in 1976 for Rothera and 1970 for Marambio in (a), 1961 for Novolazarevskaya and 1957 for Syowa in (b), 1957 for Davis in (c), 1980 for Dome C II AWS and 1957 for Amundsen Scott in (d), 1995 for Relay Station AWS in (e), and 1980 for Marble Point AWS in (f). See Fig. 6.1 for station locations.

In September, a weak positive temperature anomaly and a strong positive geopotential height anomaly (and weakening of the circumpolar westerlies) developed in the stratosphere and propagated downward to the surface in October and November, lingering into December (Fig. 6.3). A resultant strong positive surface pressure anomaly developed over the Antarctic continent, flanked by negative pressure anomalies in the middle latitudes (reflecting a negative SAM pattern, rf. SAM indices at bottom of Fig. 6.3). In particular, two very deep mid-latitude low pressure anomalies formed—one southwest of New Zealand and one in the Indian Ocean—both more than 3 std. dev. below average (Fig. 6.2g) and both aiding in transporting warm low-latitude air poleward to Antarctica. Over the continent, the positive pressure anomalies were accompanied by widespread record-setting warmth, strongest over East Antarctica and the Antarctic Peninsula (regions where the warm poleward flow was locally maximized). In October, Novolazarevskaya (4.4°C above average), Syowa (6.0°C above average), Davis (4.7°C above average), and Relay Station AWS (8.2°C above average) all set new record-high October temperatures. Davis station also had its warmest November on record (2.6°C above average), and Rothera (1.9°C above average) and Dome C II AWS (4.2°C above average) had their warmest December on record.

Annually, based on ERA5 2-m temperature averaged over the polar cap (60°S–90°S), 2025 was 1.0°C above the 1991–2020 average and the warmest year on record since 1979 (not shown). New monthly high-temperature records were set at various times of the year in nearly every region of Antarctica, including 13 new monthly high-temperature records at the nine geographically dispersed stations presented here (Fig. 6.4). While the strong positive pressure anomalies that formed in the spring played a key role in the record warmth, which appear tied to the weak stratospheric warming event (Fig. 6.3), the emergent annual-mean circulation pattern resembled a zonal wave 3 structure with three distinct negative pressure anomalies over the Southern Ocean (Fig. 6.2i). Each of these cyclonic circulations locally enhanced regional warming (Fig. 6.2j), including on the Antarctic Peninsula, where Rothera station also recorded its warmest year on record (annual average temperature of –1.4°C, 2.7°C above average; not shown), and across much of Dronning Maud Land. It is noteworthy that climate models predict a more prominent zonal wave 3 structure through the twenty-first century under anthropogenic warming (Barthélemy et al. 2026), and seven of the past eight years (2018–25) were among the eight warmest years on record based on ERA5 2-m temperature averaged over the polar cap.

c. Ice sheet surface mass balance

—L. Trusel, M. Bahrami, R. Baiman, T. Black, C. Kittel, and M. Maclennan

Surface mass balance (SMB) is the net sum of all processes that add to and remove mass from an ice sheet's surface. Over the Antarctic Ice Sheet (AIS), SMB exceeds 2500 Gt (10^{12} kg) yr^{-1} and is dominated by snowfall (Agosta et al. 2019). Sublimation and drifting snow erosion represent the largest ablation terms in the AIS SMB (van Wessem et al. 2018), given that most surface melt refreezes within the firn (Mottram et al. 2021). SMB varies strongly in space and time, exceeding 500 mm water equivalent (w.e.) yr^{-1} in high-relief coastal areas but falling below 50 mm w.e. yr^{-1} on the East Antarctic plateau (Fig. 6.5a), while peaking in autumn (March–May) and reaching a minimum in summer (December–February; Fig. 6.6a). Although only SMB on grounded ice directly affects sea level, SMB on floating ice shelves is critical for maintaining firn layer health and ice shelf stability (The Firn Symposium Team 2024). Though rare, atmospheric rivers (ARs) deliver a large fraction of AIS SMB gains (Maclennan et al. 2023; Baiman et al. 2024; Wille et al. 2025), while reduced AR activity can lead to anomalously low snowfall and a more negative mass balance (Davison et al. 2023).

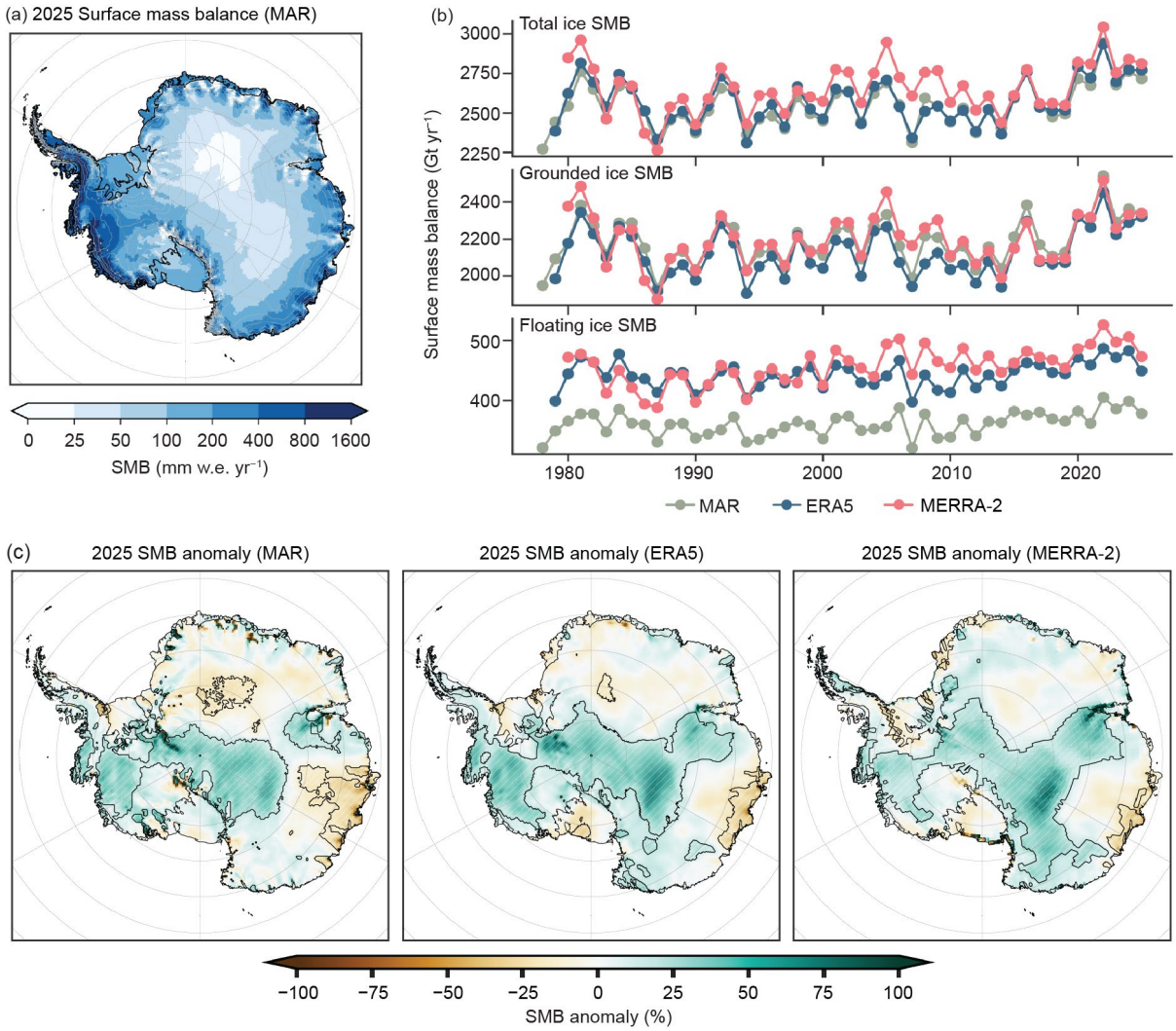

Fig. 6.5. (a) Model for Surface Mass Balance of the Arctic Ice Sheets (MAR) 2025 surface mass balance (SMB; mm water equivalent [w.e.] yr^{-1}). (b) Time series of annual surface mass balance in Gt (10^{12} kg) yr^{-1} over the full ice sheet and its grounded and floating portions. (c) Annual MAR, ERA5, and MERRA-2 SMB anomalies for 2025 relative to the 1991–2020 mean (%). The 2025 SMB anomalies are higher than the 1991–2020 std. dev. of the respective datasets in the areas outlined in black.

The 2025 SMB are estimated as total precipitation minus evaporation and sublimation (P–E) from the ERA5 (Hersbach et al. 2020) and MERRA-2 (Gelaro et al. 2017) reanalyses, and the regional climate model Model for Surface Mass Balance of the Arctic Ice Sheets (MAR) forced by ERA5, which explicitly represents SMB processes including firn evolution and meltwater runoff (Kittel et al. 2021). ERA5 and MAR have comparable spatial resolutions over Antarctica (0.25° and 25 km, respectively), both finer than MERRA-2 (0.625° × 0.5°). ERA5 (and ERA5-forced MAR) extend back to 1940, but our analysis is limited to 1979–present to avoid known pre-satellite-era biases over Antarctica (Bromwich et al. 2024). MERRA-2 begins in 1980. For spatial consistency, each dataset is bilinearly regridded to the ERA5 grid, and grounded and floating ice masks from the Antarctic Digital Database are applied (Gerrish et al. 2023). Annual and monthly SMB and ERA5 meridional moisture transport (vIVT) anomalies are computed relative to a 1991–2020 climatology. To assess synoptic drivers of SMB variability, ERA5 fields of 500-hPa geopotential height are analyzed, and the Amundsen Sea Low (ASL) position and intensity is quantified following Hosking et al. (2013). ARs are detected in MERRA-2 following Wille et al. (2021). Finally, quarterly SMB anomalies are compared with ICESat-2 ATL15 gridded rates of ice surface height change (Smith et al. 2024).

In 2025, the grounded AIS SMB equaled 2321 Gt (ERA5), 2340 Gt (MERRA-2), and 2338 Gt (MAR), representing anomalies of 1.2 std. dev. to 2.0 std. dev. above the 1991–2020 climatological means (ERA5: 2104±109 Gt yr^{-1}; MERRA-2: 2186±106 Gt yr^{-1}; MAR: 2173±98 Gt yr^{-1}). These SMBs represent the third highest in ERA5 (behind 2022 and 1981) and the fifth highest in MAR and MERRA-2. In contrast to previous years where grounded and floating SMB saw similarly strong positive anomalies, SMB over floating ice shelves was less anomalous in 2025, decreasing from 2024 according to all datasets (Fig. 6.5b), owing in part to the absence of positive SMB anomalies over the Ross and Ronne-Filchner ice shelves (Fig. 6.5c). Total and grounded SMB show a recent increase in the frequency of above-average SMB years since the early 2010s, although similarly elevated values occurred in the early 1980s (Fig. 6.5b). Including the 2025 SMB strengthens the grounded-ice SMB trend (e.g., MAR 1979–2025: 2.9 Gt yr^{-1}; $p=0.02$), but trends in all datasets remain insignificant at the 99% confidence interval and dominated by strong interannual variability. However, there are significant positive trends in floating ice shelf SMB over the full record in MERRA-2 (1.4 Gt yr^{-1}) and MAR (0.6 Gt yr^{-1}).

In contrast to the reanalyses, floating ice SMB is systematically lower in MAR both for 2025 and across the full time series (Fig. 6.5b). This offset is consistent with the fact that we quantify reanalysis SMB as P–E (e.g., Medley and Thomas 2019), whereas MAR explicitly simulates SMB, including runoff. For 2025, the MAR-ERA5 difference is ~70 Gt (MAR lower), of which ~35 Gt can be explained by runoff in MAR. The remainder likely reflects structural differences in representation of surface and boundary-layer processes between MAR and the reanalyses. We note that while runoff remains a relatively small AIS SMB term today, this discrepancy highlights why explicit firn process representation (meltwater retention and runoff; firn densification) will become increasingly important for credible ice shelf SMB projections in a warming climate (e.g., Dunmire et al. 2024).

April 2025 featured strongly positive AIS SMB (Fig. 6.6a), ranking as the highest April SMB on record in MAR and MERRA-2 and the second highest in ERA5. The synoptic pattern was characterized by an ASL that was displaced slightly east of its climatological position (Fig. 6.6b) but much deeper than average (central pressure ~1.6 std. dev. below the April climatology). This coincided with pronounced mid-tropospheric blocking east of the Antarctic Peninsula (500-hPa geopotential height anomalies up to +3.5 std. dev. above average; see Fig. 6.2c), producing a strong east–west pressure/height gradient pattern that favored sustained moisture transport into West Antarctica (Fig. 6.6b). Consistent with this circulation, April exhibited frequent episodes of anomalous poleward vIVT and a frequent occurrence of ARs (Figs. 6.6b,c), directing moisture and snowfall toward Ellsworth Land and the western Antarctic Peninsula. Precipitation was strongly orographically focused along the coastal escarpment, locally exceeding ~2 m w.e. (Fig. 6.6d). Several ARs penetrated well inland (Fig. 6.6c), helping to extend positive SMB anomalies into parts of the high elevation polar plateau (Fig. 6.6d).

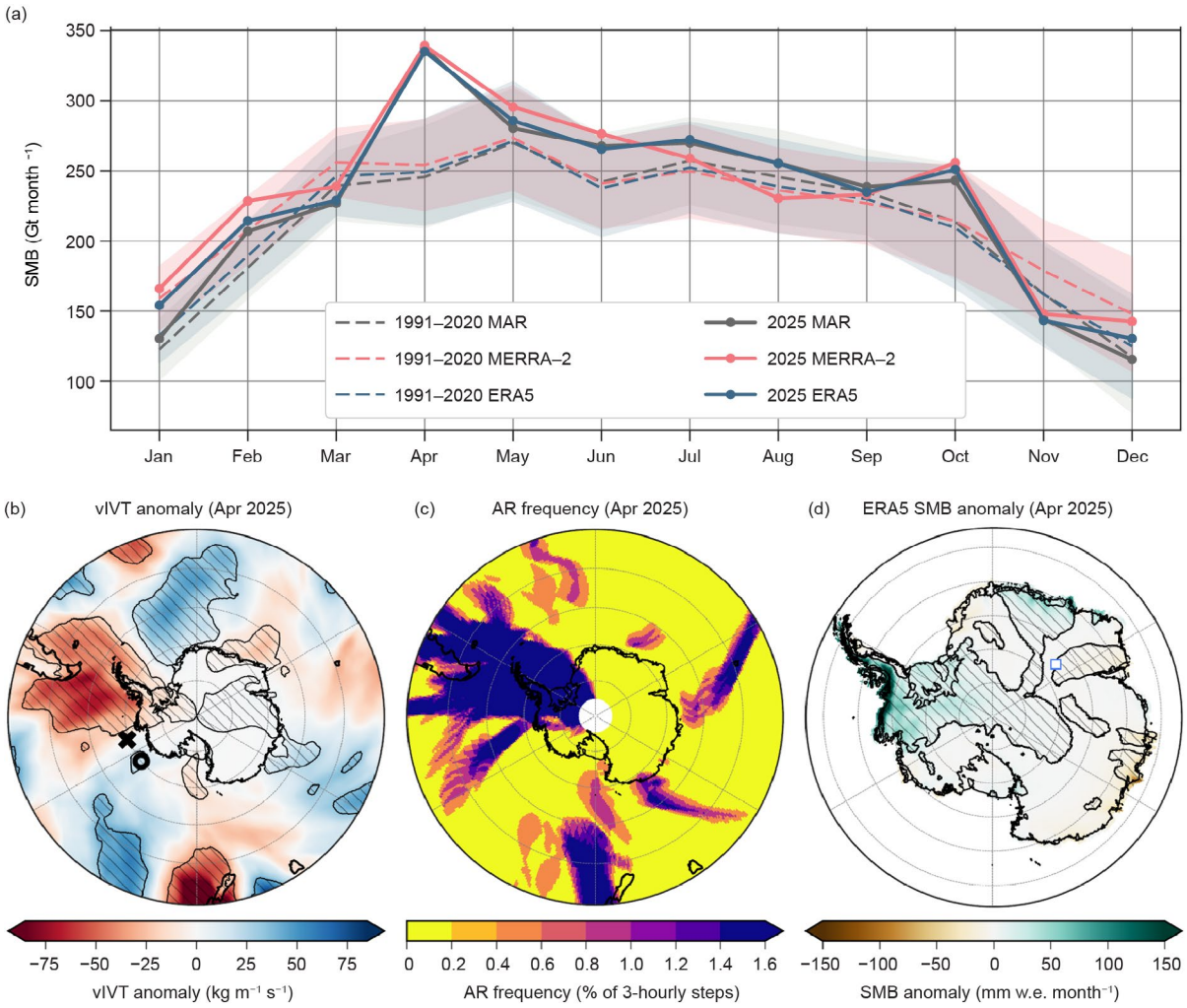

Fig. 6.6. (a) Monthly cycle of total (grounded and floating) Antarctic Ice Sheet surface mass balance (SMB) in Gt month^{-1} for the Model for Surface Mass Balance of the Arctic Ice Sheets (MAR; gray), MERRA-2 (pink), and ERA5 (blue). The 2025 values are shown with solid lines; 1991–2020 averages in dotted lines; shading indicates ±1 std. dev. (b) Apr 2025 anomalies in ERA5 meridional integrated vapor transport (vIVT) with negative values (red shades) indicating enhanced poleward moisture transport. The Apr 2025 mean Amundsen Sea Low (ASL; kg m^{-1} s^{-1}) position is marked with an X and the 1991–2020 mean position with a circle. (c) Apr 2025 atmospheric river (AR) frequency (% of 3-hr steps) from MERRA-2. (d) Apr 2025 absolute SMB anomaly (mm water equivalent [w.e.] month^{-1}) in ERA5. Outlines in (b) and (d) indicate anomalies > ±1 std. dev. relative to the 1991–2020 Apr climatology.

Finally, quarterly (91-day cycle) ATL15 estimates of surface height change (dh/dt) are compared to ERA5 SMB expressed as quarterly water-equivalent height-change rate (also see section 6e for surface height change alongside ice sheet mass balance change). There is broad spatial agreement between ERA5 SMB and ICESat-2, including coherent coastal anomaly patterns and relatively muted interior signals over the first half of 2025 (Fig. 6.7a). Notably, the effects of highly anomalous snowfall across coastal West Antarctica are revealed by positive height changes exceeding 1 m yr^{-1} for April–June 2025. A grid-cell comparison also shows a clear positive relationship between the two products (Fig. 6.7b), indicating that regions with anomalous SMB in ERA5 generally correspond to observed height changes in ATL15. In terms of magnitude, the ERA5 SMB water-equivalent dh/dt is ~40% of the ATL15 total surface dh/dt over this period, and comprises a greater percentage of the ATL15 dh/dt at snow density (e.g., ~80% at a density of 0.5 g cm^{-3}). ATL15 reflects not only SMB-driven height change but also firn processes (e.g., compaction) and potentially some residual ice-dynamic signal near fast flowing regions. Overall, this agreement provides an important, independent check that the large-scale 2025 SMB anomalies in the modeled products are physically plausible.

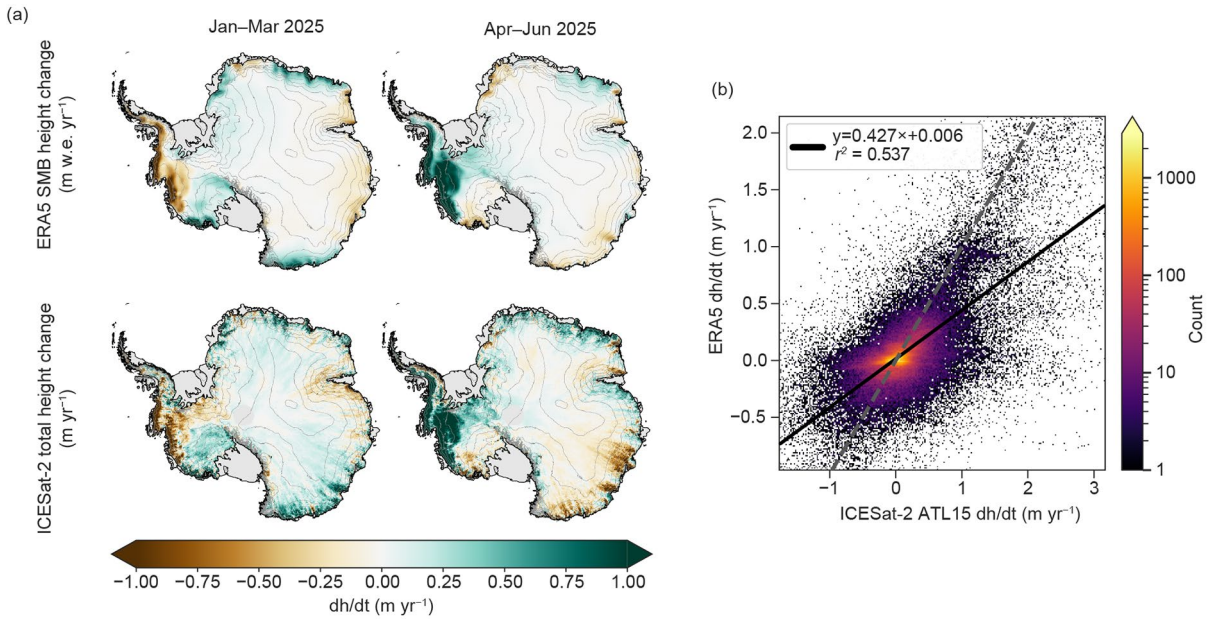

Fig. 6.7. Comparison of modeled surface mass balance (SMB)-driven height-change rates (dh/dt) from ERA5 and observed height changes (m water equivalent [w.e.] yr^{-1}) from ICESat-2 ATL15 for the first half of 2025. (a) Quarterly dh/dt (m yr^{-1}) maps showing largely coherent spatial patterns, and (b) Grid-cell ATL15 dh/dt versus ERA5 SMB water-equivalent dh/dt with colors representing point density (m yr^{-1}). The solid black line shows the best-fit regression; the dashed gray line denotes 1:1.

d. Ice sheet seasonal melt extent and duration

—M. MacFerrin, A. F. Banwell, T. L. Mote, and T. Scambos

Surface melt on the Antarctic Ice Sheet (AIS) occurs predominantly along its low-elevation coastal margins, especially on the Peninsula and on the ice shelves fringing the continent (e.g., Banwell et al. 2023). Although surface melt currently contributes only a small fraction to the overall AIS mass balance compared with snow accumulation, glacier calving, and basal melting, it is often considered to be a key measure of ice shelf stability. Meltwater that percolates into the firn and refreezes increases firn density, progressively reducing pore space and permeability. The development of near-surface impermeable layers can inhibit vertical drainage, promoting the formation of surface meltwater ponds (see Sidebar 6.1 for more details on the 2024/25 supraglacial meltwater conditions). Such ponding has been linked to ice shelf weakening and hydrofracture-driven breakup (Banwell et al. 2013); processes that may trigger upstream glacier acceleration and thinning (Scambos et al. 2014). Here, the 2024/25 Antarctic melt season is examined; the 2025/26 Antarctic melt season will be discussed in next year's report.

Daily surface and near-surface melt are mapped using satellite-derived passive-microwave brightness temperatures. The source data are distributed as daily composited polar stereographic brightness-temperatures by the National Snow and Ice Data Center (products NSIDC-0001, Meier et al. 2019 and NSIDC-0007, Gloersen 2006) spanning 1979 through the present day. Daily passive microwave brightness temperatures using the 37-GHz horizontal polarization, as well as the 37- and 19-GHz vertical polarization channels, are acquired by the Scanning Multichannel Microwave Radiometer (SMMR), Special Sensor Microwave Imager (SSM/I), and Special Sensor Microwave Imager Sounder (SSMIS) sensors aboard the NOAA Nimbus-7 and DMSP F8, F11, F13, F17, and F18 satellites. The austral melt season is defined here as 1 October through 30 April. Although small brief melt events can be measured along Antarctica's northern coastal margins throughout the year and even during the austral winter, the vast majority of melt happens during these seven months, with most melt typically occurring in December and January. An ice extent mask of 25-km grid cells for the AIS was developed from the Quantarctica v3.0 Detailed Basemap dataset (Norwegian Polar Institute 2018). All 25-km cells that contain ≥50% land ice or ice shelf are included. The AIS is divided into seven melt extent and climate regions by clustering glaciological drainage basins (based on The IMBIE Team 2020; Fig. 6.8b). The presence of liquid meltwater is determined by 37-GHz horizontally polarized brightness temperatures that exceed a dynamically established threshold each season from a simple microwave emission model that would be expected in the presence of liquid water in near-surface layers of ice and snowpack. As the melt data are binary (i.e., the algorithm indicates there is either melt or no melt); these data do not measure the intensity of the melting or the volume of meltwater present.

The method used here was first developed to track the Greenland Ice Sheet's surface melt daily (Mote and Anderson 1995; Mote 2007, 2014). Large seasonal fluctuations in passive microwave emissions from some areas of dry polar firn in Antarctica can create false positive melt indications in an unmodified version of the Greenland algorithm. This was mitigated by filtering areas that only marginally exceed the melt threshold (<10K) in the 37-GHz horizontal polarization in regions with a negative 18/19-GHz minus 37-GHz frequency gradient in the vertical polarization and has been used in previous season reports of Antarctic melt (MacFerrin et al. 2021, and each year thereafter).

Considering Antarctica as a whole, the early-to-middle portion of the 2024/25 melt season (October through January) was characterized by above-average surface and near-surface melt extent and was particularly high between mid-December 2024 and early January 2025 (Fig. 6.8b). From early February onward, melt extent declined to near-zero and remained minimal through early March. Melt was largely negligible thereafter, aside from two brief late-season spikes in early and late April.

Against this backdrop, the 2024/25 melt season was also characterized by record-high supraglacial meltwater presence, including supraglacial lakes, streams, and rivers, and based on the 2013–25 Landsat 8/9 satellite record (see Sidebar 6.1). However, above-average net snow accumulation in the 2024/25 season (section 6c) helped reduce the ice sheet's net contribution to sea level rise for the 2024/25 summer (section 6e).

Considering regional variations, the high melt extent in the early-to-mid 2024/25 melt season was observed on ice shelves in all regions except the northeastern Ross Ice Shelf (Figs. 6.8c,d). This observation contrasts to 2023/24, when only parts of the Peninsula and Maud Land and Enderby Land regions saw above-average surface melt extent, and all other ice shelf regions experienced below-average melt (MacFerrin et al. 2025).

Overall, the total number of melt days during the 2024/25 austral summer exceeded the 1991–2020 long-term average by approximately 10 days on the eastern Peninsula Larsen C Ice Shelf, 12 days to 15 days on the Fimbul Ice Shelf, and 20 days to 30 days along the eastern side of the Amery Ice Shelf. Other notable areas with above-average melt days were the North George VI, Bach, Wilkins, West, Shackleton, and Totten ice shelves.

The Antarctic Peninsula (Fig. 6.8b) saw an annual melt index of 5.55 million km^2-days, 30% above the baseline mean value of 4.28 million km^2-days. Melt extent in the Peninsula likely reached a record for the satellite era around 1–2 January 2025, with just over 50% of the ice sheet and ice shelf areas in this region showing surface melting.

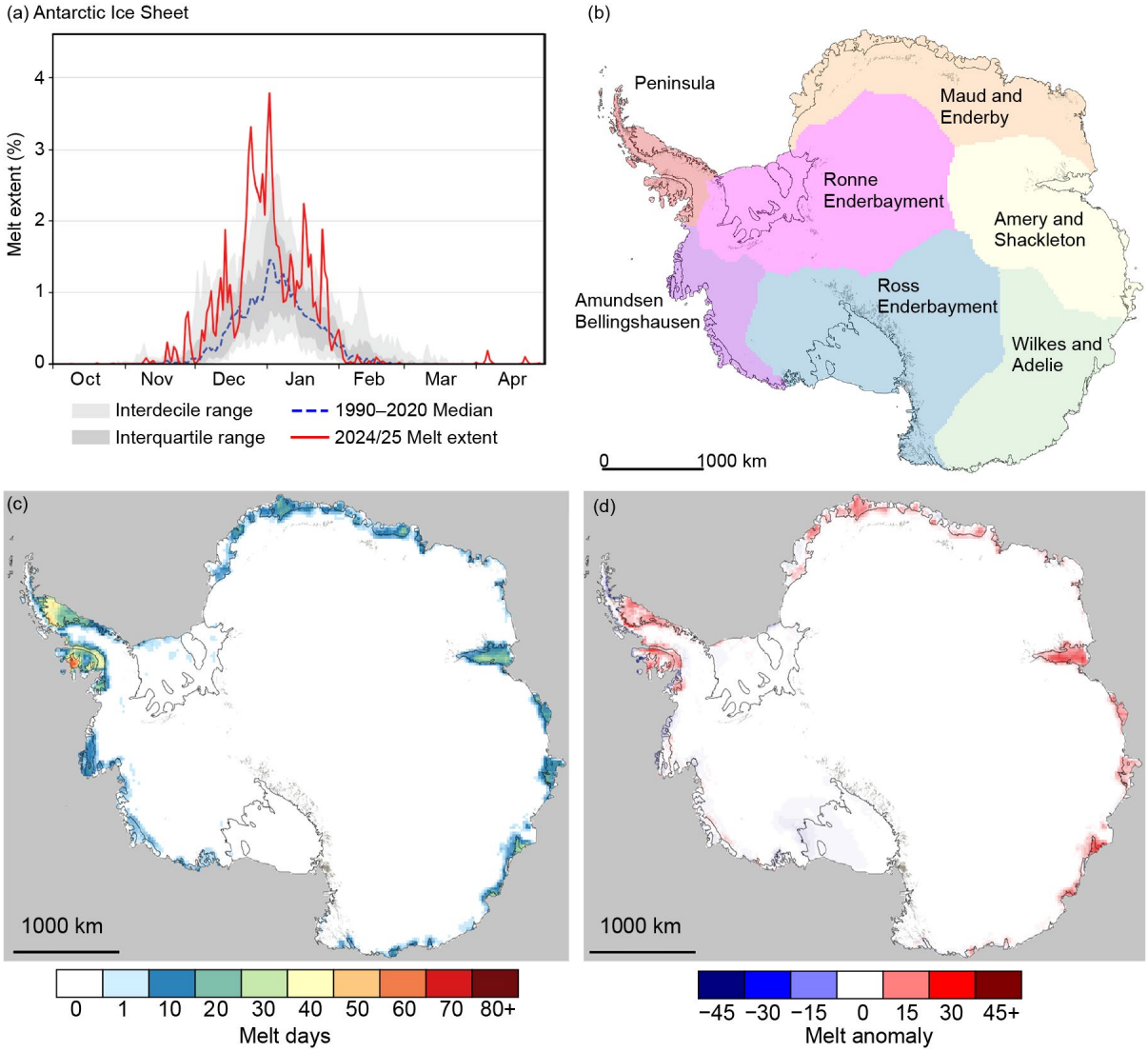

Fig. 6.8. (a) Daily surface melt extent (%; from National Snow and Ice Data Center [NSIDC]-0001, 0007) across the Antarctic Ice Sheet for the 2024/25 melt season, with 1990–2020 median values in blue and interdecile and interquartile ranges shaded in gray. (b) Reference map of Antarctic melt analysis regions. (c) Map of the sum of melt days across the Antarctic Ice Sheet in the 2024/25 melt season. (d) Map of the anomaly of the sum of melt days in the 2024/25 melt season compared to mean values from the 1990–2020 reference period.

Low air temperatures over the Antarctic Peninsula later in the melt season (section 6b) likely contributed to the observed sudden decline in melt extent and number of melt days in early February. Although air temperatures in Droning Maud Land and West Antarctica remained high relative to the average across the AIS, temperatures here rarely rose above 0°C. East Antarctica

was generally cooler than average, and overall, the atmospheric circulation anomalies were not exceptional apart from a broad positive SAM pattern (see Figs. 6.2b, 6.3), indicating that the intense summer melting (and low sea ice extent, section 6f) may plausibly be attributed to broadly warmer air temperatures (and ocean temperatures, section 6g).

The first of the two late-season spikes in melt extent in early and late April was caused by a strong atmospheric river event in early April (sections 6b, 6c) moving over the eastern Pine Island Bay region and leading to local surface melting. This air mass moved eastward, bringing the tip of the Peninsula above freezing a few days later. A later event in April appears to be due to a more typical Southern Ocean cyclone that produced warm downsloping foehn winds on the eastern Peninsula ice shelves.

Sidebar 6.1: **The exceptional nature of supraglacial meltwater in 2024/25**

—M. BAHRAMI, E. GLEN, L. D. TRUSEL, A. F. BANWELL, P. JACKSON, AND R. L. DELL

Supraglacial meltwater, including lakes and streams, develops where near-surface firn pore space is sufficiently depleted, limiting surface melt percolation and refreezing (Kuipers Munneke et al. 2014). Once established, this water can weaken ice shelves through hydrostatic loading and hydrofracture, processes implicated in past ice shelf break-ups (Scambos et al. 2000; Banwell et al. 2013, 2019; Leeson et al. 2020). Against this backdrop, the 2024/25 melt season (November 2024–March 2025) set a record for supraglacial meltwater presence across the Antarctic Ice Sheet in the 2013–25 Landsat 8/9 satellite record (Fig. SB6.1k), highlighting potentially growing ice shelf vulnerability as warming-driven melt further reduces firn pore space (Trusel et al. 2015; Veldhuijsen et al. 2024).

Supraglacial meltwater observations during the 2024/25 melt season

A continent-wide supraglacial meltwater record was generated spanning austral summers from 2013 to 2025 using a threshold-based water classification method applied to Landsat 8/9 imagery (e.g., Moussavi et al. 2020; Tuckett et al. 2025). Here, we focus on the maximum supraglacial meltwater

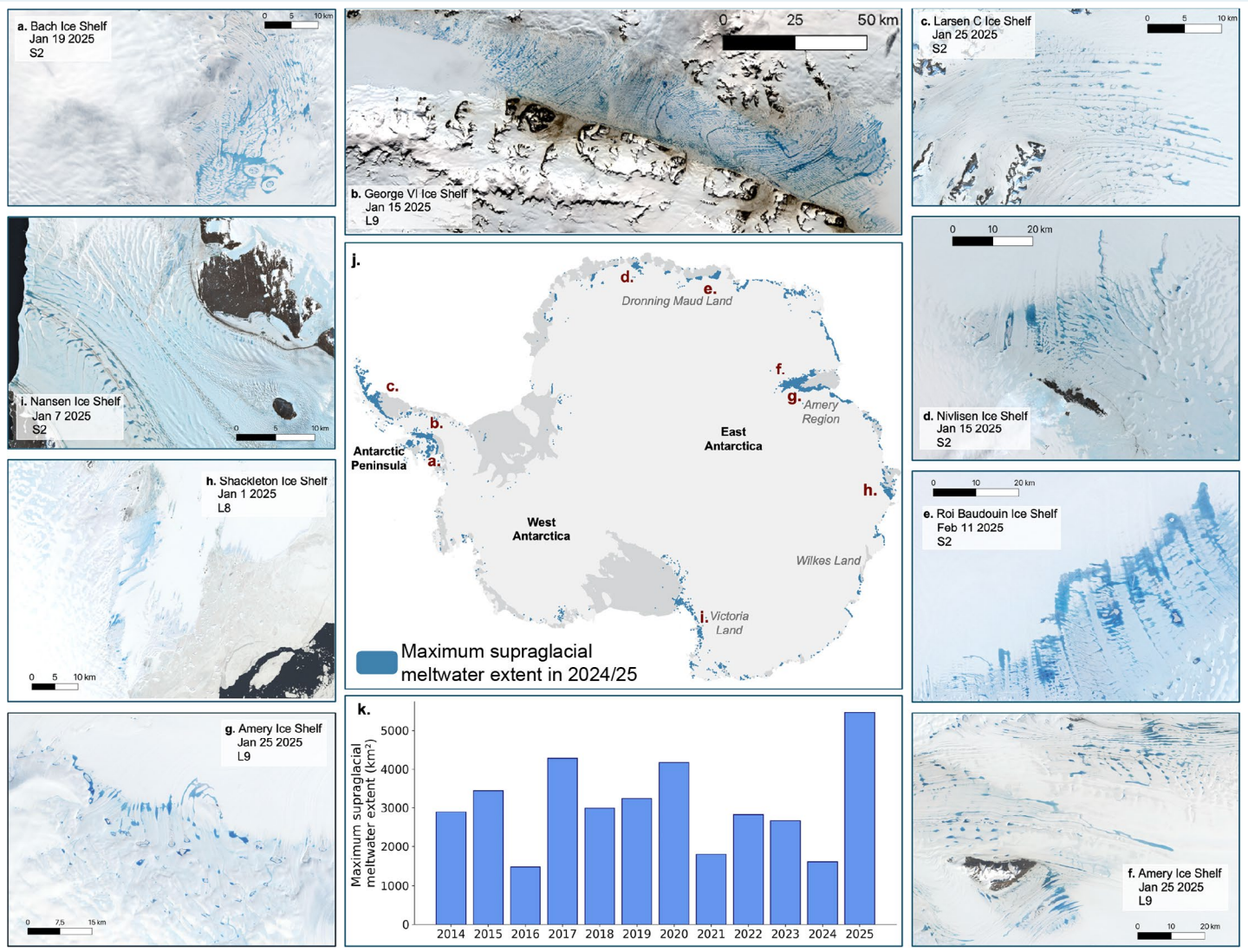

Fig. SB6.1. Supraglacial meltwater across Antarctica during the 2024/25 melt season. Representative examples of surface meltwater on ice shelves captured by Landsat 8/9 (L8, L9) and Sentinel-2 (S_2) imagery on: (a) Bach, (b) north George VI, (c) Larsen C, (d) Nivlisen, (e) Roi Baudouin, (f),(g) Amery, (h) Shackleton, and (i) Nansen. Map in (j) shows the location of each ice shelf and the maximum meltwater extent (enhanced for visualization) for the 2024/25 melt season derived from Landsat 8/9 imagery (blue). Base map of Antarctica is from Gerrish et al. (2023). Panel (k) shows maximum supraglacial meltwater extent from 2013/14 to 2024/25 based on Landsat 8/9, with the years on the x axis indicating the second year of each austral summer, i.e., 2025 corresponds to the 2024/25 season.

extent within each melt season, defined as a composite of all Landsat 8/9 water detections from November through February. Analysis of the 2024/25 melt season revealed a maximum supraglacial meltwater extent of ~5400 km^2 across Antarctica, representing the highest extent recorded since the start of the Landsat 8 era in 2013 and surpassing the previous maximum of ~4100 km^2 in 2016/17 (Fig. SB6.1k).

As in past high-melt summers, e.g., 2016/17 and 2019/20 (e.g., Banwell et al. 2021, 2023; Mahagaonkar et al. 2024; Dell et al. 2024; Arthur et al. 2022; Corr et al. 2022; Stokes et al. 2019), supraglacial meltwater in 2024/25 was mainly concentrated on the Antarctic Peninsula (AP), Dronning Maud Land (DML), and the Amery region. Across the AP, the large majority of this occurred on the north George VI Ice Shelf, which peaked at ~1127 km^2 (Figs. SB6.1b, SB6.2b), rivaling, but not surpassing, that of the 1200 km^2 reported in 2019/20 (Banwell et al. 2021), followed by Bach Ice Shelf with ~220 km^2 of meltwater area (Fig. SB6.1a). Notably, in 2024/25, meltwater ponding on George VI also occurred farther south (Fig. SB6.1b) than in previous high melt years (Banwell et al. 2021). Additional ponding was observed on inner portions of Wilkins and Larsen C ice shelves and across adjacent grounded ice (Figs. SB6.1c, SB6.2a).

Large areas of supraglacial meltwater also occurred across DML in 2024/25, reaching 1500 km^2. Approximately two-thirds of this meltwater formed on the Roi Baudouin Ice Shelf (Figs. SB6.1e, SB6.2d), with the remainder predominantly distributed across Nivlisen Ice Shelf (Fig. SB6.1d). The maximum supraglacial meltwater area in the Amery region reached ~1650 km^2 in 2024/25. Lakes occurred in Amery's eastern grounding zone, both on floating and grounded ice, along with elongated lakes across the central and southern parts of the ice shelf (Fig. SB6.2e), similar to observations in previous high-melt years (Kingslake et al. 2017; Stokes et al. 2019; Tuckett et al. 2025). Wilkes Land (325 km^2), Victoria Land (170 km^2), and Ross Ice Shelf (100 km^2) made small contributions to the Antarctic-wide total area of supraglacial meltwater, while that over Filchner-Ronne Ice Shelf (2 km^2) and coastal West Antarctica (18 km^2) was negligible.

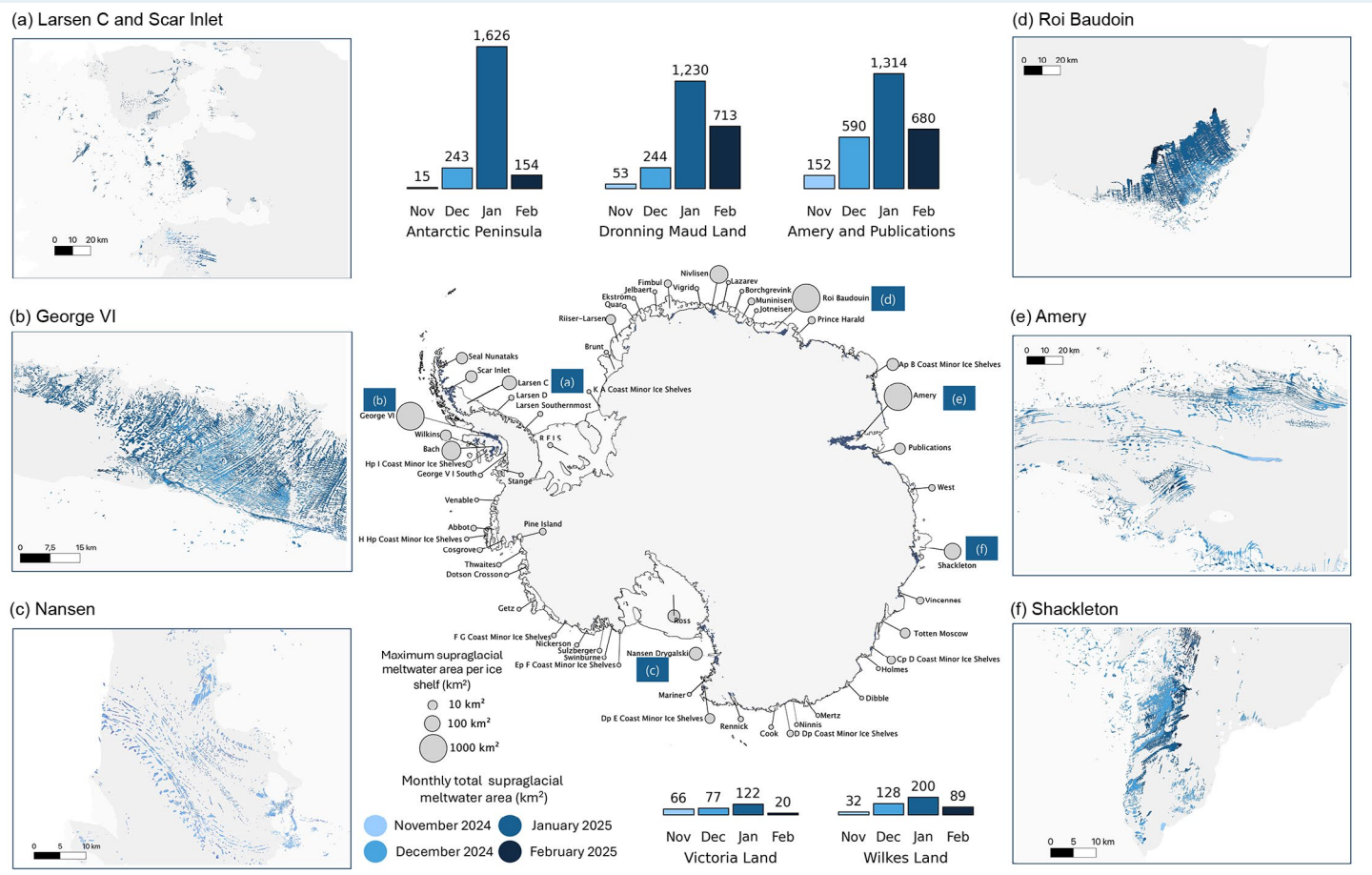

Fig. SB6.2. Antarctic-wide maximum supraglacial meltwater extent during the 2024/25 melt season and its monthly regional spatial distribution for (a) Larsen C and Scar Inlet, (b) north George VI, (c) Nansen, (d) Roi Baudoin, (e) Amery, and (f) Shackleton. Maximum 2024/25 supraglacial meltwater extent (enhanced for visualization) mapped from Landsat 8/9 imagery is shown in blue on the map of Antarctica. Circle markers are scaled by each ice shelf's maximum supraglacial meltwater area. Bar plots show the total monthly supraglacial meltwater area during the 2024/25 melt season. Panels (a)–(f) show the monthly evolution of supraglacial meltwater from Nov 2024 to Feb 2025.

The 2024/25 melt season was also characterized by active (i.e., flowing water) surface hydrological systems across multiple ice shelves. For example, a channel network on Nivlisen Ice Shelf reactivated after several years of inactivity (e.g., Dell et al. 2020), and supraglacial rivers on both Bach and Nansen ice shelves appeared to export meltwater off-shelf (e.g., Dell et al. 2026; Bell et al. 2017). Similar to previous melt years (Dell et al. 2022, 2024), widespread slush was also apparent across several ice shelves, including Roi Baudouin, Shackleton, and north George VI (Fig. SB6.1).

Potential drivers

The widespread ponding of 2024/25 reflects the combination of anomalously warm atmospheric conditions around most coastal areas during this austral summer (see Fig. 6.2b) and longer-term firn air content (FAC) depletion that has progressively reduced pore space and meltwater buffering capacity. Indeed, the largest lake coverages occur in areas where depleted FAC is reported (Banwell et al. 2021; Dunmire et al. 2024; Veldhuijsen et al. 2024).

Superimposed on this longer-term firn preconditioning, ERA5 2-m temperature anomalies (with respect to a 1991–2020 climatology) provide context for the 2024/25 conditions. The melt season began with an Antarctic-wide negative monthly temperature anomaly in November 2024 (–1.1°C) before shifting to more widespread and pronounced positive anomalies in December (+1.4°C). January 2025 recorded the strongest ice sheet-wide positive temperature anomaly in the 1979–2025 record (~+1.0°C; Fig. SB6.3a), coincident with maximum supraglacial meltwater area observed across the AP, DML, Wilkes Land, and the Amery region (Fig. SB6.2). Regionally, this peak occurred alongside temperature anomalies of around +1°C in the AP and +2°C in DML, where locally stronger anomalies reached +2.2°C in Roi Baudouin and +3.2°C in Nivlisen ice shelves, and around +2°C in the Amery Ice Shelf (Fig. SB6.3b). Anomalies remained positive in February (+0.5°C) before reducing to near-zero by March 2025.

Previous work identified a negative relationship between summer Southern Annular Mode (SAM) and meltwater area in Antarctica (Mahagaonkar et al. 2024; Tuckett et al. 2025), with negative SAM years tending to coincide with enhanced ponding. While the DJF SAM index (Marshall et al. 2003) for 2016/17 (–1.24) and 2019/20 (–0.52) is consistent with this broader pattern, the SAM was neutral (+0.05) for DJF 2024/25 (Fig. SB6.3a) and positive (+1.4) in January 2025. This indicates that the anomalously warm conditions in January 2025 occurred despite the lack of a negative SAM state that characterized previous years of elevated supraglacial meltwater extent, pointing to other mechanisms driving both anomalous warmth and lake conditions.

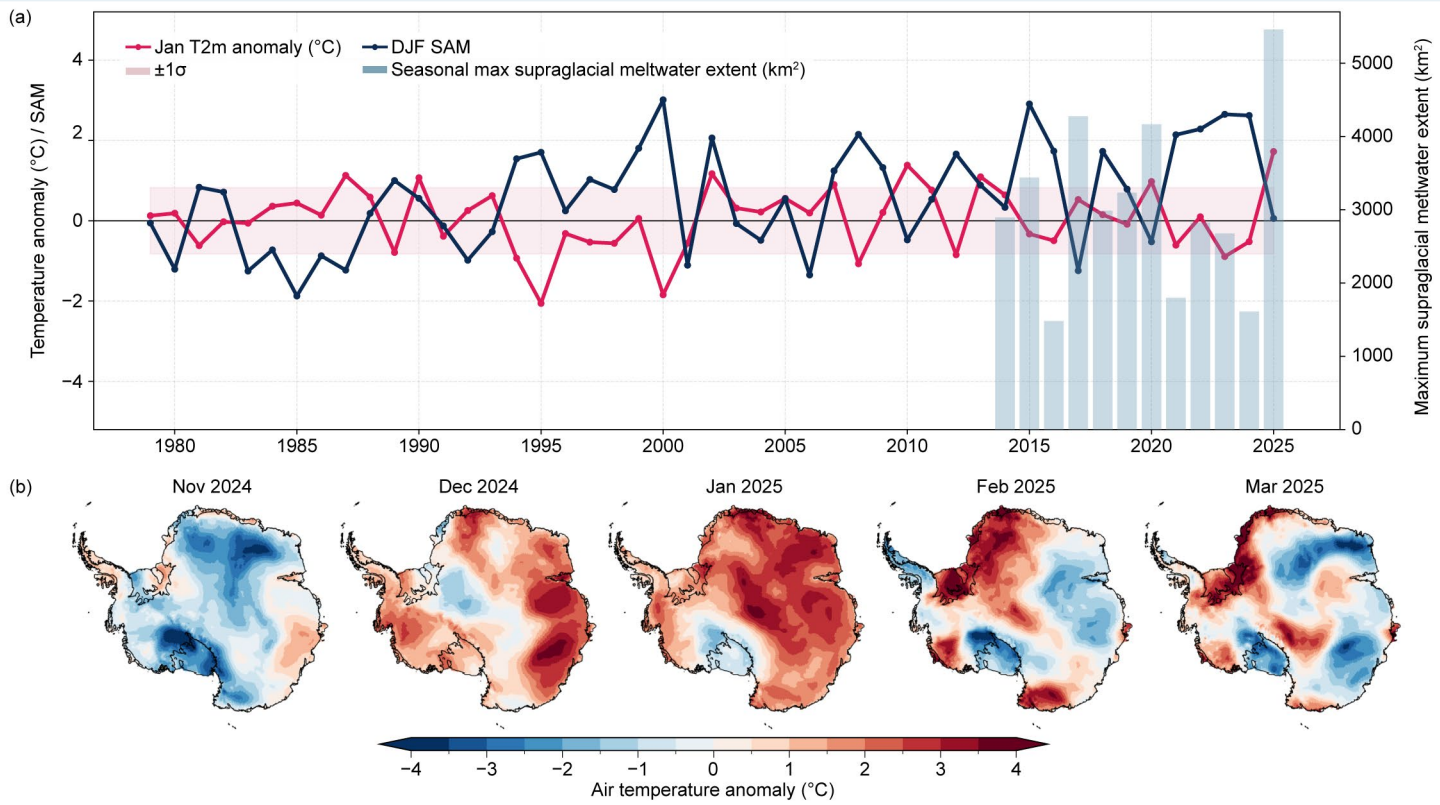

Fig. SB6.3. (a) Interannual variability for Jan 2-m temperature anomalies (T2m; °C) from ERA5 for the period 1979–2025 relative to 1991–2020 climatology (red), summer (Dec–Feb; DJF) Southern Annular Mode (SAM; blue), and maximum supraglacial meltwater extent from Landsat 8/9 (blue bars). (b) Monthly ERA5 T2m anomalies (°C). Black contours indicate ±1 std. dev. relative to the 1991–2020 climatology.

Future Outlook

Ice shelf vulnerability to surface meltwater depends both on the atmospheric forcing that produces melt and the evolving capacity of firn to buffer that meltwater. If high-melt summers became more frequent under future warming (e.g., Kittel et al. 2021), they would promote self-reinforcing expansion of surface water by lowering albedo, enhancing melt, and further reducing firn pore space, thus raising the likelihood of widespread ponding and hydrofracture where stress conditions are conducive (Bell et al. 2018).

Although runoff is a minor term in the present-day Antarctic mass budget (see section 6c), more extensive lake coverage would likely increase both lateral meltwater export as observed in 2024/25 and hydrofracture-driven vertical lake drainages (e.g., Trusel et al. 2022; Izeboud et al. 2025). Early observations from 2025/26 indicate elevated meltwater coverage across multiple regions. While it remains too early to assess whether this season will match or exceed 2024/25, the recurrence of widespread meltwater in consecutive years could represent a departure from the relatively high interannual variability that has characterized the Landsat era and move some ice shelves toward extensive lake coverages that have preceded past collapse events (Banwell et al. 2013; Leeson et al. 2020).

e. Antarctic Ice Sheet mass balance

— M. Brown, S. Adusumilli and H. A. Fricker

The Antarctic Ice Sheet (AIS) modifies global sea level through the balance between surface mass gains and dynamic mass loss of grounded ice (Otosaka et al. 2023). Surface mass gain is from snowfall accumulation, and mass loss is primarily from ice discharge across the grounding line into the floating ice shelves. Ice shelves play a critical role in slowing the rate of grounded ice flow towards the ocean, through a process called buttressing. Ice shelf mass loss, which itself does not directly contribute to global sea level, occurs through iceberg calving and basal melting. Increased ocean heat content enhances basal melting, pushing ice shelves into a negative state of balance (Adusumilli et al. 2020). This reduces buttressing and accelerates grounded ice discharge, leading to sea level rise (Smith et al. 2020; Gudmundsson et al. 2021). In recent decades, Antarctic mass loss has accelerated and exceeded ice accumulation from snowfall, but with significant variability, strengthening the need for sustained satellite-based monitoring of mass change associated with atmospheric and oceanic forcing (Fricker et al. 2025).

At the time of writing, no published estimates of total AIS height or mass change were available for 2025. Following the same approach used in previous years of this report, estimates of grounded ice surface height and mass change were derived from NASA's ICESat-2 laser altimetry and Gravity Recovery and Climate Experiment (GRACE)/GRACE-Follow On (GRACE-FO) satellite gravimetry (Clem and Raphael 2024; Raphael and Clem 2025). Only grounded ice changes are considered, as altimetry-derived height changes over floating ice shelves at sub-annual timescales remain noisy, and gravimetry cannot detect mass variations of floating ice.

Height changes were derived from ICESat-2 using measurements collected along repeated ground tracks between cycles 25 and 29, sampled at 60-m along-track resolution. These data enable estimates of annual change and three-month seasonal variability. Along-track height differences were computed between successive cycles and aggregated to produce annual (Fig. 6.9) and seasonal (Fig. 6.10) maps. Final height-change fields were smoothed using a 30-km Gaussian filter to suppress short-wavelength noise and emphasize large-scale spatial patterns.

For comparison, we also estimated mass anomalies for 2025 using satellite altimetry and gravimetry from GRACE and GRACE-FO, based on the JPL GRACE and GRACE-FO Ocean, Ice, and Hydrology Equivalent Water Height "mascon" product, Coastline Resolution Improvement (CRI)–filtered, Release 6.3 Version 4, which resolves mass variability using 300-km spherical caps (Wiese et al. 2023a). Gravity-derived mass anomalies were computed for January to November 2025 to match the ICESat-2 analysis period. Ice sheet mass anomalies were isolated by selecting mascons containing more than 10,000 km^2 of land area, as defined by the CRI land mask.

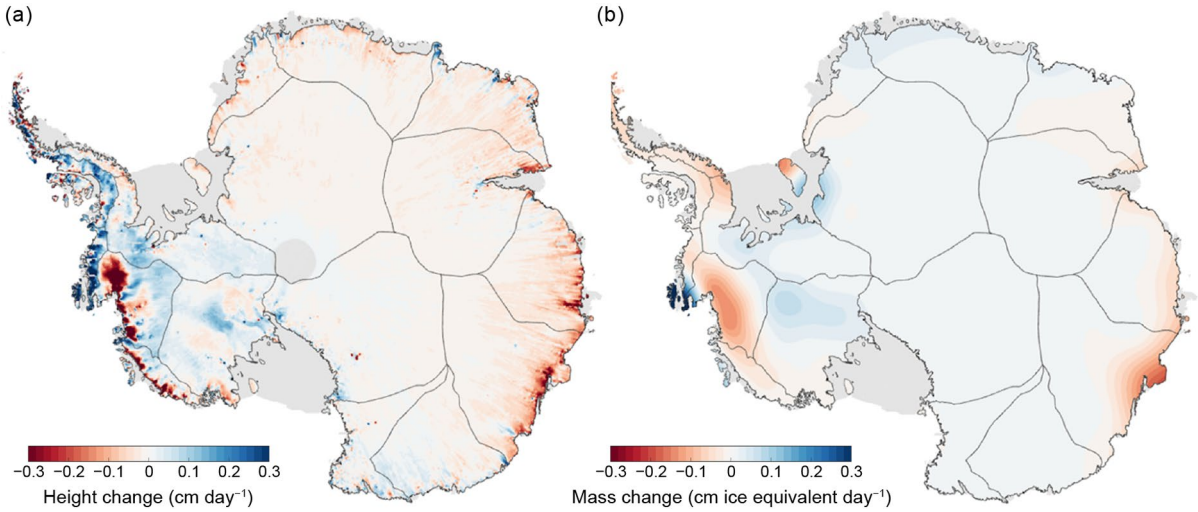

Fig. 6.9. Annual change maps for the Antarctic Ice Sheet from Nov 2024 to Nov 2025. (a) Height change (cm day^{-1}) from ICESat-2, and (b) ice equivalent mass change (cm ice equivalent day) from the Gravity Recovery and Climate Experiment Follow-On (GRACE-FO).

Area-averaged mass change rates were calculated using bilinear interpolation referenced to mascon geometric centers. Non-land regions were excluded using the BedMachine ice mask, and time series mass changes were integrated over the AIS using the Level 4 Antarctica Mass Anomaly Time Series dataset (Wiese et al. 2023b).

Maps of annual height and mass change (Fig. 6.9) reveal continued regional contrasts across Antarctica. The Antarctic Peninsula exhibits an east–west asymmetry, with surface lowering and mass loss on the eastern flank and surface rising/mass gains on the western flank. This pattern indicates differing orographic precipitation across the Peninsula during 2025, with higher precipitation on the western windward side and drier, warmer conditions on the eastern leeward side (Orr et al. 2008). This behavior was not unique to 2025 and is evident in previous versions of this report (e.g., Adusumilli et al. 2021). The West Antarctic Ice Sheet continues to experience sustained mass loss (Adusumilli and Fricker 2025). Pine Island and Thwaites glaciers maintain loss rates consistent with those observed since 2020, reflecting persistent dynamic discharge from marine-based sectors. Continued thinning, especially near grounding lines, demonstrate the ongoing dynamic ice loss due to ice–ocean processes in the Amundsen Sea sector.

The East Antarctic Ice Sheet (EAIS) experienced mean height loss of –1.26 cm in 2025, with the largest reductions concentrated near the Totten Ice Shelf. This signal departs from the historically stable or modest variability typical of most East Antarctic sectors and may reflect the

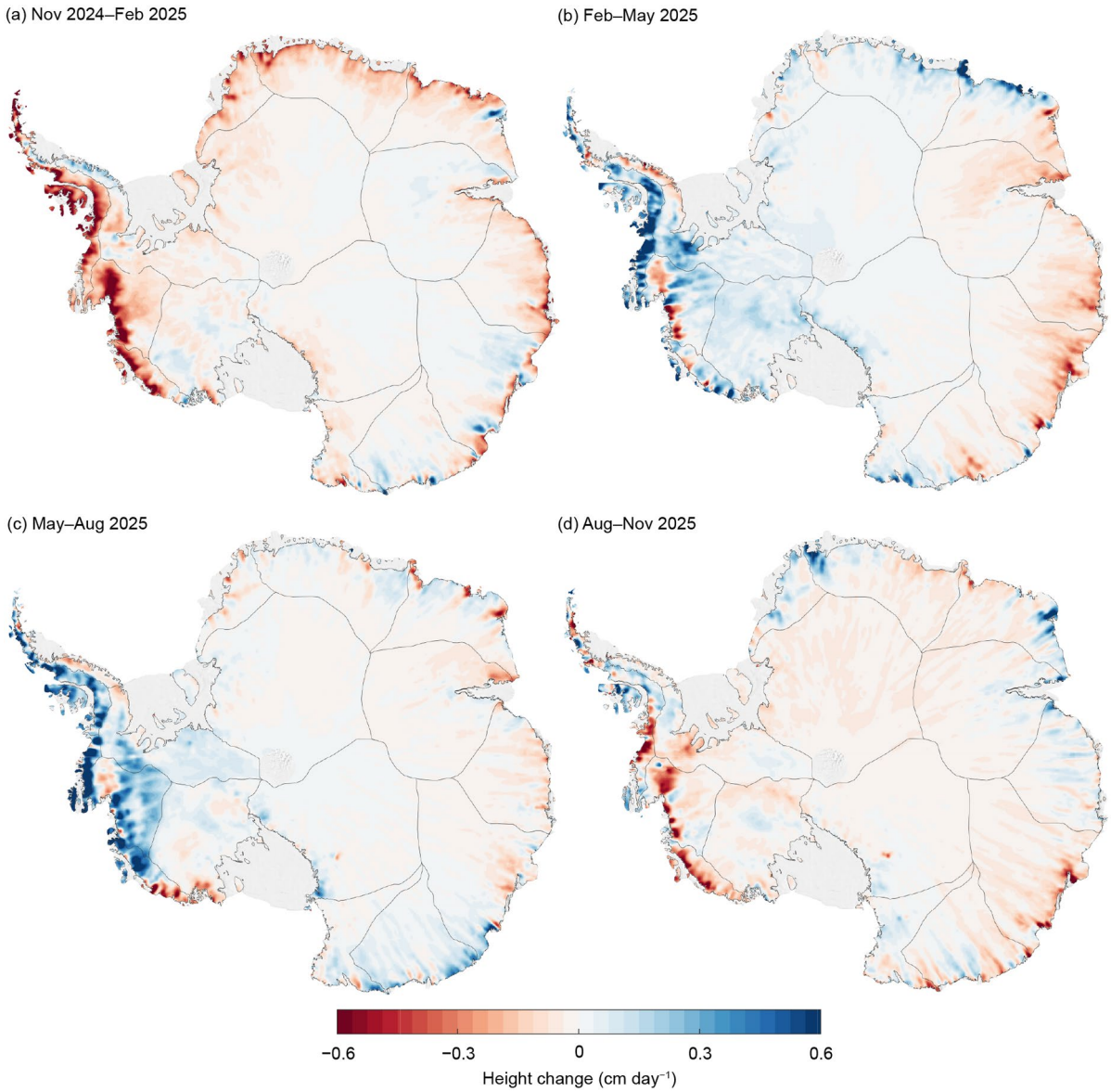

Fig. 6.10. Maps of height change from ICESat-2 shown at three-month intervals for (a) Nov 2024–Feb 2025, (b) Feb–May 2025, (c) May–Aug 2025, and (d) Aug–Nov 2025. Dates represent the central month of each three-month ICESat-2 data acquisition cycle.

below-average SMB observed in the Totten region in 2025 (Fig. 6.5) or other ice dynamics or ocean forcing. The most pronounced positive mass and height anomalies occurred between March and September, concentrated along the western coast of the EAIS. No net mass change was detected until April 2025, which started a trend linked to a 400-Gt mass gain that peaked in August before declining, yielding a net AIS annual gain of 153 Gt (Fig. 6.11). This represents the fourth-highest annual increase since GRACE observations began in 2002. The ICESat-2 three-month maps (Fig. 6.10) provide more context for these mass gains, showing that snow accumulation in the Bellingshausen Sea and Dronning Maud Land regions are responsible for offsetting the continued loss in the WAIS. And while the 2025 mass gain was dominated by anomalous snowfall, it does not reverse the long-term dynamic loss trajectory.

Instrument limitations are relevant for interpretation. Following its 2018 launch, the GRACE-FO trailing satellite (GRACE-D) experienced accelerometer degradation, and reconstructed data from the leading satellite (GRACE-C) have been used in operational products. Accelerometer measurements are sensitive to non-gravitational environmental influences, including thermospheric density variations associated with elevated solar activity during the 11-year solar-cycle peak observed in 2025. Continued integration of satellite altimetry and gravimetry remains essential for resolving short-term variability within the longer-term evolution of Antarctic mass balance and its contribution to global sea level change.

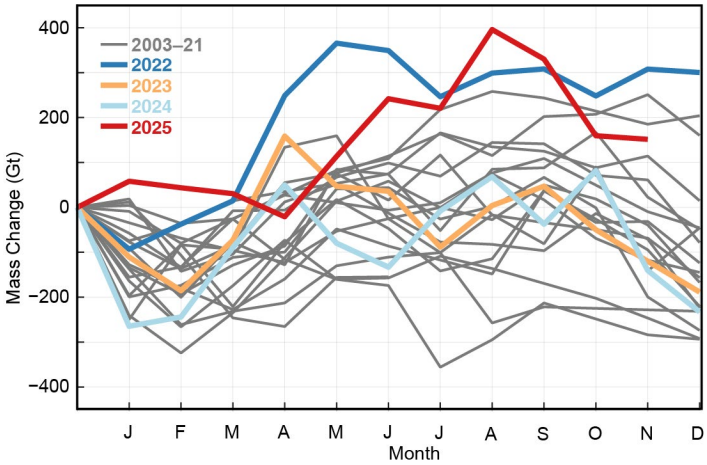

Fig. 6.11. Annual mass change (Gt) from Gravity Recovery and Climate Experiment (GRACE) and GRACE Follow-On (GRACE-FO). Time series of monthly mass changes from GRACE and GRACE-FO, with the years 2022–25 highlighted in various colors.

f. Sea ice extent, concentration, and seasonality

—P. Reid, R. A. Massom, S. Stammerjohn, S. Barreira, T. A. Scambos, and J. L. Lieser

Antarctic sea ice—formed from the freezing of seawater—is a critical component of the Southern Ocean biophysical environment and Earth's climate system. The sea ice moderates solar heating of the ocean by strongly reflecting incoming solar radiation (Riihelä et al. 2021); modulates ocean–atmosphere exchanges of heat, moisture, atmospheric gases, and momentum (Josey et al. 2024); modifies ocean properties and helps drive global ocean circulation (Meredith and Brandon 2017); protects ice shelves from potentially destructive wave action (Massom et al. 2018; Ochwat et al. 2024); and provides key habitat and food for a plethora of biota that are highly adapted to (and dependent on) its presence and seasonal rhythms (Thomas 2017).

Throughout 2025, both net Antarctic sea ice extent (SIE; Fig. 6.12a) and sea ice area (SIA; the product of SIE and concentration) were well below the long-term 1991–2020 average, except during early January. Annual daily minima of both net SIE and SIA were recorded on 1 March (1.96×10^6 km^2 and 1.21×10^6 km^2, respectively), which were fourth and second lowest on record (the record low year for both being 2023). Annual daily maximum values of net SIE and SIA were recorded on 15 and 8 September, respectively (17.85×10^6 km^2 and 13.73×10^6 km^2), with both being the third lowest on record, behind 2023 and 2024 (Reid et al. 2024). Notable features are extreme sea ice deficits in the eastern Weddell Sea–Indian Ocean sectors from March through December and year-round in the Bellingshausen Sea, which was almost ice-free until early winter. The year also included greater-than-average sea ice coverage in the eastern Ross Sea, especially in January and February. There were almost 100 days of record coastal exposure length set through the year, including the second-highest daily summertime exposure on record (13,700 km), behind 2022 (13,800 km) and almost 50% more exposure than the 1991–2020 average (Reid and Massom 2022).

The low SIE through 2025 (Fig. 6.12a) marks a continuation of the general pattern of low and record-low coverage since 2016 (Doddridge et al. 2025). In particular, and as with 2023 (Reid et al. 2024) and 2024 (Reid et al. 2025), overall sea ice seasonal growth in 2025 lagged well behind the long-term mean during the autumn-winter advance phase, which was then followed by early retreat. There is increasing evidence that changes in upper-ocean conditions, along with wind stress, may be largely responsible for the persistence in negative Antarctic SIE anomalies and reduced annual duration observed since 2016 (Cheng et al. 2022; Purich and Doddridge 2023; Maksym and Stammerjohn 2026; Silvano et al. 2025; Hobbs et al. 2026). While important, net values of SIE mask important regional and seasonal variations, and these are highlighted for 2025 below.

Five distinct periods through 2025 are identified here based on analysis of the spatiotemporal sea ice extent anomaly patterns shown in Fig. 6.12b, similar to the atmospheric seasonal analysis (see Fig. 6.2). While net SIE was close to average at the start of 2025 (Fig. 6.12a), it dipped to ~2 std. dev. below the long-term mean through March and remained 1 std. dev. to 2 std. dev. below the long-term mean throughout the year. In January through March, this net deficit was made up of several significant regional sea ice anomalies. Anomalously high SIE from ~120°W–150°W through January (i.e., 2 std. dev. to 3 std. dev. above average; Fig. 6.12a) coincided with a ridge of high pressure in the Ross-Amundsen Seas, with reduced cyclonic activity likely slowing the advection of sea ice into warmer lower latitudes where it would have rapidly melted (Himmich et al. 2024). But along the western limb of this ridge, warm northerly winds likely contributed to the anomalously low SIE over the western Ross Sea. East of the ridge, anomalously low SIE in the eastern Amundsen and Bellingshausen Seas was associated with southward advection of warm air driven by a large blocking high over the Antarctic Peninsula i.e., a likely combination of dynamic ice compaction and surface warming in January and February. The seasonal sea ice zone of the Southern Ocean is only weakly stratified, with cooler fresher waters overlying warmer much saltier waters (Pellichero et al. 2017). If the surface layer becomes less fresh (e.g., due to less seasonal sea ice melt) or the subsurface ocean becomes warmer (Wilson et al. 2026), then the upper ocean becomes even less stratified (Silvano et al. 2025), opening the door to greater upward mixing of the warm saltier waters at depth, which in turn leads to a warmer upper ocean (Spira et al. 2024), less autumn/winter sea ice production and/or greater sea ice melt in spring (see Eayrs et al. 2021, Fig. 2; Himmich et al. 2025). Unusually low SIE was

also recorded in the eastern Weddell Sea, following on from well-below-average values for all of 2024 (Reid et al. 2025). Elsewhere, sea ice coverage remained close to average across East Antarctica from January through March, except in the eastern Indian and western Pacific Ocean sectors (~60°E–110°E). There, SIE was 1 std. dev. to 2 std. dev. below average, coincident with above-normal sea surface temperatures (SSTs) to the north of the ice edge (see Fig. 6.14a) that were possibly associated with southward eddy heat transfer across the ACC in the Kerguelen

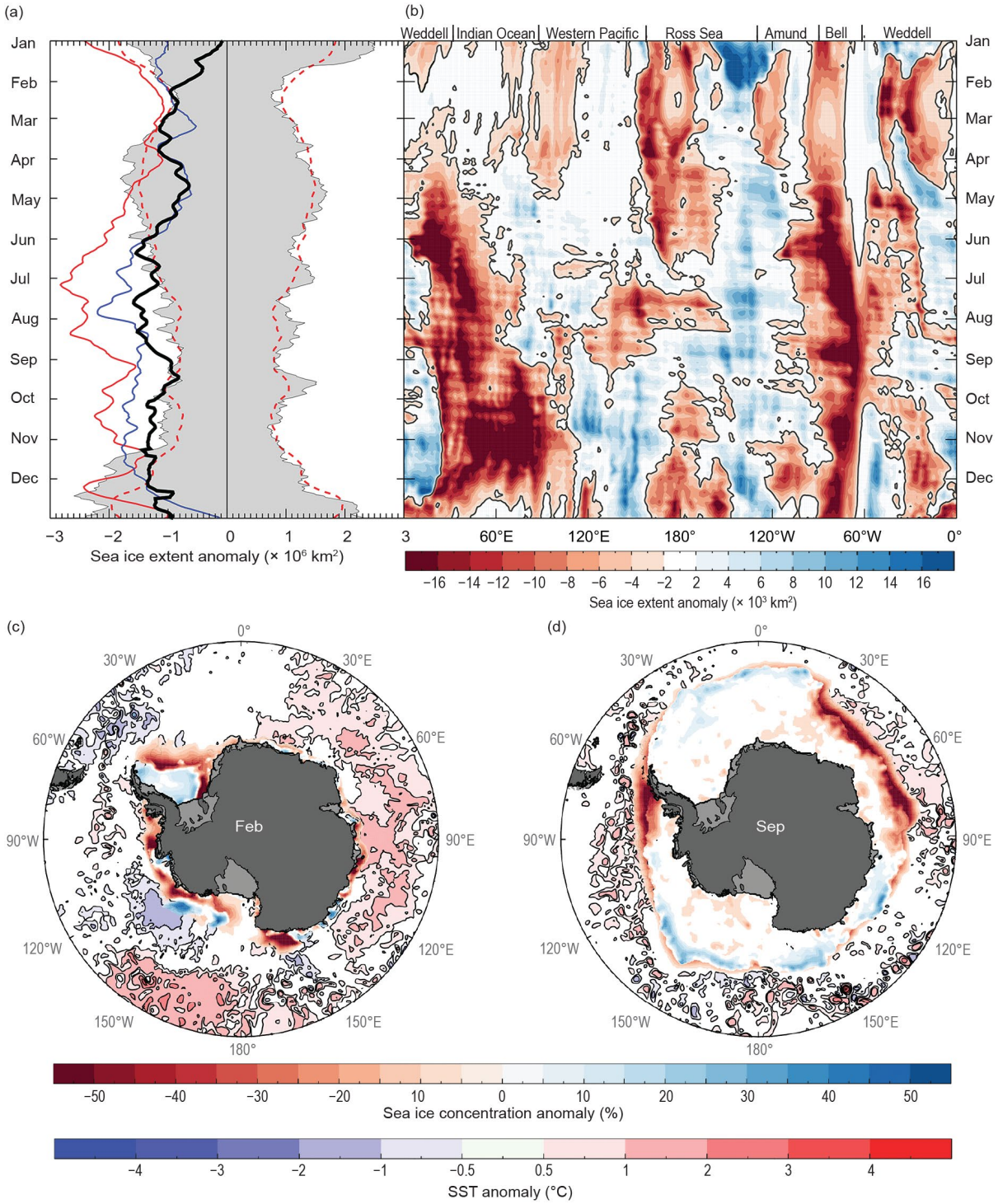

Fig. 6.12. (a) Time series of net daily sea ice extent (SIE) anomalies for 2025 (solid black line), 2024 (solid blue line), and 2023 (solid red line), based on a 1991–2020 climatology. Gray shading represents historical (1979–2023) daily SIE anomalies, red dashed line represents ±2 std. dev., and (b) Hovmöller (time–longitude) representation of daily SIE anomalies (× 10^3 km^2 per degree of longitude) for 2025. Maps of sea ice concentration anomalies (%) and sea surface temperature (SST) anomalies (°C; Huang et al. 2021) for (c) Feb 2025 and (d) Sep 2025. Sea ice concentration is based on satellite passive-microwave ice concentration data (Cavalieri et al. 1996, updated yearly and used to compute the 1991–2020 climatology and anomalies; Stewart et al. 2025 for the AMSR2 2025 sea ice concentration). See Fig. 6.1 for relevant place names.

Plateau region (Foppert 2017). Low SIE in this region has been a consistent pattern at this time of the year for the last three years.

From April through June, a general poleward intensification of low-pressure systems and a development of a high-pressure ridge in the Weddell Sea (see Fig. 6.2c) saw a change in the regional sea ice distribution pattern. Within the Weddell Sea, SIE was lower than normal, except within the central Weddell (~10°W–40°W) where SIE was higher than normal (Fig. 6.12a), possibly due to unusually strong southwesterly winds in this region (see section 6b). Farther to the east, in the western Indian Ocean sector, SIE was well below average, in conjunction with above-normal SSTs across and to the north of the ice edge. During this time, sea ice also remained low in the western Ross Sea, but advanced quickly across the eastern Ross and Amundsen Seas driven by cold southerly winds. However, farther to the east, in the Bellingshausen Sea, northerly winds exacerbated the already low sea ice conditions in that region. Across eastern Antarctica, in the southwest Pacific, sea ice coverage was close to average during these months.

July and August saw a well-defined three-wave atmospheric pattern with a deep Amundsen Sea Low (see Fig. 6.2e). This led to warm air and SST incursions into the Bellingshausen Sea and across the West Antarctic Peninsula into the eastern Weddell Sea, and into the much of the western Pacific Ocean and western Ross Sea (~120°E–180°) sectors—to suppress sea ice growth in these regions and enhance negative regional SIE anomalies through to the end of August. At this time of the year, there is typically a net eastward zonal transport of sea ice within the Weddell Sea, from 60°W through to 30°E (Kimura and Wakatsuchi 2011), and this is evident within Fig. 6.12b where positive anomalies within the central Weddell Sea advected eastward. The same zonal transport mechanism is probably also responsible for an eastward migration of negative SIE anomalies from the eastern Weddell Sea into the western Indian Ocean sector during 2025. During July and August, SIE was higher than normal in the West Pacific region (~80°E–120°E), the central Weddell Sea, and the Ross Sea (~120°W–140°W), with the latter expanding westward to 160°E during August, all associated with cold southerly winds.

From September onwards, there were regional changes in the SIE anomalies (Fig. 6.12d), driven by a weakening in the circumpolar westerly winds combined with an early September stratospheric warming (see sections 6b and 6h). Negative SIE anomalies in the eastern Weddell and southern Indian Ocean sectors during previous months expanded east into the western Pacific sector of the Southern Ocean (~20°E–110°E). The negative SIE here was perhaps enhanced by above-normal SSTs advancing across the ACC from northern latitudes in the Kerguelen Plateau region (Foppert 2017; Figs. 6.12b,d). In contrast, SIE was higher than normal in the western Pacific sector, between ~120°E and 160°E, due to the prevalence of cold southerly winds associated with the combination of an atmospheric high (~90°E–100°E) and a deep atmospheric low-pressure system centered to the west of the Ross Sea. The same low-pressure system brought warm northerly winds to the rest of the Ross Sea (to about 150°E), accelerating sea ice retreat in this region through to the end of the year. An atmospheric high-pressure system sat across the Amundsen Sea during September and October, bringing relatively calm winds and a subsequent positive SIE anomaly in the Amundsen Sea during these months. In the Bellingshausen Sea, persistently warm surface conditions since April are now reflected in the short-lived, anomalously low and already retreating winter SIE maximum in this sector.

During November, a four-wave atmospheric pattern with low-pressure centers at ~55°E, 145°E, 145°W, and 40°W (see Fig. 6.2g) significantly impacted sea ice seasonal retreat around Antarctica. Sea ice in the central-western Weddell Sea (~40°W–10°W) retreated relatively quickly, leading to negative SIE anomalies there. However, to the east of the Antarctic Peninsula and the eastern Weddell Sea, sea ice retreated slowly, influenced by cold southerly winds. The four-wave pattern also brought warm northerly winds and warmer SSTs to the Amundsen Sea, reducing the SIE in that region through to the end of the year. By the end of 2025, sea ice remained relatively highly concentrated in several regions: in the western Weddell Sea, Amundsen and eastern Ross Seas, and along the East Antarctic coastline (~130°E–160°E), with each of these regions showing some compaction of sea ice due to northerly winds.

The timings of annual sea ice advance and retreat, and resultant duration of coverage (where a sea ice year here is mid-February 2025 to mid-February 2026; Stammerjohn et al. 2008) show distinct regional anomalies (Fig. 6.13) that mirror those of the SIE (Fig. 6.12b) and SIA.

Annual sea ice advance (Fig. 6.13a) was delayed by 30 days to >60 days (compared to the 1991/92–2020/21 mean) across the Bellingshausen Sea (~60°W to ~90°W), the far eastern Weddell Sea and Indian Ocean sector (~20°E to ~60°E), along the outer ice pack of the West Pacific sector (~120°E to ~160°E), and moderately delayed (by ~15 days to 30 days) in the west-central Ross Sea (~160°E to ~160°W). Only the central-outer ice pack in the eastern Ross and western Amundsen Seas saw an appreciable early ice-edge advance (~150°W to ~115°W) by ~30 days to 60 days.

The retreat pattern (Fig. 6.13b) mostly mirrors the advance pattern where, in general, the ice-edge retreat was earlier where advance was later, and vice-versa. Notable exceptions include the broadening of exceptionally early ice-edge retreat (by 30 days to >60 days) across the entire Indian Ocean sector (~30°E to ~110°E), juxtaposed by later ice-edge retreat to the east in the Western Pacific sector (~110°E to ~160°E) where both annual advance and retreat were later than normal. Finally, the largely singular area of early ice-edge advance in the eastern Ross and western Amundsen Seas became far more attenuated in its extent, showing a much smaller area of slightly later ice-edge retreat. Taken together, the ice season duration was short across the eastern Weddell Sea and Indian Ocean, and notably also along the coastal region of the central Weddell Sea. Most of the Ross Sea and the entire Bellingshausen Sea also had a very short sea ice season. Only the western Amundsen Sea experienced a slightly longer ice season in 2025. Trends in sea ice duration (Fig. 6.13d) have changed considerably over the last few years, with smaller regions showing a trend towards a longer duration and marked increases in trends towards shorter sea ice season in the West Antarctic Peninsula–Bellingshausen Sea region by more than two days per year over the 48-year period. Another notable shorter duration trend is near ~75°E, quite possibly associated with the southward migration of warm SSTs across the ACC in this region (Foppert 2017).

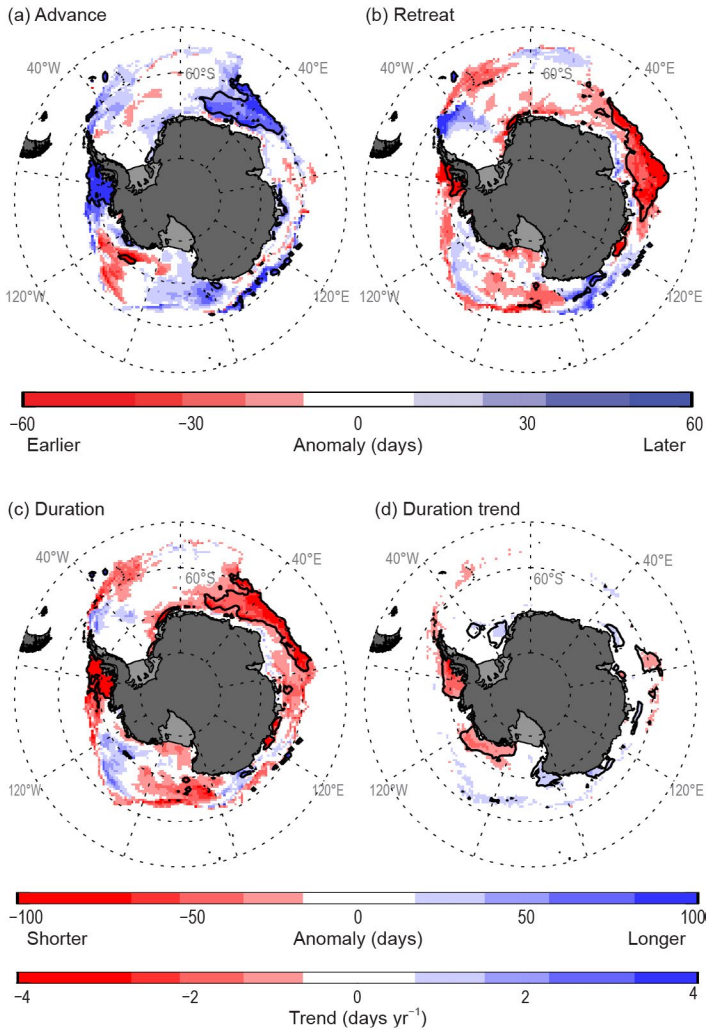

Fig. 6.13. Maps of seasonal sea ice anomaly (days) between Feb 2025 and Feb 2026 during (a) autumn ice-edge advance, (b) spring ice-edge retreat, and (c) winter ice season duration; together with (d) winter ice season duration trend (days yr^{-1}; Stammerjohn et al. 2008). The seasonal anomalies (a)–(c) are computed against the 1991/92–2020/21 climatology; the trend (d) is computed over 1979/80–2025/26. Contour lines in (a)–(c) represent where the anomalies are greater than 2 std. dev., and in (d) where the trend significance is equal to or greater than p<0.01. The 1979–2024 data are from Comiso (2023; updated yearly), while the 2025/26 data are from AMSR2 (Stewart et al. 2025); the trend is based on computed seasonal sea ice indices using the merged 1979–2024 and 2025/26 daily sea ice concentration time series.

g. Southern Ocean

—S. Thomalla, A. M. Hancock, M. Adjou, R. L. Beadling, M. du Plessis, S. Josey, Z. Kaufman, J. Milward, L. P. Pezzi, T. J. Ryan-Keogh, C. Schulz, J.-R. Shi, and E. Souza

The Southern Ocean (SO) plays a critical role in the global climate system by regulating heat and carbon exchange with the atmosphere and supplying nutrients that support ocean productivity (Frölicher et al. 2015). Here, the 2025 physical and biogeochemical state of the SO is assessed. In 2025, abnormally warm conditions prevailed, with more spatially homogenous anomalies than in recent years. Elevated air–sea heat flux anomalies across large regions of the SO indicate enhanced ocean heat uptake, which aligned with a record-setting value of upper-ocean heat content. Enhanced summer chlorophyll was observed south of the Subantarctic Front (SAF), particularly in the Atlantic. Surface dissolved oxygen anomalies were negative, consistent with warming-driven reductions in solubility. These results highlight evolving SO conditions and underscore the importance of sustained observations for tracking ongoing changes.

1. SEA SURFACE TEMPERATURE, SALINITY, AND MIXED-LAYER PROPERTIES

Sea surface temperature (SST) anomalies for 2025 (relative to a 1991–2020 climatology) were calculated from the NOAA monthly Optimum Interpolation product (Reynolds et al. 2002). Sea surface salinity (SSS) and mixed-layer depth (MLD; defined following de Boyer Montegut et al. 2004) were calculated from the Argo gridded product (Roemmich and Gilson 2009; hereafter RG09) relative to a 2004–20 climatology. As in previous years (Beadling et al. 2022; Pezzi et al. 2023; Thomalla et al. 2024, 2025), abnormally warm waters prevailed throughout most of the SO, with more spatially homogeneous anomalies, indicating coherent basin-scale warming that persisted year-round (0.4°C–0.5°C; Figs. 6.14a,b). As in 2024, surface warming was most pronounced in the western Pacific Ocean, but seasonality differed with anomalies peaking at +1.1°C (March) before weakening to near-normal conditions in November (Fig. 6.14b), whereas anomalies >+1°C persisted throughout 2024. A similar seasonal evolution was observed in the Indian Ocean with declining SST anomalies from January (~+0.7°C) to December (+0.3°C). In contrast, SST anomalies steadily intensified in the eastern Pacific Ocean from near-normal conditions in February to a maximum of ~+0.7°C in December.

In 2025, SSS anomalies exhibited both positive and negative patterns that varied regionally and seasonally (Figs. 6.14c,d). The western Pacific Ocean exhibited predominantly positive SSS anomalies, with normal conditions in March increasing to 0.11 PSU in September (Fig. 6.14d). The largest anomalies featured north of the SAF in the Atlantic and along the southern boundaries of the Atlantic and Pacific subtropical gyres (Fig. 6.14d), consistent with a gyre strengthening and enhanced poleward salt transport (Silvano et al. 2025). Consistent with 2024, all other sectors exhibited a similar seasonal cycle, but unlike the western Pacific, their summer minimum reached negative anomalies (<–0.07 PSU) before transitioning to positive anomalies from April and peaking between August and October (Fig. 6.14d).

Similar to prior years, the 2025 MLD anomaly pattern was spatially heterogeneous, with positive and negative anomalies (predominantly) north of the SAF (Fig. 6.14e). The strongest negative anomalies occurred in August (Indian), September/November (eastern Pacific), and December (Atlantic), while the western Pacific minimum anomaly occurred earlier (March) (Fig. 6.14f). Regions of negative anomalies were generally co-located with anomalously fresh and warm waters. Overall, negative anomalies were weaker in 2025 than in 2024. The strongest positive anomalies were found south of Australia in April and in November in the western Pacific.

2. AIR–SEA HEAT FLUX

The 2025 air–sea heat flux anomalies were derived from the 1991–2020 climatology using the ERA5 reanalysis (Hersbach et al. 2020). Elevated air–sea heat flux anomalies were observed across extensive regions of the western Pacific (south of New Zealand), eastern Pacific, and Atlantic, most pronounced along the Antarctic Circumpolar Current (Fig. 6.14g). The positive anomalies resulted in a SO-wide shift in ocean heat loss to heat gain during the latter half of 2025 (Fig. 6.14h). Notably, the western and eastern Pacific showed pronounced month-to-month winter variability, with basin-mean anomalies alternating by up to 40 W m^{-2} and often in opposing phase between the basins (Fig. 6.14h).

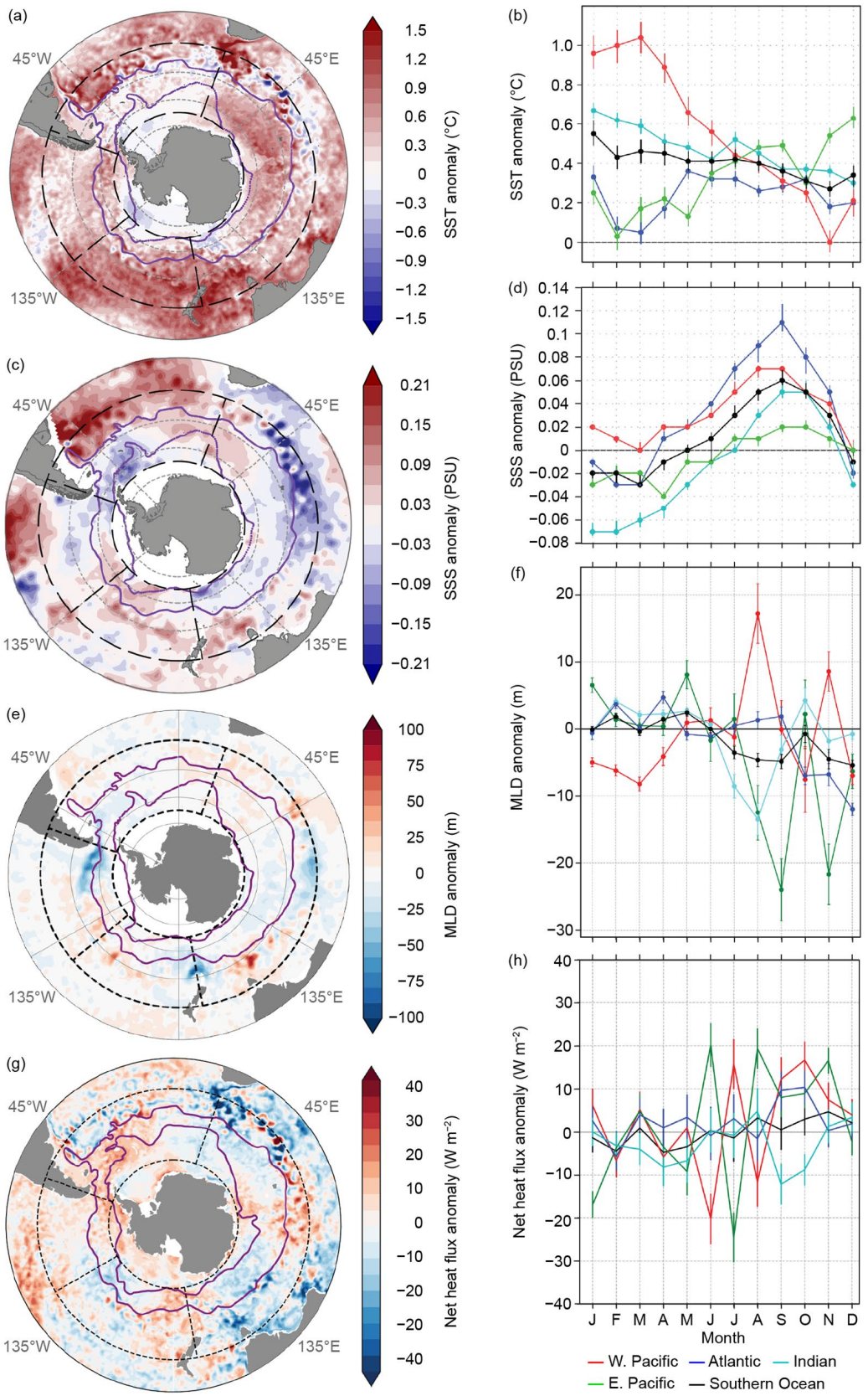

Fig. 6.14. Annual average (Jan–Dec 2025) anomalies of Southern Ocean (a) sea surface temperature (SST; °C; relative to a 1991–2020 climatology), (c) sea surface salinity (SSS; PSU), (e) mixed-layer depth (MLD; m; relative to a 2004–20 climatology), and (g) net heat flux (W m^{-2}; relative to 1991–2020 ERA5 climatology). Overlaid are the positions of the Subantarctic and Southern Boundary Antarctic Circumpolar Fronts (purple lines) defined by Orsi et al. (1995). Four distinct sectors between 40°S and 65°S are delineated by black dashed lines corresponding to the Atlantic (70°W–20°E), Indian (20°E–170°E), western Pacific (170°E–120°W), and eastern Pacific (120°W–70°W). The corresponding 2025 seasonal cycle of anomalies shown in (b) SST (°C), (d) SSS (PSU), (f) MLD (m), and (h) net heat flux (W m^{-2}) are separated according to the sectors defined above. Error bars in (b), (d), (f), and (h) represent the standard error of the climatological mean (i.e., std. dev. divided by √N, where N is the number of years in the climatology).

As in 2024 (Thomalla et al. 2025), mesoscale ocean variability left a clear imprint on air–sea fluxes north of the SAF, marked by alternating positive and negative anomalies, most evident near the Agulhas Retroflection and extending eastward into the Indian near ~40°S (Fig. 6.14g). The SO heat flux asymmetry index (Josey et al. 2023), which measures the strength of the difference in Atlantic, Indian, and Pacific sector surface heat exchange, was −0.27 in 2025, indicating that conditions were close to the climatological mean level of asymmetry for 1991–2020.

3. UPPER OCEAN HEAT CONTENT

The 0-m–2000-m upper ocean heat content (OHC) was calculated from potential temperature using the monthly gridded RG09 Argo product, with anomalies relative to the 2005–20 climatology. The 2025 OHC anomaly (Fig. 6.15a) exhibits widespread positive values, with heat gain occurring primarily north of the SAF, consistent with patterns observed in previous years (Beadling et al. 2022; Pezzi et al. 2023; Thomalla et al. 2024, 2025). Relative to 2024, OHC generally increased in 2025, while cooling occurred in the Atlantic and eastern Pacific. Based on records from the past two decades, the OHC anomaly shows a persistent long-term warming trend, reaching its highest recorded level in 2025 (Fig. 6.15b). The increase of +5.6 ZJ between 2025 and 2024 exceeds the increase of the previous two years (+4.1 ZJ and +3.2 ZJ, respectively), indicating an acceleration of heat uptake.

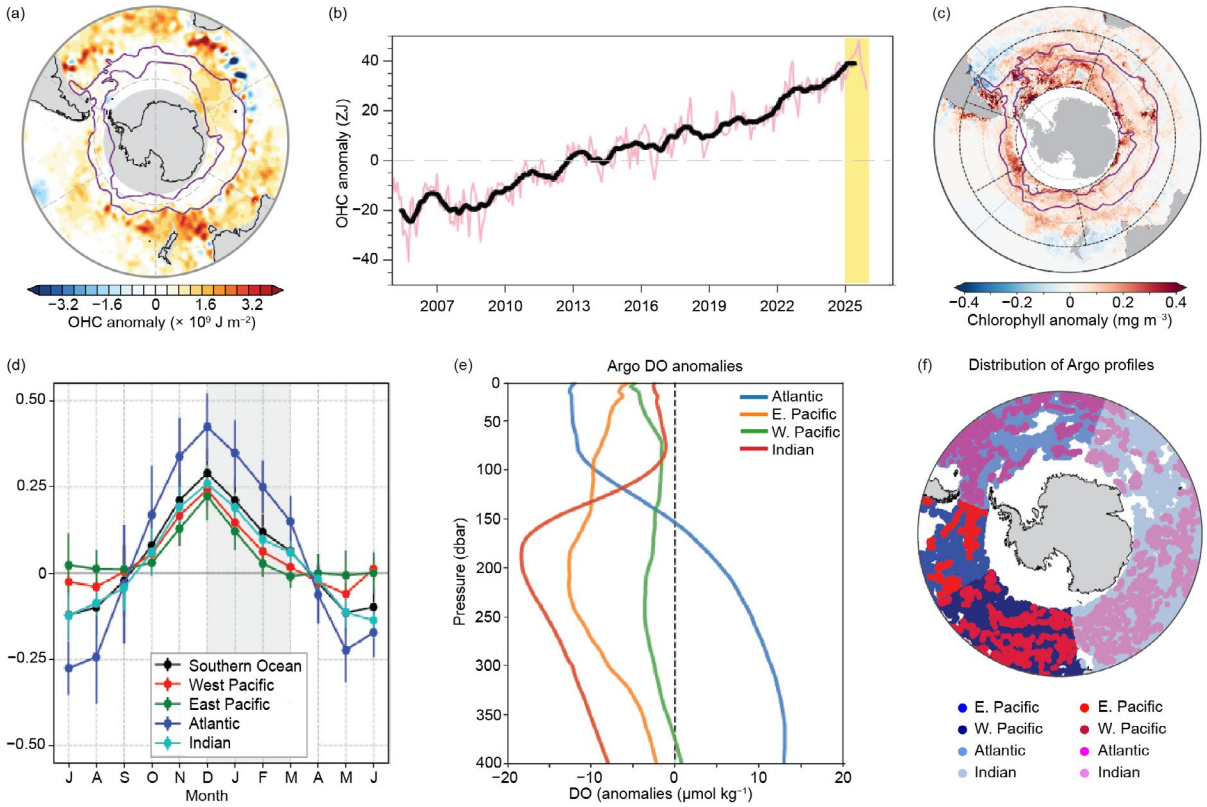

Fig. 6.15. (a) 2025 annual average ocean heat content (OHC; × 10^9 J m^{-2}) anomalies. (b) Time series of monthly average 0-m–2000-m OHC anomaly (ZJ or 10^{21} J) relative to 2004–20 Argo climatology within 40°S–65°S (red line) with 12-month running mean on top (black line) and 2025 highlighted (yellow shading). (c) Annual average (Jul 2024–Jun 2025) anomalies of eight-day, 4-km chlorophyll (mg m^{-3}) relative to 1999–2020 climatology, and (d) the 2025 seasonal cycle of anomalies for the Atlantic (70°W–20°E), Indian (20°E–170°E), western Pacific (170°W–120°W), and eastern Pacific (120°W–70°W) between 40°S and 65°S. Error bars represent the standard error of the climatological mean, i.e., std. dev. divided by √N, where N is the number of years in the climatology. Overlaid on (a) and (c) are the Subantarctic and Southern Boundary Antarctic Circumpolar Fronts (purple lines) as defined by Orsi et al. (1995). (e) Dissolved oxygen (DO) anomalies (μmol kg^{-1}) with depth (m) for Jul 2024–Jun 2025 relative to the 2004–20 Argo climatology. (f) Distribution of Argo profiles from 2004 to 2020 for the different ocean sectors (blues) relative to the distribution of profiles for the 2024/25 period (pinks and red).

4. OCEAN BIOGEOCHEMISTRY

Chlorophyll data from the eight-day (4-km) European Space Agency Ocean Color Climate Change Initiative (OC-CCI) product (v6.0; Sathyendranath et al. 2019) were processed as per Thomalla et al. (2024), with 2025 anomalies computed relative to the 1999–2020 climatology. Consistent with 2024, positive anomalies dominated south of the SAF during summer (Figs. 6.15c,d), most notably in the Atlantic, where chlorophyll concentrations were elevated. Summer anomalies were higher across all basins, with the Atlantic peaking at ~0.4 mg m^{-3} (Fig. 6.15d), nearly double that of 2024. Weaker negative anomalies occurred north of the SAF, particularly in the Atlantic downstream of South America (~−0.25mg m^{-3}) and in the Indian and western Pacific downstream of Tasmania and New Zealand (<−0.1mg m^{-3}; Figs. 6.15c,d). Dissolved oxygen (DO) anomalies (relative to the 2004–20 climatology) were derived from BGC-Argo (Wong et al. 2020) (Figs. 6.15e,f). Near-surface DO anomalies were negative in all sectors, possibly reflecting lower solubility due to increased SST. Anomalies remained negative with increasing depth in all sectors, except the Atlantic, where they were least negative near the surface (~−13 μmol kg^{-1}) and became increasingly positive from 150 m (Fig. 6.15e). Negative subsurface anomalies may reflect the spring MLD shoaling, limiting mixing with subsurface waters. While positive chlorophyll anomalies could conceivably lead to oxygen supersaturation, the largest chlorophyll anomalies occurred south of the SAF, whereas oxygen measurements used for this analysis were confined to data between 40°S and 65°S.

h. 2025 Antarctic ozone hole

—P. A. Newman, L. Coy, P. Cullis, J. De Laat, N. A. Kramarova, L. R. Lait, I. Petropavlovskikh, and M. L. Santee

The 2025 Antarctic ozone hole was smaller than average, the fourth to fifth weakest ozone hole observed since 1992. Because ozone depletion was accelerating in the 1970/80s, 2025 is compared to the mature ozone holes over the 1992-to-present period. The 2025 hole (7 September–13 October) had an average area of 18.7 million km^2 (Fig. 6.16a, magenta triangle). Against the reference period, this was the fifth smallest ozone hole on record, well below the 2006 value of 26.6 million km^2 (Fig. 6.16a, orange triangle). Other ozone hole metrics reflect this relatively weak 2025 ozone depletion. The polar ozone column minimum average (21 September–16 October) was fifth highest at 138.3 Dobson units (DU). The polar cap average (63°S–90°S; 13 September–5 October) was 246.4 DU (fourth highest). The ozone mass deficit (21 September–13 October average; the total amount of mass that is deficit relative to the amount of mass present for a value of 220 DU) was 16 million tons (fourth smallest). Together, these metrics indicate that 2025 was among the weakest ozone holes observed over the 1992–present period of severe Antarctic ozone depletion.

The day-to-day 2025 ozone hole development began in mid-July and proceeded relatively normally. The rate of ozone decline (Fig. 6.17b) was most rapid in early September, and the hole area reached a maximum of 22.9 million km^2 on 9 September (Fig. 6.17g), earlier than in recent years. Then, in mid-September, lower stratospheric temperatures (Fig. 6.17a) started to rapidly increase (section 6b) due to a series of planetary-scale wave events, which impeded further ozone hole growth. By early October, abundances of lower stratospheric ozone had stopped

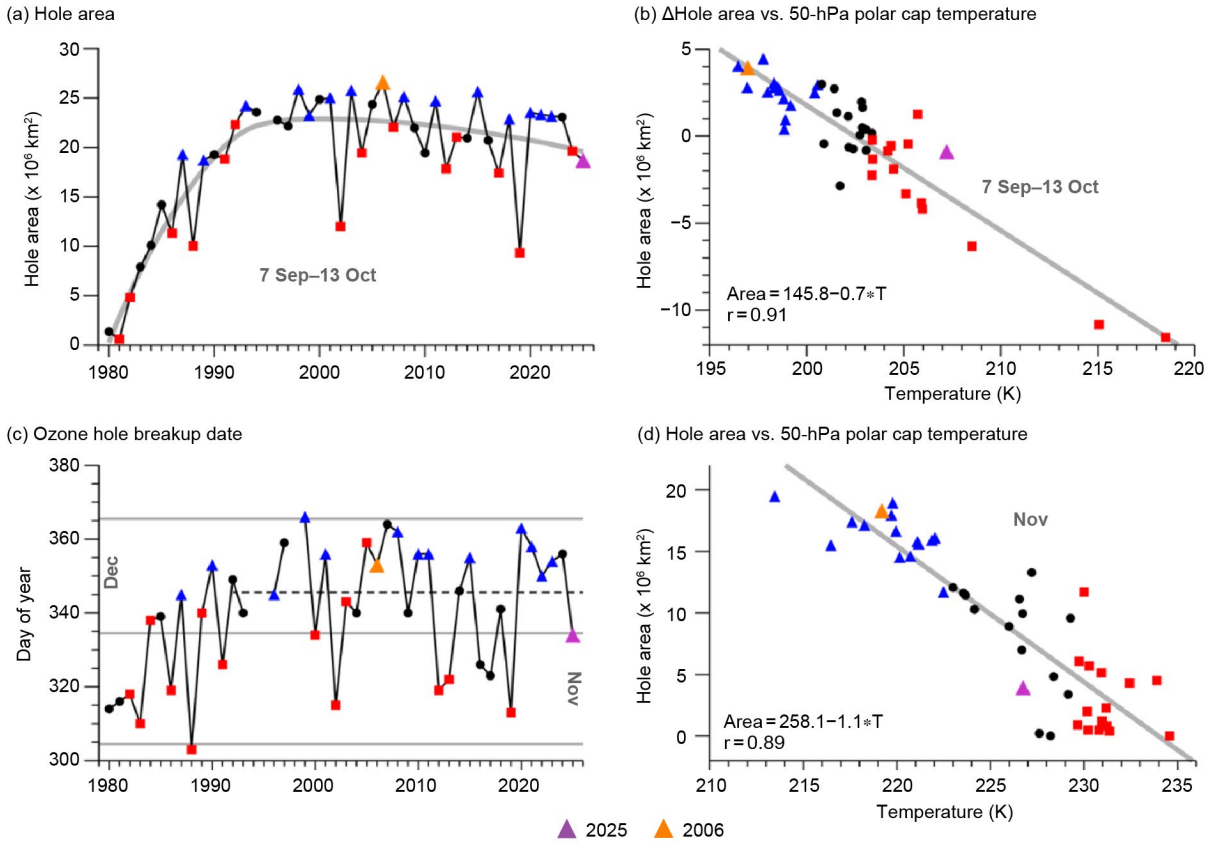

Fig. 6.16. (a) Annual 7 Sep–13 Oct average Antarctic ozone hole area (× 10^6 km^2). (b) 7 Sep–13 Oct ozone hole area anomalies vs. 7 Sep–13 Oct 50-hPa (~20-km altitude) polar cap (60°S–90°S) MERRA-2 temperatures (K). (c) Ozone hole break-up dates, where the horizontal dashed line for 11 Dec is the 1992–2024 average. (d) Nov ozone hole areas vs. MERRA-2 Nov 50-hPa temperatures. In (a), the gray curve shows a quadratic fit of effective equivalent stratospheric chlorine with a 5.2-year mean age of air (Newman et al. 2006) to the Sep hole areas (see text). Years with temperatures in the lowest (highest) third are shown as blue triangles (red squares). The years 2006 and 2025 are specifically highlighted in orange and magenta, respectively. Ozone data for 1979–92 are from Total Ozone Mapping Spectrometer (TOMS) Nimbus-7, 1993–94 are from TOMS Meteor-3, 1996–2004 are from TOMS Earth Probe, 2005–15 are from Aura Ozone Monitoring Instrument (OMI), and 2015–25 are from Suomi National Polar-orbiting Partnership (SNPP) Ozone Mapping and Profiler Suite (OMPS). The ozone hole area is the region of total column ozone values below 220 DU. There were no 1995 satellite mapper total ozone observations.

declining (Figs. 6.17b,e), leveling out at about 0.65 ppm of ozone, slightly above the 2005–24 average. Similarly, ozone in the highly depleted 12-km–20-km layer at the South Pole station had also leveled off at an above-average amount of about 40 DU (Fig. 6.17f). MLS observations of chlorine monoxide (ClO) in the vortex (Fig. 6.17d) were also lower than average in 2025 during most of the season. ClO decreased to near-zero by mid-October, ending the chemical depletion period, consistent with ozone concentrations flattening in the vortex. Compared to the extreme depletion year of 2006 (orange lines in Fig. 6.17 and orange triangles in Figs. 6.16a,b),

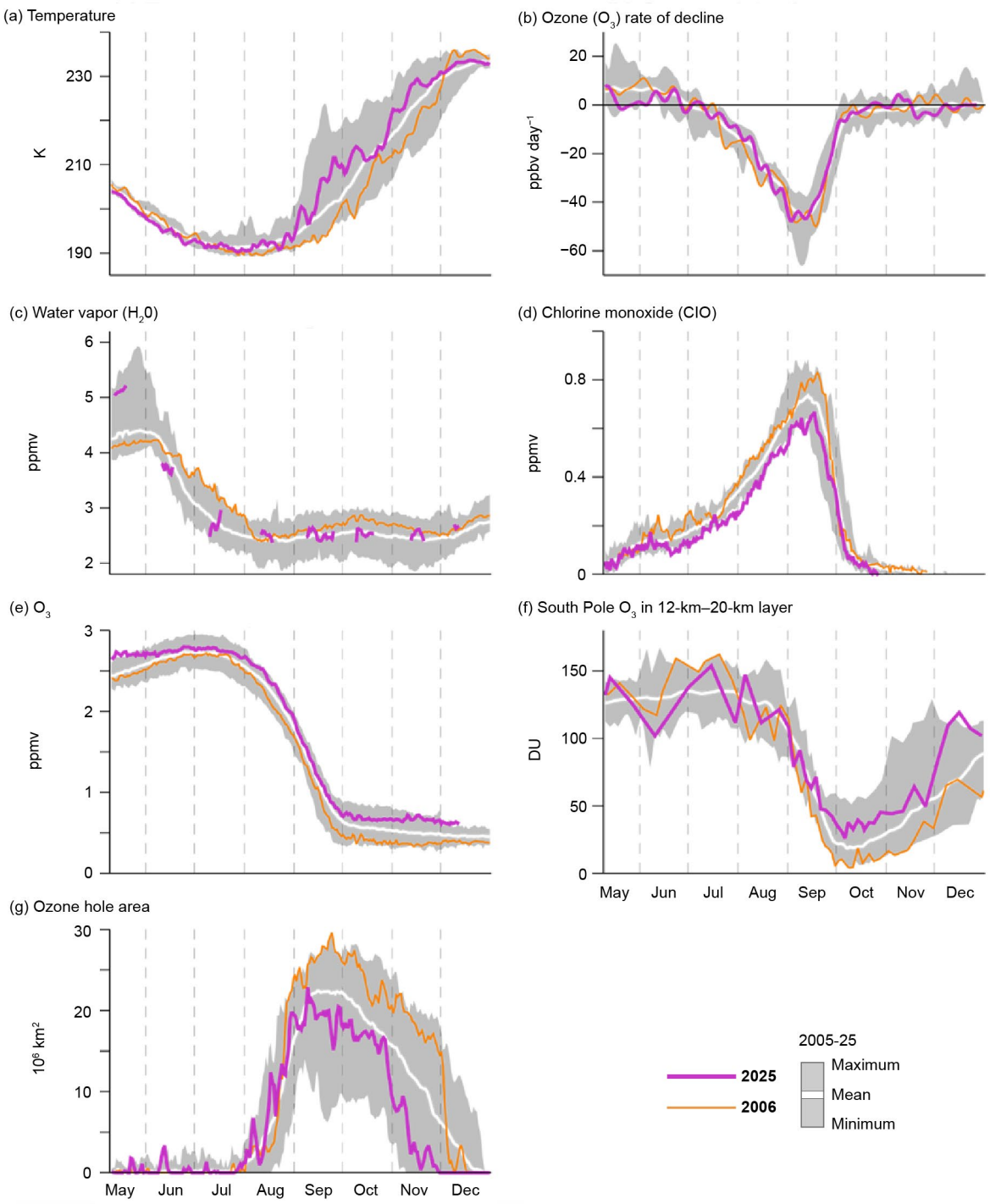

Fig. 6.17. Antarctic (a) polar cap temperature (K) at 50 hPa (~20 km, averaged 60°S–90°S) from MERRA-2. Aura MLS (updated from Manney et al. 2011) 440-K potential temperature surface (~18 km altitude) (b) ozone decline rate in the vortex (ppbv day^{-1}), (c) water vapor (H_2O; ppmv), (d) chlorine monoxide (ClO; ppbv), and (e) ozone (O_3; ppmv). (f) Lower-stratospheric ozone partial columns (12 km–20 km; DU) from South Pole ozonesondes. (g) Ozone Monitoring Instrument (OMI)/Ozone Mapping and Profiler Suite (OMPS) Antarctic ozone hole area (× 10^6 km^2; area with ozone total column less than 220 DU). The time series for 2025 (2006) is in magenta (orange). Gray shading shows daily Antarctic value ranges for 2005–24. The white lines indicate the 2005–23 long-term means.

the 2025 hole's development was less extensive than in 2006, consistent with the below-average 2025 ClO levels. This resulted in a relatively weak ozone hole by October.

The smaller-than-average austral spring depletion in 2025 is also consistent with the long-term decline of estimated chlorine and bromine levels in the Antarctic stratosphere. As noted previously, ClO values (Fig. 6.17d) were well below those in 2006 (orange line). To illustrate long-term changes in the annual ozone hole area, a quadratic regression is applied using the effective equivalent stratospheric chlorine (EESC) proxy (Fig. 6.16a). EESC is calculated using ozone depleting substance (ODS) surface observations (WMO 2022), transit times to the Antarctic stratosphere from the surface (~5.2 years), and the relative depletion efficiency of bromine with respect to chlorine (Br is ~60 more efficient than chlorine for ozone depletion). The EESC fit (gray line in Fig. 6.16a) shows a gradual 3.2 million km^2 decline in ozone hole area from 2000 to 2025.

The weak October ozone hole in 2025 is also related to higher-than-average Antarctic stratospheric temperature (Fig. 6.17a, magenta line). During the key depletion period of September to early-October, the average vortex temperature was above normal, leading to a smaller regional extent of polar stratospheric clouds (PSCs). Water vapor abundances are a key factor in PSC formation. While H_2O concentrations were elevated in May (Fig. 6.16c) due to the Hunga volcanic injection of water into the stratosphere (Millán et al. 2024), water vapor levels returned to near-normal values in August–November because of strong seasonal dehydration, also observed in 2023/24 (Santee et al. 2024; Lait et al. 2025). Polar lower stratospheric temperature is strongly correlated with ozone hole area (Fig. 6.16b). The year-to-year area anomalies in Fig. 6.16b are calculated as the difference between the Fig. 6.16a area values and the EESC gray line fit. Because the polar temperature (7 September–13 October, 60°S–90°S, 50 hPa) in 2025 was above average (Fig. 6.17a), the ozone hole area was slightly below average in 2025 (Fig. 6.16b, magenta triangle). These 2025 elevated temperatures reflect increased wave-driven warming of the Antarctic stratosphere. Both the long-term ODS decline, and above-average polar lower-stratospheric temperature led to a weak 2025 ozone hole.

The ozone hole broke up on 30 November 2025 (Fig. 6.16c, magenta triangle). The breakup is estimated by calculating when the ozone hole area falls to zero (Fig. 6.17g). The ozone hole area rapidly declined to 18.9 million km^2 by 14 September, with a slower decline to 16.9 million km^2 by 20 October. The ozone hole underwent two intervals of rapid decline in late October and mid-November. Such rapid declines are driven by planetary-scale wave events originating in the troposphere and lower-most stratosphere. These wave events deposit easterly momentum in the stratosphere that decelerates the polar vortex, warms the polar lower stratosphere by inducing a downward flow, and mixes ozone-rich air masses into the polar region. There were five significant wave events (not shown) during the 2025 austral spring that warmed the vortex. Most importantly, the wave event of 16 September 2025 largely ended the rapid ozone depletion period. The hole had considerably shrunk by early November (Fig. 6.17g) and vortex temperatures remained high because of the multiple wave events (Fig. 6.16d, magenta triangle, and Fig. 6.17a). The 30 November hole breakup was 11 days earlier than the 1992–2024 average (Fig. 6.16c, dashed line), accelerated by a wave event that began on 25 November. The greater wave activity in the September–November 2025 period led to the earlier-than-average 2025 ozone hole breakup.

Acknowledgments

- K. R. Clem and M. N. Raphael would like to extend a very warm thank you to Kathryn Marek, Antarctic Meteorological Research and Data Center, Space Science and Engineering Center, University of Wisconsin-Madison, for producing the map in Fig. 6.1.
- Work at the Jet Propulsion Laboratory, California Institute of Technology, was done under contract with the National Aeronautics and Space Administration (NASA). Support was also provided by the NASA Modeling and Analysis Program. We are indebted to the many NOAA Corps Officers and GML technical personnel who spend the winters at South Pole Station to obtain the ongoing balloon and ground-based data sets. We also acknowledge the logistics support in Antarctica provided by the National Science Foundation Office of Polar Programs.© 2024. All rights reserved.
- P. Reid and J. Lieser were supported through the Australian Bureau of Meteorology, and R. Massom by the Australian Antarctic Division. P. Reid and R. Massom were supported by the Australian Government as part of the Antarctic Science Collaboration Initiative program (Project Number ASCI000002). For R. Massom, this work was also supported by the Australian Research Council Special Research Initiative the Australian Centre for Excellence in Antarctic Science (Project Number SR200100008).
- S. Stammerjohn was supported under NSF PLR–1552226; she also thanks the Institute of Arctic and Alpine Research and the National Snow and Ice Data Center, both at the University of Colorado Boulder, for institutional and data support.
- The Southern Ocean Observing System (SOOS) is a joint international initiative of the Scientific Committee on Antarctic Research (SCAR) and the Scientific Committee on Oceanic Research (SCOR). L. P. Pezzi acknowledges support from PROANTAR's Antarctic Modelling and Observation System (ATMOS 2) Project under the CNPq/PROANTAR award 440848/2023-7 and PQ 303981/2023-7. R. L. Beadling, J. Milward, and Z. Kaufman were supported under the NSF Division of Polar Programs Grant NSF2319828. S. Thomalla is supported through the CSIR's Southern Ocean Carbon-Climate Observatory (SOCCO) Programme (http://socco.org.za/) funded by the Department of Science and Innovation (DSI/CON C3184/2023), and the CSIR's Parliamentary Grant (0000005278).
- L. P. Pezzi acknowledges support from PROANTAR's Antarctic Modeling and Observation System (ATMOS 2) Project under the CNPq/PROANTAR award 440848/2023-7 and PQ 303981/2023-7.
- R. L. Beadling and J. Milward were supported under the NSF Division of Polar Programs Grant NSF2319828.
- S. Thomalla and T. J. Ryan-Keogh were supported through the CSIR's Southern Ocean Carbon-Climate Observatory (SOCCO) Programme (http://socco.org.za/) funded by the Department of Science and Innovation (DSI/CON C3184/2023), the CSIR's Parliamentary Grant (0000005278) and the National Research Foundation (SANAP23042496681; MCR210429598142).
- T. Ziegler, M. A. Lazzara, D. Mikolajczyk, and L. M. Keller acknowledge support from the National Science Foundation, Grant Numbers 195120, 1951603, and 2301362.

Appendix 1: Acronyms

AAPP	Australian Antarctic Program Partnership
AIS	Antarctic Ice Sheet
AMRDC	Antarctic Meteorological Research and Data Center
AP	Antarctic Peninsula
AR	atmospheric river
ASL	Amundsen Sea Low
AWS	automatic weather station
ClO	chlorine monoxide
CRI	Coastal Resolution Improvement
DML	Dronning Maud Land
DMSP	Defense Meteorological Satellite Program
DO	dissolved oxygen
DOISST	Daily Optimum Interpolation Sea Surface Temperature
DU	Dobson unit
EAIS	East Antarctic Ice Sheet
EESC	effective equivalent stratospheric chlorine
FAC	firn air content
GRACE	Gravity Recovery and Climate Experiment
GRACE-FO	Gravity Recovery and Climate Experiment Follow-On
IMAS	Institute for Marine and Antarctic Studies
IMBIE	Ice Mass Balance Intercomparison Exercise
MAR	Model for Surface Mass Balance of the Arctic Ice Sheets
MLD	mixed-layer depth
MLS	Microwave Limb Sounder
NASA	National Aeronautics and Space Administration
NSIDC	National Snow and Ice Data Center
OC-CCI	Ocean Colour Climate Change Initiative
ODS	ozone depleting substance
OHC	ocean heat content
OMI	Ozone Monitoring Instrument
OMPS	Ozone Mapping and Profiler Suite
PSC	polar stratospheric cloud
S2	Sentinel-2
SAF	Subantarctic Front
SAM	Southern Annular Mode
SCAR	Scientific Committee on Antarctic Research
SIA	sea ice area
SIE	sea ice extent
SMB	surface mass balance
SMMR	Scanning Multichannel Microwave Radiometer
SNPP	Suomi National Polar-orbiting Partnership
SO	Southern Ocean
SOCCO	Southern Ocean Carbon-Climate Observatory
SOOS	Southern Ocean Observing System
SSM/I	Special Sensor Microwave Imager
SSMIS	Special Sensor Microwave Imager Sounder
SSS	sea surface salinity
SST	sea surface temperature
TOMS	Total Ozone Mapping Spectrometer

vIVT	vector-invariant water transport
WAIS	West Antarctic Ice Sheet
WMO	World Meteorological Organization

Appendix 2: Datasets and sources

Section 6b Atmospheric circulation and surface observations

Sub-section	General Variable or Phenomenon	Specific Dataset or Variable	Source
6b	Geopotential Height	ERA5	https://www.ecmwf.int/en/forecasts/dataset/ecmwf-reanalysis-v5
6b	Modes of Variability	Marshall Southern Annular Mode Index	http://www.nerc-bas.ac.uk/icd/gjma/sam.html
6b	Pressure, Sea Level or Near-Surface	ERA5	https://www.ecmwf.int/en/forecasts/dataset/ecmwf-reanalysis-v5
6b	Pressure, Sea Level or Near-Surface	University of Wisconsin-Madison Automated Weather Stations— Antarctic Meteorological Research and Data Center	https://amrdcdata.ssec.wisc.edu
6b	Pressure, Sea Level or Near-Surface	Staffed Weather Station Data	https://legacy.bas.ac.uk/met/READER/
6b	Temperature, [Near] Surface	ERA5	https://www.ecmwf.int/en/forecasts/dataset/ecmwf-reanalysis-v5
6b	Temperature, [Near] Surface	University of Wisconsin-Madison Automated Weather Stations— Antarctic Meteorological Research and Data Center	https://amrdcdata.ssec.wisc.edu
6b	Temperature, [Near] Surface	Staffed Weather Station Data	https://legacy.bas.ac.uk/met/READER/
6b	Temperature, Upper-Atmosphere	ERA5	https://www.ecmwf.int/en/forecasts/dataset/ecmwf-reanalysis-v5
6b	Wind, Upper-Atmosphere	ERA5	https://www.ecmwf.int/en/forecasts/dataset/ecmwf-reanalysis-v5

Section 6c Ice sheet surface mass balance

Sub-section	General Variable or Phenomenon	Specific Dataset or Variable	Source
6c	Atmospheric River	MERRA-2	http://gmao.gsfc.nasa.gov/reanalysis/MERRA-2/
6c	Geopotential Height	ERA5	https://www.ecmwf.int/en/forecasts/dataset/ecmwf-reanalysis-v5
6c	Grounded and Floating Ice Masks	Antarctic Digital Database	https://www.bas.ac.uk/project/add/
6c	Ice Sheet Surface Mass Balance	ERA5	https://www.ecmwf.int/en/forecasts/dataset/ecmwf-reanalysis-v5

Sub-section	General Variable or Phenomenon	Specific Dataset or Variable	Source
6c	Ice Sheet Surface Mass Balance	MERRA-2	http://gmao.gsfc.nasa.gov/reanalysis/MERRA-2/
6c	Ice Sheet Surface Mass Balance	Polar-Oriented Regional Climate Model (Model for Surface Mass Balance of the Arctic Ice Sheets [MAR])	https://arcticdata.io/catalog/view/doi%3A10.18739%2FA28G8FJ7F
6c	Ice Surface Height	CESat-2 ATL15	https://nsidc.org/data/atl15/versions/2

Section 6d Ice sheet melt extent and duration

Sub-section	General Variable or Phenomenon	Specific Dataset or Variable	Source
6d	Ice Sheet Surface Melt	Defense Meteorological Satellite Program (DMSP) Special Sensor Microwave Imager/Sounder (SSMIS)	https://nsidc.org/data/nsidc-0001/versions/6
6d	Sea Ice Extent/Area/Concentration	Nimbus-7 Scanning Multichannel Microwave Radiometer (SMMR) Sea Ice Concentration	https://nsidc.org/data/nsidc-0007

Section 6e Ice sheet mass balance

Sub-section	General Variable or Phenomenon	Specific Dataset or Variable	Source
6e	Ice Sheet Mass	Gravity Recovery and Climate Experiment (GRACE)/GRACE Follow-On (GRACE-FO)	https://podaac.jpl.nasa.gov/dataset/TELLUS_GRAC-GRFO_MASCON_CRI_GRID_RL06_V2
6e	Ice Sheet Surface Height	Advanced Topographic Laser Altimeter System (ATLAS) Ice, Cloud and Land Elevation Satellite-2 (ICESat-2)	https://nsidc.org/data/atl06/versions/5
6e	Ice Sheet Surface Height	ICESat-2	https://icesat-2.gsfc.nasa.gov/

Section 6f Sea ice extent, concentration, and seasonality			
Sub-section	**General Variable or Phenomenon**	**Specific Dataset or Variable**	**Source**
6f	Sea Ice Extent and Area	NIMBUS-7 SMMR and DMSP SSM/I-SSMIS Version 4 (NSIDC-0079)	https://doi.org/10.5067/X5LG68MH013O
6f	Sea Ice Extent and Area	AMSR2 Daily Polar Gridded Sea Ice Concentrations, Version 2 (NSIDC-0803)	https://doi.org/10.5067/W13AO54SS7CW
6f	Sea Ice Extent and Area	Sea Ice Concentration from Nimbus-7 SMMR and DMSP SSM/1-SSMIS Passive Microwave Data, Version 2 (NSIDC-0051)	https://doi.org/10.5067/MPYG15WAA4WX
6f	Sea Surface Temperature	NOAA OISSTv2.1	https://www.ncei.noaa.gov/products/optimum-interpolation-sst

Section 6g Southern Ocean			
Sub-section	**General Variable or Phenomenon**	**Specific Dataset or Variable**	**Source**
6g1	Mixed-Layer Depth	Argo Monthly Climatology	https://sio-argo.ucsd.edu/RG_Climatology.html
6g1	Sea Surface Salinity	Argo Monthly Climatology	https://sio-argo.ucsd.edu/RG_Climatology.html
6g1	Sea Surface Temperature	NOAA OISSTv2.1	https://www.ncei.noaa.gov/products/optimum-interpolation-sst
6g2	Surface Heat flux	ERA5	https://www.ecmwf.int/en/forecasts/dataset/ecmwf-reanalysis-v5
6g3	Ocean Heat Content	Argo Monthly Climatology	https://sio-argo.ucsd.edu/RG_Climatology.html
6g4	Dissolved Oxygen	Biogeochemical Argo (BGC-Argo)	https://biogeochemical-argo.org/
6g4	Ocean Chlorophyll	ESA Ocean Colour Climate Change Initiative (OC-CCI) product Version 6.0	https://www.oceancolour.org/

Section 6h 2024 Antarctic ozone hole			
Sub-section	**General Variable or Phenomenon**	**Specific Dataset or Variable**	**Source**
6h	Ozone, Lower Stratosphere	Ozone, Lower Stratosphere	https://ozonewatch.gsfc.nasa.gov/
6h	Ozone, Lower Stratosphere	Ozonesonde	https://gml.noaa.gov/dv/spo_oz/

Sub-section	General Variable or Phenomenon	Specific Dataset or Variable	Source
6h	Ozone, Total Column and Stratospheric	Ozone Mapping Instrument (OMI) Ozone Mapping & Profiler Suite (OMPS), Total Ozone Mapping Spectrum (TOMS), Earth Probe TOMS	https://ozoneaq.gsfc.nasa.gov/data/ozone/
6h	Temperature, Upper-Atmosphere	MERRA-2	https://gmao.gsfc.nasa.gov/reanalysis/MERRA-2/

Sidebar 6.1: The Exceptional Nature of Supraglacial Meltwater in 2024/25

Sub-section	General Variable or Phenomenon	Specific Dataset or Variable	Source
SB6.1	Modes of Variability	Marshall Southern Annular Mode (SAM) Index (Station-based)	https://climatedataguide.ucar.edu/climate-data/marshall-southern-annular-mode-sam-index-station-based
SB6.1	Surface Meltwater	LandSat 8/9 (L8, L9)	https://www.usgs.gov/landsat-missions/landsat-levels-processing
SB6.1	Temperature, [Near] Surface	ERA5	https://www.ecmwf.int/en/forecasts/dataset/ecmwf-reanalysis-v5

References

Adusumilli, S., and H. A. Fricker, 2025: Ice sheet mass balance [in "State of the Climate in 2024"]. *Bull. Amer. Meteor. Soc.*, **106** (8), S372–S374, https://doi.org/10.1175/BAMS-D-25-0087.1

——, ——, B. Medley, L. Padman, and M. R. Siegfried, 2020: Interannual variations in meltwater input to the Southern Ocean from Antarctic ice shelves. *Nat. Geosci.*, **13**, 616–620, https://doi.org/10.1038/s41561-020-0616-z.

——, ——, and A. S. Gardner, 2022: Ice sheet mass balance [in "State of the Climate in 2021"]. *Bull. Amer. Meteor. Soc.*, **103** (8), S325–S329, https://doi.org/10.1175/BAMS-D-21-0078.1.

Agosta, C., and Coauthors, 2019: Estimation of the Antarctic surface mass balance using the regional climate model MAR (1979–2015) and identification of dominant processes. *Cryosphere*, **13**, 281–296, https://doi.org/10.5194/tc-13-281-2019.

AMRDC, 2022: Antarctic Meteorological Research and Data Center: Automatic weather station quality-controlled observational data. AMRDC Data Repository, accessed 15 January 2025, https://doi.org/10.48567/1hn2-nw60.

Arthur, J. F., C. R. Stokes, S. S. R. Jamieson, J. Rachel Carr, A. A. Leeson, and V. Verjans, 2022: Large interannual variability in supraglacial lakes around East Antarctica. *Nat. Commun.*, **13**, 1711, https://doi.org/10.1038/s41467-022-29385-3.

Baiman, R., A. C. Winters, B. Pohl, V. Favier, J. D. Wille, and K. R. Clem, 2024: Synoptic and planetary-scale dynamics modulate Antarctic atmospheric river precipitation intensity. *Commun. Earth Environ.*, **5**, 127, https://doi.org/10.1038/s43247-024-01307-9.

Banwell, A. F., D. R. MacAyeal, and O. V. Sergienko, 2013: Breakup of the Larsen B ice shelf triggered by chain reaction drainage of supraglacial lakes. *Geophys. Res. Lett.*, **40**, 5872–5876, https://doi.org/10.1002/2013GL057694.

——, I. C. Willis, G. J. Macdonald, B. Goodsell, and D. R. MacAyeal, 2019: Direct measurements of ice-shelf flexure caused by surface meltwater ponding and drainage. *Nat. Commun.*, **10**, 730, https://doi.org/10.1038/s41467-019-08522-5.

——, R. T. Datta, R. L. Dell, M. Moussavi, L. Brucker, G. Picard, C. A. Shuman, and L. A. Stevens, 2021: The 32-year record-high surface melt in 2019/2020 on the northern George VI Ice Shelf, Antarctic Peninsula. *Cryosphere*, **15**, 909–925, https://doi.org/10.5194/tc-15-909-2021.

——, N. Wever, D. Dunmire, and G. Picard, 2023: Quantifying Antarctic-wide ice-shelf surface melt volume using microwave and firn model data: 1980 to 2021. *Geophys. Res. Lett.*, **50**, e2023GL102744, https://doi.org/10.1029/2023GL102744.

Barthélemy, L., F. Codron, J. Wille, V. Favier, and K. R. Clem, 2026: Future atmospheric rivers in Antarctica: Characteristics and impacts with the IPSL model. *J. Geophys. Res. Atmos.*, **131**, e2025JD043398, https://doi.org/10.1029/2025JD043398.

Beadling, R. L., N. M. Freeman, G. A. MacGilchrist, M. Mazloff, J.-R. Shi, A. F. Thompson, and E. Wilson, 2022: Southern Ocean [in "State of the Climate in 2021"]. *Bull. Amer. Meteor. Soc.*, **103** (8), S329–S332, https://doi.org/10.1175/BAMS-D-22-0078.1.

Bell, R. E., and Coauthors, 2017: Antarctic ice shelf potentially stabilized by export of meltwater in surface river. *Nature*, **544**, 344–348, https://doi.org/10.1038/nature22048.

——, A. F. Banwell, L. D. Trusel, and J. Kingslake, 2018: Antarctic surface hydrology and impacts on ice-sheet mass balance. *Nat. Climate Change*, **8**, 1044–1052, https://doi.org/10.1038/s41558-018-0326-3.

Bromwich, D. H., A. Ensign, S.-H. Wang, and X. Zou, 2024: Major artifacts in ERA5 2-m air temperature trends over Antarctica prior to and during the modern satellite era. *Geophys. Res. Lett.*, **51**, e2024GL111907, https://doi.org/10.1029/2024GL111907.

Cheng, L., and Coauthors, 2022: Past and future ocean warming. *Nat. Rev. Earth Environ.*, **3**, 776–794, https://doi.org/10.1038/s43017-022-00345-1.

Clem, K. R., and M. N. Raphael, Eds., 2024: Antarctica and the Southern Ocean [in "State of the Climate in 2023"]. *Bull. Amer. Meteor. Soc.*, **103** (8), S307–S340, https://doi.org/10.1175/BAMS-D-24-0099.1.

Comiso, J. C., 2023: Bootstrap Sea Ice Concentrations from Nimbus-7 SMMR and DMSP SSM/I-SSMIS, Version 4 (NSIDC-0079), NASA National Snow and Ice Data Center Distributed Active Archive Center, Boulder, Colorado USA, accessed 8 October 2025, https://doi.org/10.5067/X5LG68MH013O.

Corr, D., A. Leeson, M. McMillan, C. Zhang, and T. Barnes, 2022: An inventory of supraglacial lakes and channels across the west Antarctic ice sheet. *Earth Syst. Sci. Data*, **14**, 209–228, https://doi.org/10.5194/essd-14-209-2022.

Davison, B. J., and Coauthors, 2023: Sea level rise from West Antarctic mass loss significantly modified by large snowfall anomalies. *Nat. Commun.*, **14**, 1479, https://doi.org/10.1038/s41467-023-36990-3.

de Boyer Montégut, C., G. Madec, A. S. Fischer, A. Lazar, and D. Ludicone, 2004: Mixed layer depth over the global ocean: An examination of profile data and a profile?based climatology. *J. Geophys. Res.*, **109**, C12003, https://doi.org/10.1029/2004JC002378.

Dell, R., N. Arnold, I. Willis, A. Banwell, A. Williamson, H. Pritchard, and A. Orr, 2020: Lateral meltwater transfer across an Antarctic ice shelf. *Cryosphere*, **14**, 2313–2330, https://doi.org/10.5194/tc-14-2313-2020.

Dell, R. L., A. F. Banwell, I. C. Willis, N. S. Arnold, A. R. W. Halberstadt, T. R. Chudley, and H. D. Pritchard, 2022: Supervised classification of slush and ponded water on Antarctic ice shelves using Landsat 8 imagery. *J. Glaciol.*, **68**, 401–414, https://doi.org/10.1017/jog.2021.114.

——, I. C. Willis, N. S. Arnold, A. F. Banwell, and S. De Roda Husman, 2024: Substantial contribution of slush to meltwater area across Antarctic ice shelves. *Nat. Geosci.*, **17**, 624–630, https://doi.org/10.1038/s41561-024-01466-6.

——, M. L. Maclennan, L. Trusel, and M. Bahrami, 2026: Brief communication: Lateral surface meltwater export from Bach Ice Shelf resumes after 9-year hiatus. *EGUsphere*, **2026**, 1–11, https://doi.org/10.5194/egusphere-2026-233.

DiGirolamo, N., C. L., Parkinson, D. J. Cavalieri, P. Gloersen, and H. J. Zwally, 2022: Sea Ice Concentration from Nimbus-7 SMMR and DMSP SSM/I-SSMIS Passive Microwave Data, Version 2 (NSIDC-0051), NASA National Snow and Ice Data Center Distributed Active Archive Center, Boulder, Colorado USA, accessed 19 February 2026, https://doi.org/10.5067/MPYG15WAA4WX.

Doddridge, E. W., and Coauthors, 2025: Impacts of Antarctic summer sea-ice extremes. *PNAS Nexus*, **4**, pgaf164, https://doi.org/10.1093/pnasnexus/pgaf164.

Dunmire, D., N. Wever, A. F. Banwell, and J. T. M. Lenaerts, 2024: Antarctic-wide ice-shelf firn emulation reveals robust future firn air depletion signal for the Antarctic Peninsula. *Commun. Earth Environ.*, **5**, 100, https://doi.org/10.1038/s43247-024-01255-4.

Eayrs, C., X. Li, M. N. Raphael, and D. M. Holland, 2021: Rapid decline in Antarctic sea ice in recent years hints at future change. *Nat. Geosci.*, **14**, 460–464, https://doi.org/10.1038/s41561-021-00768-3.

Foppert, A., K. A. Donohue, D. R. Watts, and K. L. Tracey, 2017: Eddy heat flux across the Antarctic Circumpolar Current estimated from sea surface height standard deviation. *J. Geophys. Res. Oceans*, **122**, 6947–6964, https://doi.org/10.1002/2017JC012837.

Fricker, H. A., B. K. Galton-Fenzi, C. C. Walker, B. I. D. Freer, L. Padman, and R. DeConto, 2025: Antarctica in 2025: Drivers of deep uncertainty in projected ice loss. *Science*, **387**, 601–609, https://doi.org/10.1126/science.adt9619.

Frölicher, T. L., J. L. Sarmiento, D. J. Paynter, J. P. Dunner, J. P. Krasting, and M. Winton, 2015: Dominance of the Southern Ocean in anthropogenic carbon and heat uptake in CMIP5 models. *J. Climate*, **28**, 862–886, https://doi.org/10.1175/JCLI-D-14-00117.1.

Gelaro, R., and Coauthors, 2017: The Modern-Era Retrospective Analysis for Research and Applications, version 2 (MERRA-2). *J. Climate*, **30**, 5419–5454, https://doi.org/10.1175/JCLI-D-16-0758.1.

Gerrish, L., L. Ireland, P. Fretwell, and P. Cooper, 2023: Medium resolution vector polygons of the Antarctic coastline - Version 7.8. NERC EDS UK Polar Data Centre, accessed 18 February 2026, https://doi.org/10.5285/3EA85903-E068-4242-A63F-46767E16F85C.

Gloersen, P., 2006: Nimbus-7 SMMR polar gridded radiances and sea ice concentrations, version 1. Subset used: 37 & 19 GHz, h-polarization, 25 km grid, October 1979–April 1987. NASA National Snow and Ice Data Center Distributed Active Archive Center, accessed 5 May 2020, https://doi.org/10.5067/QOZIVYV3V9JP.

Gudmundsson, G. H., F. S. Paolo, S. Adusumilli, and H. A. Fricker, 2019: Instantaneous Antarctic ice sheet mass loss driven by thinning ice shelves. *Geophys. Res. Lett.*, **46**, 13 903–13 909, https://doi.org/10.1029/2019GL085027.

Hersbach, H., and Coauthors, 2020: The ERA5 global reanalysis. *Quart. J. Roy. Meteor. Soc.*, **146**, 1999–2049, https://doi.org/10.1002/qj.3803.

Himmich, K., M. Vancoppenolle, S. Stammerjohn, M. Bocquet, G. Madec, J.-B. Sallée, and S. Fleury, 2024: Thermodynamics drive post?2016 changes in the Antarctic sea ice seasonal cycle. *J. Geophys. Res. Oceans*, **129**, e2024JC021112, https://doi.org/10.1029/2024JC021112.

Hobbs, W. R., R. Holmes, and A. E. Kiss, 2026: Ocean constraints on winter Antarctic sea ice extent. *J. Geophys. Res. Oceans*, **131**, e2025JC022716, https://doi.org/10.1029/2025JC022716.

Hosking, J. S., A. Orr, G. J. Marshall, J. Turner, and T. Phillips, 2013: The influence of the Amundsen–Bellingshausen Seas Low on the climate of West Antarctica and its representation in coupled climate model simulations. *J. Climate*, **26**, 6633–6648, https://doi.org/10.1175/JCLI-D-12-00813.1.

Huang, B., C. Liu, V. Banzon, E. Freeman, G. Graham, B. Hankins, T. Smith, and H.-M. Zhang, 2021: Improvements of the Daily Optimum Interpolation Sea Surface Temperature (DOISST) version 2.1. *J. Climate*, **34**, 2923–2939, https://doi.org/10.1175/JCLI-D-20-0166.1.

Izeboud, M., B. Wouters, S. De Roda Husman, and S. Lhermitte, 2025: Damage development on Antarctic ice shelves sensitive to climate warming. *Nat. Climate Change*, **15**, 1333–1339, https://doi.org/10.1038/s41558-025-02453-4.

Josey, S. A., J. P. Grist, J. V. Mecking, B. I. Moat, and E. Schulz, 2023: A clearer view of Southern Ocean air-sea interaction using surface heat flux asymmetry. *Philos. Trans. Roy. Soc.*, **A381**, 20220067, https://doi.org/10.1098/rsta.2022.0067.

——, A. J. S. Meijers, A. T. Blaker, J. P. Grist, J. Mecking, and H. C. Ayres, 2024: Record-low Antarctic sea ice in 2023 increased ocean heat loss and storms. *Nature*, **636**, 635–639, https://doi.org/10.1038/s41586-024-08368-y.

Kimura, N., and M. Wakatsuchi, 2011: Large-scale processes governing the seasonal variability of the Antarctic sea ice. *Tellus*, **63A**, 828–840, https://doi.org/10.1111/j.1600-0870.2011.00526.x.

Kingslake, J., J. C. Ely, I. Das, and R. E. Bell, 2017: Widespread movement of meltwater onto and across Antarctic ice shelves. *Nature*, **544**, 349–352, https://doi.org/10.1038/nature22049.

Kittel, C., and Coauthors, 2021: Diverging future surface mass balance between the Antarctic ice shelves and grounded ice sheet. *Cryosphere*, **15**, 1215–1236, https://doi.org/10.5194/tc-15-1215-2021.

Kuipers Munneke, P., S. R. M. Ligtenberg, M. R. Van Den Broeke, and D. G. Vaughan, 2014: Firn air depletion as a precursor of Antarctic ice-shelf collapse. *J. Glaciol.*, **60**, 205–214, https://doi.org/10.3189/2014JoG13J183.

Lait, L. R., P. A. Newman, N. A. Kramarova, B. Johnson, M. L. Santee, I. Petropavlovskikh, L. Coy, and J. De Laat, 2025: 2024 Antarctic ozone hole [in "State of the Climate in 2024"]. *Bull. Amer. Meteor. Soc.*, **106** (8), S388–S390, https://doi.org/10.1175/BAMS-D-25-0087.1.

Leeson, A. A., E. Forster, A. Rice, N. Gourmelen, and J. M. Van Wessem, 2020: Evolution of supraglacial lakes on the Larsen B ice shelf in the decades before it collapsed. *Geophys. Res. Lett.*, **47**, e2019GL085591, https://doi.org/10.1029/2019GL085591.

MacFerrin, M., T. Mote, H. Wang, L. Liu, L. Montgomery, and T. Scambos, 2021: Ice sheet seasonal melt extent and duration [in "State of the Climate in 2020"]. *Bull. Amer. Meteor. Soc.*, **102** (8), S331–S334, https://doi.org/10.1175/BAMS-D-21-0081.1.

——, ——, A. F. Banwell, and T. Scambos, 2025: Ice sheet seasonal melt extent and duration [in "State of the Climate in 2024"]. *Bull. Amer. Meteor. Soc.*, **106** (8), S372–S374, https://doi.org/10.1175/BAMS-D-25-0087.1.

Maclennan, M. L., and Coauthors, 2023: Climatology and surface impacts of atmospheric rivers on West Antarctica. *Cryosphere*, **17**, 865–881, https://doi.org/10.5194/tc-17-865-2023.

Mahagaonkar, A., G. Moholdt, Q. Glaude, and T. V. Schuler, 2024: Supraglacial lake evolution and its drivers in Dronning Maud Land, East Antarctica. *J. Glaciol.*, **70**, e49, https://doi.org/10.1017/jog.2024.66.

Maksym, T., and S. Stammerjohn, 2026: The rise and fall of Antarctic sea ice: Large-scale variability. Sea Ice: Its Physics, Chemistry, Biology, Geology and Societal Importance, D. N. Thomas, Ed., Wiley, 215–260, https://doi.org/10.1002/9781394213764.ch06.

Manney, G. L., and Coauthors, 2011: Unprecedented Arctic ozone loss in 2011. *Nature*, **478**, 469–475, https://doi.org/10.1038/nature10556.

Marshall, G. J., 2003: Trends in the Southern Annular Mode from observations and reanalyses. *J. Climate*, **16**, 4134–4143, https://doi.org/10.1175/1520-0442(2003)016<4134:TITSAM>2.0.CO;2.

Massom, R. A., T. A. Scambos, L. G. Bennetts, P. Reid, V. A. Squire, and S. E. Stammerjohn, 2018: Antarctic Ice Shelf disintegration triggered by sea ice loss and ocean swell. *Nature*, **558**, 383–389, https://doi.org/10.1038/s41586-018-0212-1.

Medley, B., and E. R. Thomas, 2019: Increased snowfall over the Antarctic ice sheet mitigated twentieth-century sea-level rise. *Nat. Climate Change*, **9**, 34–39, https://doi.org/10.1038/s41558-018-0356-x.

Meier, W. N., H. Wilcox, M. A. Hardman, and J. S. Stewart, 2019: DMSP SSM/I-SSMIS daily polar gridded brightness temperatures, version 5. Subset used: 37 & 19 GHz, h-polarization, 25 km grid, October 1987–April 2020. NASA National Snow and Ice Data Center Distributed Active Archive Center, accessed 11 February 2021, https://doi.org/10.5067/QU2UYQ6T0B3P.

Meredith, M. P., and M. A. Brandon, 2017: Oceanography and sea ice in the Southern Ocean. *Sea Ice*, D. Thomas, Ed., Wiley, 216–238.

Millán, L., and Coauthors, 2024: The evolution of the Hunga hydration in a moistening stratosphere. *Geophys. Res. Lett.*, **51**, e2024GL110841, https://doi.org/10.1029/2024GL110841.

Mote, T. L., 2007: Greenland surface melt trends 1973–2007: Evidence of a large increase in 2007. *Geophys. Res. Lett.*, **34**, L22507, https://doi.org/10.1029/2007GL031976.

——, and M. R. Anderson, 1995: Variations in snowpack melt on the Greenland ice sheet based on passive-microwave measurements. *J. Glaciol.*, **41**, 51–60, https://doi.org/10.3189/S0022143000017755.

Mottram, R., and Coauthors, 2021: What is the surface mass balance of Antarctica? *An intercomparison of regional climate model estimates. Cryosphere*, **15**, 3751–3784, https://doi.org/10.5194/tc-15-3751-2021.

Moussavi, M., A. Pope, A. Halberstadt, L. Trusel, L. Cioffi, and W. Abdalati, 2020: Antarctic supraglacial lake detection using Landsat 8 and Sentinel-2 imagery: Towards continental generation of lake volumes. *Remote Sens.*, **12**, 134, https://doi.org/10.3390/rs12010134.

Newman, P. A., E. R. Nash, S. R. Kawa, S. A. Montzka, and S. M. Schauffler, 2006: When will the Antarctic ozone hole recover? *Geophys. Res. Lett.*, **33**, L12814, https://doi.org/10.1029/2005GL025232.

Norwegian Polar Institute, 2018: Quantarctica v3.0, detailed basemap. https://www.npolar.no/quantarctica/.

Ochwat, N. E., and Coauthors, 2024: Triggers of the 2022 Larsen B multi-year landfast sea ice breakout and initial glacier response. *Cryosphere*, **18**, 1709–1731, https://doi.org/10.5194/tc-18-1709-2024.

Orr, A., G. J. Marshall, J. C. R. Hunt, J. Sommeria, C.-G. Wang, N. P. M. van Lipzig, D. Cresswell, and J. C. King, 2008: Characteristics of summer airflow over the Antarctic Peninsula in response to recent strengthening of westerly circumpolar winds. *J. Atmos. Sci.*, **65**, 1396–1413, https://doi.org/10.1175/2007JAS2498.1.

Orsi, A. H., T. Whitworth III, and W. D. Nowlin Jr., 1995: On the meridional extent and fronts of the Antarctic Circumpolar Current. *Deep-Sea. Res. I*, **42**, 641–673, https://doi.org/10.1016/0967-0637(95)00021-W.

Otosaka, I. N., and Coauthors, 2023: Mass balance of the Greenland and Antarctic ice sheets from 1992 to 2020. *Earth Syst. Sci. Data*, **15**, 1597–1616, https://doi.org/10.5194/essd-15-1597-2023.

Pellichero, V., J.-B. Sallée, S. Schmidtko, F. Roquet, and J.-B. Charrassin, 2017: The ocean mixed layer under Southern Ocean sea-ice: Seasonal cycle and forcing. *J. Geophys. Res. Oceans*, **122**, 1608–1633, https://doi.org/10.1002/2016JC011970.

Pezzi, L. P., and Coauthors, 2023: Southern Ocean [in "State of the Climate in 2022"]. *Bull. Amer. Meteor. Soc.*, **104** (9), S351–S355, https://doi.org/10.1175/BAMS-D-23-0077.1.

Purich, A., and E. W. Doddridge, 2023: Record low Antarctic sea ice coverage indicates a new sea ice state. *Commun. Earth Environ.*, **4**, 314, https://doi.org/10.1038/s43247-023-00961-9.

Raphael, M. N., and K. R. Clem, Eds., 2025: Antarctica and the Southern Ocean [in "State of the Climate in 2024"]. *Bull. Amer. Meteor. Soc.*, **106** (8), S357–S400, https://doi.org/10.1175/BAMS-D-25-0087.1.

Reid, P., S. Stammerjohn, R. A. Massom, S. Barreira, T. Scambos, and J. L. Lieser, 2024: Sea ice extent, concentration, and seasonality [in "State of the Climate in 2023"]. *Bull. Amer. Meteor. Soc.*, **105** (8), S351–S354, https://doi.org/10.1175/BAMS-D-24-0099.1.

——, ——, ——, ——, ——, and ——, 2025: Sea ice extent, concentration, and seasonality [in "State of the Climate in 2024"]. *Bull. Amer. Meteor. Soc.*, **106** (8), S378–S381, https://doi.org/10.1175/2025BAMSStateoftheClimate.1.

Reid, P. A., and R. A. Massom, 2022: Change and variability in Antarctic coastal exposure, 1979-2020. *Nat. Commun.*, **13**, 1164, https://doi.org/10.1038/s41467-022-28676-z.

Reynolds, R. W., N. A. Rayner, T. M. Smith, D. C. Stokes, and W. Wang, 2002: An improved in situ and satellite SST analysis for climate. *J. Climate*, **15**, 1609–1625, https://doi.org/10.1175/1520-0442(2002)015<1609:AIISAS>2.0.CO;2.

Riihelä, A., R. M. Bright, and K. Anttila, 2021: Recent strengthening of snow and ice albedo feedback driven by Antarctic sea-ice loss. *Nat. Geosci.*, **14**, 832–836, https://doi.org/10.1038/s41561-021-00841-x.

Roemmich, D., and J. Gilson, 2009: The 2004–2008 mean and annual cycle of temperature, salinity, and steric height in the global ocean from the Argo Program. *Prog. Oceanogr.*, **82**, 81–100, https://doi.org/10.1016/j.pocean.2009.03.004.

Santee, M. L., and Coauthors, 2024: The influence of stratospheric hydration from the Hunga eruption on chemical processing in the 2023 Antarctic vortex. ESS Open Archive, accessed 16 January 2024, https://doi.org/10.22541/essoar.170542085.55151307/v1.

Sathyendranath, S., and Coauthors, 2019: An ocean-colour time series for use in climate studies: The experience of the Ocean-Colour Climate Change Initiative (OC-CCI). *Sensors*, **19**, 4285, https://doi.org/10.3390/s19194285.

Scambos, T. A., C. Hulbe, M. Fahnestock, and J. Bohlander, 2000: The link between climate warming and break-up of ice shelves in the Antarctic Peninsula. *J. Glaciol.*, **46**, 516–530, https://doi.org/10.3189/172756500781833043.

——, E. Berthier, T. Haran, C. A. Shuman, A. J. Cook, S. R. M. Ligtenberg, and J. Bohlander, 2014: Detailed ice loss pattern in the northern Antarctic Peninsula: Widespread decline driven by ice front retreats. *Cryosphere*, **8**, 2135–2145, https://doi.org/10.5194/tc-8-2135-2014.

Silvano, A., and Coauthors, 2025: Rising surface salinity and declining sea ice: A new Southern Ocean state revealed by satellites. *Proc. Natl. Acad. Sci. USA*, **122**, e2500440122, https://doi.org/10.1073/pnas.2500440122.

Smith, B., and Coauthors, 2020: Pervasive ice sheet mass loss reflects competing ocean and atmosphere processes. *Science*, **368**, 1239–1242, https://doi.org/10.1126/science.aaz5845.

——, B. P. Jelley, S. Dickinson, T. Sutterley, T. Neumann, and K. Harbeck, 2024: ATLAS/ICESat-2 L3B gridded Antarctic and Greenland height change, version 4. NASA National Snow and Ice Data Center Distributed Active Archive Center, accessed 16 February 2026, https://doi.org/10.5067/ATLAS/ATL15.004.

Spira, T., S. Swart, I. Giddy, and M. Du Plessis, 2024: The observed spatiotemporal variability of Antarctic winter water. *J. Geophys. Res. Oceans*, **129**, e2024JC021017, https://doi.org/10.1029/2024JC021017.

Stammerjohn, S. E., D. G. Martinson, R. C. Smith, X. Yuan, and D. Rind, 2008: Trends in Antarctic annual sea ice retreat and advance and their relation to El Niño–Southern Oscillation and Southern Annular Mode variability. *J. Geophys. Res.*, **113**, C03S90, https://doi.org/10.1029/2007JC004269.

Stewart, J. S., W. N. Meier, R. Marowitz, D. J. Scott, and H. Wilcox, 2025: AMSR2 Daily Polar Gridded Sea Ice Concentrations, Version 2 (NSIDC-0803), NASA National Snow and Ice Data Center Distributed Active Archive Center, Boulder, Colorado USA, accessed 19 February 2026, https://doi.org/10.5067/W13AO54SS7CW.

Stokes, C. R., J. E. Sanderson, B. W. J. Miles, S. S. R. Jamieson, and A. A. Leeson, 2019: Widespread distribution of supraglacial lakes around the margin of the East Antarctic ice sheet. *Sci. Rep.*, **9**, 13823, https://doi.org/10.1038/s41598-019-50343-5.

The Firn Symposium Team, 2024: Firn on ice sheets. *Nat. Rev. Earth Environ.*, **5**, 79–99, https://doi.org/10.1038/s43017-023-00507-9.

The IMBIE Team, 2020: Mass balance of the Greenland ice sheet from 1992 to 2018. *Nature*, **579**, 233–239, https://doi.org/10.1038/s41586-019-1855-2.

Thomalla, S., and Coauthors, 2024: Southern Ocean [in "State of the Climate in 2023"]. *Bull. Amer. Meteor. Soc.*, **105** (8), S355–S356, https://doi.org/10.1175/BAMS-D-24-0099.1.

——, and Coauthors, 2025: Southern Ocean [in "State of the Climate in 2024"]. *Bull. Amer. Meteor. Soc.*, **106** (8), S384–S387, https://doi.org/10.1175/BAMS-D-25-0087.1.

Thomas, D., Ed., 2017: Sea Ice. 3rd ed. Wiley-Blackwell, 664 pp.

Trusel, L. D., K. E. Frey, S. B. Das, K. B. Karnauskas, P. Kuipers Munneke, E. Van Meijgaard, and M. R. Van Den Broeke, 2015: Divergent trajectories of Antarctic surface melt under two twenty-first-century climate scenarios. *Nat. Geosci.*, **8**, 927–932, https://doi.org/10.1038/ngeo2563.

——, Z. Pan, and M. Moussavi, 2022: Repeated tidally induced hydrofracture of a supraglacial lake at the Amery Ice Shelf grounding zone. *Geophys. Res. Lett.*, **49**, e2021GL095661, https://doi.org/10.1029/2021GL095661.

Tuckett, P. A., A. J. Sole, S. J. Livingstone, J. M. Jones, J. M. Lea, and E. Gilbert, 2025: Continent-wide mapping shows increasing sensitivity of East Antarctica to meltwater ponding. *Nat. Climate Change*, **15**, 775–783, https://doi.org/10.1038/s41558-025-02363-5.

Turner, J., and Coauthors, 2004: The SCAR READER project: Toward a high-quality database of mean Antarctic meteorological observations. *J. Climate*, **17**, 2890–2898, https://doi.org/10.1175/1520-0442(2004)017<2890:TSRPTA>2.0.CO;2.

van Wessem, J. M., and Coauthors, 2018: Modelling the climate and surface mass balance of polar ice sheets using RACMO2 – Part II: Antarctica (1979–2016). *Cryosphere*, **12**, 1479–1498, https://doi.org/10.5194/tc-12-1479-2018.

Veldhuijsen, S. B. M., W. J. Van De Berg, P. Kuipers Munneke, and M. R. Van Den Broeke, 2024: Firn air content changes on Antarctic ice shelves under three future warming scenarios. *Cryosphere*, **18**, 1983–1999, https://doi.org/10.5194/tc-18-1983-2024.

Wiese, D. N., D,-N. Yuan, C. Boening, F. W. Landerer, and M. M. Watkins, 2023a: JPL GRACE Mascon Ocean, ice, and hydrology equivalent water height RL06.1 CRI filtered version 03. Ver. RL06.1Mv03. PO.DAAC, accessed 10 February 2026, https://doi.org/10.5067/TEMSC-3JC63.

——, ——, ——, ——, and ——s, 2023b: Tellus level-4 ocean mass anomaly time series from JPL GRACE/GRACE-FO Mascon CRI filtered release 06.1 version 03. Ver. RL06.1Mv03, PO.DAAC, accessed 10 February 2026, https://doi.org/10.5067/TEMSC-AT613.

Wille, J. D., and Coauthors, 2021: Antarctic atmospheric river climatology and precipitation impacts. *J. Geophys. Res. Atmos.*, **126**, e2020JD033788, https://doi.org/10.1029/2020JD033788.

——, and Coauthors, 2025: Atmospheric rivers in Antarctica. *Nat. Rev. Earth Environ.*, **6**, 178–192, https://doi.org/10.1038/s43017-024-00638-7.

Wilson, E. A., L. Arlen, and E. C. Campbell, 2026: Recent extremes in Antarctic sea ice extent modulated by ocean heat ventilation. *Proc. Natl. Acad. Sci. U.S.A.*, **123**, e2530832123, https://doi.org/10.1073/pnas.2530832123.

WMO, 2022: Scientific Assessment of Ozone Depletion: 2022. GAW Rep. 278, 509 pp.

Wong, A. P. S., and Coauthors, 2020: Argo Data 1999–2019: Two Million Temperature-Salinity Profiles and Subsurface Velocity Observations From a Global Array of Profiling Floats. *Front. Mar. Sci.*, **7**, 700, https://doi.org/10.3389/fmars.2020.00700.

STATE OF THE CLIMATE IN 2025

REGIONAL CLIMATES

A. Arguez, P. Bissolli, C. Ganter, R. Martinez, Z. Segele, L. Stevens, and Z. Zhu, Eds.

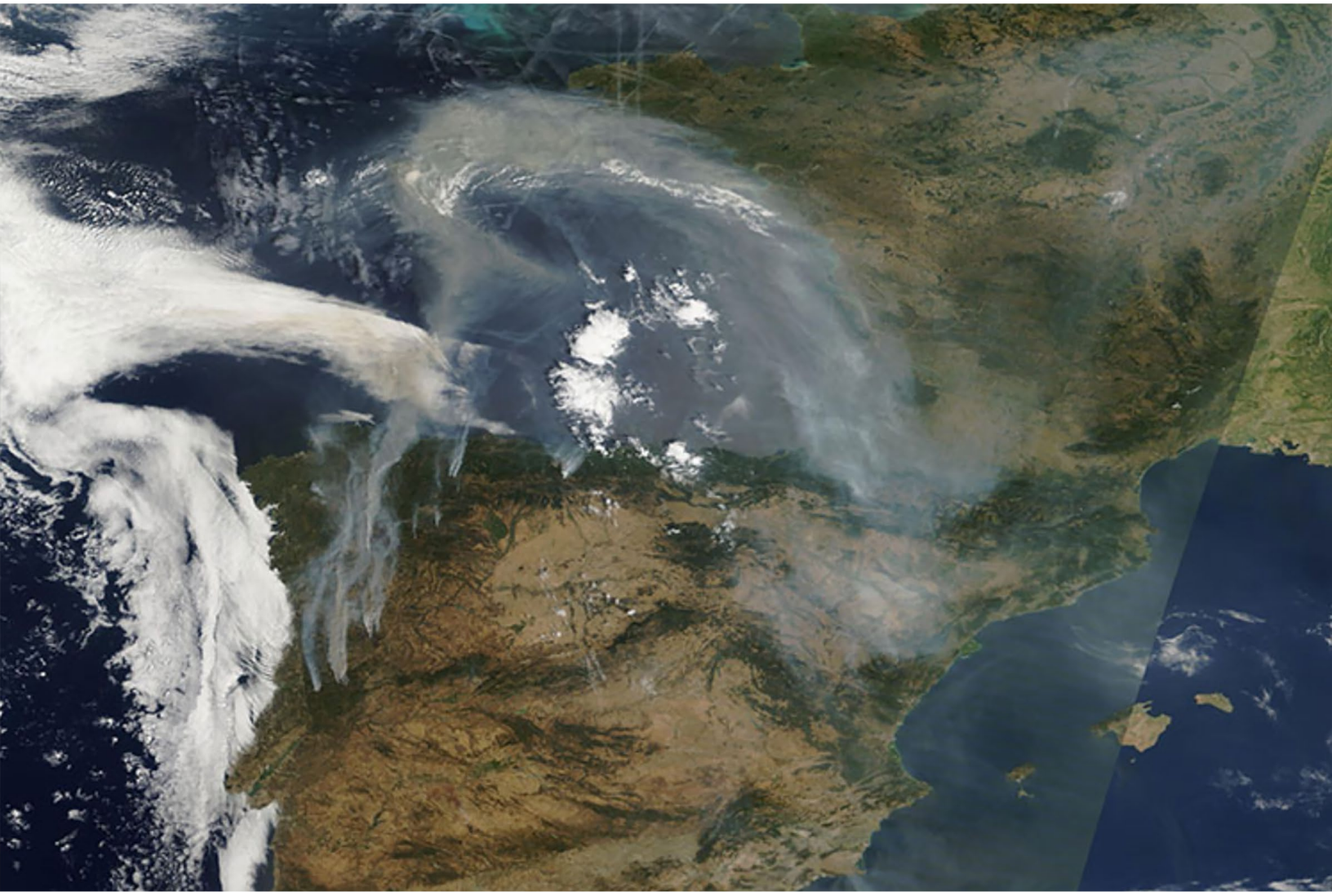

Special Online Supplement to the *Bulletin of the American Meteorological Society* Vol. 107, No. 8, August, 2026

https://doi.org/10.1175/2026BAMSStateoftheClimate_Chapter7.1

Corresponding author:
North America: Laura Stevens / laura_stevens@ncsu.edu
Central America and the Caribbean: Anthony Arguez / Anthony.Arguez@noaa.gov
South America: Rodney Martinez / rmartinez@wmo.int
Africa: Zewdu Segele / zewdu.segele@noaa.gov
Europe: Peter Bissolli / rcc.cm@dwd.de
Asia: Zhiwei Zhu / zwz@nuist.edu.cn
Oceania: Catherine Ganter / Catherine.Ganter@bom.gov.au

©2026 American Meteorological Society
For information regarding reuse of this content and general copyright information, consult the AMS Copyright Policy.

STATE OF THE CLIMATE IN 2025
Regional Climates

Editors

Jessica Blunden
James Reagan

Chapter Editors

Anthony Arguez
Josh Blannin
Peter Bissolli
Kyle R. Clem
Howard J. Diamond
Matthew L. Druckenmiller
Robert J. H. Dunn
Catherine Ganter
Nadine Gobron
Rodney Martinez
Twila A. Moon
Gary A. Morris
Marilyn N. Raphael
Renellys C. Perez
Carl J. Schreck III
Zewdu Segele
Laura Stevens
Richard L. Thoman
Denis L. Volkov
Zhiwei Zhu

Technical Editor

Lukas Noguchi
Laura Ohlmann

BAMS Special Editor for Climate

Timothy DelSole

American Meteorological Society

Cover Credit:
Dense smoke pouring northward from wildfires in Portugal and Spain on 15 August 2025. For most of its path, the smoke plume was so thick that it obscured the land from view. (Credit: Moderate Resolution Imaging Spectroradiometer [MODIS] on NASA's Terra satellite.)

How to cite this document:
Regional Climates is one chapter from the *State of the Climate in 2025* annual report and is available from https://doi.org/10.1175/2026BAMSStateoftheClimate_Chapter7.1. Compiled by NOAA's National Centers for Environmental Information, *State of the Climate in 2025* is based on contributions from scientists from around the world. It provides a detailed update on global climate indicators, notable weather events, and other data collected by environmental monitoring stations and instruments located on land, water, ice, and in space. The full report is available from https://doi.org/10.1175/2026BAMSStateoftheClimate.1.

Citing the complete report:
Blunden, J.and J. Reagan, Eds., 2026: "State of the Climate in 2025". Bull. Amer. Meteor. Soc., 107 (8), Si–S512, https://doi.org/10.1175/2026BAMSStateoftheClimate.1.

Citing this chapter:
Arguez, A., Bissolli, P., Ganter, C. , Martinez, R., Segele, Z., Stevens, L., and Zhu, Z. Eds. 2026: Regional Climates [in "State of the Climate in 2025"]. Bull. Amer. Meteor. Soc., 107 (8), S401–S509, https://doi.org/10.1175/2026BAMSStateoftheClimate_Chapter7.1.

Citing a section (example):
Minnie, C., 2026: Australia [in "State of the Climate in 2025"]. Bull. Amer. Meteor. Soc., 107 (8), S401–S509, https://doi.org/10.1175/2026BAMSStateoftheClimate_Chapter7.1.

Editor and Author Affiliations (alphabetical by name)

Agyakwah, W., ERT, Inc., College Park, Maryland; NOAA/NWS National Centers for Environmental Prediction Climate Prediction Center, College Park, Maryland

Aldeco, Laura S., Servicio Meteorológico Nacional, Buenos Aires, Argentina

Alemanno, Marco, Italian Air Force Meteorological Service, Pratica di Mare (Rome), Italy

Alfaro, Eric J., Center for Geophysical Research, University of Costa Rica, San José, Costa Rica; Center for Research in Marine Sciences and Limnology, University of Costa Rica, San José, Costa Rica

Allen, Teddy, Caribbean Institute for Meteorology and Hydrology, Bridgetown, Barbados

Alves, Lincoln. M., National Institute for Space Research (INPE), São José dos Campos, São Paulo, Brazil

Amador, Jorge A., Center for Geophysical Research, University of Costa Rica, San José, Costa Rica; School of Physics, University of Costa Rica, San José, Costa Rica

Arguez, Anthony, NOAA/NESDIS National Centers for Environmental Information, Asheville, North Carolina

Avalos, Grinia, Servicio Nacional de Meteorología e Hidrología del Perú, Lima, Peru

Ballinger, Andrew, NOAA/NESDIS National Centers for Environmental Information, Asheville, North Carolina

Bandgar, Arti, India Meteorological Department, Pune, India

Basckenstrass, Claire, Météo-France, Direction Interregionale Pour L'Ocean Indien, Réunion, France

Beauchemin, Marc, Environment and Climate Change Canada, Montreal, Canada

Bekele, E., NOAA/NWS National Centers for Environmental Prediction Climate Prediction Center, College Park, Maryland

Berne, Christine, Météo-France, Toulouse, France

Bezanilla-Morlot, Arnoldo, Institute of Meteorology, La Habana, Cuba

Bhuiyan, Md. E., Entarian, Greenbelt, Maryland; NOAA/NWS National Centers for Environmental Prediction, Climate Prediction Center, College Park, Maryland

Biernacik, Dawid, Institute of Meteorology and Water Management, National Research Institute, Warsaw, Poland

Bilotta, Rocky, NOAA/NESDIS National Centers for Environmental Information, Asheville, North Carolina

Bissolli, Peter, Deutscher Wetterdienst, WMO RA VI Regional Climate Centre Network, Offenbach, Germany

Bukunt, Brandon, NOAA/NWS Pacific Region Headquarters, Honolulu, Hawaii

Calderón, Blanca, Center for Geophysical Research, University of Costa Rica, San José, Costa Rica

Campbell, Jayaka, Department of Physics, The University of the West Indies, Kingston, Jamaica

Casella, Ana, Instituto Nacional de Meteorología e Hidrología de Venezuela (INAMEH), Caracas, Venezuela

Centella-Artola, Abel, La Habana, Cuba

Charlton, Candice S., Department of Physics, The University of the West Indies, Kingston, Jamaica

Chen, Hua, Nanjing University of Information Science and Technology, Nanjing, China

Cheng, Vincent Y. S., Environment and Climate Change Canada, Toronto, Ontario, Canada

Clarke, Leonardo, Department of Physics, The University of the West Indies, Kingston, Jamaica

Correa, Kris, Servicio Nacional de Meteorología e Hidrología del Perú, Lima, Peru

Costa, Felipe, Centro Internacional para la Investigación del Fenómeno de El Niño (CIIFEN), Guayaquil, Ecuador

Cunha, Ana P., Centro Nacional de Monitoramento e Alertas de Desastres Naturais CEMADEN, São José dos Campos, São Paulo, Brazil

De Bock, Veerle, Royal Meteorological Institute of Belgium, Brussels, Belgium

Dulamsuren, Dashkhuu, Information Research Institute of Meteorology, Hydrology and Environment, Ulaanbaatar, Mongolia

Ekici, Mithat, Turkish State Meteorological Service, Ankara, Türkiye

Ekwacu, S., Seychelles Meteorological Authority, Mahe, Seychelles

ElKharrim, M., General Directorate of Meteorology, Rabat, Morocco

Espinoza, Jhan-Carlo, Institut des Géosciences de l'Environnement (IGE), Institut de Recherche pour le Dévelopement (IRD), OSUG-B, Domaine Universitaire, Saint-Martin-d'Hères, France; Instituto de Investigación Sobre la Enseñanza de las Matemáticas, Pontificia Universidad Católica del Perú, Lima, Peru

Faye, A., University Corporation for Atmospheric Research Cooperative Programs for the Advancement of Earth System Science (CPAESS), College Park, Maryland

Fenimore, Chris, NOAA/NESDIS National Centers for Environmental Information, Asheville, North Carolina

Fleury, Michèle, Environment and Climate Change Canada, Montreal, Canada

Forde, Brendan, Environment and Climate Change Canada, Toronto, Ontario, Canada

Fuhrman, S., ERT, Inc., College Park, Maryland; NOAA/NWS National Centers for Environmental Prediction Climate Prediction Center, College Park, Maryland

Ganter, Catherine, Bureau of Meteorology, Melbourne, Australia

García Jiménez, Alejandro Jair, Servicio Meteorológico Nacional, Mexico City, Mexico

Gleason, Karin, NOAA/NESDIS National Centers for Environmental Information, Asheville, North Carolina

González, José, Instituto Nacional de Meteorología e Hidrología de Ecuador (INAMHI), Guayaquil, Ecuador

Gray, Jessie, Bureau of Meteorology, Melbourne, Australia

Hakmi, S., General Directorate of Meteorology, Rabat, Morocco

Hidalgo, Hugo G., Center for Geophysical Research, Center for Research in Pure and Applied Mathematics, University of Costa Rica, San José, Costa Rica; School of Physics, University of Costa Rica, San José, Costa Rica

Hänsch, Martje, Centro Internacional para la Investigación del Fenómeno de El Niño (CIIFEN), Guayaquil, Ecuador

Ivanov, Mirjana, Institute of Hydrometeorology and Seismology, Podgorica, Montenegro

Jadra, G., Instituto Uruguayo de Meteorología, Montevideo, Uruguay

Jha, B., ERT, Inc., College Park, Maryland; NOAA/NWS National Centers for Environmental Prediction Climate Prediction Center, College Park, Maryland

Kabidi, K., General Directorate of Meteorology, Rabat, Morocco

Kazemi, Amin Fazl, Iran National Climate and Drought Crisis Management Center, Iran National Meteorological Organization, Tehran, Iran

Kendon, Michael, Met Office Hadley Centre, Exeter, United Kingdom

Kennedy, John, Independent Researcher, Verdun, France

Khiem, Mai Van, National Center of Hydro-Meteorological Forecasting, Vietnam Meteorological and Hydrological Administration, Hanoi, Vietnam

Kim, Hyungjun, Department of AI and Futures Studies, Korea Advanced Institute of Science and Technology, Daejeon, South Korea

Korshunova, Natalia N., All-Russia Research Institute of Hydrometeorological Information, World Data Center, Obninsk, Russia

Kruger, A. C., Climate Service, South African Weather Service, Pretoria, South Africa

Kuramochi, Masaya, Tokyo Climate Center, Japan Meteorological Agency, Tokyo, Japan

Lam, Hoang Phuc, National Center of Hydro-Meteorological Forecasting, Vietnam Meteorological and Hydrological Administration, Hanoi, Vietnam

Liang, Ping, Shanghai Climate Center, Shanghai, China

Libonati, R., Federal University of Rio de Janeiro, Rio de Janeiro, Brazil

Liu, Xuefeng, Nanjing University of Information Science and Technology, Nanjing, China

Liu, Zibin, Nanjing University of Information Science and Technology, Nanjing, China

Lui, Yuk Sing, Hong Kong Observatory, Hong Kong, China

Macara, Gregor, Earth Sciences New Zealand, Lauder, New Zealand

Mamara, Anna, Climate Division, Hellenic National Meteorological Service, Elliniko, Greece

Mamen, Jostein, Climate Division, Norwegian Meteorological Institute, Oslo, Norway

Marcinonienė, Izolda, Lithuanian Hydrometeorological Service, Vilnius, Lithuania

Marengo, Jose A., Centro Nacional de Monitoramento e Alertas de Desastres Naturais CEMADEN, São José dos Campos, São Paulo, Brazil

Martinez, Rodney, World Meteorological Organization, San Jose, Costa Rica

McBride, C., Climate Service, South African Weather Service, Pretoria, South Africa

Minney, Caitlin, Bureau of Meteorology, Melbourne, Australia

Mohammadi, Marjan, Iran National Climate and Drought Crisis Management Center, Iran National Meteorological Organization, Tehran, Iran

Moise, Aurel, Centre for Climate Research Singapore, Meteorological Service Singapore, Singapore

Molina-Carpio, Jorge, Universidad Mayor de San Andrés, La Paz, Bolivia

Moody, Ronald, Meteorological Service, Jamaica

Moon, Suyeon, Climate Services and Research Division, Asia-Pacific Economic Cooperation Climate Center, Busan, South Korea

Mora, Natali, Center for Geophysical Research, University of Costa Rica, San José, Costa Rica

Morata Gasca, Ana, Agencia Estatal de Meteorología, Madrid, Spain

Mostafa, A. E., Department of Seasonal Forecast and Climate Research, Cairo Numerical Weather Prediction, Egyptian Meteorological Authority, Cairo, Egypt

Müller, Peter, GeoSphere Austria, Vienna, Austria

Nakayama, Naoki, Tokyo Climate Center, Japan Meteorological Agency, Tokyo, Japan

Nielson-Gammon, John, Texas A&M University, College Station, Texas

Nomenjanahary, T., Seychelles Meteorological Authority, Mahe, Seychelles

Orlik, Alexander, GeoSphere Austria, Vienna, Austria

Peltier, Alexandre, Météo France, Nouméa, New Caledonia

Piervitali, Emanuela, Italian Institute for Environmental Protection and Research (ISPRA), Rome, Italy

Porat, Amos, Israel Meteorological Service, Bet Dagan, Israel

Ratri, Dian Nur, BMKG, Jakarta, Indonesia

Rennie, Jared, NOAA/NESDIS National Centers for Environmental Information, Asheville, North Carolina

Reyes Kohler, A. J., Dirección Meteorológica de Chile, Santiago de Chile, Chile

Rivera, P. P., Servicio Nacional de Meteorología e Hidrología del Perú, Lima, Peru

Robjhon, M., ERT, Inc., College Park, Maryland; NOAA/NWS National Centers for Environmental Prediction Climate Prediction Center, College Park, Maryland

Rodríguez, Nathalie, Centro Internacional para la Investigación del Fenómeno de El Niño (CIIFEN), Guayaquil, Ecuador

Roebeling, Maarit, Deutscher Wetterdienst, WMO RA VI Regional Climate Centre Network, Offenbach, Germany

Ronchail, Josyane, Laboratoire LOCEAN-IPSL, Paris, France

Rubek, Frans, Danish Meteorological Institute, Copenhagen, Denmark

Runyen, Jason, NOAA National Weather Service Austin/San Antonio Office, New Braunfels, Texas

Sabeerali, C. T., India Meteorological Department, Pune, India

Salazar, Iliana, Centro Internacional para la Investigación del Fenómeno de El Niño (CIIFEN), Guayaquil, Ecuador

Samokhina, Olga. F., Yu. A. Izrael Institute of Global Climate and Ecology, Moscow, Russia

Segele, Z. T., NOAA/NWS National Centers for Environmental Prediction Climate Prediction Center, College Park, Maryland

Sensoy, Serhat, Turkish State Meteorological Service, Ankara, Türkiye

Seong, Ji-In, Climate Change Monitoring Division, Korea Meteorological Administration, Seoul, South Korea

Serna Cuenca, Julieta, Instituto de Hidrología, Meteorología y Estudios Ambientales de Colombia (IDEAM), Bogotá, Colombia

Sezaki, Fumi, Tokyo Climate Center, Japan Meteorological Agency, Tokyo, Japan

Shukla, R. P., Entarian, Greenbelt, Maryland; NOAA/NWS National Centers for Environmental Prediction Climate Prediction Center, College Park, Maryland

Sima, F., Retired, Banjul, The Gambia

Singh, B., NOAA/NWS National Centers for Environmental Prediction Climate Prediction Center, College Park, Maryland

Spence-Hemmings, Jacqueline, Meteorological Service, Jamaica

Spillane, Sandra, Met Éireann, Dublin, Ireland

Sreejith, O. P., India Meteorological Department, Pune, India

Srivastava, A. K., India Meteorological Department, Pune, India

Stella, Jose L., Servicio Meteorológico Nacional, Buenos Aires, Argentina

Stephenson, Tannecia S., Department of Physics, The University of the West Indies, Kingston, Jamaica

Stevens, Laura, North Carolina Institute for Climate Studies, North Carolina State University, Asheville, North Carolina

Takemura, Kazuto, Tokyo Climate Center, Japan Meteorological Agency, Tokyo, Japan

Taylor, Michael A., Department of Physics, The University of the West Indies, Kingston, Jamaica

Thiaw, W. M., NOAA/NWS National Centers for Environmental Prediction Climate Prediction Center, College Park, Maryland

Tran, Harrison, NOAA National Weather Service Austin/San Antonio Office, New Braunfels, Texas

Trotman, Adrian, Caribbean Institute for Meteorology and Hydrology, Bridgetown, Barbados

Turňa, Maroš, Slovak Hydrometeorological Institute, Bratislava, Slovakia

Umezu, Hironori, Tokyo Climate Center, Japan Meteorological Agency, Tokyo, Japan

Valdivieso, Cristina, Instituto Nacional de Meteorología e Hidrología de Ecuador (INAMHI), Quito, Ecuador

van der Linden, Roderick, Deutscher Wetterdienst, Offenbach, Germany

Van Meerbeeck, Cédric J., Caribbean Institute for Meteorology and Hydrology, Bridgetown, Barbados

Vazifeh, Ahad, Iran National Climate and Drought Crisis Management Center, Iran National Meteorological Organization, Tehran, Iran

Vázquez Romaña, Fabián, Servicio Meteorológico Nacional, Mexico City, Mexico

Willems, An, Royal Meteorological Institute of Belgium, Brussels, Belgium

Williams, Matthew, Department of Physics, The University of the West Indies, Kingston, Jamaica

Xu, L., Entarian, Greenbelt, Maryland; NOAA/NWS National Centers for Environmental Prediction, Climate Prediction Center, College Park, Maryland

Zhang, Peiqun, Beijing Climate Center, China Meteorological Administration, Beijing, China

Zhu, Zhiwei, Nanjing University of Information Science and Technology, Nanjing, China

Zubler, Elias, Federal Office of Meteorology and Climatology MeteoSwiss, Zurich, SwitzerlandZubler, Elias, Federal Office of Meteorology and Climatology MeteoSwiss, Zurich,

Editorial and Production Team

Allen, Jessicca, Graphics Support, Cooperative Institute for Satellite Earth System Studies, North Carolina State University, Asheville, North Carolina

Camper, Amy V., Graphics Support, Innovative Consulting and Management Services, LLC, NOAA/NESDIS National Centers for Environmental Information, Asheville, North Carolina

Carroll, Lauren, Content Team Lead, Communications and Outreach, NOAA/NESDIS National Centers for Environmental Information, Asheville, North Carolina

Crossman, Jacquelyn, NCEI Librarian, MPF-ZAI, NOAA/NESDIS National Centers for Environmental Information, Asheville, North Carolina

Haley, Bridgette O., Graphics Support, NOAA/NESDIS National Centers for Environmental Information, Asheville, North Carolina

Noguchi, Lukas, Technical Editor, Innovative Consulting and Management Services, LLC, NOAA/NESDIS National Centers for Environmental Information, Asheville, North Carolina

Ohlmann, Laura, Technical Editor, Innovative Consulting and Management Services, LLC, NOAA/NESDIS National Centers for Environmental Information, Asheville, North Carolina

Veasey, Sara W., Visual Communications Team Lead, Communications and Outreach, NOAA/NESDIS National Centers for Environmental Information, Asheville, North Carolina

7. Table of Contents

List of authors and affiliations S404
a. Overview S409
b. North America S410
1. Canada S410
2. United States S412
3. Mexico S415
Sidebar 7.1: Central Texas flooding in July 2025 ..... S418
c. Central America and the Caribbean S420
1. Central America S420
2. Caribbean S423
Sidebar 7.2: Impacts of Hurricane Melissa on the Caribbean S425
d. South America S427
1. Northern South America S427
2. Central South America S429
3. Southern South America S431
Sidebar 7.3: The late December 2025 heatwave in southeastern Brazil S434
e. Africa S436
1. Overview S436
2. Northern Africa S436
3. West Africa S439
4. Central Africa S441
5. Eastern Africa S444
6. Southern Africa S446
7. Western Indian Ocean Island countries S449
f. Europe and the Middle East S452
1. Overview S452
2. Western Europe S456
3. Central Europe S458
4. Iberian Peninsula S459
5. The Nordic and Baltic countries S461
6. Central Mediterranean region S462
7. Eastern Europe S464
8. Middle East S466
9. Türkiye and South Caucasus S467
Sidebar 7.4: Long, intense, and widespread heatwaves in Europe S470

7. Table of Contents

g. Asia S475
1. Overview S475
2. Russia S478
3. East and Southeast Asia S481
4. South Asia S483
5. Southwest Asia S487
6. Central Asia S489
Sidebar 7.5: Unprecedented 2025 autumn rainfall over East Asia S493
h. Oceania S495
1. Overview S495
2. Northwest Pacific and Micronesia S495
3. Southwest Pacific S499
4. Australia S502
5. Aotearoa New Zealand S504
Acknowledgments S507
Appendix 1: Acronyms S508
References S510

7. REGIONAL CLIMATES

A. Arguez, P. Bissolli, C. Ganter, R. Martinez, Z. Segele, A. Stevens, and Z. Zhu, Eds

a. Overview

This chapter provides summaries of the 2025 temperature and precipitation conditions across seven broad regions: North America, Central America and the Caribbean, South America, Africa, Europe and the Middle East, Asia, and Oceania. Summaries of notable weather events are also included at the discretion of the authors. Local scientists provided the annual summary for their respective regions and, unless otherwise noted, the source of the data used is typically the agency affiliated with the authors. The base period used for these analyses is 1991–2020, unless otherwise stated. Please note that on occasion different nations—even within the same section—may use unique periods to define their normal. Section introductions typically define the prevailing practices for that section, and exceptions will be noted within the text. In a similar way, many contributing authors use languages other than English as their primary professional language. To minimize additional loss of fidelity through re-interpretation after translation, editors have been conservative and careful to preserve the voice of the author. In some cases, this may result in abrupt transitions in style from section to section.

b. North America

—L. Stevens, Ed.

Above-average temperatures were recorded across the majority of Canada, the United States, and Mexico in 2025. As a whole, the temperature for North America was 1.06°C above the 1991–2020 base period, making 2025 the third-warmest year in the 176-year continental record that extends back to 1850. The latter part of the year was particularly warm, with September–November 2025 ranking as the warmest autumn on record.

Precipitation varied across North America in 2025, but overall, annual precipitation amounts were slightly drier than the 1991–2020 average for Canada and the United States, and slightly wetter than average for Mexico. Periods of extreme dryness contributed to severe wildfires in Canada and the United States.

Other notable extreme events included a major ice storm in Canada, another active U.S. tornado season, and extreme rainfall and flooding events in both the United States and Mexico. For the first time in 10 years, there were no landfalling hurricanes in the United States; however, three Category 5 storms occurred in the Atlantic, and Hurricane Erick (Category 3) struck Mexico's Pacific coast.

Information in this section relates to the geographic continent of North America. Annual temperature and precipitation data are also included for Hawaii. Tropical cyclone events affecting all regions are described further in Chapter 4. Additional information for Alaska is included in Chapter 5. Insular regions of the United States, and the sections in this report in which they are described, are as follows: Puerto Rico (section 7c1) and Guam and the U.S.-Affiliated Pacific Islands (section 7h2). Anomalies in this section are all with respect to the 1991–2020 base period, unless otherwise noted.

1. CANADA

—B. Forde, M. Fleury, V. Y. S. Cheng, and M. Beauchemin

(i) Temperature

Stations recording observations of temperature are not uniformly distributed across the country, with fewer stations in the north than in the south. To conduct a better spatial assessment of climate variations, the temperature records presented in this section are based on the Canadian Gridded Temperature Anomalies (CANGRD), which were interpolated from stations in the Adjusted and Homogenized Canadian Climate Data (AHCCD). Canada's annual average temperature for 2025 was 0.9°C above the 1991–2020 average, ranking as the ninth-warmest year since nationwide records began in 1948 (Fig. 7.1). Annual anomalies of +1.0°C were recorded in large parts of western Canada and the northern regions of eastern Canada (Fig. 7.2a), while parts of northern Nunavut reported even higher temperature departures at 2.0°C above average. Based on a linear regression of data from 1948 to 2025, the national annual average temperature has been increasing at a rate of 0.28°C decade^{-1} (±0.08°C decade^{-1} at a 95% confidence interval).

The winter (December 2024–February 2025) national temperature was the fifth warmest on record at 2.2°C above the 1991–2020 average. Anomalous warmth of +4°C extended from northern Quebec and Newfoundland to parts of northern Canada (Fig. 7.2b). Temperatures 1°C below average were observed in the southern Prairies and small regions of southern Ontario and Nova Scotia.

The spring (March–May 2025) national temperature was 0.6°C above average, ranking 17th warmest. Notable temperature anomalies of +1.5°C were recorded in the Canadian High Arctic (Fig. 7.2c), while temperatures

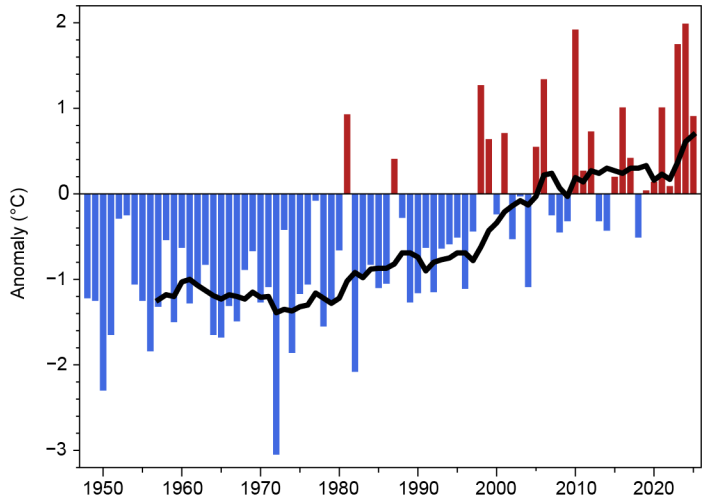

Fig. 7.1. Annual average temperature anomalies (°C; 1991–2020 base period) for Canada for the period 1948–2025. The black lines represent a lagged 10-yr running mean. (Source: Environment and Climate Change Canada.)

1°C above average were observed in most of the western provinces extending to Yukon, and in the Atlantic provinces.

The summer (June–August 2025) national temperature was the 11th warmest on record at 0.4°C above average. Temperature anomalies of +1°C were observed in British Columbia, Yukon, and most of the Atlantic provinces extending into southern Ontario (Fig. 7.2d). Some regions in the Canadian High Arctic recorded temperatures 1°C below average.

The autumn (September–November 2025) national temperature was 3.0°C above average, ranking as the warmest autumn on record. Almost all of Canada experienced above-average temperatures, with anomalous warmth of +2.5°C observed in central Canada and +5°C in central Nunavut (Fig. 7.2e). Four provinces (British Columbia, Alberta, Saskatchewan, and Manitoba) and the Northwest Territories recorded their warmest autumn on record.

(ii) Precipitation

The 10-km version of the Canadian Precipitation Analysis (CaPA) was used for this section. The CaPA is a gridded analysis that blends numerical weather prediction data, gauge observations, weather radar estimates, and satellite-based estimates.

In 2025, total precipitation across Canada was slightly less than the 1991–2020 average. Precipitation totals across the nation were generally 75%–100% of normal (Fig. 7.3a), with some areas in the Northwest Territories and northern Manitoba recording substantially drier conditions (40%–70% of normal). Small regions across British Columbia experienced wetter conditions up to 120% of normal.

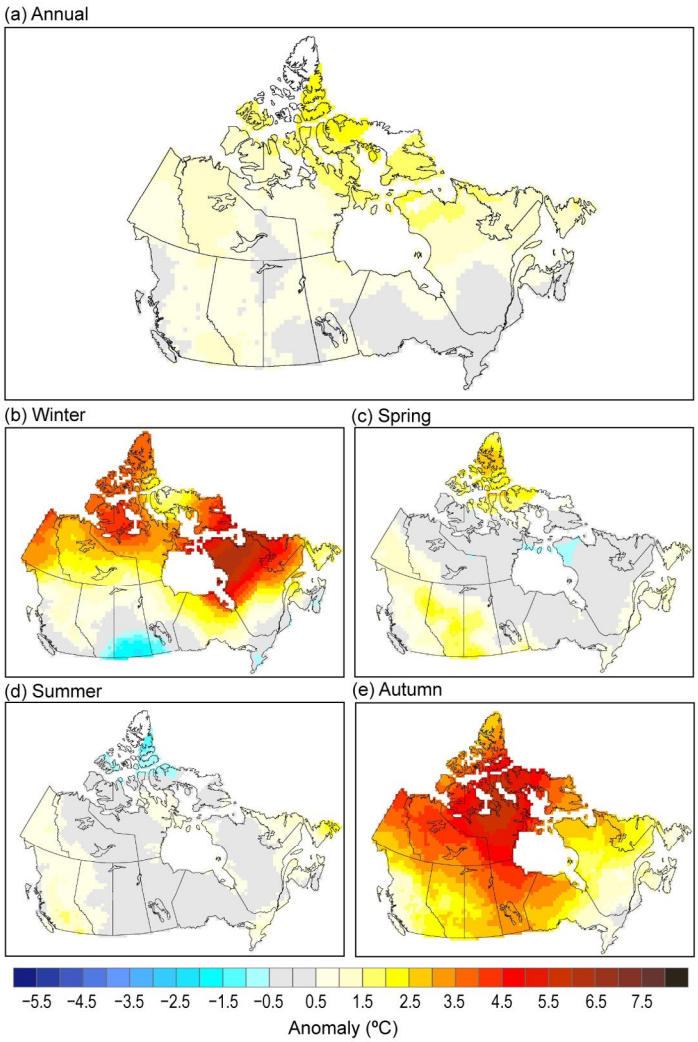

Fig. 7.2. (a) Annual 2025, (b) winter 2024/25, (c) spring 2025, (d) summer 2025, and (e) autumn 2025 average temperature anomalies (°C; 1991–2020 base period) across Canada. (Source: Environment and Climate Change Canada.)

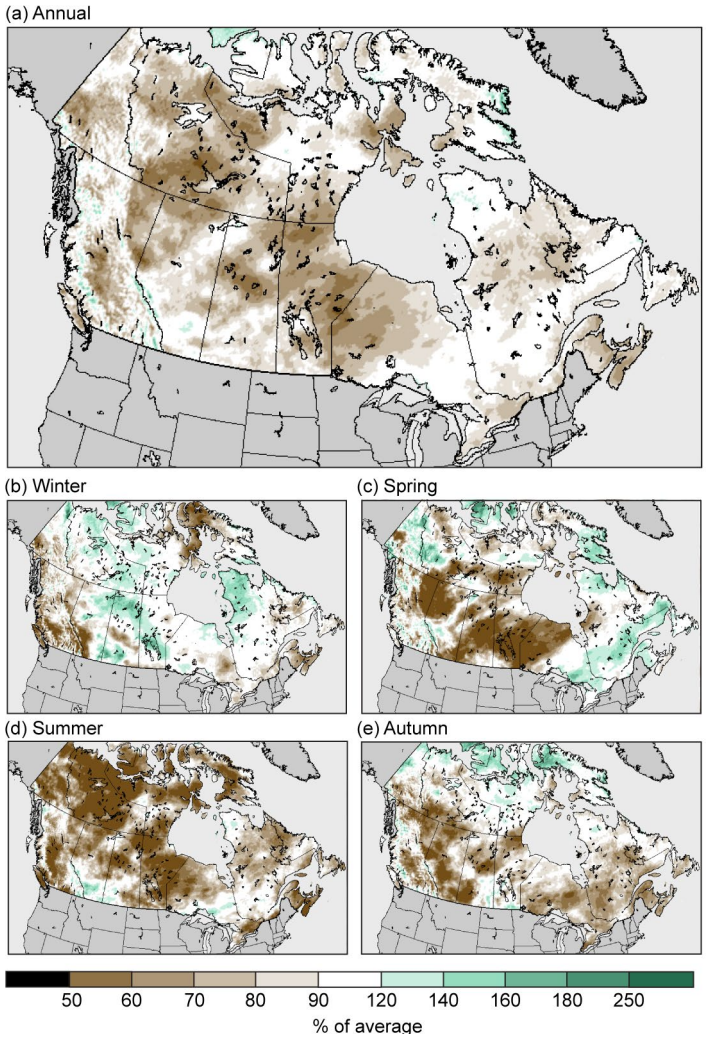

Fig. 7.3. (a) Annual 2025, (b) winter 2024/25, (c) spring 2025, (d) summer 2025, and (e) autumn 2025 total precipitation (% of average; 1991–2020 base period) across Canada. (Source: Environment and Climate Change Canada.)

Winter precipitation amounts were close to average (90%–100% of normal) for a large portion of Canada (Fig. 7.3b). In the spring, below-average precipitation occurred in much of central Canada, ranging from 40% to 70% of normal (Fig. 7.3c). The majority of Canada was drier than normal in the summer and received precipitation amounts of 40%–70% of normal (Fig. 7.3d). The dry conditions continued into autumn, with much of the country receiving only 40%–80% of normal precipitation (Fig. 7.3e).

(iii) Notable events and impacts

In 2025, a series of extreme weather events across Canada led to significant societal and economic impacts, with total insured losses reaching $2.4 billion Canadian dollars (CAD; CatIQ 2026). The year was marked by an exceptional combination of severe wildfires, widespread drought, and damaging storms.

A major ice storm from 28 to 31 March paralyzed large areas of Ontario and southwestern Quebec, becoming the second costliest on record with $490 million CAD in insured property and vehicle losses (CatIQ 2025). Some areas endured freezing rain for up to 35 hours, leading to ice accumulation of up to 25 mm and contributing to nearly 100 vehicle collisions in eastern Ontario, with multiple injuries and one fatality. The considerable weight of the ice snapped tree branches and power lines, triggering widespread, prolonged power outages (ECCC 2025).

From May through September, record-breaking heatwaves and nationwide drought conditions set the stage for Canada's second-worst wildfire season on record. Approximately 8.9 million hectares burned over five months, with Saskatchewan and Manitoba accounting for more than half of the national total (NRCan 2025). Smoke plumes spreading thousands of kilometers caused prolonged poor air quality for millions across Canada. The wildfires resulted in two fatalities and forced the evacuation of 85,000 people. According to the Insurance Bureau of Canada, national insured losses from the main fires were estimated at $370 million CAD.

At the same time, a severe precipitation deficit and reduced winter snowpack left 84% of the country under moderate to extreme drought, according to the Canadian Drought Monitor. Water systems and ecosystems were severely stressed, with reservoirs, lakes, streams, and aquifers reaching near-record lows, disrupting municipal and business water supplies. Key crops experienced notably reduced yields, especially in western and Atlantic provinces, while low water levels reduced hydroelectric power generation capacity in British Columbia.

Destructive thunderstorms further contributed to losses. A severe thunderstorm complex during 21–22 June caused powerful downbursts and subsequent flash flooding in eastern Ontario, devastating provincial parks and campgrounds and resulting in multiple injuries and one fatality. Estimated wind gusts ranged between 115 km hr^{-1} and 190 km hr^{-1}. Another episode of extremely severe thunderstorms across the Prairies during 20–21 August produced baseball-size hail, downbursts, tornadoes, and torrential rain, causing extensive damage to homes, farms, vehicles, crops, and livestock (ECCC 2025). Insured losses totaled $235 million CAD in Alberta alone, as reported by the Insurance Bureau of Canada.

2. UNITED STATES

—K. Gleason, A. Ballinger, R. Bilotta, and C. Fenimore

(i) Temperature

The annual average temperature for the contiguous United States (CONUS) in 2025 (using nClimGrid-monthly) was 0.8°C above the 1991–2020 average, which was the fourth-warmest year in the 131-year record (Fig. 7.4a). Above-average temperatures were concentrated from the Mississippi River to the West Coast (Fig. 7.5a). Based on a linear regression of data from 1895 to 2025, the annual average CONUS temperature has increased at a rate of 0.10±0.03°C $decade^{-1}$ (all uncertainties in this section represent the 95% confidence interval), and 0.29±0.07°C $decade^{-1}$ since 1970. The annual average temperature across Alaska in 2025 was 0.9°C above average and was the ninth warmest year on record. The annual temperature for Alaska over its 101-year record (1925–2025) has increased at an average rate of 0.18±0.07°C $decade^{-1}$ since 1925 (0.43±0.16°C $decade^{-1}$ since 1970). Hawaii's annual average temperature was 0.39°C above average. Over the 1991–2025 period, the state's annual temperature has risen at an average rate of 0.24±0.09°C $decade^{-1}$. All temperature trends listed above are statistically significant ($p<0.05$).

The winter (December 2024–February 2025) CONUS temperature was equal to its 1991–2020 mean value. Above-average temperatures were observed across much of the Southwest, while below-average conditions dominated the northern and central Plains, and from the Midwest to the East Coast (Fig. 7.5b). The CONUS spring (March–May) temperature tied with 1910 as the second warmest on record at 1.1°C above average with broad areas of above-average temperatures across most of the CONUS (Fig. 7.5c). The summer (June–August) CONUS temperature was 0.6°C above average, with much of the West and from the Mississippi River Valley to the Northeast experiencing above-average temperatures (Fig. 7.5d). It was the third-warmest autumn (September–November) on record for the CONUS at 1.5°C above average. Above-average temperatures were observed from the Great Lakes to the central Gulf Coast, and westward (Fig. 7.5e). Autumn was the warmest on record across Idaho, Nevada, New Mexico, Oregon, Texas, Utah, and Washington—consistent with temperatures observed in the adjacent Canadian provinces (section 7b1).

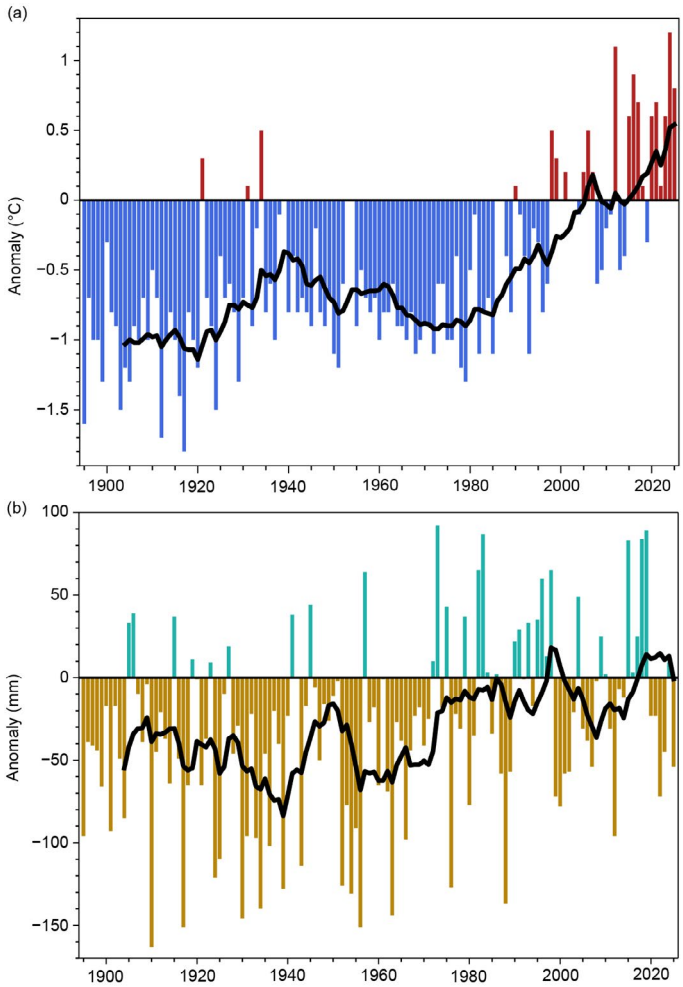

Fig. 7.4. Annual (a) average temperature anomalies (°C) and (b) precipitation anomalies (mm; 1991–2020 base period) for the contiguous United States during the period 1895–2025. The black lines represent a lagged 10-yr running mean. (Source: NOAA/NCEI.)

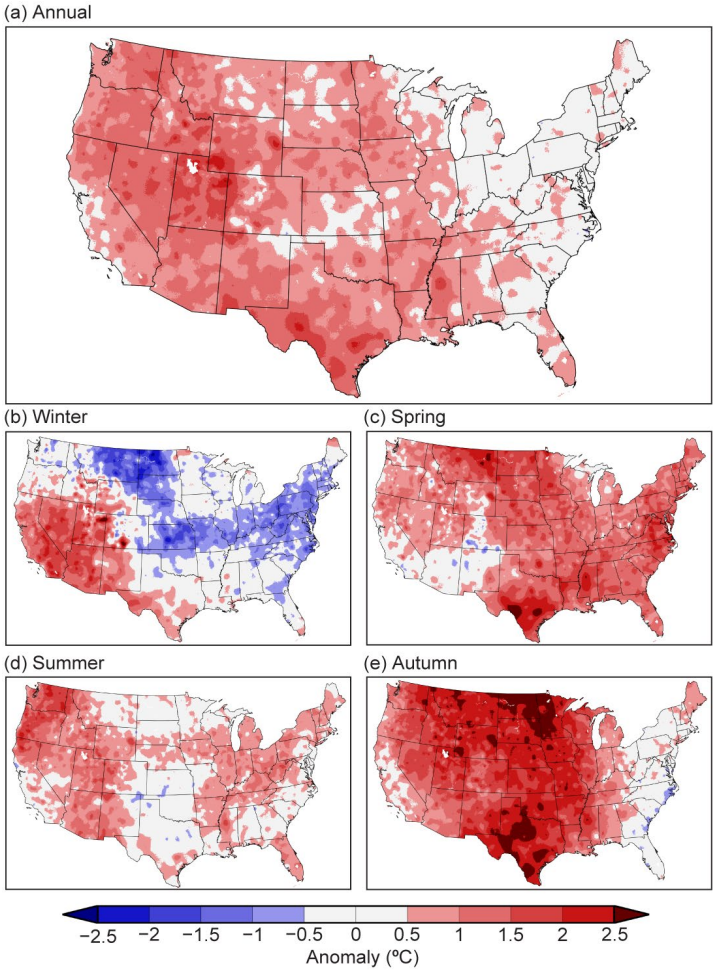

Fig. 7.5. (a) Annual 2025, (b) winter 2024/25, (c) spring 2025, (d) summer 2025, and (e) autumn 2025 average temperature anomalies (°C; 1991–2020 base period) across the contiguous United States. (Source: NOAA/NCEI.)

(ii) Precipitation

In 2025, average precipitation for the nation was 93% of the 1991–2020 average (Fig. 7.4b; using nClimGrid-monthly)—with notable dryness across parts of the Southwest, Midwest, Gulf Coast, and Northeast (Fig. 7.6a). Despite the drier-than-average year, 2025 precipitation sits within a broader statistically significant historical increase, averaging +4±2 mm decade^{-1} since 1895 (the 1970–2025 trend is not statistically significant). Total annual precipitation across Alaska was 105% of normal and has increased at an average rate of +20±11 mm decade^{-1} since 1970 (the 1925–2025 trend is not statistically significant). Hawaii's annual precipitation was its

third driest on record, at 68% of normal, contributing to a long-term decreasing trend of –21 mm decade^{-1} since 1991 (not statistically significant).

Winter precipitation across the CONUS was 84% of average with large precipitation deficits observed from the Southwest to the northern Plains and Great Lakes (Fig. 7.6b). Wet conditions were concentrated across parts of the Northwest and along a swath from eastern Texas to Virginia. Spring precipitation was 108% of average, driven by wetter conditions from the southern Plains to the East Coast (Fig. 7.6c). Summer precipitation averaged 101% of normal, with wetness in the Plains offsetting deficits across New England, including record-dry conditions in New Hampshire and significant dryness along the West Coast (Fig. 7.6d). The autumn CONUS precipitation total was 82% of average, with below-average precipitation observed from the southern Plains and Upper Midwest to the East Coast (Fig. 7.6e), though it was much wetter than average (250% of average) across parts of California, Nevada, and Arizona.

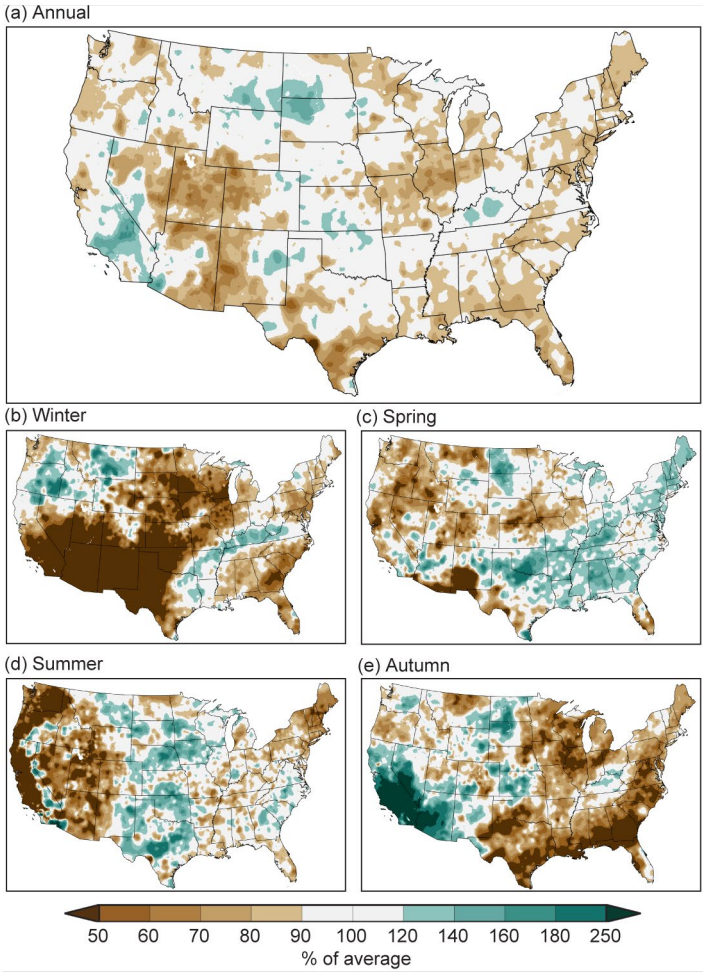

Fig. 7.6. (a) Annual 2025, (b) winter 2024/25, (c) spring 2025, (d) summer 2025, and (e) autumn 2025 total precipitation (% of average; 1991–2020 base period) across the contiguous United States. (Source: NOAA/NCEI.)

While these regional wet and dry spells varied by season, their cumulative impact was most visible in the fluctuating geographic reach of the CONUS drought footprint in 2025, which followed a pattern of spring expansion, summer contraction, and autumn resurgence. Starting at 38% coverage in January, drought expanded to a spring peak of 45% by late March. Widespread rain then triggered a decline to an annual minimum of 30% on 3 June. This recovery was brief, as conditions intensified through autumn, reaching the annual maximum of 46% in late October and mid-November. By year's end, coverage eased slightly to 43%—leaving a larger portion of the country in drought than when the year began, according to the National Drought Mitigation Center.

(iii) Notable events and impacts

According to the National Interagency Fire Center, over 77,000 wildfires occurred across the CONUS in 2025—114% of the 20-year (2001–20) average. The approximately 2 million hectares burned represented 72% of the nearly 2.8-million-hectare average. Southern California saw the most destructive activity in January; fueled by 60 km hr^{-1} Santa Ana winds and dry conditions, the Eaton Fire (5600 hectares) and the Palisades Fire (9300+ hectares) devastated the region. These fires became Los Angeles's two most destructive fires on record. Together, they destroyed over 16,000 structures and resulted in 31 fatalities (CAL FIRE 2025). Arizona's Dragon Bravo Fire was the nation's largest of the year, burning over 59,000 hectares between July and September to become the state's seventh largest on record. Conversely, Alaska's season was below average, with 405,000 hectares burned—roughly two-thirds of its 20-year average, according to the National Interagency Fire Center.

The U.S. tornado count for 2025 was 1383, the ninth-highest total on record and 113% of the 30-year (1991–2020) average (NOAA 2026). The year was marked by several notable extremes, including 300 preliminary tornado reports in March—a new March record and more than three times the average. On 20 June, the first confirmed EF-5 tornado in the U.S. since 2013 struck

Enderlin, North Dakota, resulting in three fatalities (SPC 2026a; NWS 2025). At the state level, North Dakota shattered its previous annual tornado record of 61—set in 2010—with 72 tornado reports in 2025. There were at least 67 fatalities associated with tornadoes across the United States during 2025, which was near average (SPC 2026b).

Widespread and significant flooding occurred across the CONUS during 2025, driven by a combination of atmospheric rivers, slow-moving convective systems, and tropical moisture. Significant flood events were observed in every season and region. Several historic precipitation events overwhelmed infrastructure, producing 1-in-1000-year rainfall recurrence intervals in parts of Kentucky, Tennessee, North Carolina, and Texas. These events resulted in significant loss of life. Catastrophic flooding in the Texas Hill Country in July resulted in at least 135 fatalities, while recurring storms in the Ohio Valley and severe weather across the South contributed to dozens of additional fatalities throughout the year (see Sidebar 7.1 for details on the Texas Hill Country flooding; TPR 2025).

Despite a notable season with three Category 5 Atlantic hurricanes, 2025 was the first year since 2015 without a U.S. landfall (see section 4g2 for details). However, tropical remnants caused late-season flooding, specifically Super Typhoon Halong in Alaska (see Sidebar 5.1 for details) and Hurricane Priscilla in the Southwest.

3. MEXICO

—A. J. Garcia Jimenez and F. Vázquez Romaña

(i) Temperature

Mexico's annual average temperature in 2025 was 1.2°C above the 1991–2020 average (Fig. 7.7a), marking the third-warmest year since national records began in 1953, following 2024 (+1.4°C) and 2023 (+1.3°C). Based on a linear regression of data from 1953 to 2025 (utilizing 9-km gridded interpolated station data from the Servicio Meteorológico Nacional), annual average temperatures continue to exhibit a warming trend of +0.17°C decade^{-1} ($p<0.001$), with 2025 marking the 16th consecutive year of above-average national temperatures. Above-average temperatures were notable across the north, northeast, and the Yucatán Peninsula, while isolated regions of below-average temperatures were observed in the northwest (Fig. 7.8a).

2025 was characterized by persistent warmth throughout the year, with all four seasons ranking among their five warmest on record. The winter (December 2024–February 2025) national average temperature was 0.6°C above average and the fifth warmest on record, with above-average temperatures concentrated in northern and central Mexico (Fig. 7.8b). The spring (March–May) national temperature tied for third warmest at 0.9°C above average, with anomalous warmth seen across eastern Mexico and cooler conditions in the northwest (Fig. 7.8c). The summer (June–August) national temperature was 1.6°C above average and the fifth warmest on record. Above-average temperatures were seen

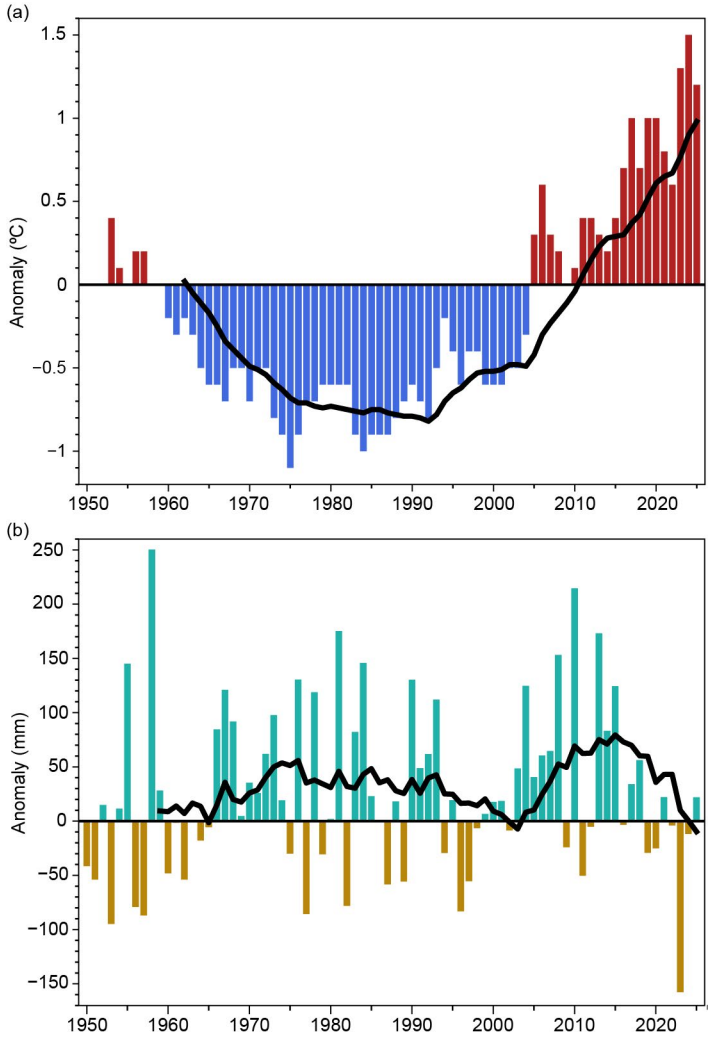

Fig. 7.7. Annual (a) average temperature anomalies (°C) and (b) precipitation anomalies (mm; 1991–2020 base period) for Mexico. Temperature records began in 1953 and precipitation records began in 1951. The black lines represent a 10-yr lagged running mean. (Source: Servicio Meteorológico Nacional.)

across most of the country, most notably in northern Mexico (Fig. 7.8d). The autumn (September–November) national temperature was 1.5°C above average and tied with 2024 as the second-warmest autumn on record. Areas of anomalous warmth were concentrated over northern Baja California, Chihuahua, Coahuila, Nuevo León, Durango, Michoacán, and Guerrero (Fig. 7.8e).

(ii) Precipitation

The national average precipitation total for 2025 was 102.9% of the 1991–2020 average (Fig. 7.9a; based on 9-km gridded interpolated station data). This near-normal precipitation accumulation ranks 2025 in the middle of the 85-year historical record. The spatial and temporal distribution of precipitation varied significantly. However, a dry start to the year was followed by extreme precipitation events in the second half. Above-average annual precipitation was observed across central and eastern regions, as well as Baja California Sur. The highest positive anomalies were concentrated over eastern Mexico, specifically the Huasteca region (including parts of San Luis Potosí, Veracruz, Hidalgo, Tamaulipas, Querétaro, and Puebla), heavily influenced by an extreme rainfall event in October. In contrast, below-average conditions were observed in northern Mexico (Fig. 7.9a).

A significant precipitation deficit was recorded during the first half of the year. National winter precipitation was only 68.5% of normal and was characterized by widespread dryness across most of the country except for parts of eastern Mexico and the Yucatán Peninsula (Fig. 7.9b). Spring precipitation was 79.1% of normal, with extreme dryness persisting in the northwest (Fig. 7.9c). The pattern shifted with the onset of the rainy season (typically commencing in June). A national

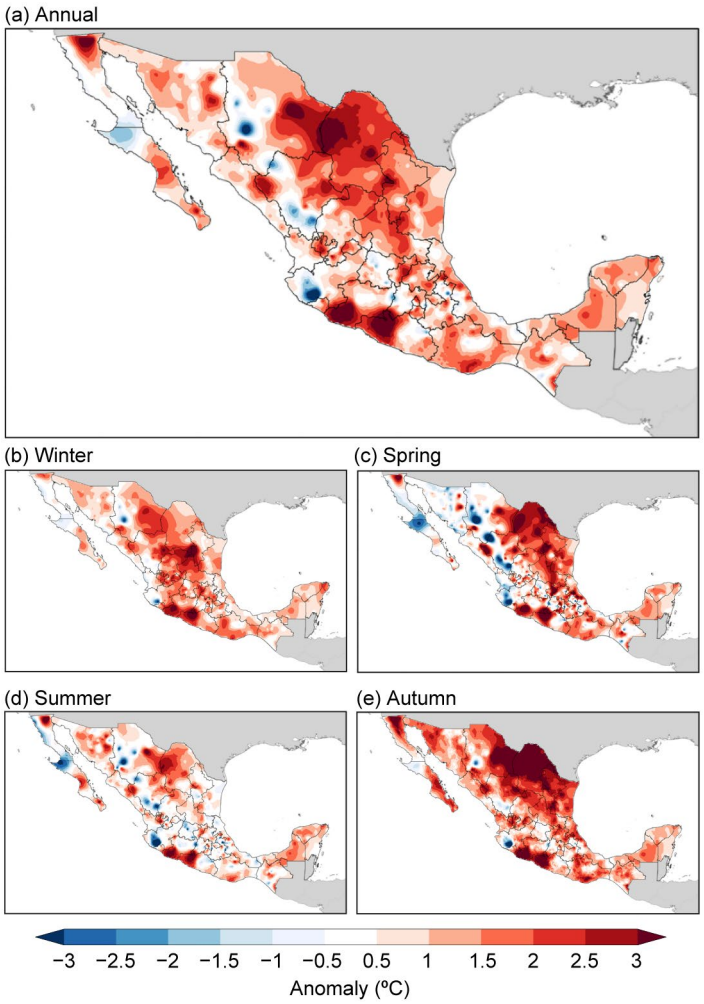

Fig. 7.8. (a) Annual 2025, (b) winter 2024/25, (c) spring 2025, (d) summer 2025, and (e) autumn 2025 average temperature anomalies (°C; 1991–2020 base period) across Mexico. (Source: Servicio Meteorológico Nacional.)

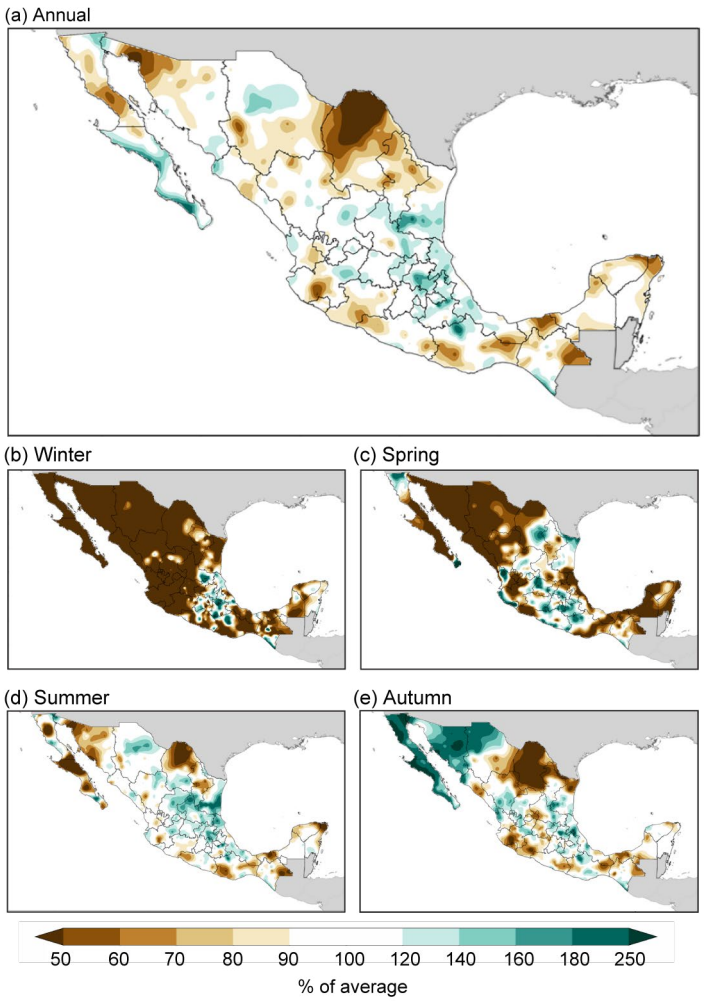

Fig. 7.9. (a) Annual 2025, (b) winter 2024/25, (c) spring 2025, (d) summer 2025, and (e) autumn 2025 average precipitation anomalies (% of average; 1991–2020 base period) across Mexico. (Source: Servicio Meteorológico Nacional.)

precipitation surplus was registered for summer with an average total that was 109.4% of normal, driven largely by the North American Monsoon (NAM). According to a new objective methodology implemented by the Servicio Meteorológico Nacional—utilizing daily radiosonde profiles and continuous wavelet transform analysis to isolate the low-frequency monsoonal signal—the 2025 NAM season lasted 99 days. The monsoon onset occurred on 18 June, bringing important above-average rainfall to the northwestern states (Fig. 7.9d). The NAM officially withdrew on 25 September, effectively separating the core monsoon precipitation from late-season transient events. Autumn precipitation was 103.7% of normal, with wet conditions across the central, eastern, and northwestern states, driven largely by several weather systems bringing extreme rainfall in October (Fig. 7.9e).

(iii) Notable events and impacts

An extreme rainfall event occurred in October 2025 in the Huasteca region of eastern Mexico, resulting from a complex interaction of meteorological systems initiated by a trough in the Gulf of Mexico. Although this system had a 10% probability of cyclonic development, it generated an abundant influx of moisture to the region. This moisture influx, combined with the region's orography and the influence of a cyclonic circulation in the Pacific, triggered the formation of high-intensity storms between 7 and 11 October. The Tlanchinol station in Hidalgo set a new daily historical record with 323.1 mm precipitation in 24 hours on 8 October, and a total event accumulation of 731.5 mm. Other record-breaking daily totals included 290.0 mm at the Macedonio Alonso (Veracruz) station and 281.7 mm at the Ávila Camacho (Puebla) station. These rains caused catastrophic flooding and landslides across five states, resulting in 83 fatalities and 17 people reported missing. Preliminary assessments by Mexico's National Center for Disaster Prevention (CENAPRED) estimate regional economic losses totaling 50 billion Mexican pesos (approximately $2.5 billion U.S. dollars), with major damage to housing, road infrastructure, and agriculture.

On 19 June, Hurricane Erick made landfall near Santiago Pinotepa Nacional, Oaxaca, as a Category 3 storm with sustained winds of 205 km hr^{-1}. Erick was the first Category 3 hurricane to impact Mexico's Pacific coast in the month of June since 1950. The storm produced extreme rainfall, notably 359.0 mm at the Presidente Benito Juárez station in Oaxaca. Impacts from Hurricane Erick resulted in two fatalities, according to the state civil protection authorities of Oaxaca and Guerrero, as well as significant damage to regional infrastructure (see section 4g3 for more details).

Sidebar 7.1: **Central Texas flooding in July 2025**

—J. RENNIE, J. RUNYEN, H. TRAN, AND J. NIELSON-GAMMON

In July 2025, catastrophic flooding affected large portions of Central Texas following intense precipitation associated with organized thunderstorm activity, amplified by anomalously high moisture originating from the tropics. The resulting flooding led to more than 135 fatalities and prompted a disaster declaration by the Texas governor. Impacts extended from the Texas Hill Country through the Greater Austin metropolitan area, with the most severely affected counties including Kerr, Kendall, Llano, Mason, Travis, Williamson, Burnet, and Tom Green. Emergency response operations were extensive. According to the NOAA Storm Events Database, on the morning of 4 July alone more than 200 individuals were rescued using helicopters and watercraft. Infrastructure damage was widespread, with numerous roads and bridges washed out, resulting in losses estimated by Climate Central to be in the hundreds of millions of U.S. dollars. The most severe impacts occurred along the Guadalupe River in Kerr County. The Texas Tribune reported 119 fatalities, including 27 individuals at a summer camp and other residents and vacationers in the area.

According to the National Hurricane Center, prior to the event, the remnants of Tropical Storm Barry moved slowly into Texas from northern Mexico, providing a moist convective environment favoring high precipitation efficiency. Low-level moisture from the Atlantic and tropical moisture drawn northward by Hurricane Flossie over the Pacific contributed to the abnormally high moisture profile. The rate at which moisture was being moved northward into Central Texas (quantified as integrated vapor transport) exceeded the 99th percentile of historically observed rates for this time of year. On 2 and 3 July, the National Weather Service noted precipitable water values in Central Texas were at or exceeding 64 mm, also corresponding to the 99th climatological percentile for the region. These anomalous moisture conditions and convective instability supported rainfall rates of as much as 150 mm per hour.

On the evening of 2 July, a broad area of thunderstorms developed over southern portions of the Mexican state of Chihuahua. This organized cluster of storms, known as a mesoscale convective vortex (MCV), slowly moved northeastward into Texas on 3 July providing multiple bands of rain wrapping into the storm's circulation. MCVs are known to be self-sustaining, lasting much longer than individual storms. In a very moist environment, as was the case in early July 2025, this can lead to prolific rainfall by concentrating moisture and repeatedly generating new storms over the same area. By the morning of 4 July, the MCV had entered the Edwards Plateau and Hill Country regions.

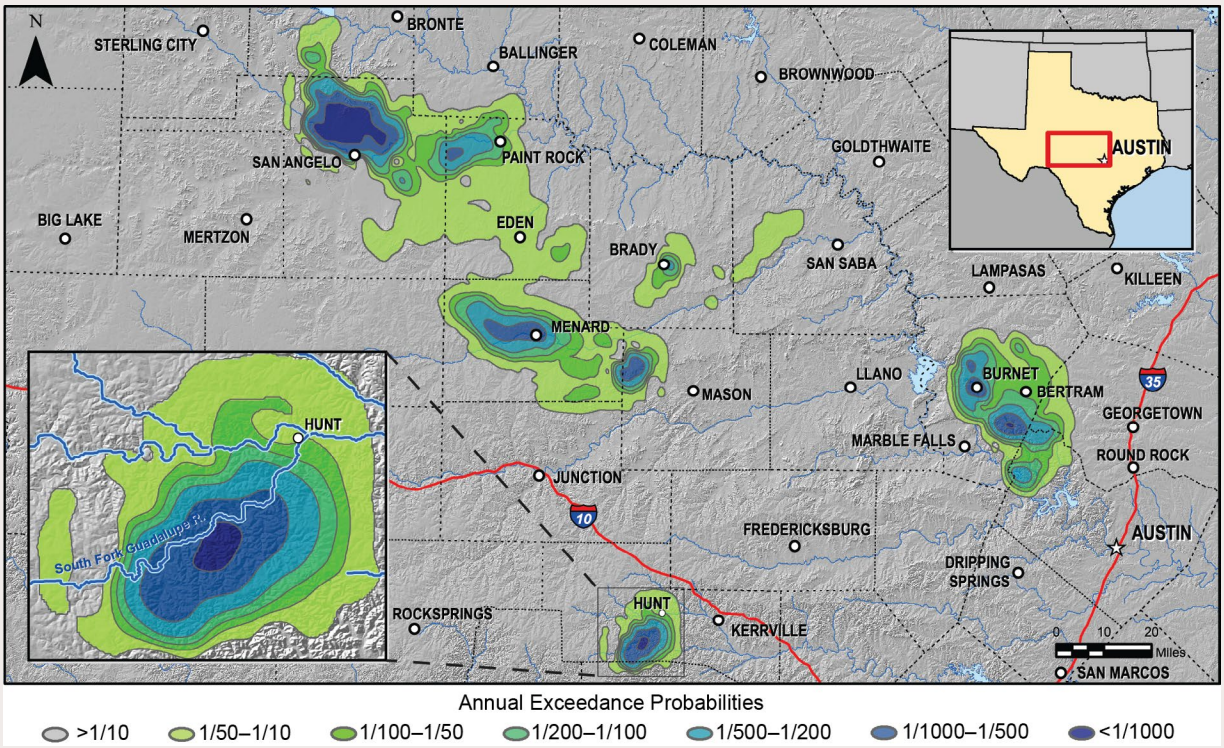

Fig. SB7.1. Annual exceedance probabilities for the highest 3-hr rainfall period in Central Texas during 3–6 July 2025. (Source: NOAA/NWS Office of Water Prediction 2025.)

The heaviest rainfall began on 3 July and continued into 5 July. Isolated rainfall totals reached 510 mm in some locations, with localized amounts of 250 mm–300 mm falling within a six-hour period. Orographic effects associated with the Texas Hill Country terrain, together with the apparent MCV, contributed additional lift and supported sustained convective development. A band of 180 mm to 300 mm of rain occurred over the South Fork of the Guadalupe River, most of which fell in just three hours. Analysis of combined rain gauge and radar observations indicates the magnitude of this three-hour event exceeded the 1-in-1000-year annual exceedance probability over areas near San Angelo and Hunt, Texas, corresponding to a 0.1% chance of occurrence at a given location in any year (Fig. SB7.1). When compared to a precipitation analysis from the 1991–2020 climatological normals, these areas received more than four months' worth of rainfall in just a two-day period.

The intense rainfall led to rapid rises in river and stream levels and widespread flash flooding. Provisional data from the U.S. Geological Survey indicates that nearly two dozen river gauges reported flooding on 4 and 5 July, including four sites reaching moderate flood stage and five reaching major flood stage. One area of localized intense precipitation developed over the South Fork of the Guadalupe River watershed in Kerr County, part of a region commonly referred to as "Flash Flood Alley" due to its susceptibility to rapid flooding. At the Kerrville, Texas, river gauge, the Guadalupe River rose from just under 0.6 m (2 ft) to over 11 m (37 ft) within a couple of hours on the morning of 4 July, briefly reaching major flood levels (Fig. SB7.2). In nearby Hunt, Texas, a river gauge recorded a rapid rise of 8 m (26 ft) in just 45 minutes before failing at a crest of 11.44 m (37.52 ft). If confirmed, this crest would exceed the previous record of 11.2 m, which was set in 1932.

Additional heavy rainfall occurred in mid-July, with 130 mm to 150 mm falling across portions of Central Texas. This secondary event prompted renewed river rises and additional water rescues. Ten river gauges again reported flooding, including four reaching the moderate flood stage, though none reached major flood levels. Rainfall totals for the month of July indicate that many counties in Central Texas experienced a top five wet July, using records dating back to 1895. Kerr County experienced its second-wettest July, trailing only 2002.

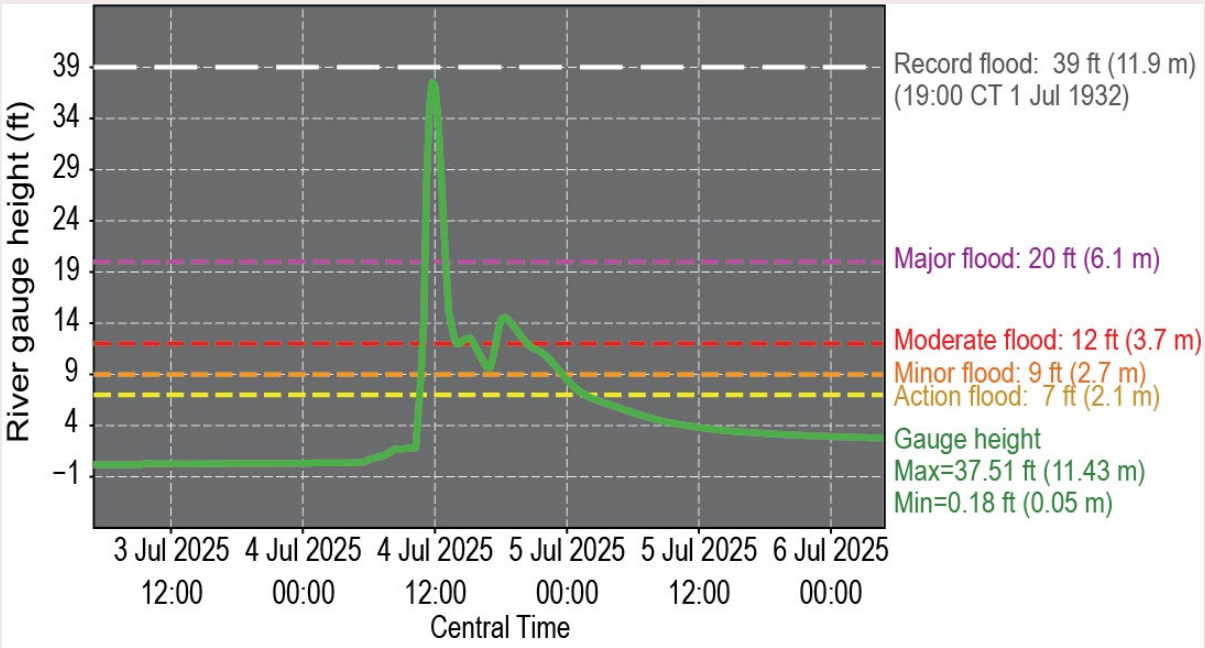

Fig. SB7.2. Hydrograph for a river gauge on the Guadalupe River in Kerrville, Texas, where major flooding occurred on 4 Jul, with a crest of over 11 m (37 ft). (Source: U.S. Geological Survey 2026; NOAA/NWS National Water Prediction Service 2026.)

c. Central America and the Caribbean

—A. Arguez, Ed.

1. CENTRAL AMERICA

—H. G. Hidalgo, J. A. Amador, E. J. Alfaro, B. Calderón, and N. Mora

Nine stations were analyzed across Central America (Fig. 7.10; Table 7.1). The station distribution is representative of the relevant seasonal and intraseasonal regimes of precipitation (Amador 1998; Magaña et al. 1999; Amador et al. 2016a,b), wind (Amador 2008), and

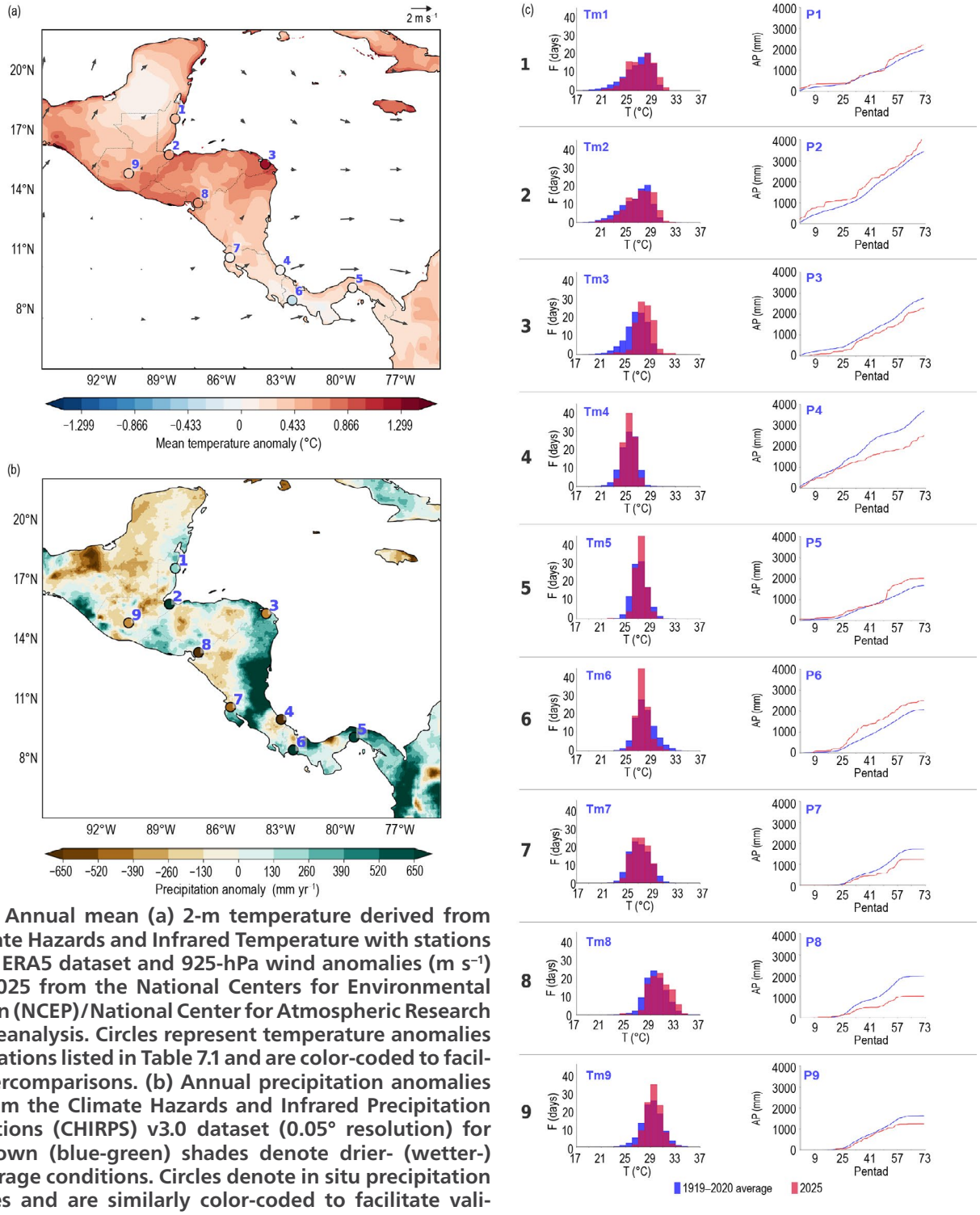

Fig. 7.10. Annual mean (a) 2-m temperature derived from the Climate Hazards and Infrared Temperature with stations (CHIRTS) ERA5 dataset and 925-hPa wind anomalies (m s⁻¹) for Jul 2025 from the National Centers for Environmental Prediction (NCEP)/National Center for Atmospheric Research (NCAR) reanalysis. Circles represent temperature anomalies for the stations listed in Table 7.1 and are color-coded to facilitate intercomparisons. (b) Annual precipitation anomalies (mm) from the Climate Hazards and Infrared Precipitation with stations (CHIRPS) v3.0 dataset (0.05° resolution) for 2025. Brown (blue-green) shades denote drier- (wetter-) than-average conditions. Circles denote in situ precipitation anomalies and are similarly color-coded to facilitate validation. (c) Time series of five-day average temperature frequency (Tm; °C) and accumulated pentad precipitation (P; mm) for each station. The solid blue lines represent the 1991–2020 climatological averages, while the red solid lines show the 2025 values. The base period for (a)–(c) is 1991–2020. (Source: National Meteorological Service [NMS; Belize], National Institute for Seismology, Vulcanology, Meteorology and Hydrology [INSIVUMEH; Guatemala], Honduran Civil Aeronautics Agency [AHAC; Honduras], National Meteorological Institute [IMN; Costa Rica], and Institute of Meteorology and Hydrology of Panama [IMHPA; Panama]).

temperature (Hidalgo et al. 2019) on the Caribbean and Pacific slopes of Central America. Precipitation and temperature data were provided either by Central America National Weather Services (CA-NWS), NOAA, or the University of Costa Rica; however, in some cases, missing 2025 daily precipitation data were filled in with the nearest grid point data from the Climate Hazards and Infrared Precipitation with stations (CHIRPs; Funk et al. 2015) and from the Climate Hazards and Infrared Temperature with stations (CHIRTs; Funk et al. 2019). CHIRPs and CHIRTs have validated well compared to meteorological station data (Alfaro-Córdoba et al. 2024). Anomalies are reported using a 1991–2020 base period and were calculated from CA-NWS data. The methodologies used for all variables are described by Amador et al. (2011).

(i) Temperature

The year 2025 was warmer than normal across most of Central America (Fig. 7.10a), with the northern countries experiencing the highest temperatures (Tm; °C). All stations (Table 7.1), except David, Panama (Tm6; −0.39°C), reported positive annual anomalies. Lempira, Honduras, reported the largest anomaly (Tm3; +1.24°C); none of the anomalies were considered to be extreme (in the 95% tails of the distribution). The temperature distributions (Fig. 7.10c) show a warm shift in 2025 relative to climatology for the two Honduran stations, and a lighter right tail of the distribution (i.e., fewer warm days) during 2025 for David, Panama.

Table 7.1. Annual temperature (°C) and precipitation (mm) anomalies for 2025 with respect to the 1991–2020 base period (normals), calculated from monthly means and accumulations, respectively.

Station	2025 Annual Temperature Anomaly (°C)	1991–2020 Annual Temperature Normal (°C)	2025 Annual Precipitation Anomaly (mm)	1991–2020 Annual Precipitation Normal (mm)
Phillip Goldson International Airport (PGIA), Belize	+0.47	26.9	+243.6	1963
Puerto Barrios, Guatemala	+0.62	26.6	+754.4	3445
Lempira, Honduras	+1.24	26.7	–459.4	2743
Limón, Costa Rica	+0.06	25.4	–1181.3	3687
Tocumen Airport, Panama	+0.14	27.2	+210.48	1794
David, Panama	–0.39	28.1	+514.9	1963
Liberia Airport, Costa Rica	+0.05	27.2	–492.3	1723
Choluteca, Honduras	+0.64	29.8	–947.8	1966
Montufar, Guatemala	+0.38	20.1	–394.0	1631

(ii) Precipitation

Annual precipitation (Fig. 7.10b) was generally below normal in the Caribbean slope from Panama to Nicaragua, except for Costa Rica, with especially large deficits along Nicaragua´s mid-southern Caribbean coast. Most of Honduras, Guatemala, and the Pacific coast of Nicaragua showed moderately drier-than-normal conditions, which is significant, as this subregion represents most of the Central America Dry Corridor (Hidalgo et al. 2019). The station observations are generally consistent with the CHIRPs dataset, except for the large (but not extreme) dry

anomalies in Limón (P4; –1181.3 mm) and in Choluteca (P8; –947.8 mm). No stations reported extreme changes in precipitation.

The northern Caribbean slope (stations 1 and 2) largely maintained wetter-than-normal conditions over the course of the year (Fig. 7.10c). The southern Caribbean slope (stations 3 and 4) reported precipitation deficits that widened to various degrees throughout the year, which was also seen in the central and northern Pacific slope (stations 7–9). The Panamanian stations in the southern Pacific slope (stations 5 and 6) showed above-normal precipitation accumulations that were largely maintained following intense wet periods (which occurred earlier in the year for David versus Tocumen Airport).

During 2025, sea surface temperature anomalies (SSTa) in the eastern tropical Pacific were generally slightly cooler than normal, and the Tropical North Atlantic Index (TNA; a measure of the SSTa in the tropical Atlantic) was warmer than normal. Although those two conditions tend to favor wet precipitation anomalies in the Pacific slope of Central America (e.g., Enfield and Alfaro 1999; Durán-Quesada et al. 2020), the lack of a strong precipitation teleconnection response may be related to the weak SSTa in both oceanic regions.

(iii) Notable events and impacts

The 2025 Atlantic tropical cyclone season brought relatively few impacts to Central America, although several fatalities were reported in Panama associated with Hurricane Melissa. Extreme rainfall events, strong winds, mudslides, landslides, and flooding accounted for most of the socio-economic losses in the region during the year, including 105 fatalities, with most occurring in Honduras and Guatemala (Table 7.2). Lightning strikes were responsible for 21 casualties across the region in 2025.

Table 7.2. Number of fatalities in several Central American countries due to hydrometeorological events and lightning strikes. (Data sources: Central American national weather services, regional newspapers, and national emergency committees, including: the National Civil Protection System [SINAP-ROC; Panama], the National Commission for Risk Prevention and Emergency Response [CNE; Costa Rica], the National System for Civil Protection, Disaster Prevention and Mitigation [El Salvador], the Permanent Contingency Commission of Honduras [COPECO; Honduras], the National Coordination for Disaster Reduction [CONRED; Guatemala], Nicaragua Investiga [https://nicaraguainvestiga.com/], and El19digital [https://www.el19digital.com/], in Nicaragua.)

Country	Hydrometeorological Events	Lightning Strikes
Panamá	1	5
Costa Rica	2	2
Nicaragua	11	1
El Salvador	6	5
Honduras	20	8
Guatemala	65	0
TOTAL	105	21

2. CARIBBEAN

—T. S. Stephenson, M. A. Taylor, A. Trotman, C. J. Van Meerbeeck, L. Clarke, T. Allen, J. Spence-Hemmings, R. Moody, C. Charlton, J. Campbell, and M. Williams

(i) Temperature

The year 2025 was the third warmest year for the Caribbean since records commenced in 1950, using the ERA5 Reanalysis dataset (Figs. 7.11a, 7.12a), as the region continues to warm at a rate of 0.13°C decade^{-1} since 1950 (0.19°C decade^{-1} since 1970). The annually-averaged 2-m temperature (26.51°C) was 0.55°C above the 1991–2020 average. Freeport (The Bahamas) experienced its warmest year since its records commenced in 1992, with an annual mean temperature of 25.9°C. Eleven of 23 reporting stations in the Caribbean islands exceeded their 90th percentile annual mean temperature. Eight of these stations recorded temperatures that ranked within the station's three warmest years. The tropical North Atlantic, a primary driver of air temperatures in the region, was warmer than normal for much of the year.

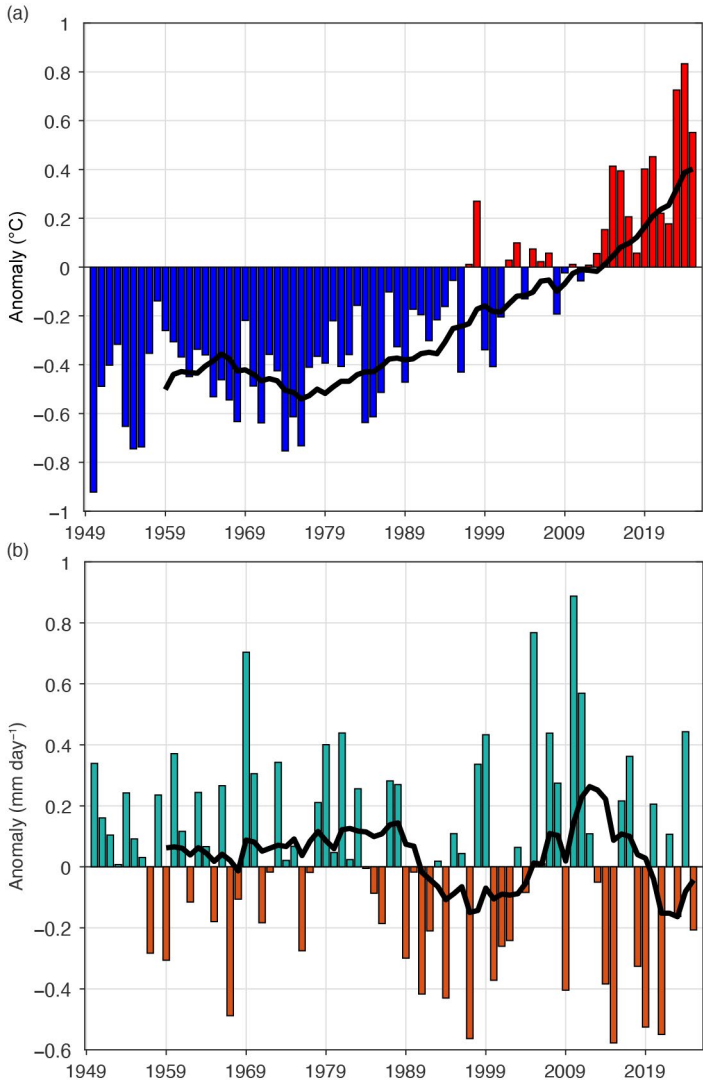

Fig. 7.11. Annually averaged (a) 2-m temperature anomaly (°C) and (b) rainfall anomaly (mm day^{-1}) time series for the Caribbean (9°N–27°N, 58°W–90°W) for the period 1950–2025 relative to the 1991–2020 base period. The black line represents the 10-year running mean. (Source: ERA5 from the Copernicus Climate Data Store.)

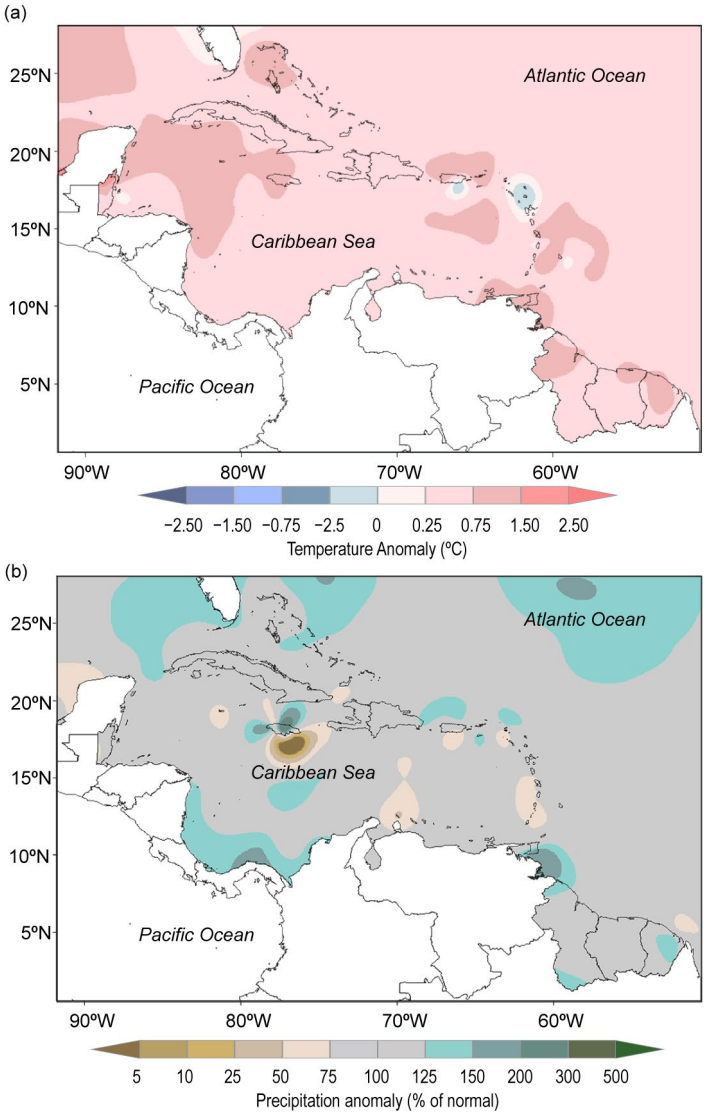

Fig. 7.12. Annual (a) mean temperature anomalies (°C) and (b) total precipitation anomalies (% of normal) across the Caribbean for 2025 relative to the 1991–2020 base period. (Source: Caribbean Climate Outlook Forum [CariCOF] and the Caribbean Institute for Meteorology and Hydrology.)

Seasonally, December–February (DJF; +0.61°C anomaly), March–May (MAM; +0.58°C), and June–August (JJA; +0.44°C) were also each the third warmest for their respective seasons for the Caribbean, while September–November (SON; +0.54°C) was fourth warmest. Some locations reported temperatures 1.5°C above normal, including New Providence (The Bahamas) and parts

of Puerto Rico (DJF). A few locations, including Antigua and St. Croix (MAM to SON), were seasonally slightly cooler than normal.

(ii) Precipitation

The Caribbean was relatively drier than normal in 2025. The annual-averaged rainfall over the region was 3.0 mm day^{-1}, which is 93.6% of the 1991–2020 average (Figs. 7.11b, 7.12b). Two stations in St. Vincent and the Grenadines experienced their driest years on record: Argyle (1309.4 mm) and ET Joshua (1147.5 mm).

In tandem with a warmer-than-normal tropical North Atlantic and weakly negative SST conditions over the equatorial Pacific, DJF rainfall was normal to above normal for most of the region; however, St. Barts and St. Croix were drier than normal. The average to above-average rainfall persisted across most of the region during MAM, with wetter-than-normal conditions over the eastern Caribbean. In contrast, northern Bahamas and Cuba recorded very dry conditions. JJA marked a shift to below-normal rainfall totals and frequency over most of the Caribbean. This was observed amid above-average North Atlantic Ocean temperatures and drier-than-usual air above the Atlantic. Drought developed across the Windward Islands during SON, as well as in a few other locations, particularly in the eastern Caribbean. Record-wet conditions were observed in parts of The Bahamas, and wet conditions prevailed for Cuba and Hispaniola, likely related to Hurricane Melissa (see Sidebar 7.2 for details).

(iii) Notable events and impacts

Several tropical systems impacted the Caribbean in 2025. On 16–17 August, Hurricane Erin, the first Atlantic hurricane of 2025, passed north of the Leeward Islands and Puerto Rico, and later east of The Bahamas, and produced strong wind gusts, heavy rainfall, and coastal flooding in the Virgin Islands, Turks and Caicos, Dominican Republic, and Puerto Rico. Widespread power outages were reported in Puerto Rico.

On 29–30 September, southeast and central Abaco in The Bahamas was impacted by tropical storm force winds related to Tropical Cyclone Imelda. The high winds resulted in power outages and flight disruptions, the latter continuing to 4 October.

On 10 October, excessive rainfall associated with Tropical Storm Jerry impacted Antigua and Barbuda, causing flash flooding, road damage, and airport closures in the twin-island nation.

On 28 October, Hurricane Melissa, a catastrophic Category 5 hurricane, made landfall in Jamaica, before sweeping across eastern Cuba and impacting Haiti and The Bahamas. Sidebars 7.2 and 4.1 (The Tropics chapter) detail the evolution and impacts of the storm.

Sidebar 7.2: **Impacts of Hurricane Melissa on the Caribbean**

—T. S. STEPHENSON, M. A. TAYLOR, A. CENTELLA-ARTOLA, A. BEZANILLA-MORLOT, AND L. CLARKE

Fig. SB7.3. Destruction of (a) the second story of a two-story building and (b) a school building in St. Elizabeth, Jamaica, as a result of the intense winds associated with Hurricane Melissa. (Source: Josh Morgerman; iCyclone.)

Icon	Category	Jamaica	Haiti	Cuba
	Deaths	46	43	0
	GDP cost	56.7	3%	3%
	Evacuations	1,100	no data	735,000
	Schools impacted	600	4,400	1,552

Fig. SB7.4. Summary of Hurricane Melissa's impacts on Jamaica, Haiti, and Cuba. The Gross Domestic Product (GDP) cost estimate for Haiti includes secondary effects such as security instability, displacement, agricultural losses, and market disruption.

Hurricane Melissa was one of the strongest Atlantic tropical cyclones on record (see section 4g2 and Sidebar 4.1 for meteorological details). The storm caused severe and widespread impacts (Figs. SB7.3, SB7.4), affecting more than eight million people across the Caribbean, particularly Haiti, Dominican Republic, Jamaica, Cuba, The Bahamas, and Bermuda, from 23 October to 1 November. Peak devastation was observed on 28–29 October when Melissa made landfall in Jamaica (Category 5) and Cuba (Category 3), bringing intense rains, strong winds, and powerful storm surge.

During 23–25 October, the strong outer bands of Melissa impacted Haiti and the Dominican Republic. In Haiti, Melissa caused flash floods, landslides, and extensive infrastructure damage, particularly in the southern parts of the country. Over 4400 schools were affected, impacting the education of more than 127,000 children. Approximately 13,300 latrines and 63 drinking water systems were damaged. Suspected cases of Cholera emerged, including 11 related deaths post-Hurricane Melissa. As of February 2026, 46 people were confirmed dead, with more than 250,000 directly impacted, according to reports by UNICEF. Across the Dominican Republic, more than 1.1 million people were without water after heavy rainfall and flooding associated with the storm disrupted water supply systems. Fifty-six aqueducts and 53 bridges were damaged. Four people were killed, and damage totaled approximately $23.36 million U.S. dollars (less than 1% of gross domestic product [GDP]).

On 28 October, Category 5 Hurricane Melissa made landfall over New Hope, Westmoreland, and was the strongest hurricane on record to make landfall in Jamaica. The country was still recovering from the severe impacts of Category 4 Hurricane Beryl that tracked south of the island on 3 July 2024. An automatic weather station at The University of the West Indies, Mona, in Kingston, Jamaica, measured a total of 345.0 mm on October 28, ~147% of the normal October monthly mean rainfall (Campbell et al. 2025). The Meteorological Service Jamaica recorded an October mean rainfall of 518 mm over the country, 248% of the month's climatological value—the extreme level of exceedance likely due to Hurricane Melissa. A storm surge of 1.2 m–4.0 m was also observed in relation to the hurricane, according to reports from the United Nations Office for the Coordination of Humanitarian Affairs (UN OCHA).

A comprehensive damage and loss assessment in relation to Melissa prepared by the UN Economic Commission for Latin America and the Caribbean in collaboration with the government estimated damage, losses, and additional costs at more than $12.2 billion U.S. dollars (56.7% of GDP in 2024), more than four times that of Hurricane Gilbert in 1988, which was previously the costliest hurricane in Jamaica's history.

Melissa caused severe damage across six of the most affected parishes—Westmoreland, St. Elizabeth, St. James, St. Ann, Trelawny, and Manchester—triggering widespread disruption to lives and livelihoods. Assessments across the social sector, which focused on aspects of population, education, health, housing, and culture, yielded the greatest loss (~23.9% of GDP). There were 124 suspected and 40 confirmed cases of Leptospirosis and 14 suspected deaths in the most affected areas post-Hurricane Melissa, according to UNICEF. In total, there were 45 confirmed deaths. Melissa caused extensive damage to homes, health facilities, and critical infrastructure, disrupting essential services and causing widespread displacement. Five major hospitals and over 100 health centers were damaged, adversely impacting access to healthcare. More than 60% of the island lost electricity, and water systems that serve approximately 50% of the country became inoperable. As of February 2026, water supply had been restored to 93% of customers, while 42,000 connections remained without service.

After crossing Jamaica, Melissa made landfall over eastern Cuba as a Category 3 hurricane on 29 October, causing strong winds and flooding, widespread power outages, extensive infrastructure damage, and agricultural losses, particularly in the eastern provinces. Water pumping, power generation, transport, and service delivery were also further constrained by fuel shortages. The government evacuated 735,000 residents. At least 1552 schools were damaged, and approximately 78,700 hectares of crops were completely destroyed, adversely impacting local food production and livelihoods (Clarke et al. 2025). As of February 2026, 871 educational institutions remained damaged, mainly due to roof collapse and structural damage. Santiago de Cuba was the most affected province, followed by Holguín and Granma, according to reports by UNICEF. Damage was reported to nearly 650 healthcare facilities, impacting health services to over 3.5 million people. More than 200,000 homes and nearly 500,000 people, particularly in Santiago de Cuba, experienced power and water outages for weeks following the storm.

Hurricane Melissa later weakened, traversing The Bahamas as a Category 1 hurricane on 30 October and eastern Bermuda as a Category 2 hurricane on 31 October. The Bahamas was impacted by high winds, storm surge, and coastal flooding, which caused transport disruption, airport closure, minor coastal damage, and temporary power outages, with no fatalities or major injuries. Approximately 1400 people were evacuated (PAHO 2025). For Bermuda, the hurricane caused widespread wind damage and power outages, affecting nearly 19,000 customers at the storm's peak. Minor road blockages and infrastructure damage were reported.

Mental health issues and increased psychosocial needs were identified in children, displaced families, and healthcare workers due to the aftermath of Hurricane Melissa (e.g., PAHO 2025). Biodiversity losses remain unquantified but likely include damage to mangroves and wetlands, degradation of forests and aquatic habitats, stress on coral reefs and seagrass beds from sedimentation and wave action, and erosion of coastal dunes and soils, adversely impacting terrestrial ecosystems and wildlife.

d. South America

1. NORTHERN SOUTH AMERICA

—A. Casella, F. Costa, J. González, M. Hänsch, N. Rodríguez, I. Salazar, J. Serna Cuenca, and C. Valdivieso

The northern South America region includes Colombia, Ecuador, French Guiana, Guyana, Suriname, and Venezuela. In this section, the 1991–2020 period is used as the reference climatology for both temperature and precipitation.

During 2025, regional climate patterns were mainly consistent with weak La Niña conditions in the early part of the year, followed by a brief neutral phase before La Niña conditions returned in October. Other climate factors, such as the warm tropical Atlantic (see section 3b for details) and the Madden–Julian Oscillation (MJO; see section 4c for details), contributed to precipitation variability in the area due to the changes in cloud convection, radiation, and wind patterns.

(i) Temperature

During 2025, annual temperatures across northern South America were mostly near to slightly above normal (Fig. 7.13). In Venezuela, maximum temperature anomalies exceeded +1.0°C in large portions of the country from January to March. From April onward, coinciding with the onset of the rainy season, temperatures decreased progressively, with widespread negative anomalies persisting through October and reaching mean values near −0.9°C. During November and December, a slight warming was observed, with positive anomalies ranging from +0.1°C to +0.6°C, mainly over the central and eastern regions.

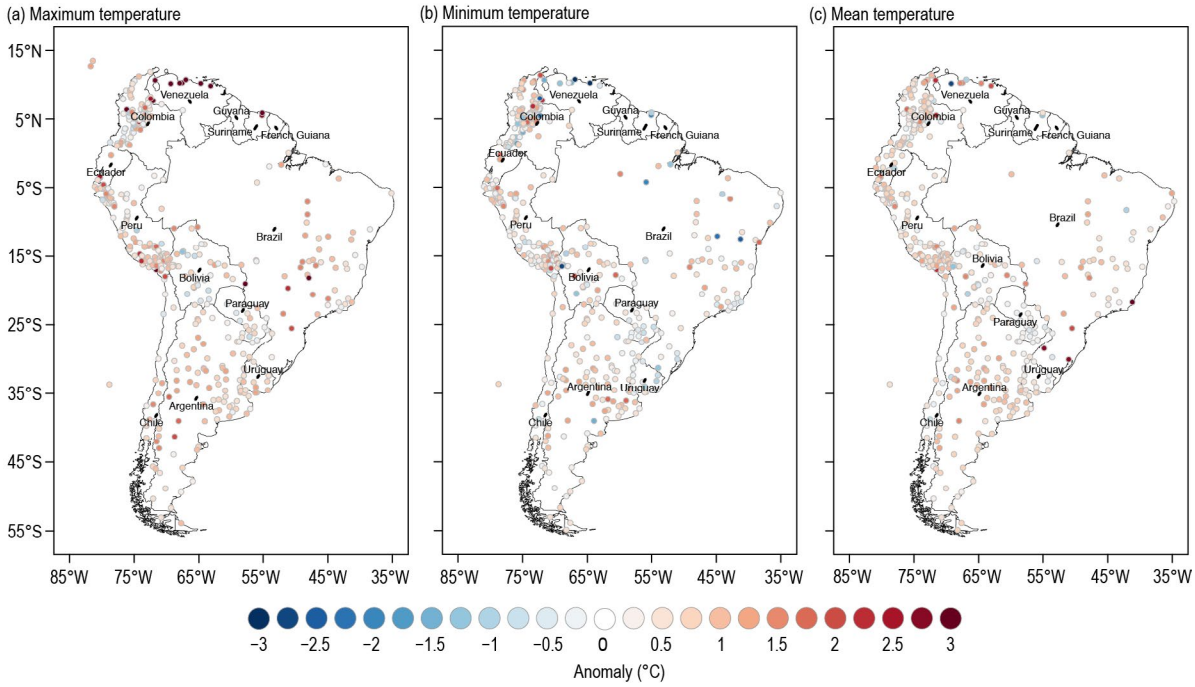

Fig. 7.13. Annual (a) maximum, (b) minimum, and (c) mean temperature anomalies (°C; 1991–2020 base period) in South America for 2025. (Source: Station data from the national meteorological and hydrological Services of Argentina, Bolivia, Brazil, Chile, Colombia, Ecuador, Paraguay, Peru, Uruguay, and Venezuela. Processed by the International Center for Research on the El Niño Phenomenon [CIIFEN].)

In Colombia, monthly temperatures were mostly near- to above normal, with anomalies up to +1.5°C in some months; however, during January and February, below-average maximum temperatures were observed over central and southern parts of the country. Notable temperature extremes were recorded during the year: the lowest minimum temperature reached 0.2°C in El Encano (Nariño) on 9 December, while the highest maximum temperature was 40.8°C in Arjona (Bolívar) on 11 March. The year ended with mean temperatures in December above normal, as an intense subsident phase of the MJO (see section 4c) transiting favored increased incoming solar radiation and suppressed convection.

In Ecuador, annual maximum, minimum, and mean temperatures were above normal in most of the country (Fig. 7.13). Mean temperatures were as high as 28.7°C along the coast in March

(+0.8°C anomaly), 17.6°C in the Andes in November (+0.5°C), and 28.2°C in the Amazon (+1.4°C). In the Amazon region, the lowest minimum temperature recorded was 14.9°C in December, which was above normal. In the Andean region, however, the lowest minimum temperature of the year was 3.0°C below normal in August.

(ii) Precipitation

Precipitation across northern South America during 2025 (Fig. 7.14) exhibited marked spatial and temporal variability, with alternating periods of deficit and excess throughout the year and extreme rainfall events in several areas.

During Venezuela's dry season (January–March), rainfall deficits prevailed at the national scale—more than 50% below normal in the Andean, eastern, and Zulia regions. With the onset of the rainy season (April–November), an abrupt transition toward wetter-than-normal conditions was observed. Between April and June, rainfall totals exceeded 150% of average in the Andean, central, western, eastern, and Zulia regions. During the second half of the year, anomalies were more heterogeneous, with moderate deficits (–18% to –34%) in the western and Zulia regions. Overall, annual precipitation anomalies were generally within ±35% of normal.

In Colombia, annual precipitation was generally above normal, particularly over central and southern sectors of the Andean and Pacific regions and parts of the southern and western Amazon. Excess rainfall of more than 160% of normal was widespread during January and February, associated with La Niña. Moderate excesses of 120%–160% of normal were recorded between March and June and in August, the latter of which was linked to the Atlantic hurricane season, which was characterized by frequent passages of tropical waves that increased moisture availability across the country. In December, severe precipitation deficits (less than 40% of average) were observed.

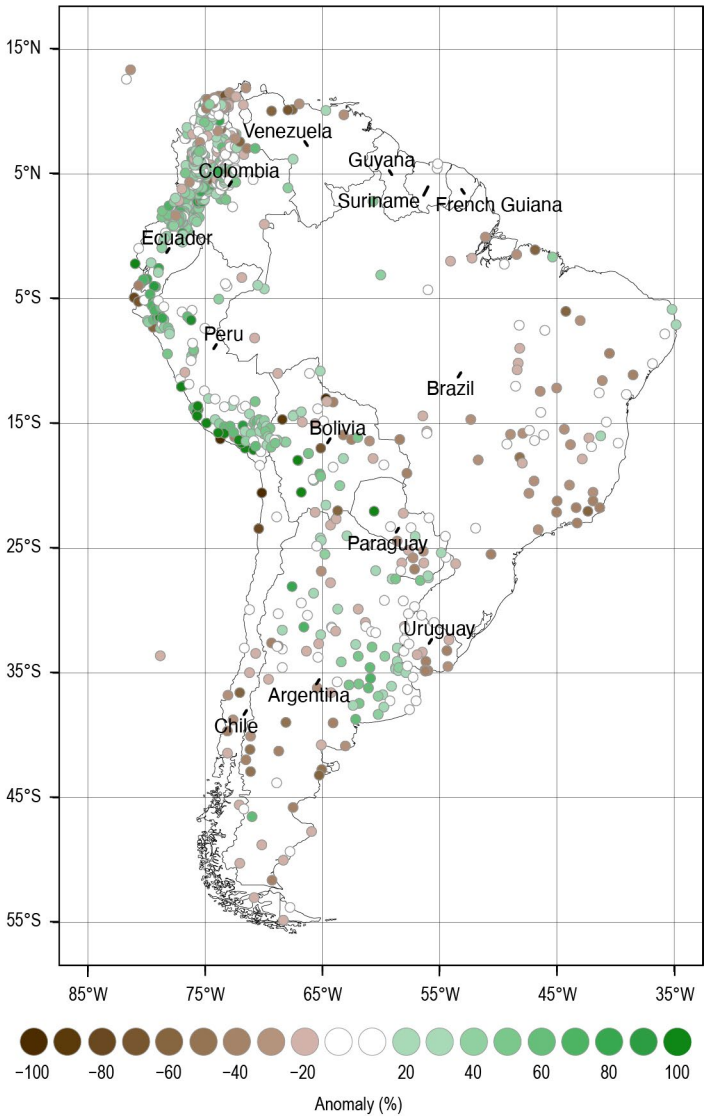

Fig. 7.14. Annual precipitation anomalies (%; 1991–2020 base period) for 2025 for South America. (Source: Station data from the national meteorological and hydrological services of Argentina, Bolivia, Brazil, Chile, Colombia, Ecuador, Paraguay, Peru, Uruguay, and Venezuela. Processed by the International Center for Research on the El Niño Phenomenon [CIIFEN].)

In Ecuador, the start of the year was marked by significantly above-normal precipitation totals, particularly notable between February and April. In the coastal region, February and March were exceptionally rainy, with accumulations exceeding 150% of normal across large areas. Rainfall totals were more extreme in some localized areas. In February, Guayaquil recorded 645.5 mm (194% of normal), while Salinas accumulated 413.6 mm (834% of normal). In March, rainfall totals in La Maná reached 819.2 mm (797% of normal). In the Andean region, precipitation was also significantly above normal in February, March, and April, with Ibarra recording 133.1 mm in February (305% of normal) and San Gabriel 326.8 mm in March (292% of normal). In the insular region, Baltra recorded 170.3 mm in February (301% of normal), and San Cristóbal registered 295.3 mm in April (342% of normal). In the Amazon region, Pastaza received up to 706.1 mm in March (166% of average). In December, precipitation deficits were recorded across the country.

(iii) Notable events and impacts

In Venezuela, heavy rainfall in June and August triggered flash floods, torrential flows, and landslides, particularly in mountainous areas. In Mesa de Aracay (Mérida State), rainfall totals of 111.4 mm over 11 hours on 24 June and 57.2 mm over 11 hours on 26 June led to torrential flows. In August, a 150-mm rainfall event in San Juan de Payara (Apure State) caused flooding across road networks and in populated areas.

In Colombia, extreme rainfall in Istmina (Chocó) in July broke the national record for maximum 24-hour precipitation with 274 mm.

In Ecuador, intense and persistent rainfall generated widespread impacts across the country over the course of the year; widespread heavy rainfall was particularly notable from January to March, affecting much of the country and prompting multiple weather alerts in early March (National Meteorological and Hydrological Service of Ecuador-INAMHI), with coastal and Amazonian provinces among the most affected. A major landslide on 13 March ruptured a key oil pipeline, causing a significant oil spill into rivers used for drinking water and irrigation. According to the Emergency Operations Committee and the Secretariat for Disaster Risk Management, 4443 adverse rainfall-related events were reported in total, mainly in the form of landslides and floods. Additionally, damage was reported for more than 85,000 households, along with impacts to the road network and the agricultural sector.

2. CENTRAL SOUTH AMERICA

—J. A. Marengo, J. C. Espinoza, L. M. Alves, J. Ronchail, A. P. Cunha, R. Libonati, J. Molina-Carpio, K. Correa, G. Avalos, R. Salinas, and P. P. Rivera

Central South America comprises Brazil, Peru, Paraguay, and Bolivia. Throughout this section, 1991–2020 is the base period used for both temperature and precipitation.

(i) Temperature

The annual mean temperature across the region for 2025 (0.76°C above normal) was among the highest in the historical record that began in 1961. Although lower than the record-breaking temperatures of 2023 and 2024, the 2025 value indicates that the climate system has not returned to pre-2010 baseline conditions. (Fig. 7.15).

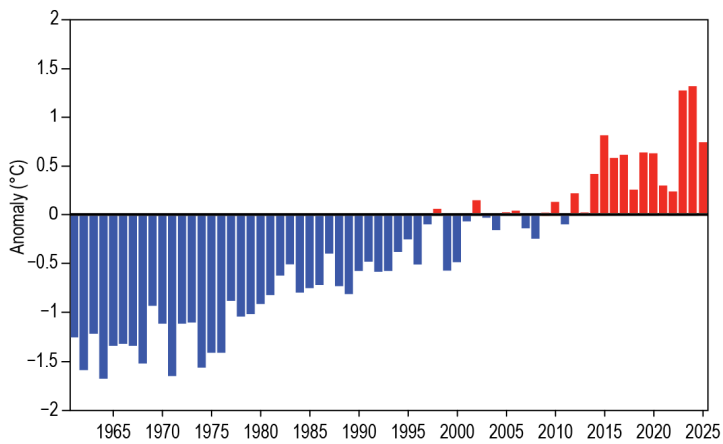

Fig. 7.15. Time series of annual mean temperature anomalies (°C; 1991–2020 base period) for the period 1961–2025 for central South America (Brazil, Bolivia, Paraguay, and Peru). (Source: NOAA/National Centers for Environmental Prediction (NCEP) Global Historical Climatology Network [GHCN] Climate Anomaly Monitoring System [CAMS] data.)

Above-normal temperatures (+1°C to +2°C anomalies) were observed across parts of the northern and central coasts of central South America, western Amazonia, the southern Andes of Peru and Bolivia, and parts of southern Brazil. Warm conditions prevailed across much of the region, particularly during austral summer (December 2024–February 2025), and several extreme summer heat records were set. On 9 January, the Dirección de Meteorología e Hidrología de Paraguay (DMH) reported a new record high temperature of 44.8°C in Mariscal Estigarribia. In mid-2025, however, cold air masses brought unusually low temperatures to central and southern Brazil; this was among the most extreme cold events in recent decades.

(ii) Precipitation

Dry conditions at the end of 2024 continued into the beginning of 2025, especially prior to the 2025 rainy season, with parts of northern Amazon countries experiencing low soil moisture, reduced river flows, and drought stress (WMO 2025). On the other hand, Bolivia experienced prolonged, unusually heavy rainfall, particularly during its rainy season, resulting in major flooding. Southern Brazil experienced intense rainfall in mid-June across several areas, with

some stations recording very high daily totals (e.g., exceeding 150 mm in 24 hours in Rio Grande do Sul), which contributed to widespread flooding.

(iii) Notable events and impacts

Figure 7.16 shows select climatic and hydrological extremes that affected central South America in 2025. Several of these events are discussed in more detail below.

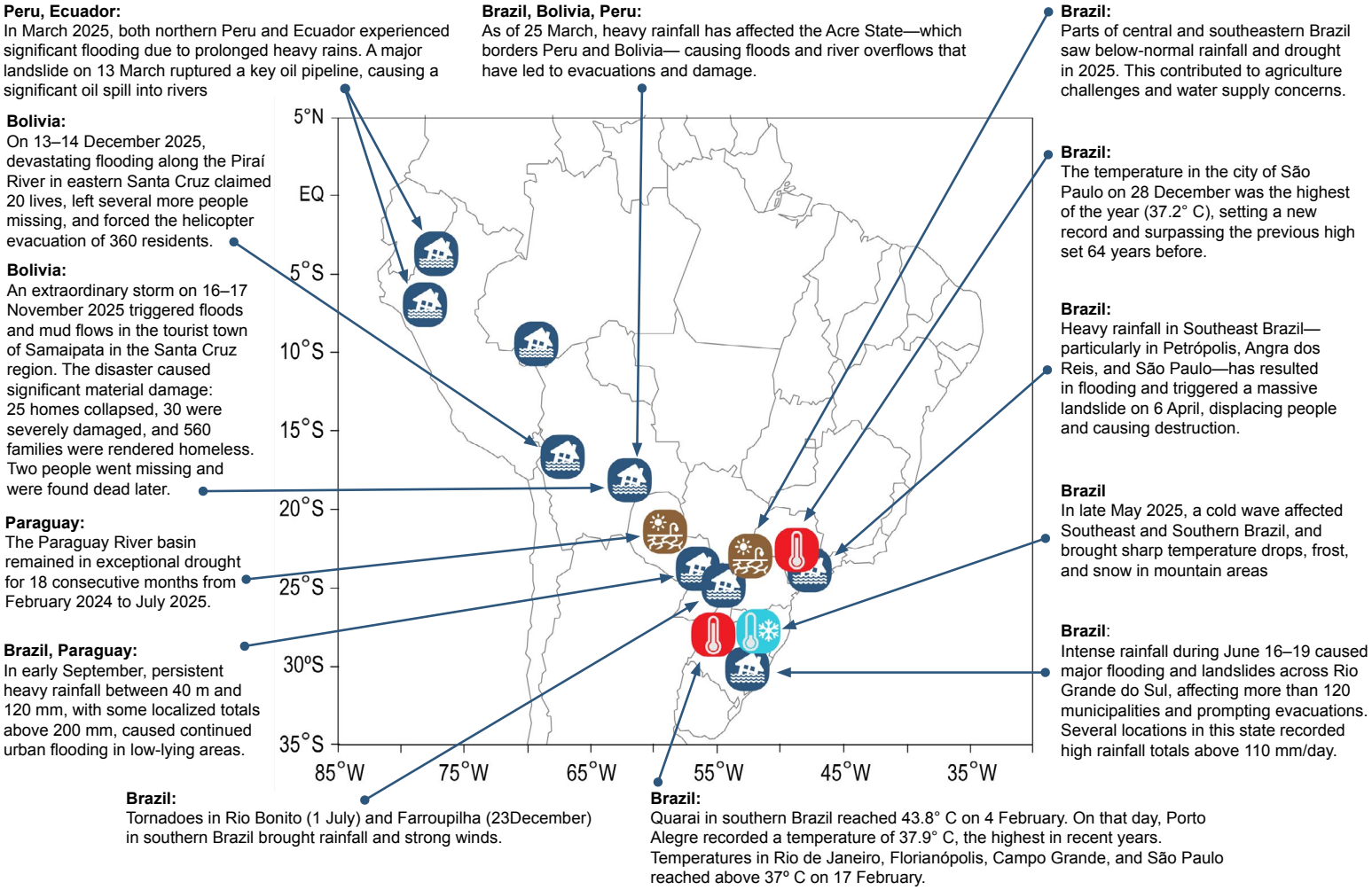

Fig. 7.16. Extreme and notable events across central South America in 2025. (Source: Peru National Meteorology and Hydrology Service of Peru [SENAMHI], Bolivia National Meteorology and Hydrology Service of Bolivia [SENAMHI], Paraguay Directorate of Meteorology and Hydrology [DMH], Brazil; National Institute of Meteorology [INMET], National Center for Natural Disaster Monitoring and Alerts [CEMADEN], National Institute for Space Research [INPE], International: UN Office for the Coordination of Humanitarian Affairs [OCHA], Reliefweb, FloodList.)

Bolivia and Brazil experienced catastrophic flooding in early 2025—resulting from an unusually prolonged wet season—in the Beni, La Paz, and Santa Cruz departments of Bolivia (National Meteorological and Hydrological Service SENAMHI, Bolivia) and in the state of Acre, Brazil, along the border with Peru and Bolivia. More than 50 fatalities and the displacement of hundreds of thousands of families were reported (National Institute of Meteorology [INMET], National Meteorology and Hydrology Service of Bolivia [SENAMHI-Bolivia], Office for the Coordination of Humanitarian Affairs [2025]). In São Paulo, 114.1 mm of rain fell in just three hours on 24 January (INMET).

On the dry side, the Integrated Drought Index (IDI; Cunha et al. 2019; Fig. 7.17) indicates that during austral summer (Fig. 7.17a), drought conditions occurred in Paraguay, central Brazil, and eastern Bolivia, whereas in autumn (Fig. 7.17b), northeast Brazil experienced moderate-to-severe drought. The situation worsened during austral winter and spring (Figs. 7.17c,d, respectively), with drought developing over central and southern Brazil due to the late onset of a weak rainy season in the region.

Seven intense heatwaves were observed in Brazil in 2025 (INMET; Marengo et al. 2026a,b). In Murtinho, Mato Grosso do Sul, near the border with Paraguay, the temperature reached 42.1°C on 20 January, surpassing the previous record of 41.8°C set several days earlier on 10 January. Quaraí in Rio Grande do Sul state in southern Brazil reached

43.8°C on 4 February, the highest temperature on record in the state since the beginning of the twentieth century. Rio de Janeiro reached 44°C on 17 February, its highest temperature in at least a decade; more than 3000 emergency room visits related to heat stress were reported. In July, the highest monthly temperature was recorded in Caxias, Maranhão State, at 41.6°C, surpassing the previous record by nearly 4°C (INMET). Near the Brazil border, Puerto Suárez, Bolivia, recorded a temperature of 39.8°C in August, one of the highest on record for that month in the country (SENAMHI-Bolivia).

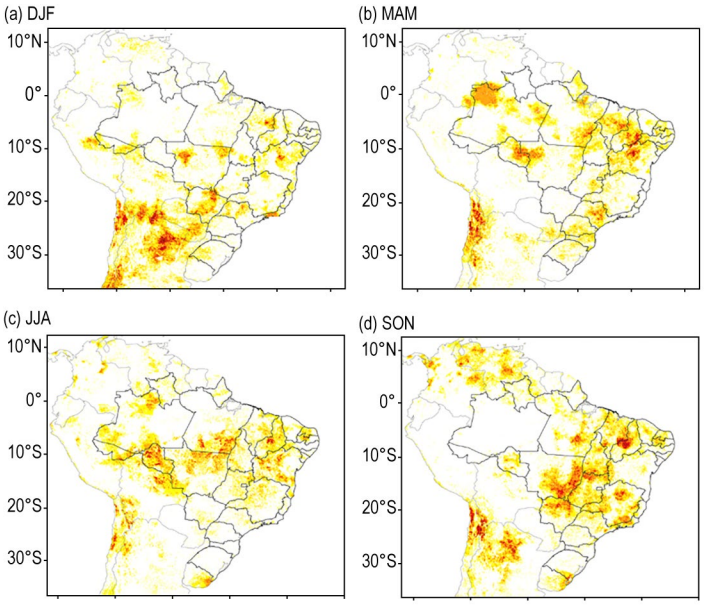

Fig. 7.17. Integrated Drought Index (IDI) maps for central South America during austral (a) summer (Dec–Feb; DJF) 2024/25, (b) autumn (Mar–May; MAM) 2025, (c) winter (Jun–Aug; JJA) 2025, and (d) spring (Sep–Nov; SON) 2025. (Source: National Center for Natural Disaster Monitoring and Alerts [CEMADEN].)

In late May, Peru, Brazil, Bolivia, and Paraguay experienced a severe cold wave, resulting in sharp temperature drops, frost, and snow in the mountainous areas of southern and southeastern Brazil. São Paulo recorded its lowest daily temperature of the year, 12.4°C, very early in the winter season on 29 May. In late June, a cold air mass lowered temperatures by several degrees across parts eastern Paraguay. Bolivia also saw notable cold conditions in austral winter 2025, particularly in the Andean highlands. In La Paz, temperatures dropped to –8.5°C in June (the mean June temperature is –1°C; SENAMHI-Bolivia). Overall in 2025, Peru experienced more friajes (local name for cold-air outbreaks) than usual, with more than 25 recorded, well above the typical annual average of approximately 18 (SENAMHI-Peru).

On 7 November, an intense series of tornadoes struck southern Brazil. Notably, an EF-4 tornado in Rio Bonito do Iguaçu (Paraná State)—one of the strongest on record in the country—generated winds of 340 km hr^{-1}. This event caused seven fatalities, hundreds of injuries, and extensive material damage (G1 2025).

3. SOUTHERN SOUTH AMERICA

—L. S. Aldeco, J. L. Stella, G. Jadra, and A. J. Reyes Kohler

This section includes Argentina, Chile, and Uruguay. Throughout this section, 1991–2020 is the base period used for both temperature and precipitation.

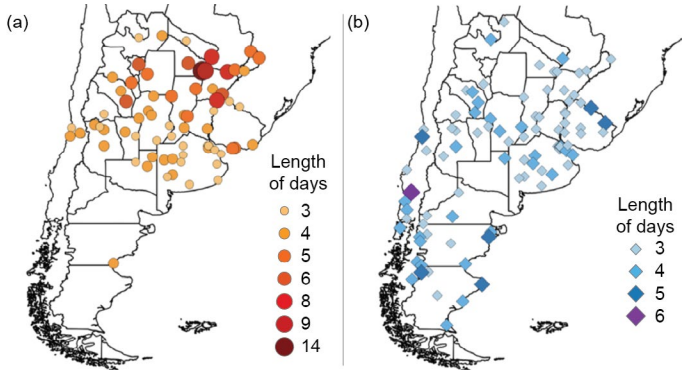

Fig. 7.18. (a) Heatwave duration from 19 Feb to 8 Mar 2025 and (b) cold wave duration from 27 Jun to 4 Jul 2025 in southern South America. (Source: National Meteorological Service of Argentina.)

(i) Temperature

Annual mean temperatures in Uruguay, northeastern Argentina, northern Chile, and southern Patagonia were close to average (±0.5°C) for 2025, while above-normal annual temperatures were observed over much of Argentina and central Chile. Overall, however, nationally averaged annual anomalies varied across the three countries: Argentina recorded its second-warmest year on record with an anomaly of +0.6°C, Uruguay was closer to normal with an anomaly of +0.26°C, and Chile observed its seventh-coolest year on record, with an anomaly of –0.4°C.

Austral summer 2024/25 was extremely warm over most of central and northern Argentina and central Chile. Two intense heatwaves developed during this period: the first between late January and mid-February and the second between mid-February and early March, affecting areas north of 40°S (Fig. 7.18a). Several daily maximum temperatures records were broken during

these episodes: at Santiago-Tobalaba (36.1°C on 8 February), La Rioja (45.0°C on 10 February), Salto (42.1°C on 10 February), Artigas (41.9°C on 11 February), and Córdoba Observatory (42.2°C on 24 February). Argentina recorded its warmest February since the start of its record in 1961.

Temperatures were near normal over most of the region during austral autumn and were characterized by subseasonal variability and synoptic forcings. Only parts of northern Argentina recorded positive anomalies above +1°C.

Winter was colder than normal in Uruguay and northeast Argentina and warmer than normal across Chilean and Argentinian Patagonia. The rest of the region experienced a near-normal winter. Between the end of June and beginning of July, a cold wave impacted most of southern South America (Fig. 7.18b) as a polar air mass gradually moved northward from the extreme south, covering the entire continent and producing a significant temperature drop accompanied by snow in several areas, even in places where it is unusual. Extreme low minimum temperatures in some locations led to new records on 30 June: Chile (–9.3°C in Chillán; –7.9°C in Temuco;) and Argentina (–12.7°C in Villa Reynolds; –8.4°C in Villa Dolores). In addition, extreme low maximum temperatures of 3°C–8°C were recorded during 29–30 June across central Argentina and Uruguay, also setting new low records in some locations.

Austral spring was warmer than normal across most of Chile and central and southern Argentina, with seasonal anomalies between +0.5°C and +2.0°C. Valdivia and Puerto Montt in Chile, and El Bolsón and Esquel in Argentina, each recorded their warmest spring since 1961. Northeastern Argentina and Uruguay, on average, had near-normal temperatures with significant subseasonal variability.

(ii) Precipitation

During 2025, below-normal annual rainfall was observed in Uruguay, northeast Argentina, and Patagonia of Chile and Argentina, while central-east and northeast Argentina saw above-normal annual rainfall. Central and north Patagonia of Chile and Argentina, as well as southern Uruguay recorded below-normal rainfall during most of the year, leading to different levels of drought.

During austral summer 2024/25, deficits of about 40%–80% below normal were recorded in northern Argentina, Patagonia of Argentina and Chile, and northern and southern Uruguay; in Argentina, La Quiaca recorded its lowest summer precipitation since 1966. In Uruguay, some stations recorded monthly rainfall about 10% of normal during December 2024 and January 2025: Laureles, in northern Uruguay, received its lowest precipitation total for January since 1980. Patagonia of Chile and Argentina recorded deficits of less than 20% of normal for the season. On the other hand, some monthly excesses were recorded in Uruguay during February: Quintana and Chapicuy in northwestern Uruguay received their highest rainfall totals for February in the record dating to 1980.

During autumn, frontal activity favored above-normal rainfall in east-central, northern Argentina and southern Uruguay (20%–60% of normal). A stationary front led to heavy precipitation in central Argentina during 15–18 May, with floods and new seasonal rainfall records set for Bahía Blanca and Junín. Deficits (20%–40% of normal) were recorded in central and north Patagonia of Chile and Argentina.

During austral winter, most of Patagonia of Chile and Argentina and eastern Uruguay had rainfall 20%–60% of normal. In Patagonia, El Bolsón and Esquel recorded their lowest seasonal precipitation since 1961. In central Chile, most of the deficit occurred during June and August, where several stations observed their third- or fourth-lowest precipitation total on record for the month. Conversely, central Argentina received more than twice its normal rainfall total: Marcos Juárez and Bolívar set new records for highest seasonal rainfall since 1961.

During spring, most of Uruguay, central Chile, and some parts of northern Argentina had below-normal rainfall. North Patagonia of Chile had the most deficits during November: Chillán set a new monthly record for the lowest rainfall since 1966. In Uruguay, rainfall of less than 60% of normal was recorded in Rocha and Treinta y Tres, the fourth-lowest precipitation total for spring since 1980 for both stations. However, above-normal precipitation was recorded in central and northeastern Argentina, with some stations setting new daily records: Laboulaye received 100.3 mm on 4 October, setting its highest daily rainfall record for this month since

1961. Central Patagonia of Chile and Argentina also had above-normal rainfall, mainly during September and October.

(iii) Notable events and impacts

Figure 7.19 shows numerous notable events that occurred across the region during 2025. Some of these events are discussed in more detail below.

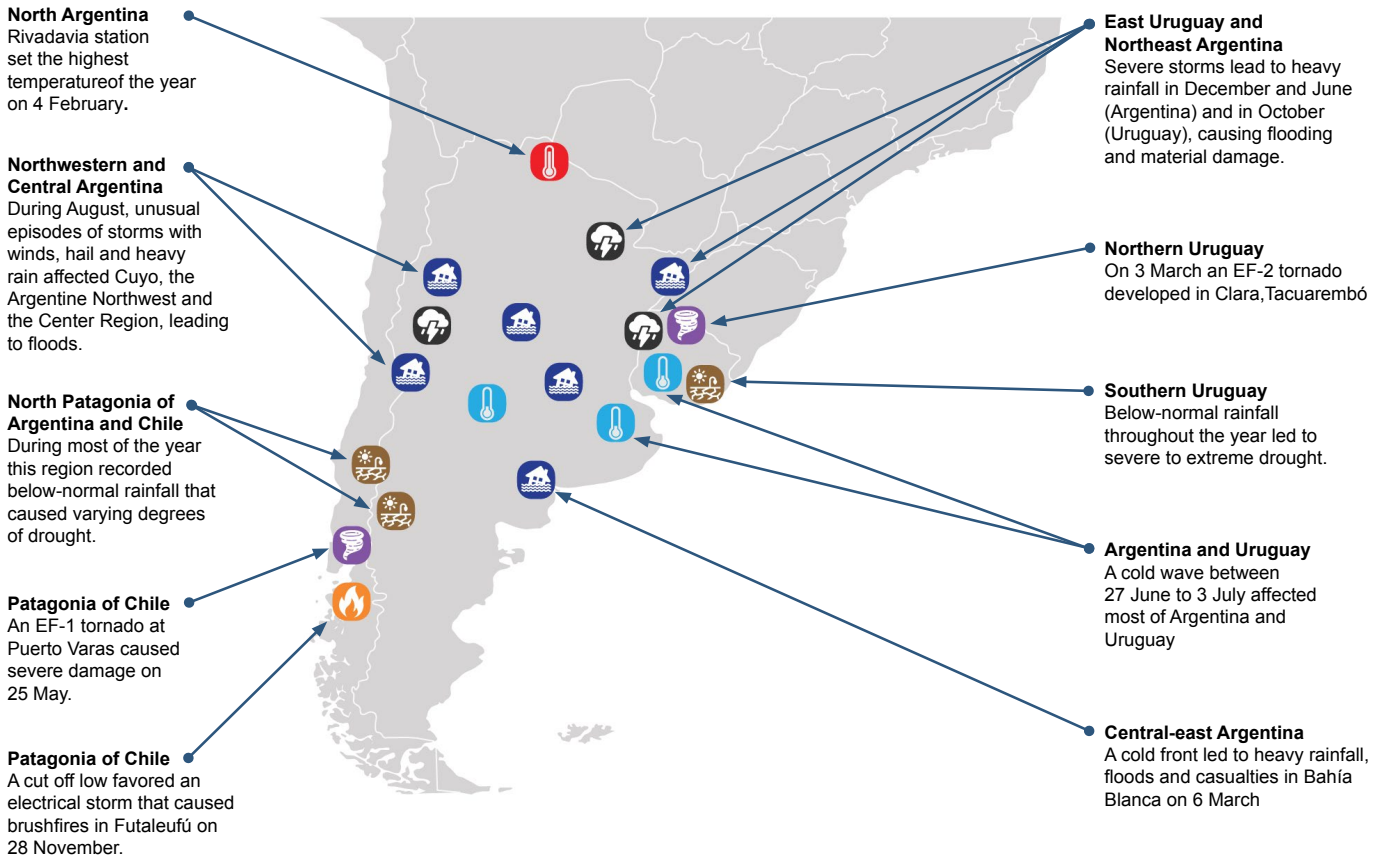

Fig. 7.19. Major extreme events for southern South America during 2025. (Sources: National Meteorological Service of Argentina [SMN], Uruguayan Institute of Meteorology [INUMET], and Meteorological Directorate of Chile [DMC].)

Some areas of southern South America experienced drought; the most affected regions were Patagonia of Chile and Argentina, as well as southern Uruguay. In southern Uruguay, deficits were recorded throughout the year, while in the Patagonia region, the driest season was austral winter. This led to moderate and extreme drought conditions, according to the U.S. Drought Monitor Standardized Precipitation Index classification (McKee et al. 1993). The drought impacted agriculture and livestock sectors and possibly contributed to the bushfires that took place in Patagonia a few months later.

In Bahía Blanca, Argentina, a cold front favored severe convection, and 209.5 mm of precipitation fell on 6 March, the highest daily total for this month since 1956. Bahía Blanca accumulated 290 mm in 12 hours and 312 mm between 4 and 8 March. This exceptional event, with a maximum rainfall intensity of 25 mm hr^{-1}, has a return period of more than 100 years.

In Paysandú, Uruguay, a severe storm on 6 October caused strong winds of up to 152 km hr^{-1}, with material damage to roofs and trees reported.

On 25 May, a tornado—classified as an EF-1 on the enhanced Fujita scale—affected the urban area of Puerto Varas city in Chilean Patagonia, causing falling trees, power outages, and roofs blown off of houses and buildings.

Sidebar 7.3: **The late December 2025 heatwave in southeastern Brazil**

—J. A. MARENGO, J. C. ESPINOZA, J. C. JIMÉNEZ-MUÑOZ, M. CALIM-COSTA, AND J. P. SIERRA

Heatwaves are natural phenomena that are intensifying due to climate change. Drivers of HWs are typically associated with large-scale patterns in the atmosphere and can involve complex interactions among atmospheric, oceanic, and land-surface conditions (Marengo et al. 2025, 2026a,b). Extended periods of extreme heat harm human health (Ebi et al. 2021) and increase the risk of fires in major ecosystems (Marengo et al. 2025). The three warmest years on record globally—2024, 2023, and 2025 (see section 2b1 for details)—also recorded the highest number of heatwaves (defined following the World Meteorological Organization criterion [Marengo et al. 2025]) in Brazil since 1980: 10, 8, and 7, respectively, according to INMET. Notably, this increase corresponds with a rise in the frequency and total number of HW days during El Niño years.

One of the impactful heatwaves of 2025 occurred during 22–30 December in the southeastern region of Brazil (along with northeastern Argentina and southern Brazil). The heatwave was caused by an atmospheric blocking pattern, a situation in which persistent high-pressure systems prevent weather systems from moving, resulting in reduced rainfall (Fig. SB7.5a) and clear skies over several days as shown by positive 850-hPa height and anticyclonic wind anomalies (Fig. SB7.5b). The combination of strong insolation and warm, dry air kept daytime temperatures high and nights warm (SB7.6a), especially in large urban centers such as São Paulo and Rio de Janeiro. Figures SB7.6b,c display time series of the daily maximum (Tmax) and minimum (Tmin) temperatures (Marengo et al. 2025) for Rio de Janeiro and São Paulo, respectively, in 2025. As highlighted by the green box, this December HW was more intense but shorter in duration those that occurred early in the year (January–March). According to INMET, São Paulo recorded a new monthly maximum temperature record of 37.2°C at the Mirante de Santana station in the northern part of the city on 28 December, breaking a

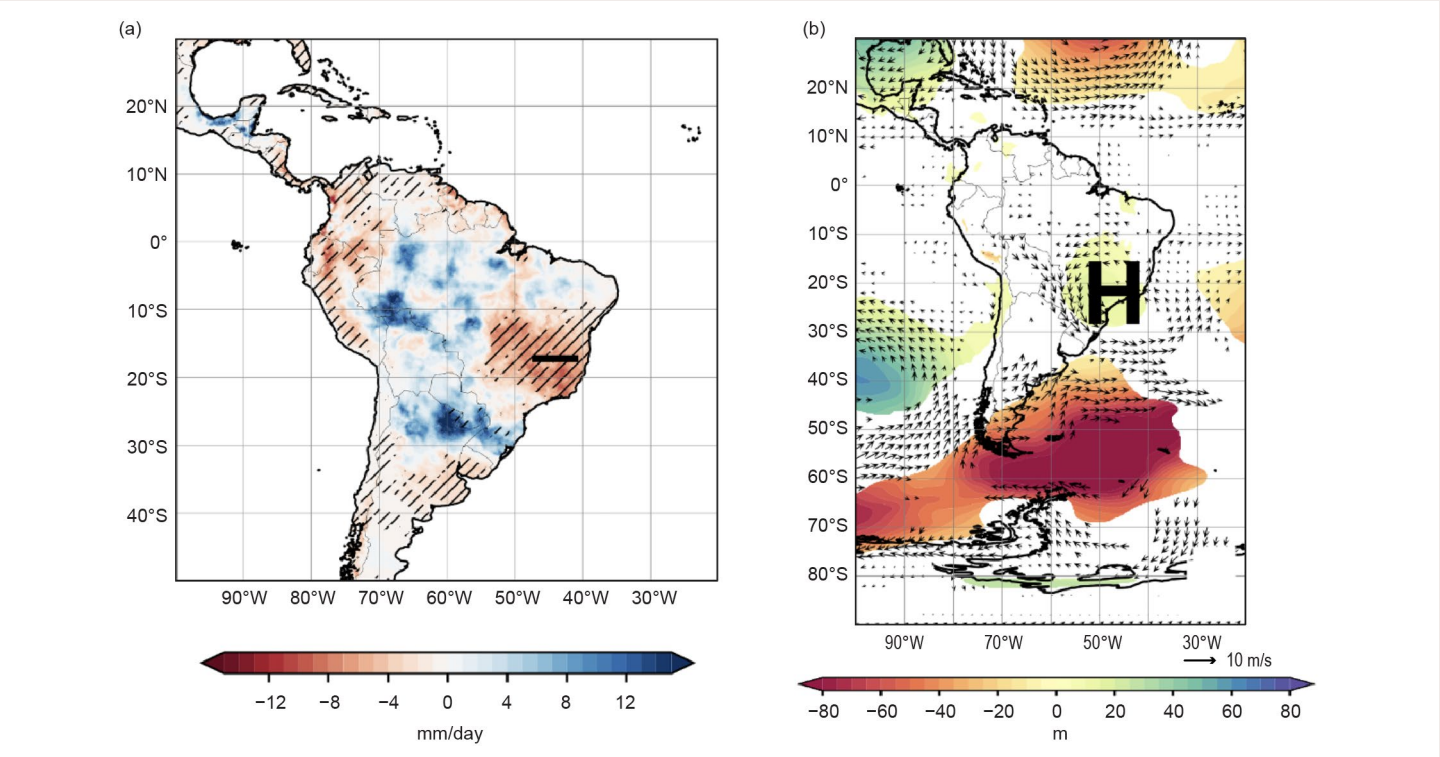

Fig. SB7.5. (a) Precipitation anomalies (mm day^{-1}) during the heatwave episode of 22–30 Dec 2025. Statistically significant anomalies (at the 95% confidence level using a two-tailed t-test) are highlighted in shaded areas. (b) The reference period is 1991–2020. Only statistically significant anomalies are shown. H denotes anticyclonic anomaly. (Source: Precipitation data are from Climate Hazards Group InfraRed Precipitation with station data; 850-hPa wind data are from ERA5.)

64-year record. On 25 December, the city of Rio de Janeiro reached a historic high of 40.1°C. These local data points exemplify the severity and spatial extent of HWs during this period.

During this event, INMET issued red (high danger) and orange (severe) heatwave alerts across several states, especially in southeastern and west-central Brazil, including São Paulo, Rio de Janeiro, Minas Gerais, Espírito Santo, Goiás, and Mato Grosso do Sul. These states have the largest populations at risk for heat stress, with about 150 million residents.

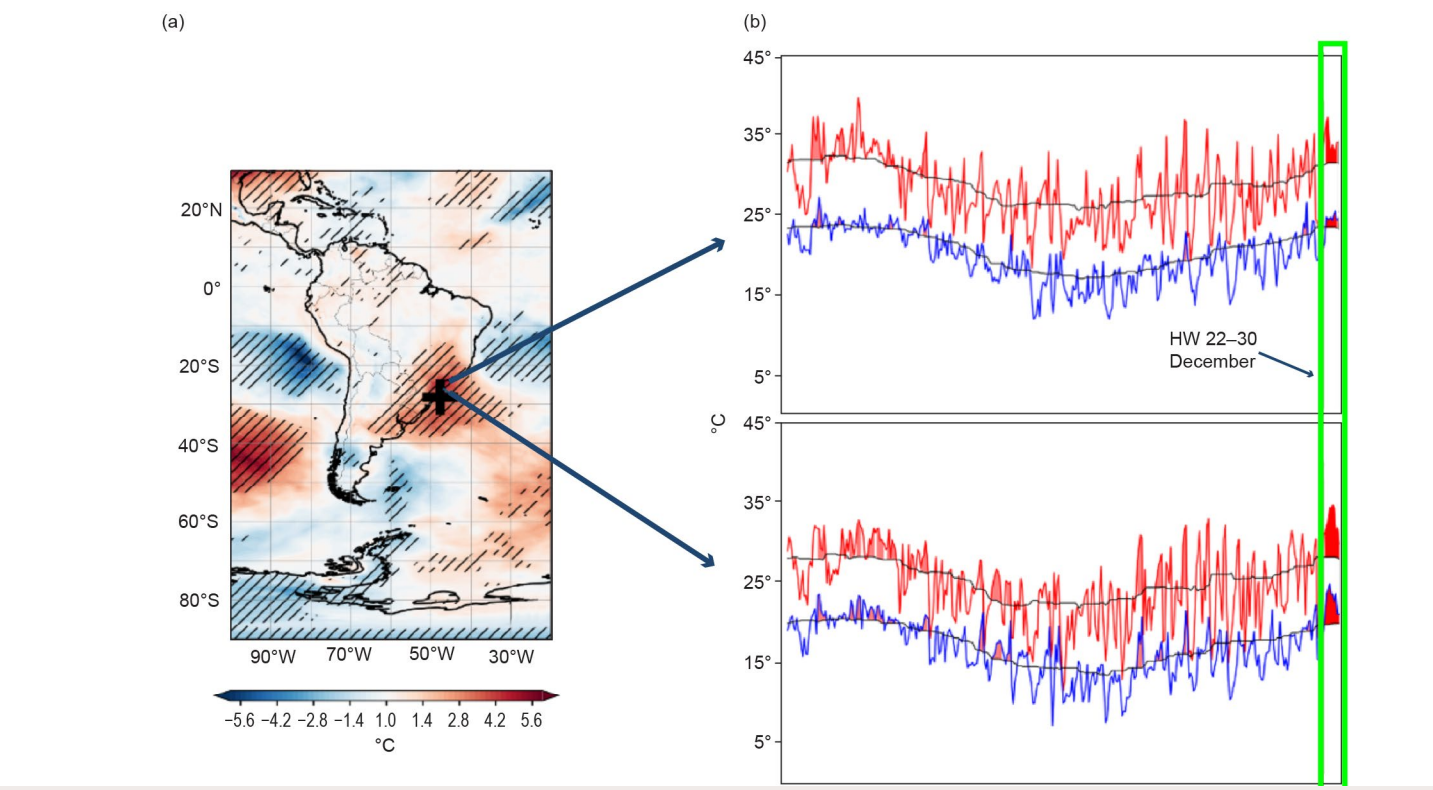

Fig. SB7.6. (a) 850-hPa temperature anomalies (°C) for the period 22–30 Dec 2025 in South America. Statistically significant anomalies (at the 95% confidence level using a two-tailed t-test) are highlighted in shaded areas. Panels (b) and (c) show time series for maximum (red lines) and minimum (blue lines) temperatures in Rio de Janeiro and São Paulo from 1 Jan to 31 Dec 2025. Values are compared to the 1991–2020 mean (represented by the black lines). (Source: 850-hPa temperature data are from ERA5; maximum and minimum temperature data are from the NOAA Climate Prediction Center temperature dataset.)

e. Africa

—Z. Segele, Ed.

1. OVERVIEW

The 2025 analysis for Africa uses rainfall data from the Global Precipitation Climatology Project (GPCP), temperature from the National Centers for Environmental Prediction (NCEP)/ National Center for Atmospheric Research (NCAR) reanalysis, and local observations from a number of meteorological and hydrological services in northern Africa, South Africa, and western Indian Ocean island countries. Notable events were compiled based on reports from government agencies, regional and international organizations, and research and early warning institutions. The climatological base period is 1991–2020, as recommended by the World Meteorological Organization (https://www.ncei.noaa.gov/products/wmo-climate-normals), and the terms "normal" and "average" are used interchangeably to refer to this climatology. Unless otherwise stated, seasons are discussed in terms of typical meteorological seasons: December 2024–February 2025; March–May 2025; June–August 2025; and September–November 2025. Both boreal and austral seasons are discussed in this section.

2. NORTHERN AFRICA

—K. Kabidi, M. ElKharrim, S. Hakmi, and A. E. Mostafa

The northern Africa subregion covers Mauritania, Morocco, Algeria, Tunisia, Libya, and Egypt. The region exhibits two distinct climates. The northern sector is characterized by a Mediterranean climate, while the southern sector features arid and semi-arid climates.

(i) Temperature

Annual mean temperatures in 2025 ranged from 18°C to 22°C in Libya and across the northern coastal belt bordering the Mediterranean Sea, while warmer conditions (>24°C) prevailed over Mauritania, southwestern Algeria, and southern Egypt. Annual mean temperature anomalies (Fig. 7.20a) exceeded +1.5°C across northern Mauritania, central Morocco, and western Algeria due to above-average maximum and minimum temperatures throughout most of the year. Except for western Egypt and eastern Libya, warm anomalies (>+0.5°C) covered the remaining parts of the region. Monthly anomalies (not shown) exceeded +3°C in southern Egypt in January, over Mauritania, Algeria, Tunisia, and western Libya in March, and over northern Mauritania, Morocco, and western Algeria in June and October.

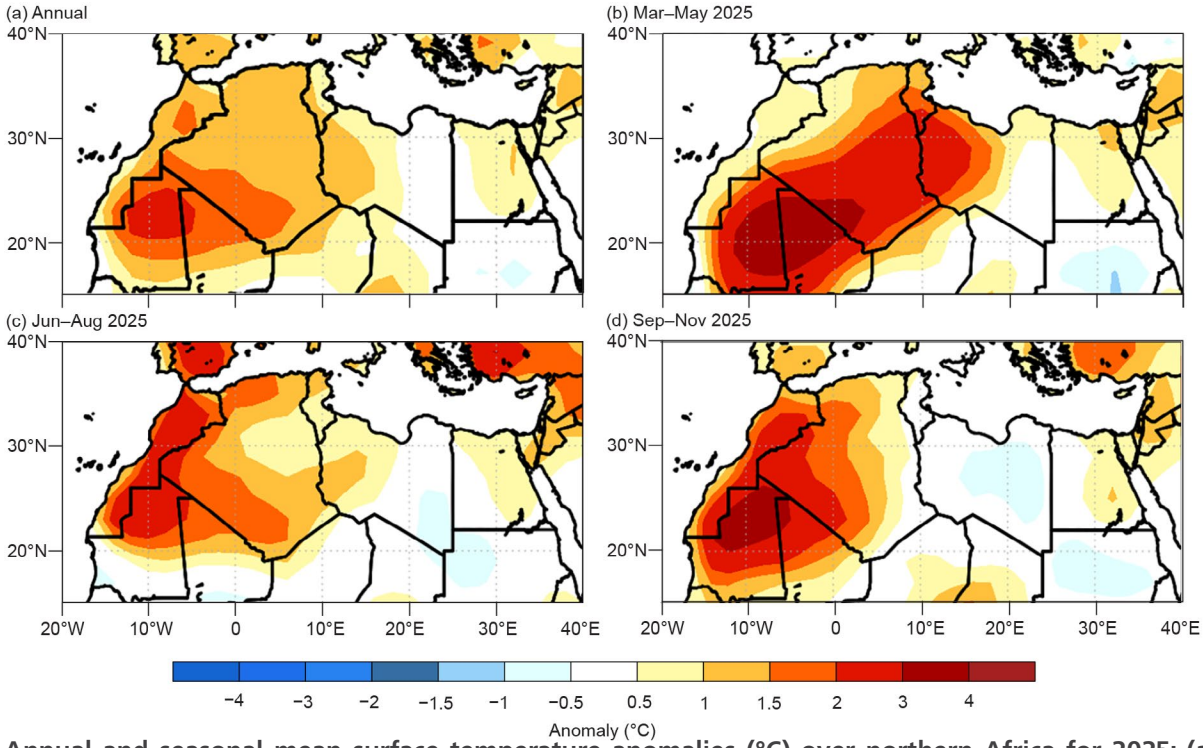

Fig. 7.20. Annual and seasonal mean surface temperature anomalies (°C) over northern Africa for 2025: (a) Annual, (b) Mar–May, (c) Jun–Aug, and (d) Sep–Nov. Anomalies are with respect to the 1991–2020 base period. (Source: NOAA/ National Centers for Environmental Prediction [NCEP].)

In winter (December 2024–February 2025; DJF; not shown), mean temperatures were above average by 1.0°C in parts of Morocco, northern Algeria, western Libya, and Egypt as a result of higher temperatures in January. For Egypt and Libya, maximum and minimum temperatures were 2.5°C and 4.0°C above average, respectively, and both were above the 90th percentile in January. Despite below-average temperatures in February and partially in December over Egypt, above-average temperatures in January led to a warmer-than-average DJF. Likewise, the national average surface temperature was 0.9°C above average in Morocco.

In spring 2025 (March–May; MAM), a ridge of warm temperatures extended across Algeria, Mauritania, and Mali. Temperature anomalies exceeded +2.0°C across most of Mauritania, northern Mali, Algeria, southern Tunisia, and western Libya (Fig. 7.20b). Although all three months were warmer than average, mean temperature anomalies were largest (>+3.0°C) and widespread in March due to high (+1.5°C to +3.0°C) above-average maximum temperatures and substantial (>+5°C) above-average minimum temperatures. In addition, minimum temperatures for MAM were above average by 3°C to 5°C and topped the 90th percentile across the region extending from Mauritania to Libya.

Mean temperatures (not shown) during summer 2025 (June–August; JJA) varied from 24°C in coastal areas to more than 36°C inland in northern Mauritania, northern Mali, and western Algeria. Summer temperatures were above average (>+0.5°C) across the region, excluding parts of western Egypt and eastern Libya (Fig. 7.20c). The largest seasonal anomaly of +2°C was concentrated in western parts of the subregion extending from Morocco to northern Mauritania and northwestern Mali. According to analysis of stations observations, the national average temperature for Morocco was 1.13°C above average and was the sixth warmest in the record dating to 1981. Similarly, stations in northern Egypt recorded temperatures that were 4.7°C above average. For Morocco, June 2025 was the third-warmest such month, registering a national average anomaly of +1.66°C. In addition, record temperatures were set at a number of cities in Morocco (e.g., Casablanca in June and Tangier and Laayoune in August). Overall, mean summer and June 2025 temperatures were above the 90th percentile for northern Morocco and western Mauritania (not shown).

During autumn (September–November; SON), mean temperatures (not shown) of more than 26°C were observed in southern Morocco, Mauritania, Mali, and southern Egypt, while northern Morocco, northern Algeria, and most of Libya recorded mean temperatures below 22°C. Temperatures were above average over western parts of northern Africa, where large positive anomalies exceeding +1.5°C dominated in Morocco, Mauritania, northern Mali, and western Algeria (Fig. 7.20d). Temperatures in these areas were above the 90th percentile due to higher maximum and above-average minimum temperatures in October and November 2025. Weaker but positive mean temperature anomalies also were observed in southeastern Egypt.

(ii) Precipitation

Annual precipitation for 2025 exceeded 100 mm in Morocco, northern Algeria, Tunisia, coasts of Libya and Egypt, and southern Mauritania (not shown). Coastal areas of Morocco, Algeria, and Tunisia, and southern Mauritania received the highest precipitation totals of more than 300 mm, but only northwestern Moroccan coast and southern Mauritania received above-average precipitation. The discussion below focuses on seasonal precipitation for December 2024 to November 2025 (Fig. 7.21).

Winter precipitation (DJF) was below average in Morocco, northern Algeria, along the northeastern Libyan coast, and northeastern Egypt, but above average in eastern Tunisia and northwestern and far eastern Libya (Fig. 7.21a). The highest deficits of up to –150 mm were recorded in northwestern Morocco, much of which was due to below-average precipitation observed in December 2024. Deficits were also large in Sinai and Alexandria in Egypt. According to station observations, winter precipitation was below average by 28.2% in northern Egypt.

In spring (MAM), northern Morocco, northern Algeria, Tunisia, and northwestern Libya received above-average precipitation (Fig. 7.21b). The highest anomalies, exceeding +50 mm, were recorded in northern Morocco, which was caused by heavy rainfall in March. According to station observations, total rainfall in March in Tangier (northern Morocco) was 349 mm, which is more than 50% of the average annual rainfall. Similarly, Chefchaouen in northern Morocco

recorded 318 mm from 7 to 15 March, which represents about a third of the average annual rainfall total. In Tunisia, seasonal precipitation was above average, primarily due to above-average rainfall in May. Kélibia in northeastern Tunisia registered a new May total record of 114 mm, breaking the previous record set in May 2023.

While southern Mauritania receives its main rains during summer, the northern sector of North Africa generally remains dry except for light rainfall in coastal areas of northeastern Algeria and Tunisia. During summer 2025, most of southern Mauritania received above-average rainfall (Fig. 7.21c). Seasonal anomalies were as high as +75 mm in southeastern Mauritania. Rainfall in northeastern Algeria and northern Tunisia was marginally deficient.

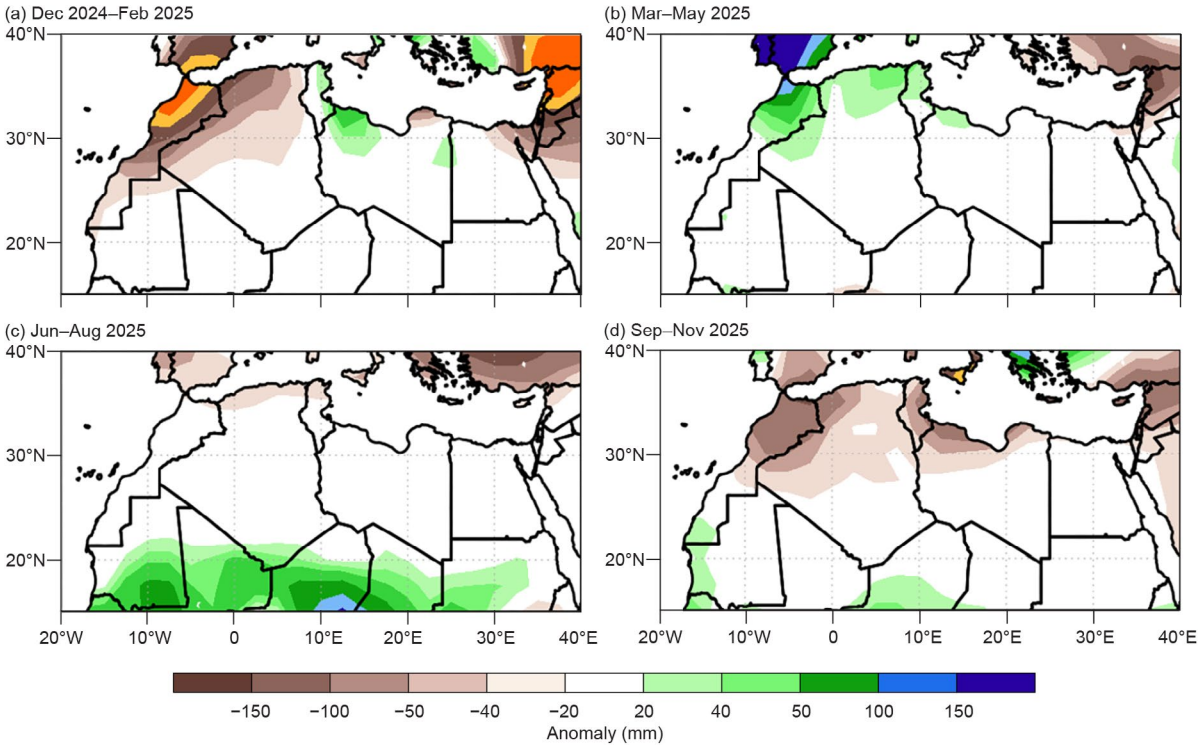

Fig. 7.21. Seasonal precipitation anomalies (mm) over northern Africa: (a) Dec 2024–Feb 2025, (b) Mar–May 2025, (c) Jun–Aug 2025, and (d) Sep–Nov 2025. (Source: Global Precipitation Data Project [GPCP] data via NOAA/National Centers for Environmental Prediction [NCEP].)

During autumn (SON), northern coastal areas of northern Morocco, Algeria, and Tunisia recorded 75 mm–200 mm of precipitation. Rainfall was 10 mm–50 mm below average in Morocco, northern Algeria, Tunisia, and northern Libya, and 10 mm–20 mm above average in western Mauritania (Fig. 7.21d). The below-average rainfall was caused by precipitation deficits in October, although marginally drier conditions were observed in the remaining months

(iii) Notable events and impacts

In May, at least five people died and around a hundred were injured following floods triggered by torrential rains in several regions of Algeria. According to the European Commission's Department for Civil Protection and Humanitarian Aid Operations (ECHO)-Flash reports, heavy rainfall in Mount El Kraâ triggered flash floods in Boussalem town, Tunisia, which led to at least one fatality on 12 October. According to news reports in Egypt, a significant rise in Nile River water levels led to flooding in parts of the Nile Delta. Violent thunderstorms struck the city of Safi in Morocco on 14 December 2025, causing rapid urban flooding and at least 37 fatalities.

In Algeria, 811 fires broke out in 2025 and destroyed ~40,000 hectares of forests in northern and central regions. In Tunisia, wildfires destroyed 4800 hectares of forests. In Egypt, prolonged heatwaves in July and August pushed temperatures above 40°C in many regions, which affected human health and increased wildfire risks.

3. WEST AFRICA

—W. Agyakwah, A. Faye, B. Jha, F. Sima, and W. M. Thiaw

West Africa stretches from the Gulf of Guinea coast in the south to around 20°N in the north, and from the Atlantic Ocean in the west to Niger in the east. It consists of two main parts: the Sahel, which runs between 12°N and 17°N from Senegal and The Gambia in the west to Niger in the east, and the Gulf of Guinea in the south, lying roughly between 4°N and 10°N.

(i) Temperature

In 2025, mean temperatures in West Africa ranged from 22°C to 30°C (Fig. 7.22a), with peaks in Mauritania, Senegal, Mali, Burkina Faso, Nigeria, and Niger. Anomalies in Mauritania reached +2°C to +3°C (Fig. 7.22b). The Gulf of Guinea was 0.5°C to 1.5°C above average, with mean temperatures between 24°C and 26°C. Observed temperatures ranged between the 70th and 97th percentiles across most of West Africa, but exceeded the 97th percentile over northeastern Nigeria (not shown).

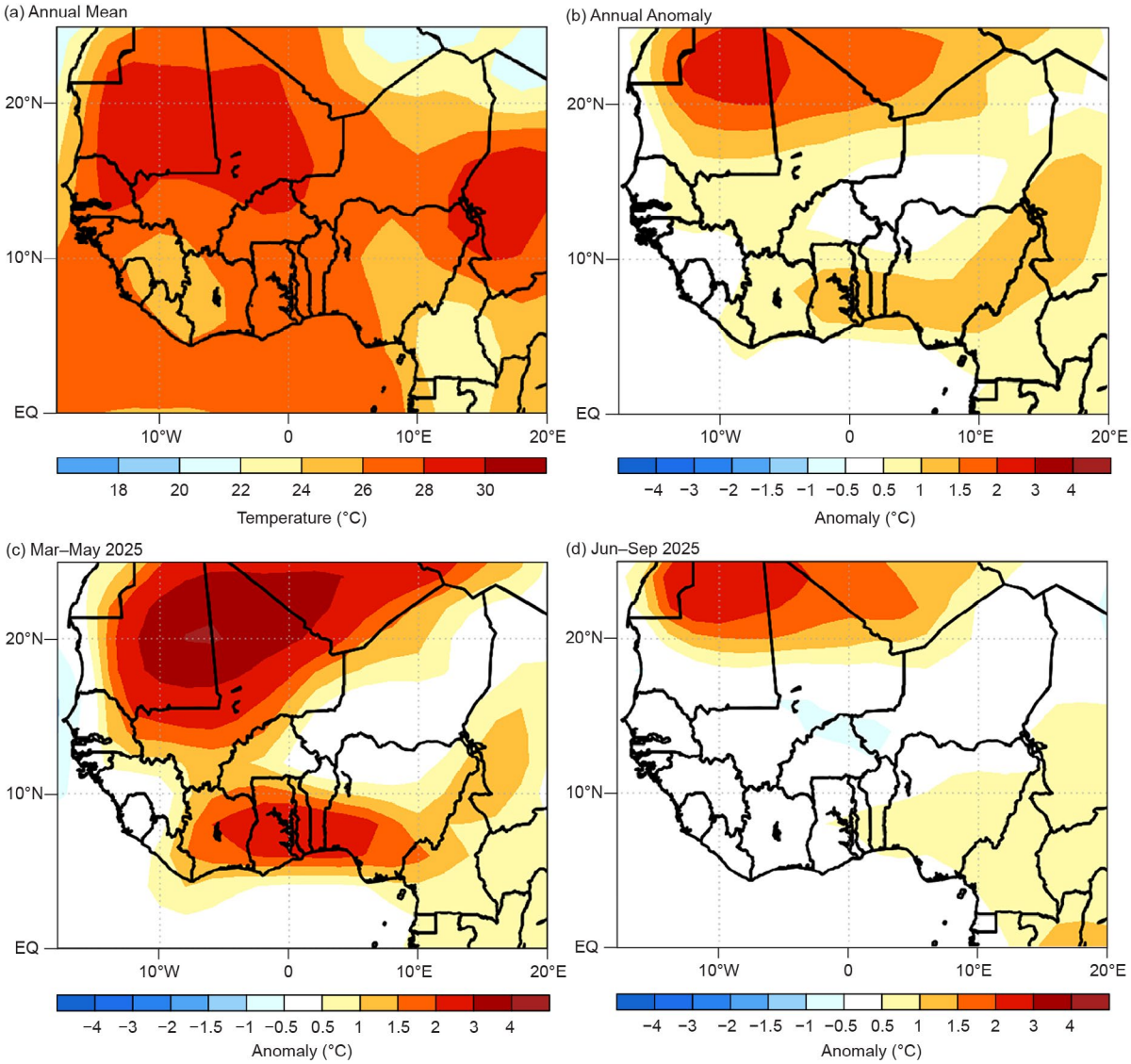

Fig. 7.22. (a) Annual mean temperatures (°C) and (b)–(d) mean temperature anomalies for West Africa in 2025. Anomalies are for (b) annual, (c) Mar–May, and (d) Jun–Sep (°C; 1991–2020 base period). (Source: NOAA/National Centers for Environmental Prediction [NCEP].)

Monthly temperatures varied widely. March–May were the warmest months, with most areas recording 2°C–4°C above-average temperatures that exceeded the 90th percentile in eastern Mauritania, northern Mali, and the Gulf of Guinea countries, including Cote d'Ivoire, Ghana, Togo, Benin, and Nigeria (Fig. 7.22c). On the other hand, mean temperatures were within ±0.5°C

of average across parts of Niger, northern Nigeria, northern Benin, eastern Burkina Faso, Sierra Leone, the Guineas, The Gambia, western Senegal, and coastal Mauritania.

During the monsoon season from June to September, central West Africa and the Gulf of Guinea experienced average or slightly below-average temperatures, while northern areas were 0.5°C–3°C above average (Fig. 7.22d). Following the monsoon season (October–December), surface temperatures remained above average (+0.5°C to +3°C) over much of the region, except in a few areas along the southern coasts of Guinea, Sierra Leone, Liberia, and Cote d'Ivoire, which experienced near-average conditions (not shown).

(ii) Precipitation

In 2025, the West African monsoon was characterized by strong spatial contrasts, with a pronounced north–south dipole pattern. The Sahel experienced a generally favorable and productive rainy season, with annual rainfall totals ranging from 200 mm to 1000 mm (Fig. 7.23a). The observed rainfall was above the 90th percentile in central Niger. In contrast, much of the Gulf of Guinea recorded annual rainfall amounts between 1000 mm and 2000 mm.

Much of the Sahel experienced above-average rainfall, with anomalies of +50 mm to +100 mm covering the western Sahel, including most of Senegal, The Gambia, southeastern Mauritania, southern Mali, and central and southeastern Niger (Fig. 7.23b). This pattern aligns with a multi-year trend of a "recovery of Sahel rainfall" observed in recent decades (Nicholson et al. 2018). While parts of the Gulf of Guinea countries, including Guinea-Bissau, western Guinea,

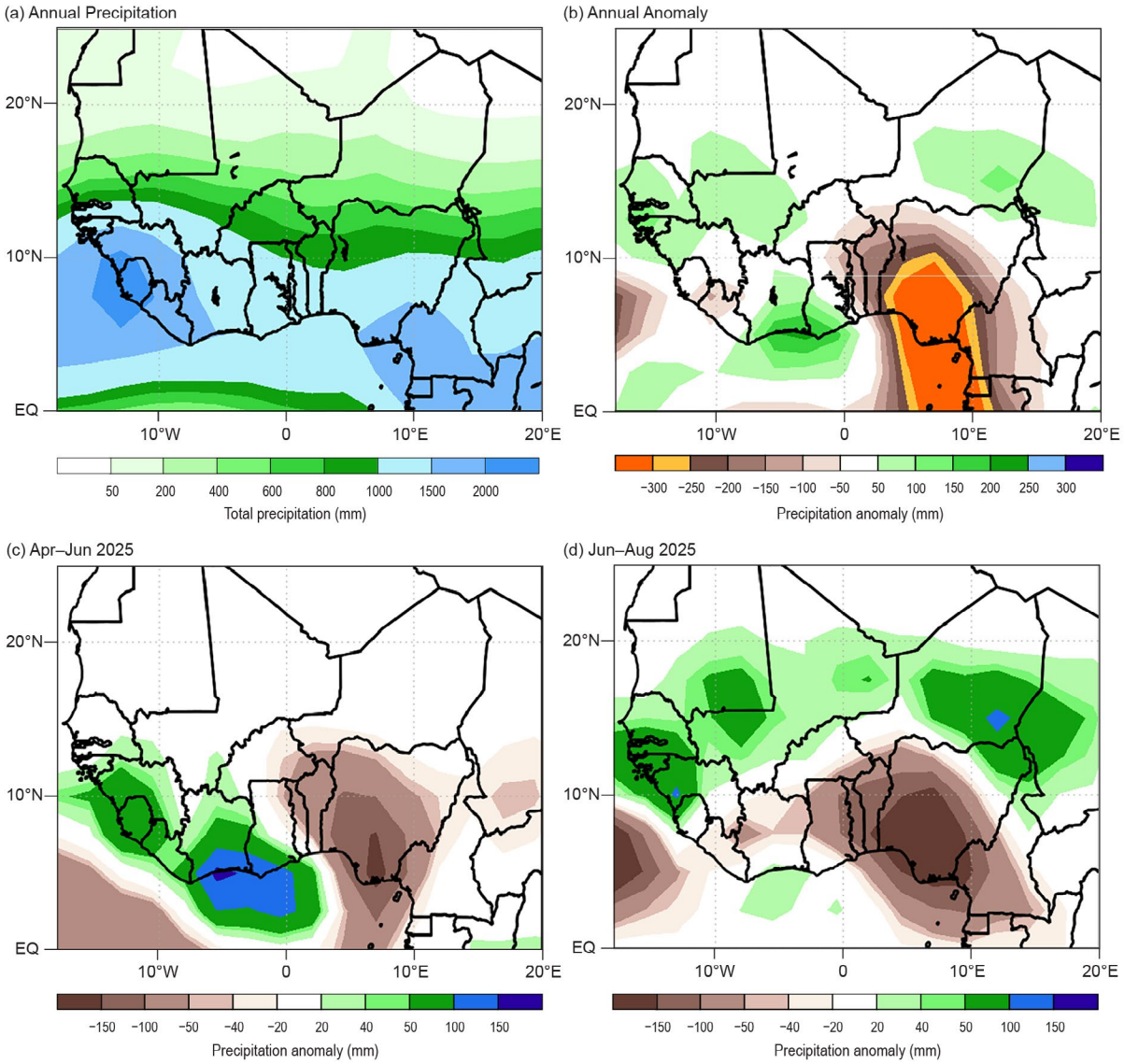

Fig. 7.23. Cumulative annual (a) total precipitation and (b)–(d) precipitation anomalies for West Africa in 2025. Anomalies are for (b) annual, (c) Apr–Jun, and (d) Jun–Aug (mm; 1991–2020 base period). (Source: Global Precipitation Data Project [GPCP] data via NOAA/National Centers for Environmental Prediction [NCEP].)

and southern Cote d'Ivoire and Ghana, recorded above-average rainfall, a large area of the Gulf of Guinea, including eastern Ghana, Togo, Benin, and central and southern Nigeria, recorded annual rainfall totals below the 15th percentile, corresponding to significant deficits of up to –300 mm. In Nigeria, the deficit started in April and accumulated through October, with the largest below-average anomaly of more than –100 mm occurring in August.

During MAM, moderate surpluses appeared in western parts of the Gulf of Guinea, while eastern areas, including most of Nigeria, remained drier than average (not shown). In April–June, deficits widened in Nigeria, Benin, and Togo, but wet conditions grew in the western and central Gulf of Guinea (Fig. 7.23c). By May–July, above-average rainfall spread across the Sahel, including Senegal, Mali, Burkina Faso, and Niger. Eastern Ghana, Togo, Benin, and much of Nigeria continued to face significant deficits (not shown).

During the core monsoon season (June–August), most of the Sahel recorded above-average rainfall (Fig. 7.23d). Seasonal rainfall anomalies exceeded +50 mm in the Guineas, Senegal, and The Gambia, much of Mali, southeast Mauritania, and eastern and central Niger. Parts of the Gulf of Guinea continued to experience drier conditions, with deficits of more than –50 mm and even exceeding –150 mm in central and southern Nigeria.

(iii) Notable events and impacts

West Africa suffered floods and landslides between May and September, mainly in Nigeria. On 28–29 May, flooding in Mokwa caused at least 200 fatalities, destroyed 265 houses, and displaced more than 3000 people, according to the European Commission. Heavy rainfall in June affected Wovi and Garjang, producing additional flooding, casualties, and property damage. Flooding intensified in July, destroying approximately 500 houses in Kabba town in Kogi State. Continued heavy rains in August affected Plateau, Bauchi, and Niger States, while flooding in Ebonyi State resulted in further fatalities. Overflow of the Benue River caused extensive damage across several communities, highlighting the cumulative impacts of persistent seasonal rainfall.

Heavy rain in Senegal caused floods on 14 July in Tambacounda, damaging infrastructure and risking livelihoods. On 15 August, flooding submerged homes in Dakar and Bamba Modou Coura, killing three in Tambacounda. In October, 178 families in eastern Senegal were displaced following water releases from the Manantali dam in Mali and heavy rainfall in the Upper Senegal River Basin, according to ReliefWeb.

In The Gambia, heavy rainfall from 30 August to 8 September destroyed roads and homes and damaged critical infrastructure. The situational report of The Gambia Government through the National Disaster Management Agency (NDMA) indicates that 1321 households were affected and 908 houses were completely destroyed. According to the International Federation of Red Cross and Red Crescent Societies (IFRC), the flooding in The Gambia caused eight deaths, destroyed homes, and displaced over 10,000 people.

During 10–11 August, Tropical Storm Erin brought heavy rains to Cabo Verde, resulting in floods, landslides, and extensive damage, particularly in São Vicente and Santo Antão. Rainfall recorded in just a few hours exceeded the annual average, overwhelming drainage systems and causing widespread damages to homes, infrastructure, and services. According to the IFRC, at least 12 people were killed and over 27,500 people affected.

4. CENTRAL AFRICA

—B. Jha, W. Agyakwah, A. Faye, and W. M. Thiaw

Central Africa has a distinct climate system characterized by a pronounced annual cycle following the north–south migration of the Intertropical Convergence Zone (ITCZ). The region spans a vast area across both the Northern and Southern Hemisphere, and stretches from the southern tip of the Democratic Republic of Congo (DRC) in the south to Chad in the north. Longitudinally, it covers approximately 5°E to 35°E. This analysis specifically examines the subregion that includes Angola, Cameroon, Chad, the Central African Republic (CAR), DRC, Gabon, Equatorial Guinea, the Republic of Congo, and São Tomé and Príncipe.

(i) Temperature

Annual mean temperatures in 2025 ranged from 20°C to 30°C across central Africa. The highest temperatures were observed in Chad, while the lowest were mainly in Angola and

southern DRC (Fig. 7.24a). Annual mean temperatures were above average by 0.5°C–1.5°C across most of the region, but anomalies were within ±0.5°C of average in Angola and southern DRC (Fig. 7.24b). The largest anomalies, exceeding +1.0°C, were limited to isolated areas in western DRC and northern Chad. While the positive anomalies in western DRC were primarily due to a significant increase in maximum temperatures, the positive anomalies in northern Chad resulted from both above-average minimum and maximum temperatures.

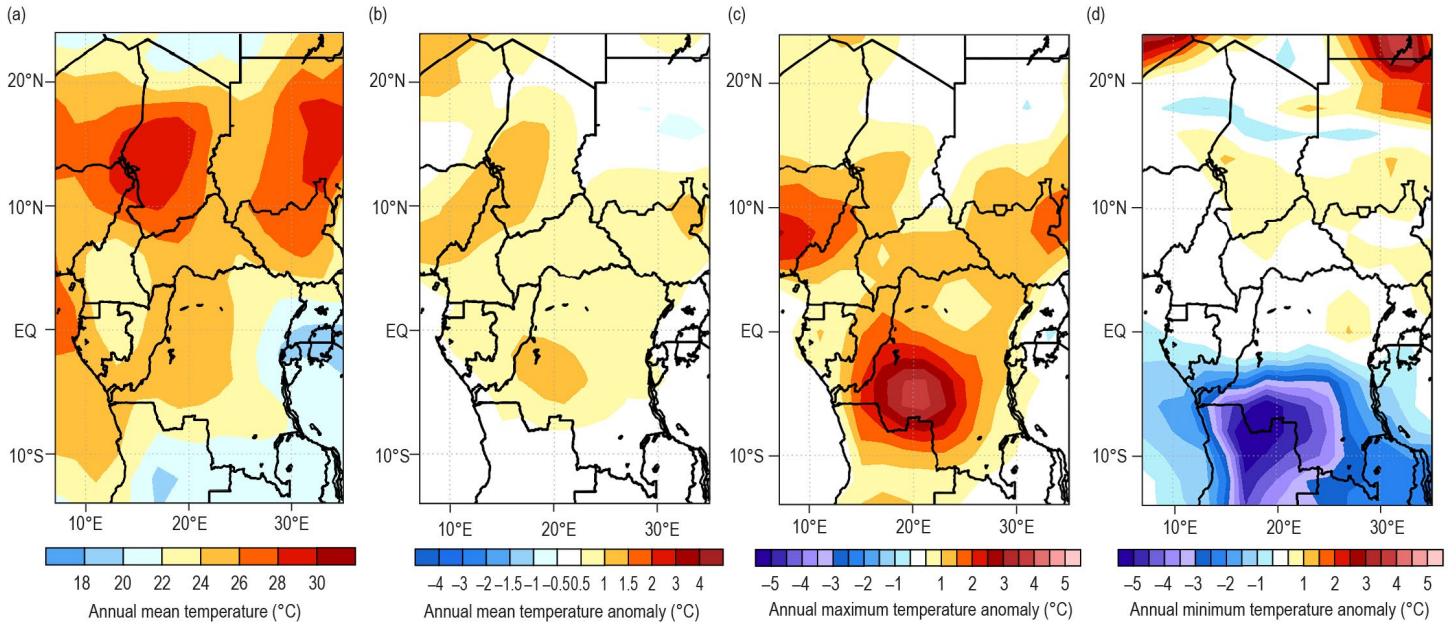

Fig. 7.24. (a) Annual mean temperatures, (b) annual mean temperature anomalies, (c) annual maximum temperature anomalies, and (d) Aug minimum temperature anomalies (°C; 1991–2020 base period) for central Africa in 2025. (Source: NOAA/National Centers for Environmental Prediction [NCEP].)

Throughout 2025, monthly mean temperature consistently stayed 0.5°C–4°C above average over most of central Africa, excluding southern DRC and Angola (not shown). The year began with mild anomalies in January over northern DRC, Congo, Gabon, Cameroon, and parts of Chad. While positive anomalies strengthened and expanded during February and March and persisted in parts of CAR through June, monthly mean temperature anomalies weakened over central DRC from April to May.

In the second half of the year, mean temperature anomalies reached +4°C in DRC as maximum temperatures topped 36°C from June to October and exceeded their long-term averages by more than 5°C (Fig. 7.24c). These above-average conditions shifted southward during September and October, as southern DRC and northern Angola also saw above-normal temperatures. In contrast to the large positive anomaly over the DRC, a pronounced center of negative temperature anomalies developed over Angola, primarily driven by a substantial drop in minimum temperatures in July and August 2025 (Fig. 7.24d). By November and December, the southern half of the region cooled relative to previous months, with temperatures across central Africa returning to near normal.

Monthly mean surface temperatures generally exceeded the 70th percentile throughout the year. The primary exception occurred during July and August, when temperatures fell below the 30th percentile in the southern DRC, Congo, Equatorial Guinea, Gabon, and Angola. From January to June and September to December, much of the region consistently experienced temperatures above the 70th percentile.

(ii) Precipitation

The main factor influencing rainfall seasonality in central Africa is the north–south migration of the ITCZ. Annual rainfall varies between 1000 mm and 2000 mm, with the highest amounts in southern and central Cameroon, Equatorial Guinea, parts of Gabon, CAR, much of the Republic of Congo, and northern and central DRC (Fig. 7.25a). Most regions experienced near-average rainfall, but areas in Cameroon, Equatorial Guinea, and Gabon faced significant

deficits exceeding –300 mm, especially in western regions. Conversely, west-central DRC saw above-average rainfall of +50 mm to +100 mm (Fig. 7.25b).

Inspection of the monthly progression shows that rainfall typically spreads to the southernmost parts of Central Africa during January–April and November–December and reaches the northernmost parts of the region during June–September. During January–March 2025 (Fig. 7.25c), rainfall was below average by as much as –100 mm over Gabon, western Congo, and Equatorial Guinea, slightly above average in parts of Angola and western DRC, and near average in most parts of DRC. Rainfall pushed northward in April and May, creating surpluses of +20 mm to +50 mm in southern and western DRC, later spreading to other regions and neighboring countries. By June, surpluses were concentrated in west-central areas, especially western DRC, eastern Gabon, and southeastern Cameroon. July saw larger surpluses of +50 mm to +100 mm over northern Cameroon, western CAR, and southern Chad (Fig. 7.25d). In August, northwestern DRC, western CAR, northern parts of Congo and Gabon, Equatorial Guinea, and Cameroon received deficient rainfall that ranked below the 15th percentile. Some pockets in north-central and eastern DRC, and parts of CAR, observed near-average or slightly above-normal rainfall. In October, widespread deficits occurred across much of central Africa, with some areas receiving rainfall totals below the third percentile.

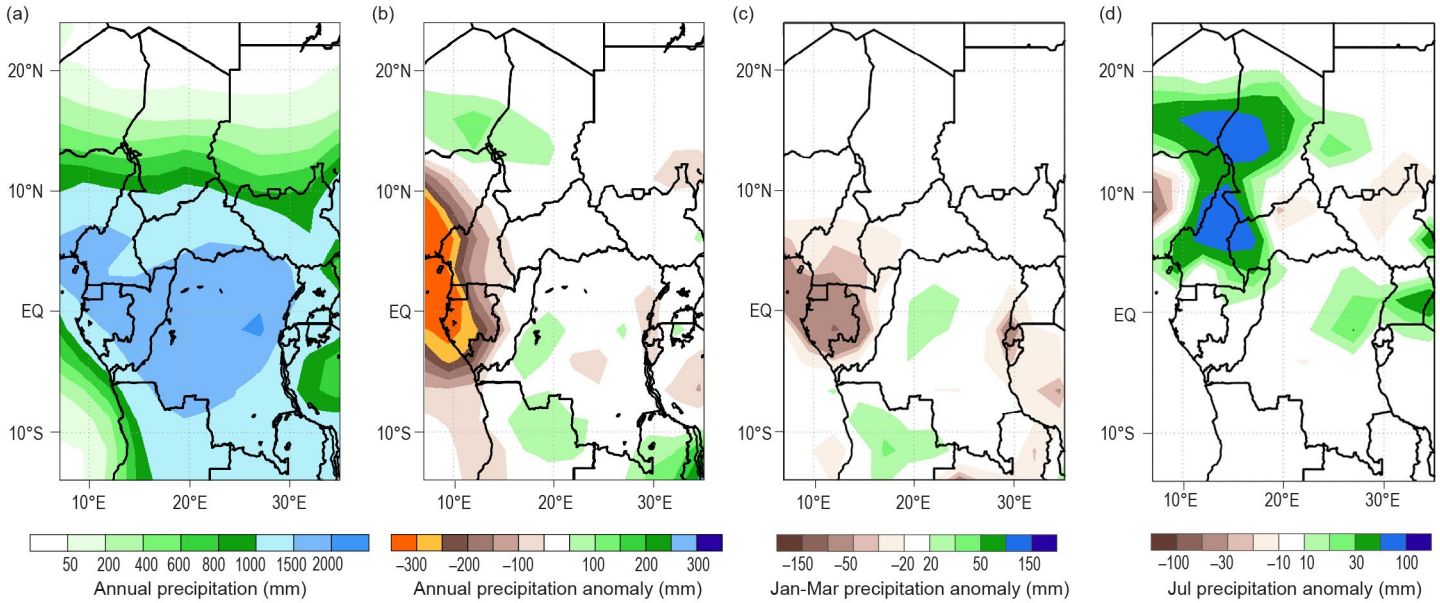

Fig. 7.25. Cumulative annual (a) total precipitation and (b)–(d) precipitation anomalies for central Africa in 2025. Anomalies are for (b) annual, (c) Jan–Mar, and (d) Jul (mm; 1991–2020 base period). (Source: Global Precipitation Data Project [GPCP]data via NOAA/National Centers for Environmental Prediction [NCEP].)

(iii) Notable events and impacts

Persistent river overflows and landslides were reported in the DRC and neighboring states. In the DRC, several disasters occurred throughout the year, as reported by ReliefWeb and the European Commission. In April, floods in Kinshasa caused 165 deaths and displaced over 7000; by 15 April, nearly 10,000 residents were displaced due to Rugumba River overflow, especially in Kalemie and Nyunzu. In May, heavy rains near South Kivu led to about 100 fatalities. June floods in Kinshasa caused 30 deaths, 44 injuries, and displaced over 36,000 people. November floods in western DRC affected 99,000 people. Heavy rains in December caused fatalities, injuries, and displacement in Boma.

According to the European Commission, floods along the Logone and Chari Rivers in Chad impacted over 123,000 people by August. In Equatorial Guinea, heavy rain in August caused floods and affected over 23,000 residents in Malabo and Luba. On 12 August, heavy rain in the Central African Republic destroyed 450 shelters in Ouham, mainly impacting displaced people. During 18–19 November, floods displaced over 22,000 people in the departments of Brazzaville and Pointe-Noire in the Republic of Congo, and resulted in injuries and damage.

5. EASTERN AFRICA

—E. Bekele, S. Fuhrman, and W. M. Thiaw

The Greater Horn of Africa (GHA), or eastern Africa, encompasses 11 countries and extends 12°S–24°N and 21°E–52°E. Its northern sector comprises Sudan, South Sudan, the northern two-thirds of Ethiopia, Eritrea, Djibouti, and the northern two-thirds of Somalia. Southern Somalia, southern and southeastern Ethiopia, Kenya, northern Tanzania, Uganda, Rwanda, and Burundi are in its equatorial sector, while the southern sector encompasses central and southern Tanzania. The region has a complex terrain, with elevation ranging from about 160 m below sea level at Ethiopia's northern exit of the Rift Valley to more than 5000 m above sea level at glaciated Mount Kilimanjaro. This complex topography is further typified by the presence of large lakes and is reflective of multi-faceted climate zones modulated by local and large-scale forcing such as the deep convective and moisture convergence zone, the El Niño–Southern Oscillation, the Indian Ocean dipole, the Madden–Julian Oscillation, and tropical–extratropical interactions. Rainfall is bimodal in the equatorial sub-region, with two distinct rainfall seasons in March–May (MAM) and October–December (OND). Seasonal rainfall is unimodal in the northern and southern sectors, spanning November–April in the south and June–September in the north.

(i) Temperature

Annual mean temperatures in 2025 exceeded 26°C across most of Sudan, Somalia, Djibouti, Eritrea, far eastern Ethiopia, and eastern Kenya (Fig. 7.26a). Although conditions were slightly above average across much of Ethiopia (+0.5°C to +1°C), annual mean temperatures remained below 22°C across most of central Ethiopia and the Lake Victoria region of equatorial East Africa (Fig. 7.26b).

Annual maximum temperatures exceeded 36°C in central and eastern Sudan, but ranged between 24°C and 28°C across central Ethiopia and the Great Lakes region of East Africa. Annual maximum temperatures were 1.5°C–2.5°C above average across far eastern South Sudan and central and northern Ethiopia (Fig. 7.26c). Annual minimum temperatures exceeding 18°C were recorded in the coastal regions of Sudan, Eritrea, Djibouti, Kenya, Somalia, and Tanzania, while central Ethiopia and parts of Tanzania experienced annual minimum temperatures below 16°C (not shown).

Anomalously warm mean temperatures were most pronounced during March–May over many parts of Ethiopia, driven by above-average maximum temperatures. In contrast, seasonal mean

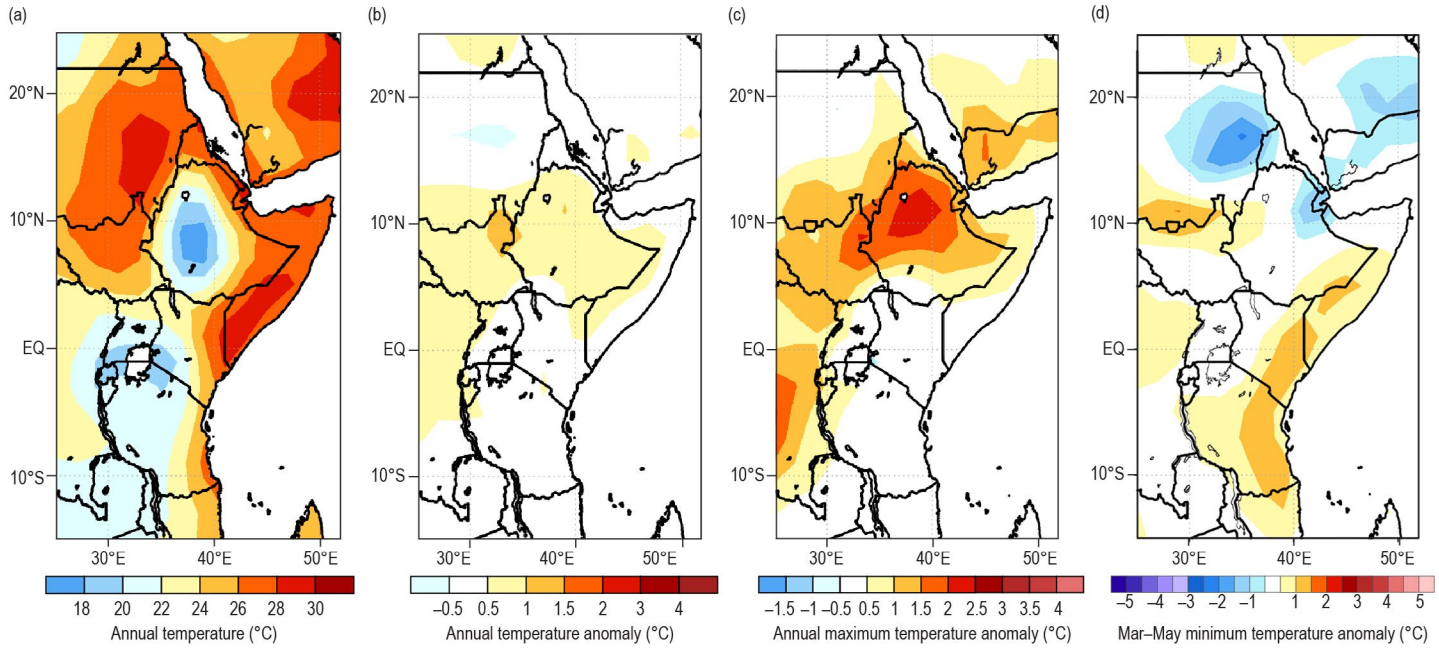

Fig. 7.26. (a) Annual mean temperatures, (b) annual mean temperature anomalies, (c) annual maximum temperature anomalies, and (d) Mar–May mean minimum temperature anomalies (°C; 1991–2020 base period) for eastern Africa in 2025. (Source: NOAA/National Centers for Environmental Prediction [NCEP].)

minimum temperatures were 1.1°C–3.5°C below average over central and eastern Sudan, parts of Eritrea, northeastern Ethiopia, and Djibouti (Fig. 7.26d).

(ii) Precipitation

Annual rainfall in 2025 exceeded 1000 mm across western Ethiopia, parts of South Sudan, Uganda, Rwanda, Burundi, and western and southern Tanzania (Fig. 7.27a). Western Kenya, central Ethiopia, northern South Sudan, northeastern Uganda, and central and northeastern Tanzania received between 600 mm and 1000 mm. Lower totals, ranging from 50 mm to 600 mm, were recorded over northern Sudan, Eritrea, Djibouti, southeastern Ethiopia, northeastern Kenya, and Somalia.

Figure 7.27b shows annual rainfall anomalies. Precipitation was below average across many parts of eastern Africa. Annual rainfall deficits exceeded –100 mm over parts of central and southern Ethiopia, northeastern Kenya, and southern Somalia. Rainfall totals fell below the 10th percentile –100 mm to –150 mm) over parts of southeastern Ethiopia and central Somalia.

During March–May, seasonal rainfall was above average in much of equatorial eastern Africa and Tanzania, with seasonal anomalies of more than +50 mm covering much of equatorial and southern sectors of eastern Africa (Fig. 7.27c). On the other hand, northern and central Ethiopia recorded below-average rainfall during MAM. Seasonal rainfall deficits were most pronounced during the October–December season (Fig. 7.27d), with most of Kenya, southern and southeastern Ethiopia, and Somalia recording OND rainfall below the 15th percentile. The lowest rainfall was recorded in eastern Kenya and southern Somalia, which was below the third percentile. The observed below-average rainfall in OND 2025 is consistent with the observed negative phases of the Indian Ocean dipole and ENSO (e.g., Black 2005; Doi et al. 2022).

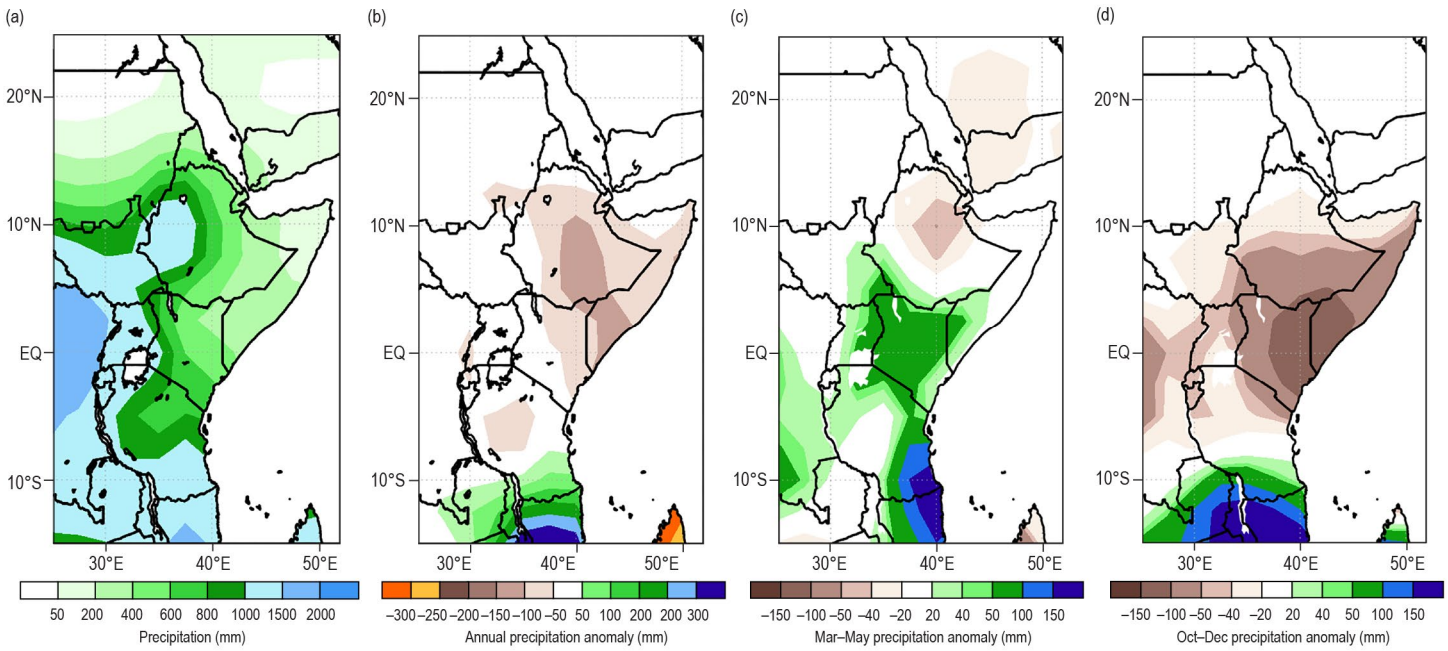

Fig. 7.27. (a) Annual total rainfall, (b) annual rainfall anomalies, (c) Mar–May rainfall anomalies, and (d) Oct–Dec rainfall anomalies (mm; 1991–2020 base period) for eastern Africa in 2025. (Source: Global Precipitation Data Project [GPCP]GPCP data via NOAA/National Centers for Environmental Prediction [NCEP].)

(iii) Notable events and impacts

Portions of eastern Africa experienced periods of abnormal heat during January–February and April–May. Central, northern, and western Ethiopia, Sudan, South Sudan, and the northeastern DRC all registered monthly mean maximum temperatures 3°C–5°C above average within these periods. In Ethiopia, Djibouti, Eritrea, and northwestern Somalia, these values met or exceeded the 97th percentile during April and May. Another period of abnormal heat occurred during September–November, with widespread seasonal mean maximum temperatures falling between the 90th and 97th percentiles. The heat was coupled with dry conditions, exacerbating the impacts to populations and agricultural activities.

Heavy rainfall during the East African "long rains" contributed to flooding through much of the region. Reports of flooding began in Uganda during late March and spread to western Kenya and southwestern and Puntland region of Somalia in April, finally reaching southwestern Tanzania in May, according to local meteorological services. According to UN OCHA, at least 45,000 people were affected and four people were killed from flash floods in Somalia. Rainfall totals during MAM reached 400 mm–500 mm in the Lake Victoria region and exceeded 500 mm in southeastern Tanzania. These totals were more than 100 mm above average in southeastern Tanzania and 50 mm–100 mm above average throughout most of Kenya.

The most notable regional climate event of 2025 was the severe drought resulting from the failure of the October–December rainfall season in many parts of Kenya, Somalia, and southern and southeastern Ethiopia. According to the U.S. Agency for International Development Famine Early Warning Systems Network (FEWSNET), drought was the primary driver for 50%–55% of the estimated 20 to 25 million affected people across Somalia, Ethiopia, and Kenya who required humanitarian food assistance in December 2025. Wide ranging impacts were reported across Somalia, southern Ethiopia, and Kenya. The National Drought Management Authority (NDMA) in Kenya reported that communities in central and eastern counties were relying on emergency water trucking. The Ethiopian Disaster Risk Management Commission (EDRMC) reported worsening water shortages and decline in livestock body conditions in southern zones. In Somalia, the Somalia Water and Land Information Management (SWALIM) system recorded significantly reduced river flows along the Shabelle and Juba Rivers. Rainfall during the OND season in southern Somalia and eastern Kenya ranked in the bottom third percentile, with seasonal accumulations failing to exceed 100 mm.

6. SOUTHERN AFRICA

—M. Robjhon, S. Fuhrman, A. C. Kruger, C. McBride, and W. M. Thiaw

Southern Africa extends from about 5°S to 35°S, and comprises Angola, Namibia, Zambia, Botswana, Zimbabwe, Malawi, South Africa, Lesotho, Eswatini, and Mozambique. Southern Africa is characterized by two main seasons: the wet and warm season from November of the previous year to April, and the dry and cold season from May to October.

(i) Temperature

Annual mean temperatures for 2025 ranged from less than 18°C to 28°C in southern Africa, with warmer conditions in eastern Mozambique and northwestern Angola and cooler conditions in South Africa, Lesotho, and southern Namibia (Fig. 7.28a). Annual mean temperatures were above average across southern portions of the region, including South Africa, Lesotho, Eswatini, southern Mozambique, southern Botswana, and Namibia. Small portions of southern and northern Angola were also warmer than average. The largest warm anomalies were observed in isolated areas in northern South Africa and bordering areas of Namibia and Botswana, where annual mean temperatures were 1.5°C to 2°C above the long-term mean (Fig. 7.28b).

Annual maximum temperatures were above average over most southern, eastern, and western areas in southern Africa (Fig. 7.28c). Positive anomalies were as large as +1.5°C to +2.5°C in northern Angola, and +1.5°C to +2°C in southern Angola and northern and southern Namibia. Portions of northern Mozambique, northern Zimbabwe, Zambia, Botswana, and central South Africa registered maximum temperatures near average. Seasonally, maximum temperatures were well above average across southern and western portions of southern Africa during the July–September (JAS) and October–December (OND) seasons (not shown). During OND, central and eastern parts of the region observed below-average maximum temperatures.

Annual minimum temperatures were 0.5°C to 2°C above average over South Africa, Eswatini, Lesotho, and parts of Botswana and Namibia (Fig. 7.28d). Minimum temperatures in the region ranged from 4°C to 8°C in parts of South Africa to 18°C to 22°C in coastal areas of Mozambique and Angola. Minimum temperatures were much cooler than average during the JAS season across Angola with anomalies reaching –3°C to –4°C. Southern parts of the region, including portions of Namibia, Botswana, and South Africa, were as much as 3°C to 3.5°C warmer than average during the second half of the year from July through December.

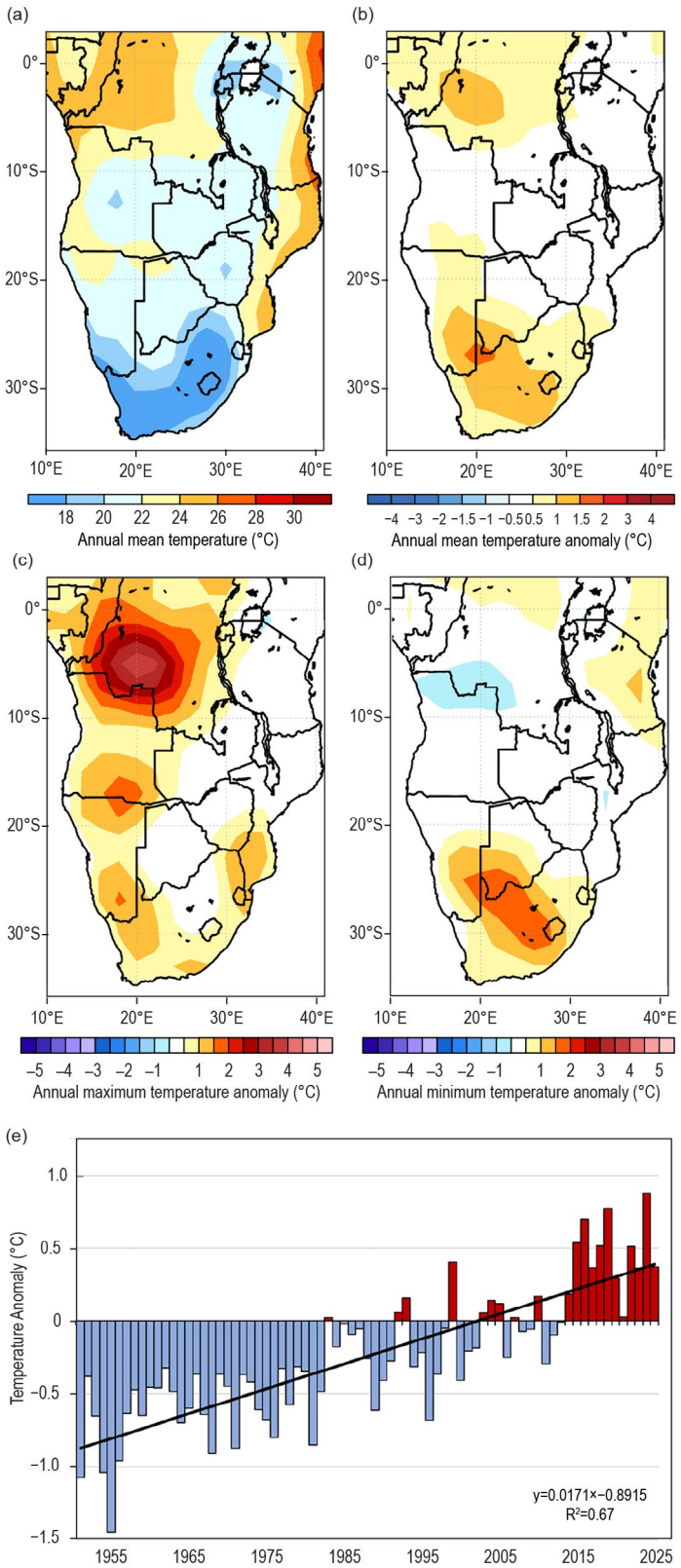

Fig. 7.28. Annual (a) mean temperatures, (b) mean temperature anomalies, (c) maximum temperature anomalies, and (d) minimum temperature anomalies (°C; 1991–2020 base period) for southern Africa in 2025. (Source: NOAA/National Centers for Environmental Prediction [NCEP].) (e) Annual average surface temperature anomalies (°C; 1991–2020 base period) for South Africa based on 26 climate stations for the period 1951–2025. The linear trend is indicated by the black solid line (Source: South African Weather Service.)

Analysis of station observations for South Africa (Fig. 7.28c) indicates that 2025 was among the 10 warmest years since 1951 based on the data of 26 climate stations, with a mean temperature that was 0.4°C above the 1991–2020 average. A linear trend analysis for the standardized surface temperature anomalies shows a warming trend of about 0.17°C decade^{-1} for the country over the period 1951–2024. This trend is statistically significant at the 5% level, according to the Student's t-test.

(ii) Precipitation

Annual rainfall totals in 2025 ranged from 200 mm to 2000 mm across southern Africa. While northern parts of the region—including northern Angola, northern Zambia, Malawi, and northern Mozambique—received over 1000 mm in rainfall, north-central Mozambique registered total rainfall in excess of 1500 mm (Fig. 7.29a). Also, eastern South Africa and parts of Lesotho recorded over 1000 mm annual

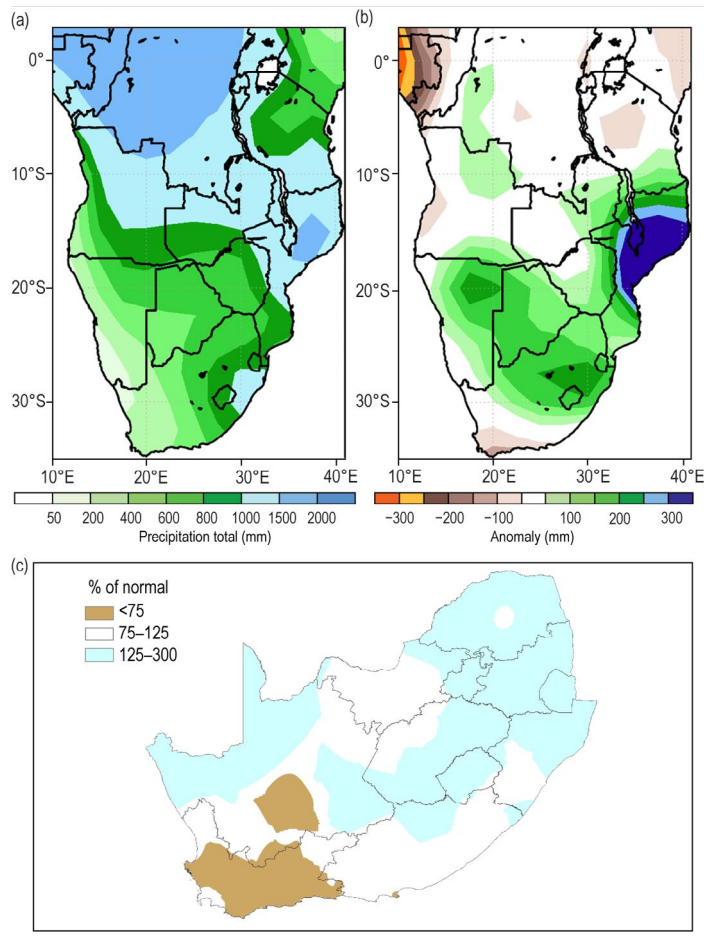

Fig. 7.29. Annual (a) total rainfall and (b) rainfall anomalies (mm; 1991–2020 base period) for southern Africa in 2025. (Source: Global Precipitation Data Project [GPCP]GPCP data via NOAA/National Centers for Environmental Prediction [NCEP].) (c) Annual rainfall anomalies (% of normal) for South Africa in 2025. (Source: South African Weather Service.)

rainfall totals. Overall, except for a few areas in western Angola and southern South Africa that received below-average annual rainfall, most of southern Africa received above-average annual rainfall. In particular, Namibia, Botswana, central and northeastern South Africa, most of Zimbabwe and eastern Zambia, southern Mozambique, and northern Malawi received above-average totals of +50 mm to +250 mm, while southern Malawi and central and northern Mozambique recorded the largest positive anomalies in excess of +300 mm (Fig. 7.29b). Moreover, according to the GPCP analysis, the 2025 annual rainfall total over southern and southeastern Africa ranked within the top 2%–10% of the wettest years on record since 1991 (not shown).

Consistent with the regional review, station-based precipitation analysis for South Africa shows that rainfall was above normal over much of the country during 2025 (Fig. 7.29c). The major exception was the Western Cape, extending into the southern interior of the Northern Cape, which received well-below-normal rainfall, with some places experiencing extremely dry conditions. Overall, the observed above-average rainfall in southern Africa in 2025 was consistent with the rainfall teleconnection patterns associated with La Niña conditions (e.g., Hoell et al. 2021).

(iii) Notable events and impacts

Flooding was the leading type of high impact event across southern Africa in 2025. Figure 7.30 shows several notable events, their geographic locations, and dates of occurrence during the year.

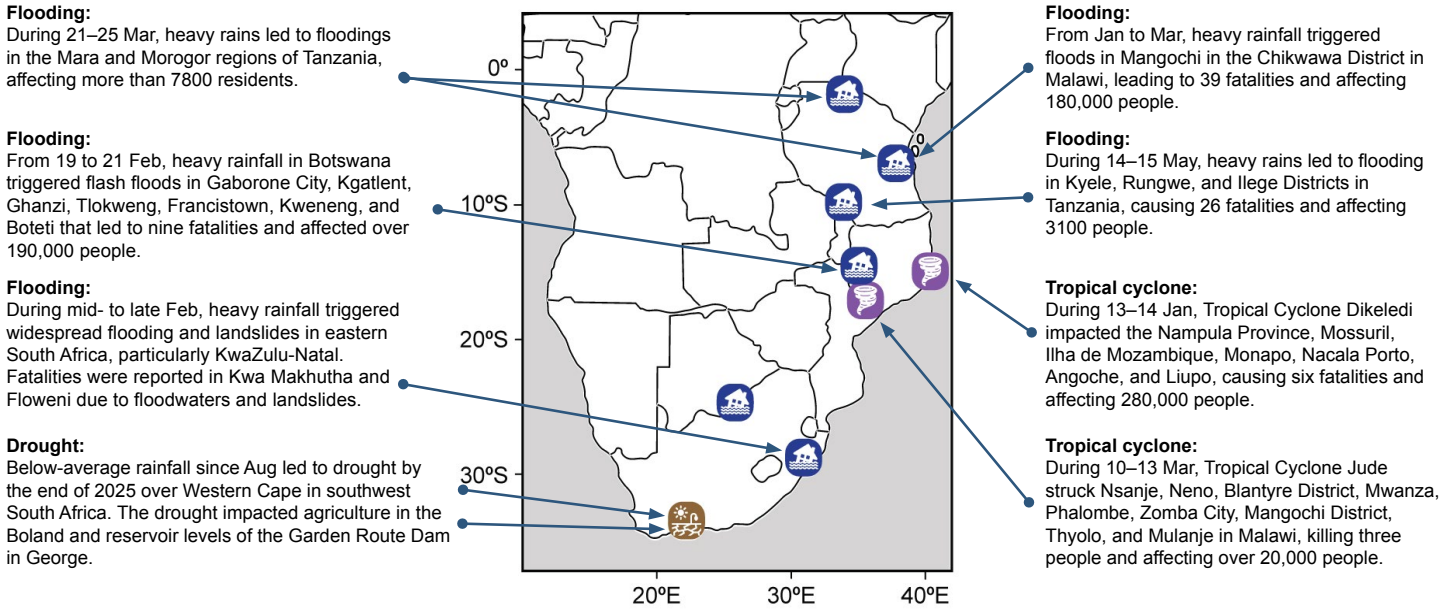

Fig. 7.30. Select extreme and notable events across southern Africa during 2025. (Source: Emergency Events Database [EM-DAT], South African Weather Service.)

In South Africa, intense and above-normal rainfall in mid-to-late February triggered widespread flooding and landslides in eastern South Africa, particularly in KwaZulu-Natal. Impacts included fatalities and casualties due to floodwater surges and landslides in residential areas such as KwaMakhutha and Folweni.

In the Western Cape of South Africa, severe drought conditions developed due to below-normal rainfall since August. Patches of extreme drought were experienced in parts of the Boland and adjoining areas. Below-normal rainfall also affected water supply as the water level of Garden Route Dam in George declined steadily throughout the year, dropping to below 50% capacity by December and prompting stricter municipal water use policy.

During 13–14 January, Tropical Cyclone Dikeledi, with a 24-hour rainfall accumulation of up to 300 mm and wind gusts of 180 km hr^{-1}, made landfall in Nampula Province in northeastern Mozambique, killing six people and affecting more than 280,000 residents across Nampula, Mossuril, Ilha de Mozambique, Monapo, Nacala Porto, Angoche, and Liupo, according to the Emergency Events Database (EM-DAT; https://www.emdat.be). Tropical Cyclone Jude crossed Mozambique during 10–12 March and brought heavy rainfall of up to 300 mm and wind gusts of up to 195 km hr^{-1}, killing at least 16 people and affecting nearly 216,000 families across many provinces, including

Zambézia, Nampula, Cabo Delgado, Niassa, Tete, and Sofala, as reported by ReliefWeb (see section 4g6 for more details on storms in the South Indian Ocean).

In Botswana, multi-day heavy rainfall in February caused widespread floods and resulted in the displacement of over 5000 people, according to ReliefWeb. During 19–21 February, heavy rain impacted Gaborone City, Kgatleng, Ghanzi, Tlokweng, Francistown, Kweneng, and Boteti, claiming nine lives and affecting over 190,000 people. Severe flooding also occurred in the Cunene and Cuvelai basins in northern Namibia and southern Angola in March and April 2025, according to reports by the Global Disaster Awareness and Coordination System and ReliefWeb.

7. WESTERN INDIAN OCEAN ISLAND COUNTRIES

—T. Nomenjanahary, S. Ekwacu, C. Backenstrass, M. Robjhon, and W. M. Thiaw

The western Indian Ocean Island countries consist of several islands scattered across the Indian Ocean, which include Madagascar, Seychelles, Comoros, Mayotte (France), Réunion (France), Mauritius, and Rodrigues (Mauritius). There are two distinct seasons: a warm and wet period spanning from November of the antecedent year to April, and a cold and dry season lasting from May to October.

(i) Temperature

The 2025 mean temperature at the Seychelles International Airport was 0.29°C above the 1991–2020 average, marking the seventh-warmest year since 1972 (Fig. 7.31a). Mean temperature anomalies ranged from +0.32°C to +0.64°C during January–March (JFM) and April–June (AMJ) and between +0.10°C and +0.16°C during July–September (JAS) and October–December (OND). The maximum temperature recorded on 3 March 2025 (34.7°C) was the second highest observed since 1972 (34.8°C). The mean temperature for May 2025 was also the second highest on record.

The annual mean temperature for 2025 over La Réunion Island (based on three stations) was 0.9°C above the 1991–2020 normal, the second-highest annual temperature since 1968. For MAM, the mean temperature was 1.4°C above normal at 25.3°C. Temperatures slightly dropped between April and June as the days grew shorter, but was still 1.1°C above normal. During JAS, the mean temperature was 0.4°C above normal, and increased to +0.8°C during OND.

For Mayotte, the annual temperature was 1.0°C above normal at the Pamandzi airport weather station, marking the fourth-highest annual temperature in the 64-year record. The average temperature was especially high during the first half of the year at 1.1°C above normal. From July to December, the anomaly was slightly lower at +0.8°C.

For Madagascar, annual mean temperatures in 2025 varied between 20°C and 26°C, with higher mean temperatures along the western and northern tiers of the island and

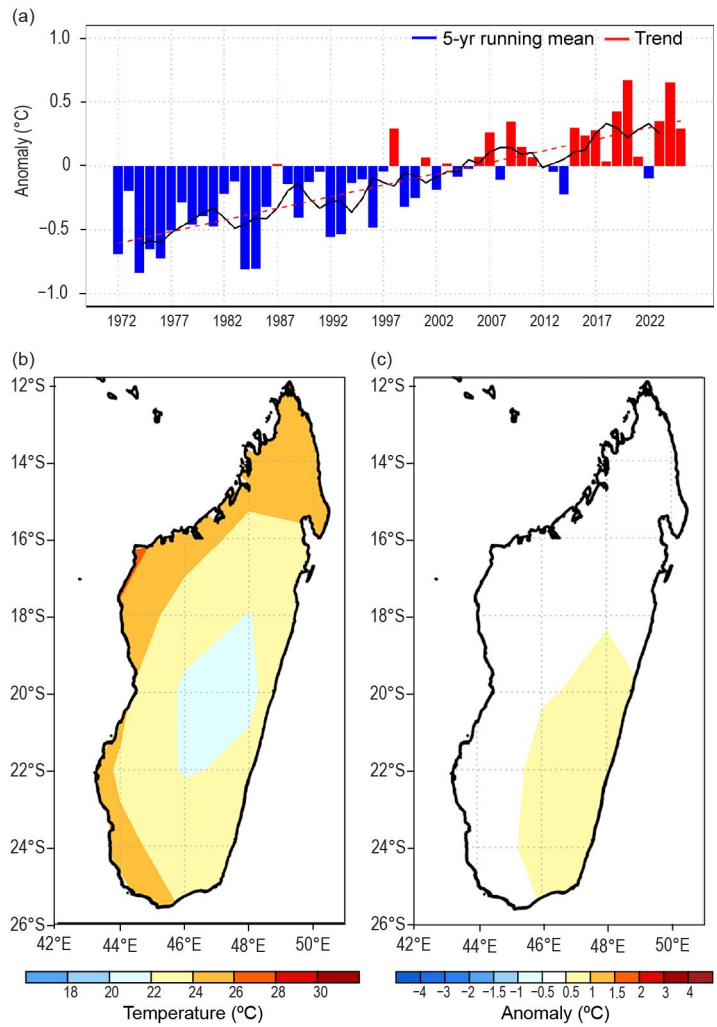

Fig. 7.31. (a) Annual mean temperature anomaly time series (°C; 1991–2020 base period) at Seychelles International Airport for the period 1972–2025 (Source: Seychelles Meteorological Authority). (b) Annual mean temperatures and (c) annual mean temperature anomalies (°C; 1991–2020 base period) for Madagascar in 2025. (Source: NOAA/National Centers for Environmental Prediction [NCEP].)

lower mean temperatures across the central highlands (Fig. 7.31b). Annual mean temperatures were 0.5°C–1°C above average over the southeastern part of the island (Fig. 7.31c), which ranked between the 90th and 97th percentile of the historical record since 1991.

(ii) Precipitation

Over the Seychelles, the 2025 total annual rainfall (1806.3 mm) was 74% of the 1991–2020 average, making it the third-driest year on record since 1972 (Fig. 7.32a). Inspection of rainfall performance for a three-month running Standardized Precipitation Index (SPI-3) in 2025 shows that the year started with a marginally positive standardized anomaly during JFM, but became mildly negative through MAM (Fig. 7.32b). Thereafter, rainfall continued to be significantly drier than average with SPI values of less than one standard deviation below the mean during the AMJ, JAS, August–October, and SON periods. Further analysis also revealed that April 2025 was the driest April on record, while October 2025 was the second-driest October since 1972.

Total annual rainfall over La Réunion for 2025 was 93% of average. However, the 2024/25 rainy season started late and ended early, culminating in a 30% drier-than-average season. In fact, January 2025, the last month of the preceding rainy season, was the driest recorded in 54 years. The subsequent dry season (May to October) was near average, while November and December received 40% more rainfall than normal.

Annual rainfall over Mayotte was near average. The 2024/25 rainy season was within 10% of the long-term average, whereas the subsequent dry season (May to October) was 25% below normal. Similar to La Réunion, the year concluded with two wetter-than-average months, as November and December received 19% more rainfall than normal, partially offsetting the preceding dry period.

Over Madagascar, total annual rainfall in 2025 ranged from 1000 mm to 2000 mm, with the highest totals in the east-central part of the island (Fig. 7.32c). While southern Madagascar received above-average annual rainfall of +50 mm to over +300 mm, the central and northern regions recorded below-average rainfall of –50 mm to over –300 mm (Fig. 7.32d). An examination of the seasonal rainfall evolution indicates that below-average rainfall dominated much of Madagascar, except over the southwestern region, which received above-average rainfall during DJF 2024/25 and MAM. Below-average

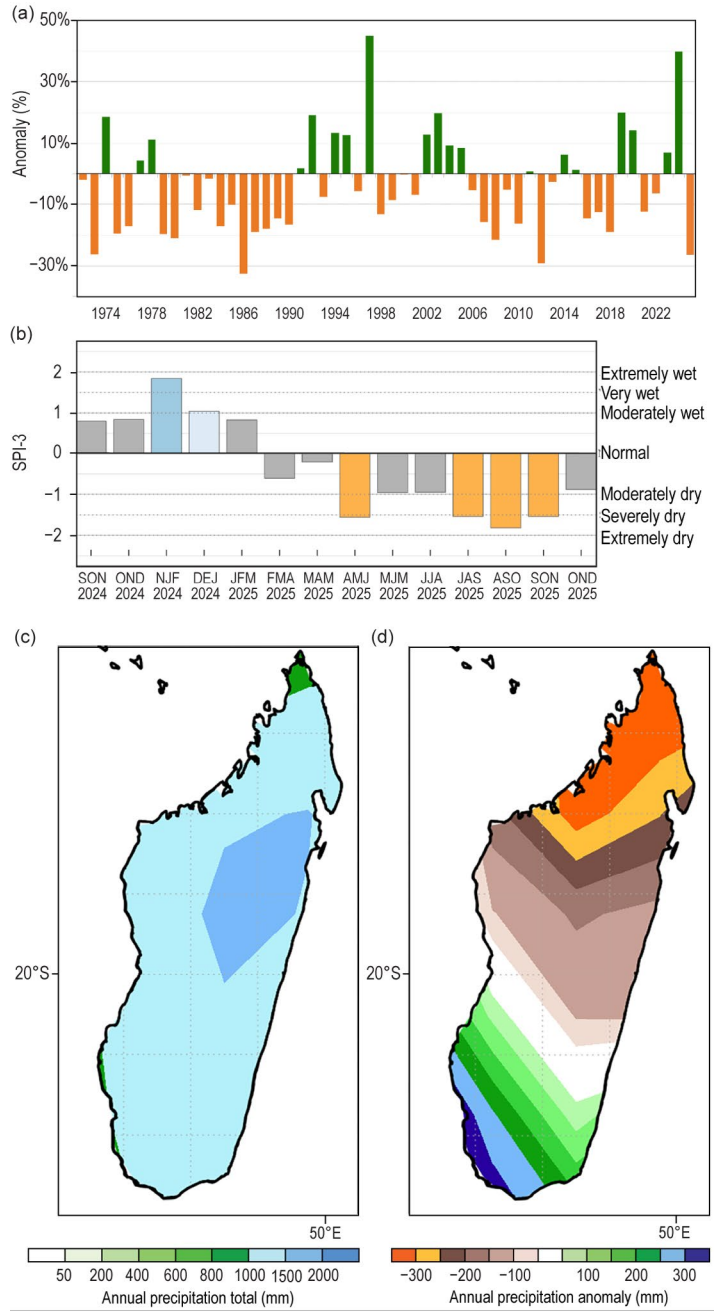

Fig. 7.32. (a) Annual rainfall anomalies (%; 1991–2020 base period) for the period 1972–2025 and (b) three-month Standard Precipitation Index (SPI-3) for 2024/25 at the Seychelles International Airport (Source: Seychelles Meteorological Authority). (c) Annual total rainfall and (d) annual rainfall anomalies (mm; 1991–2020 base period) for Madagascar in 2025. (Source: Global Precipitation Data Project [GPCP] data via NOAA/National Centers for Environmental Prediction [NCEP].)

rainfall continued over the island during JJA; above-average rainfall returned over most of the northern half of the country during SON.

(iii) Notable events and impacts

Figure 7.33 displays several notable events, their geographic locations, and dates of occurrence over the western Indian Ocean Island countries during 2025.

In the Seychelles, prolonged dry conditions affected the islands of Mahe, Praslin, and La Digue during 2025. The dry conditions that persisted from AMJ to OND resulted in a significant reduction in river flow levels and led to water supply restrictions in the Seychelles.

Over La Réunion Island, the drier-than-average 2024/25 rainy season reduced water availability and led to water supply restrictions. As a result, prolonged water outages significantly disrupted social and economic activities.

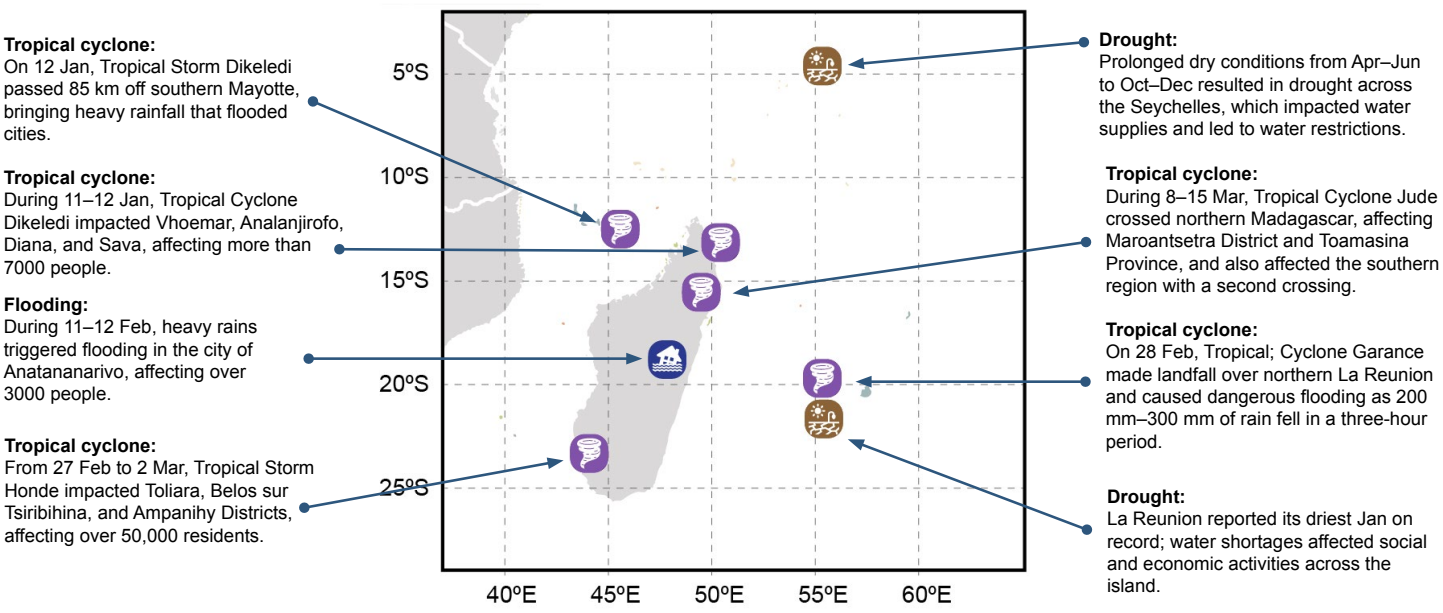

Fig. 7.33. Select extreme and notable events across western Indian Ocean Island countries in 2025. (Sources: Seychelles Meteorological Authority, Météo-France for Indian Ocean, La Réunion, Emergency Events Database [EM-DAT].)

During 11–12 January, Tropical Cyclone Dikeledi, with winds gusting up to 180 km hr^{-1}, struck Vohémar, the Analanjirofo, Diana, and Sava regions of northeastern Madagascar, causing three fatalities and affecting over 7000 people. The storm also passed within 85 km of the south coasts of Mayotte on 12 January, bringing heavy rain, especially in the south, with more than 200 mm–300 mm over a 24-hour period. Cities were flooded as this event worsened the already difficult conditions following Tropical Cyclone Chido, which had devastated the island in December 2024 (see section 4g6 for details).

Tropical Cyclone Garance hit La Réunion on 28 February 2025. Although rather small in size, the cyclone caused severe damage on the northern half of the island after it made landfall. The storm produced record-breaking heavy rainfall that led to severe flooding; several stations registered 200 mm to 300 mm in just three hours in the northern half of the Island. Winds gusts reached more than 200 km hr^{-1} over the northeastern coast, which was the most exposed part of the island.

f. Europe and the Middle East

– P. Bissolli, Ed.,
M. Roebeling, M. Alemanno, C. Berne, Christine, D. Biernacik, V. De Bock, M. Ekici, M. Ivanov, M. Kendon, J. Kennedy, I. Marcinonienė, A. Mamara, J. Mamen, A. Morata Gasca, P. Müller, A. Orlik, E. Piervitali, A. Porat, F. Rubek, S. Sensoy, S. Spillane, M. Turňa, R. Van der Linden, A. Willems, and E. Zubler

Throughout this section, 1991–2020 is the base period used for anomalies unless otherwise specified. All seasons mentioned in this section refer to the Northern Hemisphere; winter refers to the period from December 2024 to February 2025. More detailed information can be found in the Monthly Bulletins on the Climate in Regional Association VI (RA VI)–Europe and the Middle East, provided by the World Meteorological Organization (WMO) RA VI Regional Climate Centre Node on Climate Monitoring (RCC-CM). Findings are based on gridded data of interpolated CLIMAT station and ship data for temperature, as well as that of the Global Precipitation Climatology Centre (GPCC) for precipitation (if not otherwise specified); the data were also supplemented by information from National Meteorological and Hydrological Services (NMHSs) where available, as well as information from the WMO (WMO 2025). Spatial averages for subregions displayed in Fig. 7.34 are always based on these gridded data only. Whenever national data provided by the NMHSs were available, these were used for national statistics; otherwise, statistics based on gridded RCC datasets were used (as indicated in Table 7.3 in the source column). More information about the gridded RCC datasets can be found at https://www.dwd.de/EN/climate_environment/climatemonitoring/europe/maps_node.html. In the following, the WMO RA VI Region will be referred to as region. Due to the large number of countries in Europe and the limited word space for each subsection, only limited impact information can be provided here. More details about extreme events and impacts across Europe can be found elsewhere (e.g., WMO 2026).

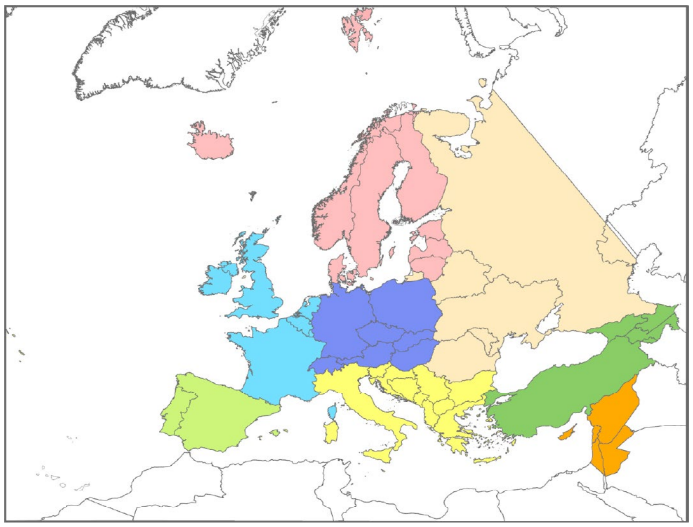

Fig. 7.34. Map of subregions in the World Meteorological Organization (WMO) Regional Association (RA) VI region of Europe.

1. OVERVIEW

Based on nine different (global) datasets, the year 2025 was the warmest on record over the region (Fig. 7.35). The region is defined as the land areas of WMO RA VI Region as displayed in Fig. 7.34 plus Greenland. The mean temperature anomaly was +1.3°C over land areas, ranging from +1.19° to +1.41°C, depending on the dataset. Based on the regional gridded RCC temperature data (interpolated climate station and ship data, Fig. 7.36), the year was also warmest on record (+1.1°C anomaly over land and sea areas of the region; +1.4°C over land only). The year was among the six warmest for all subregions with temperatures 1°C to 2°C above normal, except for Central Europe (+0.8°C, ninth warmest). Eastern Europe (+1.8°C anomaly) and the Nordic and Baltic countries (+1.4°C) each observed their second warmest year on record

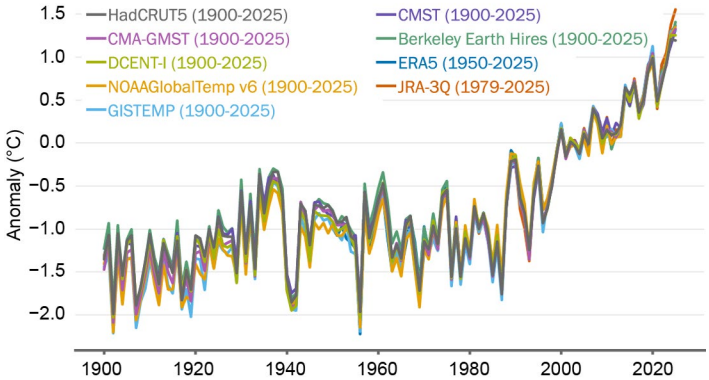

Fig. 7.35. Annual regional mean temperature anomalies for the World Meteorological Organization (WMO) Regional Association (RA) VI of Europe (°C; difference from the 1991–2020 average, land areas only) for the period 1900–2025. Data are from the following nine datasets: Berkeley Earth Hires, CMA-GMST, CMST, DCENT-I, ERA5, GISTEMP, HadCRUT5, JRA-3Q, and NOAA Global Surface Temperature (GlobalTemp) v6. For dataset and processing details, see https://www.jkclimate.fr/RegionalDashboard/wmo_ra_vi.html#WMO%20RA%20VI%20Europe (Source: WMO.)

(averaged over the subregions). The largest positive temperature anomalies (exceeding +2°C) occurred over eastern parts of European Russia and West Kazakhstan. There were no land areas with below-normal annual temperatures.

In terms of annual precipitation, 2025 was mostly drier than normal across Western Europe, Central Europe, and over the Türkiye and the South Caucasus subregion (Fig. 7.37). The Middle East saw much-lower-than-normal annual totals in 2025, marking one of the driest years on record, with only just over half of its normal precipitation in most countries of the subregion. Across the Nordic and Baltic countries, normal to drier-than-normal conditions dominated in Iceland, southern parts of Scandinavia, and southern Finland, while wetter-than-normal conditions prevailed towards northern Fennoscandia. Eastern Europe saw wetter-than-normal conditions in the north, but drier-than-normal conditions in the south (eastern Ukraine). The Iberian Peninsula also experienced mostly wetter-than-normal conditions, especially in Portugal.

In winter, above-average 500-hPa geopotential heights prevailed with the largest anomalies centered over southern Scandinavia, Poland, and the Baltic countries (Fig. 7.38). Temperatures were above normal across almost the entire region; northeastern areas saw temperatures at least 3°C higher than normal. As a result, the season was second warmest on record over Eastern Europe and also ranked second warmest for the RA VI land areas and the RA VI Region as a whole. At the surface, higher-than-normal mean sea level pressure (MSLP) dominated across the region with maximum anomalies over southern Scandinavia and Ukraine (Fig. 7.39). Winter was drier than normal across most parts of the Iberian Peninsula, Central Europe, Türkiye, and the Middle East. February saw extremely dry conditions across the entire region (land areas) recording only 70% of normal precipitation (third driest on record). Wetter-than-normal conditions in winter occurred over northern Fennoscandia, northern Russia, northwestern France, and parts of the central Mediterranean Region.

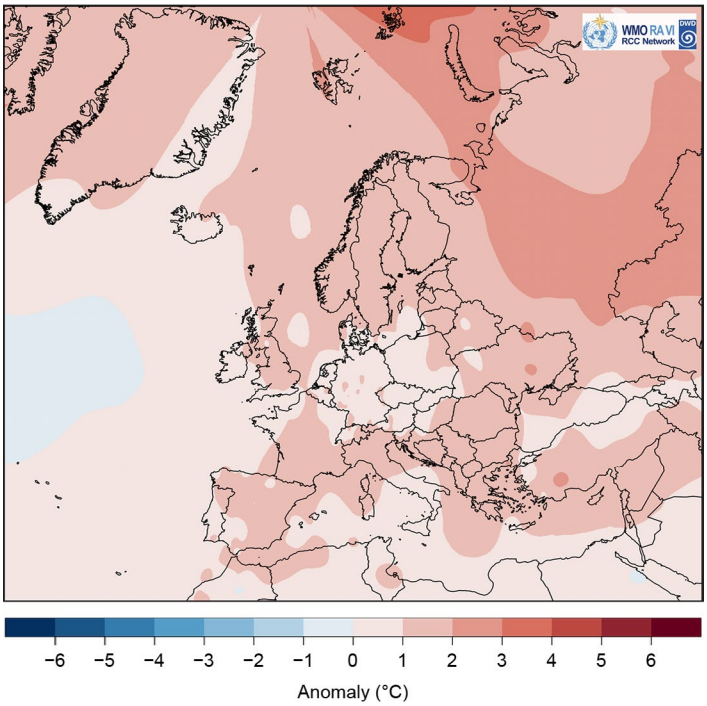

Fig. 7.36. Annual mean temperature anomalies (°C; 1991–2020 base period) for 2025. The 1991–2020 anomalies were recalculated from 1981–2010 anomalies because the 1991–2020 CLIMAT data were still not available for all countries. (Source: Interpolated climate station and ship data, Deutscher Wetterdienst [DWD].)

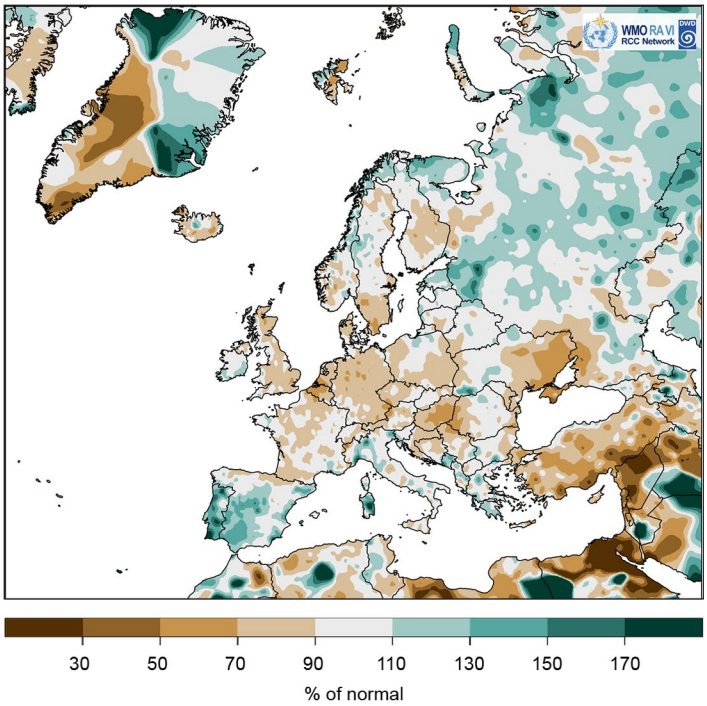

Fig. 7.37. European precipitation totals (% of 1991–2020 normal) for 2025. (Source: Global Precipitation Climatology Centre [GPCC], Schneider et al. 2022, created by Deutscher Wetterdienst [DWD].)

Spring was characterized by below-normal geopotential heights to the west of Portugal and over Svalbard and the Barents Sea. Between these two regions, above-normal heights prevailed, with the largest anomalies centered over the northern United Kingdom. The MSLP anomalies mirror this pattern, reflecting the dominant high-pressure regime across large parts of the region,

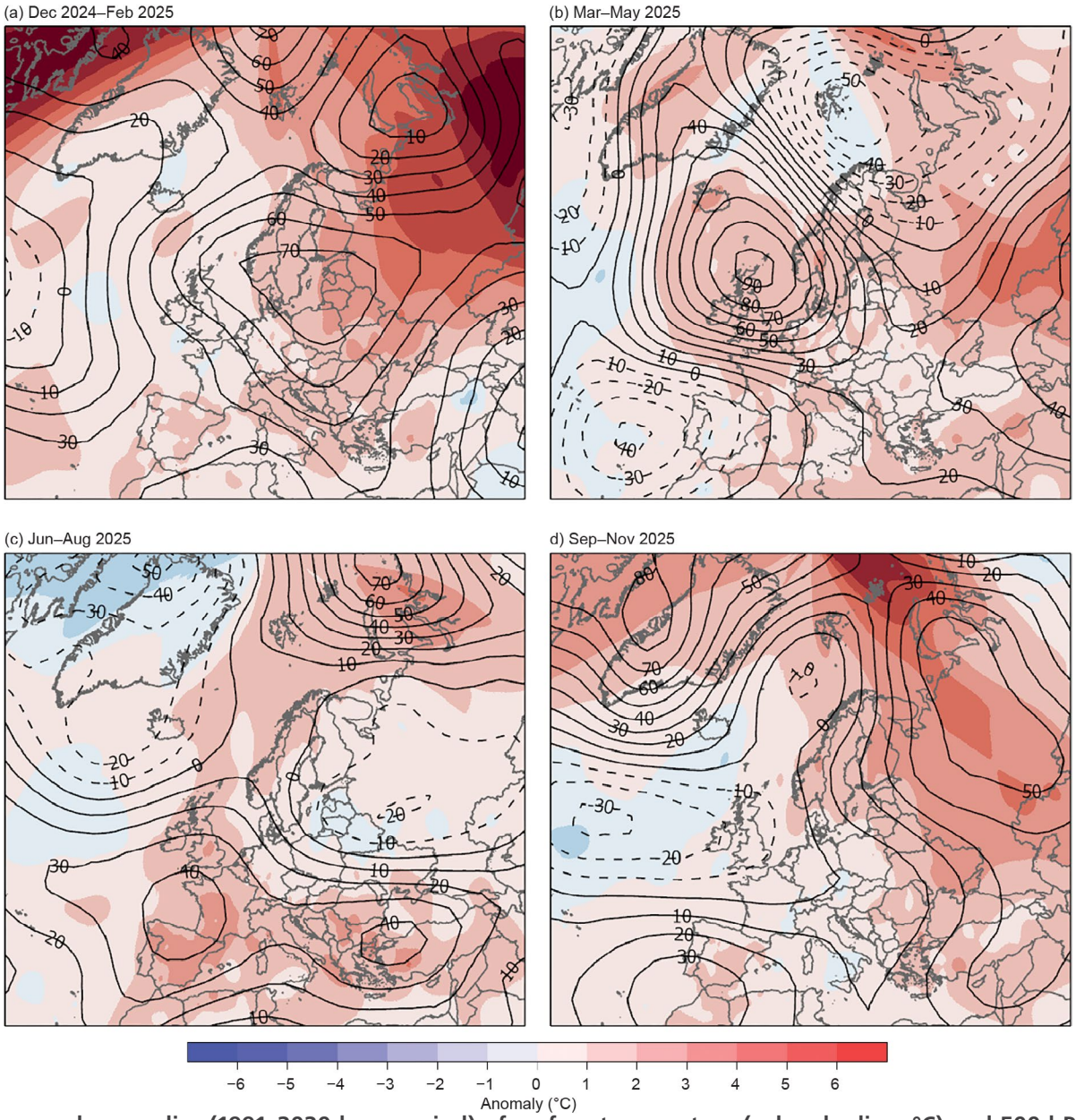

Fig. 7.38. Seasonal anomalies (1991–2020 base period) of surface temperature (color shading; °C) and 500-hPa geopotential height (contour; m; solid lines: positive, dashed lines: negative anomalies in 10-m intervals) for (a) Dec–Feb (DJF) 2024/25, (b) Mar–May (MAM) 2025, (c) Jun–Aug (JJA) 2025, and (d) Sep–Nov (SON) 2025. (Source: Interpolated climate station and ship data for temperature; National Center for Atmospheric Research [NCAR] reanalysis for 500-hPa geopotential heights, created by Deutscher Wetterdienst [DWD].)

which resulted in warmer-than-normal and especially much drier-than-normal conditions across large parts of northwestern Europe (except most of Norway). The season was third warmest on record over the RA VI land areas as a whole, and among the three warmest in Western Europe, Eastern Europe, and the Middle East. Spring precipitation was below normal in Western Europe and Central Europe with seasonal totals around 80% of normal. In contrast, wetter-than-normal conditions particularly affected the Iberian Peninsula (150% of normal) and parts of the central Mediterranean Region.

In summer, above-normal geopotential heights occurred over southern parts of the region, while below-normal heights prevailed over northwestern parts (maximum over Greenland). This reflects the high-pressure dominance in the west and south, producing a very warm, dry summer, while more cyclonic influence prevailed in the north and east with more variable, sometimes wetter, conditions. Most RA VI land areas experienced above-normal summer temperatures, with anomalies exceeding +1°C in the west and south, while below-normal temperatures were confined to the northwesternmost parts, the Baltic countries, and Belarus. The season was one of three warmest over the Iberian Peninsula, Türkiye and the South Caucasus,

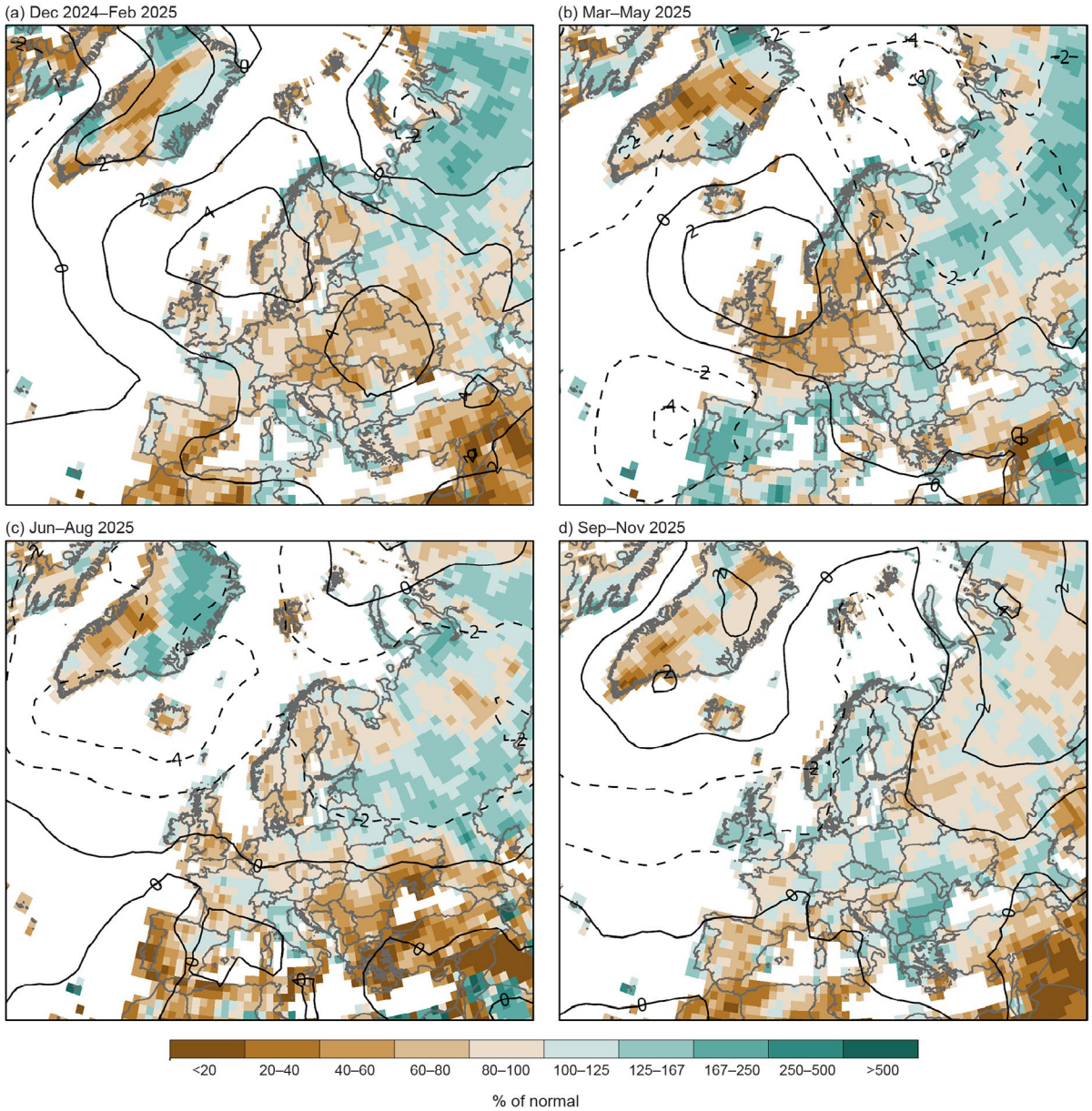

Fig. 7.39. Seasonal anomalies (1991–2020 base period) of precipitation (color shading; % of normal) and sea level pressure (contours; hPa; solid lines: positive, dashed lines: negative anomalies in 2-hPa intervals) for (a) Dec–Feb (DJF) 2024/25, (b) Mar–May (MAM) 2025, (c) Jun–Aug (JJA) 2025, and (d) Sep–Nov (SON) 2025. (Source: Global Precipitation Climatology Centre [GPCC] for precipitation, National Centers for Environmental Prediction [NCEP]/National Center for Atmospheric Research [NCAR] reanalysis for sea level pressure, created by Deutscher Wetterdienst [DWD].)

and Western Europe. Precipitation totals in summer were predominantly below normal in much of the western and southern parts of the region, as well as in parts of Northern Europe, with particularly high deficits in the southeast. For Türkiye and South Caucasus, summer was the driest on record with only about 50% of normal recorded in each month. Above-normal precipitation, in contrast, occurred over an area encompassing the Baltic States, Belarus, northern Ukraine, and parts of Russia.

In autumn, below-normal 500-hPa geopotential heights and MSLP prevailed west of Ireland over the North Atlantic, while most other parts of the region—particularly Eastern Europe—saw above-normal heights and MSLP. Autumn was the warmest on record over the land areas of the region (+1.5°C anomaly) and second warmest overall—including sea areas—with an anomaly of +1.0°C; Eastern Europe recorded its third-warmest autumn (+2.2°C anomaly). Several heavy precipitation events resulted in above-normal precipitation across Ireland and the United Kingdom,

much of Scandinavia, the western Iberian Peninsula, as well as eastern parts of Central Europe. Parts of the Balkan Peninsula recorded one of their six wettest autumns on record with totals reaching 150% to 160% of normal. Drier-than-average conditions affected most of Spain, southern France, northwestern Italy, as well as much of European Russia and Türkiye. In the Middle East, autumn and thus the first part of the 2025/26 rainfall season began with much-below-normal rainfall totals across the subregion (less than 50% of normal).

The year closed with a warmer-than-normal December, and much of the land areas in the region experienced anomalies between +3°C and +4°C in Northern and Eastern Europe. December was drier than normal in Central and southeastern Europe (largely below 40% of normal), but wetter than normal in much of Fennoscandia, European Russia, and parts of the Mediterranean region (more than 150% of normal in much of the western Mediterranean and the Middle East).

2. WESTERN EUROPE

This subregion includes Ireland, the United Kingdom, the Netherlands, Belgium, Luxembourg, and France.

(i) Temperature

The annual temperature over Western Europe for 2025 was 1.0°C above normal, the third highest on record. The year was also among the five warmest for all countries of the subregion (anomalies close to +1.0°C), except for the Netherlands and Luxembourg. In the United Kingdom, 2025 was the warmest year on record in a series from 1884.

Winter was 0.6°C warmer than normal over Western Europe; in all countries of the subregion, anomalies were positive but remained below +1°C. While anomalies over the subregion as a whole were positive in February (+0.8°C), temperatures remained near normal in January, with the largest negative anomalies, mainly between −0.5°C and −1°C, over Ireland, the United Kingdom, and Belgium.

Spring was 1.3°C warmer than normal over the subregion (third warmest). The largest anomalies occurred again over Ireland and the United Kingdom, which both experienced their warmest spring on record.

Summer was 1.7°C warmer than normal over the subregion (third warmest). The season was also among the five warmest for all countries of the subregion (anomalies above +1.0°C) except for Luxembourg. For the United Kingdom and Ireland, this marked the warmest summer on record. The largest positive anomaly over the subregion occurred in June (around +3.0°C), which was the highest on record for the subregion overall, and for the individual countries among the five highest.

Autumn saw moderate temperature anomalies overall (+0.4°C). September was near normal (−0.1°C), while both October and November were warmer than normal, with anomalies of +0.5°C and +0.8°C, respectively. In December, temperatures were markedly above normal across Western Europe (+1.5°C), with the largest anomalies observed over the Netherlands, Belgium, and Luxembourg, where temperatures were around 2.0°C above normal.

(ii) Precipitation

Over the year, large parts of Western Europe received below-normal precipitation, particularly due to much lower-than-normal precipitation in spring. The Netherlands saw a dry year, with only 77% of normal precipitation for the country as a whole. The station Uccle (Belgium) recorded 74% of its normal total. In contrast, Ireland was slightly wetter than normal, with 105% of its normal annual total.

Winter precipitation in Western Europe was near normal, but the season showed strong month-to-month contrasts: January was the month with largest wet anomaly, reaching 129% of normal, while December and February were drier-than-normal (80%). Belgium and Luxembourg saw particularly sharp contrasts: the stations Uccle (Belgium) and Findel (Luxembourg) each recorded around twice their normal monthly totals in January, but only about 60% of normal in February. For Uccle, January was its wettest on record.

Spring was significantly drier than normal for Western Europe (80% of normal), with all months seeing below-normal precipitation and the United Kingdom having its driest spring since 1974. Largest anomalies occurred in March, with the Netherlands receiving only 11% of its

normal, ranking driest on record. In Belgium and Luxembourg, the stations Uccle and Findel also recorded one of their driest months of March on record, with 13% and 22% of normal, respectively; Ireland had 40% of its normal. The other two months of the season were also mostly drier-than-normal over the subregion, except for Ireland in April (114%) and France, but deficits were generally less pronounced.

Summer precipitation was moderately dry at around 90% of normal. While July brought near-normal rainfall, both June and especially August saw drier-than-normal conditions. Uccle (Belgium) experienced its seventh driest August on record with only 21% of its normal total. With only 42% of its normal, the Netherlands was also much drier than normal in August, and the summer season overall reached just 71% of normal. Following a markedly dry spring, the accumulated precipitation for 2025 up to the end of August placed the year for the Netherlands within the driest 5% of the historical record.

Autumn was wetter than normal across Western Europe, with the subregion receiving about 110% of its normal precipitation. September was particularly wet: Ireland and the United Kingdom saw 149% and 132%, respectively, and Luxembourg recorded an exceptional 400% of normal in September, marking its wettest September on record and the wettest month ever measured at the station since observations began in 1947. November brought above-normal precipitation totals for Ireland (seventh wettest on record) and the United Kingdom (both around 130% of normal).

The year finished with below-normal precipitation in December (85% of normal). The largest deficits occurred over the Benelux countries, which recorded only one-third of their normal precipitation totals.

(iii) Notable events and impacts

Storm Éowyn, the most significant storm of 2025 in Western Europe, hit Ireland, the United Kingdom, and northwestern France on 24 January. After forming off the coast of Florida, it rapidly intensified while crossing the North Atlantic. Ireland recorded a 184 km hr^{-1} gust at Mace Head (an exposed, but lowland coastal station)—provisionally its strongest on record in Ireland—with several stations reporting record gusts and 10-minute wind speeds up to 142 km hr^{-1}. The United Kingdom saw a peak gust of 161 km hr^{-1} at Drumalbin, a lowland station southeast of Glasgow in Scotland, and a weather station on Tiree (Inner Hebrides) measured a mean sea level pressure (MSLP) of 941.9 hPa, the country's lowest since storm naming began in 2015. Twelve stations in Ireland observed their lowest hourly MSLP since storm naming began in autumn 2015; during Éowyn the lowest hourly pressure was 940.0 hPa around 0400 UTC at Belmullet, Co Mayo.

Rain and flooding occurred in southwestern France on 19 and 20 April. In these two days, the station Lubersac in that region recorded 133.1 mm of precipitation—equivalent to its normal monthly total. In autumn, the airport station Findel in Luxembourg reported its highest 24-hour precipitation total on record for both September and the entire year, measuring 126.7 mm on 9 September 2025 (data since 1947).

The last day of snowfall in Belgium in the 2024/25 season was 14 March. This was the earliest last day of snow in that country since measurements began in 1928.

There were two short heatwaves reported from the Benelux Countries (Belgium, Netherlands, Luxembourg): the first from 28 June to 2 July and the second from 10 to 15 August. The highest reported temperatures of the year were all recorded on 2 July: 39.0°C in the Netherlands, 38.3°C in Belgium, and 36.0°C in Luxembourg, although no new records were set.

Southern France experienced a turbulent end of the year. From 19 to 23 December, a long-lasting heavy rain episode caused numerous floods. In four days, totals reached 202.7 mm in Montpellier at the coast and 443.9 mm in Mont-Aigoual (mountain station).

3. CENTRAL EUROPE

This subregion includes Germany, Switzerland, Austria, Poland, Czechia, Slovakia, and Hungary.

(i) Temperature

Over Central Europe, 2025 was 0.8°C warmer than normal. All countries in the subregion registered above-normal annual temperatures with anomalies ranging from +0.5°C to +1.0°C. All seasons were warmer than normal, but none was among the five warmest.

Winter was 1.2°C warmer than normal over Central Europe. While December and January were warmer than normal over the subregion (+1.6°C and +2.2°C anomaly, respectively), temperatures were near normal in February. The most pronounced contrast occurred over eastern parts of the subregion: while Czechia, Hungary, Poland, and Slovakia saw the largest positive anomalies in December and January, the same countries experienced the most pronounced negative anomalies in February. The largest positive anomalies in February occurred over Switzerland (+1.9°C).

Spring was 0.9°C warmer than normal over the subregion. While temperatures were well above normal in March and April (+2.2°C and +1.7°C anomalies; fifth-warmest April), May was 1.3°C colder than normal. In May, the largest negative anomalies occurred over eastern parts of the subregion.

Summer was 0.7°C warmer than normal over the subregion. Substantial positive anomalies occurred only in June (+1.9°C; fifth warmest); temperatures in July and August were close to normal. In June, temperature anomalies exceeded +2°C in all countries of the subregion except for Slovakia, Czechia, and Poland. For Hungary (+2.5°C anomaly) and Switzerland (+3.8°C), June was the second warmest on record.

Temperatures were moderately above normal over the subregion in autumn (+0.5°C anomaly), with all countries seeing near-normal to slightly above-normal temperatures, with anomalies mostly below +0.5°C. While temperatures were well above normal in September (+1.3°C), October and November were near normal. December was again notably warmer than normal (+1.9°C). The strongest anomalies occurred over the eastern parts of the subregion where several countries saw temperatures more than 2.0°C above normal, including Slovakia, Hungary, and Poland.

(ii) Precipitation

In 2025, total precipitation was below normal for Central Europe (88% of normal). All countries observed drier-than-normal conditions. Hungary was the country with the greatest deficit, receiving only 74% of its normal total, marking its fourth-driest year on record. Germany and Czechia also experienced a notably drier-than-normal year, with annual totals near 80% of normal. For Czechia, 2025 was the seventh-driest year on record.

Winter was drier than normal across Central Europe, with seasonal precipitation averaging only around 80% of normal. February was particularly dry: Austria, Czechia, Germany, Slovakia, and Switzerland all received less than half of their normal precipitation. Czechia received just 30% of its normal, making this the fourth-driest February on record. In contrast, January was wetter than normal overall, especially in Germany and Switzerland, which recorded 122% and 148% of their normal totals, respectively.

In spring, drier-than-normal conditions persisted across Central Europe, with the region receiving about 76% of the normal total. For Germany, spring was the third driest on record (56% of normal). All three months were drier than normal. March showed pronounced spatial contrasts—wetter-than-normal conditions dominated in Austria and Hungary, recording 137% and 205% of their normal totals, respectively, while Germany received only 30% of its normal amount, making this the sixth-driest March on record.

Following the drier-than-normal winter and spring, the summer season continued to be predominantly drier than normal across Central Europe, with all countries recording below-normal seasonal precipitation, except Switzerland; however, there were large monthly contrasts. June was very dry in Hungary, receiving just 17% of normal precipitation—its second driest June on record—and in Slovakia, with 51% of normal. July turned wetter across most countries, except Hungary, where dry conditions persisted. The largest wet anomalies occurred in Switzerland (128% of normal), Austria (142%), and Germany and Poland (around 130%). August was again

below normal in many areas: Germany, Czechia, and Poland each received only 60% of their normal precipitation, with Poland recording its sixth-driest August on record.

Precipitation in autumn was above normal across much of Central Europe (around 110% of normal). September was particularly wet in Czechia, Slovakia, Germany, and Switzerland, where totals reached 130%–150% of normal; for Czechia, it was the ninth-wettest September on record. Slovakia also experienced a very wet November (176% of normal). Despite the overall wetter-than-normal conditions, some areas recorded deficits, including Hungary in September and October, Austria in October, and Germany in November, where monthly totals fell to 70%–80% of normal and locally even as low as 20%–40% of normal.

The year concluded with an exceptionally dry December across the subregion, with precipitation averaging only 35% of normal—ranking as the fifth-driest December on record for the subregion. Several countries also recorded one of their 10 driest Decembers at the national scale, including Czechia (37% of normal; 3rd driest), Poland (30%; 6th driest), Germany (30%; 9th driest), and Hungary (30%; 10th driest).

(iii) Notable events and impacts

Central Europe experienced a prolonged dry spell from early February to late May 2025. Germany experienced its driest February–May period since 1931, with only 118 mm of rain—53% of the 1991–2020 average. In Slovakia, some stations received under 50% of normal from October 2024 to June 2025, with local deficits exceeding 200 mm. Thanks to the wet years of 2023 and 2024, impacts in Germany were limited, but Slovakia reported notable effects, including poor plant growth, small berries, and premature leaf fall.

Following below-normal snowfall during winter in Central Europe, March and April brought major snowfall in the Alps. Switzerland saw particularly high snowfall totals after Storm Hans, with 60 cm–100 cm accumulating by 17 April. The heavy snow caused road and rail closures and power outages, and several sites set new April records for daily snowfall—Montana with 58 cm (previous record was 50 cm in 1962) and Great St. Bernard Pass with 100 cm. The snow line on the southern Alps briefly dropped below 600 m.

A long period of hot days (daily maximum temperature ≥30°C) affected much of Czechia from 22 June to 6 July, followed by another period from 8 to 16 July. The highest daily maximum temperature during these periods was 36.6°C, recorded on both 2 and 3 July.

4. IBERIAN PENINSULA

This subregion includes Spain and Portugal.

(i) Temperature

Over the Iberian Peninsula, 2025 was 1.2°C warmer than normal, ranking third warmest on record. The year was third and fifth warmest in Spain and Portugal (+1.1°C and +0.8°C anomaly, respectively). On a seasonal basis, only summer was among the five warmest over the subregion.

Winter was 1°C warmer than normal over the Iberian Peninsula. Anomalies were weaker in December (+0.4°C), when compared with those in January and February (+1.3°C in both months).

Spring was 0.4°C warmer than normal over the subregion. While March was 0.6°C below normal, both April and May saw positive temperature anomalies (+1.2°C and +0.7°C, respectively).

Summer was the warmest on record for the subregion, with an anomaly of about +2.0°C. Nationally, the season was also warmest on record for both Spain and Portugal (+2.1°C and +1.8°C). For Portugal, June was also the warmest on record (+2.1°C anomaly), while August was fifth warmest (+1.5°C). For Spain, these months were also the warmest on record (also +3.5°C and +2.0°C, respectively).

Autumn was 1.0°C warmer than normal averaged over the subregion. While October was the fifth warmest on record for the area as a whole and second warmest for Portugal (+2.2°C anomaly), September and November were slightly warmer than normal with anomalies around +0.5°C. Portugal observed below-normal temperatures in September (−0.4°C anomaly). Slightly warmer-than-normal temperatures also continued in December (+0.5°C).

(ii) Precipitation

In 2025, wetter-than-normal conditions prevailed over the Iberian Peninsula, with an average of 130% of normal for Portugal and 109% of normal for Spain as a whole; however, parts of northern Spain only received 70%–90%. Portugal saw its third-wettest year in the twenty-first century.

Winter was drier than normal across the Iberian Peninsula (about 80% of normal). The season showed pronounced month-to-month contrasts. After a very dry December 2024, January was much wetter than normal, with monthly totals reaching 180% of normal in Portugal and 136% of normal in Spain. In February, drier-than-normal conditions returned to Spain (66% of normal), particularly affecting the southeast, where rainfall amounts were just 20%–40% of normal.

Spring was among the 10 wettest on record, with precipitation reaching 150% of normal overall. In Spain, the season was fifth wettest on record with 151% of normal. March was exceptionally wet: Spain received 251% of normal, its third wettest March on record, while Portugal recorded 229%, its fifth-wettest. April remained wet, with Portugal reaching 144% of normal, whereas May brought near-normal to drier-than-normal conditions.

Summer was dry overall, with the subregion receiving about 75% of normal precipitation. For Portugal, it was the driest summer on record, with only 24% of its normal total. Spain received 81% of its normal for the summer as a whole, but above-normal rainfall in July (124%) partially mitigated the markedly dry conditions in June and August, when monthly totals were only around 70% of normal.

Autumn was drier than normal overall, with the subregion receiving about 93% of the normal amount. The season showed pronounced month to month contrasts. September and October were generally drier than normal, with Spain recording 60% of normal in both months, while November brought a return to wetter-than-normal conditions—particularly in Portugal, where precipitation was 180% of normal.

The wetter-than-normal conditions continued into December (117% of normal). Portugal experienced particularly wet conditions, reaching 137% of normal for the country as a whole. In Spain, precipitation was 109% of normal overall, but in the southeast monthly totals exceeded twice the normal amounts, and locally even three times the normal.

(iii) Notable events and impacts

Three heatwaves were observed over mainland Spain and the Baleares from June to August; Portugal also reported three summer heatwaves. The highest temperature of the year was recorded at the end of June in both countries (46.0°C in Spain [El Granado, Andalusia] on 28 June and 46.6°C in Portugal [Mora, east of Lisbon, new national record] on 29 June).

According to the Copernicus European Forest Fire Information System (EFFIS) wildfire statistics, almost 400,000 hectares (ha) was burned in Spain in 2025, the most since the start of recordkeeping in 2006. Approximately 350 fires were reported in 2025, the second highest in this period after 2022. Almost 38,000 ha of the burned area in 2025 was due to just one fire, which occurred in the Zamora Province in northwestern Spain in August. This was the largest recorded single fire in Spain. At least 12,000 people had to leave their homes; tourists were also affected due to evacuations of hotels, camping sites, and beaches.

Several intense low-pressure systems impacted the Azores Islands during the year. The most severe was post-Tropical Cyclone Gabrielle (25–26 September), which caused strong wind with gusts (154 km hr^{-1} in Faial/Horta) and heavy precipitation (daily totals over 60 mm). Gabrielle then moved farther east, reaching the mainland of the Iberian Peninsula and the western Mediterranean, causing heavy precipitation. Some areas in Spain recorded over 350 mm within two days, and Ibiza Island received 254 mm in one day (30 September), marking the wettest day for the island since 1952 when records began.

In mid-October, southeastern Spain was impacted by two more low-pressure systems. At the east coast and on the Balearic Islands, local rainfall totaled around 100 mm in an hour, and in the Ebro Delta in Catalonia, 304 mm fell in 24 hours on 11–12 October, according to the Catalan Meteorological Service. Widespread flooding, including flash floods, was reported. At least 18 people were injured, road traffic came to a standstill, and flights were canceled or diverted. Portugal recorded its highest local 24-hour precipitation total of the year—117 mm on

13 November in Guarda (northeast of Lisbon, 1000-m altitude)—when a cold front from Claudia, a North Atlantic storm, reached the country.

5. THE NORDIC AND BALTIC COUNTRIES

This subregion includes Iceland, Norway, Denmark, Sweden, Finland, Estonia, Latvia, and Lithuania.

(i) Temperature

Averaged over the Nordic and Baltic countries, the 2025 temperature was 1.4°C above normal, the second highest on record. For all countries, the year was among their five warmest; Iceland and Norway observed their warmest year on record.

Winter was 1.7°C warmer than normal over the Nordic and Baltic countries. Over the Baltic countries, seasonal anomalies exceeded +2°C, and was the fifth warmest winter in Latvia and Estonia (both +2.6°C anomaly), particularly due to a much warmer-than-normal January, which saw anomalies between +4°C and +5°C and ranked among the five warmest for all Baltic countries individually.

Spring was the fifth warmest on record over the subregion (+1.2°C anomaly), with temperature anomalies ranked among the five highest for March and April (+2.6°C and +1.2°C, respectively). While temperatures were near normal in May over the subregion as a whole, they were well-below normal over the Baltic countries. In contrast, May was warmest (+3.0°C anomaly) and the season as a whole was second warmest (+2.4°C anomaly) on record over Iceland.

Summer was 0.7°C warmer than normal over the subregion. While July was third warmest (+2.4°C anomaly) due to exceptional heatwaves (see *Notable events and impacts*) particularly affecting the Nordic countries, temperatures were close to normal in August and slightly below normal (−0.2°C anomaly) in June. July was the warmest on record for Iceland (+1.6°C) and third warmest for Norway (+2.8°C).

Autumn was the fifth warmest on record over the subregion (+1.5°C anomaly), mainly due to large positive anomalies exceeding +1.5°C over Norway, Finland, and Estonia. September saw the largest positive anomalies over the subregion (+2.2°C; second highest on record), particularly over Norway, Sweden, Finland, and the Baltic countries (anomalies between +2°C and +3°C; third to fifth warmest on record).

Overall, December was exceptionally warm across nearly the entire subregion. For all countries except Finland, temperatures were at least 3°C above normal. For Iceland and Denmark, December was the third warmest, and for Sweden it was fifth.

(ii) Precipitation

In 2025, precipitation was slightly below normal overall (95% of normal). Drier-than-normal conditions dominated across Iceland, Denmark, and southern parts of Norway, Sweden, and Finland. In contrast, central and northern parts of Norway recorded above-normal annual totals, bringing the national average to 110% of normal.

Winter precipitation was below normal overall (93% of normal), though the season featured strong month-to-month contrasts. Estonia recorded 177% of its normal total in January, the second wettest January on record for the country, while Latvia also saw a very wet month with 157% of normal, its third wettest January. February, by contrast, was much drier than normal overall (around 60% of normal), with all countries except Norway and Iceland receiving less than 50% of their normal precipitation.

Spring was drier than normal overall (93% of normal), though with notable regional differences. While drier-than-normal conditions dominated across Sweden and Denmark (60%–70% of normal), Norway experienced a markedly wetter-than-normal season with 125% of its normal. All three months showed mixed conditions and substantial variation between countries. March brought the largest deficits, with Denmark and Estonia receiving only 30%–40% of their normal totals, while at the same time Norway was much wetter than normal (140%). May was the sixth wettest on record for Latvia.

Precipitation during summer was near normal overall. While near-normal to drier-than-normal conditions dominated over the Nordic countries, the Baltic countries experienced significantly wetter-than-normal conditions with the largest anomalies in June and July (120%–170% of

normal) and Estonia recording its seventh wettest summer (137%). The Nordic countries saw a mix of wetter- and drier-than-normal summer months, with notably drier-than-normal conditions (60%–80%) in Finland in July and in Denmark and Sweden in August. Denmark saw very wet conditions in July, reaching 171% of normal and marking its ninth wettest July on record.

Autumn precipitation was near normal overall, though with pronounced regional contrasts. Conditions reversed compared to summer: wetter-than-normal conditions dominated across Norway, Sweden, and Finland while the Baltic countries generally experienced below-normal precipitation. Sweden recorded the largest wet anomaly (121% of normal), driven by a very wet September (150% of normal) and October (130%). September was also wet in Iceland, particularly in the north and east—ranking among the wettest Septembers on record at many locations.

Mixed conditions returned in December, with strong spatial contrasts across the subregion. Iceland experienced an exceptionally dry month, receiving only 25% of the normal total, its driest December on record. Finland, in contrast, recorded a notably wet month (121% of normal).

(iii) Notable events and impacts

On 18 April and repeated on 19 April, Valga and Võru in Estonia recorded 27.8°C—a new national temperature record for April. Also on 18 April, Skrīveri in Latvia recorded 28.4°C, the country's highest April temperature on record. New daily temperature records were set in Lithuania from 17 to 19 April with daily maxima between 26°C and 29°C. The heat episode was followed by rapid cooling, with severe morning frosts during the period of active vegetation. Air temperatures dropped to –5°C and locally to –10°C near the surface in the last week of April. Similar frosts returned in early May, with up to 11 consecutive nights of frost in Lithuania that damaged approximately 4000 ha of strawberry and vegetable crops.

Very heavy rain affected eastern central Sweden on 6 September, causing flooding and disrupting train and road traffic. Myckelgensjö reported a daily rain total of 140.0 mm, which was the second highest daily rain total ever recorded in Sweden in September.

On 28 October, snow depth in Reykjavík (Iceland) reached 40 cm, by far the greatest October snow depth ever recorded there. The snowfall caused major traffic disruptions and congestion in the city.

A 27 December storm (named Johannes in Sweden and Hannes in Finland) brought exceptional gusts to eastern central Sweden, with some stations recording wind gusts up to 170 km hr^{-1} with an estimated return period of more than 100 years (i.e., a 1-in-100 year event). At least four people died, and Sweden saw its most severe forest damage from a single event since 2007. Western and northern Finland were also strongly impacted; the storm ranked as Finland's third most significant windstorm of the twenty-first century (after Janika in November 2001 and Tapani in December 2011). Crossing Estonia on 27–28 December, the storm downed trees, damaged roofs, and left thousands without power.

6. CENTRAL MEDITERRANEAN REGION

This subregion includes Italy, Monaco, Malta, Slovenia, Croatia, Serbia, Montenegro, Bosnia and Herzegovina, Albania, North Macedonia, Greece, and Bulgaria.

(i) Temperature

Over the central Mediterranean region, 2025 was the fifth-warmest year on record (+1.2°C anomaly), with most countries of the subregion separately reporting one of their five-warmest years. All seasons were warmer than normal, with spring and summer both ranking fifth warmest on record for the subregion.

Winter was 1.2°C warmer than normal over the central Mediterranean region. The largest anomaly occurred in January (+2.3°C), making this the fifth warmest January over the subregion. Anomalies were largest over the Balkan Peninsula with countries reporting temperatures between 2°C and 3°C above normal. Greece reported its warmest January on record. In contrast, the weakest positive anomaly occurred in February (+0.4°C). February was colder than normal over eastern parts of the subregion, particularly in Bulgaria (–1.9°C anomaly).

Spring was 0.9°C warmer than normal over the subregion (fifth warmest on record). The largest positive anomaly occurred in March (+2.2°C; fourth warmest); March was also among the

five warmest for most countries of the subregion. In contrast, May was 0.4°C below normal over the subregion.

Summer was 1.7°C warmer than normal over the subregion (fifth warmest on record). The largest anomalies occurred in June over the subregion (+2.8°C; second warmest); June was among the four warmest for almost all countries of the subregion. In July and August, anomalies were weaker for the subregion (+1.6°C and +0.6°C, respectively), but still were close to or more than +2°C in Bulgaria, North Macedonia, Serbia, Albania, and Greece in July.

Temperatures were moderately above normal in autumn over the subregion (+0.7°C anomaly). The largest positive anomalies occurred in September (+1.7°C). Bulgaria, Croatia, Serbia, Albania, Montenegro, and Bosnia and Herzegovina all saw temperature anomalies close to or above +2°C. October was colder than normal for the subregion as a whole (−0.6°C anomaly) and also individually for all countries. November saw mostly warmer-than-normal conditions, but temperature anomalies of more than +2°C only occurred over Bulgaria and Greece.

In December, the central Mediterranean region was 1.6°C warmer than normal. Nationally, Italy recorded one of the highest anomalies (+1.7°C), making this the third warmest December on record.

(ii) Precipitation

In 2025, most of the central Mediterranean region saw near- to drier-than-normal conditions, with the largest deficits in Serbia (87% of normal). Northern Italy and western parts of Greece saw wetter-than-normal conditions with anomalies of 130%–160% of normal.

Winter precipitation was near normal, though with strong contrasts between countries and months. In January and February, drier-than-normal conditions dominated, with several countries receiving less than 60% of their normal totals. North Macedonia observed its driest February on record, with less than 20% of its normal.

Spring was wetter than normal across the subregion (116% of normal overall). March was particularly wet across most areas (145% of normal), except in Greece (64% of normal) and Bulgaria (80%). Slovenia, Croatia, and Bosnia and Herzegovina saw especially high totals, around twice their normal precipitation. March was the ninth wettest on record for Serbia (156% of normal) and 10th wettest for Italy (157%).

Summer was notably drier than normal across the subregion, with overall precipitation at around 80% of normal. All countries, except Montenegro, recorded below-normal seasonal totals. Bulgaria, Greece, North Macedonia, and Serbia were particularly dry in summer, receiving less than half of their normal precipitation totals. The season was dominated by an extreme June drought (only about 30% of normal precipitation). Croatia (16% of normal) and Serbia and Slovenia (less than 30% of normal) each recorded their driest June on record, while Italy saw its second driest (51% of normal).

Autumn was markedly wet (120% of normal overall), particularly in Albania, Bulgaria, North Macedonia, and Serbia (150%–170% of normal). The season was shaped by multiple heavy rainfall events in October and November. Bulgaria received more than twice its normal precipitation total in October, while for Albania, Serbia, and northwestern Greece, monthly totals exceeded two to three times the normal amounts in November. September, in contrast, was dominated by drier-than-normal conditions, especially in Bulgaria, North Macedonia, Greece, Croatia, and Albania (30%–60% of normal).

December was drier than normal across the subregion, with around 68% of normal precipitation. Several countries recorded 50% or less of their normal monthly totals, including Albania, Slovenia, Croatia, Bosnia and Herzegovina, North Macedonia, Montenegro, and Serbia.

(iii) Notable events and impacts

Heavy rainfall affected northwestern Italy on 15–17 April, an exceptional event for that month. The Eastern Aosta Valley recorded 300 mm in 48 hours with local maximum values up to 600 mm (return period of 300 to 1000 years) with the snowline locally dropping to 500 m on 17 April. In Piedmont, the Boccioleto station recorded 417 mm of rain in 24 hours and 565 mm in 48 hours; in Trivero-Camparient, 570.6 mm in 48 hours was recorded. These totals were more than double—and in some locations even triple—the April average. The exceptionally heavy

rains triggered river flooding and landslides. Heavy snowfall caused damage to agricultural land and roads, and initiated evacuations and power outages.

The central Mediterranean region was affected by long and intense heatwaves in July, especially in Italy and Greece (see Sidebar 7.4 for details).

On 8 July, a brief but very severe storm hit the city of Split (Middle Adriatic, Dalmatia, Croatia) and the surrounding area, bringing heavy rain, hail, and gale force winds. Marjan (a hill on the peninsula of the city of Split) and the western part of Split suffered extensive material damage, and human lives were at risk. The maximum wind gust measured in Split was 128.5 km hr^{-1} with a direction from the west, until the anemometer failed. This wind gust significantly exceeded all previously measured values from westerly and northwesterly wind directions—those from which summer thunderstorms typically approach Split.

During July and August, the central region of Montenegro faced one of its most severe wildfire seasons in the past two decades. More than 10,000 hectares of forest and agricultural land were burnt.

Heavy rain on the southern Black Sea coast of Bulgaria on 2–3 October, including 250.7 mm rain in 12 hours at Kosti, resulted in flash flooding with four deaths reported (WMO 2026). This event also brought record-breaking daily precipitation totals in central and eastern Serbia as well as abnormal early-season snow to parts of Slovenia, Serbia, and Kosovo. It also had impacts in Romania (see section 7f7).

During 18–30 November, northwestern Greece was hit by two consecutive storms, including Adel, that caused severe flooding and landslides in Epirus. An all-time station record of 592.7 mm of monthly rainfall was recorded in Corfu.

During 4–6 December, a severe weather system named Byron—characterized by heavy rain, thunderstorms, and hail—struck the entire country of Greece, causing numerous floods and extensive damage, particularly in the southern and eastern Peloponnese (Laconia and Messinia), eastern-central Greece (including West Attica), and the Dodecanese. The Enipeas River overflowed, and additional localized flooding occurred in some parts.

7. EASTERN EUROPE

This subregion includes the European part of Russia, Belarus, Ukraine, Moldova, Romania, and West Kazakhstan.

(i) Temperature

Over Eastern Europe, 2025 was the second warmest year on record (+1.8°C anomaly). The largest positive anomalies (above +2°C) occurred over Russia and West Kazakhstan. Winter and spring were also each the second warmest for the subregion.

Winter was 2.7°C warmer than normal over Eastern Europe. Seasonal anomalies reached almost +3°C in the European part of Russia (second warmest). January was much warmer than normal over the subregion (+5.3°C anomaly; warmest on record), with anomalies exceeding +4°C in all countries of the subregion. January was one of the five warmest on record for all countries of the subregion, including the warmest on record for Belarus (+5.3°C anomaly). In contrast, February was colder than normal over most of the subregion.

Spring was 1.7°C warmer than normal over the subregion, with the largest anomalies observed over Russia and West Kazakhstan. March was much warmer than normal over the subregion (+4.3°C anomaly; warmest on record), and also the warmest on record for Belarus, Romania, and Russia. In contrast, May was 0.3°C below normal.

Summer was only moderately (+0.4°C) warmer than normal over the subregion. The largest positive anomalies occurred in July (+1.2°C). In contrast, June was 0.3°C cooler than normal. While anomalies in June were mostly between –1°C and +1°C, Romania saw temperatures well above normal (+2.1°C).

Autumn was third warmest on record over the subregion (+2.2°C anomaly), mainly due to an exceptionally warm November (warmest on record) when anomalies were close to +4°C in the subregion as a whole, as well as parts of Russia, West Kazakhstan, and Ukraine. Anomalies in September and October were also positive (+1.7°C and +1.2°C).

Much warmer-than-normal conditions continued in December, with an anomaly of +2.6°C. Nationally, Belarus recorded one of the highest anomalies (+3.0°C), making this its seventh-warmest December on record.

(ii) Precipitation

Precipitation in 2025 was near normal for Eastern Europe as a whole (103% of normal). The largest deficits occurred over eastern Ukraine and adjacent parts of southern European Russia, where totals dropped to 70%–90% of normal, and locally only 50%–70%. Wetter-than-normal conditions prevailed across northern parts of European Russia.

Winter precipitation was below normal overall (92% of normal), largely due to a much-drier-than-normal February (60% of normal). Belarus, Romania, and Moldova received less than 40% of their normal precipitation totals, with Belarus experiencing its third-driest February on record.

Spring was notably wetter than normal (116% of normal), especially in Romania, Moldova, and Belarus (120%–130%). May was particularly wet (127%), with Romania and Belarus each receiving around 160% of their normal totals; in Belarus, May 2025 was among its five wettest on record. Despite the overall wetter-than-normal conditions, April was drier than normal in West Kazakhstan, Moldova, and Romania, all of which received less than 60% of their normal totals; Romania reported its sixth-driest April on record.

Summer precipitation was above normal overall, with the subregion receiving about 105% of normal precipitation, though with a large contrast among the countries. The European part of Russia, Belarus, and West Kazakhstan experienced wetter-than-normal conditions due a particularly wet June (130%–150% of normal), while dry conditions affected Moldova, Romania, and Ukraine (60%–80% of their normal summer totals). A very dry June brought around 20% of normal precipitation to Moldova and Romania and less than 50% of normal to Ukraine, marking its third-driest June on record.

Autumn precipitation was near-normal overall, with large contrast between the months and the countries. The season started with drier-than-normal conditions across most of the subregion in September. All countries (except Moldova) experienced below-normal monthly totals (60%–90%), and large parts of Ukraine, Belarus, European Russia, and West Kazakhstan received only 20%–40% of their normal precipitation, and even less locally. In contrast, October and November were wetter than normal across much of the subregion, with some areas—including Moldova, Romania, and West Kazakhstan—receiving 1.5 to 2.5 times their normal totals. December saw strong regional contrasts, with wetter-than-normal northern areas and much-drier-than-normal southwestern areas (Moldova and Romania).

(iii) Notable events and impacts

Severe ice and rime deposits (ice, wet snow) measuring 35 mm–47 mm in depth caused power outages in northwestern European Russia (St. Petersburg and Pskov regions) on 11–14 January, as numerous trees fell onto power lines and broke them.

On 25 April, unusually high daily maximum temperatures for the time of year were recorded across much of Ukraine, reaching 25°C–28°C (normal April maximum temperatures in Ukraine are around 14°C–15°C on average). Earlier, during 16–23 April, Moscow (Russia) recorded new daily maximum temperatures records nearly every day, reaching up to 25.9°C on 21 April.

A large low-pressure system swept through western Romania on 9 July, bringing violent wind gusts, heavy rain, and localized thunderstorms. The resort town of Sinaia, located in Prahova County, was one of the worst affected areas. Wind gusts exceeded 100 km hr^{-1}, tearing off the roof of the local train station, uprooting trees, and downing power lines. At least 14 people were injured.

A severe cloudburst impacted Moscow on 15 July, with 75 mm–85 mm of rain falling in less than two hours—an amount that equaled or even exceeded the city's typical monthly average for July. The intense rainfall overwhelmed stormwater systems and caused flash flooding across key districts. Metro lines were also partially disrupted, with some stations reporting temporary closures or limited access.

A large mudflow triggered by heavy rain was observed in the North Caucasus (Kabardino-Balkaria region, southern European Russia) on 31 July, with a volume of approximately three million cubic meters. As a result, a hydrological station was destroyed, the mudflow channel overflowed, and a federal road was blocked by mudflows over 200 m in length. Gas and water lines, as well as two power transmission towers, were damaged.

During 5–8 October, Cyclone Barbara formed over the Ionian Sea in the Mediterranean and moved over the Balkan Peninsula; Romania experienced heavy precipitation from the storm. From 1 to 8 October, a total of 139.4 mm was recorded in Bucharest, which was more than twice the normal precipitation for this period and came close to the October record of monthly precipitation of 143.3 mm set in 1972. Even higher totals and more severe impacts from this storm occurred on the Balkan Peninsula (see section 7f6).

8. MIDDLE EAST

This subregion includes Israel, Cyprus, Jordan, Lebanon, and Syria.

(i) Temperature

Over the Middle East, 2025 was warmer than normal (+1.2°C anomaly). The year was second warmest for Cyprus and fifth warmest for Israel, Lebanon, and Syria. All seasons, except for winter, were among their five warmest for the subregion.

Winter was 0.3°C warmer than normal over the region. The most significant anomalies occurred in January and February. January was 1.8°C warmer than normal over the subregion (third warmest) and February was 1.5°C colder than normal.

Spring was 1.5°C warmer than normal over the subregion (third warmest); Syria saw its third warmest spring on record (+1.9°C anomaly). All months of the season were warmer than normal. The largest anomalies occurred in March (+2.1°C; fifth warmest) and May (1.4°C; fourth warmest). May was particularly warm in Syria (+1.8°C; second warmest).

Summer was 1.3°C warmer than normal over the subregion (fifth warmest). For Syria, this was its second-warmest summer on record (+1.4°C anomaly); there was weak month-to-month variation.

Temperatures in autumn were warmer than normal over the subregion (+1.4°C anomaly). While temperatures were mostly near normal in September and October (+0.5°C anomaly), November was record warm across all countries, with anomalies exceeding +3°C across the subregion. December remained warmer than normal as well, though with a lower overall anomaly of +1.2°C. At the national level, the largest December anomaly occurred in Cyprus, where temperatures were +2.1°C above normal, making this the fifth-warmest December on record.

(ii) Precipitation

The Middle East saw one of its driest years on record, receiving only about half of normal precipitation. Syria, Lebanon, and Cyprus each reported their second-driest year on record with annual totals reaching only about 50% of the normal precipitation, while Israel saw its fifth driest year, receiving 68% of its normal total.

Winter was much drier than normal across the Middle East, ranking among the driest winters for the subregion, with only about 40% of normal precipitation. Syria and Israel reported their driest- and second-driest winter on record, respectively, with each receiving only around 50% of normal precipitation. January was particularly dry: Cyprus recorded 17% of normal for the month, Israel 10%, and Syria 6%; it was one of the driest Januarys on record for all three countries.

Drier-than-normal conditions continued in spring (42% of normal), ranking among the driest springs for the subregion, particularly due to a very dry April which saw 20%–40% of normal precipitation over large parts. Syria recorded its third driest spring, with a seasonal total near 30% of normal, and the 2024/25 rainy season (September to May) was one of the driest seasons in over 20 years across all Syrian territories. In some regions, it was the driest in 60 years. Israel also reported an exceptionally dry 2024/25 rainfall season. In the non-desert regions of the country, about 55% of normal rainfall was recorded, making it one of the driest rainfall seasons since records began. In Jordan, above-normal precipitation was observed during spring due to heavy rainfall in the northern and central regions in April. Despite this short-term boost, the 2024/25 rainy season still remained below normal across most parts of the country.

Summer is the dry season in this subregion with climatological averages not exceeding 1 mm month^{-1} across most of the subregion. In 2025, there was mostly very little or no precipitation across the subregion in all months.

Autumn, and thus the first part of the 2025/26 rainfall season, began with below-normal rainfall across the subregion. In Syria, both September and October had no significant rainfall; the precipitation total did not exceed 60% of normal for the season as a whole, with only about 20% at some stations. In Israel, below-average rainfall persisted until mid-November; in September, locally significant rainfall occurred in the north, with national daily rainfall records broken. From mid-November until the end of 2025, several rainfall events occurred, such that by the end of the year, cumulative rainfall totals were above average for the corresponding period—markedly so in southern Israel—while the northeastern part of the country still remained in deficit. December precipitation was well above normal (146% of normal) for the subregion as a whole.

(iii) Notable events and impacts

During spring–summer 2025, the dry rainy season led to a relatively high frequency of dust events in the region, originating both from local sources and from external transport. Syria reported 16 days with dust events during March and April.

From 23 April to 25 May, four extreme Sharav events (short, intense hot spells) occurred in Israel. Temperatures reached up to 45°C in the Jordan Valley and the Arava region. New April temperature records were set in several locations, and the highest May temperatures in decades were also observed. Due to the heat and dryness, large wildfires broke out in the Judean Foothills and the Jerusalem area, leading to road closures and the evacuation of several communities.

In summer 2025, the worst fire season in Syria in over 10 years in terms of the forest area affected by fires occurred, affecting 21,810 ha, which is about 3.7% of the total forest area.

The most destructive and deadly fire on record in Cyprus occurred during 23–25 July, destroying homes, properties, crops, livelihoods, craft units, and large areas of natural environment (vineyards, pastures). The agricultural sector recorded large damage, and even churches and ancient monuments were affected. The area of burnt land was estimated at 12,000 ha–13,000 ha in the Limassol district, roughly 1.3% of Cyprus's land area (according to satellite and official environmental analysis).

On 25 September, an exceptionally heavy rainfall event occurred in northern Israel. In the Nahariya area (northwestern coastal plain), more than 130 mm were recorded (Regba: 144 mm; Evron: 135 mm). These totals are extremely unusual for September (the long-term average is 3 mm–4 mm), and exceeded the previous September national record of 96 mm (1932) by a wide margin. Rainfall intensities during the event were also exceptional: the entire rainfall event in the Nahariya area occurred within a three to four hour span, with most (more than 100 mm) falling within just two hours.

9. TÜRKIYE AND SOUTH CAUCASUS

This subregion includes Türkiye, Armenia, Georgia, and Azerbaijan.

(i) Temperature

Over the subregion Türkiye and the South Caucasus, 2025 was 1.1°C warmer than normal. Türkiye observed its fifth-warmest year on record (+1.2°C anomaly). All seasons were warmer than normal, with summer the second warmest on record for the subregion.

Winter was 0.6°C warmer than normal over the subregion. The season was characterized by pronounced month-to-month variations. December 2024 and January 2025 were warmer than normal over the subregion (+1.1°C and +2.3°C). February, in contrast, was 1.7°C colder than normal for the subregion as a whole. Temperatures were more than 2°C lower than normal across large parts—areas over Georgia were more than 3°C below normal.

Spring was 1.2°C warmer than normal over the subregion. The largest positive anomalies occurred in March (+2.8°C; fourth warmest). With an anomaly of +3°C, March was fourth warmest on record for Türkiye. Temperatures were near normal in April.

Summer was 1.4°C warmer than normal over the subregion (second warmest). The largest anomalies occurred in July (+1.8°C; warmest on record) and August (+1.4°C; fourth warmest).

July was the warmest on record for Türkiye and third warmest for Georgia. August was third warmest for Armenia (+1.7°C anomaly).

Temperatures in autumn were above normal over the subregion (+1.2°C anomaly). While the temperatures in September and October almost equaled their long-term averages, it was 3°C above normal in November, marking the second-warmest November on record. For Türkiye and Armenia, November was third and second warmest, respectively, with anomalies close to +3°C. December remained warmer than normal, though with a lower overall anomaly of +1.6°C.

(ii) Precipitation

Türkiye and the South Caucasus saw one of the driest years on record for the subregion overall with only around 80% of normal precipitation. Türkiye reported its driest year on record (72% of normal) and Armenia its sixth driest (83%).

Winter was drier than normal across the subregion with only about 74% of normal precipitation. Türkiye observed its sixth-driest-winter season on record (72% of normal), while Georgia, in contrast, experienced a wetter-than-normal season (114%). January saw particularly dry conditions across the subregion (around 40% of normal). Armenia recorded only 18% of normal in January—its second driest on record—while Türkiye saw its third-driest January (39%). Despite the predominantly drier-than-normal conditions, February brought above-normal precipitation to the South Caucasus (120%–140%), whereas dry conditions persisted in Türkiye.

Spring was drier than normal overall (around 90% of normal), though with strong monthly contrasts. The season started with dry conditions in March with the largest deficits occurring over Türkiye, where only half the normal monthly total was registered, marking its third-driest March on record. April, in contrast, had higher-than-normal monthly totals across the subregion, averaging about 130% of normal.

Overall, summer precipitation was much lower than normal in the subregion (around 50% of normal), marking one of the driest summers on record. It was the driest summer on record for Türkiye, with less than half the normal precipitation, while Armenia (64% of normal) and Georgia (68%), reported their fourth and third driest summer on record, respectively. The season was marked by persistent precipitation deficits. Each month, the subregion received only about half of its usual rainfall. Türkiye recorded the largest deficit in June, receiving just 34% of normal precipitation—its third-driest June on record—while Armenia saw only around 20% of normal in August, ranking as its second-driest August on record.

Autumn was drier than normal overall (around 90% of normal), though with strong monthly contrasts. September saw markedly above-normal precipitation, especially in the South Caucasus, where national anomalies were 140%–170% of normal, and local totals were up to or exceeded 250%. November, in contrast, was much drier than normal across the subregion, with particularly large deficits in the South Caucasus. Armenia received less than 10% of normal—its second-driest November on record—while Türkiye recorded 57%, ranking as its 10th-driest November on record.

The year ended with near-normal (102%) precipitation in December. The South Caucasus experienced a notably wetter-than-normal month (110%–130%), while precipitation in Türkiye was close to normal (97%).

(iii) Notable events and impacts

On 5–6 February, heavy rainfall affected the city of Lankaran (southeastern Azerbaijan) and surrounding areas, leading to flooding in several districts. Rainfall totals reached 133 mm, overwhelming drainage systems and causing water accumulation in streets and residential areas. Streets in the city center were severely flooded, disrupting transportation. Several houses and agricultural lands were affected by the flooding. Twenty-two people were evacuated due to rising water levels.

A severe winter storm, accompanied by heavy snowfall and cooling, affected western Georgia from 21 February, causing widespread damage and humanitarian challenges. The snowstorm was caused by a cut-off low combined with Arctic air masses moving over the Black Sea, triggering a lake effect and intensified further in the mountainous terrain of the Caucasus mountains. The cut-off low remained almost stationary for one week. Critical impacts were still recorded on

1 March with heavy snow affecting many places. Many villages remained isolated, snowdrifts blocked roads, thousands of people were without electricity, and emergency responders faced serious challenges in reaching those in need who suffered from food shortages. At least three people died due to collapsed roofs, unavailability of essential medicines, and lack of timely medical access.

A late spring frost affected most of Türkiye, except the western, southeastern, and coastal areas, during 7–15 April. Many agricultural products, especially apricots in Malatya and hazelnuts in the Black Sea Region, were damaged by the frost.

On 15 June, maximum wind gusts reached 140 km hr^{-1} and caused damage in the city of Aparan in Armenia.

A heatwave affected most of Türkiye during 23–29 July. A temperature of 50.5°C was recorded in Silopi, Cizre, on 25 July, setting a new national temperature record for the country. Simultaneously, 66 stations broke their own temperature records (see Sidebar 7.4).

Extremely hot temperatures and heatwaves were also observed from 30 July to 8 August in Armenia, when daily maximum temperatures in Yerevan and other low-elevation areas reached as high as 42.6°C (mean daily maximum temperatures in July and August are about 30°C).

Sidebar 7.4: **Long, intense, and widespread heatwaves in Europe**

Heatwaves in Europe occur every year, but there is typically a high year-to-year variability in their spatial and temporal characteristics. In 2025, several heatwaves stood out due to their long duration, being widespread across Europe, stretching into northern latitudes, and/or reaching (locally) extremely high maximum temperatures (Fig. SB7.7).

Most heatwaves have a duration of less than one week (with a minimum of three days by definition). However, some heatwaves in 2025 persisted for longer periods, affecting Southern Europe and extending into Northern Europe, particularly Finland, northern Norway, and Sweden.

Most countries in Europe and the WMO RA VI Region (which includes additionally Türkiye, the South Caucasus countries, and parts of the Middle East) experienced at least one heatwave (according to the definition used here: daily maximum temperature reaches at least both 28°C and the 98th percentile of the 1961–90 reference period during three consecutive days). Some countries experienced multiple

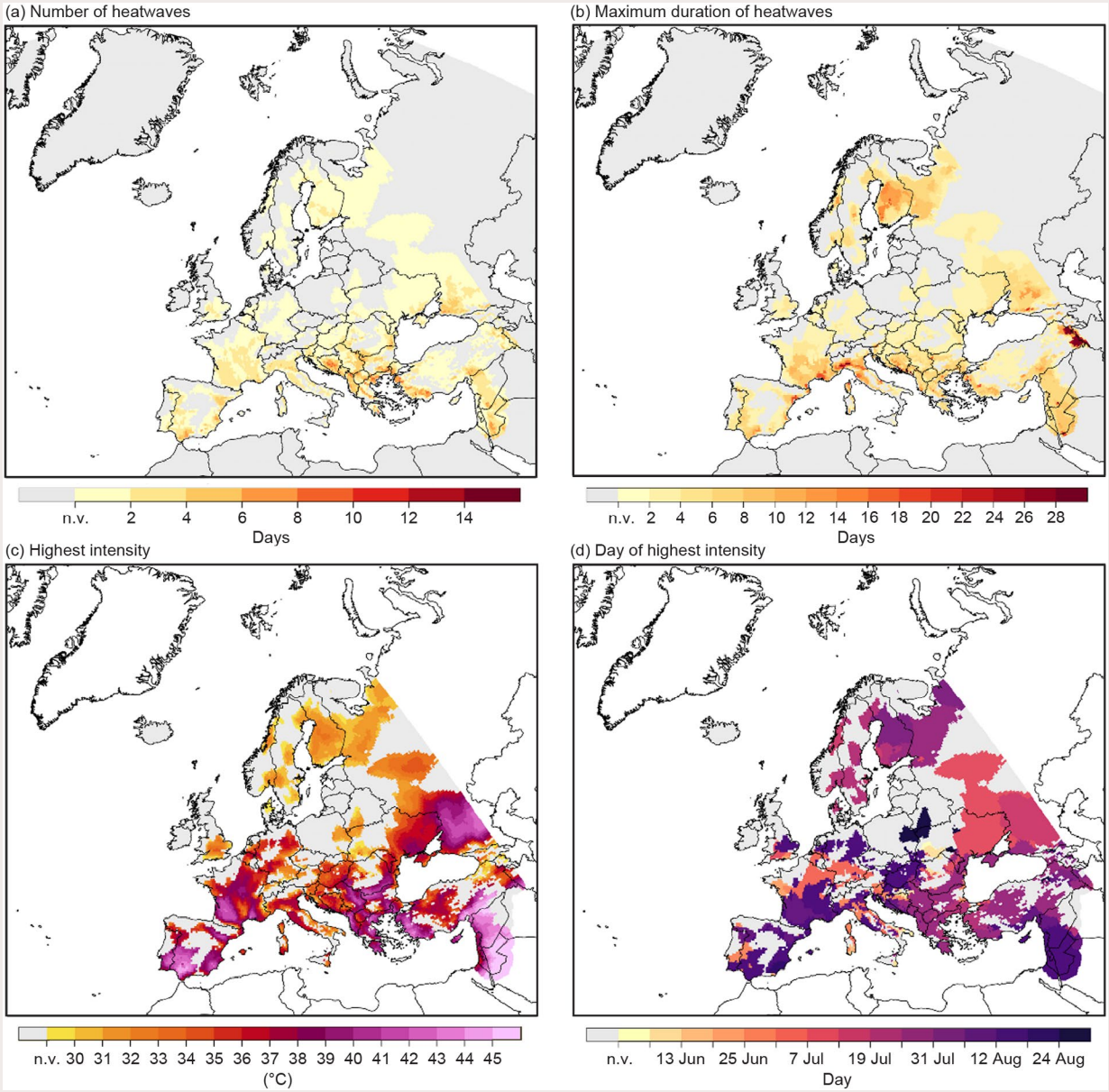

Fig. SB7.7. Maps of heatwave characteristics in Europe/World Meteorological Organization (WMO) Regional Association (RA) VI Region for summer 2025. A heatwave is defined as a period of at least three consecutive days with daily maximum temperature reaching at least both 28°C and the 98th percentile of the period 1961–90, considering the corresponding days of the year ±15 days. Data basis: Gridded daily SYNOP and E-OBS data, Cornes et al. (2018), preliminary data. The highest intensity is defined as the highest maximum temperature within the heatwave days for each grid point. (Source: Deutscher Wetterdienst [DWD].)

heatwaves; The Balkans, western Türkiye, and the Middle East had six or more.

In terms of intensity (defined here as the highest temperature reached during the heatwave), temperatures exceeded 40°C in many places in the Mediterranean region, as is typically the case. The peak of the most intense heatwave varied across the region. While some western and central parts of Europe observed their hottest day of the summer in late June or early July, the southeastern parts of the RA VI Region and also Northern Europe mainly recorded their hottest day later in July. Some places in various parts of Europe even saw their hottest day in August.

The severity of a heatwave can be quantified by the cumulative temperature anomaly (sum of anomalies over all days and grid points of the region affected by the heatwave), a simple metric that considers duration, intensity, and spatial extent of the heatwave, as shown in the bubble diagram in Fig. SB7.8. Based on this metric (which does not account for impacts of the heatwave, e.g., number of deaths, heat-related illnesses), a major heatwave that lasted three and a half weeks in July 2025 ranks as the second most severe heatwave on record for Europe since 1950.

National meteorological and hydrological services reported a large number of heatwaves for their countries in 2025, which are described here. Since there is no unique definition of heatwaves throughout Europe, not all of them fulfill the criteria used in Figs. SB7.7 and SB7.8. In Northern Europe, Iceland experienced several heatwaves during the year, among them a 10-day event in May, which affected the entire country with record maxima up to 26.6°C. Even higher temperatures occurred in summer, when a new national August maximum temperature record of 29.8°C was set on 16 August. Norway saw heatwaves throughout the country, with 28 stations recording temperatures of 30°C or higher for at least five consecutive days in July. Two stations even registered 13 such consecutive tropical days (30°C or higher), a new national record in duration. In Sweden, several stations also reported record high numbers of days with maximum temperature above 30°C. Kvikkjokk-Årrenjarka (66°53′N 18°1′E, just north of the Arctic circle) recorded 10 days with temperatures above

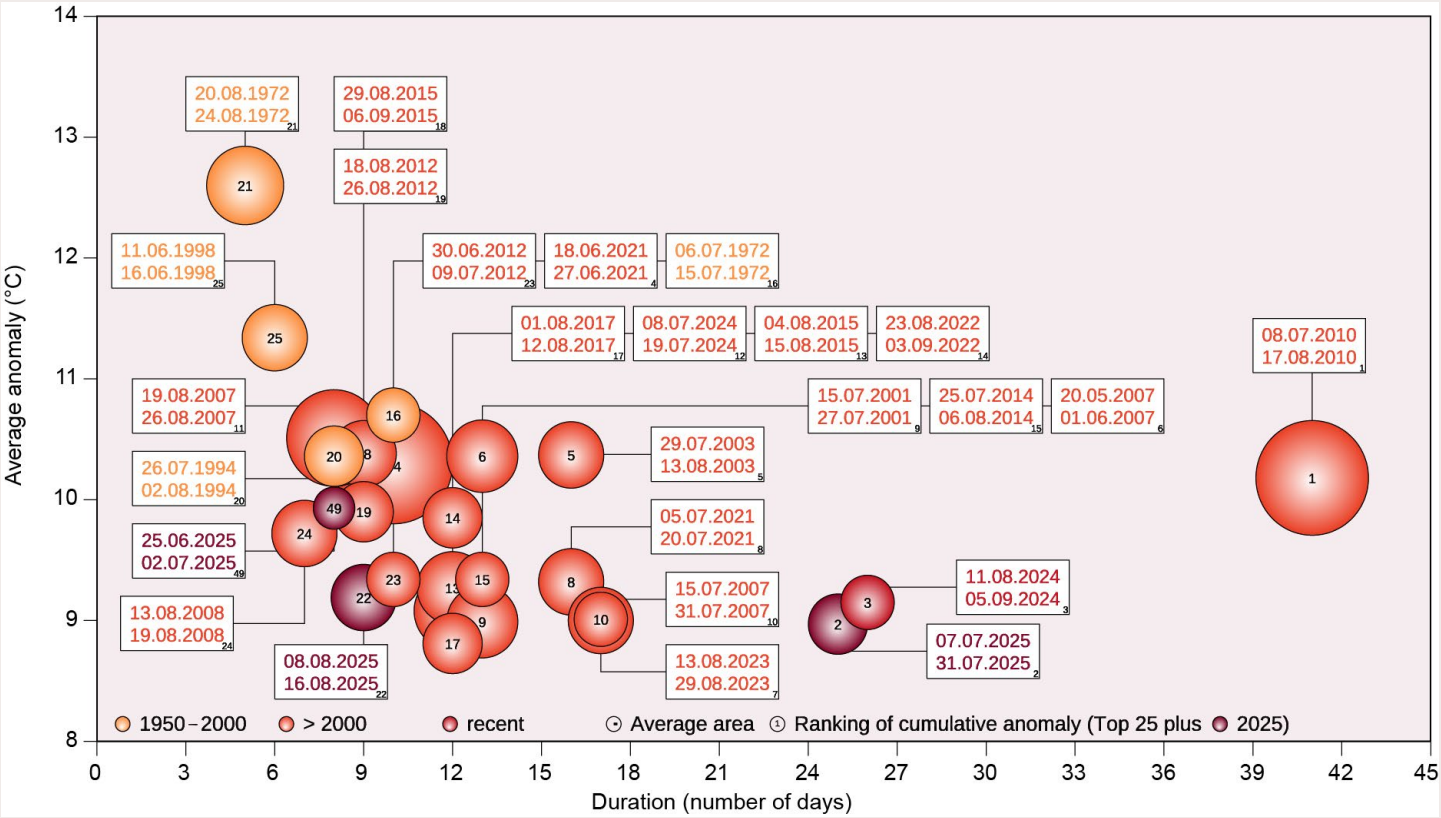

Fig. SB7.8. Bubble diagram of heatwaves in Europe for the period 1950–2025. Data basis: Gridded daily SYNOP and E-OBS data, Cornes et al. (2018). The x-axis indicates the duration of the heatwave (number of days) and the y-axis indicates the average intensity (mean deviation of all concerned grid points from the 1961–90 average; °C). The size of the bubble is proportional to the mean concerned area of the heatwave. Numbers in the bubbles refer to the ranking of the cumulative anomaly (the sum of all anomalies within the concerned area). Only the 25 most severe European heatwaves within the period 1950–2025 and all those of the year 2025, which meet the definition criteria described in Fig. SB7.7, are displayed. Annotations show the first and last day of the heatwave. Colors refer to the year of occurrence (yellow: before 2001; orange: 2001–24; dark red: 2025). (Source: Deutscher Wetterdienst [DWD].)

30°C. The previous record was four days, based on measurements extending back more than 100 years. In Finland, a heatwave that began on 11 July lasted until 5 August. From 12 July, the maximum temperature exceeded 30°C at least at one weather station in the country until 2 August, marking the longest streak of such warm days in the history of weather observations in Finland. In Meltosjärvi, Ylitornio, in southwestern Lapland, the maximum temperature exceeded 25°C on 26 consecutive days from 11 July until 5 August. This was the longest observed streak of such warm days in the region of Lapland on record. Previously, there had been 14 consecutive days with the maximum temperature above 25°C in northeastern Lapland in 1972 and in central Lapland in 1941. However, the national record of 31 consecutive days with the maximum temperature above 25°C set in Anjala, Kouvola, in 2021 remained valid.

Across Southern Europe and the Mediterranean, three heatwaves affected mainland Spain and the Baleares from June to August, while Portugal reported three summer heatwaves. In both countries, the highest temperature of the year was recorded at the end of June (46.0°C in Spain on 28 June and 46.6°C in Portugal on 29 June). Croatia's first heatwave (late June–early July) was strongest along the coast, weaker in the mainland. The season's most intense second heatwave affected the Adriatic coast and Dalmatia interior in mid-August.

During 21–27 July, a heatwave impacted Greece, which had the greatest spatial extent at the national scale, affecting many regions across the country. Several stations in the eastern mainland (Kalamata, Larissa, Serres, Sofades, Tatoi, Tithorea) recorded maximum temperatures above 43°C, with the highest values observed in Tithorea (44.3°C) and Sofades (44.2°C). The same heatwave affected most of Türkiye during 23–29 July. A temperature of 50.5°C was recorded in Silopi, Cizre, on 25 July, setting a new national temperature record for the country. At the same time, 66 stations broke their own temperature records. Cyprus had two major heatwaves in late July (the same, which affected Greece and Türkiye) and in the first half of August, each lasting eight days and setting new monthly records for maximum temperature at several stations. The highest daily maximum temperature of 45°C, recorded at the Athalassa station on 13 August, was the third highest temperature observed for this month in Athalassa since the station began operating in 1983.

Two severe heatwaves affected Israel and the West Bank area in July and August. The August heatwave was exceptional, with a duration of one week (8–14 August) and maximum temperatures reaching 45°C–48°C and even higher temperatures in the Jordan Valley and the Arava.

Table 7.3. The length of national temperature and precipitation records, annual anomalies, and rank information for each country in Europe/World Meteorological Organization (WMO) Regional Association (RA) VI region. The reference period is 1991–2020 unless otherwise specified. For some countries, instead of an area average, only the values at a single station (preferably with a long time series) are given (name of the location in brackets). Nations with an asterisk (*) represent cases where national data are not (yet) available, so statistics based on gridded products of the WMO RA VI Regional Climate Centre (RCC) were used. For precipitation, the rank ordered from wettest to driest (W) is provided for countries with above-normal precipitation and the rank ordered from driest to wettest (D) for countries with below-normal precipitation (e.g., 11W indicate the 11th-wettest year; 24D indicates the 24th-driest year).

Nation	Temp. start of record	Precip. start of record	Source	Temperature anomaly in K	Rank (ordered from warmest to coldest)	Precipitation anomaly (annual total in % of normal)	Rank
Western Europe							
Belgium (Uccle)	1833	1833	NMHS	+1.0	4	74	14 D
France	1900	1959	NMHS	+1.1	4	94	23 D
Ireland	1900	1941	NMHS	+1.0	2	105	15 W
Luxembourg (Findel)	1838	1854	NMHS	+0.7	8	113	-
Netherlands (De Bilt)	1901	1906	NMHS	+0.9	7	77	25 D
United Kingdom	1884	1836	NMHS	+1.0	1	90	78 D
Central Europe							
Austria[1]	1767	1858	NMHS	+2.2	8	90	17 D
Czechia	1961	1961	NMHS	+0.5	13	83	7 D
Germany	1881	1881	NMHS	+0.8	8	83	15 D
Hungary	1901	1901	NMHS	+1.0	7	73	4 D
Poland	1951	1951	NMHS	+0.8	9	89	20 D
Slovakia	1951	1961	NMHS	+0.9	8	94	28 D
Switzerland	1864	1864	NMHS	+1.2	4	93	61 D
Iberian Peninsula							
Portugal	1931	1931	NMHS	+0.8	5	130	23 W
Spain	1961	1961	NMHS	+1.1	3	109	25 W
Nordic and Baltic countries							
Denmark	1874	1874	NMHS	+1.0	4	91	83 D
Estonia	1922	1922	NMHS	+1.6	3	107	14 W
Finland	1900	1961	NMHS	+1.6	2	97	37 D
Iceland[2]	1874	1921	NMHS	+1.1	1	106	31 W
Latvia	1924	1924	NMHS	+1.2	4	103	34 W
Lithuania	1961	1961	NMHS	+1.0	5	97	32 W
Norway	1901	1901	NMHS	+1.5	1	110	8 W
Sweden	1858	1880	NMHS	+1.4	2	97	103 D
Central Mediterranean Region							
*Albania	1981	1901	RCC	+1.3	2	102	82 W
Bosnia and Herzegovina (Mostar/Sarajevo)	1961	1961	NMHS	+1.4/+1.3	2/3	89/91	20/28 D
Bulgaria	1981	1901	NMHS	+1.2	3	93	37 D
Croatia	1961	1961	NMHS	+1.1	3	93	20 D
Greece	1960	1960	NMHS	+1.0	2	96	25 D
Italy	1961	1961	NMHS	+1.0	4	101	23 W

Nation	Temp. start of record	Precip. start of record	Source	Temperature anomaly in K	Rank (ordered from warmest to coldest)	Precipitation anomaly (annual total in % of normal)	Rank
*Malta	1981	1901	RCC	+0.9	2	69	18 D
Monaco (Jardin Exotique)	1966	1969	NMHS	+1.3	2	81	42 D
Montenegro (Podgorica)	1949	1949	NMHS	+1.4	2	86	18 D
North Macedonia	1981	1981	NMHS	+0.8	3	93	17 D
Serbia	1951	1951	NMHS	+1.3	3	87	20 D
Slovenia	1950	1950	NMHS	+1.1	4	98	29 D
Eastern Europe							
Belarus	1981	1991	NMHS	+1.3	6	101	17 W
*Kazakhstan (western part)	1941	1901	NMHS/RCC	+2.5	1	105	48 W
Moldova (Chisinau)	1886	1886	NMHS	+0.9	5	82	34 D
Romania	1900	1961	NMHS	+1.2	4	86	-
Russia (European part)	1936	1936	NMHS	+1.7	-	103	-
Ukraine	1891	1891	NMHS	+1.2	6	93	32 D
Middle East							
Cyprus	1900	1916	NMHS	+1.9	2	53	2 D
Israel	1950	1950	NMHS	+1.1	5	68	5 D
*Jordan	1981	1901	RCC	+1.0	6	81	24 D
*Lebanon	1981	1901	RCC	+1.1	5	52	2 D
Syria	1996	1996	NMHS	+1.3	5	52	2 D
Türkiye and South Caucasus							
Armenia	1935	1935	NMHS	+1.0	6	83	6 D
*Azerbaijan	1981	1901	RCC	+1.0	6	95	32 D
Georgia	1956	1956	NMHS	+0.9	10	92	17 D
Türkiye	1971	1971	NMHS	+1.2	5	72	1 D

[1] Reference period 1961–90

[2] Precipitation statistics are given for the station of Reykjavík.

g. Asia

—Z. Zhu, Ed.

Throughout this section, the base period for climatological normals and anomalies is 1991–2020 unless otherwise noted. All seasons in this section refer to the Northern Hemisphere, with winter referring to December–February 2024/25, unless otherwise noted.

1. OVERVIEW

—Z. Zhu, P. Zhang, P. Liang, Y. S. Lui, D. N. Ratri, F. Sezaki, H. Umezu, A. Moise, M. Kuramochi, J. I. Seong, D. Dulamsuren, M.-V. Khiem, and H.-P. Lam

Annual mean surface air temperatures during 2025 were above normal across most of Asia and Siberia, except for South Asia and northwestern Southeast Asia, with anomalies of more than +1.0°C in eastern East Asia and from western Siberia to the northern Middle East. The most prominent warm center was located in Kazakhstan, where the anomaly reached +3°C (Fig. 7.40a).

Annual precipitation totals were above normal (>120% of normal) from eastern Mongolia to North China, in the interior of central Siberia to western Siberia, in and around western India, and in Southeast Asia, with the wettest anomaly center located in the northwestern Indian Peninsula. They were below normal (<80%) in the Arctic coastal areas of Siberia and from southern Central Asia to the Arabian Peninsula, with the driest anomaly center in the southern Arabian Peninsula (Fig. 7.40b).

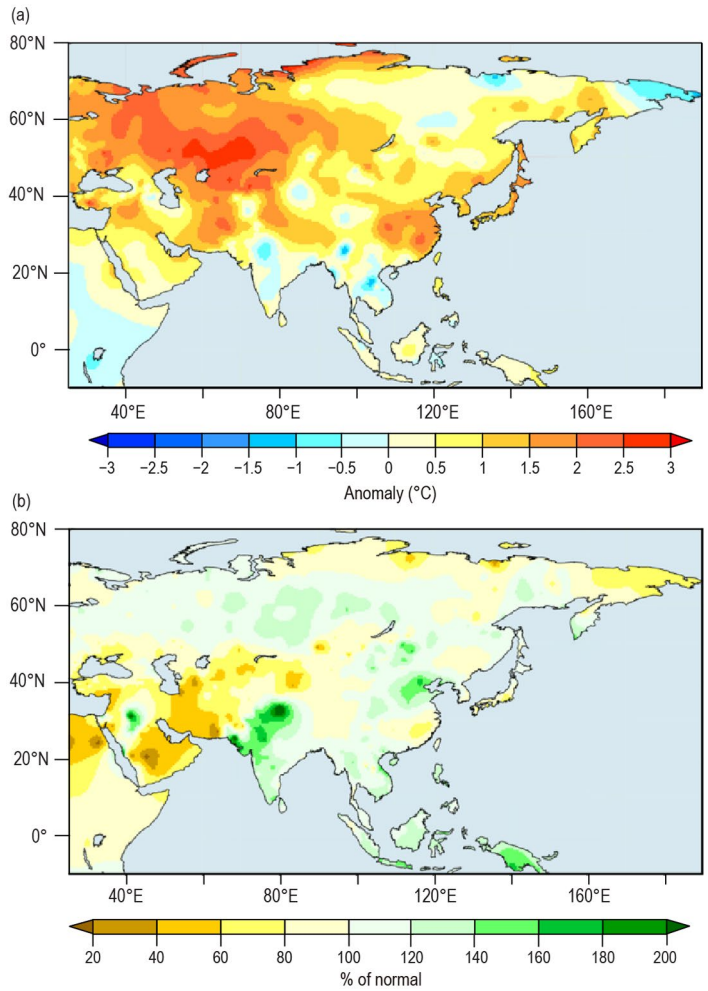

Fig. 7.40. Annual (a) mean surface temperature anomalies (°C), and (b) precipitation (% of normal) over Asia in 2025. The base period is 1991–2020.

In winter, seasonal mean temperatures were above normal (>+1.0°C) from northeastern China to eastern Mongolia, as well as in Siberia, Kazakhstan, and South Asia, while they were below normal (<–1.0°C) in western China, in and around Tajikistan, and in parts of the Indochina Peninsula (Fig. 7.41a). Seasonal precipitation was much above normal (>140%) from central to western Siberia, in and around western North China, in southern, eastern, and northern India, in and around southern Vietnam, and in parts of the Philippines and Indonesia, while it was much below normal (<60%) from eastern Japan to the Korean Peninsula, in the eastern coastal areas of China, from eastern Mongolia to western China, and from western India to the western Middle East (Fig. 7.41b).

In spring, seasonal mean temperatures were above normal in and around central China, in northern Siberia, from eastern Mongolia to southern central Siberia, and from Central Asia to the Middle East, while they were below normal in central India and in northwestern Southeast Asia (Fig. 7.41c). Seasonal precipitation was much above normal in central Mongolia, in parts of Siberia, in and around northern Saudi Arabia, in southern Oman, in India, and from southern Myanmar to southern Vietnam, while it was much below normal in western North China, east of Lake Baikal, and from southern Central Asia to southern Saudi Arabia (Fig. 7.41d).

In summer, seasonal mean temperatures were above normal in eastern East Asia, from northern central to western Siberia, and from western China to the northeastern Middle East, while they were below normal in parts of eastern Siberia, northwestern India, and in western

Myanmar (Fig. 7.41e). Seasonal precipitation was much above normal in the coastal areas of the Sea of Okhotsk, from eastern Mongolia to North China, in western Kazakhstan, in parts of the western Arabian Peninsula, in and around northwestern India, in and around northern Vietnam, and in southern Indonesia, while it was much below normal in the Arctic coastal areas from eastern to central Siberia, from western Mongolia to northwestern China, and from southern Central Asia to most of the Middle East (Fig. 7.41f).

In autumn, seasonal mean temperatures were above normal in eastern East Asia, in southern central Siberia, in the Arctic coastal areas of central to western Siberia, and from western Central

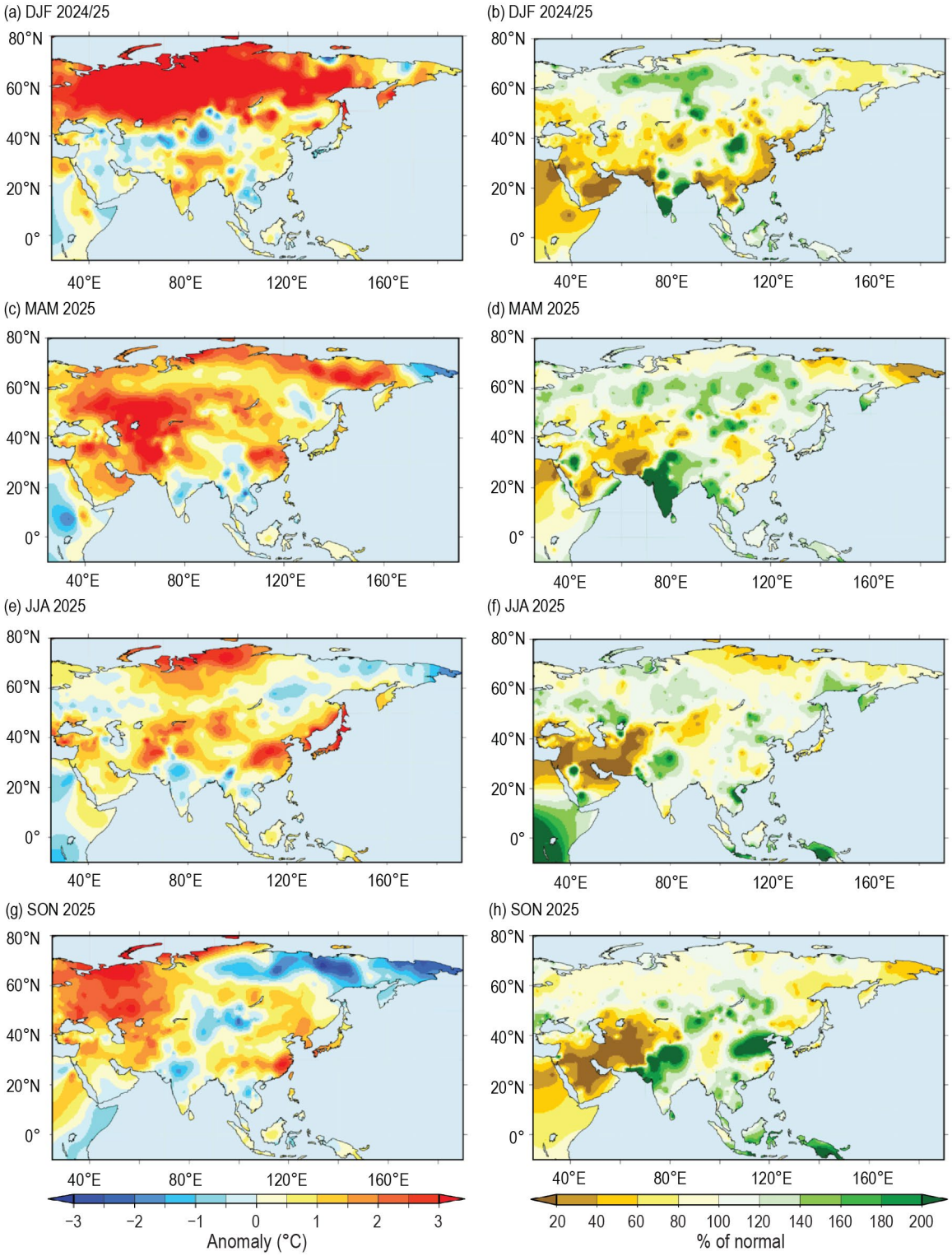

Fig. 7.41. Seasonal mean surface temperature anomalies (°C, left column) and precipitation (% of normal, right column) over Asia in 2025 for (a),(b) Dec 2024–Feb 2025; (c),(d) Mar–May 2025; (e),(f) Jun–Aug 2025; and (g),(h) Sep–Nov 2025. The base period is 1991–2020. (Source: Japan Meteorological Agency.)

Asia to the northern Middle East, while they were below normal from northern central Siberia to eastern Siberia, from western Mongolia to northwestern China, and in northwestern India (Fig. 7.41g). Seasonal precipitation was much above normal from the Korean Peninsula to North China, from east of Lake Baikal to western Mongolia, in and around northwestern India, in parts of the Indochina Peninsula, and in southern Indonesia, while it was below normal in parts of eastern Siberia and from southern Central Asia to the Middle East (Fig. 7.41h).

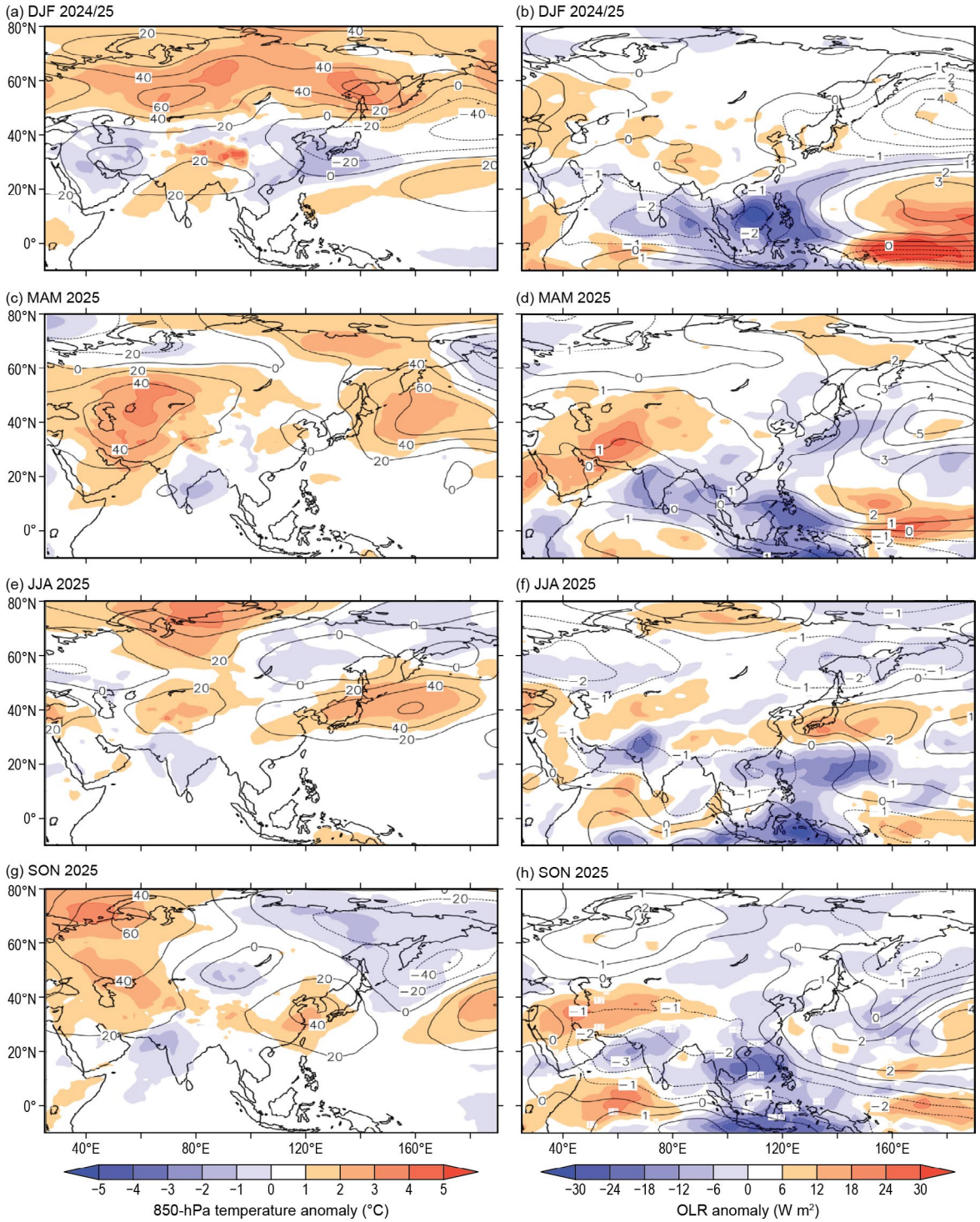

Fig. 7.42. Seasonal mean anomalies of atmospheric circulation variables in 2025 for (a),(b) Dec 2024–Feb 2025; (c),(d) Mar–May 2025; (e),(f) Jun–Aug 2025; and (g),(h) Sep–Nov 2025. Left column: 500-hPa geopotential height (contour, gpm) and 850-hPa temperature (shading, °C). Right column: 850-hPa stream function (contour, 1 × 10^6 m^2 s^{-1}) using data from the Japanese Reanalysis for Three Quarters of a Century and the Climate Prediction Center's Blended Outgoing Longwave Radiation (OLR; shading, W m^{-2}) using data originally provided by NOAA. The base period is 1991–2020. (Source: Japan Meteorological Agency.)

In winter, positive anomalies of 500-hPa geopotential height and 850-hPa temperature were observed over northern Eurasia and South Asia, while negative anomalies were observed over Central Asia and eastern East Asia (Fig. 7.42a).

In spring, positive anomalies of 500-hPa geopotential height and 850-hPa temperature were observed from Central Asia to western East Asia and from eastern Siberia to the midlatitude western North Pacific (Fig. 7.42c). The early monsoon onset in India resulted in upper-level anticyclonic circulation anomalies over Central Asia, partly contributing to the formation of downstream wavy anomaly patterns.

In summer, positive anomalies of 500-hPa geopotential height and 850-hPa temperature were observed over western Siberia and Central Asia. Positive anomalies were also observed from eastern East Asia to the midlatitude western North Pacific, along with a significant northward shift in the subtropical jet (Fig. 7.42e). The North Pacific Subtropical High (NPSH) was stronger than normal, shifted northward, and extended toward eastern East Asia, contributing to significantly above-normal temperatures in the lower troposphere. The extension of the NPSH was attributed to the intensified Pacific–Japan teleconnection pattern due to enhanced convective activity around the Philippines (Fig. 7.42f).

In autumn, positive anomalies of 500-hPa geopotential height and 850-hPa temperature were observed over Central and East Asia, while negative anomalies were found over eastern Siberia and northwestern India (Fig. 7.42g). The Siberian High developed significantly and then moved farther south than normal. In the lower troposphere, anticyclonic circulation anomalies straddling the equator were seen over the Pacific, while cyclonic circulation anomalies straddling the equator were seen from the Indian Ocean to the Maritime Continent for all seasons (Figs. 7.42b,d,f,h). The persistence of westerlies and easterlies in the lower troposphere driven by anomalous circulations was possibly associated with the development of a negative Indian Ocean dipole (IOD; see section 4f for details) from summer to autumn and the strengthening of a La Niña-like sea surface temperature (SST) pattern after summer, respectively.

2. RUSSIA

—O. F. Samokhina and N. N. Korshunova

Estimates of climate features for Russia were obtained from hydrometeorological observations of the Roshydromet Observation Network. Anomalies are relative to the 1991–2020 base period, and national rankings and percentiles reflect the 1936–2025 period of record. The boundary between Asian Russia and European Russia is considered to be 60°E.

(i) Temperature

The year 2025 in Russia was the second warmest on record, with the annual mean air temperature being 1.24°C above normal (Fig. 7.43a). The year 2020 was the warmest, at 2.03°C above normal.

Above-normal temperatures were observed over most of the Russian territory in all seasons. Annual and seasonal trends were statistically significant at the 1% significance level in both Asian Russia and European Russia, except for winter trends in the Asian part. Annual anomalies above the 95th percentile were observed throughout European Russia and in southern Asian Russia. It was the second-warmest winter since 1936 (+3.28°C), behind the record-breaking warm winter of 2019/20 (+3.80°C; Fig. 7.43b). Winter anomalies above the 95th percentile were observed at most Russian stations. January (+3.67°C) was the third warmest on record.

In January, all of European Russia experienced abnormally warm weather (Fig. 7.44) that was associated with Atlantic cyclones. In most regions, new maximum daily air temperatures were repeatedly set. As a result, the monthly mean temperatures across European Russia were 4°C–8°C above normal. A maximum anomaly of +7.2°C was recorded at the meteorological station Ryazhsk (Ryazan Region). Above-normal temperatures were observed throughout the month, with a maximum temperature of 5.2°C on 30 January. Four powerful warm spells were observed at the beginning and the end of the first 10-day period and at the end of the second and third 10-day periods. Hence, January 2025 became the warmest on record for European Russia. In western Siberia, new temperature records were also set. A maximum anomaly of +9.2°C was observed at the meteorological station Vanzhil-Kynak. Temperatures were above normal in both

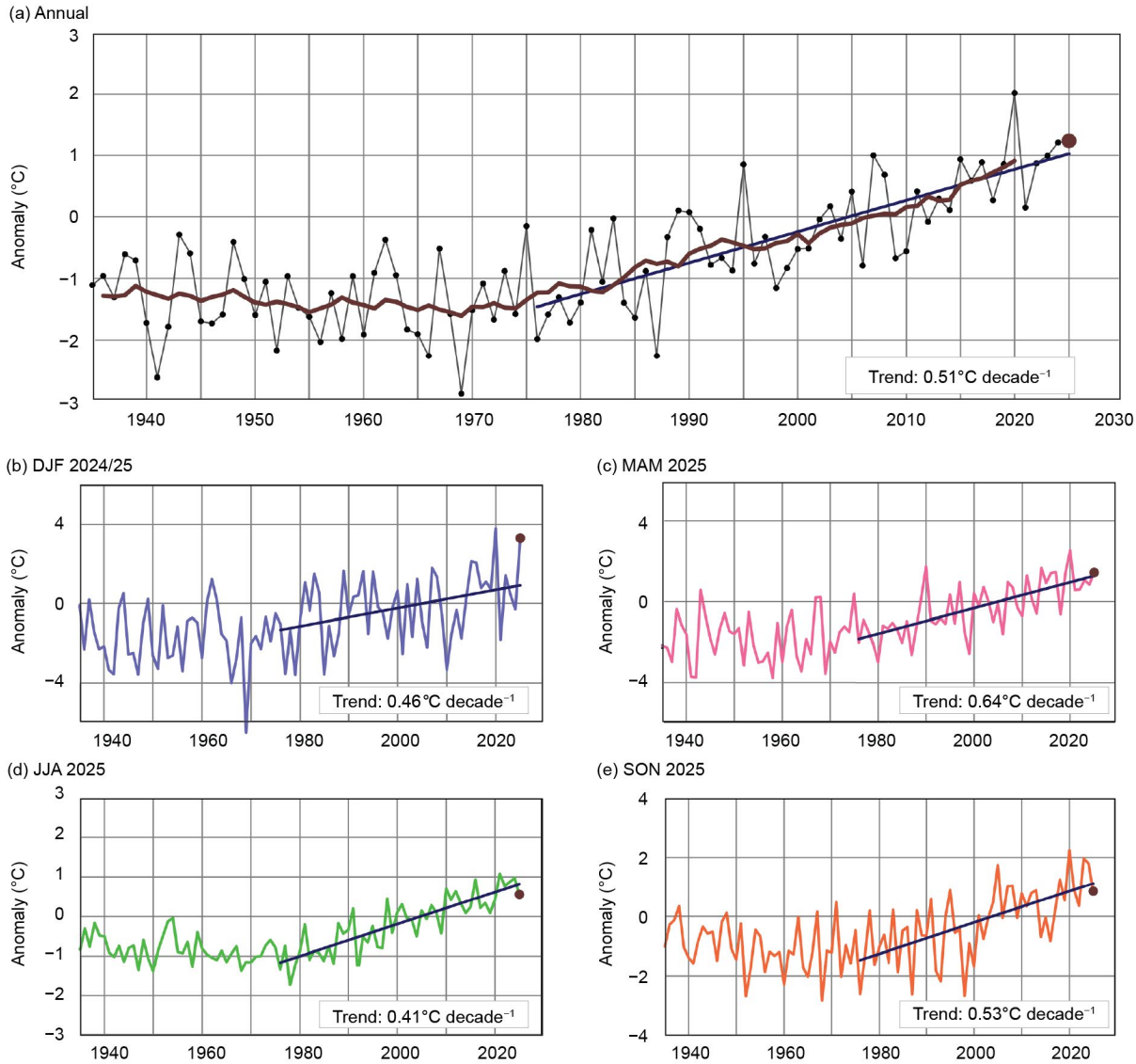

Fig. 7.43. (a) Annual and (b)–(e) seasonal. mean temperature anomalies (°C; 1991–2020 base period) averaged over the territory of Russia for the period 1936–2025: (b) Dec 2024–Feb 2025, (c) Mar–May 2025, (d) Jun–Aug 2025, and (e) Sep–Nov 2025. The dark red line on the annual mean time series is an 11-point binomial filter. The linear trend (°C decade^{-1}) is calculated for the period 1976–2025.

the first and second 10-day periods, but dropped in the third 10-day period. At the beginning of the third 10-day period, the absolute monthly air temperature maximum was exceeded.

The average spring temperature was 1.45°C above normal, the fifth highest for the season on record (Fig. 7.43c). Temperatures above the 95th percentile were recorded at all stations in central and southern European Russia, as well as in southern Asian Russia.

Summer (+0.56°C anomaly) was the eighth warmest on record (Fig. 7.43d). Temperatures above the 95th percentile were recorded in the central Siberian Plateau, Kamchatka, and Primorye.

Autumn (+0.85°C anomaly) was 11th warmest on record (Fig. 7.43e); the seasonal temperature for European Russia was 2.4°C above normal, marking its second autumn on record. In northern Asian Russia, east of the lower and middle reaches of the Yenisei, temperatures were below normal.

(ii) Precipitation

For Asian Russia and Russia as a whole, average total precipitation for 2025 was the highest since the start of the record in 1936, at 112% and 110% of normal, respectively (Fig. 7.45). Precipitation deficits were largely observed in northern Asian Russia.

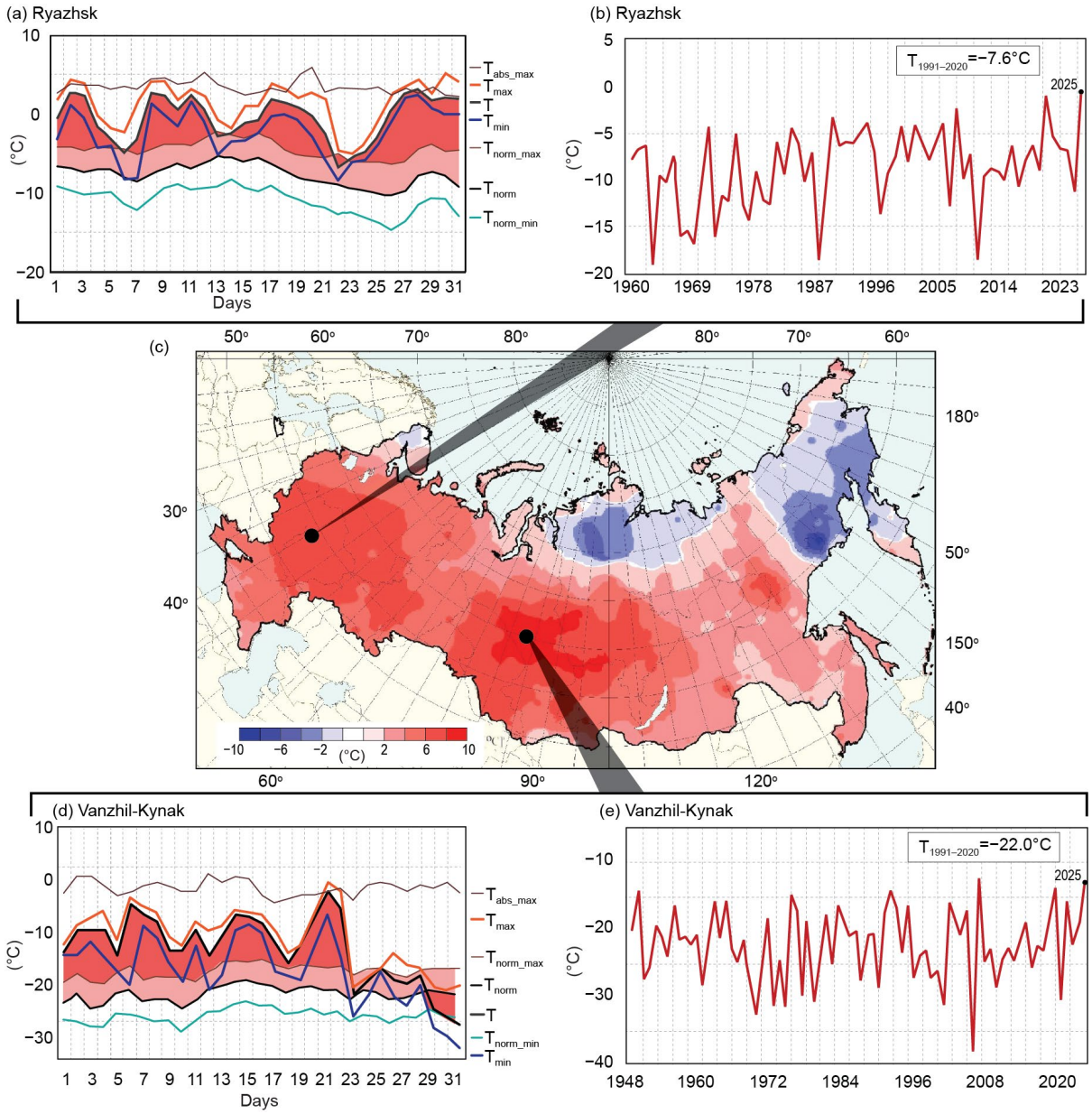

Fig. 7.44. Map: temperature anomalies across Russia (shading, contour interval is 2°C) in Jan 2025. Insets: Mean monthly temperature (°C) in meteorological stations Ryazhsk and Vanzhil-Kynak, and mean, minimum, and maximum daily temperatures (°C) in January 2025 at these stations. $T_{1991–2020}$ on plots of monthly temperatures is 1991–2020 mean. Plots of daily temperature show observed daily mean (T, black line), daily minimum (T_{min}, blue line), and daily maximum (T_{max}, red line) temperatures along with their climatological values (normal temperature [T_{norm}], black; normal minimum temperature [T_{norm_min}], blue; normal maximum temperature [T_{norm_max}], red), and absolute maximum temperature [$T_{abs–max}$], brown).

Spring and summer were both record wet, with precipitation totals 121% and 113% of normal. Across Russia as a whole, the average precipitation total for April and June was record high, at 142% and 118% of normal, respectively.

Winter was moderately wet (104% of normal) and autumn was moderately dry (96% of normal) across Russia as a whole. In October, precipitation averaged over Russia was 81% of normal, making it the fifth-driest October on record.

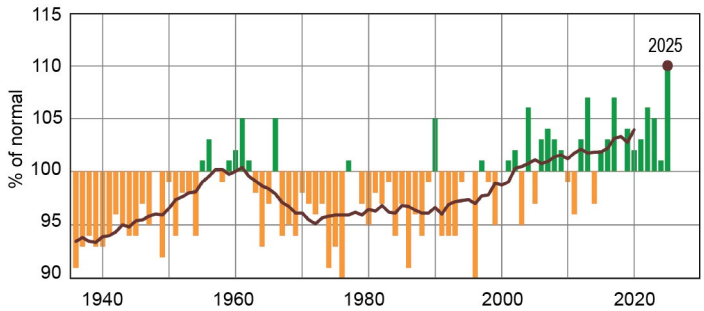

Fig. 7.45. Annual precipitation (% of normal; 1991–2020 base period) averaged over the Russian territory for the period 1936–2025. The smoothed time series (11-point binomial filter) is shown as a bold line. The black dot represents the annual precipitation % of normal for 2025.

Precipitation in Russia has increased by 1.9% per decade since the mid-1970s, especially in spring, with an increase of 5.4% per decade. However, in southern European Russia, a vast zone of reduced precipitation was observed in summer—up to −4.6% per decade.

(iii) Notable events and impacts

Information provided below was obtained through the Storm telegrams, which the Russian Research Institute of Hydrometeorological Information collects, analyzes, summarizes, and archives.

On 11–14 January, in the Leningrad and Pskov regions, severe ice and rime deposits of 35 mm–47 mm in diameter caused power outages in 17 municipal districts, with numerous fallen trees on power lines and broken electrical wires.

On 28–29 April, snowfall hit the Perm Territory, with snow depth reaching 38 cm in some areas and 33 cm in Perm. More than 5 cm of snow fell in Verkhoturye and Kachkanar. The weather caused 46 traffic accidents and suspended flights at Perm Airport for 17 hours.

On 10 May, hail measuring 20 mm–25 mm in diameter was observed in the northern and southern regions of the Stavropol Territory. Nearly 11,200 hectares of agricultural crops were damaged. In the village of Novotroitskaya, more than 900 square meters of glass were broken in a greenhouse, and 120 roofs, as well as pipe support, were damaged.

On 30 June, heavy rain in the Transbaikalia Territory caused rivers to overflow, washing out roads and railway tracks at Makaveevo Station and flooding two tracks of the Trans-Siberian Railway.

On 21–22 July, heavy rainfall triggered a mudflow of ~3 million cubic meters in the Kabardino-Balkarian Republic. The Tyrnyauz hydrological station was destroyed, the mudflow channel overflowed, and the federal road A-158 Prokhladny-Azau was blocked by 200 meters of mudflow. A bridge over the Baksan River in the lower part of Tyrnyauz was also destroyed. Gas and water lines, as well as two power transmission towers, were damaged.

On 3 August, in the Tuapse District of the Krasnodar Territory, heavy rain led to flash flooding that damaged 214 residential properties and 167 households. In the village of Lermontovo, a road bridge was destroyed. In the village of Moldovanka, two road bridges and one pedestrian bridge were damaged, and the water supply was disrupted.

On 15 December, hurricane-force winds (122 km hr^{-1}–140 km hr^{-1}) in Yuzhno-Kurilsk (Sakhalin Region) damaged multi-apartment buildings along with 20 transmission line towers, which resulted in emergency power cutoffs and cellular communication failure.

3. EAST AND SOUTHEAST ASIA

—P. Zhang, Y. S. Lui, H. Chen, D. N. Ratri, N. Nakayama, A. Moise, M. Kuramochi, J. I. Seong, D. Dulamsuren, M.-V. Khiem, and H.-P. Lam

Countries/places considered in this section include China, Hong Kong (China), Indonesia, Japan, Republic of Korea (ROK), Mongolia, Singapore, and Vietnam. Unless otherwise noted, anomalies refer to the 1991–2020 base period.

(i) Temperature

Annual mean temperatures for 2025 across East and Southeast Asia are shown in Fig. 7.40a.

In 2025, the annual mean temperature for China was 0.93°C above normal, which was the second highest since the start of the record in 1951. Every season was warmer than normal, and summer 2025 tied with the previous summer (2024) as the hottest on record.

For Hong Kong, 2025 was the sixth-warmest year since records began in 1884 with annual mean temperature of 24.3°C, 0.8°C above normal.

Japan was covered by warm air throughout most of the year, resulting in significantly above-normal annual mean temperatures in northern, eastern, and western Japan. The mean temperature in 2025 for the country as a whole was the third highest on record since 1898, following 2024 and 2023.

The annual mean temperature for the ROK was 13.7°C, which was 1.2°C above normal and marked the country's second-warmest year since 1973. Five consecutive months from June to October ranked as either first or second highest on record for their respective months.

The annual mean temperature over Mongolia was 1.6°C, marking its sixth-warmest year since 1940. The mean temperature in January was 3.6°C above normal—the fourth highest on record.

The average temperature for Indonesia in 2025 was 0.38°C above normal, making it the sixth-warmest year in Indonesia since 1981. It was the eighth-warmest year for Singapore, with the country experiencing its warmest June (tied with 1997) and November on record. The annual average temperature of Vietnam was 0.27°C above normal.

(ii) Precipitation

Annual precipitation for 2025 over East and Southeast Asia is shown in Fig. 7.40b.

The average precipitation total for China was 664.6 mm, 104.4% of normal; autumn was record wet at 133.6% of normal. The annual total rainfall in Hong Kong was 2558.7 mm, about 105% of normal.

In contrast, annual precipitation totals were below normal in western Japan and significantly below normal on the Pacific side of eastern Japan.

Total precipitation averaged over the ROK in 2025 was 1325.6 mm, near its normal of 1331.7 mm. Monthly precipitation was generally near or below normal, except in June, September, and October. The number of precipitation days (daily precipitation ≥0.1 mm) in autumn reached 34.3 days, the second highest on record.

The annual precipitation for Mongolia was 223.5 mm, close to the long-term average, ranking as the 41st-wettest year since 1940. Precipitation was significantly above normal in March, September, and November.

In Indonesia, annual total rainfall was 121% of normal, making 2025 the second-wettest year since 1991. For Singapore, the average annual total rainfall (2984.9 mm) was 118% of average (2534.3 mm), its seventh highest since 1980. In Vietnam, rainfall for 2025 was 115%–140% of normal, with many heavy rainfall events and historical 24-hour rainfall recorded.

(iii) Notable events and impacts

The rainy season progression in China was markedly earlier than normal. The Meiyu season in the middle and lower reaches of the Yangtze River began on 7 June and ended on 30 June, 7 and 16 days earlier than normal, respectively, with total rainfall 11.7% below normal. From June to August, China experienced 20 regional heavy rainfall events, characterized by frequent episodes, widespread coverage, strong local intensities, and pronounced extremes. For the rainy season in North China, both the total (356.6 mm, 261.1% of normal) and duration (59 days, 29 days longer than normal) were record high (since 1961). During summer 2025, two extraordinary rainstorms (17–23 June and 23–29 July) struck North and Northeast China. The July episode produced record-breaking precipitation totals—e.g., 605.8 mm at Yixian, Hebei—and led to the largest flood in the Haihe River on record. Autumn rain in West China lasted for 78 days with 95% above-normal rainfall, which set new records for consecutive precipitation in Chongqing and Shaanxi and led to widespread flooding along the Han and Wei Rivers.

Fourteen tropical cyclones approached Hong Kong in 2025, leading to issuance of tropical cyclone warning signals by the Observatory, the largest number since 1946 (see section 4g4 for details on the western North Pacific storm season).

Japan's summer mean temperature hit a record high since 1898. Among the 153 meteorological stations nationwide, 132 reached their highest summer mean temperatures on record (including nine tied records). A new daily high maximum temperature record for Japan of 41.8°C was set at Isesaki in Gunma Prefecture on 8 August.

In late March, large-scale wildfires swept across the Gyeongsangbuk-do in the ROK. The wildfires caused 27 fatalities, the loss of approximately 104,000 hectares of forest, and an estimated economic loss of over $700 million (U.S. dollars), the most damage on record. The summer mean temperature reached 25.7°C in the ROK, the highest since records began in 1973. Heatwaves were observed in late June and continued until mid-October, resulting in 4460 heat-related illnesses and 29 fatalities.

In Mongolia, a total of 73 weather-related hazardous and disastrous events were recorded. Two fatalities and the loss of nearly 8000 heads of livestock were reported. In addition, forest and steppe fires damaged 69 Mongolian gers (traditional, portable, dwellings used by nomads). Overall, total direct economic losses were estimated at approximately $1.2 million (U.S. dollars).

In late November 2025, Cyclone Senyar brought extreme rainfall to northern Sumatra, Indonesia, with daily precipitation exceeding 300 mm in several locales. The highest daily rainfall total of 411 mm was recorded on 26 November 2025 at the BPP Kuala rain gauge station, Aceh, with an accumulated rainfall total of 714.5 mm on 26–27 November that triggered widespread flooding and landslides, causing at least 1204 fatalities and displacement of thousands of people.

In Singapore, during the first Northeast monsoon surge, a daily rainfall total of 241.8 mm was recorded at Pulau Tekong on 10 January, which was the highest amount ever recorded by that station in January. On 1 November, a maximum temperature of 36.0°C was recorded at one station—the highest ever observed during November since records began in 1929.

In Vietnam, extremely heavy rainfall was recorded during 25–30 October from Quang Ngai to Gia Lai, with six-day totals of more than 1000 mm observed at many stations. The heavy rains caused floods in many rivers, resulting in 57 casualties and economic losses exceeding $350 million (U.S. dollars).

4. SOUTH ASIA

—O. P. Sreejith, A. Bandgar, C. T. Sabeerali, and A. K. Srivastava

Countries in this section include Bangladesh, India, Pakistan, Sri Lanka, and Nepal.

(i) Temperature

The annual mean surface temperature averaged over India during 2025 was 0.28°C above the 1991–2020 average (Fig. 7.46), making this the eighth-warmest year since nationwide records began in 1901. Seasonal mean temperature anomalies in winter (January–February, a record high of +1.17°C) and the pre-monsoon season (March–May, +0.29°C) mainly contributed to the annual warmth. The monsoon season (June–September, +0.09°C) and the post monsoon season (October–December, −0.10°C) experienced near-normal temperatures.

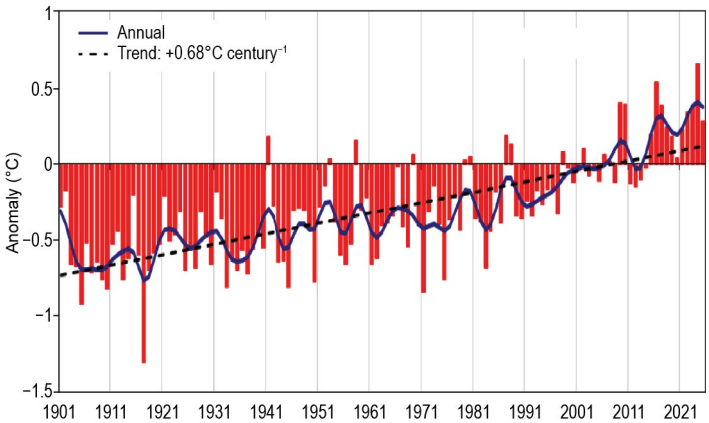

Fig. 7.46. Annual mean temperature anomalies (°C; 1991–2020 base period) averaged over India for the period 1901–2025. The smoothed time series (nine-point binomial filter) is shown as a continuous line. The dotted line represents the linear trend, which is statistically significant at the 95% confidence level.

(ii) Precipitation

The summer monsoon season (June–September) typically contributes about 75% of the annual precipitation over South Asia. In 2025, the summer monsoon set in over the Indian subcontinent (Kerala, southwestern parts of peninsular India) on 24 May, eight days earlier than its normal date of 1 June. The monsoon covered the entire country on 29 June, nine days ahead of its normal date (8 July). For India, the long-term average (LTA; 1971–2020) of the summer monsoon rainfall is 869 mm with a standard deviation of about ±10%. However, over smaller regions, the standard deviation is much larger (around ±19%). During 2025, the Indian summer monsoon rainfall (ISMR) was 108% of its LTA (Fig. 7.47), within the normal range. Rainfall distribution was generally fair over major parts of the country except for some eastern/northeastern regions. Among the four broad homogenous geographical regions of the country, northwest India, central India, and south peninsular India received seasonal rainfall of 127%, 115%, and 110% of their LTA, respectively, while east and northeast India received 80% of its seasonal rainfall. At the monthly scale, rainfall for the country as a whole was above normal during June, July, August, and September (109%, 105%, 105%, and 115% of LTA, respectively). Over the core monsoon zone, the southwest monsoon was active during the second half in June, the first week in July, and many days during the second half of August and September (Fig. 7.48); however, the monsoon was subdued during much of the first half of August. Rainfall over India was below normal (52% of its LTA) during the winter season (January–February), and above normal (142% and 111% of

LTA, respectively) during the pre-monsoon season (March–May) and post-monsoon season (October–December).

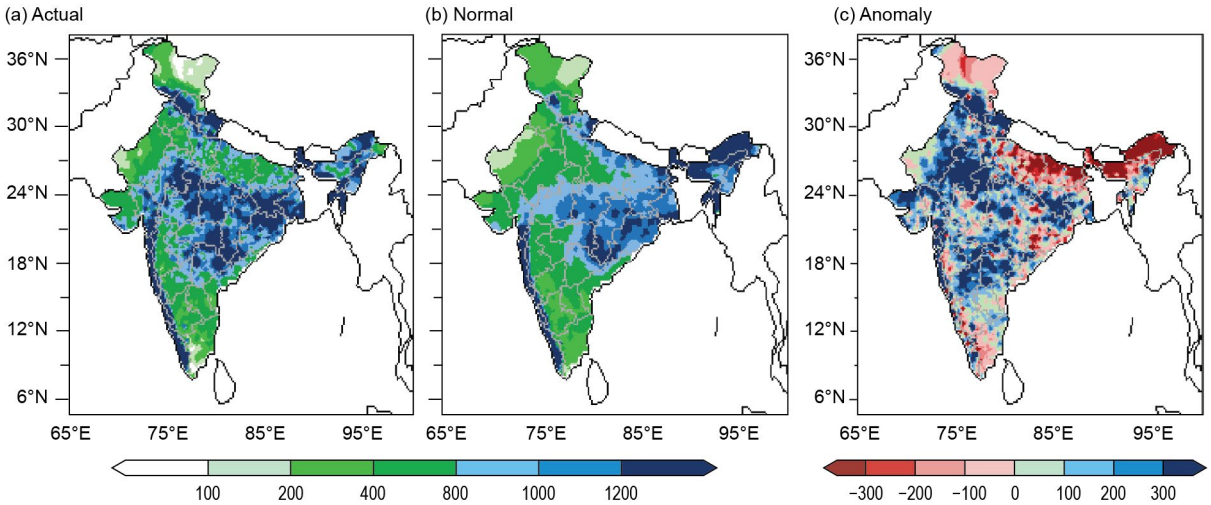

Fig. 7.47. Spatial distribution of monsoon seasonal (Jun–Sep) (a) actual, (b) normal (1971–2020 average), and (c) anomalous rainfall (mm) over India in 2025.

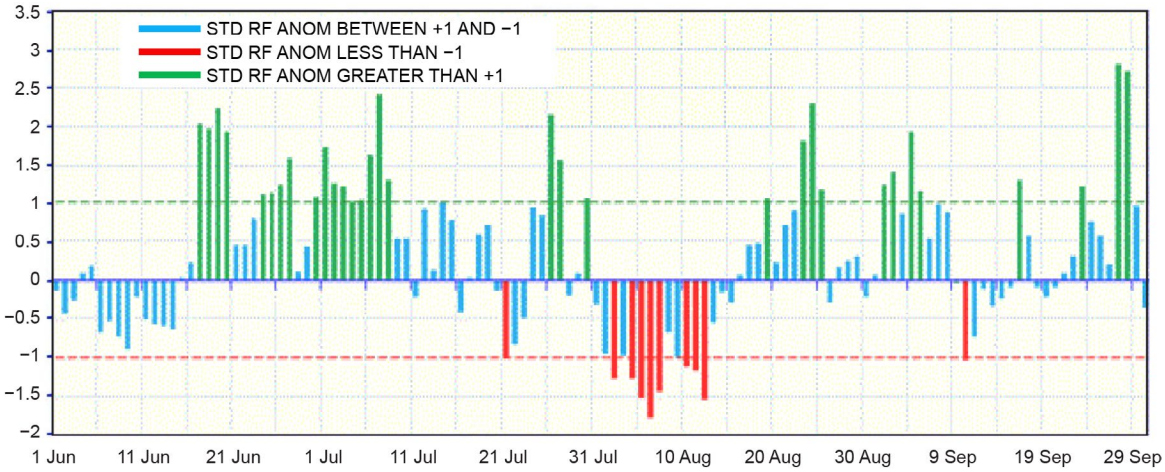

Fig. 7.48. Daily standardized rainfall anomaly time series averaged over the core monsoon zone of India for the period 1 Jun–30 Sep 2025.

Pakistan, located along the western margin of the South Asian monsoon's primary rainfall zone, typically receives about 60%–70% of its annual total precipitation during the monsoon season. The summer monsoon sets over eastern parts of Pakistan around 1 July with a standard deviation of five days. In 2025, the southwest monsoon rains commenced over Pakistan on 25 June, six days earlier than normal. The national monsoon rainfall from July to September totaled 172.8 mm, 23% above the 1961–2010 average.

During their 2025 summer monsoon seasons, both Bangladesh (May–October) and Sri Lanka (May–September) received above-normal rainfall.

Monsoon entered eastern Nepal on 29 May, 15 days earlier than the normal onset date of 13 June. It withdrew from eastern Nepal on 10 October, eight days later than the typical withdrawal date of 2 October. Although the season lasted 23 days longer than normal, rainfall during this period was only about 90% of the LTA, suggesting that the extended season did not necessarily correspond to sustained rainfall. This may reflect an uneven distribution of active and break phases, with rainfall concentrated in certain periods.

The 2025 northeast/post-monsoon season (October–December) rainfall over India was above normal (111% of LTA), while the seasonal rainfall over the core region of the south peninsula was normal (102% of LTA). Sri Lanka received above-normal rainfall during this season.

(iii) Notable events and impacts

In 2025, four cyclonic storms formed over the North Indian Ocean in the post-monsoon season (Fig. 7.49; see section 4g5 for details). Three cyclones (Montha, Senyar, and Ditwah) formed over the Bay of Bengal, while Shakti formed over Arabian Sea. Montha and Ditwah caused damage.

Heatwaves claimed about 35 lives from different parts of India in 2025, including 20 fatalities in Uttar Pradesh on 13 June and 7 in Telangana. Other fatalities were reported from West Bengal, Odisha, Kerala, Madhya Pradesh, and Maharashtra.

Bangladesh experienced an unprecedented heat wave in April 2025, which broke a 76-year record for the most consecutive days of scorching temperatures. April was also abnormally warm over northwestern parts of India and Pakistan, with maximum temperatures more than 5°C above normal on many days in the second and third weeks. Temperatures reached 49°C in the southwestern province of Balochistan on 14 and 15 April, unusually extreme for April.

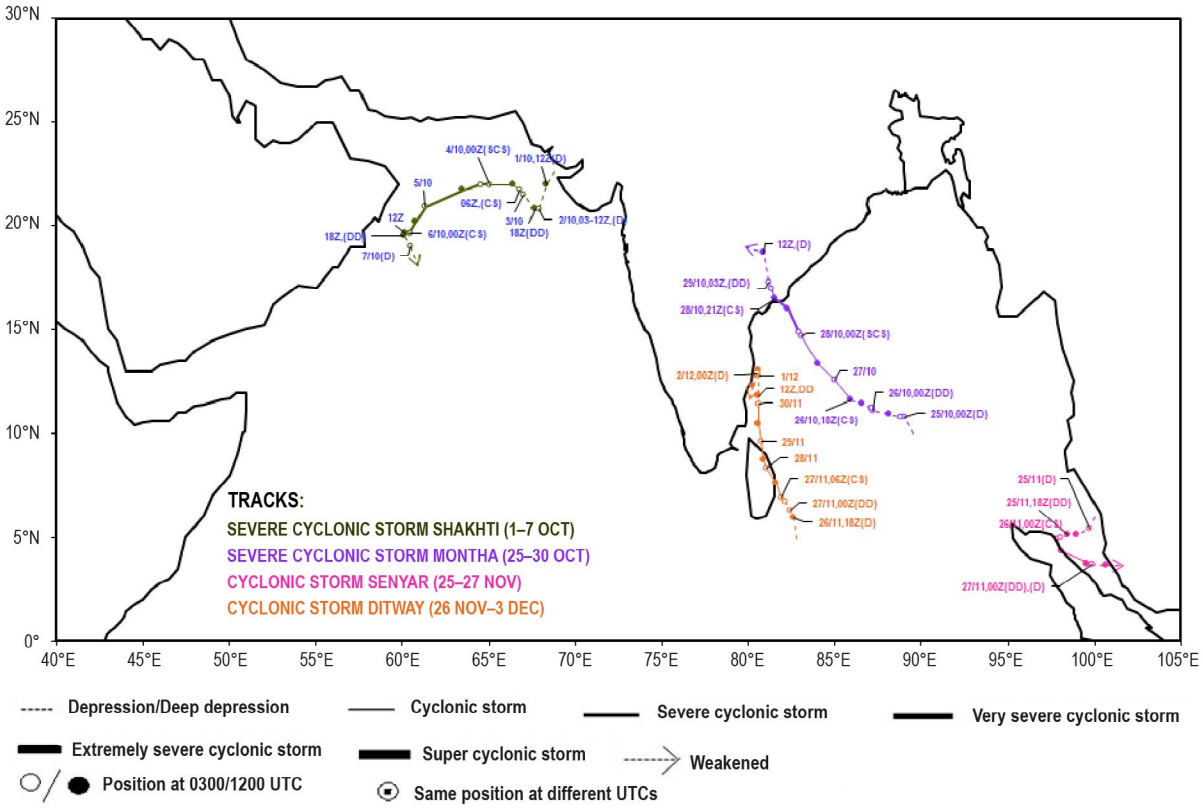

Fig. 7.49. Cyclonic storm tracks over the North Indian Ocean during 2025.

During the year, heavy rainfall, floods, cloudbursts, and landslides claimed over 1370 lives across different parts of India, including Maharashtra (210), Himachal Pradesh (160), Jammu and Kashmir (155 each), Madhya Pradesh (150), Uttarakhand (105), Uttar Pradesh (79), Rajasthan (74), West Bengal (66), Punjab (59), and Kerala (50). Thunderstorm and lightning activity also claimed more than 1310 lives across the country, including Uttar Pradesh (310), Madhya Pradesh (190), Jharkhand (170), Bihar (170), Odisha (100), West Bengal (70), and Maharashtra (60). The severity of the season was also reflected in several record-breaking short-duration rainfall events. Table 7.4 lists record 24-hour rainfall during the 2025 southwest monsoon season.

In early October, the Ilam district in eastern Nepal was severely impacted by a series of devastating landslides and floods triggered by intense rainfall. The disaster, which peaked on 4–5 October, caused significant loss of lives, destruction of infrastructure, and displacement of hundreds of families in Kathmandu and surrounding areas during the Dashain festival, the biggest and most important Hindu festival in Nepal. At least 35 fatalities were reported.

On 24 May, powerful windstorms, heavy rains, and hailstorms battered several parts of northern Pakistan, particularly Punjab, Khyber Pakhtunkhwa, and Islamabad, resulting in at least 20 deaths and 150 injuries, mostly in Punjab. From 26 June to 10 September, the monsoon season/flooding in Pakistan caused at least 900 fatalities and 1000 injuries across Pakistan, with significant infrastructure damage, including to houses and bridges. Heavy rainfall affected

Khyber Pakhtunkhwa and Balochistan provinces, causing casualties and infrastructure damage. Nationally, 6.3 million people were affected and more than 2.9 million displaced due to floods.

In mid-May, a flood crisis began in Bangladesh, primarily triggered by heavy monsoon rainfall and upstream water flow from India. During 31 May to 1 June, several landslides were reported across many Rohingya camps, which resulted in damage to thousands of shelters there. Several districts, including Sylhet, Sunamganj, Moulvibazar, Habiganj, Netrokona, Noakhali, Bhola, Khagrachari, Bandarban, and Rangamati, were severely affected. The floods resulted in loss of lives, displacement of thousands, destruction of homes and significant damage to fish farms, agriculture, and infrastructure.

Table 7.4. 24-hour rainfall totals during the Indian 2025 southwest monsoon season.

Station	24-hr Total (mm)	Date	Previous Record Total (mm)	Previous Record Date
Bhilwara	175	22 Jun	81	28 Jun 2019
Churu	85.1	30 Jun	81.9	24 Jun 1988
Mahuva	225.2	17 Jun	179.6	30 Jun 1959
Purulia	210	20 Jun	147.6	23 Jun 1996
Solan (Nauni)	85.6	29 Jun	85.3	12 Jun 1983
Tikamgarh	215	22 Jun	136	30 Jun 2011
Washim	122.4	26 Jun	121	15 Jun 2013
Guna	323	30 Jul	293.4	25 Jul 1958
Jharsuguda	205.2	06 Jul	195.1	17 Jul 2002
Khajuraho	160.4	13 Jul	143.2	07 Jul 1981
New Delhi (Ridge)	129.8	30 Jul	124	11 Jul 2003
Tadong	124.6	29 Jul	117	06 Jul 2005
Tikamgarh	215	13 Jul	180	03 Jul 1974
Bapatla	135	13 Aug	132.5	23 Aug 2000
Bijapur	151.2	06 Aug	121.2	31 Aug 1954
Gannavaram	129.6	14 Aug	122.7	31 Aug 2024
Jammu	380	27 Aug	282.2	16 Aug 2006
Karaikal	110.1	11 Aug	92.2	31 Aug 2010
Manali	102	26 Aug	88.3	14 Aug 1970
Nandigama	191.4	14 Aug	136.5	09 Aug 2008
Bilaspur	104.6	04 Sep	83.8	19 Sep 2008
Medak	196	12 Sep	192.2	21 Sep 2005
Solan (Nauni)	187	01 Sep	140.8	20 Sep 2008
Tirupattur	167.2	19 Sep	140.8	26 Sep 1978

* Based on real time available data

5. SOUTHWEST ASIA

—A. Vazifeh, A. F. Kazemi, and M. Mohammadi

This report is provided using the observed synoptic stations across Iran and the West Asia region for temperature, precipitation, standardized precipitation index (SPI), and dust event analysis. The baseline used here for comparison is 1985–2024. Particular attention is given to the interconnected phenomena of drought and dust storms. The analysis is based on Iran station data and the World Meteorological Organization's Observing Systems Capability Analysis and Review (OSCAR) synoptic station data across West Asia, with anomaly maps provided by the Iran National Climate and Drought Crisis Management Centre (NCDCM).

(i) Temperature

Several months in 2025 were among the hottest in the last 40 years for their respective months; March, June, and July were each second warmest on record and May was record warm. In Iran, the annual mean air temperature anomaly was notably elevated, particularly in the southeastern region where it exceeded +1.5°C; meanwhile, Kyrgyzstan and Tajikistan both recorded even higher anomalies, surpassing +3.5°C (Fig. 7.50a). Temperatures also showed intense positive anomalies from June to November in West Asia.

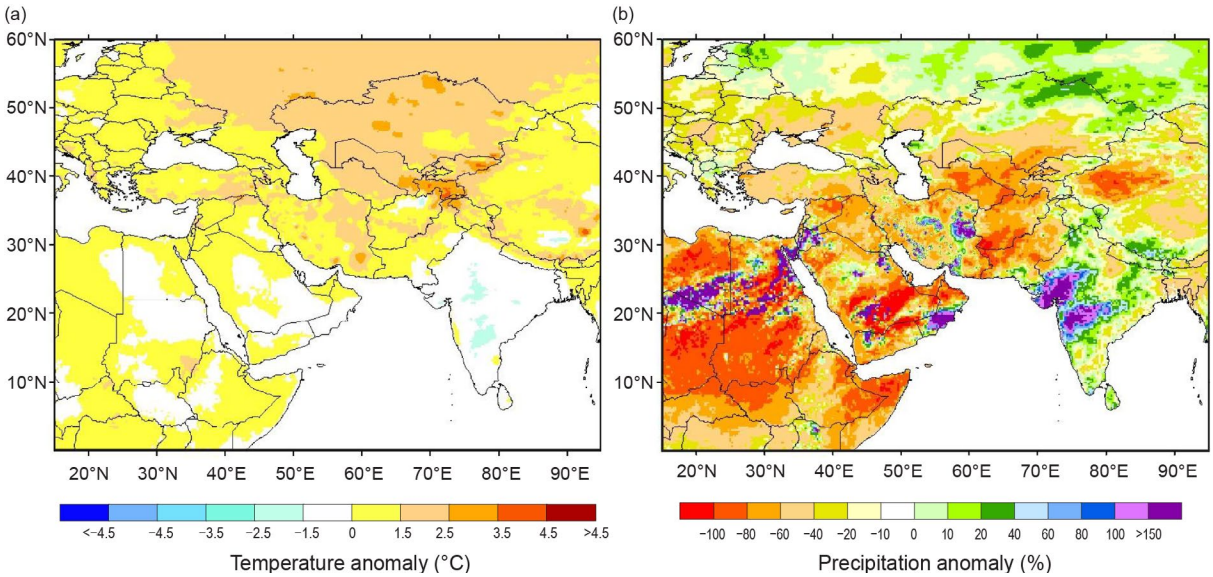

Fig. 7.50. Annual mean (a) temperature anomalies (°C) and (b) precipitation anomalies (%) in 2025.

(ii) Precipitation

Iran and neighboring countries in West Asia and Central Asia experienced one of the longest and most severe dry periods on record from late spring through mid-December 2025 (Fig. 7.50b). In many regions, it was the driest period in the last 50 years, with SPI frequently below –1 (drought) and often below –2 (severe drought).

The extended dry spell resulted in a cumulative precipitation deficit that exceeded 60% of the LTA in several key agricultural and urban watersheds. The deficit was great when the SPI below –2.0 was recorded for multiple consecutive months. The lack of precipitation had a considerable impact on water resources, including a significant depletion of freshwater reservoirs in several provinces and megacities across Iran. Major reservoirs supplying Tehran, Isfahan, and Shiraz fell to below 20% of their capacity by the end of the year, triggering water rationing in urban areas and severely limiting irrigation allocations for agriculture. The drought caused widespread crop failure, particularly in rain-fed farming regions, and led to the loss of perennial crops in drought-stricken areas. Natural ecosystems—including wetlands and forests—showed signs of severe stress, with increased tree mortality and reduced biodiversity. An intensive and prolonged dry period, combined with abnormally high temperatures, led to multiple forest fires across western and northern Iran in summer and early autumn. Due to prolonged severe droughts that continued and intensified across the country, dried beds of inland lakes increased dust storm events especially in the eastern half of Iran from summer to early mid-autumn.

(iii) Notable events and impacts

The number of dust occurrence days and anomalies for 2025 is presented in Fig. 7.51; dust occurrence is based on the horizontal visibility of <1000 m and <5000 m due to dust particle concentrations in the surface layer.

In terms of visibility below 5000 m, large areas of western and southwestern Iran, as well as parts of Iraq and Kuwait, experienced 41–85 dust days in 2025, exceeding the 2007–25 average (Fig. 7.51a). The most affected regions included western, southwestern, and eastern provinces in Iran, where dust storms occurred on more than 20% of the days in 2025. Significant positive anomalies (from 4 days to more than 10 days) were observed across western Iran, eastern Iraq, and northern Saudi Arabia, indicating a sharp increase of dust events in 2025 compared to the LTA (Fig. 7.51b). The Hawizeh Marsh region showed anomalies exceeding 15 days, reflecting the complete drying of this important wetland.

In terms of visibility below 1000 m, several regions—particularly in southwestern and western Iran—recorded 13–30 severe dust days, indicating a rise in high-intensity dust storms

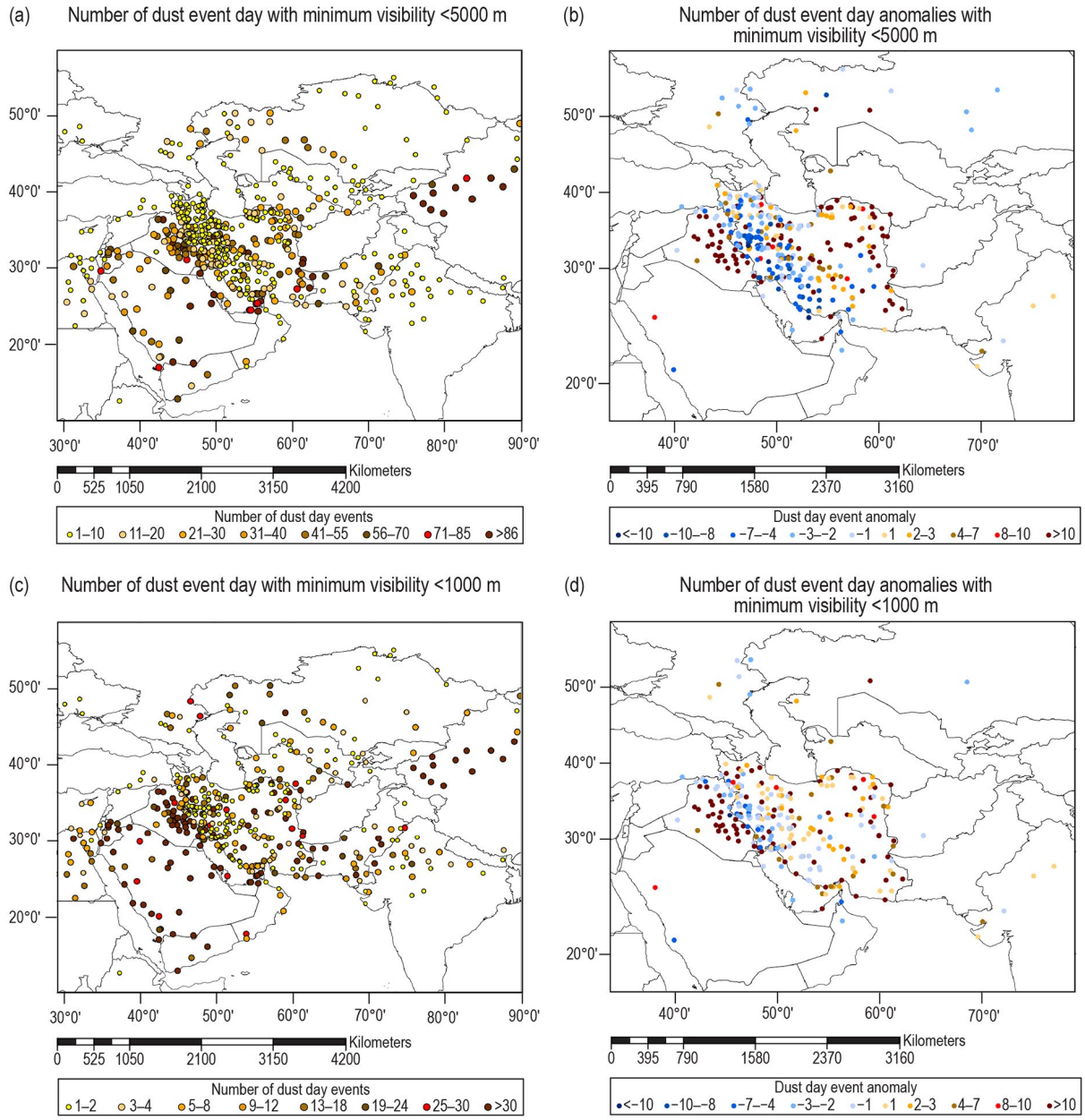

Fig. 7.51. Spatial distribution of dust event frequency and associated anomalies across West Asia in 2025. (a) Annual number of dust days with minimum visibility <5000 m; (b) Anomalies of dust days (visibility <5000 m); (c) Annual number of severe dust days with minimum visibility <1000 m; (d) Anomalies of severe dust days (visibility <1000 m). The base period is 2007–25. (Source: Islamic Republic of Iran Meteorological Organization.)

that posed significant risks to transportation, health, and economic activities (Fig. 7.51c). The severe dust storms also occurred in Iraq, Kuwait, Saudi Arabia, eastern Pakistan, Central Asia, and northwest China, each of which saw between 19 and 30 severe dust event days. The number of people who were treated or hospitalized in eastern and southwestern Iran due to air quality and dust-contaminated air was significant in summer and early autumn. Similar positive anomalies (from 4 days to more than 10 days) were concentrated in southwestern Iran, southern Iraq, Kuwait, Saudi Arabia, western Pakistan, and Central Asia, highlighting the increased frequency and duration of dust events (Fig. 7.51d). The Dasht-e Kavir and Dasht-e Lut regions in central Iran also showed elevated anomalies, suggestive of expansion of active dust sources.

The dust belt extending from the Arabian Peninsula through southern Iraq into western Iran showed the largest anomaly in dust days compared to the LTA. This corridor accounted for over 70% of all severe dust events recorded in West Asia during 2025. Emerging dust sources included dried lake beds (e.g., Lake Hamoun in eastern Iran), depleted reservoirs, and abandoned agricultural lands, particularly in regions of drought-induced cessation of irrigation. Cross-border transport of dust was intensified, with Iran receiving significant dust influx from Iraq and Syria and simultaneously exporting dust to the Persian Gulf states and western Pakistan.

A combination of warmer temperatures, less precipitation, severe drought (SPI <–2), higher dust frequency, and more dust days, which occurred more frequently than previous decades, aggravated environmental stress and affected health, agriculture, and infrastructure. Dry soils and reduced vegetation were likely to amplify dust emission, while dust deposition further reduced surface albedo and influenced local temperatures. Atmospheric dust loading potentially suppressed convective rainfall, creating a positive feedback loop that exacerbated drought conditions. Reservoir depletion and dry riverbeds (e.g., Hawizeh Marshes, Hamoun Basin) became additional dust sources, exacerbating air quality issues. The loss of stabilizing vegetation in riparian zones further increased susceptibility to wind erosion. The widespread positive anomalies of dust days showed that it was not only drier and hotter, but also significantly dustier in 2025 than the recent climatic norms in Southwest Asia, indicating an escalation in regional dust storm activity that corresponds with warming and drying trends across the Middle East. The most severe dust events were clustered in the spring and early summer months, coinciding with peak wind speeds and minimum vegetation cover, thus creating a seasonal pattern of maximum atmospheric dust loading.

6. CENTRAL ASIA

—R. P. Shukla, Md. E. Bhuiyan, M. Robjhon, L. Xu, B. Singh, and W. M. Thiaw

The climate of Central Asia varies by region and season and is influenced by terrain inhomogeneity. In this analysis, the Central Asia domain is defined as the region encompassing six countries within 20°N–60°N and 40°E–90°E. The region includes Afghanistan to the south, Turkmenistan, Uzbekistan, Tajikistan, and Kyrgyzstan (from west to east) in the center, and Kazakhstan to the north. Pakistan is not included in this Central Asia definition, but is discussed separately in this subsection because of its relevance to regional southwest monsoon variability and impacts. The NOAA Climate Prediction Center's Global Unified Temperatures and Global Precipitation Climatology Project (GPCP) data are used for most of the analysis.

(i) Temperature

During 2025, annual mean temperatures were 5°C–10°C in northern Kazakhstan and 10°C–15°C in southwestern and southern Kazakhstan (Fig. 7.52a). Annual mean temperatures were 15°C–20°C in much of Uzbekistan, Turkmenistan, southwestern Tajikistan, and parts of northern and western Afghanistan, and 20°C–30°C in southern Afghanistan and remaining parts of Pakistan. Annual mean temperatures were 0°C–5°C in eastern Tajikistan, central and eastern Kyrgyzstan, far-eastern Kazakhstan, and far-northern Pakistan, with sub-freezing temperatures occurring in isolated areas in northern Tajikistan, northeastern Kyrgyzstan, and northeastern Kazakhstan. The lowest temperatures recorded were –20°C to –10°C in parts of northern and eastern Kazakhstan, central and eastern Kyrgyzstan, and eastern Tajikistan in January and February, while the highest temperatures of 35°C–40°C occurred in parts of southern Afghanistan and southwestern Pakistan in July.

Most of Central Asia recorded annual mean temperature anomalies of +0.5°C to +2.5°C, except in far-eastern Tajikistan which had negative anomalies of –1.0°C to –0.5°C. The largest positive anomalies of +2.5°C to +3.0°C—which ranked between the 97th and 98th percentiles—were observed in parts of northern, central, and northeastern Kazakhstan (Fig. 7.52b). These large positive anomalies were also observed with respect to the maximum and minimum annual temperatures. Overall, 2025 ranked between the 90th and 98th percentiles of warmest years on record in many parts of Kazakhstan, northern Kyrgyzstan, Uzbekistan, Turkmenistan, northern and southern Afghanistan, and central and southern Pakistan.

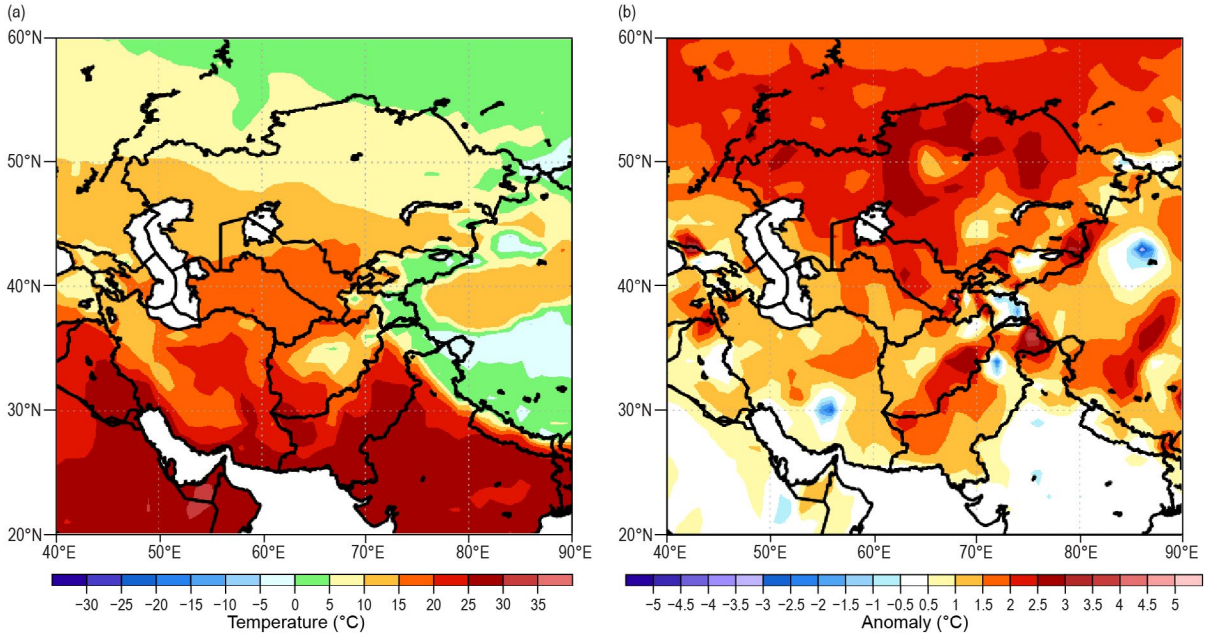

Fig. 7.52. Annual (a) mean temperature (°C) and (b) temperature anomalies (°C, 1991–2020 base period) for 2025 across Central Asia. (Source: NOAA/National Centers for Environmental Prediction.)

(ii) Precipitation

The annual total precipitation for 2025 varied greatly across Central Asia (Fig. 7.53a). The highest precipitation totals were 500 mm–700 mm in northern and eastern Kazakhstan and northern and eastern Pakistan, while 200 mm–500 mm was received in the remaining regions of

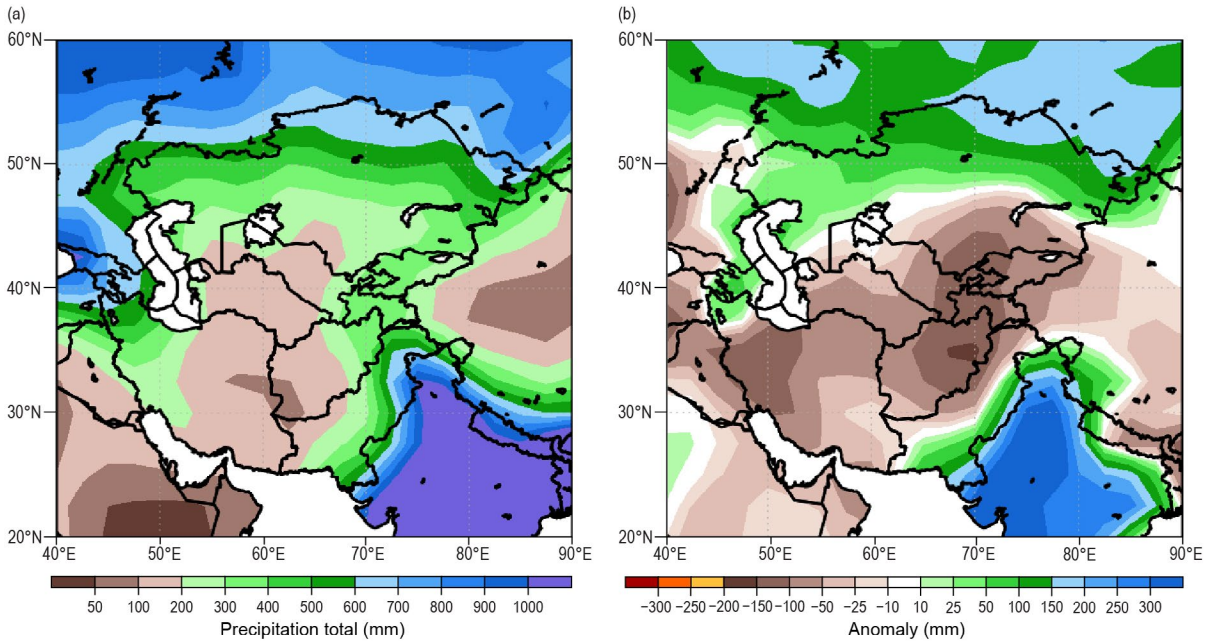

Fig. 7.53. Annual (a) precipitation totals (mm) and (b) precipitation anomalies (mm; 1991–2020 base period) for 2025 across Central Asia. (Source: NOAA/National Centers for Environmental Prediction GPCP data.)

Kazakhstan and Pakistan, Kyrgyzstan, Tajikistan, northeastern and eastern Afghanistan, and eastern Uzbekistan. The lowest totals of 50 mm–200 mm fell in western and southern Afghanistan, Turkmenistan, and parts of western and central Uzbekistan (Fig. 7.53a). The annual total precipitation was above average by 100 mm–200 mm in northern and northeastern Kazakhstan and far-eastern and southeastern Pakistan (Fig. 7.53b), ranking between the 90th and 97th percentiles of wettest years in parts of northern and northeastern Kazakhstan. The annual total precipitation was above average by 10 mm–100 mm in western and central Kazakhstan and southern Pakistan. In contrast, the annual precipitation totals were 25 mm–150 mm below average in southern Kazakhstan, Kyrgyzstan, Tajikistan, Afghanistan, Uzbekistan, Turkmenistan, and western Pakistan (Fig. 7.53b), which ranked between the 3rd and 15th percentile of driest years. Some parts of central Afghanistan received annual precipitation deficits of up to 200 mm.

(iii) Notable events and impacts

Information presented here is from the European Civil Protection and Humanitarian Aid Operations Flash and the United Nations Office for the Coordination of Humanitarian Affairs.

Minimum temperatures in April 2025 were 0°C–10°C in northern, northwestern, central, and southwestern Kazakhstan, which were 4°C–6°C above average, leading to a rapid snowmelt and overflow of rivers in northern Kazakhstan.

Total precipitation was below average in Afghanistan and Turkmenistan during March–June. During April–June (Fig. 7.54a), deficits of 25 mm–100 mm were observed across Afghanistan, many parts of Turkmenistan, Tajikistan and Uzbekistan, southern Kazakhstan, and Kyrgyzstan. The daily accumulation of precipitation averaged over Afghanistan showed that persistent below-average precipitation that started in April grew to a cumulative deficit of more than 80 mm by the end of December (Fig. 7.54b). The SPI for April–June indicated drier-than-average conditions in Afghanistan, eastern Turkmenistan, western Tajikistan, eastern Uzbekistan, and southern Kazakhstan (Fig. 7.54c). The below-average rainfall adversely affected vegetation in much of Afghanistan from May to July.

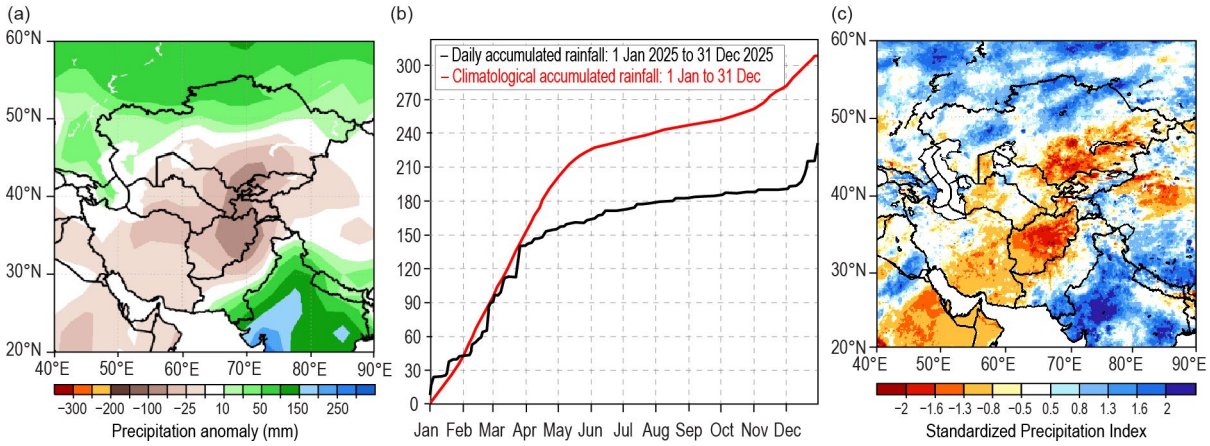

Fig. 7.54. (a) Precipitation anomalies (mm) for Apr–Jun 2025, (b) daily accumulation of rainfall averaged across Afghanistan for 2025 (black line) compared to the 1991–2020 climatological mean (red line), and (c) spatial structure of the Standardized Precipitation Index (SPI) for Apr–Jun 2025. (Sources: GPCP data for spatial precipitation; Multi-Source Weighted Ensemble Precipitation [MSWEP] for daily precipitation; MSWEP for SPI analysis.)

A heavy precipitation event during 24–27 February in Farah, Kandahar, and Helmand provinces of Afghanistan resulted in 39 fatalities and 44 injuries. During 1–7 October, heavy precipitation triggered flash flooding in central and eastern Afghanistan that resulted in three fatalities and the loss of 400 hectares of agricultural land. During 18–23 December, three deaths in Kandahar and four deaths in Herat provinces of Afghanistan were reported due to heavy precipitation and cold temperatures.

From late June to mid-September, Pakistan experienced multiple high-intensity rainfall events in Khyber Pakhtunkhwa, Punjab, Sindh, and Gilgit-Baltistan, which caused water levels to rise in Pakistan's major rivers, including the Indus, Sutlej, Ravi, Jhelum, and Chenab, that led to widespread devastation across the country. The death toll reached 1002. Over 2.9 million

people were displaced and nearly 230,000 houses were damaged or destroyed, and 220,000 hectares of rice were damaged in Punjab. Rainfall was above average across Pakistan from 21 June to 30 September 2025 (Figs. 7.55a,b). The spatial distribution of runoff indicated that flooding exhibited considerable day-to-day variation, with notable shifts across large parts of Khyber Pakhtunkhwa, Punjab, Sindh, and Gilgit-Baltistan. Significantly high runoff of 200 mm–700 mm was estimated in Punjab and Khyber Pakhtunkhwa (Fig. 7.55c).

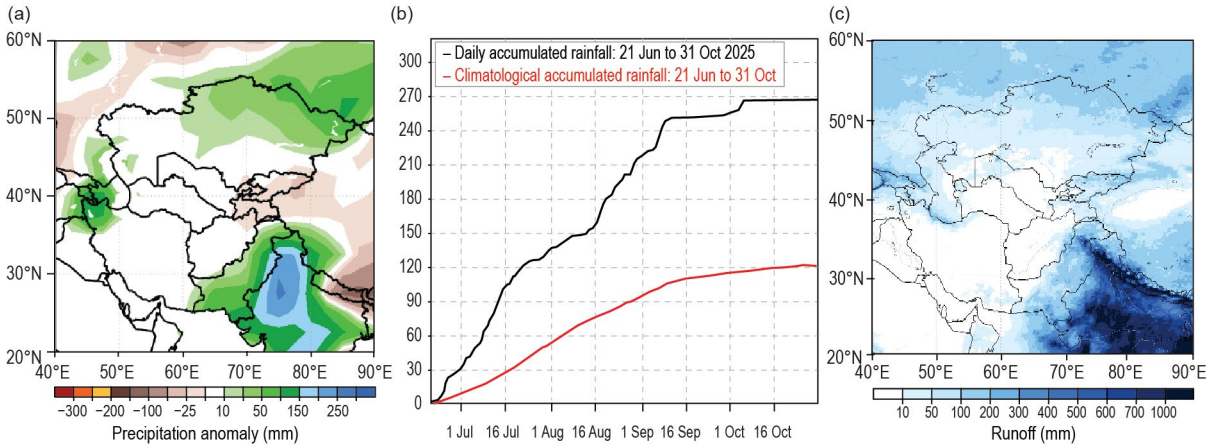

Fig. 7.55. Precipitation anomalies for Jul–Sep 2025 (mm), (b) daily accumulation of rainfall averaged across Pakistan (black line), compared to the 1991–2020 climatological mean (red line) for the period 21 Jun–31 October 2025, and (c) cumulative runoff (mm) over Central Asia during the period 21 Jun–30 Sep 2025. (Source: GPCP for precipitation; NOAA Climate Prediction Center Global Unified Gauge-based analysis of daily Precipitation; Multi-Source Weighted Ensemble Precipitation [MSWEP] for daily precipitation.)

Sidebar 7.5: **Unprecedented 2025 autumn rainfall over East Asia**

—Z. ZHU, Z. LIU, X. LIU, H. KIM, AND S. MOON

In September and October 2025, central North China experienced an unprecedented episode of extreme precipitation, resulting in severe flooding across Shandong, Henan, Hebei, Shanxi, Shaanxi, Sichuan, Jiangsu, Anhui, and Hubei provinces. This persistent and widespread rainfall adversely affected approximately 7.35 million people and led to direct economic losses estimated at $24.9 billion (U.S. dollars).

The spatial distribution of accumulated precipitation anomalies across central North China during this period exhibited a remarkable surplus, primarily concentrated in central China and the Huang River region, with maximum anomalies exceeding 600 mm (Fig. SB7.9a). The temporal evolution of daily area-mean precipitation (Fig. SB7.9b) indicates that concentrated rainfall occurred from September through early October, during which the majority of daily values significantly surpassed their climatological mean. Total precipitation for September–October, averaged over central North China, was the highest since the start of the record in 1979 (Fig. SB7.9c), more than three times the climatological mean (Fig. SB7.9b). The extreme precipitation over this region is attributed to a pair of anomalous anticyclones centered over the tropical western North Pacific and northeast Asia (Fig. SB7.9f). The circulation configuration associated with these two anomalous anticyclones passively formed a wind shear over central North China, leading to pronounced moisture convergence. Southwesterlies along the northwestern flank of the tropical western North Pacific anomalous anticyclone transported abundant moisture from the tropical oceans into North China. Meanwhile, the anomalous anticyclone over northeastern Asia inhibited further northward moisture transport, thereby promoting moisture accumulation and enhanced precipitation over central North China.

Associated with the precipitation anomalies were zonal dipole convection anomalies over the tropical Pacific (Fig. SB7.9f), as well as SST anomalies over the North Atlantic and Barents–Kara Sea (Fig. SB7.9e). The negative convection anomalies over the western Pacific excited an anomalous anticyclone to its northwest, facilitating moisture transport into central North China (Fig. SB7.9f). Meanwhile, the tropical zonal dipole convection was associated with a mid- to high-latitude Rossby wave train propagating from the North Pacific toward East Asia, as indicated by the wave activity flux in Fig. SB7.9d. The Rossby wave train was further amplified by SST anomalies over the North Atlantic and the Barents–Kara Sea (Fig. SB7.9e), ultimately leading to a quasi-barotropic anticyclonic anomaly over northeastern Asia (Fig. SB7.9d). The anomalous anticyclone impeded further northward transport of moisture, thereby contributing to the extreme precipitation over central North China.

Seasonal rainfall over central North China and adjacent East Asia was strongly shaped by the evolution of the East Asian summer monsoon frontal rainband (see section 4e for details). During 24 June–12 July, below-normal frontal precipitation was widespread over Korea and neighboring regions. The negative frontal precipitation anomalies coincided with a significantly anomalous western North Pacific subtropical high (WNPSH), indicating a dynamically unfavorable state for persistent frontal rainfall over the peninsula in the core Changma–Meiyu–Baiyu (CMB) season. In contrast, during 7–17 September, above-normal frontal precipitation occurred over Korea, with the eastward-displaced WNPSH ridge placing the region along the northwestern edge of the subtropical high. Shifts in the mid-tropospheric subtropical-high ridge during the summer-to-autumn transition could alter moisture pathways and baroclinic coupling over East Asia. Although the WNPSH typically weakens and retreats during this period, it delayed decay in 2025, and sustained enhancement of moisture transport and dynamically favorable conditions for frontal precipitation. The precipitation anomalies in autumn 2025 featured an enhanced frontal precipitation ratio under a late-season circulation configuration distinct from the CMB peak.

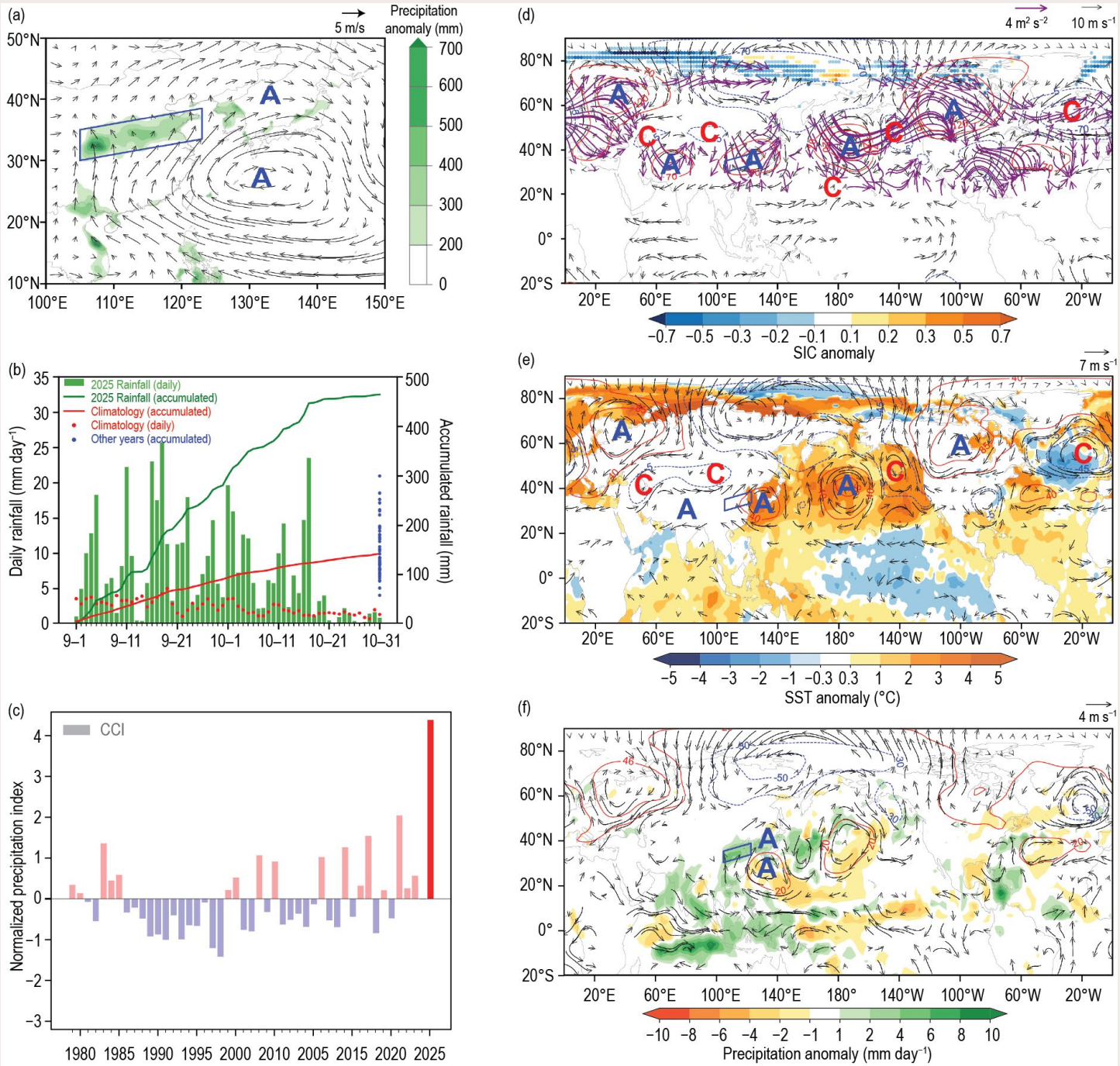

Fig. SB7.9. (a) Anomalies of accumulated precipitation (shading; mm), 850-hPa wind (vectors; m s^{-1}) during Sep–Oct 2025. (b) Daily rainfall (bars; mm day^{-1}; left axis) and daily accumulated rainfall (lines; mm; right axis) over central North China during Sep–Oct 2025. (c) Time series of normalized year-to-year central North China precipitation index (CCI; bars). Anomalies of (d) sea ice (SIC; dots), 200-hPa geopotential height (contours; gpm), wind (black vectors; m s^{-1}), and wave activity flux (purple vectors; m^2 s^{-2}), (e) 500-hPa geopotential height (contours; gpm), wind (vectors; m s^{-1}), and sea surface temperature (SST; shading; °C), and (f) 850-hPa geopotential height (contours; gpm), wind (vectors; m s^{-1}), and precipitation (shading; mm day^{-1}) for Sep–Oct 2025. The letters "A" and "C" in (d)–(f) denote centers of anticyclonic and cyclonic anomalies, respectively. The blue box outlines the central North China.

h. Oceania

—C. Ganter, Ed.

1. OVERVIEW

—C. Ganter

The region of Oceania (Fig. 7.56) began 2025 with a weak La Niña in place and ended with the re-emergence of La Niña conditions, with neutral conditions during the rest of the year (see section 4b for details). Both the northwest and southwest Pacific saw rainfall patterns consistent with La Niña; however, for Australia and New Zealand the influence was more limited. Similarly, a negative Indian Ocean dipole during austral spring (see section 4f for details) also had limited effect upon Australian rainfall.

Australia and New Zealand each reported their fourth warmest year since records began in 1910 and 1909, respectively. Both countries were surrounded by anomalously warm ocean waters throughout the year. For a second consecutive year, annual sea surface temperatures in a boxed region surrounding Australia (4°S–46°S, 94°E–174°E) were the highest on record (since 1900), according to the NOAA Extended Reconstructed Sea Surface Temperature Version 5 (ERSST v5) data.

Record-high sea levels were observed at various tide gauges across Micronesia during the year, in part due to the La Niña conditions and to the extensive record-warm water across the west Pacific. Sea level data extend as far back as 1948, for example, at Apra Harbor on Guam.

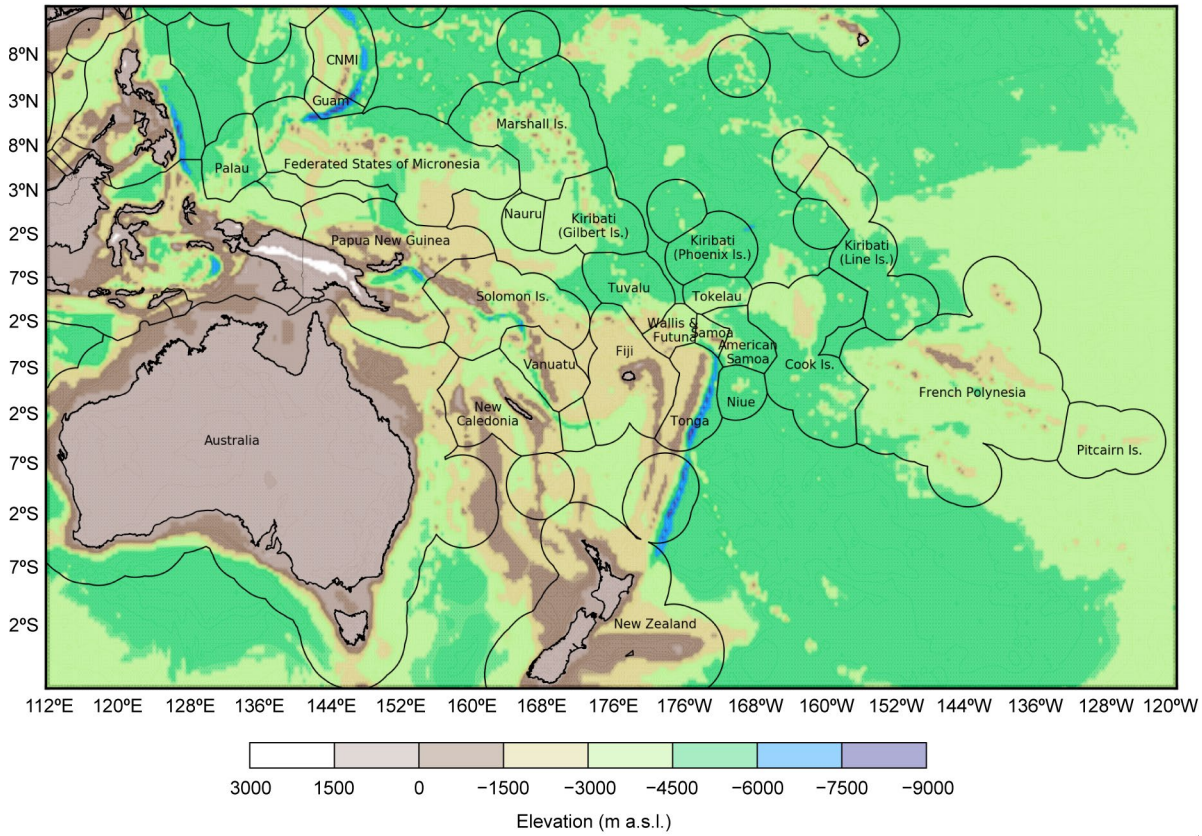

Fig. 7.56. The region of Oceania. The colors represent topographical heights, with white and brown colors ranging from around 3000 m above sea level (a.s.l) to around –1500 m a.s.l. The yellow, green, and blue indicate greater depths of up to 9000 m below sea level, with blue indicating the lowest depths.

2. NORTHWEST PACIFIC AND MICRONESIA

—B. Bukunt

This assessment covers the area from the dateline west to 130°E, between the equator and 20°N. It includes the U.S.-Affiliated Pacific Islands of Micronesia, but excludes the western islands of Kiribati and nearby northeastern islands of Indonesia (Fig. 7.56). The temperature analysis is based on data from ECMWF Reanalysis v5 (ERA5; Hersbach et al. 2023) and scripts developed by NOAA's National Weather Service (NWS). Rainfall data is a combination of

NOAA's National Weather Service (NWS) station data and the Multi-Source Weighted-Ensemble Precipitation (MSWEP; Beck et al. 2019) analyses as presented by the Bureau of Meteorology (BOM) Pacific Climate Monitoring and the Climate and Oceans Support Program in the Pacific (COSPPac) Ocean and Climate Outlook Forum. The base period is 1991–2020 unless otherwise stated.

The climate of 2025 was bookended by weak La Niña atmospheric and oceanic conditions, a pattern characterized by a consolidated warm pool in the far western Pacific and suppressed convection in the central Pacific near the equator, primarily east of 150°E. This coupling resulted in steady above-average rainfall far to the west in the vicinity of Palau contrasted by notable rainfall deficits in the equatorial atolls east of 150°E. Another zonal band of dryness was observed southeast of Guam, extending eastward to the central and northern Marshall Islands.

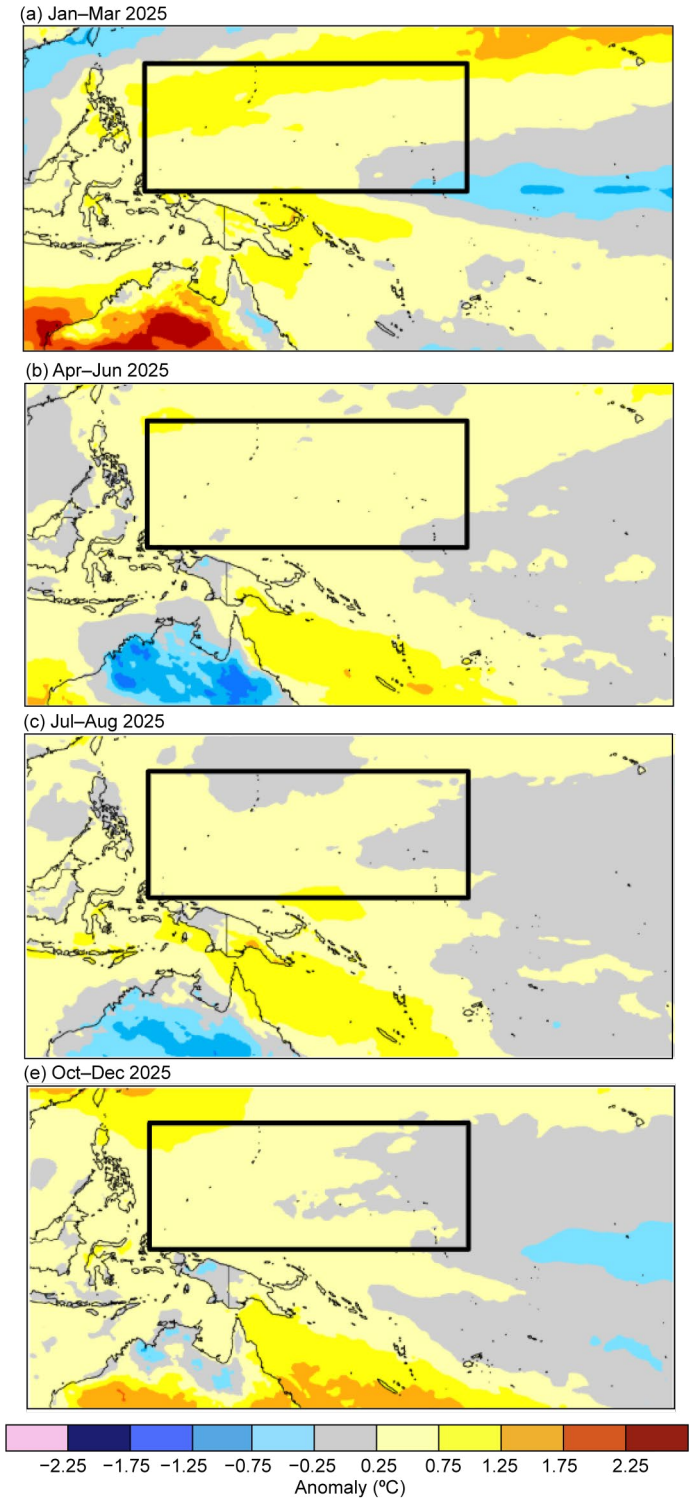

Fig. 7.57. Seasonal air temperature surface anomalies (°C) across the west-central Pacific in 2025 for (a) Jan–Mar, (b) Apr–Jun, (c) Jul–Sep, and (d) Oct–Dec. The black box in each panel defines the Micronesia region of the northwest Pacific. (Source: ERA5.)

(i) Temperature

Surface air temperatures across Micronesia were generally above normal throughout 2025 (Fig. 7.57), driven by an expansive area of above-normal sea surface temperatures (SSTs) in the western tropical Pacific Ocean. Near-normal surface air temperatures were observed in the far southeastern corner of the region for most of the year.

During the first half of the year (January–June), a broad swath of well-above-normal (within the top 10% of values in the 1991–2020 period) and record-warm SSTs were present across much of Micronesia, according to ERA5 reanalysis data (Fig. 7.58). A small portion of near-normal (middle 40%) to below-normal SSTs (lowest 30%) were evident in the southeastern corner of the region, primarily in the vicinity of Kosrae and the central to southern Marshall Islands.

During the second half of the year, the record-high SSTs shifted to above to well-above-normal across the western two-thirds of Micronesia. Surface air temperature anomalies followed this oceanic signal, with most of the region slightly warmer than normal during the latter half of the year. Near-normal air temperatures were observed near the dateline and across portions of the Marshall Islands where SSTs were closer to normal.

(ii) Precipitation

Precipitation patterns in 2025 largely followed typical La Niña expectations, with dryness observed in the near equatorial regions east of 150°E, and a secondary zonal band centered between 9°N and 14°N from Guam to the northern Marshall Islands

(Fig. 7.59). Near- to slightly-above-normal rainfall was observed in most other regions.

Station-based rainfall showed that Kapingamarangi, located near 1°N, 155°E, recorded only 68.4% of its normal total during the first half of the year, with the second half of the year receiving 86.0% of normal (Table 7.5). This deficit aligns with the suppression of convection often observed near the equator during La Niña events. Farther north, Kwajalein experienced a very dry start to 2025, receiving only 56.8% of its normal rainfall from January to June, with the second half of the year still dry, but closer to normal, at 88.9%.

In sharp contrast, islands located within the primary axis of the Intertropical Convergence Zone (ITCZ), experienced very wet conditions. Kosrae (5°N, 163°E) was exceptionally wet, particularly during the second half of the year when it received 154.1% of its normal rainfall, making 2025 its seventh wettest year in the 70-year record).

(iii) Notable events and impacts

Record-high sea levels were observed at various tide gauges across Micronesia during the year, in part due to the La Niña conditions and warm water volume buildup across the West Pacific Warm Pool. Sea level data extend as far back as 1948, for example, at Apra Harbor on Guam. The monthly mean sea level was the

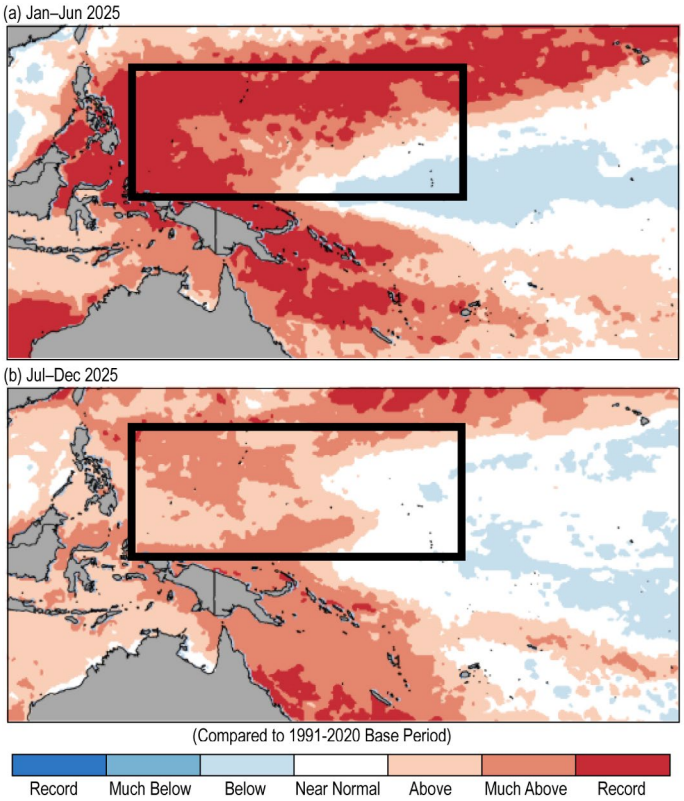

Fig. 7.58. Sea surface temperature classifications for (a) Jan–Jun 2025 and (b) Jul–Dec 2025 compared to the 1991–2020 base period. Much above normal is defined as top 10% of values, above normal is top 30%, and near normal is the middle 40% of values. The same convention applies to below normal and much below normal for the bottom 30% and bottom 10% respectively. The black boxes define the Micronesia region of the northwest Pacific. (Source: ERA5.)

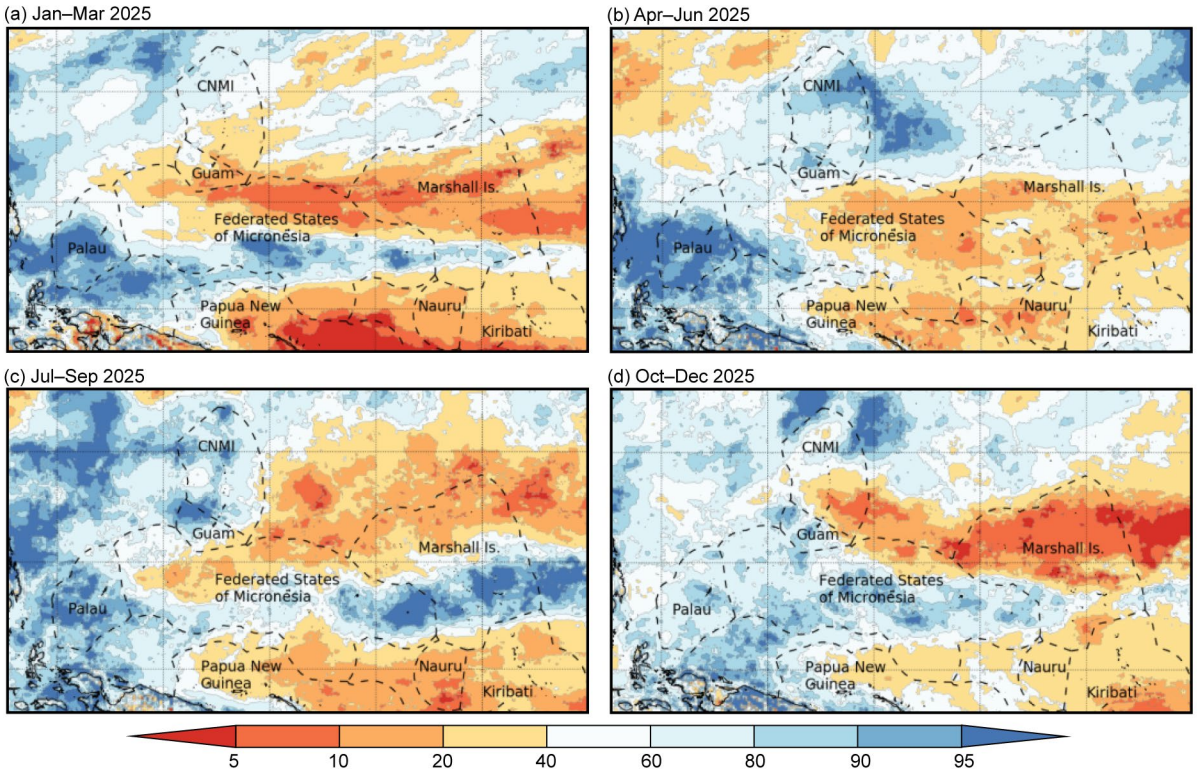

Fig. 7.59. Rainfall anomalies (% of normal; 1991–2020 base period) across the central and western Pacific in 2025 for (a) Jan–Mar, (b) Apr–Jun, (c) Jul–Sep, and (d) Oct–Nov. (Source: Bureau of Meteorology Pacific Climate Monitoring and the Climate and Oceans Support Program in the Pacific [COSPPac]/Multi-Source Weighted-Ensemble Precipitation [MSWEP].)

Table 7.5. Average rainfall total (AVG; mm) compared to rainfall total (mm) and percent of normal values (%) for select Micronesia locations in 2025 (1991–2020 base period) for Jan–Jun, Jul–Dec, and annual (Jan–Dec). Latitudes and longitudes are approximate. "Kapinga" stands for Kapingamarangi Atoll in Pohnpei State, Federated States of Micronesia. Green-filled cells with an up arrow icon (↑) indicate above-average rainfall and yellow-filled cells with a down arrow icon (↓) represent below-average rainfall. (Source: NOAA's National Weather Service.)

Location	Jan–Jun AVG Rainfall (mm)	Jan–Jun 2025 Rainfall (mm)	Jan–Jun % of Normal Rainfall	Jul–Dec AVG Rainfall (mm)	Jul–Dec 2025 Rainfall (mm)	Jul–Dec % of Normal Rainfall	Jan–Dec AVG Rainfall (mm)	Jan–Dec 2025 Rainfall (mm)	Jan–Dec % of Normal Rainfall
Saipan 15°N, 146°E	462.8	401.3 ↓	86.7 ↓	1306.1	1118.6 ↓	85.6 ↓	1768.9	1519.9 ↓	85.9 ↓
Guam 13°N, 145°E	678.7	742.4 ↑	109.4 ↑	1813.6	1739.4 ↓	95.9 ↓	2492.3	2481.1 ↓	99.6 ↓
Palau 7°N, 134°E	1798.1	1920.5 ↑	106.8 ↑	2279.4	2268.0 ↓	99.5 ↓	4077.5	4188.5 ↑	102.7 ↑
Yap 9°N, 138°E	1191.5	1244.9 ↑	104.5 ↑	1943.4	1728.2 ↓	88.9 ↓	3134.9	2973.1 ↓	94.8 ↓
Chuuk 7°N, 152°E	1678.2	1581.4 ↓	94.2 ↓	1917.7	2039.1 ↑	106.3 ↑	3595.9	3620.5 ↑	100.7 ↑
Pohnpei 7°N, 158°E	2361.2	2281.7 ↓	96.6 ↓	2308.4	2689.6 ↑	116.5 ↑	4669.6	4971.3 ↑	106.5 ↑
Kapinga 1°N, 155°E	1880.6	1285.5 ↓	68.4 ↓	1485.1	1276.7 ↓	86.0 ↓	3365.7	2562.1 ↓	76.1 ↓
Kosrae 5°N, 163°E	2635.8	2912.6 ↑	110.5 ↑	2354.8	3627.9 ↑	154.1 ↑	4990.6	6540.5 ↑	131.1 ↑
Kwajalein 9°N, 168°E	898.4	510.0 ↓	56.8 ↓	1553.7	1380.7 ↓	88.9 ↓	2452.1	1890.8 ↓	77.1↓
Majuro 7°N, 171°E	1459.0	1246.4 ↓	85.4 ↓	1875.0	2171.2 ↑	115.8 ↑	3334.0	3417.6 ↑	102.5 ↑

highest on record from April to July, and October through December (Fig. 7.60). The remaining months were all near record-high levels as well.

Saltwater inundation of low-lying coastal areas and coastal berm erosion occurred during higher tide cycles throughout the year. In July, Saipan experienced significant coastal flooding and erosion due to the combination of record-high sea levels, new moon tides, and storm surf from nearby Tropical Cyclone Krosa. Widespread coastal flooding was observed on Weno Chuuk during the full moon phase in early November.

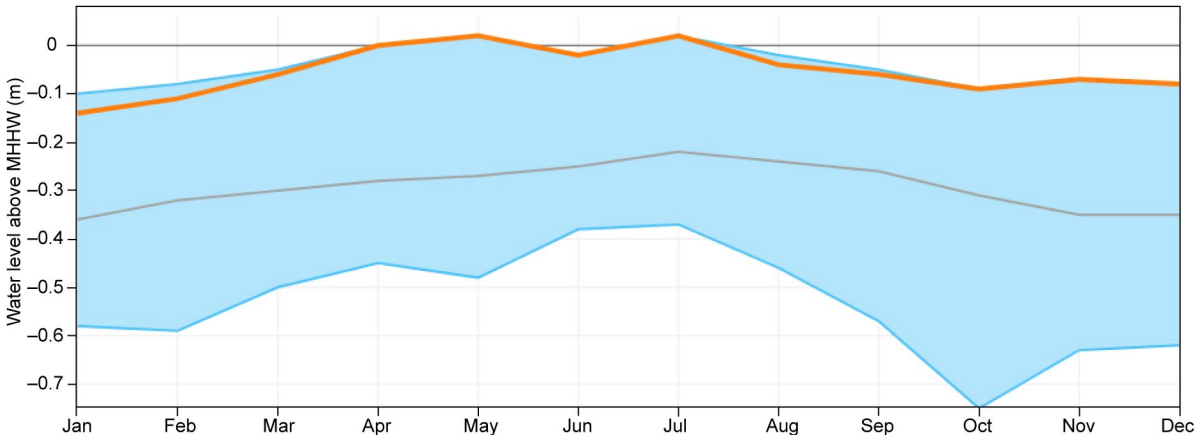

Fig. 7.60. Highest and lowest monthly mean water levels (m) at Apra Harbor, Guam, for the period 1948–2025. The 2025 monthly mean data is plotted in orange. (Source: University of Hawaii Sea Level Center and NOAA's National Ocean Service.)

3. SOUTHWEST PACIFIC

—J. Gray and A. Peltier

The Southwest Pacific region encompasses American Samoa, the Cook Islands, Fiji, French Polynesia, Kiribati, Nauru, New Caledonia, Niue, Papua New Guinea (PNG), Pitcairn Islands, Samoa, the Solomon Islands, Tokelau, Tonga, Tuvalu, Vanuatu, and Wallis and Futuna (Fig. 7.56). The analysis in this section is based on data from ECMWF Reanalysis v5 (ERA5; Hersbach et al. 2023), and the base period is 1991–2020.

The year 2025 began with a weak La Niña in the Pacific, which transitioned towards neutral in April. El Niño–Southern Oscillation (ENSO) conditions were neutral from May through November, after which weak La Niña conditions redeveloped and persisted into early 2026.

The Intertropical Convergence Zone (ITCZ) tracked along its normal climatological position from January to March and November to late December. From late April, the pattern shifted southward and did not return to its normal position until mid-May. Further deviation in the location of the ITCZ coincided with the western North Pacific summer monsoon season (mid-May–October), during which the western flank was consistently north of Guam, and the central ITCZ was more southerly than usual over Micronesia.

In contrast, shifts in the South Pacific Convergence Zone (SPCZ) were concentrated in the Southern Hemisphere tropical cyclone season (November–April), where the SPCZ was shifted south of its usual position for most of the period. The southern departure from the climatological mean was strongest in the central and eastern SPCZ, migrating southward over Vanuatu and Fiji and reaching as far east as French Polynesia. A southward shift of the SPCZ is typical for a La Niña (Brown et al. 2020; Vincent et al. 2011).

(i) Temperature

Above-average air temperatures were consistently observed across the southwestern Pacific throughout 2025. Localized temperature anomalies of +1°C to +2°C during January–March were observed in PNG, the northern Solomon Islands, and southern French Polynesia (Fig. 7.61a). For

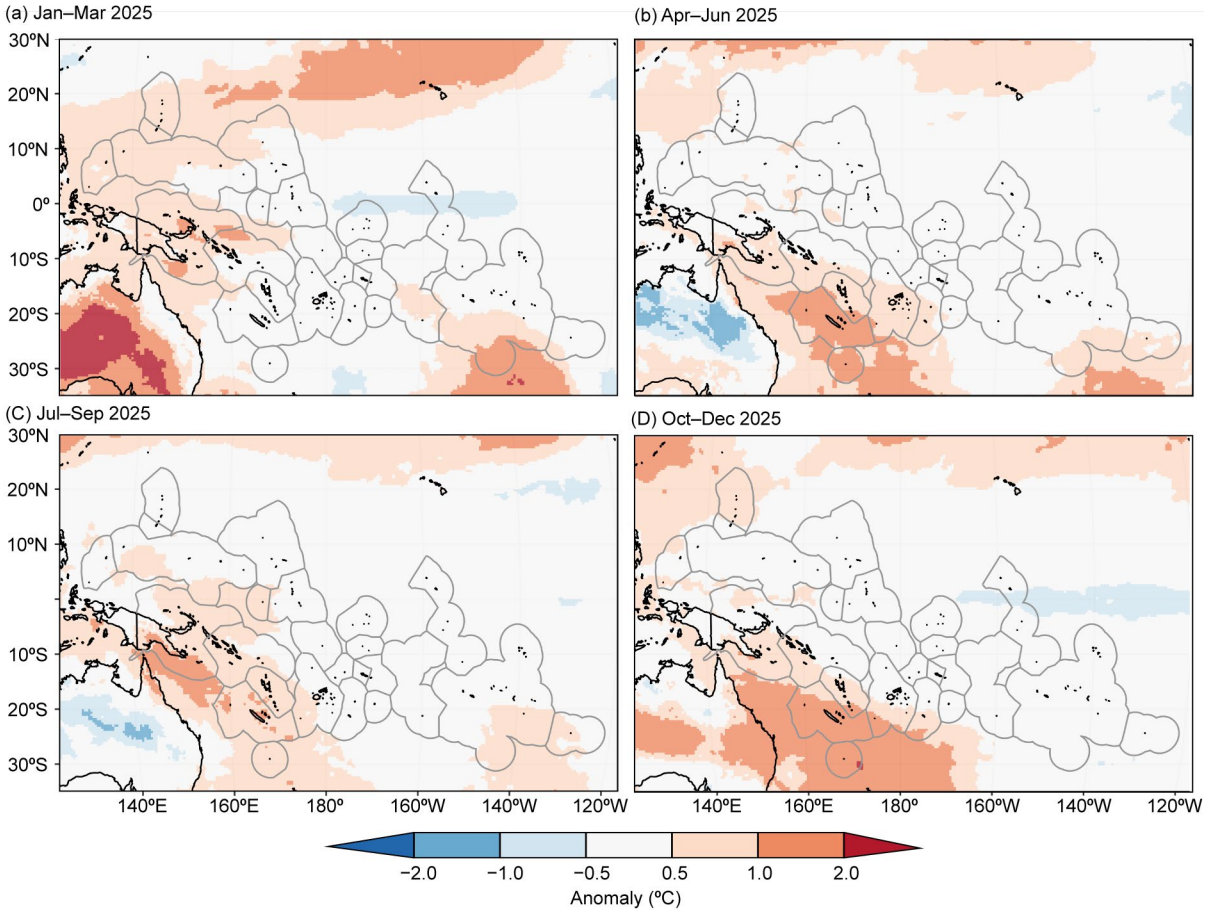

Fig. 7.61. Seasonal 2-m air temperature anomalies (°C; 1991–2020 base period) for the southwest Pacific in 2025 for (a) Jan–Mar, (b) Apr–Jun, (c) Jul–Sep, and (d) Oct–Dec. (Source: ERA5.)

these areas, the above-average air temperatures align with extreme above-average sea surface temperatures throughout 2025.

From April to June, the anomalous heat moved south, affecting New Caledonia and the southern tip of Vanuatu (Fig. 7.61b). Notably warmer temperatures throughout July–September were observed across PNG and New Caledonia (Fig. 7.61c). This trend continued into October–December for New Caledonia, with more extreme heat values shifting southward away from PNG and extending to the southern tip of Vanuatu. Below-average temperatures were observed in the northern Line Islands and the Phoenix Islands (Kiribati) in January–March, and only in the northern Line Islands during October–December (Fig. 7.61d).

(ii) Precipitation

A dry signal persisted across the equatorial South Pacific throughout 2025. The contraction of rainfall to the southwest during January–March and October–December was driven by weak La Niña conditions (Figs. 7.62a,d).

Countries that remained consistently dry throughout the year included Nauru, Kiribati (Phoenix Islands, Gilbert, and Line Islands), and parts of French Polynesia. Enhanced drier-than-normal conditions (<30% of normal) were observed from January to March and from October to December in Nauru, the Gilbert Islands (Kiribati), and the northern Phoenix and Line Islands (Kiribati); this dryness aligns with typical La Niña conditions (Juria 2025; PICOF-17 2025). Notable drought impacts from April to October were observed across Tuvalu, the Northern Cook Islands, Niue, and Tonga.

For January–March (Fig. 7.62a), above-normal rainfall was observed for New Caledonia, Vanuatu, Fiji, the southern Solomon Islands, Tonga, Niue, southern American Samoa, Samoa, Pitcairn Islands, and Wallis and Futuna. A notable monthly total during the period was recorded at Niuatoputapu, Tonga, which received 623.9 mm, its highest February rainfall total in the 78-year record.

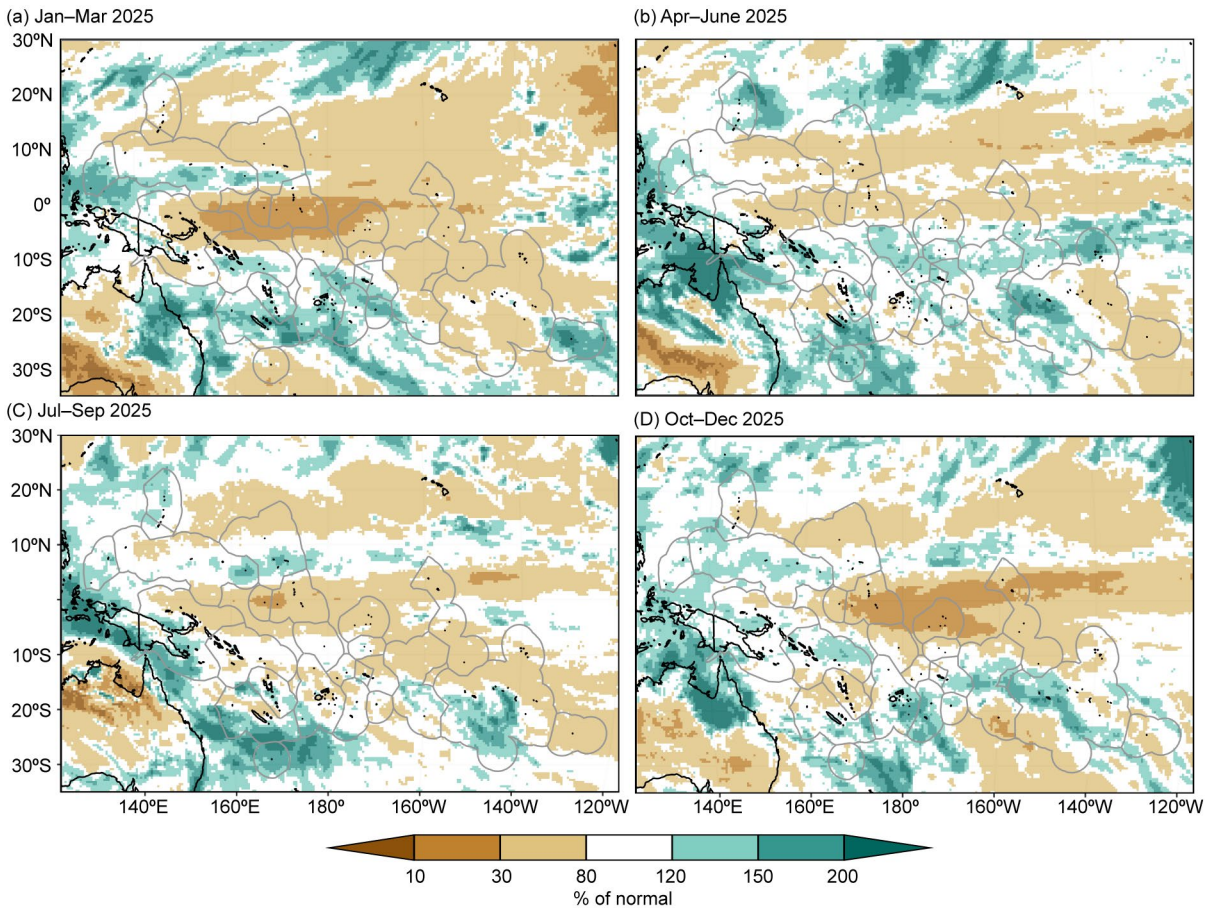

Fig. 7.62. Seasonal rainfall anomalies (% of normal; 1991–2020 base period) across the southwest Pacific in 2025 for (a) Jan–Mar, (b) Apr–Jun, (c) Jul–Sep, and (d) Oct–Dec. (Source: ERA5.)

Precipitation during April–June (Fig. 7.62b) was more widespread across the Pacific, extending into the central and eastern regions. Locations that experienced enhanced rainfall included French Polynesia (northern and central western areas), southern New Caledonia, eastern Vanuatu, the Solomon Islands, and PNG. Many rainfall events caused minor to significant flooding. Lata, in the Solomon Islands, experienced its highest monthly total of 615.1 mm for April, with records dating to 1976.

Drier-than-normal conditions (<80%) were observed during April–June in the Pitcairn Islands, eastern French Polynesia, northern Phoenix and Line Islands, Gilbert Islands, Nauru, Fiji, northeastern New Caledonia, and western Vanuatu (Fig. 7.62b).

Wetter-than-normal conditions in July–September (Fig. 7.62c) were concentrated in the far west of the basin, with higher precipitation also seen in southern French Polynesia and the Cook Islands. This western contraction of precipitation could be a product of the ITCZ and the western Pacific monsoon season, with totals >200% of normal concentrated over PNG, southern New Caledonia, southern Vanuatu, central French Polynesia, and southern Fiji.

September was particularly dry across the Pacific, with Goroka (PNG; 20.6 mm; 62-year record), Nauru (0 mm; 76-year record), and Beru (Kiribati; 35.6 mm; 67-year record) all breaking their lowest September rainfall totals. Similarly, Vunisea (Fiji; 15 mm; 88-year record) reported its second-lowest September total on record. Other locations in the western division of Fiji all recorded less than 30 mm in September, where typical rainfall is closer to 167 mm.

During October–December (Fig. 7.62d), exceptional rainfall was observed in southern New Caledonia, Fiji, Tonga, central western and southeastern French Polynesia, the central Cook Islands, and Tokelau. In November, Vanuabalavu, Fiji, set a new monthly record of 527.5 mm (41-year record), with Labasa airfield (206.2 mm, 70-year record) and Vanuabalavu (155.6 mm; 41-year record) each breaking their November daily rainfall record on 24 November.

(iii) Notable events and impacts

The 2024/25 southwest Pacific cyclone season produced seven unnamed tropical depressions and four named tropical cyclones (Pita, Rae, Seru, and Tam). The strongest storm, Tropical Cyclone Rae (Category 2), developed on 22 February, with the lowest pressure for the season of 975 hPa. Rae made landfall over the Lau and Lomaitviti groups, causing heavy rainfall, strong winds, and flooding in Fiji. Impacts from Rae led to flight cancellations, school closures (in the Lau Group, Lomaiviti, and Vanua Levu), infrastructure damage, uprooted trees, debris blocking roads, and the destruction of farms, causing food and water shortages in Sawana, according to the Pacific Islands Climate Outlook Forum (PICOF) and Radio New Zealand.

In April, landslides occurred due to persistent heavy rains in the Solomon Islands and Fiji. A landslide in the Solomon Islands on 17 April destroyed homes at Chain Valley (Borderline), central Honiara. Landslides in Fiji impacted the Wailoa (3 April) and Namosi (7 April) roads in the central division, according to PICOF.

Although PNG was forecast to be in drought from May–October in 2025, the western and central provinces experienced above-normal rainfall that led to flooding and landslides throughout May. Severe flooding also occurred on 17 October in Kanep, PNG, isolating 350 people from the community, according to PICOF, with houses, crops, livestock, bridges, roads, wooden canoes, and essential recovery tools washed away as a result. Damage to crops and livestock deaths led to food shortages in the area.

A hailstorm impacted Imaki, Tanna, Vanuatu, on 26 August. The storm was caused by a lingering trough over the southern island of Vanuatu, enhancing the deep development of towering cumulonimbus clouds and strong updrafts lifting raindrops above the freezing level in the upper atmosphere. Hail in the tropics is rare, generally occurring at higher elevations, due to warmer atmospheric conditions melting ice crystals before reaching the surface (Hand and Cappelluti 2011). Further, this was the first recorded occurrence in 23 years, according to the Vanuatu Daily Post. The last hail event in 2002 caused widespread damage and landslides.

Twenty-two people were killed and several were missing due to a landslide in Kukas village, PNG, at 2 am local time on 31 October, according to local news reports. Prolonged heavy rainfall preceding the event was a leading factor in the instability of the regolith along the slope. Kukas

village is located in the mountainous region of Enga Province, the same province where the catastrophic landslide of May 2024 occurred.

4. AUSTRALIA

—C. Minney

For this section, monthly area-averaged temperatures are based on the Australian Climate Observations Reference Network–Surface Air Temperature (ACORN-SAT) dataset (Trewin 2018), while mapped temperature analyses are based on the Australian Water Availability Project (AWAP) dataset (Jones et al. 2009), both of which begin in 1910. Area-averaged rainfall values and mapped rainfall analyses use the Australian Gridded Climate Data (AGCD) dataset (Evans et al. 2020), which began in 1900. Anomalies are based on the 1991–2020 average.

(i) Temperature

The year 2025 was Australia's fourth warmest since national records began in 1910. The area averaged mean temperature was 0.59°C above the 1991–2020 average. Every state and territory reported one of its 10 warmest years with respect to mean temperature, except Tasmania and the Northern Territory. Nationally, the area-averaged annual mean maximum temperature (Fig. 7.63) was 0.74°C above average. The area-averaged annual mean minimum temperature (Fig. 7.64) was 0.44°C above average.

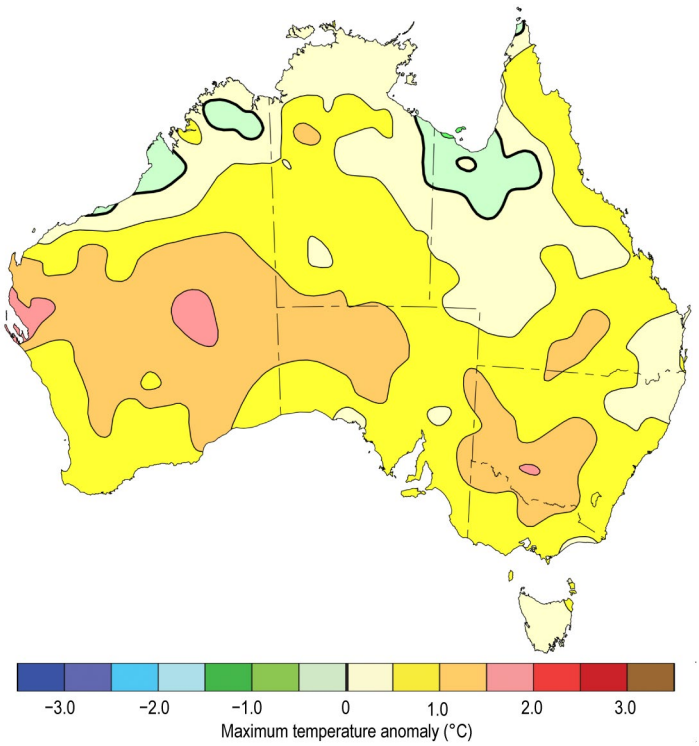

Fig. 7.63. Annual maximum temperature anomalies (°C; 1991–2020 base period) in Australia for 2025. Australian States/Territories are as follows, starting in a clockwise fashion from the west: Western Australia, the Northern Territory, Queensland, New South Wales, Victoria, and South Australia, with the island of Tasmania in the south-east. (Source: Australian Bureau of Meteorology.)

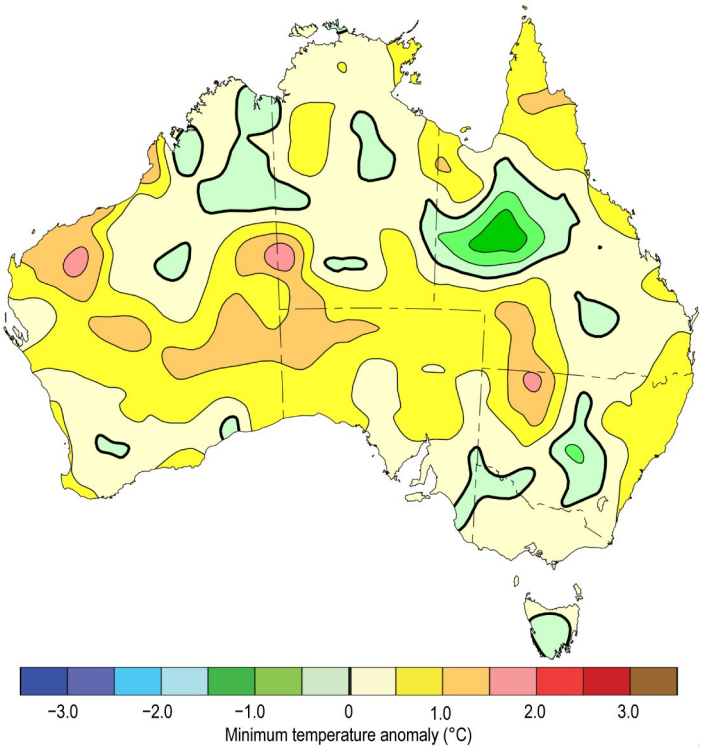

Fig. 7.64. Annual minimum temperature anomalies (°C; 1991–2020 base period) in Australia for 2025, relative to a 1991–2020 base period. (Source: Australian Bureau of Meteorology.)

Annual maximum temperatures were above average across most of the country, with anomalies of +1°C to +1.5°C across parts of southern Australia. Maximum temperatures were below average across northern Western Australia and Queensland's Gulf Country. Minimum temperatures were mostly within 1°C of average across Australia, with anomalies of +1°C to +2°C across parts of Western Australia, the Northern Territory, South Australia, and New South Wales. Minimum temperatures were 1°C to 1.5°C below average for western Queensland.

At the monthly scale, the mean national temperature was among the five warmest on record for January–March and October, including the warmest March on record. Heatwave conditions impacted large parts of the country during January to March, and persisted into early April with very-much-above-average temperatures in the southeast.

Nationally, it was the fourth-warmest austral autumn on record, particularly notable in the south where Victoria and Tasmania had their warmest autumns since records began in 1900. Austral spring for Australia was the ninth-warmest on record, even with below-average temperatures during November across the southeast due to multiple cold outbreaks during the month.

(ii) Precipitation

Nationally, the area-average annual rainfall total for Australia during 2025 was 504.5 mm, 4% above the 1991–2020 average of 486.0 mm (Fig. 7.65). Compared to the distribution across all 126 years of observations since 1900, rainfall in 2025 was above average across northern and scattered southern areas of Western Australia, northern and eastern parts of the Northern Territory, most of Queensland, and the eastern seaboard of New South Wales. Rainfall was below average for most of Tasmania, Victoria, and South Australia, southern and western New South Wales, and western and inland parts of Western Australia.

It was the driest January–May on record for parts of western Victoria and southeastern South Australia, with monthly rainfall persistently below average for the region. Low rainfall meant the absence of, or significantly later-than-average 'Autumn Break' rainfall; while there is no one agreed definition, varying by location, the Autumn Break is essential cool season rainfall required for adequate crop growth in southern agricultural regions (for a northern Victorian example, see Pook et al. 2009). Drought conditions impacted much of southern Australia, particularly during the first half of the year when record-high temperatures were also reported, as noted above. Large areas of southern Australia saw below-average rainfall for each month between April and October, except July. Low autumn rainfall impacted crop growth and followed on from below-average cool-season rainfall in both 2024 and 2023. It was the driest January–June on record for large parts of southeastern South Australia and part of southern Victoria. Drought conditions began to ease in July across southeastern Australia; however long-term (>12 months) deficiencies remained in the region at the end of the year.

It was also a drier-than-average January across much of the Northern Territory and northern and western Queensland due to minimal tropical activity. The monsoon arrived at Darwin on 7 February 2025, the latest since records began there in 1957/58, surpassing the previous latest onset date of 25 January (during the 1972/73 wet season). The average timing of the monsoon onset at Darwin is around 25 December.

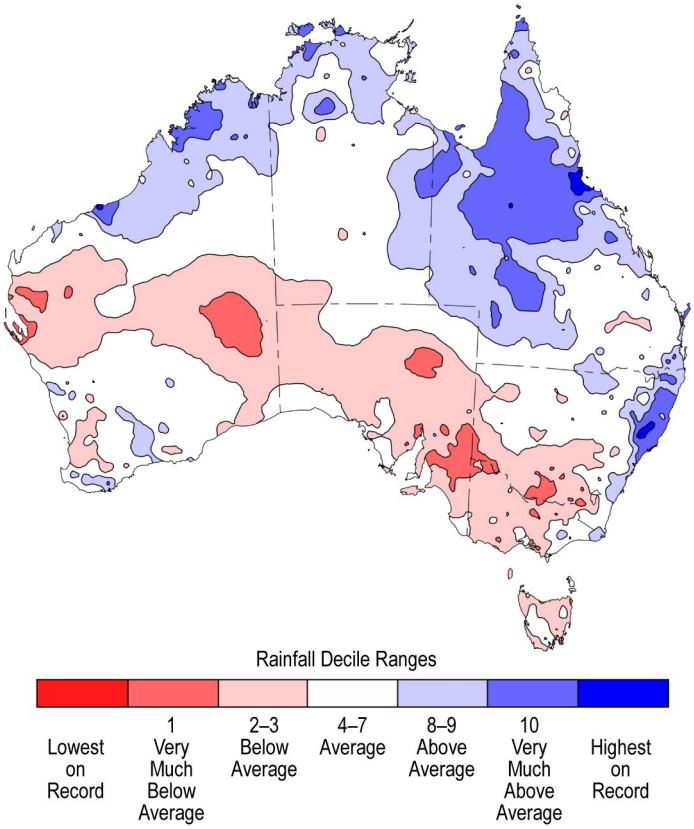

Fig. 7.65. Annual rainfall deciles in Australia for 2025, based on the 1900–2025 distribution. (Source: Australian Bureau of Meteorology.)

Annual rainfall was the highest on record for the Townsville region of northern Queensland. The Townsville Aero site recorded 2.5 times its annual average rainfall with a total of 2950.8 mm, surpassing its annual average by February.

Nationally, it was the eighth-wettest March on record, in part due to Queensland's second-wettest March due to rainfall from ex-Tropical Cyclone Alfred and widespread heavy rainfall (see *Notable events and impacts*).

A negative Indian Ocean dipole (IOD) emerged in the Indian Ocean in early September, persisting until December (see section 4f for details). While a negative IOD typically enhances spring rainfall over eastern Australia, the impact in 2025 was not pronounced.

A weak La Niña ended in March, followed by neutral ENSO conditions before a weak La Niña emerged in the tropical Pacific in late November. The timing and strength of both La Niña events meant that their influence on rainfall in Australia was likely limited. Additionally, waters surrounding Australia were overwhelmingly warmer than average during the year, with annual SSTs in the Australian region the warmest on record during 2025, according to ERSST v5 data (Huang 2017; see section 3b). These SSTs were likely enhancing heavy rainfall events by providing additional moisture and energy. SSTs in the Australian region were the warmest on record for January, February, May, July, August, September, and November, with the remaining months either second- or third-warmest on record.

(iii) Notable events and impacts

Tropical Cyclone (TC) Alfred impacted the southeast Queensland and New South Wales north coasts in early March, after slowly moving toward the southeast Queensland coast. Despite crossing the coast as a tropical low, ex-TC Alfred brought heavy rainfall and damaging winds to the area. On 9 March, it was the wettest day in the 45-year record at K'gari Eurong, with a daily rainfall total of 427.3 mm.

Heavy rainfall in late March across most of Queensland resulted in extensive flooding, including over the Georgina and Diamantina Rivers in southwest Queensland, which are within the Lake Eyre Basin. Floodwaters progressed slowly downstream, resulting in a rare instance of water reaching Kati Thanda–Lake Eyre, an ephemeral lake in South Australia. Flooding resulted in significant livestock loss, road closures, and the isolation of communities.

Tropical Cyclone Fina formed in mid-November in the Arafura Sea, north of the Northern Territory. It made landfall as a Category 2 system on the Cobourg Peninsula, Northern Territory, intensifying to a Category 3 system as it moved towards Darwin, bringing heavy rainfall, including the November daily rainfall record at Darwin Airport of 168.6 mm on 23 November, with records dating to 1941.

5. AOTEAROA NEW ZEALAND

—G. Macara

(i) Temperature

The year 2025 was New Zealand's fourth warmest year on record, based on the mean temperature from Earth Sciences New Zealand's (ESNZ) seven-station series, which began in 1909. The nationwide average temperature for 2025 was 13.51°C, 0.77°C above the 1991–2020 average. Annual mean temperatures were above average (+0.51°C to +1.20°C) for most of the country, with well-above-average temperatures (>+1.20°C) for parts of Northland and the Bay of Plenty. Annual temperatures were near average (±0.50°C of average) for the Mackenzie basin and parts of inland Southland (Fig. 7.66).

The year started on a cool note, and New Zealand's nationwide average temperature in

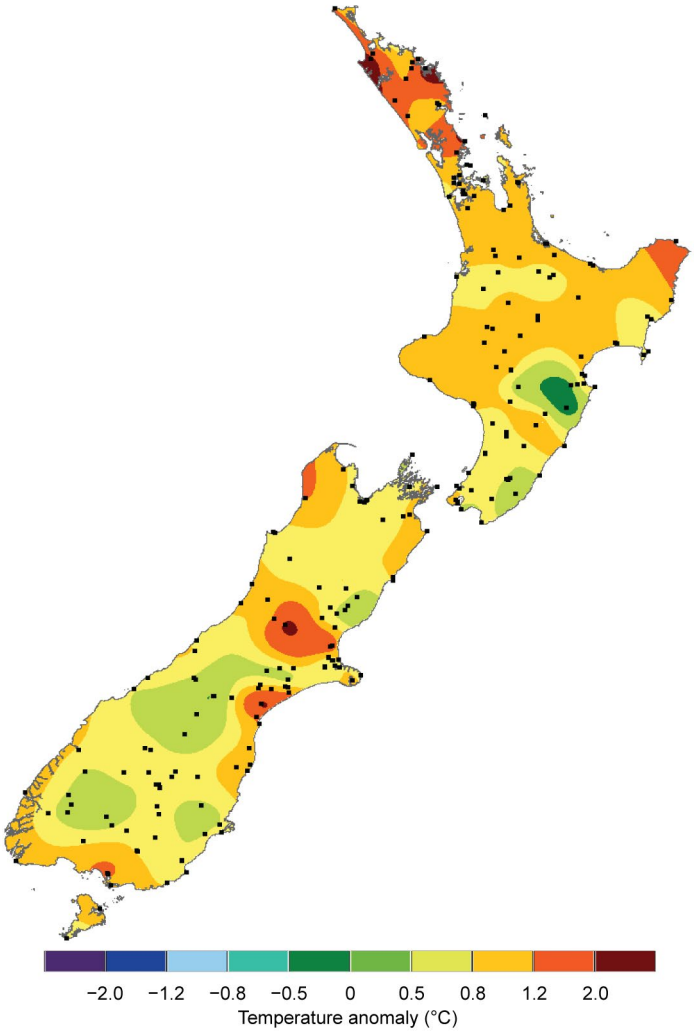

Fig. 7.66. Annual average temperature anomalies (°C; 1991–2020 base period) in New Zealand for 2025. The black dots represent the locations of climate stations used to create both the temperature and rainfall maps.

January was 0.8°C below average. This was the country's coolest January since 2017. Temperatures were mostly above average for the remaining months of the year. Regular northwesterly airflows and unusually warm sea surface temperatures near New Zealand contributed to the country's warmest November on record. The warmth continued through most of December for the North Island, and Napier (Hawke's Bay) recorded New Zealand's highest 2025 temperature: 33.8°C on 8 December. It is uncommon for New Zealand's highest temperature of the year to occur in December; the last time this happened was in 2015. Typically, the highest temperature of the year occurs in January or February. The lowest air temperature of the year was –12.9°C recorded at Mt Cook Airport (Canterbury) on 8 June.

(ii) Precipitation

Annual rainfall totals for 2025 were above normal (120%–149% of normal) for northern parts of Marlborough and Tasman, Nelson, Banks Peninsula, southern parts of the Mackenzie basin, and central parts of the North Island. Annual rainfall was below normal (50%–79%) for Hawke's Bay and much of the Wairarapa, with near-normal annual totals (80%–119% of normal) for most remaining areas of the country (Fig. 7.67). Of the regularly reporting rainfall gauges, the wettest location in 2025 was Cropp River, in the Hokitika River catchment (West Coast, South Island, 975 m above sea level), with an annual rainfall total of 10,951 mm (97% of normal). The driest of the regularly reporting rainfall sites was Alexandra (Central Otago) which recorded 307 mm of rainfall (87% of normal).

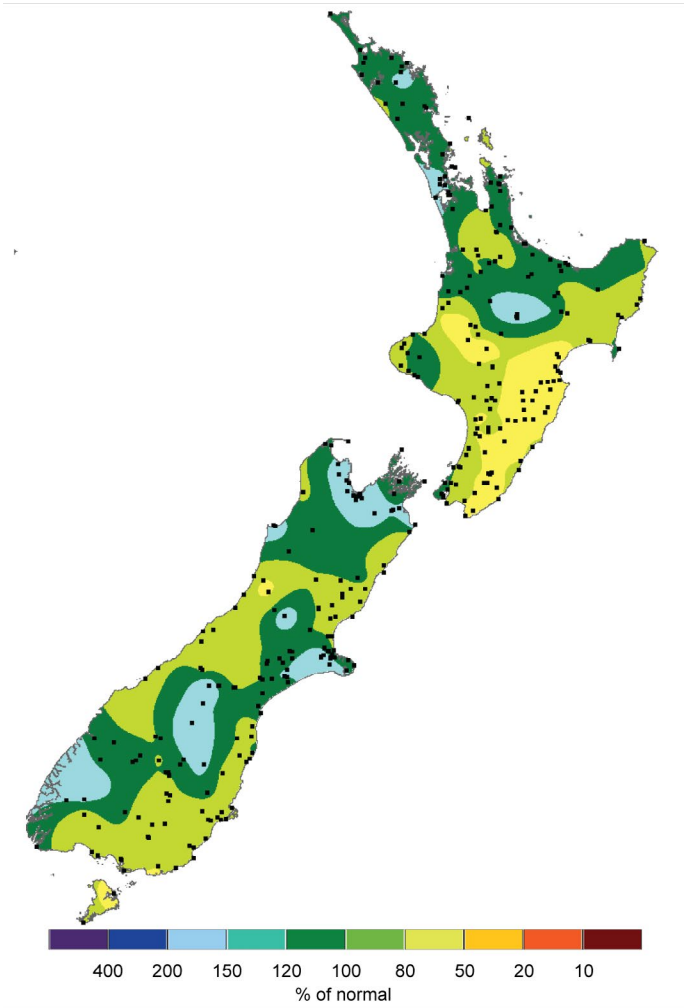

Fig. 7.67. Annual total rainfall anomalies (% of normal; 1991–2020 base period) in New Zealand for 2025.

(iii) Notable events and impacts

From 30 April to 1 May, a state of emergency was declared in Selwyn District, Christchurch, and Banks Peninsula, with significant flooding causing dozens of road closures. Akaroa recorded 223 mm of rain on 30 April, its highest one-day total since records began in 1977 and equivalent to 23% of the town's normal annual rainfall total. The rainfall resulted from a low-pressure system centered east of the South Island.

During 26–27 June, a relatively warm and moist northerly airflow brought heavy rain that caused widespread flooding in Tasman, Nelson, and Marlborough, and a state of emergency was declared for these regions. Several rural communities were evacuated, and approximately 60 northern South Island roads were closed.

On 11 July, persistent heavy rainfall associated with an atmospheric river caused significant flooding in the Tasman region. Dozens of homes suffered damage, and at least four were red-stickered (prohibited access), with 21 yellow-stickered (restricted access). Approximately 50 local roads were closed, and about 13,000 homes across Motueka and Golden Bay lost power. The Nelson-Tasman region was placed under a state of emergency, which remained in place until 17 July.

A significant wind event occurred on 23 October. This was driven by a deep low-pressure system situated south of New Zealand, combined with a large high-pressure system to the northeast of the country. In Southland and Clutha, a state of emergency was declared, which lasted for two weeks. The storm knocked out power to more than 25,000 properties. Invercargill City

Council estimated more than 1000 trees were potentially damaged. Farther north, roofs were damaged, and over 1600 properties were without power due to severe winds in Hanmer Springs.

During 8–10 November, a large wildfire burned approximately 2800 hectares in Tongariro National Park. Thirty-six residents of Whakapapa Village were evacuated, along with hikers and others at lodges and the Hilary Outdoors Centre. All tracks and huts within the Tongariro National Park were closed, as were local highways. During 8–9 December, another fire in the same area burned an additional 322 hectares.

Acknowledgments

Europe

Much of the information in this section is based on national climate reports kindly provided by the National Meteorological and Hydrological Services (NMHSs) of the World Meteorological Organization (WMO) Regional Association (RA) VI region. Specifically, data for Syria were kindly provided by the National Center of Meteorology in Syria. The information has been compiled at the WMO RA VI Regional Climate Centre (RCC) Node on Climate Monitoring, located at Deutscher Wetterdienst (DWD) in Germany. National contributions have been made to the cooperation between NMHSs and the RCC. https://rcccm.dwd.de/DWD-RCCCM/EN/products/reports/monthlyreports_national.html?nn=500112.

Appendix 1: Acronyms

ACORN-SAT	Australian Climate Observations Reference Network–Surface Air Temperature
AGCD	Australian Gridded Climate Data
AHAC	Honduran Civil Aeronautics Agency
AHCCD	Adjusted and Homogenized Canadian Climate Data
AP	accumulated pentad precipitation
AWAP	Australian Water Availability Project
BOM	Bureau of Meteorology
C3S	Copernicus Climate Change Service
CA	Central America
CA-NWS	Central America National Weather Services
CAMS	Climate Anomaly Monitoring System
CANGRD	Canadian Gridded Temperature and Precipitation Anomalies
CaPA	Canadian Precipitation Analysis
CAR	Central African Republic
CariCOF	Caribbean Climate Outlook Forum
CDP	convection diagnosis procedure
CDS	Climate Data Store
CEMADEN	National Center for Natural Disaster Monitoring and Alerts
CHIRPs	Climate Hazards and Infrared Precipitation
CIIFEN	International Center for Research on the El Niño Phenomenon
CMB	Changma-Meiyu-Baiyu
CNE	National Commission for Risk Prevention and Emergency Response
CONRED	National Coordination for Disaster Reduction
CONUS	contiguous United States
COPECO	Permanent Contingency Commission of Honduras
COSPPac	Climate and Oceans Support Program in the Pacific
DMC	Meteorological Directorate of Chile
DMH	Directorate of Meteorology and Hydrology
DRC	Democratic Republic of the Congo
DWD	Deutscher Wetterdienst
ECCC	Environment and Climate Change Canada
EDRMC	Ethiopian Disaster Risk Management Commission
EFFIS	European Forest Fire Information System
EM-DAT	Emergency Events Database
ENSO	El Niño–Southern Oscillation
ERSST	Extended Reconstructed Sea Surface Temperature
GDP	Gross Domestic Product
GHA	Greater Horn of Africa
GHCN	Global Historical Climatology Network
GlobalTemp	NOAA Global Surface Temperature
GPCC	Global Precipitation Climatology Centre
GPCP	Global Precipitation Climatology Project
IDI	Integrated Drought Index
IMHPA	Institute of Meteorology and Hydrology of Panama
IMN	National Meteorological Institute (Costa Rica)
INAMHI	National Meteorological and Hydrological Service of Ecuador
INMET	National Institute of Meteorology (Brazil)
INPE	National Institute for Space Research (Brazil)

INSIVUMEH	National Institute for Seismology, Vulcanology, Meteorology and Hydrology (Guatemala)
INUMET	Uruguayan Institute of Meteorology
IOD	Indian Ocean dipole
ISMR	summer monsoon rainfall
ITCZ	Intertropical Convergence Zone
LTA	long-term average
MCV	mesoscale convective vortex
MJO	Madden–Julian Oscillation
MSLP	mean sea level pressure
MSWEP	Multi-Source Weighted-Ensemble Precipitation
NAM	North American Monsoon
NCAR	National Center for Atmospheric Research
NCEP	National Centers for Environmental Prediction
NDMA	National Disaster Management Agency
NMHS	National Meteorological and Hydrological Services
NMS	National Meteorological Service
NPSH	North Pacific subtropical high
NWS	National Weather Service
OCHA	Office for the Coordination of Humanitarian Affairs
OLR	outgoing longwave radiation
OSCAR	Observing Systems Capability Analysis and Review
PICOF	Pacific Islands Climate Outlook Forum
PNG	Papua New Guinea
RA	Regional Association
RCC	Regional Climate Centre
RCC-CM	Regional Climate Centre Node on Climate Monitoring
ROK	Republic of Korea
SENAMHI	National Meteorology and Hydrology Service of Peru
SINAP-ROC	National Civil Protection System (Panama)
SMN	National Meteorological Service of Argentina
SPC	Storm Prediction Center
SPCZ	South Pacific Convergence Zone
SPI	Standardized Precipitation Index
SST	sea surface temperature
SSTa	sea surface temperature anomaly
SWALIM	Somalia Water and Land Information Management
T	daily mean temperature
T_{abs_min}	absolute minimum temperature
TC	Tropical Cyclone
Tm	five-day average temperature
Tmax	daily maximum temperature
Tmin	daily minimum temperature
TNA	Tropical North Atlantic index
Tnorm	normal temperature
T_{norm_max}	normal maximum temperature
T_{norm_min}	normal minimum temperature
TPR	Texas Public Radio
UN	United Nations
WMO	World Meteorological Organization
WNPSH	western North Pacific subtropical high
WWA	World Weather Attribution

References

Alfaro-Córdoba, M., N. P. Mora-Sandí, H. G. Hidalgo, and E. J. Alfaro, 2024: Central American climate extreme trends: A statistical analysis of CLIMDEX indices. *Intl. J. Climatol.*, **44**, 4115–4126, https://doi.org/10.1002/joc.8571.

Amador, J. A., 1998: A climatic feature of the tropical Americas: The trade wind easterly jet. *Tóp. Meteor. Oceanogr.*, **5**, 91–102.

Amador, J. A., 2008: The intra-Americas seas low-level jet (IALLJ): Overview and future research. *Ann. N. Y. Acad. Sci.*, **1146**, 153–188, https://doi.org/10.1196/annals.1446.012.

Amador, J. A., E. J. Alfaro, H. Hidalgo, and B. Calderon, 2011: Central America and the Caribbean [in "State of the Climate in 2010"]. *Bull. Amer. Meteor. Soc.*, **92** (6), S182–S183, https://doi.org/10.1175/1520-0477-92.6.S1.

Amador, J. A., E. R. Rivera, A. M. Durán-Quesada, G. Mora, F. Sáenz, B. Calderón, and N. Mora, 2016a: The easternmost tropical Pacific. Part I: A climate review. *Rev. Biol. Trop.*, **64** (Suppl. 1), S1–S22, https://doi.org/10.15517/rbt.v64i1.23407.

Amador, J. A., A. M. Durán-Quesada, E. R. Rivera, G. Mora, F. Sáenz, B. Calderón, and N. Mora, 2016b: The easternmost tropical Pacific. Part II: Seasonal and intraseasonal modes of atmospheric variability. *Rev. Biol. Trop.*, **64**, 23–57, https://doi.org/10.15517/rbt.v64i1.23409.

Beck, H. E., E. F. Wood, M. Pan, C. K. Fisher, D. G. Miralles, A. I. J. M. Van Dijk, T. R. McVicar, and R. F. Adler, 2019: MSWEP V2 global 3-hourly 0.1° precipitation: Methodology and quantitative assessment. *Bull. Amer. Meteor. Soc.*, **100**, 473–500, https://doi.org/10.1175/BAMS-D-17-0138.1.

Black, E., 2005: The relationship between Indian Ocean sea-surface temperature and East African rainfall. *Philos. Trans. Roy. Soc.*, **A363**, 43–47, https://doi.org/10.1098/rsta.2004.1474.

Brasil de Fato, 2025: Frente fria derruba temperaturas no Sul e Sudeste; geada, neve e ressaca estão entre os alertas (Cold front sends temperatures plummeting to the South and Southeast; frost, snow, and rough seas are among the warnings). Accessed 30 January 2026, www.brasildefato.com.br/2025/05/29/frente-fria-derruba-temperaturas-no-sul-e-sudeste-geada-neve-e-ressaca-estao-entre-os-alertas.

Brown, J. R., and Coauthors, 2020: South Pacific convergence zone dynamics, variability and impacts in a changing climate. *Nat. Rev. Earth Environ.*, **1**, 530–543, https://doi.org/10.1038/s43017-020-0078-2.

CAL FIRE, 2025: Top 20 most destructive California wildfires. 1 pp., https://34c031f8-c9fd-4018-8c5a-4159cdff6b0d-cdn-endpoint.azureedge.net/-/media/calfire-website/our-impact/fire-statistics/top-20-destructive-ca-wildfires.pdf.

Campbell, J. D., M. A. Taylor, and T. S. Stephenson, 2025: What we learn about Hurricane Melissa from two automatic weather stations at The UWI, Mona. Policy Brief 9, University of the West Indies, 2 pp., https://csgm-uwi.site/policy_briefs/Brief_9_UWI_Stations_and_Hurricane_Melissa_Measurements_Final.pdf.

CatIQ, 2025: CAD 490M—CatIQ discloses six-month industry loss estimate for the Ontario and Quebec ice storm of March 2025. Accessed 30 September 2025, https://public.catiq.com/2025/10/01/cad-490m-catiq-discloses-six-month-industry-loss-estimate-for-the-ontario-and-quebec-ice-storm-of-march-2025/.

CatIQ, 2026: Canadian insured losses from catastrophic events total CAD 2.4 B in 2025; Societal losses total 3.4 B. Accessed 20 January 2026, https://public.catiq.com/2026/01/20/canadian-insured-losses-from-catastrophic-events-total-cad-2-4-b-in-2025-societal-losses-total-3-4-b/.

CIIFEN, 2025: Boletín de Sequías. CIIFEN, accessed 7 January 2026, https://ciifen.org/boletin-de-sequias/.

Clarke, B., and Coauthors, 2025: Climate change enhanced intensity of Hurricane Melissa, testing limits of adaptation in Jamaica and eastern Cuba. WWA Scientific Rep. 76, World Weather Attribution, 67 pp., https://doi.org/10.25560/125306.

Cornes, R., G. van der Schrier, E. J. M. van den Besselaar, and P. D. Jones, 2018: An ensemble version of the E-OBS temperature and precipitation data sets. *J. Geophys. Res. Atmos.*, **123**, 9391–9409, https://doi.org/10.1029/2017JD028200.

Cunha, A. P. M. A., and Coauthors, 2019: Extreme drought events over Brazil from 2011 to 2019. *Atmosphere*, **10**, 642, https://doi.org/10.3390/atmos10110642.

Doi, T., S. K. Behera, and T. Yamagata, 2022: On the predictability of the extreme drought in East Africa during the short rains season. *Geophys. Res. Lett.*, **49**, e2022GL100905, https://doi.org/10.1029/2022GL100905.

Durán-Quesada, A. M., R. Sorí, P. Ordoñez, and L. Gimeno, 2020: Climate perspectives in the intra–Americas seas. *Atmosphere*, **11**, 959, https://doi.org/10.3390/atmos11090959.

Ebi, K. L., and Coauthors, 2021: Hot weather and heat extremes: Health risks. *Lancet*, **398**, 698–708, https://doi.org/10.1016/S0140-6736(21)01208-3.

ECCC, 2025: Canada's top 10 weather stories of 2025. Accessed 11 February 2026, https://www.canada.ca/en/environment-climate-change/services/top-ten-weather-stories/2025.html.

Enfield, D., and E. Alfaro, 1999: The dependence of Caribbean rainfall on the interaction of the tropical Atlantic and Pacific Oceans. *J. Climate*, **12**, 2093–2103, https://doi.org/10.1175/1520-0442(1999)012<2093:TDOCRO>2.0.CO;2.

Evans, A., D. Jones, R. Smalley, and S. Lellyett, 2020: An enhanced gridded rainfall analysis scheme for Australia. Bureau of Meteorology Research Rep. 41, 35 pp., https://nla.gov.au/nla.obj-2786078795/view.

Funk, C., and Coauthors, 2015: The climate hazards infrared precipitation with stations-a new environmental record for monitoring extremes. *Sci. Data*, **2**, 150066, https://doi.org/10.1038/sdata.2015.66.

Funk, C., and Coauthors, 2019: A high-resolution 1983–2016 T_{max} climate data record based on infrared temperatures and stations by the climate hazard center. *J. Climate*, **32**, 5639–5658, https://doi.org/10.1175/JCLI-D-18-0698.1.

G1, 2025: Paraná confirma sétima morte após passagem de tornados; 23 feridos estão internados (Paraná confirms seventh death after tornadoes pass through; 23 injured are hospitalized). G1, accessed 26 January 2026, https://g1.globo.com/pr/campos-gerais-sul/noticia/2025/11/11/setima-morte-tornados-parana.ghtml.

Hand, W. H., and G. Cappelluti, 2011: A global hail climatology using the UK Met Office convection diagnosis procedure (CDP) and model analyses. *Meteor. Appl.*, **18**, 446–458, https://doi.org/10.1002/met.236.

Hersbach, H., and Coauthors, 2023: ERA5 monthly averaged data at single levels from 1940 to present. Copernicus Climate Change Service (C3S) Climate Data Store (CDS), accessed 16 January 2026, https://doi.org/10.24381/cds.f17050d7.

Hidalgo, H., E. Alfaro, J. Amador, and A. Bastidas, 2019: Precursors of quasi-decadal dry-spells in the central America dry corridor. *Climate Dyn.*, **53**, 1307–1322, https://doi.org/10.1007/s00382-019-04638-y.

Hoell, A., A. E. Gaughan, T. Magadzire, and L. Harrison, 2021: The modulation of daily southern Africa precipitation by El Niño–Southern Oscillation across the summertime wet season. *J. Climate*, **34**, 1115–1134, https://doi.org/10.1175/JCLI-D-20-0379.1.

Huang, B., and Coauthors, 2017: NOAA Extended Reconstructed Sea Surface Temperature (ERSST), version 5. NOAA National Centers for Environmental Information, accessed 9 February 2026, https://doi.org/10.7289/V5T72FNM.

INMET, 2025: Verão 2024/2025 foi um dos mais quentes da história no Brasil desde 1961 (Summer 2024/2025 was one of the hottest in Brazilian history since 1961). Secretariat of Social Communication, accessed 10 January 2026, https://www.gov.br/secom/pt-br/assuntos/noticias/2025/03/verao-2024-2025-foi-um-dos-mais-quentes-da-historia-no-brasil-desde-1961.

Jones, D. A., W. Wang, and R. Fawcett, 2009: High-quality spatial climate data-sets for Australia. *Aust. Meteor. Oceanogr. J.*, **58**, 233–248, https://doi.org/10.22499/2.5804.003.

Juria, N., 2025: Micronesia climate impacts. 16th Pacific Islands Climate Outlook Forum, Pacific Regional Environment Programme and WMO, Online, 34 pp., https://www.pacificmet.net/sites/default/files/inline-files/documents/PICOF-16%20_Session%202.4_Micronesia%20climate%20impacts.pdf.

Klotzbach, P. J., M. M. Bell, and L. G. Silvers, 2025: Summary of 2025 Atlantic tropical cyclone activity and verification of authors' seasonal and two-week forecasts. Colorado State University Dept. of Atmospheric Science, 54 pp. https://tropical.colostate.edu/Forecast/2025-11.pdf.

Magaña, V., J. A. Amador, and S. Medina, 1999: The midsummer drought over México and central America. *J. Climate*, **12**, 1577–1588, https://doi.org/10.1175/1520-0442(1999)012<1577:TMDOMA>2.0.CO;2.

Marengo, J. A., and Coauthors, 2025: Climatological patterns of heatwaves during winter and spring 2023 and trends for the period 1979–2023 in central South America. *Front. Climate*, **7**, 1529082, https://doi.org/10.3389/fclim.2025.1529082.

Marengo, J. A., and Coauthors, 2026a: Characterisation of the exceptional heatwave conditions observed in Brazil during the record-hot years of 2024 and 2025. *Int. J. Climatol.*, **46**, e70219, https://doi.org/10.1002/joc.70219.

McKee, T. B., Doesken, N. J., & Kleist, J. (1993). The relationship of drought frequency and duration to time scales. Proceedings of the Eighth Conference on Applied Climatology, American Meteorological Society, 179–184. NOAA, 2026: Preliminary severe weather report database. NOAA/NWS/SPC, accessed 10 February 2026, https://www.spc.noaa.gov/climo/summary/.

Nicholson, S. E., A. H. Fink, and C. Funk, 2018: Rainfall over the African continent from the 19th through the 21st century. *Global Planet. Change*, **165**, 114–127, https://doi.org/10.1016/j.gloplacha.2017.12.014.

NOAA Office of Water Prediction, 2025: Hill Country Texas hydrologic summary (July 2025). National Oceanic and Atmospheric Administration, 2 pp., https://www.weather.gov/media/owp/oh/hdsc/docs/202507_HillCountryTX.pdf.

NOAA Office of Water Prediction, 2026:Gauge KRRT2. National Oceanic and Atmospheric Administration, accessed 19 March 2026, https://water.noaa.gov/gauges/KRRT2.

NRCan, 2025: National wildland fire situation report. Accessed 19 November 2025, https://cwfis.cfs.nrcan.gc.ca/report/archives?year=2025&month=11&day=19&process=Submit.

OCHA, 2025: Latin America & the Caribbean weekly situation update as of 28 February 2025. OCHA, accessed 9 January 2026, https://www.unocha.org/publications/report/haiti/latin-america-caribbean-weekly-situation-update-28-february-2025.

Pan American Health Organization, 2025: Public health situation analysis of Hurricane Melissa in Jamaica, Cuba, Haiti, the Dominican Republic, the Bahamas and Bermuda. PAHO, 58 pp., https://www.paho.org/sites/default/files/2025-11/phsa-1-hurricane-melissa-2025-v2.pdf.

Pook, M., S. Lisson, J. Risbey, C. C. Ummenhofer, P. McIntosh, and M. Rebbeck, 2009: The autumn break for cropping in southeast Australia: Trends, synoptic influences and impacts on wheat yield. *Intl. J. Climatol.*, **29**, 2012–2026, https://doi.org/10.1002/joc.1833.

ReliefWeb, 2025: Venezuela update: Flash flood situation Report #1, July 3, 2025. ReliefWeb, 26 pp., https://reliefweb.int/report/venezuela-bolivarian-republic/venezuela-update-flash-flood-situation-report-1-july-3-2025.

Schneider, U., P. Finger, E. Rustemeier, M. Ziese, and S. Hänsel, 2022: Global Precipitation Analysis Products of the GPCC. Deutscher Wetterdienst (DWD), 17 pp., https://opendata.dwd.de/climate_environment/GPCC/PDF/GPCC_intro_products_lastversion.pdf.

Storm Prediction Center, 2026a: F5 and EF5 tornadoes of the United States. National Oceanic and Atmospheric Administration, accessed 20 March 2026, https://www.spc.noaa.gov/faq/tornado/f5torns.html.

Storm Prediction Center, 2026b: Latest U.S. tornado statistics. National Oceanic and Atmospheric Administration, accessed 20 March 2026, https://www.spc.noaa.gov/climo/summary/.

Tanaki-New, R., 2025: Polynesia Islands climate impacts. 17th Pacific Islands Climate Outlook Forum, Pacific Regional Environment Programme and WMO, Online, 10 pp., https://www.sprep.org/sites/default/files/PICOF-17/PICOF%2017_Presentation_Session_2.iv%20Polynesia.pdf.

Texas Public Radio, 2025: Two FEMA disaster outreach centers have closed; Kerr County commissioners will hold a town hall on Oct. 8. Accessed 10 February 2026, https://www.tpr.org/live-updates/kerrville-flooding-texas-hill-country.

Trewin, B., 2018: The Australian Climate Observations Reference Network–Surface Air Temperature (ACORN-SAT) version 2. Bureau of Meteorology Research Rep. 32, 67 pp., https://www.bom.gov.au/climate/change/acorn-sat/documents/BRR-032.pdf.

U.S. Geological Survey, 2026: Monitoring location 08166200. Accessed 19 March 2026, https://waterdata.usgs.gov/monitoring-location/USGS-08166200/.

UOL, 2025: São Paulo registra 37,2ºC e bate novo recorde de calor em 64 anos (São Paulo registers 37.2ºC and breaks a new heat record in 64 years). UOL, accessed 7 January 2026, https://noticias.uol.com.br/cotidiano/ultimas-noticias/2025/12/28/sao-paulo-registra-372c-e-bate-de-novo-recorde-de-calor-em-64-anos.htm.

Vincent, E. M., M. Lengaigne, C. E. Menkes, N. C. Jourdain, P. Marchesiello, and G. Madec, 2011: Interannual variability of the South Pacific convergence zone and implications for tropical cyclone genesis. *Climate Dyn.*, **36**, 1881–1896, https://doi.org/10.1007/s00382-009-0716-3.

WMO, 2025: State of Climate in Latin America and the Caribbean, 2024. WMO, 26 pp.

WMO, 2026: Significant weather and climate events. WMO State of the Climate Rep. Suppl., 21 pp., https://wmo.int/sites/default/files/2026-03/State_of_the_Global_Climate_2025_Extreme_Supplement.pdf.